

---

***23rd International  
Conference on Infrared  
and Millimeter Waves***

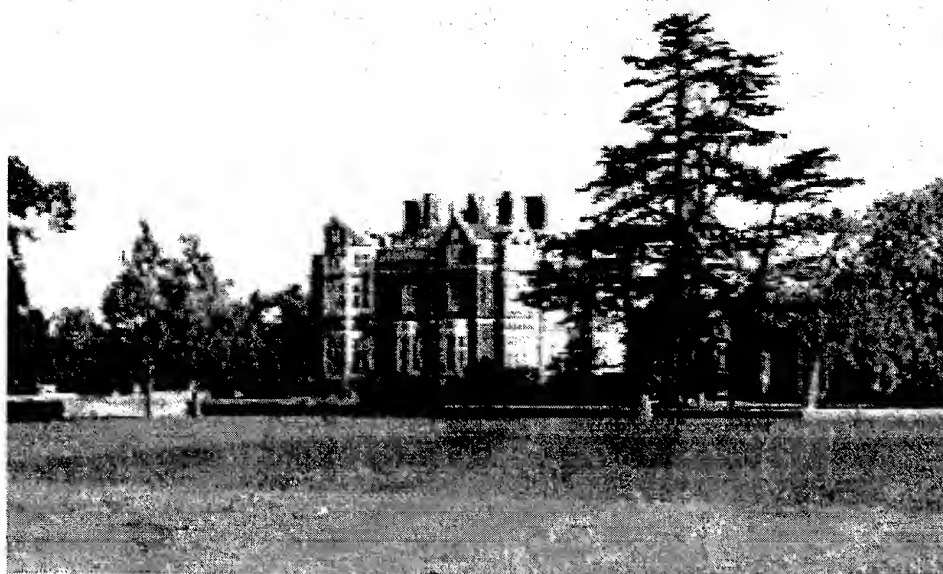
---

**Terence J. Parker  
Stephen R. P. Smith**  
*Editors*

**7-11 September 1998  
University of Essex  
Colchester, Essex  
United Kingdom**

DISTRIBUTION STATEMENT A

Approved for public release;  
Distribution Unlimited



REPORT DOCUMENTATION PAGE			Form Approved OMB No. 0704-0188	
Public reporting burden for this collection of information is estimated to average 1 hour per response, including the time for reviewing instructions, searching existing data sources, gathering and maintaining the data needed, and completing and reviewing the collection of information. Send comments regarding this burden estimate or any other aspect of this collection of information, including suggestions for reducing this burden, to Washington Headquarters Services, Directorate for Information Operations and Reports, 1215 Jefferson Davis Highway, Suite 1204, Arlington, VA 22202-4302, and to the Office of Management and Budget, Paperwork Reduction Project (0704-0188), Washington, DC 20503.				
1. AGENCY USE ONLY (Leave blank)		2. REPORT DATE September 1998		3. REPORT TYPE AND DATES COVERED Conference Digest 7 - 11 September 1998
4. TITLE AND SUBTITLE 23rd International Conference on Infrared and Millimeter Waves			5. FUNDING NUMBERS N00014-98-1-1078	
6. AUTHOR(S) Editors: Terence J. Parker, Stephen R. P. Smith				
7. PERFORMING ORGANIZATION NAME(S) AND ADDRESS(ES) Terence J. Parker Department of Physics University of Essex Colchester CO4 3SQ United Kingdom			8. PERFORMING ORGANIZATION REPORT NUMBER	
9. SPONSORING/MONITORING AGENCY NAME(S) AND ADDRESS(ES) Technical Director Office of Naval Research International Field Office Europe PSC 802 Box 39 FPO AE 09499-0700			10. SPONSORING/MONITORING AGENCY REPORT NUMBER	
11. SUPPLEMENTARY NOTES				
12a. DISTRIBUTION AVAILABILITY STATEMENT Approved for public release, distribution is unlimited			12b. DISTRIBUTION CODE	
13. ABSTRACT (Maximum 200 words) Compilation of abstracts for the conference entitled "23rd International Conference on Infrared and Millimeter Waves" held 7 - 11 September 1998 at the University of Essex, Colchester, United Kingdom				
14. SUBJECT TERMS Key Words: millimeter wave, spectroscopy, terahertz, cyclotron, gyrotron, gyroklystron, lasers, free electron laser, schottky diodes			15. NUMBER OF PAGES	
			16. PRICE CODE	
17. SECURITY CLASSIFICATION OF REPORT	18. SECURITY CLASSIFICATION OF THIS PAGE	19. SECURITY CLASSIFICATION OF ABSTRACT	20. LIMITATION OF ABSTRACT	

---

***23rd International  
Conference on Infrared  
and Millimeter Waves***

---

**Terence J. Parker  
Stephen R. P. Smith**  
*Editors*

**7-11 September 1998  
University of Essex  
Colchester, Essex  
United Kingdom**

19981030 050



The papers appearing herein comprise the proceedings of the meeting of the 23rd International Conference on Infrared and Millimeter Waves. The Programme Committee has published these proceedings on behalf of the conference organisers and sponsors. The contents of this volume have been determined by the organisers and editors, and reflect the authors' opinions, published as submitted. Their inclusion in this publication does not necessarily constitute endorsement by the publisher (The Programme Committee).

ISBN 0 9533839 0 3

Published by:

The Programme Committee  
23rd International Conference on Infrared and Millimeter Waves  
University of Essex  
Colchester CO4 3SQ, UK  
Telephone: 01206 872 827  
Fax: 01206 873 598  
e-mail: [partj@essex.ac.uk](mailto:partj@essex.ac.uk)

Additional copies of this Digest may be obtained from the University of Essex.  
For further information on price and availability please contact:

Terence J Parker  
Department of Physics  
University of Essex  
Colchester  
CO4 3SQ, UK

Tel: +44 (0)1206 872 827  
Fax: +44 (0)1206 873 598  
e-mail: [partj@essex.ac.uk](mailto:partj@essex.ac.uk)

Printed in the United Kingdom by Hobs Reprographics Ltd, Colchester



# 23rd International Conference on Infrared and Millimeter Waves

7-11 September 1998

## FINAL PROGRAM

Timetable	Symposium on Gyrotrons and similar devices	Symposium on Terahertz Technology and Applications	Symposium on Spectroscopic Techniques & Applications
Mon AM	OPENING CEREMONY, PRIZE GIVING & PLENARY LECTURE 1: K Mizuno, Development of Array Devices for the Millimeter and Submillimeter Wave Region.		
	M1: HIGH POWER DEVICES 1	M2: SOURCES 1	M3: SEMICONDUCTORS
Mon PM	M4: THEORY & EXPERIMENTS	M5: DETECTION 1	M6: SOURCES 3
	Poster session		
Tues AM	PLENARY LECTURE 2: M von Ortenberg, High Field Magneto-Spectroscopy in Condensed Matter Physics		
	Tu1: HIGH POWER TECHNIQUES	Tu2: SOURCES 2	Tu3: MAGNETIC MATERIALS
Tues PM	Tu4: HIGH POWER DEVICES 2	Tu5: QUASI-OPTICAL NETWORKS & COMPONENTS	Tu6: DETECTION 2
Wed AM	PLENARY LECTURE 3: K Wynne, Ultrafast Terahertz Pulses: A Booming Technology.		
	W1: HIGH POWER COMPONENTS & WINDOWS	W2: BEAMS & ANTENNAS	W3: DIELECTRIC MATERIALS
Thurs AM	PLENARY LECTURE 4: C M Mann, Terahertz Technology: A new era for waveguide?		
	Th1: HIGH POWER SYSTEMS & DEVICES	Th2: DIAGNOSTIC SYSTEMS	Th3: MOLECULAR MATERIALS
Thurs PM	Th4: OTHER DEVICES	Th5: SOURCES 4	Th6: SPECTRO-METRIC SYSTEMS
Fri AM	PLENARY LECTURE 5: M Makowski, Technology for Electron Cyclotron Heating and Current Drive in ITER.		
	F1: HIGH POWER DEVICES 3	F2: MATERIALS MEASUREMENT AND PROCESSING SYSTEMS	

The opening ceremony on Monday morning will begin at 0815 hours - see below.

All other morning sessions begin at 0830 hours. Afternoon sessions begin at 1400 hrs.

A poster session will be held on Monday afternoon from 1700 - 1830 hours.

(Authors of poster papers will be able to put up their posters all day on Monday)

On Monday morning there will be an opening ceremony beginning at 0815 hours, followed by the presentation of the Kenneth J Button Prize to Professor Koji Mizuno. Professor Mizuno will then deliver his plenary lecture beginning at 0830. On the other four days the conference will begin with the plenary lectures at 0830 hours.

### Time allotted for oral presentations:

Plenary Lectures: 1 hour: 50 mins for presentation and 10 mins for questions.  
 Invited Keynote papers: 30 mins: 25 mins for presentation and 5 mins for questions.  
 Contributed papers: 20 mins: 16 mins for presentation and 4 mins for questions.  
 Speakers are requested to comply with these time limits.

## **CONFERENCE ORGANISATION:**

General Chairman: Kenneth J Button

Conference Chairman: Terence J Parker

Programme Chairman: James R Birch

Technical Exhibit: Maurice F Kimmitt

Digest Editors: Terence J Parker and Stephen R P Smith

Proceedings (Journal) Editor: Kenneth J Button

## **LOCAL ORGANISING COMMITTEE:**

T J Parker (Essex) (Chairman)

J R Birch (JB Research)

M F Kimmitt (Essex)

S R P Smith (Essex)

## **PROGRAMME COMMITTEE:**

J R Birch (JB Research) (Chairman)

D V Bartlett (JET)

J M Chamberlain (Nottingham)

P R Foster (Microwave & Antenna Systems)

M F Kimmitt (Essex)

C M Mann (Rutherford Appleton Laboratory)

D H Martin (QMW)

T J Parker (Essex)

A R Phelps (Strathclyde)

K Wynne (Strathclyde)

## **PROCEEDINGS EDITOR**

Kenneth J Button

## **INTERNATIONAL ADVISORY COMMITTEE**

G F Brand	Australia	M I Petelin	Russia
B Carli	Italy	P L Richards	USA
T V George	USA	C R Pidgeon	UK
E Gornik	Austria	K Sakai	Japan
I Itoh	USA	S C Shen	China
R H Jackson	USA	Liu Shenggang	China
T O Klaassen	NL	R J Temkin	USA
J Leotin	France	M Thumm	Germany
N C Luhmann	USA	A A Vertiy	Ukraine
K Mizuno	Japan	J C Wiltse	USA
M von Ortenberg	Germany		

## FOREWORD

The Twenty Third International Conference on Infrared and Millimeter Waves is held from September 7th to September 11th, 1998, at the University of Essex in Colchester, UK. The scope of the Conference covers progress in all areas of infrared and millimeter wave science and technology, and the scientific programme has been organised into three distinct symposia which reflect current trends in the field:

Symposium on Gyrotrons and Similar Devices  
Symposium on Terahertz Technology and Applications  
Symposium on Spectroscopic Techniques and Applications.

About 230 papers will be presented by delegates from 25 countries and this demonstrates once again the vitality of work in this field.

The Local Organising Committee and the Programme Committee would like to take this opportunity to thank all authors for their high quality work which has contributed to the success of this Conference.

The organisation of the Conference would not have been possible without the generous sponsorship of the following organisations:

The University of Essex  
The Association of British Spectroscopists  
QMC Instruments Ltd  
The Institute of Physics

The generous support of commercial organisations and other institutions which have provided financial support is also gratefully acknowledged, and the names of these organisations are listed elsewhere in the Digest.

We also wish to thank the University of Essex for providing the infrastructure and facilities which were essential for organising this conference.

Terence J Parker  
Conference Chairman



## **TECHNICAL EXHIBIT**

The Technical Exhibit will be held in the Lecture Theatre Block, close to the lecture rooms. It will last for two full days, (Tuesday September 8th and Wednesday September 9th).

We wish to express our thanks to the companies and organisations listed below, who have expressed an interest in taking part or are providing technical literature for the Delegates' Kit.

Maurice Kimmitt  
Exhibit Manager

A B Millimetre, Paris, France

Crystran Ltd, Poole, UK

Edinburgh Instruments Ltd, Edinburgh, UK

EG&G Instruments, Wokingham, UK

ELVA-1 Ltd, St Petersburg, Russia

Graseby-Specac Ltd, Orpington, UK

Hamamatsu Photonics UK Ltd, Enfield, UK

L.O.T. Oriel Ltd, Leatherhead, UK

QMC Instruments Ltd, London, UK

## CONFERENCE PUBLICATIONS

### Conference Digest

The Conference Digest for the Twenty Third International Conference again attests to the strength of the field of infrared and millimeter waves.

The Digest is a convenient, timely reference in the field of infrared and millimeter waves. Additional copies of the Digest may be purchased from the University of Essex at the address given on the back of the title page. Papers in the Digest may be referred to in journal articles by citing:

Proc. 23rd International Conference on Infrared and Millimeter Waves, Colchester, UK, September 7-11, 1998, Eds. T J Parker and S R P Smith, ISBN 0 9533839 0 3.

### The Proceedings

Conference delegates are encouraged to submit a full length manuscript for publication in the monthly journal "International Journal of Infrared and Millimeter Waves". Papers published in this journal by conference delegates constitute the proceedings of the conference.

Authors must prepare final manuscripts on camera-ready templates (available from Kenneth J Button) to save time and expense. There is no page charge and there is no limit on the length of your manuscript. Your manuscript will be published in about eight weeks (no deadline). Manuscripts may be sent to K J Button at the address below at any time, before or after the Conference. Those who cannot attend the Conference this year are urged to send their manuscript for publication in the Proceedings anyway. We may miss seeing you, but we do not want to miss the chance of learning about your work.

Please send your manuscripts to:

Kenneth J Button  
Editor, *International Journal of Infrared and Millimeter Waves*  
2095 North A1A Highway  
Indialantic  
Florida 32903-2514

Telephone and Fax: (407) 777 7293

## **24th International Conference on Infrared and Millimeter Waves**

**September 6-10, 1999**

**Monterey, California**

The twenty fourth conference in this series will be held in Monterey, California. Accommodations will be at the Double Tree Hotel overlooking the harbor. Monterey is located on the California coast, between Los Angeles and San Francisco. Monterey offers many attractions, including the famous Cannery Row, Fisherman's Wharf, Wine Country and many more.

The conference will cover progress in all areas of infrared and millimeter waves, including the following topics, with special emphasis on new fields of research. Sources: lasers, free electron lasers, gyrotrons, synchrotrons, frequency mixing, calibration and standards. Detectors: receivers, mixers, amplifiers, thermal and photon detectors. Schottky diodes, Josephson and SIS devices, imaging arrays, FET amplifiers. Guided propagation and components: waveguides and other structures, Gaussian beams, integrated devices, optical fibres. Spectroscopic techniques: interferometric, laser and heterodyne spectroscopy. Spectroscopy of solids, liquids and gases. Astronomy and atmospheric physics: techniques, results and interpretation. Applications in biology and medicine. Plasma interactions and diagnostics. Technical and industrial applications: imaging, remote sensing, non-destructive testing.

General Chairman: Kenneth J Button, 2095 North A1A Highway, Indialantic, Florida 32902-2514, USA

Conference Chairman: Neville Luhmann Jr., Department of Applied Science, University of California Davis, Davis CA, USA

Further information may be obtained from Jane Keene. Tel: 925-422-2831, Fax: 925-422-6690, e-mail: keene 3@llnl.gov

# **The 1998 Kenneth J Button Prize**

**is awarded to**

**Professor Koji Mizuno**

**of Tohoku University, Sendai, Japan**

for seminal contributions to the development of techniques and technology in the field of infrared and millimeter waves. Most especially for his demonstrations and analyses of the quasi-optical coupling of millimeter and submillimeter waves with active devices, as in his pioneering work on electron-beam sources of tunable millimeter-waves, on antenna-coupled sources and detectors, on cavity-coupled source-arrays, on imaging detector arrays, and on near-field microscopy.

---

The Kenneth J Button Prize is awarded annually at the International Conference on Infrared and Millimeter Waves, in recognition of outstanding contributions to the Science of the Electromagnetic Spectrum.

The Prize is named after the founder of the Conference. It consists of a Medal and a cash award of £1500.

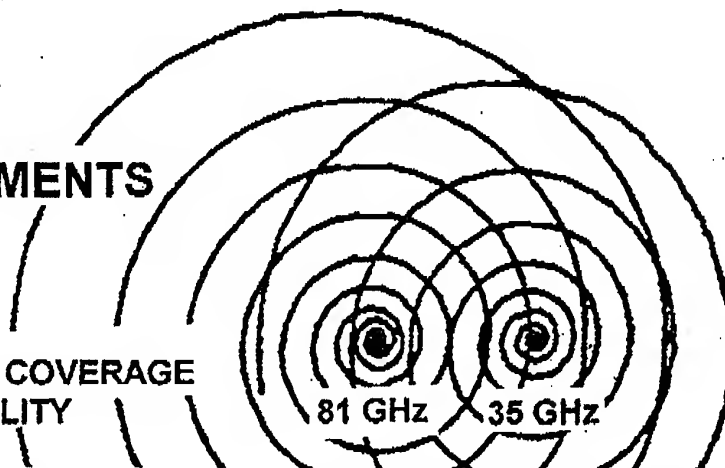
At each meeting of the Conference, a committee of the Conference's International Advisory Panel elects, from the list of nominations, the prize winner who will receive the award at the next following meeting of the Conference. Any scientist active in the field of the Conference may make a nomination for the Prize at any time by completing a nomination form which can be obtained (by mail, Fax or e-mail) from

Dr Alwyn Jones, The Institute of Physics, 76 Portland Place, London W1N 4AA, UK. Fax No. +44(0) 171 470 4848, e-mail: [physics@iop.org](mailto:physics@iop.org)

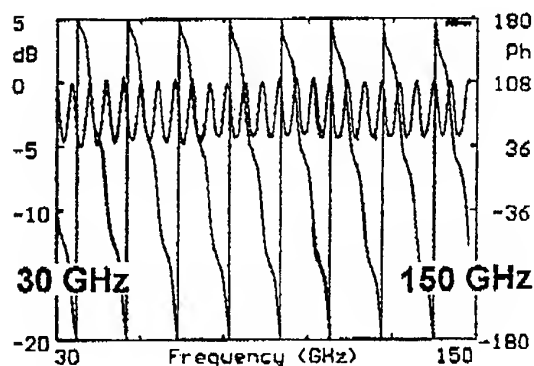


# 8-1000 GHz VECTOR MEASUREMENTS ON YOUR TABLE

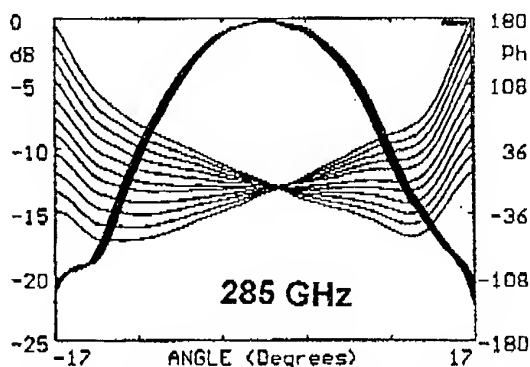
**MVNA 8-350  
CONTINUOUS FREQUENCY COVERAGE  
DUAL-FREQUENCY CAPABILITY**



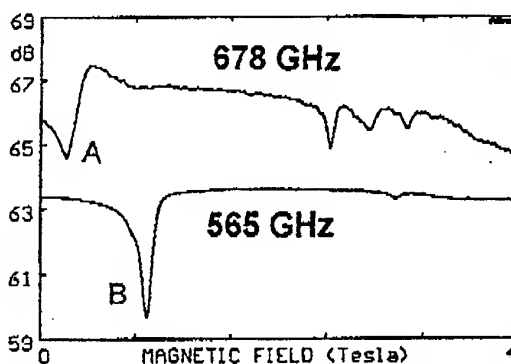
More than thirty Millimeter Vector Network Analyzers MVNA 8-350 have been produced and installed in over ten different countries since 1989. They are used by industry and universities in electrical engineering departments. Physics departments also, working for instance on plasma physics, radioastronomy, atomic physics, condensed matter physics, have found MVNA 8-350 invaluable. Various applications include measurements on waveguide and quasi-optical devices, radar modeling and propagation studies, active and passive components, antennas, dielectric, superconductive or magnetic materials, spectroscopy of atoms, molecules or radicals. MVNA 8-350 has proved to be reliable and in the past ten years no major intervention has ever been necessary on the part of the manufacturer. The figure above shows a polar plot of helicon waves observed by 35 and 81 GHz transmission across InSb at room temperature, submitted to a 0-17T magnetic field sweep (University of Nijmegen, The Netherlands). See other examples below.



Amplitude (oscillatory line, given in dB) and phase (decreasing line, given in degrees) observed by transmission across a 10mm thick slab of sapphire where the measured permittivity is  $\epsilon' = 9.40$  and the loss  $\tan \delta$  is below 0.001.



H-Plane antenna pattern of a conical horn at 285 GHz, where the horn is laterally moved by 0.2mm steps for the phase center determination, at which the observed phase variation becomes stationary.



Magnetic resonances as dips in transmission across a FeI<sub>2</sub> sample at 5K (Riken Institute, Japan). Top line (678 GHz) and bottom line (565 GHz) are recorded simultaneously, during the same magnetic field sweep (dual-frequency MVNA configuration). The phase acquisition, not shown, resolves lineshape problems. Its variations indicate that the resonances A (at top left) and B (at bottom left) belong to upwards and downwards branches, respectively, in the frequency/field diagram. Line B appears to be a single Lorentzian. Line A (quality factor close to unity) is a double Lorentzian, with a splitting of one third of the linewidth.

E-mail: [abmm001@ibm.net](mailto:abmm001@ibm.net)  
[www.abmillimetre.com](http://www.abmillimetre.com)

**ABmm**

AB MILLIMETRE  
52 RUE LHOMOND  
75005 PARIS FRANCE  
TEL: 33 1 4707 7100  
FAX: 33 1 4707 7071



---

## PLENARY LECTURES

---

**PL.1 DEVELOPMENT OF ARRAY DEVICES FOR THE MILLIMETER AND SUBMILLIMETER WAVE REGION.**

K Mizuno.

Tohoku University, Sendai, Japan.

**PL.2 HIGH FIELD MAGNETO-SPECTROSCOPY IN CONDENSED MATTER PHYSICS.**

M von Ortenberg.

Humboldt University of Berlin, Germany.

**PL.3 ULTRAFAST TERAHERTZ PULSES: A BOOMING TECHNOLOGY.**

K Wynne.

Femtosecond Research Centre, University of Strathclyde, Glasgow, UK.

**PL.4 TERAHERTZ TECHNOLOGY, A NEW ERA FOR WAVEGUIDE?**

C M Mann.

Rutherford Appleton Laboratory, Didcot, Oxon, UK

**PL.5 TECHNOLOGY FOR ELECTRON CYCLOTRON HEATING AND CURRENT DRIVE IN ITER.**

M Makowski.

ITER Garching Joint Work Site, Garching, Germany.

**M1.1 FIRST GENERATION OF MM-WAVES IN THE DUTCH FREE-ELECTRON MASER.**

*(Invited Keynote)*

A G A Verhoeven, W A Bongers, V L Bratman, M Caplan, G G Denisov, C A J van der Geer, P Manintveld, A J Poelman, J Plomp, A V Savilov, P H M Smeets and W H Urbanus

FOM-Instituut Rijnhuizen, PO Box 1207, 3430 Be Nieuwegein, The Netherlands.

**M1.2 LONG PULSE OPERATION OF 170 GHz/1 MW GYROTRON FOR ITER. *(Invited Keynote)***

V E Myasnikov, S V Usachev, M V Agapova, V V Alikaev, G G Denisov, A Sh. Fix, V A Flyagin, A Ph. Gnedenkov, V I Ilyin, A N Kuftin, L G Popov and V E Zapevalov  
Institute of Applied Physics, Russian Academy of Sciences, 46 Ulyanov st, 603600 Nizhny Novgorod, Russia.

**M1.3 EXPERIMENTAL DEMONSTRATION OF W-BAND GYRO-AMPLIFIERS WITH ENHANCED PERFORMANCE.**

M Blank, B G Danly & B Levush.

Code 6843, Naval Research Laboratory, Washington, DC 20375, USA.

**M1.4 EXPERIMENTAL 35 GHz MULTI-CAVITY GYROKLYSTRON AMPLIFIERS.**

M Garven, J P Calame, J J Choi, B G Danly, K T Nguyen & F Wood.

Code 6843, Naval Research Laboratory, Washington DC 20375 5320, USA.

**M1.5 AN ULTRA HIGH GAIN GYROTRON TRAVELING WAVE AMPLIFIER.**

K R Chu, H Y Chen, C L Hung, T H Chang, L R Barnett, S H Chen and T T Yang.  
Dept of Physics, National Tsing Hua University, Hsinchu, Taiwan, ROC.

**M1.6 DEVELOPMENT OF A W-BAND GYROKLYSTRON FOR RADAR APPLICATIONS.**

B G Danly, M Blank, J Calame, B Levush, K Nguyen, D Pershing, J Petillo, T A Hargreaves, R B True, A J Theiss, G R Good, K Felch, T S Chu, H Jory, P Borchard, B G James, W G Lawson & T M Antonsen, Jr.

Vacuum Electronics Branch, Naval Research Laboratory, Washington DC, USA.

**M2.1 PULSED GAAS-IMPATT OSCILLATORS UP TO 200 GHz. (*Invited Keynote*)**

C Benz and J Freyer.  
Technical University Munich, Germany.

**M2.2 REALISATION OF ACTIVE MODE LOCKING OF THE p-Ge HOT HOLE LASER. (*Invited Keynote*)**

J N Hovenier, M C Diez, T O Klaassen, W Th Wenckebach, A V Muravjov, S G Pavlov and V N Shastin  
Dept of Applied Physics and DIMES, Delft University of Technology, Delft, The Netherlands.

**M2.3 TECHNICAL ASPECTS OF THE MODE-LOCKED p-Ge HOT HOLE LASER.**

J N Hovenier, R N Schouten, J H Blok, T O Klaassen, W Th Wenckebach, A V Muravjov, S G Pavlov and V N Shastin.  
Dept of Applied Physics and DIMES, Delft University of Technology, Delft, The Netherlands.

**M2.4 OSCILLATION OF THE p-Ge IVB LASER WITH VERY SMALL SIZE.**

Norihisa Hiromoto, Iwao Hosako and Mikio Fujiwara.  
Communications Research Laboratory, 4-2-1 Nukui-kita, Koganei, Tokyo 184-8795, Japan.

**M2.5 CHARGING EFFECTS IN MODE-LOCKED THz p-Ge LASERS.**

R C Stribos, S H Withers, A V Muravjov, C J Fredricksen, W Trimble, S G Pavlov, V N Shastin and R E Peale  
Dept of Physics, University of Central Florida, Orlando, FL 32816, USA.

**M2.6 DESIGN AND OPTIMISATION OF QUASI-OPTICAL FREQUENCY MULTIPLIERS.**

P Arcioni, M Bozzi, G Conciauro, H L Hartnagel, L Perregrini, M Shaalan and J Weinzierl.  
University of Pavia, Dept of Electronics Via Ferrata 1, 27100 Pavia, Italy.

**M2.7 DESIGN OF GAAS/GAALAS SINGLE BARRIER VARACTORS (SBV) FOR MM-WAVE FREQUENCY MULTIPLIERS.**

J Freyer, R Meola, M Claassen & F Neugebauer.  
Lehrstuhl für Allgemeine Elektrotechnik und Angewandte Elektronik, Technische Universität München, Germany.

**M2.8 MILLIMETER-WAVE MULTI-ELEMENT FREQUENCY MULTIPLICATION USING HOLOGRAPHIC POWER SPLITTING/COMBINING.**

M Shahabadi and K Schunemann.  
Technische Universität Hamburg-Harburg, D-21071 Hamburg, Germany.

- M3.1 FREE ELECTRON LASER STUDY OF THE SUPPRESSION OF NON-RADIATIVE SCATTERING PROCESSES IN SEMICONDUCTORS.** (*Invited Keynote*)  
C R Pidgeon  
Dept of Physics, Heriot-Watt University, Edinburgh EH14 4AS, UK.
- M3.2 PROBING THE BAND STRUCTURE OF CUBIC GaN BY IR-MAGNETO-SPECTROSCOPY.** (*Invited Keynote*)  
N Puhlmann, I Stolpe, M. von Ortenberg & D Schikora.  
Institut für Physik, Humboldt-Universität zu Berlin, Berlin, Germany.
- M3.3 MEASUREMENTS OF THE INTERSUBBAND LIFETIME IN P - GaAs/AlGaAs QUANTUM WELLS USING A FREE ELECTRON LASER.**  
C D Bezant, C J Langerak, J M Chamberlain and M Henini  
Dept of Physics, University of Nottingham, Nottingham NG7 2RD.
- M3.4 THE INFLUENCE OF INTENSE THz FIELDS ON THE MAGNETO-PHOTOCONDUCTIVITY OF N-GaAs UNDER IMPACT IONISATION CONDITIONS.**  
F Ghianni, T O Klaassen and W Th Wenckebach.  
Dept of Applied Physics and DIMES, Delft University of Technology, Delft, The Netherlands.
- M3.5 ENHANCEMENT OF TUNNEL IONISATION OF DEEP IMPURITIES IN SEMICONDUCTORS IN A HIGH FREQUENCY ELECTRIC FIELD OF FAR INFRARED LASER RADIATION.**  
S D Ganichev, E Ziemann, H Ketterl, V I Perel, I N Yassievich and W Prettl  
Universität Regensburg, Germany.
- M3.6 FTIR SPECTROSCOPY OF p-DOPED GaAs/AlGaAs SUPERLATTICES.**  
S Farjami Shayesteh, G MirJalili, T J Parker and L E Vorobjev  
Dept of Physics, University of Essex.
- M3.7 FAR INFRARED CHARACTERISATION OF MIXED PHASE GaN EPILAYERS.**  
G MirJalili, S Farjami Shayesteh, T J Parker, T S Cheng and C T Foxon  
Dept of Physics, University of Essex.
- M3.8 DETERMINATION OF PLASMA FREQUENCY AND PULSE RELAXATION TIME IN DOPED SEMICONDUCTORS BY FIR SURFACE WAVES.**  
V Vaicikauskas.  
Institute of Physics, Gostauto 12, 2600 Vilnius, Lithuania

**M4.1 EXCITATION OF BACKWARD WAVES IN GYRO-FORWARD-WAVE AMPLIFIERS AND FORWARD-WAVE AMPLIFIERS DRIVEN BY LINEAR ELECTRON BEAMS.**

*(Invited Keynote)*

G S Nusinovich, M Walter and J Zhao

Institute for Plasma Research, University of Maryland College Park, MD 20742-3511, USA.

**M4.2 A NEW HYBRID ION-CHANNEL MASER INSTABILITY.**

R J Barker and Liu Shenggang.

AFSOR, USA and UESTC, P R China.

**M4.3 3-D SIMULATION DESIGN OF 3 MM SLOW WAVE STRUCTURE.**

L Song, G Caryotakis, A Vlieks and N C Luhmann Jr

College of Engineering, Dept of Applied Science Davis-Livermore, California 94550, USA.

**M4.4 AXIAL MODE LOCKING IN GYROTRONS.**

G S Nusinovich and J Zhao.

Institute for Plasma Research, University of Maryland College Park, MD 20742-3511, USA.

**M4.5 SELF-CONSISTENT TIME-DEPENDENT MODELING OF GYRO-AMPLIFIERS WITH MAGY.**

K Nguyen, M Botton, T M Antonsen, B Levush, M Blank & J Calame.

Vacuum Electronics Branch, Code 6840. Naval Research Laboratory, Washington DC 20375-5347, USA

**M4.6 A TEM-TE<sub>16,2</sub> CONVERTER BASED ON RING RESONATOR.**

Gy Reiter, Gy Veszely and T Berceli.

Budapest Technical University, Dept of Electromag. Theor. 4111 Budapest, EGRY J.U.18, Hungary.

**M4.7 A CHERENKOV MASER EXPERIMENT USING AN ELECTRON BEAM FROM A PSEUDOSPARK.**

H Yin, W He, G R M Robb, A D R Phelps, A W Cross, K Ronald, P Aitken, B W J McNeil and C G Whyte.

University of Strathclyde, Glasgow, UK.

### M5.1 RECENT DEVELOPMENTS ON SCHOTTKY DIODES FOR THz APPLICATIONS.

*(Invited Keynote)*

A Simon, C I Lin, M Rodriguez-Girones and H L Hartnagel

Institut für Hochfrequenztechnik, Merckstr 25, 64283 Darmstadt, Germany.

## M5.2 A 490 GHz SINGLE-PLANAR-DIODE SUBHARMONIC MIXER. *(Invited Keynote)*

J L Hesler, N R Erickson and T W Crowe.

Department of Electrical Engineering, University of Virginia, Charlottesville, VA, USA, and Five College Radio Astronomy Observatory, University of Massachusetts, Amherst, MA, USA.

### M5.3 FABRICATION OF QUASI-INTEGRATED PLANAR SCHOTTKY BARRIER DIODES FOR THz APPLICATIONS.

T Yasui, C M Mann, T Suzuki, H Fujiishima, S Tsunekawa and K Mizuno

RIKEN PDC, 19-1399 Koeji Nagamachi, Aoba, Sendai 980, Japan.

#### M5.4 ANTI-PARALLEL PLANAR SCHOTTKY DIODES FOR SUBHARMONICALLY PUMPED MIXER.

C I Lin, A Simon, J Zhang, P V Piironen, V S Mottonen, H L Hartnagel and A V Raisanen

Institut für Hochfrequenztechnik, TU Darmstadt, Germany, and Helsinki University of Technology, Espoo, Finland.

### M5.5 MICROSTRUCTURAL PROPERTIES OF THz SCHOTTKY MIXER DIODES.

H W Hubers and H P Roser.

German Aerospace Research Center (DLR), Institute of Space Sensor Technology,  
Rudower Chaussee 5, 12489 Berlin, Germany.

## M5.6 ANTENNA-COUPLED NANOMETER THIN FILM Ni-NiO-Ni DIODES FOR DETECTION OF CW AND PULSED 30 THz RADIATION.

C Fumeaux, W H Herrmann, F K Kneubuhl, H Rothuizen.

Institute of Quantum Electronics, ETH, Zurich, Switzerland.

## M5.7 WAVEGUIDE HETERODYNE SIS RECEIVER FOR BALLOON-BORNE SUPERCONDUCTING SUBMILLIMETER WAVE LIMB SOUNDER AT 640 GHz BAND.

Y Irimajiri, T Manabe, H Masuko, S Ochiai, M Seta, Y Kasai, T Noguchi and S C Shi  
Global Environment Division, Millimeter-Wave Remote Sensing Section,  
Communications Research Laboratory, 4-2-1, Nukui-kita-machi, Koganei-shi, Tokyo,  
184-8795 Japan.

## M5.8 METAL-HIGH $T_C$ SUPERCONDUCTOR INTERFACE RESPONSE TO MICROWAVE AND MILLIMETER WAVE RADIATION.

A Laurinavicius, K Repsas, R A Vaskevicius, A Deksnys and B Vengalis

Semiconductor Physics Institute, Vilnius, Lithuania.



**M6.1 1 W CW MILLIMETER-WAVE OSCILLATOR WITH A GUNN DIODE ARRAY.**  
(Invited Keynote)

Jongsuck Bae, Tetsu Fujii and Koji Mizuno  
Tohoku University, Sendai, Japan.

**M6.2 OPEN RESONATOR SOLID STATE MILLIMETER WAVE SOURCES.**

M A Pershin and E A Machusky  
National Technical University of Ukraine, Kiev, Ukraine.

**M6.3 A NEW CONTRIBUTION TO THE FIR LASER SYSTEMS.**

A Darwish, T Thompson and A Williams.  
Center for nonlinear optics and materials, Alabama A&M University, Normal, AL 35762.

**M6.4 OPTICALLY PUMPED SUBMILLIMETER LASER LINES FROM  $\text{CD}_2\text{Cl}_2$ .**

A Bertolini, G Carelli, N Iola, S Marchetti, A Moretti and F Strumia  
Dipartimento di Fisica dell'Universita di Pisa, CNR & INFM, Piazza Torricelli 2, I-56126 Pisa, Italy.

**M6.5 INFRARED RAMAN SOLITONS, SELF PHASE MODULATION AND SELF FOCUSING IN  $\text{CO}_2$  LASER PUMPED  $\text{NH}_3$ .**

M O Baumgartner and F K Kneubuhl.  
Institute of Quantum Electronics, ETH, Zurich, Switzerland.

**M6.6 FREQUENCY STABILISATION OF A FAR INFRARED LASER.**

R Bocquet, M Yu Tretyakov and L Margules  
Universite des Sciences et Technologies de Lille, France.

**M6.7 SMMW RING LASERS WITH OPTICAL PUMP BEAM GUIDING.**

M Raum.  
Laboratories for high frequency technology, Universitat Erlangen-Nurnberg, Cauerstr. 9, 91058 Erlangen, Germany.

**M6.8 EFFECTS OF BUFFER GAS  $\text{N}_2$  ON MINIATURE OPTICALLY PUMPED  $\text{NH}_3$  SUBMILLIMETER WAVE CAVITY LASER EMISSION AT  $67.2 \mu\text{m}$ .**

Luo Xizhang, Luo Jiancong and Qin Jiayin.  
Dept of Electronics, Zhongshan University, Guangzhou 510275, P R China.

**Tu1.1 A METHOD OF REMOTELY STEERING A MICROWAVE BEAM LAUNCHED FROM A HIGHLY OVERMODED CORRUGATED WAVEGUIDE. (*Invited Keynote*)**

C P Moeller.

General Atomics, PO Box 85608, San Diego, CA, USA.

**Tu1.2 INTERNAL MODE CONVERTER MIRROR SHAPING FROM MEASURED FIELD INTENSITY. (*Invited Keynote*)**

D R Denison, M A Shapiro, R J Temkin, S Cauffman, T S Chu and K Felch

Plasma Science and Fusion Center, MIT, Cambridge MA 02139 USA.

**Tu1.3 LOW AND MEDIUM POWER TESTS ON 4 BEAM LAUNCHING OPTICS FOR THE 1.6 MW, 0.5 s ECRH EXPERIMENT AT 140 GHz ON FTU TOKAMAK.**

A Simonetto, A Bruschi, R Bozzi, S Cirant, F Gandini, G Granucci, S Mantovani, V Meller, V Muzzini, A Nardone, N Spinicchia and C Sozzi

IFP CNR, v. R Cozzi 53, 20125 Milano, Italy.

**Tu1.4 A HYBRID MAGNET SYSTEM FOR A FAST FREQUENCY-STEP-TUNABLE HIGH POWER GYROTRON.**

K Koppenburg, B Piosczyk and M Thumm.

Forschungszentrum Karlsruhe (FZK), ITP, Association EURATOM-FZK, Postfach 3640, D-76021 Karlsruhe, Germany.

**Tu1.5 LOW POWER TEST FACILITIES FOR CHARACTERISATION OF HIGHLY OVERSIZED GYROTRON COMPONENTS.**

O Braz, A Arnold, A Mobius, H Kunkel and M Thumm.

Forschungszentrum Karlsruhe (FZK), ITP, Association EURATOM-FZK, Postfach 3640, D-76021 Karlsruhe, Germany.

**Tu1.6 MODE CONVERSION DUE TO S-BEND DEFORMATION OF AN OVERSIZED HE<sub>11</sub> WAVEGUIDE.**

B Plaum, G Gantenbein, W Kasperek, M Thumm & D Wagner.

Universitat Stuttgart, Institut fur Plasmaforschung, Pfaffenwaldring 31, D-70569 Stuttgart, Germany.

**Tu1.7 MOVABLE MIRROR SYSTEM USING SUPERSONIC MOTOR FOR THE LHD-ECH ANTENNA.**

S Sasaki, Y Kanai, K Wakabayashi, A Hayakawa, S Kawashima, F Saito, K Yamamoto, T Ohgawara, Y Obiya, S Kubo, K Ohkuba and T Watari.

Toshiba Corporation, Yokohama, Japan.

**Tu2.1 TERAHERTZ RADIATION FROM SUPERCONDUCTING YBCO THIN FILMS EXCITED BY FEMTOSECOND PULSES: DISCOVERY, DEVELOPMENT AND APPLICATIONS. (*Invited Keynote*)**

M Hangyo, M T Tonouchi, M Tani and K Sakai.

Research Centre for Superconducting Materials & Electronics, Osaka University & Kansai Advanced Research Centre, Kobe, Japan.

**Tu2.2 GENERATION OF MILLIMETER WAVE RADIATION WITH A QUASI PLANAR SUPERLATTICE DEVICE.**

E Schomburg, K Hofbeck, J Grenzer, K F Renk, D G Pavel'ev Yu Koschurinov, V Ustinov, A Zhukov, A Kovsch, A Egorov and P S Kop'ev.

Dept of Physics, Univ of Nottingham, University Park, Nottingham NG7 2RD, UK.

**Tu2.3 THz ELECTROMAGNETIC WAVE SOURCES AND DETECTORS BASED ON LT-GAAS.**

H Abe, M Tani, K Sakai and S Nakashima

Kansai Advanced Research Center, Communications Research Laboratory, 588-2, Iwaoka, Nishi-ku, Kobe, 651-2401 Japan

**Tu2.4 GENERATION OF HIGH-FREQUENCY OSCILLATIONS BY ELECTROMAGNETIC SHOCK WAVE (EMSW) SYNCHRONOUS WITH BACKWARD HARMONIC OF PERIODIC NONLINEAR TRANSMISSION LINE (NLTL) BASED ON MULTILAYER HETEROSTRUCTURE (MLHS) WITH NANOLAYERS.**

A M Belyantsev and A B Kozyrev.

Institute for physics of microstructures of RAS, 603600, Nizhny Novgorod, GSP-105, Russia.

**Tu2.5 THE FREQUENCY RESPONSE OF RESONANT CAVITY ENHANCED P-I-N PHOTODIODE.**

D S Golubovic, P S Matavulj and J B Radunovic.

Dept of Microelectronics and Engineering Physics, Faculty of Electrical Engineering, Univ of Belgrade, Bulevar revolucije 73, PO Box 35-54, 11120 Belgrade, Yugoslavia.

**Tu2.6 MIXING OF 28 THz CO<sub>2</sub>-LASER RADIATION BY NANOMETER THIN FILM Ni-NiO-Ni DIODES WITH DIFFERENCE FREQUENCIES UP TO 176 GHz. (*Invited Keynote*)**

C Fumeaux, W H Herrmann, F K Kneubuhl, H Rothuizen, B Lipphardt & C O Weiss.

Institute of Quantum Electronics, ETH, Zurich, Switzerland.

**Tu2.7 TUNABLE FAR INFRARED SPECTROSCOPY IN THE 6 TO 9 THz REGION.**

H Odashima, L R Zink & K M Evenson.

Dept of Physics, Toyama University, Japan.

**Tu2.8 DEVELOPMENT OF HIGH EFFICIENCY BACKWARD OSCILLATORS FOR MILLIMETER AND SUBMILLIMETER APPLICATIONS.**

R L Ives, M Caplan and A Tupulov

Calabazas Creek Research, Saratoga, CA 95070, USA, & Soliton-NTT Res Centre, Moscow, Russia.

**Tu2.9 STUDY ON FOLDED WAVEGUIDE TRAVELLING WAVE TUBE.**

Gun-Sik Park, Hyun-Jun Ha and Soon-Shin Jung.

Plasma and Microwave Lab, Physics Education Dept Seoul National University, Kwanak-gu Shilim-dong Seoul, Korea 151-742.

- Tu3.1 INVESTIGATION OF MAGNETIC EXCITATIONS IN RARE EARTH METALS BY FAR INFRARED ATR SPECTROSCOPY.** (*Invited Keynote*)  
S A Feiven, T J Parker, S R P Smith and D R Tilley.  
Department of Physics, University of Essex Colchester CO4 3SQ, UK; and School of Physics, Universiti Sains, Penang, Malaysia.
- Tu3.2 CALCULATION OF NON-LINEAR MAGNETIC SUSCEPTIBILITY TENSORS FOR A FERROMAGNET.**  
Siew-Choo Lim, Junaidah Osman & D R Tilley.  
School of Physics, Universiti Sains Malaysia, Penang, Malaysia.
- Tu3.3 HIGH MAGNETIC FIELD ESR OF  $\text{CsCuCl}_3$ .**  
T Yamada, S Okubo, H Ohta, H Nojiri, M Motokawa & H Tanaka.  
Kobe University, Kobe, Japan.
- Tu3.4 MILLIMETER AND SUBMILLIMETER WAVE ESR OF ALIGNED POWDER SAMPLE OF  $\text{Nd}_2\text{BaNiO}_5$ .**  
S Okubo, H Ohta, M Hayashi, T Ymada, M Motokawa, H Nojiri, I Mogi, K Watanabe, H Kikuchi and H Nagasawa  
Kobe University, Kobe, Japan.
- Tu3.5 PROSPECTS FOR THE OBSERVATION OF MAGNON MODES IN THE FAR INFRARED SPECTRUM OF A THIN ANTIFERROMAGNETIC FILM ON A METAL.**  
T Dumelow.  
Universidade Federal do Rio Grande do Norte, Natal, Brazil.
- Tu3.6 THEORY OF TRANSMISSION THROUGH LAYERED MAGNETIC STRUCTURES.**  
Xue-Fei Zhou, Jing-Ju Wang, Xuan-Zhang Wang, Siew-Choo Lim, Junaidah Osman and D R Tilley.  
Department of Physics, Harbin Normal University, China, Heilongjiang, College of Education, Harbin, China, CCAST (World Laboratory) Beijing, China, School of Physics, Universiti Sains, Penang, Malaysia and Department of Physics, University of Essex, Colchester, UK.
- Tu3.7 INFLUENCE OF MISFIT STRAINS ON THE REFLECTION OF LIGHT FROM THE INTERFACE OF YTTRIUM-IRON, GARNET FILM ON GADOLINIUM-GALLIUM GARNET SUBSTRATE IN THE NEAR INFRARED.**  
N N Dadoenkova, I L Lyubchanskii, M I Lyubchanskii and V D Poymanov.  
Donetsk Physico-Technical Institute, National Academy of Sciences of Ukraine, 72, R Luxemburg str., 340114 Donetsk, Ukraine.
- Tu3.8 METHODICS ERRORS OF MEASURING THE ELECTRONIC RELAXATION TIME IN A PARAMAGNETIC.**  
N Popenko.  
Usikov Institute of Radiophysics & Electronics, NAS of Ukraine. Kharkov.
- Tu3.9 COUPLED SPIN-ELECTROMAGNETIC SURFACE INFRARED WAVES IN FERRITE/SEMICONDUCTOR SUPERLATTICE AT QUANTUM HALL CONDITIONS.**  
Roland H. Tarkhanyan  
Inst of Radiophys & Electronics of Armenian Nat AcSci. Ashtarak-2, 378410, Armenia.

**Tu4.1 165 GHz TE<sub>31,17</sub> - COAXIAL CAVITY GYROTRON WITH QUASI-OPTICAL RF-OUTPUT. (*Invited Keynote*)**

B Piosczyk, O Braz, G Dammertz, C T Iatrou, M Kuntze, G Michel, A Mobius and M Thumm.

Forschungszentrum Karlsruhe (FZK), ITP, Association EURATOM-FZK, Postfach 3640, D-76021 Karlsruhe, Germany.

**Tu4.2 EXPERIMENTAL RESULTS FROM A HELICAL WAVEGUIDE GYRO-TWT. (*Invited Keynote*)**

G G Denisov, V L Bratman, A W Cross, W He, A D R Phelps, K Ronald, S V Samsonov and C G Whyte

Institute of Applied Physics RAS, Nizhny Novgorod, Russia, and University of Strathclyde, Glasgow, UK.

**Tu4.3 OPERATION OF A 3 MW, 140 GHz GYROTRON WITH A COAXIAL CAVITY.**

R N Avani, M Pedrozzi, K E Kreischer & R J Temkin

Plasma Science and Fusion Center, MIT, Cambridge MA 02139 USA.

**Tu4.4 DEVELOPMENT OF A MULTI-STAGE DEPRESSED COLLECTOR FOR 1 MW CW GYROTRONS.**

R L Ives, A Singh, M Gaudreau, M Mizuhara, R Schumacher and V Granatstein.

Calabazas Creek Research, Inc, Saratogo, CA, USA, Insitute for Plasma Research, College Park, MD, USA, and Diversified Technologies, Bedford MA, USA.

**Tu4.5 MICROWAVE GENERATION AT 5.7 GHz BY A 100 KW AXIAL TRANSIT-TIME OSCILLATOR.**

J J Barroso, K G Kostov and R A Correa.

National Institute for Space Research (INPE), Brazil.

**Tu4.6 FREQUENCY-STEP-TUNED OPERATION OF A QUASI-OPTICAL MODE GENERATOR.**

A Arnold, O Braz, H R Kunkel and M Thumm.

Forschungszentrum Karlsruhe (FZK), ITP, Association EURATOM-FZK, Postfach 3640, D-76021 Karlsruhe, Germany.

**Tu4.7 NUMERICAL SIMULATION AND EXPERIMENTAL STUDY OF THE HELICAL ELECTRON BEAMS ON 170 GHz/1 MW GYROTRONS.**

A N Kuftin, V K Lygin, A S Postnikova and V E Zapevalov.

Institute of Applied Physics, Russian Academy of Sciences, 46 Ulyanov st, 603600 Nizhny Novgorod, Russia.

**Tu4.8 DEVELOPMENT OF A W-BAND 120 KW GYROKLYSTRON AT IAP.**

E. V. Zasyrkin, I. G. Gachev, I. I. Antakov, M. A. Moiseev, V. K. Lygin and E. V. Sokolov.

Institute of Applied Physics, Russian Academy of Science, 46 Ulyanov Str., Nizhny Novgorod, 603600 Russia.

**Tu5.1 QUASI-OPTICAL MEASUREMENT SYSTEMS. (*Invited Keynote*)**

Richard Wylde and Graham Smith  
QMC Instruments Ltd, London, Queen Mary and Westfield College, London, Thomas  
Keating Ltd, Billingshurst, and the University of St Andrews, St Andrews, UK.

**Tu5.2 TERAHERTZ COMPONENTS FABRICATED BY A NOVEL PHOTORESIST TECHNIQUE. (*Invited Keynote*)**

C E Collins, J W Digby, G M Parkurst, R E Miles, R D Pollard and J M Chamberlain.  
Dept of Physics, University of Nottingham, Nottingham NG7 2RD.

**Tu5.3 MICRO-MACHINED WAVEGUIDE ANTENNAS FOR 1.6 TERAHERTZ.**

J W Bowen, S T G Wootton, S Hadjiloucas, B M Towlson, L S Karatzas, N J Cronin,  
S R Davies, C E Collins, J M Chamberlain, R E Miles and R D Pollard.  
Dept of Cybernetics, The University of Reading, PO Box 225, Whiteknights, Reading  
RG6 6AY.

**Tu5.4 BAND PASS FILTERS FOR THE MID INFRARED.**

K D Moeller, K R Farmer, D V P Ivanov, O Sternberg, K P Stewart and P Lalanne  
Dept of Physics and Microelectronics Research Center, New Jersey Institute of  
Technology, Newark NJ 07102, USA

**Tu5.5 THEORETICAL AND EXPERIMENTAL INVESTIGATION OF PHASE GRATINGS.**

William Lanigan, Ruth Colgan, J Anthony Murphy & Stafford Withington.  
Experimental Physics, National University of Ireland, Maynooth, Co Kildare, Ireland.

**Tu5.6 EFFICIENCY OF FIR SEW EXCITATION BY APERTURE, PRISM AND MESH METHODS.**

V Vaicikauskas, R Antanavicius and R J Anuskevicius.  
Institute of Physics, Gostauto 12, 2600 Vilnius, Lithuania

**Tu5.7 IMPROVED 2-D PHOTONIC BANDGAP MICROSTRIP STRUCTURES.**

T Lopetegi, F Falcone, B Martinez, R Gonzalo and M Sorolla  
Dept of Electrical and Electronics Engineering, Public University of Navarra, Campus  
Arrosadia, s/n E-31006 Pamplona, Navarra, Spain.

**Tu5.8 A TRANSDUCER COMBINED TAPER AND CONVERTER WITH PERIODIC WAVEGUIDE VARIATION.**

Hong-hui Yan and Hong-sheng Yang.  
Dept of Electronic Engineering, National Key Laboratory of Millimeter Waves,  
Southeast University, Nanjing, PRC.

**Tu5.9 OPTIMUM SECTIONAL WAVEGUIDE TAPERS FOR QUASI-OPTICAL TRANSMISSION LINES.**

V K Kiseliov.  
12 Ac. Proskura st., Kharkov, 310085 Ukraine.

**Tu6.1 HOT ELECTRON DETECTION** (*Invited Keynote*)

K Wood and H Araujo

QMC Instruments Ltd, Billingshurst, West Sussex, UK, and Department of Physics,  
Queen Mary and Westfield College, London, UK.

**Tu6.2 FIR PHOTOVOLTAIC EFFECT IN SILICON BIB STRUCTURES.** (*Invited Keynote*)

L Asadauskas, D Yu Kovalev, V Rylkov, B Aronzon, R Brazis and J Leotin

Semiconductor Physics Institute, Gostauto 11, 2600 Vilnius Lithuania.

**Tu6.3 PROPERTIES OF HIGH STABILITY BI MICRO-BOLOMETERS FOR THE  
DETECTION OF THz RADIATION.**

F Ghianni, F W H J Steenbrink, T O Klaassen and W Th Wenckebach.

Dept of Applied Physics and DIMES, Delft University of Technology, Delft, The  
Netherlands.

**Tu6.4 FABRICATION OF Ge:Ga FAR-INFRARED PHOTOCONDUCTOR TWO-DIMENSIONAL  
ARRAY.**

M Fujiwara, N Hiromoto, H Shibai, T Hirao and T Nakagawa

Communications Research Laboratory, 4-2-1 Nukui-Kitanachi, Koganei, Tokyo 184-  
8795, Japan.

**Tu6.5 ANTENNA COUPLED FAR INFRARED RADIATION DETECTORS.**

Yoshizumi Yasuoka.

Department of Electronic Engineering, National Defense Academy, 1-10-20  
Hashirimizu Yokosuka 239, Japan.

**Tu6.6 TRANSVERSE SEEBECK-EFFECT IN A TILTED TWO METALS MULTILAYER  
STRUCTURE.**

Th Zahner & H Lengfellner

Institut fur Experimentelle und Angewandte Physik Universitat Regensburg 93040  
Regensburg Germany

**Tu6.7 FIELDS IN THE IMAGE SPACE OF SYMMETRICAL HYPERBOLIC FOCUSING LENS.**

W B Dou, Z L Sun, X Q Tan and Z G Wang.

State Key Lab of Millimeter Waves, Dept of Radio Eng., Southeast University,  
Nanjing, 210096 P.R.China.

**Tu6.8 HTS MICROSTRIP ANTENNAS CHARACTERISED AND ANALYSED BY A HIGHER  
ACCURATE METHOD IN THE FTD.**

Geraldo F da Silveira Filho and Humberto C C Fernandes.

Dept Electrical Engineering-Technological Center, Federal University of Rio Grande  
do Norte, Natal, Brazil.

- W1.1 QUASI-OPTIC COMPONENTS IN OVERSIZED CORRUGATED WAVEGUIDE FOR MILLIMETER-WAVE TRANSMISSION SYSTEMS.** (*Invited Keynote*)  
J L Doane, H Ikezi and C Moeller.  
General Atomics, PO Box 85608, San Diego, CA, USA.
- W1.2 CVD DIAMOND WINDOWS FOR HIGH POWER GYROTRONS.** (*Invited Keynote*)  
R Heidinger, R Sporl, M Thumm, J R Brandon, R S Sussmann and C N Dodge.  
Forschungszentrum Karlsruhe, Association FZK-Euratom, Institut für Materialforschung 1, PO Box 3640, D-76021 Karlsruhe, Germany.
- W1.3 DEVELOPMENT OF A 1 MW CW WATERLOAD FOR GAUSSIAN MODE GYROTRONS.**  
R L Ives, M Mizuhara, R Schumacher and R Pendleton.  
Calabazas Creek Research, Saratoga, CA 95070, USA.
- W1.4 PRESENT DEVELOPMENTS FOR THE 140 GHz TRANSMISSION SYSTEM FOR ECRH ON THE STELLARATOR W7-X.**  
L Empacher, G Gantenbein, F Hollman, W Kasperek and H Zolm.  
Universität Stuttgart, Institut für Plasmaforschung, Pfaffenwaldring 31, D-70569 Stuttgart, Germany.
- W1.5 LOSSES IN LOW LOSS DIAMONDS AT mm RANGE.**  
B M Garin, A N Kopnin, M P Parkhomenko, E E Chigryai, V G Ralchenko and V I Konov.  
Institute of Radio Engineering & Electronics of RAS, 1 Vvedensky Sq, Fryazino, Moscow Region, 141120 Russia
- W1.6 DIAMONDS FOR HIGH-POWER GYROTRON WINDOW.**  
V Parshin, V Ralchenko and V Konov.  
Applied Physics Institution of RAS. 46 Ulyanov Str, N Novgorod 603600 Russia.



- W2.1 A SPHERICAL MAIN REFLECTOR COMPACT ANTENNA TEST RANGE FOR OPERATION UP TO SEVERAL THz.**  
C G Parini, M R Rayner and C Rieckmann.  
Electronic Engineering Dept, Queen Mary & Westfield College, Mile End Road, London E1 4NS, UK.
- W2.2 FIELD PROFILE SYNTHESIS WITH AN ANTENNA ARRAY.**  
G Michel and M Thumm.  
Karlsruhe (FZK), ITP, Association EURATOM-FZK, Postfach 3640, D-76021 Karlsruhe, Germany.
- W2.3 FREE SPACE ELECTRO-OPTIC SAMPLING OF TERAHERTZ RADIATION.**  
M Tani, K Sakai, M Herrmann and H Takahashi.  
Kansai Advanced Research Center, Kobe, Japan.
- W2.4 THE EFFECT OF RECEIVING HORN GAIN ON MEASURED RADIATION PATTERNS AS APPLIED TO THE DESIGN OF BEAM SHAPING REFLECTORS IN A GYROTRON.**  
V Natarajan, P J Sealy and R J Vernon.  
Dept of Electrical & Computer Engineering University of Wisconsin 1415 Engineering Drive Madison, WI 53711, USA
- W2.5 PHASE SINGULARITIES IN BEAMS.**  
G F Brand.  
School of Physics, University of Sydney, NSW 2006, Australia.
- W2.6 FREQUENCY RESOLVED RADIATION PATTERNS FROM LARGE APERTURE TERAHERTZ ANTENNAS.**  
P Uhd Jepsen and H Helm.  
Fakultat fur Physik Albert-Ludwigs-Universitat, Hermann-Herder-Str, 3, D-79104 Freiburg, Germany.
- W2.7 SLOT ARRAY ANTENNAS FOR 2.5 THz-CH<sub>3</sub>OH LASER RADIATION.**  
Y Yasuoka, H Kobayashi, Y Abe and Y Ohkubo.  
Dept of Electronic Engineering, National Defense Academy, 1-10-20 Hashirimizu Yokosuka, 239-8686 Japan.
- W2.8 MILLIMETER WAVE BEAM CONTROL BY THE ILLUMINATION OF A SEMICONDUCTOR.**  
G F Brand.  
School of Physics, University of Sydney, NSW 2006, Australia.
- W2.9 SIMULATION AND EXPERIMENTAL STUDY OF A WAVEBEAM REMOTE STEERING SYSTEM.**  
A Chirkov, G G Denisov, W Kasperek & D Wagner.  
Institute of Applied Physics, Russian Academy of Sciences, 46 Ulyanov Sr., 603600 Nizhny Novgorod, Russia.

- W3.1 NON-LINEAR OPTIC COEFFICIENTS OF FERROELECTRICS.** (*Invited Keynote*)  
Junaidah Osman, Y Ishibashi, D R Tilley and J F Webb.  
School of Physics, Universiti Sains Malaysia.
- W3.2 THz TIME DOMAIN SPECTROSCOPY OF ELECTRO-OPTIC CRYSTALS.** (*Invited Keynote*)  
M Schall, H Helm and S R Keiding.  
Fakultat fur Physik Albert-Ludwigs-Universitat, Hermann-Herder-Str, 3, D-79104 Freiburg, Germany.
- W3.3 MILLIMETER WAVE SPECTROSCOPY OF SUPERIONIC CONDUCTOR  $\text{LiNiO}_2$ .**  
S Ono, Y Ikeuchi, H Ohta, T Nanba, S Okubo, A Hirano and R Kanno.  
Kobe University, Kobe, Japan.
- W3.4 CHARGE DISTRIBUTIONS IN FERROELECTRIC STRUCTURES.**  
S R P Smith and T J Parker.  
Department of Physics, University of Essex Colchester CO4 3SQ, UK.
- W3.5 SURFACE OPTICS OF FERROELECTRICS.**  
Khian-Hooi Chew, R L Stamps & D R Tilley.  
School of Physics, Universiti Sains Malaysia.
- W3.6 NONLINEAR ASYMUTHAL SURFACE WAVES IN GYROTROPIC SECOND-ORDER NON-LINEAR MATERIALS COATED BY A METAL.**  
K N Ostrikov, M Y Yu, N A Azarenkov & A D Boardman.  
Institut fur Theoretische Physik 1, Ruhr-Universitat Bochum, D-44780 Bochum, Germany.
- W3.7 CHANGES OF IR PROPERTIES OF TRANSLUCENT ALUMINA INDUCED BY REACTION WITH SODIUM.**  
M Tazawa and S Tanemura.  
National Industrial Research Institute of Nagoya, Nagoya, Japan.
- W3.8 INFRARED ABSORPTION MEASUREMENTS OF TITANIUM HYDRIDE FILMS PREPARED BY RF REACTIVE SPUTTERING.**  
S Nakao, M Tazawa, P Jin, T Hirahara and K Saitoh.  
National Industrial Research Institute of Nagoya, 1-1 Hirate-cho, Kita-ku, Nagoya 462-8510, Japan.
- W3.9 IDENTIFICATION OF A Ti-RELATED ABSORPTION BAND IN  $\text{ZnSe}$ .**  
Mireya Castillo.  
Universidad Nacional Experimental del Tachira, Apartado 436, San Cristobal, Tachira, Venezuela.

**Th1.1 RECENT DEVELOPMENTS ON THE HIGH POWER ECH INSTALLATION AT THE DIII-D TOKAMAK. (*Invited Keynote*)**

J Lohr, D Ponce, R W Callis, J L Doane, H Ikezi & C P Moeller.  
General Atomics, San Diego, California, USA.

**Th1.2 STATUS OF THE 118 GHz, 0.5 MW, QUASI CW GYROTRON FOR THE TORE SUPRA AND TCV TOKAMAKS. (*Invited Keynote*)**

C Tran, E Giguet, Ph Thouvenin, P Garin, M Pain, S Alberti, M Q Tran and M Thumm.  
Thomson Tubes Electroniques, Velizy, France.

**Th1.3 A DESIGN STUDY OF A 28 GHz 200 kW GYROKLYSTRON AMPLIFIER.**

J J Choi, S W Bak, W K Han, D M Park, J G Yang and S M Hwang.  
Kwangwoon University, Dept of Radio Science & Engineering, 447-1 Wolgae-Dong,  
Nowon-Ku, Seoul, Korea 139-701.

**Th1.4 1 MW, 140 GHz GYROTRON WITH BREWSTER-WINDOW.**

G Dammertz, M Kuntze, O Braz, K Koppenburg, B Piosczyk and M Thumm.  
Forschungszentrum Karlsruhe (FZK), ITP, Association EURATOM-FZK, Postfach  
3640, D-76021 Karlsruhe, Germany.

**Th1.5 THE DESIGN OF THE ECRH LAUNCHER IN ITER.**

A G A Verhoeven, O G Kruijt, P R Prins, F J van Amerongen, W A Bongers, L de Jong, R Kruisbergen, M A Makowski and E Woldberg.  
FOM-Instituut Rijnhuizen, PO Box 1207, 3430 Be Nieuwegein, The Netherlands.

**Th1.6 DRIFT NON-LINEARITIES IN SEMICONDUCTORS GIVING RISE TO 1 THz RADIATION.**

R Brazis, R Raguotis, Ph Moreau and M R Siegrist.  
Semiconductor Physics Institute, Gostauto 11, 2600 Vilnius Lithuania.

**Th1.7 BEAM-SHAPING, DUAL MIRROR DESIGN USING MEASURED AMPLITUDE AND RECONSTRUCTED PHASE FOR THE INPUT.**

B M Harper and R J Vernon  
Dept of Electrical & Computer Engineering University of Wisconsin 1415 Engineering  
Drive Madison, WI 53711, USA

**Th2.1 COMPACT, TURN-KEY TERAHERTZ LASER SYSTEMS FOR FUSION PLASMA DIAGNOSIS. (*Invited Keynote*)**

W A Peebles, D Brower, Yong Jiang, Lei Zeng, P Pribyl and P King.  
UCLA, Los Angeles, CA, IR & T, Santa Monica, CA, and California Institute of Technology, Pasadena, CA, USA.

**Th2.2 THE CHALLENGE OF IMPLEMENTING THZ PLASMA DIAGNOSTIC SYSTEMS ON ITER. (*Invited Keynote*)**

G Vayakis for the ITER JCT and Home Teams.  
ITER Joint Central Team, 11025 North Torrey Pines Road, La Jolla, California 93037, USA

**Th2.3 CORRELATION RADIOMETRY FOR TEMPERATURE FLUCTUATION MEASUREMENTS IN FUSION PLASMAS. (*Invited Keynote*)**

Hans J Hartfuss.  
Max Planck Institut fuer Plasmaphysik, Boltzmann Str 2, D-85748 Garching, Germany.

**Th2.4 PASSIVE RANGING BY MEASUREMENT OF PHASE FRONT CURVATURE.**

D A Robertson and J C G Lesurf.  
School of Physics and Astronomy, University of St Andrews, St Andrews, Fife KY16 9SS, Scotland.

**Th2.5 COMPACT VIDEO-RATE PASSIVE MILLIMETRE-WAVE-IMAGER.**

S Price, R N Anderton, J R Borrill, P R Coward, M J Roberts, N A Salmon, G N Sinclair, M R M Wasley, K St J Murphy and R Appleby.  
DRA, Malvern.

**Th2.6 MEASUREMENT OF BUNCH SHAPE OF ELECTRONS BY COHERENT RADIATION.**

M Ikezawa, Yu Shibata and K Ishe.  
Research Institute for Scientific Measurements. Tohoku University, Japan.

**Th2.7 THE QUASI-OPTIC DIFFRACTION TOMOGRAPHY SYSTEM FOR NON DESTRUCTIVE EVALUATION.**

A A Vertiy, S P Gavrilov, I V Voinovskiy & V N Stepanuyk.  
Turkish-Ukrainian Joint Research Laboratory, Gebze-Kocaeli Turkey.

**Th2.8 CONCEALED WEAPONS DETECTION SENSOR AND SIGNAL PROCESSING DEMONSTRATION.**

A Pergande, D Eden, M McKinley, S Sutha and E Weatherwax  
Lockheed Martin Electronics and Missiles, Orlando, FL 32819, USA.

### Th3.1 TERAHERTZ SPECTROSCOPY OF BIOMOLECULES. *(Invited Keynote)*

A G Markelz and E J Heilweil.

NIST, 221/B208, Optical Technology Division, Physics Laboratory, Gaithersburg, MD 20899-0001, USA.

### Th3.2 FAR-INFRARED SPECTRA OF HIGHLY VISCOUS LIQUIDS: GLYCEROL, GLYCEROL TRIACETATE, O-TERPHYNYL.

T S Perova, D H Christensen, O Faurskov Nielsen, U Rasmussen and J K Vij.

Dept of Electronic & Electrical Engineering, Trinity College, Dublin-2, Ireland.

### Th3.3 ROTATIONAL SPECTRA OF PROTONATED RARE GAS IONS OBSERVED WITH TUNABLE FAR - INFRARED SPECTROMETER.

F Matsushima, H Odashima and K Takagi.

Department of Physics, Toyama University, Gofuku 3190, Toyama 930, Japan.

### Th3.4 FAR-INFRARED SPECTRA OF MOLECULAR MIXTURES IN THE LIQUID STATE: COMPARISON WITH THE LOW-FREQUENCY RAMAN SPECTRA.

T S Perova, D H Christensen, O Faurskov Nielsen, U Rasmussen, P Perov and J K Vij.

Dept of Electronic & Electrical Engineering, Trinity College, Dublin-2, Ireland.

### Th3.5 REVISITING WATER AT TERAHERTZ FREQUENCIES.

J R Birch and D H Martin.

Dorking, UK and Brentwood, UK.

### Th3.6 INFLUENCE OF THE MICROWAVE IRRADIATION ON THE INTERACTION OF THE WATER WITH THE NA-DNA IN THE FILMS.

T V Bolbuch, G M Glibitskiy, E A Andreev and V N Kharyanen

Institute for Radiophysics and Electronics, 12 Ac Proscura, 310085, Kharkov, Ukraine.

**Th4.1 DEVELOPMENT OF SUBMILLIMETRE WAVE GYROTRONS (GYROTRON FU SERIES) AS RADIATION SOURCES. (*Invited Keynote*)**

T Hidehara, I Ogawa, S Mitsudo & M Pereyaslavets.  
Faculty of Engineering, Fukui University, Japan.

**Th4.2 WIDE BAND FREQUENCY TUNABLE SINGLE MODE GYROTRON.**

K Yokoo, M Iguchi, N Sato and J Nishihara.  
Research Institute of Electrical Communication Tohoku University, Japan.

**Th4.3 CAVITY DESIGN FOR SECOND HARMONIC GYROTRON OPERATION.**

G F Brand.  
School of Physics, University of Sydney, NSW 2006, Australia.

**Th4.4 RESONATOR WITH GRATING FOR A QUASI-OPTICAL GYROTRON OPERATING AT THE THIRD HARMONIC FREQUENCY OF 260 GHz.**

D Guyomarc'h, J P Hogge and M Siegrist.  
Centre de Recherches en Physique des Plasmas. Association EURATOM,  
Confederation Suisse PPB-Ecublens, CH-1015 Lausanne, Switzerland.

**Th4.5 CONTINUOUSLY TUNABLE 35-190 GHz POWERFUL GYROTRONS AT GYCOM.**

E V Zasyrkin, I I Antakov, I G Gachev, S N Vlasov & E V Sokolov.  
Institute of Applied Physics, Russian Academy of Science, 46 Ulyanov Str., Nizhny  
Novgorod, 603600 Russia.

**Th4.6 GYROTRON AT THE 5<sup>TH</sup> CYCLOTRON HARMONIC.**

V L Bratman, A E Fedotov, Yu K Kalynov, V N Manuilov, M M Ofitserov, S V  
Samsonov and A V Savilov.  
Institute of Applied Physics, Russian Academy of Sciences, 46 Ulyanov St, Nizhny  
Novgorod, 603600, Russia.

**Th4.7 A HIGH-POWER, SHORT PULSE DIELECTRIC CHERENKOV MASER AMPLIFIER OPERATING IN THE SUPERRADIANT REGIME.**

S M Wiggins, D A Jaroszynski, A W Cross, A D R Phelps, K Ronald, P Aitken, B W  
J McNeil, G R M Robb, M I Yalandin, V G Shpak, S A Shunailov, M R Ulmaskulov,  
N S Ginzburg, N Yu Novozhilova. I V Zotova, A S Sergeev and N Yu Peskov.  
University of Strathclyde, Glasgow, UK, Institute of Electrophysics, RAS,  
Ekaterinburg, Russia, and Institute of Applied Physics, RAS, Nizhny Novgorod,  
Russia.

**Th5.1 A NEW FAR-INFRARED (FIR) SOURCE. (*Invited Keynote*)**

J E Walsh, J C Swartz, J H Brownell and M F Kimmitt.

Dept of Physics and Astronomy, Dartmouth College, Hanover, NH 03755, USA.

**Th5.2 A HIGH BRIGHTNESS PHOTOINJECTOR FOR FREE ELECTRON LASER APPLICATIONS. (*Invited Keynote*)**

F V Hartemann, E C Landahl, N C Luhmann, Jr, J P Heritage, G P Le Sage and C H Ho.

University of California, Davis, CA, Lawrence Livermore National Laboratory, Livermore, CA, Synchrotron Radiation Research Center, Taiwan, Republic of China.

**Th5.3 COHERENT SMITH-PURCELL RADIATION IN THE MILLIMETER WAVE REGION.**

K Ishi, Y Shibata, M Ikezawa, T Takahashi, T Matsuyama K Kobayashi and Y Fujita.

Research Institute for Scientific Measurements. Tohoku University, Japan.

**Th5.4 ENERGY-PHASE CORRELATION IN A BUNCHED ELECTRON BEAM: A NEW SCHEME FOR FREE-ELECTRON GENERATORS OF RADIATION.**

A Doria, G P Gallerano, E Giovenale, S Letardi, G Messina and C Ronsivalle.

ENEA, Dipartimento Innovazione, Divisione Fisica Applicata, Frascati, Italy.

**Th5.5 A FAR-INFRARED SMITH-PURCELL EXPERIMENT.**

G Doucas, M F Kimmitt, G Korschinek, C Walner and J E Walsh

Particle and Nuclear Physics Laboratory, University of Oxford, UK, Department of Physics, University of Essex, Colchester, UK, Fachbereich der Technischen Universitat Munchen, Garching, Germany, Department of Physics and Astronomy, Dartmouth College, Hanover, NH, USA.

**Th5.6 PROPOSAL OF THz FEL USING A PHOTOMIXING FIELD EMISSION CATHODE.**

K Yokoo.

Research Institute of Electrical Communication, Tohoku University, Japan.

**Th5.7 PREBUNCHED FREE ELECTRON LASER IN THE MILLIMETER WAVE REGION.**

Y Shibata, S Sasaki, K Ishi, S Ono, Y Inoue, M Ikezawa T Takahashi, T Matsuyama, K Kobayashi, Y Fujita & E Bessonov.

Research Institute for Scientific Measurements. Tohoku University, Japan.

**Th5.8 A KA-BAND CHI-WIGGLER FEM: EXPERIMENTAL RESULTS.**

J M Taccetti, R H Jackson, H P Freund, D E Pershing & V L Granatstein.

Vacuum Electronics Branch, Code 6840. Naval Research Laboratory, Washington DC 20375-5347, USA

**Th5.9 DETAILED MM-WAVES MEASUREMENTS AT THE DUTCH FREE-ELECTRON MASER.**

W A Bongers, G F IJ Kramer, J A Rietveld, A G A Verhoeven, P Manintveld, V L Bratman, M Caplan, G G Denisov, C A J van der Geer, A Montvai, A J Poelman, J Plomp, A V Savolov, P H M Smeets, A B Sterk and W H Urbanus.

FOM-Instituut Rijnhuizen, PO Box 1207, 3430 Be Nieuwegein, The Netherlands.

**Th6.1 DESIGN, PERFORMANCE AND APPLICATIONS OF COMPACT FAR INFRARED LASER MAGNETIC RESONANCE SPECTROMETERS. (*Invited Keynote*)**

H W Hubers and H P Roser.

German Aerospace Research Center (DLR), Institute of Space Sensor Technology, Rudower Chaussee 5, 12489 Berlin, Germany.

**Th6.2 DUAL-FREQUENCY VECTOR DETECTION IN THE 8-800 GHz INTERVAL. APPLICATION TO SPECTROSCOPY AT HIGH MAGNETIC FIELDS.**

P Goy, S Caroopen, M Gross, K Katsumata, H Yamaguchi, M Hagiwara and H Yamazaki.

AB Millimetre, Paris, France, Departement de physique de l'Ecole normale superieure, Paris, France, and The Institute of Physical and Chemical Research, Wako, Saitama, Japan.

**Th6.3 A HIGH RESOLUTION FOURIER TRANSFORM SPECTROMETER FOR THE SPECTRAL REGION BELOW 60 CM<sup>-1</sup>.**

A Atkins, G Poulter and J R Birch.

Graseby Specac Ltd, Orpington, Kent, UK, and JB Research, Dorking, Surrey, UK.

**Th6.4 A FAST SWEEPABLE BROADBAND SYSTEM FOR DIELECTRIC MEASUREMENTS AT 90-100 GHz.**

R Heidinger, R Schwab and F Koniger.

Forschungszentrum Karlsruhe, Association FZK-Euratom, Institut fur Materialforschung 1, PO Box 3640, D-76021 Karlsruhe, Germany.

**Th6.5 DIELECTRIC PROPERTIES OF MATERIALS UP TO MILLIMETER WAVELENGTHS USING WHISPERING GALLERY DIELECTRIC RESONATORS.**

G Annino, M Cassettari, I Longo and M Martinelli.

Istituto di Fisica Atomica e Molecolare, CNR, via del Giardino 7, 56127 Pisa, Italy.

**Th6.6 THE USE OF A 250 GHz GYROTRON IN A DNP/EPR SPECTROMETER.**

K E Kreischer, C Farrar, R G Griffin and R Temkin.

Plasma Science and Fusion Center, MIT, Cambridge MA 02139 USA.

**Th6.7 DIELECTRIC LOSS MEASUREMENTS WITH A CONFOCAL FABRY-PEROT RESONATOR**

J M Dutta & C R Jones

Dept of Physics North Carolina Central University Durham, NC 27707, USA

**Th6.8 THE PRECISION OF QUASI-OPTICAL NULL-BALANCED BRIDGE TECHNIQUES FOR TRANSMISSION COEFFICIENT MEASUREMENTS.**

S Hadjiloucas, J W Bowen and L S Karatzas.

Dept of Cybernetics, The University of Reading, PO Box 225, Whiteknights, Reading RG6 6AY.



- F1.1 OPERATION OF A HIGH PERFORMANCE, THREE STAGE, HARMONIC MULTIPLYING, INVERTED GYROTRON.** (*Invited Keynote*)  
H Guo, J Rodgers, V L Granatstein, G Nusinovich, M Walter and J Zhao.  
Institute for Plasma Research, University of Maryland College Park, MD USA.
- F1.2 DEVELOPMENT OF HIGH POWER GYROTRON WITH DIAMOND WINDOW.**  
K Sakamoto, A Kasugai, M Tsuneoka, K Takahashi Y Ikeda, T Imai, T Tsuyoshi and Y Mitsunaka.  
RF Heating Lab., JAERI, Naka-machi, Ibaraki, Japan.
- F1.3 EXPERIMENTAL RESULTS OF TWO HIGH-POWERED COAXIAL GYROKLYSTRONS.**  
M Castle, W Lawson, B Hogan, J Cheng, X Xu, V L Granatstein and M Reiser.  
Institute for Plasma Research & Electrical Engineering, University of Maryland College Park, MD 20742, USA.
- F1.4 STATUS REPORT ON A 110 GHz, 1 MW CW GYROTRON WITH A CVD DIAMOND WINDOW.**  
K Felch, P Borchard, S Cauffman, R W Callis, P Cahalan, T S Chu, D Denison, H Jory, M Mizuhara, D Remsen, G Saraph and R J Temkin.  
CPI, Gyrotron Engineering 811 Hansen Way, MS-B450 Palo Alto, CA 94304, USA
- F1.5 DESIGN OF A MULTI-MEGAWATT 95 GHz GYROKLYSTRON EXPERIMENT.**  
W Lawson and M R Arjona.  
Electrical Engineering Dept, Institute for Plasma Research University of Maryland, College Park, MD 20742, USA.
- F1.6 OPTIMISATION OF THE ELECTRON BEAM-CAVITY SYSTEM OF 170 GHz GYROTRON FOR ITER.**  
V E Zapevalov, V A Flyagin, N Kuftin, M A Moiseev & N A Zavolsky.  
Institute of Applied Physics, Russian Academy of Sciences, GYCOM Ltd., 46 Ulyanov st, 603600 Nizhny Novgorod, Russia.
- F1.7 HIGH POWER OPERATION OF AN 8.6 GHz COAXIAL GYROKLYSTRON.**  
W Lawson, J Cheng, B Hogan, V L Granatstein & X Xu.  
Electrical Engineering Dept, Institute for Plasma Research University of Maryland, College Park, MD 20742, USA.
- F1.8 DEVELOPMENT OF 140 GHz/1MW GYROTRON WITH A DUAL RF BEAM OUTPUT.**  
V E Myasnoikov, M V Agapova, A N Kostyna, L G Popov, G G Denisov, A A Bogdashov and V E Zepevalov  
GYCOM Ltd, Nizhny Novgorod, Russia.

- F2.1 THE BENEFITS OF MILLIMETER WAVES FOR MATERIALS PROCESSING.** (*Invited Keynote*)  
G Link, L Feher, S Rhee and M Thumm.  
Forschungszentrum Karlsruhe (FZK), ITP, Association EURATOM-FZK, Postfach 3640, D-76021 Karlsruhe, Germany.
- F2.2 OPEN RESONATOR SET-UP FOR SPATIALLY RESOLVED AND TEMPERATURE DEPENDENT MM-WAVE PROPERTY MEASUREMENTS.** (*Invited Keynote*)  
R Schwab, R Heidinger and R Sporl.  
Forschungszentrum Karlsruhe, Association FZK-Euratom, Institut für Materialforschung 1, PO Box 3640, D-76021 Karlsruhe, Germany.
- F2.3 VISUALIZATION OF PHOTO-EXCITED FREE CARRIERS BY A SCANNING NEAR-FIELD MILLIMETER-WAVE MICROSCOPE.** (*Invited Keynote*)  
T Nozokido, H Minamide, Jongsuck Bae, T Fujii, M Ito and K Mizuno.  
Photodynamics Research Center, (RIKEN), Sendai, Japan.
- F2.4 INDUCED ANISOTROPY STUDYING BY THE METHODS OF B W O-SPECTROSCOPY.** (*Invited Keynote*)  
E A Vinogradov.  
General Physics Institute, Russian Academy of Sciences, Vavilov str 38, 117942 Moscow, Russia.
- F2.5 T-RAYS IN THE NEAR-FIELD.**  
K Wynne and D Jaroszynski.  
Femtosecond Research Centre, University of Strathclyde, Dept of Physics and Applied Physics, Glasgow G4 0NG, UK.
- F2.6 MULTIMODE OPEN RESONATOR IN THE DEFECTOSCOPY OF THIN-FILMS.**  
V Derkach, A Pojedinchuk, A Brovenko and A Vertij.  
Usikov Institute for Radiophysics and Electronics, Academy of Sciences of Ukraine, 12 Ac Proskura St., Kharkov, 310085 Ukraine.
- F2.7 SURFACE IMPEDANCE MAPPING AT CRYOGENIC TEMPERATURES OF HTSC-WAFERS AT 145 GHz.**  
R Schwab, R Heidinger, J Geerk, F Ratzel, M Lorenz & H Hochmuth.  
Forschungszentrum Karlsruhe, Association FZK-Euratom, Institut für Materialforschung 1, PO Box 3640, D-76021 Karlsruhe, Germany.

- P.1 ELECTROMAGNETIC SIMULATION OF A 32 GHZ, TE<sub>021</sub> GYROTRON.**  
J J Barroso, K G Kostov and R A Correa.  
National Institute for Space Research (INPE), Brazil.
- P.2 A 4.5 MW - ELECTRON GUN FOR A COAXIAL CAVITY GYROTRON.**  
B Piosczyk.  
Forschungszentrum Karlsruhe (FZK), ITP, Association EURATOM-FZK, Postfach 3640, D-76021 Karlsruhe, Germany.
- P.3 INVESTIGATIONS OF BEAM INSTABILITIES IN THE COMPRESSION REGION OF GYROTRONS USING KINETIC THEORY AND PARTICLE-IN-CELL SIMULATIONS.**  
S Illy and E Borie.  
Forschungszentrum Karlsruhe (FZK), ITP, Association EURATOM-FZK, Hermann-von-Helmholtz-Platz 1, 4 Eggenstein-Leopoldshafen, Germany.
- P.4 DEVELOPMENT OF A SUBMILLIMETER WAVE GYROTRON (GYROTRON FU V).**  
T Idehara, I Ogawa, S Mitsudo, M Pereyaslavets, T Tsuchida & M Ui.  
Faculty of Engineering, Fukui University, Japan.
- P.5 HIGH POWER, COHERENT INGAAS/INP SEMICONDUCTOR LASER DESIGN OPERATING AT 1.55 MICRONS.**  
A R Jha.  
Jha Technical Consulting Services, Cerritos, CA 90703, USA.
- P.6 A NEW BOUNDARY DESCRIPTION IN ABSORBING-BOUNDARY CONDITIONS FOR TWO DIMENSION TLM MODELS.**  
Chendong Zhu, Liquan He and Wei Hong.  
State Key Lab of Millimetre Waves, Southeast University, Nanjing, P R China 210096.
- P.7 POWER DIVIDERS IN MILLIMETER WAVES.**  
R L M Lima and H C C Fernandes.  
Dept Electrical Engineering-Technological Center, Federal University of Rio Grande do Norte, Natal, Brazil.
- P.8 A NEW METHOD OF CIRCULAR GROOVE GUIDE ANALYSIS.**  
Hong-hui Yan, Guo-qin Huang and Hong-sheng Yang.  
Dept of Electronic Engineering, National Key Laboratory of Millimeter Waves, Southeast University, Nanjing, PRC.
- P.9 CALCULATION OF EIGENMODE MIXTURES IN OVERSIZED CORRUGATED RECTANGULAR WAVEGUIDES.**  
D Wagner, M Thumm and W Kasperek.  
Universitat Stuttgart, Institut fur Plasmaforschung, Pfaffenwaldring 31, D-70569 Stuttgart, Germany

---

**POSTER PROGRAMME (continued)**

---

- P.10 A SMALL-SIZED COMPOUND ANTENNA FOR THE AUTO-IDENTIFICATION OF DUAL-POLARISATION WAVES.**  
Wu Qun and Gun-Sik Park.  
Plasma and Microwave Lab, Physics Education Dept, Seoul National University,  
Kwanak-gu Shilim-dong, Seoul, Korea 151-742.
- P.11 AN EDUCATION PROGRAM FOR RESULTS IN 3D ON FINLINE COUPLER.**  
H C C Fernandes, L C de Freitas\_Jr and S A P Silva.  
Dept Electrical Engineering-Technological Center, Federal University of Rio Grande  
do Norte, Natal, Brazil.
- P.12 THE HIGH QUALITY MIRRORS FOR MICROWAVE RANGE.**  
V Parshin.  
Applied Physics Institution of RAS. 14 Ulyanov Str, N Novgorod, 603600 Russia.
- P.13 COMPARATIVE ANALYSIS OF MM-WAVE VCO STRUCTURES.**  
E A Machusky  
National Technical University of Ukraine, Kiev, Ukraine.
- P.14 MODELING OF MICROWAVE IMAGES OF BURIED CYLINDRICAL OBJECTS.**  
A A Vertiy and S P Gavrilov.  
Turkish-Ukrainian Joint Research Laboratory, Gebze-Kocaeli, Turkey.
- P.15 DYNAMICS OF JOSEPHSON JUNCTION UNDER GREEN NOISE.**  
S A Guz and M V Sviridov.  
Dept of Physics, Moscow Institute of Physics & Technology, Institutskiy per 9,  
Dolgoprudniy, Moscow Region 141700. Russia.
- P.16 A NOVEL METHOD FOR THE EXACT CALCULATION OF WANNIER-STARK LOCALISATION IN SUPERLATTICES**  
Y Ergun, R Amca, I Sokmen, H Sari, S Elagoz & N Balkan  
Physics Dept, University of Essex, Wivenhoe Park, Colchester, Essex CO4 3SQ
- P.17 EFFICIENCY ENHANCEMENT IN THE RELATIVISTIC MICROWAVE OSCILLATOR.**  
E Odarenko and A Schmat'ko.  
Dept of Radiophysics, Kharkov State University, Ukraine.
- P.18 DOUBLE RESONANCE IN GYRODEVICES.**  
G S Nusinovich and J Zhao.  
Institute for Plasma Research, University of Maryland, College Park, MD 20742-  
3511, USA.
- P.19 EXPERIMENTAL STUDY OF TRAPPED ELECTRONS EFFECT IN HELICAL ELECTRON BEAMS OF A MILLIMETER WAVE RANGE GYROTRON.**  
A N Kuftin and V E Zapevalov.  
Institute of Applied Physics, Russian Academy of Sciences, 22 Ulyanov st, 603600  
Nizhny Novgorod, Russia.

---

**POSTER PROGRAMME (continued)**

---

- P.20 NON-STATIONARY ANALYSIS OF HELICAL ELECTRON BEAMS WITH DIFFERENT TOPOLOGY.**  
P V Krivosheev, V K Lygin and V N Manuilov.  
Institute of Applied Physics, Russian Academy of Sciences, 24 Ulyanov st, 603600 Nizhny Novgorod, Russia.
- P.21 THEORETICAL STUDY OF THE GYROTRON BACKWARD WAVE OSCILLATOR.**  
S H Chen and K R Chu.  
Dept of Physics, National Tsing Hua University, Hsinchu, Taiwan, ROC
- P.22 THE DIFFRACTION RADIATION OSCILLATOR WITH THE WIDE-BAND ELECTRONIC FREQUENCY CHANGE.**  
M Demchenko, I Ivanchenko & V Korneynkov  
Usikov Institute of Radiophysics & Electronics, NAS of Ukraine, Kharkov.
- P.23 LOCAL PHASE INHOMOGENEITIES REVELATION IN OPTICAL OPAQUE DIELECTRIC.**  
I Ivanchenko.  
Usikov Institute of Radiophysics & Electronics, NAS of Ukraine, Kharkov.
- P.24 OFF-AXIS EXPANSION SOLUTION OF LAPLACE'S EQUATION: APPLICATION TO ACCURATE AND RAPID CALCULATION OF COIL MAGNETIC FIELDS.**  
R H Jackson.  
Vacuum Electronics Branch, Code 6840., Naval Research Laboratory, Washington DC 20375-5347, USA
- P.25 THE FEATURES OF THE SMOOTH ANODE MAGNETRON OPERATING IN A MODE CLOSE TO THE CRITICAL.**  
O P Kulagin.  
Usicov Institute of Radiophysics and Electronics, National Academy of Sciences of Ukraine, 310085 Kharkov, Ac Proscura St, 12, Ukraine.
- P.26 MILLIMETER-WAVE COLD-CATHODE COAXIAL TWT.**  
V D Yeremka and M O Khorunzhiy.  
Usicov Institute of Radiophysics and Electronics, National Academy of Sciences of Ukraine, 310085 Kharkov, Ac Proscura St, 12, Ukraine.
- P.27 THE MM-WAVE PENIOMAGNETRON.**  
V D Yeremka  
Usicov Institute of Radiophysics and Electronics, National Academy of Sciences of Ukraine, 310085 Kharkov, Ac Proscura St, 12, Ukraine.
- P.28 FREE ELECTRON MASER AMPLIFIER EXPERIMENTS.**  
C G Whyte, D A Jaroszynski, W He, A W Cross, K Ronald and A D R Phelps.  
Department of Physics and Applied Physics, University of Strathclyde, Glasgow, G4 ONG, Scotland.

---

**POSTER PROGRAMME (continued)**

---

- P.29 FREQUENCY-BROADBAND GYRODEVICES OPERATING WITH EIGENWAVES OF HELICALLY RIPPLED WAVEGUIDES.**  
V L Bratman, A W Cross, G G Denisov, W He, A D R Phelps, K Ronald, S V Samsonov and C G Whyte.  
Institute of Applied Physics, RAS, Nizhny Novgorod, Russia, and University of Strathclyde, Scotland.
- P.30 COLD AND THERMIONIC CATHODE CARM EXPERIMENTS.**  
A R Young, W He, K Ronald, A W Cross, C G Whyte and A D R Phelps.  
University of Strathclyde, Scotland.
- P.31 RECENT DEVELOPMENTS OF SCIENTIFIC INSTRUMENTS IN MILLIMETER WAVE DIVISION OF ELVA-1 LTD**  
D Korneev  
191025, Nevsky 74, 23H, St.Petersburg, Russia
- P.32 TEXTILE SEMICONDUCTORS - A NOVEL CLASS OF MM AND IR WAVE ABSORBING MATERIALS.**  
R Brazis and J Koprowska.  
Semiconductor Physics Institute, Gostauto 11, 2600 Vilnius, Lithuania.
- P.33 PUMPED PHONONS IN ATMOSPHERIC AEROSOLS**  
H A Gebbie  
Dept of Electronics & Electrical Engineering, Imperial College, London SW7.
- P.34 PROBLEMS IN THE RELATIVISTIC THEORY OF MICROWAVE PLASMA ELECTRONICS.**  
M V Kuzelev and A A Rukhadze.  
General Physics Institute, Russian Academy of Sciences, ul Vavilova 38, 117942 Moscow, Russia.
- P.35 MAGNETIC FIELD DEPENDENCE OF THZ RADIATION FROM INSB.**  
Ping Gu, M Tani and K Sakai.  
Kansai Advanced Research Center, Kobe, Japan.

# Development of array devices for the millimeter and submillimeter wave region

Koji Mizuno

Research Institute of Electrical communication, Tohoku University  
Photodynamics Research center, RIKEN  
Katahira, Aobaku-ku, Sendai 980-8577, Japan

**Abstract** - Quasi-optical dimension is practical size in the millimeter and submillimeter wave region. We have developed array devices on a substrate with quasi-optical dimension for practical use in this region. Detector arrays are used as imaging arrays, and oscillator arrays offer practical sources with combined output power and improved monochromaticity. We discuss also other devices relevant to these.

## 1. Introduction

The millimeter and submillimeter wave region lies between the microwave and the optical regions. In the millimeter and submillimeter wave region quasi-optical dimension (several ten wavelengths) is a reasonable size to handle in comparison with the dimension for the microwave or optical region. New types of devices can be realized by mounting multi-elements on a substrate with quasi-optical dimension (Fig. 1). In this paper we discuss development of these array devices such as detector arrays (imaging array), oscillator arrays and the devices relevant to these.

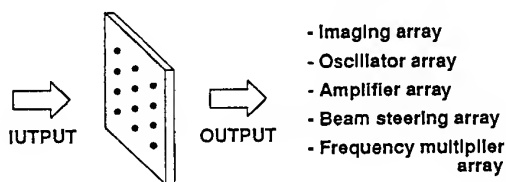


Fig. 1 Quasi-optical multi-element device.

The furthermore guiding principles for our device development are as follows: the devices should be operated at room temperature, have response time shorter than 0.1 nanosecond, and when they are oscillators outputs should be cw, single-mode, coherent and frequency-tunable. These device characteristics are quite normal and common for devices in the microwave and the optical regions, however not in the region between them.

## 2. MM-wave Imaging

Millimeter wave focal plane imaging [1] is able to provide information through clouds, smoke, and dust when visible and IR systems are unusable. It can also be used in the fields of plasma measurement,

remote sensing, etc. The resolution of the focal plane imaging is limited by diffraction and is the order of wavelength, while scanning near field microscopy achieves sub-wavelength resolution [2], which offers other applications of millimeter wave imaging technologies.

### 2-1 Focal plane imaging (Imaging arrays)

Conventional millimeter wave imaging relies mainly on the use of a single detector, with the optics mechanically scanned to obtain an image. The use of multiple detectors in an imaging array, however does not require mechanical scanning and makes real-time imaging possible. Figure 2 shows a 60 GHz imaging array [3,4] which consists of 2-element Yagi antennas with beam-lead Schottky diodes at the center of the antennas. The interval between the antennas was determined by the sampling theorem to obtain the diffraction-limited image.

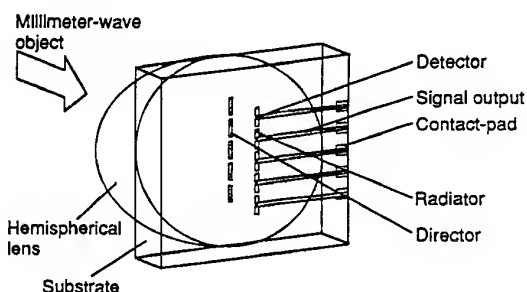


Fig. 2 Yagi-Uda antenna imaging array

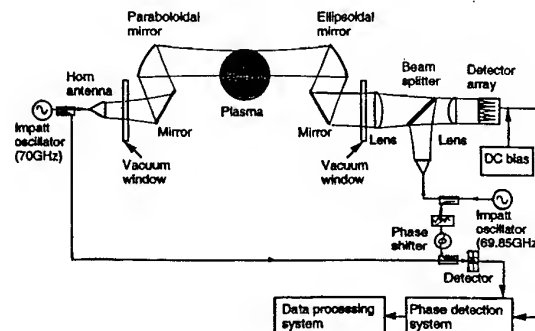


Fig. 3 Phase imaging system for plasma diagnostics

i) plasma diagnostics

The optics for mm-wave imaging radar systems can be designed using the ray tracing method. Figure 3 shows the 70 GHz optics designed for measuring 2-dimensional plasma density profile in the plasma machine of the University of Tsukuba for nuclear fusion research. Figure 4 shows measured time-revolution of the 2-dimensional density profile [5].

ii) Millimeter wave images and neural network processing [6]

A neural network signal processing has been successfully introduced to recognize mm-wave images which were distorted by speckle and/or glint through coherent illumination.

Alphabetical letters made of aluminum foil were used as test objects for evaluating our mm-wave active imaging system. Fig. 5 (a) shows experimentally-obtained images for the letters A and J. The size of each object corresponds to about 8 x 8 pixels on the image plane. The images represent power distribution of scattered signals and are strongly distorted, mainly because of speckle and/or glint resulting from the coherent illumination.

To recognize these images, a feed-forward neural network was used as a signal processor. The network consists of 10 x 10 input units, 60 hidden units and 26 output units. In Fig. 5 (b) the recognition rate is

shown as a function of the number of "teach-data" required, when 10 dissimilar alphabetical letters (A, H, J, L, O, P, S, T, V, and Z) were used as the objects. A high recognition rate of 98 % was obtained using data from five teaching trials for each letter, which shows that neural network signal processing is very suitable for mm-wave active imaging.

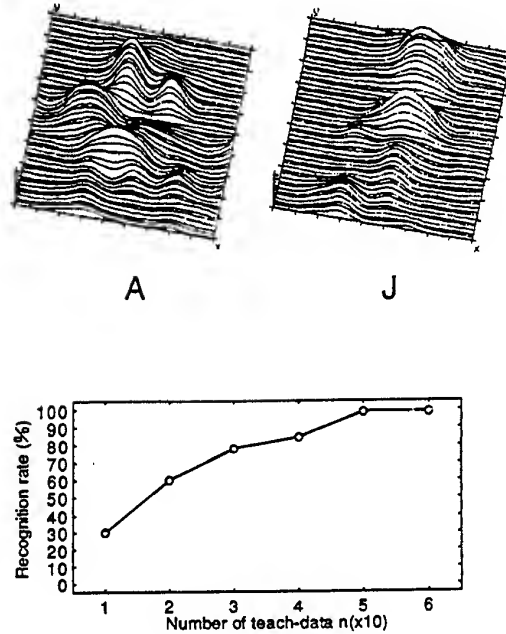


Fig. 5 (a, above) MM-wave images for the letters A and J, and (b, below) the recognition rate as a function of the number of teach-data.

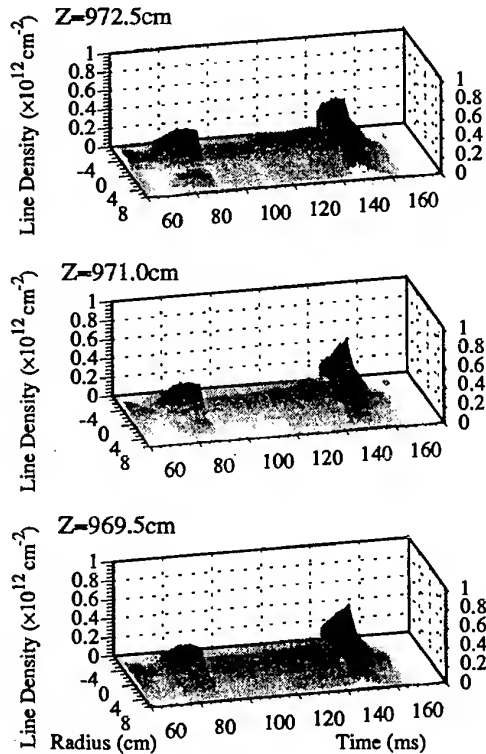


Fig. 4. Time evolution of line density radial profiles at three axial positions of a plasma at Tsukuba.

## 2-2 Scanning near-field microscopy

Diffraction limits the resolution of focal plane imaging and conventional microscopy to approximately  $\lambda/2$ . Sub-wavelength resolution has been demonstrated with scanning near-field microscopes. We proposed and demonstrated a new type of scanning near-field millimeter-wave microscopy using a metal slit at the end of a rectangular waveguide as a scanning probe [2]. The waveguide probe is shown in Fig. 6. A reduced-height waveguide forms the slit; the wide dimension of the slit and that of the waveguide are identical, but the waveguide height is reduced down to  $\lambda/60$  (0.08 mm at 60 GHz). The probe is operated above the cutoff frequency for the fundamental waveguide mode and thus provides stronger signals than point-type probes, which operate below the cutoff frequency, resulting in improved resolution or sensitivity. Also the slit type probe makes fast (but rough) scanning over a wide sample possible.

To achieve sub-wavelength resolution with a slit as a scanning probe, we adopted an image reconstruction algorithm based on computerized tomographic imaging (such as that used in x-ray CT imaging).



We have successfully observed photo-excited free carriers in a silicon substrate through this microscope [7].

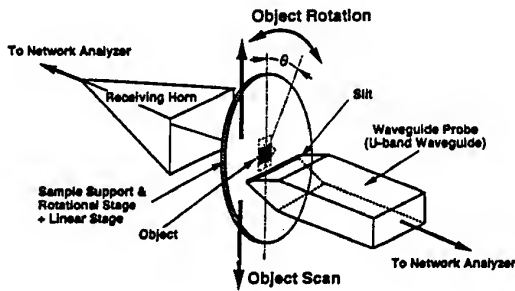


Fig. 6 Scanning near-field microscopy using a slit type probe.

### 3. Oscillator arrays

Solid-state devices, such as Gunn diodes and FET's are useful radiation sources in the microwave region because of their lower power consumption, compactness of their size, and ease of handling. However, in the short-millimeter wave region, these devices have only low power capability, typically several mW or less, and the output is noisy because of the low Q-value of the conventional waveguide resonator due to a large RF loss. In the submillimeter wave region the resonant tunneling diode (RTD) is a promising device, however its output power is less than  $\mu$ W.

Coherent power combining of these devices mounted in a Fabry-Perot resonator is one of the solutions for these problems, because the Fabry-Perot resonator could achieve a high Q-value at high frequencies even in the submillimeter wave region [8], and its quasi-optical size enables a number of oscillator elements to be mounted in the resonator.

#### 3-1 Metallic grating circuit

We have proposed a Fabry-Perot resonator [9] with a metallic grating as a resonator for millimeter and submillimeter wave oscillators with multi-elements. Figure 7 shows the configuration of the resonator. This configuration has several advantages such as capability of mounting a number of oscillator elements in a resonator, large heat dissipation power, simplicity of circuitry of biasing and capability of adjusting circuit impedance by the grating-groove dimensions.

We have developed an equivalent circuit for HEMT array in a Fabry-Perot resonator (refer to Fig. 8) and demonstrated the validity of the circuit experimentally [10]. Coherent power combining of RTD's has also been successfully observed for the fundamental  $TEM_{00}$  resonant mode at the frequency of 75 GHz [11].

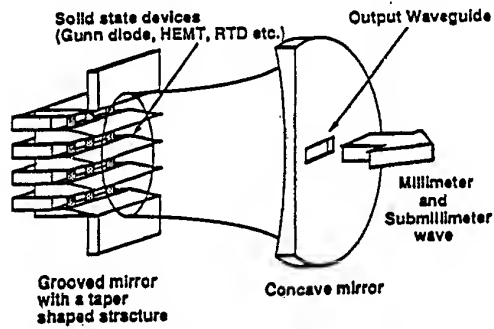


Fig. 7 Fabry-Perot resonator with a metallic grating.

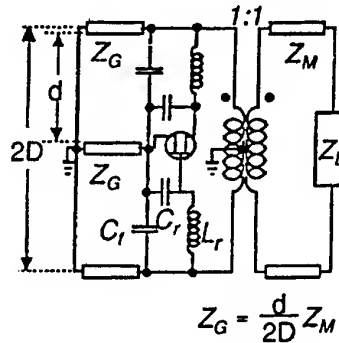


Fig. 8 An equivalent circuit for the HEMT array oscillator

#### 3-2 Horn antenna circuit

As high power solid state devices such as Gunn diodes, PHEMT's, MMIC's are recently being developed, power combining of smaller numbers of the devices could produce enough power for many practical applications. For efficient power combining of smaller numbers of devices, a new type of a waveguide power combiner has been developed [12] which incorporates an array of fundamental-mode ( $TE_{10}$ ) waveguides with diode devices, inside of an overmoded-waveguide resonator (refer to Fig. 8). An combining efficiency of above 83 % and an output power of 1.5 W (cw) at 60 GHz band have been achieved with the overmoded-waveguide oscillator containing a 3 x 3 waveguide array with Gunn diodes.

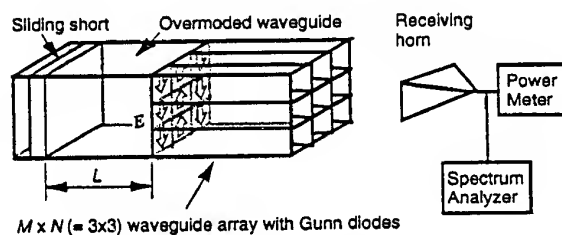


Fig. 8 Waveguide array in a overmoded-waveguide

### 3-3 Metal mesh evanescent-wave coupler

In order to extract the maximum output power from our quasi-optical oscillators, quasi-optical output coupler with adjustable coupling coefficient is needed. We have developed a metal mesh coupler which makes use of the evanescent-wave coupling between a metal mesh and a dielectric plate [13]. The transmittance of this coupler with a capacitive metal mesh can be adjusted by more than 70 % by altering the spacing between the mesh and a silicon plate by less than  $\lambda/140$  in 56-GHz experiments.

### 4. Development of fabrication processes of low-noise Schottky barrier diodes for the THz region

The dot-matrix-type Schottky barrier diode (SBD) remains an important device for detecting and mixing at terahertz frequencies, particularly in atmospheric remote sensing and plasma diagnostics. In plasma diagnostics, it is important to reduce low-frequency (1/f) diode noise, since the IF frequency used is typically below 1 GHz. We have developed submicron diode fabrication process (refer to Fig. 9) that has

resulted in a significant reduction of 1/f noise [14]. Noise performance is optimized by establishing an even distribution of gallium and arsenide at the contact surface, and different  $\text{SiO}_2$  deposition and etching techniques have been compared. CVD deposition of the  $\text{SiO}_2$  layer is preferable to RF sputtering. It was also demonstrated that ECR etching results in two orders of magnitude in noise reduction at frequencies below 100 MHz, as compared to RIE, and that thermal annealing brings further improvement of about 2 - 3 dB.

### 5. Summary

In order to develop the short-millimeter and submillimeter wave practical technologies, we have been developing quasi-optical array devices. The final goal of the submillimeter wave technologies will be to contribute to optical fiber communication technologies as modulation or sub-carrier signal sources.

### REFERENCES

- [1] K. Mizuno, '97 Topical Symposium on Millimeter Waves (Invited), Hayama, Japan, July 1997.
- [2] T. Nozokido, et al., '97 Int'l Conf. IR & MM Waves (Th 5.4), Wintergreen, July 1997.
- [3] K. Mizuno, et al., Electron. Lett., 27, 108(1991).
- [4] K. Uehara, et al., IEEE Trans. Microwave Theory Tech., 40, 806(1992).
- [5] N. Ohyama, et al., Rev. Sci. Instrum. 68, 500(1997)
- [6] K. Watabe, et al., 1996 IEEE MTT-S Symposium, San Francisco, June 1996.
- [7] T. Nozokido, et al., '98 Int'l Conf. IR & MM Waves (Invited Keynote), Essex, Sept. 1998.
- [8] K. Mizuno and S. Ono, "Ledatron" in Infrared and Millimeter Waves (Ed. K. Button), vol.1, New York:Academic press, 1979, pp. 213-233.
- [9] K. Mizuno, et al., Electron. Lett. 24, 792(1988).
- [10] H. Kondo, et al., IEEE Trans. Microwave Theory Tech. 40, 854(1992).
- [11] T. Fujii, et al., 1996 IEEE MTT-S Symposium, San Francisco, June 1996.
- [12] J. Bae, et al., '98 Int'l Conf. IR & MM Waves (Invited Keynote), Essex, Sept. 1998.
- [13] J. Bae, et al., Int. J. Infrared and Millimeter Waves 16, 377(1995).
- [14] T. Yasui, et al., '98 Int'l Conf. IR & MM Waves, Essex, Sept. 1998.

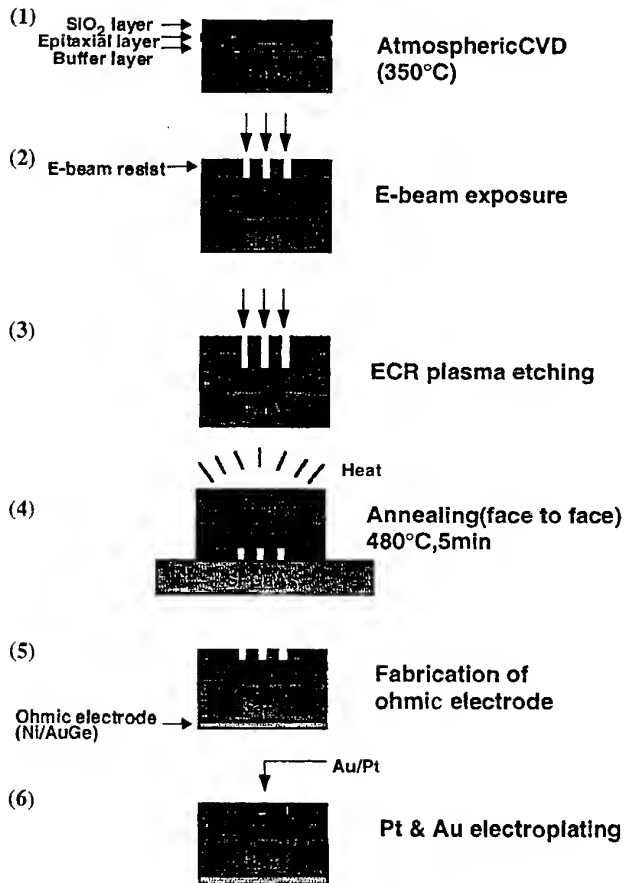


Fig. 9 Fabrication processes of Pt/GaAs Schottky diodes.

## High Field Magneto-Spectroscopy in Condensed Matter Physics

Michael von Ortenberg

Humboldt University at Berlin  
Chair for Magnetotransport in Solids  
Invalidenstrasse 110, D-10115 Berlin, Germany  
orten@physik.hu-berlin.de

### Abstract

A review of the application of high magnetic fields up to the multi-megagauss range in connection with electromagnetic radiation on selected problems in condensed matter physics is given. Special emphasis is laid on different experimental techniques. Selected problems of orbital and spin resonances are discussed as well as non-resonant phenomena.

### Introduction

The investigation of the spectral response of matter to incident electromagnetic radiation with well defined frequency is a classical experimental method for the study of matter. According to our understanding the radiation energy  $\hbar\omega$  is an excellent tool to probe the energy levels of all charged and magnetic systems, both on a macroscopic and sub-atomic level. The response of the system to the electromagnetic radiation can be resonant or non-resonant depending whether  $\hbar\omega$  fits exactly the energy separation of two levels or not. Especially in resonance pronounced effects are observed in both dispersion and absorption of the radiation. All of these transitions are affected by an external magnetic field, since the magnetic field couples with the associated magnetic moment of the system. As a matter of fact mostly the energy shift of the levels involved can be approximated in a simple linear dependence. The magnetic moment is related either to the orbital motion and hence orbital angular momentum or the spin angular momentum. Whereas the orbital angular momentum reflects the extension of the orbital motion of the charged carrier in space, the spin has no spatial extension. Interesting phenomena are the result of the coupling of the two constituents to the total angular momentum. A short-hand notation of this phenomenon is the electronic g-factor in solids. In this way not only the pure orbital and spin excitation manifest in the two research tools of cyclotron resonance and magnetic resonance respectively, but also mixed resonances as the combined spin-flip become possible. Cyclotron and magnetic resonances divide the condensed matter physics in two vast domains and both have contributed a large amount to our present knowledge about the microscopic interaction of condensed matter.

It is interesting to observe how the wavelength of the applied radiation in these experiments has shifted towards shorter values of the spectrum with the progress in magnetic field generation. Whereas the for the first cyclotron experiment [1] microwaves were applied in magnetic field of "gauss", nowadays radiation with only few micrometers wavelength are used in magnetic fields of some hundred Tesla. This factor of more than thousand reflects a dramatic development of magnet technology in this connection over the last thirty years.

### Cyclotronresonance in Semiconductors

Cyclotronresonance can be observed if the radiation frequency  $\omega$  equals the frequency of the orbital motion called cyclotron frequency  $\omega_c = eB/m$ . Here  $e$  is the elementary charge,  $B$  the external magnetic field and  $m$  the mass of the charged particle. A cyclotronresonance experiment represents therefore essentially a balance to determine the microscopic mass of the charge carrier, since for resonance holds

$$\omega = eB_r/m \quad (1)$$

and after determination of the resonance field  $B_r$  the mass  $m$  is easily derived. In a more advanced theoretical concept the mass value is related to energy bands of the charge carriers underlying the strict quantization effects of the magnetic field. In the case of many electrons occupying the states of an energy band the individuality of the different carriers manifest in a detailed lineshape of the resonance as a superposition of many weighted single particle transitions. This structure becomes more visible at higher magnetic fields, so that the latter acts as a ZOOM for studying energy band and population effects, as demonstrated in Fig. 1,

where the data of low [2] and high field cyclotron resonance on HgSe:Fe [3], respectively, are reproduced. The megagauss experiments reveals the detailed quantization structure of the quantum well sample. In the low field data not only the fundamental cyclotron resonance is observed, but also the subharmonics. This effect is due to the strong interaction of the radiation with the carrier system especially for long wavelength, which converts the incident plane wave into a strongly decaying one inside the material so that the non-local character of the interaction along the cyclotron orbit becomes evident.

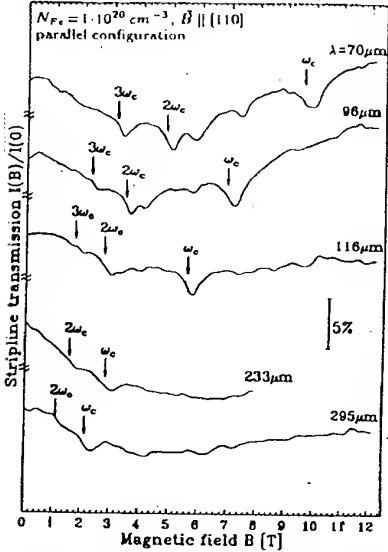


Fig. 1a Low field CR on HgSe [2]

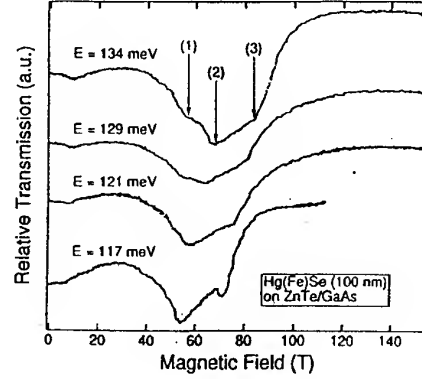


Fig. 1b High field CR on HgSe:Fe [3]

For the quantization of the orbital motion of charge carriers by an external magnetic field the magnetic length  $l = (\hbar/eB)^{1/2}$  plays a dominant role. Please note that this fundamental quantity is independent of the individual mass parameter, which means that the wavefunctions for *any* particle bearing one elementary charge - leptons, hadrons, or even mesons - are identical for the same set of quantum numbers. The magnetic length  $l$  as a tunable length measure is an excellent tool to probe man-made nanostructures [4]. The ultimate application of  $l$  to natural lattice parameters of the crystalline solid has been investigated theoretically already in the sixties resulting in the famous "Hofstadter Butterfly" representing the interference of natural lattice structure with two-dimensional flux quantization lattice perpendicular to the applied magnetic field [5]. The experimental verification of this concept is one of the most challenging problems of modern solid state physics since magnetic fields up to the order of 1000 T are necessary.

### Magnetic Resonance

Any magnetic moment  $\mu$  rotates in the presence of an external magnetic field with the Larmor frequency

$$\omega_L = g \cdot \mu_B \quad (2)$$

where  $\mu_B$  is the Bohr magneton and  $g$  the Landé  $g$ -factor. Again resonance can be observed if the Larmor and radiation frequency are equal. In the same way as for the orbital quantization the mass parameter  $m$  includes all the interesting internal interactions of the solid, here for spin systems the  $g$ -factor represents the corresponding mechanisms. Since in *hard* magnetic materials the internal fields characterizing the effective exchange interaction are in the multi-megagauss range such high fields are necessary in an experiment to compete with the internal interactions.

A very interesting behavior of integer spins in a linear antiferromagnetic chain was predicted by Haldane [6]. In contrast to spin-1/2 particles for integer spin there should be a nonvanishing gap between the effective singlet ground state and the excited triplet states. The verification of this conjecture was a challenge for submillimeter-magneto spectroscopy demonstrating again the high efficiency of this method. In Fig. 2 we have reproduced the data obtained for NENP showing clearly the different behavior of the transitions below and above the critical field  $B_c$  where the lowest excited triplet state crosses the singlet state so that the quality of the ground state is changed [7]. The corresponding scheme of the transition energies is plotted in Fig. 3. The arrows indicate the observed transitions and indicate also the strength of the resonance. After the confirmation of the Haldane conjecture various manifestations of the spin-one linear chain have been investigated corroborating this concept [8].

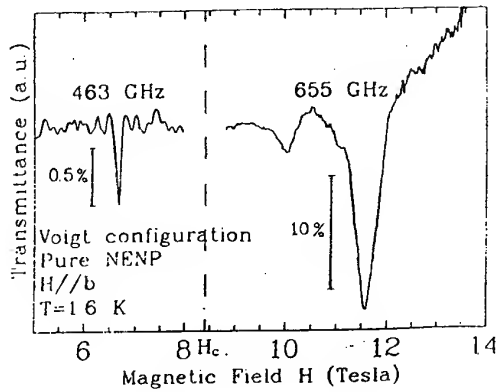


Fig 2 Magnetic Resonance on NENP [7]

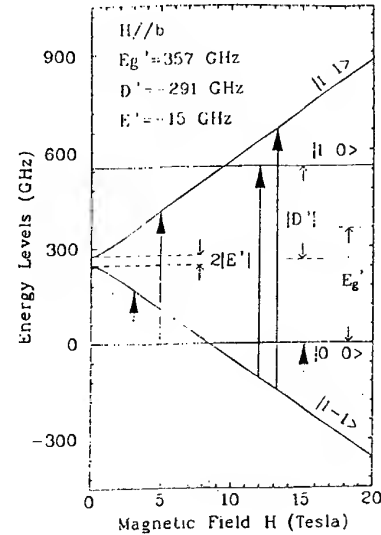


Fig 3 The transitions in NENP [7]

### Nonresonant Magneto spectroscopy

The interaction of electromagnetic radiation with a solid is most efficiently described by the complex tensor of the dielectric function, which includes the two complementary parts of absorption and dispersion [9]. Whereas in resonance spectroscopy essentially the absorption is investigated in *nonresonant* magneto spectroscopy the dispersion plays the dominant role. As a matter of fact *optical* nonresonant magneto spectroscopy can be used as a contact-less method to study quasi-DC magnetoconductivity dominated by the Shubnikov-de Haas effect. Such data for HgSe are reproduced in Fig. 4 using the strip-line technique in connection with 337  $\mu\text{m}$ -wavelength radiation of a HCN-laser [9]. For comparison also the data of the DC-magneto resistance using the four-probe technique is reproduced and corroborates the one-to-one correspondence of the observed oscillations. For this semiconductor experiment the off-resonance position was fulfilled for magnetic field intensities much

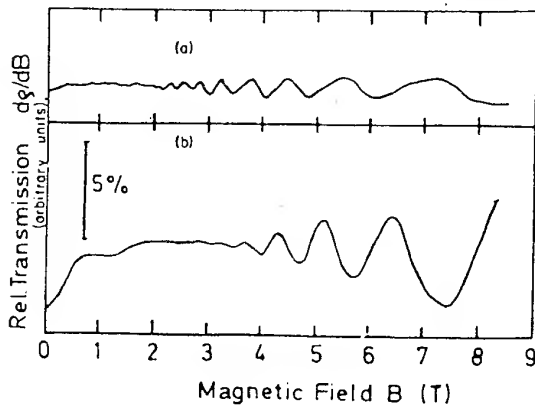
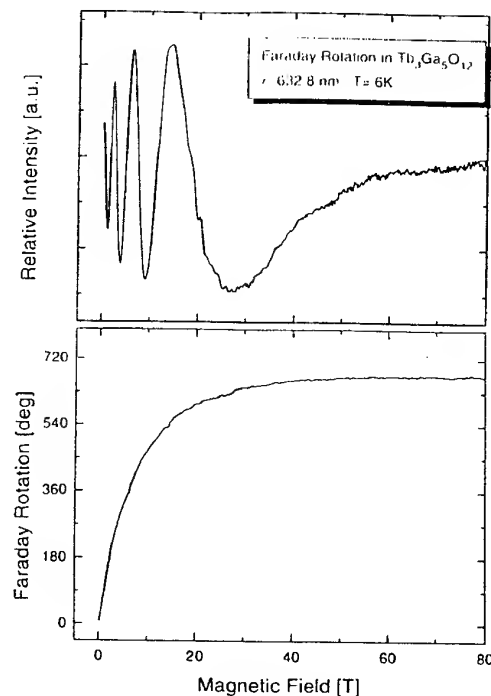
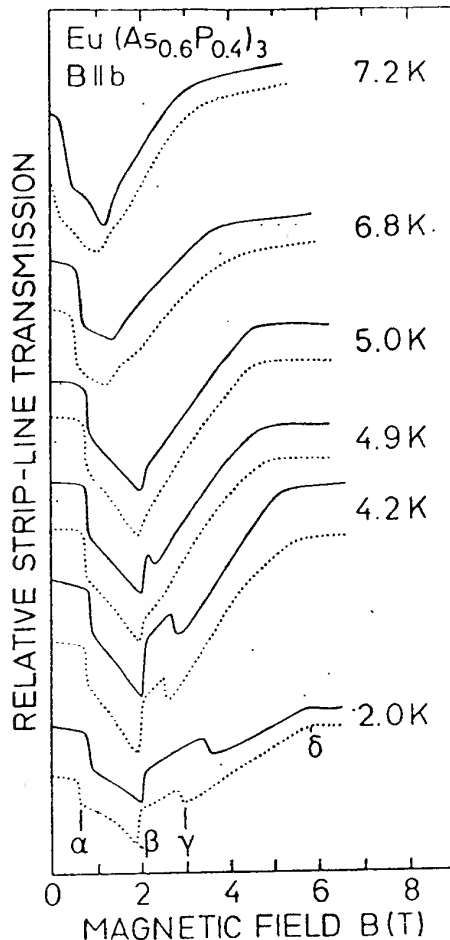


Fig. 4 The optical SdH-effect on HgSe [9]

Fig 5 Faraday rotation on  $\text{Tb}_3\text{Ga}_5\text{O}_{12}$  [10]

larger than the resonance condition in the long-wave limit. For magnetic material mostly the inverse condition at the low-field side of the resonance is applied. This means that the electromagnetic radiation is of the short-wavelength type, usually in visible range of the spectrum. In Fig. 5 we have reproduced the data of the megagauss Faraday effect on  $\text{Tb}_3\text{Ga}_5\text{O}_{12}$  in a setup using crossed polarizers [10]. One full oscillation in the data corresponds to a rotation of  $2\pi$  of the polarization vector of the linearly polarized incident radiation. Since in magnetic materials the Faraday effect is directly proportional to the magnetization of the material this quantity can directly be evaluated from the data.



Any magnetic phase transitions of a solid is reflected by a corresponding change in the optical properties. In this way even extremely small changes in the optical constants can be detected by the above mentioned strip-line technique as demonstrated for  $\text{Eu}(\text{As}_{0.6}\text{P}_{0.4})_3$  using submillimeter radiation of different wavelength. The curves for up and down sweep differ and indicate the hysteresis of the material, as shown in Fig. 6. The nearly vertical steps indicate the phase transitions.

### Summary

High field magnetospectroscopy applying a wide spectral range of electromagnetic radiation is an universal tool for the investigation of the microscopic interactions spins and orbital electrons in condensed matter. The ZOOM effect of the magnetic field the limits of field generation to higher and higher fields so that in future experiments the investigation of the "Hofstadter Butterfly" will be possible.

Fig.6 Optical detection of magnetic phases  
in  $\text{Eu}(\text{As}_{0.6}\text{P}_{0.4})_3$  [11]

### References

- 1 B. Lax, H.J. Zeiger, R.N. Dexter *Physica* 20 (1954) 818
- 2 K. Buchholz-Stepputtis, O. Portugall, M. von Ortenberg, W. Dobrowolski, Proc. "21st ICPS", Beijing 1992, ed. P. Jiang and H.-Z. Zheng, Singapore: World Scientific (1992) p. 1876
- 3 O. Portugall, N. Puhlmann, H.-U. Müller, M. Barczewski, I. Stölpe, M. von Ortenberg *Physica* 246/247 (1998) 54
- 4 M. von Ortenberg, K. Uchida, N. Miura, F. Heinrichsdorff, D. Bimberg, *Physica* 146/247 (1998)
- 5 D.R. Hofstadter, *Phys. Rev.* 14 (1976) 2239
- 6 F.D.M. Haldane, *Phys. Rev. Lett* 50 (1983) 1153
- 7 W. Lu, J. Tuchendler, M. von Ortenberg, J.P. Renard, *Phys. Rev. Lett.* 67 (1991) 3716
- 8 S. Luther, M. von Ortenberg, J. Tuchendler, J.P. Renard, *Physica* 21 (1995) 213
- 9 M. von Ortenberg, in "Infrared and Millimeter Waves" Vol. 3, ed. K.J. Button Academic Press (1980) 275
- 10 O. Tatsenko, V. Platonow, N. Puhlmann, M. von Ortenberg, to be published
- 11 M. Möllendorf, W. Bauhofer, W. Staguhn, J. Thielemann, M. von Ortenberg, *Solid State Comm.* 61 (1987) 591

## Ultrafast Terahertz Pulses: A Booming Technology

Klaas Wynne

Femtosecond Research Centre, Dept. of Physics and Applied Physics, University of Strathclyde, 107 Rottenrow, Glasgow G4 0NG, UK, E-mail: k.wynne@strath.ac.uk

### INTRODUCTION

Subpicosecond terahertz (THz) pulses or T-rays, have been around for quite some time[1] and the origins of free-space propagating few-cycle pulses can be traced back to the experiments of Heinrich Hertz in 1887. However, the recent confluence of better, smaller, faster and more reliable sources of femtosecond visible laser pulses and a renewed interest among solid state physicists and physical chemists in (time-resolved) far-infrared spectroscopy, has led to a boom in the interest in THz pulses. Over the past two to three years, many new techniques were developed for generating especially short (broadband) or especially powerful pulses. New techniques allow single shot detection of the THz pulse field as well as real-time and near-field imaging. Recent experiments have exploited the unique properties of T-rays to study ultrafast dynamics in systems varying from semiconductor heterostructures to highly excited Rydberg atoms in the gas phase. In this paper, I will attempt to give a brief (and hopefully objective) overview of what is new and interesting in this field.

### GENERATION OF T-RAYS

There are effectively two methods for generating subpicosecond THz pulses: *Photoconduction* or *optical rectification*. In photoconduction, a laser pulse incident on an absorbing semiconductor creates (real) charge carriers. Acceleration of these carriers in an electrical bias field gives rise to a transient photocurrent that radiates electromagnetic waves. In the far field the radiated electric field is given by  $E_r(t) \propto dJ_s(t)/dt$ , where  $J_s(t)$  is the time-dependent surface current. This method is typically used in conjunction with an antenna structure, which allows an external bias field to be applied. An antenna structure ideally suited to be used with low-power mode-locked lasers was developed in the 1980's at Bell Labs[2] and IBM,[3] and the most common method for generating and detecting T-rays is based on this work. In such a setup, two metal electrodes are laid down on a silicon or GaAs substrate, typically with a separation on the order of 100  $\mu\text{m}$ . [4] A beam of femtosecond laser pulses is focussed between the electrodes, in a spot with a diameter of a few microns. On the generation side the metal electrodes are biased with a few tens of volts and the generation of carriers by the pump laser triggers the emission of THz radiation. On the detection side, the incident THz beam accelerates the carriers created by the visible beam, resulting in a measurable photocurrent. Since the visible beam has to be focussed to a very tight spot in this method, only unamplified ultrafast lasers can be used. There is no overriding reason, however, why one should use such closely spaced electrodes. Large-aperture photoconducting antennas work very well for the generation of T-rays when pumped by amplified femtosecond laser pulses. The conversion efficiency (energy in the visible pulse to energy in the THz pulse) is on the order of 0.1%. Thus, 1 nJ THz pulses have been generated with a high repetition rate (250 kHz) femtosecond laser.[5] With low repetition rate (10-1000 Hz) ultrafast laser systems, far-infrared pulses with energies as high as 1  $\mu\text{J}$  have been generated.[6, 7] It has recently been suggested[8] that coherent control techniques might be used to boost the surface current and hence the T-ray conversion efficiency.

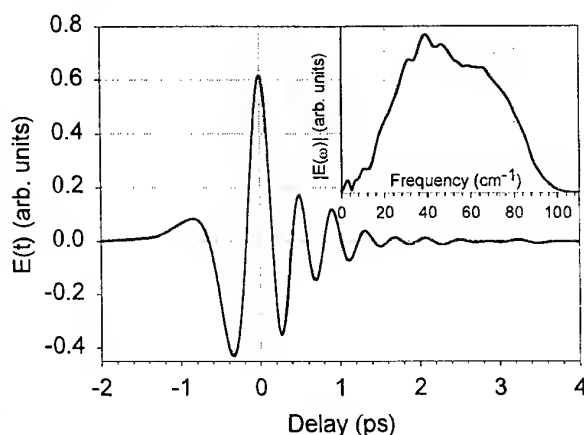


Figure 1. A THz pulse generated and detected in 1 mm long, <110> ZnTe crystals, by a 150 fs pulse at 800 nm. The inset shows the amplitude spectrum. The oscillations in the pulse are due to the finite crystal thickness. ( $1 \text{ THz} \approx 30 \text{ cm}^{-1}$ )

An external bias field is not strictly necessary for photoconductive generation of T-rays, as real carriers generated by a visible laser pulse can be accelerated in the field of the depletion layer of the semiconductor. This surface field will accelerate the carriers perpendicular to the surface of the semiconductor and hence the THz oscillating dipole will be perpendicular to the surface. Therefore, THz radiation generated through this effect is only observed if the angle of incidence of the exciting visible laser beam is nonzero. Typically, the effect maximizes at Brewster angle.

Optical rectification is distinct from photoconduction, in that the visible exciting beam creates virtual rather than real carriers. A more appropriate way to describe this is that the second-order susceptibility,  $\chi^{(2)}$ , of the crystal is used for difference frequency mixing. Thus, the second-order polarization can be written in the time-domain as  $P_{THz}^{(2)}(t) = \epsilon_0 \chi^{(2)} E_{vis}(t) E_{vis}^*(t)$ , which shows that the electric field of the THz pulse has the same shape as the intensity envelope of the visible exciting pulse. Already in the 1970's, it was shown[1] that picosecond pulses could be rectified in LiNbO<sub>3</sub> to produce pulses in the far infrared. In the last few years, it was discovered that optical rectification could be a very efficient method for generating T-rays if used appropriately. Since a subpicosecond THz pulse has a spatial length comparable to its center wavelength, it travels through a material at its phase-velocity. Therefore, for optimum conversion from visible to far-infrared wavelengths, one has to match the group-velocity of the visible pulse with the phase-velocity of the THz pulse.[9, 10] This condition is met in some zincblende, large bandgap semiconductors such as ZnTe and GaP [11] when the exciting laser has a center wavelength of *circa* 800 nm.

The reverse of optical rectification is electrooptic sampling: A THz pulse incident on an electrooptic crystal such as ZnTe will induce a birefringence through the Pockels effect. An ultrafast visible probe pulse with a variable delay co-propagating through the same crystal will experience a retardation that can be retrieved with balanced detection. Scanning the relative time-delay of the probe pulse, one can record a time-domain trace of the electric-field of the THz pulse. Using this method, signal-to-noise ratios, defined as the ratio of the THz pulse-peak to the noise background, as high as  $10^7$  have been reported.[11] However, the signal-to-noise ratio with which one can measure the peak of the THz pulse is typically on the order of  $10^2$ - $10^3$  in 100 ms. An exciting new variation on this technique, is the use of a chirped probe pulse.[12] A femtosecond pulse at 800 nm can be stretched and chirped to tens of picoseconds using a grating pair. If this chirped pulse is used in the electrooptic sampling process, there will be a relation between wavelength and relative time-delay. Thus, detection of this probe pulse with a diode-array detector allows one to measure the entire THz pulse shape in a single laser shot.

As rectification and electrooptic sampling are nonresonant effects, the minimum duration of the THz pulses that can be generated or detected is only limited by the thickness of the crystal scaled with the difference in phase and group-velocity. Thus, with *circa* 10-15 fs exciting pulses at 800 nm, it was shown that T-rays could be generated with detectable frequencies as high as 37[13] and even 44 THz.[14] At these large bandwidths, it is unavoidable that the T-ray spectrum will overlap with a phonon absorption band in the generating and detecting crystals, leading to large oscillations in the T-ray field trailing the main peak.

#### SPECTROSCOPY AND IMAGING IN THE TERAHERTZ DOMAIN

The frequency range between *circa* 100 GHz and a few THz has not been studied very well, as not many light sources are available. Fourier-transform infrared spectrometers (FTIRs) typically peter out at frequencies below about  $50 \text{ cm}^{-1}$  (1.5 THz) even when equipped with bolometric detectors and far-infrared optics. Microwave devices may go to frequencies as high as 1 THz but usually have poor tunability. Yet, this frequency range is of great interest as many low-frequency vibrational and rotational modes absorb here. The pseudo-bandgaps of superconductors and inter-bandgaps of semiconductor heterostructures are also in this range.

Over the last few years, many groups have used T-rays to study the low frequency absorption of liquids. For example, liquid water has a complicated absorption spectrum between 0 and  $1000 \text{ cm}^{-1}$  (30 THz) corresponding to librational and hydrogen bond motions. THz spectroscopy was used to study the low frequency end of the spectrum of water,[15, 16] other liquids[17, 18] and liquids in restricted geometries such as micelles.[19] Detailed comparisons could be made with Optical Kerr Effect spectroscopy (OKE), Raman scattering and molecular dynamics calculations. Similarly, THz pulses have been used to study the low-frequency absorption spectra of doped semiconductors[3] and semiconductor quantum wells.[20]

An exiting new application of THz pulses is T-ray imaging. T-ray imaging was first performed at Bell labs:[21] A T-ray beam was focussed to a tight spot and a sample scanned through the beam. Due to the long wavelengths at *circa* 1 THz, spatial resolution was limited to about a millimeter. However, because the transit-time of subpicosecond THz pulses can be measured with an accuracy of a few femtoseconds, it is possible to make tomographic images.[22] Thus, by measuring the internal reflections in a sample, for example, the various surfaces in a floppy disk, it is possible to detect hidden features. Very recently, several attempts have been made



to improve the lateral resolution by applying near-field techniques such as using small apertures in front of the sample[23] or T-ray generation in sub-wavelength regions. It was recently shown[24] that electrooptic sampling can be performed in parallel using a large area electrooptic crystal and an unfocussed probe beam, thus allowing the acquisition of T-ray images in real-time.

### TIME-RESOLVED EXPERIMENTS

It would seem that the most important feature that distinguishes femtosecond THz pulses from other sources of THz radiation, is their short duration and synchronization with other (visible light) sources. This makes it possible to perform time-resolved, pump-probe type experiments. Many absorption spectra (particularly at THz frequencies) in the condensed phase are very broad, which makes it nearly impossible to extract any information about excited state properties. Yet it is these excited state properties that are often most interesting, for example, in the study of chemical reaction dynamics or the conduction and trapping properties of carriers in semi- and superconductors.

The first such visible-pump, THz-probe experiments were performed on semiconductors,[25-30] semiconductor superlattices[31] and superconductors.[32] Excitation of a semiconductor above the bandgap with a visible ultrafast pulse creates a plasma of conduction band electrons. This gives rise to a transient absorption, which can be described using the Drude model. The time-resolved experiment gives direct information about the electron-mobility and the carrier lifetime. By pumping well above the bandgap, information can be obtained about the rates at which the carriers scatter between the different valleys.[26, 28] Recently, there has been a surge of interest in the study of Bloch oscillations, first predicted at the beginning of the century. Various groups have used a femtosecond visible excitation pulse to create coherent superpositions of Wannier-Stark exciton states in superlattices.[33] Delayed probing with a THz pulse, shows that the carriers slosh back and forth between the quantum wells. In superconductors, excitation with a visible pulse causes the breakup of Cooper pairs and collapse of the superconducting gap.[32] THz probe pulses are ideally suited to monitor these processes and the subsequent cooling and reestablishment of superconductivity.

An exciting new application of visible-pump, THz-probe spectroscopy is the study of the role of low-frequency modes in chemical and biological reaction dynamics. It is well known that, for example, low frequency librational modes in liquids play an important role in the dynamics of chemical reactions but surprisingly little is known about their microscopic properties. Two recent experiments[34, 35] have shown that an ultrafast electron-transfer reaction in solution causes a non-instantaneous reaction of the solvent. In these experiments a dye molecule in solution is excited by a visible laser pulse from its neutral ground state to its strongly dipolar excited state. The sudden creation of this dipole moment on the dye causes the surrounding polar solvent molecules to respond by rotating to adjust to the new local electric field. It was observed[35] that this sets off coherent librational wavepackets that die out in a few picoseconds.

The time-resolved experiments described so far have all used relatively low-power THz pulses with which one can passively observe reactions as they proceed. With high-power pulses, it is possible in principle to interfere with reactions actively. That this is technically non-trivial can be shown with an approximate calculation. To interfere with a reaction, one has to be able to shift the energy levels involved by a significant amount. If it is assumed that the reactant and product states have a permanent dipole moment difference of 10 D, then using the interaction Hamiltonian  $H = -\vec{\mu} \cdot \vec{E}$ , it follows that a field strength of about  $10^6$  V/cm is required to get a shift of the energy levels comparable with a typical vibrational quantum ( $\sim 170$  cm<sup>-1</sup>). As such high fields are still difficult to achieve, research in this area has concentrated on Rydberg atoms in the gas phase, as these have generally very large dipole moments. The high-energy THz pulses are generated using large area dipole antennas (*circa* 2x2 cm<sup>2</sup>), biased with large DC fields (5-10 kV/cm) and pumped with high energy ( $\sim 1$  mJ) *circa* 100 fs pulses, to produce THz pulses with an energy on the order of 1  $\mu$ J.[36, 37] The Rydberg atoms are created by multiphoton excitation of rare-earth atoms with ultrashort pulses, putting an electron in a Kepler orbit. The high-energy THz pulses, which have a focussed peak field of about 5-20 kV/cm,[36, 37] can be used to ionize the Rydberg electron or to create Rydberg wavepackets under experimental control. There has been a fair bit of controversy recently over the exact shape of the THz pulse in the focus: Since the antenna diameter is comparable to the distance between the antenna and the sample, the whole setup is in the near-field.[38] This results in severe reshaping of the THz pulse on propagating towards the sample.

### CONCLUSION

The current record bandwidth for a THz pulse is 37 THz[13] but there is no reason to believe that this could not be improved upon. Using the simple time-bandwidth relation  $\Delta\nu \cdot \Delta\tau = 0.32$ , it follows that with the shortest visible pulses achievable, *circa* 4-5 fs,[39] usable power at frequencies from 0 to 160 THz ( $\lambda = 1.8$   $\mu$ m) could be

achieved. As femtosecond lasers continue to shrink in size, it may be expected that ultrafast THz devices may well take over from FTIRs as general-purpose IR spectrometers. As it was recently shown that an entire THz time-domain trace could be acquired in a single shot,[12] these devices would combine the reliability and accuracy of FTIR with real-time speeds. The most significant aspect of ultrafast THz pulses, however, is that they are synchronized with visible or ultraviolet pulses, allowing time-domain spectroscopy. Particularly the prospect of (coherently) controlling reactions rather than just passively observing them is seen by some as one of the most exciting avenues for future research.

#### REFERENCES

1. K.H. Yang, P.L. Richards and Y.R. Shen, Appl. Phys. Lett. **19**, 285 (1971).
2. P.R. Smith, D.H. Auston and M.C. Nuss, IEEE J. Quantum Electron. **24**, 255-260 (1988).
3. D. Grischkowsky, S. Keiding, M. Exter, van and C. Fattinger, J. Opt. Soc. Am. **B7**, 2006-2015 (1990).
4. P.G. Huggard, C.J. Shaw, J.A. Cluff and S.R. Andrews, Appl. Phys. Lett. **72**, 2069-2071 (1998).
5. G. Mouret, *et al.*, Microwave Opt. Tech. Lett. **17**, 23-27 (1998).
6. D. You, R.R. Jones, P.H. Bucksbaum and D.R. Dykaar, Opt. Lett. **18**, 290-292 (1993).
7. E. Budiarto, J. Margolies, S. Jeong, J. Son and J. Bokor, IEEE J. Quantum Electron. **32**, 1839-1846 (1996).
8. A. Hache, *et al.*, Phys. Rev. Lett. **78**, 306-309 (1997).
9. A. Nahata, A.S. Weling and T.F. Heinz, Appl. Phys. Lett. **69**, 2321-2323 (1996).
10. Q. Wu and X.-C. Zhang, Appl. Phys. Lett. **70**, 1784-1786 (1997).
11. Q. Wu and X.-C. Zhang, Appl. Phys. Lett. **68**, 1604-1606 (1996).
12. Z. Jiang and X.-C. Zhang, Appl. Phys. Lett. **72**, 1945-1947 (1998).
13. Q. Wu and X.-C. Zhang, Appl. Phys. Lett. **71**, 1285-1286 (1997).
14. A. Bonvalet, M. Joffre, J.L. Martin and A. Migus, Appl. Phys. Lett. **67**, 2907-2909 (1995).
15. C. Rønne, *et al.*, J. Chem. Phys. **107**, 5319-5331 (1997).
16. J.T. Kindt and C.A. Schmuttenmaer, J. Phys. Chem. **100**, 10373-10379 (1996).
17. D.S. Venables and C.A. Schmuttenmaer, J. Chem. Phys. **108**, 4935-4944 (1998).
18. B.N. Flanders, R.A. Cheville, D. Grischkowsky and N.F. Scherer, J. Phys. Chem. **100**, 11824-11835 (1996).
19. D.M. Mittleman, M.C. Nuss and V.L. Colvin, Chem. Phys. Lett. **275**, 332-338 (1997).
20. J.N. Heyman, R. Kersting and K. Unterrainer, Appl. Phys. Lett. **72**, 644-646 (1998).
21. B.B. Hu and M.C. Nuss, Opt. Lett. **20**, 1716-1718 (1995).
22. D.M. Mittleman, R.H. Jacobsen and M.C. Nuss, IEEE J. Selected Topics Quantum Electron. **2**, 679-692 (1996).
23. S. Hunsche, M. Koch, I. Brenner and M.C. Nuss. *THz Imaging in the Near-Field*. in *CLEO/QELS'97 Technical Digest*. 1997. Baltimore: OSA.
24. Q. Wu, T.D. Hewitt and X.-C. Zhang, Appl. Phys. Lett. **69**, 1026-1028 (1996).
25. B.I. Greene, J.F. Federici, D.R. Dykaar, A.F.J. Levi and L. Pfeiffer, Opt. Lett. **16**, 48-49 (1991).
26. P.N. Saeta, J.F. Federici, B.I. Greene and D.R. Dykaar, Appl. Phys. Lett. **60**, 1477-1479 (1992).
27. W. Fishler, P. Buchberger, R.A. Höpfel and G. Zandler, Appl. Phys. Lett. **68**, 2778-2780 (1996).
28. S.E. Ralph, Y. Chen, J. Woodall and D. McInturff, Phys. Rev. B **54**, 5568-5573 (1996).
29. J. Zielbauer and M. Wegener, Appl. Phys. Lett. **68**, 1223-1225 (1996).
30. S.S. Prabhu, S.E. Ralph, M.R. Melloch and E.S. Harmon, Appl. Phys. Lett. **70**, 2419-2421 (1997).
31. R.H.M. Groeneveld and D. Grischkowsky, J. Opt. Soc. Am. **B11**, 2502-2507 (1994).
32. J.F. Federici, *et al.*, Phys. Rev. **B46**, 11153-11156 (1992).
33. T. Dekorsy, P. Leisching, K. Köhler and H. Kurz, Phys. Rev. B **50**, 8106-8109 (1994).
34. G. Haran, W.-D. Sun, K. Wynne and R.M. Hochstrasser, Chem. Phys. Lett. **274**, 365-371 (1997).
35. R. McElroy and K. Wynne, Phys. Rev. Lett. **79**, 3078-3081 (1997).
36. C. Raman, C.W.S. Conover, C.I. Sukenik and P.H. Bucksbaum, Phys. Rev. Lett. **76**, 2436-2439 (1996).
37. R.B. Vrijen, G.M. Lankhuijzen and L.D. Noordam, Phys. Rev. Lett. **79**, 617-620 (1997).
38. E. Budiarto, N.-W. Pu, S. Jeong and J. Bokor, Opt. Lett. **23**, 213-215 (1998).
39. A. Baltuska, Z. Wei, M.S. Pshenichnikov, D.A. Wiersma and R. Szipocs, Appl. Phys. B **65**, 175-188 (1997).

# TERAHERTZ TECHNOLOGY, A NEW ERA FOR WAVEGUIDE?

by C. M. Mann

Rutherford Appleton Laboratory, Didcot, Oxon, UK.

## ABSTRACT

Waveguide has for many years been the preferred choice for the low noise mixers and high efficiency frequency multipliers used in the millimetre, submillimetre and terahertz region. However, the prohibitive expense and circuit constraints relating to the precision machining required for component fabrication has limited its use to single ended receiver systems intended for radio telescopes and remote sensing instrumentation used in atmospheric science.

The use of micromachining to fabricate waveguide cavities has now been demonstrated by a number of workers in the field using a variety of techniques such as X-ray lithographic LIGA, laser ablation and silicon machining to name a few. In particular, a new promising technique that makes combined use of a thick Ultra Violet (UV) based resist has been developed. Its use allows the low cost realisation of complex three dimensional waveguide cavities thus allowing the combination of different sized waveguides, notch filters and suspended substrate channels. When combined with anisotropic silicon processing it is possible to form a high quality horn antenna. Use of new emerging micromachining techniques promises a cheap method of waveguide circuit manufacture, and in addition can often allow the fabrication of complex circuit structures that are simply impossible to realise using conventional machining techniques.

## INTRODUCTION

Waveguide's overriding limitation has been its requirement for sub-miniature circuit assembly and the prohibitive cost of the conventional machining used to realise millimetre and submillimetre wave waveguide cavities. Its use has therefore been limited to specialist applications such as remote sensing or radio astronomy where cost is not the driving factor.

### Active device

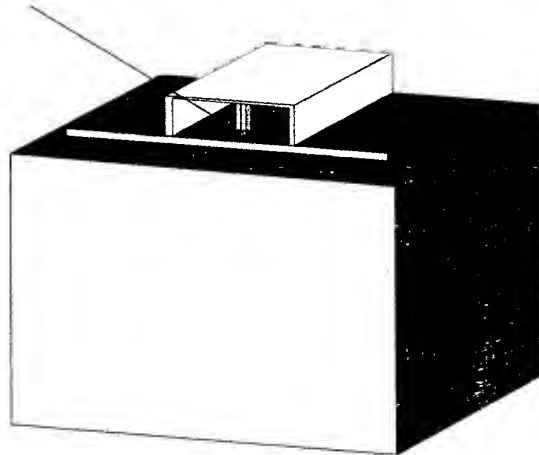


Figure 1: *Hollow metal pipe waveguide of Brown et al*

Early attempts at reducing the cost of millimetre and submillimetre wave components concentrated on the development of 'open structure' type devices. These in general consist of a planar antenna combined with a dielectric lens or micromachined horn antenna. Such devices have been used with great success but have mainly been confined to single ended mixer/detector circuits.

More complex circuits such as frequency multipliers or harmonic mixers greatly simplify system complexity but are difficult to realise using open structure circuit architecture. Conversely such devices have been realised for many years using waveguide circuitry, mainly because its natural frequency selectivity greatly eases circuit layout and

design constraints. To date the best harmonic mixers and multipliers have been realised using waveguide but still waveguide has not been the favoured choice for more general applications. However, recently a number of technological developments have led to the reassessment of waveguide as the preferred circuit medium. These include its demonstration at terahertz frequencies and the improved speed of accurate finite element circuit analysis. However, without doubt the most important reason has been the innovative use of lithographic micromachining to form waveguide circuitry.

The use of lithography to produce micromachined waveguide was first reported by Brown et al<sup>1</sup>. A schematic showing the basic concept of their hollow metal pipe waveguide technique is shown in figure 1. A photoresist waveguide former is patterned onto the surface of a semiconductor substrate. An active device such as a Schottky diode or Resonant Tunnelling Diode (RTD) is formed on the surface of the substrate and an electroformed pillar is fabricated on top of it. Finally the outer skin of the waveguide former is coated in metal and the unwanted photoresist removed by dissolution in a suitable solvent. It quickly became apparent that by using this and other lithographic techniques the cost of millimetre and submillimetre wave waveguide components could be dramatically reduced.

### TERAHERTZ WAVEGUIDE

In addition to the features described above, waveguide has a few additional advantages. It is possible to design horn antenna that have very low loss and near perfect radiation characteristics. Also, movable backshort tuners can be incorporated to allow the empirical adjustment of the RF circuit. There is currently a remote sensing requirement for heterodyne mixers operating at 2.5THz. Such mixers can be realised relatively easily using primitive corner reflectors and 4-lambda whiskers. However, such mixers have a relatively poor beam quality and are renowned for being mechanically unstable. In addition, the real impedance presented by the corner reflector antenna requires the use of unreasonably small diodes.

In order to try to circumvent these problems workers at the Rutherford Appleton Laboratory switched effort to the development of a space qualified 2.5THz waveguide mixer<sup>2</sup>. In order to realise the RF circuit, use was made of a micromachined 'planar whisker' which contacts an 0.5 $\mu$ m diameter University of Virginia NF1T2 Schottky diode. The mixer cavity is machined using state of the art conventional techniques and incorporates a corrugated feedhorn and a movable backshort. Recently this work has been further developed<sup>3</sup> and the resulting waveguide mixers have now effectively replaced those implementing a corner cube in terms of LO requirement, radiation pattern, reliability and performance. One such mixer is shown below in figure 2.

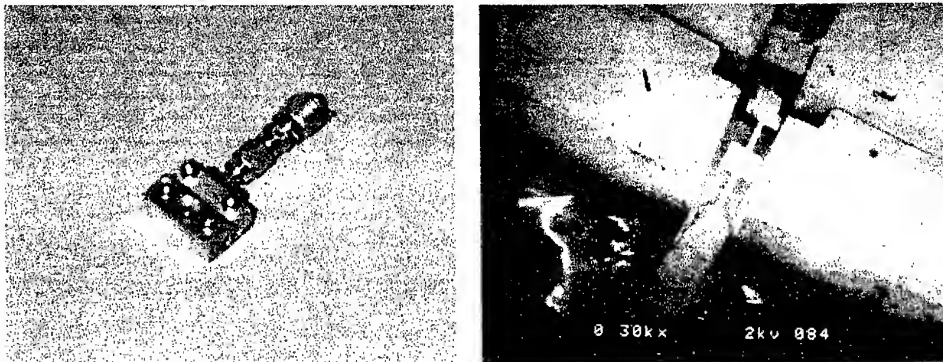


Figure 2: An RAL 2.5THz waveguide mixer and the planar whisker RF circuit

Finally, workers at JPL have also demonstrated a 2.5THz waveguide mixer. Similar performance to the RAL mixers has been obtained, however, the JPL mixer, for which the waveguide cavity is also conventionally machined, makes use of a micromachined GaAs chip incorporating a planar Schottky diode<sup>4</sup>. It should now be apparent that both whiskered and planar waveguide circuits are able to operate successfully deep into the terahertz region and are currently defining the state of the art.

### MICROMACHINED WAVEGUIDE

Once the potential for micromachined lithographic waveguide had been demonstrated new, more versatile fabrication approaches were sought. Of these by far the most exciting arose out of the development of a new ultra violet (UV) based lithographic resist SU-8<sup>5</sup>. This resist can be imaged to form vertical structures to depths of a

millimetre or more. Wall angles of  $\approx 89$  degrees can be obtained routinely making this approach perfectly adequate for most applications *down* to around 200GHz. In addition, multiple exposure techniques can be used that allow 3-dimensional structures to be realised. An example of this is shown in figure 3. The scanning electron micrograph (SEM) shows a resist structure that is  $\approx 1\text{mm}$  high and has been superimposed over an earlier image that is  $\approx 500\mu\text{m}$  high. Use of this technique allows straightforward fabrication of complex waveguide cavities that cannot be realised via the use of conventional machining.

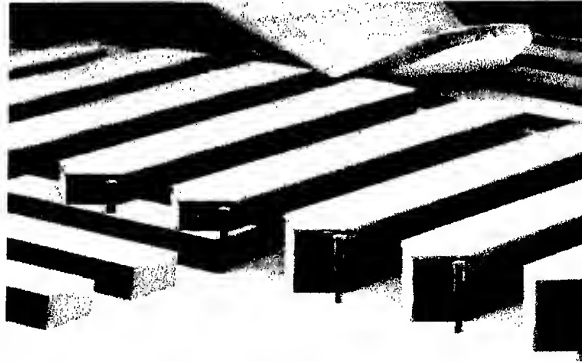


Figure 3: An example of split level deep UV lithography

Use of SU-8 resist has been combined with the anisotropic etching of silicon wafers to form an integrated waveguide to horn transition and a new novel type of horn antenna<sup>6</sup>. The process used to achieve this is shown in figure 4.

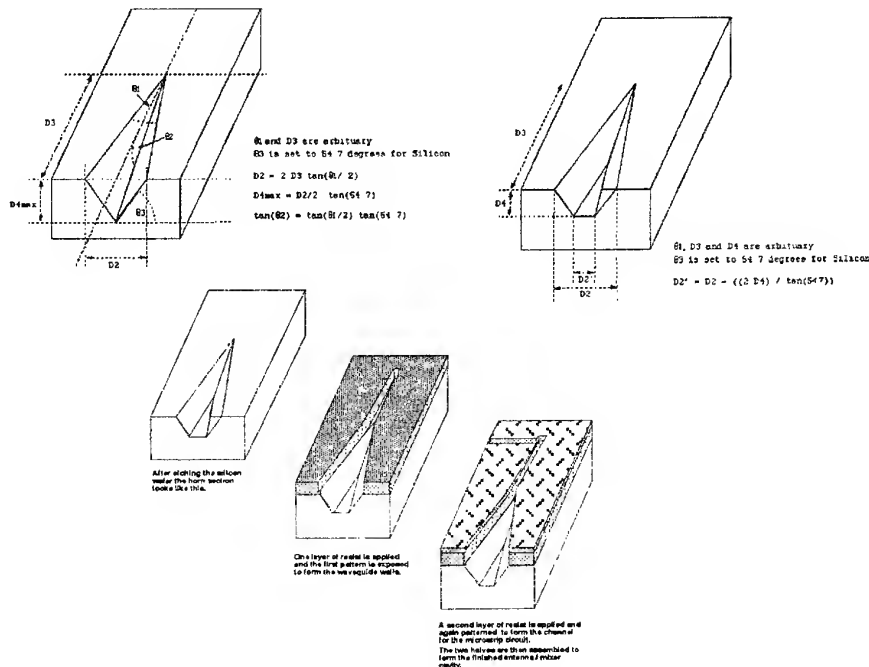


Figure 4: The fabrication process for the composite micromachined mixer cavity

Anisotropic etching of a silicon wafer can be used to produce either vertical walls or walls that incline at an angle of 54.7 degrees depending on the orientation of the crystal plane etched in the wafer. Previous techniques have used the latter method to form a pyramidal recess in the surface of the wafer, thus creating a horn with a large flare angle and wide beam widths, necessitating the use of a machined extension to improve the beam quality<sup>7</sup>. In

this case, a mask with a shallow flare angle is carefully aligned to the crystal orientation of the silicon wafer, thus resulting in a tapered 'V' type groove in which the side walls are inclined at an angle of 54.7 degrees to the horizontal. The wafer with these recesses is then planarised and coated with a thick layer of photoresist. For the 600 GHz mixer design shown in figure 5 the resist is 200 $\mu$ m deep. This mixer cavity was based on that of a 600 GHz planar diode waveguide mixer<sup>8</sup>.

Figure 5 shows a finished 600GHz mixer cavity. The main waveguide circuit incorporates microstrip channels, waveguide transformers and the antenna itself. The two halves of the mixer are fixed together, alignment being carried out with the aid of raised and recessed pins and holes.

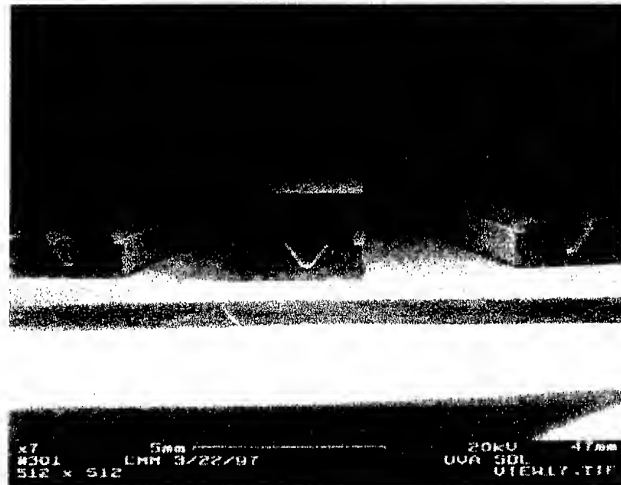


Figure 5: An SEM image of an assembled and split 600 GHz waveguide mixer cavity

## CONCLUSIONS

The future for waveguide looks very bright. Waveguide circuits at terahertz frequencies have recently been reported showing that losses are not as prohibitive as once thought. The use of micromachining techniques holds the potential to remove the last hurdle to waveguide in its domination as the circuit medium of choice, i.e., cost. The race is now on for the first RF demonstration of an all lithographically produced terahertz waveguide device.

## REFERENCES

- <sup>1</sup> D.A. Brown, A. S. Treen, N. J. Cronin, *Micromachining of Terahertz Waveguide Components with Integrated Active Devices*, 19th International Conference on Infrared and Millimetre Waves, Sendai, Japan, 1994.
- <sup>2</sup> B. N. Ellison, M.L. Oldfield, D.N. Matheson, B.J. Maddison, C.M. Mann, S. Marazita, T. W. Crowe, P. Maaskant, W. M. Kelly, *First Results for a 2.5 THz Schottky Diode Waveguide Mixer*, 7th International Symposium on Space Terahertz Technology, University of Virginia, March 1996.
- <sup>3</sup> C. M. Mann, D. N. Matheson, B. N. Ellison, M. L. Oldfield, B. P. Moyna, J. J. Spencer, D. S. Wilsher, and B. J. Maddison, *'On The Design And Measurement Of A 2.5THz Waveguide Mixer'* 9th International Conference on Space THz Technology, Pasadena, CA, March 1998
- <sup>4</sup> P. H. Siegel, M. Gaidis, S. Martin, J. Podosek, U Zimmermann, *'2.5THz GaAs Monolithic Membrane-Diode Mixer'*, 9th International Conference on Space THz Technology, Pasadena, CA, March 1998
- <sup>5</sup> K. Y. Lee, N. LaBianca, S. A. Rishton, S. Zolgharnain, J. D. Gelorme, J. Shaw, T. H.-P. Chang, *Micromachining Applications of a High Resolution Ultra thick Photoresist*, J. Vac. Sci. Technol. B 13(6), Nov./Dec. 1995.
- <sup>6</sup> T. W. Crowe, P. J. Koh, W. L. Bishop, C. M. Mann, J. L. Hesler, R. M. Weikle, P. A. Wood, D. N. Matheson, *Inexpensive Receiver Components for Millimetre and Submillimetre Wavelengths*, 8th International Symp. on Space THz Technol., Harvard University, March 1997.
- <sup>7</sup> G. M. Rebeiz, *Millimetre-Wave and Terahertz Integrated Circuit Antennas*, Proc. IEEE Vol. 80, No. 11, pp. 1748-1770, Nov. 1992.
- <sup>8</sup> J. L. Hesler, W. R. Hall, T. W. Crowe, R. M. Weikle, II, B. S. Deaver, Jr., R. F. Bradley, and S.-K. Pan, *Fixed-Tuned Submillimetre Wavelength Waveguide Mixers Using Planar Schottky Barrier Diodes*, IEEE Trans. Microwave Theory Tech., May 1997.

## Technology for Electron Cyclotron Heating and Current Drive in ITER

M. Makowski

ITER Garching Joint Work Site, Boltzmannstr. 2  
85748 Garching, Germany

### Abstract

Electron cyclotron heating and current drive (EC H&CD) systems in concert with other forms of auxiliary heating will provide a wide variety of functions on ITER, the International Thermonuclear Experimental Reactor. The scale of the proposed system presents many challenges with regard to source technology, efficient long-distance high-power transmission, and injection of power into the tokamak. EC H&CD is in a good position to be a major source of auxiliary power on ITER due to the simplicity of the injection physics, the flexibility provided by the transmission technology, its high delivered power density, and the range of applications it provides.

### Introduction

On ITER, the International Thermonuclear Experimental Reactor, electron cyclotron heating and current drive (EC H&CD) can be used to assist in plasma initiation and shut-down, to access the H-mode confinement in D-T Ohmic plasmas, to provide on- and off-axis current drive for profile control and stabilization of MHD instabilities, for wall conditioning, and for bulk heating to increase the plasma temperature to ignition values.

With the design developed during the EDA (Engineering Design Activity) a total of 50 MW of power is delivered to the torus using two equatorial ports 2.6 m in height by 1.6 m in width. With the current design, this allows for injection of up to ~40 MW per port. Evacuated waveguide transmission lines carry power from the gyrotron sources to the port up to the launcher. Toroidally steerable mirrors inject the power into the torus through a slotted shield-blanket mounted on the port plug assembly.

### Physics Overview

Modeling of standard ignited scenarios and advanced discharges has shown that launch of elliptically polarized ordinary-mode electron

cyclotron waves from the low-field side of the device provides the necessary capabilities for start-up, heating, and current drive

In order to provide these capabilities with a single frequency source over the full range of central magnetic fields an injection system providing some steering capability must be used. Toroidal steering is found to provide significantly greater functionality than poloidal steering. The ability to provide some frequency tuning would increase the flexibility of the system. For most scenarios, current drive efficiencies in the range  $(0.1 - 0.3) \times 10^{20} \text{ A/Wm}^2$  are expected.

In addition, two 3 MW start-up systems are required at lower frequencies (90 and 140 GHz). No steering capability is required for this application, but toroidal injection at a fixed angle of  $\sim 20^\circ$  improves the absorption efficiency. The start-up systems can also be used for wall conditioning.

### ITER Systems

Gyrotrons have been selected for the sources on ITER due to their demonstrated ability to generate high power for a long pulse length with high efficiency when operated with a depressed collector. The goal of the R&D now in progress is the demonstration of steady-state,  $\geq 1 \text{ MW}$  output power,  $\sim 50\%$  efficient, 170 GHz sources. The results of the ITER gyrotron development program are summarized in Fig. 1 which plots output power versus pulse length for prototype 170 GHz tubes developed within the program. Both diode and triode tubes have been developed and tested. During the EDA the following have been achieved on separate occasions:

- 3.6 MJ at 170 GHz in long pulse (450 kW, 8 s) operation (Japanese Home Team);
- Demonstration of a single stage depressed collector at 110, 140, and 170 GHz (Multiple Parties);
- Demonstration of CW operation at 110 GHz (US Home Team);

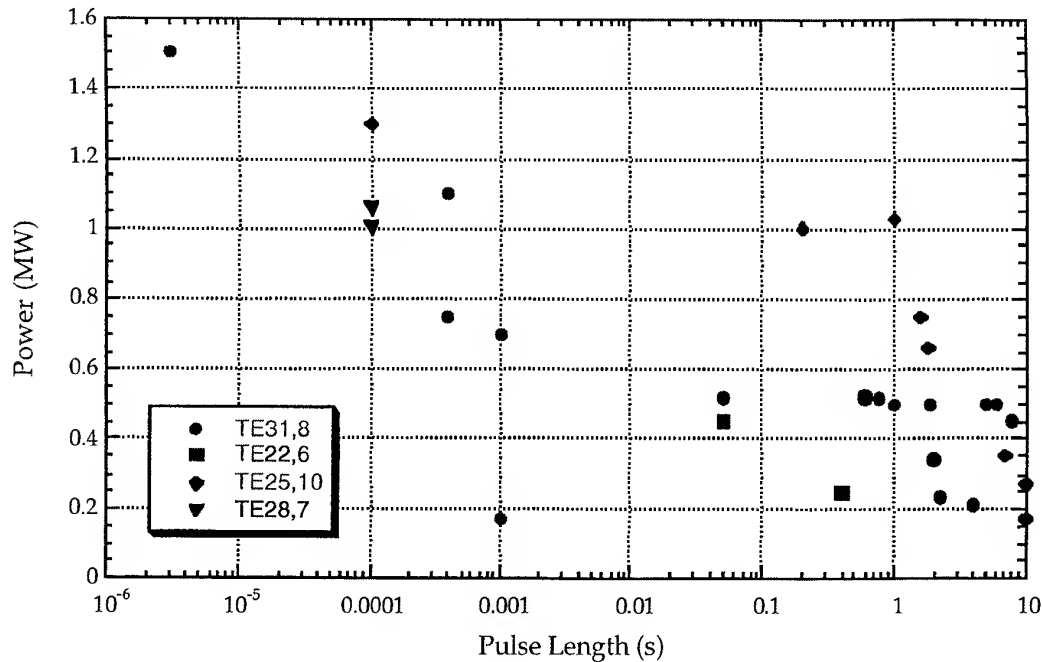


Fig. 1. Results from the ITER 170 GHz gyrotron development program are displayed as a plot of achieved output power versus pulse length. Both diode and triode type tubes have been developed and operation in several different volume modes demonstrated. A variety of volume modes, as shown in the legend, have been tested in the course of the development.

- Demonstration of 1 MW output at up to 1 s at 170 GHz and 2 s at lower frequencies (Russian Home Team).

Thus all performance goals have been demonstrated at least separately. The goal of the work in the EDA Extension is the integral demonstration of a full performance tube.

Diamond disks have been chosen for use as the barrier window on the torus and will also be used as the output window on the tubes due to the material's high thermal conductivity, low loss tangent, high mechanical strength, and availability in large diameters ( $> 100$  mm). As a result of the material properties it is possible to fabricate a single disk, 1 MW, 170 GHz, edge cooled window with water as the coolant. The more demanding application is that of barrier window, as here, not only must the window transmit the power with low loss as for the gyrotron output window, but it must also withstand 0.5 MPa pressure as part of the primary confinement and be resistant to neutron and gamma irradiation.

One of the major successes of the development program has been the demonstration of the needed component in the form of a water cooled single disk diamond window. The work was a

collaborative effort between the European and Japanese Home Teams. Within a two year period the technology to manufacture large diameter diamond disks was developed, the material quality improved to the point that 2 MW CW windows are theoretically feasible, the technique to bond the disks to metal tubes was developed, prototype bonded disks were subjected to the tube bakeout cycle establishing the feasibility of their use on gyrotrons, high power tests of the material at 170 GHz were made, and a complete window assembly was fabricated, installed and successfully tested on a 170 GHz high power tube.

In order to prevent leakage of water into the vacuum in the event of a failed window, the edge may be "encased" with a thin  $\sim 0.5$  mm thick layer of electrodeposited copper. The window temperature does not increase significantly with the added thermal resistance of the copper layer due to the high thermal conductivity and low loss tangent of diamond.

Evacuated circular corrugated waveguide is used to transmit the power from the gyrotron to the torus. The waveguide run is composed of standard waveguide components such as miter bends, DC breaks, and vacuum pumping sections. Quasi-optical components, such as



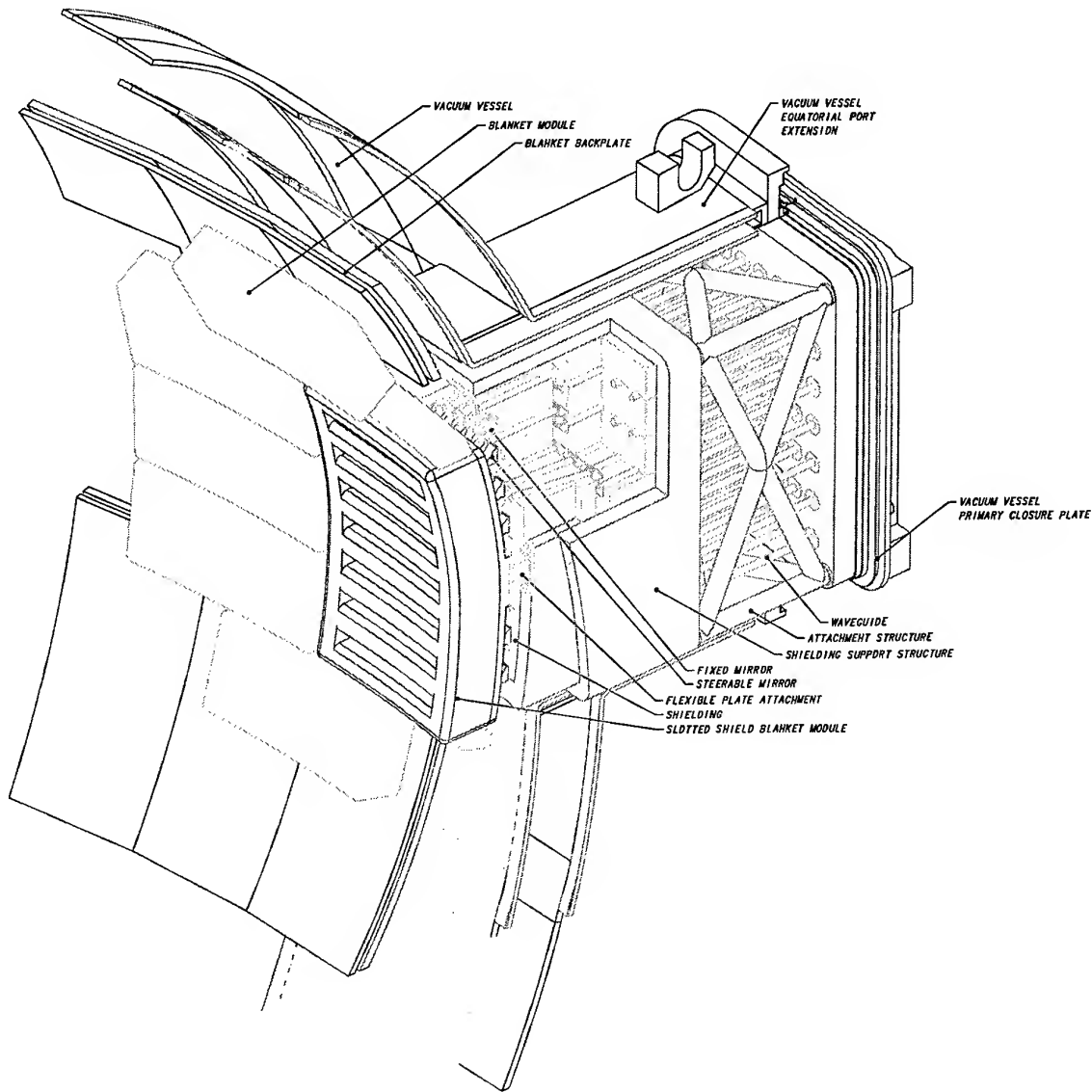


Fig. 2. Isometric view of the EC H&CD in-vessel launcher system as viewed from inside the vacuum vessel. The toroidally slotted shield-blanket is in the foreground. Fixed and steerable optics are located in the region immediately behind the shield-blanket. A pair of miter bends are used to form a labyrinth with staggered shielding on either side to prevent neutron streaming. Waveguide runs continue to the closure plate at the back of the port.

polarizing and phase correcting optics, are also used at the output of the gyrotron to condition the output beam for long distance transmission. The estimated transmission efficiency for the system is 85%. As they enter the port the waveguides are configured in a 7 x 7 array allowing injection of ~40 MW/port.

Specialized designs are required to transport the power through the interspace, the region of the port between the cryostat and vacuum vessel. This is accomplished through the use of mode conserving sections of deformable waveguide.

An S-shaped deformation arises as a result of the relative motion between the two structures which, due to the symmetry of the deformation, gives rise to specific length to diameter ratios for which the net mode conversion of the bend is nearly zero. Low-power measurements in scaled experiments have verified the predicted performance.

In an effort to standardize interfaces between systems as much as possible, the concept of the integrated equatorial port has been developed. Here a standardized port-plug assembly

provides a frame which houses the differing systems such as diagnostics, RF heating systems (electron cyclotron, ion cyclotron, and lower hybrid), breeder blankets, and limiters. Figure 2 shows this concept as it applies to the EC H&CD system.

As the waveguides pass the port-plug, a "dog-leg" is formed using a pair of miter bends in order to reduce neutron streaming. The waveguide runs are terminated within the equatorial port at a point behind the backplate. The beams radiating from the ends of the waveguides illuminate an array of fixed mirrors which reflect the beams downward onto a set of steerable mirrors. The vertical axis of rotation of the second mirror allows the beams to be steered toroidally as required for heating and current drive. Waveguides are shifted to one side of the port in order to obtain the greatest possible toroidal injection angles. Toroidal injection angles in the range  $15^\circ - 45^\circ$  can be achieved for most of the array and larger angles for restricted portions of it.

#### Future Work

Future work will concentrate on developing detailed designs of critical components and reducing the system cost.

Design studies and detailed analysis have shown that a steerable injection system is feasible but that a reliable design for the steering mechanism, bearings, and cooling system will be needed. For this reason, a remote steering concept has also been proposed which potentially does not require mechanical components in the vacuum vessel. The remote steering concept uses square corrugated waveguide and is based on the principle that in highly oversized waveguide an input pattern consisting of a restricted spectrum of wavenumbers is repeated periodically with a characteristic length. Thus a beam injected into the waveguide at an angle at one end of the waveguide is launched with the same angle at the output end. The length can be reduced by one half due to symmetry. In this case, a beam injected at angle  $\theta_{in}$  is launched at  $-\theta_{in}$ .

Development can be extended based on two considerations. The first is cost. The diamond window appears to be the ultimate window and is expected to remain an expensive item so alternative concepts should still be sought. Development of higher unit power tubes would also aid in reducing system costs. This can be accomplished either through improvements in

the current (cylindrical cavity) tube design or by means of an alternative, but related type of tube, the coaxial gyrotron. Secondly, in order to improve the flexibility of the system and provide as many functions as possible, some degree of frequency tunability would be very useful. The desired frequency agility can likely be achieved with "course" step-tunable gyrotrons (widely spaced discrete frequencies matched to the gyrotron oscillation frequencies and corresponding to passbands in the single disk windows). One of the challenges in this area is the development of efficient multi-mode internal mode-converters. For finer step-tuning or for a continuously tunable source such as the free electron maser, a true wide-band window, such as a Brewster angle window, is required.

#### Summary

The design of the electron cyclotron system for ITER provides the desired capabilities in the areas of start-up, heating, and current drive. Both on- and off-axis current drive is possible over the desired range of central fields. An injected power density of  $\sim 40$  MW/port ( $\sim 10$  MW/m<sup>2</sup>) is achievable while still complying with ITER design constraints imposed by shielding, safety, and maintenance as well as conforming to the envelope provided by the integrated port-plug concept.

The overall system has been designed to be compatible with future technologies. The goal is to provide a system which maintains its inherently broadband characteristics. In this way step tunable gyrotrons and continuously tunable masers can be adopted as these technologies mature. Generally, windows are the most frequency sensitive elements in the system. Broadband window options included a double disk diamond window and a Brewster angle window.

#### Acknowledgments

The contributions of the Home Teams are gratefully acknowledged and appreciated. This report was prepared as an account of work performed within the ITER Joint Central Team under the Agreement among the European Atomic Energy Community, the Government of Japan, the Government of the Russian Federation, and the Government of the United States of America on Cooperation in the Engineering Design Activities for the International Thermonuclear Experimental Reactor ("ITER EDA Agreement") under the auspices of the International Atomic Energy Agency (IAEA).

## First generation of mm-waves in the Dutch Free-Electron Maser

A.G.A. Verhoeven, W.A. Bongers, V.L. Bratman\*, M. Caplan\*\*,  
G.G. Denisov\*, C.A.J. van der Geer, P. Manintveld, A.J. Poelman,  
J. Plomp, A.V. Savilov\*, P.H.M. Smeets, W.H. Urbanus.

FOM-Instituut voor Plasmafysica 'Rijnhuizen', Association EURATOM-FOM

tel.: (31)30-6096999, fax: (31)30-6031204, e-mail: verhoeven@rijnh.nl

P.O. Box 1207, 3430 BE Nieuwegein, the Netherlands

\*Institute of Applied Physics, Nizhny Novgorod, Russia

\*\*Lawrence Livermore National Laboratories, Livermore, CA, USA

### Abstract

A free-electron maser (FEM) has been built as a pilot experiment for a mm-wave source for applications on future fusion research devices such as ITER, the International Tokamak Experimental Reactor. A unique feature of the Dutch Fusion-FEM is the possibility to tune the frequency over the entire range from 130 to 260 GHz at an output power exceeding 1 MW. In the first phase of the project, the so-called inverse set-up is used. The electron gun is mounted inside the high-voltage terminal. The entire beam line was tested successfully with extremely low loss current, lower than 0.05 %. First generation of mm-waves was achieved in October 1997. Up to now a peak power exceeding 730 kW was measured at 200 GHz and 350 kW at 167 GHz. Output power, start-up time and frequency correspond well with simulation results. Parameter scans for the longitudinal undulator gap, accelerator voltage, waveguide settings and reflection coefficient have given a wide range of interesting data.

### Introduction

The free-electron maser consists of a 12 A thermionic electron gun and a 2 MeV electrostatic accelerator, see fig. 1. The undulator and mm-wave system are located inside a terminal at 2 MV level. The terminal is placed inside a steel vessel of 11 m length and a diameter of 2.6 m, filled with SF<sub>6</sub> at 7 bar. After interaction with the mm waves in the undulator, the energy of the spent electron beam is recovered by means of a decelerator and a multi-stage depressed collector. This approach is expected to lead to an overall system efficiency of 50 % [1]. For long-pulse generation a low loss current, lower than 20 mA, is essential. Therefore, the electron beam line is entirely straight from gun to collector. The mm waves are directed sideways from the electron beam by means of a stepped waveguide. This is a symmetrical step in the transverse dimension of a low-loss HE<sub>11</sub> waveguide. Furthermore, an adjustable reflector enables adjustment of the feedback power over the entire range from 0 - 100% [2]. In the first phase of the project, the inverse set-up is used. Now, the electron gun is mounted inside the high-voltage terminal at -2 MV. The undulator and waveguide system are outside the pressure vessel at ground potential for easy adjustments and fine-tuning of the entire system.

Therefore, the decelerator and depressed collector are not installed yet, which means that the FEM pulses are limited to 10 - 20  $\mu$ s.

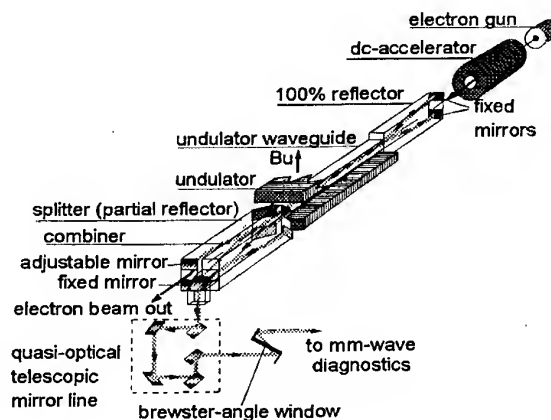


Fig. 1. The beamline system, showing the electron gun, the dc-accelerator, the 100% reflector, the undulator, the splitter/combiner, the outcoupling waveguide and the confocal mirror system to the brewster-angle window

### First Experimental Results

In October 1997, the FEM generated mm-wave power for the first time. Using an electron beam current of 6 A and an accelerator voltage of 1.76 MV, the mm-wave pulse started after 3  $\mu$ s and lasts for 3  $\mu$ s, reached a peak power level of 375 kW, see fig. 2. Output power and start-up time correspond well with simulation results.

In the present set-up (without electron beam recovery) the accelerating voltage drops rapidly during the pulse (1 kV per A of beam current per  $\mu$ s, so for 6 A this means: 6 kV/ $\mu$ s). Due to a bandwidth of the mm-wave cavity of 4% the pulse length is limited to a few  $\mu$ s, since the gain curve thus rapidly shifts across the cavity bandwidth. Consequently, the output power drops sharply.

The highest power achieved so far is just over 700 kW. See fig. 3 [4]. The mm-wave power signal is peaked and drops sharply.

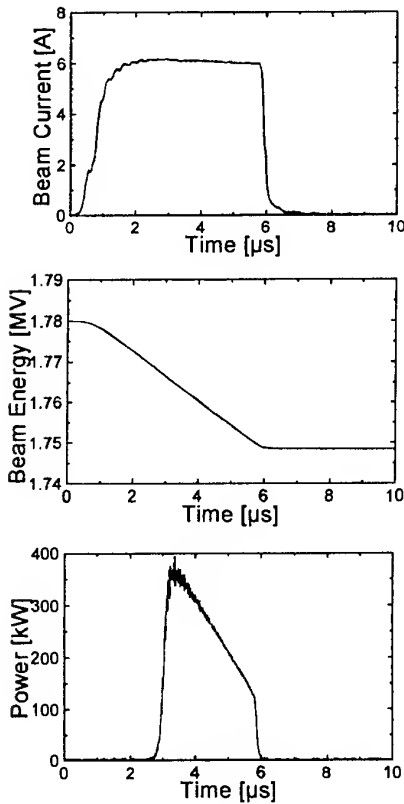


Fig. 2. One of the first high-power experiments. Plotted are the beam current vs. time, the accelerator voltage and the mm-wave power as measured by a fast broadband detector. With these parameters the spectrum is very pure and the output power grows to about 375 kW. Feedback coefficient: 0.35.

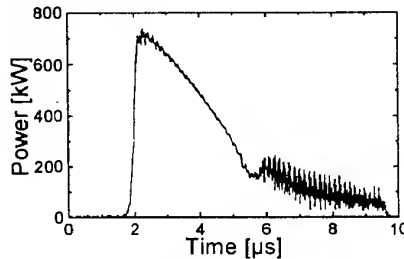


Fig. 3. Highest power achieved so far, reaching just over 700 kW. Accelerator voltage at start: 1.77 MV. Feedback coefficient: 0.6. Beam current 8 A.

At very similar parameters the output power behaviour can be completely different by just changing the starting value of the acceleration voltage. See fig. 4. This effect is believed to be caused by the different starting conditions of the different longitudinal modes in the mm-wave cavity in relation to the gain curve of the interaction between the mm-waves and the electron beam and is subject of further investigations.

### Simulation of the Interaction

The interaction between the electron beam and the mm waves inside the Fusion-FEM has been simulated using several codes. Very often the CRMFEL (Cyclotron Resonance Maser Free Electron Laser) code was used. CRMFEL is a fully three dimensional (3-D), non-linear, particle-EM wave interaction code. Until recently these simulations were done with a single-frequency, stationary version of this amplifier code. Simulations indicated that for a 12 A beam the net mm-wave power generated is above 1 MW for all frequencies between 130 GHz (at 1.35 MeV) and 260 GHz (at 2 MeV).

Simulations with a modified non-stationary (space charge and high gain included) code developed jointly by the University of Maryland and LLNL indicate that a parameter regime can be found with a pure single-frequency operation, without any sidebands. A result of a simulation with this code is given in fig. 5.

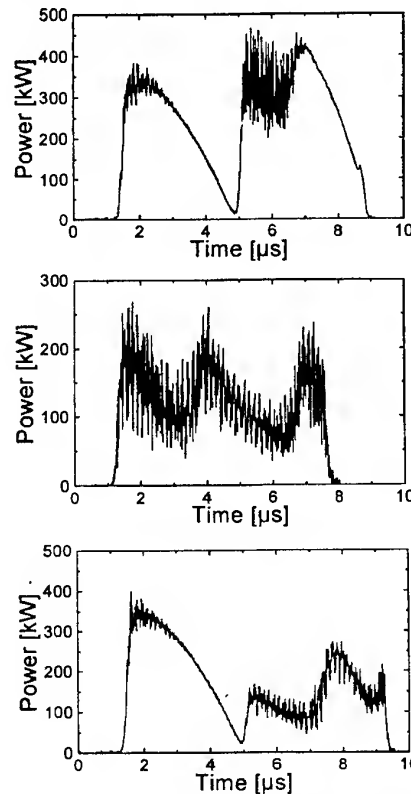


Fig. 4. At very similar parameters (feedback coefficient: 0.7, beam current 6 A), the output power can be completely different by just changing the start value of the acceleration voltage. Acceleration voltages at start are as follows:

Top: 1.754 MV.  
Middle: 1.755 MV.  
Bottom: 1.769 MV.

Parameters are very similar to those used during the first experiments, including the time behaviour of the accelerator voltage. The reflection coefficient of the mm waves, the size of the electron beam and especially the distance between the two undulator sections have a strong effect on the FEM behaviour.

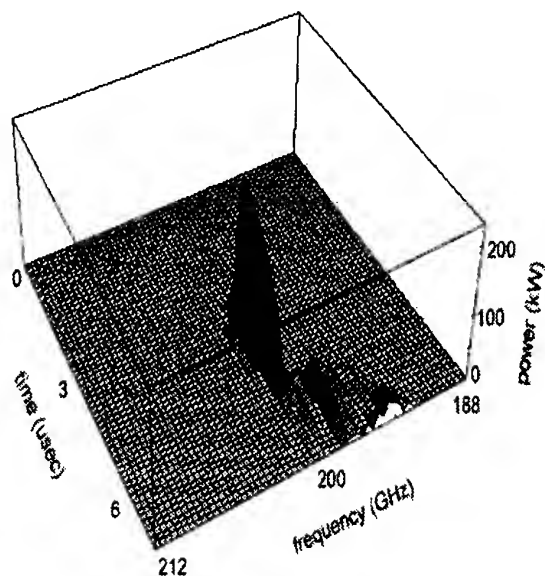


Fig. 5. Frequency spectrum as calculated by Malt 1D code [5]. Beam current is 6 A. Voltage droop is 6 kV/μs. Accelerator voltage starts at 1.75 MV. Measured data for mm-wave reflection and transmission coefficients are taken into account. The beam radius is 1.4 mm. At these parameters it can be noted that a pure frequency develops and decays followed by a much broader frequency spectrum.

#### Experiments at 167 GHz.

With the cavity tuned at a different setting around 167 GHz in stead of 200 GHz a new series of experiments were performed. In fig. 6 a few examples are given at accelerator voltage levels of 1.6 MeV and a beam current of 7 A.

#### Conclusions

In the first phase of the project, experiments were done in the inverse set-up. The entire beam line was tested successfully with extremely low loss current, lower than 0.05 %. This included the accelerating structure up to 2 MV level and the transport through the undulator and waveguide system. First generation of mm-waves was achieved in October 1997. Highest peak power measured so far is 730 kW at 200 GHz. This was achieved with a beam current of 7.2 A and an accelerator voltage of 1.77 MV. Output power, start-up time and frequency correspond well with simulation results.

After the series of experiments in the inverse set-up, the equipment will be reinstalled in the final set-up. From that moment on (now scheduled for the first half of 1998), the pulse length can be extended up to 100 ms.

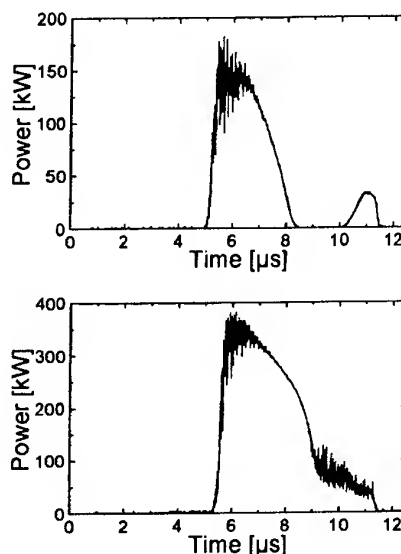


Fig. 6. At cavity settings around 167 GHz. (feedback coefficient: 0.7, beam current 6 A), the output power reaches a maximum of 350 kW

#### Acknowledgements

This work was performed as part of the research programme of the association agreement of EURATOM and FOM with financial support from NWO and EURATOM.

#### References

1. W.H. Urbanus, *et al.*, Proc. 10th Workshop on ECE and ECRH, EC10, Edited by A.J.H. Donne and A.G.A. Verhoeven (World Scientific, Singapore, 1998), pp. 497-506.
2. W.A. Bongers, *et al.*, This conference
3. M. Valentini, *et al.*, Nucl. Instr. and Meth. A375, pp. 409-416 (1997).
4. A.G.A. Verhoeven, *et al.*, APS, Pittsburgh, Nov. 1997, Phys. of Plasmas. Vol. 5, no. 5 (May 1998), p 2029
5. A.G.A. Verhoeven, *et al.*, Brussels, 2nd Europe. Top. Conf. on RF Heating and Current Drive of Fusion Devices, Jan. 1998. Plasma Physics and Contr. Fusion **40** (1998) pp. 1-18.

## Long-pulse Operation of 170 GHz/1 MW Gyrotron for ITER

V.E. Myasnikov, S.V. Usachev, M.V. Agapova, V.V. Alikaev,  
G.G. Denisov, A.Sh. Fix, V.A. Flyagin, A.Ph. Gnedenkov,  
V.I. Ilyin, A.N. Kuftin, L.G. Popov, V.E. Zapevalov

GYCOM Ltd., 46 Ulianov St., Nizhny Novgorod, 6003600, Russia

### Abstract

The design and test results of 170GHz/1MW gyrotron for ITER are reported. Stable operation at the TE<sub>25,10</sub> mode was achieved for a number of regimes: 1MW/1 s, 500 kW/5 s, 270kW/10 s, etc. The maximal efficiency was 34 % without depressed collector operation. Obtained experimental results are in a good agreement with numerical simulation data. RF pulse energy was limited by single-disc BN window capacity at the level of about 2.5 MJ.

### 1. Introduction

According to ITER requirements the gyrotron should produce output power of 1MW/CW with depressed collector operation efficiency not less than 50 %.

Preliminary numerical simulations and experimental tests of short-pulse gyrotron prototypes have shown that 170GHz/1MW level regimes can be reached at TE<sub>31,8</sub>, TE<sub>28,7</sub> and TE<sub>25,10</sub> operating modes [1]. For ITER gyrotron the TE<sub>25,10</sub> operating mode was chosen, because it permits to have minimum cavity specific losses, as well as to use the available superconducting magnet with room temperature bore diameter of 140 mm.

A 170GHz/1MW gyrotron was designed, manufactured and tested. Excluding the depressed collector and output window, the main gyrotron assemblies are designed for CW operation.

### 2. Design of 170 GHz/1 MW gyrotron

A 170GHz gyrotron was developed on the base of 1MW/110GHz-140GHz gyrotrons creation experience [2, 3]. The cavity in a form of 35.6 mm cylinder with smooth curve transition sections [4] is equipped by the intensive water cooling system. Water flow for cavity and mode converter cooling of about 40 l/min is provided at pressure drop of about 4 bar. The built-in converter of the TE<sub>25,10</sub> mode into wave beam consists of a visor of optimized shape and three mirrors.

Output window is a critical component of the 170GHz/ 1MW/ CW gyrotron. Here, the design was done with single-disc BN output window of 123 mm diameter with edge water cooling. This window has loss tangent  $\tan \delta = 1.1 \cdot 10^{-3}$  at 170 GHz and is obviously not adequate for 170 GHz/1 MW/CW gyrotron.

The collector is equipped by an additional sweeping coil, which increases the effective collector surface up to 5000 cm<sup>2</sup>. Water flow for collector cooling of about 1200 l/min is provided at pressure drop of about 4 bar. Calculations and experimental study shows, that this collector can dissipate up to 1.5 MW.

### 3. The experimental results and discussion

The gyrotron tests were carried out on the special set-up at "Kurchatov institute". Gyrotron conditioning was performed according to the technique, optimized during many years of such class gyrotron tests. The gyrotron vacuum level was monitored by an inside electron-discharge pump. Also, integrated getter blocks of large capacity were used for maintenance the good vacuum conditions. The calorimetric dummy load for output power measurement at pulse length up to 0.1 s was used. For longer pulses the load formed with absorbing bricks was applied. The output power was measured in these regimes by means of calorimetry in window cooling system. Percentage of window dissipated power relatively to gyrotron output power was periodically checked with dummy calorimetric load and quoted as 5.3 % to 5.5 %. Also, power dissipation in the cavity and mode converter visor was calorimetrically measured. It was about 3.5 %, that corresponds to a value of increase factor with reference to ideal copper ohmic losses of 1.8.

Oscillation frequency was about 170.17 GHz and frequency drift during RF pulse did not exceed 50 MHz ( $\Delta f/f_0 = 3 \cdot 10^{-4}$ ). There was no frequency change from pulse to pulse, so there were no plastic deformations of the cavity.

Experimental dependencies of gyrotron output power and efficiency versus beam current (a) and beam voltage (b) are shown in Fig. 1. The stable tendency of an efficiency growth with increase of beam voltage and optimum range versus beam current may be observed. The maximum output power of 1000 kW at 1.0 s pulse length was achieved and limited by collector overloading. Optimum efficiency was 34.8 % ( $P_{out} = 870$  kW,  $U_b = 76$  kV,  $I_b = 34$  A) that is in a good agreement with simulating data and results of short-pulse prototype tests [1].

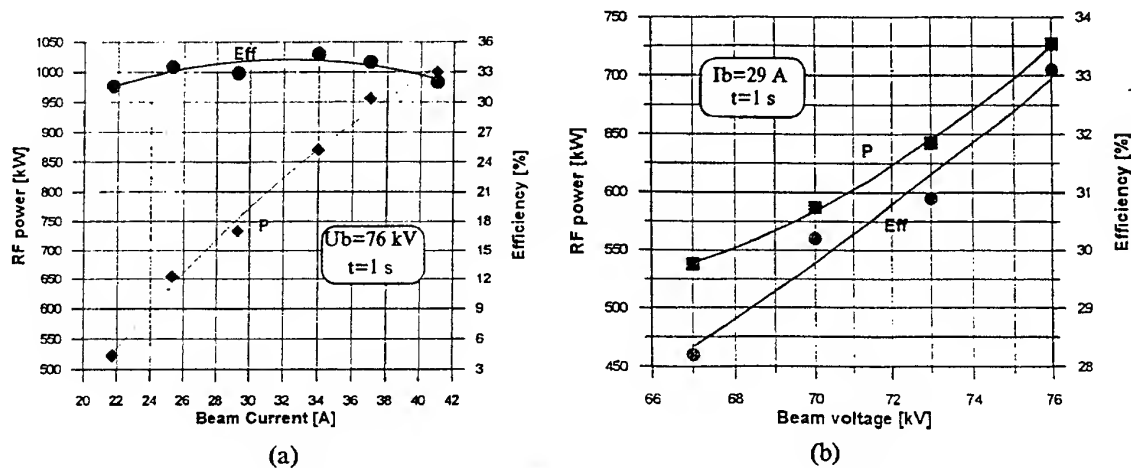


Fig. 1: Output power and efficiency versus beam current (a) and beam voltage (b)

During tests the temperature distribution over window surface was measured by means of videocamcorder with computer data processing. Dependencies of window maximally heated up area temperature versus pulse output energy are shown in Fig. 2. RF pulse energy was limited at about 2.5 MJ (500 kW/ 5 s ; 270 kW/ 10 s etc.) by window temperature rising up to 1200 °C.

#### 4. Conclusion

Stable operation of the TE<sub>25,10</sub> mode gyrotron at 170.17 GHz was demonstrated. The output power of 1 MW with efficiency of 32 % at pulse length of 1.0 s was reached. The maximum pulse output energy of about 2.5 MJ was limited by single-disc BN window capacity. The maximum efficiency was 34% (870 kW/ 76 kV/34 A/1 s) without a depressed collector. Achieved experimental results are in a good agreement to numerical simulation and test results of short-pulse prototypes. An advanced 170GHz gyrotron with new window, one-stage depressed collector and CW adequate cooling of all elements is planned to be tested in 1998. It is expected to reach 1MW/10-20 s with efficiency of 50 %.

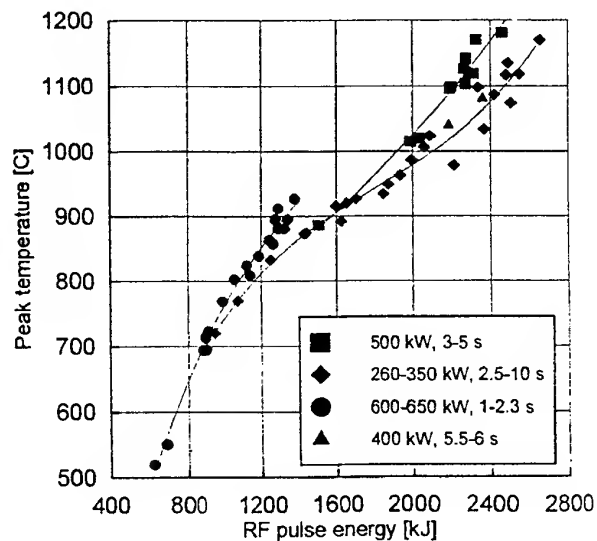


Fig. 2: Maximum window temperature versus RF pulse energy

#### References:

- [1] V.E. Zapevalov, V.E. Myasnikov, et al. Development of 1 MW output power level gyrotron for ITER, 22 Int. Conf. on IR&MM Waves. 1997, p. 108-109
- [2] V.E. Myasnikov, et al. Long-pulse operation of 110GHz/1MW gyrotron, 22 Int. Conf. on IR&MM Waves. 1997, p. 102-103
- [3] V.E. Myasnikov, et al. Megawatt power Long-pulse 140GHz gyrotron, 21 Int. Conf. on IR&MM Waves. 1996.
- [4] V.E. Zapevalov, et al. Izv. Vuzov., Radiofizika, v. 37, No. 3, pp. 381-386.

## Experimental Demonstration of W-Band Gyro-Amplifiers with Improved Performance\*

M. Blank, B.G. Danly, B. Levush

Code 6843 Naval Research Laboratory, Washington, D.C. 20375

### Abstract

W-band gyrokystron and gyrotwyston amplifier experiments are currently underway at the Naval Research Laboratory. Recently, a four cavity gyrokystron amplifier achieved 84 kW peak output power, corresponding to 34% efficiency, with a 56 kV, 4.4 A electron beam. A five cavity gyrokystron produced 72 kW peak output power at 50 dB saturated gain. A four section gyrotwyston amplifier demonstrated 50 kW peak output power at a center frequency of 93.9 GHz with 925 MHz full width half maximum (FWHM) bandwidth. Results from several experiments are discussed and compared with theoretical performance predictions.

### Gyro-Amplifier Experiments

Several  $TE_{011}$  mode W-band gyro-amplifiers operating near the fundamental cyclotron frequency have been built and tested. Each circuit consists of four interaction sections separated by drift sections cutoff to the operating mode. For each circuit, a coaxial drive cavity was used. Drive power is coupled from a cylindrical waveguide to the  $TE_{411}$  mode of the outer coax through a single aperture. Power is then coupled to the  $TE_{011}$  mode in the inner cavity through four slots positioned 90 degrees apart around the azimuth of the common wall. The input cavity parameters were determined through theoretical modeling with HFSS, a finite element code that computes field distributions and S-parameters for passive 3D structures.

Because the intermediate cavities are terminated by drift sections that are cutoff for the  $TE_{011}$  operating mode, the diffractive Q's are quite large. The desired Q values (100-200) are achieved by ohmically loading the cavities with rings of lossy ceramic placed at one end of each cavity. In the output sections, where no ceramic loading is used, power is diffractively coupled through a 5 degree linear uptaper to the collector radius. For each circuit, the parameters of the intermediate cavities and the output cavities/sections were determined through cold test measurements. A 2 kW peak power, mechanically tunable Extended Interaction Oscillator was used to supply the drive power. The tests were typically performed with 2  $\mu$ sec pulses at 250 Hz for 0.05% duty. The measured results for five recently demonstrated W-band gyro-amplifier circuits are shown in Table 1.

Circuit	Peak Output Power (kW)	Efficiency (%)	Bandwidth (MHz)	Gain (dB)	Power x BW (kW-GHz)
WGKL1	67	28	460	29	30.8
WGKL2	60	25	640	27	38.4
WGKL3	84	34	370	42	31.1
WGKL4	72	27	410	50	29.5
WGTWY1	50	18	925	30	46.3

Table 1. Measured performance of NRL W-band gyro-amplifiers.

Results from the WGKL1 circuit [1], which was used to benchmark the design tools, and WGKL2 [2], the low duty prototype for the 10 kW average power radar driver [3], have been previously reported. The WGKL3 circuit was designed to demonstrate high peak output power and efficiency at moderate bandwidths. The efficiency and peak output power as functions of drive frequency for a 56 kV, 4.4 A electron beam are shown in Fig. 1. In the figure, experimental data points are indicated by the filled circles and the predictions of theory are shown by the solid line. The measured results are in good agreement with theoretical predictions. Also shown on Fig. 1 are the



resonant frequencies and  $Q$ 's for each cavity, determined by modeling (cavity 1) and cold test (cavities 2-4). The high efficiency is achieved through the combination of the high  $Q$  output cavity and the minimized stagger tuning of the intermediate cavities about the resonant frequency of the output cavity.

The five cavity WGKL4 circuit was designed to demonstrate large gain, as well as high power and efficiency. A peak saturated output power of 72 kW was produced for a 54 kV, 5 A electron beam with 1 W drive power, corresponding to 50 dB saturated gain. In the experiment, the drive power was measured at the output of the EIO driver and the losses in the drive line and input cavity were not taken into account.

In the four section WGTWY1 circuit, the output cavity was replaced by a traveling wave section to maximize the bandwidth of the device. Figure 2 shows the measured and theoretically predicted peak output power and efficiency versus drive frequency for a 57 kV, 5 A electron beam. As shown in Fig.2, the measured FWHM bandwidth was 925 MHz and the peak output power was 50 kW, corresponding to a power-bandwidth product of 46.25 kW-GHz. This power-bandwidth product represents a significant increase over the power-bandwidth product of the gyrokystron amplifiers (see Table 1). The measured data and predictions of non-linear theory are in good agreement. The cavity and output section parameters are also indicated on the plot. The traveling wave output section has a measured  $Q$  of 70, which is 15% below the minimum diffractive  $Q$ .

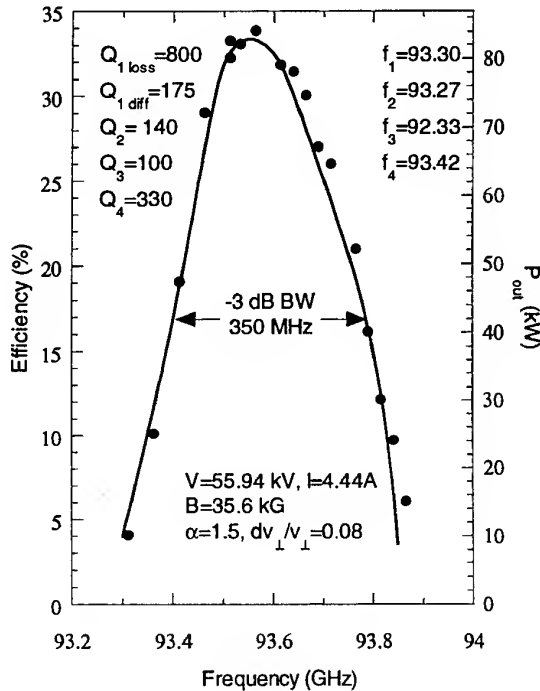


**Figure 1.** Measured (filled circles) and theoretical (solid line) peak output power and efficiency versus drive frequency for the WGKL3 circuit.

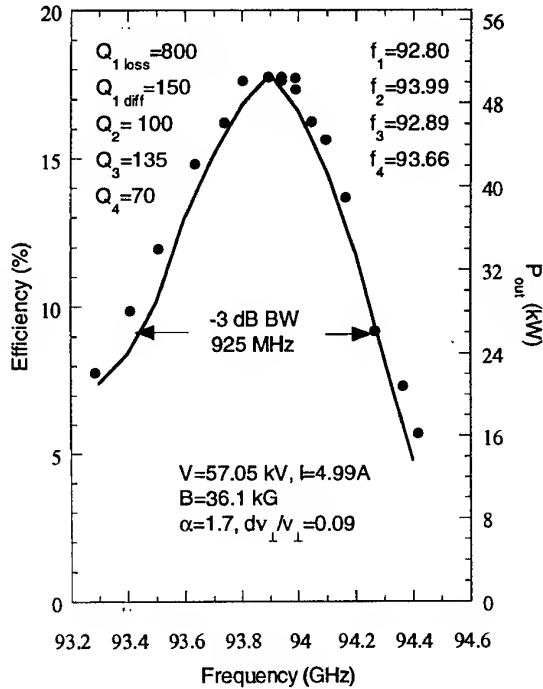


**Figure 2.** Measured (filled circles) and theoretical (solid line) peak output power and efficiency versus drive frequency for the WGTWY1 circuit.

## References

\* This work supported by the Office of Naval Research. The computational work was supported in part by a grant of HPC time from the DoD HPC Center NAVO.

1. M. Blank *et al.*, "Experimental demonstration of a W-band gyrokystron amplifier," *Phys. Rev. Lett.* Vol. 79, No. 22, pp. 4485-4488, December 1997.
2. M. Blank *et al.*, "Experimental Investigation of W-band (93 GHz) gyrokystron amplifiers," *IEEE Trans. Plasma. Sci.*, Vol. 26, No. 3, June 1998.
3. B.G. Danly *et al.*, "Development of a W-band gyrokystron for radar applications," this digest.

## Experimental 35 GHz Multi-Cavity Gyroklystron Amplifiers

M. Garven<sup>†</sup>, J. P. Calame, J. J. Choi<sup>†</sup>,  
B. G. Danly, K. T. Nguyen\* and F. Wood<sup>‡</sup>

Code 6843, Naval Research Laboratory, Washington, DC 20375, U.S.A.

<sup>†</sup>University of Maryland, College Park, MD 20742

<sup>\*</sup>Present address: Kwangwoon University, Seoul, Korea

<sup>\*</sup>KN Research, Silver Spring MD 20906

<sup>‡</sup>DynCorp, Rockville, MD 20850

### Abstract

Experimental studies of a three-cavity, Ka-band gyrokystron amplifier employing stagger-tuning have been completed. A peak power of 225 kW at 34.90 GHz, with a -3 dB bandwidth of 0.82%, a saturated gain of 30 dB and an efficiency of 31% was obtained. The design of a four cavity gyrokystron with improved gain (> 45 dB) will also be presented.

### Introduction

Gyrokystron amplifiers operating in the Ka-band are attractive for the next generation of millimeter wave radars [1,2] and are currently under investigation at the Naval Research Laboratory [3]. The advantages of operating in the millimeter wave band include the ability to achieve high angular resolution with an antenna of modest dimensions, improved radar scattering from small targets and the potential for higher absolute bandwidth. Such sources must also be capable of operating at high average power with typical duty cycles ranging from 10% to CW. The three-cavity, 35GHz gyrokystron amplifier experiment is presented as a significant result towards the goal of higher average power, broader bandwidth sources.

### Experimental Set-up

A schematic of the three-cavity, gyrokystron amplifier experiment is shown in Fig. 1. An electron beam of up to 12 A is produced from a thermionic, double anode magnetron injection gun by applying voltages of 65-75 kV. The magnetic field at the cathode can be varied with the gun coils to control the beam velocity ratio,  $\alpha$  ( $v_z/v_z$ ). The beam is adiabatically compressed as it enters the region of high magnetic field (approx. 13 kG) generated by the 14 coil superconducting magnet. The three cavities of the gyrokystron circuit are positioned in the region of constant magnetic field. Each cavity operates in the  $TE_{011}$  cylindrical mode. Drive power is directed into a passive  $TE_{011}$  coaxial resonator which surrounds the

$TE_{011}$  input cavity. Power is coupled to the circular-electric mode inside the inner cavity by four axial slots placed every 90 degrees in azimuth. The cold-test resonant frequency of the input cavity is 34.89 GHz and the loaded  $Q_L$  is 188 (primarily diffractive due to the coupling slots). The intermediate (buncher) cavity employs an annular ring of lossy ceramic against the upstream endwall to provide the desired cold-test  $Q_L$  of 194 and a resonant frequency of 34.62 GHz. The downstream end of the output cavity employs an outward radial step and a nonlinear uptaper to achieve a cold-test  $Q_L$  of 175 and a resonant frequency of 34.83 GHz. The frequency upshift due to the presence of the electron beam is approximately 70 MHz. The drift tubes between cavities are loaded with lossy ceramic rings to suppress instabilities.

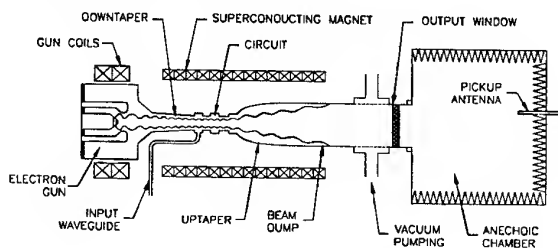


Figure 1. Schematic diagram of the experiment.

A 3.81 cm, half-wavelength thick BeO disk positioned immediately after the pumping manifold functions as the output window. The experiment employed two different diagnostic systems for measuring output power. The main diagnostic was an anechoic chamber joined to the output waveguide which had an absolute accuracy of 8% and a relative accuracy of 0.25%. A high-average power calorimeter with 5% absolute accuracy was also used to confirm the higher power measurements.

### Results

Systematic studies were performed over a wide range of operating voltage, current, magnetic field and drive frequency. A peak power of 225 kW at

34.90 GHz, with a -3 dB bandwidth of 0.82%, a saturated gain of 30 dB, and an efficiency of 31% was obtained. These values were measured with a beam voltage of 70.2 kV, a current of 10 A, a magnetic field of 13.1 kG and a pulse width of 2  $\mu$ s. The beam velocity ratio  $\alpha$  was determined to be  $1.27 \pm 0.05$  using a capacitive probe placed just upstream of the input cavity. The frequency response for this case is shown in Fig. 2.

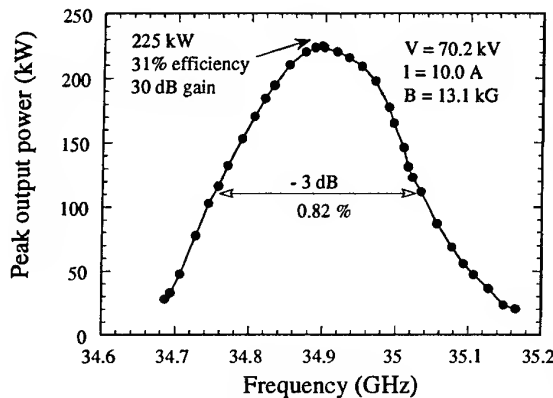


Figure 2 Experimental frequency response at 13.10 kG.

Additional enhancements in bandwidth were achieved with magnetic field adjustments and changes in beam voltage and current, at the expense of output power. For example, raising the voltage to 73.10 kV and the nominal magnetic field to 13.40 kG produced a -3 dB bandwidth of 0.94% but with a lower peak output power of 200 kW (shown in Fig. 3). The beam current was 10 A, and the efficiency was 27.5% for this case. Detailed studies of how the bandwidth varies with operating parameters will be presented, along with comparisons to theory. In general, the measured bandwidth of the three-cavity device is 2.0-2.7 times as large as that obtained from the previous two-cavity gyrokystron experiment [3].

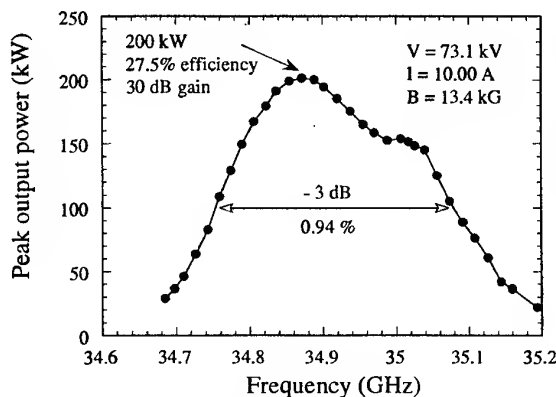


Figure 3 Experimental frequency response at 13.40 kG.

### Four-cavity Gyrokystron Amplifier

Future efforts in the Ka-band region at the Naval Research Laboratory include developing a four-cavity gyrokystron to increase the saturated gain to 40-45 dB while maintaining bandwidths in the 0.6-0.9% range and output powers greater than 200 kW.

Preliminary design studies have been completed using a time-dependent version of the non-linear code MAGYKL [4]. These studies suggest that the above requirements of improved gain (45 dB) with greater than 200 kW output power and 0.6-0.9% bandwidth can be met. This can be achieved by the addition of a second buncher cavity with very similar design criteria as the buncher cavity in the present three-cavity design. The status of the four-cavity gyrokystron will be presented.

### Conclusions

A three-cavity, Ka-band gyrokystron amplifier has demonstrated a peak output power of 225 kW at 34.90 GHz, with a -3 dB bandwidth of 0.82%, 30 dB saturated gain and 31% efficiency. Variation in magnetic field was found to have a strong influence on power-bandwidth tradeoff. The design of a four-cavity, Ka-band gyrokystron amplifier indicates that improved gain (>45dB) can be achieved and a four-cavity gyrokystron experiment is currently underway.

### Acknowledgments

This work was supported by the Office of Naval Research and the Naval Research Laboratory. The authors would like to thank Dr. Monica Blank for many useful discussions. We also acknowledge excellent technical support from R. Myers, F. Robertson, B. Sobocinski, G. Longrie and D. Lobas.

### References

- [1] I. I. Antakov et al, "35 GHz Radar Gyrokystrons," 18<sup>th</sup> Int. Conf. IR & MM Waves, Colchester, 1993.
- [2] A. A. Tolkachev, "Gyrokystron-based 35 GHz Radar for Observation of Space Objects," 22<sup>nd</sup> Int. Conf. IR & MM Waves, Wintergreen VA, July 1997.
- [3] J. J. Choi *et al*, IEEE Trans. Plasma Sci. **26**(3), June 1998.
- [4] P. E. Latham, W. Lawson and V. Irwin, IEEE Trans. Plasma Sci. **22**, 804, 1994.

## **An Ultra High Gain Gyrotron Traveling Wave Amplifier**

**K. R. Chu, H. Y. Chen, C. L. Hung, T. H. Chang, L. R. Barnett**

Department of Physics, National Tsing Hua University

**S. H. Chen**

National Center for High-Performance Computing

**T. T. Yang**

Synchrotron Radiation Research Center

Hsinchu, Taiwan, ROC

In contrast to conventional linear beam devices, the electron beam employed in the gyrotron has a transverse motion at the electron cyclotron frequency. It is this property that allows the beam to selectively interact with a high order waveguide mode at a high cyclotron harmonic by properly matching the resonance conditions. However, the extra degree of freedom provided by the multitude of cyclotron harmonics can also generate numerous spurious oscillations. In the case of the gyrotron traveling wave amplifier (gyro-TWT), interactions in the backward wave region are absolute instabilities (oscillations due to an internal feedback), whereas those in the forward wave region are normally but not always convective instabilities. The gyro-TWT is a complicated case because it exploits a convective instability near the cutoff frequency which will turn into an absolute instability at sufficiently high beam current when the unstable spectrum extends into the backward wave region. These various absolute instabilities can easily be the dominant sources of oscillations in an unsevered interaction structure. For example, in a fundamental harmonic gyro-TWT operating at the lowest order waveguide mode, a second harmonic absolute instability has been observed [1] at beam current as low as 0.1 A. The instability was shown to compete with and eventually suppressed by the amplified wave, but linearity was affected at low drive powers.

Feedback due to reflections at the input/output couplers and structural nonuniformities presents a different oscillation problem (referred to as the reflective oscillation) in the high gain regime. Even when the gain is kept below the oscillation threshold, reflective feedback can still cause ripples in the gain and output power spectra.

Reflective oscillations are common in traveling wave structures. The feedback loop can be effectively cutoff by a sever as has been a standard practice in conventional TWT's. The absolute instability, a much more serious problem to the gyro-TWT than to the conventional TWT, is basically different from the reflective oscillation in that the backward wave associated with the absolute instability is internally generated by the ac beam current. In the experiment of Ref. 2, a sever was used as a remedy for the absolute instability. But the two stages, though separated by the sever, are coupled by the beam. With the beam providing an internal path, the sever does not really quite cut the interaction structure into two isolated sections to produce a substantial stabilizing effect. With the sever, the start-oscillation current can be increased from 0.1 A to 0.9 A, but still well below what is required for high power generation.

Recently an interaction structure with distributed wall losses was shown to be effective in suppressing both types of oscillations [3]. The losses are distributed over much of the linear interaction region. Like the sever, the lossy section cuts off the path of the reflective feedback loop. In contrast to the sever, however, it is an integral part of the linear amplification stage. To the predominantly backward power flow of the absolute instability, the lossy section also functions as an effective energy sink. The absolute instability threshold can be raised to 26 A as a result.

The distributed-loss structure can in principle yields ultra high stable gain. The scheme is based on the different responses to wall losses between the cold tube and hot tube modes. The cold tube mode has all of its energy in the electromagnetic fields. In a hot tube, however, energy of the beam generated mode resides not only in the electromagnetic fields but also in the kinetic energy of the oscillatory motion of the

electrons, the latter being an integral part of the hot tube mode. The lossy wall absorbs the electromagnetic energy but not the oscillatory energy of the electrons. Thus, wall losses of the amplifier circuit attenuate the reflected wave (basically a cold tube mode) far more than it reduces the gain of the amplifying wave (a hot tube mode). As shown in an early analysis [4], the reduction in hot tube gain due to wall losses is only one third of the cold tube attenuation over the same distance.

Such unequal effects can be exploited to achieve both high gain and reflective stability at the same time. The lossy and conducting wall sections form the linear and nonlinear stages of the amplification, respectively. The linear section is made sufficiently long to provide the desired gain while the nonlinear section is kept at a minimum length to enhance the threshold of absolute instabilities.

This talk will present theoretical and experimental studies of a high gain gyro-TWT based on the distributed-loss scheme. High gain operation enhances the possibility of spurious oscillations caused by various internal and external feedback mechanisms. Thus the physics issues involved are the identification, characterization, and suppression of possible sources of oscillations.

Three types of oscillations have been analyzed theoretically. Each type of oscillation exhibits different characteristics. Experiments have been conducted to investigate these oscillations and their stabilization by proper distribution of wall losses. Based on these results, a Ka-band gyro-TWT with 93 kW saturated peak output power at 70 dB stable gain, and 26.5 % efficiency has been demonstrated in stable operation.

1. L.R. Barnett, L.H. Chang, H.Y. Chen, K.R. Chu, Y.K. Lau, and C.C. Tu, Phys. Rev. Lett. **3**, 1062 (1989).
2. K.R. Chu, L.R. Barnett, W.K. Lau, L.H. Chang and C.S. Kou, in Technical Digest of International Electron Devices Meeting (IEEE, New York, 1990). P.699.
3. K.R. Chu, L.R. Barnett, H.Y. Chen, S.H. Chen, Ch. Wang, Y.S. Yeh, Y.C. Tsai, T.T. Yang, and T.Y. Dawn, Phys. Rev., Lett. **74**, 1103 (1995).
4. Y.Y. Lau, K.R. Chu, and L.R. Barnett, Int. J. Infrared and Millimeter Waves **2**, 395 (1981).

## Development of a W-Band Gyroklystron for Radar Applications<sup>1</sup>

B.G. Danly, M. Blank, J.P. Calame, B. Levush, K. Nguyen<sup>2</sup>(, D. Pershing<sup>3</sup>(, J. Petillo<sup>4</sup>(  
Vacuum Electronics Branch, Code 6840, Naval Research Laboratory, Washington, D.C. 20375

T.A. Hargreaves, R.B. True, A.J. Theiss, G.R. Good  
Electron Devices Division, Litton Systems, Inc., San Carlos, CA

K. Felch, T.S. Chu, H. Jory, P. Borchard, B.G. James  
Microwave Power Tube Products Division, Communications and Power Industries, Palo Alto, CA

W.G. Lawson and T.M. Antonsen, Jr.  
Electrical Engineering Dept., University of Maryland, College Park, MD

### Abstract

A four-cavity, high average power gyrokystron amplifier designed to operate at 94 GHz has been designed and built. This device is scheduled to be tested during 1998. The status of the project is outlined in this paper.

### Introduction

There is currently a need for high-power, W-band amplifiers for a variety of millimeter-wave radars. To meet this need, a 94-GHz gyrokystron amplifier has been designed by a collaboration of the Naval Research Laboratory (NRL), Litton Electron Devices, Communications and Power Industries (CPI), and the University of Maryland. This four-cavity gyrokystron is designed to be capable of delivering 10 kW of average power and has been fabricated in U.S. industry. The design of this amplifier is based on the series of high peak power, low-duty factor experiments on gyrokystron amplifiers which have been carried out at NRL during the past two years [1,2,3]. This amplifier is will produce in excess of 80 kW peak power at 20% efficiency with a bandwidth of 600 MHz and 41 dB saturated gain. The amplifier is designed to operate at up to 12.5% RF duty factor (15% beam duty factor), for an average power of 10 kW at 94 GHz. Following successful operation of this amplifier, it will be delivered to the NRL Radar Division for incorporation into a millimeter wave radar system.

### Amplifier Design and Project Status

The gyrokystron amplifier operates at the fundamental of the cyclotron frequency in the TE<sub>01</sub> mode. Details of the device design parameters are listed in Fig. 1. The gyrokystron will utilize a magnetron injection gun designed to produce a 65-kV, 6-ampere electron beam with very low velocity spread ( $(v_{\parallel}/v_{\perp}) = 1.8\%$ ) at a velocity ratio ( $v_{\parallel}/v_{\perp}$ ) of 1.5. The electron gun cathode has been successfully tested at CPI, where it required 22 W heater power to reach 1060 °C<sub>B</sub>. The cathode uniformity was better than the pyrometer instrumental limit of 5 °C<sub>B</sub>. This magnetron injection gun represents the smallest MIG that CPI has ever built. Cavities have been fabricated at both Litton and CPI, following detailed design work at NRL [4]. Particular areas of emphasis in the circuit design have been the thermal capacity of the penultimate

<sup>1</sup> Work sponsored by the Office of Naval Research. Work at Litton and CPI sponsored under NRL Contract N00014-94-C-2136.

<sup>2</sup>( KN Research, Inc.

<sup>3</sup>( Mission Research Corp.

<sup>4</sup>( Science Applications International Corp.

cavity, the stagger tuning of the resonant frequencies of each of the 4 cavities, and manufacturing and assembly issues. Recent calculations using the MAGY gyrokystron code have also indicated an increased heat load in the drift tubes from non-resonant RF resulting from the bunched electron beam [5]. Detailed thermal and mechanical stress analysis of the circuit under the high thermal load accompanying the 10 kW average power operation has been carried out. The input window is in WR-10 rectangular waveguide, and the output is in 1.284" ID circular waveguide. The required input power is approximately 50 W at the input window flange and will be provided by a CPI coupled-cavity TWT (VTW-6495). The drive level of this CCTWT is approximately +4dBm.

The amplifier utilizes a diamond output window in the first device. The first device will be tested with a liquid helium (LHe) filled magnet system, however, a cryogen-free superconducting magnet is presently being built for this gyrokystron and will be delivered with the gyrokystron to the Radar Division. In addition, an all-high temperature superconducting magnet is being fabricated by Intermagnetics General Corp. for this gyrokystron [6]. This HTS magnet will operate with a closed-cycle cryo-cooler at approximately 15K. To date, the LHe magnet has been successfully tested. The major components of the tube have been completed, and the gyrokystron has been successfully processed and pinched-off.

Parameter	Design Value
Frequency	94 GHz
Operating Mode	TE <sub>01</sub>
Peak Power	80 kW
Average Power	10 kW
Max. Beam Duty Factor	15%
Bandwidth [-3 dB]	> 600 MHz
Drive Power	40 W
Cathode Voltage	- 65 kV
Mod-anode Voltage	18 kV
Peak Current	6 A

Fig. Design Parameters for 94 GHz gyrokystron

(Azimuthal and Elevation) and low cross polarization mode content. A quasi-optical TEM<sub>00</sub> mode antenna duplexer will be mounted on the antenna with a design similar to past high power millimeter wave radar duplexers, albeit at a much higher power.

Following successful demonstration of this device at high average power, the gyrokystron will be delivered to the NRL Radar Division for the millimeter wave radar project. In the initial installation of the radar, the amplifier will be mounted in a trailer with the pedestal and dish antenna mounted on top of the trailer. The transmission line from the gyrokystron to the antenna is presently being designed. This transmission line must incorporate provision for handling the full 10 kW average power over the instantaneous bandwidth of >600 MHz (2 GHz in future upgrades), with two rotary joints

### Conclusions

The 94 GHz gyrokystron has been completed; testing is scheduled to begin during the summer of 1998. When successful, this amplifier will enable the development of a millimeter wave radar with more than an order of magnitude more power than present day radars at comparable frequencies.

### References

- [1] M. Blank *et al.*, "Experimental demonstration of a W-band gyrokystron amplifier," Phys. Rev. Lett. Vol. 79, No. 22, pp. 4485-4488, December 1997.
- [2] M. Blank *et al.*, "Experimental Investigation of W-band (93 GHz) gyrokystron amplifiers," IEEE Trans. Plasma. Sci., Vol. 26, No. 3, June 1998.
- [3] M. Blank, B.G. Danly, B. Levush "Experimental Demonstration of W-Band Gyro-Amplifiers with Improved Performance", This Conference Digest, 1998.
- [4] D. Pershing, K. Nguyen, J. Petillo, J.P. Calame, B.G. Danly, B. Levush, "Circuit Design of the NRL/Industrial 94 GHz Gyrokystron Amplifier", Proc. 22<sup>nd</sup> Int. Conf. IR and MM Waves, Th1.4, 1997.
- [5] K. Nguyen, M. Botton, T.M. Antonsen, B. Levush, M. Blank, J.P. Calame, "Self-consistent time-dependent modeling of gyro-amplifiers with MAGY", This Conference Digest, 1998.
- [6] D. Hazelton, B.G. Danly, D. Gubser, "Cryogen-free high temperature superconducting magnet for 94 GHz gyrokystron powered radar applications", Proc. Amer. Soc. Naval Engineers, ASNE98 Conference, Washington, DC, 1998.

## Pulsed GaAs-IMPATT Oscillators up to 200 GHz

C. Benz, J. Freyer

Technische Universität München, Lehrstuhl für Allgemeine Elektrotechnik und Angewandte Elektronik  
Arcisstr. 21, D-80290 München, Germany, e-mail: benz@aet.e-technik.tu-muenchen.de

### Abstract

GaAs Double-Read IMPATT diodes for pulsed operation are optimised for extremely high current densities ( $200 \text{ kA/cm}^2$ ) at frequencies up to 200 GHz. Active device and resonator impedance are determined by the help of simulation programmes. The used mounting technique without parasitic elements ensures low loss impedance transformation of the investigated IMPATT diodes. The experimental results (176 GHz: 1 W; 198 GHz: 0.3 W) fit quite well to the applied oscillator model.

### Introduction

In the past few years significant progress has been achieved in mm-wave power generation using GaAs transit time devices [1]. Due to their excellent noise behaviour in cw-mode at upper D-band frequencies [2, 3], these devices are used for pulsed operation, too. Since very promising results were obtained with pulsed Double-Read IMPATT diodes [4], investigations concentrate on the optimisation of these structures for operation at extremely high current densities.

### Device Design

The realisation of mm-wave oscillators at elevated frequencies is concerned with high dc-current densities to be supplied to the IMPATT diode. In the cw-mode dc-input power and thus maximum current density of the active element are thermally restricted. Since at pulsed operation this limitation is not as severe, extremely high current densities can be applied, to increase the avalanche frequency and thus the oscillation frequency of the diode. The applied device structure has to be well designed for efficient heat transfer to the heat sink in order to decrease the thermal resistance and thus the maximum device temperature during operation.

The applied active devices in this paper are Double-Read GaAs IMPATT diodes which have been already successfully realised for cw-operation [1]. The avalanche region of this device type was designed by Monte Carlo simulation and the drift regions for electrons and holes, respectively, are optimised for pulsed operation. For typical dc current densities in the range of  $150 \text{ kA/cm}^2$  to  $200 \text{ kA/cm}^2$ , the electric field strength within the drift zones must be below breakdown field to prevent carrier generation due to impact ionisation. The real part of the device impedance must compensate at least the total losses of the diode contacts and the resonator (about  $2.4 \cdot 10^{-6} \Omega \text{cm}^2$ ). By the help of a large-signal drift-diffusion model [6] the optimum length and doping concentration of the drift zones are determined for a given current density and frequency range. Thus, successful design of IMPATT-structures up to 200 GHz was performed. In Fig. 1 an optimum diode structure for a frequency range between 160 GHz and 200 GHz at dc current density of  $175 \text{ kA/cm}^2$  is given.

### Resonator Structure

Generally, the realisation of oscillators at pulsed operation is related to the application of waveguide resonators with inductive post structure, where the waveguide height is reduced to 1/3 of the normal height for impedance matching of devices with relatively large areas. Since there is a great demand on mechanical precision and tuning behaviour at G-band frequencies (140 GHz - 220 GHz, waveguide height:  $650 \mu\text{m}$ ), the application of this resonator structure appears quite critical. First experiments carried out at D-Band frequencies (110 GHz - 170 GHz) [4] and simulations from a finite element programme qualifies also the full height waveguide resonator with inductive post structure for pulsed operation. Impedance matching of active device and load resistance can be achieved for oscillation frequencies up to 200 GHz if the impedance transformation to the relatively low device impedance is carried out by appropriate choice of only the resonator post height and diameter. Conventional stand-off technology for the encapsulation of the active device is not applicable due to the relatively high values of the parasitic elements and the small degree of reproducibility. Even the module technique [1], which represents the monolithic integration of an active element and the surrounding stand-off structure with well defined parasitics can not be applied, since also the parasitics of this encapsulation technique lead to a drastic reduction of the small negative device resistance or to a quenching at all. Therefore,



a new mounting technique without parasitic elements for large area devices is developed, which ensures low loss impedance transformation of the investigated IMPATT diodes. By the help of standard photoresist technology the active device structure and a truncated cone of Au on top of the device are fabricated. The truncated Au-cone adjusts the height of the post above the waveguide bottom. The monolithic realisation of the element ensures high reproducibility and sensitive adjustment of the load resistance for impedance matching. The single elements are bonded by thermocompression on the metallised diamond heat-sink on the bottom of the resonator. The total applied resonator structure consists of the full height waveguide section with inductive post structure and a sliding short for tuning as illustrated in Fig. 2.

### Experimental Results

The applied Double-Read IMPATT structures (see Fig. 1) are grown in an MBE system on GaAs  $n^+$ -substrates. During growth attention is focused on exact compliance with length and doping concentration of the individual layers. The diodes have been optimised with regard to low internal losses by the application of a Ti-Schottky contact on the highly doped  $n^+$ -GaAs epitaxial layer [5]. For the  $p^+$ -ohmic contact Ti/Pt/Au is used. The truncated cone of Au for post height adjustment is galvanically grown on the upper  $n^+$ -contact of the active device. For optimum heat transfer from the chip to the diamond heat sink, the pressure in the thermocompression process has to be adjusted precisely according to the applied device diameters. Experiments are carried out at dc current densities of 150 kA/cm<sup>2</sup> and 175 kA/cm<sup>2</sup>. For a current density of 175 kA/cm<sup>2</sup>, which is equivalent to an applied dc input power density of about 2 MW/cm<sup>2</sup>, the pulse length is reduced from 75 ns (used for operation at 150 kA/cm<sup>2</sup>) to 55 ns to ensure a device temperature of about 500 K for optimal operation. The devices have diameters between 24  $\mu$ m and 37  $\mu$ m. The results for rf-output power as a function of oscillation frequency are given in Fig. 3. At 176.5 GHz a maximum rf-output power of 1 W could be realised. Up to now the maximum oscillation frequency of 198 GHz is realised with 0.3 W rf-output power. The results are in good agreement with those of a self-consistent steady state oscillator simulation where oscillation frequency and rf-output power can be calculated as a function of the sliding short position [7]. Herein the nonlinear device is characterised by the drift-diffusion model and the load impedance of a given resonator geometry is described by a finite element programme. The theoretical results from Fig. 3 are calculated for a value of the total losses of  $2 \cdot 10^{-6} \Omega \text{cm}^2$ . Fig. 4 shows as an example the resonator and diode impedance loci in dependence of frequency and rf-voltage  $U_1$ , respectively, for the realised oscillator at 176.5 GHz. At the point of intersection oscillation condition is fulfilled and stable operation of the oscillator is obtained. The representation in Fig. 4 is associated with the given rf-output power at this frequency in Fig. 3.

### Conclusion

With the help of a large-signal drift-diffusion model, a GaAs Double-Read IMPATT diode is designed for pulsed operation up to 200 GHz for extremely high current densities. An appropriate resonator structure consisting of a full height waveguide section with inductive post structure is realised for optimum impedance matching between active device and load resistance. Using the applied mounting technique without parasitic elements low loss transformation of the negative device resistance is ensured. Rf-output power of 1 W at 176.5 GHz and 0.3 W at 198 GHz are realised. The experimental results are in good agreement with the applied oscillator model.

### Acknowledgement:

We are grateful to H. Grothe for supplying the MBE-material. Financial support of the DFG (SFB 348) is kindly acknowledged.

### References:

1. M Tschernitz, J Freyer, Electronics Letters 31, 582 (1995)
2. M Pöbl, W Bogner, L Gaul, Electronics Letters 30, 1316 (1994)
3. M Tschernitz, Ph. D. Thesis, Technical University of Munich (1995)
4. C Benz, J Freyer, Proc. of 21<sup>st</sup> Intern. Conf. on Infrared and Millimeter Waves, Berlin, Germany (1996)
5. J Freyer, M Tschernitz, H Grothe, W Harth, Proc. of 3<sup>rd</sup> Intern. Workshop on Terahertz Electronics, Zermatt, Switzerland (1995)
6. L Gaul, Ph. D. Thesis, Technical University of Munich (1993)
7. T Bauer, J Freyer, Proc. of Intern. Workshop on Millimeter Waves, Orvieto, Italy (1996)

## List of Figures:

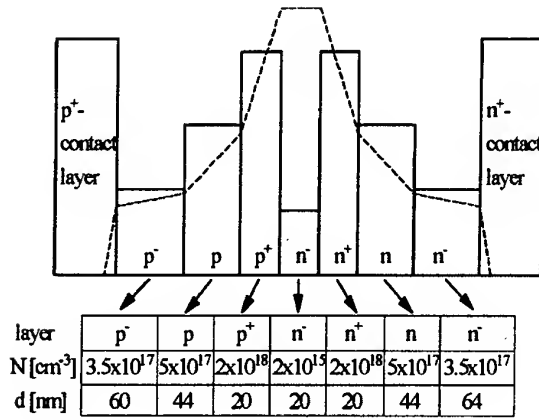


Fig. 1:

Structure of the applied Double-Read IMPATT diode for 160 GHz to 200 GHz.

(The dashed line shows the electric field distribution)

The table represents doping concentration and thickness of the corresponding layers.

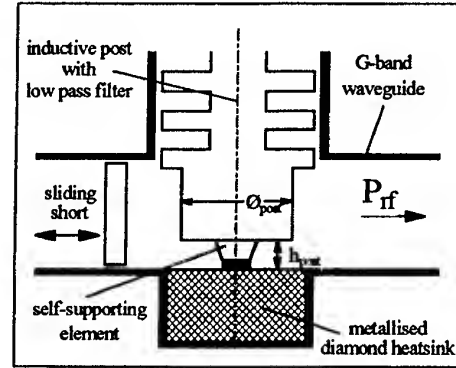


Fig. 2:

Schematic cross-section of the applied resonator structure, with low loss mounting technique of the active device.

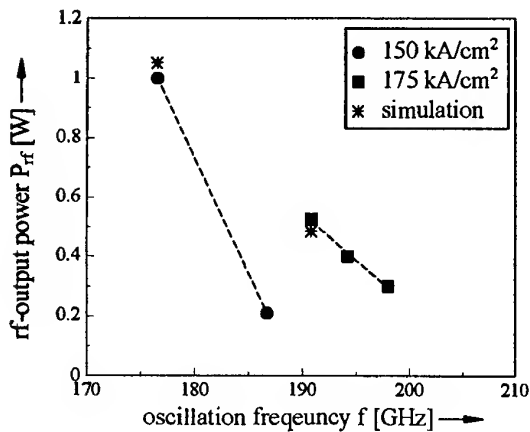


Fig. 3:

Measured peak rf-output power  $P_{rf}$  versus oscillation frequency of the investigated oscillators. Parameter is the applied dc-current density. The theoretical results are shown by (\*).

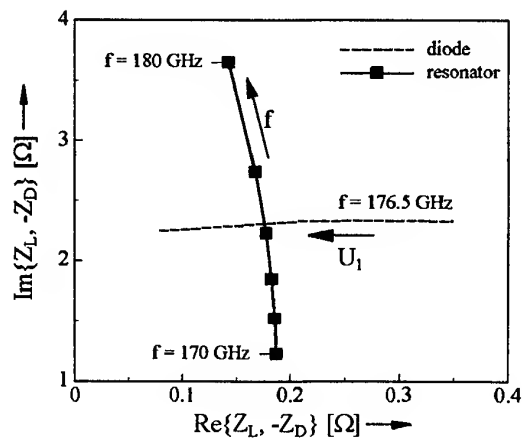


Fig. 4:

Impedance locus of resonator and Double-Read IMPATT diode.

G-band resonator:  $h_{post} = 18 \mu\text{m}$ ,  $\phi_{post} = 500 \mu\text{m}$  (see Fig. 2)

Diode:  $J_0 = 150 \text{ kA/cm}^2$ ,  $T = 500 \text{ K}$

## Realization of active mode locking of the p-Ge hot hole laser.

J.N. Hovenier, M.C. Diez, T.O. Klaassen and W.Th. Wenckebach,

Department of Applied Physics and DIMES, Delft University of Technology,  
P.O.Box 5046, 2600 GA Delft, The Netherlands,

and

A.V. Muravjov, S.G. Pavlov and V.N. Shastin,

Institute for Physics of Microstructures, Russian Academy of Sciences,  
GSP-105, Nizhny Novgorod 603600, Russia.

### Introduction

Until now little work has been performed to optimize the *short pulsed* characteristics of the p-Ge hot hole laser in order to optimize this source for time resolved THz experiments. Some time ago we proposed a method to achieve gain modulation that might result in active mode locking of the laser [1]. Recently we reported on the first experimental observation of mode locked operation [2,3]. Here we will discuss the experimental realisation of active mode locking and present recent results on wavelength, small signal gain and pulse shape of this mode locked THz laser, with emphasis on the behaviour at  $B \approx 0.5$  T. We show that the system is capable of producing 100 ps FWHM pulses.

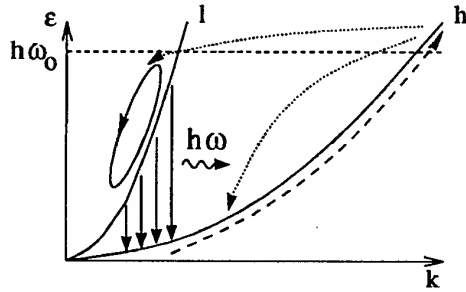


Figure 1: Mechanism for population inversion : the pumping cycle from heavy (h) to light (l) hole subband is indicated.

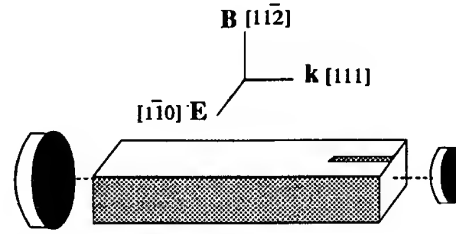


Figure 2: p-Ge laser cavity design.

The operation of the p-Ge hot hole laser [4] is based on the acceleration of holes in  $\vec{E} \perp \vec{B}$  fields at  $T \leq 20$  K. For  $E/B \approx 1.5$  kV/cmT the heavy holes are scattered by optical phonons - partially into the light hole band - whereas the light holes are accumulated on closed trajectories below the optical phonon energy (see fig. 1). The resulting population inversion between the lh- and hh-band leads to emission in the 1.5-4.2 THz range. An electric field component  $\parallel \vec{B}$  causes an acceleration of the holes  $\parallel \vec{B}$ . This leads to optical phonon scattering of *light* holes too, and thus to a decrease of population inversion. Application of a radio frequency (RF) electric field  $\parallel \vec{B}$  at *half* the roundtrip frequency of the laser cavity then leads to modulation of the gain at the roundtrip frequency -the gain reaches a minimum at maximum amplitude of the rf field, i.e. twice per cycle - and possibly to mode locking [1].

The laser sample was cut from a single crystal of Ga doped Ge, with  $N_{Ga} = 7.10^{13} \text{ cm}^{-3}$ , in the form of a rectangular parallelepiped of  $5 \times 7 \times 49.46$  mm. The high voltage electric excitation field ( $\vec{E} \parallel [1\bar{1}0]$ ) is applied to ohmic contacts covering two opposite lateral surfaces of the sample in pulses of a few  $\mu\text{s}$  long to avoid excessive heating. The magnetic field ( $\vec{B} \parallel [11\bar{2}]$ ) is applied perpendicular to the long axis and to  $\vec{E}$  (Voigt configuration). The RF electric field  $\parallel \vec{B}$  for gain modulation is applied also in short pulses to additional ohmic contacts of  $1 \times 10$

mm<sup>2</sup> on the lateral sides of the sample. The RF frequency of 386.1 MHz equals half the laser cavity round trip frequency. Two gold mirrors, evaporated on quartz substrates and isolated by 10  $\mu$ m Teflon films are attached to the ends of the sample. The entire system is immersed in liquid helium. At the side of the smaller, 4 mm diameter, mirror, laser radiation is coupled out and detected with fast room temperature GaAs Schottky diode detectors. The signal is displayed using a 1 GHz bandwidth, 5 GS/s, oscilloscope to monitor the overall pulse envelope. For a detailed study of the waveform of individual pulses, a 6 GHz bandwidth real time oscilloscope was used. The overall response time of the electronic system was found to be 100 ps.

### Pulsed operation

To better understand the mode locked operation, first the time- and wavelength resolved properties of the laser under unmodulated, pulsed, operation is discussed. The absence of frequency selective elements in the present cavity together with the inherently broad band nature of the lh- to hh- hole transition, causes laser action to occur simultaneously at a large number of longitudinal modes. In fig. 3 the observed frequency band as a function of the applied B-field

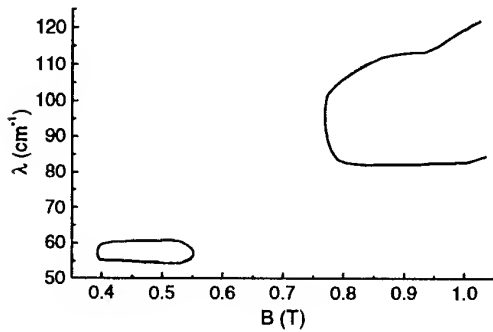


Figure 3: Laser emission band as a function of applied B-field

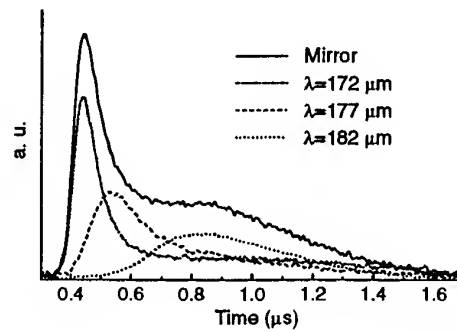


Figure 4: Time resolved optical output for different wavelengths at B=0.5T

is shown. The gap in the spectrum results from optical absorption due to acceptors in the crystal. In fig. 4 the time dependence of the optical pulse for B=0.5 T at three different wavelengths is shown, together with the pulse shape of the total optical output, measured using a mirror instead of a grating as reflecting element. The zero of the time scale coincides with the start of the E-field excitation pulse. It is clear that laser action starts at short wavelengths and shifts towards longer wavelengths during the optical pulse. Similar effect are observed for  $B \geq 0.75$  T. From the growth of intensity in the early part of these pulses, the wavelength dependent effective small signal gain has been determined to be  $g_{(172)}=0.015 \text{ cm}^{-1}$ ,  $g_{(177)}=0.0026 \text{ cm}^{-1}$  and  $g_{(182)}=0.0021 \text{ cm}^{-1}$ .

### Mode locked operation

With the RF modulation field applied, active mode locking of the laser is achieved [2,3]. The emission band is about the same as observed for pulsed operation, although the pulse delays are slightly larger. In figs. 5 and 6 the typical time dependent optical output under mode locked conditions, at B=0.5 T and  $\lambda \approx 172 \mu\text{m}$ , is shown.

In the early stage of laser action (fig. 5) a regular train of pulses with a 1.3 ns separation, the cavity round trip time, is observed. The growth of intensity reflects the small signal gain per round trip. With increasing amplitude also a decrease of pulse width, typical for mode locked

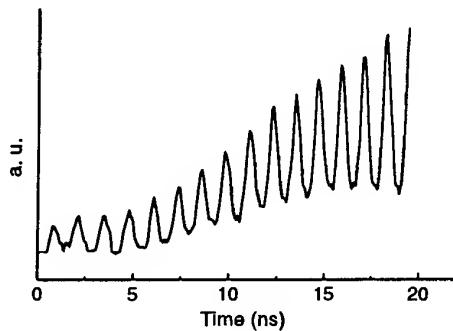


Figure 5: Laser output in early part of emission: small signal gain region

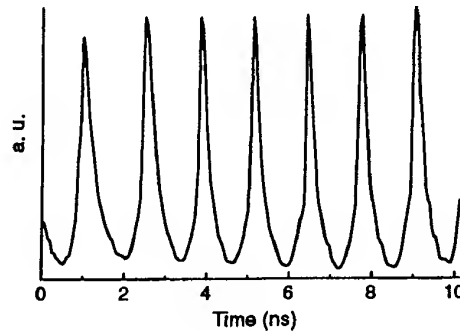


Figure 6: Pulse train in saturated gain region

operation, is observed. The small signal gain is found to be slightly larger than for pulsed operation. Because the rf modulation causes a loss in overall roundtrip gain, clearly a substantial increase of the gain in the unmodulated part of the crystal with respect to that under quasi CW operation must occur. Under saturated gain conditions, a train of constant amplitude, narrow pulses is observed (fig. 6). As shown in fig. 7, the minimum width of these pulses is found to be about 100 ps FWHM. In view of the system risetime of 100 ps, it is conceivable that the actual pulse width can even be shorter.

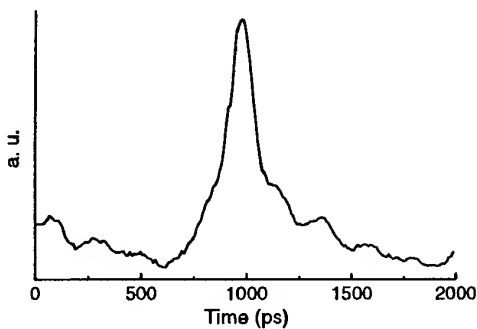


Figure 7: Shape of micropulse in saturated gain region

In the 177-182  $\mu\text{m}$  region where laser action is delayed compared with that at 172  $\mu\text{m}$ , merely a low intensity amplitude modulated output is seen. Probably due to the much smaller gain at these wavelengths, the gain modulation does not lead to genuine mode locking. Because of the change of wavelength during the optical pulse, stationary mode locking at 172  $\mu\text{m}$  is only of short duration: near the end of the emission the pulse train therefore shows an irregular behaviour. Introduction of a, frequency selective, mesh outcoupler might yield a more stable mode locked output.

This work is part of the research program of the European TMR network "INTERACT"

#### References.

- [1] R.C. Strijbos, J.G.S. Lok, W.Th. Wenckebach, J. Phys.: Condens. Matter 6(1994)7461.
- [2] J.N. Hovenier, A.V. Muravjov, S.G. Pavlov, V.N. Shastin, R.C. Strijbos, W.Th. Wenckebach, Appl. Phys. Lett. 71(1997)443.
- [3] J.N. Hovenier, T.O. Klaassen, W.Th. Wenckebach, A.V. Muravjov, S.G. Pavlov, V.N. Shastin, Appl. Phys. Lett. 72(1998)1140.
- [4] Opt. Quantum Electron. 23(1991) Special Issue on Far-infrared Semiconductor Lasers, Eds. E. Gornik and A.A. Andronov.

# Technical aspects of the mode locked p-Ge hot hole laser

J.N. Hovenier, R.N. Schouten, J.H. Blok, T.O. Klaassen, W.Th. Wenckebach,

Department of Applied Physics and DIMES Delft University of Technology,  
P.O.Box 5046, 2600 GA Delft, The Netherlands,  
and

A.V. Muravjov, S.G. Pavlov and V.N. Shastin,

Institute for Physics of Microstructures, Russian Academy of Sciences,  
GSP-105, Nizhny Novgorod 603600, Russia.

## Introduction

The laser action of the p-Ge hot hole laser is based on a population inversion between the light and heavy hole band at temperatures below  $\approx 20$  K [1]. This population inversion is created through the acceleration of the light and heavy holes in crossed electric and magnetic fields. The heavy holes are then accelerated up to energies above the optical phonon energy (37 meV); consequently they are scattered strongly, partially into the light hole band. The light holes do not reach the optical phonon energy and are accumulated on closed trajectories, and exhibit a much longer lifetime than that of the heavy holes. The resulting population inversion leads to frequency tunable emission in the 1.5-4.2 THz range. A component of  $E \parallel \vec{B}$  causes an acceleration of the holes  $\parallel \vec{B}$ , such that also the *light* holes will reach the optical phonon energy and scatter at optical phonons. This leads to a destruction of the population inversion and thus of the laser gain. In [2] we proposed to use a radio frequency (RF) electric field  $\parallel \vec{B}$  to modulate the gain. As the gain reaches a minimum at maximum amplitude of the rf field, i.e. twice per cycle, an RF field at *half* the cavity round trip frequency leads to gain modulation at the roundtrip frequency, and thus active mode locking of the laser. In fig. 1 the sample magneto-resistance and necessary E and B fields for laser action are shown.

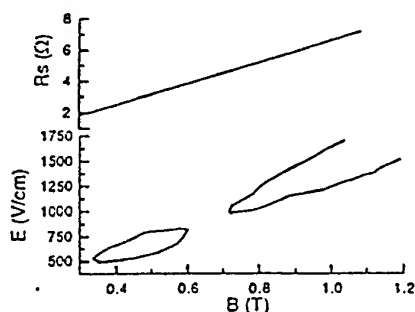


Fig. 1. Sample resistance and active E-B region

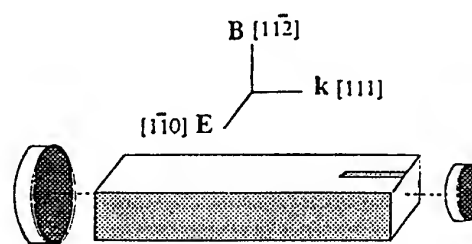


Fig. 2. p-Ge laser cavity design.

## Experimental setup and results

The laser sample was cut from a single crystal of Ga doped Ge,  $N_{Ga} = 7.10^{13} \text{ cm}^{-3}$ , in the form of a rectangular parallelepiped of  $5 \times 7 \times 49.46$  mm (fig. 2). The high voltage electric excitation field is applied to ohmic contacts covering two opposite lateral surfaces of the sample in pulses of a few  $\mu\text{s}$  long to avoid excessive heating. The magnetic field is applied perpendicular to the long axis and to  $\vec{E}$  (Voigt configuration). The RF electric field  $\parallel \vec{B}$  for gain modulation is applied also in short pulses to additional ohmic contacts of  $1 \times 10 \text{ mm}^2$  on the lateral sides of the sample. Two gold mirrors, evaporated on quartz substrates and isolated by  $10 \mu\text{m}$  Teflon films are attached to the ends of the sample. The entire system is immersed in liquid helium. At the side of the smaller, 4 mm diameter, mirror, laser radiation is coupled out and detected. The High Voltage pulser consists of a large low inductance capacitor bank and a fast switch

with the following specifications: flatness is better than 1% over a  $10\mu\text{s}$  pulse, risetime  $\leq 500\text{ns}$ ,  $V_{\text{max}}=1800\text{V}$ ,  $I_{\text{max}}=500\text{A}$  and output impedance  $Z_0=4\Omega$ . A balanced  $Z_0=4\Omega$  transmission line for this HV pulse was made from  $75\mu\text{m}$  thick KAPTON film with  $5\text{mm}$  wide copper conductors on both sides. For the gain modulation, a high voltage proof buffer amplifier with a  $250\text{W}$  @  $386\text{MHz}$  output was developed. The RF power is transferred to the Ge- sample by a  $50\Omega$  coax cable. Inside the home build cryostat, as close as possible to the sample, a resonant circuit and transformer to match the  $\approx 10\Omega$  resistance between the RF contacts on the Ge crystal to the  $50\Omega$  cable is situated. The homogeneous electromagnet ( $B_{\text{max}} \approx 1.5\text{T}$ ) with a  $65\text{mm}$  bore, can be rotated to adjust the angle between E- and B-field to obtain optimum laser action. The spectrum of the laser output is measured with a resolution of about 1% using a  $7.9$  grooves/mm Littrow grating. The optical output can be detected with a variety of far infrared detectors, and monitored with different oscilloscopes (see fig. 3 for the experimental setup).

Detector	Sens.	Risetime	NEP	Oscilloscope	Bandwidth	Sampling
Pyro 1	1 KV/W	100 $\mu\text{s}$	4.7E-9	Tektronix TDS 620	0.5GHz	2GS/s
Pyro 2	100 V/W	10 $\mu\text{s}$	1.5E-8	Tektronix TDS 680	1GHz	5GS/s
Micro bolo	1 V/W	50 ns		Tektronix 7250	6GHz	real time
Ge	2 KV/W	350 ns		H.P. 54120B	34GHz	
Schottky	60 V/W	50 ps	5E-9	+ 54123A preamp		

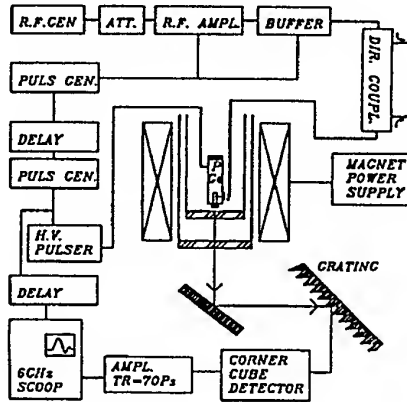


Fig. 3. Experimental setup

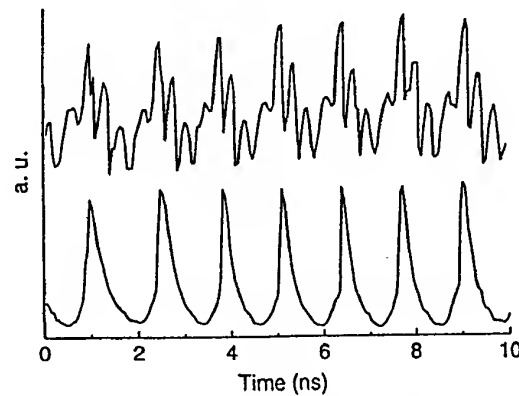


Fig.4. Mode locked Pulse train.

Fig. 4 shows pulse trains under mode locked operation; FIR pulses at  $1.3\text{ ns}$  cavity round trip time, with a  $150\text{ ps}$  FWHM [3]. The upper trace gives the signal of a corner cube Schottky detector with inferior video circuit showing many internal reflections. The lower trace depicts the signal using a Schottky detector with factory optimized video circuit. Now the limit of the rise time of our overall electronic system ( $100\text{ps}$  with Tek. 7250) is reached. Probably FIR pulses are shorter than we can detect at this moment. The H.P. 54120B scope has a  $10\text{ps}$  resolution, but because of its slow sampling rate, the signal is build up from many sequential pulses. Although mode locked pulses can be observed with that system, more work on laser stability and trigger circuit has to be performed before effective risetimes below  $100\text{ ps}$  can be realized.

#### References

- [1] Opt. Quantum Electron. 23(1991) Special Issue on Far-infrared Semiconductor Lasers, Eds. E. Gornik and A.A. Andronov.
- [2] R.C. Strijbos, J.G.S. Lok, W.Th. Wenckebach, J. Phys.: Condens. Matter 6(1994)7461.
- [3] J.N. Hovenier, T.O. Klaassen, W.Th. Wenckebach, A.V. Muravjov, S.G. Pavlov, V.N. Shastin, Appl. Phys. Lett. 72(1998)1140.

# Oscillation of the p-Ge IVB Laser with Very Small Crystal Size

Norihisa Hiromoto, Iwao Hosako, and Mikio Fujiwara

Communications Research Laboratory  
4-2-1 Nukui-kita, Koganei, Tokyo 184-8795, Japan  
FAX: +81-423-27-6941, E-mail: [hiromoto@crl.go.jp](mailto:hiromoto@crl.go.jp)

**Abstract:** Pulse oscillation has been obtained from p-Ge IVB lasers with a Ga-doped Ge crystal of  $1 \times 1 \times 5 \text{ mm}^3$  under the [100] uniaxial stress, which is the smallest in the sizes previously reported so far. Electric power needed to lasing was only 300 W. This small power is important to keep the crystal at the low temperature and to achieve the continuous wave (CW) oscillation in future.

## 1. Introduction

The p-type Ge IVB (intervalence band) laser<sup>[1-3]</sup> is the promising coherent source in the far-infrared region because of its small size, reasonable output power, wide tunable-wavelength range, narrow line-width, long life-time, and so on.

Although only the pulse oscillation was achieved with the pulse widths of the order of  $\mu\text{s}$  so far, the miniaturization of the p-type Ge laser rods has been recently studied in order to accomplish high-duty-cycle pulse oscillation and continuous wave oscillation in near future<sup>[4,5]</sup>.

In this paper, we report the laser oscillation from a very small ( $1 \times 1 \times 5 \text{ mm}^3$ ) rod of the p-type Ge crystal to which uniaxial stress is applied.

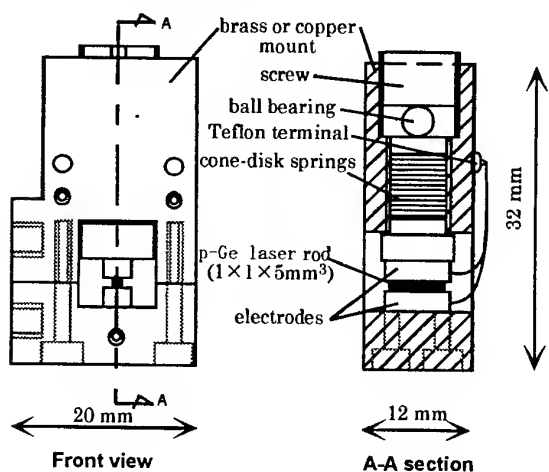


Fig. 1 A p-type Ge laser mount which applies the [100] uniaxial stress to the small laser rod.

## 2. Fabrication and Experiment

The p-type Ge laser rods of rectangular shape were fabricated by the same process as the case of the Ge:Ga photoconductors.<sup>[6]</sup> The size of the rods is  $1 \times 1 \times 5 \text{ mm}^3$ , the ohmic electrodes are  $1 \times 5 \text{ mm}^2$  area, and all surfaces are (100).

The p-type Ge crystal has acceptor (Ga) concentration of  $1 \times 10^{14} \text{ cm}^{-3}$  and compensation of  $5.6 \times 10^{17} \text{ cm}^{-3}$ .

Figure 1 shows a mount which applies uniaxial stress to the small p-type Ge laser rod in the direction of the electrodes.

The p-type Ge laser was cooled at 4.2 K in the liquid He dewar, and it was oscillated under the crossed electric and magnetic fields in the Faraday configuration. The electric pulse width applied was typically  $2 \mu\text{s}$ . Far-infrared power was measured with a stressed Ge:Ga photoconductor<sup>[6]</sup> which responded to the light of shorter wavelengths than  $200 \mu\text{m}$ .

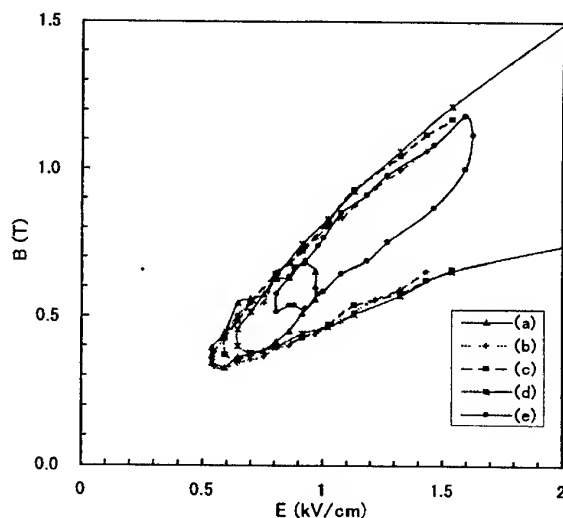


Fig. 2 Lasing regions on the plane of electric and magnetic fields. Stresses applied to the p-Ge crystal are (a)  $1300 \text{ kg/cm}^2$ , (b)  $3500 \text{ kg/cm}^2$ , (c)  $4100 \text{ kg/cm}^2$ , (d)  $5000 \text{ kg/cm}^2$ , and (e)  $6500 \text{ kg/cm}^2$ .



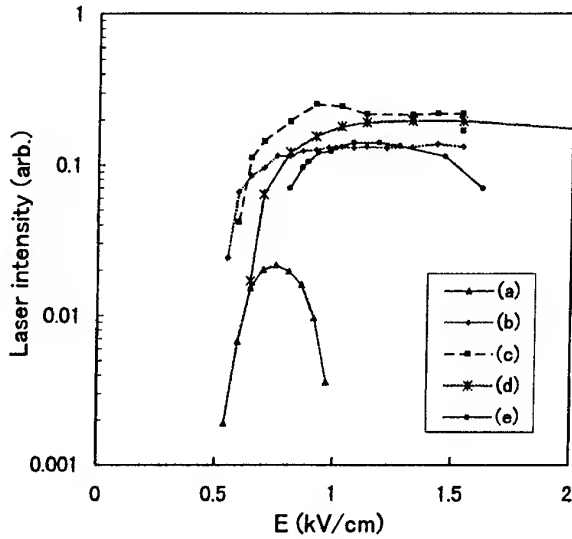


Fig. 3 Far-infrared intensity of the laser oscillation as functions of the electric field. Conditions of stresses for (a) to (e) are the same as Fig. 2.

### 3. Results

The lasing regions on the plane of electric and magnetic fields are shown in Fig. 2. Uniaxial stresses applied to the small p-Ge laser rod were (a) 1300 kg/cm<sup>2</sup>, (b) 3500 kg/cm<sup>2</sup>, (c) 4100 kg/cm<sup>2</sup>, (d) 5000 kg/cm<sup>2</sup>, and (e) 6500 kg/cm<sup>2</sup>. Lasing occurs only in the lower electric and magnetic fields for the smallest stress (a), but it occurs only in the higher fields for the largest stresses (d). The widest lasing regions are achieved for around the stresses of (b), (c) and (d). The minimum fields necessary for lasing increase with the stress.

Figure 3 shows the measured far-infrared laser intensity as functions of the electric field for the same stress conditions as in Fig. 2. The laser intensity increases, it has the maximum at the stress of (c), and then it decreases, as the stress increases.

Figure 4 shows the input voltage and current for the small p-Ge laser. The minimum electric power needed for lasing was only 300 W. The largest duty cycle was achieved at a 1.4 kHz pulse repetition rate, and it was larger than  $2 \times 10^{-3}$ .

### 4. Discussion

The previous studies revealed that both the lasing regions and the intensity of laser emission were remarkably increased by the uniaxial stress,<sup>[9,10]</sup> but their experiments were made under relatively small stresses, that is smaller than only 500 kg/cm<sup>2</sup>.

We found that the large uniaxial stress as 3000-4000

kg/cm<sup>2</sup> was the most effective for the laser oscillation of the p-Ge laser.

Increase in the lasing regions and the laser intensity appeared in Figs. 2 and 3 can be explained by the decrease of ionized impurity-scattering probability between holes due to the splitting of the valence bands<sup>[11]</sup> caused by the uniaxial stress. Increase of the minimum fields for lasing is also related to the band splitting which diminish the transition probability from heavy to light holes by the optical-phonon emission under the lower electric fields.

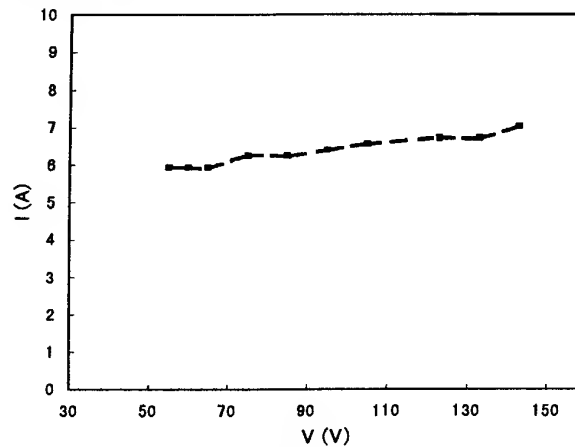


Fig. 4 Input current and voltage for the small p-type Ge laser of  $1 \times 1 \times 5$  mm<sup>3</sup>-volume.

### References

- [1] A. A. Andronov, I. V. Zverev, V. A. Kozlov, Yu. N. Nozdrin, S. A. Pavlov, and V. N. Shastin, *JETP Lett.* **40**, 804-807 (1984).
- [2] S. Komiyama, N. Iizuka, and Y. Akasaka, *Appl. Phys. Lett.* **47**, 958-960 (1985).
- [3] E. Gornik ed, *Special Issue on Far-Infrared Semiconductor Lasers*, *Opt. Quantum Electron.* **23** (1991).
- [4] E. Brundermann, H. P. Roeser, W. Heiss, E. Gornik, and E. E. Haller, *Appl. Phys. Lett.* **67**, 3543-3545 (1995).
- [5] E. Brundermann, A. M. Linhart, H. P. Roeser, O. D. Dubon, W. L. Hansen, and E. E. Haller, *Appl. Phys. Lett.* **68**, 1359-1361 (1996).
- [6] N. Hiromoto, M. Saito, and H. Okuda, *Jpn. J. Appl. Phys.* **29**, 1739-1744 (1990).
- [7] N. Hiromoto and M. Fujiwara, *Jpn. J. Appl. Phys.* **35**, 4685-4688 (1996).
- [8] N. Hiromoto, T. Itabe, H. Shibai, H. Matsuhara, T. Nakagawa, and H. Okuda, *Appl. Opt.* **31**, 460-465 (1992).
- [9] S. Komiyama and S. Kuroda, *Phys. Rev. B* **38**, 1274-1280 (1988).
- [10] V. I. Gavrilenko and V. V. Nikonorov, *Opt. Quantum Electron.* **23**, S217-S220 (1991).
- [11] G. E. Pikus and G. L. Bir, *Sov. Phys. Solid State* **1**, 1502 (1960).

## Charging effects in mode-locked THz p-Ge lasers

R. C. Strijbos,<sup>1</sup> S. H. Withers,<sup>1</sup> A. V. Muravjov,<sup>1</sup> C. J. Fredricksen,<sup>1</sup>  
W. Trimble,<sup>1</sup> S. G. Pavlov,<sup>2</sup> V. N. Shastin,<sup>2</sup> and R. E. Peale<sup>1</sup>

<sup>1</sup> Department of Physics, University of Central Florida, Orlando, FL 32816,  
Fax: (407) 823-5112, E-mail: rsb@physics.ucf.edu

<sup>2</sup> Institute for Physics of Microstructures, Russian Academy of Sciences,  
GSP-105, Nizhny Novgorod 603600, Russia

The p-Ge far-infrared laser ( $50 - 140 \text{ cm}^{-1}$ ) is based on a population inversion between light and heavy hole valence subbands in strong crossed electric and magnetic fields ( $\mathbf{E} \perp \mathbf{B}$ ) at helium temperature. Recently, active mode locking by rf gain modulation at one end of the laser rod in the Voigt configuration [1, 2] yielded 200 ps pulses with  $\sim W$  peak power. Fig. 1(a) shows the experimental scheme with contacts, mirrors and applied fields. The gist of this method is that a small electric field component  $E_L$  along  $\mathbf{B}$  accelerates light holes beyond the optical phonon scattering threshold, thereby decreasing their lifetime and reducing gain. In our active mode-locking experiments [2] we have found that the rf  $E_L$ -field modulation is offset by a 'DC'  $E_L$  field due to charging, with significant impact on short pulse formation [2]. An analysis of this offset is presented here.

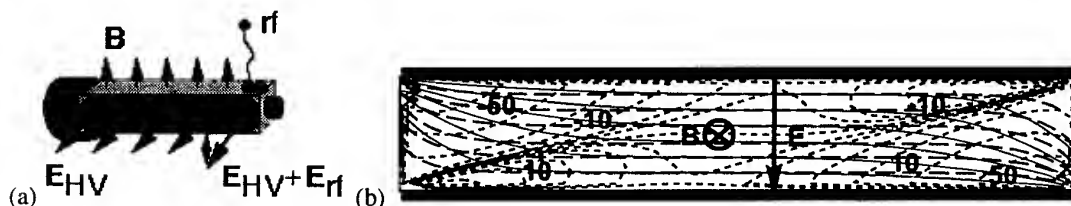


**Figure 1:** (a) Experimental set-up (b) Equipotential lines (each 100 V) in the sample cross-section  $\perp \mathbf{B}$  for  $f = 0$  (no space-charge, long-dashed lines) and  $f = 0.7$  (solid lines). The short-dashed contour lines indicate space charge (in units of  $\epsilon \times 10^6 \text{ Vm}^{-2}$ ) formed for  $f = 0.7$ . A constant Hall-angle ( $\alpha_H = 45^\circ$ ) is assumed and  $V_{\text{appl}} = 700 \text{ V}$ .

Fig. 1(b) shows the electric field distribution found by solving Poisson's equation for a cross-section  $\perp \mathbf{B}$  of our  $d \times h \times l = 7 \times 5 \times 42 \text{ mm}$  laser crystal in Voigt configuration, where  $d$  is the distance between HV contacts,  $h$  the distance between rf contacts, and  $l$  the crystal length. Near the long ends of the laser rod, the total transverse electric field  $E_T$  is larger and rotated over an angle  $\phi$  with respect to the applied field  $E_{\text{appl}}$  due to the usual Hall effect. Apparently, space-charge effects due to current saturation (modeled here by taking the transverse conductivity  $\sigma_T = j_T/E_T \propto E^{-f}$  with  $0 \leq f \leq 1$  a free parameter determining the degree of saturation [3]) significantly enlarge the affected area.

Since  $\mathbf{E}_{\text{appl}} \parallel [1\bar{1}0]$  and  $\mathbf{B} \parallel [112]$ , there is no symmetry plane  $\perp \mathbf{B}$ , and a significant current component  $j_L \parallel \mathbf{B}$  occurs even in perfectly crossed  $\mathbf{E}$  and  $\mathbf{B}$  fields [4, 5]. In Voigt configuration, where the sample dimensions  $\parallel \mathbf{B}$  are relatively small, a  $E_L$  field due to charging will built up in order to make  $j_L$  zero and meet the boundary conditions. In principle, this  $E_L$  field can be compensated by turning the laser crystal over a small angle  $\alpha$  around its long axis (see insets in Fig. 3). However, due to the inhomogeneity of  $E_T$  (Fig. 1(a)), also this  $E_L$  field differs strongly between the central part of the sample and near its long-ends. This can be directly concluded from Fig. 2, showing the Monte Carlo results [4] for the current  $j_L \parallel \mathbf{B}$  when  $E_T$  is rotated over  $\phi$  due to the Hall effect. Additionally,  $j_L$  depends strongly on the ratio  $E/B$  [4, 5]. Turning the sample now optimizes the gain (by minimizing  $E_L$ ) only in the central part, and additional local gain increase between the additional contacts can be achieved by applying a bias  $U_2 - U_1$  to them (see inset in Fig. 3). This allows also to optimize gain modulation and improve active mode locking [2].

In Fig. 3 the change  $\Delta(U_2 - U_1)$  is plotted versus  $\Delta\alpha = \alpha - \alpha_0$  ( $\alpha_0$  is the center of the angle range of lasing). Clearly, for most values of  $\alpha$ , the  $U_2 - U_1$  value without external biasing (denoted by solid symbols in Fig. 3(a)) differs significantly from the  $U_2 - U_1$  values for which lasing is optimal (denoted by open triangles) as obtained by external biasing. This is due to the effects described above. Moreover, the curves in Fig. 3 have non-zero slopes

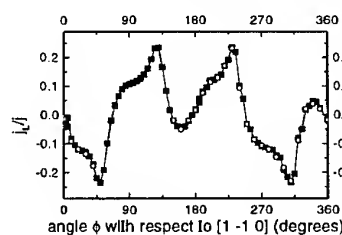


**Figure 2:**  $j_L/j$  versus  $\phi$ ;  $T = 20 \text{ K}$ ,  $E = 1.35 \text{ kV/cm}$ ,  $B = 1.0 \text{ T} \parallel [112]$ ,  $N_l = 1.3 \times 10^{14} \text{ cm}^{-3}$ ,  $p_0 = 7 \times 10^{14} \text{ cm}^{-3}$ , Brooks-Herring model with self-consistent screening

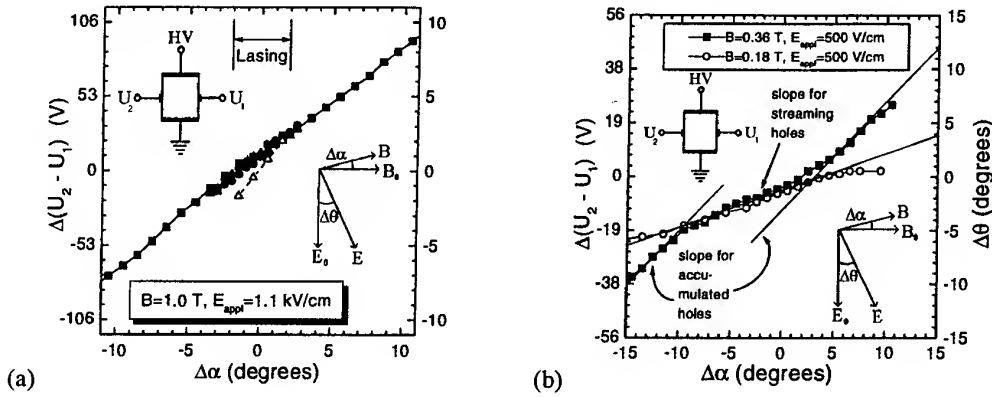


**Figure 3:** Effect of magnetic-field tipping on the potential  $U_2 - U_1$  between rf contacts.

(and in Fig. 3(b) a clear change of slope is observed), indicating another remarkable effect of charging: when the magnetic field  $B$  is tipped (by turning the sample over an angle  $\Delta\alpha$ ), also the total electric field *inside the sample* rotates over an angle  $\Delta\theta \approx \Delta\alpha$  in order to (largely) maintain the perpendicularity of  $E$  and  $B$ . This can be understood in terms of a two conductivity model [4], simplifying the complicated hole motion into a longitudinal motion along  $B$  (determined by  $\sigma_L = j_L/E_L$ ) and transverse motion perpendicular to  $B$  (determined by  $\sigma_T = j_T/E_T$ ), where  $j_L, j_T$  and  $E_L, E_T$  are the longitudinal and transverse hole currents and total electric field components, respectively. When  $\sigma_L$  is larger than  $\sigma_T$ , and the magnetic field is tipped ( $E \not\perp B$ ), additional charging of the sample sides with the rf contacts occurs. The resulting potential difference is estimated to be  $(U_2 - U_1)/h \propto (1 - \sigma_T/\sigma_L)E_0 \sin \alpha$ , where  $E_0$  is the total transverse electric field in the region between the additional contacts. Hence the slope becomes steeper when  $\sigma_L/\sigma_T$  increases and is zero when  $\sigma_L = \sigma_T$ . Analysis of the slopes yields  $\sigma_L/\sigma_T \approx 4$  for Fig. 3(a) and the steeper slopes in Fig 3(b), and  $\sigma_L/\sigma_T \approx 1.4$  for the less steep slopes in Fig 3(b). These values agree well with those expected from Monte Carlo simulations for accumulated and streaming holes, respectively [4].

Finally, Fig. 4 shows the perturbing  $E_L$  field and hence the gain modulation to be more localized to the area directly in between the additional contacts due the space-charge effects because of the difference in  $\sigma_L$  and  $\sigma_T$  and because of current saturation.

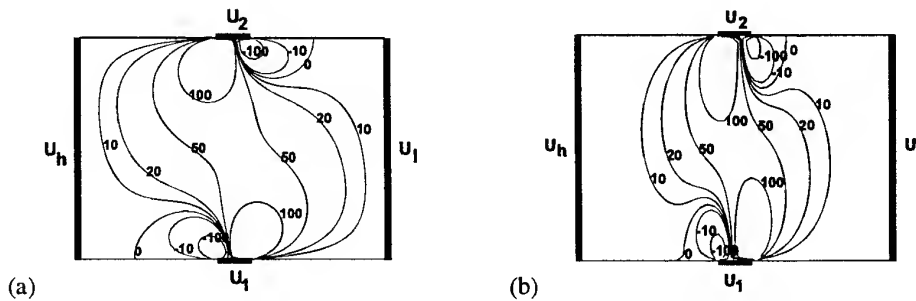


**Figure 4:** Distribution of  $E_L$  components;  $U_h = 700$  V,  $U_l = 0$  V; the additional contacts have a width  $w = 0.8$  mm, and  $U_2 = 375$  V and  $U_1 = 325$  V. (a)  $\sigma_L/\sigma_T = 1, f = 0$ . (b)  $\sigma_L/\sigma_T = 5, f = 0.7$ .

1. J. N. Hovenier, A. V. Muravjov, S. G. Pavlov, V. N. Shastin, R. C. Strijbos, and W. Th. Wenckebach, *Appl. Phys. Lett.* **71**, 443 (1997).
2. A. V. Muravjov, R. C. Strijbos, C. J. Fredricksen, H. Weidner, W. Trimble, A. Jamison, S. G. Pavlov, V. N. Shastin, and R. E. Peale, in *Radiative Processes and Dephasing in Semiconductors* (OSA-TOPS, Washington DC, 1998), to be published.
3. R. C. Strijbos, A. V. Muravjov, and W. Th. Wenckebach, pp. 627–629, in Ref. 6.
4. R. C. Strijbos, Ph.D. thesis, Delft University of Technology, 1997.
5. R. C. Strijbos, S. I. Schets, and W. Th. Wenckebach, pp. 469–471, in Ref. 6.
6. *Hot Carriers in Semiconductors*, K. Hess, J.-P. Leburton, U. Ravaioli, Eds. (Plenum Press, New York, 1996).

## DESIGN AND OPTIMISATION OF QUASI-OPTICAL FREQUENCY MULTIPLIERS

P. Arcioni<sup>1</sup>, M. Bozzi<sup>1</sup>, G. Conciauro<sup>1</sup>, H. L. Hartnagel<sup>2</sup>, L. Perregini<sup>1</sup>, M. Shaalan<sup>2</sup>, J. Weinzierl<sup>3</sup>.

<sup>1</sup> University of Pavia, Department of Electronics, Via Ferrata 1, 27100, Pavia, Italy.

Phone +39-382-505223 Fax +39-382-422583 E-mail p.arcioni@ele.unipv.it

<sup>2</sup> Darmstadt University of Technology, Merckstr. 25, 64283, Darmstadt, Germany.

<sup>3</sup> University of Erlangen, Cauerstr. 9, 91058 Erlangen, Germany.

### Abstract

This paper presents a novel CAD-tool for the design and the optimisation of quasi-optical frequency multipliers. A brief description of the theoretical background of this approach is presented. Moreover, the design and the fabrication of a frequency tripler, based on Hetero-structure Barrier Varactors and operating at 430 GHz, is discussed.

### 1. Introduction

The design of quasi-optical frequency multipliers requires an accurate modelling of the planar antenna integrated with the non-linear devices as well as of the external system of dielectric slabs and filters [1]. This analysis is very complicated and time-consuming when using general-purpose simulation tools.

In this paper we present a CAD-tool for the analysis and the automatic optimisation of quasi-optical frequency multipliers, operating in the millimetre and sub-millimetre wave range. Our code is able to simulate the non-linear device, the planar antenna and the embedding layered structure as a whole. The analysis of the multiplier is performed under the simplifying approximation of an infinite array excited by a uniform plane wave incident from the broadside direction. The array parameters are deduced from a full-wave analysis, based on the Method of the Moments, while the solution of the non-linear circuit is found by the Harmonic Balance method. This analysis algorithm is integrated into an optimisation routine, which adjusts the antenna geometry and the layered structure, in order to maximise the overall conversion efficiency of the multiplier.

### 2. Modelling of Quasi-Optical Multipliers

The modelling of the multiplier is based on the approximation of the infinite array [2]. The input wave is a uniform plane wave, incoming from the broadside direction, and the electric field is vertically polarised. Under these assumptions, the analysis of the antenna reduces to the investigation of the single unit cell of the array (Fig. 1). The unit cell consists of a rectangular waveguide with two electric walls and two magnetic walls (according to the polarisation of the electric field), containing a layered medium. It includes a thin metal layer (with an arbitrarily shaped aperture) and, possibly, a number of dielectric slabs and filters. The non-linear device is connected between the terminals A and B.

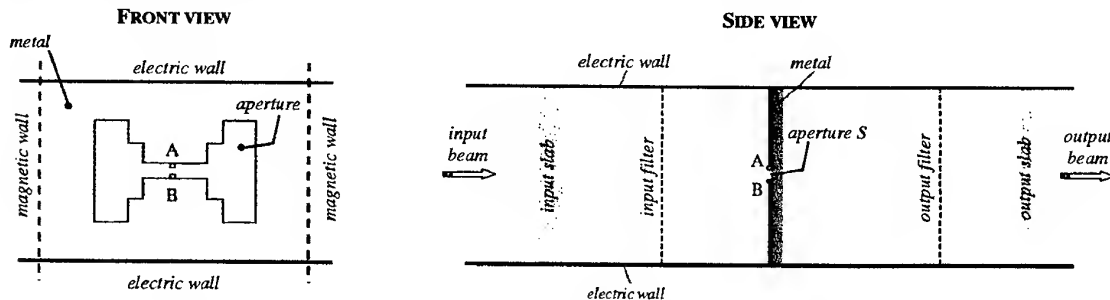


Fig 1 - Elementary unit cell of the array: front view (left) and side view (right).

These assumptions lead to the equivalent circuit sketched in Fig. 2. The antenna is modelled by a Thevenin equivalent circuit, including the open circuit voltage  $V_0$  (generated by the input power at the fundamental frequency  $f_0$ ) and the impedance  $Z(f_0)$  seen at the terminals A-B in the absence of the incident wave at all the harmonics.

The diode is represented by its non-linear impedance  $Z_{NL}(v)$ , which is a function of the voltage  $v$  between the terminals A and B. The analysis of the multiplier requires the solution of a twofold problem: the former is the calculation of  $V_0$  and  $Z(f_0)$ , deduced from a full-wave analysis, based on the Method of the Moments [3].

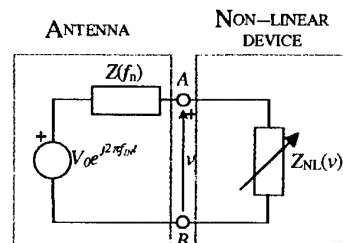


Fig 2 - Lumped element circuit representing the elementary cell of the array.

The latter is the modelling of the non-linear device, which leads to a lumped element circuit, whose characteristics can be either extracted from the measurement of test structures or theoretically calculated using analytical models. Once the equivalent model has been determined, the non-linear circuit is solved using the Harmonic Balance technique.

Following this approach, we have developed a specialised computed code, for the analysis and the optimisation of quasi-optical frequency multipliers. The available power per unit cell at  $f_N$ , the antenna geometry and the layered structure, together with the characteristics of the non-linear device, represent the input data for the analysis code. The analysis algorithm is embedded in an optimisation routine, which is able to adjust the antenna geometry and the layer position and characteristics (layer thickness, dielectric constant, ...), in order to maximise the multiplier efficiency.

The validation of the analysis results has been performed, comparing the calculation of the antenna impedance with the results provided by MDS-Momentum, and the Harmonic Balance method with publications in literature. In both the cases, we found a good agreement.

### 3. A 430 GHz Frequency Tripler

This code has been used for the design and optimisation of a quasi-optical frequency tripler, based on Heterostructure Barrier Varactors, operating at 430 GHz (Fig. 3a). It consists of a  $10 \times 10$  slot antenna array on a GaAs substrate. The HBVs are monolithically integrated on one side of the slots and consist of four GaAs/AlGaAs hetero-structure barriers (Fig. 3b). The tripler chip has been fabricated at the Darmstadt University of Technology. The design and the fabrication of the tripler have been recently presented [1].

It has been proved that a proper tuning of the position and the electrical characteristics of the external elements allows for obtaining an antenna impedance very close to the optimal one, both at the fundamental frequency and at the output harmonic.

The computation time required for a single analysis of such a structure is in the order of few seconds on a Sun Sparcstation 10, while a whole optimisation of the antenna and of the embedding system (dielectric slabs and filters) can be performed in a couple of hours.

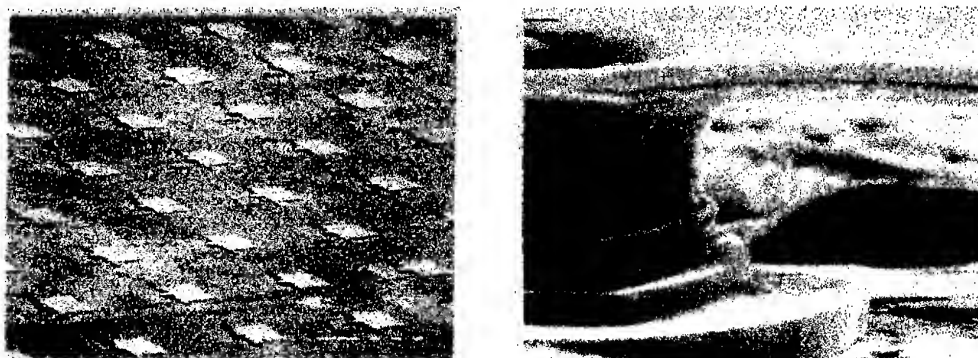


Fig. 3 - a. Photograph of the  $10 \times 10$  slot array (left). b. SEM photograph of the four-barrier HBV (right)

### 4. Improvements

The assumption of the infinite array, which our algorithm is based on, results very reasonable in the calculation of the antenna impedance, at least for the elements not too close to the boundary of the chip. Nevertheless, this method does not account for the power coupling of the array with the quasi-optical gaussian beam. Moreover, it is not possible to evaluate the diffraction effects in the tuning of external filters and slabs. We are embarked [4] in the extension of the theory described in this paper, with the aim of including in the analysis the gaussian coupling effects. It is possible to expand the gaussian beam on a basis of plane waves, incident on the antenna from different directions, and so calculate the efficiency of the multiplier embedded in a gaussian system.

### 5. Acknowledgements

This work is supported by the European Commission under the TMR Programme contract n. ERBFMRXCT960050 and by the University of Pavia under F.A.R. 1997/98 Funding.

### 6. References

- 1 P Arcioni et al., Proc. of the 9th Intern. Symposium on Space Terahertz Technology, Pasadena, CA (1998).
- 2 T K Wu, Frequency Selective Surface and Grid Array, John Wiley and Sons (1995).
- 3 P Arcioni et al., Proc. of ESA Workshop on MM Wave Techn. and Applications, Espoo, Finland (1998).
- 4 P Arcioni et al., submitted to the 6th IEEE Int. Conf. on Terahertz Electronics, Leeds, UK (1998).

## Design of GaAs/GaAlAs Single-Barrier Varactors (SBV) for mm-Wave Frequency Multipliers

Jürgen Freyer, Renato Meola, Manfred Claassen, Frank Neugebauer

Lehrstuhl für Allgemeine Elektrotechnik und Angewandte Elektronik, Technische Universität München  
Arcisstraße 21, 80333 München, Germany

The single-barrier varactor (SBV) has become an alternative multiplier device for mm-wave applications as compared to the Schottky diode [1,2]. Due to its symmetric capacitance-voltage characteristic, the multiplier rf-circuit can be less complex, e.g. for triplers no bias and no idler circuits are necessary. For optimum multiplier operation besides the demand of a high ratio of maximum to minimum capacitance (which determines the cut-off frequency and conversion efficiency), the onset voltage of conduction current should be as high as possible to ensure large rf-input power. According to the SBV structure of Fig. 1, the following parameters of the SBV are optimised: Al-concentration and width of the barrier as well as doping concentration and widths of the adjacent layers.

To determine the device properties, a simulation programme was developed which considers thermionic field emission as well as tunnelling [3]: First, the conduction band shape and the field distribution are computed as functions of the applied voltage neglecting conduction current which results in the capacitance-voltage characteristic. The conduction current and therewith the onset voltage are achieved from the solution of the Schrödinger equation which delivers the quantum mechanical transmission factor for thermionic emission and tunnelling across the barrier.

Following previous investigations on GaAs/GaAlAs SBV's from literature, mainly an Al-concentration of 70 % is used [1,2] which, however, is not optimum. Fig. 2 shows the theoretical results of the onset voltage versus Al-concentration for a current density of  $1 \text{ kA/cm}^2$  with 20 nm barrier width. The barrier is undoped and the doping concentration of the depletion layer is  $1 \cdot 10^{17} \text{ cm}^{-3}$ . It can be seen that the onset voltage for 50 % Al-concentration is nearly twice that of 70 % Al-concentration.

Fig. 3 demonstrates the dependence of the maximum capacitance on the doping concentration of the adjacent depletion layer again for a barrier width of 20 nm. The effective space charge layer of the SBV consists of the width of the hetero-barrier and two layers on both sides of the barrier corresponding to the Debye length. Since the Debye length decreases with increasing doping, the effective space-charge layer reduces. Therefore, high doping concentration would lead to a large maximum capacitance. However, with increasing doping concentration, the modulation of the space charge region due to the applied voltage decreases also, from which a larger value of the minimum capacitance follows. So, for optimisation of the ratio  $C_{\text{max}}/C_{\text{min}}$ , a depletion layer with two step-wise constant doping concentrations is proposed. A high doping concentration near the barrier enhances the maximum capacitance, an adjacent lower doping concentration allows larger space charge layer modulation resulting in a smaller minimum capacitance at higher maximum voltage.

An increase of the hetero-barrier width on the one hand leads to an increase of the onset voltage, but on the other hand also to a reduction of the ratio  $C_{\text{max}}/C_{\text{min}}$ . Fig. 4 shows the contrary behaviour of  $C_{\text{max}}/C_{\text{min}}$  and the onset voltage versus the barrier width for constant doping concentration and for the splitted depletion layer. From the results of Fig. 4 the conversion efficiency of the SBV applied as tripler can be computed for different widths of the hetero-barrier. It follows a smooth maximum at a hetero-barrier width of 20 nm for both constant and step-wise constant doping in the depletion layer. The maximum conversion efficiency of the two different structures, however, differs essentially: 13.8 % for constant and 21.8 % for step-wise constant doping concentration with 70 GHz fundamental frequency. Table 1 summarises the results of an optimised SBV structure. The total length of the depletion layer is limited by velocity saturation.

SBV's with step-wise constant doping concentration in the depletion layer according to Table 1 have been successfully fabricated by MBE technique and monolithically integrated in microstrip circuits for a frequency tripler from 70 GHz to 210 GHz. Output power of 1.4 mW with an efficiency of 2.8 % has been achieved [4].

### References

- 1 E L Kollberg, A Rydberg, Electron. Letters, 25, pp.1696-1698, 1989
- 2 D Choudhury, M A Frerking, P D Batelaan, IEEE Trans. MTT, 41, pp. 595-599, 1993
- 3 F Neugebauer, Diplom-Thesis, Technical University Munich, 1997
- 4 R Meola, J Freyer, "Monolithically integrated SBV for frequency triplers", to be published

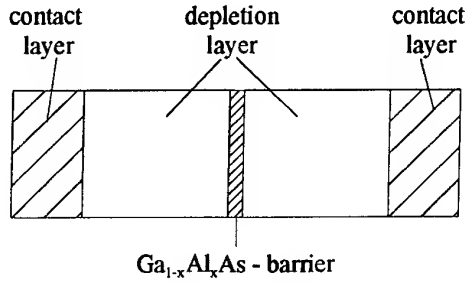


Fig. 1: Schematic structure of a SBV

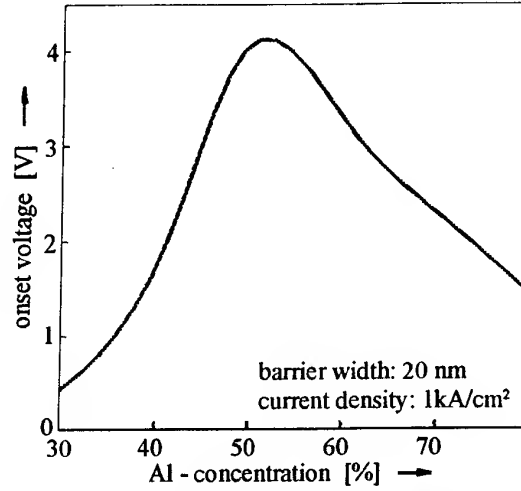


Fig. 2: Onset voltage versus Al - concentration for a SBV with constant doping profile in the depletion layer

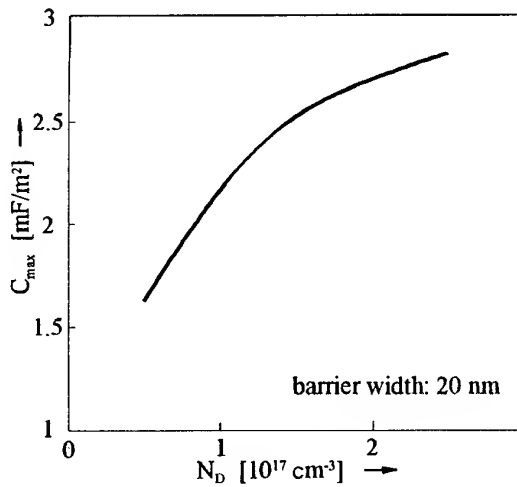


Fig. 3: Maximum capacitance versus doping concentration for a SBV with constant doping profile in the depletion layer

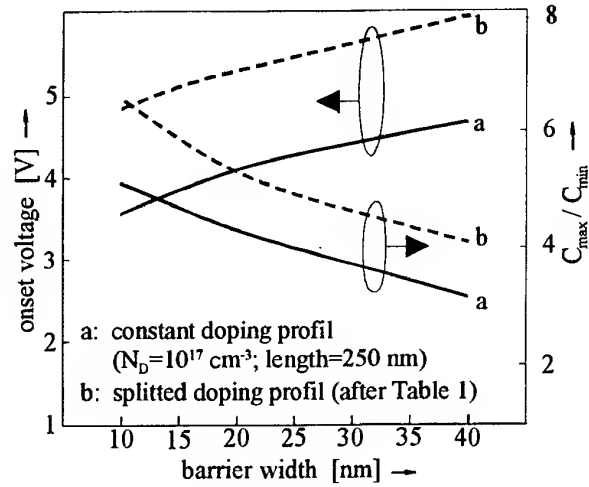


Fig. 4: Onset voltage and capacitance ratio versus barrier width for a SBV with constant and splitted doping profile in the depletion layer

Ga <sub>1-x</sub> Al <sub>x</sub> As - barrier	splitted depletion layer		contact layer
x = 50 %	N <sub>D1</sub> =10 <sup>17</sup> cm <sup>-3</sup>	N <sub>D2</sub> =5·10 <sup>16</sup> cm <sup>-3</sup>	N <sub>DC</sub> =5·10 <sup>18</sup> cm <sup>-3</sup>
d = 20 nm	d <sub>1</sub> = 50 nm	d <sub>2</sub> = 200 nm	

Table 1: Parameters of an optimised SBV structure for 70 GHz fundamental frequency

# Millimeter-Wave Multi-Element Frequency Multiplication Using Holographic Power Splitting/Combining

Mahmoud Shahabadi and Klaus Schünemann

Arbeitsbereich Hochfrequenztechnik, Technische Universität Hamburg-Harburg  
D-21071 Hamburg, Germany, e-mail: schuenemann@tu-harburg.de

## Abstract

The realization of a multi-element solid-state frequency multiplier primarily relies on an efficient method of power splitting and combining. It will be shown that the newly introduced method of holographic power splitting/combining almost entirely meets the requirements on power splitters/combiners at millimeter and submillimeter-wave frequencies. A possible setup for a millimeter-wave multi-element frequency multiplier working on the basis of this holographic approach will be presented.

## 1 Introduction

The efficiency of millimeter-wave frequency multipliers exploiting nonlinear elements such as varactor diodes mostly shows a maximum within a determined range of input power levels, so that the increase of the input power of a frequency multiplier does not generally lead to a higher output level. To achieve higher power levels, one may obviously utilize a multi-element configuration of frequency multipliers in which every single element receives the optimum power level at its input. Evidently, the essential components for such a multi-element arrangement are power splitters and combiners to be connected to the input and output port of each frequency multiplier, respectively.

Spatial power splitting/combining seems to be the method with the lowest losses at very high frequencies. For instance, the state-of-the-art terahertz multi-element frequency multiplier presented in [1] applies the mentioned technique to an array of  $12 \times 12$  planar Schottky diodes jointed to bow-tie antennas. However, to reach a constructive superposition in free space, the neighboring antennas should be located within a close spacing of less than half a wavelength, which necessitates the miniaturization of the frequency multiplier.

In contrast to the above procedure, we will make use of the newly developed method of holographic power combining [2], [3] which imposes no severe restriction on the dimensions of the circuit, while it maintains a very high splitting/combining efficiency. As a consequence, circuit miniaturization can advantageously be avoided, and the multipliers can be manufactured in well-studied, efficient technologies.

For a more detailed explanation, we firstly review the operating principle of holographic power splitting in the coming section. Later, the implementation of a multi-element frequency multiplier will be discussed.

## 2 Holographic Power Splitting

We approach the problem of power splitting in free space from the point of view of *wavefront transformation*. That is to say, the process of power splitting may be imagined as the transformation of the wavefront equivalent to the input electromagnetic beam into a desirable wavefront. The latter should clearly be constituted by a set of wavefronts each of which corresponds to one of the output beams.

A hologram is capable of carrying out the aforementioned transformation if it stores the desired output wavefronts as the *object wave* while the input beam plays the role of the *reference wave*. At millimeter and submillimeter-wave frequencies, the required hologram can, in some special cases, be realized by a dielectric periodic structure [2], [3]. Fig. 1(a) depicts a possible configuration for a holographic power splitter. In this arrangement, the main reflector along with its feed system provides the input beam to the hologram. This computer-generated hologram transforms the uniform input beam into a defined number of output beams to be collected by appropriate antennas that supply the individual circuits. Assuming a simple rectangular profile for the periodic structure, we arrive at a relatively large splitting efficiency by optimizing the geometrical parameters of the hologram and the antennas. This has been shown in the diagram of Fig. 1(b) as a function of the normalized inter-element spacing  $D/\lambda_0$  where  $\lambda_0$  denotes the free-space wavelength. According to Fig. 1(b), a high efficiency will be maintained nearly independent of the spacing  $D$ .

In summary, the considerable features of this method, which have also been observed in experimental investigations, are its scalability up to even the frequencies of the optical range, high efficiency, and broad-band character [3].

## 3 Multi-Element Frequency Multiplication

Fig. 2 illustrates how the method of holographic power splitting can be applied to a multi-element frequency multiplier. In this setup, the purpose of the power splitter seen on the input side is the coherent distribution of the input power



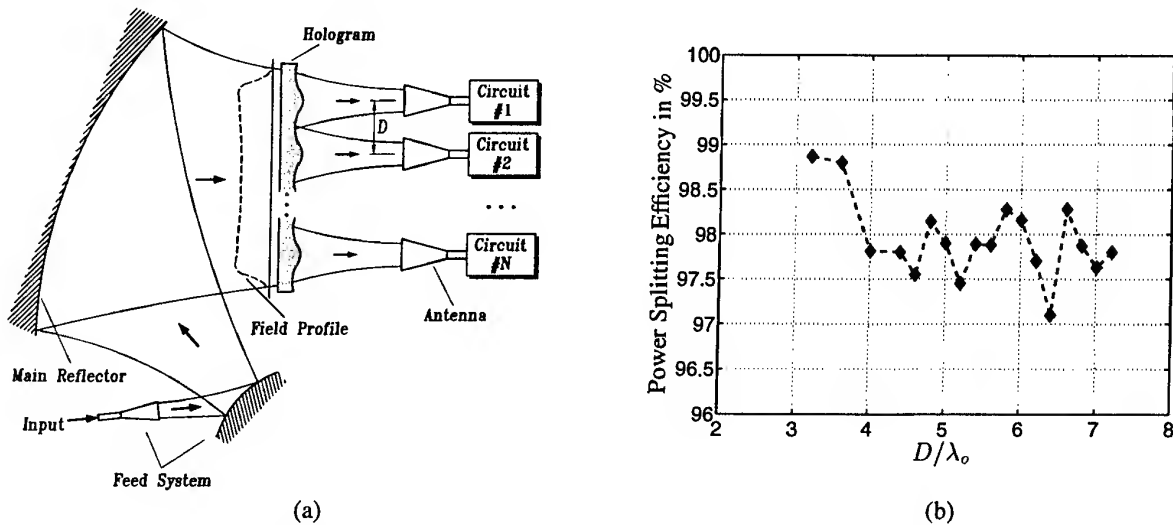


Fig. 1: (a) A holographic power splitter, (b) achieved splitting efficiency as a function of the normalized spacing.

among the multipliers. After undergoing a frequency multiplication, this signal appears at the output ports where an array of beam launchers along with a hologram combines the output signals to a common output at a multiple of the input frequency.

## 4 Conclusions

In this contribution, we have demonstrated a new quasi-optical scheme for multi-element frequency multiplication. On the one hand, this method avoids circuit miniaturization, and on the other hand it establishes at a moderate complexity a high efficiency as well as a relatively large bandwidth.

## 5 Acknowledgment

This work has been supported by the Deutsche Forschungsgemeinschaft.

## References

- [1] A. Moussessian, et. al., *Dig. IEEE MTT-S Int. Microw. Symp.*, Denver, June 1997, pp. 683–686.
- [2] M. Shahabadi and K. Schünemann, *Proc. 26th European Microw. Conf.*, Prague, Sept. 1996, pp. 115–119.
- [3] M. Shahabadi and K. Schünemann, *IEEE Trans. Microw. Theory Tech.*, vol. MTT-45, pp. 2316–2323, Dec. 1997.

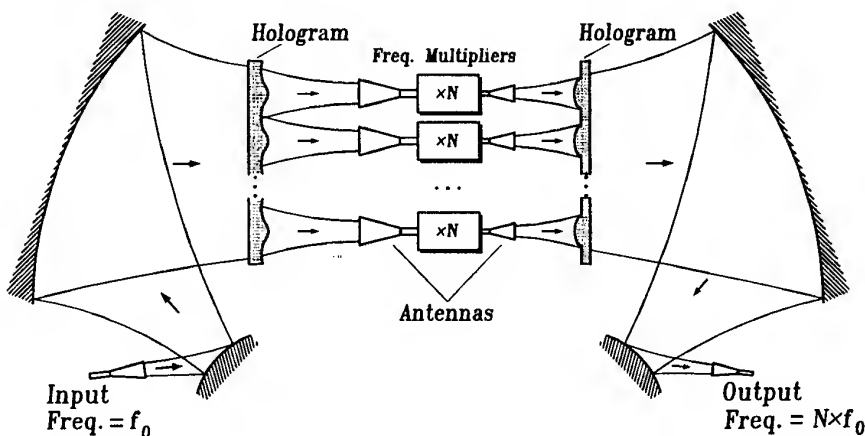


Fig. 2: A multi-element frequency multiplier using holographic power splitting/combining.

## Free Electron Laser Study of the Suppression of Non-Radiative Scattering Processes in Semiconductors

C. R. Pidgeon

Department of Physics, Heriot Watt University, Edinburgh EH14 4AS, UK.

### Introduction

A brief review is given of pump/probe studies of far infrared inter-sub-level relaxation between conduction band states in doped "quasi" quantum dots (created by the application of a magnetic field along the growth direction of an InAs/AlSb quantum well) and of mid-infrared interband recombination in narrow gap semiconductors, using the free electron laser at FOM-Rijnhuizen (FELIX). In the former case we are concerned with the suppression of LO phonon scattering in "quasi" quantum dots in a collaborative programme between the universities of Heriot Watt, Surrey and Imperial College [1]; in the latter case we are studying the suppression of Auger recombination in the lead salts due to their "mirror" energy band structure, in a programme between the universities of Heriot Watt, Surrey, Linz and Leoben [2]. The experiments were all performed at FELIX, which is continuously tuneable in stages from 4.5 to 100 $\mu$ m. FELIX delivers "macropulses" of typically 4 $\mu$ s in duration at a frequency of 5Hz, and each macropulse consists of a train of micropulses separated by 40ns, which have an energy of 1-10 $\mu$ J. The micropulse length is controllable in the range 1-10ps. The sample was mounted in one case in vacuum on a cold finger in the Faraday configuration of a horizontal bore superconducting magnet [1], and in the other case in a continuous flow cryostat [2]. The temperature could be varied from 4 to 300K. For the pump/probe experiments the FEL was split into pump and probe beams and calibrated wire-mesh attenuators were used to independently control the intensities so as to achieve full saturation by the pump but linear absorption only by the probe. The intensities used were estimated to be typically 40kW/cm<sup>2</sup> and 0.89kW/cm<sup>2</sup> for the pump and probe respectively.

### Suppression of LO phonon scattering in "quasi" quantum dots [1]

Electronic lifetimes of 2D systems in magnetic fields are of fundamental interest in part because the quantisation effect of the magnetic field mimics the effect of a quantum dot potential with an easily variable degree of confinement. The magnetic field perpendicular to the layers forces the electrons into confined orbits and the density of states becomes a ladder of broadened delta-functions similar to that of a quantum dot. Recently much work has been carried out on the so-called "phonon bottleneck" which has been claimed to inhibit the cooling of carriers in quantum dots. However, partly as a result of different groups using different growth techniques for interband photoluminescence samples and partly on fundamental grounds, this is controversial and is the subject of much debate. In the present work we observe clear phonon suppression in "quasi" 0-D dots by a time-resolved intraband (cyclotron resonance) absorption measurement [1]. This provides unambiguous evidence for the phonon bottleneck effect independently of arguments concerning which processes dominate in the interband photoluminescence measurements such as electron-hole scattering. Further, because of the very clean model system (much sharper interfaces and no wetting layer etc), the interpretation is not complicated by detailed questions about different growth techniques and the quality of different sample (dot) structures. The results should assist in the understanding of which aspect of these processes is fundamental and which is dependent on sample structure.

Resonant longitudinal optic (LO) phonon absorption has long been known to be responsible for the magnetophonon effect, which generates oscillatory structures in a variety of transport properties such as magnetoresistance [3]. At resonant phonon scattering (RPS) the LO phonon absorption/ emission

probability is strongly enhanced giving rise to large changes in the electron energy relaxation lifetime [4]. Resonant phonon scattering occurs when

$$\Delta l \cdot \hbar \omega_c = \hbar \omega_{LO} \quad (1)$$

where  $\hbar \omega_{LO}$  is the LO phonon energy,  $\hbar \omega_c = \hbar e B / m^*$  is the cyclotron resonance (CR) energy, and  $\Delta l$  is an integer. In the present work we have utilised the pump/probe technique for the first time with CR to quantitatively determine the relaxation time associated with the phonon bottleneck effect away from RPS in an InAs/AlSb quantum well [1]. This narrow gap material ( $E_g = 0.42\text{eV}$  in InAs) has sufficient band non-parabolicity so that higher Landau levels are bent out of resonance. The Landau level ladder is thus truncated and saturation is possible over a wide range of energies, enabling determination of energy relaxation lifetime both below and above the LO phonon energy.

Our results and calculation for InAs/AlSb show lifetimes on-resonance which are consistent with those found previously in InAs/GaSb [4,5], where lifetimes at RPS were sub-picosecond. However, in these earlier experiments the pump-probe technique was not available, and the sample used was not of the high mobility and narrow linewidth used in the present work. Under these circumstances it was not possible to observe the strong phonon bottleneck effect away from RPS reported here.

In summary, we have measured the relaxation lifetime of carriers in a quasi quantum dot resulting from a 2DEG in a magnetic field [1]. The measurements have been made both with the level separation equal to the phonon energy and away from this condition. A bottleneck exists in LO phonon cooling of carriers away from the resonance, which is independent of temperature in the range 4-80 K. The fact that the LO phonon cooling is significantly quenched away from the resonant phonon scattering condition, may have important consequences for quantum dot devices based on either inter- or intraband optical transitions, since it confirms the existence of the LO phonon bottleneck between the lowest dot states, even at the higher temperatures. On the other hand the lifetimes found here under bottleneck conditions ( $\sim 50\text{ps}$ ) may not be deleterious since they are similar to the lifetimes predicted to be necessary for dot operation [6].

#### Auger recombination dynamics of lead salts under ps FEL excitation [2]

The lead salts are of interest both fundamentally, because of their novel band structure, and from a device point of view since they are widely used in mid-infrared (MIR) optoelectronic emitters and detectors. A particular feature of this system – i.e. their near “mirror” conduction and valence bands – has been cited as potentially leading to much smaller Auger scattering rates than found in III-V material systems. However, theory predicts that there may nevertheless still remain a substantial contribution to this unwanted recombination process through intervalley scattering [7-10], although later theories [8-10] including more realistic band structure pictures suggest that this should not be as serious as originally predicted [7]. Understanding accurately how the recombination processes change with carrier density is important for emission devices which operate far from equilibrium, and in particular in the continuing quest for the development of compact MIR room temperature lasers. A recent design study suggesting the possibility of cw room temperature MIR operation of GaSb/PbSe/GaSb double heterostructure lasers [11] depends critically on the theoretical prediction of a low value of Auger coefficient,  $C$  [10]. Although considerable research has been done on the recombination processes, with the exception of one report [12] almost all previous work has utilised techniques using relatively long pulse or cw radiation, and experimentally reported values for  $C$  vary over an order of magnitude.

We have made direct pump-probe measurements of radiative and non-radiative recombination in epilayers of PbSe under high excitation with an rf linac-pumped (ps) free electron laser (FELIX), in the temperature range 30 to 300K [2]. For temperatures below 200K and carrier densities above the threshold for stimulated emission, stimulated recombination represents the most efficient recombination mechanism with kinetics in the 50-100ps regime, in good agreement with earlier reports [12]. Above this temperature Auger recombination dominates on a 0.1-2ns time scale. The sophistication of a 3-beam pump-probe experimental technique described below has enabled an analysis of the decay at times longer than 100ps, in terms of the non-parabolic anisotropic band structure of the lead salts, to give the Auger coefficient,  $C$ ,

quantitatively over a wide temperature range, 30-300K. The results are in good agreement with theory for non-parabolic, anisotropic bands [13,14] and non-degenerate statistics [8], and confirm that the original parabolic band calculations [7] underestimated the measured lifetime by more than an order of magnitude [8-10,12]. Finally the Auger results for the lead salts are compared with earlier measurements taken at FELIX [15-17] for  $\text{Hg}_{1-x}\text{Cd}_x\text{Te}$  of a composition such that the bandgap for the two semiconductors is the same at  $T = 100\text{K}$  [15-17]. It is found that  $C$  for PbSe is between one and two orders of magnitude lower than for  $\text{Hg}_{1-x}\text{Cd}_x\text{Te}$  over the whole temperature range for comparable values of bandgap. This results in domination of stimulated radiative recombination even at quite low carrier concentrations.

This review summarises the collaborative work of many workers as indicated in references [1] and [2]. We wish to thank Dr. A. van der Meer and the FELIX staff for technical assistance. We are grateful to Ivair Gontijo and Ray Murray for helpful discussions concerning the "phonon bottleneck" problem. This work was undertaken as part of the joint EPSRC (UK) and FOM (NL) programme at FELIX. CJGML and HAP are grateful for the support of EPSRC research assistantships (UK). Three of us are grateful for EPSRC studentships and for CASE awards with DERA, Malvern (ARH, CMC and PCF). ACR is grateful to the British Council for a Commonwealth fellowship. The lead salts work was supported by the Österreichischer Fonds zur Förderung der Wissenschaftlichen Forschung.

## References

- [1] B N Murdin, A R Hollingworth, M Kamal-Saadi, R Kititschke, C M Ciesla, C R Pidgeon, P C Findlay, H A Pellemans, C J G M Langerak, A C Rowe, R A Stradling and E Gornik, *Phys. Rev. B* (1998), to be published.
- [2] P C Findlay, C R Pidgeon, R Kititschke, A Hollingworth, B N Murdin, C J G M Langerak, A F G van der Meer, C M Ciesla, J Oswald, A Homer, G Springholz and G Bauer, *Phys. Rev. B* (1998), to be published.
- [3] D J Barnes, R J Nicholas, F M Peeters, X G Wu, J T Devreese, J Singleton, C J G M Langerak, J J Harris and C T Foxon, *Phys. Rev. Lett.*, **66**, 794 (1991).
- [4] T A Vaughan, R J Nicholas, C J G M Langerak, B N Murdin, C R Pidgeon, N J Mason and P J Walker, *Phys. Rev. (Rapid Commun.)* **B53**, 16481 (1996).
- [5] X. Wu and F.M. Peeters *Phys. Rev.* **B55**, 9333 (1997).
- [6] M. J. Steer, D. J. Mowbray, W. R. Tribe, M. S. Skolnick, M. D. Sturge, M. Hopkinson, A. G. Cullis, C. R. Whitehouse and R. Murray, *Phys. Rev.* **B54**, 17738 (1996)
- [7] P R Emtage, *J. Appl. Phys.* **47**, 2565 (1976)
- [8] O Ziep, O Mocker, D Genzow and K H Hermann, *Phys. Stat. Solidi* **90b**, 197 (1978).
- [9] M Mocker and O Ziep, *Phys. Stat. Solidi* **115b**, 415 (1983).
- [10] R Rosman and A Katzir, *IEEE J. Quant. Electron.* **QE-18**, 814 (1982)
- [11] Z Shi, *Appl. Phys. Lett.* **72**, 1272 (1998).
- [12] R Klann, T Hofer, R Buhleir, T Elsaesser and J W Tonn, *J. Appl. Phys.* **77**, 277 (1995).
- [13] D L Partin, *IEEE J. Quant. Electron.* **QE24**, 1716 (1988)
- [14] M Tacke, *Infrared Phys. Technol.*, **36**, 447 (1995).
- [15] C M Ciesla, B N Murdin, T J Phillips, A M White, A R Beattie, C J G M Langerak, C T Elliott, C R Pidgeon and S Sivananthan, *Appl. Phys. Lett.* **71**, 491 (1997).
- [16] C M Ciesla, PhD thesis, Heriot Watt, November 1997 (unpublished).
- [17] A R Beattie and A M White, *J. Appl. Phys.* **79**, 802 (1996).

# Probing the Band Structure of Cubic Galliumnitride by IR-Magnetospectroscopy

N. Puhlmann\*, I. Stolpe\*, M. von Ortenberg\*, and D. Schikora†

\*Institut für Physik, Humboldt-Universität zu Berlin, Invalidenstrasse 110, D-10115 Berlin, Germany

†Universität /GH Paderborn, Warburgerstrasse 100, D-33095 Paderborn, Germany

## Abstract

*For the first time we present high field cyclotron resonance measurements on p-type cubic GaN. Megagauss peak fields up to 300 T are generated by the semidestructive single-turn coil technique within a time scale of about 5  $\mu$ s. Different lines of a CO<sub>2</sub> laser are used as radiation source. Transmission changes in the order of 1% of zero field transmission are clearly resolved. For a detailed interpretation of the experimental data the Landau level scheme of cubic GaN is calculated.*

## I. Introduction

The recent progress in fabricating bright light emitting diodes [1,2] and laser diodes both operating in the blue-to-violet wavelength range [3] as well as heterostructure field effect transistors operating up to 300°C [4] has considerably increased the interest in the details of the band structure of GaN. Despite of the fundamental technological interest basic experimental data are rare in literature. The first experimentally determined value of the electron effective mass ( $m^*=0.2 m_e$ ) in highly conducting n-type single crystals of GaN was reported many years ago [5]. More recently cyclotron resonance (CR) experiments on conduction band electrons in GaN films [6] and GaN/AlGaIn films [7,8] have been published. Most of the results reported up to now refer to wurtzite type material, since GaN naturally crystallizes in this structure. However, it was shown recently that also the epitaxial growth of cubic GaN on GaAs (001) substrates is possible [9]. By use of far infrared spectroscopy Mirjalili et al [10] have very recently determined electron and hole effective masses in GaN epilayers with cubic and wurtzite structure, respectively. A direct determination of effective masses in cubic GaN using cyclotron resonance, however, has to the best of our knowledge not yet been published. This lack of experimental results is mainly due to the missing of either high quality material or sufficiently high magnetic fields. The necessary condition for the observation of cyclotron resonance  $\omega_c \tau \gg 1$ , where  $\omega_c$  is the cyclotron frequency and  $\tau$  the mean collision time, can only be fulfilled at higher fields for samples with low carrier mobility. The present paper describes CR experiments on p-type cubic GaN in extremely high magnetic fields and reveals by the different observed transitions the detailed structure of the valence bands.

## II. Experimental techniques

The single-phase c-GaN layers were grown on GaAs(001) substrates by plasma-assisted MBE monitored continuously by RHEED. The thickness of the layers was always in the order of one micrometer, so that the corresponding carrier system is 3D. The layers were additionally doped with Mg. Despite of the

well-known difficulties in producing ohmic contacts on p-type GaN [10] the Hall effect proves unambiguously the p-type character of the layers.

For the magneto-spectroscopical experiments we used a multi-megagauss generator producing fields in the order of 300 T within a pulse length of 5  $\mu$ s in a copper single-turn coil with a useful volume of about 1 cm<sup>3</sup> [11,12]. All experiments were performed without additional polarization of the CO<sub>2</sub>-laser radiation in Faraday geometry with the magnetic field oriented parallel to the [001] direction of the epitaxial layer. The radiation was focused on the sample of about 1.5 by 1.5 mm<sup>2</sup> by means of mirror optics. A fast HgCdTe detector located outside the Faraday cage was used for the detection of the transmitted radiation intensity.

## III. Results and Discussion

Figure 1 shows the relative transmission of CO<sub>2</sub>-laser radiation ( $\lambda=10.65 \mu$ m) versus the magnetic field for different temperatures. Two pronounced resonance structures are observed at room temperature in the transmitted radiation intensity as shown in the upper curve of Fig.1. The solid curve indicates a classical oscillator fit for a layered structure. Note, that despite of the low depth of the transmission minima in the order of only a few percent, the resonances can be clearly resolved, due to the excellent signal to noise ratio of the measuring system. Evaluation of different reference samples as are substrate, substrate with GaAs-buffer layer, and substrate/GaAs/GaN with and without Mg-doping ensures that both of the observed resonance lines are related to the p-type GaN. An analysis of the different data reveals that the resonance field of the transmission minimum at around 91 T does not scale with the radiation energy but extrapolates to a finite offset, as shown in Fig. 2. This effect is probably due to nonparabolicity effects in the bandstructure and not an indication for an impurity transition. There is strong evidence by the temperature dependence of the resonance intensity that the observed two resonances are caused by quasi-free holes and not by impurities, as shown in Fig. 1. The medium and high field resonances vanish completely at low temperatures. Another interesting and

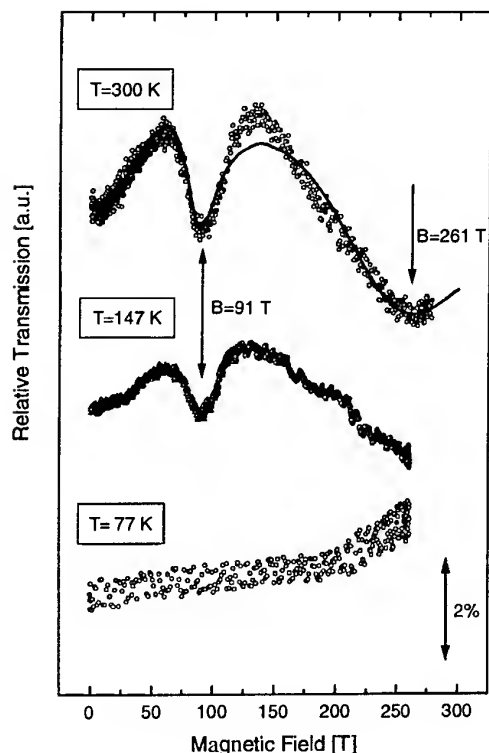


Fig. 1: Temperature dependent cyclotron resonance in *p*-type cubic GaN. The radiation energy is  $E=116.4$  meV. The points are the experimental data, whereas the solid line was simulated according to Drude's theory.

completely unexpected feature is the temperature independent increase in the normalized radiation intensity of about 1.5% in the field range from  $B=0$  to  $B=50$  T. The simulation of the data in an extended oscillator model in a multilayer structure, as shown by the solid curve in Fig. 1, is only possible, if we assume a third very broad resonance at low magnetic fields. The line shape of the transmission curve was simulated according to Drude's theory in a layered structure, taking into account interference effects in the layer and assuming three resonances at field strength of  $B=9$  T,  $B=91$  T and  $B=261$  T, respectively. From a physical point of view the existence of such an additional resonance is very questionable, however, and might be entirely due to the application of the oversimplified classical model. The estimated line width of the resonances is in good agreement with the DC-mobility of the carriers in the order of  $200 \text{ cm}^2/\text{Vs}$ , however.

To our knowledge no *k**p*-model for c-GaN has been established so far in contrast to the wurtzite modification [13]. However, Kim et al. have pointed out the group theoretical relations between the effective mass tensors and the related Rashba-Sheka-Pikus and Kohn-Luttinger Hamiltonian parameters for wurtzite and zincblende GaN [14]. For the calculation of the Landau levels for a magnetic field parallel to the

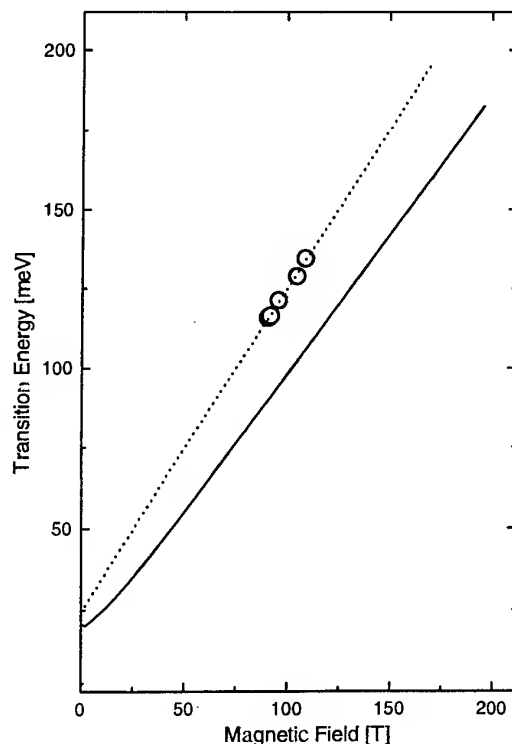


Fig. 2: Transition energy of the „medium field resonance line“ vs. resonance field. The points are the experimental data, the dashed line represents a least square fit, whereas the solid line refers to *k**p*-theory.

[001]-orientation we have applied a 6x6 Hamiltonian splitted into two submatrices 3x3 for the "a"- and "b"-set, respectively. The parameters used are  $\gamma_1 = -(A+2B)/3 = 2.463$ ,  $\gamma_2 = -(A-B)/6 = 0.647$ ,  $\gamma_3 = -C/6 = 0.975$ ,  $\kappa = 0$ , and  $\Delta = 19$  meV for the spin-orbit splitting [14]. Since for wurtzite GaN the temperature dependence of the Luttinger parameters is negligible we expect to hold the same for the cubic modification and apply the model for the entire temperature range of our experiments. The lowest Landau levels for the "a"- and "b"-set for  $k_z = 0$  are plotted as a function of the magnetic field up to 300 T in Fig. 3. Due to the missing crystal field splitting in the cubic modification the splitting of the valence bands at zero magnetic field is less pronounced than for wurtzite GaN. To locate possible transitions between the levels we have also calculated the square of the transition matrix elements between the levels involved for a transition energy of  $\hbar\omega = 116.4$  meV. The arrows indicate the lowest transitions which should be observable according to the model, whereas the thickness of the arrow lines indicate qualitatively the strength of the matrix elements. We obtain clearly for both "a"- and "b"-set a low field transition of medium intensity starting from an excited state at about 120 T. The energy difference to the ground state is of about  $E \approx 15$  meV. A careful evaluation of the

experimentally observed temperature dependence of the integrated resonance intensity of the 91 T line (Fig. 1) yields a rough estimation of the activation energy of about  $E_A \approx 20$  meV, which is in fairly good agreement with the theory. The transition energy of this line is plotted as a function of the magnetic field in Fig. 2 (solid line). Since the initial- and the final state belong to different valence bands, separated at zero magnetic field by a spin-orbit splitting of  $\Delta = 19$  meV, the resonance line does not scale with the energy, thus explaining the experimentally found offset of about 25 meV (dashed line in the insert of fig. 2).

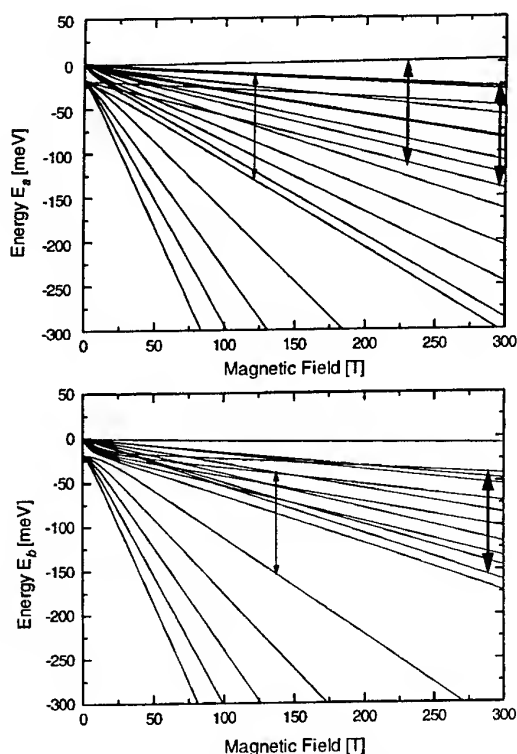


Fig. 3: Landau-Level scheme for the 3 highest valence bands in cubic GaN for the „a“ and „b“ set in the upper and lower part, respectively, as calculated in a *kp*-model. The magnetic field was assumed to be parallel to the [001] orientation. The arrows indicate the lowest transitions with relatively strong matrix elements and a transition energy of  $E = 116.4$  meV

Different transitions at magnetic fields between 230 T and 300 T contribute to an observable broad CR line. For this group the transitions starting from excited states and higher fields are definitely stronger than the transition from the ground state at about 220 T. This means that the theoretical model supports the general tendency of a freeze-out effect of the observable transitions in agreement with the experimental findings of vanishing intensity at low temperatures. With respect to the resonance position theory reproduces the splitting of two resonance groups. The resonance field is, however, only qualitatively reproduced. This fact is not only due to the crude extrapolation of the band

parameters from wurtzite to zincblende structure but also to the strong coupling to the optical phonons [15].

## References

- [1] S. Nakamura, M. Senoh, N. Iwasa, S. Nagahama, Jpn. J. Appl. Phys. Part 2, **34**, L 797 (1995)
- [2] S. Nakamura, M. Senoh, S. Nagahama, N. Iwasa, T. Yamada, T. Mukai, Jpn. J. Appl. Phys. Part 2, **34**, L 1332 (1995)
- [3] S. Nakamura, M. Senoh, S. Nagahama, N. Iwasa, T. Yamada, T. Matsuhita, H. Kiyoku, W. Sugimoto, Jpn. J. Appl. Phys. Part 2, **35**, L 74 (1996)
- [4] M. Asif Khan, M.S. Shur, J.N. Kuznia, Q. Chen, J. Burn, W. Shaff, Appl. Phys. Lett. **65**, 1121 (1994)
- [5] A.S. Barker, M. Ilegems, Phys. Rev. B **7**, 743 (1973)
- [6] M. Drechsler, D.M. Hoffmann, B.K. Meyer, T. Detchprohm, H. Amano, I. Akasaki, Jpn. J. Appl. Phys. Part 2, **34**, L 1178 (1995)
- [7] Y.J. Wang, R. Kaplan, H.K. Ng, K. Doverspike, D.K. Gaskill, T. Ikeda, I. Akasaki, H. Amono J. Appl. Phys. **79**, 8007 (1996)
- [8] W. Knap, H. Alause, J.M. Bluet, J. Camassel, J. Young, M. Asif Khan, Q. Chen, S. Huant, M. Shur, Solid State Com. **99**, 195 (1996)
- [9] O. Brandt, H. Yang, B. Jenichen, Y. Suzuki, L. Daweritz, K. Ploog, Phys. Rev. B, **52**, R 2253 (1995)
- [10] G. Mirjalili, R.A. Levett, T. J. Parker, T. S. Cheng, C. T. Foxon, Proc. 22nd Intl. Conf. on Infrared and Millimeter Waves, Wintergreen (VA), (1997), ed. H.P. Freund
- [11] N. Puhlmann, O. Portugall, M. Barczewski, I. Stolpe, H.-U. Müller, M. von Ortenberg Physica B **246/247**, 323 (1998)
- [12] O. Portugall, N. Puhlmann, I. Stolpe, M. Barczewski, H.-U. Müller, M. von Ortenberg, Physica B **246/247**, 54 (1998)
- [13] S.L. Chuang and C.S. Chang, Phys. Rev. B **54**, 2491 (1996)
- [14] K. Kim, W.R.L. Lambrecht, B. Segall, M. van Schilfhaarde, Phys. Rev. B **56**, 7363 (1997)
- [15] X. Wu and F.M. Peeters, Phys. Rev. B **55** 15438 (1997)

## Measurements of the Intersubband Lifetime in a p-GaAs/AlGaAs Quantum Well using a Free Electron Laser.

Christopher D Bezan<sup>1</sup>, Casper J Langerak<sup>2</sup>, J. Martyn Chamberlain<sup>1</sup> and Mohammed Henini<sup>1</sup>

<sup>1</sup> Department of Physics, University of Nottingham, Nottingham NG7 2RD., UK

<sup>2</sup> FOM Institute for Plasmaphysics "Rijnhuizen", PO Box 1207, 3430 BE Nieuwegein, NL.

### ABSTRACT

This contribution reports recent saturation-absorption and pump-probe studies of the intersubband lifetime of holes at energies below the LO-phonon energy in a p-type GaAs/Al<sub>0.33</sub>Ga<sub>0.67</sub>As multiquantum well. In the case of the saturation-absorption measurement, the lifetime is limited by the width of the Free Electron Laser (FEL) pulse, and is found to be greater than 1.7 ps at 4K. In the pump and probe investigation, a lifetime of approximately 300ps is found for this multiquantum well of well-width 7nm. The implications of this result are discussed in comparison with the equivalent data for electron systems.

### INTRODUCTION

The band architecture of two dimensional hole systems (2DHS) realised in GaAs/AlGaAs systems is now becoming increasingly well understood [1]; the complexity of 2DHS contrasts strongly with the companion two dimensional electron systems (2DES) displaying a wide range of effective masses and a large and complex non-parabolicity. Furthermore, the band structure and its attendant parameters show considerable variations as the substrate growth orientation and confinement lengths are changed [2]. It is evident that this range of carrier-transport parameters may be of considerable value to device designers; it has recently been suggested that 2DHS terahertz emitters can be fabricated [3], taking advantage of their large joint densities-of-states and the breakdown of intersubband selection rules [4]. In order to exploit this freedom to design suitable emitting structures in 2DHS, however, a much better understanding is required of such important parameters as the intersubband lifetime,  $\tau$ .

Over the last few years, a considerable number of studies of  $\tau$  for *electrons* in wide GaAs QW wells and related systems have taken place (see: Murdin et al [5] for a review). These studies have

focused on the dependence of  $\tau$  on temperature, well-width, laser-intensity and other parameters when the intersubband separation is below the optical phonon energy (36.7meV for GaAs). The outcome of these measurements is that below a certain critical carrier (electron) temperature (about 35K),  $\tau$  is chiefly determined by acoustic phonon emission; above this temperature LO phonon emission is dominant.

The present experiments report the first attempts to pursue similar measurements in the companion p-type system. Although a FEL has been used to measure  $\tau$  in a sample of In<sub>0.5</sub>Ga<sub>0.5</sub>As / Al<sub>0.5</sub>Ga<sub>0.5</sub>As [6], the pump energy in that experiment greatly exceeded the LO phonon energy, which renders comparisons difficult.

### EXPERIMENTAL DETAILS

The sample was a 10x MQW grown on (311)A substrate using Si as a dopant. Each well was doped to a density of  $3 \times 10^{11} \text{ cm}^{-2}$ ; the well-width was 7nm. Figure 1 shows the calculated band structure of this sample. The 4K linear FIR absorption has been discussed elsewhere [7], and the complexity of this spectrum is attributed to the strong non-parabolicity. Depolarisation shift effects [8] are important in these structures for the polarisation conditions in the FEL, and give rise to enhanced absorptions at energies greater than the Fermi edge absorption. For this reason, the FELIX experiments were conducted at wavelengths (around 57 $\mu\text{m}$ ), which were slightly lower than those corresponding to the  $k=0$  absorption. Details of the saturation-absorption set-up have been given elsewhere [9]. Figure 2 shows the saturation absorption behaviour when the sample is irradiated with a train of micropulses of width 1.7 ps at a wavelength of 57 $\mu\text{m}$ . These results indicate that  $\tau$  exceeds 1ps. Calculations of the effective hole temperature ( $T_{\text{eff}}$ ) have been undertaken and indicate that during the experiment  $T_{\text{eff}} \approx 40\text{K}$ . In the second experiment, a pump-probe arrangement was used with FELIX again tuned to approximately 57  $\mu\text{m}$ ;



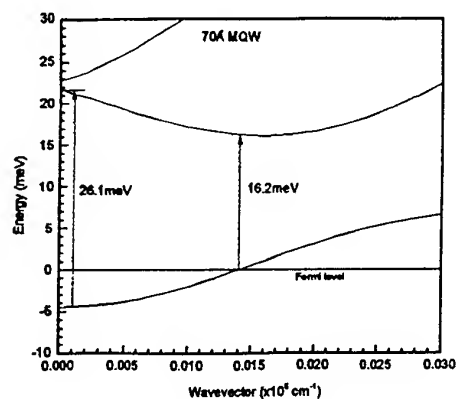


Fig. 1 Valence Band Structure for p-QW

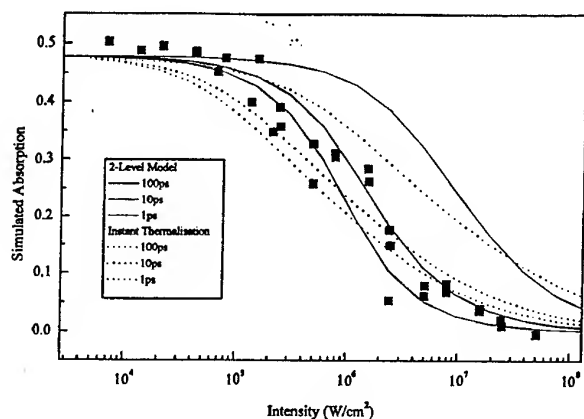


Fig 2. Saturation-absorption at  $57\ \mu\text{m}$  this wavelength corresponded to the HH1-LH1 absorption ; the sample was mounted behind a pinhole in a liquid helium cryostat at a temperature of 5K. The pump radiation was directed onto it using a focusing mirror. A small part of the pump beam was diverted to act as a probe (of intensity approximately 1% of the pump) and a delay line was used to temporally separate pump and probe.

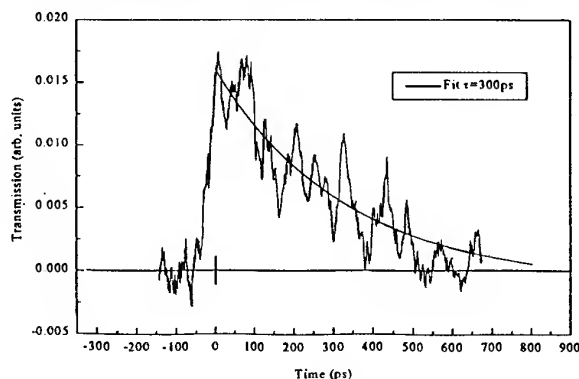


Fig.3 Decay of the probe signal at  $57\ \mu\text{m}$  The change in transmission as the absorption recovers was measured with a Ge:Ga detector. Figure 3 shows the decay of the  $57\ \mu\text{m}$  probe beam following excitation. The pump-probe effect is rather small (2-4%), but nevertheless is clearly present above the noise. A number of rather crude

fits to the decay data is shown , from which an approximate value of  $\tau$  of 300ps is determined.

## DISCUSSION AND CONCLUSION

Figure 1 shows the valence band structure for the 7 nm well-width sample used in this experiment. It is clear that the ground (HH1) state has a hole-character, whereas the next (LH1) state has an electron character. This ordering of valence bands clearly resembles the situation in a conventional band-to-band laser. Sun et al [ 3] have discussed the possibility of constructing a terahertz frequency laser using transitions occurring near the inverted effective mass region . The present experiment, for the first time in a hole system, provides evidence that the lifetime of carriers may be long enough to allow population inversion and strongly indicates the feasibility of such a p-QW system exhibiting optical gain at terahertz frequency.

## ACKNOWLEDGEMENTS

The support of EPSRC, FOM and the EC in this work is acknowledged. CDB acknowledges a CASE studentship supported by Toshiba Research Centre, Cambridge.

## REFERENCES

- [1] B.E. Cole, B. F. Peeters, A. Ardavan, S. O. Hill, J. Singleton, W. Batty, J.M. Chamberlain, A. Polisskii, M. Henini, T. Cheng, J Phys: Condens. Matter 9 (1997), 3163.
- [2] B.E.Cole, J.M. Chamberlain, M. Henini, T.S. Cheng, W. Batty, A. Wittlin, J. Perenboom, A. Ardavan, A. Polisski, J. Singleton, Physical Review B 55 (1997) 2503.
- [3] G Sun, Y Lu and J B Khurgin Applied Physics Letters 72 (1988) 1481.
- [4] B.W. Kim and A. Majerfeld, J.Appl. Phys. 77 (1995) 4552.
- [5] B.N. Murdin, W. Heiss, C J G M Langerak, S-C Lee , I Galbraith, G Strasser, E Gornik, M Helm and C R Pidgeon, Physical Review B55 ( 1997) 5171.
- [6] Z. Xu, P.M. Fauchet, C.W. Rella, B.A. Richman, H.A. Schwettman and G.W. Wicks, Physical Review B 51 (1995) 10 631.
- [7] B.E.Cole, J.M. Chamberlain, M. Henini, V. Nakov and G. Gobsch, Journal of Applied Physics 80 (1996), 6058.
- [9] B E Cole, CJGM Langerak, B N Murdin, C D Bezant, J M Chamberlain, C R Pidgeon, M Henini and V Nakov , Physica E, in press (1998)

# The influence of intense THz fields on the magneto-photoconductivity of n-GaAs under impact ionization conditions

F. Ghianni, T.O. Klaassen and W.Th. Wenckebach,

Department of Applied Physics and DIMES, Delft University of Technology,  
P.O.Box 5046, 2600 GA Delft, The Netherlands

## Introduction

The influence of THz radiation on the magneto-photoconductivity of epitaxial n-GaAs under low temperature impact ionization conditions has already been subject of investigation by other authors. Impact induced negative photoconductivity (PC) at long wavelength under *non-resonant* conditions [1], and the influence of impact ionization on the saturation of the (positive PC)  $1s-2p^+$  donor transition [2] were studied. In both cases however, relatively low intensity THz radiation was used.

In the present study, the behaviour of the resonant PC under *intense* THz radiation at the  $1s-2p^+$  and the cyclotron resonance (CR) transitions is studied. Preliminary experiments at  $T=4.2K$  and  $\lambda = 118.8 \mu m$  have been carried out as a function of dc bias current, magnetic field and THz intensity.

## Experiment

The GaAs:Si sample used in the experiments consists of a  $10 \mu m$  epitaxial layer grown on a Si GaAs substrate with  $N_d=4.10^{14}cm^{-3}$  and  $N_a \leq 1.10^{14}/cm^{-3}$ .

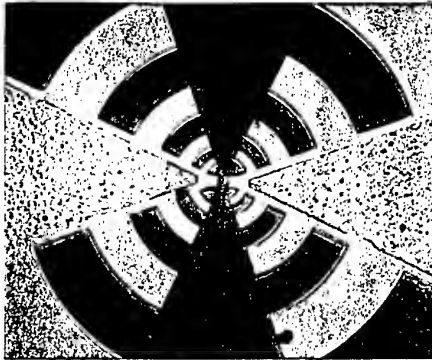


Fig. 1. THz antenna on n-GaAs; the electrode is also visible

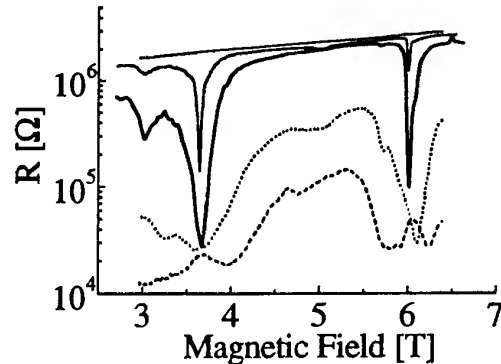


Fig. 2. Magneto resistance at  $BC=30$  nA for various THz intensities

In fig. 1 a photo of the planar logperiodic antenna is shown. AuGeNi electrodes with a  $15 \mu m$  separation are fabricated underneath the  $220$  nm thick gold antenna to provide a good ohmic contact with the epitaxial GaAs layer. The area between the antenna tips is  $3 \times 3 \mu m^2$ . The far infrared beam is focussed onto the antenna by an (externally adjustable) polyethylene Fresnel lens, instead of by the usual Si hyperhemispherical lens. Therefore the optical coupling efficiency in this setup is only of the order of 1%. Nevertheless, using a conventional OPFIR laser, intensities of the order of  $1$  kW/cm<sup>2</sup> at the apex of the antenna can be obtained. In order to position the antenna in the beam focus, the sample is placed on a small x-y translation stage. The sample insert is placed in the bore of a 7T superconducting solenoid, immersed in liquid helium. The experiments have been performed using a constant bias current; the voltage across the sample - with and without far infrared (FIR) illumination - is monitored using a sample and hold technique. In fig. 2 the influence of the intensity of the  $118.8 \mu m$  THz field on the PC is shown for a low bias current (BC), i.e. with not to large impact ionization effects. The

upper, straight, curve shows the sample magneto-resistance without illumination. The other four curves give  $R(B)$  under FIR illumination. The FIR intensity increases by about 25 dB from top curve to bottom curve. The lowest intensity trace shows the well known shape of the spectrum at low FIR and BC intensity. The donor transitions  $1s$ - ( $1\bar{1}0$ ) at 3.0T,  $1s$ - $2p^+$  at 3.66T and the cyclotron resonance (CR) transition at 6.07T are easily discernable; also non-resonant PC is observed. With increasing THz intensity the transitions broaden due to saturation effects. As expected, the value of  $R$  decreases towards higher FIR intensity, be it that at the highest intensity at the center of both the  $1s$ -  $2p^+$  and the CR transition a relative *increase* of  $R$  occurs, similar to that observed in earlier publications [3,4].

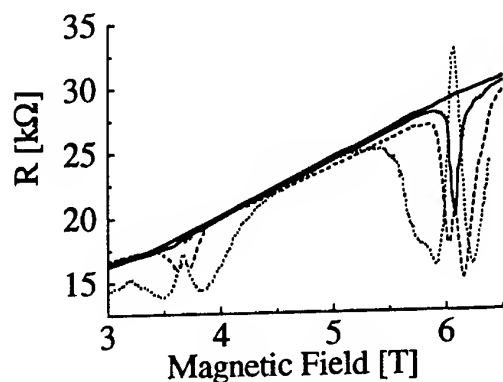


Fig. 3. Magneto resistance at  $BC=10 \mu A$  for various THz intensities

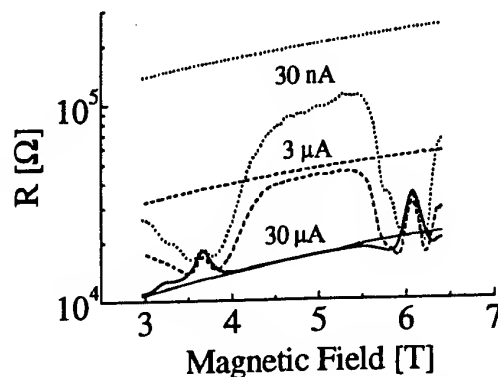


Fig. 4. Magneto resistance at high THz intensity for various BC values

In fig. 3 similar data are shown, but now under strong impact ionization conditions. With increasing THz intensity the  $R$  value at the CR transition becomes even larger with than without THz illumination: negative photoconductivity. This trend is more clearly seen in fig. 4 where traces for 3 different bias currents with and without high intensity FIR are given. Under strong impact ionization (lower trace) a negative PC is observed for both donor transitions and for the CR; the non-resonant PC tends to become negative too.

### Conclusions

These preliminary experimental data seem to indicate the presence of counteracting effects. The bias current, through the impact ionization, excites electrons into the conduction band, whereas the THz field, through stimulated optical transitions, tends to restore the population in the low lying donor states. Possibly the strong negative PC at the  $1s$ - $2p^+$  and CR transitions is due to stimulated transitions from electrons in the conduction band to lower bound states, by which the number of free electrons, and thus the sample conductivity, will be diminished. For instance at  $B=3.66T$  the  $2p^+$ - $1s$  transition could play such a role when the  $1s$  groundstate is depopulated through impact ionization. At  $B=6.07T$  one might speculate about the occurrence of stimulated transitions from high lying donor states ( $1,1,\nu$ ) to low lying states ( $0,-1,\nu$ ). The energy difference between any such pair of states equals the CR energy. Although formally parity forbidden, these transitions certainly will gain transition probability under these extreme ionization conditions.

### References

- [1] E. Schöll, W. Heisel, W. Prettl, Z. Phys. B 47(1982)285.
- [2] M. Weispfenning, F. Zach, W. Prettl, Int. J. Infrared and Millimeter Waves 9(1988)1153.
- [3] M. Weispfenning, W. Prettl, Proceedings of the 14th IRMMW Conference, SPIE Vol. 1240(1989)134.
- [4] P.C.M. Planken, P.C. van Son, J.N. Hovenier, T.O. Klaassen, W.Th. Wenckebach, B.N. Murdin, G.M.H. Knippels, Infrared Phys. Technol 36(1995)333.

## Enhancement of tunnel ionization of deep impurities in semiconductors in a high frequency electric field of FIR laser radiation

S.D. Ganichev<sup>1,2</sup>, E. Ziemann<sup>1</sup>, H. Ketterl<sup>1</sup>, V.I. Perel<sup>2</sup>, I.N. Yassievich<sup>2</sup> and W. Prettl<sup>1</sup>

<sup>1</sup>Institut für Experimentelle und Angewandte Physik, Universität Regensburg, D 93040 Regensburg, Germany

<sup>2</sup>A. F. Ioffe Physicotechnical Institute, Russian Academy of the Sciences, St. Petersburg, 194021, Russia

### Abstract

An enhancement of tunnel ionization of deep impurities in semiconductors in a high frequency electric field of FIR laser radiation as compared to static and quasi-static fields has been observed experimentally. A theory of this effect has been developed.

### Introduction

Here we report on the experimental observation of an enhancement of tunneling in alternating electric fields. In contrast to the quasi-static regime, where electrons tunnel at constant energy in a time much shorter than the reciprocal radiation frequency  $\Omega^{-1}$ , in the high-frequency regime electrons can absorb energy from the radiation field during tunneling leaving the barrier at higher energy. By this the effective width of the tunneling barrier is reduced and thus, the tunneling probability enhanced. This effect has been observed at tunneling ionization of deep impurities in semiconductors. In contrast to tunneling ionization of atoms, where only electron tunneling takes place [1], ionization of impurities in solids is accomplished by two simultaneous tunneling processes, electron tunneling and the redistribution of the vibrational system by defect tunneling [2]. In the quasi-static regime the electron tunnels at the momentary magnitude of the electric field in a time shorter than the period of oscillation, thus the electric field acts like a static field. The ionization probability is independent of frequency and increases with rising field strength  $E$  like  $\exp(E^2/E_c^2)$  where  $E_c$  is a characteristic field [3]. In the high frequency regime the ionization probability, being characterized by the same field dependence, substantially increases with increasing frequency [4].

### Results and Discussion

Measurements have been carried out on different types of deep impurities in semiconductors: substitutional impurities with weak electron phonon coupling and auto-localized  $DX^-$  centers, with strong electron phonon coupling in the temperature range from 20 K to 150 K. Tunnel ionization has been achieved by far-infrared laser radiation

with photon energies much smaller than the thermal impurity ionization energy  $\varepsilon_T$ . The ionization probability has been determined by detecting photo-conductivity. The radiation source applied was a pulsed far-infrared molecular laser optically pumped by a TEA-CO<sub>2</sub> laser. Using NH<sub>3</sub> as active gas, 40 ns pulses with a peak power of 100 kW have been obtained at frequencies of 25, 21, 13 and 6.7 THz

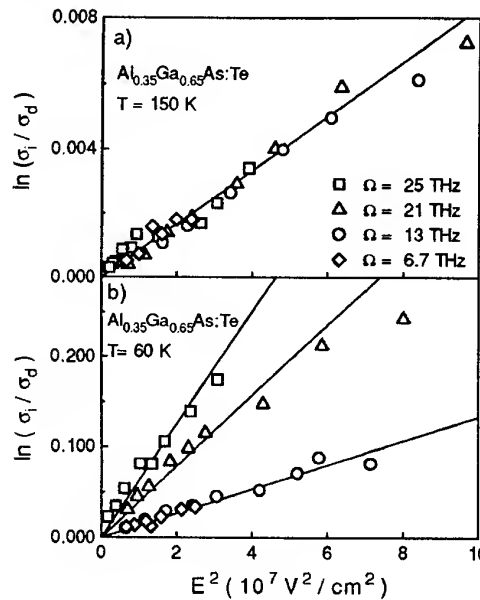


Fig. 1

Fig. 1 shows experimental results obtained with  $DX^-$  centers in AlGaAs:Te at  $T = 150$  K and  $T = 60$  K. The ratio of the conductivity under irradiation to the dark conductivity  $\sigma_i/\sigma_d$ , which is proportional to the ionization probability, is plotted as a function of the square of the peak electric field strength  $E$ . The ionization probability at  $T = 150$  K is independent of radiation frequency and increases with rising  $E$  like  $\exp(E^2/(E_c^*)^2)$  where  $E_c^*$  is a characteristic electric field strength. Such a behavior has been observed for all materials at sufficiently high temperatures. In contrast to these observations at  $T = 60$  K the ionization probability gets frequency dependent and is drasti-

cally enhanced with rising frequency  $\Omega$ . The ionization probability still depends exponentially on the square of electric field strength, but the magnitude of  $E_c^*$  decreases strongly with increasing frequency. We have shown that the ionization probability depends on alternating electric field strength as [4]

$$e(E) \propto \exp \left[ \frac{E^2}{(E_c^*)^2} \right] \quad \text{with} \quad (E_c^*)^2 = \frac{3m^*\hbar}{e^2(\tau_2^*)^3} \quad (1)$$

and

$$(\tau_2^*)^3 = \frac{3}{4\Omega^3} (\sinh(2\Omega\tau_2) - 2\Omega\tau_2) \quad (2)$$

The tunneling process is controlled by  $\Omega\tau_2$  where the tunneling time  $\tau_2$  depends on temperature like  $\tau_2 = \hbar/2kT \pm \tau_1$  [5]. Here  $\tau_1$  is of the order of the period of the impurity vibration and plus and minus correspond to substitutional and auto-localized impurities, respectively.

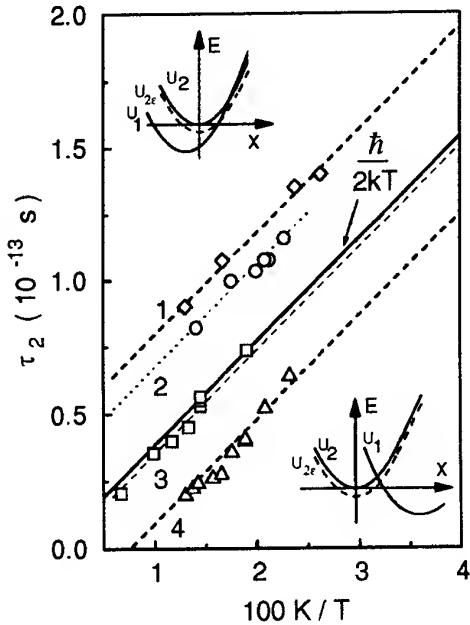


Fig. 2

The experimentally determined temperature dependence of  $\tau_2$  for both types of impurities is shown in Fig. 2 where  $\diamond$ -Ge:Cu;  $\circ$ -Ge:Hg are substitutional impurities and  $\square$ -DX<sup>-</sup> centers in  $\text{Al}_{0.35}\text{Ga}_{0.65}\text{As}$ ;  $\triangle$ -DX<sup>-</sup> centers in  $\text{Al}_{0.5}\text{Ga}_{0.5}\text{Sb}$  are auto-localized impurities. Insets show schematically adiabatic potential structures corresponding to substitutional impurities (top left) and auto-localized impurities (bottom right).

Varying the temperature and the radiation frequency the dependence of the effective time  $\tau_2^*$  has been obtained from measured values of  $E_c^*$  for various frequencies, temperatures and all investigated

materials. In Fig. 3 the ratio  $\tau_2^*/\tau_2$  determined experimentally is plotted as a function of  $\Omega\tau_2$  and compared to calculations after Eq. (??).

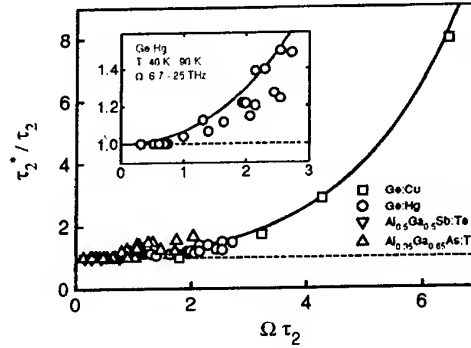


Fig. 3

To show in detail the transition from the quasi-static regime  $\Omega\tau_2 < 1$  to the high frequency regime  $\Omega\tau_2 > 1$  the data obtained for Ge:Hg are plotted in the inset for  $\Omega\tau_2$  on an exaggerated scale. Note that even a ratio  $\tau_2^*/\tau_2$  slightly larger than one causes a considerable enhancement of tunneling in an alternating field as compared to static fields, because the tunneling probability depends exponentially on the third power of tunneling time (Eq. (??)).

We have shown that typically the limit  $\Omega\tau_2 = 1$  is in the range of terahertz frequencies where high electric fields can easily be applied in a contact-less manner by powerful far-infrared lasers. Our measurements have been carried out with deep impurities in semiconductors, however, because tunneling is crucial in numerous processes in physics, chemistry, and biology we expect that an enhancement of tunneling by contact-less application of coherent radiation will have significant consequences.

#### Acknowledgments

Financial support by the Deutsche Forschungsgemeinschaft is gratefully acknowledged.

#### References

- [1] L.V. Keldysh, Zh. Eksp. Teor. Fiz. **47**, 1945 (1964) [Sov. Phys. JETP **20**, 1307 (1965)].
- [2] V.N. Abakunov, V.I. Perel, and I.N. Yassievich, *Nonradiative Recombination in Semiconductors*, edited by V.M. Agranovich and A.A. Maradudin, Modern Problems in Condensed Matter Sciences Vol. 33 (North Holland, Amsterdam, 1991).
- [3] S.D. Ganichev, W. Prettl, and P.G. Huggard, Phys. Rev. Lett. **71**, 3882 (1993).
- [4] S.D. Ganichev, E. Ziemann, Th. Gleim, W. Prettl, I.N. Yassievich, V.I. Perel, I. Wilke, and E.E. Haller. Phys. Rev. Lett. **80**, 2409 (1998).
- [5] S.D. Ganichev, W. Prettl and I.N. Yassievich, Phys. Solid State **39**, 1703 (1997).

# FIR spectroscopy of p-doped GaAs/Al<sub>x</sub>Ga<sub>1-x</sub>As superlattices

S Farjami Shayesteh<sup>1,a</sup>, G Mir Jalili<sup>1,b</sup>, T J Parker<sup>1</sup> and L E Vorobjev<sup>2</sup>

<sup>1</sup>Department of Physics, University of Essex, Colchester CO4 3SQ, UK

<sup>2</sup>Department of Semiconductor Physics, St Petersburg State Technical University, St Petersburg, Russia

<sup>a</sup>now at Department of Physics, University of Gilan, Gilan, Iran

<sup>b</sup>now at Department of Physics, University of Yazd, Yazd, Iran

We examine some consequences of the phonon and plasmon modes of low dimensional semiconductors that are important in far infrared spectroscopy, with particular reference to oblique incidence reflection spectroscopy, dispersive Fourier transform spectroscopy and attenuated total reflection (ATR) spectroscopy. In modelling long period superlattices the phonon resonances are determined by a modified effective medium [1] and take into account the directional dependence of plasmons in the wells of the MQWs, whereas, in short period superlattices the resonances are shifted from their bulk frequencies due to phonon confinement [2]. We apply ATR spectroscopy to the study of superlattice structures and surface modes and use the technique to probe both of the principal components of the superlattice dielectric tensor, and to investigate surface phonon polaritons and guided wave polaritons.

Attenuated total reflection provides a large out-of-plane electric field component and induces coupling to a series of surface polaritons whose mode frequencies depend sensitively on the components of the dielectric tensor parallel and normal to the layers,  $\epsilon_{xx}$  and  $\epsilon_{zz}$ . We present details of the technique and show how its application to superlattice samples can probe some interesting phonon and plasmon phenomena. Due to different band structures for samples grown in different directions ((001) GaAs/Al<sub>0.5</sub>Ga<sub>0.5</sub>As and (311) GaAs/Al<sub>0.33</sub>Ga<sub>0.67</sub>As), superlattices are likely to exhibit interesting orientation-dependent phenomena, such as a reduction of the in-plane effective mass [3]. Superlattice periods are typically orders of magnitude less than far infrared wavelengths. It is therefore always reasonable in practice to consider a superlattice as a single uniaxial medium. The modified bulk slab model has been applied to the phonon and plasmon response [1] of such samples. The principal components of the dielectric tensor at frequency  $\omega$  for a structure with alternate layers of thickness  $d_1$  and  $d_2$  are given by:

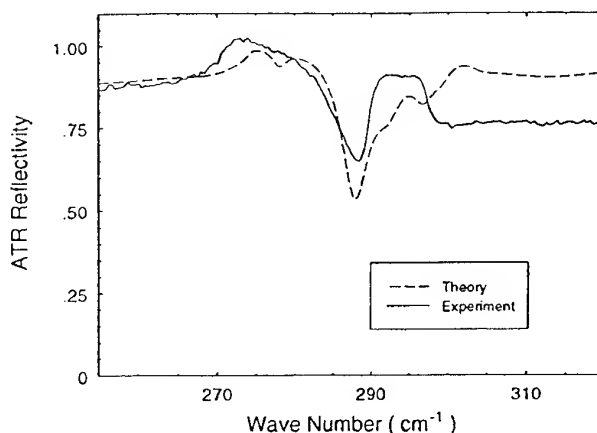
$$\epsilon_{xx}(\omega) = (\epsilon_{xx1}(\omega)d_1 + \epsilon_{xx2}(\omega)d_2)/(d_1 + d_2)$$

$$\epsilon_{zz}^{-1}(\omega) = (\epsilon_{zz1}^{-1}(\omega)d_1 + \epsilon_{zz2}^{-1}(\omega)d_2)/(d_1 + d_2)$$

where  $\epsilon_{xx1}$ ,  $\epsilon_{xx2}$  are the components of the dielectric function in the plane parallel to the quantum layers and  $\epsilon_{zz1}$ ,  $\epsilon_{zz2}$  are the components of the dielectric function in the direction perpendicular to the plane of the MQWs. In considering the free carrier contribution it must be noted that carriers are quasi two-dimensional and confined to the wells.

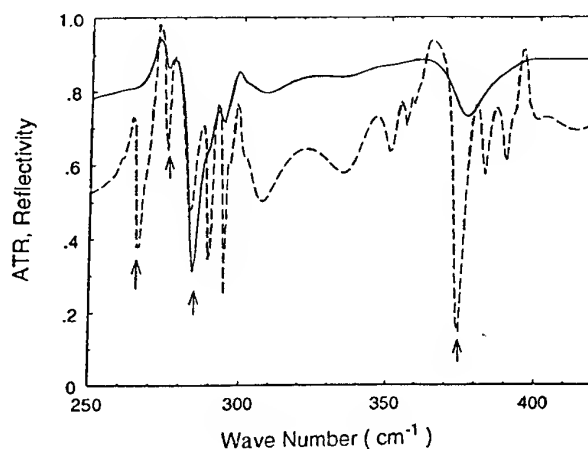
Far infrared measurements were made by polarised oblique incidence reflectivity and ATR spectroscopy using a silicon prism at 20° internal angle of incidence in s and p-polarisation. Measurements were made at 0.5 cm<sup>-1</sup> resolution. The detector was a liquid He-cooled Si bolometer. Fig. 1 shows a 77 K ATR spectrum of a multiple quantum well sample in p-polarisation. The calculated ATR spectrum shows a

Fig. 1. Measured (solid line) and calculated (dashed line) p-polarisation ATR reflectivity spectra of sample GA2 in the GaAs reststrahl region. The air gap is 7  $\mu$ m and the angle of incidence 20°.



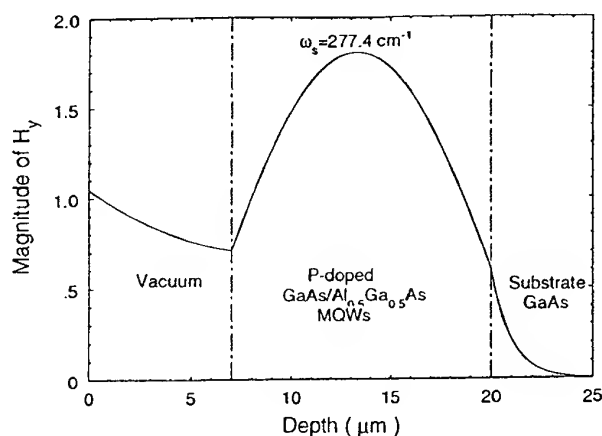
series of plasmon-phonon polaritons in the range of the plasma response which are sensitive to  $\epsilon_{zz}$ , and hence to the hole distribution. The best-fit theoretical spectra correspond to plasma frequencies of 150 and 90  $\text{cm}^{-1}$  which are dependent on the propagation direction of holes in the wells. Dips in the ATR

Fig.2. Theoretically modelled p-polarisation ATR spectra of sample GA2 with full damping and 10% of the full damping for the phonons and plasmons



reflectivity are expected when the scan line crosses a dispersion curve. The dispersion curve shows that there are, in fact, four surface mode branches, but only one interaction is strong enough to produce a clear feature in the measured spectrum, due to high damping. In Fig. 2 we compare calculated ATR spectra with

Fig.3. The calculated magnetic field profile in p-polarisation of sample GA2 at 277.4  $\text{cm}^{-1}$  and 77 K, showing a guided wave mode.  $q_z$  is real in the MQW layer and imaginary in the gap and substrate. The depth is measured from the sample surface.



full damping and 10% of full damping for the phonons and plasmons, demonstrating that for full damping the ATR features are difficult to resolve. The p-polarised field profile of the MQW sample at 277.4  $\text{cm}^{-1}$  and 77 K shows a guided wave mode (Fig. 3).  $q_z$  is real in the MQW layer and imaginary in the vacuum.

#### References

1. S Farjami Shayesteh, T Dumelow, T J Parker, G Mir Jalili, L E Vorobjev, D V Donetsky, and A Kastalsky, *Semicond. Sci. Technol.* 11, 323 (1996).
2. T Dumelow, T J Parker, S R P Smith, and D R Tilley, *Surf. Sci. Report.* 17, (19963)
3. S Farjami Shayesteh, T J Parker, G Mir Jalili, B E Cole, J M Chamberlain and N M Henini, *Proc. 21st Int. Conf. on Infrared & Mm. Waves, Berlin, (1996)*, Eds. M von Ortenberg and H-U Mueller, paper CTh13.

## Far Infrared Characterisation of Mixed Phase GaN Epilayers

G Mirjalili<sup>1,a</sup>, S Farjami Shayesteh<sup>1,b</sup>, T J Parker<sup>1</sup>, T S Cheng<sup>2</sup>, and C T Foxon<sup>2</sup>

<sup>1</sup>Department of Physics, University of Essex, Colchester CO4 3SQ, UK

<sup>2</sup>Department of Physics, University of Nottingham, Nottingham NG7 2RD, UK

<sup>a</sup>Now at Department of Physics, University of Yazd, Yazd, Iran,

<sup>b</sup>Now at Department of Physics, University of Gilan, Gilan, Iran

Polarised oblique incidence FIR reflection spectroscopy at room temperature has been used to investigate the phonon frequencies of mixed phase GaN epilayers deposited by MBE on GaP substrates as the epilayers switch from the  $\alpha$ - to the  $\beta$ -phase crystal structure. The amount of GaAs in the epilayers has been measured and found to correlate well with the use of As during growth.

The crystal structure of GaN depends strongly on the growth conditions and orientation of the substrate surface. Strite et al. [1] have shown that the wurtzite phase often coexists with the cubic phase. GaN films deposited on [001] GaP substrates grown by MBE exhibit mixed structures ( $\alpha$ -,  $\beta$ -GaN), and Chen et al. [2] have demonstrated that by varying the arsenic flux and using different substrate temperatures during the growth of the epilayer, a film with a wurtzite ( $\alpha$ -GaN), zincblende ( $\beta$ -GaN), or mixed crystal structure can be grown.

We have previously reported on GaN epilayers in the cubic and wurtzite phases on GaP substrates [3]. Here we describe studies on mixed phase GaN layers on GaP substrates. The measurements enable us to determine the transverse optic (TO) and longitudinal optic (LO) phonon frequencies at the centre of the Brillouin zone, and this enables the amount of GaAs that emerges during growth to be determined. The samples were grown by MBE using elemental solid sources of Ga and As and an activated nitrogen source. Prior to growth the substrates were heat-cleaned under either active nitrogen or arsenic flux at 620 °C to remove any residual surface oxide [2]. We have studied four samples grown under different conditions, each consisting of a thin epilayer of mixed phase GaN grown on a GaP substrate. Far infrared measurements were made by s- and p-polarised reflection spectroscopy at 45° angle of incidence at 300 K, and spectra are interpreted by comparing with spectra of  $\alpha$ - and  $\beta$ -phase epilayers of GaN deposited on the same substrate [3].

Examples of p-polarisation spectra of samples MG80, MG85, MG88, and MG89 obtained at 300 K in comparison with  $\alpha$ -phase sample MG84 and  $\beta$ -phase sample MG108 are shown in Fig. 1. To account

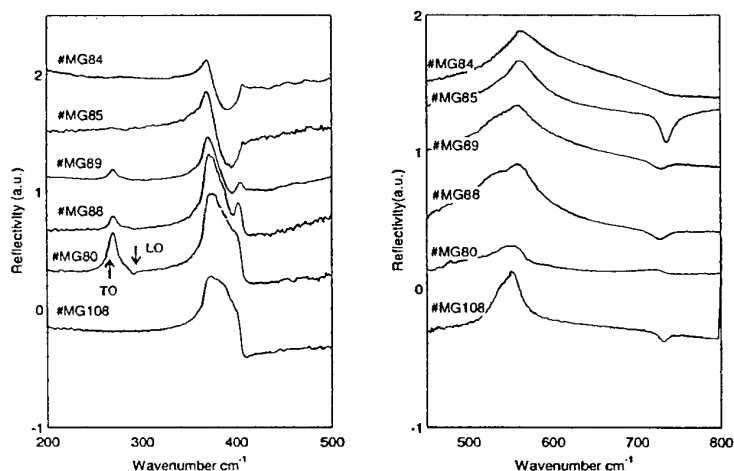


Fig. 1. Comparison of p-polarisation spectra of mixed phase samples (MG85, MG89, MG88, and MG80) with the spectra of samples MG84 ( $\alpha$ -GaN) and MG108 ( $\beta$ -GaN). Left: GaP reststrahl region, and right: GaN reststrahl region. The graphs are displaced vertically for clarity.

for all features observed in these spectra, we have modelled the reflectivity using a standard matrix optics model using three layers: (1) a GaN epilayer, (2) a very thin layer of GaAs, and (3) the GaP substrate. We obtained a good fit between the experimental and theoretical spectra, as shown in Fig. 2. The results have been used to determine the phonon frequencies of each of the epilayers and thicknesses of the GaN and GaAs thin films, so we could calculate the fraction of



GaAs in the grown epilayers. The parameters used in modelling are listed in Table 1 [4], which also includes results from electron microscopy.

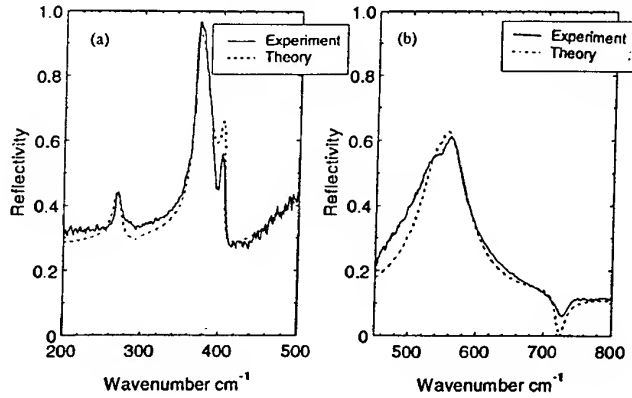


Fig. 2. p-polarisation spectra of sample MG88 in left: the GaP reststrahl region, and right: the GaN reststrahl region.

From the table and Fig. 1 we see that as the As flux increases a peak arising from the GaAs TO frequency appears in the spectra, increasing in size as the flux increases. In sample MG80, the sample grown with the highest As flux, this peak is largest. We have modelled the GaAs modes with bulk GaAs phonon parameters; if a GaAs alloy were present, the LO and TO frequencies would be shifted from the bulk frequencies [5]. This implies that the ternary alloy  $\text{GaAs}_x\text{N}_{1-x}$  is not present in our samples, which is consistent with [2, 4] which also indicate that no alloy is present in the epilayers. Furthermore, with increasing As flux the GaN TO frequencies decrease. Indeed, in the absence of an As flux the TO frequency has a maximum value equal to the  $\alpha$ -GaN TO frequency at  $560 \text{ cm}^{-1}$  (sample MG84). With an arsenic flux of about  $1.2 \times 10^{-5}$  Torr, the TO frequency has a minimum value of about  $553 \text{ cm}^{-1}$  (sample MG88) which is fitted with the  $\beta$ -GaN phases in the epilayers. In spite of the presence of both  $\alpha$ - and  $\beta$ -GaN, there is no evidence of segregation in the phonon frequencies. The TO frequencies for the mixed phase are between the TO frequencies of the  $\alpha$ - and  $\beta$ -phases, but the LO frequency is usually less than those of either the  $\alpha$ - or the  $\beta$ -phases.

Sample	As-flux (Torr)	$T_{\text{growth}}$ $^{\circ}\text{C}$	$d_{\text{epilayer}}$ ( $\mu$ )*	$d_{\text{GaAs}}$ ( $\mu$ )	$d_{\text{GaN}}$ ( $\mu$ )	$\gamma_{\text{GaN}}$ ( $\text{cm}^{-1}$ )	$\gamma_{\text{GaAs}}$ ( $\text{cm}^{-1}$ )	$\text{TO}_{\text{GaN}}$ ( $\text{cm}^{-1}$ )	$\text{LO}_{\text{GaN}}$ ( $\text{cm}^{-1}$ )	GaAs %	epilayer phase <sup>M</sup>
MG84 <sup>W</sup>	0	620	0.48	0.00	.48	70	-	560	740	0	$\alpha$ -GaN
MG85	$1.2 \times 10^{-6}$	620	0.42	0.02	.40	15	6	558	734	4.4	$\alpha$ -GaN $\beta$ -GaN
MG89	$2.0 \times 10^{-6}$	620	0.55	0.08	.50	25	5	556	728	14	$\alpha$ -GaN $\beta$ -GaN
MG88	$4.2 \times 10^{-6}$	620	0.45	0.15	.40	50	6	554	729	33	$\alpha$ -GaN, $\beta$ - GaN GaAs
MG80	$1.2 \times 10^{-5}$	620	0.60	0.45	.15	35	5	553	734	75	$\beta$ -GaN GaAs
MG108 <sup>C</sup>	$2.4 \times 10^{-5}$	700	0.20	0.00	.20	17	-	553	733	0	$\beta$ -GaN

Table 1. W: wurtzite structure, C: cubic structure, M: from electron microscopy, \*: nominal thickness.

#### References

1. S Strite, M E Lin and H Morkoc, Thin Films, 231, 197 (1993)
2. T S Chen, L C Jenkins, S E Hooper, C T Foxon, J W Orton, and D E Lacklinson, Appl. Phys. Letters, 66, 1509 (1995)
3. G Mirjalili, T Dumelow, T J Parker, S Farjami Shayesteh, T S Chen, C T Foxon, L C Jenkins, and D E Lacklinson, Infrared Phys. and Techn., 37, 389 (1996)
4. Y Xin, P D Brown, R E Dunin-Borkowski, C J Humphreys, T S Cheng and C T Foxon, Crystal Growth, 171, 321 (1997)
5. O.K. Kim and W G Spitzer, J. Appl. Phys., 130, 4362 (1979)

## Determination of plasma frequency and the pulse relaxation time in doped semiconductors by FIR Surface Waves

V.Vaicikauskas

Institute of Physics, Gostauto 12, 2029 Vilnius, Lithuania, Fax: (3702) 235182, e-mail: vikvai@ktl.mii.lt

**Theory.** The conventional method for determination of parameters of plasma oscillations in semiconductors is IR reflectivity [1]. In the homopolar semiconductors possessing a diamond structure, e.g. Si and Ge plasma reflection edge is't affected by lattice vibrations and this method gives good results. In polar semiconductors longitudinal modes involve collective ion and electron motion and plasma reflectance edge is affected by phonons.. Effective dielectric permittivity of semiconductor with one type of phonons and one type or carriers can be expressed:

$$\varepsilon = \varepsilon_{\infty} \left( 1 + \frac{\frac{\omega_{LO}^2 - \omega_{TO}^2}{\omega_{TO}^2 - \omega^2 + i\omega\Gamma} - \frac{\omega_p^2}{\omega(\omega - i\gamma)} \right), \quad (1)$$

where  $\omega_{TO}$ ,  $\omega_{LO}$ , are frequencies of transverse and longitudinal optical phonons,  $\Gamma$  and  $\gamma$ , are damping constants of phonons and plasmons,  $\gamma = 1/\tau = e/\mu m^*$ ,  $\mu$  is mobility of electrons,  $\tau$  is pulse relaxation

time,  $\omega_p = \sqrt{\frac{Ne^2}{m^* \varepsilon_0 \varepsilon_{\infty}}}$  is plasma frequency (in  $\text{cm}^{-1}$ ). Surface Electromagnetic Waves (SEW) wavevector

$$k = \frac{\omega}{c} \sqrt{\frac{\varepsilon}{\varepsilon + 1}} \approx 1 - \frac{1}{2\varepsilon}.$$

The positive contribution of phonons into  $\varepsilon$  decreases when  $\omega$  moves away from phonon frequency, whereas negative contribution of free carriers increases with the wavelength according to Drude law. So, in the FIR region, contribution of free carriers becomes dominant. The SEW propagation distance  $L$  and real part of SEW refraction index  $n'_{\text{ef}} = ck'/\omega$  can be expressed:

$$L = \frac{\omega_p^2 \varepsilon_{\infty}}{2\pi\gamma\omega^2}, \quad n'_{\text{ef}} - 1 = \frac{\omega^2}{2\varepsilon_{\infty}\omega_p^2} \quad (2)$$

**Experimental results.** The experimental arrangement and technique used for measurement  $L$  and  $n'_{\text{ef}}$  have been described previously [2].

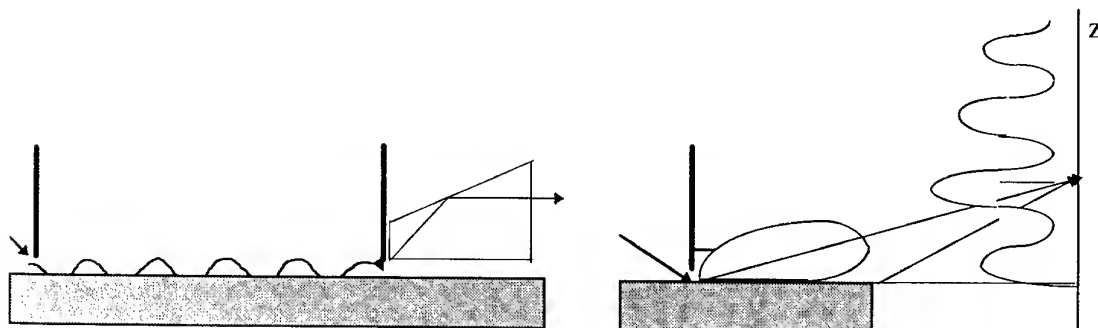


Fig.1. A scheme of amplitude (a) and phase (b) SEW spectroscopy.

Experiments were carried out using the automatic homemade SEW spectrometer. The pulse optically pumped  $\text{CH}_3\text{OH}$ -laser operating at frequencies 85, 103, 128, 142 and  $238\text{cm}^{-1}$  was used for SEW excitation. The pumping of was accomplished by the pulse  $\text{CO}_2$ -laser ( $\tau = 100\mu\text{s}$ ,  $P_{\text{pulse}} = 0.1 \div 0.5\text{kW}$ ) with the  $150\text{mm}^{-1}$  rotating grating output mirror.

The imaginary part of the SEW refraction index was determined from the intensity  $I(x)$  dependence on the distance  $x$  along the interface (fig.1a). In order to obtain the real part of  $n_{\text{ef}}$  (phase spectroscopy) the interference measurements have been carried out (Fig.1b). After the SEW excitation they propagate along the interface, transform into bulk waves at the sample edge and interfere with that part of the bulk wave that has been diffracted on the screen. The condition of interference maximum at the point  $z_m$  can be written in this way:

$$a \times n_{\text{ef}} + \sqrt{(b^2 + z_m^2)} - \sqrt{z_m^2 + (a+b)^2} = \frac{m + \Delta}{v}, \quad (3)$$

where  $a$  is distance between the screen and the sample edge,  $b$  is distance from the sample edge to the observation plane,  $m$  are even numbers for maximums and odd numbers for minimums,  $v$  is linear frequency (in  $\text{cm}^{-1}$ ). The value  $\Delta$  is introduced to account the possible phase shift between the bulk wave and the SEW. So, the interferogram modulation depth relies on the SEW excitation efficiency, the propagation distance  $L$  and on the distance between the sample edge and the screen used for SEW excitation. From the  $m$  dependence on  $z_m$  at few distances the  $n_{\text{ef}}$  can be determined. In the FIR region the modulation pattern is deeper modulated in comparison with  $10\mu\text{m}$  region in metals, because SEW excitation efficiency in the FIR region is higher. Namely, at  $97\mu\text{m}$  line about 40% of incident radiation transforms into SEW for  $N = 2 \times 10^{18}\text{cm}^{-3}$ . So, positions of extremums are clearly expressed and can be determined with high accuracy. The precision can be even increased by using cooled semiconducting FIR detectors instead of pyroelectric ones.

In the spectral range where phonon contribution becomes appreciable  $L$  and  $n_{\text{ef}}$  must be calculated exactly. It must be mentioned from (2), that from the experimentally measured complex SEW refraction index the plasma frequency and the plasmon damping constant  $\gamma$  (or  $\tau$ ) can be determined independently. They are presented in Table 1 and compared with these obtained by the IR reflectance method.

Table 1. Plasma frequency and plasmon damping constant measured by SEW and IR Reflectance methods

Parameter	SEW ( $103\text{cm}^{-1}$ )	IR reflectance
$\omega_p$	510	506
$\gamma$	74	71

Another way to determine both  $\gamma$  and  $\tau$  is to measure  $L$  at two FIR laser lines and from the obtained two pairs of  $\omega_p^2/\gamma$  (from (2)). This method is even more simple because it is carried out at one geometry of the experiment.

We obtained nonlinear dependence  $L(N)$  in GaAs (Te) in the concentration range  $(10^{17} - 10^{18})\text{cm}^{-3}$ . It is caused firstly by the dependence of effective mass  $m^*$  of carriers on  $N$  due to nonparaboly of the conduction band. The pulse relaxation time  $\tau$  is determined by the scattering mechanism. At low dopant concentrations in  $\text{A}^3\text{B}^5$  semiconductors, carriers scatter mainly by acoustic modes. In the strongly doped crystals combined scattering by ions of admixtures and polar lattice vibrations dominate. We obtained a "hump" in  $L(N)$  dependence in GaAs(Te) at  $N$  approximately  $2 \times 10^{18}\text{cm}^{-3}$ , which was explained by isostructural phase transition [3]. In this case scattering by impurity ions falls down when the separated admixture ions transform into some correlated state.

1. B.V. Tata and A.K. Arora. Infrared Physics. **24**, 547 (1984).
2. V. Vaicikauskas. Infrared Physics and Technology. **36**, 475 (1995).
3. N.A. Semikolenova. Fizika Tverdogo Tela. **22**, 137 (1988).

## **Excitation of Backward Waves in Gyro-Forward-Wave Amplifiers and Forward-Wave Amplifiers Driven by Linear Electron Beams**

G.S. Nusinovich, M. Walter, and J. Zhao

Institute for Plasma Research  
University of Maryland  
College Park, MD 20742-3511 USA

Excitation of parasitic backward waves is one of the most important issues for all microwave amplifiers based on interaction between electrons and forward traveling waves propagating in waveguides. This excitation restricts the interaction length, and therefore, limits the gain of amplifiers. It may also cause some restrictions on the operating bandwidth.

We developed the theory describing the self-excitation conditions for backward waves in the presence of the large-amplitude forward waves. This theory is applicable to a wide class of traveling-wave amplifiers, including gyro-traveling-wave tubes (gyro-TWTs) and gyrotwistrons as well as conventional twistrons and traveling-wave tubes (TWTs). Our formalism is based on a two-step procedure. First, the large-signal amplification of a forward wave is considered which allows one to determine the optimal parameters of the device in the absence of backward wave parasites. Second, the conditions of self-excitation of backward waves in the presence of the forward wave are studied.

The results illustrating the effect of suppression of backward waves by forward waves operating in large-signal regimes are obtained for gyro-TWTs and TWTs as well as for output waveguides of gyrotwistron and twistrons. These results allow one to determine the maximum ratio of the coupling impedance of an electron beam to the backward wave parasite to that for the operating forward wave, at which the forward wave amplification remains stable. For twistor configurations with well prebunched electron beams this maximum ratio is larger than for gyro-TWTs and TWTs with a relatively low input power level. This shows that twistor-type devices are more stable with respect to parasitic backward wave excitation than single-stage traveling-wave devices.

Our formalism can easily be generalized for the analysis of multi-stage forward-wave amplifiers as well as for including the effects of electron velocity spread, distributed wall losses and other factors important for operation of real devices.

This work has been supported by the U.S. Department of Defense Multidisciplinary University Research Initiative (MURI) program and by the Naval Research Laboratory.

## A New Hybrid Ion-Channel Maser Instability

Robert J. Barker \*, Liu Shenggang\*\*

**Abstract:** A new hybrid ion-channel maser instability, in which the electron cyclotron maser instability mechanism and the ion-channel instability maser instability mechanism are combined, is proposed and studied. The features and the dispersion equation of the new maser are given in the paper with detailed discussion.

### I. Introduction

An ion-channel can be formed due to either intense laser beam or relativistic electron beam injection. Based on this effect, varieties of ion-channel lasers' and ion-channel masers' instabilities have been presented and studied [1]-[5]. Now a new instability scheme is proposed, in which the ion-channel maser instability and the electron cyclotron maser instability are combined. Theoretical analysis and the dispersion equation of the new instability mechanism are given in the paper. It shows that this new hybrid ion-channel maser instability has some interesting features.

### II. Analysis

In an ion-channel, the force affecting the electron motion is

$$\vec{F}_i = -\frac{|e|^2 n_p}{2\epsilon_0} R \vec{e}_R \quad (1)$$

It is a centripetal force, we get the cyclotron frequency as

$$\omega_0^2 = \omega_p^2 / 2\gamma_0, \quad \omega_p^2 = \frac{|e|^2 n_p}{m_0 \epsilon_0} \quad (2)$$

$n_p$  is the ion density and  $\gamma_0$  is the relativistic factor of the electron beam. Almost all electromagnetic instabilities of ion-channel laser' and maser' are based on equ.(2).

If there exists an axial magnetic field  $B$ , we have a combined force:

$$\vec{F} = \vec{F}_i + \vec{F}_m = -\left[ \frac{|e|^2 n_p}{2\epsilon_0} R + |e| B_0 v_\theta \right] \vec{e}_R \quad (3)$$

It shows that both  $F_i$  and  $F_m$  are centripetal force. Then we get the electron cyclotron frequency:

$$\omega_0 = \frac{\omega_{c0}}{2\gamma_0} \left( 1 + \left( 1 + \frac{2\gamma_0 \omega_p^2}{\omega_{c0}} \right)^{1/2} \right) \quad (4)$$

Where  $\omega_{c0} = \frac{|e|B_0}{m_0}$

When  $\omega_{c0} \gg \omega_p$ , we get  $\omega_0 = \omega_c = \frac{\omega_{c0}}{\gamma_0}$ , when  $\omega_p^2 \gg \omega_{c0}^2$ , we get  $\omega_0 = \frac{\omega_p}{\sqrt{2\gamma_0}}$ .

The former one is the base of Electron Cyclotron Maser instability, the  $\gamma_0^{-1/2}$  energy dependence of which is  $\gamma_0^{-1}$ , while the second one is the base of ion-channel maser instability, the energy dependence is  $\gamma_0^{-1/2}$  [3]. Now equ.(4) shows that for the new hybrid one, the energy dependence is not  $\gamma_0^{-1}$ , nor  $\gamma_0^{-1/2}$ , it is a new interaction scheme.

### III. Dispersion Equation

By using the fluid model the following dispersion equations of the hybrid ion-channel maser instability can be obtained:

$$(k_z^2 - k_{z0}^2) = -\frac{j\omega\mu_0}{P_E} \int J_\varphi \cdot E_\varphi^* ds = \frac{\omega\mu_0|e|n_b}{P_E} \left( j \frac{\omega_0^2}{\Omega} R_1 + (\omega_0 + \Omega) R_0 \varphi_1 + R_0 \omega_0 k_{z0} z_1 \right) \cdot E_\varphi^* \Big|_{R=R_0} \quad (5)$$

Where

$$\Omega = \omega - k_{z0} v_{z0} - \omega_0 \quad (6)$$

$$R = \frac{\Delta_R}{\Delta} \quad (7)$$

$$\bar{f} = -|e|(\bar{E}_1 + \bar{v}_0 \times \bar{B}_1) R_0 \varphi_1 = \frac{\Delta_\varphi}{\Delta} \quad (8)$$

$$z_1 = \frac{\Delta_z}{\Delta} \quad (9)$$

$$\Delta = \gamma_0^3 \Omega^4 \left( (1 + \gamma_0^2 \beta^2) \left( \Omega^2 - \omega_0^2 - \frac{\omega_p^2}{\gamma_0} \right) - (\omega_0 - \omega_c)^2 (1 + \gamma_0^2 \beta_{||}^2) \right) \quad (10)$$

Where  $\bar{f}$  is the force due to the electromagnetic wave field:

$$\bar{f} = -|e|(\bar{E}_1 + \bar{v}_0 \times \bar{B}_1) \quad (11)$$

Substituting the field expressions into the above equations we can get the complete form of the dispersion equation.

#### IV. Conclusion

A new kind of ion-channel maser instability is proposed and studied in the paper. This hybrid ion-channel maser is based on the combination of magnetic electron cyclotron maser and the ion-channel maser instabilities. The theoretical analysis given in the paper shows that the new hybrid ion-channel maser instability has the following features:

1. The new instability mechanism is based on the hybrid cyclotron frequency that has a special energy dependence ( $1/2 < q < 1$ ). According to [3], the energy dependence can be written as  $\gamma_0^{-q}$ , it showed in [3] that there are three kinds of the dependence:  $q=1$ , is the electron cyclotron maser instability;  $q=1/2$  is the ion-channel maser instability and  $q=0$  is the Free Electron Laser instability. Now we get a new one the  $q$  of which should be ( $1/2 < q < 1$ ). Actually, there is another one, the Electrostatic Electron Maser [5], the energy dependence is also  $q=1/2$ . Therefore, there are four different kinds of energy dependence for different instability mechanisms:  $q=0$ ,  $q=1/2$ ,  $1/2 < q < 1$  and  $q=1$ . It shows that the instability mechanism is also negative mass effect, and the energy dependence is weaker than that of magnetic electron cyclotron maser and stronger than that for the ion-channel maser.

2. The character of the singularity in the dispersion equation of the new maser instability is different from that of electron cyclotron maser and the ion-channel maser. There are

two singularities:  $\Omega = 0$  and  $\left( (1 + \gamma_0^2 \beta^2) \left( \Omega^2 - \omega_0^2 - \frac{\omega_p^2}{\gamma_0} \right) - (\omega_0 - \omega_c)^2 (1 + \gamma_0^2 \beta_1^2) \right) = 0$

. The last one was never seen in published papers.

3. Comparing with the electron cyclotron maser and the ion-channel maser, the new hybrid ion-channel maser may have some advantages: At first, because of the ion neutralization the beam density can be increased, secondly, since  $q < 1$ , for the same electron energy, the operating frequency may be higher. In addition, since the interaction takes place in the ion-channel region, stronger interaction efficiency is expected.

\*AFSOR, USA; \*\*UESTC, P.R.China.

#### References

1. David H. Whilttom, Phys. Fluids, B4(3), 730, 1992,
2. David H. Whilttom, Andrew M. Sessler and J. M. Dawson, Phys. Rev. Letters, 64,21,2511,1990.
3. K. R. Chen, J.M.Dawson, A.T. Lin and T. Katsouleas. Phys. Fluids, B(3),5, 1270, 1991,
4. Chang J. Tang, Pukun Liu and Liu, Shenggang. J. Phys. D. Appl. Phys. 29, 90, 1996,
5. Liu Shenggang, Robert J. Barker, et al. Unpublished paper,
6. Liu, Shenggang et al. J. Appl. Phys. 59,3621, 1986.

### 3-D Simulation Design of 3mm Slow Wave Structure

L. Song , G. Caryotakis<sup>1</sup>, A. Vlieks<sup>1</sup> and N. C. Luhmann Jr

Department of Applied Science, University of California, Davis, CA 95616

(1) Stanford Linear Accelerator Center Menlo Park, CA 94025

A new type of slow wave structure is proposed for use in next generation millimeter wave sources for a variety of applications [1][2]. The structure is compatible with fabrication techniques such as LiGA (Lithographie, Galvanoformung, Abformung) as well as more conventional approaches such as EDM (Electrical Discharge Machining), which are expected to result in favorable manufacturing cost. This paper is concerned with the design and modeling of the slow wave structure using the 3-dimensional code MAFIA [3]. It is found that structures, such as shown in Fig. 1, are capable of providing high R/Q and thus conversion efficiency, either for narrow or wide bandwidth use. The rectangular structure is chosen because of the fabrication requirements.

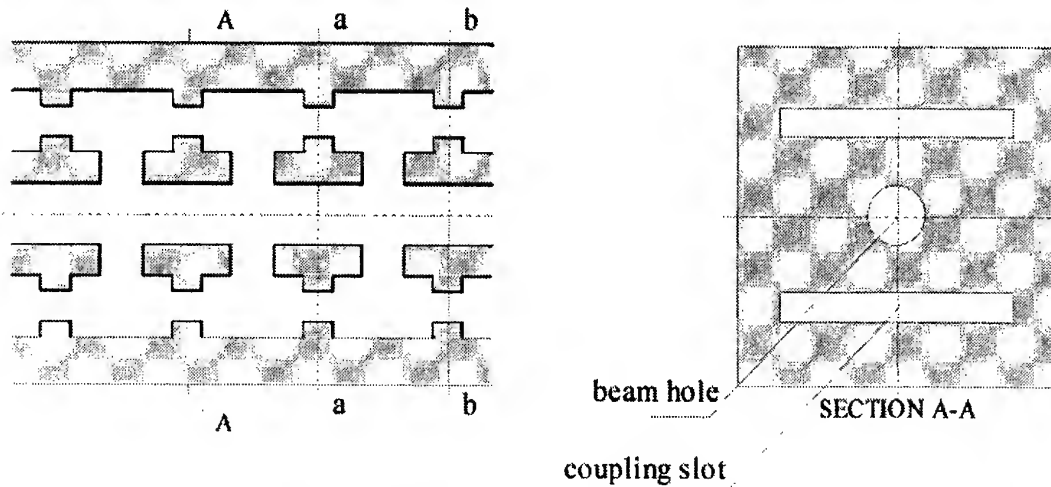


Figure 1. Schematic of 2mm x 2mm cross-section slow wave structure

The periodic structure of the output cavity results in the dispersion relation shown in Fig. 2. It is observed that the hybrid  $HE_{10}$  and  $HE_{01}$  cavity modes and the  $HE_{20}$  and  $HE_{02}$  slot modes are degenerate, unlike those in traditional cylindrical structure designs. The  $EH_{11}$  and  $HE_{11}$  modes are separated by a stop band due to the cutoff frequency of the coupling slot. Also, it is found that TE and TM modes can not exist independently since they must satisfy periodic boundary conditions in coupled-cavity slow wave structures. In this sense, the present structure differs from conventional cylindrical corrugated waveguide such as those employed in backward wave oscillators (BWOs) and mode converters. For such BWO type slow wave systems, the  $TM_{0m}$  and  $TE_{0m}$  mode can exist independently. The  $EH_{11}$  cavity mode is proven to be the optimal operating mode because of its strong interaction with the electron beam. Its cold pass band is 20.037GHz. The self oscillation problem with other harmonic modes is also ameliorated by the choice of the  $EH_{11}$  mode.



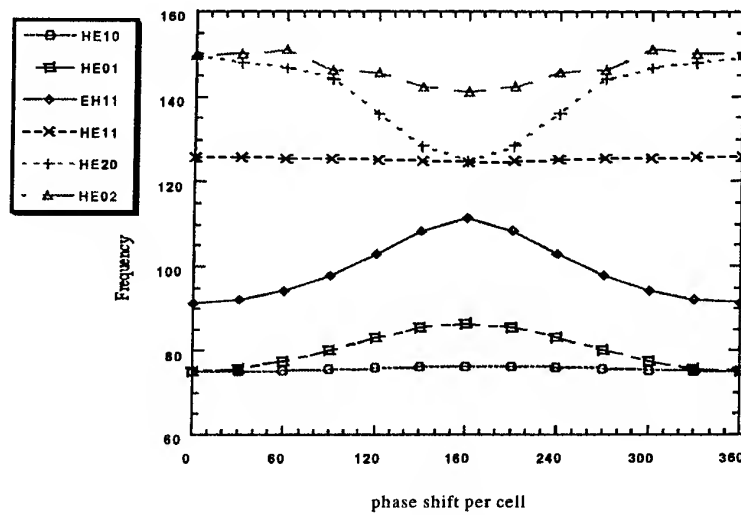


Figure 2. Dispersion Characteristic of Periodic 3mm Slow Wave Structure

A realistic 3-dimensional nonperiodic five section coupled cavity was also simulated to obtain the eigenmodes shown in Fig. 3, which agree very well with scaled x-band cold test measurements. The fifth eigenmode, i.e. the quasi- $2\pi$  mode on the  $EH_{11}$  curve, is the interaction point. Its z-component electric field profile along the z-axis was measured by a bead perturbation experiment. Also, the cavity quality factor  $Q_0$ ,  $R/Q$  values for each cell and the total structure ( where  $R$  is the reentrant cavity impedance ) were also obtained and found to be in reasonable agreement with predictions.

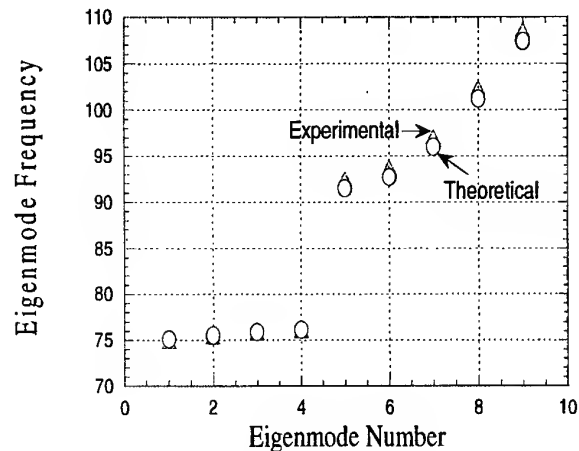


Figure 3. Theoretical and experimental eigenmodes of 5-cell 3mm slow wave structure

This work has been supported by AFOSR under Grant F49620-95-1-0253 (MURI) and Contract F30602-94-2-0001 (ATRI).

#### References:

1. G. Caryotakis, SLAC-PUB-7731 Jan. 1998.
2. G. Caryotakis, SLAC-PUB-7624 Aug. 1997.
3. Carol L. Kory et.al NASA Technical paper 3513 1995.

## Axial Mode Locking in Gyrotrons

G.S. Nusinovich and J. Zhao

Institute for Plasma Research  
University of Maryland  
College Park, MD 20742-3511 USA

Recently, a new gyrotron configuration, the inverted gyrotwyston, was studied experimentally [1]. In this device, electrons are prebunched in an input waveguide, which is followed by a drift section. Then, the prebunched electron beam enters an output cavity where it excites oscillations at the signal frequency or its harmonic. An intriguing feature of the experiment [1] was the dependence of the output power on the signal frequency; when this frequency was increased, the device's radiation exhibited two narrow, isolated peaks followed by a large (1.3%) continuous bandwidth. This bandwidth is much larger than the width of a resonance curve of one mode, which is a typical scale of operation in the cavity.

Gyrotron cavities are usually formed by slightly irregular open waveguides excited at frequencies close to cut-off. In such cavities, as the number of axial variations,  $\ell$ , increases, the diffraction quality factor,  $Q_D$ , decreases as  $1/\ell^2$  [2]. Therefore, as  $\ell$  grows the width of the resonance curve,  $\omega/Q$ , widens, which may lead to their overlapping. This fact allows one to assume that in the experiment [1], first, two modes with  $\ell = 1$  and  $\ell = 2$  were excited, which have narrow resonance curves. Then a set of low-Q modes with  $\ell \geq 3$  and overlapping resonance curves was excited in a continuous way. As a result, the phase locking of such modes may occur.

In our paper we develop the theory describing this effect. The results are in reasonable agreement with experimental data.

This work has been sponsored by the U.S. Department of Defense Multidisciplinary University Research Initiative (MURI) program under AFOSR Grant No. F4962001528306.

1. H. Guo et al., Phys. Rev. Lett. 79, 515 (1997).
2. L.A. Weinstein, *Open Resonators and Waveguides* (Boulder, CO: Golem Press, 1969); S.N. Vlasov et al., Radiophys. Quantum Electron. 12, 971 (1969).

## Self-consistent Time-dependent Modeling of Gyro-amplifiers with MAGY

K. Nguyen\*, M. Botton†, T.M. Antonsen†, B. Levush, M. Blank, and J. Calame

Vacuum Electronics Branch  
Naval Research Laboratory  
Washington D.C. 20375

### Abstract

In this paper, the modeling of several recent experiments on gyrokystron amplifier at the Naval Research Laboratory using the quasi three-dimensional code MAGY is presented. Amplifiers in both Ka- and W-bands have been studied. Using known experimental input parameters, code-predicted salient amplifier performance characteristics, e.g. efficiency, bandwidth, drive curve, have been found to be in good agreement with experimental results. The self-consistency of MAGY also reveals the existence of RF excitation at the drive frequency in cutoff drift sections driven by the bunched electron beam. This phenomenon may impact the design and use of lossy ceramics in drift-sections of high-average power devices due to thermal considerations.

### Introduction

Detailed and accurate nonlinear simulations of the interaction between the electromagnetic (EM) fields and the electron beam in vacuum electron devices are essential to the understanding of their performance. This understanding is critical to the design and development of future devices. This is the essential impetus for the recent development of the self-consistent, time-dependent, quasi three-dimensional, new MAGY code [1]. Differently from the Finite-Difference-Time-Domain Particle-in-cell (PIC) approach, MAGY employs a reduced description approach in which the electromagnetic fields are described by a superposition of the waveguide Transverse Electric (TE) and Transverse Magnetic (TM) eigenmodes. Furthermore, the temporal evolution of the EM complex field amplitudes and of the electron beam are assumed to be slow relative to the RF period; hence, allowing for the averaging over time-scale on the order of the RF period. The fast-time-scale averaging and RF-fields reduced description approach substantially reduces the computational resources compared to that required by PIC codes. However, unlike other reduced description codes, MAGY does not incorporate restricting assumptions on the physics involved, and thus, does not compromise on the fidelity of the results. For instances, in MAGY, the RF field profiles, rather than being restricted to a fixed form, freely evolve in response to the interaction with the electron beam. This capability is achieved in the new MAGY code via a novel formulation of the generalized telegrapher's equations together with the fast-time-scale averaging of the fully-relativistic electron equations of motion. Even though, the new MAGY code is intended for the modeling of both slow and fast-wave devices. In this paper, we shall only report results on a type of fast-wave devices, the gyrokystron amplifiers.

### Ka-band and W-band Gyrokystron Modeling

Several experiments on gyro-amplifiers have recently been performed at the Naval Research Laboratory. The goal is toward extending the bandwidth and average power of these devices for the next generation of millimeter wave radars and for communications applications [2]. To illustrate the capability of the new MAGY code, we will report here the comparison with experimental results of one such devices: a two-cavity 35-GHz gyrokystron [3] which operates in the cylindrical  $TE_{01}$  mode. In Figure 1, the geometry and axial RF field profile for the Ka-band gyrokystron are shown. Also shown in this figure is the comparison of simulated drive curve and saturated frequency-response (bandwidth) curve against experimental data with good agreement. Similar agreement for the 94-GHz gyrokystrons has also been obtained. It should be noted that for the input parameters used in the comparison: the cavity quality factors (Q) and resonance frequencies are from experimental cold-test measurements, the beam voltages and

\* KN Research, Silver Spring, MD 20906

† University of Maryland, College Park, MD 20742

currents are measured values, and the beam velocity ratio ( $\alpha$ ) and perpendicular velocity spread are deduced from beam optics simulations.

### Beam-induced RF Excitation in Cut-off Drift Section

This physical phenomenon, previously not been observed with reduced description codes, has been self-consistently simulated with MAGY. Non-resonant RF excitation at the drive frequency is observed in cut-off drift sections. The RF amplitude is found to scale linearly with the bunched electron beam perturbed current. The origin of this phenomenon is similar to that of a driven harmonic oscillator. The presence of RF in the drift section has important consequence in the use of lossy dielectrics in cutoff drift-section, especially for high-average power devices. Subsequent to the discovery of this phenomenon, a model has been incorporated into MAGY to estimate the power loading on lossy ceramics due to beam-driven RF excitation. This model was benchmarked against a particle-in-cell code, MAGIC, with excellent agreement, and has been employed to provide information about the thermal stress on the ceramics in the last drift-section of the high-average power 94-GHz gyrokyklystron [2].

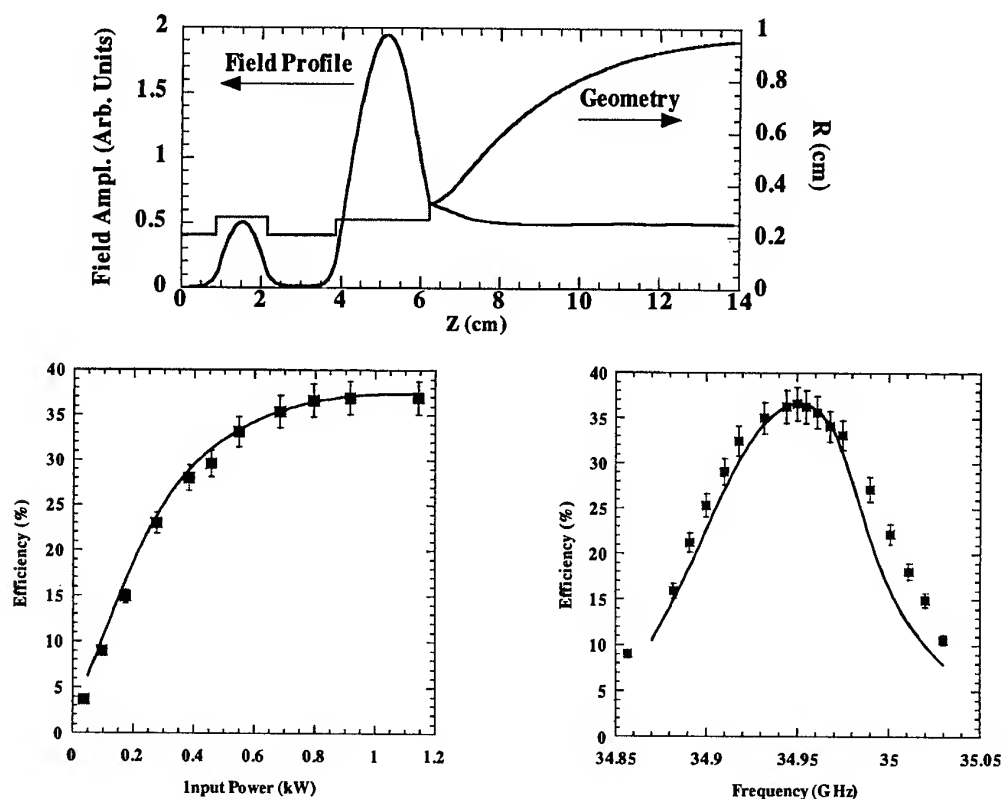


Figure 1: Geometry and field profile for a two-cavity gyrokyklystron (top) Comparison with experimental data: drive curve at 34.95 GHz (bottom left) and frequency response with input power of 920 W (bottom right). Resonance frequency and quality factor are 34.89 GHz and 188 for first cavity and 34.895 GHz and 191 for second cavity. Beam current and voltage are 8.2A and 70 KV with velocity ratio of 1.35 and perpendicular velocity spread of 5%.

[1] M. Botton, et al., "MAGY: A time-dependent Code for Simulation of Slow and Fast Microwaves Devices," *IEEE Trans. Plasma Sci.*, Vol.26, No. 3, June 1998.

[2] B.G. Danly, et al., "Development of a W-band Gyrokyklystron for Radar Applications," This Conference Digest 1998.

[3] J.J. Choi, et al., "Investigation of a High-power Two-cavity 35GHz Gyrokyklystron Amplifier," *IEEE Trans. Plasma Sci.*, Vol.26, No. 3, June 1998.

## A TEM-TE<sub>16,2</sub> converter based on ring resonator

Gy. Reiter, Gy. Veszely and T. Berceli

Budapest Technical University, Department of Microwave Telecommunications  
Goldmann t. 3. Budapest, 1111 Hungary

### Abstract

A mode transducer is described consisting of a surface excited ring resonator and iris-coupled resonators. An equivalent network is determined and used for the proper construction of the transducer.

### Introduction

Recently a mode transducer using a microstrip-slot antenna was developed by the authors [1], [2]. At higher frequencies (above 100GHz) and higher azimuthal mode numbers ( $m > 30$ ) the realization satisfying the strict symmetric conditions of the microstrip-slot antenna is impossible. In this paper another excitation method is proposed.

### Construction

The construction of the proposed transducer can be seen in Fig. 1. At the left side there is a coaxial input which excites the circular input resonator. Instead of the coaxial input a circular waveguide with TM<sub>01</sub> mode

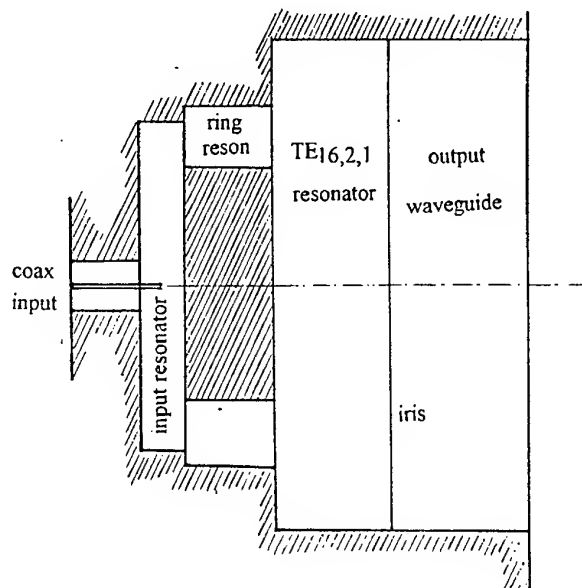


Fig. 1. The construction

can be used as well. The length of the input resonator is much shorter as the wavelength belonging to the uppermost frequency of the transducer. The rotational symmetrical coaxial or circular excitation generates  $\varphi$ -independent fields. Consequently in the input resonator TM<sub>0n0</sub> modes are present. There are 16 symmetrically placed coupling holes on the common wall of the input resonator and the ring resonator. Through these holes - among others - the modes with the 16 azimuthal indices are excited. The ring resonator is used in the TE<sub>16,0,1</sub> mode and the length of it is chosen so that its resonant frequency equals the midband frequency of the transducer. On the common wall of the ring resonator and the TE<sub>16,2,1</sub> resonator there are 32 symmetrically placed coupling holes.

One or more  $TE_{16,2,1}$  resonators can be applied which are separated by irises.

### The network model

In [3], [4] a network model was elaborated for the modeling of aperture coupled resonator systems. If the symmetric demands are appropriately satisfied then mode purity is valid, the network is separated into independent parts and this makes possible the application of the construction methods well known from the theory of microwave filters.

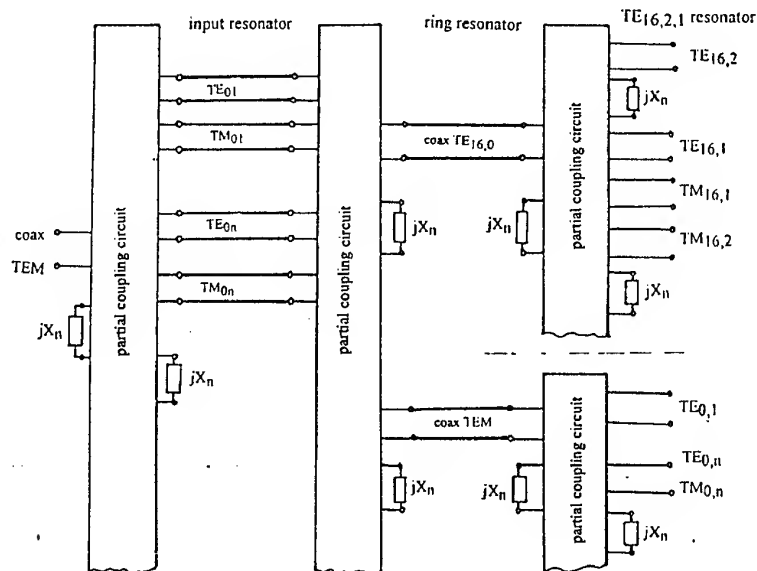


Fig. 2 . The network model

The network model consists of transmission line sections, coupling circuits and lumped reactances. The transmission lines model the propagating waveguide modes, the lumped reactances are the pure imaginary wave impedances of the cut-off modes, the coupling circuits express the mode converting effect of the coupling holes. The first partial coupling circuit transforms the input coaxial or circular waveguide field into the  $TM_{0n}$  field of the input resonator, the second one transforms this circular symmetrical field to the modes of the ring resonator among which the modes with the 16k azimuthal indices are the important for us. If the coupling holes between the ring and  $TE_{16,2,1}$  resonators are perfectly symmetrical then there are no mode conversion between the modes of 16k and other azimuthal index and the last coupling circuit is separated into isolated parts. We choose the length of the ring resonator to be equal to the half wavelength of the  $TE_{16,0}$  mode. This length possibly must strongly differ from the integer multiple of the half wavelength of the unwanted modes. Similarly must be adjusted the lengths of the  $TE_{16,2,1}$  resonators to depress the  $TE_{16,1}$ ,  $TM_{16,1}$  and  $TM_{16,2}$  modes.

### Acknowledgement

This work was supported by the US-Hungarian Joint Fund. We would like to thank Dr. R. Temkin of the MIT Plasma Fusion Center for the helpful discussions.

### References

- [1] Gy. Reter et al., Conference Digest of the 21th Int. Conf. on Infrared and Millimeter Waves, Berlin 1996, AT4.
- [2] F. Volgyi et al., Conference Digest of the 22th Int. Conf. on Infrared and Millimeter Waves, Wintergreen, Virginia 1997, 33.
- [3] Gy. Reiter, Proc. of the URSI Electromagnetic Wave Theory Symposium held in Delft, the Netherlands, 1965, 357.
- [4] Gy. Reiter, Proc. of the URSI Electromagnetic Wave Theory Symposium held in Budapest, 1986, 500.

## A Cherenkov Maser Experiment Using an Electron Beam from a Pseudospark

H. Yin, W. He, G.R.M. Robb, A.D.R. Phelps, A.W. Cross,  
K. Ronald, P. Aitken, B.W.J. McNeil and C.G. Whyte

Department of Physics and Applied Physics  
University of Strathclyde  
Glasgow, G4 0NG, UK

### Abstract

Experimental and computer simulation results are presented of the first free electron maser experiment using a pseudospark (PS) cathode. A pulsed, 75kV, 10A electron beam of normalized brightness  $10^{11} \text{Am}^2 \text{rad}^{-2}$  from a PS device was used to achieve coherent microwave amplification in a 60cm long alumina-lined waveguide using the Cherenkov maser mechanism. A gain of 30dB has been measured from a PS beam noise level of 2.7W at a frequency of 25.5GHz and in the  $\text{TM}_{01}$  radiation mode.

### Introduction

A pseudospark discharge[1] is a low pressure, transient hollow cathode glow gas discharge which occurs in a special geometry and can use several kinds of gases, e.g., argon, nitrogen, and hydrogen. The background gas pressure is such that  $pd$ , the product of the gas pressure  $p$  and the distance  $d$  between the front faces of the cathode and anode, is on the left-hand side of the Paschen curve between the Paschen minimum and vacuum breakdown. The pseudospark discharge offers possibilities for fast, high repetitive rate, high power closing switches[2] and of electron beam production at high current density ( $> 10^4 \text{Acm}^{-2}$ ), high brightness (up to  $10^{12} \text{Am}^2 \text{rad}^{-2}$ ), narrow beam diameter ( $< 4\text{mm}$ ), very low emittance (tens of mm mrad) and variable duration (tens of ns to hundreds of ns)[3]. It is therefore very attractive as an electron beam source for high power sources of microwave radiation, such as free electron lasers (FELs), cyclotron autoresonance masers (CARMs) and Cherenkov

masers. In this paper we present the first free electron maser experiment using the novel PS beam. Simulation and analysis of these results are also presented.

### Experimental setup

A schematic outline of the PS-based Cherenkov maser apparatus is shown in Fig.1. The main components of the experiment are the pseudospark-based electron beam source, the magnetic field for beam transport, the Cherenkov interaction waveguide, electrical/beam diagnostics and the microwave launching/diagnostic system.

A linear electron beam was extracted from the anode of an 8-gap pseudospark discharge chamber. The beam was then transported to the interaction space by a 80cm long 0-0.3T solenoid. The waveguide where the interaction between the electron beam and the waveguide modes takes place is a section of 60cm long cylindrical waveguide, 4.75mm in radius, lined with a 1.75mm thick layer of dielectric (alumina). The microwave radiation was launched into free space by a conical horn antenna. A double screened microwave diagnostics system was situated  $\sim 1\text{m}$  from the antenna. The discharge voltage was measured by an instantaneous capacitive voltage probe. The discharge current was monitored by an in-line current shunt. Two Rogowski coils were inserted into the system to measure the beam current entering and exiting the Cherenkov interaction region. A field-free collimator of cylindrical shape was used immediately after the anode to measure the beam brightness.

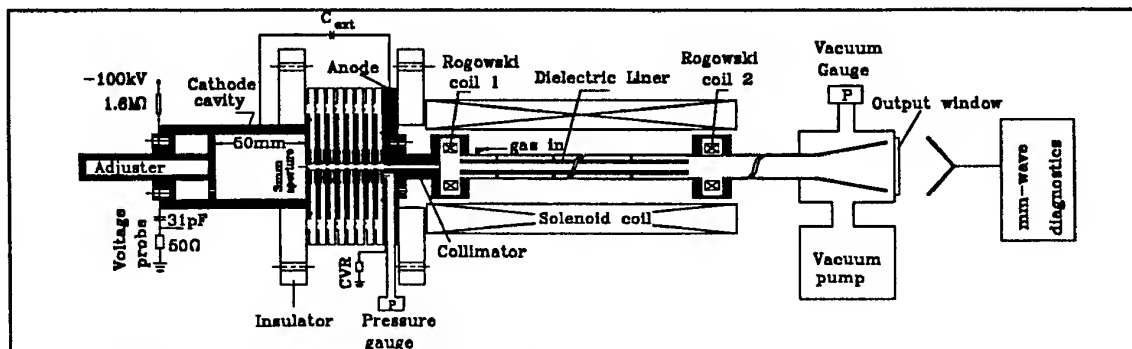


Fig. 1 A schematic outline of the PS-based Cherenkov maser experiments

The presence of the dielectric in the interaction cavity slows down the electromagnetic wave phase velocity. This allows a resonant interaction to occur between a TM or HE waveguide mode and the electron beam. Coherence of the radiation generated arises due to bunching of the electrons in the beam into phase with the electromagnetic wave. The bunching of the electrons in a Cherenkov maser is axially distributed because of the axial electric field of the electromagnetic wave mode.

### Microwave diagnostic results

Microwave pulse duration and temporal profile from the PS-based Cherenkov maser were obtained from a crystal detector signal observed on an oscilloscope, time-correlated with the electron-beam current and voltage profiles. It was observed that removal of the dielectric liner resulted in the loss of the microwave amplification and the amplitude of the amplified microwave pulse was independent of the guide magnetic field over the range 0.13 to 0.26 T.

The microwave spectrum with and without Cherenkov amplification at an applied discharge voltage of  $\sim 80$  kV were analyzed using a series of in-waveguide cut-off filters. The results showed that the signal without the amplification, ie PS beam noise, had a wide frequency distribution but was below W-band (62.5 GHz) frequency. The microwave output of the maser had roughly two frequency components: one was between 25.5-28.6 GHz corresponding to the high voltage beam during the hollow cathode phase, another between 28.6-41.8 GHz corresponding to the lower voltage beam from the conductive phase.

To verify the operation mode of the maser, the far-field output radiation pattern from the conical horn antenna of aperture diameter 60 mm was measured. The output microwave pattern associated with the azimuthal E-field component was measured to be independent of the presence of the dielectric and close to zero and hence confirmed the operation of a TM mode. The measured pattern associated with the radial E-field component was in good agreement with the results from bench experiments in which a 27 GHz microwave signal was launched in a  $TM_{01}$  mode using the same launching horn.

The absolute power of the microwave output from the Cherenkov maser was calculated to be  $2.0 \pm 0.2$  kW (without considering any losses within the detecting system) by integrating the measured normalized mode pattern and multiplying with the measured maximum power density. After similar treatment the microwave signal without maser amplification was found to be 2.7 W in the frequency range 25.5-28.6 GHz. This corresponded a gain of  $29 \pm 3$  dB.

### Modelling results

A 3-D numerical simulation code was developed to complement the experimental investigations of the Cherenkov maser. The code integrates the Lorentz equations of motion for the electrons self-consistently with Maxwell's wave equation for a  $TM_{0n}$  waveguide mode in the steady-state limit. It includes the effect of resonant space-charge forces and electron energy spread. Figure 2 shows a graph of predicted output power from the Cherenkov maser as a function of interaction length for a beam voltage  $V=75$  kV and a beam current  $I=10$  A. Only  $TM_{01}$  and  $TM_{02}$  modes lie within the frequency range of the noise from the PS discharge. The microwave power at  $z=0$  was assumed to be 3 W for both modes. The beam was assumed to have an axial velocity spread of 3% and a radius of 1.5 mm. The predicted power at  $z=60$  cm is  $\sim 3$  kW for the  $TM_{01}$  mode and 3 W for the  $TM_{02}$  mode.

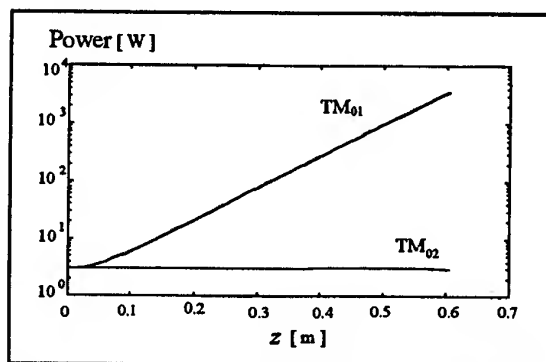


Fig. 2 Predicted output power of the  $TM_{01}$  and  $TM_{02}$  modes as a function of  $z$

### Conclusion

In this first PS-based free electron maser experiment, a Cherenkov maser amplifier was operated. The microwave radiation was allowed to build up from the PS beam noise. The frequency of the microwaves produced by the Cherenkov system was measured to be mainly 25.5-28.6 GHz and the dominating mode was identified as being  $TM_{01}$ . A peak power of  $\sim 2$  kW and a gain of  $\sim 30$  dB were achieved.

### Acknowledgements

H. Yin would like to thank the Committee of Vice-Chancellors and Principals of the Universities of the United Kingdom and the University of Strathclyde for financial support

### References

1. K. Frank and J. Christiansen, IEEE Trans. Plasma Sci., 17, 748, (1989)
2. H. Riege and E. Boggasch, IEEE Trans. Plasma Sci., 17, 775, (1989)
3. T. Y. Hsu and M. A. Gunderson, Appl. Phys. Lett., 61, 2515, (1992)



## Recent Developments on Schottky Diodes for THz Applications

A. Simon, C. I. Lin, M. Rodriguez-Gironés, H. L. Hartnagel

Institut für Hochfrequenztechnik, Merckstr. 25, 64283 Darmstadt

Fax: + 6151/164367, e-mail: hfmwe015@hrzpub.th-darmstadt.de

### Abstract

Advances in Schottky diode design and technology are reported that lead to significant performance improvements at THz frequencies. Whisker contacted substrateless varactors provide doubler efficiencies of 40% at 150 GHz and tripler efficiencies of 16% at 300 GHz, 8% at 480 GHz and 7% at 630 GHz. European activities on planar Schottky devices and integrated receiver structures are presented.

### Introduction

GaAs Schottky barrier diodes are a key element as frequency multiplier in an all-solid-state local oscillator and as mixer element in heterodyne receivers. Especially whisker-contacted Schottky diodes have been the preferred nonlinear element at frequencies above 300 GHz. The main limitation of whiskered diodes is that no integration is possible. Therefore, competitive planar Schottky barrier diodes technologies have been developed in the last decade [1,2].

In the submillimeter-wavelength range there is a need for compact and reliable sources of local oscillator power. All-solid-state sources that use GaAs Schottky varactors to multiply the output of Gunn or Impatt devices are reliable, compact and are relatively inexpensive. Recently, fundamental sources can provide sufficient input power to frequencies up to approximately 150 GHz. Therefore, a chain of frequency doublers or triplers is required to cover the frequency range up to 1000 GHz.

GaAs Schottky diodes have been used as the nonlinear element in the mixer of heterodyne receivers due to the high cut off frequency and low parasitics. Improvements of other mixer technologies (i. e. SIS) have reduced the Schottky mixer activities in the past years and the applications have mainly focused on 2.5 THz mixers where Schottky diodes remain the devices of choice. Recently new activities consider fully integrated planar Schottky diodes to provide reliable integrated front ends. The most attractive benefit of Schottky diodes for this revitalization is that they require no cooling. Especially for space applications this is a demanding issue.

### Varactor Optimisation

For multiplier applications in the submillimeterwave regime several phenomena limit the performance. Very high current densities and a low heat conductivity of GaAs limit the power handling capabilities. An increased series resistance at high frequencies (skin effect) and velocity saturation effects lead to a decrease of the efficiency.

The improvement potential of a standard honeycomb style whisker-contacted diode were based on new strategies reducing velocity saturation effects and improvements of the fabrication process. Substrateless Schottky diodes, proposed in 1995 [3], offer the prospect to increase the power handling capabilities and to receive a minimum series resistance. Important characteristics of a varactor diode are the capacitance modulation ratio  $C_{jo} / C_{min}$ , the breakdown voltage  $U_b$ , and the series resistance  $R_s$ . Recently new passivation techniques are in use to increase the breakdown voltage and the capacitance modulation ratio for a specific doping level.

For the passivation and definition of the anodes,  $SiO_2$  has been used almost exclusively in the past. It is a reliable process and the definition of the anodes can be done very accurately. We investigated several alternative passivation techniques to improve the varactor performance. We have established a new polyimide passivation technique that lead to an improvement in the breakdown voltage and the capacitance modulation ratio. Fig. 1 gives a comparison of the breakdown voltage of  $SiO_2$  layers and of the polyimide passivation as a function of the GaAs-doping concentration. At the same doping concentration the polyimide passivation offers a 30-50% higher breakdown voltage compared with the best reported values of CVD- $SiO_2$ . This behavior gives a new flexibility to the design of varactor diodes. For the same amount of input power higher doping levels are possible. This leads to a smaller series resistance and a reduction of the velocity saturation effect.

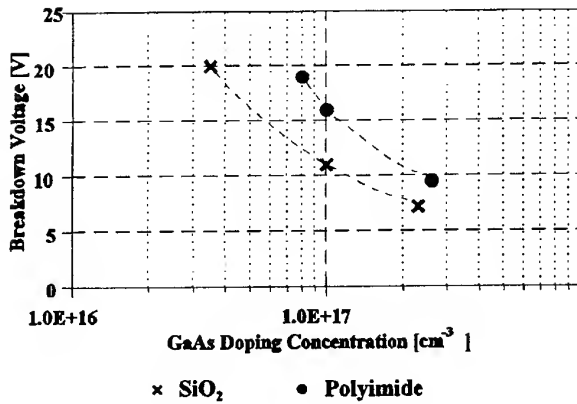


Fig. 1: Breakdown voltage as a function of the GaAs doping concentration

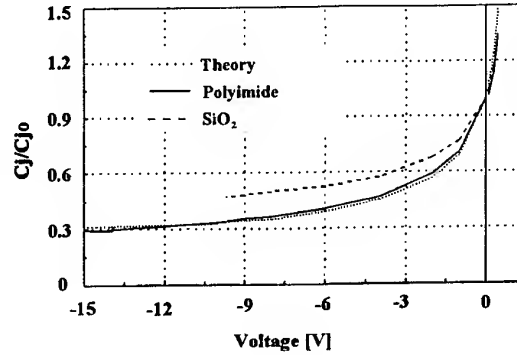


Fig. 2: Capacitance modulation ratios depending on the passivation

Additionally to the improvement of the breakdown voltage the polyimide passivation offers a C-V characteristic close to the theoretical limit. Fig. 2 shows the C-V characteristics of two substrateless diodes with identical diode parameters and SiO<sub>2</sub> and polyimide passivation. The capacitance modulation ratio of the SiO<sub>2</sub> passivation is smaller in the same voltage range (0 - 10.5 V). The capacitance modulation of the polyimide passivation shows almost the same characteristic as the calculated value.

Table 1 shows the output power and efficiency achieved with different diodes. Some of these multipliers yielded record output power and efficiency. At around 500 GHz the best achieved output powers have been around 1 to 1.2 mW. Therefore, the result at 480 GHz (2 mW) is outstanding recently. It is important that the efficiency does not degrade between 300 and 640 GHz. With optimised complex doping structures we can further increase the capacitance modulation ratio (SLHA5010, hyper-abrupt doping profile).

Table 1 : Multiplier performances

$\nu_{in}$ [GHz]	$\nu_{out}$ [GHz]	Diode	$P_{in}$ [mW]	$P_{out}$ [mW]	Efficiency [%]
75	150	SLHA5010	25	10	40
89	267	SLV2818	30	5.6	18.7
93	279	SLV2018	50	6	12
101	202	DAPV3016	40	5	12.5
100	300	SLV2818	35	5.5	15.7
126	378	SLV2818	84	4.1	4.9
160	480	SLV0910	25	2	8
210	630	SLV0510	10	0.7	7
266	800	SLV0510	6	0.2	3.3
375	1125	SLV0310	4.1	0.02	0.5

### Integrated Mixer

Whiskered mixer diode technology has been in use mainly for 2.5 THz mixers where no competitive device concept is available recently. The main shortcoming of the whiskered device technology is that any integration of other mixer components or several diodes in a mixer is not possible. An important advantage that remained for Schottky mixers is that no cooling is necessary for a proper operation. Therefore, due to a mature planar Schottky diode technology that is now available many activities in Europe and the United States are now based on integrated structures. The possibility to fabricate subharmonically pumped mixers or fully integrated front-ends that provide reproducibility, reliability and low costs mainly motivate these activities. In Europe the activities focus on integrated front-ends for operation at 650 GHz with integrated diode, RF- and IF filter, transmission lines and planar antenna [4]. In addition subharmonically pumped mixers with an anti-parallel diode pair at 220 GHz and 650 GHz are in progress [5]. In the United States the activities concentrate on integrated filter-diode structures for waveguide mixers at 640 GHz and 2.5 THz[6].

### Conclusion

New technologies have improved the performance of Schottky barrier varactor diodes significantly in the last two years. All-solid-state local oscillators with sufficient output power are now available up to 800 GHz. Further improvements are necessary and possible to cover the frequency range up to 1.5 THz. Planar diode technology is starting to become an attractive technology for oscillators up to 400 GHz.

Planar mixer diode technology has become a mature technology and many activities are now based on integrated structures to overcome serious shortcomings of the whiskered diode technology. The possibility to fabricate subharmonically pumped mixers or fully integrated front-ends that provide reproducibility, reliability and low costs mainly motivate these activities.

### Acknowledgment

The authors would like to express their acknowledgment to Dr. H. Grothe and Dr. J. Freyer, both from the Technical University of Munich, Germany, for supplying high-quality epitaxial materials.

### References

1. W. L. Bishop, K. McKinney, R. L. Mattauch, T. W. Crowe und G. Green, "A novel whiskerless Schottky diode for millimeter and submillimeter wave applications," *IEEE MTT-S Int. Microwave Symp. Dig.*, June 1987, pp 607-610
2. A. Simon, A. Grüb, V. Krozer, K. Beilenhoff and H.L. Hartnagel, "Planar THz Schottky Diode Based on a Quasi-Vertical Diode Structure", *4th Int. Symp. on Space Terahertz Technology*, pp 392-403, 1993
3. A. Simon, A. Grüb, M. Rodriguez-Gironés and H. L. Hartnagel, "A Novel Micron-Thick Whisker Contacted Schottky Diode Chip", *Sixth Int. Symp. on Space Terahertz Technology*, pp 5-12, 1995
4. J. Mees, H. Ekstrom, E. Kollberg, G.V. Eleftheriades, J.R. Mosig, A. Räisänen, P. Piironen, H. L. Hartnagel, A. Simon, T. Vaupel, V. Hansen, "Open Structure Integrated Schottky Receiver for Space Applications", *Proc. 20th ESTEC Antenna Workshop on Millimeter Wave Antenna Technology and Antenna Measurements*, 18.-20. Juni 1997, ESTEC, Noordwijk
5. C. I. Lin, A. Simon, J. Zhang, P. V. Piironen, V. S. Möttönen, H. L. Hartnagel, A. V. Räisänen, "Anti-Parallel Planar Schottky Diodes for Subharmonically Pumped Mixer", *ibidem*
6. P. H. Siegel, R. P. Smith, M. Gaidis, S. Martin, J. Podosek, U. Zimmermann, "2.5 THz GaAs Monolithic Membrane-Diode Mixer a New Planar Circuit Realization for High Frequency Semiconductor Components", *Ninth Int. Symp. on Space Terahertz Technology*, March 17-19<sup>th</sup>, 1998, Pasadena

## A 490 GHz Single-Planar-Diode Subharmonic Mixer

Jeffrey L. Hesler, Neal R. Erickson<sup>†</sup>, and Thomas W. Crowe

Department of Electrical Engineering  
University of Virginia  
Charlottesville, VA 22901

<sup>†</sup>Five College Radio Astronomy Observatory  
Department of Physics and Astronomy  
University of Massachusetts  
Amherst, MA 01003

### Abstract

The modeling and design of a 490 GHz single-planar-diode subharmonic mixer is presented. The mixer was designed using HP's High Frequency Structure Simulator to determine the effect of the planar diode on the mixer impedances. The fixed-tuned RF bandwidth of the mixer is predicted to be greater than 40 GHz. Mixer results will be presented at the conference.

### Introduction

This paper will describe the design and testing of a 490 GHz single-planar-diode subharmonic mixer. There are two main goals for this research: first to produce a set of spares for the existing SWAS [1] mixers, and second to develop a prototype for new broadband, rugged, low-power submillimeter wave mixers. The existing SWAS mixers use whisker-contacted diodes, and while possessing the required sensitivity, present potential problems with reliability. For this reason it is desirable to have equally sensitive spares that are more rugged; a requirement which can be satisfied using planar Schottky diodes [2]. The second goal of this research is to develop a sensitive fixed-tuned room-temperature mixer with broad RF and IF bandwidths that is rugged and uses a relatively simple block geometry, in particular one that is compatible with molding and micromachining block fabrication techniques [3]. The use of an E-plane split block design, with the RF and LO guides machined in the same plane of the block makes this design amenable to these inexpensive block fabrication techniques. The single-diode subharmonic mixer is a particularly interesting candidate for use at submillimeter wavelengths, not only because of the reduced LO frequency, but also because of its ability to operate with very little LO power. In addition, with proper design the single-diode subharmonic mixer can show sensitivity comparable to other mixer configurations [4].

### Mixer Block Configuration

The mixer geometry, shown in Fig. 1, is similar to that of the whisker-contacted Schottky diode mixer described in [4]. The mixer block, machined at Millitech Corp. [5], is split in two parts in the E-plane of the RF and LO waveguides, which simplifies mixer assembly and reduces the losses in the waveguides. The planar diode is mounted on a 25  $\mu\text{m}$  thick fused quartz substrate and then placed in a channel which runs perpendicular to the RF and LO waveguides. The planar diode is positioned across the RF waveguide, and is grounded at the bottom of the waveguide. A three-section low-pass filter prevents the RF signal from traveling up the microstrip channel. The LO signal is coupled from a waveguide into the microstrip channel, and a low-pass filter above the LO waveguide couples the IF and DC signals to the diode.

### Mixer Block Design

The mixer was designed using Hewlett Packard's High Frequency Structure Simulator to model the waveguides, planar diode chip, and quartz circuit. A coaxial probe was artificially introduced at the junction during the finite element modeling to allow the direct prediction of the diode embedding impedance. The circuit was designed to present an LO embedding impedance of  $40 + j160\Omega$ , and an RF impedance of  $55 + j95\Omega$ . Harmonic balance simulations were performed for the University of Virginia SC1T5 planar diode ( $\eta=1.17$ ,  $I_{\text{sat}}=3 \cdot 10^{-17}$  A,  $R_s=14\Omega$ , and  $C_{j0}=2$  fF), and for the above embedding impedances the simulation predicted a mixer

conversion loss of 8.5 dB (DSB) and noise temperature of 1000 K (DSB) with 1 mW of LO power. Assuming conductor and dielectric losses in the horn, waveguide, microstrip, and diode of 2 dB total, and an IF noise temperature of 60 K, the system noise temperature is then predicted to be 2500 K (DSB). The fixed-tuned RF bandwidth of the mixer is predicted to be greater than 40 GHz.

#### Preliminary Testing

The noise temperature of the mixer was measured at room temperature, yielding an overall system noise temperature of 14,000 K (DSB) using 1.2 mW of LO power. A variable attenuator was used to vary the IF noise temperature from 80 K to 370 K, thus allowing the measurement of  $T_{\text{mix}}=10300$  K (DSB) and  $L_{\text{mix}}=16.8$  dB (DSB). Correction of the IF standing-wave-ratio of 3 is predicted to improve the performance to  $T_{\text{mix,c}}=6700$  K (DSB) and  $L_{\text{mix,c}}=15.5$  dB (DSB). Additional test results will be presented at the conference.

#### Conclusions

Using this design we expect to achieve performance comparable with the SWAS mixer, but with larger fixed-tuned bandwidth and greater ruggedness. These properties, combined with the low LO power requirement, make this mixer a promising candidate for use at submillimeter wavelengths.

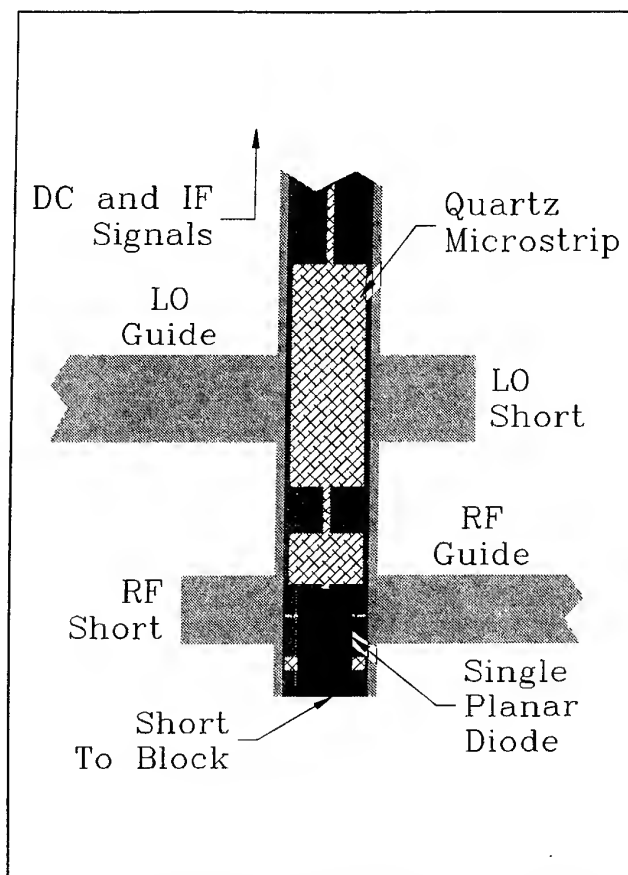


Fig. 1. Schematic of single-diode subharmonic mixer.

#### References

1. P.F. Goldsmith, et al., "The Submillimeter Wave Astronomy Satellite," IEEE MTT-S Digest, pp.395-398,1991.
2. W.L. Bishop, E. Meiburg, R.J. Mattauch, T.W. Crowe and L. Poli, "A  $\mu\text{m}$ -thickness, planar Schottky diode chip for terahertz applications with theoretical minimum parasitic capacitance," *IEEE-MTT-S Int. Microwave Symp. Dig.*, 1990, pp. 1305-1308.
3. T.W. Crowe, P.J. Koh, W.L. Bishop, C.M. Mann, J.L. Hesler, R.M. Weikle II, P.A.D. Wood, D. Matheson, "Inexpensive Receiver Components for Millimeter and Submillimeter Wavelengths," *Proc. of Eighth Int. Symp. on Space THz Tech.*, Cambridge, MA, March 25-27 1997.
4. N.R. Erickson, "Low-Noise Submillimeter Receivers Using Single-Diode Harmonic Mixers," *Proc. of the IEEE*, Vol. 80, pp. 1721-1728, Nov 1992.
5. Millitech Corp., South Deerfield Research Park, P.O. Box 109, South Deerfield, MA 01373, U.S.A.

# Fabrication of Quasi-Integrated Planar Schottky Barrier Diodes for THz Applications

T. Yasui<sup>1</sup>, C. M. Mann<sup>3</sup>, T. Suzuki<sup>5</sup>, H. Fujishima<sup>1</sup>, S. Tsunekawa<sup>4</sup>, and K. Mizuno<sup>1,2</sup>

<sup>1</sup> Photodynamics Research Center, RIKEN, Sendai 980, Japan

<sup>2</sup> Research Institute of Electrical Communication, Tohoku University, Sendai 980, Japan

<sup>3</sup> Rutherford Appleton Laboratory, Chilton, Didcot, United Kingdom

<sup>4</sup> Institute for Materials Research, Tohoku University

<sup>5</sup> Sendai National College of Technology, Sendai 989-3124, Japan

**INTRODUCTION:** Schottky barrier diodes (SBDs) still remain the most important semiconductor device used for direct detection and heterodyne mixing of terahertz frequency signals. This is particularly true for space applications and plasma diagnostics where the Schottky diodes ability to operate at ambient temperatures greatly reduces radiometer complexity and cost. This paper describes the fabrication of a new quasi-integrated planar (QUIP) SBD chip [1] that has been used in a 2.5 THz waveguide mixer. For a more detailed description of the mixer design see ref. [2]. Use is made of the same circuit architecture. A schematic diagram showing the basic concept of the QUIP SBD chip is shown in figure 1.

QUIP SBD chip has Schottky diode anodes and the ohmic contact on the front face of the chip which has dimensions of 395 x 400  $\mu\text{m}$ . This front side ohmic forms the top face of the waveguide which in turn feeds a corrugated conical feedhorn antenna. A planar whisker with an integrated IF filter was used to contact one of the 0.25-0.3  $\mu\text{m}$  diameter anodes. The QUIP SBD chip realizes easier handling, simplifies mixer block fabrication, and also minimizes losses between the antenna and the diode by allowing the SBD contact to be placed virtually at the feed of the antenna.

**PROCESS OPTIMIZATION:** The QUIP SBD fabrication procedure is very similar to that used for the fabrication of the conventional back contacted Schottky diode chips used in corner cube mixers [3, 4]. This new design of chip combined with an optimized fabrication process has been successfully fabricated and its use resulting in reduced receiver noise. A fabrication process has been developed, which minimizes intrinsic diode noise. This process has to be performed carefully particularly when active GaAs surface is directly exposed to radical and/or ions, as is the case in the use of atmospheric CVD, ECR plasma etching, wet etching and electroplating. It was found that the ECR plasma etching reduces defects at the surface than the RIE does, and thus significantly lowers the 1/f noise from the diodes. The noise spectrum for various etching techniques have been compared in figure 2. To realize atomic scale perfection of the GaAs surface, we combined the ECR plasma etching with wet etching and surface passivation by  $(\text{NH}_4)_2\text{S}_x$ , resulting in the diode noise closing to the thermal and the shot noise limit as shown in figure 3

**MIXER PERFORMANCE:** The preliminary RF experimental results at 2.5 THz are very encouraging and are displayed in figure 4. A double sideband receiver noise temperature of 24,000 K was obtained

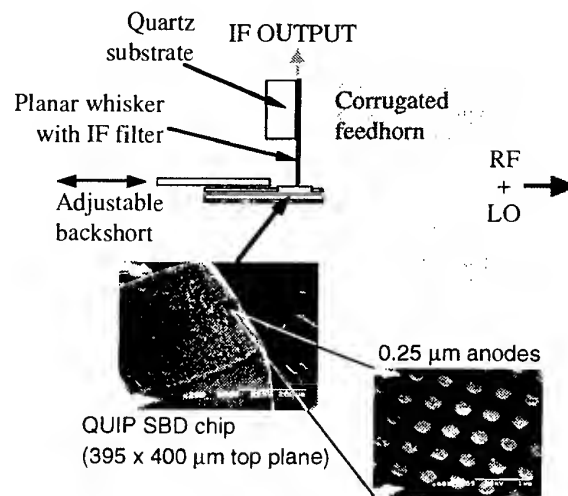


Figure 1: The basic quasi-integrated planar diode concept and QUIP SBD chip

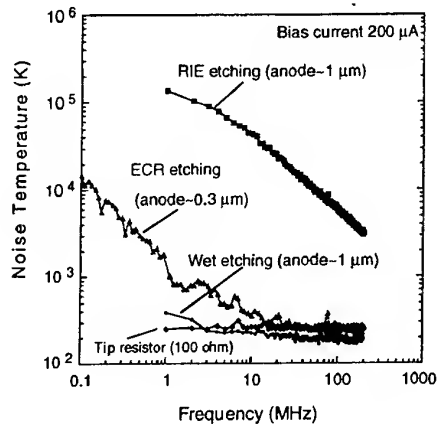


Figure 2 : Diode noise temperature for various etching procedures

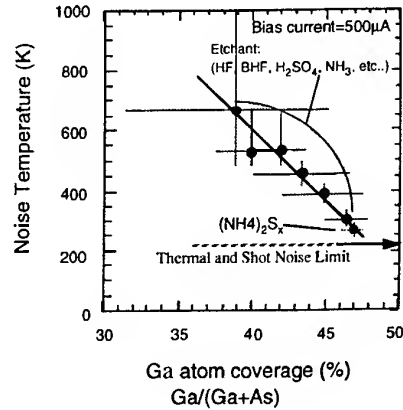


Figure 3 : Diode noise temperature at 200 MHz for various passivation procedures

at the first iteration. Importantly the LO requirement has been reduced to levels comparable to that required by a corner reflector mixer, showing that the loss associated with the waveguide mount is reasonable. These mixer performances at 2.5 THz show the usefulness of our diode fabrication processes.

**CONCLUSIONS:** We have refined THz Schottky diode fabrication processes using in-situ diode noise measurement. The new quasi integrated planar diode chip was successfully fabricated. Good mixer performance at 2.5 THz has been obtained using this new chip.

**ACKNOWLEDGEMENTS:** Thanks are given to Dr. J.

J. Chang for his discussions about the QUIP chip diode concept. Part of this work was carried out at the Laboratory for Electronic Intelligent Systems, Research Institute of Electrical Communications, Tohoku University, supported by the Heiwa Nakajima foundation and a Grant-in-Aid of Scientific Research from the Ministry of Education, Science, Sports and Culture of Japan.

## REFERENCES

- [1] C. M. Mann, T. Yasui, T. Suzuki, H. Fujishima, and K. Mizuno, Quasi-Integrated Planar Schottky Barrier Diodes for 2.5 THz Receivers, The 9th International Symposium on Space THz Technology, Pasadena, CA., USA, March 1998.
- [2] C. M. Mann, D. N. Matheson, B. N. Ellison, M. L. Oldfield, B. P. Moyna, J. J. Spencer, D. S. Wilsher, and B. J. Maddison, On The Design And Measurement Of A 2.5 THz Waveguide Mixer, The 8th International Symposium on Space Terahertz Technology, JPL, Pasadena, March 1998
- [3] T. Suzuki, H. Shinohara, T. Nozokido, Y. Kudo, H. Warashira, and K. Mizuno, Noise Dependence of Submillimeter Wave Pt/GaAs Schottky Diodes on Interface Defects and Temperature, Proc. of the 16th International Conf. on IR & MMW, pp. 472-473, Lausanne, Switzerland, August 1991.
- [4] T. Yasui, T. Suzuki, H. Fujishima, M. Arasawa, T. Nozokido, T. Yamada, S. Tsunekawa, and K. Mizuno, Development of Low Noise Schottky Barrier Diode for the THz Region and Semiconductor Surface Analyses, Technical Report of IEICE, ED96-180, MW96-143, ICD96-168 (1997-01), pp. 1-8 (in Japanese).

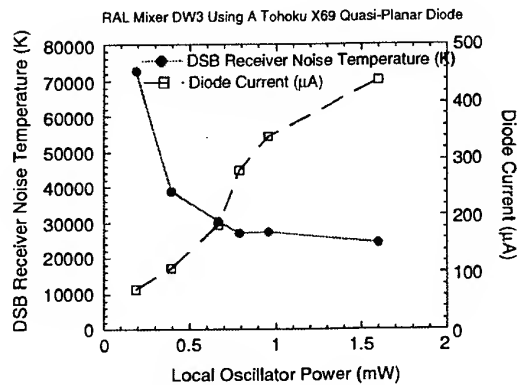


Figure4 : 2.5THz mixer RF performance for Tohoku diode X69 in RAL mixer DW3

## Anti-Parallel Planar Schottky Diodes for Subharmonically Pumped Mixer

C. I. Lin<sup>1</sup>, A. Simon<sup>1</sup>, J. Zhang<sup>2</sup>, P. V. Piironen<sup>2</sup>, V. S. Möttönen<sup>2</sup>, H. L. Hartnagel<sup>1</sup>, A. V. Räisänen<sup>2</sup>

<sup>1</sup>Institut für Hochfrequenztechnik, TU Darmstadt, Merckstrasse 25, D-64283 Darmstadt

Fax: +49-6151-164894, e-mail: hfmwe013@hrz2.hrztu-darmstadt.de

<sup>2</sup>Helsinki University of Technology, FIN-02150 Espoo, Finland

### Abstract

Anti-parallel planar Schottky diodes using the Quasi-Vertical Schottky Diode (QVD) geometry, developed by TU Darmstadt, are realized and applied to a subharmonically pumped waveguide mixer at 220 GHz, realized by Helsinki University of Technology. Because of the geometry, the diode has low parasitics, vertical current flow and improved heat sink capability, and is less affected by the skin effect. The technology and the electrical characteristics of the Anti-Parallel Quasi-Vertical Schottky Diode (APQVD) are presented.

### Introduction

GaAs-Schottky diodes are used as the nonlinear element (varistor) in the mixer of heterodyne receivers for THz applications because of its high cutoff frequency and low parasitics as compared with other semiconductor devices. Planar Schottky diodes offer possibilities to integrate more than one diode and other system components such as filters and antennas by using coplanar waveguide (CPW) or microstrip designs.

The Quasi-Vertical planar Schottky Diode (QVD), developed by TU Darmstadt [1], is based on the substrateless whisker contacted Schottky diode concept [2], which is geometrically the same as the conventional whisker contacted Schottky diodes, but with extremely reduced size of the diode chip. Therefore, like the whisker contacted Schottky diodes, QVD has vertical current flow and offers low parasitics. The modeling of the whisker contacted Schottky diodes can also be applied to QVD without any modification. In addition, because of the reduced distance from the diode to the ohmic contact metal, it has better heat sink capabilities and is less affected by skin effect in comparison to conventional whisker contacted Schottky diodes or other planar concepts [3]. Based on the concept of QVD, the Anti-Parallel Quasi-Vertical Schottky Diode (APQVD) has been developed and fabricated.

### Diode Design

Both diodes of APQVD have the same structure as a single QVD. Fig. 1 shows a side view of the mesa region of the single QVD. According to the experiences [1, 4], a doping level of  $3 \times 10^{17} \text{ cm}^{-3}$  and a thickness of 100 nm is chosen for the active n-layer, while the anode diameter is set to be 0.8  $\mu\text{m}$ . The thickness of the  $n^+$ -layer of 2  $\mu\text{m}$ , which is chosen to be as thick as the skin depth of the  $n^+$ -layer at an RF signal frequency of 220 GHz, eliminates the influence of the skin effect. While the conventional whisker contacted Schottky diodes use the whisker as the main heat sink due to the low thermal conductivity of the 100  $\mu\text{m}$  thick GaAs substrate, the QVDs use not only the air-bridge, but also the backside ohmic contact metal as heat sink because of the dramatically reduced thickness

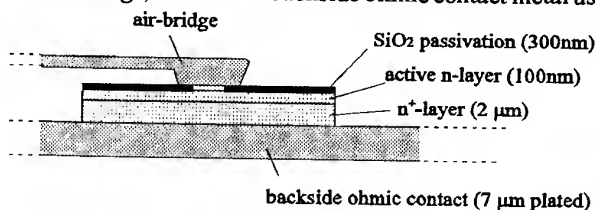


Fig. 1: Sketch of the mesa region of a QVD chip

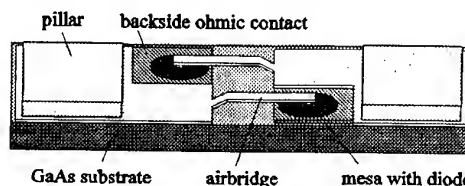


Fig. 2: Geometrical structure of an APQVD chip

of the  $n^+$ -layer. The vertical current flow in the QVD enables the direct implantation of the model of whisker contacted Schottky diodes to the QVD model [4, 5, 6]. Only by adding the parasitic lump elements, which stem from the air-bridges and the contact pads [7], the QVD model complete.

Several specifics of the APQVD structure can be pointed out here:

- Reduced chip thickness of 10  $\mu\text{m}$ : Compared with whisker contacted devices a general problem of planar devices is the stray capacitance introduced by the contact pads. But the need of short air-bridges to reduce the air-bridge inductance decreases the distance of the pads and increases therefore the stray capacitance between the pads. In order to reduce the stray capacitance of the pads, a reduced substrate thickness of 10  $\mu\text{m}$  is achieved by using the etch-separation technique from the front side of the sample.



- High air-bridges: By using high air-bridges of 2  $\mu\text{m}$  over the mesa and 4  $\mu\text{m}$  over the backside ohmic contact metal the stray capacitance of the air-bridges is reduced to a negligible value.
- Pillars for flip-chip technique: APQVDs are soldered onto the microstrip RF filter by using the flip-chip technique. To prevent any possible damage of the air-bridges while handling such a thin device, two pillars of about 6  $\mu\text{m}$  are fabricated onto the contact pads.

Accurate modeling of the APQVD employed in the mixer is fundamental to design the circuitry in the mixer. The modeling is divided into two parts: modeling of the diode and of the parasitic part around the diode. With the experiences in conventional and substrateless whisker contacted diodes there was no difficulty to get a proper model of the diode [4, 5, 6]. For the study of the parasitic lump elements of the APQVD, Helsinki University of Technology has used the electromagnetic structure simulator HFSS, whose S-parameter results are fitted with the equivalent circuit and therefore the values of parasitic elements can be evaluated [7]. Simulated values of the model of an APQVD, which are used in the equivalent circuit and embedded into the microwave circuit simulator MDS for simulation of the mixer performance are: Air-bridge inductance = 8.7 pH, Air-bridge to cathode capacitance = 1.1 fF, Pad-to-pad capacitance = 11.4 fF, Pad to microstrip-ground capacitance = 0.69 fF, Series inductance = 0.8 pH, zero bias junction capacitance = 1.2 fF and Reverse saturation current =  $2.55 \cdot 10^{-17} \text{ A}$ .

### APQVD Fabrication and Characterisation

The fabrication process is based on the technologies of single QVD which we have developed in the last years [8]. Fig.3 shows a SEM picture of an APQVD that shows that the air-bridge is several microns over the mesa. The pillars are even higher than the air-bridges for the handling during the flip-chip soldering.

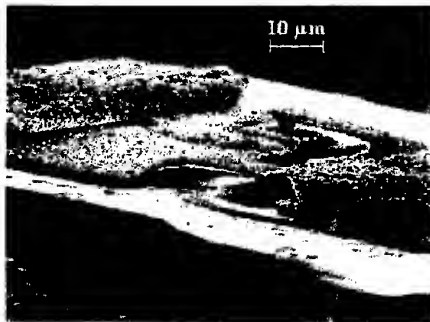


Fig. 3: Side view of an APQVD

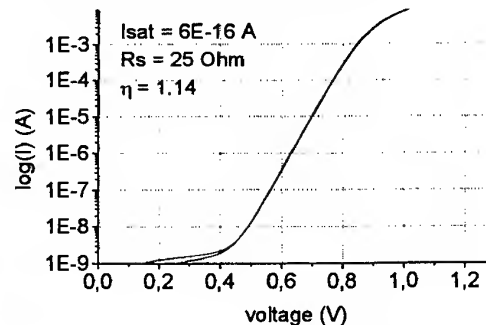


Fig. 4: I/V-characteristics of two diodes of an APQVD

Fig. 4 shows measured I/V curves of a APQVD. The noise temperature measurement at 1.4 GHz is performed on each diode of the mounted APQVD at different bias currents. At a typical bias current of 500  $\mu\text{A}$  for a single mixer diodes, a noise temperature of 350 K is achieved which is comparable to whisker contacted ones.

### Conclusion

Anti-parallel planar Schottky diodes using quasi-vertical structure are developed. To reduce to parasitic capacitance of the contact pads, reduced chip thickness of 10 microns and high air-bridges are realized. For a reliable handling of this thin device two flip-chip pillars are introduced in the fabrication. The DC measurements show that the characteristics are comparable to whisker contacted ones and the variation of the anode diameters is little. Several batches of diodes were already finished and delivered for RF measurements. The first successful flip-chip mounted APQVD has shown a at 1.4 GHz measured diode noise temperature of 350 K at a bias current of 500  $\mu\text{A}$ . Further measurements on mixer performance is being in progress.

### References

1. A. Simon *et al.*, Proc. 4<sup>th</sup> Int. Symp. on Space Terahertz Technology, 392 (1993)
2. C. I. Lin *et al.*, Proc. 8<sup>th</sup> Int. Symp. on Space Terahertz Technology, 224 (1997)
3. U. V. Bhapkar *et al.*, MTT, 40, 886 (1992)
4. K. Huber *et al.*, Proc. 5<sup>th</sup> Int. Workshop on Terahertz Electronics (1997)
5. T. Crowe, Int. J. Infrared Millimeter Waves, 10, 765 (1989)
6. H. Hjelmgren *et al.*, Solid-State Electronics, 34, 587 (1991)
7. B. K. Kormanyos *et al.*, MTT, 41, 1730 (1993)
8. A. Simon *et al.*, Proc. 8<sup>th</sup> Int. Symp. on Space Terahertz Technology, 179 (1997)

## Microstructural Properties of THz Schottky Mixer Diodes

H.-W. Hübers, H. P. Röser

German Aerospace Center (DLR)  
Institute of Space Sensor Technology  
Rudower Chaussee 5, 12489 Berlin, Germany  
heinz-wilhelm.huebers@dlr.de

### Introduction

Schottky diodes are widely used as mixers in low noise mm and submm wave THz heterodyne receivers. In order to optimize their performance a detailed understanding of the underlying physical mechanisms is necessary. We have investigated the microstructural properties of the potential barrier of Pt/n-GaAs diodes such as defects at the metal-semiconductor interface and spatial inhomogeneities.

### Experimental Setup and Analysis

Current voltage (I-V) characteristics of different Schottky diodes were measured in the temperature range from 80 K to 300 K by the use of a closed cycle He refrigerator. The temperature was measured with a Si temperature sensor diode mounted closely to the Schottky diode. To allow for thermal equilibrium a delay of about 15 minutes between two measurements was held. The stability of the temperature was better than  $\pm 0.1$  K. The diodes which we have investigated are listed in table 1. It is worth noting that all diodes were used as mixers in THz heterodyne receivers.

Diode	Manufacturer	$n_D [10^{17} \text{ cm}^{-3}]$
SDO 20	Farran Tech.	0.5
DA499	TU Darmstadt	1.0
HSD3S	Tohoku U	1.0
1T6	U Virginia	1.0
1I7a	U Virginia	3.0
1I7b	U Virginia	3.0
1I7c	U Virginia	3.0
1T12	U Virginia	3.0
1I12	U Virginia	4.5
1T14	U Virginia	10.0
1T15	U Virginia	10.0

Table 1: Manufacturers and doping densities  $n_D$  of the investigated diodes.

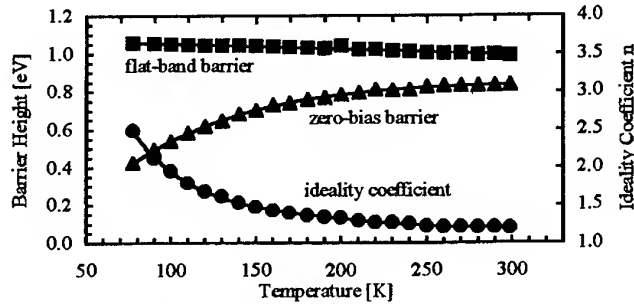


Fig. 1: Barrier heights and ideality coefficient of the diode 1I7c.

The I-V curves of the diodes shift with decreasing temperature towards higher voltages and become steeper. From a least squares fit of the standard expression for the I-V curve of a Schottky diode [1, p. 99] one can determine the ideality coefficient  $n$  and the zero bias barrier height  $\Phi_{b0}$ . Fig. 1 shows the results for the diode 1I7c. While the ideality coefficient decreases with increasing temperature the zero-bias barrier height increases.

### Defects at the Interface

According to [2] one can determine the so called flat-band barrier height  $\Phi_{bf} = n \Phi_{b0} - (n-1) (kT/q) \ln(N_c / N_d)$ . Here  $N_c$  is the effective density of states in the conduction band,  $N_d$  is the ionized donor density,  $k$  is the Boltzmann constant,  $T$  is the temperature and  $q$  is the electronic charge.  $N_c$  and  $N_d$  are functions of the temperature which is taken into account in our analysis. It is worth noting that the flat-band barrier height is independent of the current transport mechanism and can be determined also for highly doped diodes as in our case where tunneling contributes significantly to the total current. One can show that the flat-band barrier height is the same as the barrier height determined by the capacitance-voltage method [2]. As an example fig. 1 shows the flat-band barrier height of the diode 1I7c. It decreases linearly with increasing temperature. From a linear fit  $\Phi_{bf}(T) = \alpha T + \Phi_{bf}(T=0)$  to the temperature dependent flat-band barrier height it is possible to derive the temperature coefficient  $\alpha$ . Fig. 2 shows the flat-band barrier height at 300 K as a function of the temperature coefficient. One can clearly distinguish two groups. While the first group has a flat-band barrier height of  $1.02 \pm 0.01 \text{ eV}$  and a temperature coefficient of  $-0.23 \pm 0.02 \text{ meV/K}$  the diodes of the second group have a barrier height of  $0.92 \pm 0.02 \text{ eV}$  and a temperature coefficient of  $-0.002 \pm 0.004 \text{ meV/K}$ . It is worth noting that even diodes which are nominally the same can belong to both groups (e.g. diodes 1I7a,b,c in fig 2).

The barrier height as well as the temperature coefficient of the diodes of the first group can be well explained by the theory of Tersoff [3,4]. This theory contains an adjustable parameter which accounts for the chemical nature of the metal. With this parameter one yields a barrier height of 1.02 eV. In this framework the

temperature coefficient is governed only by the temperature dependence of the direct ( $E_g$ ) and the indirect ( $E_g^i$ ) band gap, i.e.  $\alpha = dE_g/dT - 1/2 dE_g^i/dT$ . With the appropriate values this yields  $\alpha = -0.18$  meV/K in well agreement with our measurements. For the diodes of the second group the barrier height and the temperature coefficient are governed by defects at the interface. In this case the Fermi Level is pinned by defects and the temperature dependence of the barrier follows the ionization entropy of the defects which changes weakly with temperature [5]. In addition, defects at the interface result in a reduction of the barrier height. The maximum reduction is given by  $\delta\Phi_B \approx N_I / D_{MIGS}$  where  $N_I$  is the density of the interface defects and  $D_{MIGS}$  is the density of the metal induced gap states [6]. For these diodes the reduction is about 0.1 eV and  $D_{MIGS} \approx 3.7 \times 10^{14}$  eV<sup>-1</sup> cm<sup>-2</sup> [6] yielding  $N_I \approx 3.7 \times 10^{13}$  cm<sup>-2</sup>. This is about one fiftieth of the total density of sites in a GaAs (100) plane.

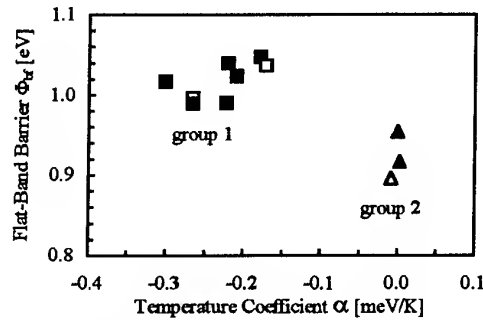


Fig. 2: Flat band barrier height as a function of the temperature coefficient. The open symbols belong to the diodes 117a,b,c.

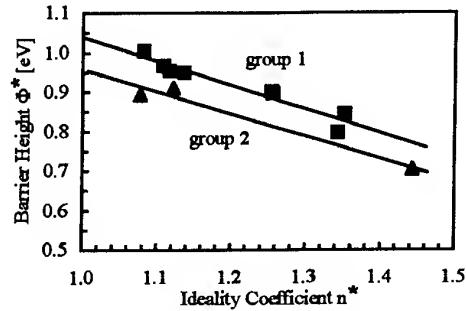


Fig. 3: Barrier height  $\Phi^*$  as a function of the ideality coefficient  $n^*$  (explained in the text).

### Spatial Inhomogeneities at the Interface

Very often the ideality coefficient of a Schottky diode is bigger than predicted by the thermionic emission theory even if tunneling of electrons through the barrier and image force lowering are included. As Tung [7] has pointed out spatial inhomogeneities at the metal-semiconductor interface can explain these "anomalous" ideality coefficients. According to Tung the zero-bias barrier height and the ideality coefficient depend in a complicated way on the density and distribution of spatial inhomogeneities at the metal-semiconductor interface. With an increasing density and an increasing distribution of the inhomogeneous patches the ideality factor increases while the zero-bias barrier height decreases. In fig. 3 the zero-bias barrier height corrected for lowering due to image force and tunneling [1],  $\Phi^* = \Phi_{b0} + \delta\Phi_{if} + \delta\Phi_{tunn}$ , is shown as a function of the ideality coefficient (also corrected for image force and tunneling,  $n^* = n \cdot (n_{tunn} - 1) \cdot (n_{if} - 1)$ ). A linear extrapolation to  $n^* = 1$  yields the barrier height in the absence of spatial inhomogeneities, tunneling and image force lowering. The values of 1.04 eV for the diodes with  $\alpha \approx -0.22$  meV/K and 0.95 eV for the diodes with  $\alpha \approx 0$  meV/K are in agreement with the flat-band barrier height.

### Conclusion

Microstructural properties of the metal semiconductor interface determine the barrier height and the temperature dependence of the Schottky diodes. A defect free Pt/n-GaAs potential barrier has a height of 1.02 eV and a temperature coefficient of -0.23 meV/K. Both values are in good agreement with current theories of the Schottky barrier formation. Defects at the interface pin the Fermi level and consequently lower the barrier up to 0.1 eV. In addition, the temperature coefficient is close to 0 meV/K because it is governed by the ionization entropy of the defects which is almost independent of the temperature. An ideality coefficient bigger than predicted by thermionic emission and tunneling theory can be attributed to spatial inhomogeneities at the interface. This results in a smaller zero-bias barrier height because the current flows preferentially through patches with a smaller than the average barrier height. Our measurements show that spatial inhomogeneities contribute significantly to the barrier lowering in Pt/n-GaAs Schottky diodes.

### References

1. E. H. Rhoderick, R. H. Williams, *Metal-Semiconductor Contacts*, 2nd ed. (Clarendon Press, Oxford, 1988)
2. V. W. L. Chin, M. A. Green, J. W. V. Storey, *J. Appl. Phys.* **68**, 3470 (1990).
3. J. Tersoff, *Phys. Rev. B* **32**, 6968 (1985).
4. H.-W. Hübers, H. P. Röser, submitted to *J. Appl. Phys.* (1998).
5. P. Revva, J. M. Langer, M. Missous, A. R. Parker, *J. Appl. Phys.* **74**, 416 (1993).
6. W. Mönch, *Semiconductor Surfaces and Interfaces*, 2nd ed. (Springer, Berlin, 1995)
7. R. T. Tung, *Phys. Rev. B* **45**, 13509 (1992).
8. R. F. Schmitsdorf, T. U. Kampen, W. Mönch, *J. Vac. Sci. Technol. B* **15**(4), 1221 (1997).

## Antenna-coupled Nanometer Thin-film Ni-NiO-Ni Diodes for Detection of cw and Pulsed 30 THz Radiation

C. Fumeaux<sup>1</sup>, W. Herrmann<sup>1</sup>, F.K. Kneubühl<sup>1</sup>, H. Rothuizen<sup>2</sup>

<sup>1</sup> Institute of Quantum Electronics, Swiss Federal Institute of Technology (ETH), CH-8093 Zürich, Switzerland (Tel.: +41-1-633 23 40, Fax: +41-1-633 10 77, e-mail: infrared@iqe.phys.ethz.ch)

<sup>2</sup> IBM Research Laboratory, Säumerstrasse 4, CH-8803 Rüschlikon, Switzerland

### Abstract

Thin-film nanometer Ni-NiO-Ni diodes with a contact area of  $110 \text{ nm} \times 110 \text{ nm}$  are integrated with  $5 \mu\text{m}$  dipole, bow-tie and spiral antennas. We report on their performance as detectors for 30 THz ( $\approx 10 \mu\text{m}$ ) cw CO<sub>2</sub>-laser radiation and 35 ps OFID CO<sub>2</sub>-laser pulses.

Point-contact Metal-Oxide-Metal (MOM) diodes [1][2] are applied since the late 1960 as detectors and mixers of infrared and visible laser radiation. Here we report on the realization of thin-film Ni-NiO-Ni diodes with integrated infrared antennas for  $10 \mu\text{m}$  radiation. These devices constitute a mechanically stable alternative to the point-contact MOM diodes suitable for field applications.

Our development of thin-film Ni-NiO-Ni diodes with integrated dipole, bow-tie and spiral antennas as detectors and mixers has been described previously [3-10]. Our thin-film diodes are fabricated on SiO<sub>2</sub>/Si substrates with the help of electron-beam lithography at the IBM Research Laboratory (Rüschlikon, Switzerland). We have reduced the contact area to  $110 \text{ nm} \times 110 \text{ nm}$  in order to achieve a fast response of the device.



Fig. 1: Electron micrograph of our thin-film Ni-NiO-Ni diode with integrated bow-tie antenna.

Figure 1 shows an electron-microscope image of one of our Ni-NiO-Ni diodes integrated with a bow-tie antenna with a flare angle of  $60^\circ$ . The antenna improves the coupling of the incident radiation fields to the diode with

dimensions much smaller than the wavelength of the incident radiation.

The nonlinearity of our diodes at infrared frequencies is accurately described by the second derivative  $I''(V)$  of the static current-voltage characteristic  $I(V)$  measured at 10 kHz (Fig. 2). The corresponding zero-bias resistance is in the range of  $100 \Omega$ .

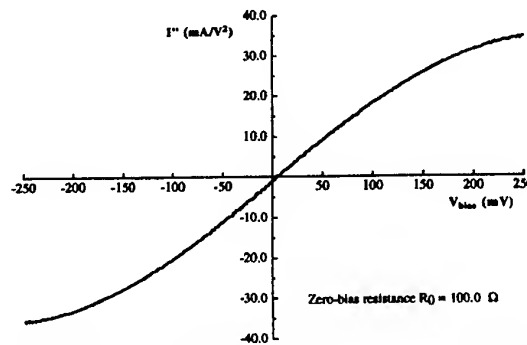


Fig. 2: Second derivative of the current-voltage characteristics  $I(V)$ .

The dc response of our diode used as a detector of cw CO<sub>2</sub>-laser radiation consists of a polarization-dependent part  $V_p$  due to antenna coupling and rectification by a fast tunneling process [11] and a polarization-independent part  $V_{ip}$  mainly of thermal origin (Fig. 3).

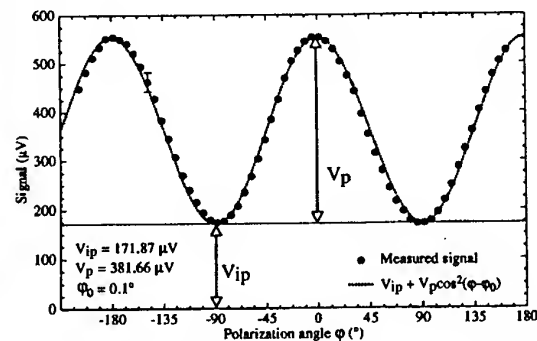


Fig. 3: Polarization dependent response of the MOM diode with integrated bow-tie antenna.

For linearly polarized antennas, the polarization-dependent part of the signal is described by a cosine square curve with a maximum for the polarization parallel to the antenna axis in accordance with antenna theory [12]. Optimum detection of cw-30THz radiation with bow-tie antennas was achieved for an overall arm-length of  $4.6 \mu\text{m}$  which confirms that the dominant modes propagate at the dielectric wavenumber [13].

We have also performed detection measurement of cw CO<sub>2</sub>-laser radiation with thin-film diodes integrated with spiral antennas with a diameter in the order of  $5 \mu\text{m}$  (Fig. 4). These devices generate the comparatively highest signals. However, the central asymmetric feed structure necessary to relax fabrication tolerances was shown to introduce a polarization-dependent antenna responsivity that differs from the expected circular polarization [6].



Fig. 4: Electron micrograph of the spiral antenna.

The application of 35 ps 10.6  $\mu\text{m}$  CO<sub>2</sub>-laser optical-free-induction-decay (OFID) pulses gives information on the speed of the different conduction mechanisms in our Ni-NiO-Ni diodes. The response of our diode to an incident short pulse is represented in Fig. 5. A thermal relaxation is observed after a fast peak caused by rectification of the antenna currents in the diode.

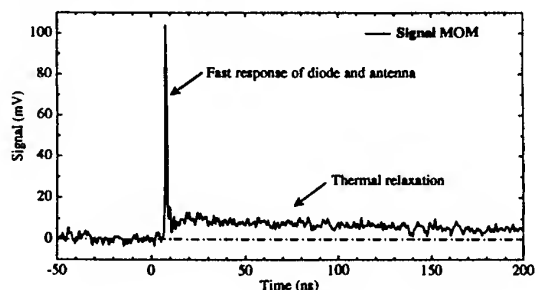


Fig. 5: Response to a 35 ps 28 THz OFID CO<sub>2</sub>-laser pulse.

A good approximation of this thermal relaxation is achieved by the sum of two exponential decay functions

with characteristic times  $\tau_1 \approx 100 \text{ ns}$  and  $\tau_2 \approx 15 \text{ ns}$  (Fig. 6). These two distinct exponential relaxations are explained by thermal diffusion in the Ni and in the SiO<sub>2</sub> layers of our structures.

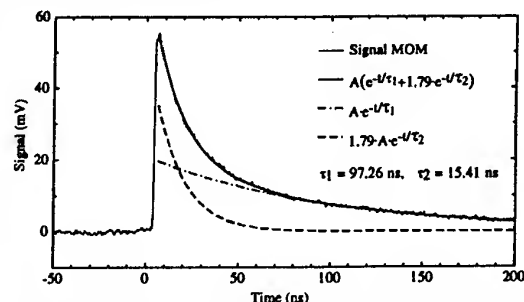


Fig. 6: Thermal response of the MOM diode to a 35 ps 28 THz CO<sub>2</sub>-laser pulse.

Our experiments show the potential application of antenna-coupled thin-film MOM diodes as fast detectors. In addition we have demonstrated the efficiency of planar infrared antenna for frequencies in the order of 30 THz. This development extends present millimeter-wave techniques to the mid-infrared.

## References:

- [1] L.O. Hocker, D.R. Sokoloff, V. Daneu, A. Szoke, A. Javan: *Appl. Phys. Lett.* **12**, 401-402 (1968)
- [2] S.M. Faris, T.K. Gustafson, J.C. Wiesner: *IEEE J. QE-9*, 737-745 (1973)
- [3] E. Wiesendanger, F.K. Kneubühl: *Appl. Phys.* **13**, 343-349 (1977)
- [4] I. Wilke, W. Herrmann, F.K. Kneubühl: *Appl. Phys. B* **58**, 87-95 (1994)
- [5] I. Wilke, Y. Oppliger, W. Herrmann, F.K. Kneubühl: *Appl. Phys. A* **58**, 329-341 (1994)
- [6] C. Fumeaux, G.D. Boreman, W. Herrmann, H. Rothuizen, F.K. Kneubühl: *Appl. Opt.* **36**, 6485-6490 (1997)
- [7] C. Fumeaux, W. Herrmann, H. Rothuizen, P. De Natale, F.K. Kneubühl: *Appl. Phys. B* **63**, 135-140 (1996)
- [8] C. Fumeaux, W. Herrmann, F.K. Kneubühl, H. Rothuizen, B. Lipphardt, C.O. Weiss: *Infrared Phys. & Techn.* **38**, 393-396 (1997)
- [9] C. Fumeaux, W. Herrmann, F.K. Kneubühl, H. Rothuizen, B. Lipphardt, C.O. Weiss: *Appl. Phys. B* **66**, in print (1998)
- [10] C. Fumeaux, W. Herrmann, F.K. Kneubühl, H. Rothuizen: *Infrared Phys. & Techn.*, in print (1998)
- [11] M. Heiblum, S. Wang, J.R. Whinnery, T.K. Gustafson: *IEEE J. QE-14*(3), 159-169 (1978)
- [12] R.C. Johnson: "Designer notes for microwave antennas", Artech House, Boston-London (1990)
- [13] R.C. Compton, R.C. McPhedran, Z. Popovic, G.M. Rebeiz, P.P. Tong, D.B. Rutledge, *IEEE Trans. AP-35*, 622-631 (1987)

## Waveguide Heterodyne SIS Receiver for Balloon-borne Superconducting Submillimeter-Wave Limb Emission Sounder at 640-GHz band

Y. Irimajiri<sup>(1)</sup>, T. Manabe<sup>(1)</sup>, H. Masuko<sup>(1)</sup>, S. Ochiai<sup>(1)</sup>,  
M. Seta<sup>(1)</sup>, Y. Kasai<sup>(1)</sup>, T. Noguchi<sup>(2)</sup>, and S. C. Shi<sup>(3)</sup>

<sup>(1)</sup>Communications Research Laboratory, Ministry of Posts and  
Telecommunications, 4-2-1, Nukui-kita, Koganei, Tokyo 184-8795, Japan

<sup>(2)</sup>Nobeyama Radio Observatory, National Astronomical Observatory,  
Nobeyama, Nagano 384-1305, Japan

<sup>(3)</sup>Laboratory for Radio Astronomy, Purple Mountain Observatory,  
2 West Beijing Road, Nanjing, JinagSu 210008, China

### Abstract

Submillimeter-wave waveguide type SIS receiver has been built for atmospheric research. The mixer uses Nb/AlOx/Nb SIS junctions using PCTJ.  $T_{rr}$  of about 700 K in DSB has been achieved in the frequency range 605 - 650 GHz. The SIS receiver will be installed in the balloon-borne superconducting submillimeter-wave limb emission sounder (BSMILES).

### 1. Introduction

Balloon-borne limb emission sounder at the submillimeter-wave using superconducting low noise receiver is developed for observations of stratospheric minor constituents. Emission line spectra from ozone and chlorine monoxide will be observed. From the observed line intensity and shape of the spectra, height profile of volume mixing ratio of the gases will be given by scanning antenna elevation angle. The main purpose is to research on ozone depletion mechanism in detail.

### 2. SIS receiver

SIS (Superconductor Insulator Superconductor) mixer with Nb/AlOx/Nb SIS junction using PCTJ (Parallel-Connected Twin Junctions) [1] [2] is designed and fabricated. The waveguide

tunerless SIS mixer mount for the 640-GHz band is designed based on that for the 200-GHz band, that is, the dimensions of the mixer mount are scaled down with respect to frequency. SIS junction chip is fabricated in the clean room facility of Nobeyama Radio Observatory (NRO), National Astronomical Observatory (NAO), Japan. The normal resistance ( $R_n$ ) of 10  $\Omega$ , current density ( $J_c$ ) of 5.5 kA/cm<sup>2</sup>, junction size of 1.25 x 1.25  $\mu\text{m}^2$ , and  $\omega R_n C_j$  product of 8 are designed. The  $\omega R_n C_j$  product was determined to be 4 for 200-GHz band SIS mixer. However, it is difficult to fabricate SIS junction with the same  $\omega R_n C_j$  value in the submillimeter-wave range. In this case, SIS junction with high current density of 10 kA/cm<sup>2</sup> should be fabricated. Therefore, the  $\omega R_n C_j$  product of 8 is determined at the sacrifice of the band width.

The receiver noise temperature is measured by Y-factor method. The measurement system is shown in Fig.1. LO signal in the frequency range 600 - 650 GHz is supplied by Gunn oscillator followed by a doubler and a tripler. LO signal is injected by a mylar film into the SIS mixer which is cooled by a mechanical cooler down to 3.95 K. The ratio of the IF output power for hot (room temperature of 295 K) and cold load (liquid nitrogen temperature of 77 K) inputs is measured. From the ratio which is called Y-factor, the receiver noise temperature is ob-



## Metal - High $T_C$ Superconductor Interface Response to Microwave and Millimeter Wave Radiation

A. Laurinavičius, K. Repšas, R. A. Vaškevičius, A. Deksnys, and B. Vengalis

Semiconductor Physics Institute, A. Goštauto 11, 2600 Vilnius, Lithuania

Fax: (3702) 627123, E-mail: laurinavicius@uj.pfi.lt

There are several papers [1-5] where the response of high- $T_C$  superconducting films to microwave radiation were investigated. In this paper, we present the experimental results of normal metal - high  $T_C$  superconductor point contact response to microwave radiation.

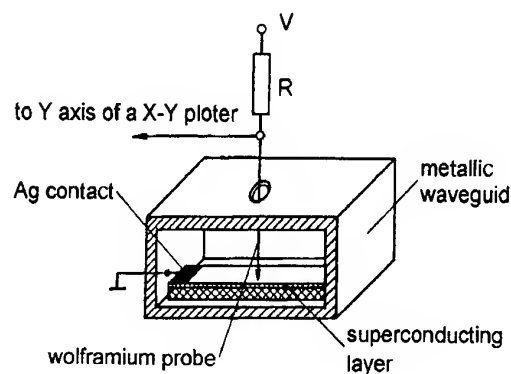


Fig.1. Schematic diagram of the experimental set-up.

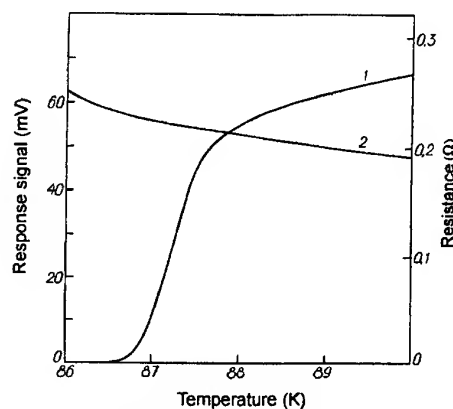


Fig.2. Point contact response signal (curve 2) and resistance (curve 1) dependencies on temperature. Microwave power and wave frequency are 115 mW and 10 GHz, respectively. Bias voltage is 3V.

The experiment was carried out at microwave and millimeter wave ranges. The incident power was 0-115 mW. The superconducting Bi-Sr-Ca-Cu-O layers with a thickness of about  $30\mu\text{m}$  were used for the investigation. Samples were prepared on cleaved MgO(100) faces by the so-called melt processing technology, i.e. by melting and recrystallizing coatings of the superconducting powder. The schematic diagram of the experimental set-up is shown in Fig.1. The sample used for the investigations was placed on the wide wall of the rectangular waveguide. Bias voltage  $V$  was applied to the point contact tungsten probe-superconducting layer through the load resistance  $R$ , which was much higher than the point contact one. The next silver-superconducting sample contact was connected with the metallic waveguide wall.

The response measurement results are shown in Fig.2. It is seen that the response has weak dependence on temperature even in the region of the transition from the normal state to the superconductive one. The response was also observed in room temperature. From these facts, we can conclude that the response is not related to the superconducting phenomenon. We thus assume that the response could be associated with the degraded metal-high  $T_C$  superconductor interface. Such assumption have been confirmed by N. A. Tulina [6], who investigated metal-high  $T_C$  superconductor point contact dc properties. The increase of the response when temperature is decreased and the large point contact resistance show that the nature of the interface layer should be semiconductive. Such response behaviour is well known in Ge and Si semiconductors.



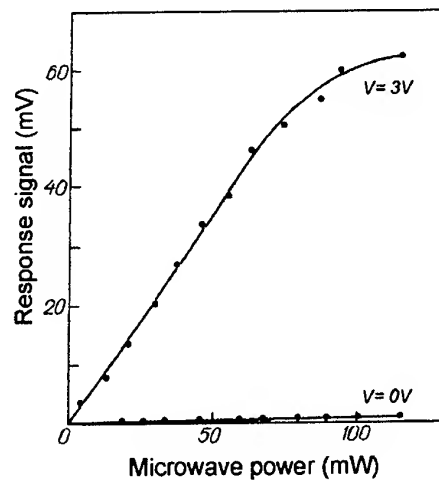


Fig. 3. Point contact response signal and detection voltage-power characteristics.

In Fig.3 the response ( $V=3V$ ) and detection ( $V=0V$ ) voltage-power characteristics are presented at 86K temperature. A small detection signal shows that the voltage-current characteristic of the point contact is very close to symmetric. This means that the inner electric field in the degraded layer is very small. The application of the bias voltage annuls the voltage-current characteristic symmetry and a relatively large response signal appears. The dependence of the response signal on the microwave power (small scale) has a linear character, which could have practical applications.

#### References

1. L. Ngo Phong and I. Shih, J. Appl. Phys., v. 74, pp. 7414-7421 (1993).
2. B. E. Grabow, B. G. Boone and R. M. Sova, J. Appl. Phys., v. 74, pp. 6985-6987 (1993).
3. B. E. Grabow and B. G. Boone, J. Appl. Phys., v. 76, pp. 5589-5591 (1994).
4. F. Anisimovas, A. Deksnys, K. Repšas, A. R. Vaškevičius, Lithuanian J. Phys., v.34, 248-253 (1994).
5. A. Laurinavičius, K. Repšas, A. R. Vaškevičius, V. Lissauskas, D. Čepelis, Proc. 3rd European Conf. on Appl. Supercond., The Netherlands, v. 1, pp. 393-396 (1997).
6. N. A. Tulina, Physica C, v. 291, pp. 309-314 (1997).

# 1 W CW Millimeter-Wave Oscillator with a Gunn Diode Array

Jongsuck Bae, Tetsu Fujii, and Koji Mizuno

Research Institute of Electrical Communication, Tohoku University,  
2-1-1 Katahira, Aoba-ku, Sendai 980-8577, Japan.  
e-mail: bae@riec.tohoku.ac.jp

**ABSTRACT** - A millimeter-wave oscillator which incorporates an overmoded-waveguide resonator with an array of  $TE_{10}$ -mode waveguides containing Gunn diodes, has been developed as a means for achieving highly efficient spatial power combining. The oscillator with a  $3 \times 3$  waveguide Gunn diode array has achieved a power combining efficiency of more than 50 % and an output power of 450 mW (CW) at 98.8 GHz.

## INTRODUCTION

Spatial power combining techniques are useful to generate coherent and intense millimeter and submillimeter waves using solid-state devices, such as HEMT's and HBT's, with lower capability for radiation power. Many authors developed quasi-optical oscillators [1]-[4] as a spatial power combiner that can accommodate a large number of devices. On the other hand, recently, high power devices, such as Gunn and IMPATT diodes, PHEMT's, and MMIC's [5] have been developed, which can be used to produce several tens of mW, even at frequencies above 90 GHz. Thus combining power from twenty of these source devices or even less could produce enough rf-power for many practical applications at millimeter wavelengths. However, quasi-optical oscillators must use a number of source elements of more than 25 for efficient power combining, as described by Mink [6]

For efficient spatial power combining of smaller numbers of the devices, a new type of a waveguide power combiner has been developed, which incorporates an array of fundamental-mode ( $TE_{10}$ ) waveguides with diode devices, inside of an overmoded-waveguide resonator (refer to Fig. 1). An efficiency of about 83 % and an output power of 1.5 W (CW) at 61.4 GHz have been achieved with the overmoded-waveguide oscillator containing a  $3 \times 3$  waveguide array with Gunn diodes [7]. In this paper, the overmoded-waveguide oscillator newly developed at W-band is presented.

## RESONATOR CONFIGURATION

Figure 1 shows the experimental configuration of a waveguide array oscillator with Gunn diodes. The oscillator consists of an  $M \times N$  ( $3 \times 3$ ) array of fundamental-mode ( $TE_{10}$ ) waveguides with pyramidal horn couplers at both ends, a metal overmoded waveguide with a cross section of greater than an operating wavelength, and a sliding short. The Gunn diodes are mounted at the cen-

ter of the  $TE_{10}$ -mode waveguides and are biased by a dc-power supply through an insulated metal post [8].

The resonator configuration allows the oscillator to operate in a single mode even though an overmoded-waveguide is used as a resonator. Referring to Fig. 2, the  $3 \times 3$   $TE_{10}$ -mode array transfers energy selectively to a  $TE_{30}$ -mode in the overmoded-waveguide through the horn couplers with conversion efficiency of 100 %, because their electric and magnetic fields at the boundary between the horn array and overmoded waveguide are exactly the same.

The overmoded-waveguide resonator not only improves efficiency, but also provides a large heat sink for the Gunn diodes, which have a low dc-rf conversion efficiency. Therefore, the overmoded-waveguide power

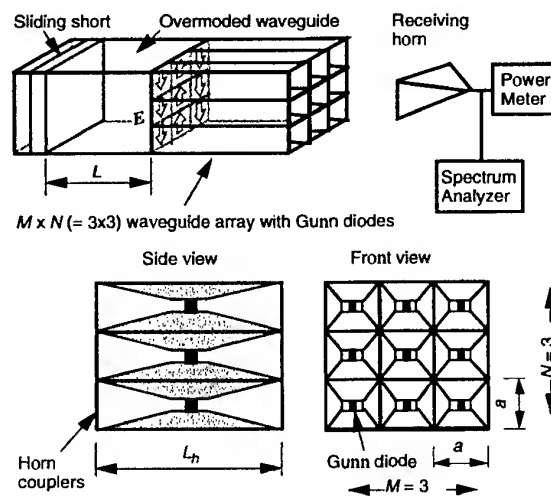


Fig. 1 Experimental configuration of the overmoded-waveguide oscillator with Gunn diodes.

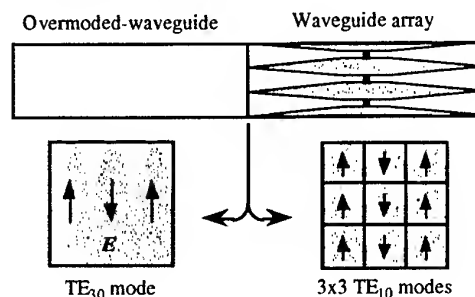


Fig. 2 Mode conversion between a  $3 \times 3$   $TE_{10}$  mode array and the  $TE_{30}$  mode in the overmoded-waveguide resonator.

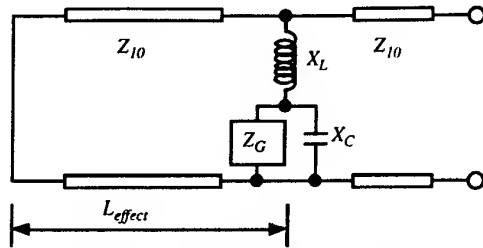


Fig. 3 Equivalent circuit for the overmoded-waveguide oscillator.

combiners can be used to achieve high output power with high combining efficiency at millimeter wavelengths.

### EQUIVALENT CIRCUIT

Figure 3 shows the equivalent circuit developed for the overmoded-waveguide oscillator. When the oscillation mode in the resonator is  $TE_{30}$ , the propagation constant in the overmoded waveguide matches that of the  $TE_{10}$ -waveguide formed by the horn aperture. The attenuation constants do differ: in the overmoded waveguide the attenuation constant is decreased by 1/3 times compared to that in the  $TE_{10}$ -waveguide. The overmoded-waveguide resonator acts therefore as a  $TE_{10}$ -waveguide with a smaller propagation loss. Consequently, we can apply the same equivalent circuit design techniques used for conventional waveguide resonators containing Gunn diodes [9] [10]. In Fig. 3,  $L_{effect}$  is an effective resonator length between the Gunn diode and sliding short,  $Z_{10}$  is the characteristic impedance of the  $TE_{10}$ -waveguide,  $X_L$  and  $X_C$  are reactances of the bias post, and  $Z_G$  is the impedance of the Gunn diode. The parameters,  $X_L$  and  $X_C$ , are calculated using the induced EMF method [9].

### EXPERIMENTAL SETUP

In Fig. 1, the Gunn diodes used are of InP-type, Japan Energy Co., NT-W90, and have a maximum rated output power of about 90 mW in CW at 94 GHz. The  $TE_{10}$ -waveguides are standard W-band waveguides with the horn couplers which have square apertures with dimensions of  $a=b=15$  mm. The length of the waveguide,  $L_h$ , is 60 mm. The oscillation frequencies and output power for the oscillator were measured using a W-band standard horn antenna connected to a spectrum analyzer (HP-8563A) and a power meter. The receiving horn antenna was placed at a distance of 1.3 m from the oscillator.

### EXPERIMENTAL RESULTS

Figure 4 compares the measured frequency spectra for the oscillators with one and nine diodes at 98.8 GHz. The measured C/N ratio for the oscillator with nine diodes is -91.3 dBc/Hz at a 100 kHz offset which is com-

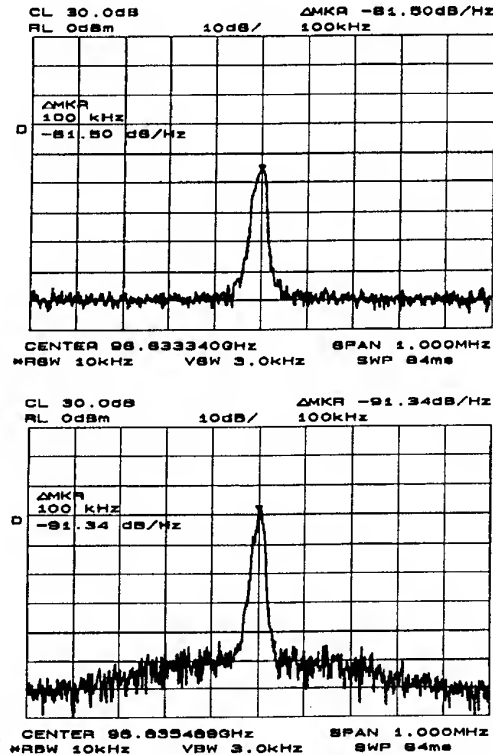


Fig. 4 Measured frequency spectrum of the overmoded-waveguide oscillators with one Gunn diode (a), and nine diodes (b).

pared to -81.5 dBc/Hz measured for that with a one diode. The C/N ratio reduction indicates that power from the nine diodes has been successfully combined coherently in the overmoded-waveguide resonator.

In order to confirm the  $TE_{30}$  oscillation mode, radiation patterns from the output horn array were measured. The measured radiation patterns for  $H$ - and  $E$ -planes are shown in Fig. 5. The oscillation frequency was 98.4 GHz. The solid curves indicate the theoretical radiation patterns for the  $TE_{30}$  oscillation mode. The coincidence between the two patterns shows that the oscillation mode in the overmoded-waveguide oscillator is  $TE_{30}$ .

The total output power of the oscillator was estimated from the power detected by the W-band standard horn and the theoretical radiation patterns for the  $TE_{30}$  mode. Figure 6 shows the measured frequencies (a), and corresponding total output power for the oscillator in the  $TE_{30}$  mode (b), as a function of the length,  $L$ , between the sliding short and the horn array. The solid lines indicate the theoretical frequencies calculated using the equivalent circuit for the oscillator. The measured tuning frequency range is about 2 GHz at a center frequency of 98.5 GHz. The maximum output power is about 450 mW at 98.8 GHz, demonstrating a power combining efficiency of about 51 %. For some applications using this oscillator in guided wave systems, the  $TE_{30}$  output mode can be easily converted to  $TE_{10}$  through waveguide circuit techniques.

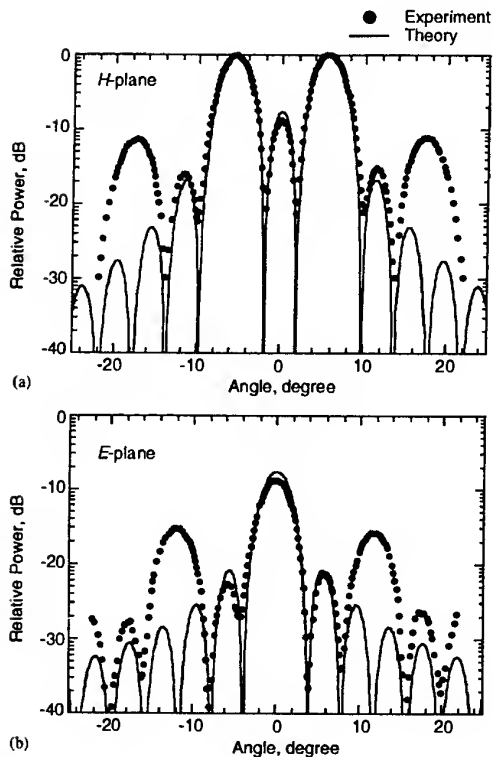


Fig. 5 Measured and theoretical (a) *H*- and (b) *E*-plane patterns of the output beam from the overmoded-waveguide oscillator in the  $TE_{30}$  mode at 98.4 GHz. The radiation angles are measured from the center of the surface of the output horn antenna array.

### CONCLUSION

We have demonstrated the use of an overmoded-waveguide resonator with a fundamental-mode waveguide array, as a coherent power combiner with millimeter wave solid state devices. The experimental results have shown that the oscillator with a 3x3 Gunn diode array can produce an output power of greater than 400 mW even at high frequencies above 98 GHz.

This research was partially supported by the Ministry of Education, Science, Sports and Culture, Grant-in-Aid for Scientific Research (B), 09450134, 1998.

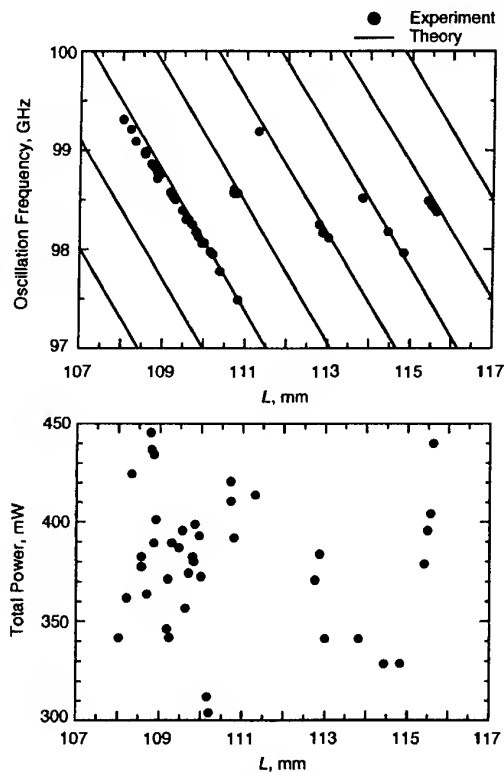


Fig. 6 Measured oscillation frequencies (a), and total output power (b), in the overmoded-waveguide oscillator operating in the  $TE_{30}$  mode as a function of the spacing,  $L$ , between the sliding short and horn array.

### REFERENCES

- [1] K. Mizuno, T. Ajikata, M. Hieda, and M. Nakayama, *Electron. Lett.*, vol. 24, pp. 792-793, 1988.
- [2] B.M. Weikle II, M. Kim, J. B. Hacker, M. P. Delisio, Z. B. Popovic, D. B. Rutledge, *Proc. IEEE*, vol. 80, no. 11, pp. 1800-1809, 1992.
- [3] Workshop digest of 1997 IEEE MTT-S Int. Microwave Symp., "WFF: Quasi-optical power combining", Denver, Colorado.
- [4] H. Kondo, M. Hieda, M. Nakayama, T. Tanaka, K. Osakabe, and K. Mizuno, *IEEE Trans. Microwave Theory Tech.*, vol. 40, no. 5, pp. 472-478, 1992.
- [5] P. Huang, E. Lin, R. Lai, M. Biedenbender, T. W. Huang, H. Wang, C. Geiger, T. Block, and P. H. Liu, 1997 IEEE MTT-S Int. Microwave Symp., TH1C-1, Denver, Colorado, 1997.
- [6] J. W. Mink, *IEEE Trans. Microwave Theory Tech.*, vol. MTT-34, no. 2, pp. 273-279, 1986.
- [7] J. Bae et al., 1998 IEEE MTT-S Int. Microwave Symp., TH4A-2, Baltimore, MD, 1998.
- [8] J. Bae et al., *Conf. Dig. of the 22nd Int. Conf. IR&MMW*, Wintergreen, Virginia, 1997, pp. 247-245.
- [9] R. L. Eisenhart and P. J. Khan, *IEEE Trans. Microwave Theory Tech.*, vol. MTT-19, no. 8, pp. 706-719, 1971.
- [10] K. Chang and R. L. Ebert, *IEEE Trans. Microwave Theory Tech.*, vol. MTT-28, no. 4, pp. 295-305, 1980.

# OPEN RESONATOR SOLID-STATE MILLIMETER-WAVE SOURCES

Mykola A. Pershin, Eugene A. Machusky

Design Bureau "Storm"  
National Technical University of Ukraine "Kyiv Polytechnical Institute",  
Build-11, Politechnichna, 16, Kyiv, Ukraine, 252056  
tel/fax (044)-274-10-15, e-mail: persh@rtus.ntu-kpi.kiev.ua

Quasioptical electrodinamical structures are perspective at millimeter and submillimeter wavelengths especially with diode and transistor active elements due to the simplicity of active circuit installation. High  $Q$  of open resonators gives the possibility of oscillator noise minimization. Simple is mechanical tuning and matching.

Generally oscillators resistance system include active element, open resonator and coupling-matching circuit. Coupling-matching circuit realizes impedance transformation to optimal power or noise point of active element, selects the resonant frequency and forms the necessary field configuration (as primary antenna).

At the negative active resonance port the coupling system can give the reaction of series ( $Z$ ) or parallel ( $Y$ ) type. The main (open) cavity can also give the reaction of series or parallel type depending on coupling features. Than it is possible to realize four resonant structures:

1.  $Z$  coupling -  $Z$  resonator;
2.  $Y$  coupling -  $Z$  resonator;
3.  $Z$  coupling -  $Y$  resonator;
4.  $Y$  coupling -  $Y$  resonator.

With  $Z$  (series) representation of active element ( $Z_D = R_D + jX_D$ ) under practical condition  $|X_{GE}| > |R_{GE}|$  the reaction of complex electrodinamical structure at the negative resistance terminals at the resonant frequency must be of  $Z$ -type. Then the partial  $Q$  of open resonator and coupling resonator must have different meanings in different above mentioned structures. In Fig. 1 there is shown equivalent circuits of practical structures N 2 and N 3, where  $n_1, n_2, n_3$  - coupling factors of different parts of oscillating system;  $Z_L$  - useful load;  $Z_A$  ( $Y_A$ ),  $Y_{OR}$  ( $Z_{OR}$ ),  $Z_F$  ( $Y_F$ ) - parameters of coupling circuit, open resonator and losses of free space.

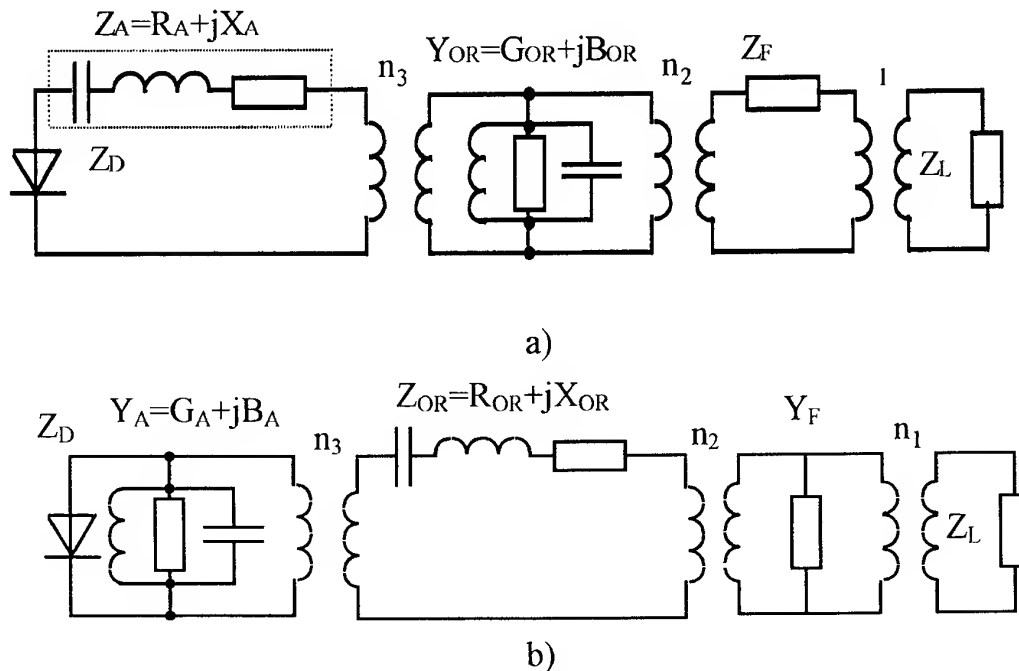


Fig. 1

For the structure "Z coupling - Y resonator" (Fig. 1,a) impedance components of resonant circuit at the active elements terminals are:

$$R_s = R_A \frac{1 + \alpha + \xi_L^2}{1 + \xi_L^2}; \quad X_s = R_A \left( \xi_A - \frac{\alpha \xi_L}{1 + \xi_L^2} \right),$$

$$\xi_L = 2Q_L(\Delta\omega/\omega_o);$$

$\omega$  - oscillator frequency;  $\omega_o$  - open resonator frequency;

$Q_L$  - loaded Q of open resonator;

$$\xi_A = 2Q_A(\Delta\omega/\omega_{oA});$$

$\omega_{oA}$  - resonant frequency of coupling-matching (antenna) circuit;

$Q_A$  - quality factor of unloaded antenna;

$\alpha$  - coupling factor of antenna - open resonator [1].

Typically  $Q_{OR} \gg Q_A$  and at resonant antenna frequency

$$X_s|_{\xi_A=0} = R_A \frac{\alpha \xi_L}{1 + \xi_L^2};$$

and fixing capability of system at the active elements terminals is

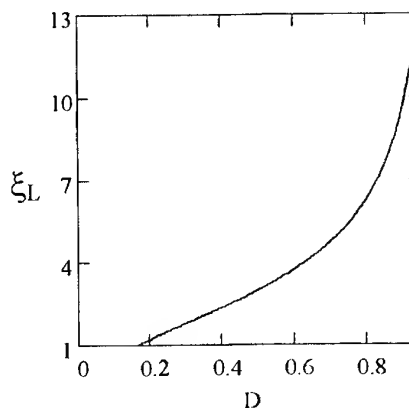
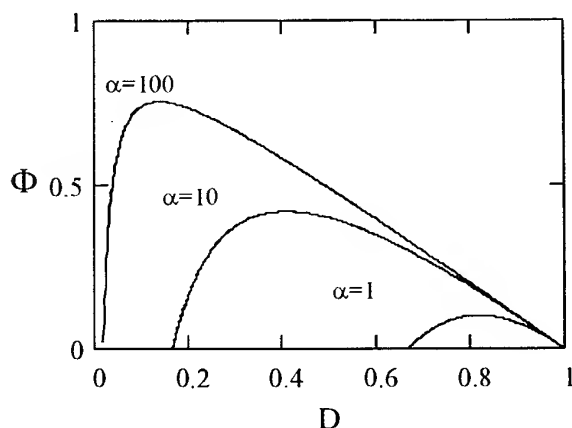
$$\frac{\partial X_s}{\partial \omega}|_{\xi_A=0} = 2 \frac{Q_L}{\omega} \alpha R_A \frac{\xi_L^2 - 1}{\xi_L^2 + 1} = 2 \frac{Q_L}{\omega} R_D \Phi = 2 \frac{Q_L}{\omega} R_D \frac{2(1-D)}{\alpha} \left( \frac{\alpha + 2}{2} - \frac{1}{D} \right),$$

where  $\Phi = Q_{OSC}/Q_L$  [2];  $Q_{OSC}$  - loaded Q of oscillator;  $D = R_A/R_{D OPT}$ ;

$$\xi_L = \pm \sqrt{\frac{\alpha D}{1-D}} - 1.$$

Parameters  $\Phi$  and  $D$  give the possibility to estimate oscillator quality (Fig. 2) and to obtain optimal parameters of coupling-matching (antenna) circuit.

Experimental results will be presented for optimally tuned mm-wave oscillators and for other oscillator circuits.



1. Kotserzhinskii B.A., Machusskii E.A., Pershin N.A., Taranenko V.P. Solid-state oscillators with quasioptical resonant systems. Radioelectronics and communications systems (Izvestiya VUZ. Radioelektronika). Vol. 30, No. 10, pp. 11-20, 1987

2. Machusskii E.A. Stabilizing the frequency of diode microwave oscillators. Radioelectronics and communications systems (Izvestiya VUZ. Radioelektronika). Vol. 30, No. 10, pp. 25-31, 1987.

### **A New contribution to the FIR laser systems**

**A. Darwish\*\*, T. Thompson\*\*, A. Williams\***

**\*Center for Nonlinear Optics and Materials  
Alabama A&M University, Normal, AL 35762**

**\*Laser-Matter Research Labs, P.O. BOX 245, Normal, AL, 35762**

**\*\*EB52, National Aeronautics and Space Administration, Marshal Space Flying Center , AL 35812**

#### **Abstract**

As a new research program at AL A&M University, we have built a FIR laser which is pumped by CO<sub>2</sub> laser. The system was tested and new FIR lines from CH<sub>3</sub>OH were observed. A tentative assignment for these lines will be presented as well as the complete design for the FIR laser system.

## Optically pumped submillimeter laser lines from $\text{CD}_2\text{Cl}_2$

A. Bertolini, G. Carelli, N. Ioli, S. Marchetti\*, A. Moretti and F. Strumia

Dipartimento di Fisica dell'Università di Pisa, CNR and INFM

Via Buonarroti 2, 56127 Pisa, Italy

\*IFAM-CNR Via del Giardino 7, 56126 - Pisa, Italy

The deuterated dichloromethane molecule is a near-prolate asymmetric top rotor (asymmetry factor  $\kappa = -0.97$ ), belonging to  $\text{C}_{2v}$  symmetry point group [1]. We investigated the  $\nu_8$  IR absorption band by using a CW waveguide  $\text{CO}_2$  laser having a tunability of 300 MHz in order to pump infrared transitions with large offset. As a FIR laser resonator we used a Fabry-Perot cavity described in details elsewhere [2]; in order to make easier the search of new FIR lines it is equipped with an electret microphone for an optoacoustic monitoring of absorption transitions. With this system we could observe 16 new lines, ranging from 212.63 to 983.3  $\mu\text{m}$ . The precision in the wavelength measurements is  $10^{-3}$ . For each of them we also measured the infrared absorption offset relative to the  $\text{CO}_2$  line center, the polarization relative to that of the  $\text{CO}_2$  pumping laser, the optimum operating pressure and the relative intensity. The polarization has been measured by means of a mesh polarizer. The pump offset is measured using the Transferred Lamb Dip [TLD] technique [3]. In table I are given the data for the new lines and for six old ones whose offset was unknown.

Pump Line	Wavelength ( $\mu\text{m}$ )	Rel. Pol	Offset (MHz)	Rel. Power	Press. (Pa)	Comments
10R(18)	506.7	$\perp$	- 60	M	8	old
	287.5	$\perp$	- 60	S	8	
10R(14)	247.8	$\parallel$	- 140	W	6	
	587.2	$\perp$	90	M	8	
10R(12)	705.7	$\perp$	- 70	VW	8	
	643.2	$\perp$	130	MW	7	
10R(08)	447.5	$\perp$	- 50	M	9	
	586.5	$\perp$	90	MS	10	
10R(06)	438.2	$\parallel$	45	M	10	
	695.2	$\perp$	95	W	12	old
10R(04)	543.2	$\perp$	- 30	W	8	
	587.5	$\perp$	- 10	W	10	
10P(10)	983.3	$\perp$	- 80	M	10	
10P(12)	212.6	$\parallel$	- 80	M	8	
	260.1	$\perp$	- 80	M	8	
	476.3	$\perp$	80	M	10	
10P(14)	328.3	$\perp$	- 30	W	6	
	270.4	$\parallel$	100	S	8	
	376.5	$\perp$	100	M	8	
10P(16)	588.7	$\perp$	15	M	8	old

Table I. New FIR laser lines of  $\text{CD}_2\text{Cl}_2$ .

The assignment of the FIR laser lines of  $\text{CD}_2\text{Cl}_2$  is complicated by the presence of two chlorine isotopes,  $^{35}\text{Cl}$  and  $^{37}\text{Cl}$  and by the possible interaction between the  $\nu_8$  and the  $\nu_2$  bands. For this reason it was not possible to assign the IR transitions, while tentative assignments can be proposed for the FIR laser transitions when two lines having different polarizations and sharing the same upper level are present. For the first time we obtained a large number of lines with a polarization perpendicular to that of the pump laser and combining our experimental results with previous known laser lines it was possible to assign 15 Q-R FIR emission doublets.

The rotational levels of the molecule are identified by  $J$ ,  $K_+$ ,  $K_-$ . Given the slightly asymmetry, the K-splitting is negligible and the energy of the level can be written as:

$$E_{JK} = (B + C)/2J(J + 1) + (A - (B + C)/2)K^2$$

where the rotational constants of the excited levels are obtained from Fourier Transform IR absorption



spectrum [4], and K is  $K_{-}$ . Our assignments are given in table II. Column one gives the pump laser line and the offset relative to the centerline; column two the experimental wavenumber; column 3 the calculated one; column four the quantum numbers of the levels involved in the laser emission.

Pump line	Offset (MHz)	Pol.	$\nu_{\text{exp}}$ ( $\text{cm}^{-1}$ )	$\nu_{\text{calc}}$ ( $\text{cm}^{-1}$ )	(J,K) $\rightarrow$ (J',K')
10R(18)	- 60	$\perp$	19.736	19.707	(72,15) $\rightarrow$ (72,14)
		$\parallel$	34.783	34.818	(72,15) $\rightarrow$ (71,14)
10R(14)	90	$\perp$	17.030	16.989	(56,13) $\rightarrow$ (56,12)
		$\parallel$	28.727	28.742	(56,13) $\rightarrow$ (55,12)
10R(12)	- 70	$\perp$	14.170	14.270	(52,11) $\rightarrow$ (52,10)
		$\parallel$	25.208	25.184	(52,11) $\rightarrow$ (51,10)
10R(12)	130	$\perp$	15.547	15.629	(45,12) $\rightarrow$ (45,11)
		$\parallel$	25.100	25.074	(45,12) $\rightarrow$ (44,11)
10R(08)	- 50	$\perp$	22.346	22.425	(38,17) $\rightarrow$ (38,16)
		$\parallel$	30.469	30.400	(38,17) $\rightarrow$ (37,16)
10R(08)	90	$\perp$	17.050	16.989	(33,13) $\rightarrow$ (33,12)
		$\parallel$	23.946	23.915	(33,13) $\rightarrow$ (32,12)
10R(06)	95	$\perp$	14.384	14.270	(41,11) $\rightarrow$ (41,10)
		$\parallel$	22.821	22.875	(41,11) $\rightarrow$ (40,10)
10R(04)	- 30	$\perp$	18.409	18.348	(18,14) $\rightarrow$ (18,13)
		$\parallel$	22.158	22.126	(18,14) $\rightarrow$ (17,13)
10R(04)	- 10	$\perp$	17.021	16.989	(20,13) $\rightarrow$ (20,12)
		$\parallel$	21.286	21.187	(20,13) $\rightarrow$ (19,12)
10P(10)	- 80	$\perp$	10.170	10.193	(37,8) $\rightarrow$ (37,7)
		$\parallel$	17.880	17.959	(37,8) $\rightarrow$ (36,7)
10P(12)	- 80	$\perp$	38.447	38.734	(40,29) $\rightarrow$ (40,28)
		$\parallel$	47.037	47.129	(40,29) $\rightarrow$ (39,28)
10P(12)	80	$\perp$	20.995	21.066	(43,16) $\rightarrow$ (43,15)
		$\parallel$	30.175	30.091	(43,16) $\rightarrow$ (42,15)
10P(14)	- 30	$\perp$	30.460	30.579	(48,23) $\rightarrow$ (48,22)
		$\parallel$	40.634	40.653	(48,23) $\rightarrow$ (47,22)
10P(14)	100	$\perp$	26.560	26.502	(50,20) $\rightarrow$ (50,19)
		$\parallel$	36.982	36.996	(50,20) $\rightarrow$ (49,19)
10P(16)	15	$\perp$	16.987	16.989	(58,13) $\rightarrow$ (58,12)
		$\parallel$	29.172	29.162	(58,13) $\rightarrow$ (57,12)

Table II. Assignments of  $\text{CD}_2\text{Cl}_2$  laser transitions.

#### References

1. R.W. Davis, A.G. Robiette and M.C.L. Gerry, J. Mol. Spectrosc. 85, 399 (1981).
2. A. Bertolini, G. Carelli, N. Ioli, C.A. Massa, J.C.S. Moraes A. Moretti and F. Strumia, Int. J. Infr. MMWaves 18, 779 (1997).
3. M. Inguscio, A. Moretti and F. Strumia, Opt. Commun. 30, 355 (1979).
4. J.L. Duncan, G.D. Nivellini and F. Tullini J. Mol. Spectrosc. 118, 145 (1986).

# Infrared Raman Solitons, Self-phase Modulation and Self Focusing in $\text{CO}_2$ -Laser Pumped $\text{NH}_3$

M. O. Baumgartner and F. K. Kneubühl

Institute of Quantum Electronics, Swiss Federal Institute of Technology (ETH), CH-8093 Zürich, Switzerland  
(Tel: +41-1-633 23 40 Fax: +41-1-633 10 77, e-mail: infrared@iqe.phys.ethz.ch)

Stimulated Raman scattering is a nonlinear process, that has been studied extensively by many groups. Nevertheless, the presence of soliton-like pulses in the depletion region of the pump pulse is not yet completely understood. The origin of such spontaneous solitons is the rapid phase variation of the Stokes field induced by the quantum fluctuations of the electromagnetic field in vacuum.

With the aid of a pulsed  $\text{CO}_2$ -laser system [1] including a fast plasma shutter we have observed the first spontaneous Raman solitons in the forward stimulated Raman scattering (SRS) by the far-infrared-active laser gas  $\text{NH}_3$ . The measured SRS processes are rotational transitions at  $58\text{ }\mu\text{m}$  and  $72.6\text{ }\mu\text{m}$  optically pumped with pulses of preselected duration and wavelengths of  $10.37\text{ }\mu\text{m}$  and  $10.35\text{ }\mu\text{m}$  respectively. Our experimental arrangement shown in Fig. 1 enables us to measure the depleted pump pulse with the SRS solitons and simultaneously the scattered far-infrared radiation (FIR) with the corresponding dip. Such a measurement is shown in Fig. 2.

In addition we have measured the statistics of the relative delays and relative amplitudes of these spontaneous Raman solitons at  $10.37\text{ }\mu\text{m}$  wavelength. We performed these statistics on the basis of 1000 shots with a shot to shot variation of the pulse intensity within the limit of 10%. The Histogramms are shown in Fig. 3.

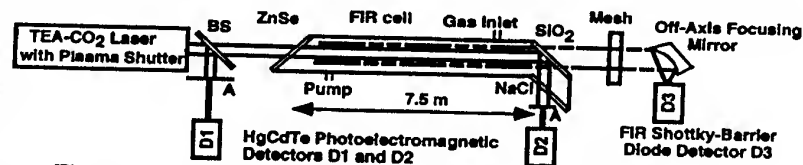


Fig. 1: Experimental arrangement for SRS of  $\text{CO}_2$ -laser radiation by  $\text{NH}_3$

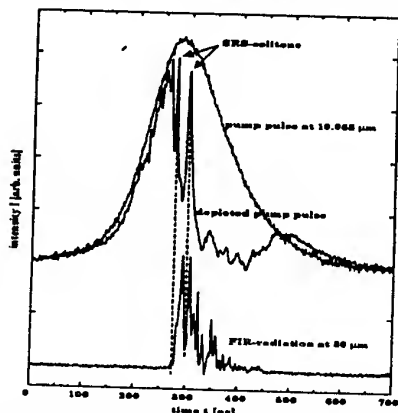


Fig. 2: Multiple SRS solitons in the depleted pump pulse with the corresponding dips in the FIR

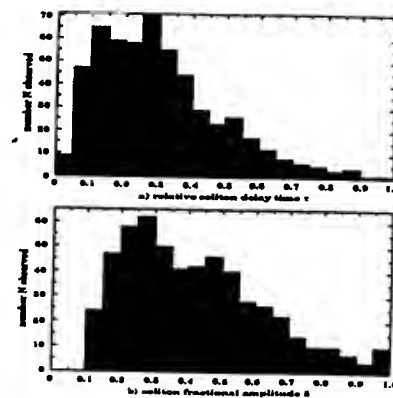


Fig. 3: Histogramms of a) spontaneous SRS solitons delay times measured relative to the duration of the temporal depletion region and b) solitons fractional heights

For 362 of these 1000 shots we observed unambiguous multiple solitons within one pump pulse. In total we measured 542 solitons in our 1000 pump pulses. Subsequently, we compared these results with earlier measurements performed by MacPherson et al. [2] in para-hydrogen pumped by a frequency doubled Nd:YAG laser and with the calculations by Englund and Bowden [3].

As reported by Girdauskas et al. [4] the mutual diffractive focusing of laser and Stokes beams has a strong influence on the gain of the observed SRS as well as on the process of Raman soliton generation. Therefore, we have measured the

magnitude of self focusing shown in Fig. 4 for two different intensities of the CO<sub>2</sub> 10(R4) laser transition. In this figure the relative intensity is the intensity transmitted through an aperture at the end of the FIR cell versus the total intensity of the laser beam. In order to determine the nonlinear refractive index  $n_2$  for NH<sub>3</sub>, we have measured for the first time the corresponding self-phase modulation with the set-up shown in Fig. 5. Fig. 6 shows the result for the 10.37  $\mu\text{m}$  (10R4) CO<sub>2</sub>-laser emission. The total self-phase modulation is a linear function of the NH<sub>3</sub> gas pressure due to the maximal relative refractive index change of  $\Delta n_{\text{max}}/n_0 \approx 5 \cdot 10^{-7}$ . Making use of these data we evaluated the cubic refractive index  $n_2$  as a function of the NH<sub>3</sub> pressure. Thus, we determined the nonlinear refractive index  $n_2$  of NH<sub>3</sub> for the wavelengths at the CO<sub>2</sub>-laser emissions 10(R4), 10(R6) and 10(R8). No phase change could be observed at 9(P20). This is in agreement with the fact that NH<sub>3</sub> has no vibrational resonance at that wavelength.

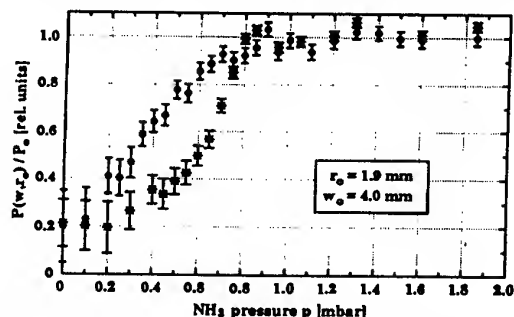


Fig. 4: Normalized transmission of self-focused laser beam. Dots represent the measurement with  $P_0 = 150$  kW, while stars indicate the result for  $P_0 = 75$  kW

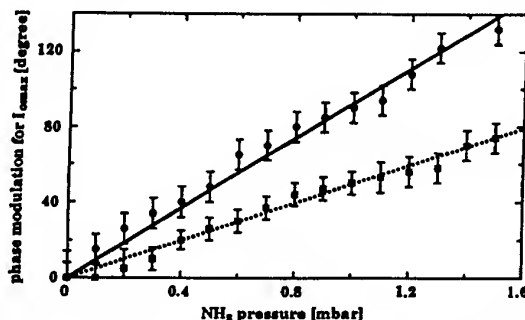


Fig. 6: Self-phase modulation for the maximal intensity  $I_{0\text{max}}$  at the laser emission 10.365  $\mu\text{m}$  (10R4) as a function of the ammonia pressure  $p$ . Phase modulation for the intensity  $I_{0\text{max}}$  with a pulse energy  $E_1 = 70$  mJ (full line and circles). Phase modulation with an intensity attenuated by a factor 1/2 and the corresponding pulse energy  $E_2 = 35$  mJ (dotted line and squares)

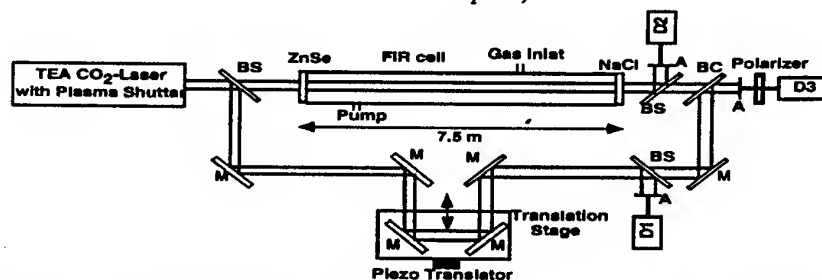


Fig. 5: The set-up for the measurement of the total self-phase modulation in NH<sub>3</sub> includes BS: beam splitter, BC: beam combiner, M: mirror, A: aperture, D1-D3: fast HgCdTe-photoelectromagnetic detectors for 10  $\mu\text{m}$  radiation. Aperture A insures that only the onaxis modulation is measured

#### References:

- [1] A. W. Källin, R. Kesselring, Cao Hongru and F. K. Kneubühl, *Infrared Phys.* 33, 73-112 (1992)
- [2] D. C. MacPherson, R. C. Swanson and J. L. Carlsten, *Phys. Rev. A* 40, 6745-6747 (1989)
- [3] J.C. Englund and M. C. Bowden, *SPIE Conference Proceedings No. 874*, "Nonlinear Optical Beam Manipulation, Beams Combining in Atmospheric Propagation", 218 (1988)
- [4] A. Dement'ev, V. Girdauskas and A. Rodin, *SPIE Conference Proceedings No. 2800*, ICONO95, "Nonlinear Optical Interactions and Wave Dynamics", 341-350 (1995)

#### Acknowledgements:

This study is supported by the Swiss National Science Foundation GRD/EMD Bern and ETH Zurich.

## Frequency stabilization of a Far Infrared laser

R. Bocquet<sup>†</sup>, M. Yu. Tretyakov<sup>††</sup>, L. Margulès<sup>†</sup>

<sup>†</sup>: Laboratoire PhLAM, Physique des Lasers Atomes et Molécules  
Université des Sciences et Techniques de Lille  
59655 Villeneuve d'Ascq Cedex France  
Email: [bocquet.robin@univ-lille1.fr](mailto:bocquet.robin@univ-lille1.fr)

<sup>††</sup>: Applied Physics Institut of the Russian Academy of Science  
46 Ulyanova Street  
603600 Nizhnii Novgorod GSP-120 Russia  
Email: [trt@pop.sci-nnov.ru](mailto:trt@pop.sci-nnov.ru)

### Abstract

All the spectrometers based on the use of a far infrared laser present the drawback of the laser frequency uncertainty. Even if the knowledge of the laser frequency is very precise, a shift of the laser cavity length is always present, limiting the spectrometer frequency accuracy at 1 MHz. The goal of this paper is to give a solution to this drawback in demonstrating the feasibility of a frequency stabilization of the far infrared laser.

### Introduction

Since 1990, we are using at Lille (France), a far infrared (FIR) spectrometer for spectroscopic applications [1]. This experiment consists to mix the output radiation from an FIR laser with the radiation from a synthesizer, operating in the range 2-18 GHz, to produce sidebands in the FIR region. These sidebands with a tunability of 32 GHz serve as a source for the spectrometer. The drawback of this experiment is the knowledge of the FIR laser frequency. The uncertainty of the measured absorption line frequency is indeed proportional to the laser line frequency uncertainty. Figure 1 shows an example of FIR laser gain curve.

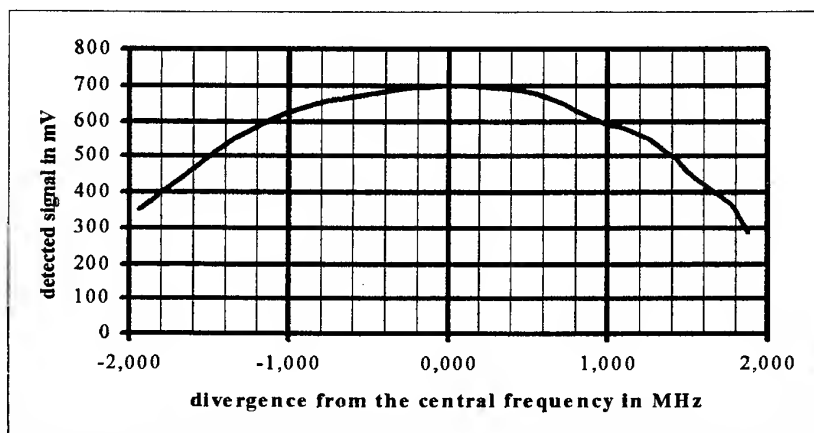


**Figure 1 : FIR laser gain curve for the vinyl fluoride line centered at 634.222 GHz pumped by the 10P20 CO<sub>2</sub> line**

One can see on this characteristic example, a bandwidth of the order of 4 MHz. This means that we can tune the laser radiation frequency over this range. One can also imagine the difficulty to tune the laser cavity length just at the top of the gain curve. We can reach in these conditions, an accuracy between 500 kHz and 1 MHz for the absorption line frequency measurements [2].

The goal of this short paper is to show the possibility of a frequency stabilization of the FIR laser to increase the frequency accuracy of the experiment.

### Experimental set up

Figure 2 gives a scheme of the experimental set up used to stabilize the FIR laser.

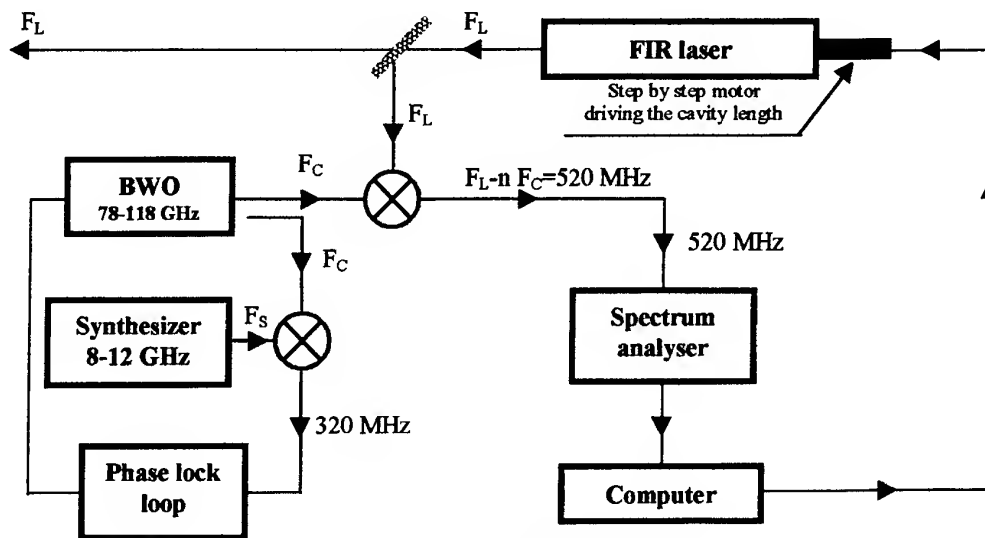


**Figure2 : Experimental set up**

A part of the FIR laser output power is used to generate a beat note around 520 MHz, with the radiation from a backwardwave oscillator (BWO) in the range 78-118 GHz, phase locked on a 8-12 GHz synthesizer. The beat note frequency is measured by a spectrum analyser and sent via a GPIB bus to the computer which drives the step by step motor of the laser cavity. We are then able to control the FIR laser frequency by tuning the cavity length.

### Results

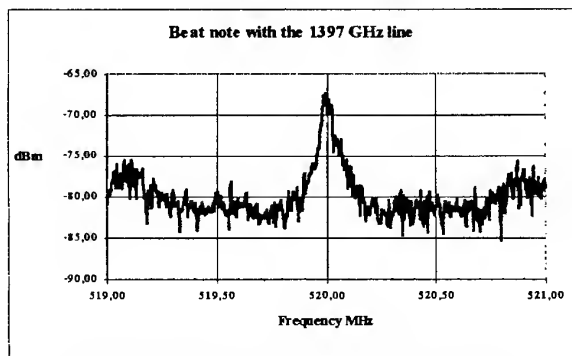


**Figure3 : beat note with the 1397 GHz line**

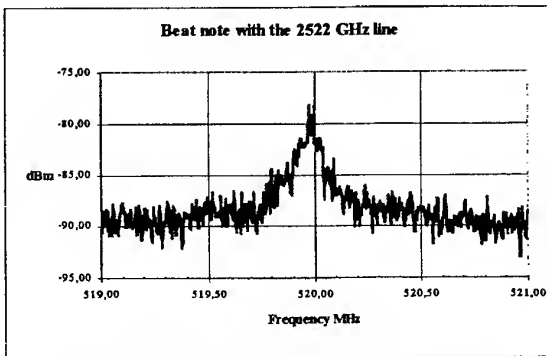


**Figure4 : beat note with the 2522 GHz line**

The two examples given in figures 3 and 4 show beat notes around 520 MHz with signal to noise ratios better than 10 dB. So, they can be used to stabilize the FIR laser up to 2500 GHz. We tried the stabilization in spectroscopic configuration with the OCS molecule. We measured 31 times on 4 days, the same transition at 899015.989 MHz. These trials give a 60 kHz standard deviation. The theoretical laser accuracy was 25 kHz, but the standard deviation found, takes into account other experimental parameters such as the signal ratio of the observed line, the accuracy of the software which measure the transition, the line deformation due to the optical path.

### References

- 1 D. Boucher, R. Bocquet, J. Burie, W. Chen, *J. Phys. III France* 4,1467-1480 (1994)
- 2 X. Li, R. Bocquet, D. Petitprez, D. Boucher, L. Poteau, J. Demaison, *J. Mol. Spectrosc.* 172,449-455 (1995)

## SMMW Ring Lasers with Optical Pump Beam Guiding

Michael Raum

Lehrstuhl für Hochfrequenztechnik, University Erlangen-Nürnberg, D-91058 Erlangen, Germany  
email: michael@lhft.e-technik.uni-erlangen.de

### Introduction

The OH radical, one of the radicals involved in stratospheric chemistry, emits radiation at a frequency around 2.514 THz. For its remote sensing, airborne heterodyne receivers with a local oscillator frequency near the emission line are required. As local oscillators, methanol gas lasers on the 2.522 THz line pumped by a CO<sub>2</sub> laser on its 9 P 36 line are used. The design of a SMMW laser head for airborne applications, which require compactness, efficiency and reliability [1] at this frequency will be introduced.

### Optical Pump Beam Guiding

The ring resonator of the SMMW laser head (perimeter  $L_0$ ) consists of four mirrors (figure 1). The pump beam is injected into the SMMW resonator via a pinhole in a plane mirror 1. Mirror 2 is a focussing mirror (focal length  $f_B$ ) serving for pump beam guiding as well as for SMMW beam guiding. The outcoupling of the SMMW radiation takes place at a hybrid hole mirror 4.

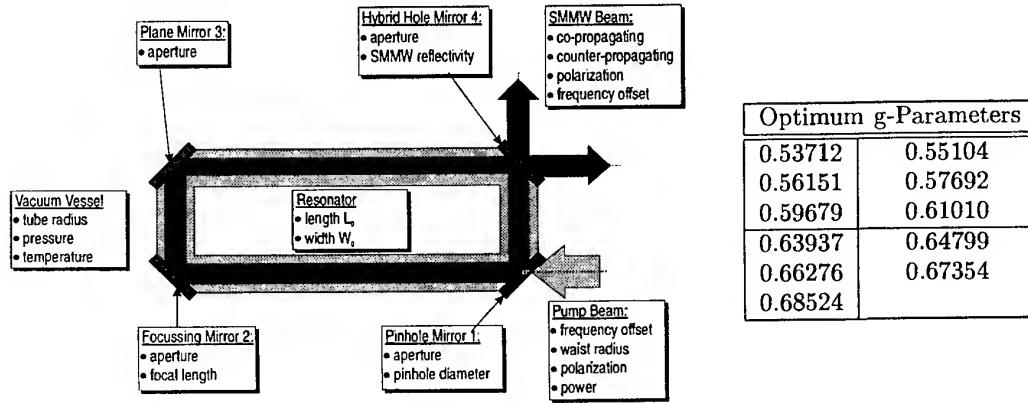


Figure 1: Resonator geometry and parameters important for SMMW output power; table of standard resonator g-parameters

The most important constructional parameters to be determined are the focal length  $f_B$  and the perimeter of the ring resonator  $L_0$ . It is useful to introduce the  $g$ -parameter of the resonator  $g = 1 - \frac{L_0}{2 \cdot f_B}$  as a characteristic measure for the resonator geometry. In order to maximize the SMMW beam volume, but minimize its spotsizes on the mirrors, a  $g$ -parameter around  $g \approx 0.6$  is adequate [2]. But not every  $g$ -parameter provides good pump beam guiding;  $g$ -parameters obeying

$$g = \cos \left[ \frac{\pi \cdot i}{m+1} \right] \quad (1)$$

with  $i$  and  $m$  integers lead to refocussing of the pump beam on the pinhole in the  $m+1$  roundtrip [3], and the remnant pump power is lost. From the viewgraphs given in [4], eleven geometries of resonators providing good pump beam guiding can be derived (see table in figure 1). With perimeter length  $L_0$  and  $g$ -parameter (i. e. the focal length) known, one is able to completely design the ring resonator. With the Rayleigh length of the SMMW beam

$$z_{R,L} = \frac{L_0}{2} \cdot \sqrt{\frac{1+g}{1-g}} \quad (2)$$

the SMMW beam geometry is now perfectly known. The waist radius of the pump beam to be coupled into the resonator is characterized by a pump beam factor  $f_{pb}$  via

$$w_{0,P} = f_{pb} \cdot \sqrt{\frac{z_{R,L} \cdot \lambda_P}{\pi}} \quad (3)$$

and has a maximum spot size of the pump beam

$$w_{P,max} = \frac{1}{f_{pb}} \cdot \sqrt{\frac{L_0 \cdot \lambda_P}{\pi} \cdot \left[ \frac{z_{R,L}}{L_0} + \frac{L_0}{4 \cdot z_{R,L}} \right]} \quad (4)$$

on the focussing mirror. An optimum pump beam factor can be found by compromising between a small  $f_{pb}$  requiring large mirror apertures and a large  $f_{pb}$  increasing the pump beam losses at the necessarily large pinhole;  $f_{pb} = 0.22$  is a good solution.

### Measurement Results

Two SMMW laser heads have been realized in close accordance to the given design process. The first one was based on a 1.5 m perimeter length design with  $g$ -parameter of  $g_1 = 0.551$ , the second one includes a 2 m perimeter length resonator with  $g$ -parameter of  $g_2 = 0.61$ . The perimeter length is thermally compensated by a INVAR-aluminium frame [5]. To provide a tuning range of more than one SMMW wavelength ( $> 119 \mu\text{m}$ ) with an accuracy corresponding to the emission linewidth ( $< 1 \mu\text{m}$ ), a two stage tuning unit consisting of a differential screw and a piezoelectric stack is used.

The measured SMMW laser output power of the strongest SMMW mode, the radial  $\text{TEM}_{01}$  mode, is shown in figure 2 (left) in comparison to the  $\text{TEM}_{00}$  mode for the case of the 1.5 m resonator system.

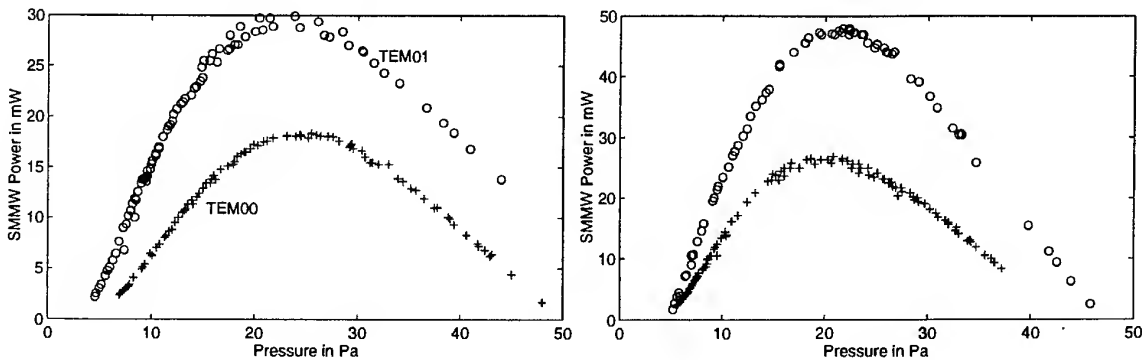


Figure 2: Pressure scans for the  $\text{TEM}_{00}$  and the  $\text{TEM}_{01}$  mode of the 1.5 m laser system (left) and the  $\text{TEM}_{00}$  mode of the 2 m laser system (right).

Both characteristics have been measured at the copropagating end of the SMMW laser for a pump power of 20 W. The better conditions for the  $\text{TEM}_{01}$  mode compared to the  $\text{TEM}_{00}$  mode can be explained by the heating of the laser gas on the optical axis and the fact that the hybrid hole outcoupler is not optimized for this resonator length. A maximum output power of 18 mW for the  $\text{TEM}_{00}$  mode, which is of special interest for the heterodyne application, and 30 mW for the  $\text{TEM}_{01}$  mode have been observed. The scattering in the higher power part of the  $\text{TEM}_{01}$  mode scan is due to two modes of the pump laser competing with each other; the measurements on the envelope are to be taken as valid.

The outcouplers have been optimized meanwhile. The pressure characteristics of the  $\text{TEM}_{00}$  mode in the 2 m resonator system are shown in figure 2 (right). The maximum output powers are 49 mW in the copropagating direction and 27 mW in the counterpropagating direction.

### Conclusions

The design of SMMW ring lasers using a focussing mirror for optical pump beam guiding has been described. The features of two compact system prototypes optimized for the  $119 \mu\text{m}$  methanol line have been presented, measurement results have been given.

### References

1. G. Chin. *International Journal of Infrared and Millimeter Waves*, 8(10):1219-1234, 1987.
2. M. Raum. *5th International Workshop on Terahertz Electronics*, Grenoble 1997.
3. G. A. Koepf and N. McAvoy. *IEEE Journal of Quantum Electronics*, QE-13(6):418-421, 1977.
4. M. Raum. *International Journal of Infrared and Millimeter Waves*, 16(12):2147-2161, 1995.
5. M. Raum. *4th International Workshop on Terahertz Electronics*, Erlangen 1996.

## Effects of Buffer Gas N<sub>2</sub> on Miniature Optically Pumped NH<sub>3</sub> Submillimeter Wave Cavity Laser Emission at 67.2μm

Luo Xizhang, Luo Jiancong, Qin Jiayin

Department of Electronics, Zhongshan University, Guangzhou 510275, P.R.China

### ABSTRACT

The effect of buffer gas N<sub>2</sub> on miniature optically pumped NH<sub>3</sub> submillimeter wave (SMMW) cavity laser emission at 67.2μm was studied theoretically and experimentally. It has been found that:

1. N<sub>2</sub> had a positive effect on laser output of 67.2μm,
2. sharp absorption in laser spectrum under certain gases mixture pressure corresponded to the threshold of "bottleneck effect".

### INTRODUCTION

NH<sub>3</sub> pumped by TEA-CO<sub>2</sub> laser line has been known as an effective SMMW emission source [1, 2]. In mini-cavity laser, NH<sub>3</sub> operates with very high pressure (compared with the conventional cavity laser), interaction of Raman processes has significant effect on SMMW emission, leading to high power output, wide band spectral characteristics and wide range frequency tunability [3]. However, the efficiency of this laser is very low (less than a percent). This low efficiency is largely caused by the so called "bottleneck effect" - a large accumulation of population in lower laser level caused by a slow vibration relaxation rate and thus a great reduction of population between the upper and the lower laser levels [4]. In this paper, based on the density matrix equation theory, the effect of buffer gas NH<sub>3</sub> was calculated and was verified by experiment.

### THEORETICAL DISCUSSION

Our calculation was based on the density matrix equation theory and the gain superposition principle, which have been described in detail elsewhere [3]. The relevant energy levels of NH<sub>3</sub> molecule and that of buffer gas N<sub>2</sub> were shown in Fig. 1. NH<sub>3</sub> was a six-level system and level J=5 (v=0) of N<sub>2</sub> was near-resonant with level s(5,0) (v=2) of NH<sub>3</sub> ( $\Delta E < 2.5 \text{ cm}^{-1}$ ).

The effect of buffer gas N<sub>2</sub> was included in our calculation. In the presence of N<sub>2</sub>, the relaxation time  $\tau$  was determined by the collision between NH<sub>3</sub> molecules and by the collision between NH<sub>3</sub> and N<sub>2</sub> molecules as follows (collision between N<sub>2</sub> molecules had no effect on  $\tau$ ):

$$\frac{1}{\tau} = \frac{1}{\tau_{AA}} + \frac{1}{\tau_{AB}} \quad (1)$$

$$\frac{1}{\tau_{AB}} = \eta \pi (d_A + d_B)^2 \left[ \frac{2kT(m_A + m_B)}{\pi m_A m_B} \right]^{1/2} n_B \quad (2)$$

Where the subscripts A and B denoted NH<sub>3</sub> and N<sub>2</sub> respectively, m- the molecule mass, d- the diameter of the molecule, n- the number of molecule per unit volume, T- the absolute temperature of the system.  $\eta$ - the probability of de-exciting a NH<sub>3</sub> molecule in a given collision with a N<sub>2</sub> molecule.

---

\* This work is supported by the National Natural Science Foundation of China.



$\eta$  should be deduced and calculated by quantum theory. For simplicity, it was assumed that  $\eta$  was 1 for near-resonant or resonant energy transfer caused by collision between  $\text{NH}_3$  and  $\text{N}_2$  molecules and was 0 for off-resonant energy transfer.

### RESULTS AND DISCUSSION

The calculated spectrum characteristics of miniature OPSMMW cavity laser emission at  $67.2\mu\text{m}$  was shown in Fig. 2 and was verified by our experiment. Compared with that of our early work [3], it could be seen that:

1. a very wide band ( $\sim 13\text{GHz}$ ) laser emission was roughly the same as that without buffer gas  $\text{N}_2$ .
2. sharp absorption appeared in the spectrum under certain gases mixture pressure (35 Torr in our case), about 20% more SMMW laser power was output.

Under certain gases pressure, "bottleneck effect" became serious and dominated the transition where AC Stark splitting centers of each Raman process was located, there the population inversion was broken and SMMW laser transition stopped, leading to sharp absorption in the spectrum. With higher pressure, collision between  $\text{NH}_3$  and  $\text{N}_2$  molecules became more frequent, the effective near-resonant energy transfer from  $\text{NH}_3$  molecules in lower laser level to  $\text{N}_2$  molecules greatly reduced the influence of the undesired "bottleneck effect". Obviously, the gases mixture pressure under which the sharp absorption appeared corresponded to the threshold of "bottleneck effect".

The study of the threshold of "bottleneck effect" would lead to a more comprehensive understanding of the mechanism of buffer gas and would be significant to the optimized operation of OPSMMW laser.

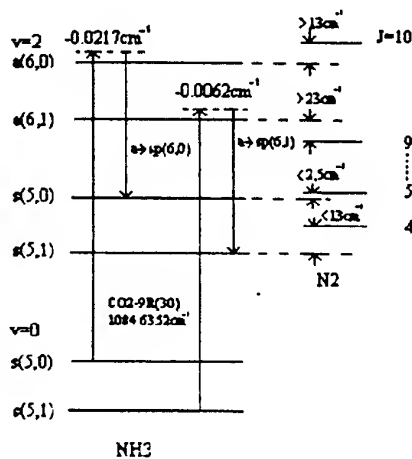


Fig. 1, Part of energy levels of  $\text{NH}_3$  and  $\text{N}_2$  related to  $67.2\mu\text{m}$  emission

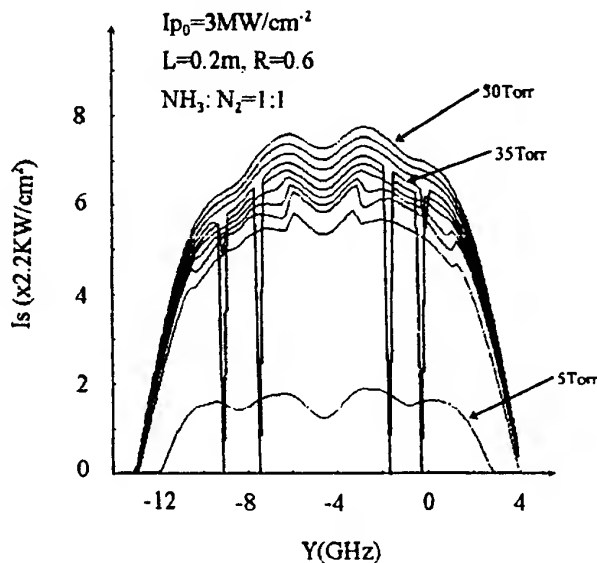


Fig. 2, The calculated spectrum characteristics of mini-OPSMMW  $\text{NH}_3$  cavity laser emission at  $67.2\mu\text{m}$  (with buffer gas  $\text{N}_2$ )

### REFERENCES:

1. H.O.Everitt et al., Appl. Phys. Lett., 49(16), 995(1986).
2. Lin Yikun et al., Int. J. IR-MMW, 10(12), 1427(1989).
3. Luo Xizhang et al., Int. J. IR-MMW, 18(3), 653(1997).
4. T.Y.Chang et al., J. Opt. Soc. Am., 66(4), 362(1976).

## A Method of Remotely Steering a Microwave Beam Launched from a Highly Overmoded Corrugated Waveguide

C.P. Moeller

General Atomics, P.O. Box 85608, San Diego CA 92186-5608, USA

A primary application of high power millimeter waves is electron cyclotron heating and current drive in magnetically-confined plasma research. Transmission of the power from generator to load, if skin effect losses, risk of microwave breakdown, and first wall penetration area are to be minimized, can best be accomplished by using corrugated waveguide having transverse dimensions  $\gg \lambda_0$ , where  $\lambda_0$  is the free space wavelength. However, for a fixed frequency or even a step tunable source, such as a gyrotron, localization of current drive requires toroidal or poloidal steering, depending on electron temperature [1].

Although this steering can be accomplished by rotatable mirrors within the vacuum vessel, engineering details are challenging, and reliability remains a question [2]. A method of controlling the angle at which a microwave beam is launched from a corrugated waveguide is described which places the only moving parts many meters from the waveguide output. This approach was first developed as an alternative to the internal moving mirror baseline design for ITER [3].

### Description and Results

The proposed scheme for remote beam steering requires the use of a square or rectangular corrugated waveguide. Designating  $b(z)$  as the waveguide height in the steering plane ( $y$ - $z$  plane), and  $b_0$  the waveguide height at the output, it is necessary that  $b_0 > 10\lambda_0$  for this scheme to be useful. Designating the transverse dimension orthogonal to  $b$  as  $a$  (along  $x$ ), the effective wave number in the  $y$ - $z$  plane is  $k_{\parallel} = [(2\pi/\lambda_0)^2 - (\pi/a)^2]^{1/2}$ . To avoid the complication of diffraction in the  $x$ - $z$  plane outside the waveguide, we will let  $a \rightarrow \infty$ , so that the geometry is truly 2D and  $k_{\parallel} = 2\pi/\lambda_0 = k_0$ .

A Gaussian-like beam will be emitted from the output of a square or rectangular corrugated waveguide at  $\phi$  radians with respect to the waveguide ( $z$ ) axis if the  $E_y$ -field component has the profile at the outlet:  $\sin(\pi y/b_0) \exp(i\phi k_0 y)$ . This profile can be expanded in terms of the normal modes of the waveguide as  $E_y = \sum_{n=1}^{\infty} B_n \sin(n\pi y/b_0)$ , where the coefficients are given by:

$$B_n = \frac{-i4nu \{ \exp[i\pi(u-n)] + 1 \}}{\pi [u^2 - (n+1)^2] [u^2 - (n-1)^2]}, \quad (1)$$

where  $u = \phi k_0 b_0 / \pi$ . If these mode amplitudes could be excited at some remote point such that the modes arrived at the waveguide output with the phases required by (1), remote steering would be achieved.

It is interesting to see which modes contribute to the far field radiation pattern for a given value of  $u$  in (1). A 2D far field pattern [4] for the case  $u = 14$  (which corresponds to  $\phi = 11.1^\circ$  for  $b_0 = 6.35$  cm at 170 GHz) is plotted in Fig. 1 for modes of index 14, 13-15, and 12-16. The five modes account for 99.3% of the total radiated power. When  $u$  is not an integer, the basic behavior is the same so that the output pattern shape only changes weakly with  $\phi$ .

The required mode amplitudes can be excited most easily by the inverse process, e.g., launching a beam into the waveguide input at angle  $\phi$ . In addition, the correct phases are given by (1), so with this excitation, it is "only" necessary for the relative phases to replicate at the waveguide output.

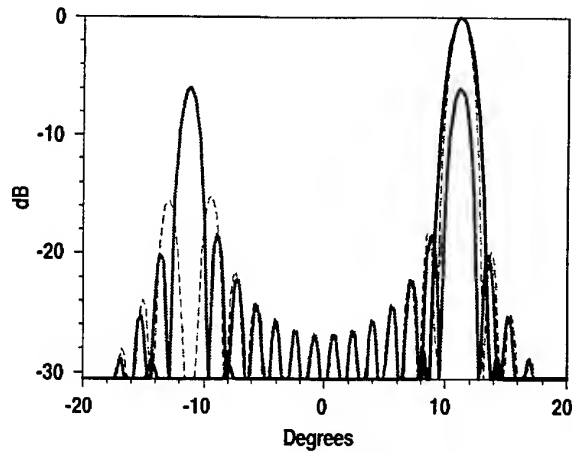


Fig. 1. The far field pattern of the  $N = 14$ ,  $N = 13-15$ , and  $N = 12-16$  modes having amplitudes given by Eq. (1) radiated from an aperture of height  $b_0 = 6.35$  cm at 170 GHz. The corresponding power in the main lobe is 50%, 83.5%, and 99.3%.

The accumulated phase difference between any two modes of indices  $m$  and  $n$  along a waveguide of length  $L$  (which in general may be tapered) is given by:

$$\Delta \psi_{m,n} = \int_0^L \left\{ k_0^2 - [m\pi/b(z/L)]^2 \right\}^{1/2} - \left\{ k_0^2 - [n\pi/b(z/L)]^2 \right\}^{1/2} dz \quad (2)$$

$$= \frac{\pi^2}{2} \frac{k_0 L I_1}{(k_0 b_0)^2} (n^2 - m^2) \left[ 1 + \frac{1}{4} (\phi_n^2 + \phi_m^2) \frac{I_2}{I_1} + \frac{1}{8} (\phi_n^4 + \phi_n^2 \phi_m^2 + \phi_m^4) \frac{I_3}{I_1} + \dots \right]$$

where  $I_p = b_0^{2p} \int_0^1 dt / b(t)^{2p}$ ,  $\phi_p = p\pi/k_0 b_0$ , and  $b(t) \geq b_0$ . Considering first only the lowest order term of (2), if we choose  $k_0 L = (4/\pi)(k_0 b_0)^2/I_1$ , so that  $\Delta \psi_{1,2} = 6\pi$ , then  $\Delta \psi_{m,n} \approx 2\pi(n^2 - m^2)$ . Therefore, if  $\phi_n^2$  and  $\phi_m^2 \ll 1$ , so that the higher terms of the binomial expansion can be neglected, all the incident modes come back into phase over this length, and the tilted input beam is replicated at the waveguide output. It was pointed out by G. Denisov [5] that the tilted beam would also be replicated at  $L/2$ , but at  $-\phi$ , thereby reducing both the required waveguide length and the phase error.  $k_0 L = (2/\pi)(k_0 b_0)^2/I_1$  will be used in all plots that follow. In particular, if  $b(z/L) = b_0$ ,  $k_0 L = 2(k_0 b_0)^2/\pi$ .

Figure 2 shows examples of a 2D far field pattern of a beam steered through a uniform waveguide, which shows a useful range of about  $\pm 10^\circ$ . The steering range can be extended to  $\pm 15^\circ$ , as shown in Fig. 3 by reducing  $L$  by  $-\Delta L$  where  $\Delta L/L = 1 - 4N\pi/(\Delta \psi_{N,N+1} - \Delta \psi_{N,N-1})$  and  $N$  is chosen so that  $N - 1/2 < u \leq N + 1/2$ .  $\Delta L/L$  varies approximately as  $\phi^2$ . Varying the length with angle requires a line stretcher or a means of changing the effective position at which the input beam enters the waveguide.

Regarding any further steering range extension, for modes having significant amplitudes in Eq. (2),  $\phi_n$  and  $\phi_m \approx \phi$ , so phase errors can only be reduced by reducing  $I_2/I_1$  and  $I_3/I_1$ . The form of  $b(z/L)$  that has been examined so far is  $b(t) = b_0(R - (R - 1)t^k)$ , where  $Rb_0$  is the input height and  $b_0$  is the output height. For  $k = 1$ ,  $k_0 L = 2R(k_0 b_0)^2/\pi$ , and for  $R = 3$ , for example,  $I_2/I_1 = 0.48$  and  $I_3/I_1 = 0.30$ .

For  $k = 2$ ,  $k_0 L = 4R(k_0 b_0)^2/\pi \{1 + \ln[(1 + \alpha)/(1 - \alpha)]/2R\alpha\}$ , where  $\alpha = \sqrt{(1 - 1/R)}$ . For  $R = 3$ ,  $I_2/I_1 = 0.39$  and  $I_3/I_1 = 0.22$ , which further reduces the phase error, although unlike the linear taper, this parabolic taper has no set of normal modes, so mode mixing near  $\phi = 0$  needs to be examined. Figure 4 shows that with  $R = 3$  and  $k = 2$ , steering  $\pm 24^\circ$  is possible.

The performance of various profiles with and without  $\Delta L$  length correction is summarized in the Table 1 for the same  $k_0 b_0$  as in the examples above. The last column in the table, "ohmic loss," is the ratio of the total attenuation in the taper to that of a uniform waveguide having the same  $k_0 b_0$  and radiating at the same exit angle  $\phi$ . Compared to the  $HE_{1,1}$  mode, the  $HE_{n,1}$  mode has  $n^2$  times the loss, but still varies as  $1/b^3$  locally.

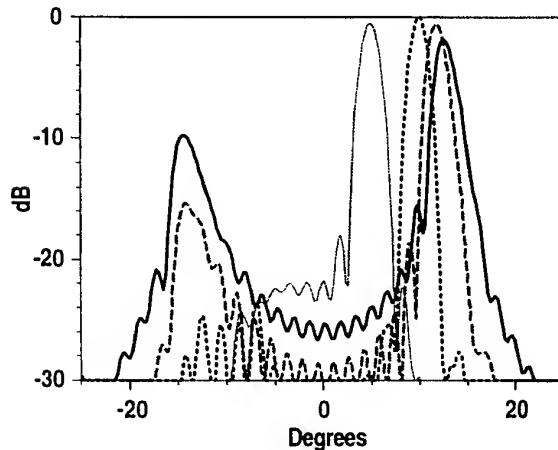


Fig. 2. Radiation patterns of a remotely steered Gaussian beam from a uniform waveguide of height  $b_0 = 6.35$  cm at 170 GHz. Ratio of power in range  $(\phi - 5^\circ, \phi + 5^\circ)$  to total power:  $5^\circ$ : 97.3%;  $10^\circ$ : 98.6%;  $12^\circ$ : 93.6%;  $13^\circ$ : 78.7%;  $L = 8.996$  m.

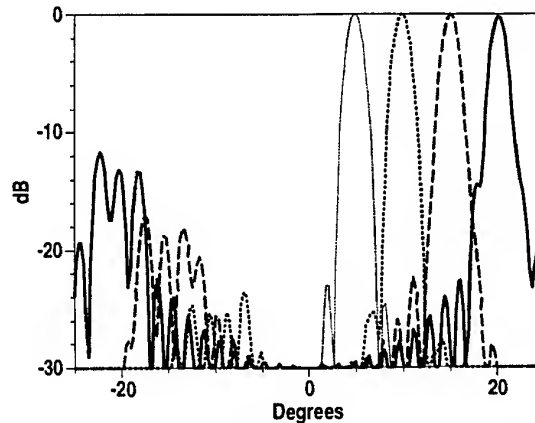


Fig. 3. Radiation patterns of a remotely steered Gaussian beam from a uniform waveguide of height  $b_0 = 6.35$  cm at 170 GHz. Ratio of power in range  $(\phi - 5^\circ, \phi + 5^\circ)$  to total power:  $5^\circ$ : 99.8%;  $10^\circ$ : 98.6%;  $15^\circ$ : 95.5%; and  $20^\circ$ : 87.4%;  $L = 9.150$  m,  $\Delta L$ :  $-3.2, -15.1, -32.5, -57.0$  cm.

### Windows

A window is often required near the vacuum vessel to separate its vacuum from the waveguide vacuum. If the disk or plate thickness is chosen so that  $\rho = 0$  for an incident angle  $\theta$ , where  $\rho$  is voltage reflection coefficient, then as a function of steering angle  $\phi$ :

$$\rho(\phi, \theta) \approx \frac{-i(\sqrt{\epsilon} - 1/\sqrt{\epsilon}) \tan[N\pi(\theta^2 - \phi^2/2\epsilon)]}{2 + i(\sqrt{\epsilon} + 1/\sqrt{\epsilon}) \tan[N\pi(\theta^2 - \phi^2/2\epsilon)]} \quad (3)$$

where  $\epsilon$  is the relative dielectric constant of the disk and  $N$  is the number of half wavelengths in the dielectric. As an example, let  $\epsilon = 5.7$  (diamond) and  $N = 5$ . Then for  $\theta = 0$ ,  $\rho^2 \leq 2 \times 10^{-3}$  over  $-11^\circ \leq \phi \leq 11^\circ$ , while for  $\theta = 10.5^\circ$ ,  $\rho^2 \leq 2 \times 10^{-3}$  over  $\pm 20^\circ$ .

### Conclusions

We have shown that it is theoretically possible to steer the exit angle  $\phi$  of a Gaussian-like beam radiated from a highly overmoded rectangular corrugated waveguide as much as  $\pm 24^\circ$  by injecting a similar beam in to the uniform or tapered waveguide at a specific distance from the exit (typically 10s of meters). This distance takes the approximate form  $L_0 \times [1 - (\phi/\phi_0)^2]$ , where  $L_0$  and  $\phi_0$  are constants dependent on the taper profile and  $k_0 b_0$ .

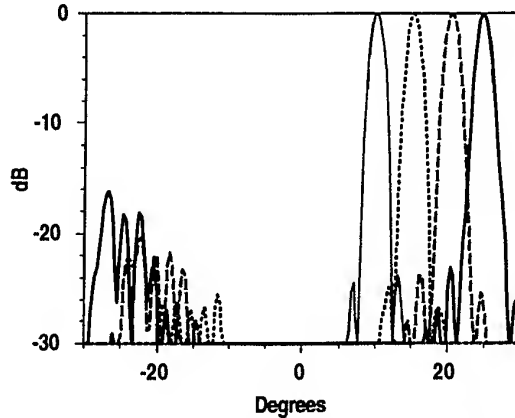


Fig. 4. Radiation patterns of a remotely steered Gaussian beam from a parabolically tapered (3:1 in:out) waveguide of output height  $b_0 = 6.35$  cm at 170 GHz. Ratio of power in range  $(\phi - 5^\circ, \phi + 5^\circ)$  to total power:  $10^\circ$ : 99.7%;  $15^\circ$ : 99.0%,  $20^\circ$ : 97.2%;  $24^\circ$ : 95.2%;  $L = 37.380$  m,  $\Delta L$ : -23.8, -51.5, -90.5, -132.3 cm.

Table 1: Summary of Examples

Taper/ $\Delta L$ Length	$\phi^\circ$	$\eta$ at $\phi$	$L$ m	$\Delta L$ at $\phi$ , cm	Ohmic Loss
uniform/ $\Delta L = 0$	12/13	93.6/78.7	8.996	0	1
uniform/ $\Delta L \neq 0$	15/20	95.5/87.4	9.147	-32.5/-57.0	1
lin $R = 2/\Delta L = 0$	15/16	95.6/87.3	17.984	0	0.75
lin $R = 2/\Delta L = 0$	15/16	97.4/91.8	27.052	0	0.67
lin $R = 3/\Delta L \neq 0$	20/24	96.2/93.5	27.436	-84.7/-119.4	0.67
par $R = 2/\Delta L = 0$	15/16	97.1/91.4	22.220	0	0.68
par $R = 2/\Delta L \neq 0$	20/24	96.3/93.5	22.536	-68.7/-99.3	0.68
par $R = 3/\Delta L \neq 0$	20/24	97.2/95.2	37.380	-90.5/-132.3	0.59

### References

- [1] R. W. Harvey, W. M. Nevins, G. R. Smith, B. Lloyd, M. R. O'Brien, and C. D. Warrick, Nucl. Fusion **37**, 69 (1997).
- [2] R. Prater, H. J. Grunloh, C. P. Moeller, J. L. Doane, R. A. Olstad, M. A. Makowski, R. W. Harvey, in Electron Cyclotron Emission and Electron Cyclotron Heating," in Proc. 10th Joint Workshop on Electron Cyclotron Emission and Electron Cyclotron Resonance Heating, April 6-11, 1997, Ameland, The Netherlands (Work Science Publishing, Singapore, 1995), pp. 534-537.
- [3] R. Prater, H. J. Grunloh, C. P. Moeller, J. L. Doane, R. A. Oldstad, M. A. Makowski, R. W. Harvey, *ibid* pp. 537-539.
- [4] Microwave Antenna Theory and Design edited by S. Silver (Peter Peregrins Ltd., London, 1984), pp. 182-183.
- [5] G. Denisov, private communication at the conference referenced in [3].

## Internal Mode Converter Mirror Shaping from Measured Field Intensity

D.R. Denison, M.A. Shapiro, R.J. Temkin

Plasma Science and Fusion Center  
Massachusetts Institute of Technology  
167 Albany St., Cambridge, MA 02139, USA

S. Cauffman, T.S. Chu, K. Felch

Microwave Power Tube Products Division  
Communications and Power Industries  
811 Hanson Way M/S B-450  
PO Box 50750, Palo Alto, CA 94303-0750, USA

### Abstract

A new approach to mode converter mirror design is presented. The proposed method uses field intensity measurements and a fast numerical phase retrieval algorithm to fully account for the mode converter field structure in the mirror design. Phase-correcting mirrors are designed from this reconstructed field to synthesize a desired beam on the output window of the gyrotron. The method is applied to a 110 GHz gyrotron internal mode converter to produce a 1.52cm waist Gaussian beam at the gyrotron window. Cold test measurements of the mirrors validate the proposed method, producing a Gaussian beam with the specified characteristics.

### Introduction

Quasi-optical internal mode converters ([1],[2]; see Figure 1) designed from theory and numerical simulations effectively transform the high-order gyrotron cavity mode into a free space beam; however, the measured field intensity pattern on the gyrotron window typically exhibits unpredicted behavior that can reduce the overall power handling capability of the window (e.g. [3]). The disagreement between theory and experiment most likely arises from an incomplete theory of the rippled-wall launcher and/or machining errors in the launcher. MIT has developed an alternative approach to mode converter design that uses measured field intensities following the launcher, along with numerical phase retrieval, to account for the full field structure inside the mode converter [4]. A pair of phase-correcting mirrors are then designed from these measured field patterns to produce the desired beam on the window.

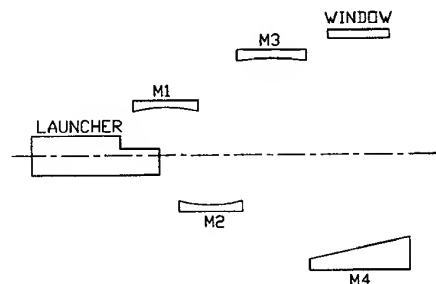


Figure 1: Internal mode converter schematic.

### Approach to Mode Converter Design

Consider the internal mode converter depicted in Figure 1. The proposed design approach employs

the following steps [4]:

1. Design and build (from theory) the launcher and first two mirrors to produce a quasi-Gaussian beam at the surface of mirror 3.
2. Measure the field intensity over several planes parallel to the surface of mirror 3.
3. Retrieve the phase of the beam from the intensity measurements to reconstruct the full field structure of the wave incident on mirror 3.
4. Shape phase-correcting mirrors 3 and 4 to transform the incident wave into the desired field pattern on the window.

### Phase Retrieval and Mirror Shaping

Because of the difficulty in measuring the phase at gyrotron frequencies ( $> 100$  GHz), we rely on a numerical iterative phase retrieval algorithm that uses the measured field intensity over two or more planes to determine the phase of the beam [5,6]. This method propagates the field from plane to plane, and upon each propagation updates the phase function with the measured intensities as constraints. MIT has developed a FORTRAN code implementation of the algorithm which uses an FFT to rapidly compute the inter-plane propagation. The code has been extensively tested for both simulated and experimental data, and it accurately recovers the phase [4].

The mirror shaping procedure is essentially identical to that of phase retrieval, and is similar to that discussed in [7,8]. With the incident beam amplitude and desired window field amplitude as input, the phase retrieval procedure finds a set of self-consistent phases for those amplitudes. The phase correctors then transform the incident and output phases into the self-consistent phases to satisfy the overall beam synthesis problem.

### Design and Experiment: 110 GHz Gyrotron

The 10-cm diameter, double-disk sapphire window in a CPI 110 GHz high-power gyrotron [3] has been replaced with a 5-cm edge-cooled diamond window. The new window requires a well-formed Gaussian beam over its aperture, and the above procedure was used to retrofit the existing mode converter with a pair of phase correcting mirrors to provide the desired Gaussian beam. The mode converter was first placed in a cold test configuration (external to the tube) at CPI and measurements were made over several consecutive planes following the second mirror (M2 in Figure 1). The phase of the beam was then retrieved with the MIT phase retrieval code and the mirrors (M3 and M4 in Figure 1) shaped to synthesize a 1.52-cm waist beam at the window aperture. This beam size corresponds to 99.5% of the beam power passing through the window and minimizes edge heating and diffraction while maintaining an acceptable power density over the window surface. The shaped mirrors were simulated in an independent physical optics code [2], which demonstrated that the mirrors do produce the specified Gaussian beam at the window.

The shaped mirrors were mounted on the mode converter in a cold test set-up and the output beam was measured over planes — perpendicular to the direction of propagation — before, at, and after the window plane. Figure 2(a) shows the measured field intensity at the window. The beam is a centered Gaussian with a  $x$ -waist size of 1.7cm and a  $z$ -waist of 1.6cm. These values are slightly larger than the specified waist of 1.52cm, but the wider beam does not adversely affect the power transmission through the window. Integrating the measured intensity over the window aperture indicates that roughly 98% of the power incident on the window plane will pass through the aperture. Figure 2(b) compares an ideal Gaussian beam with a waist of 1.6cm to the measured beam along the  $z$ -axis. The beam has an excellent Gaussian profile over the range of measurable intensity. Measurements on planes following the window show that the beam propagates perpendicularly to the window plane and evolves as a nearly ideal Gaussian.

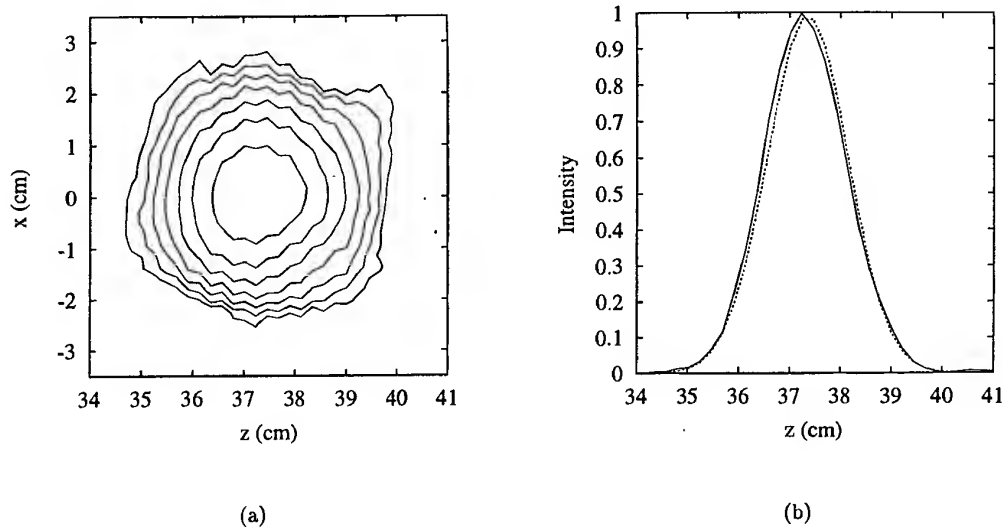


Figure 2: (a) Measured field intensity at window. Contours of constant  $|E_x|^2$  are at 3dB intervals from peak. (b) Measured (solid) and Ideal Gaussian (dashed) field intensity at window along the z-axis.

### Conclusions

We have presented a new approach to internal mode converter design that uses measured field intensities over several planes along with a rapid phase retrieval algorithm to fully describe the true fields in the mode converter. The reconstructed beam serves as input to a mirror shaping procedure that synthesizes a specified output beam from the incident wave. The method was used to modify the internal mode converter for a CPI 110 GHz gyrotron with a diamond window in order to generate a Gaussian beam at the window aperture. Cold test results of the shaped mirrors reveal that the new method works very well, producing a Gaussian beam with the desired size and propagation behavior.

### References

1. G G Denisov *et. al.*, Int. J. Electronics 72, 1079 (1992)
2. M Blank *et. al.*, IEEE Trans. Plasma Sci. 24, 1058 (1996).
3. K Felch *et. al.*, IEEE Trans. Plasma Sci. 24, 558 (1996).
4. D R Denison *et. al.*, 22nd Int. Conf. IRMM Waves Conf. Dig., 81 (1997).
5. B Z Katsenelenbaum and V V Semenov, Rad. Eng. & Elec. Phys. 12, 223 (1967).
6. A P Anderson and S Sali, IEE Proc. 132 Pt. H, 291 (1985).
7. A A Bogdashov *et. al.*, Int. J. IRMM Waves 16, 735 (1995)
8. Y Hirata *et. al.*, IEEE Trans. Microwave Theory Tech. 45, 72 (1997)

## Low and medium power tests on 4 beams launching optics for the 1.6 MW ECRH experiment at 140 GHz on the FTU tokamak

A.Simonetto, A.Bruschi, R.Bozzi, S.Cirant, F.Gandini, G.Granucci, S.Mantovani\*, V.Mellera, V.Muzzini, A.Nardone, N.Spinicchia, C.Sozzi

IFP CNR, v. R.Cozzi 53 - 20125 MILANO ITALY

\*CRE ENEA, v. E.Fermi 27 - 00044 Frascati (RM) ITALY

### Introduction

The Electron Cyclotron Resonance Heating experiment [1] on the FTU tokamak in Frascati is performed with four 400KW, 0.5s gyrotrons at 140GHz [2]. The RF power is injected from the low field side, usually at the first harmonic EC resonance in the ordinary mode. Second harmonic, extraordinary mode can also be used.

Each gyrotron's output beam is corrected for astigmatism and filtered of spurious mode content with a matching optics unit provided by the manufacturer, and the resulting nearly gaussian beam is matched to the transmission line with an elliptical mirror and a polarizer made of two flat corrugated mirrors [3]. The transmission line is made of about 40 m of aluminium corrugated waveguide [4] with an internal diameter of 88.9 mm carrying the HE11 mode. Four quasi optical 90° bends are required to reach the tokamak.

ECRH experiments have been made at short and medium pulse length using a single gyrotron in the last few years [5], the power being launched into the plasma in the equatorial plane from the open end of the corrugated waveguide.

The four beam launching optics has now been installed on FTU to deliver the full power scheduled with good control over the resonance position, and low and medium power laboratory tests were made on the assembled unit before it was mounted on the tokamak.

### Launching optics

The launching optics [1,6] consists of four mirrors per transmission line, three of which under vacuum. The first mirror is outside the vacuum and can be used to switch the power into an external calorimetric load for high power transmission line tests. The last mirror of each line can be adjusted in elevation independently on the others, allowing a wide poloidal scan of the resonance position without adjustment of the toroidal field: -50 mm to +250 mm for line 1, +150 mm to -50 mm for line 2, -150 mm to +50 mm for line 3, -250 mm to +50 mm for line 4, i.e. up to 75% of the minor radius of the vessel (333 mm). Also the azimuth can be varied independently to allow angled RF launch into the plasma after one to three bounces on two flat steel surfaces (with >1µm gold plating) inserted into the narrow port duct of FTU. Electron cyclotron current drive experiments can thus be performed at three discrete angles of incidence (about 10, 20 and 30 degrees).

### Millimeter wave tests

The most extensive measurements were made using a Varian VKT2438N4 10 W Extended Interaction Oscillator feeding a horn-mirror antenna [7] whose output beam closely matches the HE11 from the corrugated waveguide. The radiated power was sampled with a thin partially absorbing target made with black plastic antistatic sheet. The temperature increase of the target was measured with an infrared camera with a telescope lens to give good spatial resolution, using a frame grabber to acquire a frame sequence in order to check for the onset of the vertical image spurious elongation due to hot air convection. The target was placed at 45° to the beam, and the camera's line of sight was perpendicular to the beam, to avoid image distortion. The variation in beam size across the field of view is negligible. The best compromise between detector noise and hot air convection was found at a temperature increase between 10 and 20 °C, which was reached in about five seconds. Fig. 1 shows a typical image.

The beam shapes were measured placing the target at the position of the plasma center, and moving each of the four beams at three different positions, at plasma center and close to full upper/lower range. The beam radius along the toroidal (horizontal) direction is quite close to the design specifications but in the poloidal (vertical) direction the beam is on average 25% larger. This was expected, being a consequence of the beam truncation at a radius equal to the amplitude  $e$ -folding width, which had to be applied to the last mirror because of the dimension of the FTU port duct. Table 1 below lists the measured beam radii at the center position, together with the design specifications. The size of one pixel was taken as the error bar. One can see that the poloidal size of the beams, which is the most significant for plasma heating, is anyway 21 to 37% better than in the preliminary experiments (where it was about 30.5 mm). This translates into a volume power density at plasma center that is 46 to 89% larger than before. The variation of beam radius when moving the resonance position along the vertical plane is usually within 10%.

The angled launch was tested in the equatorial plane for one to three bounces on the side plates. The beam shape was quite good, with small diffraction lobes appearing only with three bounces. Configurations with four and five bounces were also tested, although not useful for ECRH because the plasma absorption would decrease



too much. Appreciable distortion to the beam was found as one might expect, but the beam shape would still be acceptable for plasma heating.

In the angled launch configuration the beam path from the final mirror to the plasma increases with the number of bounces, and the increased beam diameter may cause interaction with the side plates at the end of the narrow port duct. As a consequence of the interaction, a spurious beam may appear opposite to the main one. Attempts to estimate this effect taking IR images of the expected spurious beam gave no signal above the noise for one and two bounces, and a level of  $-14.3$  dB for three bounces. To expand the 8 bit image level, the main and spurious beams were measured in different temperature ranges (2 and 50 °C) when equilibrium had been reached after ten seconds of heating.

A better picture of the beams was taken at low power, using a modulated solid state generator to feed the same horn-mirror antenna. The RF power was measured with a sensitive heterodyne receiver, using a lock-in to detect the modulation in the receiver's output signal. The receiver was moved across the beam using IFP's automated test range. These measurements are intrinsically more precise and have a wider dynamic range, but since they take a much longer time, they were made only on each beam at its center position, and on beam 3 at one bounce. The measured beam shape is well fitted with a gaussian (Fig. 2), with a sidelobe level of  $-17$  to  $-19$  dB in the vertical (poloidal) direction and always below  $-25$  dB in the horizontal (equatorial) plane. The  $-25$  dB threshold is comparable to the sidelobe level in the horn-mirror antenna. Table 2 shows the beams' amplitude  $1/e$  radii as determined from these data. The results are close to the ones estimated from thermal images.

### Conclusions

The four-beam optics for ECRH can deliver millimeterwave power in a narrow region in the FTU plasma. The beam's shape is elliptical and the diameters have been measured and found to be close to what expected. The sidelobes produced by diffraction are small under all circumstances, and the multi-bounce angled launch can deliver power to the plasma with a well controlled  $k_{\parallel}$  spectrum.

### References

- [1] L.Argenti et al, Proc. of 17th Symp. on Fusion Technology, Roma 1992, Vol.1,432  
S.Cirant et al, Proc. 9th Joint Workshop on ECE and ECRH, 105(1995)
- [2] GYCOM Ltd, Nizhny Novgorod, Russia
- [3] A.Bruschi et al, Int.J. of Infrared and Millimeter Waves, 15,8(1994)1413
- [4] General Atomics, San Diego, CA
- [5] S.Cirant et al, Proc. 10th Joint Workshop on ECE and ECRH, 369(1997)
- [6] A.Bruschi et al, to be presented at 20th Symp. on Fusion Technology, Marseille, September 7-11, 1998
- [7] Thomas Keating Ltd, Billingshurst, West Sussex, UK

Table 1

Beam	Spec's	x(mm)	y(mm)
1	18.1	$17.6 \pm .5$	$24.2 \pm .5$
2	17.4	$17.7 \pm .5$	$23.0 \pm .5$
3	17.4	$17.9 \pm .5$	$22.2 \pm .5$
4	18.1	$18.5 \pm .5$	$25.2 \pm .5$

Table 2

Beam	x(mm)	y(mm)
1	20.8	26.0
2	19.9	23.8
3	20.1	23.0
4	20.3	25.3

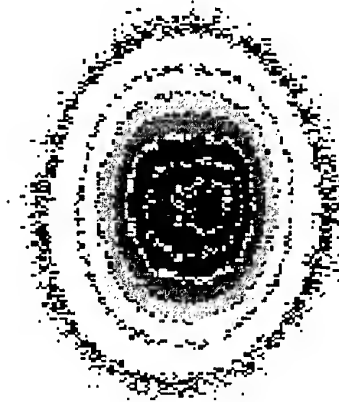


Figure 1 - Typical thermal image. Contours are evenly spaced over the range 0-100%

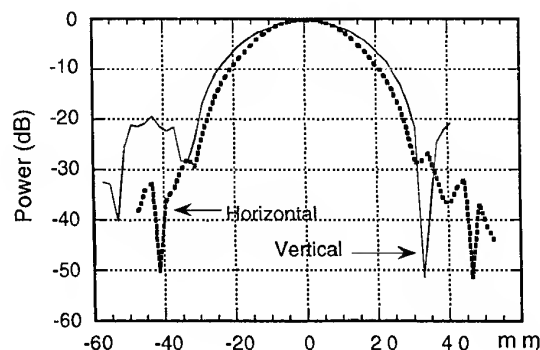


Figure 2 - Horizontal and vertical cross sections of beam 2 in dB. Central resonance.

## A Hybrid Magnet System for a Fast Frequency-Step-Tunable High-Power Gyrotron

K. Koppenburg<sup>†)</sup>, B. Piosczyk, M. Thumm<sup>†)</sup>

Forschungszentrum Karlsruhe, Association EURATOM-FZK,

Institut für Technische Physik, Postfach 3640, D-76021 Karlsruhe, Germany

<sup>†)</sup> also Universität Karlsruhe, Institut für Höchstfrequenztechnik und Elektronik, Kaiserstr. 12, D-76128 Karlsruhe, Germany; e-mail: kai.koppenburg@itp.fzk.de

### Abstract

The design problems of magnet systems for fast (2s) frequency-step-tunable high-power gyrotrons are discussed. A hybrid magnet consisting of a superconducting ( $B \leq 6.5$  T) and a fast variable normal conducting magnet ( $\Delta B \sim \pm 0.25$  T) is presented and the specific problems are considered.

### Introduction

Fast frequency-tunable gyrotrons are of interest for controlling instabilities in magnetically confined plasmas in large fusion reactors like e.g. ITER [1]. The confining magnetic field depends on the radial position in stellarators and tokamaks. Hence, the electron cyclotron resonance interaction between the RF wave and the plasma electrons occurs only in a small plasma layer where the resonance condition is approximately fulfilled. The possibilities to reach other plasma flux surfaces are a change of the gyrotron frequency or mechanically steerable mirrors in the plasma vessel making use of the Doppler effect. Since it is difficult to find a material for such mirrors and a reduction of the number of movable parts is desired, it is obvious that the first solution is more promising.

coils. To prevent quenching the sc solenoids,  $\partial B / \partial t$  is limited to a maximum of  $\sim 0.1$  Tesla/minute. This results in a frequency change of  $\leq 42$  MHz/s. To detect and suppress plasma instabilities in the ITER tokamak the estimated time duration for a frequency variation is of the order of seconds for several GHz [1]. To fulfill these demands at FZK different hybrid magnet systems including one or more fast tunable normal conducting (nc) solenoids are under investigation; the currently favoured one is shown in Figure 1.

### Fast frequency tunability of gyrotrons

**Mechanical tuning :** Several possibilities for mechanical tuning have been considered but found to be impractical for high-power devices [3].

**Electrical tuning :** Electrical tuning is achieved by a variation of the accelerating and modulating voltages in a gyrotron. With the gyrofrequency of the electrons  $\Omega[\text{GHz}] = 28B[\text{T}]/\gamma$  and the relativistic factor  $\gamma = 1 + U[\text{kV}]/511$  the relation between the accelerating voltage and the output frequency, which is always very close to  $\Omega$  or its harmonics, is simple. Unfortunately, the tuning range is limited to  $\sim 0.1\%$  if the quality factor  $Q$  of conventional gyrotrons is about 1000, as is usually the case. For gyrotrons with triode guns theoretical investigations were made in [4] which show that a very fast switching between operating modes is possible by variation of both the accelerating and modulating voltages.

**Magnetic tuning :** The most simple tuning method is changing the magnetic field  $B$ . Since  $\Omega$  is directly proportional to  $B$  and the dependence on the accelerating voltage is small, it is possible to switch between the operating modes by changing the current in the solenoids. The main problem of this frequency step tuning is the large time constant of a current change in large sc magnets. A possible solution is therefore a small auxiliary nc magnet located between the sc-solenoid and the gyrotron. The frequency range of such a system is limited by the maximum reachable B-field of the nc-solenoid.

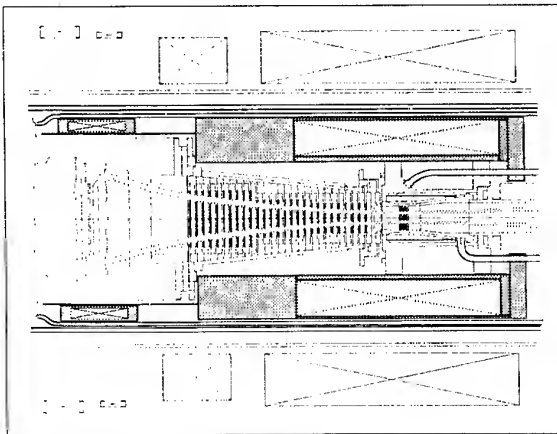


Fig. 1: Gyrotron with hybrid magnet system consisting of two normal conducting solenoids

A 1 MW frequency-step-tunable gyrotron for ITER that operates between 114 and 166 GHz is under development at FZK [2]. In a first step the frequency change has been performed by a slow variation of the magnetic field due to a modification of the current flow in the superconducting (sc)

### Superconducting wires

The losses in sc-wires are dependent on the pinning forces of the penetrated flux in the material. If the Lorentz force density exceeds the pinning force density, the critical current is reached and the wire quenches (becomes normal conducting). The three main reasons for the sc quenching during a current change are the following. Since the technical superconductors magnetization curve is a hysteresis

loop a variation of the magnetic flux is a dissipative process, which produces heat. The area under this curve is a measure for the energy losses. The second reason is the movement of the wires due to the strong forces. The friction heats up the material. The third reason is the eddy current in the copper coat of the sc, produced by the movement of the wire in the B-field and the  $\partial B/\partial t$  itself. Thus the field variation at the sc has to be small enough, that the heat energy can be carried off by the copper and helium, to prevent a temperature increase higher than  $T_c$ .

### Screening cylinders

The first idea to prevent the sc-coils from quenching was a copper cylinder between the nc and the sc-solenoids. A fast change of the magnetic field affects a screening eddy current in the cylinder with the opposite direction of the current change in the nc-coil, so that the B-field change at the sc-magnets is slowed down. For a current variation within 1 s the delay time in a 6 mm thick copper cylinder is  $\sim 14$  ms. Unfortunately the eddy current is like a further magnet which also has an effect on the field at the cavity axis. Therefore a gyrotron operation is not possible until  $I_{cyl}=0$ . For this reason the effect is the same as if the screening time delay is added to the variation time of the magnetic field. Since the time constants of the planned nc-solenoids which are in the order of 150 ms are essentially higher than the delay time of the copper coat, for the magnet system at FZK there are no advantages to use a screening cylinder.

### Operating modes

The development is based on a 140 GHz, 1MW gyrotron designed for operation in the  $TE_{22,6}$  mode. The possible working modes with a similar electron beam radius corresponding to the  $TE_{22,6}$  mode are shown in Table 1. During the experiment the calculated beam radius has been optimized for highest output power.

Mode	Calculated beam radius [mm]	Optimized beam radius [mm]	f [GHz]	$\Delta B$ [Tesla]
$TE_{20,6}$	7.64	7.75	132.6	-0.3
$TE_{21,6}$	7.79	7.88	136.3	-0.152
$TE_{22,6}$	7.94	7.94	140.1	0.0
$TE_{23,6}$	8.07	8.09	143.8	0.148
$TE_{24,6}$	8.21	8.23	147.5	0.296

Tab. 1: Possible working modes with parameters

With the estimated  $B_{max}=\pm 0.25$  Tesla of the nc solenoid the maximal possible frequency variation is  $\sim \pm 6.25$  GHz. To work with the  $TE_{20,6}$  and the  $TE_{24,6}$  mode the current density in the nc magnet has to be increased by 20%.

### Simulations

To calculate the field profiles, currents and energy densities, forces, power and cooling consumptions and the resulting beam radius a program based on the laws of Biot-Savart and Lorentz was written. Results for the planned hybrid magnet system with two nc-solenoids (Figure 1) are shown in Table 2. The maximum current density of  $768 A/cm^2$  requires for a continuous wave operation a water cooling set for the nc-solenoids.

Mode	$R_b$ [mm]	J [ $A/cm^2$ ]	$F_{zGun}$ [N]	$F_{zRes}$ [N]	$P_{Mag}$ [kW]
$TE_{20,6}$	7.73	-768	-145.3	153.1	6.8
$TE_{21,6}$	7.87	-365	-67.7	71.4	1.5
$TE_{22,6}$	7.99	0	0	0	0
$TE_{23,6}$	8.11	422	75.0	-79.3	2.1
$TE_{24,6}$	8.22	768	134.0	-141.7	6.8

Tab. 2: Simulation results

It is very important to minimize the total force to prevent lifting the hanging sc-magnet system. The maximum of less than 8N is a good solution for this problem. The calculated beam radius with the hybrid magnets (curve) agree, as demonstrated in Figure 2, very well with the experimental measurements in Table 1.

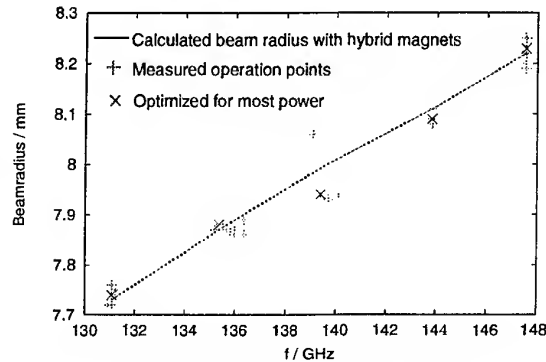


Fig. 2: Electron beam radius depending on frequency

### RF output system

The investigations of diamond brewster output windows in [5] have demonstrated that frequency tuning over a wide frequency band is possible. In [6] it is shown, that the output of the quasi-optical mode converter for the  $TE_{22,6}$  mode at 140 GHz is very similar to that of the  $TE_{19,5}$  mode at 117.8 GHz and the  $TE_{25,7}$  mode at 162.2 GHz. Since the modes of Table 1 have nearly the same Brillouin angle and caustic radius these operating modes work very fine too.

### References

- [1] O. Dumbrajs, J.A. Heikkinen, H. Zohm, Current Profile Control using Fast Frequency Tuning in ECRH and ECCD, Proceedings of the 10th Joint Workshop on ECE and ECH, 91, 1997
- [2] G. Dammertz, M. Thumm et al., Influence of window reflections on gyrotron operation, IRMW Conference Digest, 150, (1997)
- [3] O. Dumbrajs, Tunable Gyrotrons for Plasma Heating and Diagnostics, Riga Aviation University Scientific Reports, Volume 2, (1997/98)
- [4] O. Dumbrajs and G.S. Nusinovich, IEEE Transactions on Plasma Science 20, 452, (1992)
- [5] O. Braz, M. Thumm et al., Frequency Step-Tuned Operation of a 1 MW, D-Band Gyrotron using a Brewster Output Window, ITG-Fachbericht 150, (1998)
- [6] G. Michel, M. Thumm et al., Advanced Quasi-Optical Mode Converter for a Step-Tunable 118-162 GHz, 1MW Gyrotron, IRMW Conference Proceedings, ISBN 3-00-000800-4, (1996)

## Low Power Test Facilities For Characterization of Highly Oversized Gyrotron Components

O. Braz<sup>1,2</sup>, A. Arnold<sup>1,2</sup>, A. Möbius<sup>3</sup>, H.-R. Kunkel<sup>1</sup>, M. Thumm<sup>1,2</sup>

Forschungszentrum Karlsruhe (FZK), <sup>1</sup>ITP, Association EURATOM-FZK, Postfach 3640,  
D-76021 Karlsruhe, Germany

<sup>2</sup>Universität Karlsruhe, Institut für Höchstfrequenztechnik und Elektronik (IHE), Kaiserstr. 12,  
D-76128 Karlsruhe, Germany

<sup>3</sup>Innovative Microwave Technology GmbH, Luisenstr. 23, 76344 Eggenstein- Leopoldshafen, Germany

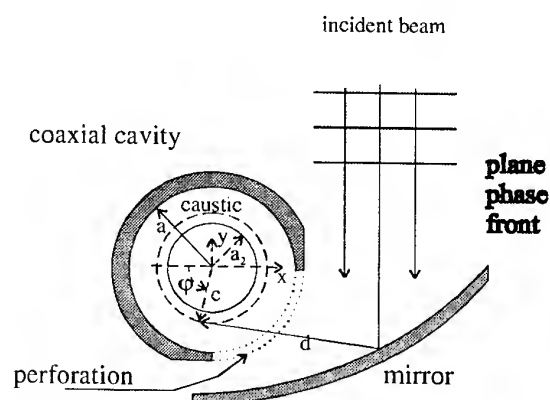
### Abstract

To verify the proper behavior of highly oversized gyrotron components required for the generation and transportation of high power micro- and millimeter-waves, special test facilities are needed. This paper summarizes the status of such low power tests developed at the Forschungszentrum Karlsruhe during the last few years.

### Introduction

In order to increase the generated rf-power of gyrotrons at very high frequencies the size of the ratio of the cavity radius to the wavelength has to be increased to keep the Ohmic losses within technically acceptable limits. This requires the operation in high asymmetric  $TE_{m,n}$  modes. For launching the generated power through a broadband Brewster window, transmission through an  $HE_{11}$  or a quasi-optical waveguide and for plasma heating the gyrotron cavity mode has to be converted into a linearly polarized Gaussian wave beam. This is performed by helically cut antennas with feed waveguide deformations, serving as mode converters, and a series of phase correcting and astigmatism removing mirrors that have to be integrated into the ultra high vacuum system of the tube. Theoretical predictions for these components have to be checked experimentally since for this frequency range and size of the components neither a purely geometrical optical description nor a fully 3D- numerical method based on field discretization is possible. Once these components are integrated into the tube their replacement and alignment is difficult. For this reason their proper performance has to be verified experimentally in advance.

### Quasi-optical mode generation



The main need for the low power analysis of microwave transmission components that are integrated into the gyrotron is the low power generation of high order rotating modes. The principle of the arrangement can be seen in the sketch to the left. The parallel incident rays are reflected by means of a quasi-parabolic mirror such that the reflected rays form a cylindrical caustic which is coincident with the caustic formed by the rays of the desired waveguide mode. Modes of extremely high order such as the  $TE_{+76,2}$  require a coaxial cavity for increased mode selection. To maintain a high quality factor of the cavity the transverse aperture has to be closed by a perforated wall. A detailed description of the

theoretical performance has been given in earlier papers [1, 2, 3]. A variety of mode generators have been built and investigated [4, 5, 6]. Their theoretically predicted behavior has been confirmed by experiments. However additional knowledge has been obtained during this experimental investigation. A complex theoretical description of these additional results would be very difficult. The main tool for the measurements has been the k-spectrometer [7], which requires an extremely high dynamic range of the detecting electronics. For this reason a new analyzer providing a dynamic range of more than 110 dB over the entire frequency range from 70 GHz up to 170 GHz [5, 6] has been constructed.

The measured effects are:

A: Drop of resonant frequency due to the perforation. This drop can be evaluated to be

$$\Delta f \approx 1,4 \cdot f_s / 1000$$

where  $f_s$  is the design frequency of the non perforated cavity.

B: Undesired coupling to  $\Delta m = \pm 1$  modes. This coupling into the undesired modes in all cases has been considerably below 5%, which is determined by an effectively larger radius at the location of the perforation (Fig. 2 a)). For the investigation of transmission line components the effect of these spurious modes is negligible.

C: For extremely high order modes the axial field profile of the beam launched onto the cavity has to match the cavity's field profile (Fig. 2 c)). The required matching can be achieved by either turning the horn antenna as shown in the Fig. 2 b) or appropriate tapering of the coupling holes and/or achieving a narrow waist of the beam launched onto the cavity.

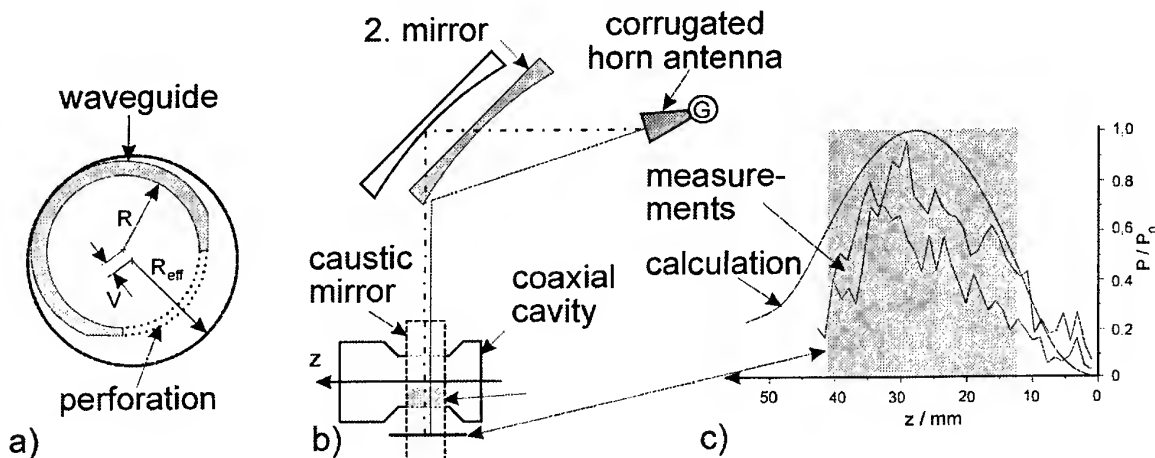


Fig. 2:

### Summary and conclusions

In order to achieve a high mode purity quasi-optical mode generators individually have to be optimized by experiment. The most convenient way is by applying k-spectrometer measurements. By this analysis a series of discrepancies with the theoretical predictions have been found.

The high benefit from low power measurements has been demonstrated by analyzing several quasi-optical mode converter systems. Significant differences in the experimental behavior of the tube compared to theoretical predictions in all cases have been explained by cold test measurements.

### References

1. N.L. Alexandrov, A.V. Chirkov, G.G. Denisov, D.V. Vinogradov, W. Kasperek, J. Pretterebner, D. Wagner, *Int. Journal of Infrared and Millimeter Waves*, **13**, 1369-1385 (1992).
2. N.L. Alexandrov, G.G. Denisov, D.R. Whaley, M.Q. Tran, *Int. Journal of Infrared and Millimeter Waves*, **79**, 215-226, (1995).
3. M. Pereyaslavets, O. Braz, S. Kern, M. Losert, A. Möbius, M. Thumm, *Int. Journal of Electronics*, **82**, 107-115, (1997)
4. Braz, O., Arnold, A., Kunkel, H.-R., Thumm, M., *Proc. 22<sup>nd</sup> Int. Conf. on Infrared and Millimeter Waves*, Wintergreen, Virginia, 21-22, (1997).
5. O. Braz, M. Losert, A. Möbius, M. Thumm, R. Coudroy, E. Giguet, C. Tran, M. Q. Tran, D. R. Whaley, *Proc. 20<sup>th</sup> Int. Conf. on Infrared and Millimeter Waves*, Lake Buena Vista, Florida, 281-282, (1995).
6. O. Braz, A. Arnold, M. Losert, A. Möbius, M. Pereyaslavets, M. Thumm, V.I. Malygin, *Proc. 21<sup>st</sup> Int. Conf. on Infrared and Millimeter Waves*, Berlin, ATh6, (1996)
7. W. Kasperek, G.A. Müller, *Int. Journal of Electronics*, **64**, 5-20, (1988).

## Mode Conversion due to S-Bend Deformation of an Oversized HE<sub>11</sub> Waveguide

B. Plaum<sup>1</sup>, G. Gantenbein<sup>1</sup>, W. Kasperek<sup>1</sup>, M. Thumm<sup>2</sup>, D. Wagner<sup>1</sup>

<sup>1</sup>Universität Stuttgart, Institut für Plasmaforschung  
Pfaffenwaldring 31, D-70569 Stuttgart, Germany

<sup>2</sup>Forschungszentrum Karlsruhe, Association EURATOM-FZK, Institut für Technische Physik and  
Universität Karlsruhe, Institut für Höchstfrequenztechnik und Elektronik,  
P.O. Box 3640, D-76021 Karlsruhe

### 1 Introduction

The movement of the vacuum vessel of large fusion devices like ITER leads to an s-bend type deformation of the connected waveguide antennas. The mode conversion in such a deformed HE<sub>11</sub> waveguide has been calculated and compared with measurements.

### 2 Calculation of the expected mode conversion

The mode conversion in s-bends was described in [1] using a simplified model with only one spurious mode. The calculations show, that for an optimum bend-length of 1.4 times the beat wavelength between the HE<sub>11</sub> mode and the spurious mode (TE<sub>01</sub>), the whole power in the spurious mode will be converted back into the HE<sub>11</sub> mode in the second half of the bend.

For the calculation of the expected mode conversion, the coupled mode equation was used:

$$\frac{\partial A_i}{\partial z} = \gamma_i A_i + \sum_{j=1}^{N, i \neq j} C_{ji} A_j$$

where  $A_i$  is the amplitude of the  $i$ 'th mode,  $\gamma_i = \alpha_i + j\beta_i$  is the propagation constant of the mode, and  $C_{ij}$  is the coupling coefficient for the  $i$ 'th mode and the  $j$ 'th mode. A program was developed to integrate the coupled mode equation numerically. The coupling coefficients for curved corrugated waveguides derived by Li and Thumm [2] are used by the program. The code can take into account an arbitrary number of spurious modes as well as ohmic losses. The s-bend geometry is approximated by a 3<sup>rd</sup> order polynomial [1]:

$$y(z) = \frac{zD}{2L^3}(3L^2 - 4z^2)$$

where  $z$  is the coordinate along the bend,  $D$  is the total displacement of the bend and  $L$  is the total bend length (see Fig. 1). For the calculations, the following parameters were used:

Total deflection $D$ :	27 mm
Frequency:	140 GHz
Corrugation depth	0.41 $\lambda/4$ ( $\approx 220 \mu\text{m}$ )
Waveguide diameter:	70 mm

Fig. 2 shows the fractional power sum of spurious modes at the bend output for different lengths of the bend. One can see, that for a length of 6.6 m, the spurious modes approach a minimum.

### 3 Comparison with measurements

To confirm these calculations, a low power experiment has been designed and built. The available waveguide has a diameter of 70 mm and is coated with 70  $\mu\text{m}$  of Al<sub>2</sub>O<sub>3</sub>. The wall impedance due to the dielectric layer corresponds to a corrugation depth of 220  $\mu\text{m}$  for the HE<sub>11</sub> mode. To generate the HE<sub>11</sub> mode, a lens horn antenna has been used and attached directly to the waveguide (See Fig. 3). The results presented

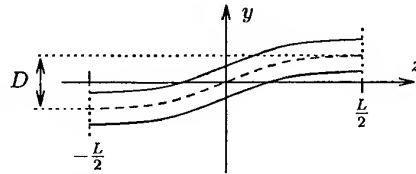


Fig. 1: Geometry of an s-bend

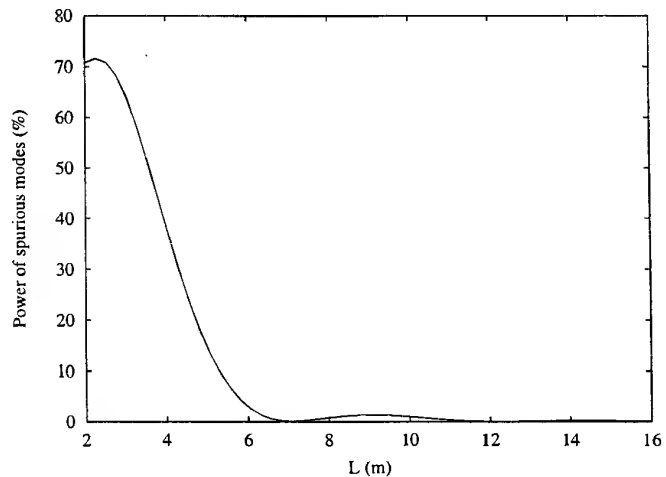


Fig. 2: Content of spurious modes at the output of a s-bend for different lengths.

here are the co-polarised components of the electric field at a distance of 2.12 m from the open end of the bend. For the optimum length of 6.6 m, the spurious mode content is less than 0.5 % at the bend output. The far field of such a mode mixture is a gaussian-like beam which is expected for the  $HE_{11}$  mode (see Fig. 4). To further check the codes and to compare the results with measurements, calculations have been performed for a bend length of 3.3 m, which leads to a higher amount of spurious modes (see Fig. 2). The power of the  $HE_{11}$  mode is only 42 % of the total power for this bend length. For this case, the far field was also calculated and measured (see Fig. 5) and a good agreement is found.

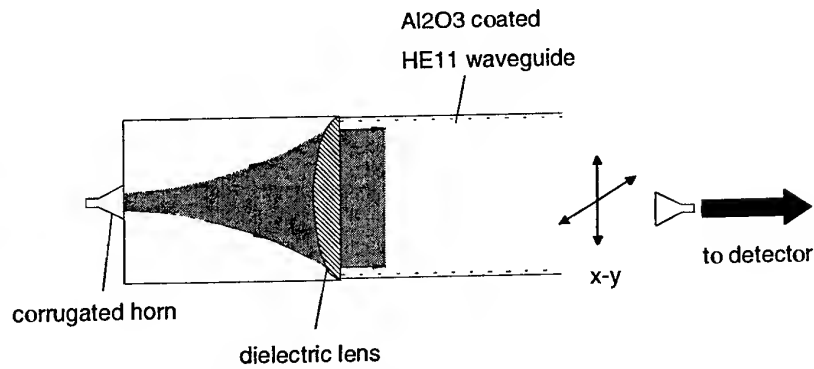


Fig. 3: Experimental set-up for far-field and near-field measurements

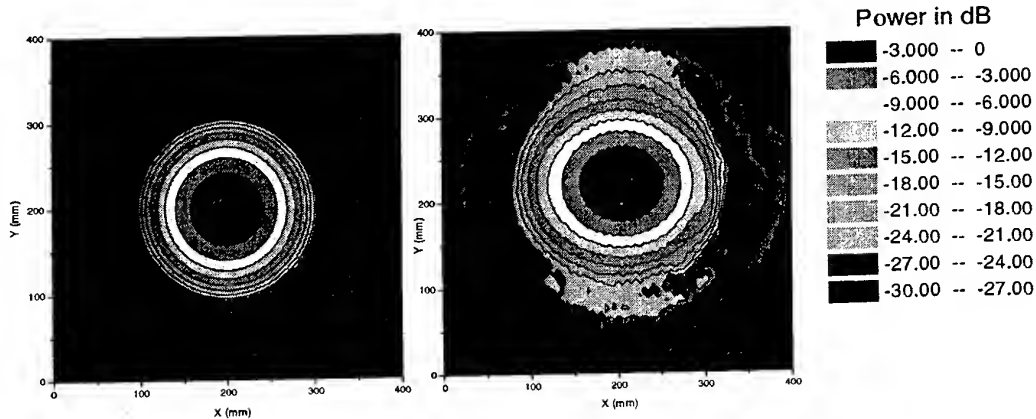


Fig. 4: Far field of a mode mixture at the output of an s-bend (length: 6.6m) calculated (left) and measured (right).

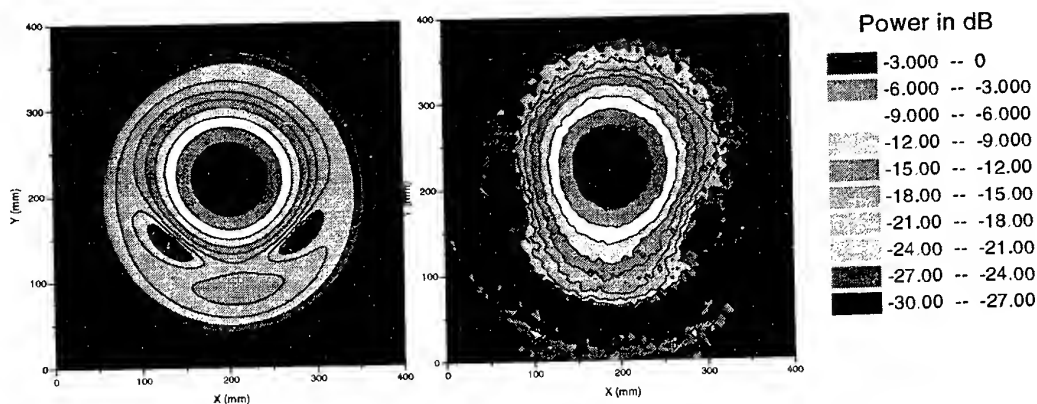


Fig. 5: Far field of a mode mixture at the output of an s-bend (length: 3.3 m) calculated (left) and measured (right).

### 3 References

- [1] Doane, J. L., Mode Conversion in S-Bends, ITER ECRH Meeting
- [2] Li, H., and Thumm, M., Mode conversion due to curvature in corrugated waveguides. *Int. J. Electronics* (1991), 333-347.

## Movable mirror system using supersonic motor for the LHD-ECH antenna

S. Sasaki, Y. Kanai, K. Wakabayashi, A. Hayakawa, S. Kawashima, F. Saito, K. Yamamoto (1),  
T. Ohgawara (1), Y. Obiya (1), S. Kubo (2), K. Ohkubo (2), and T. Watari (2)

Machinery and Equipment Dept., Toshiba Corp., 2-4 Suehiro-cho, Tsurumi-ku, Yokohama 230-0045, JAPAN,

(1) Toshiba Engineering Corp., 66-2 Horikawa-cho, Saiwai-ku, Kawasaki 210-0913, JAPAN

(2) National Institute for Fusion Science, Toki-shi, Gifu 509-5202 JAPAN

### Abstract

An antenna with supersonic motors for the ECH (Electron Cyclotron Heating) system on LHD (Large Helical Device) enabled the operation under high magnetic field ( $\sim 4$  T). Four antenna mirrors provide a well focused millimeter wave beam of  $15 \times 50$  [mm] (waist size), with steering range of  $\pm 220$  mm (radial)  $\pm 180$  mm (toroidal) at the mid plane. Aluminum (A5052) and stainless steel (SUS304) mirrors are cooled by water, capable for CW and 500 kW - 1 MW transmission.

### I. Introduction

LHD is a heliotron type plasma device at NIFS (National Institute for Fusion Science), which has superconducting magnets with major radius of 3.9 m. The ECH antenna is designed to meet various requirements; a) non-magnetic materials, b) 1 MW-CW transmission, c) 2-axis mirror drive system, d) well focused beam, d) compact dimensions compatible to the limited port size [1,2]. This antenna is relevant to the ITER (International Fusion Experimental Reactor) class superconducting fusion device with a megawatt level ECH heating.

### II. ECH transmission system

The ECH transmission system conveys 84 GHz, 82.6 GHz, and 168 GHz microwave to the antenna. Each transmission line have total length of 120 - 150 m and 17 - 20 miter bends, operated with filling air or flowing dried air. The corrugated waveguide has 88.9 mm diameter, and corrugation with 0.8 / 0.6 / 0.6 [mm] period, depth and width. The miterbend has a flat mirror with 1 MW - CW transmission capability. The waveguides were aligned using a transit within  $\sim 0.3$  mm linearity. Bend mirrors were adjusted using He-Ne laser within 0.5 - 1 mrad precision. Four transmission lines were connected to the antennas at 5.5 U and 9.5 U ports, through BN (water cooled) or SiN (water and dry air cooled) windows.

### III. Antenna system

The antenna unit has 84 GHz and 168 GHz launchers, Fig. 1. Each launcher has four mirrors; m1: flat mirror (SUS) driven by supersonic motors, m2: concave mirror (SUS), m3: flat mirror (Al), and m4: concave mirror (Al). Rotation angles of m1 mirror around the horizontal and vertical axes are  $\pm 8^\circ$  and  $\pm 3^\circ$ , respectively. The m1 and m2 mirror, has  $\sim 250 \times 300$  [mm] dimensions and circular water channels, Fig. 2(a), designed for 1MW-CW transmission. The plasma facing mirrors m3 and m4, has  $\sim 300 \times 450$  [mm] dimensions and rectangular water channels, Fig. 2(b), bearable for 500 kW - CW transmission at 168 GHz. The concave mirrors were machined with the precision of  $20 \mu\text{m}$  ( $< 1/80\lambda$ ). Center area (20 mm dia.) of mirrors were polished for the laser alignment. Those mirrors are assembled on the antenna unit with a flange with  $1040 \times 565$  [mm] dimensions and four support pipes of 2320 [mm] length. Two of those pipes are employed as water channels. A corrugated

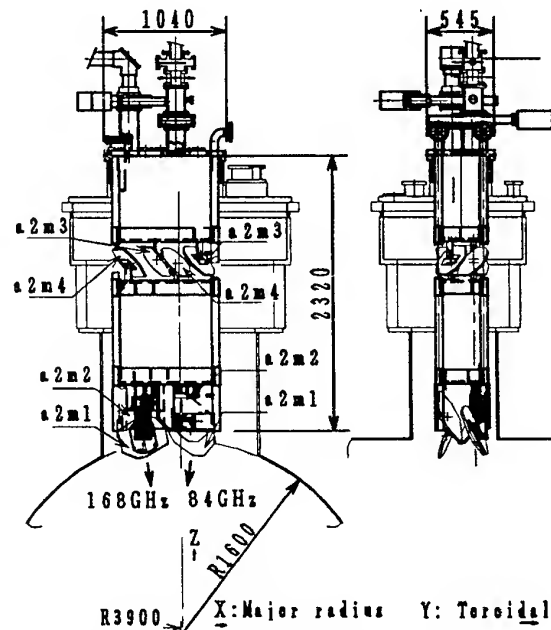


Fig. 1 ECH antenna system on LHD



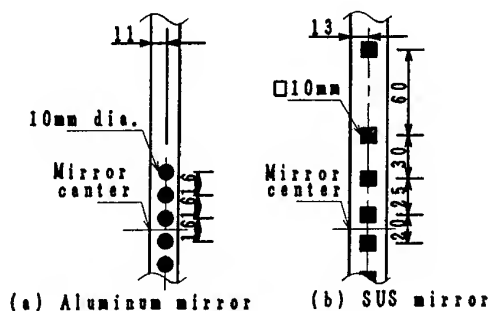


Fig. 2 Water cooling channel  
(a) Aluminum, and (b) SUS mirrors.

waveguide is put in one of the support pipes as a spare microwave launcher. The final flat mirror, m1, is controlled by supersonic motors by mechanical links and optical positioning sensor, which has been tested at the magnetic field up to 4 T. A Molybdenum compounds coating is employed for the link system to avoid lubrication. The positioning accuracy, due to the backlash of the link system, is within 5 mm. Full stroke motion of the mirror takes about 60s.

#### IV. Test and installation

Helium leak test is performed from the flange and the water channel ( $10 \text{ kg/cm}^2$ ). Flat mirrors, m1 and m3, were adjusted using He-Ne laser. The traces of the He-Ne laser at the mid-plane is compared to the calculation in Fig. 3 (a) and (b). After installation, the laser spot was geometrically measured relative to the vacuum vessel. The millimeter beam profiles were measured using HE11 mode exciters, Fig 4 (a) and (b), which shows good focuses with radially 15 mm and toroidally 50 mm waist size.

#### V. Plasma production and conclusion

The first plasma of LHD was produced on March 31, 1998 using 84 GHz and 82.6 GHz microwave at 1.5 T operation (second harmonics). In the experiment, it is concluded that the positioning of the microwave beam to the ECR region is important for the initial plasma production. The ECH antenna with well focused beam, wide positioning ability in the high magnetic field ( $\sim 4 \text{ T}$ ), and 0.5 - 1 MW CW transmission capability, satisfies the further experimental plans in LHD.

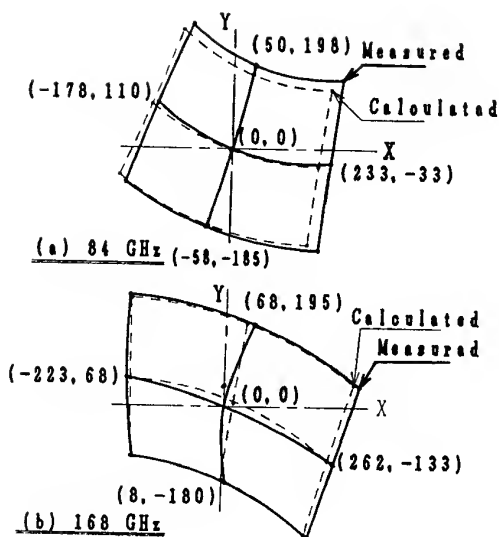


Fig. 3 Mirror alignment test using He-Ne laser. (a) 84 GHz, (b) 168 GHz.

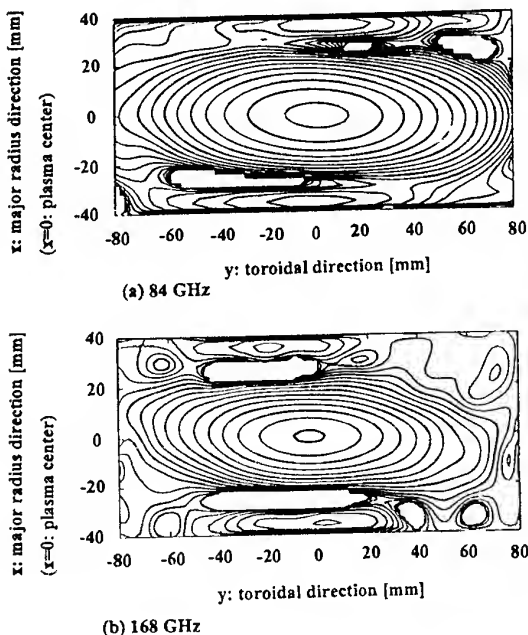


Fig. 4 Low power microwave test.  
(a) 84 GHz, (b) 168 GHz.

#### References

- 1 S. Kubo, et al., Fusion Eng. & Design 26, 319 (1995).
- 2 S. Kubo, et al., Conf. Digest 19th Int. Conf on IR & MM Waves p.500 (1994, Sendai).

# Terahertz Radiation from Superconducting YBCO Films Excited by Femtosecond Laser Pulses - Discovery, Development and Applications -

Masanori Hangyo<sup>1</sup>, Masayoshi Tonouchi<sup>1,2</sup>, Masahiko Tani<sup>3</sup> and Kiyomi Sakai<sup>3</sup>

<sup>1</sup>Research Center for Superconducting Materials and Electronics, Osaka University,  
Suita, Osaka 565-0871, Japan

<sup>2</sup>JST/CREST

<sup>3</sup>Kansai Advanced Research Center, Communications Research Laboratory,  
Ministry of Posts and Telecommunications, Iwaoka, Kobe, Hyogo 651-2401, Japan

## Abstract

Ultrashort electromagnetic (EM) pulses ( $\sim 450$  fs in time width) are emitted from current biased high- $T_c$  superconducting films by exciting with femtosecond laser pulses. The EM pulses (called THz radiation) are also emitted from high- $T_c$  superconducting films under external magnetic fields or in magnetic-flux trapped states. The THz radiation is ascribed to the ultrafast modulation of transport, shielding and persistent currents associated with the breaking of the Cooper pairs. As applications of these phenomena, we propose and demonstrate a new superconducting optical memory and noncontact supercurrent mapping system.

## Introduction

In 1995, we found that ultrashort EM pulses are emitted from current-biased superconducting YBCO films by exciting with femtosecond laser pulses [1,2]. The Fourier spectrum of them extends up to  $\sim 3$  THz and therefore they are referred to as THz radiation hereafter. Later, we found that THz radiation is emitted from YBCO films under external magnetic fields or in magnetic-flux trapped states even without a bias current [3]. These phenomena indicate that high- $T_c$  superconductors are interesting materials from the view point of ultrafast optoelectronics.

In this paper, we describe a basic idea of the THz radiation from the high- $T_c$  superconductors, fundamental characteristics of the radiation and recent progress including various applications [4,5].

## Basic Idea

It is well known that the THz radiation is emitted from an ultrafast photoconductive switch (Auston switch) by exciting with femtosecond laser pulses. The transient photocurrent  $J$  is the source of the THz radiation, whose far-field electric field is given by  $E \sim dJ/dt$ . This is illustrated in Fig. 1 (a) schematically. On the other hand, what happens when a superconducting bridge with supercurrent flow is irradiated with femtosecond laser pulses? The optical pulses may destroy part of the Cooper pairs and change them into quasiparticles. The quasiparticles undergo scattering by electrons and phonons and as a result decrease of the supercurrent may occur. After energy relaxation, the photogenerated quasiparticles recombine into Cooper pairs and the recovery of the supercurrent occurs. If the decrease and recovery of the supercurrent occurs in a subpicosecond time scale, the THz radiation is emitted. This is shown in Fig. 1 (b) schematically.

## Radiation Characteristics

Figure 2 (a) shows the waveform of the THz radiation from a dipole antenna type device made of a superconducting YBCO film on an MgO substrate. The device is excited by laser pulses with 80 fs in time width and 80 MHz in repetition rate. A low-temperature grown GaAs photoconductive antenna is used to record the waveform. A sharp pulse with 600 fs time width is observed followed by a weak replica due to multiple reflection in the MgO substrate. Figure 2 (b) shows the Fourier transform spectrum of the pulse. The component extends from 0.1 to 2 THz. The radiation power is proportional to the square of the bias current and laser power. The waveform and its temperature

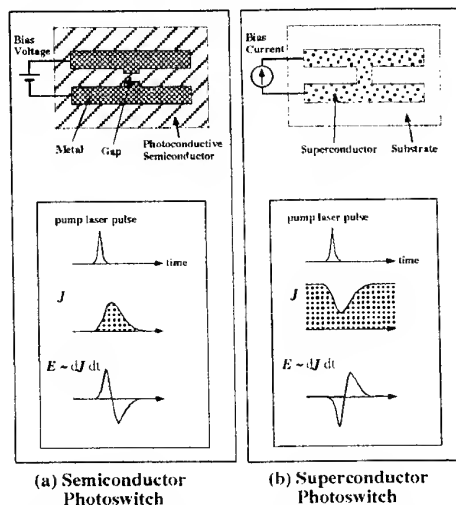


Fig.1. Comparison of the THz radiation from a semiconductor and superconductor.

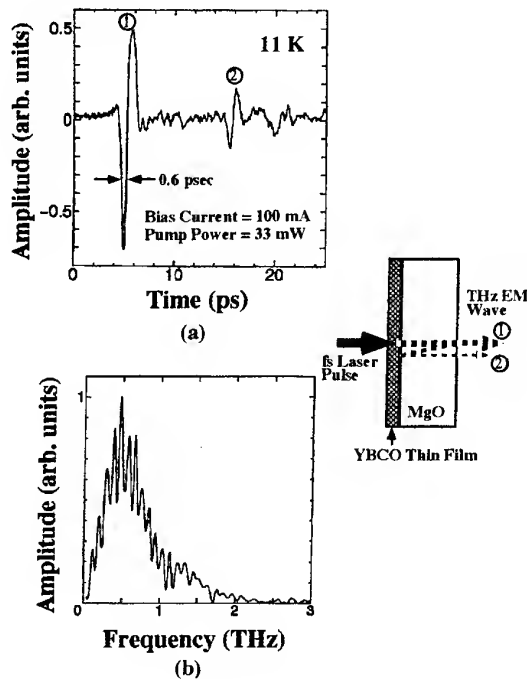


Fig. 2. (a) Typical waveform of the electric field and (b) its Fourier spectrum.

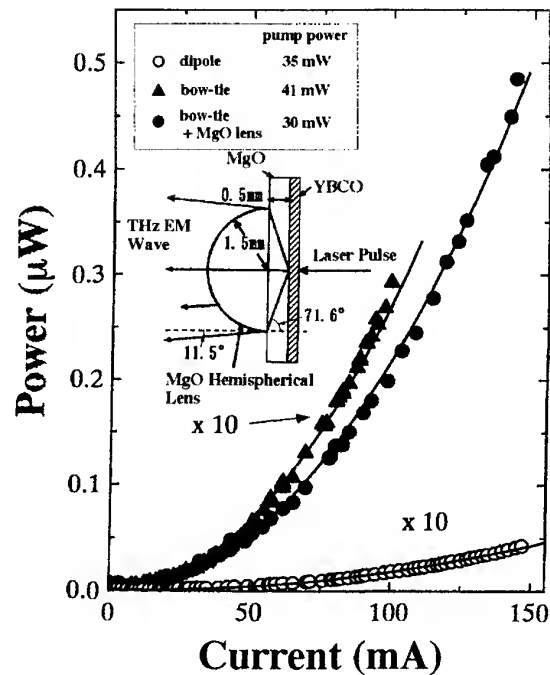


Fig. 3. Comparison of the radiation power for three cases

dependence are analysed by using the rate equations for photogenerated quasiparticles and phonons. The result indicates that the recombination time of the quasiparticles is less than 500 fs and increases rapidly with approaching  $T_c$ .

In order to increase the radiation power, the bow-tie antenna is adopted instead of the dipole one and an MgO hemispherical lens is attached to the back surface of the substrate. The result of this improvement is shown in Fig. 3. The radiation power detected by an InSb hot electron bolometer increases by two orders of magnitude compared to that from the dipole antenna type device without the MgO lens and reached 0.5  $\mu\text{W}$  by the 30 mW excitation.

### Radiation Related to Magnetic Fields

Thus far, the THz radiation is emitted from current biased thin film devices. However, we found that the THz radiation is emitted from the YBCO devices under external magnetic fields even without a bias current. Figure 4 (a) shows the waveform radiated from the bow-tie antenna type device under the external magnetic field  $B = 150$  G. Without the magnetic field, no signal is observed. By applying the magnetic field, the THz radiation is observed and the polarity of the waveform is changed by reversing the magnetic field. The radiation mechanism is interpreted in terms of the ultrafast shielding current modulation by the laser pulses. The radiation is even observed after applying and removing the external field as shown in Fig. 4 (b). The radiation after removing the external field is related to the persistent current associated with the magnetic flux trapped in the film. The radiation intensity decreases to some finite levels with the characteristic time constant of several minutes.

### Application to New Magnetic-Flux Trap Memory

We proposed and demonstrated a new type of superconducting optical flux-trap memory using the THz radiation from magnetic-flux trapped states [5]. Figure 5 (a) shows the structure of the memory cell and Fig. 5 (b) shows the change of the waveform with the bias current and the laser spot position. The cell has a hole in the center of the

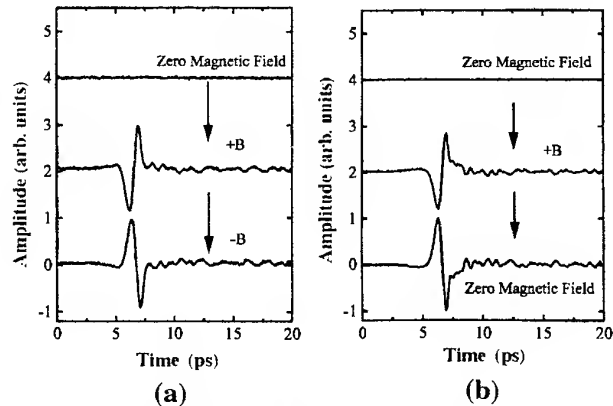


Fig. 4. Radiation under (a) external magnetic fields and (b) magnetic flux trapped state.

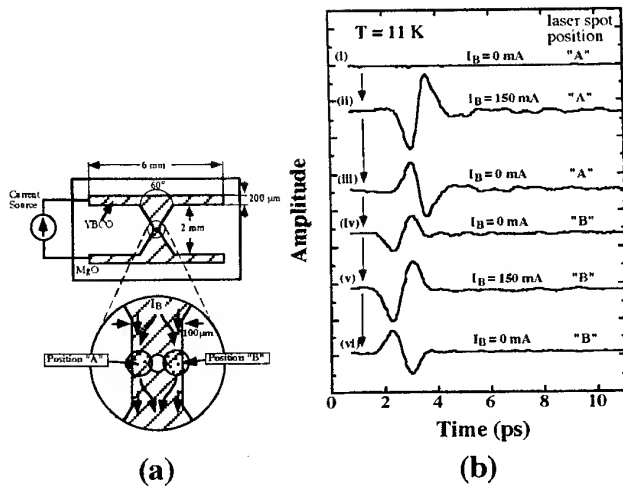


Fig. 5. (a) Structure of the memory cell and (b) change of the waveform with the bias current and laser spot position.

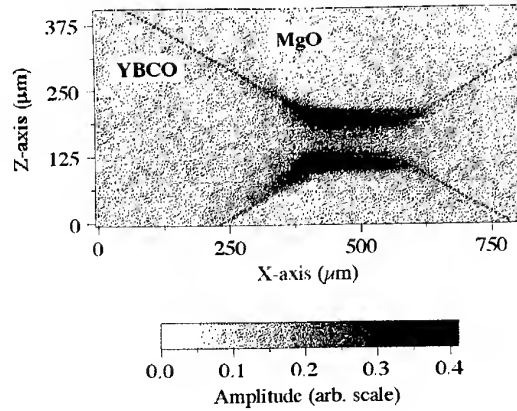


Fig. 6. Mapping of the THz radiation amplitude for the bow-tie antenna type device.

bridge to trap the magnetic flux. The direction of the magnetic flux trapped in the hole can be changed by the combination of the bias current direction and the laser spot position. The polarity of the THz radiation (read-out signal) reflects the direction of the magnetic flux. By integrating this memory cell two-dimensionally, it is possible to make a new type of superconducting optical flux-trap memory.

### Two-Dimensional Mapping of Supercurrent Distribution

Since the amplitude of the THz radiation excited by the femtosecond laser pulses is proportional to the supercurrent density at the laser spot, the two-dimensional supercurrent distribution can be obtained from the THz radiation intensity by scanning the excitation laser beam. Figure 6 shows the distribution of the THz amplitude (root of the intensity) near the bridge of the bow-tie antenna type device under a bias current of 100 mA. The diameter of the laser spot is  $\sim 30$  μm, which determines the spatial resolution. Since the MgO hemispherical lens 3 mm in diameter is attached to the back surface of the substrate, the amplitude in the central part of the bridge is enhanced. It is seen that the supercurrent flows near the edge of the bridge. Until now, the supercurrent distribution is obtained indirectly from the magnetic field measured by a magneto-optical film or Hall sensor. The present method provides a new direct noncontact method for measuring the supercurrent distribution.

### Summary

It is found that ultrashort electromagnetic pulses  $\sim 500$  fs in time width are emitted from superconducting films by exciting with femtosecond laser pulses under current biased, external magnetic field and flux trapped states. The radiation intensity is proportional to the square of the bias current and the laser intensity. A new type of optical flux-trapped memory can be made utilizing this phenomenon. A new method for measuring the supercurrent distribution using the photoexcited THz radiation is also demonstrated.

The ultrafast optical response and THz radiation from high- $T_c$  superconductors open a new field "Superconducting Optoelectronics" combining the superconducting electronics and optoelectronics.

### Acknowledgments

This work was partly supported by a Grant-in-Aid for Scientific Research from the Ministry of Education, Science, Sports and Culture, Japan. This work was also partly supported by the public participation program for the promotion of creative info-communications technology R&D of Telecommunications Advanced Organization of Japan (TAO).

### References

1. M Hangyo *et al.*, Conf. Digest of 12th Int. Conf. on Infrared and Millimeter Waves, Orlando, 1995, p. 233.
2. M Hangyo *et al.*, Appl. Phys. Lett. **69**, 2122 (1996).
3. M Tonouchi *et al.*, Jpn. J. Appl. Phys. **36**, L93 (1997).
4. M Hangyo *et al.*, IEICE Trans. Electron. **E80-C**, 1282 (1997).
5. M Tonouchi *et al.*, Appl. Phys. Lett. **71**, 2364 (1997).

## Generation of millimeter wave radiation with a quasi-planar superlattice device

E.Schomburg<sup>a,b</sup>, K.Hofbeck<sup>b</sup>, J.Grenzer<sup>b</sup>, K.F.Renk<sup>b</sup>, D.G.Pavel'ev<sup>c</sup>, Yu.Koschurinov<sup>c</sup>,  
V.Ustinov<sup>d</sup>, A.Zhukov<sup>d</sup>, A.Kovsch<sup>d</sup>, A.Egorov<sup>d</sup>, and P.S.Kop'ev<sup>d</sup>

<sup>a</sup> Department of Physics, University of Nottingham, University Park, Nottingham NG7 2RD, UK

<sup>b</sup> Institut für Experimentelle und Angewandte Physik, Universität Regensburg, Germany

<sup>c</sup> Department of Radiophysics, Nizhny Novgorod State University, Russia

<sup>d</sup> A.F.Ioffe Physico-Technical Institute, St.Petersburg, Russia

**A quasi-planar structured GaAs/AlAs superlattice, mounted into a waveguide, delivered tuneable radiation around 55 GHz (power: 400  $\mu$ W). Harmonic radiation at frequencies up to 220 GHz was observed. We associate the generation of this radiation with current oscillation caused by travelling dipole domains.**

### 1. Introduction

Almost three decades ago, Esaki and Tsu [1] proposed to use semiconductor superlattices, having a negative differential conductance, for the generation of microwave radiation. A doped wide-miniband superlattice, built into a resonator, has been used as the active device of a microwave oscillator with emission frequencies from 6 to 30 GHz [2]. Recently, it has been demonstrated [3, 4], that a superlattice, not coupled to a resonator, can show microwave emission due to self-sustained current oscillations, with oscillation frequencies corresponding to a transit frequency for travelling dipole domains. The occurrence of travelling dipole domains in superlattices was predicted earlier [5]. In this contribution, we report on a millimeter wave oscillator based on a quasi-planar superlattice electronic device (SLED).

### 2. Experimental

The SLED was fabricated using a superlattice (doping  $10^{17} \text{ cm}^{-3}$ ), grown by molecular beam epitaxy, with 140 periods of 37 Å GaAs layers and 9 Å AlAs layers. The quasi planar SLED (Fig.1a; a detailed description is given in [6]) consisted of a  $n^+$  GaAs substrate (area  $200 \times 300 \mu\text{m}^2$ , height  $40 \mu\text{m}$ ) supporting a small area (cross section  $7 \times 7 \mu\text{m}^2$ ) and a large area (cross section  $70 \times 150 \mu\text{m}^2$ ) superlattice mesas, both covered with ohmic contacts and connected by the  $n^+$  GaAs substrate. The mesa with the smaller cross section acted as an active element responsible for the millimeter wave emission. The active element was connected to a metallic contact pad ( $100 \mu\text{m}$  long and  $25 \mu\text{m}$  wide) partly carried by a polyimide film; the contact pad protruded ( $80 \mu\text{m}$ ) beyond the  $n^+$  GaAs substrate.

The SLED was mounted (Fig.1b) in a metallic waveguide structure (impedance about  $100 \Omega$ ) having both a V-band (50 - 75 GHz) and a D-band (110 - 170 GHz) output. The contact of the large mesa was connected to the waveguide by indium

solder and the active superlattice to a voltage supply. A mixer and a spectrum analyser were used for monitoring the millimeter wave generation.

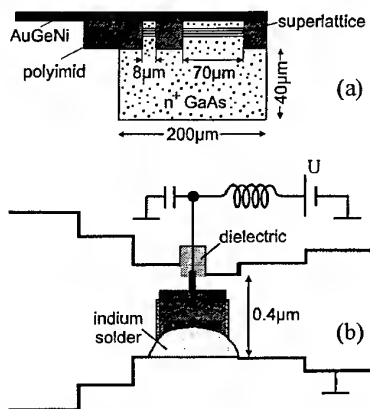


**Fig.1:** (a) Quasi-planar SLED and (b) SLED in a waveguide.

### 3. Results

The current-voltage characteristic (Fig.2a) of the SLED in the waveguide exhibited a negative differential conductance in a large voltage region, where current jumps downwards and upwards followed by smooth parts occurred. These current jumps indicate the formation of travelling dipole domains in the active element [3, 4, 6]. From the peak current we estimated a peak current density of about  $60 \text{ kA/cm}^2$  corresponding to a drift velocity of  $v_p = 4 \cdot 10^6 \text{ cm/s}$ .

Narrowband microwave emission at a fundamental frequency  $\nu_1$  between 54 and 60 GHz was found between 1.8 and 2.5 V (Fig.2b). The line was tuneable by about 400 MHz/0.1 V. A maximum output power of about 400  $\mu\text{W}$  was observed corresponding to an efficiency of 1 % for the conversion from dc to rf power. The emission line had, relative to the centre frequency, a full width at half maximum of  $10^{-5}$ .

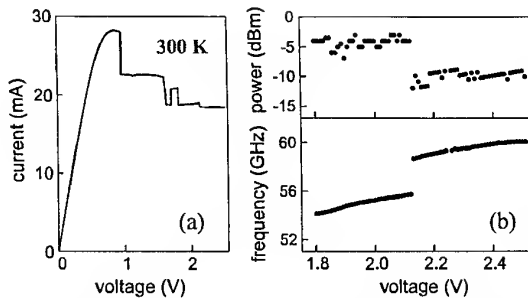


**Fig.2:** (a) Current-voltage characteristic of a SLED and (b) tunability and power of the fundamental harmonic.

Besides a fundamental line, higher harmonics at  $\nu_n = n\nu_1$  ( $n=2, 3, \dots$ ) were observed (Fig.3); the power in a harmonic decreased with increasing order. Using a short-circuit plunger at the V-band output in order to tune the power of the higher harmonics monitored at the D-band output, a maximum power of 100  $\mu$ W (efficiency about 0.2 %) for the second harmonic was observed; powers of 16  $\mu$ W (for the third) and 0.2  $\mu$ W (for the fourth) were found.

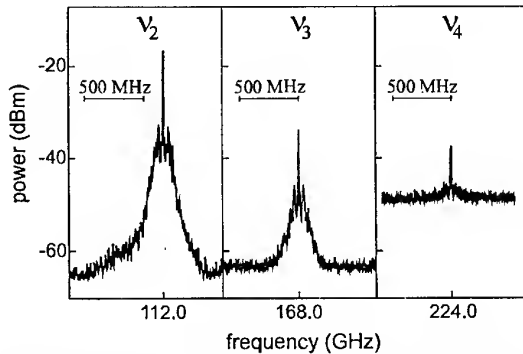


**Fig.3:** Spectra of harmonics for a fundamental at  $\nu_1 = 56$  GHz.

#### 4. Discussion

The conduction in the active superlattice was attributed to electron transport in the lowest miniband (width 70 meV), with a negative differential mobility due to Bloch oscillations of the miniband electrons. When the SLED was biased in the region of negative differential mobility, a dipole domain was periodically formed, which travelled through the active superlattice and was quenched at the anode. This domain propagation gave rise to a current oscillation exciting the millimeter wave radiation in the waveguide. The fundamental frequency corresponded to the transit frequency of a travelling dipole domain and was about  $0.8 v_p/L$ , where  $L$  ( $\sim 0.64 \mu\text{m}$ ) is the length of the superlattice. The observation of higher harmonics

indicate the nonsinusoidal character of the current oscillation. A detailed treatment of dipole domains in a superlattice is published in [7]. We suggest that the propagation of dipole domains in the active superlattice was influenced by a feedback of the field in the waveguide; this feedback was responsible for the tunability and the frequency jump at about 2.1 V. We do not yet know the origin of the sidebands observed in the spectra (Fig.3).

#### 5. Conclusion

In conclusion, we have presented an active two-terminal device for generation of millimeter wave radiation and have demonstrated generation of radiation up to 220 GHz.

E.S. would like to thank the European Commission (EC) for financial support through the INTERACT Project (FMRXCT 960092).

#### 6. References

1. L. Esaki, and R. Tsu, IBM J. Res. Dev. **14**, 61 (1970).
2. J. Grenzer, A.A. Ignatov, E. Schomburg, K.F. Renk, D.G. Pavel'ev, Yu. Koschurinov, B. Melzer, S. Ivanov, S. Schaposchnikov, P.S. Kop'ev, Ann. Phys. **4**, 184 (1995).
3. K. Hofbeck, J. Grenzer, E. Schomburg, A.A. Ignatov, K.F. Renk, D.G. Pavel'ev, Yu. Koschurinov, B. Melzer, S. Ivanov, S. Schaposchnikov, and P.S. Kop'ev, Phys. Lett. A **218**, 349 (1996).
4. E. Schomburg, S. Brandl, K. Hofbeck, T. Blomeier, J. Grenzer, A.A. Ignatov, K.F. Renk, D.G. Pavel'ev, Yu. Koschurinov, V. Ustinov, A. Zhukov, A. Kovich, S. Ivanov, and P.S. Kop'ev, Appl. Phys. Lett. **72**, 1498 (1998).
5. M. Büttiker and H. Thomas, Phys. Rev. Lett. **38**, 78 (1977).
6. E. Schomburg, K. Hofbeck, J. Grenzer, T. Blomeier, A.A. Ignatov, K.F. Renk, D.G. Pavel'ev, Yu. Koschurinov, V. Ustinov, A. Zhukov, S. Ivanov, and P.S. Kop'ev, Appl. Phys. Lett. **71**, 401 (1997).
7. E. Schomburg, T. Blomeier, K. Hofbeck, J. Grenzer, S. Brandl, I. Lingott, A.A. Ignatov, K.F. Renk, D.G. Pavel'ev, Yu. Koschurinov, B. Ya. Melzer, V.M. Ustinov, S.V. Ivanov, A. Zhukov, and P.S. Kop'ev, Phys. Rev. B (1998) in press.

# THz electromagnetic wave source and detector based on an LT-GaAs

H. Abe\*, M. Tani\*, K. Sakai\*, and S. Nakashima\*\*

\*Kansai Advanced Research Center, Communications Research Laboratory,  
588-2, Iwaoka, Nishi-ku, Kobe-shi, Hyogo 651-2401, Japan

\*\*Department of Applied Physics, Osaka University,  
2-1, Yamadaoka, Suita, Osaka 565-0871, Japan

## Abstract

This paper describes the emission and detection properties of photoconductive antennas fabricated on low-temperature-grown GaAs (LT-GaAs) substrates grown at several different growth temperatures. The devices showed almost the same spectral bandwidth and amplitude for emissions at ordinary operating conditions but they showed a clear relation between the spectral bandwidth and the carrier lifetime of LT-GaAs substrate for detections.

## 1 Introduction

The LT-GaAs<sup>1)</sup> is grown by molecular beam epitaxy at relatively low substrate temperatures (<300°C) followed by thermal annealing (~600°C). It exhibits ultrashort lifetime of photogenerated carriers (< 1ps), reasonably good mobility (~200 cm<sup>2</sup>/vs), and a high breakdown field (~500 KV/cm). THz electromagnetic wave sources and detectors are fabricated by printing a metallic antenna on the LT-GaAs substrates. The device is called photoconductive antenna<sup>2)</sup>. We have investigated the relation between the carrier lifetime and the spectral bandwidth as well as the relation between the carrier lifetime and the amplitude of the photoconductive antenna as the wide-bandwidth source and detector.

## 2 Experimental

### 1) Devices

The 1.5- $\mu$ m-thick LT-GaAs film was grown by molecular-beam epitaxy at temperatures between 160°C and 300°C on a 400- $\mu$ m-thick semi-insulating GaAs (SI-GaAs). The film was subsequently annealed at 600°C under an As overpressure for about 5 minutes. The carrier lifetime of the LT-GaAs layers was measured by using the time-resolved photoreflectance method. The decay time of the transient reflectivity change is plotted as a function of the growth temperature in Fig.1. The sample which was grown at 180°C demonstrates the shortest carrier lifetime (0.24 ps). The 30- $\mu$ m-long dipole antenna with a small photoconductive gap (5  $\mu$ m) was placed in the center of a 10- $\mu$ m-wide, 6mm-long coplanar transmission line. The same antenna pattern was printed on the fabricated LT-GaAs substrates which were used as the source and detector.

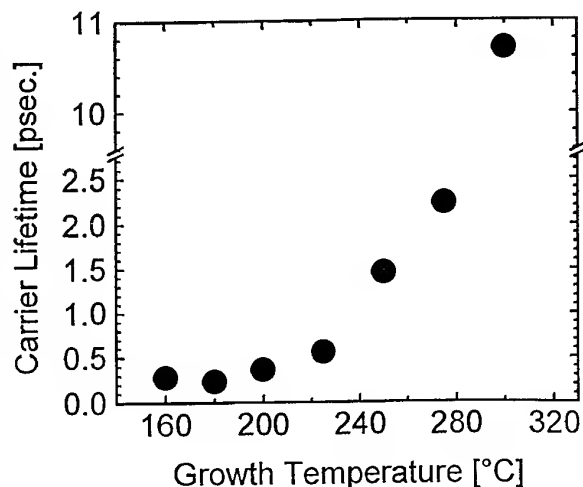


Fig. 1. Growth temperature dependence of the carrier lifetime for LT-GaAs layers.

### 2) Sources

The THz electromagnetic wave pulses from an each biased photoconductive switch excited with about 30-mW femtosecond (fsec) laser pulses were observed by using a standard THz time-domain experimental setup<sup>3)</sup>. A photoconductive antenna having a wide bandwidth was used as the detector. The intensity and the bandwidth of the Fourier-transformed amplitudes were almost the same. Systematic variations could not be seen for the devices fabricated on the substrates grown at different growth temperatures.

### 3) Detectors

The fabricated photoconductive antennas were used as detectors<sup>4)</sup> by exciting the gap with about 2-mW fsec laser pulses. An electromagnetic wave source which emits THz radiation as high as 5THz was used. The THz pulses were also observed by the THz time-domain experimental set-up. The Fourier-transformed amplitudes of the measured electromagnetic wave pulses are shown in Fig. 2. They are normalized at a peak amplitudes of the measured electromagnetic wave pulses even though the amplitude increased slightly when the carrier lifetime decreased. As expected, the spectral response extends to higher frequencies as the carrier lifetime decreases. The 3-dB down frequency ( $f_{3dB}$ ) and the carrier lifetime ( $\tau$ ) have a relation as  $f_{3dB}=A+B/\tau$  with  $A=1.38\text{THz}$  and  $B=0.21$ , which suggests that the  $f_{3dB}$  is determined not only by the lifetime. The constant term (A) corresponds to the sharp rise of the photoresponse. The second term ( $B/\tau$ ) reflects the influence of the carrier lifetime.

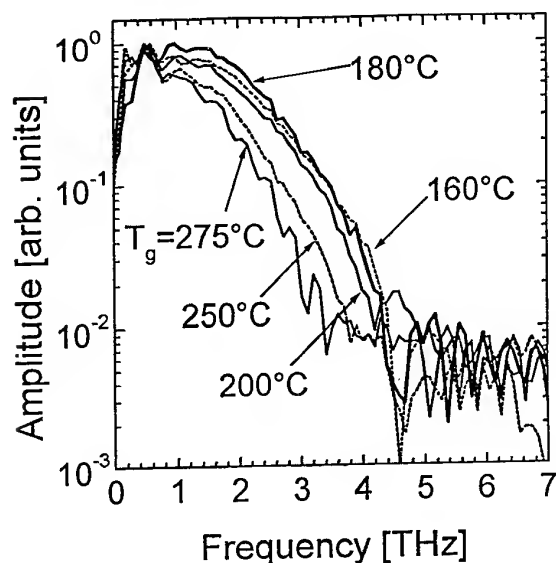


Fig. 2 Fourier-transformed amplitudes of THz pulses detected by using photoconductive detectors which were fabricated on the LT-GaAs grown at different temperatures.

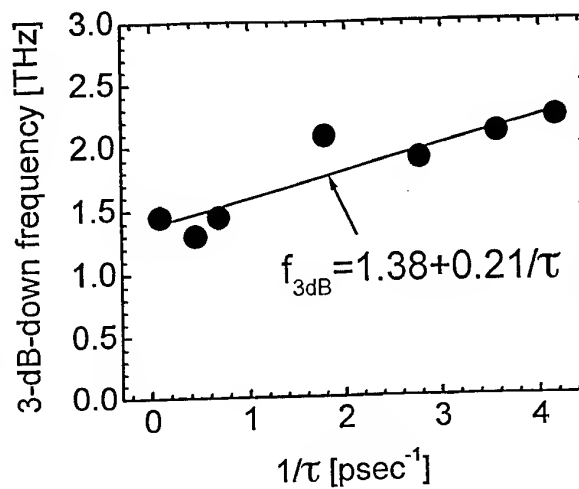


Fig. 3 Three-dB down frequencies of photoconductive detectors plotted as a function of the reciprocal of the carrier lifetime.

### References

1. S. Gupta, J. f. Whitaker, and G. A. Mourou: IEEE J. Quantum Electron., **28**, 2464 (1992).
2. P. R. Smith, D. H. Auston, and M. C. Nuss: IEEE J. Quantum Electron., **24**, 255 (1988).
3. M. van Exter, C. Fattinger, and D. Grischkowsky: Appl. Phys. Lett., **55**, 337 (1989).
4. F. W. Smith, H. Q. Le, V. Diadiuk, M. A. Hollis, and A. R. Calawa: Appl. Phys. Lett., **54**, 890 (1989).



# **Generation of high-frequency oscillations by electromagnetic shock wave (EMSW) synchronous with backward harmonic of periodic nonlinear transmission line (NLTL) based on multilayer heterostructure (MLHS) with nanolayers**

A.M.Belyantsev, A.B.Kozyrev

Institute for Physics of Microstructures of RAS  
603600, Nizhny Novgorod, GSP-105, Russia

In our previous works [1] we suggested using dispersive NLTL based on MLHS with nanolayers of the type  $(iAlAs-nGaAs-iAl_xGa_{1-x}As-n^+GaAs-iAlAs)_n$  for direct effective transformation of a videopulse into a radiopulse with filling frequency of the order of 100 GHz (generation of high-frequency (HF) oscillations). The mechanism of this transformation is EMSW front instability to the largest-period wave running in synchronism with it. In this case the front of EMSW can be considered as traveling source of radiation leaving behind an increasing «wake» of oscillations with period equal to the period of the synchronous wave and running out of it with the velocity proportional to the difference between phase and group velocity. The promoting of the above mechanism of generation for obtaining longer radio pulses is limited by HF losses in such transmission lines. To overcome the restrictions on the duration of the generated radiopulse connected with HF losses it is suggested in this publication to use a synchronism not with a forward harmonic [1] (the group velocity  $v_g$  is aligned with phase velocity  $v_p$ ) but with a backward one (group velocity is opposite to the phase velocity). The computer modelling has shown the attenuation of oscillations in latter case to be by an order less, all other factors being the same.

The necessary dispersion for generation of HF oscillations in the case of planar geometry can be easily realized if one metal strip has branches (arms) and the capacitance cross links between branches are organized through thin dielectric layer (Fig. 1a) for adaptable dispersion control. The transmission line becomes a discrete one and, accordingly, has space harmonics and, hence, backward ones. The equivalent circuit diagram of such transmission line represents itself an LC ladder with capacitance cross links [1]. Dispersion characteristics of NLTL for cross link coefficient  $\gamma = C^*/C_0 = 0.2$  ( $C_0$  is saturated capacitance of NLTL section,  $C^*$  is cross link capacitance) are presented in Fig. 2. The advantage of the system is the ease of the dispersion control by means of variation of only one parameter (cross link capacitance). As it is easy to see from Fig. 2a the space harmonic is forward at the wave number  $0 \leq \phi \leq \pi$  (fundamental harmonic of wave group  $\phi_n = \phi_0 + 2\pi n$ ) and backward at  $\pi \leq \phi \leq 2\pi$  (the first harmonic of wave group  $\phi_n = -\phi_0 + 2\pi n$ ).

In microstrip NLTL with asymmetric MLHS as nonlinear medium all oscillations behind the front of intensive EMSW propagate as in a linear transmission line since  $C(V)$  characteristic of the asymmetric MLHS exhibits hysteretic properties (Fig. 1b). Losses in microstrip NLTL are connected mainly with losses in the conductor plates (because of the skin-effect) and can be taken into account in calculations by the resistance  $R_1(\omega)$  in the equivalent circuit diagram [1].

As in the case of distributed NLTL in the case of discrete NLTL the transformation to the traveling coordinate can be performed and eigenvalues of the obtained differential-difference equation found. The attenuation of oscillations in generated radiopulse (in the stationary case) will be determined by the imaginary

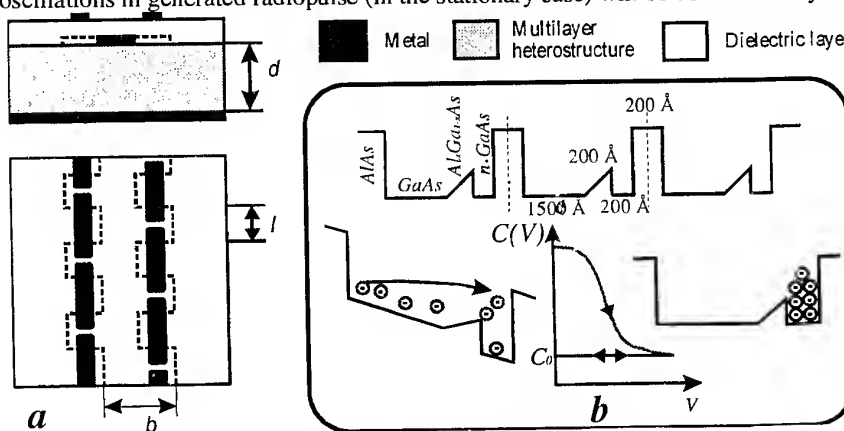


Fig. 1: a) NLTL on the basis of MLHS with nanolayers.

b) Profile of the conduction band diagram of MLHS and its  $C(V)$  characteristic.

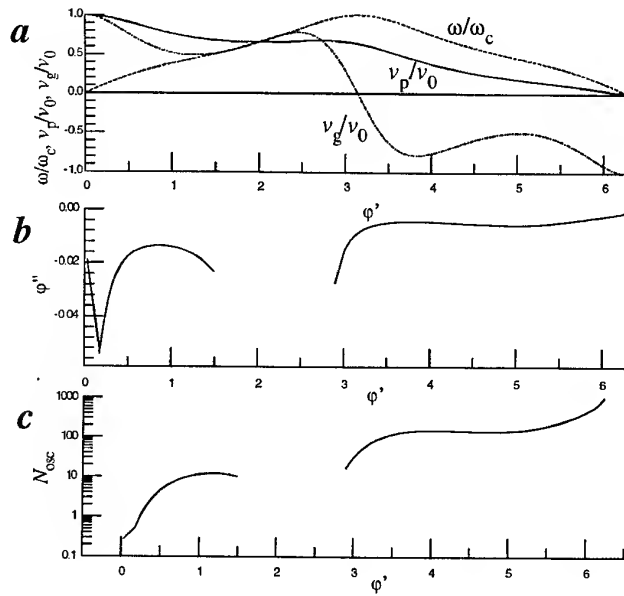


Fig.2: a) Dispersion characteristics of microstrip periodic NLTL (dependence of the relative phase velocity  $v_p/v_0$ , group velocity  $v_g/v_0$  and relative frequency  $\omega/\omega_c$  on the wave number  $\phi'$ ,  $v_0 = (L_0 C_0)^{-1/2}$ ,  $\omega_c = 2/(L_0 C_0)^{-1/2}$ ).

b) Dependence of the increment of attenuation  $\phi''$  on the wave number  $\phi'$ .

c) Dependence of the number of oscillations in the stationary radiopulse on wave number  $\phi'$ .

part of the eigenvalues. In doing so the ratio of the amplitude of  $n$ -th oscillation to the amplitude of the first one will be described by the following formula:

$$\frac{A_n}{A_1} = \exp\left\{2\pi(n-1) \frac{\phi''}{\phi'}\right\} \equiv \exp\left\{\pi(n-1) \frac{R_1(\omega)/Z_0}{\phi' \cdot (v_g/v_0 - v_s/v_0)}\right\}$$

where  $\phi = \phi' + i\phi''$  is the relative wave number or phase shift per one section,  $v_s$  is the shock wave velocity,  $R_1(100 \text{ GHz})/Z_0 = 0.0073$ . Fig.2b,c represents the dependencies of the attenuation increment  $\phi''$  and of the stationary radiopulse duration (number of oscillations which corresponds to the attenuation by  $e$  times) on the wave number if the skin-effect losses in NLTL shown in Fig. 1a are taken into account. As it is easy to see there is some optimal value of the wave number for both forward and backward waves corresponding to the maximum duration of the stationary radiopulse. However in the case of the backward wave this value is approximately by an order higher than in the case of the forward wave. Therefore, as far as generation of the long radiopulse with high filling frequency is concerned the synchronism with the backward wave is more preferable.

As it is easy to see from the given above formula, the decrease of the attenuation in the case of the backward waves is explained by the high relative velocity of energy coming out of the EMSW front (the group velocity is negative  $v_g < 0$ ) from the one hand and large value of the wave number  $\phi'$  from the other one.

Just as at the synchronism with forward harmonics so also with backward ones the direct transformation of a short videopulse into a radiopulse (100 GHz, 5-10 V) in microstrip transmission lines based on MLHS with nanolayers is possible. However in the case of the synchronism of EMSW front with the backward harmonic the generated radiopulse can be significantly longer. It is obvious that carried out investigations does not take into account coupling between harmonics in wave group. However, modifying design of microstrip line (transmission line with normal dispersion coupled with transmission line with anomalous dispersion) a situation when wave groups will be presented mainly by zero forward and backward harmonics can be easily realized. In this case the main results of this publication are held.

This work was made possible under the grant from Russian Foundation for Basic Research (project N 96-02-19284).

# The Frequency Response of Resonant Cavity Enhanced P-i-N Photodiode

Dušan S. Golubović, Petar S. Matavulj, and Jovan B. Radunović

Department of Microelectronics and Engineering Physics,  
Faculty of Electrical Engineering, University of Belgrade  
Bulevar revolucije 73, P. O. Box 35-54, 11120 Belgrade, Yugoslavia

Frequency response of homostructure GaAs *resonant cavity enhanced* (RCE) P-i-N photodiode [5] designed for high speed applications [3] is analyzed. Complete phenomenological model for two valley semiconductor [1, 2] is used in analysis. Stability and convergence of applied numerical algorithm are provided by implementation of conditions described in [1, 2]. As we presume monochromatic and completely coherent incident light, quantum efficiency is given by [4]

$$\eta = (1 - R_1) \frac{(1 - e^{-\alpha d})(1 + R_2 e^{-\alpha d}) + \frac{2\sqrt{R_2}\alpha}{\beta} e^{-\alpha d} \sin(\beta d) \cos(\beta d + \phi_2)}{1 - 2\sqrt{R_1 R_2} e^{-\alpha d} \cos(2\beta d + \phi_1 + \phi_2) + R_1 R_2 e^{-2\alpha d}} \quad (1)$$

where  $R_1$  and  $R_2$  are power reflectivities,  $\phi_1$  and  $\phi_2$  are corresponding phase shifts and together represent resonant cavity parameters which were constant during the simulations. In our simulations are  $R_1 = 0.3$ ,  $R_2 = 0.9$ ,  $\phi_1 = 0$  and  $\phi_2 = \pi$ .  $\beta$  is propagation constant,  $d$  is thickness of absorption i-layer and  $\alpha$  is absorption coefficient at applied wavelength.

Incident light power is  $W = 0.007 \text{ pW}$  and it was also constant during the simulations. For applied light power, maximal concentration of photogenerated carriers is ten times less than concentration of donor ( $\gamma = 0.1$ ), response is linear [1, 2], so that bandwidth usage for response characterization is justified. The analysis has been carried out for sub-micron thicknesses of absorption layer, two different active areas ( $A = 70 \mu\text{m}^2$  and  $A = 700 \mu\text{m}^2$ ) and different bias voltages ( $0 \text{ V} \leq V_{cc} \leq 10 \text{ V}$ ).

Figure 1 shows the dependence of bandwidth on the thickness of absorption layer of RCE P-i-N photodiode. For bias voltage  $V_{cc} = 5 \text{ V}$  and active area  $A = 700 \mu\text{m}^2$  curve increases permanently. According to the results represented in [1] we conclude that bandwidth is limited only by RC-constant for all thicknesses of absorption layer. For the same value of active area and bias voltage  $V_{cc} = 2 \text{ V}$ , the curve has maximum but for higher thicknesses of i-layer. For active area  $A = 70 \mu\text{m}^2$  the maximum appears for lower thicknesses of absorption layer and curve decreasing may be observed. In the increasing region of the curve the predominant limiting factor is RC-constant. Appearance of the bandwidth maximum, is predominantly caused by carrier transit time. This is the difference in bandwidth behaviour when compared with conventional P-i-N photodiode in the submicron region [1]. It's easy to notice significant difference in curve slopes for active area  $A = 70 \mu\text{m}^2$  in the decreasing region. For  $V_{cc} = 5 \text{ V}$  beyond maximum the bandwidth slowly decreases. Electrons are localized in the satellite valleys and holes are in saturation owing to high values of the electric field. But, holes are slower and therefore they represent the main limiting factor. For electric field value corresponding to absorption layer thickness  $d \approx 0.8 \mu\text{m}$ , electron velocity becomes lower than the hole velocity and then electrons, which are not in saturation, start to limit the bandwidth. For bias voltage  $V_{cc} = 2 \text{ V}$  electrons are localized in the satellite valleys and holes are in saturation. But, electrons are always slower than holes. In this case they predominantly limit the bandwidth and curve decreasing is well observed. In all cases electrons are localized in satellite valleys and nonstationary effects are not noticeable.

Figure 2 shows the dependence of bandwidth on the applied bias voltage of RCE P-i-N photodiode for absorption layer thickness  $d = 0.6 \mu\text{m}$ . Dash curve represents bandwidth without RC-constant influence

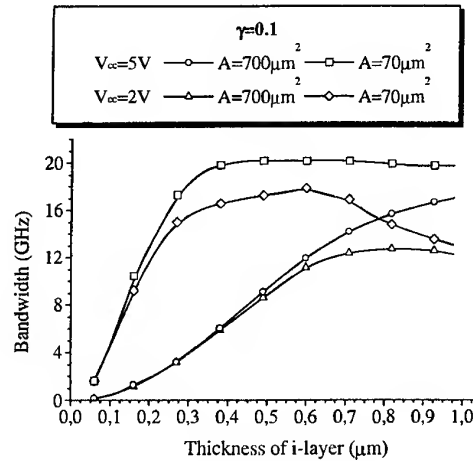


Fig. 1. The bandwidth versus thickness of i-layer for two different bias voltage  $V_{CC} = 5 \text{ V}$  and  $V_{CC} = 2 \text{ V}$  and two different values of active area  $A = 700 \mu\text{m}^2$  and  $A = 70 \mu\text{m}^2$ .

( $R = 0 \Omega$ ). For bias voltages  $V_{cc} \leq 1 V$  electrons are localized in the central valley where their mobility is much larger than holes mobility. Therefore, bandwidth is predominantly limited by holes. For bias voltages  $1 V \leq V_{cc} \leq 2 V$  intervalley transfer is significant. Owing to intervalley transfer the bandwidth increases slower but holes are still the main limiting factor. Maximum corresponds to holes saturation. Beyond maximum the bandwidth increase has much lower slope, because electrons are localized in the satellite valleys where their velocity is small. For  $V_{cc} \geq 6 V$  electron velocity becomes larger than holes saturation velocity and holes influence becomes significant again. Two other curves represent bandwidths when RC-constant influence is present, for two active areas in fact two capacitance values.

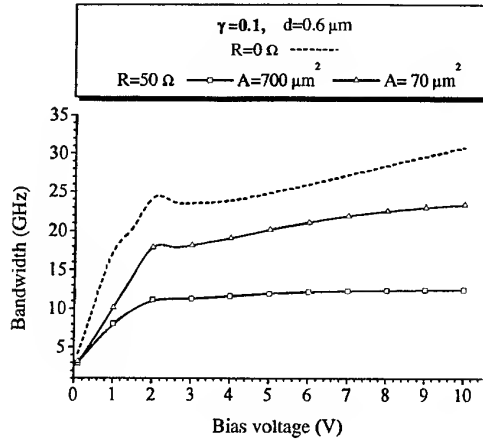


Fig. 2. The bandwidth versus bias voltage for two different values of load resistance  $R = 0 \Omega$  and  $R = 50 \Omega$  and two different values of active area  $A = 700 \mu m^2$  and  $A = 70 \mu m^2$ . (of course). We may also observe that bandwidth-quantum efficiency product, for special combinations of bias voltages and active areas, has maximum for thicknesses less than  $1 \mu m$ . This provides speed increasing without reducing photodiode's gain.

We may conclude, in general, that RC-constant presence reduces the bandwidth and decelerates the bandwidth slope vs bias voltage. For active area  $A = 70 \mu m^2$  nonstationary effects, described above, are observed but less than in the case when RC-constant is zero. For active area  $A = 700 \mu m^2$  nonstationary effects, owing to large RC-constant, cannot be observed. Maximum is not present, and curve slope for  $V_{cc} \geq 2 V$  is almost zero. In both cases, for applied bias voltage range, the bandwidth is limited by carrier transit time.

Figures 3a) and 3b) show the dependence of bandwidth-quantum efficiency product on the absorption layer thickness of RCE P-i-N photodiode. Significant difference is observed when compared with conventional P-i-N photodiode [1]. Oscillatory behaviour is a consequence of resonant cavity presence. In case of RCE P-i-N photodiode, it is possible to provide, for special absorption layer thicknesses, very large bandwidth-quantum efficiency product, even 30% larger than in case of conventional P-i-N photodiode (for the same bias voltages and active areas,

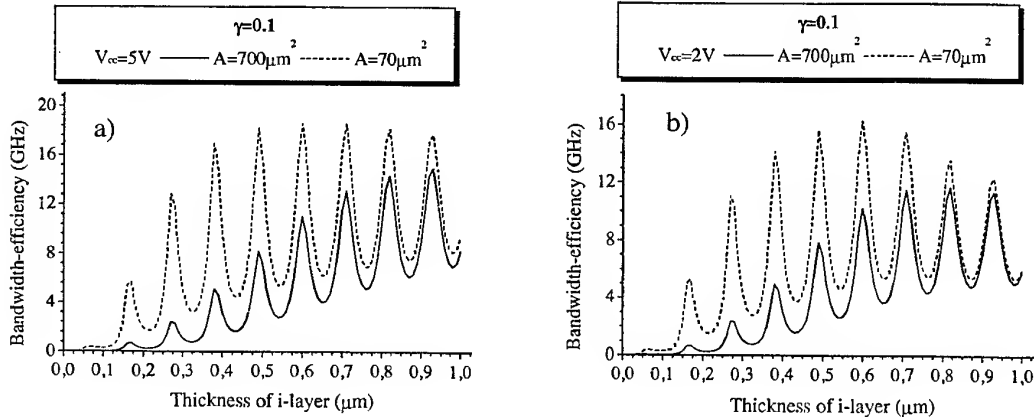


Fig. 3. The bandwidth-quantum efficiency product versus the i-layer thickness for two different values of active area  $A = 700 \mu m^2$  and  $A = 70 \mu m^2$  and bias voltage a)  $V_{CC} = 5 V$ , b)  $V_{CC} = 2 V$ .

#### References

- 1 P. S. Matavulj, D.M. Gvozdić, and J. B. Radunović, *Journal of Lightwave Technology*, 12, 2270 (1997)
- 2 P.S. Matavulj, D.M. Gvozdić, and J. B. Radunović, *MIEL '97*, 1, 331 (1997)
- 3 H. H. Tung and C. P. Lee, *IEEE Journal of Quantum Electronics*, 5, 753 (1997)
- 4 P. L. Nikolić, D. M. Gvozdić, and J. B. Radunović, *MIEL '97*, 1, 327 (1997)
- 5 A. Srinivasan, S. Murtaza, J. C. Campbell, and B. G. Streetman, *Appl. Phys. Lett.*, 5, 535 (1995)

# Mixing of 28 THz CO<sub>2</sub>-Laser Radiation by Nanometer Thin-film Ni-NiO-Ni Diodes with Difference Frequencies up to 176 GHz

C. Fumeaux<sup>1</sup>, W. Herrmann<sup>1</sup>, F.K. Kneubühl<sup>1</sup>, H. Rothuizen<sup>2</sup>, B. Lipphardt<sup>3</sup>, C.O. Weiss<sup>3</sup>

<sup>1</sup> Institute of Quantum Electronics, Swiss Federal Institute of Technology (ETH), CH-8093 Zürich, Switzerland

(Tel.: +41-1-633 23 40, Fax: +41-1-633 10 77, e-mail: infrared@iqe.phys.ethz.ch)

<sup>2</sup> IBM Research Laboratory, Säumerstrasse 4, CH-8803 Rüschlikon, Switzerland

<sup>3</sup> Physikalisch-Technische Bundesanstalt (PTB), D-38116 Braunschweig, Germany

## Abstract

Difference frequencies up to 176 GHz between CO<sub>2</sub>-laser transitions at 28 THz (10.7  $\mu$ m) are generated by thin-film nanometer-scale Ni-NiO-Ni diodes (MOM, MIM) with integrated bow-tie antennas and rhodium waveguides.

The mixing of infrared radiation with point-contact Metal-Oxide-Metal (MOM) diodes was first demonstrated by Hocker et al. in 1968 [1]. Since then, the range of operation of these devices has been extended to the visible [2]. These diodes have been intensively used in absolute frequency measurements and high-resolution spectroscopy. In 1973, Javan and co-workers [3] reported the first fabrication of thin-film diodes and demonstrated their mixing capability at approximately 1 THz. In this paper we report on the first successful mixing of two 28 THz (10.7  $\mu$ m) CO<sub>2</sub>-laser transitions in the 10P branch with difference frequencies up to 176.2 GHz performed by thin-film Ni-NiO-Ni diodes with integrated bow-tie antennas (Fig. 1) and new integrated rhodium waveguides. The fast response of our Ni-NiO-Ni diodes is due to their extremely thin NiO layer required for nonlinear electron tunneling and to their sufficiently small contact area of 110 nm  $\times$  110 nm that implies a short RC time constant. The fabrication and development of our thin-film Ni-NiO-Ni diodes with integrated dipole, bow-tie and spiral antennas and their application to the detection of 10  $\mu$ m CO<sub>2</sub>-laser radiation is described elsewhere [4-6]. First mixing experiments with our thin-film diodes are reported in [7]. They resulted in difference frequencies up to 85 MHz.

For the measurements described here [8,9], the diode is based on a high-resistivity ( $> 3$  k $\Omega$ -cm) silicon substrate with weak losses in the microwave region [10] and low attenuation of the antenna currents at infrared frequencies. The previous connections to the diode with bond-wires [7] have now been replaced by coplanar rhodium waveguides and indium solder flip-chip connections, which guarantee excellent high-frequency transmission and permit the

illumination of the antenna from the back side of the substrate.



Fig. 1: Electron micrograph of our thin-film Ni-NiO-Ni diode with integrated bow-tie antenna

The radiation of two CO<sub>2</sub>-lasers with wavelengths near 10.7  $\mu$ m was focused on the diode. The total infrared power on the diode was approximately 400 mW. The two lasers constitute part of the permanent frequency-measurement chain of the PTB (Braunschweig, Germany) [11]. Part of the mixing performed is shown in Table 1. In the second-order mixing experiment, the difference-frequency signal of two adjacent laser lines at 58.7 GHz was externally mixed with microwaves and measured with a spectrum analyzer. The higher-order mixing processes required irradiation of the diode with the microwaves produced by a Gunn oscillator working at the frequencies 58.8 GHz  $\pm$  50 MHz. The measured mixing signals listed in Table 1 show significant signal-to-noise (S/N) ratios, especially in the third-order mixing with 47 dB for a bandwidth of 100 kHz (Fig. 2). The highest difference frequency of 176.19 GHz was generated by mixing the 10P(30) and 10P(36) emissions with the third harmonic of the Gunn oscillator in a fifth-order mixing process.

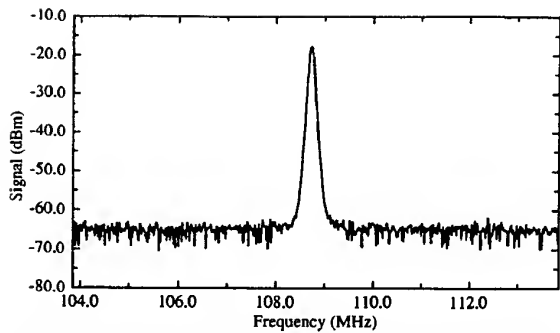


Fig. 2: Third-order mixing signal with a laser difference frequency of 58.7 GHz and a 100 kHz detection bandwidth

The mixing signals as a function of the polarization of the incident  $10.7 \mu\text{m}$   $\text{CO}_2$ -laser radiation are represented in Fig. 3 in the case of third-order mixing. The perfect polarization dependence demonstrates that our bow-tie antennas show almost complete polarization as predicted by the antenna theory of microwave techniques [12]. This can be explained by the fact that in our range of difference frequencies, the polarization-independent thermal effects are too slow to influence the mixing signal.

Our experiments represent the first mixing of  $10 \mu\text{m}$   $\text{CO}_2$ -laser radiation with thin-film MOM diodes with difference frequencies in the 50 to 200 GHz range.

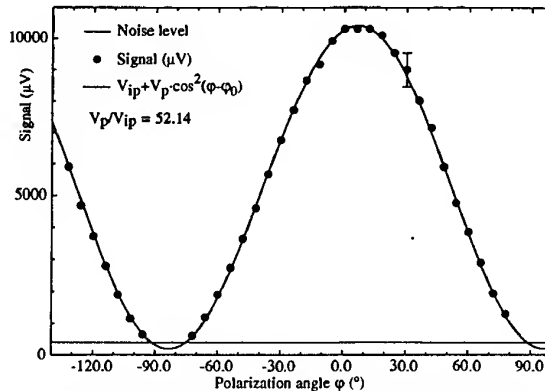


Fig. 3: Polarization dependence of the third-order mixing signal with a difference frequency of 58.7 GHz between the two  $\text{CO}_2$ -lasers

Mixing process	Mixing order	Laser difference frequency $\Delta\nu$	S/N ratio	Bandwidth	Polarization contrast
10P32-10P34 (external mixing)	2	58.7 GHz	22 dB	100 kHz	34.4 dB
10P32-10P34 + MW 58.8 GHz	3	58.7 GHz	47 dB	100 kHz	34.4 dB
10P30-10P34 + 2 $\times$ MW 58.8 GHz	4	116.7 GHz	19 dB	100 kHz	> 25 dB
10P36-10P30 + 3 $\times$ MW 58.8 GHz	5	176.2 GHz	14 dB	300 kHz	-

Table 1: Mixing with our thin-film Ni-NiO-Ni diodes.

## References:

- [1] L.O. Hocker, D.R. Sokoloff, V. Daneu, A. Szoke, A. Javan: Appl. Phys. Lett. **12**, 401-402 (1968)
- [2] H.-U. Daniel, M. Steiner, H. Walther: Appl. Phys. **25**, 7-12 (1981)
- [3] J.G. Small, G.M. Elchinger, A. Javan, A. Sanchez, F.J. Bachner, D.L. Smythe: Appl. Phys. Lett. **24**, 275-279 (1974)
- [4] I. Wilke, W. Herrmann, F.K. Kneubühl: Appl. Phys. **B 58**, 87-95 (1994)
- [5] I. Wilke, Y. Oppliger, W. Herrmann, F.K. Kneubühl: Appl. Phys. **A 58**, 329-341 (1994)
- [6] C. Fumeaux, G.D. Boreman, W. Herrmann, H. Rothuizen, F.K. Kneubühl: Appl. Opt. **36**, 6485-6490 (1997)
- [7] C. Fumeaux, W. Herrmann, H. Rothuizen, P. De Natale, F.K. Kneubühl: Appl. Phys. **B 63**, 135-140 (1996)
- [8] C. Fumeaux, W. Herrmann, F.K. Kneubühl, H. Rothuizen, B. Lipphardt, C.O. Weiss: Infrared Phys. & Techn. **38**, 393-396 (1997)
- [9] C. Fumeaux, W. Herrmann, F.K. Kneubühl, H. Rothuizen, B. Lipphardt, C.O. Weiss: Appl. Phys. **B 66**, in print (1998)
- [10] A. Rosen, M. Caulton, P. Stabile, A.M. Gombar, W.M. Janton, C.P. Wu, J.F. Corboy, C.W. Magee: RCA Rev. **42**, 633-660 (1981)
- [11] H. Schnatz, B. Lipphardt, J. Helmcke, F. Riehle, G. Zinner: Phys. Rev. Lett. **76**, 18-21 (1996)
- [12] J.D. Kraus: "Antennas", second edition, McGraw-Hill, New York (1988)

## Acknowledgements:

This study is supported by GR/EMD, Bern; Swiss Federal Institute of Technology (ETH), Zürich; and IBM Research Laboratory, Rüschlikon.

## Tunable Far-Infrared Spectroscopy in the 6 to 9 THz Region

Hitoshi Odashima,<sup>1</sup> Lyndon R. Zink,<sup>2</sup> and K. M. Evenson<sup>2</sup>

<sup>1</sup>Department of Physics, Toyama University, Gofuku 3190, Toyama 930-8555 Japan; and

<sup>2</sup>Time and Frequency Division, National Institute of Standards and Technology, 325 Broadway, Boulder, Colorado 80303, U.S.A.

### Abstract

We generated tunable far-infrared radiation up to 9.1 THz by mixing CO<sub>2</sub> laser, <sup>15</sup>NH<sub>3</sub> laser, and microwave radiation in a metal-insulator-metal diode. We used this radiation to measure accurately the torsion-rotation transitions of CH<sub>3</sub>OH and the pure rotational transitions of HF and HCl in the 6-9 THz region.

### Introduction

The far-infrared (FIR) region (1–10 THz) is sometimes referred to as “the gap in the electromagnetic spectrum”, because it is difficult to produce tunable, coherent radiation. For high-resolution spectroscopy in this frequency region, Evenson and his coworkers developed a tunable far-infrared (TuFIR) spectrometer in which tunable, coherent far-infrared radiation is produced by difference frequency generation from two CO<sub>2</sub> lasers in a metal-insulator-metal (MIM) diode [1,2]. This TuFIR spectrometer covers the frequency region up to 6.5 THz limited by the maximum frequency difference between two CO<sub>2</sub> lasers [3]. In the previous conference, we reported the extension of tunable FIR spectroscopy up to 7.9 THz, replacing one of two CO<sub>2</sub> lasers in the traditional TuFIR spectrometer with a <sup>15</sup>NH<sub>3</sub> laser which oscillates at lower frequencies than those of a CO<sub>2</sub> laser and thus provides higher difference frequencies[4]. With this ammonia-TuFIR spectrometer, we measured torsion-rotation transition frequencies of CH<sub>3</sub>OH with an accuracy better than 1 MHz. However, we failed to observe the CH<sub>3</sub>OH spectrum over 8 THz because of reduced MIM diode efficiency at higher frequencies and reduced FIR detector sensitivity of the gallium-doped germanium (Ge:Ga) photoconductor whose sensitivity peaks around 3 THz. In the present work, we will report the further extension of tunable FIR spectroscopy into the 8-10 THz region with an improved ammonia-TuFIR spectrometer in which both a higher sensitivity beryllium-doped germanium (Ge:Be) photoconductor and a more powerful <sup>15</sup>NH<sub>3</sub> lower frequency laser are used.

### Experimental details and results

The radiation from a CO<sub>2</sub> laser (frequency  $\nu_1$ ), a <sup>15</sup>NH<sub>3</sub> laser ( $\nu_2$ ), and a microwave (MW) synthesized sweeper ( $1 \leq \nu_{\text{MW}} \leq 20$  GHz) is mixed in a W-Co MIM diode. Two tunable FIR frequencies:  $\nu_{\text{FIR}} = |\nu_1 - \nu_2| \pm \nu_{\text{MW}}$  are generated. The synthesized FIR frequency is changed by tuning the microwave source. Details of our <sup>15</sup>NH<sub>3</sub> laser are found in Refs.[4,5] and details of the ammonia-TuFIR spectrometer are described in Ref.[4] except for the following changes. The generated FIR radiation is detected by a Ge:Be photoconductor. Using 38- $\mu\text{m}$  CH<sub>3</sub>OH FIR laser line, we have confirmed that this detector is a few times more sensitive at 7.6 THz than the Ge:Ga detector used previously. To generate a difference frequency over 9 THz, we pumped the  $aR(2,0)$  <sup>15</sup>NH<sub>3</sub> transition by a two times more powerful CO<sub>2</sub> laser which provides a power of ~35W for the pump  $R(42)_1$  CO<sub>2</sub> laser line. The <sup>15</sup>NH<sub>3</sub> oscillates on  $aP(7,3)$  line at a lower frequency as well as  $aP(4,0)$ ,  $aP(4,3)$ ,  $aP(5,3)$ ,  $aP(6,0)$ , and  $aP(6,3)$  with a typical power of 0.3–1.2 W, and a grating selects one of them. At first, CH<sub>3</sub>OH was chosen as a sample gas to demonstrate the generation of FIR radiation over 9 THz because of its rich torsion-rotation spectrum in this frequency region. Three transitions up to 9.1 THz were measured. A plot of the observed absorption from the  $A, (n,K,J) = (1,7,19) \leftarrow (0,6,19)$  transition at 9.1 THz is shown in Fig. 1, where  $n$  is the torsional quantum number. With a traditional TuFIR spectrometer, pure rotational transitions of light molecules, such as HF and HCl, were measured accurately below 6.5 THz [1].

Table 1

Observed Frequencies of CH<sub>3</sub>OH, HF, and HCl.

CH <sub>3</sub> OH	Transition <sup>a</sup>	Obs. Freq. (MHz) <sup>b</sup>
E, (1,-4, 20)←(0,-3,19)		8 083 380.39(64)
E, (1,2, 13)←(0,1,12)		8 510 223.84(80)
A, (1,7,19)←(0,6,19)		9 063 067.34(56)
HF	Transition	Observed Frequency
	$J = 6 \leftarrow 5$	7 341 700.96(35)
	$7 \leftarrow 6$	8 542 410.96(98)
H <sup>35</sup> Cl	Transition	Observed Frequency
	$J = 11 \leftarrow 10$	6 801 958.73(23)
	$12 \leftarrow 11$	7 403 057.80(35)
	$14 \leftarrow 13$	8 591 531.68(46)
H <sup>37</sup> Cl	Transition	Observed Frequency
	$J = 11 \leftarrow 10$	6 791 867.06(22)
	$12 \leftarrow 11$	7 392 100.67(52)
	$14 \leftarrow 13$	8 578 884.52(63)

<sup>a</sup>The assignment of CH<sub>3</sub>OH transition is given by (*n, K, J*).

<sup>b</sup>The estimated uncertainties of the last quoted digits (2σ) are given in parentheses.

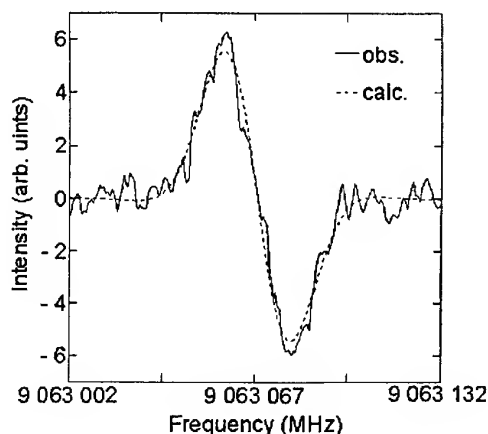


Fig.1

A plot of the observed absorption from the  $A$ , ( $n, K, J$ ) = (1,7,19) ← (0,6,19) transition of CH<sub>3</sub>OH.

We have made extended measurements of higher- $J$  transitions of HF, H<sup>35</sup>Cl, and H<sup>37</sup>Cl with this ammonia-TuFIR spectrometer in the 6-9 THz region. The observed frequencies are summarized in Table 1 with the estimated 2σ uncertainties.

## Discussion

Our previous and present experimental results show that the third-order generation, in which tunable FIR radiation is obtained from a CO<sub>2</sub> laser, a <sup>15</sup>NH<sub>3</sub> laser, and MW radiation, works up to 9.1 THz. Because of its wide tuning range (±20 GHz), this ammonia-TuFIR spectrometer provides nearly complete coverage of the 6-9 THz region. We have successfully applied this spectrometer for the observation of the rotational transitions of HF and HCl. The measured accurate frequencies of strong absorption lines of these stable molecules should be useful for calibration standards in this frequency region. The observed spectrum in Fig.1 shows a good signal-to-noise ratio even at 9.1 THz; however, to observe FIR spectrum over 9.1 THz, we should provide a <sup>15</sup>NH<sub>3</sub> laser power for lower frequency lines than  $aP(7,3)$  enough both for frequency stabilization (~100 mW) and for FIR generation (~150 mW), using a more efficient <sup>15</sup>NH<sub>3</sub> laser. At higher frequencies, more sensitive detection of a smaller amount of FIR radiation is required. A Si:B photoconductor whose sensitivity peaks around 11 THz could be used near 10 THz. We believe that this TuFIR technique should be applicable up to ~10 THz with a Si:B detector and that "the gap in the electromagnetic spectrum" should disappear.

## References

1. K. M. Evenson, D. A. Jennings, and F. R. Petersen, Appl. Phys. Lett. **44**, 576 (1984).
2. I. G. Nolt, J. V. Radositz, G. DiLorenzo, K. M. Evenson, D. A. Jennings, K. R. Leopold, M. D. Vanek, L. R. Zink, A. Hinz, and K. V. Chance, J. Mol. Spectrosc. **125**, 274 (1987).
3. F. Matsushima, K. M. Evenson, and L. R. Zink, J. Mol. Spectrosc. **164**, 517 (1994).
4. H. Odashima, M. Tachikawa, L. R. Zink, and K. M. Evenson, the 22nd international conference on IR & MMW, Wintergreen, 1997; Opt. Lett. **22**, 822 (1997) and J. Mol. Spectrosc. **188**, 245 (1998).
5. M. Tachikawa and K. M. Evenson, Opt. Lett. **21**, 1247 (1996).



## Development of High Efficiency Backward Wave Oscillators for Millimeter and Submillimeter Applications

R. Lawrence Ives, Malcom Caplan, Andrej Tulupov\*

Calabazas Creek Research, Inc.  
20937 Comer Drive  
Saratoga, CA 95070, USA

\*Soliton-NTT Research Centre  
Krasnobogatyrskaya, Moscow, Russia 105023

Calabazas Creek Research, Inc. and Soliton-NTT Research Centre are developing advanced backward wave oscillators (BWOs) that will incorporate a depressed collector for energy recovery and improved output coupling of the RF signal for improved mode purity. In addition, advanced magnetic technology will be utilized to reduce the weight of the permanent magnet. Successful development will result in devices that require significantly less input power, require less cooling, have reduced weight, and have improved mode purity than sources now in use.

BWO sources are presently used for ground based atmospheric sensing of trace chemicals, testing of solid state sensors, and basic spectroscopy research. The innovative developments proposed here will allow these devices to be used for airborne and/or space atmospheric sensing missions, as well as reduce the cost and complexity of the BWO sources, making their unique tunability and output power capability more accessible to research laboratories around the world.

The technical objectives of the current program are as follows:

- Develop depressed collector designs for BWOs in the range of 300 GHz to 900 GHz such that the maximum input power requirement is 10 watts or less for 5-20 mW of output power.
- Develop depressed collector designs that can sufficiently reduce the dissipated power of the spent electron beam to allow air cooling rather than water cooling.
- Develop mode converter designs that facilitate single mode operation over the tuning range of the BWO.
- Develop new designs for the permanent magnet system that will result in a 30% or greater weight reduction.

Soliton-NTT research Centre currently produces BWOs in the 300 GHz to 1100 GHz frequency range. A recently delivered 800 GHz to 1100 GHz BWO is currently on loan to the Jet Propulsion Laboratory in Pasadena, California and is performing well. That device incorporates multiple sheet beams and requires approximately 100 W of input power and water cooling. Unfortunately, this prevents its use in airborne or satellite applications. The output also contains a large mixture of modes, which reduces the percentage of usable power.

In order to incorporate the depressed collector, it will be necessary to redesign the cathode structure, electron gun, and beam focusing and transport system. Soliton will be investigating use of a single, cylindrical beam rather than the existing multiple sheet beams, though implementation of the depressed collector with sheet beams should be practical. Depressed collector design will be performed using advanced finite difference and finite element particle simulation codes that include secondary electron emission.

The program will also investigate techniques for improving the output mode purity of the RF output. This will involve coupling to the RF power emerging from the slow wave structure and using advanced mode converters and tapers to control the transition into the overmoded output waveguide. This analysis will utilize advanced scattering matrix design codes and slow wave circuit codes.

A new magnet design will be required to incorporate changes in the electron beam system, depressed collector, and output waveguide structure with the mode converters and tapers. The goal will be to reduce the weight of the magnet by 30% from that of the current device. The program will utilize new design techniques developed at the U.S. Army Research Laboratory and the computer codes Maxwell 2D and Maxwell 3D.

This research is funded by Small Business Innovation Research Grant Number NAS8-98186 from the U.S. National Aeronautics and Space Administration.

# Study on Folded Waveguide Traveling Wave Tube

Gun-Sik Park, Hyun-Jun Ha and Soon-Shin Jung

Physics Education Department, Seoul National University, Seoul, Korea

## Abstract

Ku-band folded waveguide type TWT is in fabrication. This particular type of TWT draws attention for its robust structure and easier coupling. The linear theory predicts a gain of 2 dB/cm and a bandwidth 37% at the center frequency of 14 GHz when the parameters of the circuit are  $b=0.469\text{cm}$ ,  $l=0.746\text{cm}$ ,  $h=2.017\text{cm}$ . A dispersion relation is derived using an equivalent circuit model and is compared with HFSS simulation. Electron beam and its diagnostics, solenoid, RF circuit, and other components in fabrication are discussed.

## Summary

Broadband operation(14- 14.5 GHz) is realized by slowing down the phase velocity of electromagnetic wave close to the velocity of the electron beam. A linear theory of slow-wave interaction in folded waveguide has been developed.

$$\delta \bar{k} (\Delta_m + \delta \bar{k})^2 \left( \frac{1 - \delta \bar{k}}{2k_{01}^2} \right) - C^3 = 0$$

$$\text{where } C^3 = \frac{1}{\gamma_o^3 \beta_{zo}^3} \frac{b}{a} \left( 1 + \frac{h}{l} \right) \left( \frac{a}{l} \right)^2 \left( \frac{\bar{\omega}}{k_c a} \right)^2 \left( \frac{|e| I_o}{\epsilon_o m_o c^3} \right) \left( \frac{G_m C_b}{k_o} \right)$$

$$\Delta_m = \frac{\bar{\omega}}{\beta_{zo}} - \bar{k}_{o1} - \frac{(2m+1)\pi}{k_c l} \quad \bar{k}_{o1} = \frac{l+h}{l} \sqrt{\frac{\omega^2 - \omega_c^2}{c^2}} \quad \bar{k} = k/k_c \quad \bar{\omega} = \omega/\omega_c \quad \bar{k}_o = \sqrt{\bar{\omega}^2 - 1}$$

The linear theory predicts a gain of 2 dB/cm and a bandwidth 37% at the center frequency of 14 GHz, when the parameters of the circuit are  $b=0.469\text{cm}$ ,  $l=0.746\text{cm}$ ,  $h=2.017\text{cm}$  as shown Fig. 1. A dispersion relation is derived using an equivalent circuit model and is compared with HFSS simulations as shown in Fig. 2. The schematic of the experimental setup is shown in Fig. 1. Here an electron beam of 6 kV and 0.2 A is used. The minimum radius of the beam is 0.5 mm. To study the effect of magnetic field on the stability of the electron beam and interaction between the beam and waves, the solenoidal coils are used. Iron pole pieces are used to confine the flux and limit the leakage of flux into the gun region. The magnetic field is estimated by Maxwell 2D code and its profile is shown in Fig. 5. To produce the highly stiff field gradient at the beginning of the interaction circuit, a special flange partly made of the iron is fabricated. The beam stability is studied with this field as shown in Fig. 6. The electron beam diagnostic using a cerium glass is prepared. To increase an overall efficiency of the folded waveguide TWT, the depressed collector will be used. The power supply fabricated by LG Precision is prepared as shown Fig. 8. The power supply can provide the electrode voltage ranged from 0 to -10 kV, the beam current of 0~1 A with the pulse duration of 10  $\mu\text{s}$ .

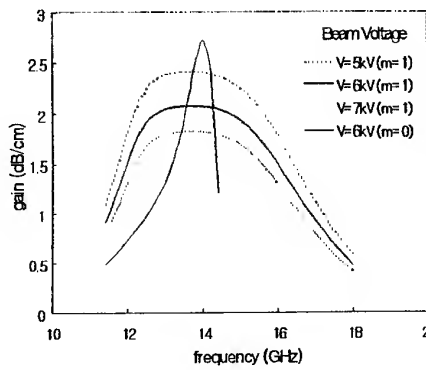


Fig. 1. The gain vs. beam voltage

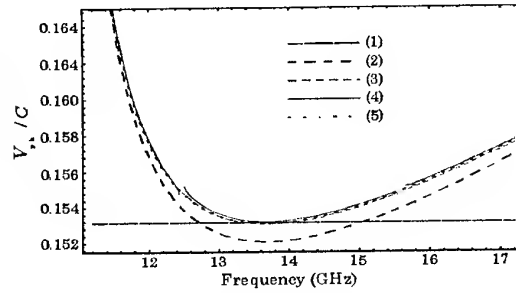


Fig. 2. Phase velocity of waves in a folded waveguide (1) beam line (2) obtained by considering bend as straight (3) obtained by considering both straight and bend section (4) obtained by dispersion relation (5) simulated by HFSS

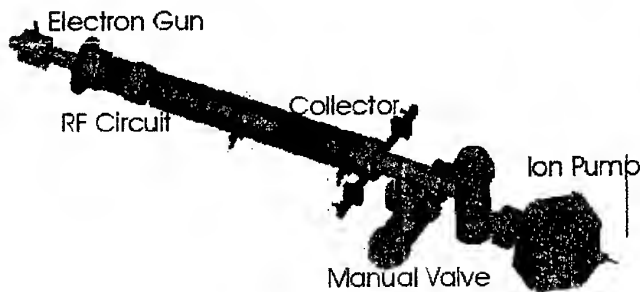


Fig. 3. Schematic of folded waveguide TWT System

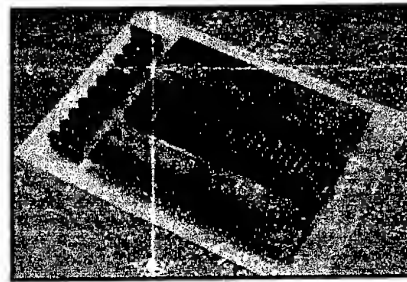


Fig. 4. Folded waveguide TWT interaction circuit

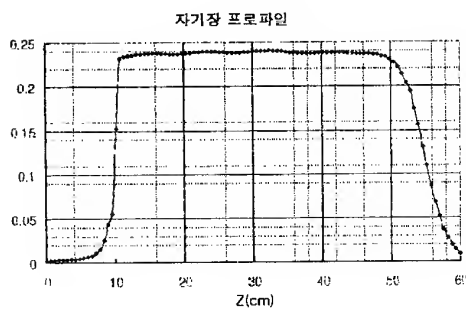


Fig. 5. Magnetic field profile

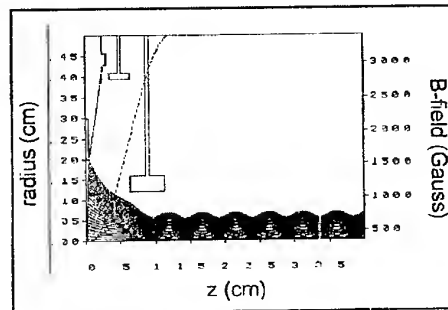


Fig. 6. Computer simulation of electron gun with magnetic field

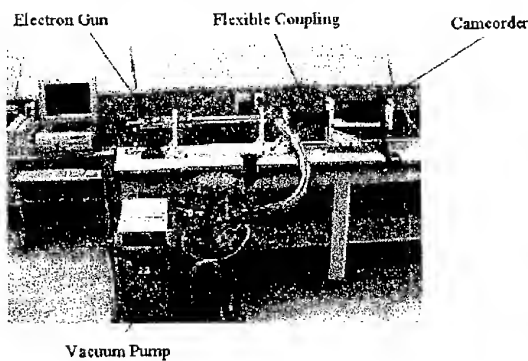


Fig. 7. Electron beam diagnostic system

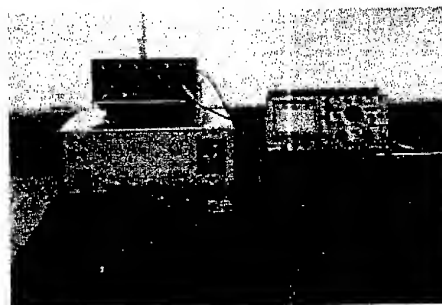


Fig. 8. Power supply and dummy load

## Investigation of Magnetic Excitations in Rare Earth Metals by Far Infrared ATR Spectroscopy

S A Feiven<sup>1</sup>, T J Parker<sup>1</sup>, S R P Smith<sup>1</sup> and D R Tilley<sup>1,2</sup>

<sup>1</sup>Department of Physics, University of Essex, Colchester, CO4 3SQ, UK

<sup>2</sup>School of Physics, Universiti Sains Malaysia, 11800 USM, Penang, Malaysia

### Introduction

In recent years we have developed a high resolution ( $0.015 \text{ cm}^{-1}$ ) far infrared Fourier transform spectrometer for investigating bulk and surface magnetic polaritons in antiferromagnetic and ferrimagnetic media in the frequency range from about 10 to  $100 \text{ cm}^{-1}$  [1]. Bulk excitations are investigated using polarised oblique incidence reflection measurements, and surface excitations are investigated using polarised attenuated total reflection (ATR) spectroscopy [2,3]. Measurements can be made at temperatures in the range 1.6-300 K with the specimen located in a magnetic field of up to 7 Tesla in the Voigt configuration. In previous work with this instrument we have investigated bulk and surface magnetic excitations in the bulk antiferromagnet  $\text{FeF}_2$ , and used the results to study non-reciprocal behaviour in an applied magnetic field and obtain experimental determinations of the magnetic polariton dispersion curves. In more recent work, the feasibility of using far infrared spectroscopy to probe magnetic excitations in highly conducting media has been established [4].

For decades the spectroscopic investigation of magnetic excitations in conducting media has presented formidable problems because coupling to the magnetic excitations is screened by the high reflectivity (typically ~99%) due to the conduction electrons. For measurements on Dy and Tb, Sievers in 1970 [5] made far infrared transmission lines by rolling alternate thin layers of metal and polyethylene into "jelly roll" coils which were used as transmission lines. However, he reported that the sample surface is not well defined in such a structure, and the method is only suitable for studying polycrystalline samples. In 1994 Abraha and Tilley [6] reported theoretical work which indicated that the weak coupling expected in a simple reflection experiment (~1%) might be significantly enhanced by carrying out a suitable ATR experiment. In this paper we report ATR measurements which establish the feasibility of using FIR spectroscopy to investigate magnetic excitations in conducting media like the rare earth metals for the first time. The measurements are made on plane single crystal samples in an experimental configuration which matches very closely the configuration analysed theoretically.

### Rare Earth Magnetism

Rare earth (RE) metals crystallise in an hcp structure. Dy orders magnetically in a helical phase below  $T_N = 179 \text{ K}$  in which the spins align in the ab-plane (normal to the hexagonal c-axis) with a helix angle  $\psi$  between the spin direction in neighbouring ab-planes. Below  $T_F = 89 \text{ K}$ , the spins align ferromagnetically ( $\psi = 0$ ) along an "easy" direction  $a$  in the ab-plane. There are 6 possible equivalent easy directions  $a$ , every  $60^\circ$ , which are orthogonal to the corresponding "hard" directions  $b$ .

Cooper [7] has given a comprehensive review of the magnetic properties of RE metals. With a magnetic field  $B_0$  applied along an easy axis, magnetic resonance is observed at a frequency  $\omega_R$  given by

$$\omega_R^2 = \omega_A \omega_B$$

with

$$\omega_A = \omega_0 + \omega_2 + \omega_6; \quad \omega_B = \omega_0 + 6\omega_6$$

where  $\omega_2$  and  $\omega_6$  are connected with the rank 2 and rank 6 components of the single ion spin-Hamiltonian operators, and  $\omega_0 = g\beta B_0/\hbar$ . At low temperatures,

$$\omega_A \approx 8 \text{ cm}^{-1} + \omega_0; \quad \omega_B \approx 35 \text{ cm}^{-1} + \omega_0; \quad \omega_0 \approx 0.62 B_0 \text{ cm}^{-1} \text{ (} B_0 \text{ in Tesla).}$$

Our measurements involve a sample cut with its face normal to a b-axis (hard axis). The magnetic field  $B_0$  is applied along an easy (a) axis. The ATR reflectivity is measured at this surface with radiation propagating in the bc-plane and with its E-field along the a-axis (s-polarisation configuration). The relevant components of the magnetic susceptibility are

$$\chi_{cc} = 2.30 \frac{\omega_A}{\omega_R^2 - \omega^2}; \quad \chi_{cb} = 2.30 \frac{i\omega}{\omega_R^2 - \omega^2} = -\chi_{bc}; \quad \chi_{bb} = 2.30 \frac{\omega_B}{\omega_R^2 - \omega^2}$$

with all frequencies in  $\text{cm}^{-1}$  units. The permeability tensor is given by  $\mu = 1 + \chi$ , and damping should be included in a full treatment, so that  $\mu(\omega)$  is complex.

Abraha and Tilley [6] have discussed the far-infrared reflectivity of this system, following earlier work on surface polaritons by Almeida and Tilley [8]. A reflectivity experiment in s-polarisation involves the Voigt permeability  $\mu_v = \mu_{cc} - |\mu_{cb}|^2/\mu_{bb}$ . The reflection coefficient for reflection at an interface between media 1 and 2 has the form

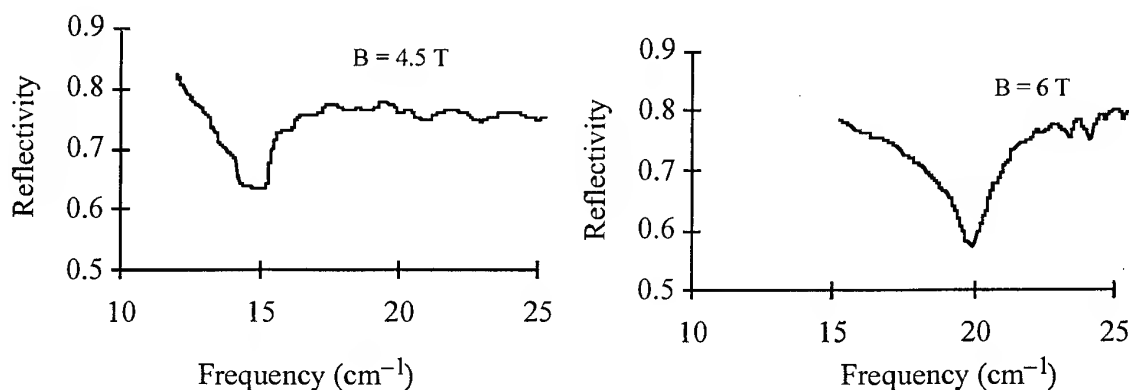


Fig. 1. Reflectivity of Dy metal at  $B_0 = 4.5 \text{ T}$  and  $6.0 \text{ T}$ .

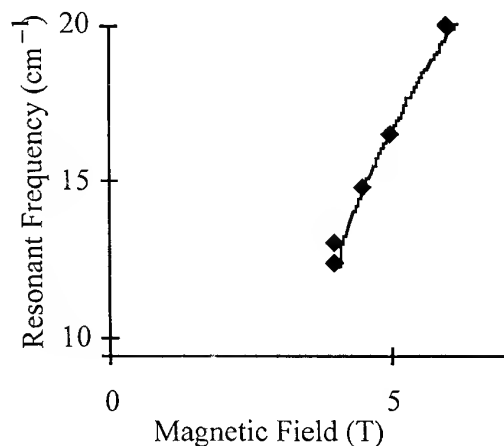


Fig. 2. Dependence of resonance frequency in Dy on magnetic field at  $T = 40 \text{ K}$ .

$$R = \left| \frac{1-f}{1+f} \right|^2$$

where  $f$  is an appropriate ratio of impedances, i.e.  $\mu_1 q_2 / \mu_2 q_1$ , where the normal components of wave-vector  $q_i$  are given by

$$q_i^2 = k_0^2 (\epsilon_i \mu_i - \sin^2 \theta_0)$$

with  $k_0$  the wavevector in the external medium, where the angle of incidence is  $\theta_0$ . It can be seen that a low reflectivity will be obtained under the impedance matching conditions  $f \approx 1$ , i.e.  $\mu_1 q_2 \approx \mu_2 q_1$ . If medium 2 is a rare earth metal, the dielectric permittivity  $\epsilon_2$  is large and complex, so  $f$  is normally large and complex, and  $R \approx 1$ . In order that a significant change in reflectivity  $R$  is observable,  $\mu_2$  needs to be  $\sim 0$ . In fact, because of the fact that both  $\epsilon_2$  and  $\mu_2$  are complex, the maximum change in  $R$  occurs when  $\text{Re}\{\mu_2\}$  is negative, so the observed resonance is technically a surface polariton. Moreover, the larger  $\epsilon_1$  (assumed real), the larger the change in  $R$ . The above expressions apply to isotropic media; the situation is somewhat more complicated for anisotropic media, but for a RE metal  $\mu_2$  can be approximately equated to the Voigt permeability  $\mu_v$ , and the experimentally observable reflectivity resonance corresponds roughly to a zero in  $\mu_v$ .

### Results and conclusions

The experiments described here are essentially ATR experiments, in which the reflectivity is observed in oblique incidence reflection at an interface between a high permittivity medium (a silicon prism) and the rare earth metal. The measurements were made on a b-cut single crystal of Dy with the sample in the Voigt geometry at 40 K using various values of the applied magnetic field. The spectra shown in Fig. 1 clearly show a dip of  $\sim 25\%$  in the reflectivity near the resonance with a linewidth of about  $2 \text{ cm}^{-1}$ . The improvement in detectability of the resonance using ATR with a Si prism rather than simple reflection from a vacuum/RE metal interface is significant. Similar measurements attempted using ordinary oblique-incidence reflectivity showed no observable features at all, corresponding to coupling of less than the detectable limit of  $\sim 1\%$ . The possibility of a small gap between the prism and the metal surface, though essential for observation of surface polaritons in dielectric resonances, does not appear to have a fundamental importance in the magnetic resonance case. A graph of the mode frequency as a function of applied magnetic field, Fig. 2, shows a field dependence similar to that calculated by Rossol and Jones in 1966 [9]. No further calculations of this behaviour have been reported in the literature, presumably because theoretical progress has lacked the stimulation of experimental work. The theory summarised above will be developed further to permit a detailed comparison with experiment.

The measurements reported here thus establish the feasibility of using far infrared ATR spectroscopy to carry out detailed investigations of magnetic excitations in metals for the first time.

### References

1. T.Dumelow, D.E.Brown and T.J.Parker, Proc. 18th Int. Conf. on Infrared and Mm. Waves, Colchester, September 1993, Proc. SPIE, Vol. 2104, p. 633.
2. M.R.F.Jensen, S.A.Feiven, T.J.Parker and R.E.Camley, Proc. 21st Int. Conf. on Infrared and Mm. Waves, Berlin, July 1996, ISBN 3-00-000800-4, paper CM12.
3. M.R.F.Jensen, G.Mirjalili, S. Farjami Shayesteh, S.A.Feiven, T.J.Parker, and R.E.Camley, *ibid*, paper CTh2.
4. S.A.Feiven, T.J.Parker and S.R.P.Smith, Inst. of Phys. Conf.: CMMP, Exeter, December, 1997, Paper AM.P1.28.
5. A.J.Sievers, J, Appl. Phys., 41, 980 (1970).
6. K. Abraha and D.R. Tilley, *Infrared Phys. Technol.*, 35, 681-699 (1994)
7. B.R. Cooper, *Solid State Physics* (ed. F. Seitz, D. Turnbull and H. Ehrenreich), Vol. 21, p.293. Academic Press, New York (1968)
8. N.S. Almeida and D.R. Tilley, *Solid State Commun.*, 73, 23 (1990)
9. F.C. Rossol and R.V.Jones, J. Appl. Phys. 37, 1227 (1966)

### Calculation of nonlinear magnetic susceptibility tensors for a ferromagnet

Siew-Choo Lim<sup>(1)</sup>, Junaidah Osman<sup>(1)</sup> and D. R. Tilley<sup>(1,2)</sup>

1. School of Physics, Universiti Sains Malaysia, 11800 USM, Penang, Malaysia

2. Department of Physics, University of Essex, Colchester CO4 3SQ

We derive expression for the nonlinear susceptibilities for a simple ferromagnet in a static magnetic field. We neglect exchange effects and consider only the dipolar interactions and magnetic anisotropy. We use continuum approach to transform the quantum mechanical equations of motion for spin operators to the semi-classical Landau-Lifshitz equations of motion:

$$\frac{d\mathbf{M}}{dt} = \frac{d\mathbf{m}}{dt} + \frac{\eta}{M_0} \mathbf{M} \times \frac{d\mathbf{m}}{dt} \quad (1)$$

for magnetization where  $\mathbf{M} = \mathbf{m} + M_0 \hat{z}$  with  $M_0$  as the magnitude of the equilibrium magnetization. The damping, second term in (1) with  $\eta$  as the damping parameter, is included to take account of the magnetic relaxation of the interactions between magnetization and the applied field  $\mathbf{H}$ . The static part of  $\mathbf{H}$ ,  $\mathbf{H}_d$ , includes magnetic anisotropy  $H_A$  and may include a demagnetizing field. The expressions for  $\tilde{\chi}$  are obtained by inverting the equation of motion in equivalence to the formulation in nonlinear optics [1,2] with the rf magnetization  $\mathbf{M}(\omega)$  expanded as a power series in the rf field:  $\mathbf{M} = \tilde{\chi}^{(1)} \mathbf{H} + \tilde{\chi}^{(2)} \mathbf{H}\mathbf{H} + \tilde{\chi}^{(3)} \mathbf{H}\mathbf{H}\mathbf{H}$ . For simplicity, we consider only a single-frequency input wave and second-order nonlinear effects namely second harmonic generation (SHG) and optical rectification (OR). Here we give expressions for the tensor elements in the circular polarization frame (+z) and discuss magnitudes, frequency and field dependences for two.

In the (+z) frame, SHG has three nonzero tensor elements  $\chi_{++z}^{\text{SHG}}$ ,  $\chi_{--z}^{\text{SHG}}$  and  $\chi_{z+-}^{\text{SHG}}$ ; and OR has four namely  $\chi_{++z}^{\text{OR}}$ ,  $\chi_{+-z}^{\text{OR}}$ ,  $\chi_{-z-}^{\text{OR}}$  and  $\chi_{-+z}^{\text{OR}}$ . As examples, expressions for  $\chi_{++z}^{\text{SHG}}$  and  $\chi_{-z-}^{\text{OR}}$  are found to be  $\chi_{++z}^{\text{SHG}} = -\frac{1}{2M_0} (1 + i\eta)^2 / [f_d (1 + i\eta) + 2f] [f_d (1 + i\eta) + f]$  and  $\chi_{-z-}^{\text{OR}} = -\frac{1}{2M_0} (1 - i\eta) / f_d [f_d (1 - i\eta) - f]$  where  $f_d = H_d / M_0$  and  $f = \omega / \gamma \mu_0 M_0$  is the normalized frequency. Graphs below illustrate the field and frequency dependences of

$\chi_{++z}^{\text{SHG}}$  and  $\chi_{-z-}^{\text{OR}}$ . The relevant parameters used are:  $M_0=0.175$ ,  $H_A=0.006$ , and  $\eta=0.05$ . As expected resonances are observed at the input and output frequencies. Resonances due to the field demagnetization effect are also observed.

We would like to thank the Malaysian Government for supporting the work under IRPA Grant No. 09-02-05-6001.

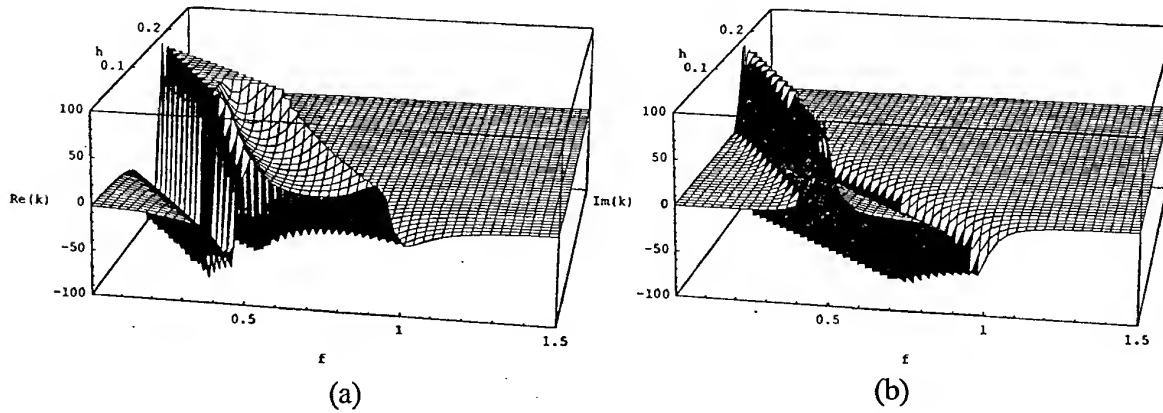


Fig. 1. Frequency and field dependences of  $\chi_{++z}^{\text{SHG}}$ . (a) real part and (b) imaginary part.

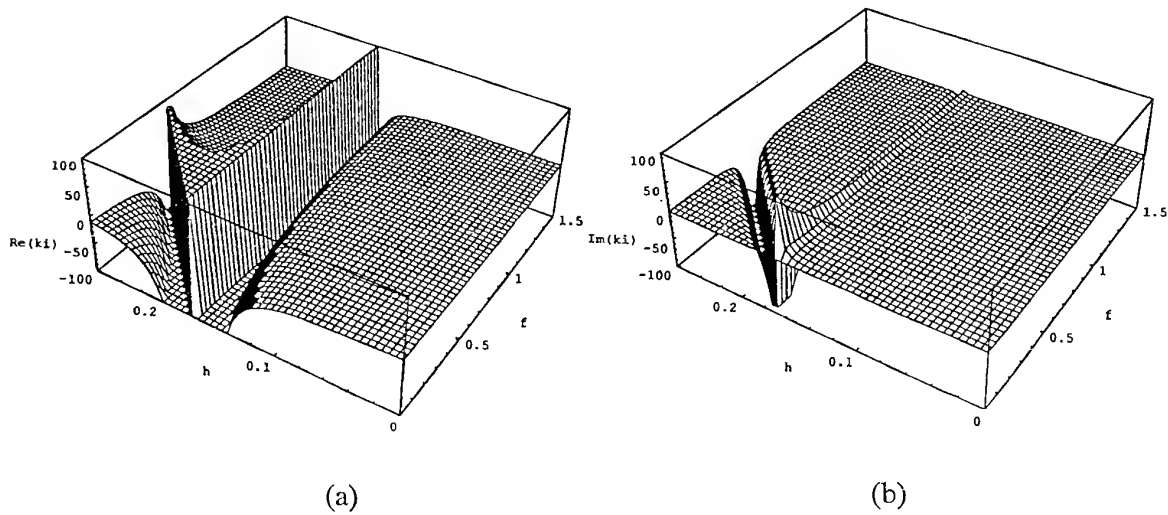


Fig. 2. . Frequency and field dependences of  $\chi_{-z-}^{\text{OR}}$ . (a) real part and (b) imaginary part.

1. M. G. Cottam, ed. *Linear and Nonlinear Spin Waves in Magnetic Films and Superlattices* (World Scientific, Singapore, 1994).
2. Junaidah Osman, Y. Ishibashi and D. R. Tilley, submitted to Jpn. J. Appl. Phys.



# High Magnetic Field ESR of CsCuCl<sub>3</sub>

T. Yamada<sup>1)</sup>, S. Okubo<sup>2)</sup>, H. Ohta<sup>1)</sup>, H. Nojiri<sup>3)</sup>, M. Motokawa<sup>3)</sup>, H. Tanaka<sup>4)</sup>

<sup>1)</sup> Department of Physics, Faculty of Science, Kobe University,  
1-1 Rokkodai, Nada, Kobe 657-8501, Japan

<sup>2)</sup> The Graduate School of Science and Technology, Kobe University,  
1-1 Rokkodai, Nada, Kobe 657-8501, Japan

<sup>3)</sup> Institute for Materials Research, Tohoku University,  
1-1 Katahira, Aoba, Sendai 980-8577, Japan

<sup>4)</sup> Department of Physics, Faculty of Science, Tokyo Institute of Technology,  
2-12-1 Ohokayama, Meguro, Tokyo 152, Japan

CsCuCl<sub>3</sub> is one of the well-known hexagonal ABX<sub>3</sub> type compound. Cu<sup>2+</sup> ions form chains parallel to the *c*-axis. The exchange interaction along the *c*-axis is ferromagnetic and Dzyaloshinsky-Moriya (D-M) interaction exists due to the cooperative Jahn-Teller distortion. Due to the combination of these interactions, the spins form a long period incommensurate helical structure along the *c*-axis below  $T_N=10.5$  K. The chains form an antiferromagnetic triangular lattice and the spins form the 120° structure in the *c*-plane. High field magnetization measurements at 1.1 K [1] revealed a small jump at  $H_c=12.5$  T for  $H \parallel c$  and a plateau around 11 T for  $H \perp c$ . The small jump for  $H \parallel c$  cannot be expected from the mean field theory but can be explained by the theory considering the quantum effect proposed by H. Shiba and T. Nikuni [2]. Its suggests that the anomalous jump is a quantum-fluctuation-induced phase transition and it was confirmed by the neutron diffraction experiments [3], ESR [4, 5] and NMR [6]. On the other hand, A. E. Jacobs, T. Nikuni and H. Shiba proposed a theory in the case of  $H \perp c$  that an incommensurate-commensurate phase transition is expected around the field of the plateau of the magnetization [7], but this transition was not found in the previous experiments up to 14 T [3, 5]. However, recent neutron diffraction experiment using a new repeated pulsed magnet up to 25 T by H. Nojiri *et al.* [8] revealed that an incommensurate-commensurate phase transition is observed at around 17 T, which was higher than the critical field proposed theoretically. To investigate this incommensurate-commensurate phase transition, we have performed the submillimeter wave ESR of CsCuCl<sub>3</sub> for  $H \perp c$  at 4.2 K in the frequency region from 50 to 625.5 GHz using the pulsed magnetic field up to 25 T. The details of our experimental setup can be found in refs.[9] and [10]. Figure 1 shows some examples of the ESR absorption lines observed at 4.2 K. The results are summarized in fig. 2. The major absorption lines in fig. 2 show a small anomaly at around 17 T, which correspond to the critical field of the incommensurate-commensurate transition observed by recent neutron measurement [8]. The minor absorption lines in fig. 2 show that their frequencies decrease as the external field is increased and approach zero at 17 T. These results support the results of the recent high field neutron diffraction measurement and the connection with the magnetization will be discussed.

## References

1. H. Nojiri, Y. Tokunaga and M. Motokawa, J. Phys. (Paris) **49** Suppl. C8 1459 (1988).
2. T. Nikuni and H. Shiba, J. Phys. Soc. Jpn. **62** 3268 (1993).

3. M. Mino, K. Ukukata, T. Bokui, M. Arai, H. Tanaka and M. Motokawa, *Physica B* **201** 213 (1994).
4. H. Ohta, S. Imagawa, M. Motokawa and H. Tanaka, *J. Phys. Soc. Jpn.* **62** 3011 (1993).
5. H. Ohta, S. Imagawa, M. Motokawa and H. Tanaka, *Physica B* **201** 208 (1994).
6. M. Chiba, K. Ohara, Y. Ajiro and T. Morimoto, *J. Phys. Soc. Jpn.* **62** 4186 (1993).
7. A. E. Jacobs, T. Nikuni and H. Shiba, *J. Phys. Soc. Jpn.* **62** 4066 (1993).
8. H. Nojiri, K. Takahashi, T. Fujita, M. Arai and M. Motokawa, to appear in *Physica B* (1997).
9. N. Nakagawa, T. Yamada, K. Akioka, S. Okubo, S. Kimura and H. Ohta, *Int. J. Infrared & MMW* **19** 167 (1998).
10. S. Kimura, H. Ohta, M. Motokawa, S. Mitsudo, W-J Jang, M. Hasegawa and H. Takei, *Int. J. Infrared & MMW* **17** 833 (1996).

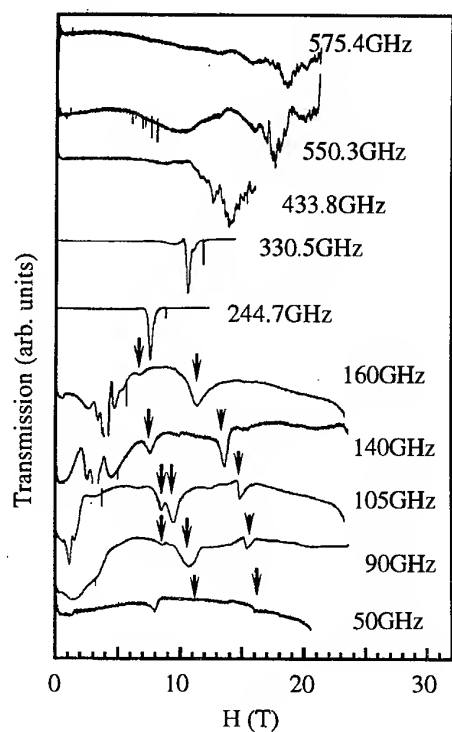


Fig. 1 Typical absorption lines of  $\text{CsCuCl}_3$  for  $H//a$  observed at 4.2K. Arrows indicate the minor absorption lines.

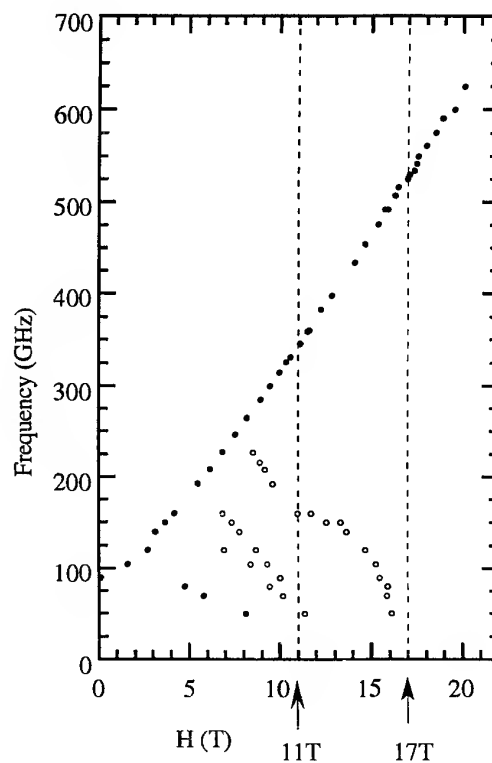


Fig. 2 Frequency-field relation of  $\text{CsCuCl}_3$  for  $H//a$  observed at 4.2K. Solid and open circles correspond to major and minor absorption lines, respectively.

# Millimeter and Submillimeter wave ESR of aligned powder sample of $\text{Nd}_2\text{BaNiO}_5$

S. Okubo<sup>1)</sup>, H. Ohta<sup>2)</sup>, M. Hayashi<sup>2)</sup>, T. Yamada<sup>2)</sup>,  
M. Motokawa<sup>3)</sup>, H. Nojiri<sup>3)</sup>, I. Mogi<sup>3)</sup>, K. Watanabe<sup>3)</sup>, H. Kikuchi<sup>4)</sup>, H. Nagasawa<sup>4)</sup>

<sup>1)</sup>The Graduate School of Science and Technology, Kobe University,

1-1 Rokkodai, Nada, Kobe 657-8501, Japan

<sup>2)</sup>Department of Physics, Faculty of Science, Kobe University, 1-1 Rokkodai, Nada, Kobe 657-8501, Japan

<sup>3)</sup>Institute for Materials Research Tohoku University, 1-1 Katahira, Aoba, Sendai 980-8577, Japan

<sup>4)</sup>Institute of Physics, University of Tsukuba, 1-1-1 Tennoudai, Tsukuba 305-8571, Japan

The studies of Haldane system have attracted much attention since Haldane's conjecture in 1983.  $\text{Y}_2\text{BaNiO}_5$  is known as the typical Haldane system with the Haldane gaps of about 100K [1].  $\text{NiO}_6$  octahedra form Ni-O-Ni 1D antiferromagnetic chains. On the other hand,  $\text{Nd}_2\text{BaNiO}_5$  has the same crystal structure as  $\text{Y}_2\text{BaNiO}_5$  but  $\text{Nd}_2\text{BaNiO}_5$  is a 3D antiferromagnet because the magnetic  $\text{Nd}^{3+}$  ions induce interchain exchange interactions. The 3D antiferromagnetic order is observed below  $T_N=48$  K from the neutron diffraction measurement [2]. Therefore the investigation of  $(\text{Y}_x\text{Nd}_{1-x})_2\text{BaNiO}_5$  system is an interesting problem to see the crossover from the 1D Haldane system to 3D antiferromagnet. However, little is known about the magnetic properties of  $\text{Nd}_2\text{BaNiO}_5$  than those of  $\text{Y}_2\text{BaNiO}_5$ . Therefore we decided to investigate the magnetic properties of  $\text{Nd}_2\text{BaNiO}_5$ .

In our previous paper [3] we reported the high field magnetization and the submillimeter wave ESR measurements of  $\text{Nd}_2\text{BaNiO}_5$  powder sample. From the high field magnetization measurement two magnetic phase transitions were observed at 9.6 T and 16.2 T, and the magnetization curve has a round shape above each transition and the shape differs from those of the spin-flop and metamagnetic transition curves of usual antiferromagnets. A lot of AFMR modes, which come from the very complicated magnetic structure, were observed by our submillimeter ESR measurement up to 383 GHz and AFMR modes change at the critical field 9.6 T. However, to gain information of anisotropy, we prepared the aligned powder sample of  $\text{Nd}_2\text{BaNiO}_5$  and performed the high field magnetization and submillimeter wave ESR measurement. The high field magnetization was measured by means of pickup method using the pulsed magnetic field up to 30T at 4.2 K. The millimeter and submillimeter wave ESR measurements were performed in the frequency region from 50 to 762 GHz by using Gunn Oscillator, BWO and FIR laser. The pulsed magnetic field up to 30 T was also used. Our millimeter and submillimeter wave ESR system in Kobe University is described in refs. 4 and 5. The differential magnetization at 4.2 K clearly shows two magnetic transitions at 9.6 T and 16.2 T for  $H//c$  which corresponds to the direction of applied field in the preparation of aligned sample. From the magnetization curve, it is obvious that these magnetic phase transitions are metamagnetic phase transitions. Typical AFMR absorption spectra of aligned powder sample of  $\text{Nd}_2\text{BaNiO}_5$  at 1.8 K are shown in Fig. 1. In the case of powder sample broad absorption features were seen in the spectra, but sharp absorption features are seen for aligned sample. Especially, strong absorption line A is observed below the critical field  $H_{C1}=9.6$  T above 310 GHz. The information of the magnetic anisotropy is well separated by the measurement using the aligned powder sample. The arrows in Fig. 1 indicate the minor absorption lines. Figure 2 shows the frequency-field diagram observed 1.8 K and 4.2 K. Difference of measurement temperature is due to the difference of the measuring system. It is clear that AFMR modes change at the critical field  $H_{C1}$ . Two distinct AFMR modes A and B were observed in the high frequency. AFMR mode B has an antiferromagnetic gap of about 240 GHz at zero magnetic field. Antiferromagnetic gap of AFMR mode

A at zero magnetic field were estimated to be about 1 THz by the extrapolation. High frequency measurement by using the FIR laser makes it possible to estimate antiferromagnetic gap of AFMR mode A. The AFMR mode A is mainly coming from the resonance of  $\text{Ni}^{2+}$  ion, while the AFMR mode B is mainly coming from the resonance of  $\text{Nd}^{3+}$  ion, because the stronger exchange field is expected at the  $\text{Ni}^{2+}$  ion site than at the  $\text{Nd}^{3+}$  ion site. Higher field and higher frequency measurements are still required to understand the whole magnetic properties of  $\text{Nd}_2\text{BaNiO}_5$ .

#### References:

1. J. Darriet and L. P. Regnault, *Solid State Commun.* **86**, 409 (1993).
2. V. Sachan, D. J. Buttrey, J. M. Tranquada and G. Shirane, *Physical Review B* **49**, 9658 (1994).
3. S. Okubo, H. Ohta, M. Hayashi, H. Kikuchi, M. Motokawa and H. Nagasawa, to appear in *Physica B* (1998).
4. M. Motokawa, H. Ohta and N. Makita, *Int. J. Infrared MMW* **12**, 149 (1991).
5. S. Kimura, H. Ohta, M. Motokawa, S. Mitsudo, W-J Jang, M. Hasegawa and H. Takei, *Int. J. Infrared MMW* **17**, 833 (1996) 833.

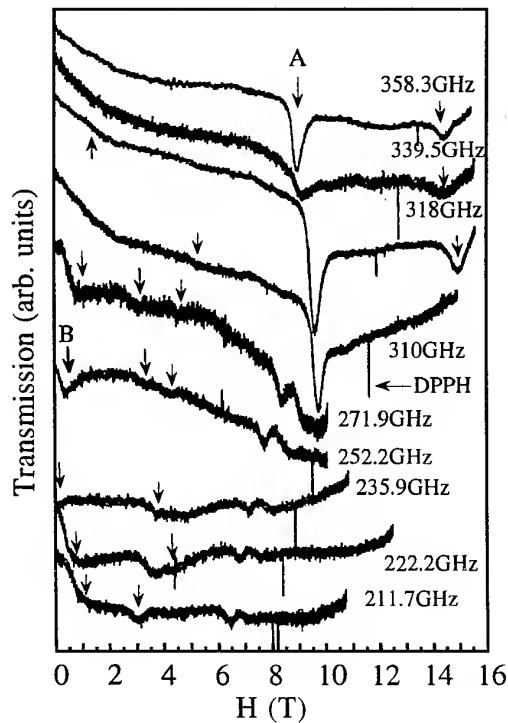


Fig. 1 Frequency dependence of AFMR absorption lines of aligned sample observed at 1.8K. The applied field direction corresponds to the aligned direction.

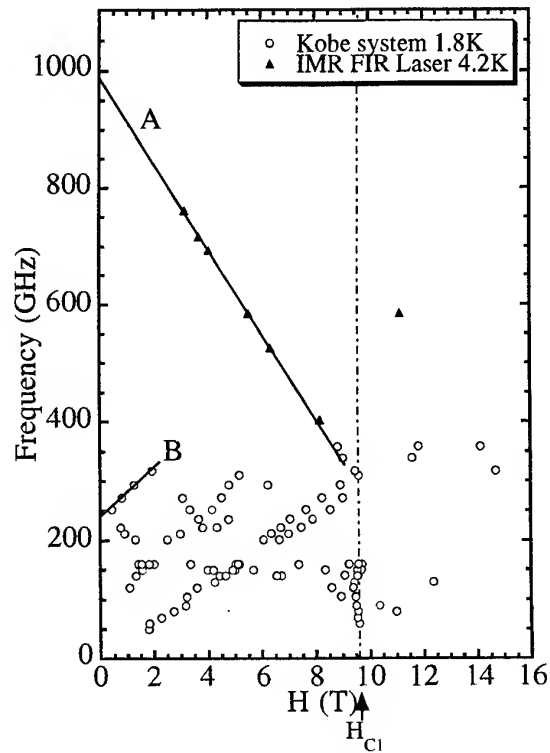


Fig. 2 Frequency-field diagram of  $\text{Nd}_2\text{BaNiO}_5$  observed at below  $T_N$ .

## Prospects for the Observation of Magnon Modes in the Far Infrared Spectrum of a Thin Antiferromagnetic Film on a Metal

Thomas Dumelow

Departamento de Física, Universidade Federal do Rio Grande do Norte, 59072-970 Natal RN, Brasil

Far infrared spectroscopy has up to now proved very useful in measuring the magnon spectrum of bulk antiferromagnetic materials. Of increasing recent interest, however, is the emergence of a range of layered magnetic structures, many of which incorporate antiferromagnetic layers. Since layer thicknesses in such structures may be in the order of 10 nm, compared with a free space wavelength of infrared radiation of order 100  $\mu\text{m}$ , the prospects for the use of far infrared spectroscopy for investigating such thin layers do not, at first sight, look very promising.

In this paper, we concentrate on the expected far infrared spectrum for an antiferromagnetic film in contact with a metal, and show that for this particular geometry magnon modes should indeed be observable. It should be noted that a number of systems of interest at present are in fact ferromagnet/antiferromagnet bilayers. Since many ferromagnets are themselves metals, the results presented in this paper are likely to be of considerable relevance to the study of such systems. We use as our model a thin film of the uniaxial antiferromagnet  $\text{FeF}_2$  (using 4.2 K parameters) deposited on a highly metallic substrate (using parameters of the order expected for iron at low temperature). The uniaxis of the antiferromagnet is in the plane of incidence.

A useful way to consider the modes expected is in terms of surface polariton modes at the antiferromagnet/metal interface. In the structure considered these modes are unusual for two reasons:

- i. Surface magnon polariton modes at the antiferromagnet/metal interface may exist in either s- or p-polarisation. Nevertheless, when the substrate is highly metallic, field continuity dictates that, in s-polarisation, there is a essentially no associated  $\mathbf{E}$  field, so the modes carry negligible energy. In this paper we therefore concentrate on p-polarisation modes.
- ii. There is no wavevector restriction on these surface polariton modes. This contrasts with conventional surface modes, such as for an antiferromagnet in contact with vacuum, which only exist if the in-plane wavevector exceeds a minimum value - this restriction usually means that a special geometry, such as that used in attenuated total reflection spectroscopy, is required for their observation. For the antiferromagnet/metal case, however, they should be observable using simple oblique incidence reflection spectroscopy. This has an analogy with so-called 'Berreman' modes observed in the oblique incidence spectroscopy of alkali halides deposited on metals.

The surface polariton description, based on a mode localised at the antiferromagnet/metal interface, predicts the excitation, using p-polarisation oblique incidence relectivity from vacuum, of a mode at the top of the reststrahlen band. However, a such a description does not include the effect of the vacuum/antiferromagnet interface, which shifts the mode to lower frequency. This is shown in the 75° oblique incidence reflectivity spectra, calculated for a range of antiferromagnet film thicknesses, shown in Fig. 1. The calculated surface mode frequency occurs, if the substrate is sufficiently metallic, at the upper interface of the reststrahl and bulk mode regions, in this case corresponding to 52.8  $\text{cm}^{-1}$ . For a layer thickness of 30  $\mu\text{m}$  this is approximately correct. However, for such thick layers it is impossible in practice to separate the mode from the interference modes in the bulk region at higher frequency. For thinner layers, the mode shifts down in frequency towards the bottom of the reststrahl region, ending up as a strong mode a the transverse magnon frequency  $\omega_{\perp}$ . The mode is quite distinct, even with a film thickness as thin as 0.02  $\mu\text{m}$ . In s-polarisation or at normal incidence there is no mode absorption clearly visible for such a thin film, showing that the surface mode effect significantly enhances the possibility of detecting any magnon modes in this type of structure.

In Fig. 2 we consider the reflectivity from the 0.02  $\mu\text{m}$  structure for a series of incident angles. It is clear that the strength of the observed dip increases markedly with incidence angle. It therefore appears that one should perform such experiments as near to grazing incidence as possible.

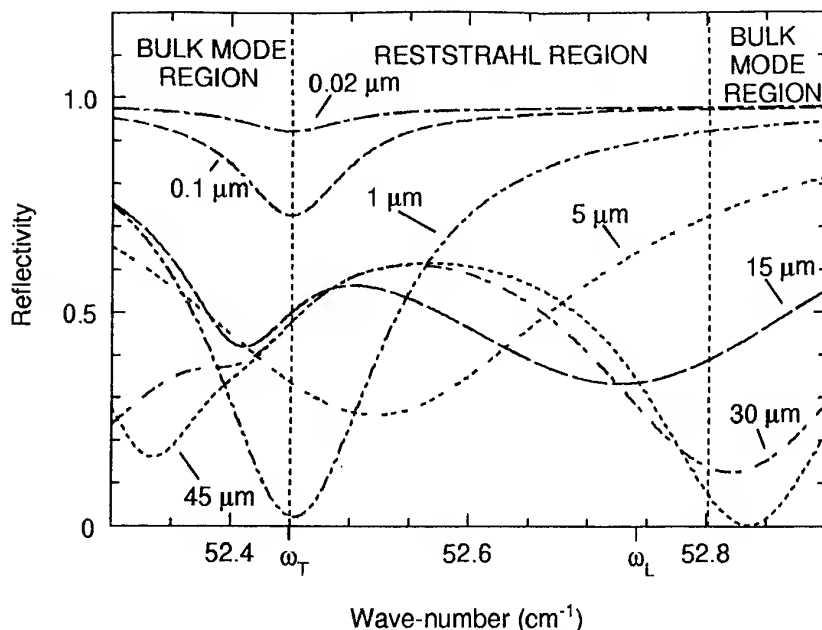


Fig. 1: Calculated  $p$ -polarisation  $75^\circ$  reflectivity off an  $\text{FeF}_2$  film deposited on a highly metallic substrate, for a series of layer thicknesses.

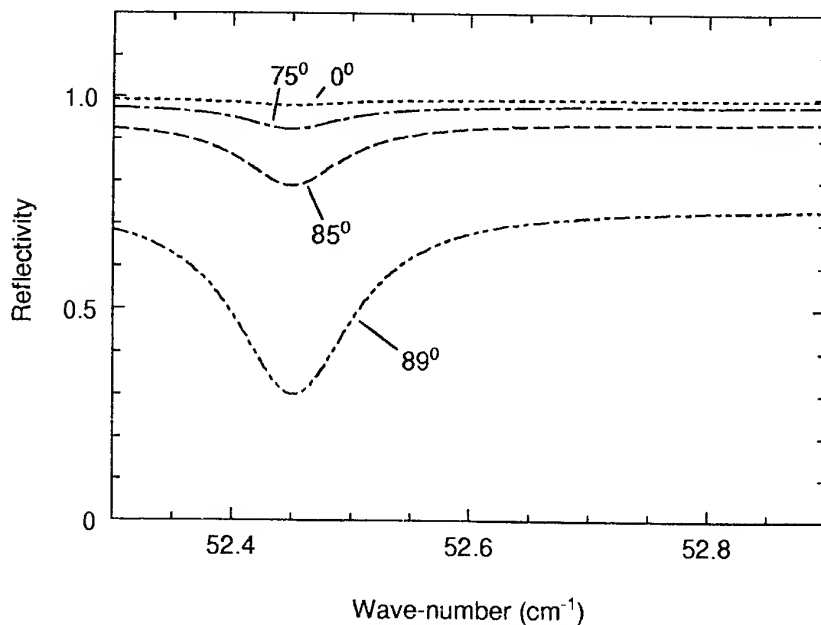


Fig. 2: Effect of incident angle on  $p$ -polarisation reflectivity off  $0.02 \mu\text{m}$   $\text{FeF}_2$  deposited on a highly metallic substrate.

The above analysis shows that it should be possible to observe thin film magnon modes using the right geometry. Although the description has been based on the excitation of surface polariton modes, for very thin films there is considerable deviation from a simple surface polariton picture due to the presence of the upper vacuum/antiferromagnet interface, as shown by the shift in mode frequency with film thickness. In fact, if the film is thin enough, the field across the layer is essentially constant. In this case the mode can be considered as occurring at  $\omega_T$ , excited by a power flow along the film, parallel to the surface.

## Theory of transmission through layered magnetic structures

Xue-Fei Zhou<sup>1,2</sup>, Jing-Ju Wang<sup>1,2</sup>, Xuan-Zhang Wang<sup>1,3</sup>, Siew-Choo Lim<sup>4</sup>, Junaidah Osman<sup>4</sup>  
and D.R. Tilley<sup>4,5</sup>

1. Dept of Physics, Harbin Normal University, Harbin 150080, China
2. Heilongjiang College of Education, Harbin, China
3. CCAST (World Laboratory), PO Box 8730, Beijing 100080, China
4. School of Physics, Universiti Sains Malaysia, 11800USM Penang, Malaysia
5. Dept of Physics, University of Essex, Colchester CO4 3SQ, UK

We have previously[1] discussed normal-incidence transmission through a magnetic Fabry-Perot (FP) resonator with a magnetic field applied normal to the interfaces. For both ferromagnets and antiferromagnets the propagating eigenstates are the states + and - of circular polarization; except around the resonance frequency fringes are predicted at positions that depend on the magnetic field value so that the FP is a tunable circular polarizer. Here we discuss the extension to a finite superlattice, that is, a stack of  $N$  bilayers each of which comprises a thickness  $d_M$  of a magnetic medium and  $d_N$  of a non-magnetic medium.

Within one magnetic layer the solution of the wave equation is  $a_n \exp(ikz) + b_n \exp(-ikz)$  where  $k^2 = (1 + \chi)\epsilon\omega^2/c^2$  in which  $\epsilon$  is the dielectric constant and  $\chi$  is  $\chi^+$  or  $\chi^-$  [1]. Transmission through the superlattice is governed by the transfer matrix  $T$  which relates  $(a_{n+1}, b_{n+1})$  to  $(a_n, b_n)$  and the Bloch vector  $Q$  is given by  $\cos[Q(d_M + d_N)] = \text{Tr}(T)/2$  [2]. Fig. 1 below shows dispersion graphs  $f = \omega/\omega_m$  versus  $Q$  in a field  $H_0 = 1.5M_s$  for a YIG/N superlattice with  $d_M = d_N = 1\text{mm}$ , where  $M_s$  is the static magnetization and we use standard numerical values for YIG[1] with  $\epsilon(N) = 5.0$ .  $\chi^-$  is resonant at  $f = 0.5$  so the lowest stop band is the magnetic reststrahl and higher stop bands result from Bragg reflections;  $\chi^+$  is not resonant so the only stop bands are the Bragg ones.

Reflection and transmission for a finite superlattice of  $N$  layers is calculated by combining electromagnetic boundary conditions at the vacuum interfaces with propagation through the superlattice described by the matrix  $T^N$ . Computed transmission graphs corresponding to Fig. 1 are shown in Fig. 2. One feature is the presence of regions where  $\tau \approx 0$ ; these are the stop bands of Fig. 1. The lowest such region in Fig. 2a is the magnetic reststrahl and it is absent from Fig. 2b. The other low-transmission regions in Fig. 2a and both of those in Fig. 2b are the Bragg stop bands. Close fringes with spacing given by  $\delta(QND) = \pi$  are seen on both graphs and in addition a slow modulation arising from  $d_M$  is present.

We have presented graphs for frequency dependence in a ferromagnet-based superlattice in order to illustrate the main physical principles. For ferromagnets the resonance frequency is typically in the microwave region and field scans are more practical. However, the formalism applies also for antiferromagnets with the relevant forms of  $\chi^\pm$  [1] and in that case with resonance in the FIR frequency scans are possible. For antiferromagnetic films with  $d_M \sim 1\mu\text{m}$ , additional fringes arising from exchange modes can be seen[3,4]. We are currently extending the present formalism to include exchange.

This work was supported by IRPA (Malaysian Government) Grant 09-02-05-6001, by National Science Foundation of China Grant 19574014 and by the Outstanding Youth Science Foundation of Heilongjiang Province. XZW thanks the Third World Academy of Science (TWAS) and Universiti Sains Malaysia for support to visit USM.

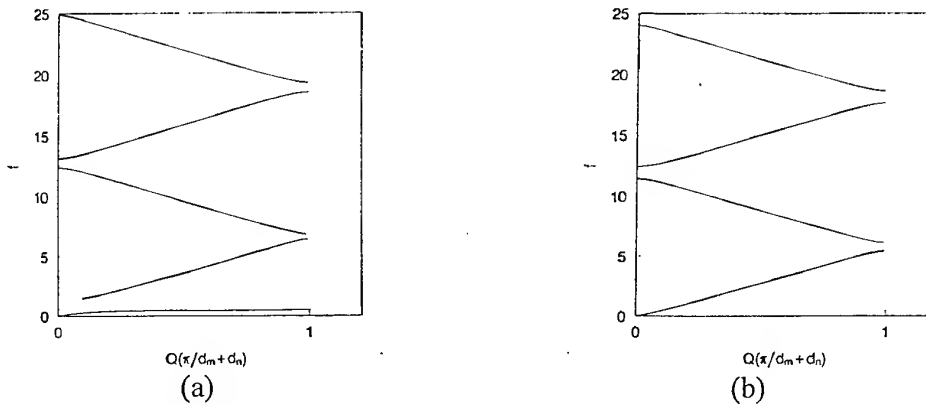


Fig. 1. Superlattice dispersion curves. (a)  $\chi^-$  and (b)  $\chi^+$

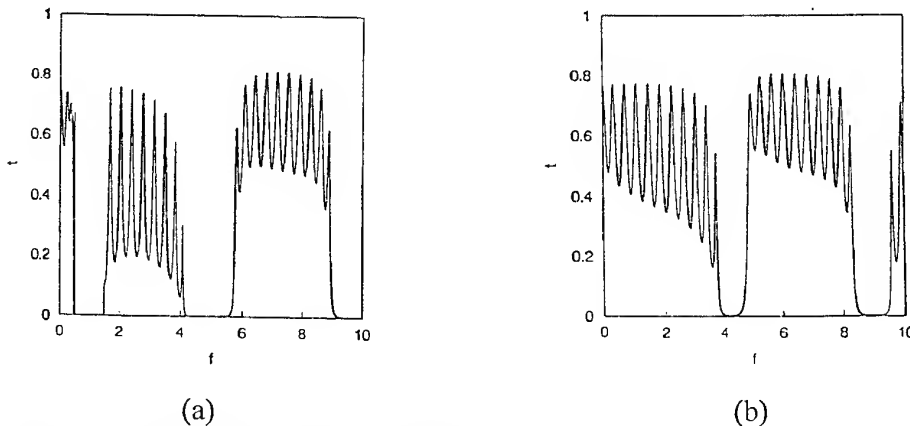


Fig. 2. Transmission curves corresponding to Fig. 1.

1. Siew-Choo Lim, Junaidah Osman and D.R. Tilley, *J. Phys.: Condens. Matter* **9**, 8297 (1997)
2. N. Raj and D.R. Tilley, *Phys. Rev. B* **36**, 7003 (1987)
3. M. Lui, C.A. Ramos, A.R. King and V. Jaccarino, *J. Appl. Phys.* **67**, 5518 (1990)
4. Siew-Choo Lim, Junaidah Osman and D.R. Tilley, *J. Phys.: Condens. Matter* **10**, 1891 (1998)



# INFLUENCE OF MISFIT STRAINS ON THE REFLECTION OF LIGHT FROM THE INTERFACE OF YTTRIUM-IRON GARNET FILM ON GADOLINIUM-GALLIUM GARNET SUBSTRATE IN THE NEAR INFRARED

N.N. Dadoenkova, I.L. Lyubchanskii, M.I. Lyubchanskii, V.D. Poymanov

Donetsk Physical & Technical Institute of the National Academy of Sciences of Ukraine,  
340114, Donetsk, UKRAINE

It is well known that elastic strains arise near real interface between crystal media (so called pseudomorphic strains) which are induced by misfit of crystal lattice constants of different materials in layered structures [1]. Thicknesses of corresponding deformed layers, which are determined by elastic parameters of materials, can reach the values which are equal to a few hundred angstroms [1]. Therefore, for a real situation such deformed layers can lead to additional contribution induced by elasto-optical interaction to optical effects at interfaces.

In a few publications (see, for example, [2,3]) it was investigated some peculiarities of reflection, transmission and propagation of electromagnetic waves (EMW's) at the presence of intermediate layers located near interfaces in layered structures. However, in mentioned above articles it was not taken into account the contribution of elastic strains in reflection coefficients of EMW. It should be noted that elasto-optical contribution into reflection of light in nonmagnetic metals was investigated theoretically and experimentally (by ellipsometric methods) in [4].

The aim of present communication is to investigate contribution of pseudomorphic layer near interface of magnetic and nonmagnetic media to reflection coefficients of EMW. As the object of research we consider bilayer structure, formed by magnetic film of yttrium-iron garnet (YIG)  $Y_3Fe_5O_{12}$  on nonmagnetic substrate of gadolinium-gallium garnet (GGG)  $Gd_3Ga_5O_{12}$ .

Let us consider magnetic film of YIG (medium 1) on nonmagnetic substrate GGG (medium 2) with thicknesses  $d_1$  and  $d_2$  correspondingly. Interface between YIG and GGG ( $z = d_1$ ) is parallel to XOY-plane. Reflection plane is XOZ. For simplicity we shall investigate the transversal magneto-optical configuration. At this case magnetization vector in magnetic film is oriented perpendicularly to the reflection plane. For geometry under consideration normal EMW's in magnetic medium can be presented as pure TM- and TE-modes. The dielectric permeability tensor  $\epsilon_{ij}(z)$  for such system has the form:

$$\epsilon_{ij}(z) = \begin{cases} \delta_{ij} & z < 0 \\ \epsilon_{ij}^{(1)}(z) & 0 < z < d_1 \\ \epsilon_{ij}^{(2)}(z) & d_1 < z < d_1 + d_2 \\ \delta_{ij} & d_1 < z < d_1 + d_2 \end{cases} \quad (1)$$

Tensors  $\epsilon_{ij}^{(1,2)}(z)$  have the following structure:

$$\epsilon_{ij}^{(1,2)}(z) = \epsilon_{(0)ij}^{(1,2)} + \Delta\epsilon_{ij}^{(1,2)}(z) \quad (2)$$

where  $\epsilon_{(0)ij}^{(1,2)}$  are dielectric permeabilities of undeformed media

$$\epsilon_{(0)ij}^{(1)} = \begin{pmatrix} \epsilon_{(0)}^{(1)} & 0 & i\epsilon_{(0)}^{'(1)} \\ 0 & \epsilon_{(0)}^{(1)} & 0 \\ -i\epsilon_{(0)}^{'(1)} & 0 & \epsilon_{(0)}^{(1)} \end{pmatrix}, \quad \epsilon_{(0)ij}^{(2)} = \begin{pmatrix} \epsilon_{(0)}^{(2)} & 0 & 0 \\ 0 & \epsilon_{(0)}^{(2)} & 0 \\ 0 & 0 & \epsilon_{(0)}^{(2)} \end{pmatrix} \quad (3)$$

and  $\Delta\epsilon_{ij}^{(1,2)}(z)$  are additional terms induced by strains, which can be written in well-known form [5]:

$$\Delta\epsilon_{ij}^{(1,2)} = p_{ijkl}^{(1,2)} u_{kl}^{(1,2)} \quad (4)$$

In Eq.(4)  $p_{ijkl}^{(1,2)}$  and  $u_{kl}^{(1,2)}$  are components of photoelastic and deformation tensors. Pseudomorphic strains (or misfit  $f_m$ ) is determined by the relation [1]

$$f_m = \frac{a_f - a_s}{a_s} \quad (5)$$

where  $a_f$  and  $a_s$  are lattice parameters of the film and substrate. These strains are located in magnetic film as well as in nonmagnetic substrate in sublayers with thicknesses  $h_1$  and  $h_2$  below and above interface [1].

Electric field of reflected EMW is determined by the following expression

$$\mathbf{E}(z) = \mathbf{E}_0(z) + \mathbf{E}_s(z) \quad (6)$$

where  $\mathbf{E}_0(z)$  is the contribution to the total electric field of EMW from non-strained bilayer and  $\mathbf{E}_s(z)$  is the strain-induced electric field of reflected wave (for the details see [6]):

$$E_{is}^{(r)}(z) = \int_0^{d_1} G_{ik}^{(1)}(z-z') \Delta\epsilon_{kl}^{(1)}(z') E_l^{(1)}(z') dz' + \int_{d_1}^{d_1+d_2} G_{ik}^{(2)}(z-z') \Delta\epsilon_{kl}^{(2)}(z') E_l^{(2)}(z') dz' \quad (7)$$

In Eq.(7) the Green functions  $G_{ik}^{(1,2)}(z-z')$  are solution of wave equations for both media.

Two cases are considered: i) incident light is polarized along  $OX$ -axis; ii) incident light is polarized along  $OY$ -axis. Analytical expressions for Green functions  $G_{ik}^{(1,2)}(z-z')$  and reflected electric fields are obtained and angular dependencies for reflection coefficients for TM- and TE-modes [7] for YIG-GGG bilayer (on the base of data from [8]) in the near infrared region ( $\lambda = 1.15\mu\text{m}$ ) are investigated.

This work is supported in part by Ukrainian State Foundation of Basic Research under grant No. 2.4/247.

#### References.

1. S.C. Jain, A.H. Harker, R.A. Cowley, Phil.Mag. A. 75, 1461 (1997).
2. N.P. Zhuk, O.A. Tretyakov, Proceedings of Ukrainian Academy of Sciences. 4, 59 (1984) - in Russian; Surface (Poverkhnost'), 8, 45 (1986) -in Russian.
3. G.V. Rozhnov, Zh. Eksp. Theor. Phys. (Sov. Phys. JETP). 96, 1137 (1989); 103, 740 (1993) - in Russian.
4. K. Pedersen, O. Keller, Appl. Opt. 25, 226 (1986).
5. W.A. Wooster. Tensors and group theory for physical properties of crystals. Clarendon Press, Oxford, 1973.
6. N.N. Dadoenkova, I.L. Lyubchanskii, M.I. Lyubchanskii, V.D. Poymanov, Phys. Solid State (Fiz. Tverd. Tela) (1998) - submitted in Russian.
7. M. Born, E. Wolf. Principles of optics. Pergamon Press, Oxford, 1964.
8. B. Knoerr, W. Tolksdorf, Mat. Res. Bull. 19, 1507 (1984).

# METHODOLOGICAL ERRORS IN MEASURING TIME OF ELECTRONIC RELAXATION IN A PARAMAGNETIC.

Popenko N.A.

Usikov Institute for Radiophysics and Electronics NAS of Ukraine,  
12 Acad. Proskura st., 310085 Kharkov, Ukraine.  
Tel. (380572)448594, fax: (380572)441105. E-mail: buran@ire.kharkov.ua

The investigation into nonlinear spin dynamics under the conditions of quantum of electromagnetic radiation exceeding the energy of heat disordering is considered the most interesting from the point of view of getting the information about the properties of the substances. One of the central problems in creating spectrometers which provide carrying out these experiments is creating a resonance cell. In mm range high-quality open resonators (OR) are used for this purpose, they provide high sensitivity and resolution of the experiment. As a rule these are two-mirror ORs with a paramagnetic placed on the plane mirror. But for investigation into the samples with high losses, e.g. semimagnetic semiconductors, such a resonator does not give an opportunity to obtain the best characteristics of the spectrometer. In this case the problem lies in disturbance of the resonance oscillation because of the scattering and absorption of electromagnetic waves from the sample. This leads to decrease of Q-factor of oscillations. This problem may be solved with a three-mirror OR which is composed of two metal mirrors placed on the opposite facet of dielectric prism and a dielectric mirror - boundary «dielectric-air» under TIR effect [1]. Due to a regulated coupling coefficient of the OR with the sample placed near TIR edge, the resonance properties of such an OR in a wide range of dielectric constants of the samples may be preserved. It is necessary to note that application of resonance systems for studying nonlinear processes in a paramagnetic requires special investigation into their properties as the resonance system with a paramagnetic reveals both stability and bistability when the electronic transition is saturated.

The paper is devoted to the methodological basis of investigation into the nonlinear processes in a substance (e.g. process of relaxation in electron spin system of a paramagnetic) in mm wave range. The characteristics of this nonlinear dissipation system have been calculated for different time of electron relaxation.

In the general case the resonance cell is an OR with a saturating paramagnetic. The behaviour of such a system may be described in the framework of a theoretical model [2]. We will consider the described above three-mirror OR.

We are considering the propagation of plane electromagnetic waves in this OR. Plane waves are propagating between semi-transparent metal mirrors with the reflection coefficient R and the transmission coefficient T and its TIR facet:

$$H_j(z, t) = H_j \exp[i(\omega t \pm kz)] + c.c., \quad (1)$$

The resonance oscillation is set in the three-mirror resonator when the following boundary conditions are fulfilled:

$$\begin{vmatrix} H_I(0) \\ H \end{vmatrix} = \begin{vmatrix} \sqrt{T} & \sqrt{Rr(H)}e^{i\beta} \\ -\sqrt{Rr(H)}e^{i\beta} & \sqrt{T} \end{vmatrix} \quad (2)$$

where H - field amplitude in the resonator,  $H_I$  - amplitude of incident electromagnetic wave;  $\beta$  - phase shift per single passing;  $r(H)$  - reflection coefficient from the nonlinear boundary formed by the TIR facet and a paramagnetic sample placed near it. After falling on the first semi-transparent metal mirror, an incident wave is propagating further in the direction of the TIR facet and after being reflected from it goes to the second metal mirror. The full cycle of a wave going through the OR is finished when it comes back to the first metal mirror. In the general case the equation which connects the waves propagating in the resonator looks as follows:

$$H = \frac{H_I \sqrt{T}}{1 - Rr(H)^2 \exp(i2\beta) \exp(-\alpha L)} \quad (3)$$

The value  $r(H)$  is determined on the basis of the solved problem of diffraction of plane electromagnetic wave from the three-layer system: dielectric - dielectric - paramagnetic, under condition when the electron spin transition is saturated. In this case the paramagnetic permeability is determined by the expression [3].

The numerical analysis of such a system for different concentration of paramagnetic centers, time of relaxation and also coupling coefficient of the OR with the sample has shown that with a certain correlation of the described above parameters the transition into bistability can be observed. The three equation roots (3) as frequency function are shown in Fig. 1. It is important to underline that when the coupling coefficient of the OR with the sample is changed, return to stability is possible. According to the given data it becomes clear that when the relaxation processes in the substance are studied, the choice of parameters of the resonance system should be determined by the bistability phenomenon.

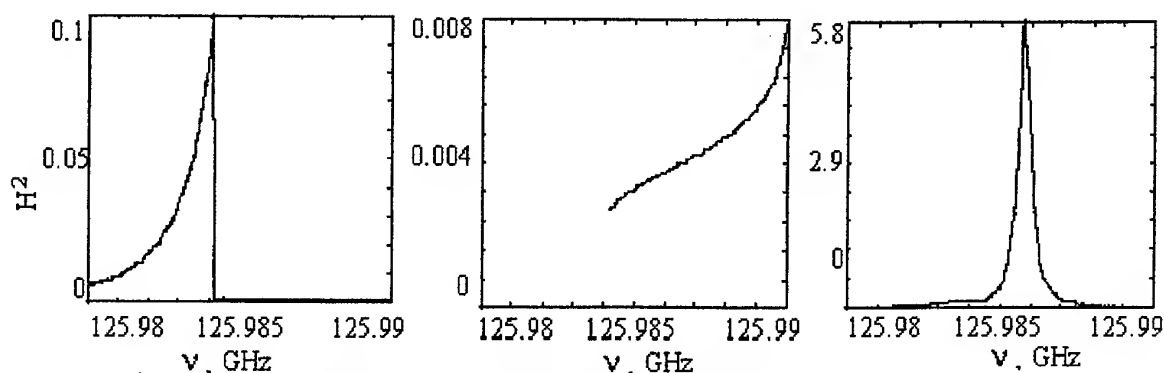


Fig. 1. Dependence of the intensity resonance field on the frequency.

The calculation of the parameter plane has been carried out, namely the concentration of paramagnetic centers - coupling coefficient of the OR with the sample. This plane is divided into two areas corresponding to stability and bistability of the resonance system (Fig. 2). The location of the boundary between these two planes depends greatly on the time of relaxation of the substances under the investigation.

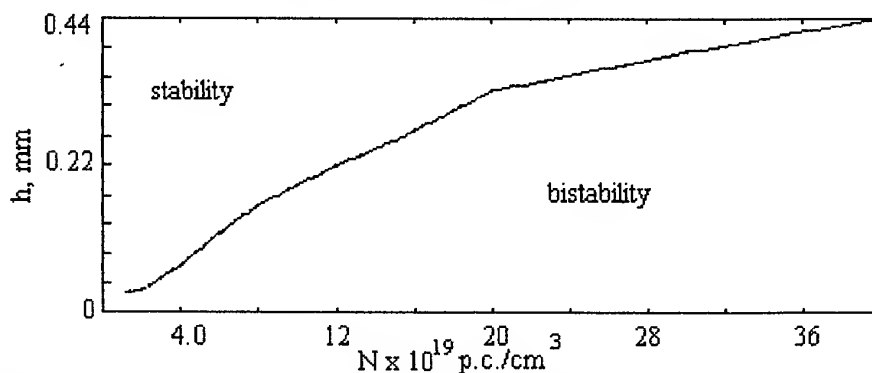


Fig. 2. The parameter plane such as concentration of paramagnetic centers - coupling coefficient of the OR with the sample (distance between the TIR facet and the sample) for different system parameters.

Thus, the calculation of the dependences of the intensity of the resonance field on the frequency for the three-mirror OR with a saturating paramagnetic has revealed the existence of bistability in such a system and has determined the limits of the bistability area which depends on the parameters.

**Acknowledgements.** The author thanks prof. S. Tarapov and researcher I. Gudim for the valuable discussions.

#### References.

1. Vertiy A., Popenko N., Tarapov S. *Izvestiya VUZov, Radiophysics*, **27**, N6, p.775-782, 1984 (in Russian)
2. H.M. Gibbs. *Optic Bistability; Controlling Light with light*. Academic Press. Orlando, FL, 1985.
3. C. Poole. *Electron Spin Resonance*. John Wiley & Sons. New York. 1983.

## Coupled Spin-Electromagnetic Surface Infrared Waves in Ferrite/Semiconductor Superlattice at Quantum Hall-Effect Conditions

Roland H. Tarkhanyan

Institute of Radiophysics & Electronics of Armenian National Academy of Sciences  
Ashtarak-2, 378410, Armenia. E-mail: office@irphe.sci.am

The principal result of this report is the existence of coupled magnon-plasmon surface polaritons (MPSP) on the lateral surface of a superlattice that consists of alternating layers of GaAs-AlGaAs quantum well system and ferrimagnet insulator. Dispersion relations for MPSP at quantum Hall-effect conditions are considered when a static quantizing magnetic field is perpendicular to the quantum well plane.

Propagation of coupled spin-electromagnetic surface waves on the lateral surface of a ferrite-semiconductor superlattice is the subject of interest in this work. The waves arise from the coupling between two-dimensional magnetoplasmons, magnons and fluctuating infrared electromagnetic fields in quantum Hall-effect conditions. A peculiarity of the dispersion relation is the existence of a static quantizing magnetic field which is perpendicular to the GaAs-AlGaAs quantum well plane. This work continues our study of coupled spin-electromagnetic waves in bigyrotropic media. A previous investigation was performed for the waves localized at the boundary of vacuum with the superlattice in the presence of a non-quantizing static magnetic field parallel to the lateral surface of the superlattice [1]. Two TE and two TH polarized nonradiative surface waves have been found in the case of the Voigt configuration. The nonreciprocity between opposite propagation directions has been shown to be just a result of the nonreciprocity of the waves in the presence of an applied field. Some new resonance frequencies for the considered waves have been found also.

In this work most particular attention is paid to those collective modes which propagate in arbitrary directions with respect to the quantizing magnetic field. The principal new result is the existence of nondumping and nonradiative superslow spin-electromagnetic waves with quantizing frequencies propagating along the lateral surface of the superlattice. These waves are solutions of Maxwell equations in their full form, transport equation for an average charge carrier at quantum Hall-effect conditions and equations of motion for precessing moments of magnetization in ferrite layers.

The effective anisotropic medium method is used to express the dielectric and magnetic permeability tensors of the superlattice in terms of the individual layers' permeabilities. This method is based on the use of continuity of some macroscopic field components at the interfaces of the layers and is valid only if the period of the superlattice is less than the coupled surface polariton wavelength. In the case of arbitrary thickness of the superlattice the dispersion relations are quite complicated transcendental equations. That is why the magnetostatic approximation is used for the surface waves.

The localization conditions impose some restrictions on the values of static magnetic field and direction of propagation as well as on free two-dimensional carrier concentration. The regions of existence for surface waves in the frequency-2D wave number plane are very sensitive to these parameters. To derive an analytical expression for the phase velocity of the surface waves the cases of a thick and thin superlattice are considered. It is important to point out that the positive and negative values of the normal component of the 2D wave vector are only equivalent in the case of superlattices with finite thickness.

- [1]. Roland G. Tarkhanyan. Proc. of International SPIE conference on Mm and Submm Waves. 1995, vol. 2558, San-Diego.

## 165 GHz, TE<sub>31,17</sub> - Coaxial Cavity Gyrotron with Quasi-Optical RF - Output

B. Piosczyk, O. Braz<sup>+</sup>, G. Dammertz, C.T. Iatrou<sup>++</sup>, M. Kuntze, G. Michel<sup>+</sup>, A. Möbius<sup>+++</sup>,  
M. Thumm<sup>+</sup>,

Forschungszentrum Karlsruhe, Association EURATOM-FZK, ITP, D-76021 Karlsruhe, Germany

e-mail: bernhard.piosczyk@itp.fzk.de

<sup>+</sup> also Universität Karlsruhe, Institut für Höchstfrequenztechnik und Elektronik

<sup>++</sup> National Technical University of Athens, Greece

<sup>+++</sup> IMT GmbH, Luisenstr. 23, D-76344 Eggenstein, Germany

### Introduction

A coaxial cavity gyrotron operated at 140 GHz in the TE<sub>28,16</sub> mode and at 165 GHz in the TE<sub>31,17</sub> mode with an rf-output power of 1.5 MW is under development at FZK. In order to investigate the basic operating problems in a first step experiments with a gyrotron equipped with an axial waveguide output have been performed. The achieved results were in good agreement with numerical calculations [1,2]. In a second step, the 140 GHz, TE<sub>28,16</sub> gyrotron has been operated with a dual rf-beam output. For the first time the possibility of internal splitting of the generated rf-power has been demonstrated successfully [3]. The development of rf-windows is progressing very fast. CVD-diamond windows with a transmission capability even above 2 MW at the frequencies considered here seem to be close to realization. Therefore, in the recent experiment the 165 GHz, TE<sub>31,17</sub> gyrotron has been equipped with a q.o. system for transmission of the rf-power through a single window. The results of this experiment are given here.

### Design and experimental set-up

A schematic layout of the gyrotron is shown in Fig.1. With exception of the cavity and the quasi-optical (q.o.) output system the same components are used as in the previous experiments [1-3]. The emitter ring of the electron gun has been renewed since the last experiment because the emission properties of the emitter were

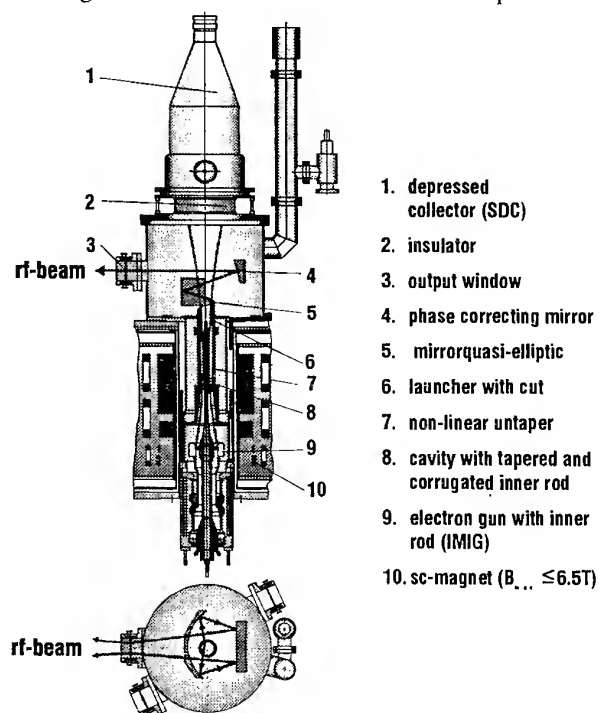


Fig. 1: Schematic layout of the 165 GHz, TE<sub>31,17</sub> gyrotron

deteriorated due to exposure to air for several times. The dimensions of the TE<sub>31,17</sub> cavity with the coaxial insert are as in the set-up with the axial rf-output [2]. The high volume cavity mode is directly transformed to a homogeneously distributed paraxial beam. The design of the q.o. system is based on a hybrid geometrical optical and physical optical technique [4]. It consists of a Vlasov launcher with a single cut and two mirrors. The rf-power is radiated with a transverse angle of divergence of about 142° towards the first quasi-elliptic mirror. The second mirror has a phase-correcting surface in order to generate approximately a homogeneous rf-field distribution with a high Gaussian content in the window plane. Since the transmission for neighbouring cavity modes is good, frequency step tuning can be performed. Stray radiation due to diffraction losses has been estimated to be ≤ 5% and the absorption losses to about 7% resulting in total losses of about 12%. A fused silica window with a thickness of about 13 half wavelengths at 165 GHz is used. The reflection coefficient was measured to be ≤ 1% at 165 GHz.

### Experimental operation and results

The measurements have been performed in pulsed operation. Most data have been taken with an rf-pulse length of 0.5 ms and a repetition rate of 1 Hz. In single pulses the pulse length has been extended up to 15 ms limited by the capability of the HV power supply. The rf-output power  $P_{out}$  has been measured calorimetrically. For measuring of the distribution of the rf-output power an infrared camera has been used. The microwave

diagnostic system allows to measure the frequency and to observe whether there is single or multimode oscillation during a pulse. A concentricity of the electron beam relative to the coaxial insert and to the outer cavity wall within  $\leq 0.2$  mm has been achieved by adjusting as well the sc-magnet and the coaxial insert.

The  $TE_{31,17}$ -mode has been found to oscillate with a frequency of 165.0 GHz in very good agreement with the design. A wide single mode operating range has been observed as shown in Fig. 2 for a given magnetic field. The calculated value is in reasonable agreement with the experiment. A maximum rf-output power of 1.2 MW with an efficiency of 25% was measured. The efficiency increased to 35% when operating with the single-stage depressed collector (SDC). Fig.3 gives the rf-output power in dependence of the cathode voltage  $U_c$  for a constant magnetic field and an approximately constant beam current. The calculations have been performed with a selfconsistent, time dependent multimode code using the experimental parameters as input. Six neighbouring modes of the  $TE_{m,17}$  series have been considered as possible competitors in the calculations. Total rf-losses inside the tube of 12% have been taken into account. At a cathode voltage  $U_c \leq 77$  kV the  $TE_{32,17}$  mode is oscillating with a frequency  $f = 167.24$  GHz. The relatively low value of the measured rf-output power in comparison to the calculations in this mode is presumably due to the rf-reflection of about 14% at the output window. Above  $U_c \approx 89$  kV the  $TE_{30,17}$  mode oscillating at a frequency of 162.82 GHz is expected. The measured rf-output power in the  $TE_{31,17}$  mode is in good agreement with the calculations for  $U_c \leq 84$  kV. At cathode voltages above 84 kV the measured rf-power increases slower than the calculated value. The difference between the experiment and calculations rises up to about 15%. Further investigations are needed for clarification.

The rf-power distribution in the window plane is not as homogeneous as expected from the previous design because for the design of the q.o. system partially geometrical optical tools have been used. However, there is good agreement between the measured and the calculated distribution when the calculations are performed fully according to physical optics.

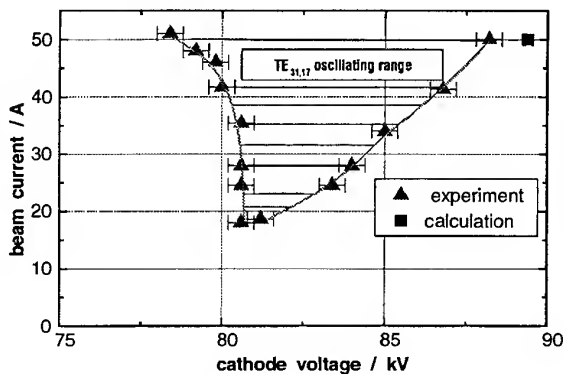


Fig. 2: Single-mode operating range.  
 $B_{cav} = 6.55$  T

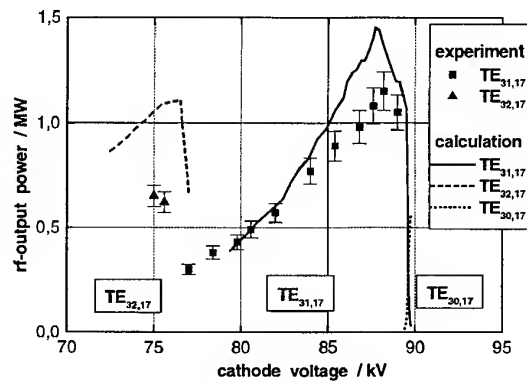


Fig. 3:  $P_{out}$  vs.  $U_c$  for  $I_b \approx 50$  A and  $B_{cav} = 6.63$  T  
 $\alpha \approx 0.9$  ( $U_c = 75$  kV) – 1.1 ( $U_c = 87$  kV)

### Conclusions and outlook

The measured rf-output power is in good agreement with calculations at lower cathode voltages. At higher values of  $U_c$  around the maximum efficiency the experimentally achieved rf-output power is approximately 15% lower than the calculated values. The reason for the observed deviation is not clear yet and needs further investigations. In particular, the influence of rf-power reflection from the output window on the operation will be proved and further calculations of the mode competition will be performed with the multimode code. In order to prove the tools for designing of the q.o. output system the phase correcting mirror has been redesigned fully according to physical optics for a homogeneous field distribution in the window plane and is now under fabrication.

### References

- [1] B. Piosczyk et al., "A 1.5-MW, 140-GHz,  $TE_{28,16}$ -coaxial cavity gyrotron", *IEEE Transactions on Plasma Science*, **25**(3), 1997, pp. 460-469.
- [2] C.T. Iatrou et al., "Design and experimental operation of a 165 GHz, 1.5 MW coaxial-cavity gyrotron with axial RF output", *IEEE Transactions on Plasma Science*, **25**(3), 1997, pp. 470-479.
- [3] B. Piosczyk et al., "Coaxial cavity gyrotron with dual rf-beam output", *IEEE Transactions on Plasma Science*, **26**(3), 1998.
- [4] G. Michel et al., "Design of a quasi-optical mode converter for a coaxial 165 GHz  $TE_{31,17}$  gyrotron", *Conf. Digest of the 22nd Int. Conf. Infrared and Millimeter Waves*, Wintergreen, Virginia, USA, 1997, pp.25-26.

## Experimental results from a helical waveguide gyro-TWT

G.G. Denisov<sup>1)</sup>, V.L. Bratman<sup>1)</sup>, A.W. Cross<sup>2)</sup>, W. He<sup>2)</sup>, A.D.R. Phelps<sup>2)</sup>, K. Ronald<sup>2)</sup>,  
S.V. Samsonov<sup>1)</sup> and C.G. Whyte<sup>2)</sup>

<sup>1)</sup> Institute of Applied Physics RAS, 603600 Nizhny Novgorod, Russia

<sup>2)</sup> Department of Physics and Applied Physics, University of Strathclyde, Glasgow, G4 0NG, UK

### Abstract

A novel gyro-TWT amplifier, based upon a new microwave system in the form of a helical corrugation of the inner surface of a circular waveguide, has produced promising first experimental results. In the regime of single-frequency amplification at 9.1 GHz and 9.4 GHz, the gyro-TWT operating at the second cyclotron harmonic with a 200 keV, 25 A electron beam having a large axial velocity spread of ~30% and moving in a weak magnetic field of 0.22 T generated the high output power of 1 MW corresponding to a gain of 23 dB and an efficiency of 20%.

### Introduction

Hitherto, conventional gyro-TWT's have presented difficulties as broad band and high efficiency amplifiers. This is due to a twofold problem related to the unfavourable wave dispersion of a smooth waveguide. Close to cut-off the wave group velocity is small and therefore the amplifier is susceptible to oscillation, and far from cut-off, at high Doppler upshifts, the system's efficiency suffers due to particle velocity spread, whilst remaining vulnerable to oscillation at lower frequency (near cut-off) resonances. An ideal eigenwave dispersion for a gyro-TWT would be one which has small ("zero") axial wavenumbers ( $k_z$ ), while at the same time possessing a large wave group velocity  $\partial\omega/\partial k_z$  which is finite and approximately constant. As shown by [1,2] such an eigenwave dispersion may be realised in an oversized circular cylindrical waveguide with a helical corrugation of the inner surface. This helical corrugation couples two rotating partial waves of a

regular waveguide with cut-off frequencies near and far below the operating frequency. The first partial wave resonantly interacts with the electrons and the admixture of the second wave makes the group velocity of the eigenwave non-zero. Changing the geometrical parameters of the corrugation one can control the eigenwave group velocity and adjust it to the longitudinal velocity of an electron beam for a rather broad frequency band around the point where the longitudinal wavenumber is equal to zero. These features allow a very attractive regime of gyro-TWT operation to be realised where the interaction is less prone to oscillations and simultaneously possesses a weak sensitivity to the spread in electron velocity (as in the gyrotron).

### Experimental setup

In this paper we present the results of a joint experiment which was carried out at the high-current direct-action accelerator at the University of Strathclyde as shown in figure 1. The diode was operated in the space-charge limited regime of electron field emission, using a velvet surface to enhance the electron emission properties of the central cathode disk. A stacked double-Blumlein pulsed high voltage source was used to provide the accelerating field. Fast electron beam diagnostics were constructed, having response times typically 5-15ns, which permitted time-correlated observation of the evolution of the pulse parameters. The electron accelerating potential was measured using a resistive divider, while the beam current was measured at the cavity using a self-integrating Rogowski coil, inserted in the beam tube.

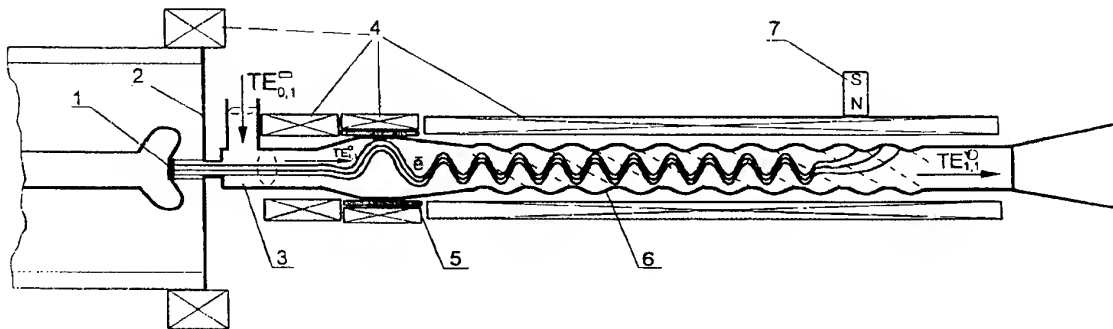


Fig.1. Schematic diagram of the gyro-TWT with a helical waveguide: 1 - velvet cold cathode; 2 - anode; 3 - wave launcher (converter of  $TE_{0,1}$  mode of a rectangular waveguide into  $TE_{1,1}$  mode of a circular waveguide); 4 - coils generating DC guiding magnetic field; 5 - kicker; 6 - operating helical waveguide; 7 - deflecting magnet.



A 200 keV/25 A rectilinear electron beam with a diameter of 8 mm and flat-top duration of 50-100 ns was produced from a "cold" velvet cathode. The microwave pulse duration and temporal profile were obtained from a crystal detector observed on an oscilloscope, time correlated with the electron beam pulse and voltage profiles (Fig.2).

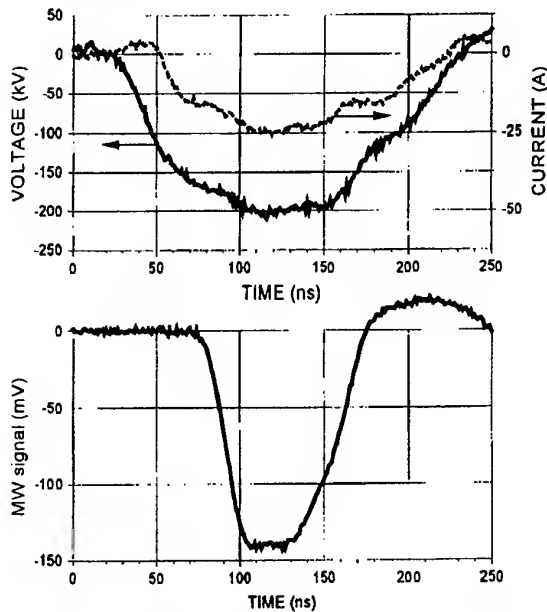


Fig.2. Oscilloscope traces: Top - beam voltage and current, Bottom - microwave signal.

A DC single-period bifilar spiral kicker transformed the straight beam into a helical one gyrating around the axis with a variable transverse velocity  $\beta_{\perp}=0-0.6$ . The use of a thin solid electron beam encircling the axis enhances mode selection for gyrodevices: only co-rotating resonant modes with azimuthal indices ( $m$ ) equal to the cyclotron harmonic number ( $s$ ),  $m=s$ , are excited. The electron velocities and their spreads were estimated experimentally from a scintillator placed at different distances from the kicker. For the operating transverse velocity  $\beta_{\perp}=0.5-0.6$  a large spread in axial velocity of about 30% was measured. The magnitude of the axial magnetic field generated by a water-cooled DC coil was up to 0.3 T which allowed realisation of a second harmonic helical gyro-TWT in the X-band. In this amplifier the operating eigenwave was formed by mutual scattering of near-cutoff (co-rotating with electrons)  $TE_{2,1}$  and counter-rotating  $TE_{1,1}$  partial waves on a three-fold helical corrugation (Fig.3).

A 40 cm long waveguide of 14.5 mm mean radius with a helical corrugation of 1.5 mm amplitude and 37.5 mm period was used as an operating microwave system. The calculated and measured dispersions of the waveguide are in good agreement (Fig.2) [2, 3].

The eigenwave  $W_1$  has the desirable dispersion and can be matched with the electron beam for a rather wide frequency band. Numerical simulations predict for the helical gyro-TWT with these parameters efficiency of  $\sim 30\%$  and 3dB frequency bandwidth of  $\sim 10\%$  (for a deeper corrugation the bandwidth can be widened up to 20-25%).

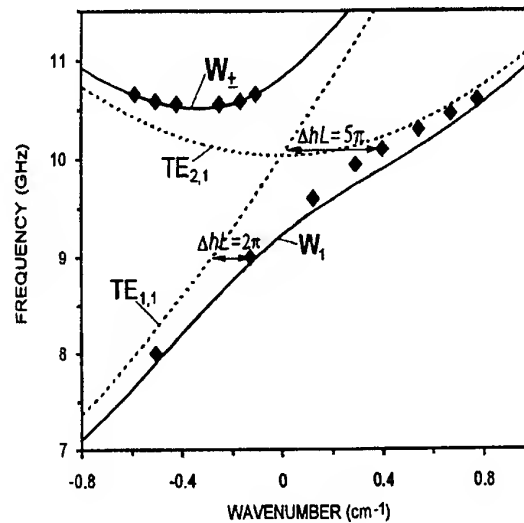


Fig.3. Dispersion diagram for the operating helical waveguide: dotted and solid lines correspond to partial and eigen modes, respectively, ♦ - results of "cold" measurements.

#### Second harmonic gyro-TWT experimental results

For the operating amplification regime, the driving RF signal was produced by one of two pulsed magnetrons with operating frequencies of 9.4 and 9.1 GHz, a maximum power of 25 kW and pulse duration of 1  $\mu$ s. Nearly 50% of the magnetron power was transported through a long rectangular waveguide to a specially designed broad-frequency-band launcher which was 90% efficient in coupling the radiation from the rectangular waveguide to the circular beam transport region. The circular beam transport region supported only the fundamental  $TE_{1,1}$  mode for the operating frequency. Its radius was then increased to match that of the interaction region. A linearly polarised wave was injected into the helical waveguide of which half of the incident power, with the correct rotation of the electric-field vector, participated in the interaction. Therefore, the maximum input power in the operating eigenwave of the helical waveguide was approximately 5.5 kW. For gyro-TWT operation at frequencies below cutoff of the parasitic (gyrotron-like) mode  $W_{\perp}$  (Fig.2), all the output power is contained in the wave  $W_1$  which is then easily transformed into a  $TE_{1,1}$  mode and radiated in a nearly Gaussian wave beam. The output power was measured using attenuators and sensitive

semiconductor detectors, calibrated with the magnetrons. Cutoff waveguide filters were also used for measuring the radiation frequency.

At the operating magnetic field of 0.22 T the transverse electron velocity was limited to a value of  $\beta_{\perp}=0.5$  because of self-excitation of the mode of operation as observed by oscillations at frequencies 10-10.5 GHz where the wave reflection coefficient from the input was relatively high. Therefore the achieved amplification and power were slightly less than the calculated values for the saturation regime. When the parasitic oscillations were close to their starting regime they were easily suppressed if the magnetron was switched on.

For both operating frequencies of the magnetrons, 9.4 and 9.1 GHz, and fixed parameters of the electron beam and magnetic field the same output power was measured. An important measurement with the use of elliptical waveguide polarisers in front of the microwave detection system confirmed that the output  $TE_{1,1}$  wave had a circular polarisation with a rotation opposite to the electron rotation in the magnetic field. In the regime of single-frequency amplification, the gyro-TWT provided a maximum output power of 1 MW, a gain of 23 dB and an efficiency of 20%. Further experiments are now in progress at the Institute of Applied Physics, Nizhny Novgorod, Russia and at the University of Strathclyde, Glasgow, UK.

#### Acknowledgements

The work was supported by the United Kingdom DERA, Gycom, Ltd., Nizhny Novgorod, Russia and the Russian Foundation for Basic Research under Grant 98-02-17208.

#### References

1. G.G. Denisov and S.J. Cooke. Digest 21st Int. Conf. IR&MM Waves, Berlin, Germany, 1996, p.AT2.
2. G.G. Denisov, V.L. Bratman, A.D.R. Phelps, and S.V. Samsonov. IEEE Trans. on Plasma Sci. (to be published June 1998).
3. G.G. Denisov, V.L. Bratman, A.D.R. Phelps and S.V. Samsonov. Digest 22nd Int. Conf. IR& MM Waves, Virginia, USA, 1997, p. 289.

# Operation of a 3 MW, 140 GHz Gyrotron with a Coaxial Cavity

R. Advani, M. Pedrozzi, K.E. Kreischer, R. Temkin

Plasma Science and Fusion Center, Massachusetts Institute of Technology  
Cambridge, MA 02139

and M.E. Read

Physical Sciences, Inc., Alexandria, VA

## Abstract

Operational details of a 3 MW, 140 GHz gyrotron are reported in this paper. A  $TE_{21,13}$  coaxial gyrotron has been designed to operate at an efficiency of at least 30%. Initial operation of this gyrotron in the low velocity ratio regime yielded power levels of ~1 MW. Subsequently problems were found with the power output section leading to its redesign. Also, the large cathode emitter was found to be defective and has now been replaced.

## Introduction

CW gyrotrons operating at 140-170GHz are typically designed to produce 1 MW per tube. This has been due to technological limitations imposed by the cavity heat load, mode competitions and the output window. The coaxial gyrotron attempts to increase this value to 3 MW per tube, thus reducing the number of tubes required for the future fusion experiments and the total system costs. Recent improvements in window design with double-disk, diamond, and dome-shaped windows mean that future tubes will be mostly limited by the maximum average cavity heat loading. About  $1.8 \text{ kW/cm}^2$  can be handled in present designs.

The main advantages of a coaxial conductor in a gyrotron are[1]:

- Causes rarefied mode spectrum around the design mode
- Reduces the quality factor of competing modes
- Volume modes (higher radial index) can be chosen decreasing the ohmic losses
- Reduces voltage depression

Due to the ability to choose a volume mode in coaxial gyrotrons, greater output can be expected at the same level of cavity ohmic power.

## Experimental set-up

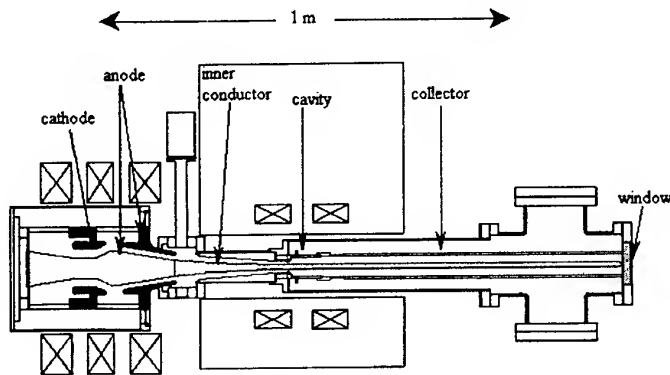


Figure 1: Schematic of the Coaxial Gyrotron

The experimental set-up is shown in Fig. 1, and the theoretical operating parameters are summarized in Table 1. The electron gun is an inverted magnetron injection gun (IMIG) designed and built by PSI [2]. A 6.5 T superconducting magnet is used for the main magnetic field, and three gun coils allow the adjustment of the magnetic field at the cathode. The inner conductor is made in two parts and is held at the anode and at the end of the tube and does not interfere with either the electron beam or microwave power. It is possible to isolate the gun from the tube by

retracting the coaxial conductor and closing a valve. In order to simplify the design, the power at the output end is extracted longitudinally through a conventional quartz window. A previous design included a mode converter that directed the power through a side window.

## Initial operation

In spite of all these advantages, the operation of the coaxial gyrotron has proven to be a challenge. Alignment of the inner conductor, beam (magnetic field), and the outer cavity to a accuracy of less than 0.25 mm has been difficult. Nevertheless we have been successful in operating the coaxial gun to parameters of 95 kV, 76 Amps, and the initial operation gave us 1 MW, at 140 GHz, with a 14% efficiency[3]. The peak power was found in the  $TE_{27,11}$  mode. In initial operations, the gyrotron was operated in a low velocity ratio regime ( $\alpha \approx 1.1$ ) and with a magnetic compression less than the design parameter.

The initial operation used a mode converter and the power was extracted radially, which is complicated because of the coaxial conductor. Upon opening the tube after the initial runs, we saw evidence of some power hitting the flanges instead of making it out of the tube.

### Improved design

Consequently, the output section of the tube was simplified. The mode converter was removed and replaced by a straight section of copper pipe which would now make the power output axial. This redesign ensured that all the power would exit the tube and be measured. A schematic of the old design and the new one is shown in Fig. 2.

Frequency	140 GHz
Mode	TE <sub>21,13</sub>
Voltage	95 kV
Current	76 A
Velocity Ratio	1.7
Efficiency	41 %
Magnetic field	5.5 T
Compression	38
Cavity radius	2.33 cm
Coaxial insert radius	0.602 cm
Beam radius	0.812 cm
Emitter radius	5.01 cm
L/l	8.5
Diffraction Q	1400
Avg. ohmic losses	1.8 kW/cm <sup>2</sup>
Voltage depression	5.1 kV
Satellite modes	TE <sub>18,14</sub> , TE <sub>22,13</sub>

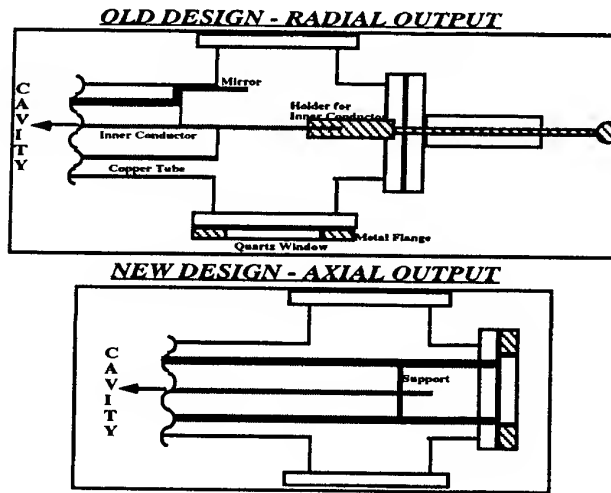


Table 1: Design parameters of the coaxial gyrotron.

Figure 2: Initial design and new design

The design and construction of this modification is complete and we re-tested the tube. In this iteration we first tested the tube in the empty cavity mode where the coaxial conductor was removed and the mode spectrum and power were measured. The measured frequencies of the modes were consistent with theory, but the power output continued to be low, less than 1 MW.

### Beam asymmetry measurements

Since the power output was low even in the empty cavity experiments, we decided to measure the electron beam. We first let the electron beam strike a witness plate and when that showed us that we may have severe asymmetries we followed it up with a rotating probe experiment. This experiment consisted of a simple 30° sector of Copper which could be rotated in the azimuthal direction. This probe would thus measure the current at different azimuthal positions. This measurement of the beam with the rotating probe is shown in Fig.3. It shows that the beam is quite asymmetric. Therefore we are now replacing the cathode emitter with a new one. After that, the alignment mechanism is going to be further improved and further testing will be done with the coaxial conductor reinserted. Besides the experimental work, a numerical analysis of the data will also be presented. A theoretical study of the sensitivity of the tube (and gun) to

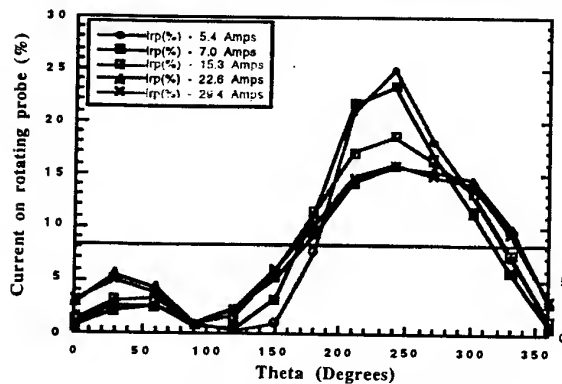


Figure 3: Measurement of beam measured by the 30° sector as a percentage of the total current.

small misalignments in radius or axial displacements, of the anode will also be presented. A study of the critical parameters (velocity ratio and spread) versus changes in voltage, current, and magnetic field will be shown.

### References

- 1 V.A. Flyagin, N.S. Nusinovich, Proceedings of the IEEE, 76, pp. 646, 1988.
- 2 M.E. Read, G. Nusinovich, O. Dumbrajs, G. Bird, J.P. Hogge, K.E. Kreischer and M. Blank, IEEE Trans. Plasma Science, vol 24, no 3, 1996.
- 3 J.P. Hogge, K.E. Kreischer, M.E. Read, 20<sup>th</sup> International Conference on Infrared and Millimeter Waves, pp. 417-418, Orlando, December 1995.

## Development of a Multi-Stage Depressed Collector System for 1 MW CW Gyrotrons

R. Lawrence Ives, Amarjit Singh\*, Marcel Gaudreau+,  
Max Mizuhara, Rich Schumacher, Victor Granatstein\*

Calabazas Creek Research, Inc.  
20937 Comer Drive  
Saratoga, CA 95070, USA

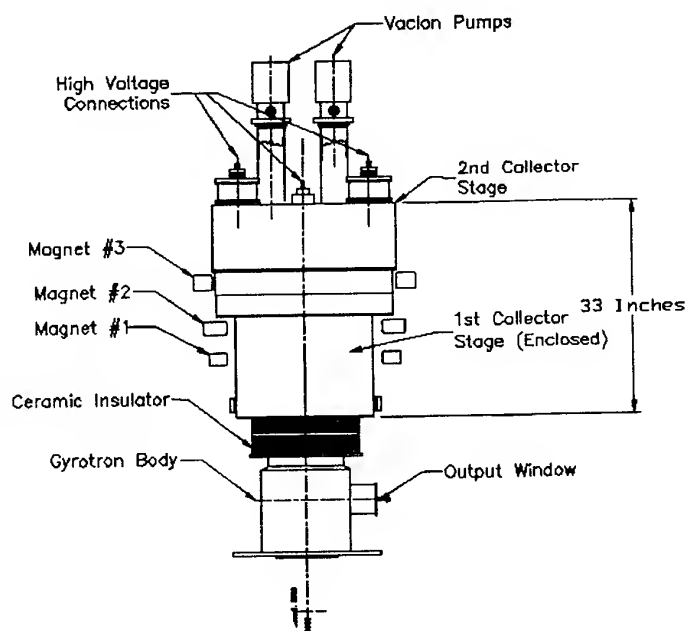
\*Institute for Plasma Research  
223 Paint Branch Road  
College Park, MD 20742, USA

+Diversified Technologies, Inc.  
35 Wiggins Ave.  
Bedford MA, 01730, USA

Calabazas Creek Research, Inc., in cooperation with the Institute for Plasma Research at the University of Maryland and Diversified Technologies, Inc., is continuing the development of the multi-stage depressed collector system described at the 23rd IR&MM Conference in Wintergreen, VA. Recently developed analytical tools demonstrate the importance of considering high energy, backscattered electrons in the design of the collector structure. The collector described in last year's presentation was predicted to achieve 70% collector efficiency with no return current when only primary electrons were considered. Analysis including secondary electrons resulted in a drop in predicted efficiency by 8% with approximately 2 amps of returned current to the body and gun sections of the tube. This clearly represents an unacceptable situation, so the electrical, magnetic, and mechanical design of the collector is being modified with consideration for the effect of secondary electrons.

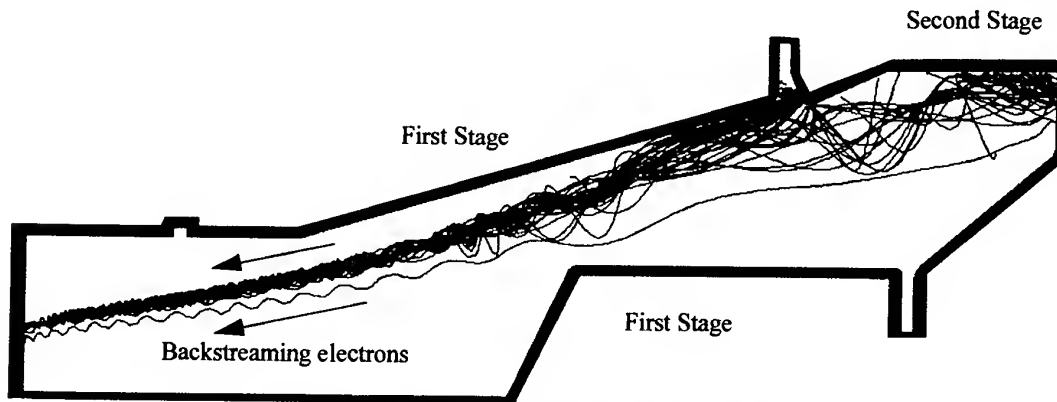
The emission of secondary electrons depends on the impact angle and energy of the primary electron. Depending on the structural details of the surface, the characteristics of the secondary electrons can be quite different. This program will examine the nature of secondary emissions for machined copper surfaces and for ion-textured copper surfaces. Recent research at the NASA-Lewis Research Center is providing new information on secondary electrons emitted from these surfaces. In particular, the effect of ion-texturing on secondary electron generation may provide a means of dramatically lowering the number of electrons emitted. This program will analyze the potential benefits of ion-texturing and techniques for implementing it in the depressed collector.

The development of the collector will be able to provide high levels of energy recovery for gyrotrons operating with similar size electron beams at frequencies between 80 GHz and 170 GHz. This is expected to include most gyrotrons in the 500 kW to 1 MW CW power range. Development of a single collector applicable to gyrotrons in this range will lower development and manufacturing costs and promote standardization of collector and power supply designs.



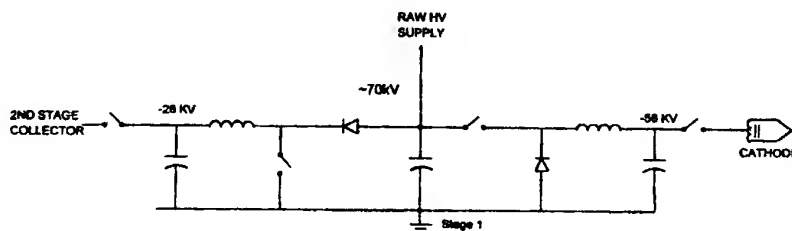
Outline drawing of two stage depressed collector for 1 MW CW gyrotrons

The second major effort in the program is to design a system that will provide all required power for the gyrotron and magnet coils, exclusive of the superconducting magnet. Recent developments by Diversified Technologies will dramatically reduce the cost of the power supply system by using advanced, solid state switching technology.



Trajectory plot for original two stage depressed collector design showing only reflected primary electrons and low energy secondary electrons. Collector efficiency is 62% with 2.0 amps of returned current.

It is currently estimated that this technology will reduce the cost of the power supply system to less than one third that of conventional, tube-based supplies. A schematic diagram of the power supply system for the cathode and collector is shown below. Energy recovered by the second collector stage is modified by a voltage boost circuit and fed back into the main filter capacitor of the beam voltage supply. The cathode supply consists of a basic buck regulator, which provides -58 kV to the cathode through a solid state switch for beam modulation and arc interruption. The efficiency of the solid state supplies exceeds 98%, and the reliability and performance is significantly higher than tube-based supplies.



Three port converter for recovering energy from the depressed collector and recycling it to the cathode/beam supply.

The third aspect of the current research is to develop a computer control system to facilitate operation of the gyrotron and ensure optimized efficiency at all power levels. The user will be able to modify operation of the tube by specifying the desired output power through a graphical user interface or to specify operation according to a predefined schedule of output power versus time. The computer control system will modify the appropriate supplies to deliver the requested output power while also maximizing energy recovery. The solid state power supplies are capable of responding in 10s of milliseconds to computer requested changes in voltage or current. This will allow the gyrotron to respond to diagnostic feedback from the plasma in time scales of a few hundred milliseconds, allowing modes of gyrotron operation not currently possible with manual control.

The current program will include development, manufacture, and test of a multi-stage depressed collector on a 1 MW CW gyrotron. The program also includes development of the software to optimize energy recovery of the gyrotron independent of operating frequency, power level, or detailed beam characteristics. The computer software will characterize the performance of individual gyrotrons during initial testing and store this information for recall during actual operation. This will facilitate implementation of the computerized power supply system and multi-stage collector on a wide variety of gyrotrons.

This program is funded by the U.S. Department of Energy through SBIR Grant Number DE-FG03-97ER82342.

# MICROWAVE GENERATION AT 5.7 GHz BY A 100 kW AXIAL TRANSIT-TIME OSCILLATOR

J. J. Barroso, K. G. Kostov\*, and R. A. Corrêa

National Institute for Space Research (INPE), P.O. Box 515, 12201-970 São José dos Campos, SP, Brazil

\*On leave from Dept. of General Physics, Sofia University, 5 J. Bourchier Blvd., Sofia 1126, Bulgaria

## Abstract

A description is given of a microwave tube based on the transit-time effect and conditions accounting for its feasibility as a high-power, pulsed microwave source are outlined. The device comprises a temperature-limited diode gun operating at 33-kV cathode voltage and 40-A beam current. As indicated by 2.5D particle-in-cell simulations, a 5.7-GHz single frequency radiation has been generated at the peak-power output level of 100kW.

## Introduction

The mechanism by which a stream of electrons crossing a resonant structure transfers energy to cavity's characteristic modes is called a transit-time effect. Perhaps, the simplest microwave tube is the transit-time oscillator [1], which consists of a cylindrical cavity with the end plates forming a diode in which propagates a rectilinear electron beam. Early works on transit-time effect date back to the 1930's with a developmental 3-GHz device of 0.25% efficiency [2]. Nevertheless, the transit-time based oscillator can achieve a significant efficiency to be worth considered as an attractive microwave source by virtue of its simplicity, as diode and resonator are combined into a single unit that makes for a compact, lightweight device. Recent advancements in the pulse technology has revived the concept of transit-time oscillator as an attractive source of high-power microwaves [3].

This article deals with 2½D, electromagnetic PIC computer simulation [4] of an axial transit-time oscillator, which operates without external guiding magnetic field. The diode runs in the temperature-limited regime producing a 40-A beam current at 33 kV cathode voltage and the transit-time oscillator is designed to operate at 5.74GHz in the lowest order  $TM_{010}$  cavity mode. Peak output power of 100 kW is obtained, which translates into a 7.5% beam to microwave power conversion efficiency.

## Numerical Simulation

Fig. 1 shows the elements of the oscillator, where the electrons are accelerated through the diode gap and then collected at the anode to the right. In the simulation of the transit-time oscillator operation, square cells of

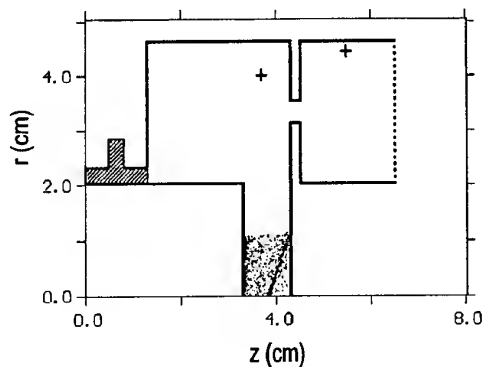


Fig. 1. Simulation setup.

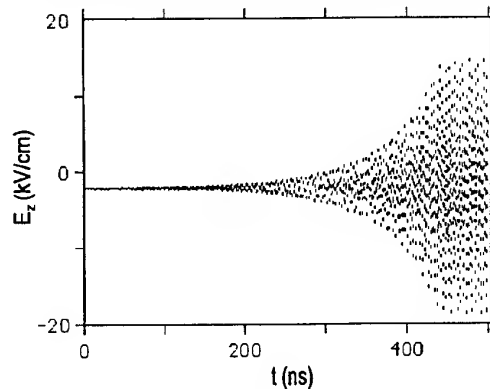


Fig. 2. Time history of the RF field

1mm in size have been used with over one thousand particles representing the 40-A electron beam, whose configuration space is also shown in Fig. 1. The RF fields have started to grow after a time span of 200ns as indicated in Fig. 2, that displays the time history of the electric field at the observation point  $z=3.8\text{cm}$ ,  $R=4.0\text{cm}$ . More detailed information about the axial electric field is provided by Figs. 3(a) and 3(b).

As for the radiation that leaks into the output TEM guide through the annular aperture, Fig. 4 shows the spectrum of the radial electric field at the point  $z=6.0\text{cm}$ ,  $r=4.5\text{cm}$ . The spectrum has a sharp peak of 0.7kV/cm in amplitude centered at 5.7GHz. The corresponding output power (Fig. 5) is obtained by integration of the Poynting flux across the section at  $z=6.0\text{cm}$  of the outlet. First we note in Fig. 5 that the pulsating power is always positive, indicating that the output signal is a pure traveling wave that propagates to the right. We can see also that within a 1ns interval there exist twelve peaks, twice as much as in the time plots of the electric (Fig. 3(a)) fields. This corresponds to two pulses per period, as expected from the Poynting vector calculation involving the cross product  $E \times B$ .

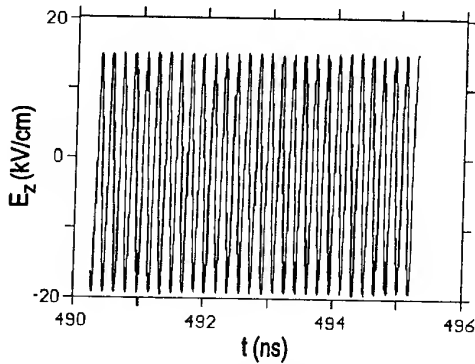


Fig. 3(a). Time variation of electric field

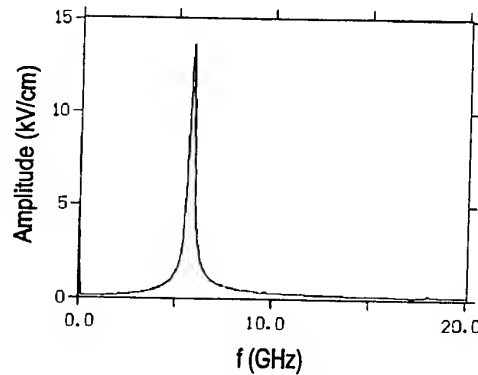


Fig. 3(b). Spectrum of the electric field

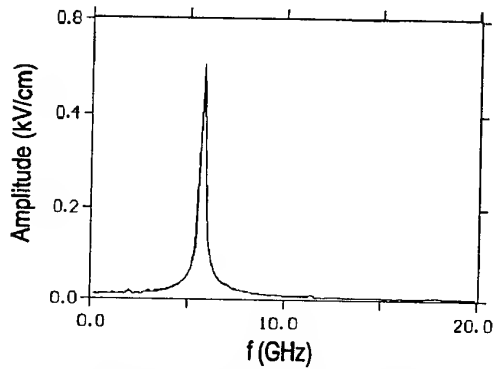


Fig. 4 Frequency spectrum in TEM guide

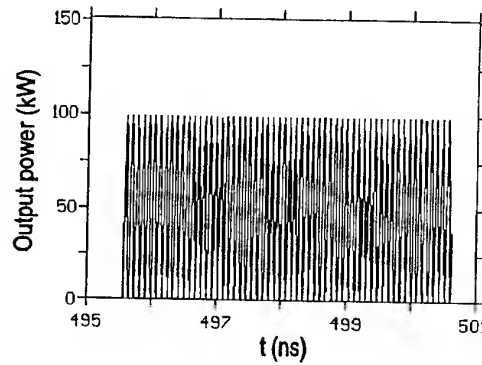


Fig. 5. Time plot of the output RF power

### Conclusions

We have devised a single-frequency oscillator that comprises a temperature-limited diode gun operating at 33kV cathode voltage and 40A beam current. The diode gap acts as a mode resonator that excites an intermediate coaxial  $TM_{010}$  cavity, which in turn is coupled by an annular aperture to an output TEM coaxial guide having characteristic impedance of  $50\Omega$ .

On the basis of 2.5D particle-in-cell simulations, the device has produced an output peak power of 100kW which translates into a DC to RF power conversion efficiency of 7.5%. Oscillations reach the steady-state regime on a time scale of a few hundreds of microseconds after the beam has become density-modulated in high-voltage gap, where RF electric field intensities of 65kV/cm have been noticed.

The device, rugged from both a mechanical and thermal standpoint, has a simple structure with cylindrical symmetry for easy machining and assembly. The peak power density of  $420\text{kW/cm}^2$  restrains the oscillator from operating in CW regime, since this value far exceeds the limit of  $3\text{kW/cm}^2$  for presently available cooling techniques. Nevertheless, for a pulse duration  $\tau_p = 10\mu\text{s}$  and repetition frequency of 250Hz the average ohmic heating density on the anode inner surface reaches the acceptable value of  $1.0\text{kW/cm}^2$ . For OFHC copper, the corresponding temperature rise during the application of the pulse can be estimated by [5]  $\Delta T(^{\circ}\text{C}) = 0.3P_s(\text{W/cm}^2)\sqrt{\tau_p(\text{s})}$ , where  $P_s$  is the peak power density at surface, giving  $400^{\circ}\text{C}$ . As for the emission density, the cathode should operate at a current density of  $13.0\text{A/cm}^2$ , for which an efficient pulsed thermionic emitter can fulfill this requirement.

### References

1. C. H. Birdsall and W. B. Bridges, *Electron Dynamics of Diode Regions*, New York: Academic Press, 1966, Sec. 1.06.
2. F. B. Llewellyn and A. E. Bowen, *Bell System Technical Journal*, **18**, 280, (1939).
3. M. J. Arman, *IEEE Trans. Plasma Sci.*, **24**, 964 (1996)
4. V. P. Tarakanov, "User's Manual for Code KARAT" 1994, Berkeley Research Associates, Inc., Springfield, VA, USA.
5. G. B. Collins, "Microwave Magnetrons", (M.I.T. Radiation Laboratory Series, vol. 6, New York: McGraw-Hill, 1948, Sec. 12.6.



## Frequency-Step-Tuned Operation of a Quasi-Optical Mode Generator

A. Arnold<sup>1)2)</sup>, O. Braz<sup>1)2)</sup>, H.-R. Kunkel<sup>1)</sup>, M. Thumm<sup>1)2)</sup>

<sup>1)</sup> Forschungszentrum Karlsruhe (FZK), ITP, Association EURATOM-FZK,  
Postfach 3640, D-76021 Karlsruhe, Germany

<sup>2)</sup> Universität Karlsruhe, Institut für Höchstfrequenztechnik und Elektronik,  
Kaiserstr. 12, D-76128 Karlsruhe, Germany

### Abstract:

In future ECRH systems it will be necessary to heat the fusion plasma at different locations. One possibility is to feed in millimeter-waves with different frequencies. As millimeter waves sources gyrotrons, each operating at different frequencies, are foreseen. In order to check the proper behaviour of the required multi-mode quasi-optical converter system cold test measurements are necessary. A possibility for using already existing mode generators at these other frequencies and other modes will be presented.

### Introduction

In a gyrotron it is possible to generate different frequencies by applying different magnetic fields in the resonator to excite different modes. Experiments on an existing 1 MW, 140 GHz  $TE_{22,6}$ -gyrotron with a built-in quasi-optical mode converter have shown a series of oscillation in the range from 114 GHz to 166 GHz [1]. For further experiments the modes  $TE_{19,5}$  at 117.80 GHz,  $TE_{22,6}$  at 140.10 GHz and  $TE_{25,7}$  at 162.30 GHz seem to be most important.

Since the gyrotron cavity mode has to be converted into a linearly polarized Gaussian beam, a multi-mode quasi-optical mode converter system working at least with these three modes has to be developed. To prove the steady performance when fed with different TE-modes low power measurements are necessary. This requires a low power mode generator working at the three modes mentioned above. An existing mode-generator [2] designed for a  $TE_{22,6}$ -mode at 139.86 GHz was tuned to excite a  $TE_{25,7}$ -mode at 162.108 GHz. The preliminary results are shown in the next paragraph.

### $TE_{22,6}$ -Mode-Generator generating $TE_{25,7}$ -Modes at 162.108 GHz

A summary of the principle of the quasi-optical mode generation method used here is given in another paper at this conference [3]. For an increased mode selection a coaxial cavity shown in Fig. 1 is used.

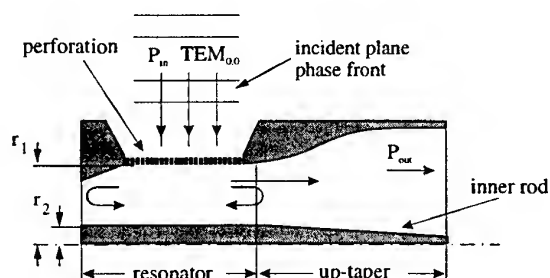


Figure 1: Cross-section of a coaxial cavity of a mode generator.

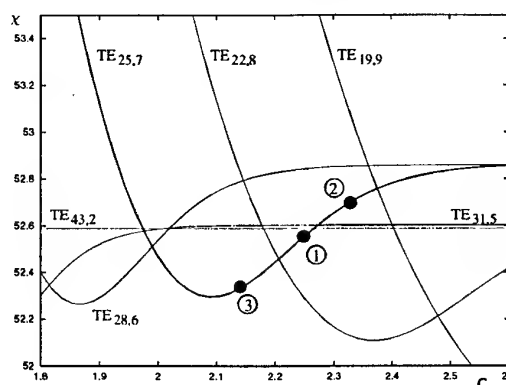


Figure 2: Eigenvalues as a function of  $C$  for certain modes.

To excite only one mode one must choose not only a good coupling but also the right dimensions of the coaxial cavity. By simply tuning the frequency up to where the desired  $TE_{25,7}$ -mode was expected, a mixture with a strong contribution of the  $TE_{31,5}$ -mode was detected. Due to the almost identical eigenvalue the separation between these two modes was found to be the most critical.  $C = r_1/r_2$  describes the ratio of the cavity's radius to the radius of the inner rod. Fig. 2 shows the eigenvalues  $\chi$  as a function of  $C$ . To get highest performance for the  $TE_{22,6}$ -mode  $C = 2.27$  was chosen, but for this case two modes had nearly the

same value of  $\chi$  (point 1 in fig. 2); both were excited and could not be separated. The problem was solved by using a slightly thinner inner rod with  $C = 2.35$  (point 2). Together with a measured cavity's operating quality factor  $Q = 3300$  the eigenvalues differ sufficient to get a mostly pure mode. Fig. 3 shows a plot of the measured E-field distribution after up-tapering the mode-generator's waveguide mouth to a diameter of 70 mm. The mode purity measurements have been determined by using a wavenumber spectrometer (k-spectrometer)[4]. The k-spectrum shown in fig. 4 presents a first overview about the generator's mode

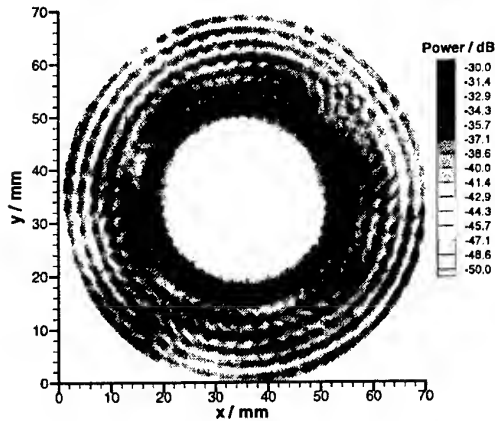


Figure 3: Measured E-field distribution of the  $TE_{25,7}$ -mode.

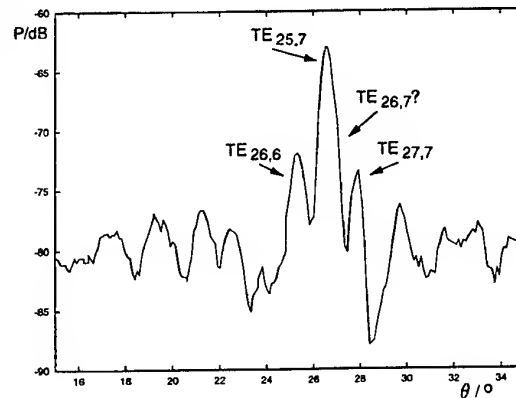


Figure 4: Mode spectrum.

content. Every mode is given a discrete angle  $\theta$  it propagates inside a waveguide and is radiated through an leakage structure. A receiving antenna gives the power and therefore the mode distribution as a function of  $\theta$ . Three modes contain most of the power. Besides the  $TE_{25,7}$ -mode the other two could be determined to be the  $TE_{26,6}$ - and  $TE_{27,7}$ -modes. After a correction for the coupling mechanism of the leakage structure the following table gives the shares. Due to the small difference in their Brillouin angles, compared to the  $TE_{25,7}$ -mode, the also expected  $\Delta m = \pm 1$  modes (e.g.  $TE_{26,7}$ ) need further investigations.

Mode	detection level dB	correction dB	level referring to $TE_{25,7}$	share %
$TE_{25,7}$	-63.0	0.0	0.0	82.7
$TE_{26,6}$	-72.0	+0.3	-8.7	10.7
$TE_{27,7}$	-73.4	-0.6	-11.0	6.6

As a preliminary result 82.7% of the total power is in the desired mode.

### Summary

A quasioptical coaxial mode generator originally designed for a  $TE_{22,6}$ -mode at 140 GHz has been operated at a frequency of 162 GHz in the  $TE_{25,7}$ -mode. First measurements on this have been presented and the performance is astonishingly good even though only the inner rod was slightly changed. Concerning the generator's mode-selection the cavity's radius proportions have been found to be the most sensitive point what modes are excited in the cavity. The next step is to examine whether it also works at 117 GHz and at last to find a configuration where all three frequencies work without changing the generator, and have a versatile device for measurements on multi-mode-converters. One possibility is to use a thicker inner rod with a  $C$  about 2.15 (point 3 in fig. 2).

### References

1. O. Braz et. al., IEEE Transactions on infrared and millimeter waves, Vol. 18, No. 8 (1997)
2. M. Pereyaslavets et. al., Int. Journal of Electronics, Vol. 82, 107-115 (1997)
3. O. Braz et. al., 23rd International Conference on Infrared and Millimeter Waves (1998)
4. W. Kasperek, G. A. Müller, Int. Journal of Electronics, Vol. 64, 5-20 (1988)

# Numerical Simulation and Experimental Study of the Helical Electron Beams of 170 GHz/1MW Gyrotrons

A.N.Kuftin, V.K.Lygin, A.S.Postnikova, V.E.Zapevalov

Institute of Applied Physics Russian Academy of Sciences,  
46 Ulyanov Street, 603600 Nizhny Novgorod, Russia

## Abstract

The report presents the results of the numerical simulation and experimental study of the helical electron beams (HEB) formed in magnetron-injection guns of 170 GHz/1MW gyrotrons. The dependence of HEB parameters on the beam current is analyzed. The evolution of the transverse velocity distribution functions is traced at the variation of the beam current.

## Introduction

Achievement of 1MW output power of 170 GHz gyrotrons for ITER with an operating voltage  $U=80$  kV and the efficiency  $\approx 35\%$  or more is required to a magnetron-injection gun (MIG) which should provide formation of a beam with a current  $I \approx 40$  A and a pitch-factor  $g \approx 1.25$  or higher ( $g = v_{\perp}/v_z$ ,  $v_{\perp}$ ,  $v_z$  - oscillatory and longitudinal velocity in operating space). The specified restrictions were taking into account for design of particular guns for gyrotrons with different working mode. The results of a new numerical simulation procedure and experimental data concerning four possible versions of guns with different radiuses of cathodes  $R_c$  are presented.

## Numerical Simulation

The results of a new numerical simulation procedure for each beam type the dependencies  $t_{\perp}$  and  $\delta v_{\perp}$  on the beam current, including results for the model with finite initial velocities are received. It was found, that there are the small divergences between the data obtained from numerical simulation at the total formation length and the ones find out from calculation in the cathode region only. The observed distinctions are caused by different value of the beam potential, used at the finding  $t_{\perp}$  and  $\delta v_{\perp}$ . According to results of the trajectory analysis, the value of the beam voltage depression is rather close to the theoretical estimations [1]. Evolution of  $f(v_{\perp})$  for each beam type along the formation region and when the current grows is traced.

The allowable value of radius of the cathode for a chosen operating mode is defined by the value of an acceptable electrical field on the cathode  $E_c$ , which, as a rule, is necessary not above than 6 kV/mm. Width of the emitter is selected with the account of extreme allowable density of an emission current (usually it is not recommended to exceed 3 A/cm<sup>2</sup>). At selection of an optimum configuration of electrodes the value of velocity spread  $\delta v_{\perp}$  was not allowed above than 30%. The specified restrictions were taking into account of particular guns for gyrotrons with different operating modes. Then from numerical simulation dependencies  $\delta v_{\perp}(I)$  and  $t_{\perp}(I)$  for

the each gun were received. Calculations were performed as using model with zero initial velocities (EPOS-R [2]) as taking into account initial velocities (EPOS-V [3]). Evolution of transverse velocity distribution function  $f(v_{\perp})$  is traced with a beam current growth. The sensitivity of the beam parameters to influence of thermal deformations of a gun and possible technological errors is investigated. The transformation of distribution function  $f(v_{\perp})$  can serve one of attributes of loss of beam stability [4]. In considered guns infringement unimodality of oscillatory velocity distribution function is not registered at currents of a beam, even exceeding design value of the current ( $I=40$ A). The specified circumstance allows to hope, that offered MIG will provide formation of a stable beam with acceptable parameters.

For the operating mode the TE<sub>31,8</sub> in the frame of limitations on an electrical field  $E_c$ , optimum radius of the cathode

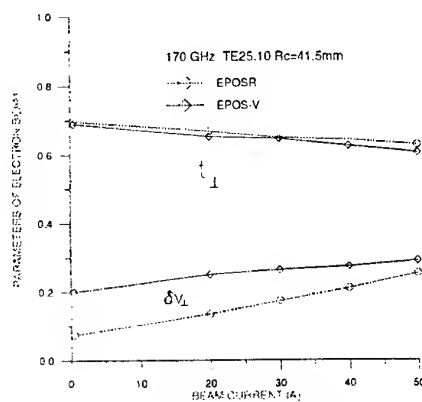


Fig.1.  $\delta v_{\perp}$  and  $t_{\perp}$  vs. beam current

$R_c = 51\text{mm}$ . Thus on the cathode  $E_c \approx 5.8\text{ kV/mm}$ . For gyrotron with an operating mode the  $TE_{28.7}$  two versions of guns with different radiuses of cathode were designed. In the first version a gun with  $R_c = 45.2\text{mm}$  was used. The necessary  $g$  value need an increased electrical field on the cathode  $E_c \approx 6.3\text{ kV/mm}$ . In the second variant the reduction  $E_c$  to  $5.5\text{--}5.7\text{ kV/mm}$  was reached by using of the cathode with increased average emitter radius ( $R_c = 47.5\text{mm}$ ). Finally for the operating mode the  $TE_{25.10}$   $R_c = 41.5\text{ mm}$  was chosen. For all gun variants dependencies  $\delta v_{\perp}(I)$  and  $t_{\perp}(I)$  and evolution  $f(v_{\perp})$  are investigated, including the disturbing factors presence also. Fig.1 shows typical dependencies.

### Experimental Study

The measurements were carried out for guns with  $R_c = 45.2\text{mm}$  and  $R_c = 41.5\text{mm}$  by the modified method of the retarding field in the scale down regime [5] at the automated experimental set up [6]. Beams with caught electrons are compared with beams, in which these electrons are intercepted by a special additional diaphragm. HEB formed in such conditions we shall name "primary beam". Besides knowledge of the characteristics even for a primary beam allows to predict real beam stability and stability of gyrotron operation in oscillation regimes, when reflected electrons take places. A beam, which is measured without interception of reflected electrons, we shall name "resulting beam". Below we will mark for simplicity resulting beam measurements as 1D regime, and primary beam measurements as 2D regime. The velocity spread, average oscillatory energy and oscillatory velocity distribution function dependencies on the beam parameters were traced (fig.2, fig.3.). The received dependencies  $\delta v_{\perp}$  and  $t_{\perp}$  are compared with results of numerical simulation and good correlation is observed.

### Conclusion

Methods of numerical simulation and experimental research of HEB were developed. HEBs properties including the electron distribution functions over transverse velocities were studied numerically and experimentally in various regimes. In result of numerical simulation and series of experiments an electron gun, ensuring formation of an electron beam with parameters, necessary for the  $170\text{ GHz/1MW}$  gyrotron, is created.

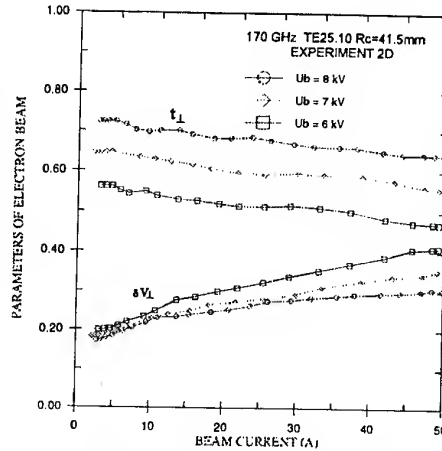


Fig.2.  $\delta v_{\perp}$  and  $t_{\perp}$  vs. beam current

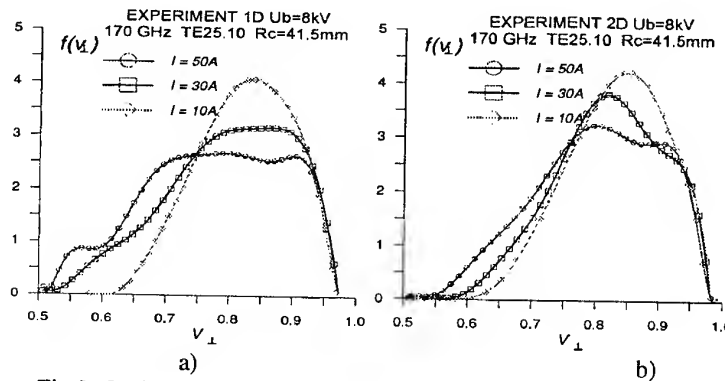


Fig.3. Oscillatory velocity distribution functions at various currents.

### References

1. Sh.E. Tsimring. Int. J. of Infrared and MM waves, 14, 817, 1993.
2. V.K.Lygin., V.N.Manuilov, Sh.E. Tsimring Elektron. tekhnika, ser.1, Elektronika SVCH, n.7., 38, (1987).
3. V.K.Lygin Int. J. of Infrared and MM waves, v.16, n.2., 363, (1995).
4. V.A.Flyagin, A.L.Goldenberg., and V.E.Zapevalov Conference Digest, 18th Int. Conf. on IR and MM Waves, University of Essex, Colchester, UK, v.2104, 581, (1993).
5. A.L.Gol'denberg, E.G.Avdoshin. Izv. Vyssh. Ucheb. Zavedenii, Radiofizika, 16., 1605(1973).
6. A.N.Kuftin, et al. Digest of 21st Int. Conf. On IR and MM Waves., 188(1997).

## Development of a W-band 120 kW gyrokystron at IAP

E. V. Zasytkin, I. G. Gachev, I. I. Antakov, M. A. Moiseev, V. K. Lygin  
and E. V. Sokolov

Institute of Applied Physics, Russian Academy of Science,  
46 Uljanov Str. 603600 Nizhny Novgorod, Russia

### INTRODUCTION

In recent years, a great progress in the development of high power W-band gyro-amplifies has been attained. At Institute of Applied Physics (IAP), a pulsed four cavity gyrokystron amplifier has produced 65 kW peak output power in the  $TE_{011}$  cavity mode at 26% efficiency with 300 MHz bandwidth [1]. In a CW version of this tube, the output power of 2.5 kW with 25% efficiency and the same bandwidth has been realized. At Naval Research Laboratory, two four cavity pulsed gyrokystrons with the operating  $TE_{011}$  mode have produced 67 kW output power with 450 MHz bandwidth, and 60 kW peak power with 640 MHz bandwidth [2]. A four section W-band gyrotwystron demonstrated 50 kW peak output power at 17% efficiency with 925 MHz bandwidth [3]. Recent investigations at IAP have been focused on output power enhancement in mm wave gyro-amplifiers. This paper presents the initial results of an experimental study of a two-cavity W-band gyrokystron operating in the  $TE_{021}$  mode.

### DESIGN AND EXPERIMENTAL RESULTS

This tube utilizes a diode magnetron injection gun to produce a hollow annular electron flow with a voltage up to 60 kV and a current up to 18 A. The cathode diameter is 28 mm, beam diameter in the interaction region is 5.5 mm. It means that electron beam is injected into the second radial maximum of the cavity RF field.

The RF circuit consists of two oversized cylindrical cavities operating in the  $TE_{021}$  mode at the fundamental cyclotron frequency. The length and quality factor of the input cavity are  $2\lambda$  and 150, respectively. The output cavity length is about  $2.1\lambda$  and its  $Q$ -factor is 500. The calculated eigen-frequencies are a) 92.7 GHz for the first cavity, and b) 92.96 GHz for the output one. The drive power is coupled into the circuit through an input circular waveguide inside cathode, then input  $TE_{01}$  mode is transformed to the  $TE_{02}$  mode by an inner mirror transformer, and then  $TE_{02}$  wave excites the operating mode in the first cavity. As a driver, a 100  $\mu$ sec, 2 kW mechanically tunable gyrottron with the operating  $TE_{011}$  mode was used in this experiment. Its frequency may be varied from 92.3 GHz to 93.7 GHz. The initial examination of this gyrokystron has been performed at a beam voltage of 50 kV. Fig. 1 shows the measured dependencies of the output power and efficiency on a beam current. The magnetic field in the circuit and the cathode drive power and frequency were adjusted to maximize the output power at each data point. The maximum peak power of about 120 kW with 23.5% efficiency occurred at 10.4-A beam current. Gain of about 18 dB has been observed. The central operating frequency was 93.2 GHz. At higher beam current, a breakdown problem in the tube has taken place. The main reasons of a breakdown are a poor vacuum in the tube and some faults of a gun design.

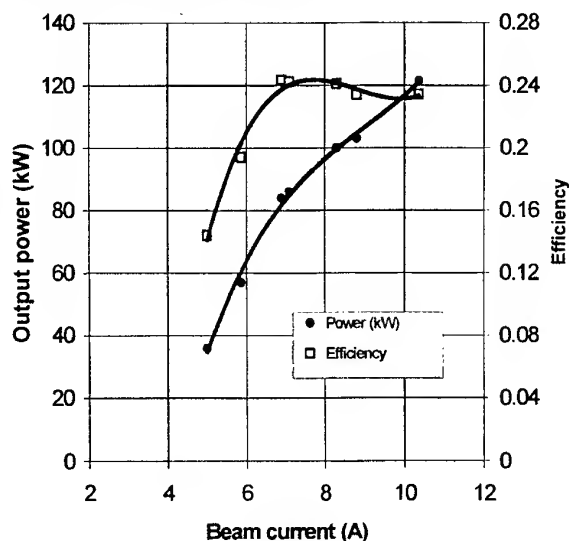


Fig.1. Output power vs beam current.

### REFERENCES

1. I. I. Antakov, E. V. Zasytkin, E. V. Sokolov, Conf. Digest of the 18<sup>th</sup> Int. Conf. on Infrared and MM Waves, Proc SPIE. **2104**, 166 (1993)
2. M. Blank, B. G. Danly, B. Levush, P. E. Latham, D. Pershing, Phys. Rev. Lett. Vol.79, 4485 (1997)
3. M. Blank *et al.* Abstracts of the 11<sup>th</sup> Int. Conf. on High-Power Electromagnetics, Tel Aviv, Israel (1998)

# QUASI-OPTICAL MEASUREMENT SYSTEMS

Richard Wylde

Department of Physics and QMC Instruments Ltd.,  
Queen Mary and Westfield College, Mile End Road, London, E1 4NS, UK and  
Thomas Keating Ltd., Station Mills, Billingshurst, West Sussex, RH14 9SH, UK

Graham Smith

Department of Physics and Astronomy University of St Andrews  
North Haugh, St Andrews, Fife KY16 9SS, UK

July 3, 1998

## 1 Introduction

There is now a complete and mature methodology for the design of Quasi-Optical (QO) measurement systems. Any measurement system that can be made in waveguide at W-band or above can almost invariably be constructed using quasi-optics with higher performance. The technique first came to prominence in the development of mm-wave astronomical systems, Martin-Puplett Interferometers and a variety of diagnostics for Fusion plasma studies. More recently, quasi-optics have been used in radiometer and Radar systems, as well as a variety of materials studies such as electron cyclotron and electron spin resonance. Our aim in this paper is to outline the methodology, and give typical performance of components built at QMC instruments, Thomas Keating and St. Andrews University. In the presentation, we will illustrate the typical performance of quasi-optical systems with two recent examples from the fields of Plasma Fusion Diagnostics and Electron Spin Resonance.

## 2 Beam forming and receiving components

Although research into quasi-optical oscillators, multipliers and mixers has been making significant progress, at present the most effective way of impedance matching such devices is still in single-mode waveguide, (over limited frequency ranges). However, above 150GHz waveguide losses start to become prohibitive and for many measurement systems it becomes preferable to transform to low loss optics for the rest of the system processing.

### 2.1 Corrugated horns

The most efficient way of transforming from single-mode waveguide to a free-space single-mode Gaussian beam is by using corrugated horns which can offer  $> 97\%$  coupling efficiencies with losses  $< 0.25\text{dB}$ , and this is now the preferred antenna in most QO measurement systems.

### 2.2 Lenses and Off-axis mirrors

Lenses (made from HDPE or PTFE) offer a compact and relatively inexpensive method for refocussing beams, where the surface of the lens is typically blazed to provide quarter wavelength matching layers to reduce reflections. However, for the highest performance, off-axis mirrors are nearly always preferred because of their wideband performance, negligible ohmic losses and the elimination of reflections between focussing elements. Using mirrors it is possible to transmit power over wide frequency ranges through complex optical systems with losses waveguide flange to waveguide flange substantially less than 1dB. Moreover, modern CNC tools are now reducing the absolute cost difference between lenses and mirrors.

### 2.3 Corrugated Pipes

Where beams must be transported over considerable distances, through long narrow apertures (such as the bore of a cryostat), corrugated pipes have proved extremely useful and are commonly used in fusion

diagnostic systems and for material studies at cryogenic temperatures. High coupling efficiencies to quasi-optical beams, low losses (0.01dB/m) and good mode and polarisation integrity have all proved to be key advantages.

### 3 Beam processing components

#### 3.1 Polarisers/Roof Mirrors

Polarisation manipulation is often at the heart of many QO systems and wire grid polarisers together with roof mirrors are almost ideal components at mm-wave frequencies. They have been combined in a number of systems to provide adjustable phase shifters attenuators, SSB filters, duplexers and diplexers as well as polarising interferometers. Free standing wire grids have been constructed with tungsten wire at diameters down to 5 microns at 10 micron spacing offering excellent performance into the Terahertz region.

#### 3.2 Filters

High performance quasi-optical low-pass, band-pass, and high pass filters have been demonstrated at mm-wave and sub-mm wave frequencies: Drill plate filters, alkali-halide and multilayer mesh filters all have a role to play in QO systems.

#### 3.3 Fabry-Perot Cavities

High Q Fabry-Perot cavities with beam-splitter coupling have been demonstrated with Finesses of 1500 at 90GHz for critically coupled cavities, with Q's of several hundred thousand. These have been used as filters, frequency discriminators, impedance matching devices, oscillator stabilisation elements, cavity dumping as well as measurements on low loss materials.

#### 3.4 Beam Dumps (RAM)

Some applications require high performance beam-dumps which absorb mm-wave power from all angles with limited scattering or re-radiation of power. Eccorb AN72 at 90GHz will typically reflect significantly more than 1% of the power at normal incidence. Higher performance has been obtained using injection moulded plastics RAM square tiles. Carbon is introduced into a polypropylene base and small square moulded sharp pointed pyramids reduce the area normal to any incident beam. Above 200 GHz, specular and near in scattered reflection from such RAM is lower than 0.1%.

#### 3.5 Free Space Isolators

Free space isolators or circulators may be constructed by placing a 45 degree Faraday rotators between two angled 45 degree polarisers. Quasi-optical Faraday rotators have been demonstrated at frequencies from 10GHz to 300GHz using permanently magnetised hard ferrites (strontium and barium hexaferrites) as well as the more traditional microwave soft ferrites. The soft ferrites potentially offer lower loss but require biasing from large permanent magnets. The hard ferrites have the considerable advantage that they are not aperture limited while still having impressive performance in terms of loss and isolation. At St.Andrews we have constructed narrow-band rotators near 35GHz with 1m apertures with 20dB isolation. At higher frequencies and smaller apertures, it is possible to obtain wide-band performance with > 30dB isolation, and losses < 0.5dB at 90GHz, < 1dB at 140GHz, < 2.5dB at 280GHz.

### 4 QO systems

Quasi-optical system design involves designing optics with sufficient beam throw to incorporate all the desired optical components while taking into account diffraction, cross-polarisation, excitation of higher order modes as well as standing waves between components such as the oscillator and mixer (which is a common problem in these very low loss systems). A properly designed system can have almost negligible losses over frequency ranges covering many waveguide bands. In the presentation we will illustrate quasi-optical system design and outline typical performance in two recently constructed systems:

- Electron density measuring interferometer at the Large Helical Device at NIFS in Nagoya, Japan. and a
- 180 GHz High field Electron Spin Resonance Spectrometer in St.Andrews, Scotland.

## Terahertz Components Fabricated by a Novel Photoresist Technique

Caroline E. Collins<sup>1,2</sup>, John W. Digby<sup>2</sup>, Geoff M. Parkhurst<sup>2</sup>, Robert E. Miles<sup>1</sup>,  
Roger D. Pollard<sup>1</sup>, and J. Martyn Chamberlain<sup>2</sup>.

<sup>1</sup>*Institute of Microwaves and Photonics, School of Electronic and Electrical Engineering,  
University of Leeds, Leeds. LS2 9JT, UK.*

<sup>2</sup>*Department of Physics, University of Nottingham, Nottingham NG7 2RD.*

### ABSTRACT

This paper reports two new techniques for fabricating millimetre-wave and terahertz rectangular waveguide components using an advanced negative UV photoresist. These structures have highly accurate dimensions, are cheap and easy to manufacture and are physically robust. S-parameter measurements show that they achieve low loss. The second technique offers the possibility of assembling complex structures in a relatively simple fashion.

### INTRODUCTION

Commercial interest in the millimetre-wave frequency range is increasing for a variety of applications including automotive radar, passive imaging, and sensing. Interest is also increasing in exploiting the large bandwidths available in the submillimetre-wave range as soon as a suitable cost-effective technology becomes available [1]. Rectangular waveguide is commonly used in the millimetre and submillimetre wave range owing to its low loss, although it becomes more difficult and expensive to machine at these frequencies due to its small size and consequently tighter manufacturing tolerances. Previous attempts at fabricating micro-machined rectangular waveguides [2] using conventional monolithic circuit techniques have exhibited high loss ( $>40\text{dB/wavelength}$  at  $100\text{GHz}$ ). Micromachined waveguides using standard UV resist formers have also been reported [3], but these guides suffer from a height limitation which implies a difficulty in coupling into standard waveguides, and they are therefore lossy. The LIGA x-ray lithographic process has been used in the micro-machining of tall, high-aspect-ratio structures [4], but this process is both time-consuming and expensive to implement. A recently introduced negative photoresist (known as EPON SU-8<sup>TM</sup> [5]) is capable of producing features in excess of  $1\text{mm}$  in height with large aspect ratios in a single UV exposure. This paper reports two new techniques

for the fabrication of micro-machined rectangular waveguides using SU-8 photoresist and presents some measured S-parameter results.

### WAVEGUIDE FABRICATION TECHNIQUES

The fact that SU-8 is a negative resist and cannot easily be removed after UV exposure means that a completely different fabrication technique is required to that previously reported [3]. The first waveguide fabrication procedure is detailed in Fig 1. A thick layer of SU-8 is first spun onto a semiconductor substrate and baked. The sample is then exposed, baked again, and developed to reveal "troughs" which will become the waveguide structures. The sample is sputtered with gold to a thickness of  $600\text{nm}$  (2 skin depths at W-band) to coat the inside walls. It is then attached to a sample holder with epoxy. The waveguide walls are therefore supported by hardened SU-8 making the guides physically robust and easy to handle. The sample holder already contains W-band flange detail to allow the micro-machined waveguides to be connected directly onto standard waveguides for measurement purposes. Finally a pre-sputtered lid is attached over the lithographically formed troughs to complete the waveguide.

In a development of this method, micro-machined rectangular waveguides (known as "T-guides") are fabricated in two halves. The T-guide fabrication procedure is detailed in Figure 2. A sacrificial layer of aluminium is first evaporated onto a semiconductor substrate, and then a thick layer of SU-8 photoresist is spun on top and baked. This SU-8 layer will eventually form the bottom and top walls of the waveguide. This first layer of SU-8 is exposed, a second thick layer is applied, and the whole sample baked again. The second layer is then exposed, carefully lining up the alignment marks on the mask with those already exposed on the first layer of resist, and the sample is given a post-exposure bake and developed. The second resist



layer forms the side walls of the waveguide; one waveguide piece also contains locating pins and the other matching holes to enable the halves to be snapped together with the edges exactly aligned. Subsequent immersion in potassium hydroxide solution removes the sacrificial aluminium layer, and releases the SU8 waveguide halves; these are sputtered with gold to a thickness of at least 600nm (2 skin depths at W-band) to coat the inside walls. The locating pins are designed slightly smaller than the holes to allow for this thickness of sputtered gold. The final stage in the procedure is to simply snap the two waveguide halves together. These guides were clamped between metal test blocks containing W-band flange detail to enable them to be connected to standard waveguide flanges. The lower block contained a shallow groove into which the SU8 pieces could simply slide to achieve alignment..

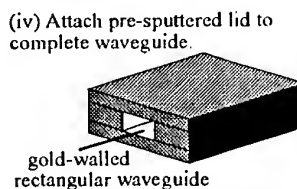
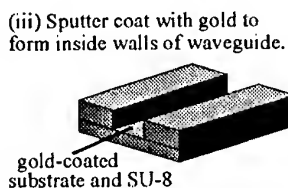
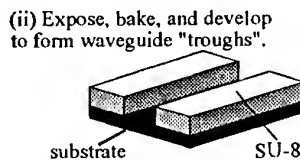
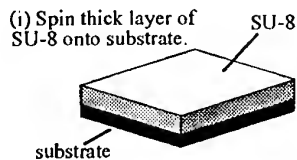
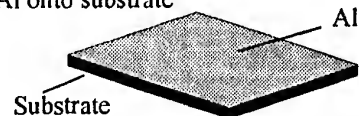
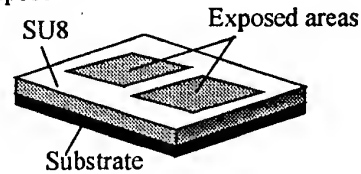


**Fig 1.** Fabrication of micro-machined rectangular waveguide using EPON SU-8™ photoresist.

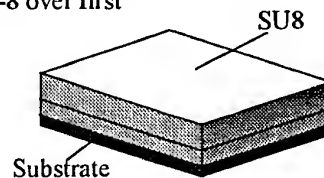
(i) Evaporate sacrificial layer of Al onto substrate



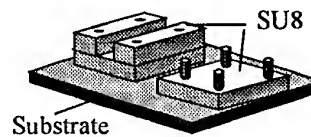
(ii) Spin on thick layer of SU-8 and expose



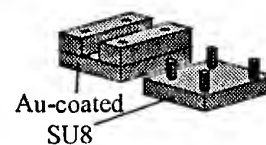
(iii) Spin second layer of SU-8 over first



(iv) Expose second layer, bake, and develop leaving waveguide halves



(v) Etch away Al and sputter waveguide pieces with Au



(vi) Connect top and bottom to complete waveguide

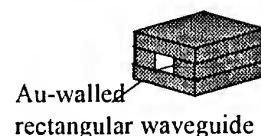


**Fig 2:** Fabrication of T-Guides

## MEASURED RESULTS

The results presented here are for a straight piece of 17mm long, cross-section 2.54mm by 700 $\mu$ m ( $\approx$  half height) waveguide made by the first technique. A standard TRL calibration was performed at the waveguide test ports of a W-band vector network analyser and the micro-machined waveguide was then connected between the test ports and its S-parameters measured. The measurements displayed a periodic ripple caused by multiple reflections between the full to reduced height waveguide junctions, which was removed from the measurements by renormalising the S-parameters to the characteristic impedance of the micro-machined sample rather than the full height test port impedance. The renormalised measurement results obtained are shown in Fig 3 and demonstrate low insertion loss, in spite of the join between the two waveguide halves occurring in the narrow walls. The measured sample was several wavelengths long, and the results actually correspond to an insertion loss of between 0.2dB and 0.4 dB per wavelength over most of the measurement frequency range, as shown.

## CONCLUSIONS

A new technique for micro-machining millimetre-wave rectangular waveguides has been demonstrated and characterised electrically. The process uses a photoresist which requires only a single UV exposure to form features up to 1mm in height; the new technique is therefore simple, cost-effective and also highly accurate. The measured results presented show that the micro-machined waveguides achieve lower loss than previously reported on-chip waveguides [2,3] due to their additional height, as well as being physically more robust. This new technique will also be useful at submillimetre-wave frequencies, where standard machining becomes even more difficult, and lends itself well to the possible integration of active devices.

## ACKNOWLEDGEMENTS

This work is supported by the UK Engineering and Physical Sciences Research Council (EPSRC) as part of the TINTIN program. The authors wish to thank Terry Moseley of the University of Leeds for machining the sample holders.

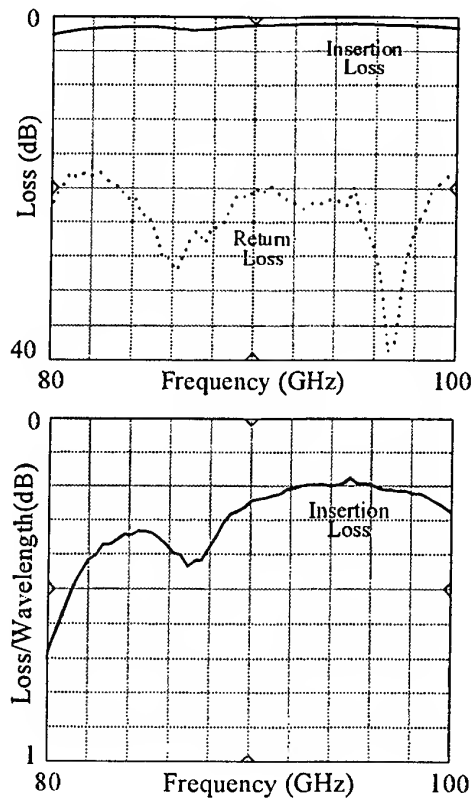


Fig. 3 Measured S-parameters of micro-machined waveguide.

## REFERENCES

- [1] J. M. Chamberlain and R. E. Miles (editors), *New Directions in Terahertz Technology*, Kluwer Academic Publishing, Dordrecht, 1997.
- [2] S. Lucyszyn, Q. H. Wang, and I. D. Robertson, "0.1THz Rectangular Waveguide on GaAs Semi-Insulating Substrate," *Electronics Letters*, vol. 31, no. 9, pp. 721-722, 27th April 1995.
- [3] C. E. Collins, J. W. Digby, R. D. Pollard, R. E. Miles, G. M. Parkhurst, J. M. Chamberlain, D. P. Steenson, N. J. Cronin, L. S. Karatzas and J. W. Bowen, "W-Band Measurements of 100 $\mu$ m Height Micro-Machined Air-Filled Rectangular Waveguides," in *1997 IEEE Int. Micr. Symp. Dig.*, pp. 1439-1442, Denver, CO, June 1997.
- [4] S. W. Moon *et al.* "Terahertz Waveguide Components Fabricated Using a 3D X-ray Microfabrication Technique," *Electronics Letters*, vol. 32, no. 19, pp. 1794-1795, Sept 12th 1996.
- [5] K. Y. Lee *et al.*, "Micromachining Applications of a High Resolution Ultrathick Photoresist," *J. Vac. Sci. Technol. B*, vol. 13, no. 6, pp. 3012-3016, Nov/Dec 1995.

## Micro-machined Waveguide Antennas for 1.6 Terahertz

J.W. Bowen<sup>1</sup>, S.T.G. Wootton<sup>2</sup>, S. Hadjiloucas<sup>1</sup>, B.M. Towilson<sup>1</sup>, L.S. Karatzas<sup>1</sup>, N.J. Cronin<sup>2</sup>, S.R. Davies<sup>2</sup>, C.E. Collins<sup>3,4</sup>, J.M. Chamberlain<sup>3</sup>, R.E. Miles<sup>4</sup> and R.D. Pollard<sup>4</sup>

<sup>1</sup> Department of Cybernetics, The University of Reading, PO Box 225, Whiteknights, Reading RG6 6AY, UK

<sup>2</sup> School of Physics, University of Bath, Claverton Down, Bath BA2 7AY, UK

<sup>3</sup> Department of Physics, University of Nottingham, Nottingham NG7 2RD, UK

<sup>4</sup> Department of Electronic and Electrical Engineering, The University of Leeds, Leeds LS2 9JT UK

Recent advances in micro-machining techniques have opened up the possibility of fabricating integrated components, based around hollow metal waveguide technology, which are intended for operation at frequencies ranging from 100 GHz to in excess of 1 THz. The fabrication technique is such that the waveguide wall surface quality is superior to that in a comparable conventionally machined waveguide. Losses of 0.6 dB per guide wavelength at 200 GHz have been demonstrated [1]. This paper describes a new type of horn antenna that can be fabricated monolithically with the micro-machined waveguide. A series of 1.6 THz radiation pattern measurements for different designs are presented. These represent the first measurements on micro-machined waveguide components to be carried out at frequencies above 1 THz.

During the waveguide fabrication process a layer of metallisation is initially deposited on the surface of a semiconductor wafer substrate. A thick layer of photo-resist is then built up on top of the metal layer and exposed through a mask so that regions of it can be developed away in a pre-defined pattern. This leaves raised areas of photo-resist on the surface of the metallisation. A further metal layer is then evaporated over the whole surface. This is strengthened by electro-plating with additional metal. Dissolving the remaining photo-resist leaves hollow metal waveguide structures on the surface of the substrate.

While the fabrication process places no limits on the extent to which the lateral dimensions of the waveguide may be tapered, the maximum height that the structure may have is governed by the thickness of the photo-resist layer that may be deposited. Furthermore, it is not possible to gradually taper the waveguide height. This means that structures approximating pyramidal or conical horns, with tapers in both dimensions, cannot be fabricated using this technique. H-plane scalar horns can be made although, unfortunately, they have unacceptably broad E-plane patterns. In an aperture antenna, the far-field antenna pattern is related to the electrical field distribution across the antenna by a Fourier transform. Thus, increasing the effective aperture of an antenna results in a reduction of the far-field beamwidth. This principle is employed in the design of the micro-machined antenna. Removing a tapered slot from the upper surface of a scalar horn (Figure 1) reduces the E-plane beamwidth at the expense of a slight increase in the H-plane beamwidth. The slot allows the E-plane fields to extend outside the confines of the waveguide but is sufficiently narrow near its apex to prevent significant radiation. This is because, in this region, components of the field in close proximity to each other are in anti-phase. As the slot taper opens up, the fields extend further outside the waveguide and regions are formed where the anti-phase components of the field no longer cancel each other, particularly in the vicinity of the slot where there is a strong field concentration. Radiation is launched from this point.

Fabrication of the antenna requires some further processing steps. After the metal layer has been evaporated over the substrate and photo-resist to form a basic scalar horn structure, a second layer of photo-resist is applied, exposed through a mask and developed so that the metal where the slot is to be formed is left uncovered. This is etched away to form the slot. The top layer of photo-resist can then be removed and the structure strengthened by electro-plating before removing the remaining photo-resist.

Using microwave (X-band) scale-models it was found that, with appropriate choice of the antenna dimensions, equal 3 dB beamwidths of 27° could be obtained in both E and H-planes and that the beam axis was angled at 22.5° up from the plane of the substrate. The maximum side-lobe and cross-polar levels were at -14 dB and -8 dB respectively. A return loss of -19 dB was measured. These figures apply to an antenna equal in height to full-height waveguide.

The antennas fabricated for testing at 1.6 THz were all fed by a 5 guide-wavelength long, 1/4-height open-ended waveguide with dimensions 140 µm × 17.5 µm. Quarter-height waveguide was chosen because it provides a better impedance match to devices and because it is difficult to build up thicker layers of photo-resist which maintain good definition. For lower frequency operation, where tolerances are less tight, an alternative technique for depositing the photo-resist may be used which allows taller structures to be made. Versions with aperture widths of 3, 4, 5 and 6 free-space wavelengths were made, with an overall antenna length of 3.5 free-space wavelengths.

the far-field of the beam from an optically-pumped FIR laser operating on the 1.6266 THz difluoromethane line. As the output from the laser is horizontally polarised, a Martin-Puplett interferometer was used to rotate the plane of polarisation through  $90^\circ$  for the co-polar H-plane and cross-polar E-plane measurements. The interferometer was also used to switch between horizontal and vertical polarisations for determination of the cross-polar levels. Good repeatability was shown between E-plane pattern measurements made on three different  $3\lambda$  wide antennas.

Figure 2 shows representative measured E and H-plane antenna patterns for the  $3\lambda$  and  $6\lambda$  antennas. The H-plane patterns show a monotonic decrease in beamwidth as the antenna width is increased. In each case, they were measured in the plane corresponding to the peak of the E-plane radiation pattern. The E-plane patterns have more complicated behaviour. The substrate plane corresponds to  $0^\circ$ . At  $3\lambda$ , the peak occurs at about  $8^\circ$ . The  $4\lambda$  pattern peaks at  $58^\circ$ , while the peaks in the  $5\lambda$  and  $6\lambda$  patterns occur at increasingly shallow angles. The  $5\lambda$  and  $6\lambda$  patterns also show some bifurcation of the main lobe. Cross-polar levels were better than -15 dB. The general behaviour observed is in agreement with numerical simulations using Hewlett Packard's High Frequency Structure Simulator (HFSS). Discrepancies between measurements and simulations may be due to the presence of the baffle and the substrate edge, which, to date, have not been modelled in the simulations. The E-plane patterns for these antennas are rather broader than seen in scale models; this is a consequence of the micro-machined antennas being based on quarter height waveguide. Simulations suggest that exponentially tapered antennas may produce improved antenna patterns with quarter-height waveguide.

1. G.M. Parkhurst, *et al.* Proc. SPIE 3465, In Press, 1998.

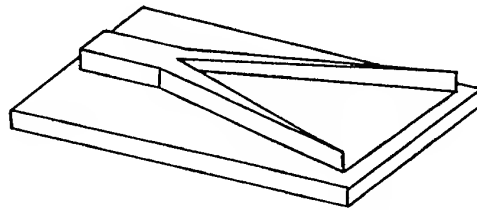


Figure 1. Micro-machined antenna.

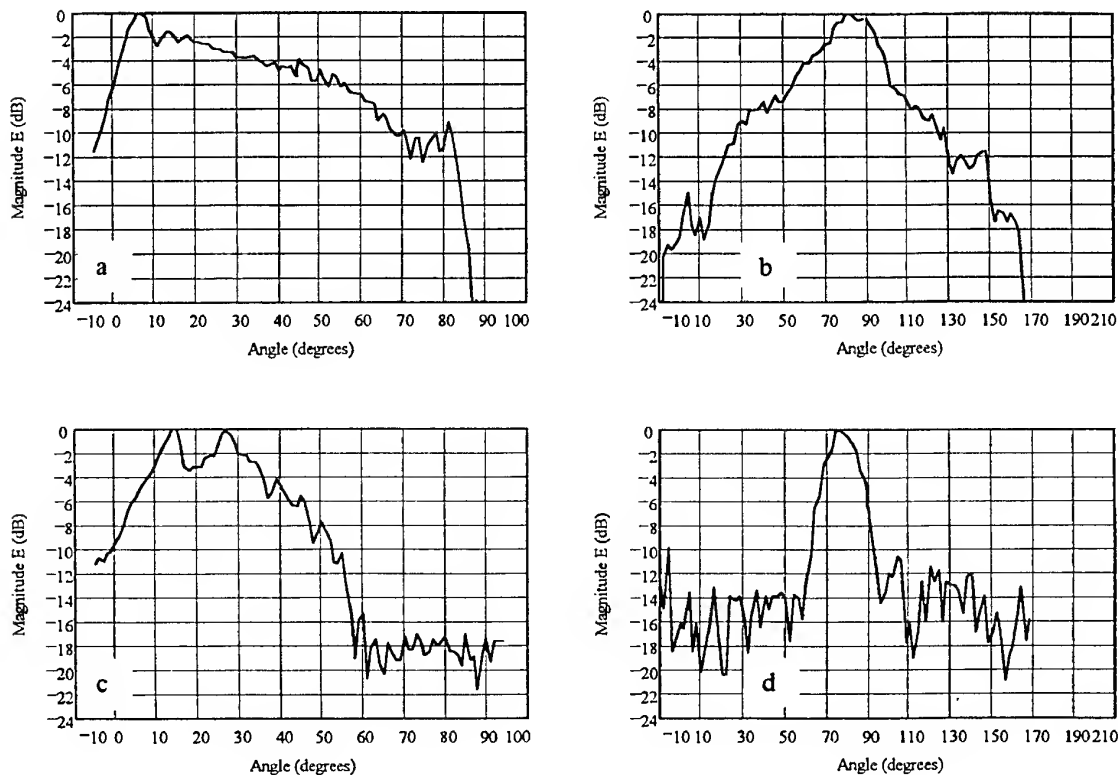


Figure 2. Measured 1.6 THz patterns. a)  $3\lambda$  antenna E-plane, b)  $3\lambda$  H-plane, c)  $6\lambda$  E-plane, d)  $6\lambda$  H-plane.

## Band pass filters for the Mid-Infrared

K. D. Möller<sup>a</sup>, K.R. Farmer<sup>a</sup>, D.V.P. Ivanov<sup>a</sup>, O. Sternberg<sup>a</sup>, K.P. Stewart<sup>b</sup>, and P. Lalanne<sup>c</sup>

<sup>a</sup> Department of Physics and Microelectronics Research Center, NJIT, Newark, NJ 07102

<sup>b</sup> Code 551, Goddard Space Flight Center, Greenbelt MD 20771

<sup>c</sup> Institut d'Optique Theorique, CNRS, BP 147, F91403, Orsay Cedex, France

In the far infrared spectral region, Chase and Joseph [1] studied six cross shaped grids, each having a different shape of the crosses. The specification of the shapes of the crosses are given in Fig 1a. These grids are considered as "free standing without substrate".

We have used the A. Golden program [2], and calculated the transmission of these six cross shaped grids, see Fig. 1b, assuming no substrate and infinite conductivity.

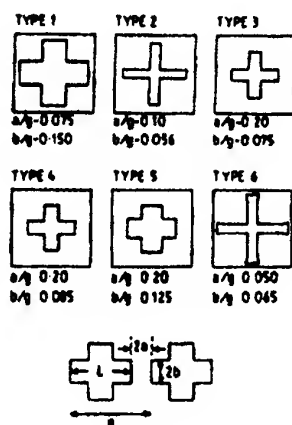


Fig. 1a.

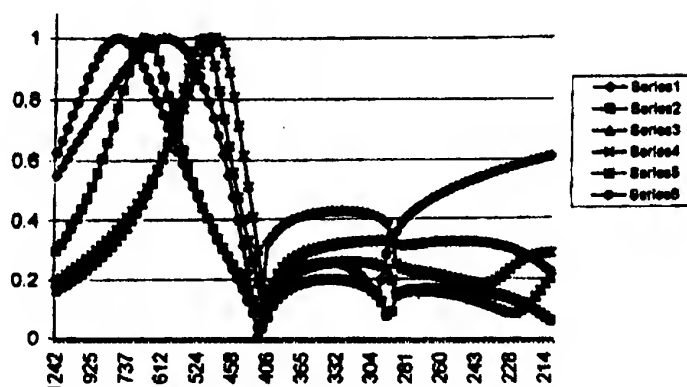


Fig. 1b.

In a paper by Möller et al [3] an empirical formula for the peak transmission wavelength was derived on "dipole" considerations. This formula,  $\lambda_R = 2g - 4a - 2b$ , compares well with a formula,  $\lambda_R = 2g - 3.6a - 2.7b$ , which was derived, using a least square fit procedure, from the data obtained with the A. Golden [2] program. In comparison, Chase and Joseph [1] derived from their experimental data a similar, but slightly different formula,  $\lambda_R = 2.1g - 4.2a + 2.1b$ .

One of us, P. Lalanne, has studied 6 cross shaped grids with the same set of specifications as shown in Fig. 1a. He used the "rigorous coupled wave analysis" method, and calculated the transmission for free standing grids, for  $g = 2.143 \mu$ , thickness  $.2\mu$ , and assumed for the entire spectral region the complex index of refraction  $3.84 + i 11.4$ , see Fig. 2a. A least square fit for the peak transmission wavelengths resulted in  $\lambda_R = 2.86g - 5.27a + 4.9b$ . For grid #2 the transmission has been calculated for thickness' of  $.2$ ,  $.4$ , and  $.8\mu$ , see Fig. 2b.

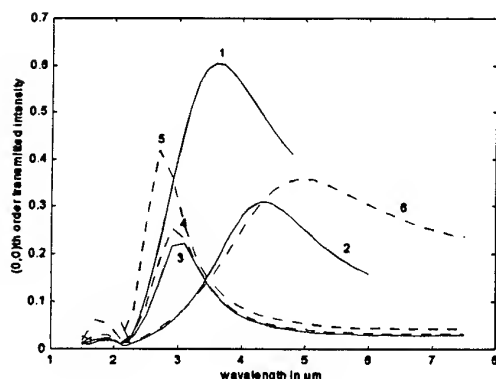


Fig.2a.

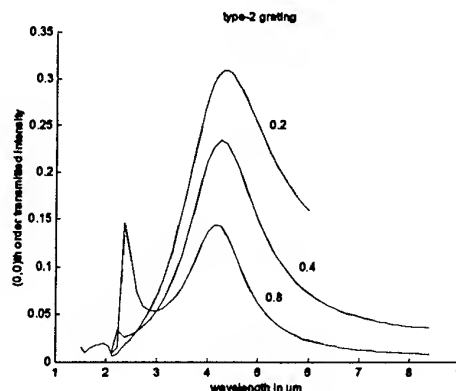


Fig.2b.

In Fig.2b one observes two peaks, as observed for "thick" grids by Ruprecht et al [4] and predicted theoretically, for infinite conductivity and "thick" grids, by Compton et al [5].

In Fig.3 we show the transmission of a capacitive cross shaped grids on a Si substrate with the dimensions of  $g = 16.4\mu$ ,  $2a = 2.5\mu$ ,  $2b = 4.9\mu$

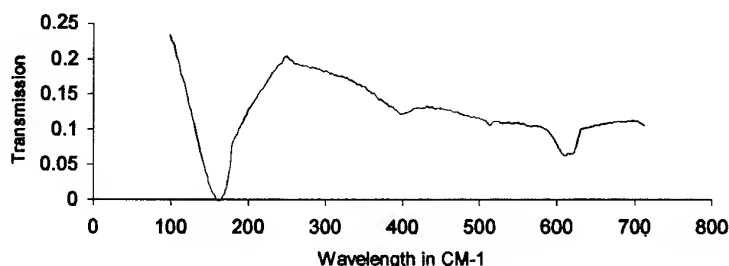


Fig.3

For grids with  $g = 16.4$  microns, the peak frequency shifts from about  $450\text{ cm}^{-1}$  for a free standing inductive grid to about  $165\text{ cm}^{-1}$  for a capacitive grid on Si substrate. A shift proportional to the refractive index has been predicted by Dawes et al[6]

We acknowledge support both from New Jersey Commission on Science and Technology through the New Jersey MEMS center and from a seed research grant through NJIT's Microelectronics Research Center.

- [1] S. T. Chase and R. D. Joseph, *Appl.Opt.*, **22**, 1775 (1983).
- [2] A. Golden, University of Chicago.
- [3] K. D. Möller, J. Warren, J. B. Heaney, and C. Kotecki, *Appl.Opt.*, **35**, 6210 (1996).
- [4] R. Ruprecht, W. Bacher, P. Bley, M. Harmening, and W. K. Schomburg, *KfK-Nachr.Jahrg.* **23**, 2-91, 18-123, (1991).
- [5] R. C. Compton, R. C. McPhedran, G. H. Derrick, and L. C. Botten, *Infrared Physics*, **23**, 239 (1983).
- [6] D. H. Dawes, R. C. McPhedran, and L. B. Whitbourn, *Appl.Opt.*, **28**, 3498 (1989).

## Theoretical and Experimental Investigation of Phase Gratings.

William Lanigan<sup>1</sup>, Ruth Colgan<sup>1</sup>, J. Anthony Murphy<sup>1</sup> & Stafford Withington<sup>2</sup>

<sup>1</sup>Experimental Physics Department, National University of Ireland, Maynooth, Co. Kildare, Ireland

<sup>2</sup>Cavendish Laboratory, Cambridge University, Madingley Road, Cambridge CB3 0HE, England

### Introduction

Phase gratings are now being incorporated into submillimetre-wave array receivers as beam multiplexing devices [1,2]. They have the advantage of being relatively easy to manufacture because of the long wavelength. Transmission gratings can be machined from suitable transparent dielectric materials such as Teflon or quartz. Phase gratings find ready application in submillimetre-wave heterodyne imaging, where optical coupling provides the most efficient way of combining LO power for systems limited to one source.

In this investigation we restrict our study to binary phase gratings in which the optical path length through the grating takes on just two values. A Dammann phase grating [3,4] is an example of a binary grating designed to produce a finite array of diffraction spots of equal intensity. In the paper we summarise our investigations into theoretical modelling of phase gratings using Gaussian beam mode analysis. This can be used as a powerful theoretical tool in predicting grating operation with finite throughput optics, quantifying bandwidth effects and manufacturing tolerances. We also present some experimental measurements for a scale model millimetre-wave phase grating which operates at 100 GHz.

### Beam Mode Analysis of Phase Gratings

The basic operation of a phase grating can be understood in terms of Fourier optics. The grating consists of an array of basic cells with the transmission function of the on-axis cell being given by the aperture function  $t(x,y)$ . The transmission of an ideal grating with rectangular symmetry is given by sum:  $\sum_{m,n} t(x-m\Delta x, y-n\Delta y)$ , where  $\Delta x$  and  $\Delta y$  are the grating periods in the  $x$  and  $y$  directions, respectively. In a typical submillimetre-wave system the grating will be illuminated by some incident quasi-Gaussian field  $\psi(x,y)$  produced by the LO source feed. If one assumes that the extent  $\psi(x,y)$  is less than that of the grating, then at the output plane (the Fourier plane of the plane where the grating is placed), the resultant field obeys the usual Fourier Transform relationship:  $E(u,v) = [\sum_{m,n} T(u,v) \delta(u - m\Delta u) \delta(v - n\Delta v)] * \mathcal{F}(u,v)$ , where capital symbols represent Fourier Transforms. The output field is therefore an array of images of the quasi-Gaussian field  $\mathcal{F}(u,v)$ , with the intensity of the various images determined by the amplitude envelope function  $T(u,v)$  [5].

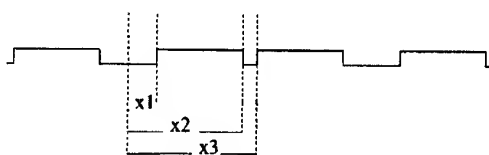
In order to model the effect of the finite throughput of the optics, with the consequent spatial filtering effects on the output array of images, it is convenient to apply a Gaussian beam mode analysis of a typical phase grating set-up. Because of the symmetry of the grating, a phase modulated quasi-Gaussian input field,  $\psi(x,y)\exp(i\phi(x,y))$ , can most conveniently be expressed as a sum of Hermite-Gaussian beam modes,  $\sum_{m,n} A_{mn} \psi_{mn}(x,y)$ . Higher order modes are of much greater spatial extent than the fundamental and may be truncated at optical components between the grating and the output plane. Such stops will act as effective low pass filters for the beam modes, placing a limitation on the maximum number of output beams possible [6]. Clearly, for the system to operate efficiently as a multiplexer, the throughput of the optics between the grating and the output plane must be sufficiently great. A careful modal analysis must therefore be an important aspect of the design of any compact multiplexing quasi-optical system.

Phase gratings only operate correctly over a finite bandwidth, which may pose a limitation for certain applications. Two effects occur if the wavelength of the LO beam does not correspond to the design wavelength of the grating: (i) the actual inter-beam separation in the output plane will change, and (ii) the different phase delays for the grating will not be as designed. The effect is to change  $T(u)$ , and thus the relative intensities of the output array of image beams. These effects can be readily modelled using Gaussian beam modes by recalculating the mode coefficients. It is worth noting that mixer sensitivity to local oscillator power for optimised performance is usually not so critical that such a small variation in the output beam intensities would cause a significant deterioration in performance across the array. Manufacturing tolerances can in a similar fashion be quantified using beam mode analysis by modelling the effects of small resultant variations in the phase delays and cell widths.

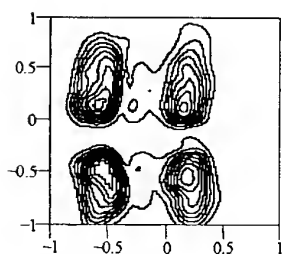
### Experimental Testing of Phase Gratings

We have developed a test facility at Maynooth to evaluate the performance of our grating designs. The facility is built for operation at 100GHz for the scale modelling of submillimetre-wave gratings. This frequency provides a reasonable compromise between the size of the quasi-optical components and their ease of manufacture. The test facility source consists of the Gunn oscillator, isolator and a conical horn antenna. The beam from this source is brought to a waist at the grating plane by an off-axis parabolic mirror and the output from the grating is collected and imaged onto the detector plane by a second matching mirror. The crystal detector is fed by conical horn, and mounted on a XY raster scan mechanism which has a useable scan area of 550mm  $\times$  550mm. This mechanism is computer controlled and has a step resolution of 0.03mm. Data can be collected from any user-defined area within the limits of the scanner and is read from the detector via a variable gain scaling amplifier and a 12 bit A/D converter.

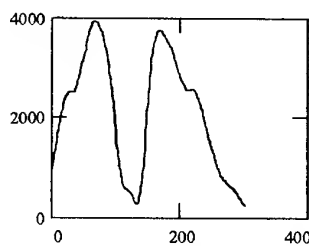
The plots below show the results obtained from our first  $2 \times 2$  Quartz grating. As is clear from the example grating designed and tested, the scheme is particularly suitable for the coupling of LO power in sparse array heterodyne systems.



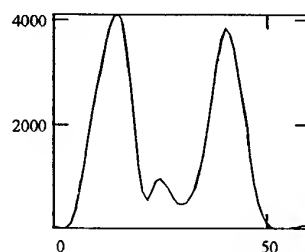
Cross section through two cells.



Contour plot of beam pattern



Cut through bright spots in Y



Cut through bright spots in X

### Conclusions

In this paper we have summarised a theoretical and experimental investigation of phase gratings for LO beam multiplexing at submillimetre wavelengths. Gaussian beam mode analysis was found to be a powerful theoretical tool in analysing the operation and limitation of such gratings in practical systems. The theoretical bandwidth of a typical grating was found to be of the order of 15%, which would be adequate for astronomical array receivers operating in the submillimeter waveband.

### References

1. Klein, T., Ediss, G.A., Gusten R., Hausschildt, H., Kasemann, C., 8<sup>th</sup> Int. Sym.Space THz, Harvard, 1997.
2. Delgado G. F. and Johansson J. F., in Multi-feed Systems for Radio Telescopes, A.S.P. Conf. Ser. 75, 1995.
3. Jahns J., Downes M.M., Prise E.M., Streibl N. and Walker S.J., Optical Engineering, 28, 1267, 1989
4. Dammann H., Klotz E., Optica Acta, 24, 505, 1977
5. Murphy J.A., Murphy J.A. 1995, 3<sup>rd</sup> Int. Workshop THz Electron, Zermatt, 1995.
6. Murphy J.A., Withington S. and Egan A., IEEE Trans. Microwave Theory Tech., 41, 1700, 1993



## Efficiency of FIR SEW excitation by aperture, prism and mesh methods

V.Vaicikauskas, R.Antanavicius, R.Januskevicius

Institute of Physics, Gostauto 12, 2029 Vilnius, Lithuania, Fax: (3702) 235182, e-mail: vikvai@ktl.mii.lt

The efficiency of the Surface Electromagnetic Waves (SEW) excitation was widely investigated in the near infrared region ( $\lambda \approx 10\mu\text{m}$ ) [1]. The prism couplers are commonly used in this spectral range. It was found, that the optimum coupling gap height  $d$  between the prism and the sample exists and it is determined by dielectric properties of the supporting sample surface and overlayer material as well as the angle of incidence. The value of  $d$  was found to be of the order of one half to one third of the theoretical extension distance of the SEW field into the air overlayer and equals to about  $25\mu\text{m}$  [2]. For SEW excitation on Cu film, a maximum coupling efficiency  $\eta$  of 3.4% occurred for a prism internal angle of  $66.8^\circ$ . A coupling efficiency of only 1% was observed for a right-angle prism. After more complete investigation of radiation losses under SEW excitation in the prism-gap-sample system the  $\eta$  of 8% was achieved [3]. Authors of [4] published the contraversary to the previous works statement that  $d$  does not depend on the SEW extension distance  $\delta$  into the air but depends on the wavelength of SEW and  $\delta$  equals to about  $2\lambda$ . It is well known, that in the radiofrequency region  $\eta$  reaches even 92% for rectangular waveguide and about 60% for the prism coupler.

The SEW extension distance into the air  $\delta_1$  is inversely proportional to the difference of surface polariton wavevector and light wavevector  $\omega/c$  [1]. For plasmons it can be derived:

$$\delta_1 = \begin{cases} v_p/4\pi v^2, & \text{when } v=1/\lambda \ll v_t \\ v_p/4\pi v^{3/2} v_t^{1/2}, & \text{when } v \gg v_t \end{cases} \quad v_t \text{ is collision frequency of electrons.}$$

**Experimental setup and results.** The experimental arrangement used has been previously described [5]. Briefly, the SEW were excited by the FIR radiation ( $97\mu\text{m}$ ) incident upon the input screen (blade) (Fig.1). Backward SEW

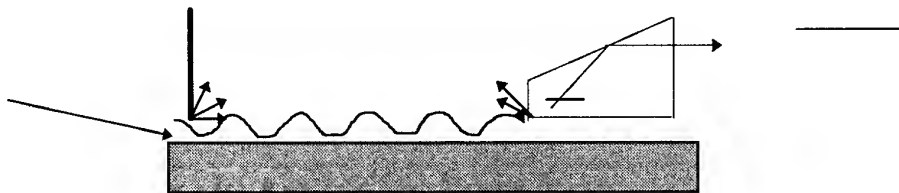


Fig.1. The input (blade) and output (Si prism) couplers for SEW experiments.

decoupling into the bulk wave was accomplished by using a Si ATR prism. The screen and prism gap heights were adjusted by micrometers for optimum coupling efficiency. The propagation distance  $L$  of the SEW was determined by adjusting the separation distance between elements and by measuring a decoupled signal. Transited and reference signals were detected by pyroelectric detectors. We used an electronic two channel peak detector for amplitude measurement of both transmitted and reference signals. The negative reciprocal of the slope of a semilog plot of the signal vs separation distance provided  $L$ . In order to determine the field distribution behind the screen, the prism was detached out and the detector was scanned vertically. To receive only the part of bulk radiation the sample surface partially was coated with thin absorbing film. Experimentally determined efficiency  $\eta$  can be expressed as  $\eta = I(1-\rho_1)(1-\rho_2)/I_0 \times \exp(-a/L)$ , where  $\rho_1$  and  $\rho_2$  are losses due to the reflectance on the front surface of blade and Si prism, respectively,  $a$  is the distance between elements,  $I$  and  $I_0$  are incident and transited through the system radiation. The samples used for the SEW excitation were steel coated with Ge film (thickness 0.3 and  $0.6\mu\text{m}$ ), doped GaAs ( $N=1.4 \times 10^{18} \text{cm}^{-3}$ ) and  $\text{SrTiO}_3$  crystals. The obtained values of  $L$ ,  $\eta$ ,  $d$  (of input screen) measured at  $97\mu\text{m}$  and calculated SEW extension depth into the air are presented in Table 1.

For limited size  $\Phi_0$  of the beam, when  $\Phi_0$  can be compared with  $L$ , it is necessary to account the distribution of intensity in the beam crossection. For the effective SEW excitation in materials possessing high

mean part of dielectric permittivity (metals) by using the Gauss beam necessary to fulfil 3 requirements: 1)  $k_0 \epsilon^{1/2} \sin \Theta = k_x'$ , where  $k_x'$  is SEW wavevector in the presence of a prism,  $\epsilon$  is dielectric permittivity of prism,  $\Theta$  is angle of incidence into base of prism; 2)  $\Phi_0 \ll L$ ; 3)  $\Phi_0 \approx L_p$ , where  $L_p$  is SEW propagation distance determined by radiation losses in the presence of a prism. The analytical expression for the SEW excitation efficiency by prism was obtained by Otto [4]. Outgoing from the prism base radiation possesses diffraction and as a consequence part of radiation transforms into SEW, whereas other part of radiation transforms into bulk radiation under the sample. It is well known from diffraction theory that the light wavevector changes under diffraction and it depends on the gap or hole size relative to the light wavelength. So, the prism gap or aperture gap serves as a k-filter for the adjustment of incident light wavevector with that of the SEW. Because effects of order  $d/\lambda$  play their part, the requirements for prism manufacturing are strict, especially in the near infrared.

Table 1. SEW propagation distance  $L$ , coupling efficiency  $\eta$ , optimum gap height  $d$  and calculated SEW field extension into the air distance  $\delta_1$ .

Sample	$\lambda, \mu\text{m}$	$L, \text{cm}$	$\eta, \%$	$d, \mu\text{m}$	$\delta_1, \mu\text{m}$
Steel	100	$(30.9)_{\text{theor}}$	-	-	2872
Steel+Ge(0.6 $\mu\text{m}$ )	97	4.05	41	290	387
Steel+Ge(0.3 $\mu\text{m}$ )	97	7.31	39	470	684
n-GaAs	97	0.61	32	170	183
SrTiO <sub>3</sub>	97	0.81	29	140	185

Parameters used in calculations (Steel:  $\omega_p=33000\text{cm}^{-1}$ ,  $\omega_t=560\text{cm}^{-1}$ , Ge:  $n=4.0$ , n-GaAs:  $\omega_p=398\text{cm}^{-1}$ ,  $\gamma = 37 \text{ cm}^{-1}$ ). On the steel without film the  $L$  can not be measured experimentally in a conventional way.

We also used the metal wire mesh as a SEW input coupler instead of the blade. The mesh was made of Ni wires with thickness of  $10\mu\text{m}$  mounted on the brass ring at  $t=100\mu\text{m}$  period. The mesh was placed on the sample surface at an angle  $\Theta$  of about 10 degrees, whereas input beam was directed into the mesh at an angle of SEW excitation ( $k_m = \omega/c \times \sin \Theta + 2\pi m/t$ ). Therefore, we achieved only 17% efficiency in steel+Ge samples. Such a relatively low value of  $\eta$ , may be, is the reason of poor quality of such mesh in comparison with sinusoidal one.

As a conclusion, we must state that in the FIR region efficiency of the SEW excitation is significantly higher in comparison with  $10\mu\text{m}$  region. The optimum gap height correlates with optical constants of material to be used for SEW excitation. The optimum values of gap were obtained to be a bit less than the calculated extension distances.

1. Surface Polaritons. Ed. V.M.Agranovich and D.L. Mills. North Holland. 717p., (1982).
2. D.I.Begley, D.A.Bryan, R.W.Alexander, R.J.Bell. Applied Optics. **16**, 1549 (1977).
3. G.N.Zhizhin, V.I.Silin, V.A.Yakovlev. Kvantovaya Electronika. **13**, 137 (1986).
4. R.Miller, D.L.Begley, and R.J.Bell. Applied Optics. **16**, 3077 (1977).
5. V.Vaicikauskas. Infrared Physics and Technology. **36**, 475 (1995).
6. A.Otto. Z.Phys. **216**, 398 (1968).

## Improved 2-D Optimized Photonic Bandgap Microstrip

Txema Lopetegi, Francisco Falcone, Beatriz Martínez, Ramón Gonzalo, Mario Sorolla

*Microwave and Millimeter Wave Group. Electrical and Electronic Engineering Department.  
Public University of Navarra. Campus Arrosadía s/n. E-31006 Pamplona, Spain*

### Abstract

Novel 2-D photonic bandgap structures in microstrip technology have been recently proposed to obtain deep and wide stopbands. They are periodic 2-D patterns formed by circles etched in the ground plane of the microstrip line. To increase the width and depth of the stopband it is necessary to increase the ratio between the circle radius and the period of the structure but the ripple in the passband is also increased. Here we propose to employ optimal design method in order to increase the bandwidth and to reduce the ripple at the same time. Simulations demonstrate good agreement with measurements.

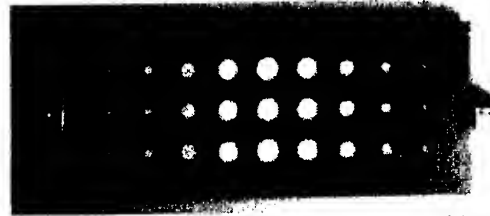


Fig. 1. PBG microstrip structure tapered with a Hamming window

### Introduction

PBG are periodic structures where propagation of electromagnetic waves is not allowed in some frequency bands [1]. Primary research on PBG was realised in the optical frequency bands [2], but lately, PBG designs in the microwave region have been proposed for very promising new applications as described in [3]. Because of its distributed structure, PBG's are suitable for broadband designs.

A simple way to produce a PBG structure in microstrip technology is to drill the periodic pattern in the dielectric substrate or by etching circles in the ground plane, also following the periodic pattern. The last approach is simpler, compatible with monolithic technology and obtains good depth and width in the rejected frequency band [3].

The obtained performance can be substantially improved applying tapering techniques to the periodic pattern. This paper shows the practical application of this idea, i.e. tapering with the use of a Hamming window [4]. The simulation results and measurements show considerable improvement in the side-lobe level and increase in the bandwidth of the device.

### PBG design

The PBG structure is realised in microstrip technology by etching circles in the ground plane, following the periodic pattern (fig. 1). The distance  $a$  between the center of the circles is constant. Only three rows of circles are necessary following [3]. In the top plane there is the classical conductor strip having a width corresponding to the conventional  $50\ \Omega$  microstrip line. This periodic structure can be analyzed like a single mode Bragg reflector so that the reflected frequency satisfies the Bragg condition:

$$2k = k_{\text{Bragg}} = 2\pi/a \quad (1)$$

being  $k$  the guided mode wavenumber and  $a$  the structure period [4].

Similar behavior (non-transparent frequency band) was observed in twisted dielectric waveguides that have been analyzed satisfactorily in terms of Bragg Theory and Mode Coupling (the Cross-Section Method) [5].

Tapering the periodic pattern of the PBG structure, it seems feasible to obtain similar benefits as the obtained by tapering the corrugation amplitude of circular corrugated waveguide Bragg reflectors and resonators in Free Electron Lasers [4]. In this paper two PBG structures have been simulated, measured and compared. Both have been designed at 4 GHz (supposing  $\lambda_g$  of conventional microstrip, [3]) having the same number of periods (9); but in one of them the radius of all the circles is constant,  $r = 3.5\ \text{mm}$ , obtaining a ratio  $r/a = 0.25$ , which scales the optimum design in [3] in order to use our HP<sup>TM</sup> 8753D Vector Network Analyzer (up to 6 GHz). In the other structure, a tapering based on a Hamming Window with  $r_{\text{max}} = 4.2\ \text{mm}$  has been applied:

$$r(z) = r_{\text{max}}(0.54 - 0.46 \cos(2\pi z/L)) \quad (2)$$

but the first and last samples have been neglected. The circuits have been fabricated in a substrate with  $\epsilon_r = 10.2$  and thickness  $h = 50\ \text{mils}$ , by means of a numerical milling machine.

To study the effect of variation of the  $r_{\text{max}}/a$  ratio, other tapered structures have been simulated, for ratios 0.3, 0.35 and 0.4.

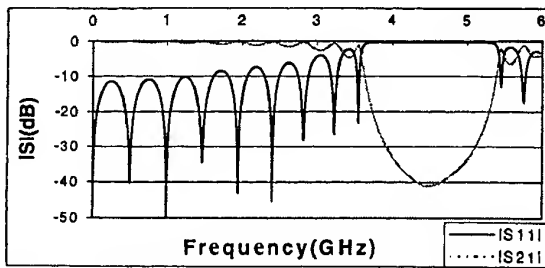


Fig. 2. Measurements of PBG uniform structure.

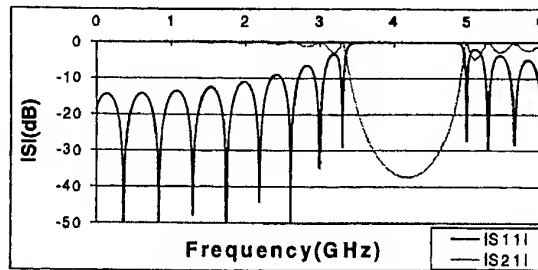


Fig. 4. Simulation of PBG uniform structure.

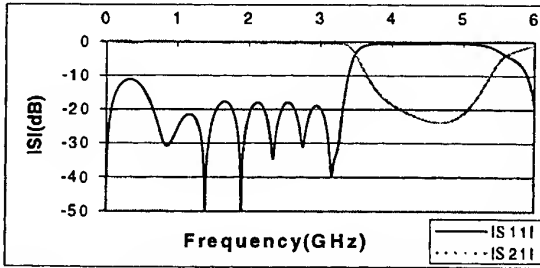


Fig. 3. Measurements of PBG tapered structure.

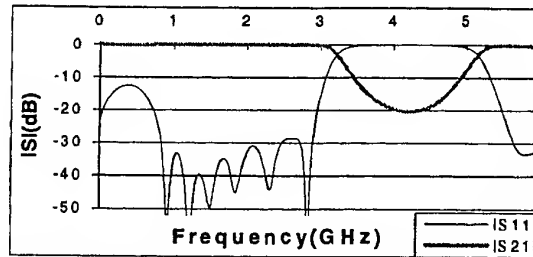


Fig. 5. Simulation of PBG tapered structure

### Simulation and measurement

The circuits have been simulated with *HP<sup>TM</sup>* Momentum and *MDS* software. The measurements were taken with a *HP<sup>TM</sup>* 8753D-network analyzer. The results are included in figures 2,3,4 and 5.

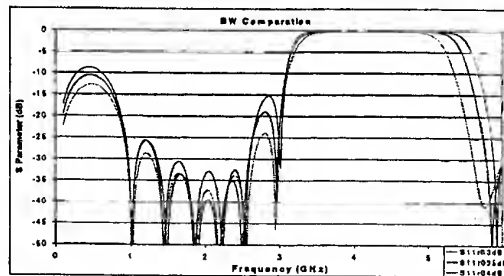
A reasonable agreement between simulation and measurement is obtained, providing slight mismatch introduced in the constructed prototype (due to connector unions). Comparing the performance offered by both PBG structures, the optimized PBG shows a larger relation between the rejected frequency band and the first side-lobe. The rejected band amplitude level in the tapered PBG structure is not as good as that of the uniform structure although it is still good.

The bandwidth obtained in the rejected frequency is similar in both cases. To increase the bandwidth, larger  $r/a$  ratios can be used, although side-lobe levels also increase, as it can be seen in figure 6.

### Conclusions

In a uniform microstrip PBG structure there is a design trade-off because an increase of the circle radius means that the rejection amplitude and bandwidth increases, as well as the amplitude of the sidelobes (and, therefore, the ripple in the pass band).

The use of tapering techniques (windows) in PBG structures has the effect of reducing the level of the sidelobes giving the chance of increasing circle radius (further than in the uniform case) to obtain greater bandwidths and rejection amplitudes.

Fig. 6. Comparison of  $S_{11}$  as a function of  $r/a$ 

### References

1. J. D. Joannopoulos, R. D. Meade, and J. N. Winn, *Photonic Crystals: Molding the Flow of Light*. Princeton, NJ: Princeton University Press, 1995.
2. E. Yablanovich, "Inhibited spontaneous emission in solid-state physics and electronics", *Phys. Rev. Lett.*, vol 58, no. 20, pp. 2059-2062, May 1987.
3. V. Radisic, Y. Qian, R. Coccioli, and T. Itoh, "Novel 2-D photonic bandgap structure for microstrip lines" in *IEEE Microwave and Guided Wave Lett.*, vol 8, No. 2, pp. 69-71, Feb. 1998
4. C. K. Chong et al., "Bragg reflectors", *IEEE Transactions on Plasma Science*, vol. 20, No. 3, pp. 393-402, Jun. 1992
5. B.Z. Katsenelenbaum et al., *Theory of Nonuniform Waveguides - the Cross-Section Method*. IEE Electromagnetic Waves Series, 44, London, 1998

# A Transducer Combined Taper and Converter with Periodic Waveguide Variation

Hong-hui Yan and Hong-sheng Yang

Dept. of Electronic Engineering  
National Key Laboratory of Millimeter Waves  
Southeast University, Nanjing, 210096, P. R. China

**Abstract** — A transducer combined taper and converter is presented. As an example, a  $TE_{02}$ -to- $TE_{01}$  mode transducer of this kind at 70 GHz is designed by numerically solving the proper coupled wave differential equations. The input and output radius are 0.0224 m and 0.0139 m respectively. The design considers five modes ( $TE_{01}^O$  through  $TE_{05}^O$ ). The converter is highly efficient (99.28%) and the length is short (0.6395 m).

## I. INTRODUCTION

Gyrotron is an efficient source of high power millimeter wave. On the other hand, the circular groove guide comparing with the traditional guides has advantages at the same band when transmitting in main mode  $TE_{11}^H$  [1]: large power capacity, low loss, large scale, wide bandwidth. So we pay our attention to the system that is based on gyrotron and circular groove guide. Considering the output mode of the gyrotron that are always higher order modes and the different cross section between the gyrotron output window and the circular groove guide, it is necessary to design a transducer between them. In traditional method, at first, using a taper to vary the output radius of gyrotron to the radius of circular groove guide, then change the mode in the way as

$$TE_{0n}^O \xrightarrow{1} TE_{01}^O \xrightarrow{2} TE_{11}^O \xrightarrow{3} TE_{11}^H.$$

In step 1 and 2, it usually uses the periodic wall perturbation technology [2][3][4]. This structure is long. We find that the taper and the step 1 converter both change the radial profile and leave the azimuthal profile unchanged. So it is possible to combine them in one section, named "combined transducer", to decrease the total length.

## II. ANALYSIS AND COMPUTATIONAL RESULTS

The  $TE_{0n}^O$ -to- $TE_{0q}^O$  coupled mode equation can be written in the form [3]

$$\frac{dA_n}{dz} = -\gamma_n(z)A_n + \sum_{q \neq n} C_{nq}(z)A_q \quad (1)$$

where

$$C_{nq}(z) = \frac{\beta_n + \beta_q}{\sqrt{\beta_n \beta_q}} \frac{D_n D_q}{(D_q^2 - D_n^2)} \frac{1}{a(z)} \frac{da(z)}{dz} \quad (2)$$

and  $\gamma_n = \alpha_n + j\beta_n \cdot |A_n|^2$  is the power transported in the +z direction by nth mode.  $D_n$  is the nth zero of  $J'_0(x)$  (excluding the one at  $x=0$ ),  $a(z)$  is the local wave guide radius. Proper  $a(z)$  variation can convert the power from  $TE_{0n}^O$  to wanted  $TE_{0q}^O$  mode.

To realize the converter function, we use the technique similar to that of periodic wave guide perturbations. According to the fact that the radius varies from input radius to output radius while modes are converting, the other higher order modes may be excited and the alteration of wave number along the transmitting direction is not negligible [4]. So, we assume that the function  $a(z)$  is expressed in the Fourier series form

$$a(z) = \left( r_2 + \frac{r_1 - r_2}{2} \left( 1 + \cos\left(\frac{z\pi}{L}\right) \right) \right) \cdot \frac{(1 - \sum_{n \geq 1} \varepsilon_n \cos(nk_p z))}{(1 - \sum_{n \geq 1} \varepsilon_n)} \quad (3)$$

where

$$k_p = \beta_n - \beta_q \quad (4)$$

$\beta_n, \beta_q$  are the undisturbed wave numbers of the interacting mode  $TE_{0n}^O, TE_{0q}^O$ .  $r_1$  and  $r_2$  are input and output radius respectively.  $L$  is the combined transducer length. The coefficient  $\varepsilon_m$  could be optimized by

numerically solving the equations (1).

The first item of expression (3) is used to ensure

$$\left. \frac{da(z)}{dz} \right|_{z=0} = \left. \frac{da(z)}{dz} \right|_{z=L} = 0 \quad (5)$$

If the above relationship (5) is not satisfied, other higher order circular electric waves will be exited obviously [5]. It is a disadvantage especially at the output port. The expression (3) also ensure

$$a(0)=r_1 \quad \text{and} \quad a(L)=r_2 \quad (6)$$

Of course,  $k_p L$  must be integer times of  $2\pi$  at the same time. The second item of expression (3) has infinite terms. However, in fact, as shown later, the converter efficiency is enough high when using only finite terms. We can find that the higher the order, the smaller the corresponding coefficient  $\varepsilon_n$ . So, the higher order coefficient  $\varepsilon_n$  could be neglected if the order  $n$  is big enough. And we assume that the undisturbed radius is  $r_0 = \frac{r_1}{(1 - \sum_{n \geq 1} \varepsilon_n)}$ .

Now, we design a  $TE_{02}^0$ -to- $TE_{01}^0$  combined transducer at 70 GHz as an example. The input radius  $r_1$  is 0.0224 m. The desired output radius  $r_2$  is 0.0139 m. To make the combined transducer as short as possible, we assume  $k_p L = 2\pi$ .

Through solving the equation (7) developed by Buckley *et al.* [3], we could get the estimate value  $\varepsilon_1 = 0.4015$ .

$$\frac{D_n D_q}{(D_q^2 - D_n^2)} k_p L \varepsilon_1 (1 - \varepsilon_1 + \frac{5}{4} \varepsilon_1^2) = \frac{\pi}{2} \quad (7)$$

The  $\varepsilon_1$  precise value and the higher order  $\varepsilon_n$  are obtained by numerical solving the coupled mode equations (1). The efficiency is further increased by empirically altering the undisturbed radius value  $r_0$ . In this design,  $r_0 = 0.0347$  m.

The radial variation is

$$a(z) = 1.3369(0.0139 + 0.00425(1 + \cos(\frac{z\pi}{0.6395}))) \times (1 - 0.433 \cos(9.8257z) + 0.10 \cos(19.6541z) + 0.044 \cos(29.4771z) + 0.033 \cos(39.3028z) + 0.004 \cos(49.1285z)) \quad (8)$$

From expression (8), we can find that the coefficient  $\varepsilon_n$  becomes small while the corresponding order becomes large. The result is shown in fig.1

The  $TE_{02}^0$ -to- $TE_{01}^0$  conversion efficiency is 99.28%, the length is 0.6395 m. The separate powers of the five modes

are listed in table 1.

Table 1 Separate-power at end of converter

Mode	$TE_{01}^0$	$TE_{02}^0$	$TE_{03}^0$	$TE_{04}^0$	$TE_{05}^0$
power (%)	99.28	0.031	0.076	0.51	0.11

### III. CONCLUSION

Computer-aided optimization calculations of the combined transducer for use with 70 GHz gyrotron operating in  $TE_{02}^0$  mode are presented which take into account  $TE_{01}^0$  through  $TE_{05}^0$  modes. The advantages of the structure are high efficiency (99.28%) and short length (0.6395m). This structure finishes converting  $TE_{02}^0$ -to- $TE_{01}^0$  mode and varying radius simultaneously. It is smooth and the first derivatives at both ends are zero.

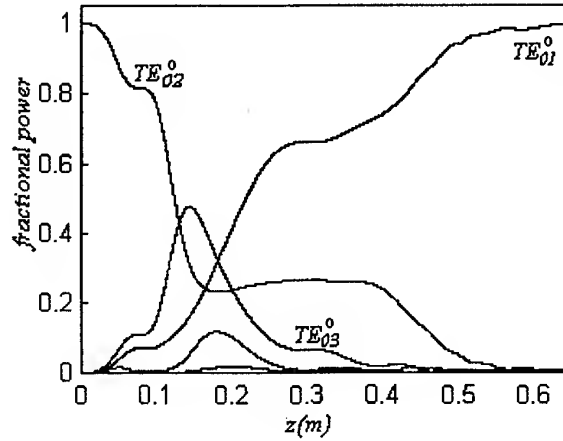


Fig.1 Calculated fractional power in five modes ( $TE_{01}^0$  through  $TE_{05}^0$ ) of  $TE_{02}^0$ -to- $TE_{01}^0$  combined transducer

### IV. REFERENCES

- [1] H. S. Yang, J. L. Ma, and Z. Z. Lu, IEEE trans. On. MTT vol.43, No.2, pp755- 764, 1995
- [2] N. F. Kovalev, I. M. Orlava, and M. I. Peletin, Radio Physics, Quant. Electron vol.11, pp.449-450, 1969.
- [3] M. J. Buckley and R. J. Vernon, IEEE Trans. Micro-wave Theory Tech., vol.38, pp.712-721, 1990.
- [4] M. Thumm, Int. J. Electron, vol.57, pp.1225, 1984
- [5] H. G. Unger, B.S.T.J, vol.37, pp899-912, 1988

# OPTIMUM SECTIONAL WAVEGUIDE TAPERS FOR QUASI-OPTICAL TRANSMISSION LINES

V.K. Kiseliiov

Institute for Radiophysics and Electronics of the National Academy of Sciences of Ukraine

Address: 12, Ac. Proskury st., Kharkov, 310085, Ukraine

Tel: +38 0572 448335, E-mail: kiseliiov@ire.kharkov.ua

## Introduction

The matching considerations must be embodied in the short-millimeter/submillimeter designs involving quasi-optical transmission lines of a class "Hollow Dielectric Waveguide" (HDW) [1-3] in order to provide the working mode transmission at a minimum extension of the matching components and without essential power loss. The thorough study [4] of commonly used waveguide tapers joining two different-size waveguides in a smooth way revealed that optimum, minimum-size tapers providing the adiabatic transition of the working mode are formed by parabola. Unfortunately, when extended in the axial direction, a parabolic surface is too much difficult in the manufacture. Therefore parabolic tapers are hardly producible even in the planar version. For 3-D optical and quasi-optical waveguides of circular, rectangular and other cross-sectional shapes, the things with parabolic tapers get much worse, and only a linear taper having the appearance of a truncated cone generated by a straight line is possible. However to provide adiabatic transition areas in the optical and quasi-optical regions, the linear tapers are required to be rather extended too. In addition, the dissipation loss which is proportional to the taper length essentially increases. In this connection, a sectional waveguide taper representing a succession of ordinary tapers – sections – seems reasonable to try.

A new method of the design of adiabatic optimum sectional waveguide tapers for 3-D quasi-optical lines of the HDW type is suggested. It calculates the optimum, in terms of a minimum extension and dissipation loss, approximation of a parabolic taper by a finite number of the ordinary, highly manufacturable linear sections. The calculation formulas are presented.

## Discussion

A sectional waveguide taper (SWT) joining two quasi-optical hollow dielectric waveguides of characteristic sizes (diameters)  $D_0$  and  $D_n$  is shown in Fig.1 and represents a set of linear-taper sections  $LS_m$ ,  $m=1, \dots, n$  approximating the parabolic surface. The both waveguides and the SWT are similar in the shape of their cross sections and in the nature of their boundaries; the working (fundamental) mode is assumed to be common. The quasi-optical conditions  $ka_0 \gg 1$ ,  $ka_n \gg 1$ , where  $a_0 = D_0/2$ ,  $a_n = D_n/2$ , and  $k = 2\pi/\lambda$  is the wavenumber are valid. The adiabatic transition condition of the SWT is formulated in terms of the ray model [5] of the waveguide modes as the "nonseparated propagation" conditions

$$\varphi_m(n) \leq \theta_m(n), \quad m=1, \dots, n, \quad (1)$$

for the local plane waves or for the ray family describing the fundamental mode

in each SWT section. Here  $\varphi_m(n)$  is the angle between the generator of the  $m$ -th linear section and the Z axis;  $\theta_m(n)$  is the local angle between the Z axis and the generator of the ray cone in the widest cross section  $A_m - A'_m$  (of the  $m$ -th linear section) onto the azimuthal X-Z plane. Relation (1) is the basic formula for finding all the necessary geometrical parameters of the optimum sectional waveguide taper (OSWT).

A minimum possible length of each linear section (as well as the SWT length as a whole) is found when (1) is considered at the shortest wavelength  $\lambda_{min}$  of the operating range. This gives the system

$$(D_m(n) - D_{m-1}(n)) / (2 l_m(n)) = \tilde{U}_1 \cdot \lambda_{min} / (\pi D_m(n)), \quad m=1, \dots, n \quad (2)$$

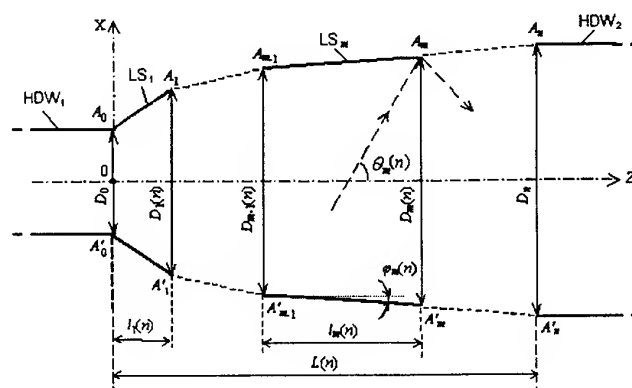


Fig. 1

of  $n$  algebraic relations between the sought values  $l_m(n)$  and  $D_m(n)$  of the adiabatic SWT and the given parameters  $D_0$ ,  $D_n$ ,  $\lambda_{\min}$ , and  $\tilde{U}_1$ , where  $\tilde{U}_1$  is the fundamental mode parameter. System (2) yields the SWT length as a nonlinear function of intermediate diameters  $D_m(n)$ . The minimum of this function determines the OSWT geometry and can be obtained with the unique set of  $D_m(n)$  values

$$D_m(n) = D_0 + m(D_n - D_0)/n = D_n[q + m(1-q)/n], \quad m=1, \dots, n, \quad (3)$$

where  $q=D_0/D_n$  is the OSWT unitless parameter. With (2) and (3), the rest geometrical parameters can be found as follows

$$l_m(n) = \pi \cdot D_n^2 (1-q) [q + m(1-q)/n] / (2n\lambda_{\min} \tilde{U}_1), \quad m=1, \dots, n; \quad (4)$$

$$\varphi_m(n) = \tilde{U}_1 \lambda_{\min} / (\pi \cdot D_n [q + m(1-q)/n]), \quad m=1, \dots, n; \quad (5)$$

$$L(n) = \sum_{m=1}^n l_m(n) = \pi \cdot D_n^2 (1-q^2) [1 + (1-q)/(n(1+q))] / (4\lambda_{\min} \tilde{U}_1). \quad (6)$$

The break points  $A_0, \dots, A_n$  of the OSWT generator (see Fig. 1) lie on the parabola whose axis is parallel to the Z axis and whose vertex is at point  $C_n$  with coordinates  $X(C_n) = -D_n(1-q)/(4n)$ ,  $Z(C_n) = -\pi D_n^2 [q + (1-q)/(2n)]^2 / (4\tilde{U}_1 \lambda_{\min})$ . The symmetrical points  $A'_0, \dots, A'_n$  lie on another parabola whose axis is parallel to the same axis but the vertex is at point  $C'_n$  with coordinates  $X(C'_n) = -X(C_n)$ ,  $Z(C'_n) = Z(C_n)$ . The focus-to-directrix distance of the both parabolas is  $p = \tilde{U}_1 \lambda_{\min} / 2\pi$ , which is independent of  $n$  and  $q$ . Hence these parabolas are identical. They have the same focal plane but their foci are symmetrically displaced by  $\Delta_n = \mp D_n(1-q)/(4n)$  from the Z axis. In the limit case  $n \rightarrow \infty$ , these enveloping parabolas merge giving the contour of the adiabatic parabolic taper.

Fig. 2 plots the relative difference  $\delta L(n)$  between the lengths of the OSWT and the ideal parabolic taper joining the circular HDWs with the fundamental mode  $HE_{11}$  ( $\tilde{U}_1 = 2.405$ ). It is seen that  $\delta L(n)$  rapidly falls as  $n$  rises, and already at  $n \geq 10$  the difference, even for the widely different diameters  $D_0$  and  $D_n$  ( $q \ll 1$ ), becomes less than 10 percent. When the minimum loss condition is not the deciding factor in the design, the number of the sections (which depends on  $q$ ) may be reduced. For example, at  $q=0.5$ , the four-section OSWT is possible, which is only 8 percent longer than the ideal parabolic taper but 19 percent shorter than the linear analog. For  $n \geq 7$ , the fundamental mode loss (without regard for the loss by the mode transformation) is found [6] to be almost the same as that in the parabolic taper.

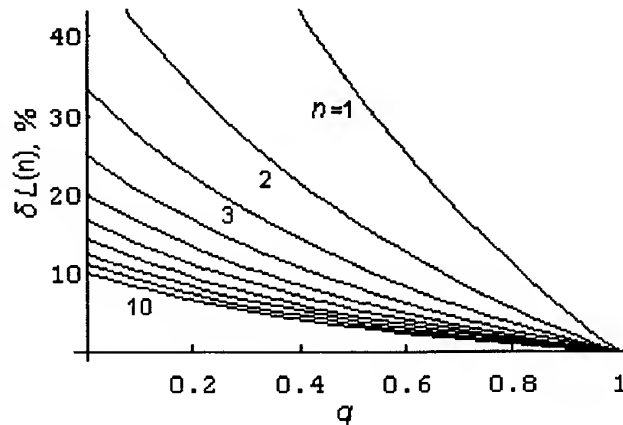


Fig. 2

### Conclusion

Keeping the main characteristics of parabolic tapers essentially the same, the presented OSWT design gains in the manufacturability. The suggested method can be used not only for hollow dielectric waveguides but for other waveguide types as well.

1. E A Marcanti and R A Schmeltzer, Bell Syst. Tech. J. 43, 1783 (1964).
2. Yu N Kazantsev and O A Kharlashkin, Radio Eng. and Elect. Physics. 16, 1040 (1971) (in Russian).
3. Yu N Kazantsev and O A Kharlashkin, Radio Eng. and Elect. Physics. 29, 78 (1984) (in Russian).
4. W K Burns, A F Milton, and A B Lee, Appl. Phys. Lett. 30, 28 (1977).
5. A W Snyder and J D Love, Optical Waveguide Theory. Chapman and Hall, London- New York (1983).
6. V K Kiseliyov and T M Kushta, Proc. IRE NAS of Ukraine. 128 (1990) (in Russian).



# Hot-Electron Detection

K. P. Wood<sup>1</sup> and H. Araújo<sup>2</sup>

<sup>1</sup> QMC Instruments Ltd., Station Mills, Billingshurst, West Sussex, RH14 9SH

<sup>2</sup> Physics Department, Queen Mary and Westfield College, London E1 4NS

## Abstract

We present a brief discussion of the hot electron mechanism and its use in radiation detection. We comment on the performance and design considerations of established n-InSb devices operating at 4.2 K. More recent working designs using cyclotron resonance to enhance absorption at terahertz frequencies are also outlined. We also discuss superconducting hot-electron devices made from thin niobium films.

## 1 The hot-electron effect

Electrons excited by the absorption of incident photons will transfer excess energy either by heating the lattice through an inelastic electron-phonon scattering mechanism or to other electrons by direct electron-electron inelastic scattering. In most materials the characteristic timescales of the two processes are such that energy is transferred to the lattice.

Some systems exist however where the relative importance of these two competing processes is reversed. After absorbing a photon, an electron – or small number of initial energetic electrons – can share energy with a great number of other electrons before energy relaxation to the lattice phonons takes over. This happens when  $\tau_e \ll \tau_{e-ph}$ , where  $\tau_e$  is the inelastic electron scattering time, and  $\tau_{e-ph}$  the inelastic electron-phonon interaction time. Therefore, there is an equilibrium of electron excitations during a time of the order of  $\tau_{e-ph}$ , before they thermalise with the phonon bath. During that period, the electron distribution can be regarded as having an effective temperature  $T^*$  greater than the phonon temperature,  $T_0$ . These so-called hot-electron phenomena were predicted and identified as early as the 1950s [1, 2].

Bolometric detection relies on materials with a steep temperature dependence of electrical resistance. A superconductor at its transition temperature, or a semiconductor held at low temperature are therefore good candidates to convert a temperature rise due to radiation absorption to an electrical signal. In *hot-electron* bolometers, the change in resistance is non-thermal in nature, therefore inherently fast. This temperature dependence can have different characteristics. In a superconductor, absorption of radiation produces an increase in the number of quasiparticles, which *increases* its resistance by a partial destruction of superconductivity. On the other hand, in semiconductors, where the large energy gap forbids carrier creation at such low frequencies, radiation absorption brings about an increase in the carrier mobility, resulting in a *decrease* of resistance. In both cases, the response speed is ultimately determined by the electron-phonon interaction, which is the bottleneck of the cooling process. This can range between  $\sim 10^{-12}$  s for the high- $T_c$  superconductors, and  $\sim 10^{-6}$  s in semiconductors such as n-InSb.

## 2 n-InSb hot-electron bolometers

The Drude theory can be invoked to obtain classical formulae which accurately predict the measured characteristics of hot-electron devices like, for example, undoped n-InSb at 4.2 K. The link between dissipation at the radiation frequency,  $\omega$ , and the detection mechanism is well established

in the expression for the electrical conductivity:

$$\sigma = \frac{\sigma_0}{1 + \omega^2 \tau_e^2},$$

where  $\tau_e$  is the electron scattering time, and  $\sigma_0$ , the dc conductivity, is given by

$$\sigma_0 = \frac{ne^2 \tau_e}{m^*},$$

with  $n$  the carrier concentration and  $m^*$  the effective carrier mass. It is the carrier mobility, through its dependency on  $m^*$ , that provides the sensitivity of the detector resistance on the electron temperature.

A responsivity which is constant at long wavelengths and then falls as  $\lambda^2$  as  $\omega^2 \tau_e^2 \gg 1$  is therefore predicted. A real working device for the cm wavelength range was first constructed from germanium. In InSb, where the effective carrier mass is much smaller, absorptivity is constant for wavelengths longer than  $\sim 500 \mu\text{m}$  in modern materials, and it is this spectral bandwidth which makes the InSb device so useful.

Noise from these devices is dominated by Johnson noise, and the output noise spectrum from such a system exhibits a very low value of the  $1/f$  'knee' frequency. Room temperature preamplifiers are now available which permit the overall system noise to be limited by the noise performance of the detector itself. Low-pass filters have also been developed in recent years which transmit detectable frequencies with good efficiency and at the same time give good blocking at all unwanted higher frequencies. Consequently, modern systems have the convenience of long cryogen hold-times. Since the late 1970s this kind of InSb detector has been widely used as a diagnostic tool in many fields at millimetre and sub-millimetre wavelengths. Typical performance parameter values are as follows:

* Wavelength range at max. sensitivity	0.5 to 10 mm.
* Detector optical responsivity	$\geq 5,000 \text{ V/W.}$
* Detector optical N.E.P.	$\leq 5 \times 10^{-13} \text{ W Hz}^{-1/2}$
* Detection time constant at 4.2 K	$\leq 1 \mu\text{s.}$

## 2.1 InSb in a magnetic field

The hot-electron mechanism in semiconductors is significantly altered by the application of a magnetic field. In a field,  $B$ , the conduction band is confined to discrete Landau levels, and only relatively narrow band photoconductive transitions are possible at the cyclotron resonance frequency given by

$$\nu = \frac{eB}{2\pi m^*}.$$

The small effective carrier mass in InSb ( $0.016 m_e$ ) means that higher cyclotron resonance frequencies are reached using modest magnetic field strengths. For example, a 1 Tesla (10 kGauss) field corresponds to a resonance frequency of approximately 2 THz. The magnetic enhancement constitutes an increase in absorptivity of approximately one order of magnitude at 1.5 THz and up to two orders at 2.5 THz. Measurements of InSb in superconducting coil magnets indicate that the resonance peak frequency varies linearly with magnetic field strength well into the THz region, until the lower energy side of the *reststrahlen* band is reached at  $\lambda=60 \mu\text{m}$  ( $160 \text{ cm}^{-1}$ ). Beyond the high frequency edge of the *reststrahlen* band, the application of even higher magnetic fields would see the resonance peak continue through the mid-IR region. Although such a system would be sophisticated to use optimally, the possibility exists for a narrow band tunable InSb detector operating within a superconducting coil magnet with almost complete coverage through the millimetre region to perhaps the near-IR.

In the commercial detector systems currently available, permanent magnets are used to keep systems simple and relatively inexpensive. At lower field strengths it is possible to configure the

detector element in a spread magnetic field geometry so that enhancement of absorptivity occurs at a range of frequencies. In these modest fields, freeze-out of carriers into discrete levels is not complete and a balanced contribution is possible between absorption by both free and bound electrons. In this way, the tail of the hot electron response can be extended from 500 GHz to 1500 GHz and beyond.

Recent advances in permanent magnet technology enable much higher field strengths to be generated in passive NeFeB magnets, and work is currently under way to optimise an InSb system to give a response range from 10 mm to 60  $\mu\text{m}$  (30 GHz to 5 THz.)

### 3 Superconducting hot-electron bolometers

In the early 1980s, Sergeev and co-workers [3] reported on the non-thermal response of ultrathin ( $\sim 100 \text{ \AA}$ ) niobium films to electromagnetic radiation. In particular, they determined the frequency-independent nature of radiation absorption in the band between  $10^{10}$ – $10^{15}$  Hz, and attributed the effect to the heating of quasiparticles.

The first generation Nb detectors were made from ultrathin films deposited on high thermal conductivity substrates, such as sapphire. The geometry of the devices (a number of thin strips  $\sim 1$  mm long by  $\sim 1 \mu\text{m}$  wide connected in parallel) helps to eliminate the slower thermal bolometric effect so that the frequency response curve has only one time-constant – that of the hot-electron response. Typical  $50 \Omega$  devices now commercially available have a response time of  $\sim 1$  ns, optical NEPs of a few tens of  $\text{pW/Hz}^{1/2}$ , and optical voltage responsivities of tens of V/W. Besides short response times, they are also attractive for their wide radiation bandwidth, which extends to the ultraviolet.

One advantage of a 'cold' lattice is that the device may be coupled to the input signal with greater efficiency using a planar antenna. This also allows the downscaling of the bolometer element with significant improvement in responsivity and NEP.

Faster cooling of the hot-electron population in ultra-low noise systems is an on-going development issue for heterodyne detection applications. A diffusion-cooling mechanism for superconductor bridges of sub-micron dimensions has recently been proposed [5], that exploits the escape of hot-electrons from the microbolometer element before they can interact with phonons. Bandwidths well into the GHz range and unprecedented noise temperatures in the submillimetre spectral region have been achieved in Nb bolometric mixers, while electron-phonon cooling in the same material would limit its speed to  $\sim 100$  MHz [6].

#### Acknowledgment

H. Araújo is supported by research grant PRAXIS XXI/BD/5134/95 FCT, Portugal.

#### References

- [1] E. S. Borovik, Dokl. Akad. Nauk SSSR **91**, 771 (1953).
- [2] H. Frohlich and B. V. Paranjape, Proc. Phys. Soc. Lon. **B69**, 21 (1956).
- [3] A. V. Sergeev *et al.*, Sov. Phys. JETP Lett. **34**, 268 (1981); Sov. Phys. JETP Lett. **36**, 296 (1982); Sov. Phys. JETP **59**(2), 442 (1984).
- [4] E. M. Gershenzon *et al.*, IEEE Trans. Magn. **27**(2), 2836 (1991).
- [5] D. E. Prober, Appl. Phys. Lett. **62**(17), 2119 (1993).
- [6] B. S. Karasik, M. C. Gaidis, W. R. McGrath, B. Bumble and H. G. LeDuc, IEEE Trans. Appl. Supercond. **7**(2), 3580 (1997).

## FIR photo-voltaic effect in silicon BIB structures

L. Asadauskas<sup>1,2</sup>, D. Yu. Kovalev<sup>3</sup>, V. Rylkov<sup>3,4</sup>, B. Aronzon<sup>3,4</sup>, R. Brazis<sup>1</sup>, J. Leotin<sup>2</sup>

<sup>1</sup>Semiconductor Physics Institute, A. Goštauto 11, 2600 Vilnius, Lithuania

<sup>2</sup>Laboratoire de Physique de la Matière Condensée, Université Paul Sabatier,  
118 route de Narbonne, 31062 Toulouse Cedex, France

<sup>3</sup>Russian Research Center "Kurchatov Institute", Moscow 123182, Russia

<sup>4</sup>Scientific Center for Applied Electrodynamics, Moscow 127412, Russia

### 1. Introduction

Semiconductor structures with a blocked impurity band (BIB) are found to be the most sensitive far infrared (FIR) detectors allowing for a single-photon counting [1]. The theory of BIB detectors is based on the photo-conductivity which originates from the carrier release from the impurity band to the valence band in the active layer and their transport through the pure (blocking) layer in the presence of bias electric field [2,3]. Previous works have been focused on a rather high bias regime seeking for the highest quantum yield [4,5]. In contrast to this, we have undertaken refined measurements focused on the possibilities of BIB detector operation at low bias voltage. What we have observed is the photo-current flow in the BIB circuit without any bias.

In the present paper we report the first data on the short-circuit current and the photo-electromotive force, their dependence on the lattice temperature and the background FIR photon flux in BIB structures.

### 2. Experiment

The boron-doped BIB structures have been grown by chemical vapor deposition epitaxy on silicon substrates. The rear contact layer ( $p^{++} = 10^{19} \text{ cm}^{-3}$ ,  $d_{++} = 1.5 \text{ } \mu\text{m}$ ) has been deposited on the substrate ( $p = 5 \times 10^{16} \text{ cm}^{-3}$ ,  $d = 520 \text{ } \mu\text{m}$ ) and the blocking ( $i < 5 \times 10^{13} \text{ cm}^{-3}$ ,  $d_i = 3 \text{ } \mu\text{m}$ ) and the active layers ( $p^+ = 10^{18} \text{ cm}^{-3}$ ,  $d_a = 4.5 \text{ } \mu\text{m}$ ) on it. The front contact layer has been obtained by epitaxial deposition of a thin highly doped  $\text{Ge}_{12}\text{Si}_{88}$ -alloy ( $p^{++} = 10^{19} \text{ cm}^{-3}$ ,  $d_{++} = 0.1 \text{ } \mu\text{m}$ ). The heterojunction bringing about the additional energy barrier [6] is introduced in order to reduce the carrier injection from the contact layer to the valence band of the active layer.

In the spectral measurements the photon flux has been directed onto the sample through the 35 mm long cone with the front diameter of 11 mm and the rear diameter of 1.5 mm. The wave number of incident radiation has been limited to the range of  $100\text{--}700 \text{ cm}^{-1}$  with two broad maxima centered at  $300 \text{ cm}^{-1}$  and  $550 \text{ cm}^{-1}$ . The photo-current spectral characteristics have been measured following standard Fourier transform procedure of the Bruker IFS 113v spectrometer. The BIB detector spectral response has been normalized to the spectral response of a standard bolometer.

Current-voltage characteristics have been measured under illumination by two different sources. In the first case a broadband constant-intensity photon flux of the Bruker IFS 113v spectrometer has been used. In the second case the BIB structure has been closed in a hermetic He-cooled shield together with the solid-state  $5.25 \text{ } \mu\text{m}$ -laser.

### 3. Results and discussion

**3.1. Broad-band illumination.** Current-voltage characteristics of the BIB structures illuminated by the broad-band radiation do not go through zero manifesting an internal photo-effect (Fig. 1). The current is referred to as a positive when the holes are streaming from the active layer through the blocking layer. One needs to apply a stopping voltage in order to compensate the photo-emission-induced current. The photo-electromotive force measured in this way is found to decrease with the rise of temperature (insert in Fig 1). The absolute value of zero-bias photo-current changes non-monotonously with a maximum at  $T = 10\text{--}12 \text{ K}$ .

The zero-bias photo-current dependence (Fig. 2) on the photon energy manifest a threshold at photon energy about  $38 \text{ meV}$ . The shape of the zero-bias photo-current dependence on temperature (insert in Fig. 2) does not much depend on the photon energy in the wave number range of  $400\text{--}500 \text{ cm}^{-1}$  though there are some indications of a reduced temperature dependence near the red border of the internal photo-effect. The latter is indicated in Fig. 2 by arrow which correspond to the acceptor (B) state ionization energy.

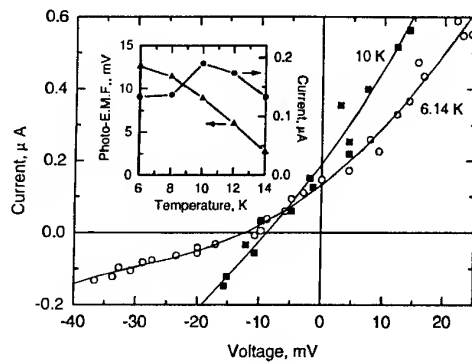


Fig. 1. - Current-voltage characteristics of the BIB structures. Short-circuit photo-current and photo-electromotive force is shown in the insert as a function of the lattice temperature.

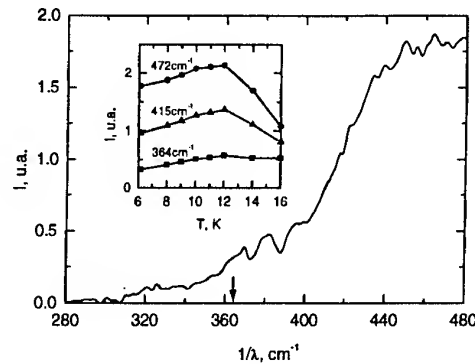


Fig. 2. - Short-circuit photo-current spectrum of the BIB structures at the temperature of 6 K. The photo-current at selected photon wave numbers is shown in the insert as a function of temperature.

**3.2. Laser illumination without a background radiation.** An experiment with the sample housing in the dark He-cooled shield together with the infrared laser emitting considerably higher energy photons is aiming at the verification of the universality of the observed photo-voltaic effect. The photo-voltaic effect is found to persist even at this quite high photon energy (200 meV).

The current-voltage characteristics obtained at laser illumination exhibit the same sign of the photo-voltaic effect as in the case of a broad-band illumination. However, the photo-current in the laser experiment is by two orders of magnitude lower than in the broad-band illumination experiments. This can be explained by much lower intensity of the laser radiation compared to the intensity of the broad-band photon beam. The zero-bias photo-current direction is found to be independent of the photon energy. Both experiments are in agreement manifesting jointly a slightly non-monotonous photo-current dependence on temperature.

The effect is suggested to originate from two co-operative processes. The first is the photo-emission of holes from the front Ge/Si contact to the active layer. The hole energy relaxation time in the active layer is short because they are captured to the neutral acceptor band. The holes can be thermally or optically excited again to the valence band, or fill in the impurity band owing to recombination with the negatively charged acceptors. In any case, the extra charge of photo-injected holes in the active layer is screened by the highly conductive system of holes of the impurity band, and the space charge is localised at the active/blocking layer interface. The second process is the hole photo-emission from the interface across the blocking layer to the rear contact. Both the processes are influenced by the space charge peculiarities at the SiGe/Si and the active/blocking layer interfaces, as well as by the streams of thermally activated holes or the holes released by photons from the rear contact.

#### 4. Conclusion

One can conclude that the total hole photo-emission current in the BIB structures illuminated both by low-energy and high-energy photons flows along the photon flux direction when the bias voltage is zero. This new puzzling photo-emission signal opens a new possibility for IR detection at zero dark current.

#### References

1. M D Petroff, M G Stapelbroek, and W A Kleinhans, *Appl. Phys. Lett.*, **51**, 406 (1987).
2. F Szmulowicz, F L Madarsz, J. *Appl. Phys.*, **62**, 2533 (1987).
3. V D Shadrin and V T Coon, I K Blokhin, *J. Appl. Phys.*, **74**, 6927 (1993).
4. J E Huffman, A G Crouse, B L Halleck, T V Downes and T Herter, *J. Appl. Phys.*, **72**, 273 (1992).
5. S Pasquier, G Sirman, C Meny, A Murray, M Griffin, P Ade, L Essaleh, J Galibert and J Leotin, in "*Millimeter and Submillimeter Waves*" edited by M N Afsar (Proceedings of SPIE vol. 2211, 1994)
6. T L Lin, and J Maserjian, *Appl. Phys. Lett.*, **57**, 1422 (1990).

## Properties of high stability Bi microbolometers for the detection of THz radiation.

F. Ghianni, F.W.H.J. Steenbrink, T.O. Klaassen and W.Th. Wenckebach,

Department of Applied Physics and DIMES, Delft University of Technology,  
P.O.Box 5046, 2600 GA Delft, The Netherlands

### Introduction

Bolometers have been used for optical detection in a wide wavelength range over the last decades. Antenna coupled thin film Bi microbolometers have been used for room temperature detection of THz radiation [1]. They are relatively cheap and easy to fabricate using standard lithographical techniques. Because of the smallness of the bolometer elements, they can be made very fast without an appreciable loss of sensitivity. The video bandwidth of commonly used pyroelectric detectors can also be raised, but only at the cost of a strong decrease in sensitivity. Moreover, the relatively large electrical capacitance of the active element limits the upper video frequency. Short THz pulses are therefore often monitored using Schottky barrier diode detectors. The ultimate bandwidth of these detectors, if the video output has been designed properly, can be larger than 5 GHz. However, these detectors are very expensive, often strongly wavelength dependent due to the antenna structure used, rather fragile and difficult to align. For many THz applications such an extreme video bandwidth is unnecessary, whereas at the same time broad wavelength coverage is often required. Fast, antenna coupled microbolometers promise to be a good choice to monitor THz pulses at those intermediate bandwidths at room temperature. They combine a reasonable sensitivity with relatively high video speed. Moreover, using a broadband planar THz antenna to couple the THz field to the bolometer, a wavelength independent sensitivity over about a decade is possible. The disadvantage of this type of bolometers, however, is that performance decreases with time over a period of several months. Evidently, more work on long term stability must be performed.

In this contribution we report on the results of a new fabrication technique for bolometers on a Si substrate. The influence of the insulating SiO<sub>2</sub> layer thickness on sensitivity and response time of the bolometer is studied. One of the goals of this research is the construction of a sensitive detector array, with sub-nanosecond time resolution, that will enable the time resolved monitoring of the wavelength dependent output of our mode locked p-Ge THz laser [2].

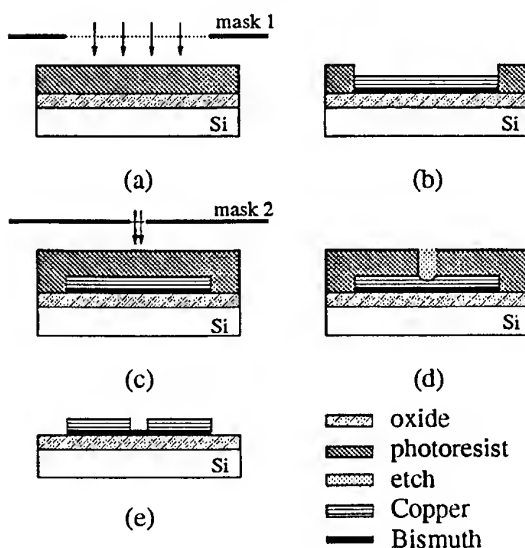


Fig. 1. Antenna/bolometer patterning technique

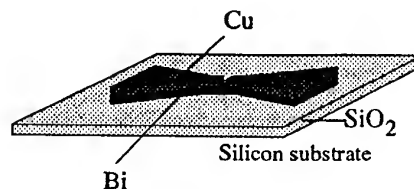


Fig. 2. Antenna/bolometer sample

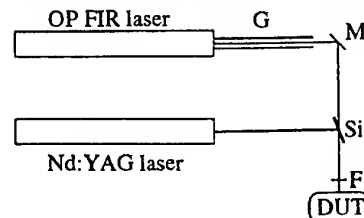
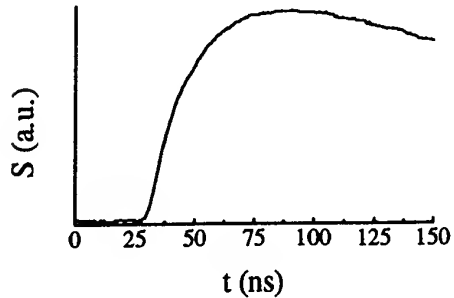


Fig. 3. Nd:YAG laser FIR pulse slicing setup

### Fabrication

The antenna and bolometer thin films used in the experiments are deposited in a single step process, as it is assumed that the single step of Bi and Cu evaporation gives less  $1/f$  noise than a two step evaporated film because of contamination by processing [1] and oxidation of the bolometer material. Successively, layers of 5 nm Ti, 100 nm Bi and 200 nm Cu are evaporated on Si substrates with  $\text{SiO}_2$  isolation layers of various thickness. During evaporation of Bi the substrate is at a temperature of about  $80^\circ\text{C}$ ; the evaporation rate is  $0.2\text{ nm/s}$ . The film layer thickness is monitored with a crystal quartz monitor. Lift-off is performed and the bolometer pattern is wet etched after developing a second illuminated photoresist layer, see fig 1.



$\text{SiO}_2$	S	video BW	NEP
nm	V/WmA	MHz	$\text{WHz}^{-1/2}$
15	1.2	9	$2.10^{-9}$
100	6.3	8	$4.10^{-10}$
190	11		$2.10^{-10}$
475		3	

Fig. 4. Thermal time constant measured with FIR slicing technique

Table 1. Experimental data for various bolometers

### Results

Most bolometers, fabricated in the apex of either a bowtie or a logperiodic antenna, proved to be stable over a period of at least 6 months. The resulting resistance values fell in the  $70 - 140\ \Omega$  range, and did not increase in time with more than 20 %. The low value of  $-2.2 \times 10^{-3}\ \text{K}^{-1}$  found for the temperature coefficient [1], may be due to non ideal evaporation conditions such as the relative high substrate temperature ( $80^\circ\text{C}$ ). SEM photographs did show a rather irregular Bi surface.

Typical values for the DC responsivity S [V/WmA], determined from I-V curves, are given in Table 1.

The THz coupling efficiency is measured using a conventional OPFIR laser at  $118.8\ \mu\text{m}$ . The beam is focused by a Fresnel lens on the antenna backed by a Si hyperhemispherical lens; efficiencies of the order of 20 % of the theoretical maximum are observed.

The video bandwidth, set by the bolometer thermal time constant, is determined from the respons of the bolometer on a sudden (10 ns) shut-off of the FIR beam, using a 532 nm Q-switched Nd:YAG laser pulse to block the FIR transmission of a Si wafer. (see figs. 3,4). The noise voltage at 1 mA bias current, measured with a HP 4195A network/spectrum analyzer, is about  $2.10^{-9}\text{VHz}^{-1/2}$  up to a bandwidth of 200 MHz. NEP values, shown in the table, are a few orders of magnitude lower than for pyroelectric detectors at equal bandwidth [3].

These preliminary experiments show that in order to decrease the response time of the detector, more work on the bolometer design is necessary.

### References

- [1] D.P. Neikirk, W.W. Lam, D.B. Rutledge, Int. J. Infrared and Millimeter Waves, 5(1984)245
- [2] J.N. Hovenier, T.O. Klaassen, W.Th. Wenckebach, A.V. Muravjov, S.G. Pavlov, V.N. Shastin, Appl. Phys. Lett. 72(1998)1140.
- [3] T.Hwang, S.E. Schwarz D.B. Rutledge, Appl. Phys. Lett. 34(1979)773.

## Fabrication of Ge:Ga Far Infrared Photoconductor two-dimensional array

M. Fujiwara(1), N. Hiromoto(1), H. Shibai(2), T. Hirao(2), and T. Nakagawa(3)

- (1) Communications Research Laboratory, Ministry of Posts and Telecommunications  
4-2-1 Nukuikita, Koganei, Tokyo 184-8795, Japan  
FAX: +81-42-327-6941, e-mail: fujiwara@crl.go.jp  
(2) Nagoya University  
(3) Institute of Space and Astronautical Science

**Abstract:** We are developing the A  $20 \times 3$  Ge:Ga far-infrared photoconductor array which is directly hybridized to a Si p-MOS readout integrated circuit (IC) by indium bump technology. We describe the design of the detector array, as well as the fabrication process and the performance of the Ge:Ga photoconductor array.

### Introduction

Gallium-doped germanium (Ge:Ga) extrinsic semiconductors have been used as sensitive far-infrared detectors with a cutoff wavelength at  $110 \mu\text{m}$ [1], especially for applications in astronomy[2] and spectroscopy of molecules, solid, and plasma. Development of arrays of Ge:Ga photoconductors is now an important issue for research fields to take two-dimensional THz images, especially for observation in space[3,4].

We are developing Ge:Ga far-infrared photoconductor direct hybrid arrays for applying to focal-plane detectors of the Far Infrared Surveyor (FIS), one of the two main instruments of the Infrared Imaging Surveyor (IRIS) satellite. In order to fabricate a two-dimensional Ge:Ga photoconductor array, we make a transparent electrode for placing the detectors in a "longitudinal" configuration in which the electric field is applied parallel to the photon influx. In this paper, we report on the basic idea and the design of direct hybrid two-dimensional array, and on the performance of the 16-element Ge:Ga photoconductor linear array in the recently fabricated by an improved process.

### Fabrication of detector arrays

The transparent electrode for detectors must be good in two characteristics, which are transmission of far-infrared radiation and ohmic contact. The transparent electrode was made by implanting  $\text{B}^+$  ions on one surface of a Ge:Ga wafer with Ga concentration of  $2 \times 10^{14} \text{ cm}^{-3}$ .  $\text{B}^+$  ions were implanted at a density of  $5 \times 10^{13} \text{ ions/cm}^2$  at 40 keV and the Ge:Ga wafers were annealed at  $320^\circ\text{C}$  for 1 h in an atmosphere of  $\text{N}_2$ .

The far-infrared transmittance of the ion-implanted Ge:Ga specimens were measured at a temperature of 4.2 K by use of a Fourier spectrometer. We estimated the far-infrared absorption at the  $\text{B}^+$  layer by comparing the transmission between the wafers with and without ion-implantation. The transmittance of far-infrared radiation through the ion-implanted layer at a

wavelength of  $100\text{-}\mu\text{m}$  was about 84%[5,6]. We chose a 0.5 mm-thick wafer for the photoconductor array.

After making the transparent electrode,  $\text{B}^+$  ions were implanted on the back surface at a dose density of  $1 \times 10^{14} \text{ ions/cm}^2$  at 40 keV and  $2 \times 10^{14} \text{ ions/cm}^2$  at 60 keV. This condition is the same as the metallic ohmic electrodes for the single-element photoconductors[7,8]. Following a 5-min annealing in  $\text{N}_2$  atmosphere at  $320^\circ\text{C}$ , a  $5000\text{-}\text{\AA}$ -thick Au on  $500\text{-}\text{\AA}$  Cr layer was evaporated onto the ion implanted surfaces.

A metal pattern was formed on the transparent electrode to optically separate the pixels, to increase conductance on the front surface, and to make bonding pads. One pixel has  $500 \times 500 \mu\text{m}^2$  windows. Width of the metal pattern between pixels is  $50 \mu\text{m}$ . In the first fabrication, we had used  $\text{Si}_3\text{N}_4$ , instead of photoresist, and transparent electrodes had gotten damage due to using strong acid during lift-off process. Therefore, in this time these patterns were formed by photoresist lift-off technique, and hence we obtained unharmed transparent electrode with metal windows.

The ditches  $50 \mu\text{m}$  in width and  $30 \mu\text{m}$  deep were digged on the back metal surface by wet etching with a 4:1 mixture of  $\text{HNO}_3\text{:HF}$  for the purpose of electrically separating pixels.

Fig. 1 shows the pattern of the transparent electrode and the back metal electrode of the  $20 \times 3$  Ge:Ga detector array. There is a guard ring on the back electrode, which will be connected to ground level.

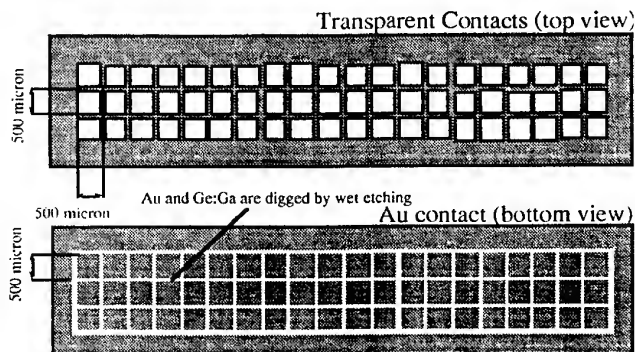


**Fig. 1 Design of Ge:Ga Photoconductor  $20 \times 3$  Array  
with a Transparent Contact**



### Performance of detectors with transparent electrode

We tested the 16-element linear array which is connected to transimpedance amplifier array with 6 G $\Omega$  feedback resistors. Fig. 2 shows typical responsivity and NEP of the detector with transparent electrode as functions of the bias field, for step change in the photon influx (DC), and for 7.5 Hz and 15 Hz chopped light. Difference between responsivities for step change and for chopped light implies the existence of the slow transient response[7,8], and difference between 7.5 Hz and 15 Hz is due to the moderately-fast response[9]. Background photon influx was  $4 \times 10^6$  photon/sec. For comparison, we tested a single element detector too. Responsivities nonlinearly increased as the bias field increased. The bias electric field at which the best NEP was achieved was about 1.2 V/cm.

When the detector was cooled at 2.1 K, the best responsivity and NEP were obtained to be 15.2 A/W and  $3.2 \times 10^{-17}$  W/Hz $^{1/2}$  respectively at a bias field of 1.2 V/cm. Comparing with first fabrication detector array[5,6], responsivities and NEPs were improved due to the success in making good transparent electrode.

We also estimated the value of crosstalk between neighboring detectors, and the result was less than 10% including the electrical crosstalk in the readout circuits.

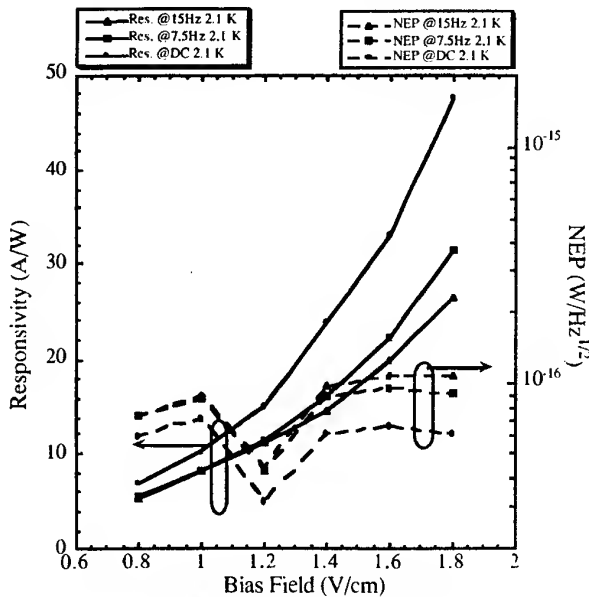


Fig. 2 Responsivity and NEP as functions of bias field.

### Fabrication of direct hybrid two-dimensional detector array

We are developing two-dimensional photoconductor array which is directly hybridized to a cryogenic Si p-MOS FETs' readout circuit with the  $20 \times 3$  format. The preliminary model of Si p-MOS IC readout circuits are the source-follower-per-detector type. For the following model, we will adopt

capacitive transimpedance amplifier with feedback capacitance (CTIA) type. Si p-MOS FETs with gate 200  $\mu$ m wide and 1.5  $\mu$ m long are used in the circuit. The technique for electrical connection between Ge:Ga and Si IC is very important because the difference in the coefficient of thermal expansion could cause significant mechanical stress. The displacement between the Ge:Ga photoconductor array and the Si p-MOS IC is about 12  $\mu$ m when they are cooled from 300 K to 4.2 K. Theoretically, indium columns of 100-200  $\mu$ m in diameter and 100-200  $\mu$ m high have enough capability to absorb the stress caused by the thermal strain between the Ge:Ga array and the Si p-MOS read out circuit[10,11]. Therefore, the hybridization will be achieved by indium bump technology. Fig. 3 shows the structure of the hybrid. 100-200  $\mu$ m diameter indium balls are used for thermo-sonic compressing. The direct hybrid two-dimensional array will bring the enormous improvement in performance for taking two-dimensional 3 THz images.

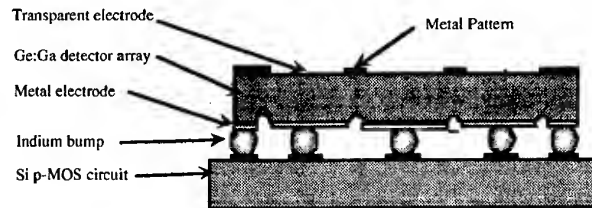


Fig. 3 Structure of the direct hybrid detector array

### Reference

- [1] P. R. Bratt: *Infrared Detectors II*, eds. R. K. Willardson and A. C. Beer (Academic Press, New York, 1977) Semiconductors and Semimetals.
- [2] H. Shibai *et al.*: *Astrophys J.* **428** (1994) 354.
- [3] J. W. Beeman *et al.*: *Infrared Phys.* **35** (1994) 827.
- [4] E. F. Erickson *et al.*: *Proc. ESA Sympo. on Submillimetre and Far-Infrared Space Instrumentation (ESA SP-388, 1996)* p. 41.
- [5] M. Fujiwara and N. Hiromoto: *Digest of Int'l Conf. Infrared & Millimeter Waves M3.7* (1997).
- [6] N. Hiromoto *et al.*: *Proc. SPIE on Infrared Astronomical Instrumentation*, **3354** (1998).
- [7] N. Hiromoto *et al.*: *Jpn. J. Appl. Phys.* **29** (1990) 1739.
- [8] N. Hiromoto *et al.*: *Jpn. J. Appl. Phys.* **35** (1996) 1676.
- [9] M. Fujiwara and N. Hiromoto: *Jpn. J. Appl. Phys.* **36** (1997) 4262.
- [10] J. T. Longo *et al.*: *IEEE Trans. Elec. Dev.* **25** (1978) 213.
- [11] N. Oda, private communication, (1998).

## Antenna Coupled Far-Infrared Radiation Detectors

Yoshizumi Yasuoka

Department of Electronic Engineering, National Defense Academy,  
1-10-20 Hashirimizu Yokosuka 239, Japan

Point contact antenna coupled devices such as MOM diodes, Schottky diodes and warm carrier devices are known as a detector and mixer in the millimeter wave and infrared frequency regions. Although these devices were easy to fabricate, the extreme mechanical instability of these devices made them impractical except for special applications, and encouraged the fabrication of stable, thin-film devices through recently developed microfabrication techniques.

In order to obtain high sensitive thin-film antenna coupled devices, it is necessary to fabricate a thin-film antenna which can receive the submillimeter and infrared radiation efficiently. It is also necessary to fabricate a detector which has  $I$ - $V$  characteristics persisting up to frequencies of signals received by the antenna.

The thin-film antennas such as bow-tie, spiral, long wire, log-periodic, microstrip and slot have been fabricated using recently developed microfabrication techniques, and the operation properties in the millimeter wave and/or far-infrared frequency regions have been investigated. In these antennas, the slot antenna is one of the leading candidates for a far-infrared array antenna because it has a main lobe normal to the substrate and its wide ground plane makes the microfabrication process easy. We have fabricated thin-film slot array antennas for 94GHz, 700GHz, 2.5THz and 28THz radiation, and have investigated the receiving properties of the antennas at the frequencies. Figure 1 shows a fabricated 4-array antennas for 700GHz radiation, as an example.

Regarding the detectors, we have fabricated antenna coupled pin-hole type and edge type warm carrier devices which have a contact area less than  $8 \times 10^{-10} \text{cm}^2$ , and detection properties have been investigated at 94GHz, 700GHz and 28THz. In Fig. 2, an edge type warm carrier device is shown.

At the conference, I will discuss the trends of thin-film antennas and detectors for far-infrared radiation.

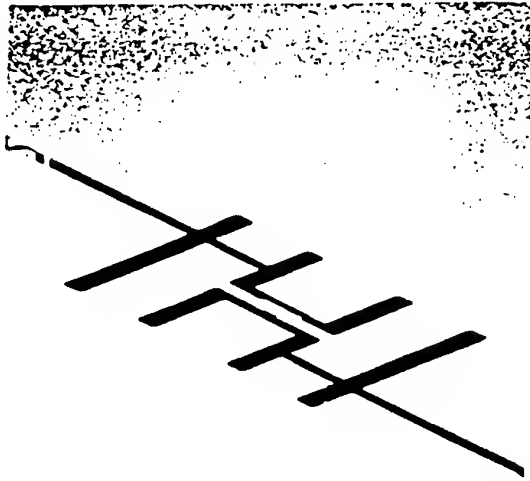


Fig.1. SEM photograph of a fabricated 4-slot array antenna for 700GHz radiation.

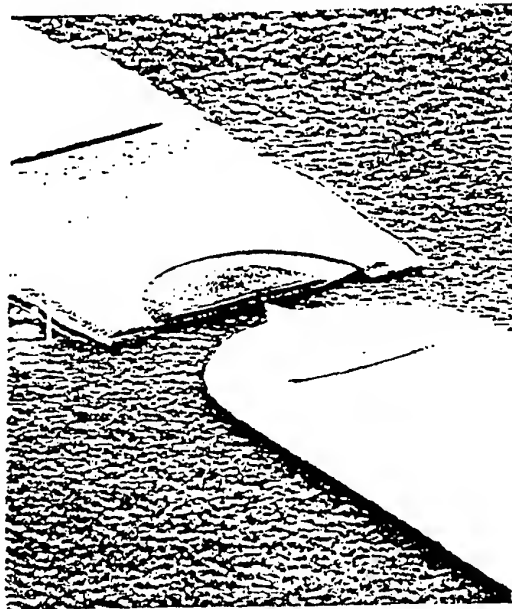


Fig.2. SEM photograph of a fabricated edge type thin-film warm carrier device for 700 GHz radiation.

## Transverse Seebeck-effect in a tilted two metals multilayer structure

Th. Zahner and H. Lengfellner

*Institut für Experimentelle und Angewandte Physik, Universität Regensburg, 93040 Regensburg, Germany*

Thermoelectric fields transverse to an applied temperature gradient have been observed in a tilted metallic multilayer structure, prepared by sintering of a compressed stack of copper/constantan foils. These structures represent a new class of thermoelectric devices, applications for detection of light are demonstrated.

### Introduction

Normal state  $\text{YBa}_2\text{Cu}_3\text{O}_{7.8}$  and  $\text{Bi}_2\text{Sr}_2\text{CaCu}_2\text{O}_8$  thin films, oriented grown off-c-axis generate a thermoelectric response due to the transverse Seebeck-effect, and applications for detection of pulsed and continuous laser radiation have been reported [1,2]. As this effect occurs in these materials because of their thermoelectric anisotropy, the question arises, if such thermoelectric anisotropy can also be obtained by artificial creation of tilted layered materials. In this paper we report on first investigations of the transverse thermoelectric response of a tilted multilayer structure made with the metals copper and constantan.

According to the tensorial description of the Seebeck-effect, the electric field  $\mathbf{E}$  due to a temperature gradient  $\nabla T$  in a material is given by  $\mathbf{E} = \mathbf{S} \cdot \nabla T$ , where  $\mathbf{S}$  is the Seebeck tensor.

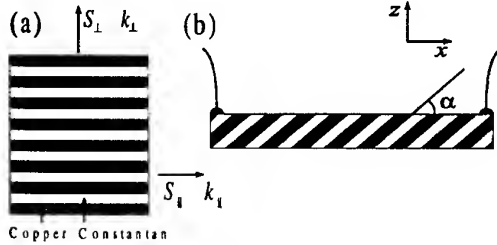


Fig. 1: (a) Multilayer stack with „in-plane“  $S_{\parallel}$ ,  $k_{\parallel}$  and „out-of-plane“  $S_{\perp}$ ,  $k_{\perp}$  transport properties and (b) sample with tilt angle  $\alpha$

For materials of tetragonal symmetry and the coordinate system of Fig. 1b, where  $\alpha$  is the tilt angle between the „in-plane“-direction of the material and the surface of the sample,  $\mathbf{S}$  has the form

$$\mathbf{S} = \begin{pmatrix} S_{\parallel} \cos^2 \alpha + S_{\perp} \sin^2 \alpha & 0 & \frac{1}{2} \sin(2\alpha)(S_{\parallel} - S_{\perp}) \\ 0 & S_{\parallel} & 0 \\ \frac{1}{2} \sin(2\alpha)(S_{\parallel} - S_{\perp}) & 0 & S_{\parallel} \sin^2 \alpha + S_{\perp} \cos^2 \alpha \end{pmatrix}$$

Here

$$S_{\parallel} = \frac{1}{\sigma_{\text{Cu}} + \sigma_{\text{Const}}} (\sigma_{\text{Cu}} S_{\text{Cu}} + \sigma_{\text{Const}} S_{\text{Const}}) = 0.4 \frac{\mu\text{V}}{\text{K}},$$

$$S_{\perp} = \frac{1}{R_{\text{Cu}} + R_{\text{Const}}} (R_{\text{Cu}} S_{\text{Cu}} + R_{\text{Const}} S_{\text{Const}}) = -35 \frac{\mu\text{V}}{\text{K}}$$

are the absolute thermopowers (Fig. 1a) of the multilayer cube, derived by calculating the absolute

thermopowers of copper and constantan in parallel or in series [3], with  $S_{\text{Cu}} = 1.7 \frac{\mu\text{V}}{\text{K}}$ ,  $S_{\text{Const}} = -37 \frac{\mu\text{V}}{\text{K}}$  the thermopowers,  $R_{\text{Cu}} = 0.25 \frac{\text{cm}^2\text{K}}{\text{W}}$ ,  $R_{\text{Const}} = 5.1 \cdot 10^5 \frac{\text{cm}^2\text{K}}{\text{W}}$  the thermal resistances and  $\sigma_{\text{Cu}} = 5.9 \cdot 10^5 \frac{1}{\Omega\text{cm}}$ ,  $\sigma_{\text{Const}} = 0.2 \cdot 10^5 \frac{1}{\Omega\text{cm}}$  the conductivities of copper (Cu) and constantan (Const) [4].

A temperature gradient  $\nabla T$  along the  $z$ -axis (Fig. 1b) therefore generates a transverse thermoelectric field  $E = \frac{1}{2} \sin(2\alpha)(S_{\parallel} - S_{\perp}) \cdot \nabla_z T$  in  $x$ -direction and by heating over a length  $l$  a thermoelectric voltage

$$U = \frac{1}{2} \sin(2\alpha)(S_{\parallel} - S_{\perp}) \cdot \nabla_z T \cdot l \quad (1)$$

is obtained at the electrical contacts.  $\nabla_z T$  can be deduced from the heat flow equation

$$Q = k_z \cdot \nabla_z T \quad (2)$$

where  $Q$  is the absorbed flux of heat and

$$k_z = k_{\parallel} \sin^2 \alpha + k_{\perp} \cos^2 \alpha \quad (3)$$

is the thermal conductivity in  $z$ -direction. Here,

$$k_{\parallel} = \frac{1}{2} (k_{\text{Cu}} + k_{\text{Const}}) = 2.1 \frac{\text{W}}{\text{cmK}},$$

$$k_{\perp} = 2 \frac{k_{\text{Cu}} \cdot k_{\text{Const}}}{k_{\text{Cu}} + k_{\text{Const}}} = 0.4 \frac{\text{W}}{\text{cmK}}$$

are the thermal conductivities of the multilayer stack (Fig. 1a), with  $k_{\text{Cu}} = 4 \frac{\text{W}}{\text{cmK}}$  and  $k_{\text{Const}} = 0.2 \frac{\text{W}}{\text{cmK}}$  the thermal conductivities of copper and constantan [4].

### Experiments

A multilayer structure was prepared by sintering of a compressed stack of copper/constantan foils of 0.1 mm thickness (Fig. 1a). Sintering was accomplished at 950 °C within 1 h, in a tube furnace flushed by argon gas to prevent oxidation. Samples were obtained by cutting the sintered stack obliquely to its axis. Thus samples with various tilt angles  $\alpha$  (Fig. 1b) and thickness of 10  $\mu\text{m}$  - 2 mm were prepared.

First experiments have been performed with a sample shown in Fig. 1b, with length 8 mm between contacts, width 6 mm, thickness  $d = 2$  mm and tilt angle  $\alpha = 15^\circ$ . Sample heating has been accomplished by diode laser irradiation  $\lambda = 689$  nm,  $P = 10$  mW of the sample surface, which was blackened to improve absorption. The sample was bonded onto a metal

support serving as a heat sink. A thermoelectric signal obtained from this arrangement is shown in Fig. 2. At  $t = 0$  the diode laser is switched on, the thermoelectric signal rises within  $\approx 0.1$  s to a voltage of 150 nV and then decreases to zero when the laser is switched off.

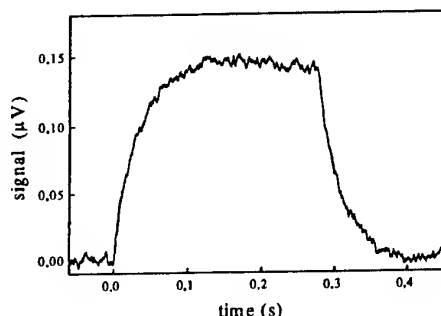


Fig. 2: Signal obtained by  $Q = 10 \frac{\text{mW}}{\text{cm}^2}$  diode laser irradiation from a  $\alpha = 15^\circ$  sample.

With Eqs. (1-3),  $Q = 10 \frac{\text{mW}}{\text{cm}^2}$  and  $l = 0.8$  cm a signal of 180 nV is estimated, well comparing with the measurement. The observed rise- and fall-time of the thermoelectric response is given by the time necessary to establish a temperature gradient within the sample. As the heat propagates by diffusion, this time is governed by the heat diffusion time  $\tau_{\text{diff}} = \frac{l^2}{D_z} \approx 0.2$  s, where the thermal diffusion constant in  $z$ -direction  $D_z = \frac{k_z}{c \cdot \rho}$  is estimated using  $k_z(\alpha = 15^\circ)$ , the specific heat  $c = \frac{1}{2}(c_{\text{Cu}} + c_{\text{Const}})$  and the density  $\rho = \frac{1}{2}(\rho_{\text{Cu}} + \rho_{\text{Const}})$  of the sample ( $c_{\text{Cu}} = 0.38 \frac{\text{J}}{\text{g} \cdot \text{K}}$ ,  $c_{\text{Const}} = 0.41 \frac{\text{J}}{\text{g} \cdot \text{K}}$ ,  $\rho_{\text{Cu}} = 8.96 \frac{\text{g}}{\text{cm}^3}$ ,  $\rho_{\text{Const}} = 8.90 \frac{\text{g}}{\text{cm}^3}$  [4]).

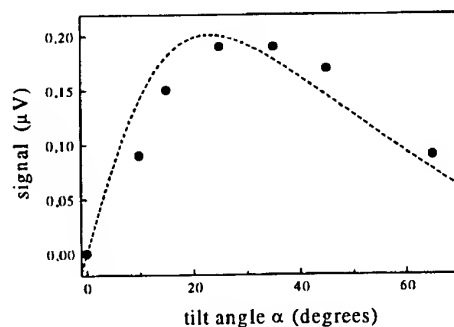


Fig. 3: Signal in dependence of tilt angle for constant irradiation density. Dashed line is calculated, see text.

The thermoelectric signal, obtained by laser irradiation ( $Q = 10 \frac{\text{W}}{\text{cm}^2}$ ,  $l = 0.8$  cm) of several samples with different tilt angles  $\alpha$  is shown in Fig. 3. The drawn curve is calculated using Eqs. (1-3), giving a tilt

angle dependence of  $U \propto \frac{\sin(2\alpha)}{k_1 \sin^2 \alpha + k_2 \cos^2 \alpha}$  in good agreement with the experiment.

To shorten the response time, a sample with tilt angle  $\alpha = 35^\circ$  was thinned to a thickness of 10  $\mu\text{m}$ . A thermoelectric signal obtained upon irradiation with a Nd:YAG laser pulse ( $\lambda = 1064$  nm, pulse duration  $\approx 15$  ns, pulse intensity  $E_{\text{pulse}} = 0.5 \frac{\text{mJ}}{\text{cm}^2}$ ) shows a decay time of  $\approx 1$   $\mu\text{s}$  and a signal height of about 1 mV (Fig. 4). Again, the decay time is consistent with the diffusion time, and the signal height can be estimated from  $\nabla_z T \approx \frac{E_{\text{pulse}}}{\tau_{\text{diff}} \cdot k_z} = 150 \frac{\text{K}}{\text{cm}}$  to be  $U \approx 1$  mV.

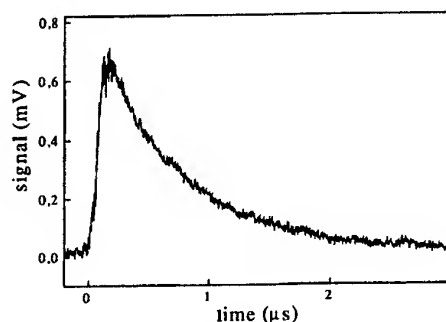


Fig. 4: Signal of a 10  $\mu\text{m}$  thick sample upon irradiation with a Nd:YAG laser pulse.

### Summary

The experiments show that artificially created tilted metallic multilayer structures show an off-diagonal Seebeck-effect in close analogy to the off-diagonal Seebeck-effect observed in tilted  $\text{YBa}_2\text{Cu}_3\text{O}_{7-\delta}$  and  $\text{Bi}_2\text{Sr}_2\text{CaCu}_2\text{O}_8$  superconductor films in the normal state. Tilted multilayer structures may therefore be useful as a new class of thermoelectric devices based on off-diagonal thermoelectricity. As an application, we described the use of a copper/constantan multilayer structure for detection of laser radiation.

\*\*\*

Financial support by the Deutsche Forschungsgemeinschaft (DFG) (H.L.) and the Bayerisches Staatsministerium für Unterricht, Kultus, Wissenschaft und Kunst (Th.Z.) is gratefully acknowledged.

### References

- 1 S. Zeuner, W. Prettl, and H. Lengfellner, Appl. Phys. Lett. 66(14), 1833 (1995).
- 2 Th. Zahner, R. Schreiner, R. Stierstorfer, O. Kus, S.T. Li, R. Rössler, J.D. Pedarnig, D. Bäuerle, and H. Lengfellner, Europhys. Lett. 40(6), 673 (1997).
- 3 D.K.C. MacDonald, *Thermoelectricity: An introduction to the Principles* (Wiley, New York, 1962).
- 4 Landolt-Börnstein, *physikalisch-chemische Tabellen* (Springer, Berlin, 1992).

## Fields in the image space of symmetrical focusing lens

W.B. Dou Z.L. Sun X.Q. Tan Z.G. Wang

State Key Lab of Millimeter Waves  
Dept. of Radio Engr., Southeast University  
Nanjing, 210096, P.R. China

### ABSTRACT

The fields refracted by circular symmetric hyperbolic lens illuminated by a linearly polarized wave incident obliquely on the aperture are calculated from the induced surface currents. The image structures for different focal ratio are compared with the classical Airy pattern, deduced by scalar analysis, of optical focusing systems.

### 1. INTRODUCTION

Millimeter wave imaging now attracts more attentions. One approach is focal plane imaging system. Focal plane array technology has been adopted as design approach for imaging systems in the 2 mm to 3mm wavelength range<sup>1</sup>. However, the limited volume available restricts  $f/D$  for lens systems to values  $\leq 1.25$ , which seriously restricts imaging capability. To evaluate the imaging performance it is necessary to get the field distribution in the focal plane of a focusing lens. It is useful for selecting the feed element, evaluating the packing efficiency and coupling between lens and feed element. The usual optical analysis of the focal region is inadequate for investigating this possibility. Airy's well-known equation  $2J_1(u)/u$ , for the amplitude distribution in the focal plane of a circular lens, is valid only for the large focal ratios  $f/D$  common in optical systems. Although both amplitude and phase near the focus of a lens have been studied extensively at both optical and microwave frequencies, the scalar-wave theory used gives no information on the detailed configuration of the electromagnetic fields in the image. A vector solution is therefore sought for the fields in the focal region of a lens.

### 2. ANALYSIS

The configuration to be analyzed is shown in Fig.1. A linearly polarized wave is incident obliquely on the surface  $S_2$ . Using the ray tracing method the fields on surface  $S_2$  can be gotten. Then the fields in the focal plane are calculated by following equation<sup>2</sup>

$$\vec{E}_p = -\frac{j}{4\pi\omega\epsilon} \int_s [(\vec{J} \cdot \nabla) \nabla + k^2 \vec{J} - j\omega\epsilon \vec{J}_m \times \nabla] \frac{\exp(-jk r_s)}{r_s} ds \quad (1)$$

where  $r_s$  is the distance between source point and field point.  $\vec{J}$  and  $\vec{J}_m$  are given by

$$\vec{J} = \vec{n} \times \vec{H}, \quad \vec{J}_m = -\vec{n} \times \vec{E} \quad (2)$$

where  $\vec{H}$  and  $\vec{E}$  are the fields on the surface  $S_2$  of the lens. It is assumed that the polarization of

incident wave is in X-Z plane. If the polarization is in Y-Z plane, similar results also can be obtained.

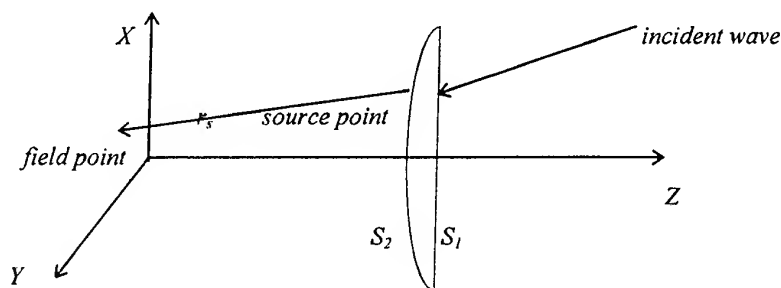


Fig.1 Geometry of symmetric focusing lens

Vectorial equation (1) can be decomposed to three scalar equations for  $E_x$ ,  $E_y$  and  $E_z$ , respectively. Then integration surface is divided to many small areas, doing integration to each area and adding up all the contributions of every area the fields in focal plane can be obtained. It can be seen from calculations:

1. The fields in the axial region of focal plane are almost same as the fields in the aperture of corrugated horn under balanced hybrid conditions.
2. The calculated image structures for different focal ratio ( $f/D$  is equal to 1.0, 1.3, 1.75 respectively) are different to some extent from the classical Airy pattern. Its shape is wider than the Airy pattern and gradually close to the Airy pattern with  $f/D$  increasing.
3. For the considered situation here,  $E_y$  and  $E_z$  are small compared to the  $E_x$ .

### 3.CONCLUSION

The field distribution in the focal plane of a symmetrical hyperbolic lens is calculated by a well-known electromagnetic field formula. They provide much information which is useful for selecting the feed element, evaluating the packing efficiency and coupling between lens and feed element. It is also useful for the design of multiple beam antenna in communication systems.

### 4.REFERENCES

1. P.F. Goldsmith, et al, "Focal Plane Imaging Systems for Millimeter Wavelength", *IEEE Trans.*, MTT-41, No.10, pp.1664-1676, 1993.
2. S. Silver, "Microwave Antenna Theory and Design", *IEE Series on Electromagnetic Waves*, No.19, 1984.
- [3] S. D. Gray, "A Nulling Performance Comparison Between a Single- and Multiple-Aperture Multiple-Beam Antenna", *IEEE Trans.*, AP-43, No.11, pp.1319-1324, 1995.

# HTS MICROSTRIP ANTENNAS CHARACTERIZED AND ANALYZED BY A HIGHER ACCURATE METHOD IN THE FTD

Geraldo F. da Silveira Filho and Humberto C.C. Fernandes

Department of Electrical Engineering - Technological Center  
Federal University of Rio Grande do Norte,  
P. O. Box 1583 - Tel/Fax: +55 84 2153731 - E-mail: humbeccf@ct.ufrn.br  
59.072-970 - Natal/RN - Brazil

**Abstract** - A more accurate analysis and design for HTc superconducting microstrip patch antenna is presented in this work. The concise Transverse Transmission Line (TTL) method in the Fourier Transform Domain (FTD) along with the Transmission Line Model are applied. Since the TTL is a full wave method and very much suitable on microwave and millimeter-wave components study, it gives accurate effective dielectric constant which contributes definitively to obtain all others antenna parameters with higher precision such as length, efficiency, bandwidth, quality factor, radiation patterns.

## I. INTRODUCTION

Modern societies depend principally on an efficient communication system, capable to transmit, receive and handle information with reliability, precision and each time faster. As a consequence, devices and equipments are required to supply those needs, and must conciliate lightweight, to be highly efficient with low cost and reduced dimensions.

HTS Microstrip patch antenna holds these characteristics, can be used in many applications over the broad frequency range from microwave to millimeter-wave and HTS antenna shows a substantial improvement over an identical antenna made with normal metals, with a higher gain and radiation efficiency [1], especially when the number of radiating elements increases, due to superconducting thin-films have quite lower microwave surface resistance ( $R_s$ ) compared to normal conducting films [2].

The applied theories are the Transverse Transmission Line (TTL) method [3] in conjunction with the theory of the rectangular-patch antenna [4] to design and analyze the related antenna. Various applications using the rigorous TTL method has been presented by H. C. C. Fernandes et al. [3],[5]. This complete and efficient method provides appropriate analysis for various others planar structures, giving precise effective dielectric constant ( $\epsilon_{eff}$ ) for these structures, which is quite important to design and to calculate antenna parameters with accuracy.

## II. THEORY - TTL METHOD

Considering the microstrip patch antenna, as a session of a microstrip line, a set of equations that represent the electromagnetic fields in the  $x$  and  $z$  direction as function of the electric field in the  $y$  direction are obtained applying the TTL method. Starting from the Maxwell's equations, two components can be used to represent the electric and magnetic fields: the transverse ( $y$ ) and tangential ( $t = x$  and  $z$ ) components to the patch antenna and after various algebraic manipulations the general equations for the structure in the FTD is obtained, for example, for the  $x$  direction:

$$\tilde{E}_{xi} = \frac{-j}{k_i^2 + \gamma_i^2} \left( \alpha_n \frac{\partial}{\partial y} \tilde{E}_y + \omega \mu_o \Gamma \tilde{H}_y \right) \quad (1) \quad \tilde{H}_{xi} = \frac{-j}{k_i^2 + \gamma_i^2} \left( \alpha_n \frac{\partial}{\partial y} \tilde{H}_y + \omega \epsilon_i \Gamma \tilde{E}_y \right) \quad (2)$$

where  $\gamma^2 + k^2 = \alpha_i^2 - \Gamma^2$  and  $\alpha_i$  is the spectral variable.

After the application of the boundary conditions, the Moment method is used to eliminate the electric fields and to obtain the homogeneous matrix equation for the calculation of the complex propagation constant. The roots of this matrix are the attenuation constant ( $\alpha$ ) and phase constant ( $\beta$ ). The effective dielectric constant is obtained from  $\epsilon_{eff} = (\beta/k_0)^2$ , where  $k_0$  is the free space wave number.

## III. RESULTS

The results, including design parameters, efficiency, bandwidth, quality factor and radiation patterns are shown, demonstrating the accuracy of the superconducting microstrip patch antenna parameters due to the dynamic method application, are presented in Figs. 3 and 4.



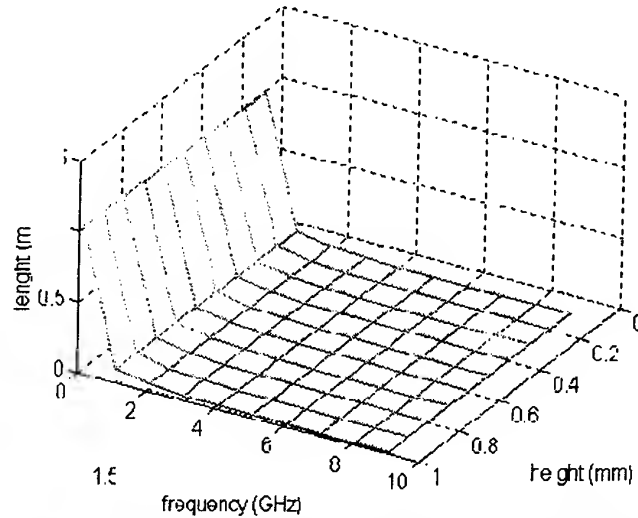


Fig. 3. Element length comparison between HTS antenna (red) and metallic patch radiator (green). Details:  $W=9.8$  mm,  $\epsilon_r = 2.32$ , natural scale.

#### IV. CONCLUSION

The rectangular patch antenna was analyzed using The TTL Method. Results for the patch antenna design and bandwidth were presented, confirming the exactness of the TTL method applied. A more accurate value of the effective permittivity gives a better value for the element length which contributes definitively to all others parameters. To sum up, The Transverse Transmission Line - TTL is an efficient and accurate method for rectangular microstrip antenna patch analysis and design. This is a very versatile method that can be used with a lossless or semiconductor substrate in various planar structures. This work was supported by CNPq and CAPES.

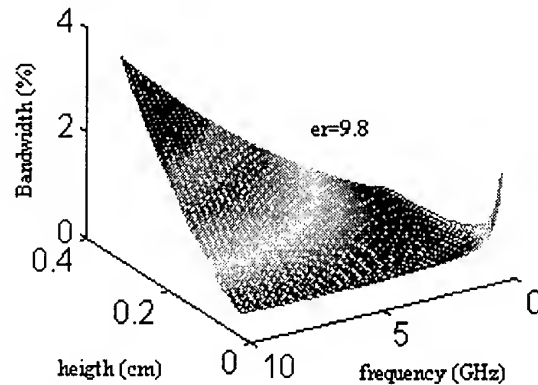


Fig. 4. 3-D presentation of bandwidth as functions of frequency and height.

#### V. REFERENCES

1. H. C. C. Fernandes and Geraldo F. da S. Filho, "Recent Advances on Superconducting Microstrip Patch Antennas", *Progress in Electromagnetics Research Symposium - PIERS*, Julho 1998.
2. M.A.Richard, K.B.Bhasin, P.C.Claspy, "Superconducting Microstrip Antennas: An Experimental Comparison of two Feeding Methods", *IEEE Trans. on Antennas and Propagation*, Vol.41, No.7, pp.967-974, July 1993.
3. H. C. C Fernandes, "Attenuation And Propagation In Various Finline Structures", *International Journal of Infrared and Millimeter Waves*, Vol. 17, N° 08, pp. 1419-1430, Aug. 1996.
4. I.J. Bahl and P. Bhartia, "Microstrip Antennas", Artech House, 1980.
5. H. C. C. Fernandes, A. J. Giarola and D. A. Rogers, "PACMO: A Comprehensive CAD Package for Microwave Devices", *IEEE Transactions on Education*, Vol. E-26, No. 4, pp. 162- 164, Nov. 1983.
6. S. A. Bokhari, Jean-François Z., J. R. Mosig and F.E.Gardiol, "A Small Microstrip Patch Antenna with a Convenient Tuning Option", *IEEE Trans. on Antennas Propagation*, Vol. 44, No. 11, pp.1521-1528, Nov. 1996.

## Quasi-Optic Components in Oversized Corrugated Waveguide for Millimeter-Wave Transmission Systems

John L. Doane, Hiro Ikezi and Charles Moeller

General Atomics, P.O. Box 85608, San Diego CA 92186-5608

### INTRODUCTION

Propagation of the  $HE_{11}$  mode in corrugated waveguide is attractive for low-loss transmission. This mode has a well-defined polarization that is independent of transverse position across any waveguide cross section. Diffraction effects at discontinuities are small, because the field is very small at the waveguide walls. In oversized waveguide, the longitudinal field components are also small everywhere. Hence in many situations the  $HE_{11}$  mode behaves like a plane wave.

Quasi-optical components based on plane wave designs have been designed and successfully implemented in oversized corrugated waveguides. We describe below components based on miter bend mirrors, grid polarizers, and plastic films.

### COMPONENTS BASED ON MITER BENDS

A simple broadband polarization rotator is a useful component for rotating the  $HE_{11}$  mode polarization by any angle. It consists of an ordinary  $90^\circ$  miter bend between two  $135^\circ$  miter bends. The polarization is rotated by two times the angle between the incidence polarization and the plane of the miter bends. Figure 1 shows the measurement setup with a  $90^\circ$  polarization rotation in 63.5 mm corrugated waveguide. At both ends of the polarization rotator in Fig. 1 are broadband transitions from WR8 waveguide to 63.5 mm corrugated waveguide. In the broadband transitions, a taper and horn are attached to a miter bend with a paraboloidal mirror. The radiation patterns from one of these transitions measured at 110 and 165 GHz were in close agreement with the theoretical  $HE_{11}$  patterns. The total insertion loss of two transitions in series was about 1 dB at both frequencies, in agreement with the expected 10% loss per transition.

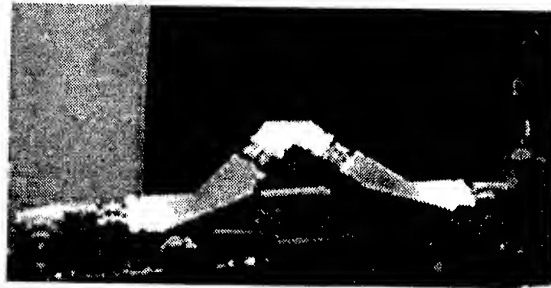


Fig. 1. Broadband polarization rotator in 63.5 mm waveguide.

Polarizing miter bends using grooved mirrors have been described earlier [1]. Since then, similar polarizers have been made in 31.75 mm and 88.9 mm waveguide miter bends for use near 84, 110, and 168 GHz. Sinusoidal grooves are used when there is concern over field enhancement at high power. Some of these polarizers allow remote control of the polarization even when the waveguide is evacuated. Simple circular polarizers were made for 60 GHz in 63.5 mm waveguide miter bends with fixed mirrors. Circular polarization is desirable for transmission through rotary joints, for example.

By using grooved mirrors above the frequency where Bragg diffraction may occur, we can make low pass filters such as those previously made for rectangular waveguide [2,3]. The best performance is obtained when the electric field is in the plane of the miter bend. Using theory for sinusoidal shaped grooves [4], we found that excellent low pass filters could be made. Figure 2 shows the response measured with a scanning Michelson interferometer for one of these filters in 63.5 mm waveguide. The vertical line shows the designed cutoff frequency of 168 GHz. The measured structure was in agreement with theory except for the peak near 200 GHz. This peak was found to be an artifact of the measurement due to Bragg diffraction occurring at 180 degrees to the ray incident on the mirror.

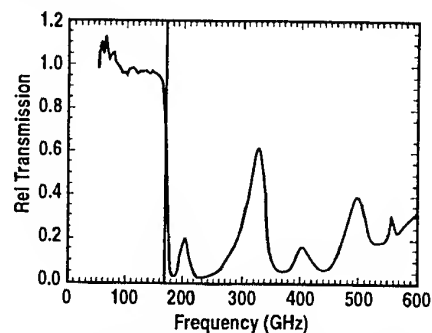


Fig. 2. Transmission through 63.5 mm miter bend low pass filter as measured by Michelson interferometer.

### COMPONENTS BASED ON GRID POLARIZERS

Standard free space grid polarizers consist of either parallel gold lines photolithographically deposited on Mylar® film or of parallel stretched thin wires. Figure 3 shows such a polarizer that can be rotated between two back-to-back miter bends (the broadband transitions seen in Fig. 1 are also visible in this figure). An absorber is glued to a metal cap on the unused miter bend port. This device can be used as a polarization diplexer, or as a variable beam combiner and splitter.

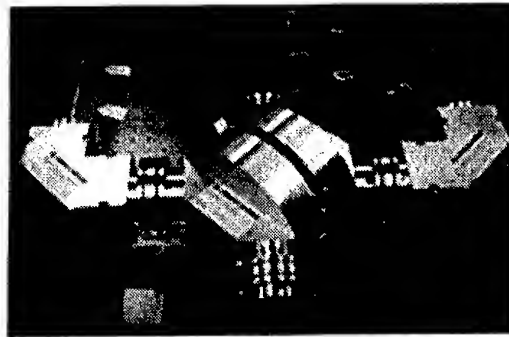


Fig. 3. Measurement of 63.5 mm variable beam combiner with rotatable grid polarizer.

In addition, polarization filters can be made by grid polarizers that are inserted between two corrugated waveguides. The polarization parallel to the grid is reflected. We have made remotely controllable rotatable filters of this type.

### COMPONENTS BASED ON PLASTIC FILMS

To evaluate various plastics, we pressed films of the same type together to make a total thickness of 2.2 mm. Broadband measurements made with the Michelson interferometer showed that capacitor grade polypropylene and polystyrene had much less loss than Mylar® (see Fig. 4).

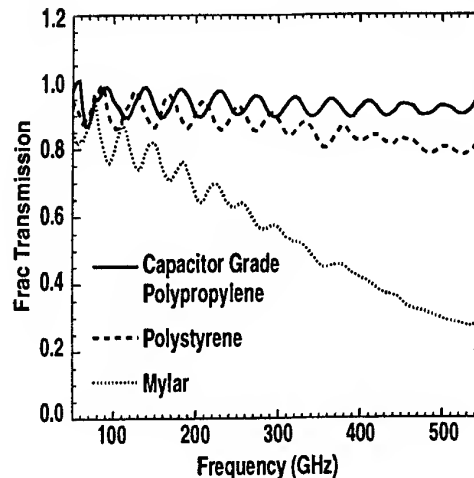


Fig. 4. Transmission through 2.2 mm thick stacks of various plastic films. The individual film thicknesses were 12.7  $\mu\text{m}$ , 25  $\mu\text{m}$  and 31.75  $\mu\text{m}$  for the Mylar®, polypropylene, and polystyrene, respectively.

Using closely spaced parallel films of 32  $\mu\text{m}$  thick polystyrene, artificially birefringent structures were made with low reflections. One such device is a polarimeter to determine the wave polarization [5]. Each time the polarimeter is rotated, two measurements of the polarization can be obtained by analysis of the power received in a horn placed behind the rotating films. Rotational speeds up to 20 rotations per second are used. The measurements can be averaged to remove noise even in low power measurements.

The polarimeter was attached to the rear of a high power 31.75 mm miter bend whose mirror was made of high thermal conductivity diamond coated with suitable metallic and resistive layers. This mirror coupled a small amount of the power from the high power waveguide to the polarimeter. Representative measurements are shown in Fig. 5 for the polarization from a high power polarizing miter bend as a function of rotation angle of the grooved mirror. The theoretical polarizations are shown by the solid line and the polarimeter measurements are shown as points.

Another artificially birefringent device with the polystyrene film is used as a remotely controllable polarization rotator for 60 GHz in 63.5 mm waveguide. The total differential phase shift between the polarizations parallel and perpendicular to the films was adjusted to 90°. In combination with a fixed miter bend circular polarizer, this device produces an output polarized at 45° to the film direction.

Bragg reflection notch filters were made by using 150 to 200 periodically spaced polypropylene films each 25  $\mu\text{m}$  thick. The films were spaced by thin rings of corrugated waveguide machined precisely to the same thickness. A narrowband measurement of such a notch filter is shown in Fig. 6. Other similar filters exhibited nearly 40 dB notches near 82.6 and 84 GHz. Broadband measurements with the Michelson interferometer showed low loss between the high loss harmonics.

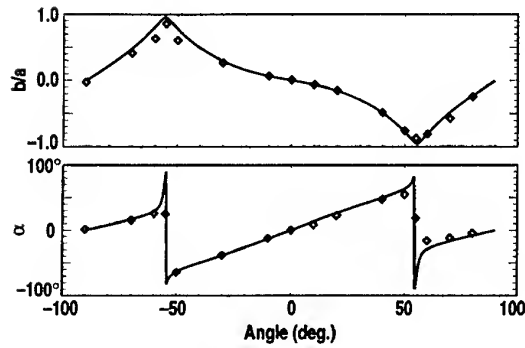


Fig. 5. Polarization parameters as a function of rotation angle of the mirror in a polarizing miter bend, as measured at 110 GHz at low power by a spinning polarimeter. The ellipticity  $b/a$  is the ratio of the minor and major axes, and  $\alpha$  is the orientation angle of the major axis.

#### ACKNOWLEDGMENT

Measurements shown in Figs. 2 and 4 were made by Max Austin of the University of Texas using the DIII-D scanning Michelson interferometer developed by the University of Maryland. This work was supported by General Atomics and the U.S. Department of Energy under Contract No. DE-AC03-89ER51114.

#### REFERENCES

- [1] J.L. Doane, *Int. J. Infrared MM Waves*, **13**, 1727 (1992).
- [2] G.D. Tait, 5th Int'l Conf. Infrared MM Waves, Wurzburg, paper T4-8 (1980).
- [3] A. Cavallo and R. Cutler, *Rev. Sci. Instrum.*, **56**, 931 (1985).
- [4] G. Whitman and F. Schwering, *IEEE Trans. Antennas Prop.*, AP-25, 869 (1977).
- [5] H. Ikezi, C.P. Moeller, J.L. Doane, et al., "Millimeter Wave Polarimeter," submitted to *Rev. Sci. Instr.* 1998.

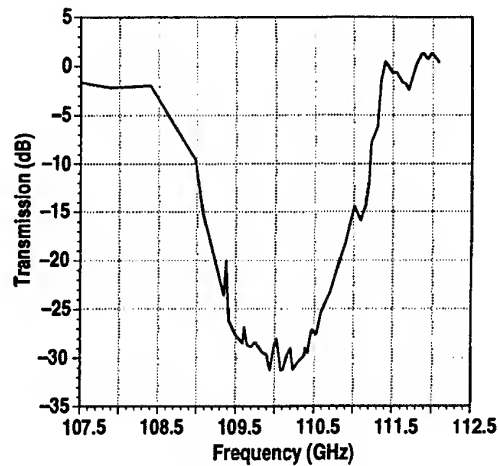


Fig. 6. Transmission through a 110 GHz Bragg reflection notch filter in 63.5 mm waveguide. Data were taken point-by-point. Baseline (reference) signal with no notch filter was manually subtracted.

## CVD DIAMOND WINDOWS FOR HIGH POWER GYROTRONS

R. Heidinger<sup>1)</sup>, R. Spörl<sup>1)</sup>, M. Thumm<sup>2)</sup>, J.R. Brandon<sup>3)</sup>, R.S. Sussmann<sup>3)</sup>, C.N. Dodge<sup>4)</sup>

<sup>1)</sup> Forschungszentrum Karlsruhe, Association FZK- Euratom, Institut für Materialforschung I,  
Postfach 3640, D-76021 Karlsruhe, Germany

<sup>2)</sup> Forschungszentrum Karlsruhe, Association FZK- Euratom, Institut für Technische Physik,  
and University Karlsruhe, Institut für Höchstfrequenztechnik und Elektronik  
Postfach 3640, D-76021 Karlsruhe, Germany

<sup>3)</sup> DeBeers Industrial Diamond Div., Charters, Ascot, SL59PX, UK

<sup>4)</sup> Diamanx Products Ltd., Freeport, P.O. Box 6, Ballasalla, Isle of Man, IM996AQ, UK

### Abstract

The recent development of large size CVD diamond wafers with low mm-wave losses has enabled the manufacture of output windows for Megawatt gyrotrons. The progress in the window development is illustrated with a 100 mm dia. x 1.6 mm thick window disc mounted on double metal cuffs with a UHV compatible diffusion bond. In the disc, excellent properties ( $\tan\delta < 10^{-5}$ , good homogeneity) were established. Further up-scaling potential is demonstrated with a 120 mm dia. x 2.2 mm CVD diamond window disc.

### Introduction

The challenge of realising output windows for high power gyrotrons that generate in continuous wave (CW) operation power levels of at least 1 MW has called for extensive materials development and window design activities in the recent years. In the search to overcome the limitations for transmissible mm-wave power for Electron Cyclotron (EC) wave systems, which are projected to serve in the next step fusion machines at frequencies between 90 GHz and 170 GHz, a number of different window designs have been developed based on sapphire (cryogenically N<sub>2</sub> or Ne cooled), high resistivity grades of silicon (CO<sub>2</sub> gas pressure cooled) or boron nitride (water cooled, restricted to EC wave pulses).

As excellent resistance against thermal crack formation is one of the major materials performance criteria [1], diamond received particular attention when the possibility of manufacture of large size diamond plates by the Chemical Vapour Deposition (CVD) process was demonstrated. Apart from the outstanding thermal and mechanical parameters, low levels of mm-wave absorption which is parameterised by the dielectric loss tangent ( $\tan\delta$ ) must be attained. The first experience with early CVD diamond material, often 'black grades', was rather discouraging, as  $\tan\delta$  levels were prohibitively high ranging between  $10^{-3}$  and  $10^{-2}$  in the interesting frequency range [2,3]. Progress in material development became substantial, after special 'white' grades were identified which showed  $\tan\delta$  levels below  $10^{-4}$  [3,4] and thus became competitive to Sapphire. When the first full size windows were produced successfully with losses in the range of  $10^{-4}$ , it became evident that inhomogeneities in mm-wave absorption along the disc axis, as well as in the radial direction, were of concern [5]. In the present paper, window material from further refined CVD diamond grades is presented which combine good homogeneity with very low  $\tan\delta$  level and which can be mounted into window structures which opens a new horizon for high power gyrotrons.

### Characteristics of the window material

The new types of CVD diamond material were studied in form of two large discs. The first one was produced to serve as 'standard window type' with 4 inch diameter with actual geometries of 100 mm x 1.6 mm. It was given the internal name 'Super-FZK', in continuation of a series of names starting with the 'FZK' disc presented previously [5]. The second one was produced to investigate and to demonstrate the growth process adopted for even more extended window geometries, such as for Brewster windows. This disc was denominated 'Star of FZK', its dimensions are 120 mm x 2.2 mm. The older 'FZK' disc which will serve as a reference component in this paper had the size of 105 mm x 2.2 mm.

All three discs were produced using the microwave plasma assisted CVD (MPACVD) technique [6]. Reactor geometry and processes were developed specially for the synthesis of large diameter, high quality diamond discs. Following synthesis, material was removed from both growth and nucleation surfaces by lapping to achieve a thickness tolerance better than  $\pm 20 \mu\text{m}$  and surface Ra values less than 200 nm.

### Dielectric measurements

For the measurements of mm-wave properties, two different set-ups were used which determined the permittivity ( $\epsilon_r$ ) and the dielectric loss tangent at 145 GHz based on the open resonator technique with a quasi-hemispherical resonator geometry. The temperature dependent data were obtained with a fixed mirror system installed in a liquid flow cryostat, spatially resolved measurements (line scans, mapping) were obtained with a new system where the specimen can be shifted together with the plane mirror over the mm-wave beam by computer driven positioning devices. Details on both measuring facilities and their resolution has been published recently elsewhere [7].

The temperature dependent measurements between 70 K and 370 K showed for all three discs no significant changes with temperature. Whereas no difference occurred in the permittivity, which amounted to  $\epsilon_r = 5.67 (\pm 0.01)$ , striking reductions in  $\tan\delta$  of more than one order of magnitude could be observed for the two new discs. The increased scattering in loss tangent data for the 'Super-FZK' window disc was due to the fact, that material came close to a perfect ultralow loss dielectric. Here the lowest loss tangent so far reported for a CVD diamond material at 145 GHz (300 K) was obtained with  $\tan\delta = 6 (\pm 2) \cdot 10^{-6}$ . Even in the large 'Star of FZK' losses hardly exceeded  $2 \cdot 10^{-5}$ .

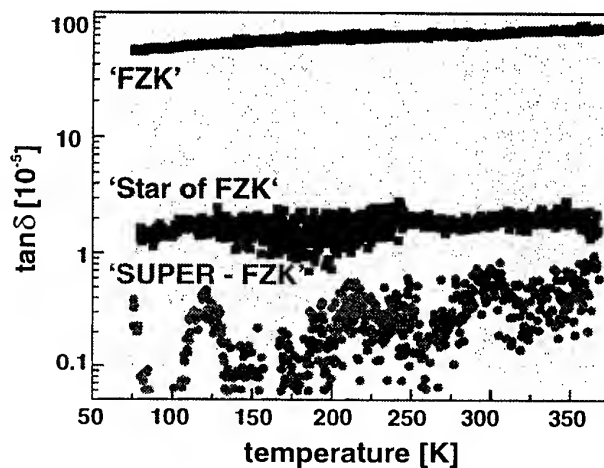


Fig. 1 Temperature dependence of  $\tan\delta$  at 145 GHz for the 'FZK', 'Star of FZK' and 'Super-FZK' window discs.

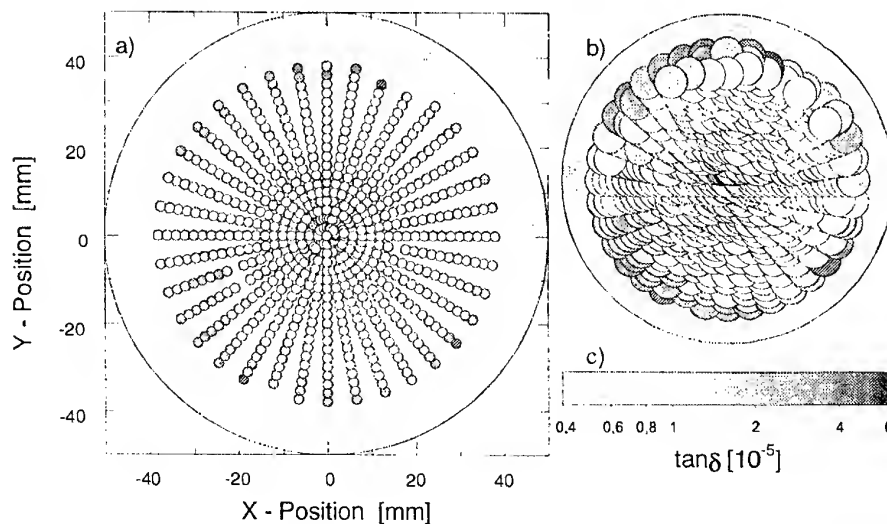


Fig. 2  $\tan\delta$  mapping for the 'Super-FZK' window disc: a) demagnified spot size, b) actual spot size of 6mm and c)  $\tan\delta$  grey scale.

It was clear from the earlier paper [5] that different surface contributions to the loss typically arise at the nucleation and the growth face, which may be eliminated by polishing off an appropriate material quantity, but bulk losses could superimpose these. In the present new discs, no significant differences were observed along the growth axis by alternative placing the nucleation and the growth face into the resonator.

As for the distribution of the losses observed across the area of the disc, the  $\tan\delta$  map plotted in Fig. 2 shows the good homogeneity of losses in the 'Super-FZK' window disc. The circles plotted in Fig. 2a do not represent the actual spot size of the measurement, but are demagnified for a clear lay-out, whereas for the actually mapped area ( circle diameter = real spot size  $\sim 6$  mm ) is given in Fig. 2b. Obviously in the central region ( about 60 mm in diameter ), which is the most critical for a gyrotron window,  $\tan\delta$  values did not go beyond the  $10^{-5}$  level. A line scan across the 'Star of FZK' window disc gives evidence of constant low loss area (  $\tan\delta < 3 \cdot 10^{-5}$  ) in the inner area of at least 80 mm dia ( cf. Fig.3 ). The increase in the outer area may be enlarged by diffraction at the disc edges.

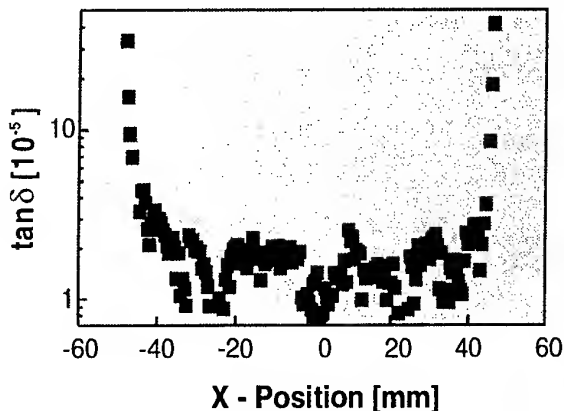


Fig.3 Line scan across the diameter of the 'Star of FZK' window disc.

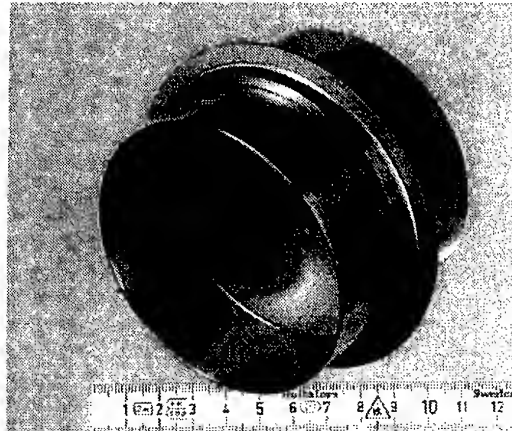


Fig.4 The 'Super-FZK' disc mounted into a test structure for high power mm-wave tests.

#### Mounting of the window material

To prepare for high power testing, the 'Super-FZK' window disc was mounted on double inconel cuffs using an ultrahigh vacuum ( UHV ) compatible, aluminium based diffusion bond. The leak rate for the assembly was measured at  $< 10^{-9}$  mbar-l/s. The cuff dimensions were chosen to allow a clear aperture of transmission of 80 mm in diameter and sufficient material at the edge for efficient water cooling. The whole cuff assembly was then baked at temperatures up to 450°C for more than 24 hours, which represents a typical out-gassing cycle, and subsequent tests confirm vacuum tightness.

#### Acknowledgement

Parts of this work have been performed in the framework of the Nuclear Fusion Project of the Forschungszentrum Karlsruhe within the European Fusion Technology Programme.

#### Literature

- [ 1 ] R. Heidinger, J. Nucl. Mater., 179-181 (1991), pp64-69
- [ 2 ] M.N. Afsar, H. Chi, Digest 18<sup>th</sup> Int. Conf. IR & MM Waves, Colchester (UK), 1993, SPIE Vol.2104, pp185-186
- [ 3 ] R. Heidinger, Digest 19<sup>th</sup> Int. Conf. IR & MM Waves, Sendai (J), 1994, JSAP Cat No. AP941228, pp277-278
- [ 4 ] R.S. Sussmann, J.R. Brandon, G.A. Scarsbrook, C.G. Sweeney, T.J. Valentine, A.J. Whitehead, C.J.H. Wort, Diamond and Related Materials, 3 (1994), 303-312
- [ 5 ] R. Heidinger, R. Schwab, R. Spörl, M. Thumm, Digest 22<sup>nd</sup> Int. Conf. IR & MM Waves, Wintergreen (USA), 1997, pp142-143
- [ 6 ] R.S. Sussmann, J.R. Brandon, S.E. Coe, C.S.J. Pickles, C.G. Sweeney, A. Wasenczuk, A.J. Whitehead, C.J.H. Wort, C.N. Dodge, Proc. Ultrahard Materials Technical Conference, Windsor (CDN), 1998, pp. 477-496
- [ 7 ] R. Schwab, R. Spörl, J. Burbach, R. Heidinger, F. Königer, Proc. of ITG Conference on Displays and Vacuum Electronics, Garmisch-Partenkirchen (D), 1998, ITG Report No. 150, pp. 363-368

## Development of a 1 MW CW Waterload for Gaussian Mode Gyrotrons

R. Lawrence Ives, Max Mizuhara, Rich Schumacher, Rand Pendelton

Calabazas Creek Research, Inc.

20937 Comer Drive

Saratoga, CA 95070, USA

Calabazas Creek Research, Inc. has developed a 1 MW CW waterload for Gaussian mode gyrotrons operating at frequencies between 30 GHz and 180 GHz. The interior of the Load Section consists of a metal cylinder coated with a lossy dielectric material that absorbs the RF power. The amount of power absorbed per RF bounce is a function of the RF frequency and the thickness of the dielectric coating. The dielectric coating is plasma sprayed on the inside surface of an aluminum cylinder, which ensures a strong bond between the two materials. The thickness of the coating can be controlled to .005 cm.

It is important that the absorbed power be less than  $150 \text{ W/cm}^2$ . Previous devices using this technique experienced damage to the dielectric coating at higher power levels. The intensity of the RF beam on the load surface was modeled using Gaussian optical techniques. The thickness of the loss coating was then specified to ensure that the absorbed power would be well below critical levels. For the prototype load, maximum absorbed power is calculated to be  $70 \text{ W/cm}^2$  at 170 GHz and  $65 \text{ W/cm}^2$  at 110 GHz.

The power is distributed in the load by a rotating copper reflector that sweeps the RF beam circumferentially around the structure. This eliminates hot spots caused by constructive interference, which has been seen in similar waterloads using static structures.

Power absorbed in the dielectric coating is conducted through the aluminum cylinder, and the heat is removed by water cooling. For 1 MW CW operation, 760 liters/minute of flow is specified to maintain temperatures at acceptable levels. The structure was modeled using finite element computer codes to predict the temperature in the loss coating and the aluminum cylinder. Analysis predicts that the maximum temperature in the dielectric will be less than  $320^\circ\text{C}$  and the maximum temperature in the aluminum will be less than  $150^\circ\text{C}$ . Maximum allowable temperatures are  $500^\circ\text{C}$  and  $300^\circ\text{C}$ , respectively. The prototype waterload incorporates temperature resistance devices (RTDs) to monitor temperature during operation to verify the computer predictions.

The Load Section can be operated vertically or horizontally and with an internal vacuum or pressurized gas to 1.5 atmospheres. Absorbed power can be monitored calorimetrically.

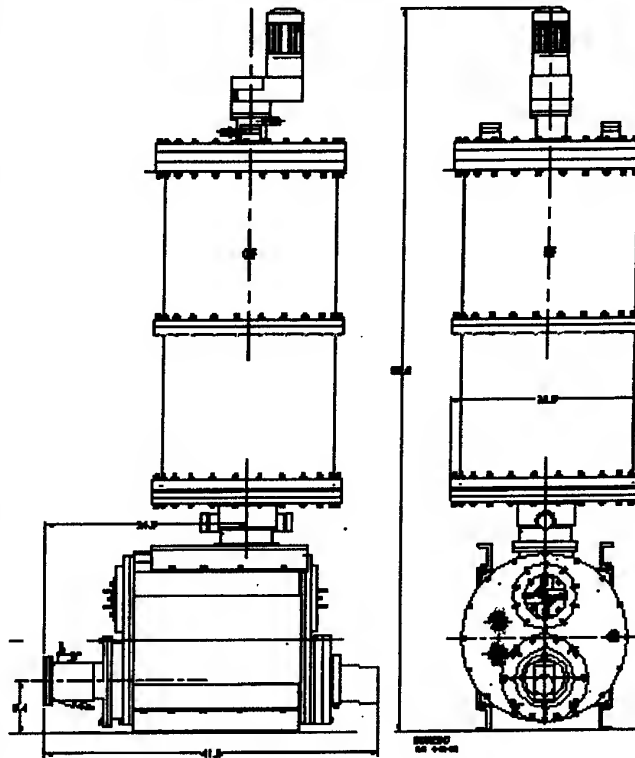




Maximum diameter of the RF beam must be less than 6.0 cm at the load input and less than 28 cm wide at the rotating reflector. The Mirror Section was developed to provide for focusing and alignment of the RF beam emerging from the gyrotron. A series of three mirrors can correct for minor asymmetries and beams that do not emerge from the gyrotron perpendicular to the output window. In addition, the Mirror Section can dissipate up to 75 kW CW of spurious RF power.

The Mirror Section includes an RF sampler port and an arc detector port. The first mirror can also incorporate ports for imaging the gyrotron window with video and infrared cameras. Each of the three alignment and focusing mirrors can be externally adjusted without compromising the vacuum integrity of the device. The vacuum pump port for the waterload system is located in the Mirror Section.

This presentation will describe the design of the waterload and compare experimental predictions with available experimental results.



#### Mirror Section Specifications

Length	0.93 meters (36.7 inches)
Width (diameter)	0.53 meters (20.8 inches)
Height	0.57 meters (22.4 inches)
Weight	135 kg (300 lbs) (estimated)
Max. power dissipation	75 kW CW
Number of mirrors	3
Diagnostics	RF sampler, video port, infrared imaging port, calorimetric power, arc detector port

#### Load Section Specifications

Length	1.68 meters (66.1 inches)
Diameter	0.60 meters (23.5 inches)
Weight	220 kg. (500 lbs.) (estimated)
Max. power dissipation	1 MW CW
Flow rate (full power)	760 liters/m (200 gpm)
Pressure drop	TBD
Internal pressure	Vacuum to 1.5 atmospheres
Orientation	Vertical or horizontal
Interlocks	Water flow, reflector rotation
Input mode	Gaussian
Max. RF beam size	6.0 cm (2.4 inches) diameter
Diagnostics	Calorimetric power

## Present Developments for the 140 GHz Transmission System for ECRH on the Stellarator W7-X

L. Empacher, G. Gantenbein, F. Hollmann, W. Kasperek, H. Zohm

Universität Stuttgart, Institut für Plasmaforschung, Pfaffenwaldring 31, D-70569 Stuttgart, Germany

V. Erckmann, M. Weißgerber

Max-Planck-Institut für Plasmaphysik, EURATOM-Association, D-85748 Garching, Germany

For the future stellarator W7-X of IPP at Greifswald, a powerful electron cyclotron heating facility is under design which will include 10 gyrotrons at 140 GHz with a CW power of 1 MW each plus 2 optional gyrotrons at 70 GHz. The millimetre wave power will be transmitted via two multi-beam waveguides with a length of about 50 m. A description of the transmission system is found in [1]. In this paper, issues for the mirror development are discussed.

### Determination of optimised mirror surfaces

In a multi-beam waveguide, the surface of the mirrors has to meet the following requirements:

The input plane must be imaged to the output plane. This can be fulfilled by paraboloids. On the other hand the beams must be transmitted with the lowest possible mode conversion. For the central beam, the proper phase-correction is performed by ellipsoids. The off-axis beams may need other surfaces.

As the requirements are contradictory, optimisation calculations have been performed. The surface  $h(x_s, y_s)$  of the mirrors was taken as

$$h(x_s, y_s) = \frac{1}{4\sqrt{2}f} x_s^2 + \frac{\sqrt{2}}{4f} y_s^2 + \frac{p}{16f^2} (x_s^3 + 2x_s y_s^2)$$

where  $f$  is the focal length and  $p$  characterises the shape of the surface ( $p = 1$ : off-axis paraboloid,  $|p| < 1$ : off-axis ellipsoid;  $p = 0$ : toroid). Analytical formulae are obtained by tracing the beams along their central rays through the mirror system. At each reflection point, the local curvature of the mirror is taken to calculate the new beam parameters, and at the output plane, gaussian beam mode analysis is performed with respect to the input beam. Diffraction calculations have been used to check the analytical formulae; both methods are in good agreement. Experiments have been performed which confirmed these calculations [2]. A general finding is that the optimum surface of the mirrors is described by a shape parameter which lies between the limits imposed by the requirements above. Furthermore, the configuration of the mirrors determines if the mode conversion on successive mirrors cancels or adds up. An example for the mode conversion of a 4-mirror MBWG in an optimum configuration ( $f = 1000$  mm, beam waist  $w_0 = 20$  mm, off-axis shift in the plane of incidence  $\Delta x = 100$  mm) as a function of the mirror shape is given in Fig. 1.

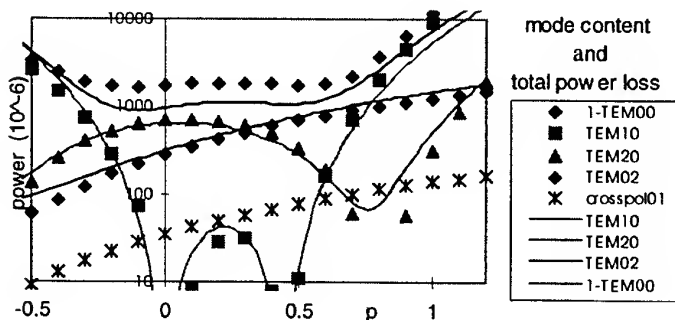


Fig. 1

Mode conversion after 4 mirrors as a function of the shape parameter  $p$ ,  $\Delta x = 100$  mm,  $\Delta y = 0$ ,  $f = 1000$  mm,  $w_0 = 20$  mm

Symbols: results from diffraction calculations, solid lines: analytic formulas.

The total mode conversion loss is low (below 0.2 %) in the region  $-0.2 < p < 0.6$  with the minimum at  $p = -0.1$ . For comparison, geometrical optics results in  $p = +1$ , whereas the optimum surface for single beam transmission is

described by  $p = -0.48$ . If the results are applied to the beam parameters chosen for W7-X [1], negligible mode conversion losses are expected.

### Mirror design

To reach the theoretical predictions also in the experiment, the design of the mirrors must guarantee a stable surface under different heat loads imposed by the millimetre waves. The mechanical design which is investigated at present consists of a thick (52 mm) aluminium honeycomb structure which gives high stability at relatively low weight. The cooling channels are machined into an explosion-bonded copper surface (typ. 8 mm) and are closed by electro-forming techniques. Thermomechanical calculations have been started and tests are in preparation to get information on possible deformation due to surface heating by microwaves.

To get exact data for the ohmic loss of different copper surfaces (plane; shallow diagnostic gratings; polarising grooves) with typical machining quality (NC-milled and slightly polished), a resonator technique was used c.f. [3]. The quality factor  $Q_2$  of a nearly spherical 2-mirror resonator is measured as a reference. After folding this resonator via a sample under test, a 3-mirror resonator is formed with a reduced quality  $Q_3$ , from which an effective surface resistance (including polarisation and angle of incidence) of the sample can be calculated:

$$R_{s,eff} = \frac{1}{4} \omega_0 \mu_0 \cdot (1/Q_3 - 1/Q_2)$$

The ohmic loss  $\Delta P$  per reflection is given by

$$\Delta P = 4R_{s,eff}/Z_0$$

Here  $\omega$  is the angular frequency,  $\mu_0$  and  $Z_0$  the permeability and impedance of the vacuum. Results for copper are given in Fig.2 as a function of the angle of incidence. Typically, the measured loss is about a factor of 1.3 above the theoretical value for plane and shallow grating surfaces; for polarizers with the electric field perpendicular to the grooves the loss is significantly higher as the wave can penetrate into the grooves. For the W7-X transmission system, this results in a maximum loss of 3 kW per beam with thermal loads of up to 100 W/cm<sup>2</sup> on the mirror surface. With the cooling structure foreseen, the resulting temperature rise of the surface is below 70 K according to first calculations. Measurements are underway.

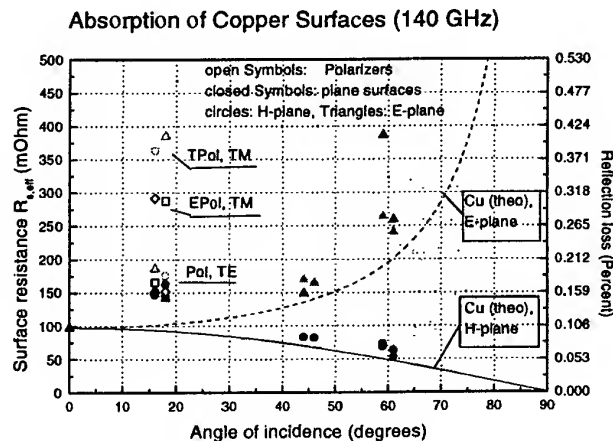


Fig.2: Ohmic loss measured on different copper surfaces as a function of the angle of incidence (symbols). For comparison, the theoretical loss for a plane surface with H-plane polarisation (solid line) and E-plane polarisation (dotted line) is shown..

### Conclusions

It has been shown, that the mirrors for the multi-beam waveguide can be optimised for low mode conversion. The mechanical design of the mirrors is in good progress. The ohmic loss measured with a 3-mirror resonator are in very good agreement with theory, the resulting thermal loads are compatible with the present design of the cooling structure of the reflectors.

### References

1. L Empacher et al., In Fusion Technology 1996, Elsevier Science B.V. Amsterdam (1997), 541-544.
2. L Empacher et al., Proceedings of the 10th Joint Workshop on ECE and ECRH, ed. T Donne and T Verhoeven, World Scientific, Singapore (1997), 561-568.
3. R G Jones, Electronic letters, **11**, 525 (1975).

## LOSSES IN LOW LOSS DIAMONDS AT MM RANGE

B.M. Garin, A.N. Kopnin, M.P. Parkhomenko, E.E. Chigryai

Institute of Radio Engineering & Electronics of RAS,  
1 Vvedensky Sq., Fryazino, Moscow Region 141120, Russia  
Telefax: +7 (095) 702-9572; e-mail: ask@ms.ire.rssi.ru

V.G. Ralchenko and V.I. Konov

General Physics Institute of RAS, 38 Vavilov st., Moscow 117942, Russia  
E-mail: ralchen@ran.gpi.ru

### Introduction

In various low loss materials the theoretical lower limit of lattice loss (absorption) at the MM and SMM ranges is determined by the multiphonon (mainly two-phonon) absorption in corresponding ideal crystal [1,2]. This loss may be named "intrinsic" lattice loss (ILL). In some cases an addition lower bound on the loss may be due to not intrinsic lattice loss, connected with lattice disorder, defects and impurities or to the loss connected with free carriers of charge [3-5]. It had been predicted theoretically in [1,3,4] that in the diamond type lattice structure crystals at the millimeter (MM) and submillimeter wavelengths range it is possible to expect the extremely low ILL. Furthermore the diamond is characterised by the lowest limits both for lattice and free carriers charges induced losses among various diamond type crystals [3-5].

The progress in the synthesis technique of polycrystal diamond films by the method of the chemical vapour deposition (CVD) and creation of diamond plates with great diameter (5-10 cm) and thickness (up to 1-2 mm) gives the measurement possibilities for low loss diamonds at MM range and the opportunities for the design of diamond windows for the most powerful MM waves sources (gyrotrons). In literature the results of the loss measurements in synthetic diamonds at MM range [6-8] and also at lower frequencies [9] are available. But the loss nature is not revealed and the influence of the diamond synthesis conditions on the loss and the possibilities of the significant loss reduction are not practically researched. The present work is devoted to these problems.

### Theoretical estimations of intrinsic lattice loss in diamond

In [4,5] the rough theoretical estimations of absolute loss tangent  $\tan\delta$  values have been obtained for the ILL in the diamond, silicon, germanium respectively:  $\tan\delta \sim 10^{-9}$ ,  $3 \cdot 10^{-8}$  and  $2 \cdot 10^{-7}$  at the wavelength  $\lambda = 2$  mm and home temperature. At the present time the lowest losses among condensed substances at the given conditions have been observed in the gold doped silicon (Si:Au) [5,10]. And these losses, including the record breaking low loss ( $\tan\delta \sim 3 \cdot 10^{-6}$  at  $\lambda = 2$  mm and temperature  $T = 20$  C [10]), are due to free carriers of charges as it follows from its measured temperature and frequency dependencies. Hence in silicon the ILL  $\tan\delta \leq 10^{-6}$ . From the theoretical estimations, mentioned above, it follows that the ILL in diamond is 1/30 of the ILL in silicon. From the comparison of it with the mentioned experimental data it follows that the  $\tan\delta$  value for the ILL in the diamond should be  $\leq 3 \cdot 10^{-8}$  at the same conditions.

### Experimental results

At the present work the series of low loss synthetic diamonds created in GPI of RAS by method of plasma-chemical deposition from the  $\text{CH}_4\text{-H}_2\text{-O}_2$  mixtures in the microwave discharge [11] have been experimentally investigated. The deposition velocities was of 2-5  $\mu\text{m}/\text{hour}$ , nitrogen impurity concentrations was  $(8-30) \cdot 10^{17} \text{ cm}^{-3}$ . The specimens, separated from substrate, had the form of discs with the diameter  $\varnothing$  55-60 mm and thickness up to 1.3 cm. The measurements was made in IREE of RAS in the open resonators [5] at the range 2.15-6.8 mm. The results of some measurements are presented in the tables 1,2. The loss values in the researched initial specimens are in the interval:  $\tan\delta = (1-10) \cdot 10^{-4}$ . The tendency have been observed of the loss decrease with the decrease of deposition velocity and nitrogen concentration. In addition, the considerable reduction of loss after annealing on air at  $T = 550$  C have been found:  $\tan\delta$  from  $\sim 1.5 \cdot 10^{-4}$  to  $\sim 5 \cdot 10^{-5}$  in specimen No.111.

Table 1. Losses at  $\lambda = 2.15-6.8$  mm in specimen No.79.

$\lambda$ [mm]	2,15	3,9	6,0	6,8
$\tan\delta$ [ $10^{-4}$ ]	1,5 $\pm$ 3	4	5	9,5

Table 2. Losses  $\tan\delta$  at  $\lambda = 2,15$  mm and home temperature in synthetic diamonds.

Specimen number	Mean Thickness [ $\mu\text{m}$ ]	Deposition velocity [ $\mu\text{m}/\text{hour}$ ]	$\tan\delta$ [ $10^{-4}$ ]
92	1280	5,0	8
83	190	4,6	10
79	490	4,5	1,5 $\pm$ 3
70	230	3,9	<5
111	490	3,7	1 $\pm$ 2
93	430	3,2	2
56	270	2,7	2
100	640	2,6	1,5 $\pm$ 3,5
AST	180	2,5	<2

### Interpretation and conclusions

The loss dependence on frequency  $f$  at the given range (table 1) can be approximated by the law  $1/f$ . The observed loss in the diamonds can be explained by the loss on the electric conductance in the inclusions of nondiamond phases with very inhomogeneous distribution of local dynamic conductivity  $\sigma$ , containing amorphous carbon and nanographite. According to the nonelastic light scattering spectroscopy data, the relative volume concentrations of the inclusions is not more than  $10^{-3}$ . According to the proposed loss mechanism the more weak frequency dependence (compared with the  $1/f$  law) at  $f \ll 10$  GHz [9] is connected with the decrease of amount of local regions that satisfy the condition  $\tau_M^{-1} \ll \omega$  (where:  $\tau_M = \epsilon\epsilon_0/\sigma$  and  $\epsilon$  are respectively the local values of the Maxwell's electric relaxation time and dielectric permittivity;  $\epsilon_0$  is the electric constant;  $\omega = 2\pi f$ ). The relatively weak loss dependence on temperature [9] can be naturally explained by the weak dependence of the conductivity in the nondiamond inclusions. The observed losses differ by its temperature-frequency dependencies from the ILL (the latter must considerably increase with increase of frequency and temperature [1-4]) and significantly exceed its estimated values (see above). So the intrinsic lattice loss in diamond (such as in other diamond type crystals including silicon [5,10]) are not experimentally revealed to the present time.

From the obtained data and consideration and also from the ILL estimations it follows that there are possibilities of further significant loss reduction in diamond and achievement of lowest losses in it compared with other materials in MM and next ranges. Moreover the estimations have been obtained using the loss and thermal conductivity values that there is a principle possibility of creation the diamond windows for gyrotrons with power  $> 10$  MW in continuous regime at the MM range.

This work was carried out at the support of the Russian Scientific-Technical Program "Microwave Physics" (Project No.3.19).

### References

1. A.V. Galdetskii, B.M. Garin, Preprint No.17(320). Moscow, Inst. of Radio Engineering & Electronics of RAS, 1981; the same, All-Union Conf. "Designing and Appl. of Radio-electronic Devices on dielectric waveguides and resonators", Saratov, Russia, 1983. Digest, p.98 [in Russian].
2. B.M. Garin, 18th Int. Conf. on IR & MM Waves, Colchester, 1993, Digest, vol.1, p.509.
3. B.M. Garin, A.N. Kopnin, M.P. Parkhomenko, et al, 1st Ukrainian Symp. "Physics and Technology of MM and SubMM Radio Waves", Khar'kov, Ukraine, 1991. Digest, vol.1, p.86 [in Russian].
4. B.M. Garin, Russian Conf. "Dielectrics-93", St.-Petersburg, 1993. Digest, vol.1, p.98 [in Russian]; Third Int. Conf. on Millimeter-wave and Far-Infrared Sci. and Technol., Guangzhou, China, 1994. Digest, p.275.
5. B.M. Garin, A.N. Kopnin, M.P. Parkhomenko, et al, Technical Phys. Lett. 20, 878 (1994); B.M. Garin, A.N. Kopnin, M.P. Parkhomenko, et al, 21st Int. Conf. on IR & MM Waves, Berlin, 1996. Digest, paper CT15.
6. R. Heidinger, 19th Int. Conf. on IR & MM Waves, Japan, 1994. Digest, p.277.
7. R.S. Sussman, J.R. Brandon, G.A. Scarsbrook, et al, Diamond Related Materials 3, 303 (1994).
8. V.V. Parshin, V.A. Khmara, V.I. Mankeev, et al, 9th Joint Russian-German Meeting on ECRH and Gyrotrons, Proc., 1997, p.143; R. Spörl, R. Schwab, R. Heidinger, ibid, p.167.
9. A. Ibarra, M. Gonzalez, R. Vila, et al, Diamond Related Materials 6, 856 (1997).
10. R. Heidinger, J. Molla, V.V. Parshin, Digest of 21st Int. Conf. on IR & MM Waves. Berlin, 1996.
11. V.G. Ralchenko, A.A. Smolin, V.I. Konov, et al, Diamond Related Materials 6, 417 (1997).

## Diamonds for High-Power Gyrotron Window

Vladimir Parshin (1), Victor Ralchenko and Vitaly Konov (2)

(1) Applied Physics Institute RAS, 46 Ulyanov st., N. Novgorod, 603600, Russia.

Fax: 007 8312 362061; e-mail: parsh@appl.sci-nnov.ru

(2) General Physics Institute RAS, 38 Vavilov st., Moscow 117942, Russia.

### Abstract

The CVD diamond disks were tested as the material for gyrotron windows. The losses and refractive index were measured at frequencies 70-200 GHz and temperature 20-600C.

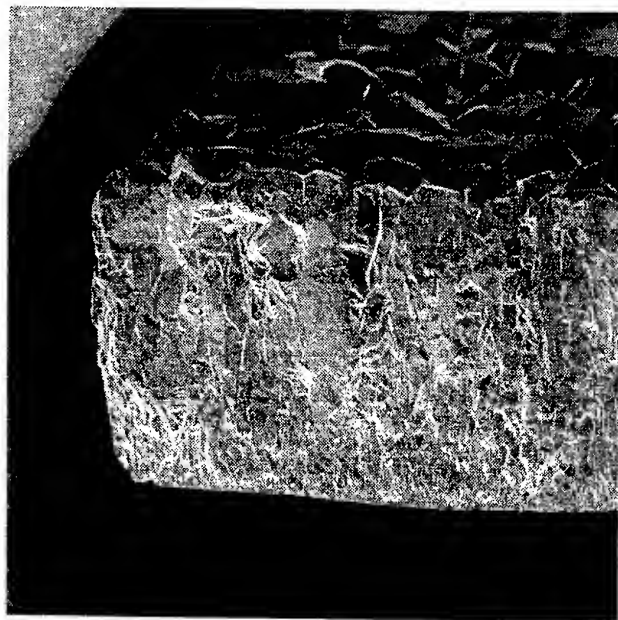
The dielectric parameters and thermoconductivity are high enough to use these diamonds as a real high-power CW-gyrotron window.

### Introduction

Due to low absorption and extremely high thermoconductivity diamond is considered to be an ultimate material for output windows in high-power (>1 MW) continuous wave gyrotrons. In this paper we present the results of dielectric properties testing of chemical-vapor-deposited (CVD) polycrystalline diamond disks. The losses and refractive index were measured at frequencies 70-200 GHz in the temperature range 20-600C.

### Growing conditions and thermoconductivity

The diamond disks of 100 mm diameter and up to 1.3 mm thickness were produced by a joint group of



General Physics Institute and Diagascrown Ltd. (Moscow) using a microwave plasma deposition from  $\text{CH}_4\text{-H}_2\text{-O}_2$  gas mixtures [1]. Deposition parameters were systematically varied to grow the material of a better quality. Mapping of thermal conductivity (TC) over the disk diameter by a laser flash technique revealed nearly uniform TC profiles, the TC values exceeding 18 W/cmK at room temperature. Here we describe the results obtained for one of the best samples grown at the rate of 2.4 micron/hour and containing 1 ppm of nitrogen impurity. Fig. 1 shows a micrograph of as-grown 1.1 mm thick diamond plate with columnar grains seen in cross-section. The disk was polished from both sides to reduce the roughness at the top faceted surface and remove a defective fine-grained layer at the bottom side. Finally, the resonance thickness = 0.74 mm ( $2\lambda/2$ ) at  $f = 170$  GHz was reached with thickness deviation being only 5 micron over the whole area of the 50 mm diameter disk.

Fig. 1. SEM picture of as-grown 1.1 mm diamond film (fractured surface).

### Microwave measuring technique

The refractive index ( $n$ ) and loss tangent ( $\text{tg}\delta$ ) were measured at Applied Physics Institute using a high Q-factor Fabry-Perot resonator. The measurements were made by using traditional for us method of measuring the refractive index and loss tangent at the resonance frequency of the plan parallel disk [2]. But for the measuring of so negligible losses and especially at high temperatures the method was a bit developed:

While measuring we do not take off the disk to obtain the Q-factor of empty resonator. For  $\text{tg}\delta$  calculation we used two values of resonator width curve for the two terminal plate position: when its surfaces are in max. and in min. of standing wave in resonator. In this way we get rid of many errors connected with the calculation of parasitic scattering; influence of heating air turbulence; with the mechanical replacing of the disk position and etc. So, by this way we essentially simplified the measuring procedure. Finally, we got the scattering of  $\text{tg}\delta$  measurements  $\sim 2 \cdot 10^{-6}$  for diamond disks with the thickness =  $2\lambda/2$  at 170 GHz.

### Refractive index and loss tangent measurements

The temperature dependencies of refractive index, loss tangent and resonance frequency are presented in Fig. 2. The loss tangent is as low as  $\text{tg}\delta=8 \cdot 10^{-6}$  at  $T=20^\circ\text{C}$  increasing to  $12 \cdot 10^{-6}$  at  $T=400^\circ\text{C}$ , while the refractive index increases from  $n=2.381$  to  $n=2.390$ .

The loss tangent frequency dependencies have been measured at the range of 70-200 GHz. The results are presented on Fig. 3. But we had only two well measured points, i.e. at the resonance frequencies of the plate. The scattering of results at other frequencies do not permit to define clearly the law of frequency dependence. The source of errors is connected with an inhomogeneity of the disk on one side and the changing of resonator beam diameter with the frequency changing on the other side. So, we can say only that  $\text{tg}\delta$  at 85 GHz is approximately twice as higher in comparison with 170 GHz.

By using both of these results (Fig. 2 and Fig. 3.) we can say that the main mechanism of absorption is connected with the free charge carriers produced by an impurity, because the activation temperature of intrinsic conductivity is higher than  $500^\circ\text{C}$ .

The absorption at room temperature is still far from the theoretical limit [3]. From theoretical estimations and some modern data it follows that the lattice absorption in perfect crystal should be at least  $\text{tg}\delta < 3 \cdot 10^{-8}$  at 150 GHz. Much greater losses observed in real CVD diamonds can be connected with various lattice defects as disorder, non-diamond phases (amorphous carbon and graphite) and mainly with an electrically active impurities. It is expected that further progress in CVD process will lead to diamond plates of better quality.

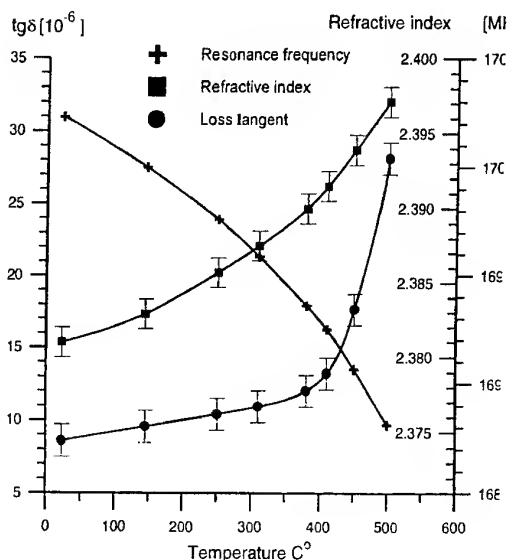


Fig. 2. Refractive index, loss tangent, and resonance frequency versus temperature as measured for 0.74 mm thick polished disk.

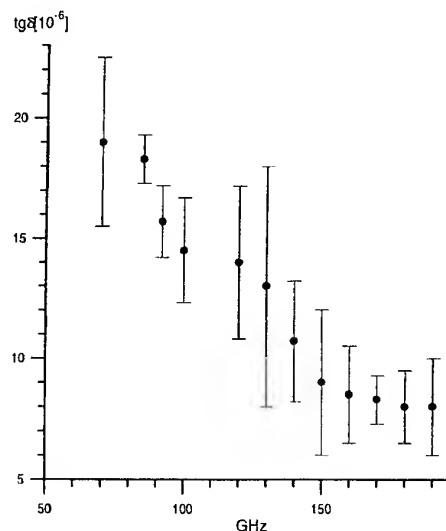


Fig. 3. Loss tangent frequency dependence as measured for 0.74 mm thick polished disk.

### Conclusion

All parameters needed for temperature regime calculation of real diamond window have been got. The calculation shows that the window with diamond like the one having been measured is able to transmit more than 1 MW of microwave power in continuous wave operation.

### Acknowledgements

Experiments described were supported partially by Russian State Program "Fundamental Physics of Microwaves" and Russian Foundation for Basic Research (RFBR), Grant N 96-03-32798.

The authors express their deep gratitude to all of these sources of support.

### References

1. V.G. Ralchenko, A.A. Smolin, V.I. Konov, K.F. Sergeichev, I.A. Sychov, I.I. Vlasov, V.V. Migulin, S.V. Voronina and A.V. Khomich, *Diamond and Related Materials*, V.6, p. 417, (1997).
2. Yu.A. Dryagin, V.V. Parshin, *Int. J. of IR. & MM Waves*, V.13, pp.1023-1032, (1992).
3. B.M. Garin, *Conf. Digest "Dielectrics-93"* St. Petersburg, Russia V.1, pp.98-99, (1993).

## A SPHERICAL MAIN REFLECTOR COMPACT ANTENNA TEST RANGE FOR OPERATION UP TO SEVERAL THz.

C.G. Parini, M.R. Rayner & C. Rieckmann

Electronic Engineering Dept., Queen Mary & Westfield College, London E1 4NS, U.K.

### Introduction

The principle behind a Compact Antenna Test Range (CATR) is to produce a quasi-plane wave test region by collimating the field from a point source using a parabolic reflector. The test region (or quiet zone) where the antenna under test (AUT) is placed being located only a short distance in front of the compact range collimator. Several variations on this basic theme have been successfully used over the years including the use of Cassegrain (or Gregorian) reflector systems, dual shaped folded reflector systems, and dual cylindrical reflectors. However which ever configuration is chosen the one common factor is that the single most expensive item in the construction of a CATR is the manufacture of the main reflector. This is true for two reasons :-

- (i) The size of the reflector needs to be considerably larger than the quiet zone size required. For the most common single offset CATR the quiet zone is approximately 30% of the size of the main reflector. This has, to date, only been overcome using the dual shaped folded CATR at the expense of having two reflectors of near equal size to give a quiet zone of about 80% of the reflector size.
- (ii) The surface accuracy of the reflector directly determines the phase quality of the quiet zone. A displacement of the reflector surface by  $0.01\lambda$  from the true paraboloid results in a phase change at the quiet zone of  $7.2^\circ$ . Since the generally accepted definition of a CATR quiet zone is one with less than  $\pm 0.5\text{dB}$  amplitude ripple and  $\pm 5^\circ$  degrees of phase ripple, surface quality needs to be very high. This is a particularly serious problem for millimetre wave operation and has to date limited the upper frequency of CATR operation to about 200GHz.

Thus the compact range reflector is a large high surface accuracy structure which is either constructed from an accurately machined mould using composites or aluminium honeycomb sandwich, or directly machined from solid metal. However it has been shown [1] that the panel joint severely degrades the performance of the CATR when high gain millimetrewave AUT's are tested.

The next generation of radiometers being actively considered by the European Space Agency (ESA) will operate up to 1.5 THz and so there is a need to be able to measure these antennas radiation patterns accurately in order that they may be calibrated accurately for radiometric measurements [2]. One such example is the proposed MASTER Plus instrument which is a radiometer operating from 200GHz to 550GHz with a main reflector diameter of 2 metres and antenna gains in excess of 70dB. A CATR to test such an antenna would require a reflector surface accuracy of 3 microns which most certainly challenges the state of the art in conventional reflector manufacture. In this paper we describe the advantages of making the shape of the CATR reflector *spherical*. The principle advantage is that only one radius of curvature is needed for all the reflector and so manufacturing costs can be significantly reduced.

### The Dual Reflector Feed System

The proposed CATR consists of a spherical main reflector and two shaped subreflectors to control the illumination of the main reflector by the feed. This concept is an extension of the dual reflector feed system (DRFS) being developed at QMW, figure 1, [3] and is analogous to a compensated spherical scanning reflector. The principle of the DRFS is based on the fact that a single offset reflector configuration for the CATR leads to the quiet zone size (defined as being the region within which the amplitude ripple remains less than  $\pm 0.5\text{dB}$  and  $\pm 5^\circ$  of phase) being approximately one third the diameter of the CATR reflector. This is because, with a simple feed, it is necessary to keep the edge illumination low to avoid excessive diffraction but this results in a large feed illumination taper over the reflector thus limiting the region over which the field is "quiet". However using Geometrical Optics (GO) reflector synthesis techniques a dual reflector feed system can be designed providing the ability to shape the illumination reaching the main reflector to give uniform field and fast roll off at the reflector edge.

### Size Of Quiet Zone Achievable

By using a Physical Optics reflector analysis package to determine the quality of the quiet zone for a number of CATR designs based on our GO synthesis we have found that the quiet zone needs to be approximately  $30\lambda$



smaller than the main reflector diameter. Clearly for large millimetrewave CATR's the potential for very efficient conversion of the main reflector diameter to quiet zone diameter is possible.

### Tri-Reflector CATR With Spherical Main Reflector

The principle advantage of a spherical main reflector is that only one radius of curvature is needed for all the reflector and so manufacturing costs can be significantly reduced. For millimetrewave operation very high quality spherical surfaces can be made using optical mirror technology. For example a CATR operating at 500GHz would require a reflector surface accuracy of better than 3 microns r.m.s. The most cost effective way of achieving this is to use a spherical reflector manufactured using techniques developed for optical telescope mirrors. There is a considerable amount of information in the open literature concerning manufacture of such mirrors, and single piece mirrors up to 2.5 metres diameter have been successfully manufactured in significant numbers using a variety of materials and construction methods. A large number of mirror blanks used for telescopes are delivered as spherical blanks and then the final grinding and polishing process creates the desired paraboloidal surface. A typical optical mirror blank can be delivered ground spherical, at this point the surface accuracy is 5 microns. The next phase of the manufacturing process is fine grinding which yields a surface accuracy of 0.25 microns. For optical mirrors the final process is that of polishing which then achieves a surface accuracy of typically 0.02 microns. Clearly for the CATR application the surface accuracy achieved at the end of the fine grinding stage would be more than adequate. Since the polishing process is by far the most time consuming of the finishing process, a substantial reduction in the cost of the reflector would be seen, compared to those for optical use.

### Construction Of A Demonstrator

As a proof of concept QMW will be constructing a spherical tri-reflector CATR with a 1 metre diameter main reflector and 8 micron surface accuracy for operation at up to 200GHz. It is envisaged that the design will feature a dual reflector feed system that is Gregorian in nature in order to provide maximum isolation between the dual reflector feed system and the quiet zone, figure 2. This work is being supported by the U.K. EPSRC.

### References

1. PHILIPPAKIS, M., and PARINI, C.G. : "Diffraction effects of tape covering the gaps of a panelled 'compact range' operating at millimetrewaves", Proc. IEE - Microw. Antennas. propag., Vol. 141, No. 2, April 1994, pp 114-122
2. HEWISON, T.J. and SAUNDERS R., "Measurements of the AMSU-B antenna pattern", IEEE Trans. Geoscience & Remote Sensing, Vol. 34, No. 2, March 1996.
3. DESCARDECI, R. & PARINI, C.G., "Dual reflector feed system for a compact antenna test range", Proc. IEE 9th International Conference on Antennas & Propagation, Technical University of Eindhoven, April 1995. pp141-4.

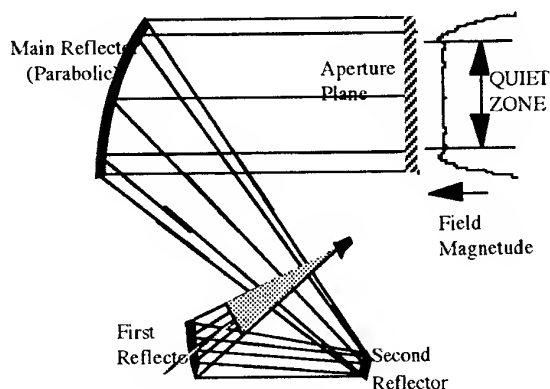


Figure 1 Plan view of typical tri-reflector CATR.

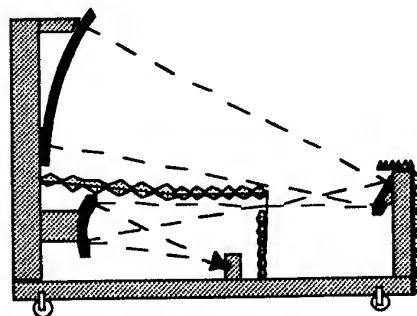


Figure 2 Proposed 200GHz CATR demonstrator

## Field Profile Synthesis with an Antenna Array

G. Michel, M. Thumm

Forschungszentrum Karlsruhe, ITP, Association FZK-Euratom  
P.O. Box 3640, D-76021 Karlsruhe, Germany  
and Universität Karlsruhe, Inst. f. Höchstfrequenztechnik u. Elektronik  
Kaiserstr. 12, D-76128 Karlsruhe, Germany

**Abstract:** An algorithm for the synthesis of a microwave beam with desired characteristics is discussed. The beam is composed by an array of identical antennas with a given radiation pattern.

**Keywords:** Katsenelenbaum Algorithm, Antenna arrays, Power combining, Field profile synthesis

### Introduction

The Katsenelenbaum algorithm [1] can be used for the synthesis of a particular amplitude distribution by means of a phase corrector. This is now an established method in gyrotron technology for the generation of a microwave beam with desired characteristics.

A similar problem—however at a larger scale—occurs in wireless power transmission (WPT). Here, a beam is desired which gives maximum transmission efficiency between the transmitting and receiving apertures which are both limited in their size. For this problem, gradient search methods have been applied in order to optimize the field distribution on the transmitting aperture.

In [2] the proposal was made to use an incompletely filled transmitting aperture (with the same active area as the compact aperture) in order to overcome the limit imposed by the diffraction expansion. The division into sub-apertures leads to the technical realization of such an aperture by means of an antenna array.

### Beam Synthesis

For reasons of simplicity, we will concentrate on the one dimensional case, but everything can be translated into two dimensions. Let us first have a look at the propagation operator. In [1], the Fresnel approximation of the Kirchhoff integral is used. For the sake of speed and accuracy, we will use the so called plane wave decomposition. I.e. we decompose the field into its plane wave spectrum (which is infinitely dense in free space), then each plane wave or mode is propagated according to its transverse wavenumber with an appropriate phasor. Finally, the field at the target aperture (which can be the receiving or transmitting aperture) is composed out of these modes. For the observable  $u$  we thus obtain along the optical axis  $z$

$$u(x, z_1) = \mathcal{F}^{-1} e^{-j(z_1 - z_0) \sqrt{k_0^2 - k_x^2}} \mathcal{F} u(x, z_0) \quad (1)$$

where  $\mathcal{F}$  represents the (fast) Fourier transform,  $k_0$  is the free-space wavenumber and  $k_x$  the transverse wavenumber.

When the field of a single antenna is  $s(x)$ , we obtain for the total field of an equidistant array (the transmitting aperture)

$$u_0(x) = \sum_n A_n s(x - n \Delta x) \quad (2)$$

where  $\Delta x$  is the distance between the antennas and  $A_n$  are the (still unknown) complex amplitudes. With the translation rule of the Fourier transform we obtain for the spectrum  $U_1$  of the field in the receiving aperture

$$U_1(k_x) = S(k_x) \cdot e^{-j(z_1 - z_0)\sqrt{k_0^2 - k_x^2}} \sum_n A_n e^{jn\Delta x k_x} = \tilde{S} \sum_n A_n e^{jn\Delta x k_x} \quad (3)$$

where  $S(k_x)$  is the spectrum of the field of a single antenna. In this equation,  $A_n$  and  $U_1$  are still unknown. We have no constraints for  $A_n$  (they are represented by the fact that we have a finite  $n$ ) and for  $U_1(k_x)$  we have the constraint that  $u_1(x)$  is limited to a certain region or must have a certain amplitude distribution.

The sum in (3) represents a Fourier series. This leads to an error correction scheme between  $A_n$  and  $u_1(x)$ :

$$\frac{U_1}{\tilde{S}} = \sum_n A_n e^{jn\Delta x k_x}. \quad (4)$$

We start with a sensible initial distribution for  $u_1$ , transform it into spectral domain, divide it by  $\tilde{S}$ , approximate it with the right hand side of (4), go back to spatial domain, apply the constraints and so on. Finally we obtain:

```

1 begin
2    $S := e^{-j\Delta x \sqrt{k_0^2 - k_x^2}} \cdot \text{fft}(s)$ 
3    $u := \text{initial\_field}$ ;
4    $\text{continue} := \text{True}$ ;
5   while  $\text{continue}$  do
6      $U := \text{fft}(u)$ ;
7      $U / = S$ ;
8      $A := \text{fft}(U)$ ;
9      $U := \text{ifft}(A)$ ;
10     $U * = S$ ;
11     $u := \text{ifft}(U)$ ;
12    if  $u \approx \text{apply\_constraints}(u)$ 
13      then  $\text{continue} := \text{False}$  fi;
14     $u := \text{apply\_constraints}(u)$ ;
15  od
16 end
```

After termination of the loop we have gained the desired  $A_n$ . Note that the Fourier transform in lines 8 and 9 is not the same as in lines 6 and 11. The former represents the Fourier series in (4) and the latter the one in (1). When we look at (4), we see that the right hand side can be seen as a spectrum of the spectrum. Thus,  $x$  is the "frequency" of this spectrum. Since this frequency is sampled with  $\Delta x$ , the approximation corresponds to a periodic function with period  $B = 2\pi/\Delta x$ . Beyond this bandwidth the approximation is rather bad, but since the approximation is multiplied by  $\tilde{S}$  (which decreases with increasing wavenumber) afterwards, this error is less effective.

### Summary

An algorithm for field profile synthesis by means of an antenna array was presented. Another variant of the algorithm for non-identical antennas as well as a numerical example can be found in [3]. The authors wish to thank S.S. Shaposhnikov and B.Z. Katsenelenbaum from the Moscow Radiotechnical Institute (MRTI) for providing their papers and for valuable discussions.

### References

- [1] B.Z. Katsenelenbaum, V.V. Semenov, *Synthesis of Phase Correctors Shaping a Specified Field*, Radio Eng. Electronic Phys. 12/1967. p. 223
- [2] S. S. Shaposhnikov et. al., *Innovative Approach to the Small Divergence Wave Beam*, WPT'95 Conference, Japan (Kobe), Report 4-2, 1995
- [3] G. Michel, M. Thumm, *Field Profile Synthesis with an Antenna Array*, Int. J. of Infrared and Millimeter Waves, Vol. 19, No. 3 (1998), p. 419

# Free Space Electro-Optic Sampling of Terahertz Radiation

Masahiko Tani, Kiyomi Sakai, Michael Herrmann and Hironori Takahashi\*

Kansai Advanced Research Center, Communications Research Laboratory  
588-2 Iwaoka, Kobe 651-2401, Japan  
tel: +81-78-969-2214, fax: +81-78-969-2219, e-mail: tani@crl.go.jp

\*Hamamatsu Photonics K.K.  
5000 Hirakuchi, Hamakita 434-8601, Japan

## 1. Introduction

It is well known that pulsed terahertz (THz) radiation can be detected by photoconductive antennas gated by femtosecond laser pulses. The detection bandwidth is, however, limited to less than 5 THz due to the finite carrier mobility and the RC constant of the device. The electro-optic (EO) effect, on the other hand, has an almost instantaneous response even in the femtosecond regime, and can be used for high-speed detection of THz radiation. Ultra-wideband (>3 THz) detection of THz radiation in free space by using the EO effect in nonlinear crystals (EO-sampling) has recently been exploited and demonstrated by several groups [1-3]. The EO crystals used so far are limited to several types: LiNbO<sub>3</sub> [3], LiTaO<sub>3</sub> [3,4], ZnTe [1], and GaP [5]. Among these crystals, ZnTe seems to be the most promising because it has a relatively large EO coefficient and, more importantly, a good phase velocity matching between optical and THz pulses. In this paper we have investigated the applicability of ZnSe, ZnS, and ZnTe (as a reference) crystals as EO-sampling detector for THz radiation. We have found that ZnSe has a similar detection efficiency to ZnTe. Since the detection bandwidth and efficiency are strongly dependent on the crystal thickness, we have also investigated the crystal-thickness-dependence of the EO signals using ZnTe.

## 2. Experiment

The properties of the investigated crystals are listed in Table I. All the crystals have the zinc-blende structure and a direct optical band gap greater than 2 eV, and all were cut to have a (110) surface. The typical crystal size was 5x5 mm<sup>2</sup> and thickness  $t=0.3$  mm unless otherwise specified. The experimental setup is illustrated in Fig. 1. The laser source was a mode-locked Ti:sapphire laser operated at a wavelength of 830 nm and a repetition rate of 82 MHz. The optical pulse width was about 70 fs. The THz emitter was a biased (150 V) stripline on low-temperature-grown GaAs which was excited with a pump beam power of 20 mW. The THz

Table I. Properties of the EO crystals.

Crystals	Band gap (eV)	$\epsilon_0/\epsilon_\infty$	TO phonon (THz)	EO coefficient (pm/V)	$n_{opt}^3 r_{ij}$ (pm/V)
ZnTe	2.28	9.67/7.28	5.3	$r_{41}=4.45$	103
ZnSe	2.58	7.6/5.4	6.39	$r_{41}=2.0$	31
$\beta$ -ZnS	3.6	8.0/5.1	8.2	$r_{41}=1.2$	15

radiation was focused on the EO crystal by using a pair of off-axis parabolic mirrors. The polarization of the THz radiation was directed parallel to the <001> crystal axis, and thus the refractive index in the <1-10> direction was

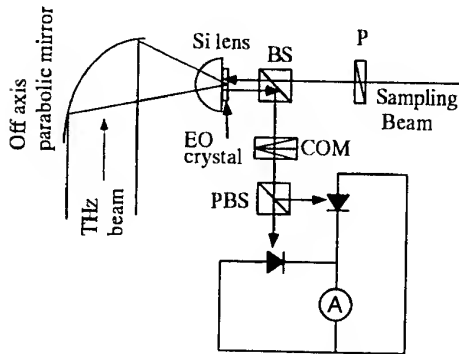


Fig. 1 Experimental setup for free space EO sampling. P: polarizer, BS: beam splitter, PBS: polarizing BS, COM: compensator ( $\lambda/4$ -plate).

modulated by the electric field. The sampling optical beam was focused on the EO crystal and reflected at the flat surface of the Si hemispherical lens to interact collinearly with the THz radiation pulses. The polarization of the sampling beam was set at 45° to the <001> axis. The change of the optical polarization due to the phase retardation ( $\Delta\phi$ ) of the polarization component along the <1-10> direction was detected by a pair of balanced photo-detectors with an appropriate polarizing optics. The time-resolved waveform of the THz radiation was recorded by changing the time delay between the excitation and the sampling optical pulses.

The phase retardation of the sampling beam is given by the following equation (which neglects the optical absorption in the crystal).

$$\Delta\phi(T) = \frac{\omega}{c} n_{opt}^3 r_{41} \int_0^d E_{THz} \left( \frac{z}{c} \Delta n + T \right) dz \quad (1)$$

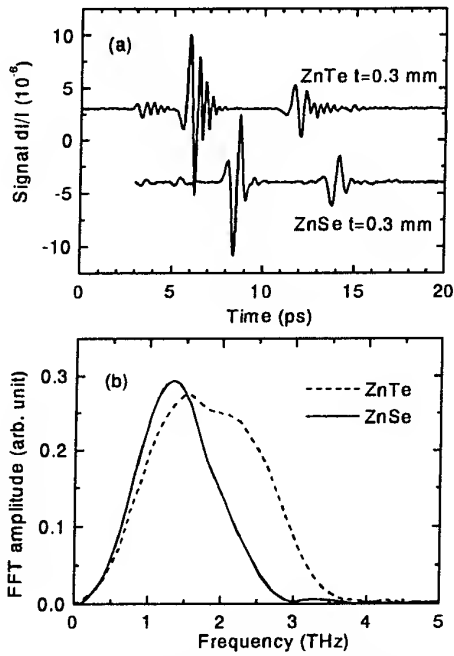


Fig. 2 (a) EO signal detected with ZnTe and ZnSe and (b) their Fourier transform spectra.

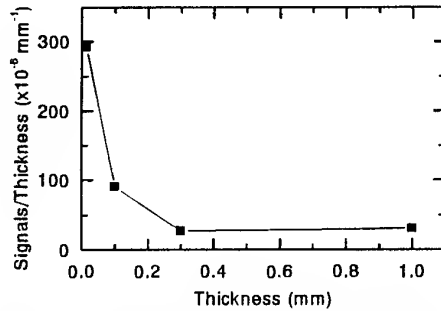


Fig. 3 The signal amplitude normalized by the crystal thickness at with various crystal thicknesses of ZnTe.

any meaningful signal using the ZnS crystal at our detection noise level ( $\sim 5 \times 10^{-7}$ ). The weakness of ZnS signal is attributable to a poor phase velocity matching of the THz and optical pulses ( $\Delta n > 0.5$ ) and a small EO coefficient.

We also measured the crystal-thickness-dependence of the EO signal amplitude using ZnTe ( $t = 14 \mu\text{m}, 0.1 \text{ mm}, 0.3 \text{ mm}, 1 \text{ mm}$ ). The result is shown in Fig. 3. It is surprising that the decrease in signal amplitude is not proportional to the crystal thickness. The EO signal normalized by the crystal thickness (peak-signal/thickness) increases by almost an order of magnitude when the crystal thickness decreases from 1 mm to 14  $\mu\text{m}$ . This cannot be explained simply by the phase mismatch or the absorption of THz wave in thicker crystals, because the  $l_c$  of ZnTe is more than 1 mm and the absorption is less than 20% for frequencies below 2 THz.

#### 4. Conclusion

We found that ZnSe is a promising EO crystal for the detection of THz radiation because its detection efficiency is comparable to that of ZnTe but it is optically more transparent and more robust. We also found that the detection efficiency normalized by the crystal thickness increased as the thickness of ZnTe decreased.

where  $T$  is the time delay between the optical and THz pulses,  $\omega$  is the angular frequency of the optical pulses,  $c$  is the velocity of light,  $n_{opt}$  is the refractive index for the light,  $r_{41}$  is the EO coefficient of the crystal,  $E_{THz}$  is the electric field of the THz pulses, and  $d$  is the thickness of the EO crystal. The term  $\Delta n$  is the difference between the refractive indices of THz and optical pulses, which is defined as

$$\Delta n = n_{eff} - n_{THz} = n_{opt} - \lambda_{opt} \frac{dn_{opt}}{d\lambda} \bigg|_{\lambda_{opt}} - n_{THz} \quad (2)$$

where  $n_{eff}$  is the effective refractive index for the optical pulse including the effect of the group velocity dispersion,  $n_{THz}$  is the refractive index at THz frequencies, and  $\lambda_{opt}$  is the wavelength of the optical pulse. Equation (1) tells us that when the phase mismatch between the optical and THz pulses is negligible over the total crystal thickness compared with a cycle of THz radiation ( $1/f_{THz} = \lambda_{THz}/c > d\Delta n/c$ ), the optical phase retardation  $\Delta\phi$  (EO signal) is proportional to the electric field  $E_{THz}(T)$  (and also to the crystal thickness  $d$ ). On the other hand, when the phase mismatch is large compared to a cycle of the THz radiation ( $1/f_{THz} = \lambda_{THz}/c < d\Delta n/c$ ), the signal is proportional to the integral of the THz electric field and goes to zero at the phase mismatch limit. To get the best possible detection efficiency we have to choose an appropriate crystal thickness, which is given by the coherence length  $l_c$  ( $=\pi/\Delta k = \lambda_{THz}/2|\Delta n|$ ) of the THz and optical pulses.

#### 3. Results and Discussion

Figure 2(a) shows the EO sampling signal for ZnTe and ZnSe. The signals before and after the main peak are respectively due to the optical and THz pulse reflections within the crystal. It is noteworthy that the signal amplitude of ZnSe is similar to that of ZnTe, while the figure of merit of ZnSe for the refractive index change ( $n_{opt}^3 r_{41}$ ) is estimated to be about one third that of ZnTe. The Fourier transform spectra of the signals in Fig. 2(a) are shown in Fig. 2(b). The bandwidth of the spectrum of ZnSe is a little narrower than that of ZnTe. This may be because the use of the ZnSe results in less efficient phase velocity matching of THz radiation and optical pulses at higher frequencies and because the use of ZnTe also results in stronger absorption of THz radiation by TO phonons in ZnSe. Unfortunately, we were unable to detect

1. Q. Wu and X.-C. Zhang, IEEE J. Selected Topics in Quantum Electronics, **2**, 693 (1996).
2. A. Nahata *et al.*, Appl. Phys. Lett. **69**, 2321 (1996).
3. C. Winnewisser *et al.*, Appl. Phys. Lett. **70**, 3069 (1997).
4. Q. Wu and X.-C. Zhang, Appl. Phys. Lett. **68**, 1604 (1996).
5. Q. Wu and X.-C. Zhang, Appl. Phys. Lett. **70**, 1784 (1997).

# The Effect of Receiving Horn Gain on Measured Radiation Patterns as Applied to the Design of Beam Shaping Reflectors in a Gyrotron

Vimalkaushik Natarajan, Phil J. Sealy and Ronald J. Vernon

University of Wisconsin  
Madison, WI 53706, USA

## Abstract

The effects of the receiving horn gain pattern on near field radiation pattern measurements are discussed in terms of radiation from overmoded waveguides and reflectors encountered in gyrotron related work.

## Introduction

Using measured data for the amplitude and phase distributions of input radiation patterns in the design of reflector systems for gyrotrons has been found to give better results in some cases than using input data obtained from theory [1]. Amplitude measurements at different planes have been carried out for reconstructing the phase distribution for mirror design. These pattern measurements have been made by using a simple open-end rectangular waveguide as the receiving antenna (probe). However, the patterns measured are not the necessarily the true patterns that exist in space, but rather the patterns modified by the receiving probe. Using a receiving probe of inappropriate dimensions can significantly change the shape of the measured pattern. In some cases, it may be of interest to extract the true pattern from the measured patterns. Other times it may be sufficient to check if the measured pattern is indeed a satisfactory approximation to the true pattern for its intended use. For these purposes two models for the relationship between the measured and the true patterns have been analyzed, namely a "point-to-point" model and a "global" model. These two models were compared with the radiation patterns measured at the University of Wisconsin-Madison, Microwave Laboratory. The inclusion of the effects of the receiving pattern of the probe on near-field pattern measurements has been studied in depth for the purpose of obtaining far-field patterns from the near field measurements [2]. However, the application of these techniques for the above purposes seems not to have been widely considered in gyrotron related development.

## Formulation of the Gain Function for the Receiving Probe

The receiving probe used in this investigation was (usually) a simple open-end rectangular waveguide of dimensions such that only its dominant mode could propagate at the frequency of interest. The electric field radiated from such a waveguide when transmitting has been found to be given approximately by expressions derived in [3]. (Better approximations exist, but will not be considered in this summary.) Figure 1. shows the variation of these field amplitudes in the E- and H-planes for an F-band waveguide ( $a = 2.03$  mm,  $b = 1.02$  mm) at 110 GHz. From the Lorentz reciprocity theorem, we know that the receiving pattern of this aperture antenna is the same as the transmitting pattern. Thus the signal strength that is excited in this waveguide when it is receiving depends on the direction from which the radiation is coming (as well as its polarization). When such a receiving antenna is used in an arc scan type measurement made at a large distance from the radiating aperture ( $r > 2D^2/\lambda$ , i.e. in the far field) the effect of the receiving probe pattern can be neglected. However, if the probe is moved in a straight line scan, the receiving pattern of the probe may need to be taken into account even in the far field region, if the angle  $\theta$  of the received radiation with respect to the waveguide axis varies by more than about  $5-10^\circ$  over the length of the scan.

## Analytical Models for Including the Gain Pattern of the Receiving Probe

For extracting the actual pattern radiated from an aperture, two models have been analyzed. Consider an aperture  $S'$  made up of many small Huygen's sources radiating together in free space as shown in Fig. 2. If the receiving probe is not far from the radiating aperture, the radiation from each elemental source reaches the receiving horn at a different angle. Thus, the receiving pattern of the receiving probe must be taken into account for each radiating element. We call this model the point-to-point model. It is a rigorous and realistic method of including the effect of the receiving probe. However, it is somewhat more complicated to extract the actual fields radiated using this model because the gain function is inside of the integral over the source area. Hence another useful model, the global model, in which the gain function is not part of the integrand has been analyzed for easier compensation. In this model, all the rays are assumed to originate from a global "center" situated on the surface of the aperture. Clearly, as one goes farther away from the aperture, the two models will give the same results.

### Theoretical and Measured Data

Both theoretical and experimental work was done for radiation from a Vlasov launcher and a  $TE_{0,2}$  mode from an open-ended circular waveguide. Figure 3 shows the comparison of different models for the gain function and measured radiation patterns for a  $TE_{0,2}$  mode radiated from a circular waveguide. It can be inferred that the effect of the receiving probe is significant and that the global model is a reasonable approximation for extracting the true pattern from the measured radiation patterns in this case. A better model for the probe radiation pattern will produce improved agreement between theory and experiment.

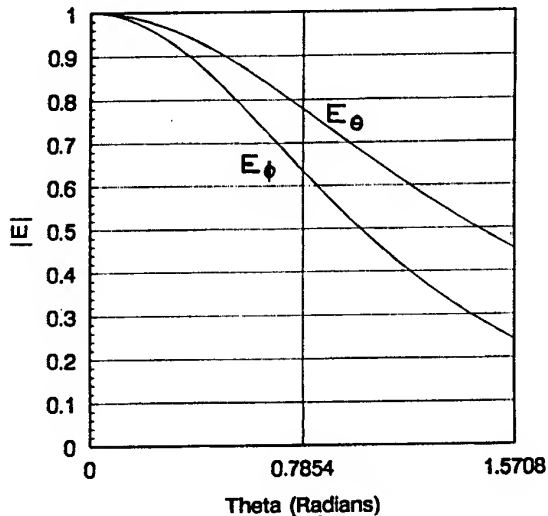


Fig. 1. Variation of the radiated  $E_\theta$  and  $E_\phi$  in the E- and H-planes respectively for an F-band waveguide ( $a = 2.03$  mm,  $b = 1.02$  mm) at 110 GHz according to [3].

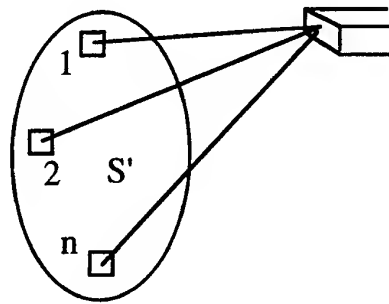


Fig. 2. Infinitesimal Huygen's sources radiating from an aperture in a near field measurement.

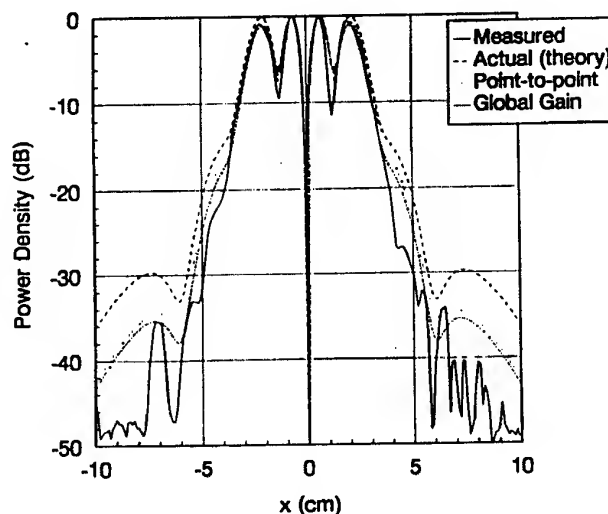


Fig. 3. Comparison of measured and theoretical radiation patterns for a  $TE_{02}$  mode radiating from a 27.8 mm diam. circular waveguide at 60 GHz. The receiving probe was an open-end V-band waveguide. The scan was taken at a distance of 5 cm from the aperture.

1. B. M. Harper and R. J. Vernon, "Beam-Shaping, Dual-Mirror Design Using Measured Amplitude and Reconstructed Phase for the Input," This conference.
2. A. D. Yaghjian, "An Overview of Near-Field Antenna Measurements," IEEE Trans. on Ant & Prop., AP-34, 30, (Jan., 1986).
3. S. Silver, "Microwave Antenna Theory and Design," McGraw-Hill, (1947).

## PHASE SINGULARITIES IN BEAMS

G.F. Brand

*School of Physics, University of Sydney NSW 2006, AUSTRALIA*

### Introduction

Beams of electromagnetic radiation with phase singularities can transport angular momentum and exert torques on objects. These beams and their effects have been studied at optical and at millimeter wavelengths. In this paper we discuss the generation of such beams and describe a particularly efficient way of generating these beams at millimeter wavelengths employing a specially-configured blazed grating.

### Phase singularities

One example of a beam with a phase singularity is the cylindrical variety of higher-order modes that can be generated by a laser, the Laguerre-Gaussian modes. The beam is linearly-polarized and the field has an azimuthal dependence  $E \propto \exp(il\phi)$ . Consider the case where  $l \neq 0$ . Imagine a loop encircling the axis of the beam. Around this loop the phase changes by  $l$  times  $2\pi$ . Now imagine the loop becoming infinitesimally small. The loop reduces to a point on the axis where the phase can take on any value between 0 and  $l$  times  $2\pi$ . Ambiguity is avoided only if the amplitude of the field on the axis is exactly zero. It follows that the beam must be hollow. The axis of the beam is described as a *phase singularity*. The integer  $l$  is known as the *topological charge*.

Such phase singularities have been studied at optical wavelengths[1] and at millimeter wavelengths[2,3,4]. Much of the interest stems from the fact that a beam like this, with this  $\exp(il\phi)$  dependence, carries orbital angular momentum and any interaction with matter is inevitably accompanied by a transfer of angular momentum.

### Diffraction gratings

#### A. Plane gratings

A family of grating patterns is shown in Fig. 1. An analysis of the diffraction from Figs 1(a), (b) and (c) shows that at the first interference maxima, the beams carry singularities of topological charge  $p = 0, 1$  and  $2$ , respectively. The straight through beam in each case carry no topological charge.

In the millimeter-wave experiment described in Ref. [3], the grating pattern was etched onto copper-coated printed-circuit board.

#### B. Blazed gratings

While a plane grating is easy to manufacture, it is very inefficient. Most of the wave continues on in the straight through direction and has no phase singularity. A more efficient approach is to employ the principle of the blazed grating. A suitable choice of blaze angle and period can ensure that almost all of the radiation is diffracted in the one direction. A forked blazed grating would therefore be expected to produce a beam with a phase singularity with very great efficiency.

To test this idea we designed a grating for use with a 105 GHz IMPATT source (wavelength 2.86 mm). The grating was milled from an aluminium block with a blaze angle of  $10^\circ$  and a period  $D = 8.36$  mm. A view of the blazed forked grating is shown in Fig. 2. When the angle of incidence  $\phi = 20^\circ$ , all of the radiation will be diffracted into the direction of the  $m = 1$  interference maximum, at an angle  $\phi' = 0^\circ$ , which in this case coincides with the principal diffraction maximum.



### Experiment

The results are shown in Fig. 3. All of the radiation was diffracted into the expected direction. The beam diffracted from the grating carried a phase singularity while the one diffracted from a conventional blazed grating, with the same blaze angle and period, did not. Agreement with theory is excellent.

Support has come from the Australia Research Council, the University of Sydney and the Science Foundation for Physics within the University of Sydney.

1 I.V. Basistiy, M.S. Soskin and M.V. Vasnetsov, *Optics Comm.* 119, 604 (1995).

2 G.A. Turnbull, et al, *Optics Comm.* 127, 183 (1996).

3 G.F. Brand, *J. Mod. Optics* 44, 1243 (1997).

4 G.F. Brand, *J. Mod. Optics* 45, 215 (1998).

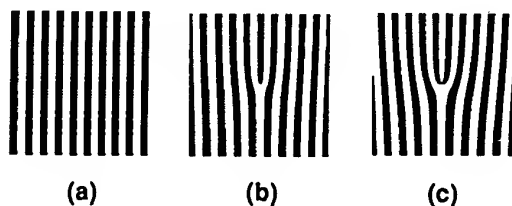


Fig. 1. Plane forked gratings. (a)  $p = 0$ , (b)  $p = 1$ , (c)  $p = 2$ .

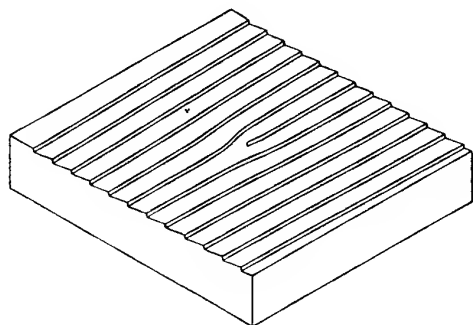


Fig. 2. An isometric view of the forked blazed grating.

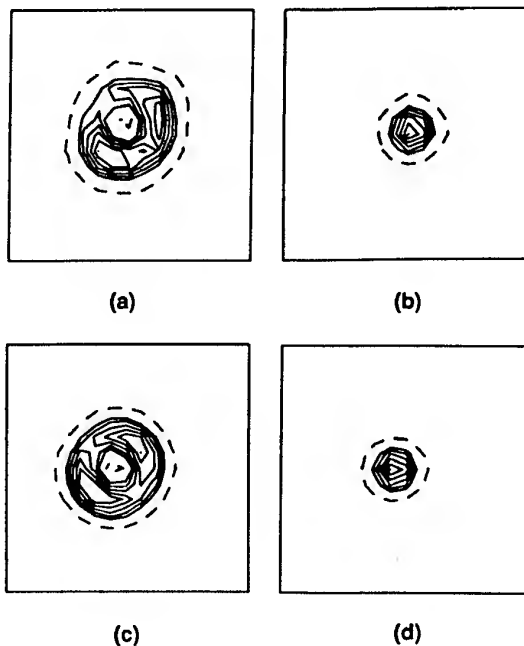


Fig. 3. Contours of intensity in the vicinity of the  $m = 1$  interference maximum for the forked and conventional blazed gratings with  $\phi = 20^\circ$ . (a) and (b) are experimental results for the forked and conventional gratings, respectively. (c) and (d) are the corresponding calculated results. Contours for 0.2 (dashed), 0.5, 0.6, 0.7, 0.8, 0.9 and 1.0 of the maximum intensity are shown. The scanned area is  $80 \text{ mm} \times 80 \text{ mm}$ .

# Frequency-resolved radiation patterns from large-aperture terahertz antennas

P. Uhd Jepsen and H. Helm

Fakultät für Physik, Albert-Ludwigs-Universität,  
Hermann-Herder-Strasse 3, D-79104 Freiburg, Germany  
email: jepsen@uni-freiburg.de

## Introduction

In the recent years there has been considerable interest in the generation of high-power subpicosecond terahertz (THz) radiation. These THz pulses typically consist of one cycle of the electric field, with a highly asymmetric temporal pulse shape. The pulse consists of a short (FWHM 0.5 ps) positive peak followed by a long weak negative tail. The field strength of the first, positive peak is approximately 10 times larger than the field strength of the negative tail, so within a limited time window the pulse therefore resembles a unipolar pulse, consisting only of a half cycle of the electric field. The approximate unipolar shape of the pulse is applied in a new type of experiment conducted mainly by the groups of P. Bucksbaum and R. Jones [1-4]. In these experiments the interaction between unipolar THz pulses and Rydberg atoms is investigated. One of the key parameters in these experiments is the temporal shape of the THz pulses [5]. The temporal and spectral shape of the THz pulse is mainly determined by (a) the generation process and (b) propagation effects. The generation process has been investigated in detail [6-8], but the effects of propagation is still relatively unexplored, with a few exceptions [9,10].

In the work presented here we measure the spatial distribution of radiation (the radiation pattern) emitted from a high-power THz antenna. We find that the radiation is emitted in a beam with frequency-dependent divergence proportional to wavelength, and with a spatial profile closely resembling that of a Gaussian beam. We have determined the radiation pattern of the THz beam at the focal point of a focusing mirror, and comparison of the radiation patterns of the unfocused and focused beams shows that the THz beam propagation is diffraction limited.

## The experiment

In Fig. 1 we show the experimental setup. The THz emitter is driven by femtosecond laser pulses from a Ti:sapphire regenerative amplifier. The emitter consists of a GaAs wafer with active emitting area of  $1 \times 1 \text{ cm}^2$ . A small fraction of the pump beam is split off and used for the detection. We apply the novel technique of free-space electro-optic sampling [11,12] to detect the temporal shape of the THz pulses. The THz beam is directed from the emitter to the detector by either a plane mirror or an off-axis paraboloidal mirror with focal length  $f$ . The distance between emitter and detector is  $2f$ . In this way we are able to compare the unfocused and focused radiation patterns directly. The emitter and the guiding optics in the THz beam path are mounted on a translation stage so that the radiation pattern can be moved across the detector. The radiation pattern at a specific frequency is recorded in the following manner. First temporal traces of the THz pulse are measured as the emitter and guiding optics is moved parallel to the detector plane. Then the spectra of the temporal traces are found by Fourier transformation. The frequency dependent radiation patterns are then obtained by plotting specific frequency components of the spectra versus the translation relative to the detector. In Fig. 2 we show temporal and spectral traces obtained by moving the emitter and guiding optics  $\pm 19 \text{ mm}$  from the propagation axis. The effect of focusing is seen as on-axis pulse shortening and, correspondingly, spectral broadening. The on-axis FWHM of the pulse decreases from 0.8 ps to 0.6 ps upon focusing, and the 10% bandwidth limit increases from 1.0 THz to 1.3 THz. Whereas the pulse shape is relatively insensitive to the off-axis position in the case of the unfocused beam, it can be seen that the focusing only works well close to the propagation axis. In Fig. 3 we show the radiation pattern as function of frequency for the unfocused and focused beams, respectively. The different amplitudes of the traces reflects the useful bandwidth of the THz pulses. Together with the experimental data points we have plotted Gaussian beam profiles fitted to the experimental data. From these fits it is clear that the

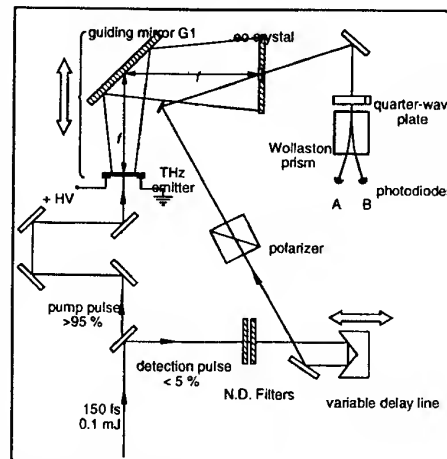


Figure 1: Experimental setup

FWHM of the pulse decreases from 0.8 ps to 0.6 ps upon focusing, and the 10% bandwidth limit increases from 1.0 THz to 1.3 THz. Whereas the pulse shape is relatively insensitive to the off-axis position in the case of the unfocused beam, it can be seen that the focusing only works well close to the propagation axis. In Fig. 3 we show the radiation pattern as function of frequency for the unfocused and focused beams, respectively. The different amplitudes of the traces reflects the useful bandwidth of the THz pulses. Together with the experimental data points we have plotted Gaussian beam profiles fitted to the experimental data. From these fits it is clear that the

spatial profile of the THz beam is Gaussian. In Fig. 4 the  $e^{-1}$ -radius of the fitted Gaussian profiles are plotted versus frequency. In order to determine whether the propagation of the THz beam can be described by Gaussian beam optics we have compared the experimentally obtained spot sizes with the spot sizes predicted by Gaussian optics. The only free fitting parameter is the spot size of the laser beam illuminating the THz emitter. The fitted curves are shown together with the experimental data in Fig. 4. The general agreement is good, especially in the case of the focused beam. We hence conclude that the far-field propagation of the THz beam can be described by Gaussian beam optics.

The radiation pattern in the near field can be modelled both in the time domain and in the frequency domain by results from diffraction theory [10]. We are currently working on a full vector-based simulation of the radiation field based on Kirchhoff diffraction integrals. With this simulation we will be able to model the temporal and spectral behaviour of the emitted THz pulse with high precision.

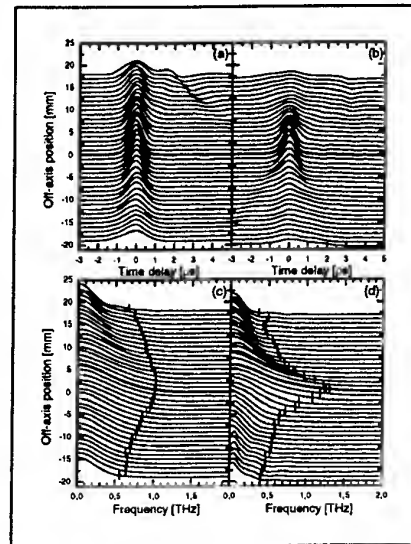


Figure 2: Temporal (a and b) and spectral (c and d) pulse traces of unfocused and focused THz beams

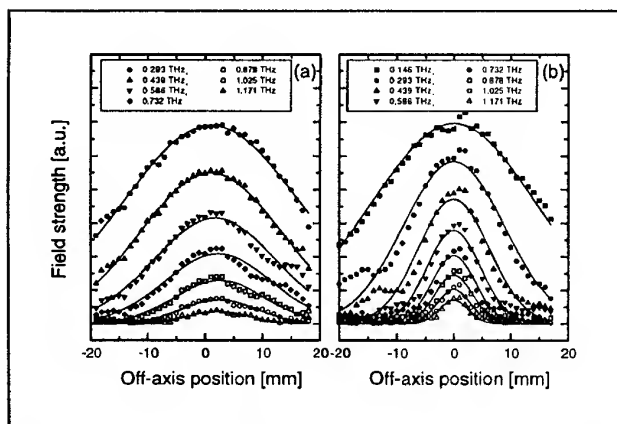


Figure 3: Radiation patterns of (a) unfocused and (b) focused THz beams

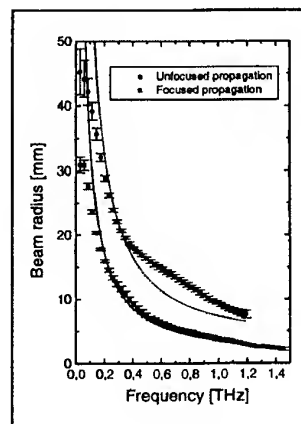


Figure 4: Frequency-dependent spot size of the unfocused and focused THz beam

## References

1. D. You, R. R. Jones, P. H. Bucksbaum, and D. R. Dykaar, *Opt. Lett.* **18** (4) 290 (1993)
2. R. R. Jones, D. You, and P. H. Bucksbaum, *Phys. Rev. Lett.* **70** (9) 1236 (1993)
3. C. Raman, C. W. S. Conover, C. I. Sukenik, and P. H. Bucksbaum, *Phys. Rev. Lett.* **76** (14) 2436 (1996)
4. R. R. Jones, *Phys. Rev. Lett.* **76** (21) 3927 (1996)
5. N. E. Tielking, T. J. Bensky, and R. R. Jones, *Phys. Rev. A* **51** (4) 3370 (1995)
6. P. K. Benicewicz, J. P. Roberts, and A. J. Taylor, *J. Opt. Soc. Am. B* **11** (12) 2533 (1994)
7. G. Rodriguez and A. J. Taylor, *Opt. Lett.* **21** (14) 1046 (1996)
8. A. J. Taylor, G. Rodriguez, and D. Some, *Opt. Lett.* **22** (10) 715 (1997)
9. D. You and P. H. Bucksbaum, *J. Opt. Soc. Am. B* **14** (7) 1651 (1997)
10. E. Budiarto, N.-W. Pu, S. Jeong, and J. Bokor, *Opt. Lett.* **23** (3) 213 (1998)
11. Q. Wu and X.-C. Zhang, *Appl. Phys. Lett.* **67** (24) 3523 (1996)
12. P. Uhd Jepsen, C. Winnewisser, M. Schall, V. Schyja, S. R. Keiding, and H. Helm, *Phys. rev. E* **53** (4) R3052 (1996)

## Slot Array Antennas for 2.5THz-CH<sub>3</sub>OH Laser Radiation

Y. Yasuoka, H. Kobayashi, Y. Abe, and Y. Ohkubo

Department of Electronic Engineering, National Defense Academy,

1-10-20 Hashirimizu Yokosuka 239-8686 Japan

### Introduction

Point contact antenna coupled devices such as MOM diodes, Schottky diodes and warm carrier devices are known as a detector and mixer in the millimeter wave and infrared frequency regions [1]. Although these devices were easy to fabricate, the extreme mechanical instability of these devices made them impractical except for special applications, and encouraged the fabrication of stable, thin-film devices through recently developed microfabrication techniques [2].

In order to obtain high sensitive thin-film antenna coupled devices, it is necessary to fabricate a thin-film antenna which can receive the submillimeter and infrared radiation efficiently, as well as the detector which maintains its  $I$ - $V$  characteristics up to the frequencies of the signals received by the antenna.

The thin-film antennas such as bow-tie, spiral, long wire, log-periodic, microstrip and slot have been fabricated using microfabrication techniques, and the operation properties have been investigated in the millimeter wave and/or far-infrared frequency regions. In these antennas, the slot antenna is one of the leading candidates for a far-infrared array antenna because it has a main lobe normal to the substrate and its wide ground plane makes the microfabrication process easy [3]. We have fabricated thin-film slot array antennas for 94 and 700GHz radiation, and have discussed the receiving properties of the antennas at the frequencies [4], [5]. In the present paper, slot array antennas were fabricated, and the

receiving properties for 2.5THz-CH<sub>3</sub>OH radiation were studied.

### Antenna Properties

Figure 1 shows the SEM photograph of the fabricated three-slot array antenna. The antenna was fabricated on the fused quartz ( $\epsilon_r = 3.8$ ) substrate by a photolithographic method. The length and width of the slot are  $85\mu\text{m}$  ( $0.72\lambda_0$ ) and  $9.4\mu\text{m}$  ( $0.08\lambda_0$ ), respectively. The distance between the slots is  $30\mu\text{m}$  ( $0.5\lambda_d$ ), where  $\lambda_d$  is the wavelength in the dielectric substrate and is given in terms of the free-space wavelength  $\lambda_0$  by  $\lambda_d = \lambda_0/\epsilon_r^{1/2}$ . In order to detect the signal received by the antenna, a bismuth bolometer is formed at the center of the slot antenna. To apply the bias current to the bolometer, the  $2\mu\text{m}$ -width DC cuts (narrow slits) were made on the ground plane.

In the experiments, 2.5THz-CH<sub>3</sub>OH laser was used as a source, and the detected voltage was measured with a lock-in amplifier. The power gain was derived from the detected voltage and the radiation power of the laser by a method similar to that used in the millimeter wave case [6].

Figure 2 shows the antenna patterns of the single-slot antenna and three-slot array antennas for 2.5THz-CH<sub>3</sub>OH laser radiation as well as the theoretical antenna patterns. Here, E-plane is along the electric field direction of the slot, while the H-plane is along the magnetic field. In regard to the E-plane in Fig.2(a), the directive pattern becomes sharper as the

number of slot increases. On the other hand, the pattern does not change significantly in the H-plane as shown in Fig.2(b). From these facts, it is confirmed that improvement of the gain is caused by the placement of the parasitic slots in the E-plane and that the slots effectively work as well as the ones in the millimeter wave region even at 2.5THz. The measured power gain of the three-slot antenna is 5dBi as expected from the theory, and it is 3dB higher compared to the one of the single-slot antenna.

### Conclusion

The three-slot array antennas were fabricated on fused quartz substrates, and the receiving properties were investigated at 2.5THz. It was found that fabricated three-slot array antenna has the power gain of 5dBi as expected from the theory even at 2.5THz, and the power gain is 3dB higher than that of the single-slot antenna. It would be expected that the gain would increase further by increasing the number of the parasitic slot as well as that in the millimeter wave region.

### References

- [1] Y.Yasuoka, T.Okuda, and N.Inoue, Jpn. J. Appl. Phys., 27, L886 (1988).
- [2] C.Fumeaux, W.Herrmann, H.Rothuizen, P.De Natale, and F.K.Kneubühl, Appl. Phys. B63, 135 (1996).
- [3] S.S.Gearhart and G.M.Rebeiz, IEEE Trans. Microwave Theory Tech. 42, 2504 (1994).
- [4] H.Kobayashi and Y.Yasuoka, Trans. IEICE, J80-B- II, 862 (1997).
- [5] H.Kobayashi and Y.Yasuoka, IEEE Trans. Microwave Theory Tech. 46 (1998).
- [6] H.Kobayashi and Y.Yasuoka, Trans. IEICE, J79-B- II, 53 (1996).

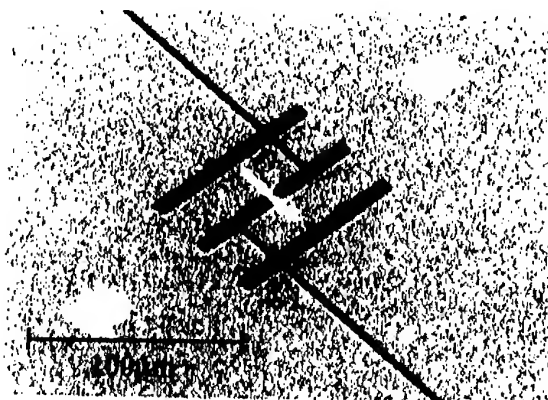


Fig.1. SEM photograph of the three-slot array antenna.

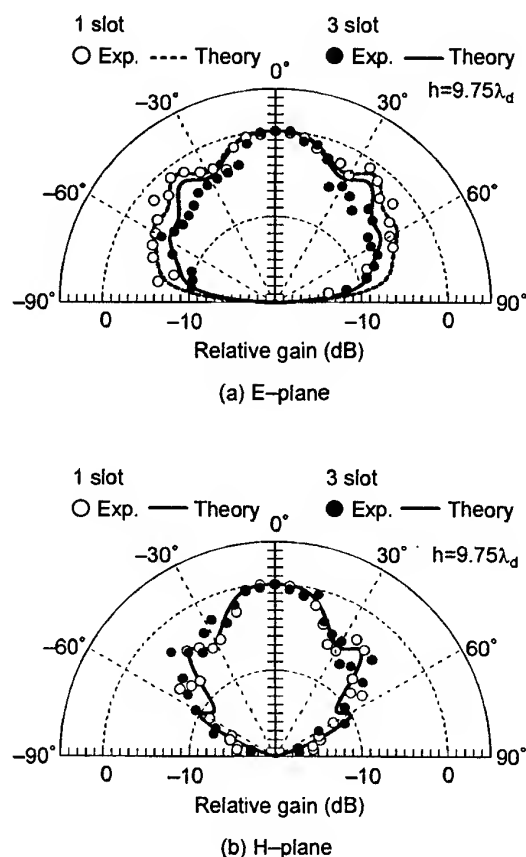


Fig.2. Antenna patterns of the single-slot and three-slot array antennas for 2.5THz-CH<sub>3</sub>OH laser radiation.

# MILLIMETER-WAVE BEAM CONTROL BY THE ILLUMINATION OF A SEMICONDUCTOR

G.F. Brand

*School of Physics, University of Sydney NSW 2006, AUSTRALIA*

## Introduction

The aim of this work is to use diffraction gratings to control a millimeter-wave beam propagating in free space. The diffraction gratings are produced by projecting a grating pattern onto a semiconductor wafer. Where the light falls the conductivity is high because of the formation of a photo-induced electron-hole plasma, elsewhere the conductivity remains low.

An earlier experiment[1] on the diffraction by transmission through such a grating of a millimeter-wave gave results that agreed well with the calculations. However most of the beam proceeded in the straight through direction and only a small fraction was diffracted to the sides.

In the work described here the millimeter waves are reflected from the face of the wafer. We are particularly interested to see under what conditions diffraction into the specular angle may be destructive so that all the radiation goes into adjacent interference maxima. This would allow for example the direction of the beam to be controlled by changing the period of the pattern projected onto the semiconductor. Some preliminary results are reported.

## Reflection grating

Consider an ideal grating made of strips of two types of material with reflection coefficients  $\rho_1$  and  $\rho_2$ , as shown in Fig. 1, illuminated by a plane wave. In the Fraunhofer approximation, the intensity of the diffracted beam in the  $m = 0$  direction, i.e., at the specular angle, is

$$I = \frac{I_0}{4} |\rho_1 + \rho_2|^2$$

and in the  $m = \pm 1$  directions, the directions of the first interference maxima, is

$$I = \frac{I_0}{4} \left( \frac{2}{\pi} \right)^2 |\rho_1 - \rho_2|^2.$$

Our aim of having (i) destructive interference of the beam at the specular angle and hence no reflection in that direction and (ii) constructive interference in the directions of the adjacent interference maxima so most of the beam goes into these directions is achieved if we can create strips with  $\rho_2 = -\rho_1$ . Then,  $|\rho_1 + \rho_2| = 0$  and  $|\rho_1 - \rho_2| = 2\rho_1$ .

## Reflection coefficients for silicon slab with conductor backing

The properties of different reflectors can be found by applying Fresnel's equations. A high-resistivity silicon wafer of thickness  $l = \frac{N\pi}{2nk}$ ,  $N$  odd (where  $n$  is the refractive index and  $k$  is the wavenumber) with a perfect

conductor backing it would be very effective. The diffraction patterns expected when the wafer is a circular disk, radius 25 mm, and the pattern projected on it has a period of 20 mm and the conductivity of the areas where the light falls is 2, 5, 10, 20, 50 S m<sup>-1</sup> is shown in Fig 2. The 105 GHz source is 500 mm from the wafer, the angle of incidence is 20° and, at the specular angle, the detector is 500 mm from the wafer. The pattern is scanned from -200 mm to +200 mm in a direction perpendicular to the specular beam.

If the illumination is not sufficiently intense and the conductivity not sufficiently high, the diffracted signal remains small and most of the beam is specularly reflected.

### Experiment

One set of experimental results is shown in Fig. 3. Because the silicon wafers available to us had a thickness of 0.38 mm, a 0.58 mm layer of mylar was added in order to locate the conductor at the optimum distance behind the front face. The semiconductor was illuminated by a pulsed arc lamp (Oriel Series Q flashlamp with a 5 J xenon bulb). Fig. 3(a) shows the detected signal at the specular angle and Fig. 3(b) in the direction of the first interference maximum.  $\sigma$  is estimated to be  $40 \text{ S m}^{-1}$  at the pulse maximum.

### Concluding remarks

This is contribution to a more general program to develop ways of controlling millimetre-waves and integrating millimetre-wave and optical techniques. This approach offers optical control of the intensity and direction of millimetre-wave beams propagating in space, and the pattern is projected from a distance, rather than having optical fibres or masks in contact with the semiconductor, and so offers great flexibility.

Support has come from the Australia Research Council, the University of Sydney and the Science Foundation for Physics within the University of Sydney.

1 G.F. Brand, Int. J. Infrared and Millimeter Waves 17, 1253 (1996).

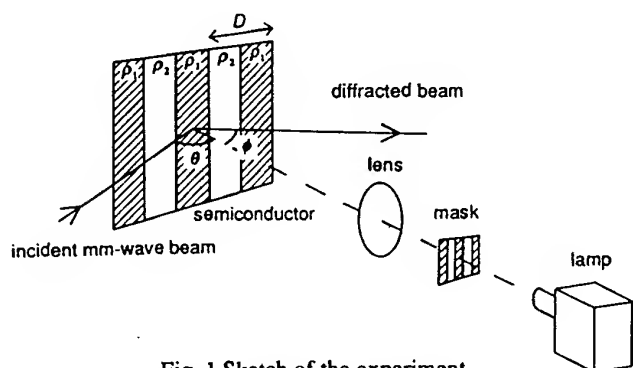


Fig. 1 Sketch of the experiment.

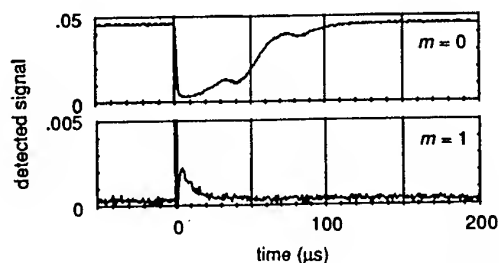


Fig. 3 Experimental results. Upper trace: diffraction into the  $m = 0$  (specular) direction; lower trace: into the  $m = 1$  direction.

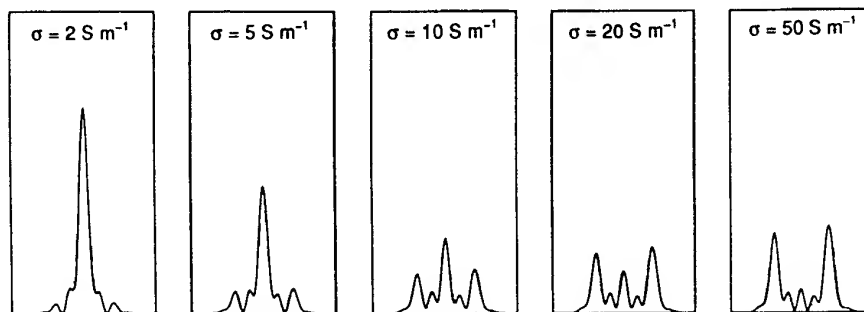


Fig. 2 Calculated diffraction patterns for a range of conductivities.

## Simulation and Experimental Study of a Wavebeam Remote Steering System

A.V.Chirkov,<sup>1</sup> G.G.Denisov,<sup>1</sup> W.Kasperek,<sup>2</sup> D.Wagner<sup>2</sup>

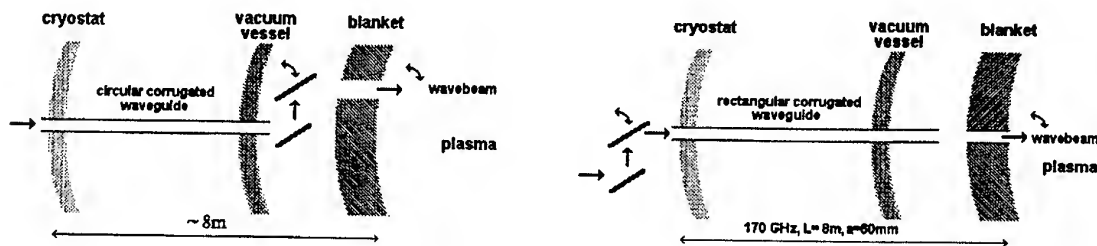
<sup>1</sup>Institute of Applied Physics, Russian Academy of Sciences, 46 Ulyanov St., 603600 Nizhny Novgorod, Russia

<sup>2</sup>Universitaet Stuttgart, Institut fuer Plasmaforschung, Pfaffenwaldring 31, D-70569 Stuttgart, Germany

### Introduction

The present design for the ITER ECW launcher is based on individual circular corrugated waveguides running until the vacuum vessel. At each waveguide end, a pair of mitre bends (one of them being movable) provides steering of the beam between 0° and 40°. The power is launched through slits in the blanket, which thus provides screening for the optics.

An alternative to circular waveguides as planned for the reference launcher are corrugated square or rectangular waveguides, as proposed in [1]. These waveguides show imaging characteristics for length  $L_B \approx 8a^2/\lambda$  [2]; the effect can be used for remote scanning of the beam: a wave which is coupled to the waveguide at an angle leaves the waveguide at the output at the same angle, provided that the length is properly chosen.



Current and alternative launcher schemes

The range of acceptance angles calculated in [1] is about  $\pm 10^\circ$ , which is less than the optimum of  $30^\circ$ ; however, according to our proposal the length of the waveguide could be halved and thus the scanning range could be increased.

To get a safe data base for the realisation of this concept, theoretical and experimental studies were performed.

### Calculations and Measurements

The procedure of the field calculation in a waveguide is based on the fast mode decomposition-composition and it takes, for example, 4 seconds for Pentium-100 for  $128 \times 128$  field calculation on the basis of  $2^{14}$  modes.

For the field calculation in free space a code compatible with the previous one was developed. This code allows field calculation for arbitrary apertures and distances from the waveguide end.

Steering angle at input ( $\varphi$ )	Power in the main lobe	Direction of the main lobe
0.0	> 0.99	- $\varphi$
2.5	> 0.99	- $\varphi$
5.0	> 0.99	- $\varphi$
7.5	0.985	- $\varphi$
10.0	0.985	- $\varphi$
11.0	0.98	- $\varphi$
12.5	0.92	- $\varphi$
15.0	0.40 / 0.60	- $\varphi$ / + $\varphi$
16.9	0.90	+ $\varphi$
20.3	0.80	- $\varphi$

Calculations were performed mainly for two frequency ranges, around 140 GHz and 170 GHz, for a square waveguide cross-section of  $60 \times 60$  mm. A Gaussian beam is assumed to be injected into the waveguide.

The fields were analysed by calculating the matching coefficient to the input beam, and by calculating the power in the wanted output beam relative to the total launched power which gives the practical efficiency, i.e. the power available in a beam with a divergence of a few degrees.

In the Table, the output beam efficiencies are listed as a function of the steering angle  $\varphi$  for a frequency of 142.21 GHz, a waveguide cross-section of  $60 \times 60$  mm and a fixed length of  $L = 6720$  mm, which is optimal for  $\varphi = 10$  degrees.

At a frequency of 170 GHz, the results are similar for the corresponding fixed waveguide length of  $L = 8033$  mm.



To prove the calculations, experiments have been performed around 140 GHz and 170 GHz. A corrugated square waveguide (total length 8.4 meters, in 20 pieces) with a side-length of 60 mm was fabricated. The waveguide was excited by a lens horn, which emits a Gaussian beam with a waist radius of about 22 mm. This lens horn could be rotated around the waveguide input. Measurements of amplitude and phase distribution were performed in the output plane of the waveguide and compared to the theoretical patterns. Additionally, far-field patterns were recorded at a distance of 1.7 meters, which would correspond approximately to the plasma at half radius. The results shown in Fig. 1 and 2 validate the concept.

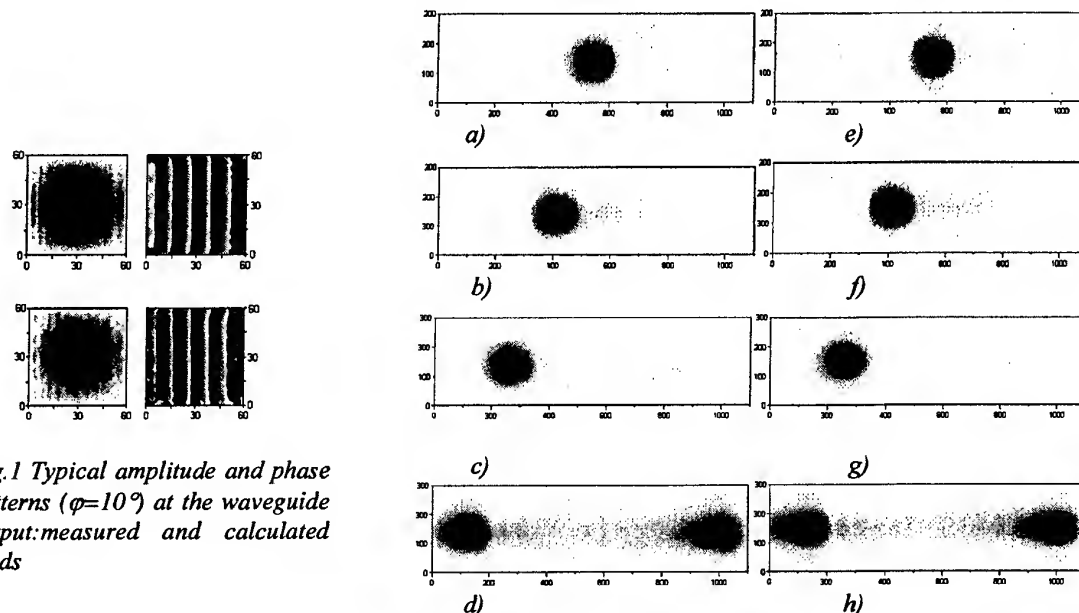


Fig. 1 Typical amplitude and phase patterns ( $\varphi=10^\circ$ ) at the waveguide output: measured and calculated fields

Fig. 2 Far field amplitude patterns (distance 1687mm from the waveguide output): a, b, c, d - measured, e, f, g, h - simulated. Launching angles: a, e -  $0^\circ$ ; b, f -  $5^\circ$ ; c, g -  $10^\circ$ ; d, h -  $14.4^\circ$ .

#### Compatibility with ITER Machine

This concept of beam steering can be integrated into the present waveguide launcher design by the following:

- Exchange of the circular corrugated waveguide by a square corrugated waveguide. For a cross-section of 60x60 mm, the length should be about 8.1 meter, a cross-section of 50x50 mm yields  $L=5.6$  meter. These data are compatible with the present launcher with respect to power capability and dimensions.
- Exchange of the movable mitre bend in the launcher by fixed mirrors, which are set to the mean launcher angle  $\varphi_0$ . For this case, the scanning range of the launcher is  $\varphi_T = \varphi_0 \pm \varphi$ .
- Addition of a scanning unit outside of the launcher module. For toroidal scanning only, this module can be very compact and can consist of one modified mitre bend per waveguide.
- The vacuum barrier windows should be placed into the square corrugated waveguide to make full use of the advantages of the remote steering system. In this case, some reflections will occur when the beam is steered, which however are tolerable (max. 0.3 %).

#### Summary

We have studied an alternative concept for the ITER ECRH antenna which do not include moveable parts close to the plasma. A waveguide solution is based on the present concept but modified by the use of square waveguides. This would allow continuous angle variation in a limited range of up to  $30^\circ$ . In addition to the theoretical analysis, this concept has been demonstrated experimentally.

#### References:

1. Prater, R. et al., 1997, The ECH launcher for ITER, Proc. of the 10th workshop on ECE and ECRH, EC-10, Ameland, The Netherlands, April 1997.
2. Semenov, and Rivlin, 1981, Laser Focus Feb. 1981, p.82-84.

## Nonlinear Optic Coefficients of Ferroelectrics

Junaidah Osman<sup>1</sup>, Y. Ishibashi<sup>2</sup> D.R. Tilley<sup>1,3</sup> and J.F. Webb<sup>1</sup>

1. School of Physics, Universiti Sains Malaysia, 11800 USM Penang, Malaysia
2. Dept. of Applied Physics, School of Engineering, Nagoya University, Nagoya 464-01, Japan
3. Dept. of Physics, University of Essex, Colchester CO4 3SQ, UK

Ferroelectric crystals have large nonlinear optical coefficients in the visible and near infrared because of the lattice deformability. We have shown[1] how to calculate the coefficients through the resonant region in the FIR from the Landau-Devonshire expression for the free energy  $F$  in terms of the polarization  $P$ :

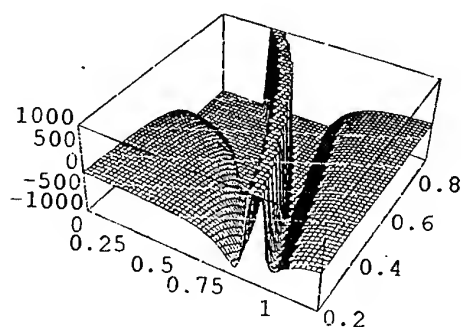
$$F = \frac{1}{2} \frac{A}{\epsilon_0} P^2 + \frac{1}{4} \frac{B}{\epsilon_0^2} P^4 + \frac{1}{6} \frac{C}{\epsilon_0^3} P^6 \quad (1)$$

where  $P^2 = P_x^2 + P_y^2 + P_z^2$  and  $A = a(T - T_C)$ . The frequency dependence is deduced from an equation of motion  $m\ddot{P}_i + \gamma\dot{P}_i = -\partial F / \partial P_i + E_i$  where  $\vec{E}$  is the FIR field. This is nonlinear in  $\vec{P}$  but linear in  $\vec{E}$ ; it is inverted to give  $\vec{P} = \tilde{\chi}^{(1)} \vec{E} + \tilde{\chi}^{(2)} \vec{E} \vec{E} + \tilde{\chi}^{(3)} \vec{E} \vec{E} \vec{E}$  where tensor contractions are implied. We have given expressions[1] for all the  $\tilde{\chi}^{(2)}$  effects in the ferroelectric phase (they vanish in the paraelectric phase) and for the main  $\tilde{\chi}^{(3)}$  effects. Here we discuss the magnitudes, temperature and frequency dependences of the elements  $\chi_{zzz}^{(2)}$  for second harmonic generation (SHG) and the Pockels effect when the FIR and static E fields lie along the direction of the static polarization  $\vec{P}_0$ . We discuss second-order transitions,  $C = 0$  and  $B > 0$ , and take numerical values for BaTiO<sub>3</sub>.

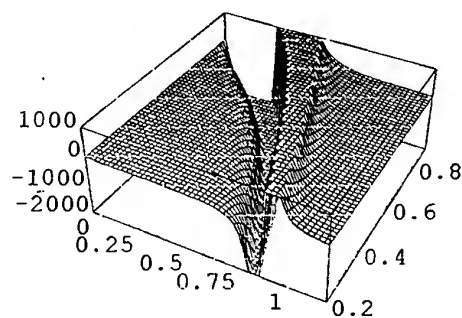
The static parameters are  $a$  and  $B$ . The former, which is dimensionless, is the inverse of the Curie constant so[2]  $a = 5.882 \times 10^{-6}$ .  $B$  is found from  $P_0^2 = -\epsilon_0 A / B$  and the textbook temperature dependence of  $P_0$  [3] gives  $B = 1.89 \times 10^{-15} \text{ m}^3/\text{Joule}$ . The parameter  $m$  can be found from the soft-mode frequency[3] and we estimate  $m = 6.44 \times 10^{-21} \text{ kg m}^3 \text{ s}^{-2} \text{ A}^{-2}$ . The SHG is given by[1]  $\chi_{zzz}^{SHG} = -1.5 B P_0 s(2\omega) s^2(\omega)$  where  $s(\omega) = (2|A| - i\epsilon_0 \omega \gamma - \epsilon_0 m \omega^2)^{-1}$ .  $\chi_{zzz}^P$  is given by a similar expression except that the numerical factor is 6 and  $s(2\omega)$  is replaced by  $s(0)$ . We put  $f = \omega / (2\pi f_0)$  where  $\epsilon_0 m (2\pi f_0)^2 = 2aT_C$  with  $f_0 = 4.53 \times 10^{13} \text{ Hz}$ , and  $t = T/T_C$ . In SI units ( $\text{mV}^{-1}$ ) the SHG and Pockels tensor elements then are  $\chi_{zzz}^{SHG} = -9.37 \times 10^{-9} (1-t)^{1/2} (1-t-2igf-4f^2)^{-1} (1-t-igf-f^2)^{-2}$  where  $g = \gamma / f_0$  and

$\chi_{zz}^P = -3.748 \times 10^{-8} (1-t)^{-1/2} (1-t-igf-f^2)^{-2}$ . These have resonances at the soft-mode frequency  $f$  (and for SHG also  $2f$ )  $= f_S = (1-t)^{1/2}$  and strong temperature dependences. A rule of thumb for magnitudes is  $\chi^{(2)} \approx 10^{-11}$  and on this scale the values quoted are very large. The magnitudes follow from the large Curie constant so physically they result from the lattice deformability. The graphs below show  $10^9 \chi^{(2)}$  ( $\text{mV}^{-1}$ ) versus  $f$  on a scale of 0 to 1.2 (P) or 1 (SHG) and  $t$  on a scale 0.2 to 0.9 with  $g = 0.1$ .  $\text{Re}(\chi^P)$  and  $\text{Im}(\chi^P)$  display the soft-mode resonance while  $\text{Re}(\chi^{SHG})$  and  $\text{Im}(\chi^{SHG})$  have resonances at  $f_S$  and at  $f_S/2$ . For illustration the vertical axes are truncated at  $10^3$  ( $\chi = 10^{-6} \text{ Vm}^{-1}$ ) but as  $t \rightarrow 1$  the values go beyond  $10^4$ .

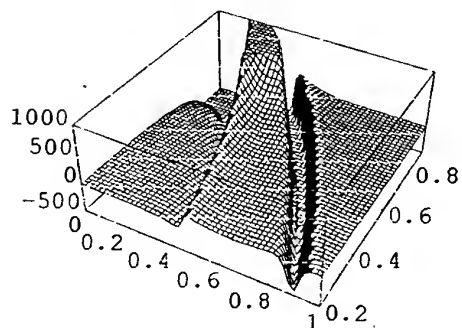
This work was supported by IRPA (Malaysian Government) Grant 09-02-05-6001 and by JSPS Travel Grants to YI and DRT.



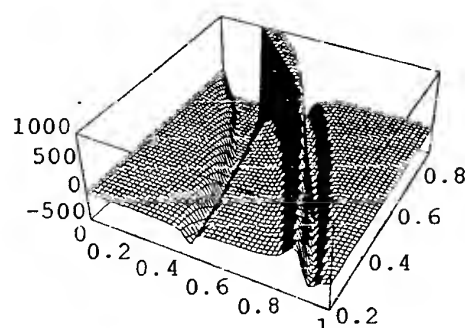
$\text{Re}(\chi_{zz}^P)$



$\text{Im}(\chi_{zz}^P)$



$\text{Re}(\chi_{zz}^{SHG})$



$\text{Im}(\chi_{zz}^{SHG})$

### References

1. Junaidah Osman, Y. Ishibashi and D.R. Tilley, submitted to Jpn J. Appl. Phys.
2. J.C. Burfoot and G.W. Taylor, Polar Dielectrics and their Applications (Macmillan, London 1979)
3. C. Kittel, Introduction to Solid State Physics (6/e, John Wiley, New York 1986)

## THz Time Domain Spectroscopy of Electro-Optic Crystals

M. Schall<sup>1</sup>, H. Helm<sup>1</sup>, and S. R. Keiding<sup>2</sup>

<sup>1</sup>Dept. of Molecular and Optical Physics, University of Freiburg, Germany  
Hermann-Herderstr. 3, D-79104 Freiburg, Tel.: \*\*49-761-203-5909, Fax.: -5955

<sup>2</sup>Department of Chemistry, University of Aarhus, Denmark  
e-mail: Michael.Schall@physik.uni-freiburg.de

### Abstract

We report an experimental investigation of the far-infrared properties of the non-linear crystals LiNbO<sub>3</sub>, LiTaO<sub>3</sub>, ZnTe and CdTe. Using Terahertz time domain spectroscopy (THz-TDS) we have measured the complex frequency response up to 3 THz (100 cm<sup>-1</sup>) for these electro-optic crystals with high accuracy (<0.5%). We have found additional absorption features, in particular in CdTe.

Recently there have been remarkable progress in the electro-optic (eo) detection and generation of subpicosecond terahertz (THz) pulses[1]-[3]. Especially in detecting high power THz pulses the eo technique shows the best performance and enables 2-dim THz sampling to obtain images [4].

In order to optimize the THz system it is crucial to know the optical characteristics of the eo material in the far infrared (FIR) regime. We report an experimental investigation of the dielectric properties of the eo crystals LiNbO<sub>3</sub>, LiTaO<sub>3</sub>, ZnTe and CdTe using terahertz time domain spectroscopy (THz-TDS) in the frequency range between 100 GHz and 3 THz at room temperature [5].

We are using a standard THz time domain spectrometer (Fig. 1), which is capable to generate and detect FIR radiation in the frequency range between 0.1 THz and 4.5 THz [6]. The THz spectrometer is driven by laser pulses of 25 fs duration supplied from a Titan:Sapphire at 80 MHz repetition rate. By comparing the complex fourier spectrum of a THz pulse transmitted through a sample with a reference spectrum without a sample, we determine the complex dielectric function i.e. both the index of refraction and the absorption of the eo crystals. For the birefringent crystals both ordinary and extraordinary dielectric parameters have been obtained using polarized THz radiation.

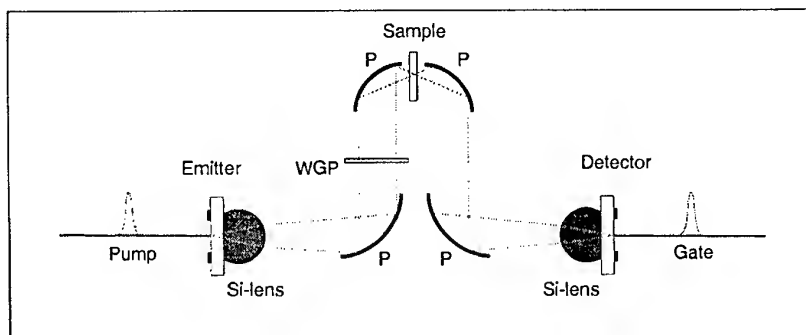


Figure 1: *Experimental setup of the THz spectrometer. (P) paraboloidal mirror, (WGP) wire grid polarizer.*

Experimental results for the index of refraction and the absorption coefficient versus the frequency are illustrated in Fig. 2 for  $\text{LiNbO}_3$  and  $\text{ZnTe}$ . In contrast to the isotropic semiconductor  $\text{ZnTe}$ , the dielectric crystal  $\text{LiNbO}_3$  shows a large birefringence in the THz range. The simplest approach to represent the results is the Lorentzian single oscillator model for both index of refraction and absorption. This allows us to compare the data with the existing literature. Besides the large Lorentzian absorption profile due to the first transverse optical (TO) lattice resonance we have found additional absorption features in the semiconductors.

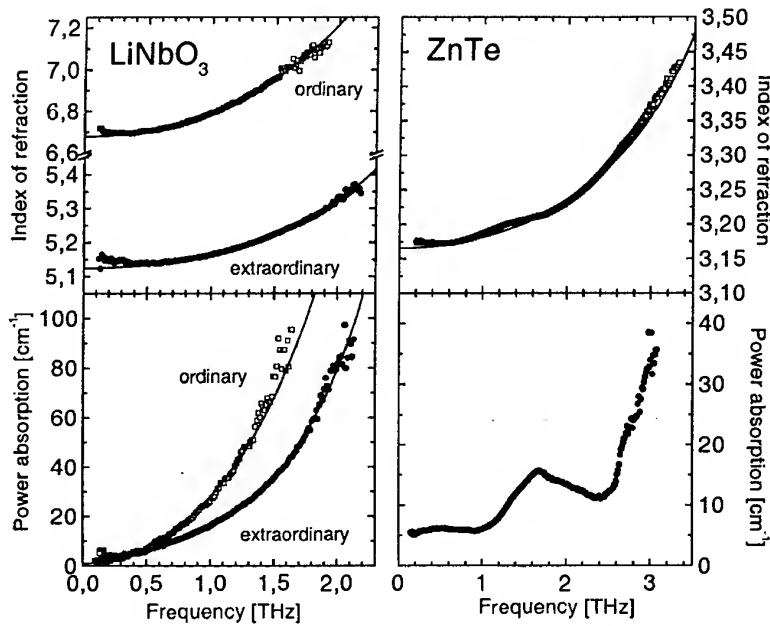


Figure 2: Index of refraction and absorption coefficient of  $\text{LiNbO}_3$  and  $\text{ZnTe}$  in the FIR regime obtained by THz-TDS. The Lorentzian fits are represented by solid lines.

## References

- [1] Q. Wu, X.-C. Zhang, Appl. Phys. Lett. **68**, (1996)
- [2] P. U. Jepsen, C. Winnewisser, M. Schall, V. Schyja, S. R. Keiding, H. Helm, Phys. Rev. E **53**, (1996)
- [3] A. Nahata, A. S. Weling, T. F. Heinz, Appl. Phys. Lett. **69**, 2321 (1996)
- [4] Q. Wu, T. D. Hewitt, X.-C. Zhang, Appl. Phys. Lett. **69**, 1026 (1996)
- [5] M. Schall, H. Helm, S. R. Keiding to be published
- [6] D. Grischkowsky, S. Keiding, M. van Exter, C. Fattinger, J. Opt. Soc. Am. B **7**, 2006 (1990)

# **Millimeter Wave Spectroscopy of Superionic Conductor LiNiO<sub>2</sub>**

**S. Ono<sup>1)</sup>, Y. Ikeuchi<sup>1)</sup>, H. Ohta<sup>1)</sup>, T. Nanba<sup>1)</sup>,  
S. Okubo<sup>2)</sup>, A. Hirano<sup>3)</sup>, R. Kanno<sup>3)</sup>**

<sup>1)</sup>*Department of Physics, Faculty of Science, Kobe University,  
1-1 Rokkodai, Nada, Kobe 657-8501, Japan*

<sup>2)</sup>*The Graduate School of Science and Technology, Kobe University,  
1-1 Rokkodai, Nada, Kobe 657-8501, Japan*

<sup>3)</sup>*Department of Chemistry, Faculty of Science, Kobe University,  
1-1 Rokkodai, Nada, Kobe 657-8501, Japan*

LiNiO<sub>2</sub> is known to be a superionic conductor and promising for electrode material in secondary Li batteries especially when it is stoichiometric. [1] But the composition of LiNiO<sub>2</sub> is very sensitive to the synthesis composition, especially the sintered temperature, and it can be easily lead to a decomposition to Li<sub>1-x</sub>Ni<sub>1+x</sub>O<sub>2</sub>. However, Kanno *et al.* succeeded in synthesizing nearly stoichiometric LiNiO<sub>2</sub> by controlling synthesis condition. [1] Previously we performed the reflection measurements in the millimeter wave region using stoichiometric LiNiO<sub>2</sub> in order to obtain the information about the diffusive motion of Li<sup>+</sup> ions separately by observing ionic plasmon whose existence can be proved as a definite increase in a reflectivity towards a low energy side in the millimeter wave region because of the difference between the mass of Li<sup>+</sup> and that of electron. [2] The first observation of ionic plasmon has been performed for alkali silver iodide superionic conductors MAg<sub>4</sub>I<sub>5</sub> (M=Rb, K and NH<sub>4</sub>) by Awano *et al.* [3] The reflectivity and ionic conductivity of these substances become high above T<sub>c</sub>. In this paper, we obtained new sample of LiNiO<sub>2</sub>, which had superior quality, synthesized by Kanno *et al.* and we have performed more detailed temperature dependence in the wider wave number region. The temperature dependence reflection measurements of LiNiO<sub>2</sub> were performed at 79 K, 197 K, 300 K, 340 K and 380 K in the spectral region from 5 cm<sup>-1</sup> to 60 cm<sup>-1</sup> using the beam line BL6A-1 of UVSOR, the electron storage ring facilities of Institute of Molecular Science in Okazaki. Figure 1 shows the reflectivity spectra of our sample. As a result of our measurements of stoichiometric LiNiO<sub>2</sub> sintered at 650°C, we observed significant increase of the reflection especially below 10 cm<sup>-1</sup> for the temperature region above 300 K. The reflectivity is almost the same at 79 K and 197 K in all spectral region. However, the reflectivity starts to rise at 300 K and changes its value significantly from about 0.3 to 0.8 in the low energy region below 10 cm<sup>-1</sup> as the temperature is increased. On the other hand, no significant change of the reflectivity is observed in the high energy region at 300 K, 340 K and 380 K. These results suggest that the diffusive motion of Li<sup>+</sup> ions starts at 300 K and keeps increasing above 300 K. The results at 79 K and 197 K are consistent with the result of our previous reflection measurements of LiNiO<sub>2</sub>. Thus, we suggest that the rise of the reflection can be attributed to Li<sup>+</sup> ionic plasmon in LiNiO<sub>2</sub>. The experimental results and the analysis of our measurements will be presented.

## References

1. R. Kanno, H. Kubo and Y Kawamoto. :J. Solid State Chem. 110 , 216 (1994).
2. H. Ohta, T. Nanba, A. Hirano and R. Kawamoto. :Digest of 21st IR and MM Wave Conference Berlin. CTh3, (1996).
3. T. Awano, T. Nanba and R. Kanno. :Solid State Ionics. 53-56 , 1296 (1992).

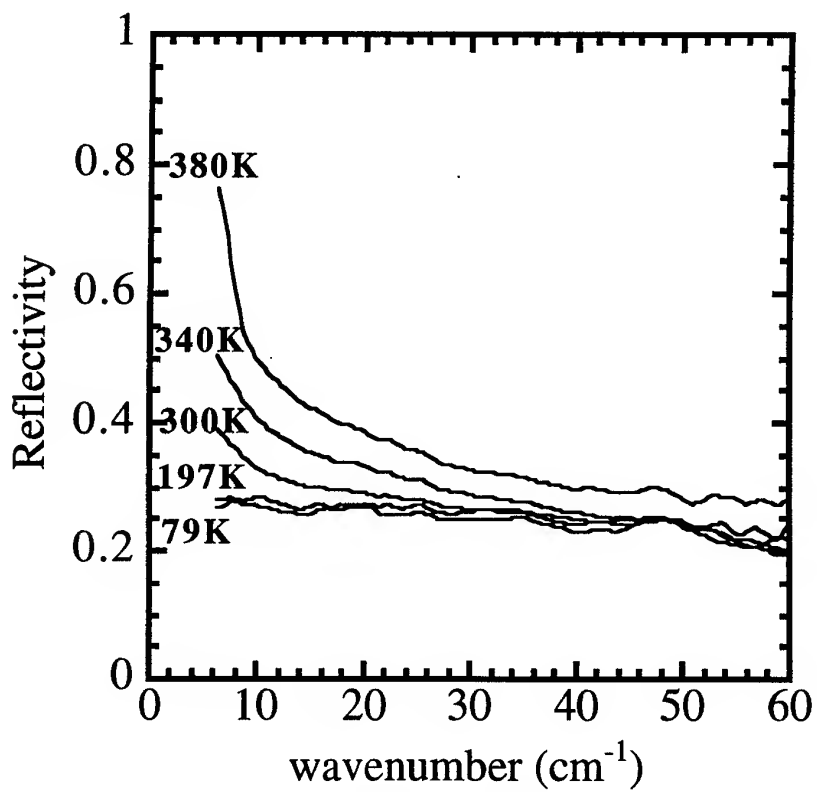


Fig.1 The temperature dependence of reflectivity spectra of  $\text{LiNiO}_2$  sample sintered at 650 °C.

## Charge distributions in ferroelectric structures

S R P Smith and T J Parker

Department of Physics, University of Essex, Colchester CO4 3SQ, UK

### Abstract

The switching behaviour of thin film ferroelectric structures is determined primarily by the properties of the free charges at boundary layers between domains of opposite polarisation. We have used a Landau theory model to describe the hysteresis curves (polarisation vs. applied voltage) as measured in typical experiments on thin film ferroelectric capacitor structures, in which it is shown that the free charges play a crucial role in satisfying the electrostatic boundary conditions and conditioning the switching properties. These free charges form a surface plasmon at the domain boundaries. We will discuss ways in which these plasmons can be investigated by infrared spectroscopy.

### 1. Introduction

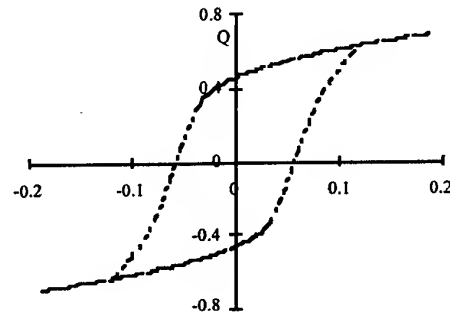
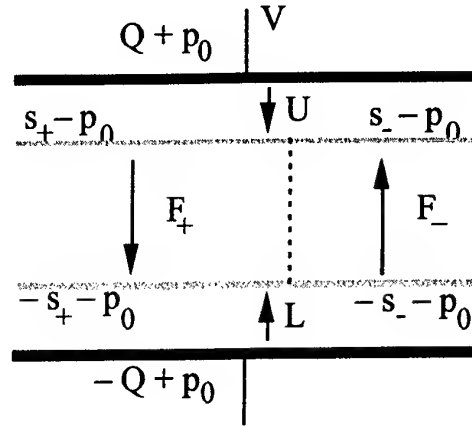
Layered ferroelectric structures continue to attract interest because of their device applications. The simplest structure is a single layer of a ferroelectric medium in a capacitor geometry with metal electrodes on the surfaces. Since the ferroelectric alignment (assumed to be normal to the plane) can be reversed by applying an appropriate voltage  $V$  to the plates, the device can act as a memory element. The commonly observed property of such a structure is the hysteresis loop – variation of stored charge  $Q$  with applied voltage  $V$ . The Landau-Devonshire model of a ferroelectric has for many years been used to model the behaviour of bulk ferroelectrics. In its basic form, this model predicts that  $Q$  will change discontinuously at the switching voltage  $V_c$ , whereas experimental measurements always show a continuous variation of  $Q$  with  $V$ . We have recently developed a new model<sup>[1]</sup> to explain the polarisation switching in layered ferroelectric structures in which we show that the hysteresis behaviour is crucially dependent on the existence of domains within the layer, and that, given a suitable configuration of these domains, the Landau-Devonshire model can be used to explain the type of hysteresis curve observed experimentally.

Free electric charges must exist at the interface between domains in order to satisfy the electrostatic boundary conditions. The motion of these free charges will determine the dynamics of the switching process, and it is therefore of considerable interest to study their behaviour. The free charges form a 2-d plasmon at the interface between domains. The purpose of this paper is to show that useful information about this plasmon (i.e. charge density and mobility) is obtainable by far-infrared spectroscopy studies. Such measurements are likely to provide the most direct method of investigating the properties of the charge layers and the way in which they determine the switching behaviour of thin film ferroelectric structures.



## 2. Model for ferroelectric capacitor structure

The basic model for the capacitor structure is shown. There are four regions: upper and lower non-switching layers U and L, and a switching layer F divided into two domains  $F_+$  and  $F_-$  of opposite polarisation, with relative fractions  $f_+$  and  $f_-$ . Switching is achieved by motion of the domain wall between  $F_+$  and  $F_-$ . The surface charge densities on the top and bottom plates are  $(\pm Q + p_0)$  respectively ( $p_0$  is the long term equilibrium density at zero applied voltage); the charge densities in the boundary regions between  $F_{\pm}$  and U are  $(s_{\pm} - p_0)$ , and  $(-s_{\pm} - p_0)$  between  $F_{\pm}$  and L. Continuity of the normal component of displacement field  $D$  in the boundary regions enables  $s_{\pm}$  to be determined, using the Landau-Devonshire model for the dependence of polarisation  $P$  on electric field  $E$  in each of the 4 regions. The basic assumption is that the charge in the two boundary layers is mobile within the layer but cannot move vertically in the structure, so the total charge  $s_0 = f_+ s_+ + f_- s_-$  must remain constant. Given these assumptions, a hysteresis curve (a plot of  $Q$  vs.  $V$ ) typical of experimental measurements is obtained, as shown. The dashed lines show the parts of the curve where the fractions  $f_{\pm}$  are changing, with  $f_+ = 0$  on the bottom solid curve and  $f_- = 0$  on the upper solid curve.



## 3. Surface plasmons

The free charges in the boundary layers will behave as a surface plasmon, providing a surface plasmon polariton<sup>[2]</sup> (an electrostatic excitation pinned at a charged surface) with characteristic frequency  $\Omega_s = \sigma e / m \epsilon_0 c$ , where  $\sigma \sim p_0 \sim 0.1 \text{ C m}^{-2}$  is the surface charge density. If the top surface of the structure is designed as a metallic grating of period  $d$ , this polariton should be observable in far infrared spectroscopy at a resonant frequency  $\omega \sim \sqrt{\pi \Omega_s c / \epsilon d}$ , where  $\epsilon$  is the dielectric constant of the ferroelectric. With  $d \sim 0.5 \mu\text{m}$ , the resonant frequency  $\omega \sim 40 \text{ cm}^{-1}$  is within the far infrared range, and should provide a measurable excitation spectrum.

The mechanism by which polarisation reversal occurs in a ferroelectric structure is still an open question. A far infrared reflectivity experiment would provide the only method of directly investigating the behaviour of the compensation charge layers in such structures.

## 4. References

1. S.R.P. Smith, J. Phys. C: Solid State Physics (to be published, 1998)
2. M.G. Cottam and D.R. Tilley, *Introduction to Surface and Superlattice Excitations*, Cambridge University Press (Cambridge) 1989.

# Surface Optics of Ferroelectrics

Khian-Hooi Chew<sup>1</sup>, R. L. Stamps<sup>2</sup> and D. R. Tilley<sup>1,3</sup>

1. School of Physics, Universiti Sains Malaysia, 11800 USM Penang, Malaysia
2. Dept. of Physics, University of Western Australia, Nedlands, WA 6907, Australia
3. Dept of Physics, University of Essex, Colchester CO4 3SQ, UK

Ferroelectric films are of topical interest, partly because of their use in memory devices[1]. One issue is whether the critical temperature  $T_C$  and other properties are functions of film thickness. The experimental evidence is contradictory but attempts have been made to develop a theory by adding symmetry-allowed terms to the Landau free energy[2]. For a film with in-plane polarization  $P(z)$  the free energy per unit area is an integral over a function which includes a term  $(1/2)D(dP/dz)^2$ . The Euler-Lagrange equation contains  $Dd^2P/dz^2$  and the theory is completed with boundary conditions  $\vec{n} \cdot \nabla P + \delta^{-1}P = 0$  at the surfaces. Up to now attempts to determine the parameters  $D$  and  $\delta$  have concentrated on static properties like specific heat and dielectric constant. Our proposal is that optical (FIR) probes may prove better. We use an equation of motion  $m\ddot{P}_i + \gamma\dot{P}_i = -\partial F/\partial P_i + E_i$  where  $\vec{E}$  is the optical field. The full theory[3] covers both linear and nonlinear optical effects and various ways to measure  $D$  and  $\delta$  emerge. Here we describe the simplest form of the linearized theory. Assuming  $\delta^{-1} = 0$  and  $T > T_C$  (paraelectric phase) we find that the (in-plane) FIR polarization  $Q$  satisfies

$$Dd^2Q/dz^2 + [m\omega^2 - (T - T_C)/\varepsilon_0 C + i\omega\gamma]Q + E = 0 \quad (1)$$

where  $C$  is the Curie constant. This is solved together with the Maxwell wave equation. Plane wave solutions  $\exp(\pm ik_{1,2}\omega_0 z/c)$  are found, where  $k_1$  and  $k_2$  are the roots of

$$\alpha k^4 - (f^2 + 1 - t + igf + \alpha\varepsilon_\infty f^2)k^2 + \varepsilon_\infty f^2(f^2 + 1 - t + igf - \beta/\varepsilon_\infty) = 0 \quad (2)$$

Here  $\omega_0^2 = T_C/\varepsilon_0 mC$ ,  $f = \omega/\omega_0$ ,  $g = \gamma/\omega_0$ ,  $\alpha = D/mc^2$ ,  $\beta = C/T_C$  and  $\varepsilon_\infty$  is the high-frequency dielectric constant. Typical values are  $\omega_0$  in the far infrared,  $g$  in the range  $10^{-2}$  to  $10^{-1}$ ,  $\beta$  in the range 1 to 10 and  $\varepsilon_\infty$  in the range 2 to 5.  $D$  is unknown and the question is whether it can be determined by FIR measurements. To fix ideas, if we assume a Landau coherence length  $(\varepsilon_0 DC/T_C)^{1/2}$  of around 100nm then we expect  $\alpha$  in the range  $10^{-3}$  to  $10^{-2}$ .

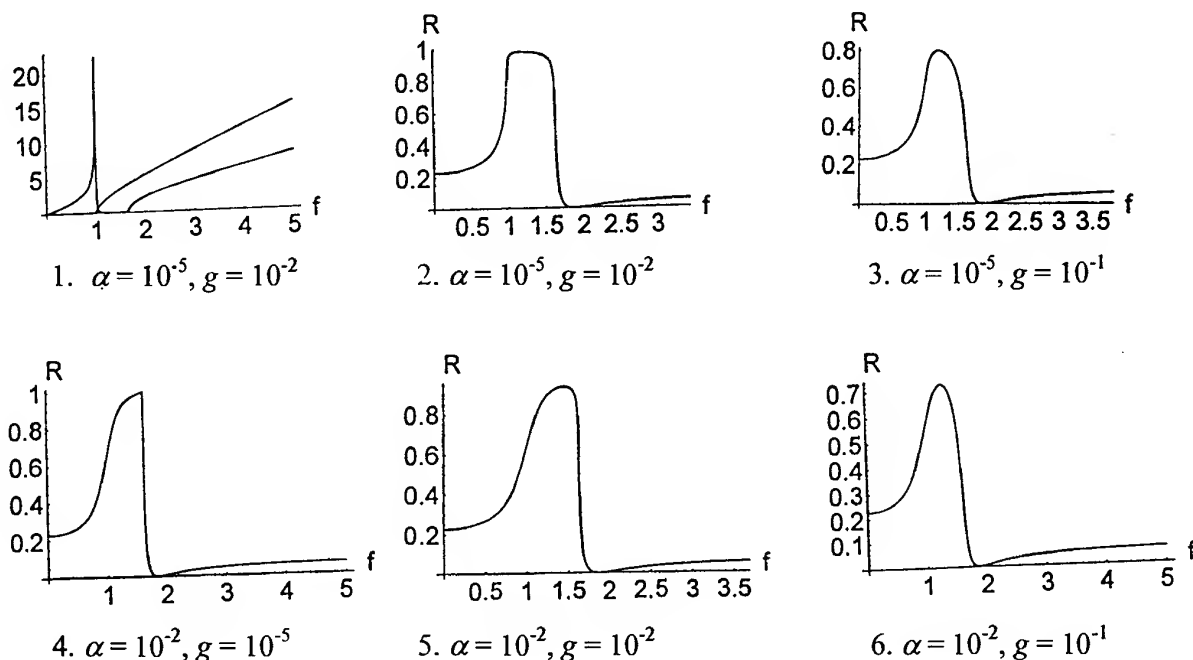
The graphs are drawn for  $\varepsilon_\infty = 3$ ,  $\beta = 5$ ,  $t = 2$  and differing  $\alpha$  and  $g$ . The first plot shows  $\text{Re}(k_1)$  and  $0.01\text{Re}(k_2)$  for the small values  $\alpha = 10^{-5}$  and  $g = 0.01$ .  $k_1$  is the usual polariton curve and the corresponding reflectivity is  $R \approx 1$  in the reststrahl region where  $k_1$  is

imaginary. Here  $k_2$  is real though larger than  $k_1$  so we ask if coupling to  $k_2$  leads to enough reduction in  $R$  to enable determination of  $D$ . The normal incidence reflectivity  $R = |r|^2$  is calculated using the electromagnetic boundary conditions together with  $dQ/dz = 0$ . We find

$$r = \frac{f(k_2^2 + k_1 k_2 + k_1^2 - \epsilon_\infty f^2) - k_1 k_2 (k_1 + k_2)}{f(k_2^2 + k_1 k_2 + k_1^2 - \epsilon_\infty f^2) + k_1 k_2 (k_1 + k_2)} \quad (3)$$

Graph 2 shows  $R$  corresponding to Graph 1. For this small value of  $\alpha$   $k_2$  is large so that coupling to  $k_2$  is small and  $R$  has the usual reststrahl form. Graph 3 shows the usual effect of larger damping in rounding  $R$  across the reststrahl. Graph 4 is for a larger value of  $\alpha$  and very small  $g$ . Here  $k_2$  is smaller by about an order of magnitude than in Graph 1 so that coupling is stronger. The  $k_2$  dispersion curve crosses the vacuum light line near the lower boundary of the reststrahl and it is seen the presence of the  $k_2$  mode reduces the left side but leaves the right side sharp. Graphs 5 and 6, for more realistic  $\alpha$  and  $g$ , show the different effects of  $k_2$  coupling and damping. The differences in shape are sufficient to make it likely that data analysis will be able to determine both  $\alpha$ , i.e.  $D$ , and  $g$  to good accuracy.

This work was supported by by IRPA (Malaysian Government) Grant 09-02-05-6001.



### References

1. J.F. Scott, *Ferroelectrics Review* 1,1 (1998)
2. D.R. Tilley, *Ferroelectric Thin Films: Synthesis and Basic Properties*, ed. C.P. de Araujo, J.F. Scott and G.W. Taylor (Gordon and Breach 1996), 11.
3. R.L. Stamps and D.R. Tilley, unpublished.

## Nonlinear Azimuthal Surface Waves in Gyrotropic Second-Order Nonlinear Materials Coated by a Metal

K. N. Ostrikov<sup>1,2</sup>, M. Y. Yu<sup>1</sup>, N. A. Azarenkov<sup>2</sup>, A. D. Boardman<sup>3</sup>

<sup>1</sup>Institut für Theoretische Physik I, Ruhr-Universität Bochum,  
D-44780 Bochum, Germany

<sup>2</sup>Kharkov State University and Scientific Center for Physical  
Technologies, Novgorodskaya st., 2/93, 310145 Kharkov, Ukraine

<sup>3</sup> Physics Department, Joule Laboratory, Salford University, M5 4WT, Salford, UK

Nonlinear effects associated with azimuthal surface waves in cylindrical samples of second-order nonlinear materials with metal coating are studied. The propagation in the azimuthal direction along the circumference of a waveguide structure leads to a discreteness of the ASW spectrum. This results in the possibility of realization of the nonlinear interactions, which are otherwise not possible for ordinary surface waves with continuous spectrum.

The wide use of the second-order nonlinear materials in a number of modern technologies stimulated detailed studies of the influence of various nonlinear effects on electromagnetic wave propagation in such media. Specific nonlinear effects significantly depend on the geometry of the problem as well as on the type of the propagating mode. Here we are interested in second-order nonlinear processes which can be realized in cylindrical samples of second-order nonlinear materials coated by a metal film. In such structures the very specific type of waves, namely the azimuthal surface waves (ASW), can propagate [1-5]. The electromagnetic energy of ASW is located near the interface between a nonlinear medium and a metal coating, and their amplitudes monotonously decrease from it. For this reason the ASW can be treated as pure surface modes. They propagate in the azimuthal direction along the circumference of the cylinder (across the waveguide axis) and reflect simultaneously the properties of both travelling and standing waves. Moreover, the propagation along the circumference of the waveguide results in a number of peculiarities of the ASW compared with the ordinary surface-type waves. One of the main peculiarities of the ASW is the discreteness of the spectrum (the dispersion properties are described by the dependence of the eigenfrequency  $\omega$  on the azimuthal mode number  $m$ ). It is expected that the discreteness of the ASW spectrum  $\omega = \omega(m)$  makes possible to realize a number of nonlinear processes which are forbidden for ordinary SW. Particularly, it is demonstrated here that the phase synchronization and mode selection conditions are much more easily satisfied for ASW than for the usual SW with continuous spectrum. Unfortunately, to the best of our knowledge, nonlinear processes involving the ASW have not been previously addressed in the scientific literature.

Consider an axially infinite cylindrical metal waveguide of radius  $a$  filled by a spatially homogeneous gyrotropic second-order nonlinear material. The material is characterized by the standard permeability tensor of a gyrotropic medium with the diagonal components  $\epsilon_{xx} = \epsilon_{yy}$  and  $\epsilon_{zz}$  and off-diagonal components  $\epsilon_{xy} = -\epsilon_{yx}$ . The analysis of the linear problem [1] shows that the purely surface waves can propagate in the azimuthal ( $\phi$  axis) direction only in the frequency ranges  $\omega_l < \omega < \omega_e$ ,  $\omega_{11} > \omega > \omega_h$ , where  $\omega_{11} = \omega_e/2 + (\omega_h^2 - 3\omega_e^2/4)^{1/2}$ ,  $\omega_e$  is the electron cyclotron,  $\omega_l$  and  $\omega_h$  are the lower hybrid and upper hybrid frequencies, respectively. It is important to note that the character of ASW propagation is nonreciprocal. In our case this means that in the first frequency range the ASW can propagate only with  $m > 0$ , while in the second only with  $m < 0$ .

In this paper we are interested in two main second-order nonlinear processes, namely, the second harmonic generation and the interaction between three eigenmodes with the mode numbers  $m_1$ ,  $m_2$ , and  $m_3$ . In the second harmonic generation process the azimuthal mode numbers and the eigenfrequencies of the ASW satisfy  $\omega_2 = 2\omega_1$  and  $m_2 = 2m_1$ . The nonlinear three-wave interactions processes are only possible if the spatial and temporal synchronization conditions  $\omega_3 = \omega_1 + \omega_2$  and  $m_3 = m_1 + m_2$  are satisfied. The possibilities of realization of the above conditions are addressed in details for both frequency ranges of existence and a broad range of the parameters involved. The process of generation of azimuthal-type signals with double frequency can be realized even in the case when the phase synchronization conditions are not satisfied. However, in this case the efficiency of the process is low since the generated double-frequency signal is not the eigenmode of the waveguide structure, but rather a forced oscillation disappearing with the switching off the pump wave with the fundamental frequency. Therefore, to increase the efficiency of the second harmonic generation it is necessary to provide excitation at the second harmonics of the eigenwave by resonance. One can show that such kind of interaction is realized in the frequency ranges where by adjustment of other parameters of the waveguide the linear dependence of the ASW eigenfrequency on the azimuthal mode number over all the frequency range involving both the

first and the second harmonics is obtained. Particularly, this situation can be realized in the case when the transverse dimension of the metal cylinder fully filled by a gyrotropic nonlinear medium significantly exceeds the skin depth of the ASW, and the inequalities  $4\omega_1^2 \ll \omega_c^2$  and  $\Omega_c^2/\epsilon_0 \gg \omega_c^2$ , where  $\epsilon_0$  is the static dielectric constant of the nonlinear medium, hold.

Analogous conditions govern the possibility for realizing the interaction between the three lowest-order azimuthal eigenmodes, namely with  $m_1 = 1, m_2 = 2$ , and  $m_3 = 3$ . If  $(4\omega_1)^2 \sim \omega_c^2$  holds, the wave process with the frequency  $4\omega_1$  and the azimuthal wavenumber  $4m_1$  is not an eigenmode of the structure and cannot effectively participate in the above-mentioned process. Therefore, in the latter case only three azimuthal surface modes are involved in a nonlinear three-wave interaction. Such interaction is not possible for surface waves propagating across the external magnetic field in the planar sample of a nonlinear material covered by a metal film (i.e., the planar analog of the ASW problem) [6]. This is due to the fact that in the latter case the SW are characterized by a continuous spectrum. This means that for certain frequencies the linear dependence of the eigenfrequency on the wavenumber, complicated finite-spectrum interactions involving a large number of waves are unavoidable [6]. Another significant difference between the cylindrical and planar geometries is that the tangential component of the SW electric field is equal to zero in the planar case, and differs from zero in the cylindrical case. Since these components of the electric field appear in the expressions for the nonlinear polarization of the medium, the efficiency of nonlinear mode coupling in the cylindrical case is higher. However, under certain conditions the tangential component of the ASW electric field  $E_\phi$  is smaller than the normal one  $E_r$ , and this fact allows one to reduce the number of the second-order nonlinear susceptibilities [7] incorporated into the definition of the second-order nonlinear polarization. In that cases the terms which are proportional to  $E_{rk}E_{rl}$  and  $E_{rk}H_{zl}$ , where  $H_{zl}$  is the axial component of the ASW magnetic field,  $k$  and  $l$  are the numbers of waves participating in the nonlinear interaction, make the most significant contribution in the efficiency of the nonlinear process.

In this paper the nonlinear dispersion relations for waves taking part in the nonlinear interactions are derived in a general form, incorporating also the third-order nonlinear processes by means of the formalism of the second and third-order nonlinear susceptibilities. By using standard procedures [7], the corresponding sets of coupling equations describing the nonlinear second harmonic generation and wave interaction processes are also obtained. In the case of second harmonic generation the characteristic temporal scales of the energy exchange between the first and the second harmonics are defined. For three-wave processes the threshold values of the pump wave amplitude are estimated for several conditions. The temporal scales of the parametric decay process of ASW are also defined. For the third-order nonlinear processes, it is shown that the value of the nonlinear phase shift of the ASW can provide the valuable information about the third-order nonlinear susceptibilities. However, a detailed investigation of the latter process is outside the scope of this paper.

The nonlinear processes studied above can be useful for production of compact phase shifters and frequency convertors, with broad frequency ranges based on second-order nonlinear materials. They have also direct relevance to modern low-temperature plasma technologies. This is due to the fact that the ASW alongside with the non-symmetrical SW can be used for the production of large-diameter technological plasmas [5]. Moreover, due to the purely transverse propagation with respect to a discharge chamber axis, the ASW can produce and sustain technological plasmas in the cylindrical chambers with transverse sizes comparable or even larger than the longitudinal ones. In such structures the traditionally used axially-symmetric and nonsymmetric travelling surface waves propagating along the waveguide axis cannot be responsible for the discharge production. Therefore, the comprehensive studies of the nonlinear effects involving ASW in solid-state nonlinear gyrotropic materials as well as in gas-discharge plasmas are warranted.

The work of K. N. Ostrikov was supported by Alexander-von-Humboldt Foundation.

#### References.

1. V. A. Girka, Girka I. A., Kondratenko A. N., and Tkachenko V. I., *Sov. J. Commun. Technol. and Electronics* **33**, 1031 (1988); **34**, 296 (1989); **34**, 1527 (1989).
2. N. A. Azarenkov, Kondratenko A. N., and Ostrikov K. N., *Sov. Radiophys.* **36**, 325 (1993).
3. N. A. Azarenkov, and Ostrikov K. N., *Physics Reports* **310**, 67 (1998).
4. K. N. Ostrikov, Osmaev O. A., *Contrib. Plasma Physics* **34**, 661 (1994).
5. V. Viel, J. Bernard, and G. Laval, *J. Phys. D: Appl. Phys.* **29** 1500 (1996).
6. K. N. Ostrikov, *Contrib. Plasma Phys.* **35**, 481 (1995).
7. Y. R. Shen, *Principles of Nonlinear Optics* (John Wiley, New York, 1984).

## Changes of IR Properties of Translucent Alumina Induced by Reaction with Sodium

Masato TAZAWA and Sakae TANEMURA

National Industrial Research Institute of Nagoya  
Nagoya, 462-8510, Japan

### Introduction

Alumina ceramics are considered to be very reliable materials for industries because of their excellent mechanical, thermal, and optical properties. Translucent aluminae which are allowing light to pass through but not transparent are used as an arc tube material of high pressure sodium lamps. It is also known that they could be degraded by reaction with sodium inside.

In our previous work [1] we reported that the surface structure of translucent aluminae can be estimated by spectral reflectance in reststrahlen band (500 - 1000  $\text{cm}^{-1}$ ) and effective medium approximation. In this paper we observed changes in surface structure and spectral reflectance in reststrahlen band by reaction with sodium at high temperature.

### Experimental and Results

Samples were two translucent alumina plates (HICERAM lid, NGK Insulators, Japan) whose grain sizes were 15 and 30  $\mu\text{m}$ . The specific gravity, 3.85  $\text{g}/\text{cm}^3$ , was satisfactorily identical with the theoretical density of  $\alpha\text{-Al}_2\text{O}_3$  and we confirmed that the porosity was negligibly small using optical microscopy and SEM observations. As shown in our previous work [1], microscopic observations showed layered structures with various orientations on each grain of alumina (Fig. 1-a). The thickness of the layer was estimated several hundred nanometers from AFM observations.

The reaction with sodium in an accelerated way, vacuum evaporated sodium was deposited on the samples and they were kept at high temperature (ex. 900  $^\circ\text{C}$ ). The microscopic observations showed that many pits whose diameter was several micrometers were formed on each alumina grain (Fig. 1-b). The instrument for the measurement of spectral reflectance in the reststrahlen band (500 - 1000  $\text{cm}^{-1}$ ) was an FT-IR (Jasco, FT/IR-620V). The measured spectral reflectance are shown as solid curves in Figs. 2-a and b for before and after the reaction with sodium, respectively.



Fig. 1 Optical microphotograph of a sample (grain size : 30  $\mu\text{m}$ )  
(a) before reaction with sodium and (b) after the reaction.

### Discussion

Measured spectral reflectance shown in Figs. 2-a and b show some difference from calculated spectral reflectance using published optical constants [2] of  $\alpha\text{-Al}_2\text{O}_3$  single crystal. As shown in our previous work [1], the origin of this difference was identified as the surface structure on the grains after some calculation based on the effective medium approximation and the distribution of the probability of the depolarization factor can be determined by comparison of the measured and calculated reflectance.

According to Andersson and Ribbing [3], the dielectric constants ( $\epsilon_{tot}$ ) of the system can be calculated using the optical constants of single crystalline  $\alpha$ -Al<sub>2</sub>O<sub>3</sub> :

$$\epsilon_{tot} = \epsilon + f(\epsilon - \epsilon_m)\epsilon_m \int_0^1 \frac{1}{\epsilon_m + L(\epsilon - \epsilon_m)} w(L) dL \quad (1)$$

where  $f$  is the total volume fraction of inhomogeneities compared with the total volume contained in the skin depth,  $\epsilon$  and  $\epsilon_m$  are dielectric constants of alumina and air respectively, and  $w(L)dL$  is the probability that the inhomogeneity has effective depolarization factor,  $L$ , in the increment of  $L$ ,  $dL$ .

In our calculation  $w(L)$  was assumed the normal distribution with the boundary condition  $w(1)=0$ :

$$w(L) = \frac{1}{\sigma\sqrt{2\pi}} \exp\left[-\frac{1}{2}\left(\frac{L-m}{\sigma}\right)^2\right] \quad (2)$$

where  $\sigma$  and  $m$  are the standard deviation and the mean value of  $L$  respectively.

The parameters  $f$  in eq. (1), and  $\sigma$  and  $m$  in eq. (2) are determined by the least square method between the calculated and the measured reflectance. The dotted curves in figs. 2-a and b are calculated with best fit parameters shown in table 1. Fig. 2 shows that the fitting is better in case of before reaction than after. This is because the diameter of pits on grains was comparable to the wavelength so that the effective medium approximation might not be applicable perfectly. From table 1, we can see that both samples have almost same parameters but the volume fraction decreases slightly.

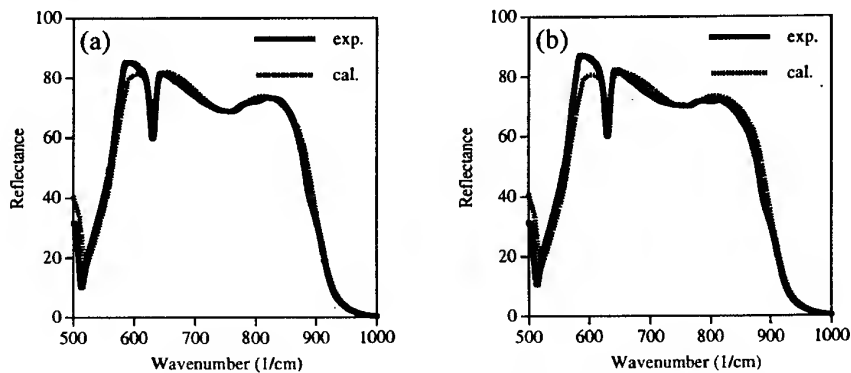


Fig. 2 Measured and calculated spectral reflectance, (a) before the treatment, (b) after the treatment.

Table 1

	$\sigma$	$m$	$f$
before degradation	0.064	0.246	0.034
after degradation	0.063	0.249	0.026

### Conclusion

Spectral reflectance in the reststrahlen band is changed slightly when translucent alumina degrades by reaction with sodium. Using effective medium approximation, we can determine the distribution of depolarization factor. Diameters of the pits caused by reaction with sodium on grains are comparable to wavelength in reststrahlen band so that the effective medium approximation might not be applicable perfectly.

### ACKNOWLEDGEMENT

The authors would like to thank Mr. T. Ohashi of NGK Insulators, Ltd. for giving the samples.

### REFERENCES

- [1] M. Tazawa and S. Tanemura, Conference Digest of Twentieth International Conference on Infrared and Millimeter Waves, pp. 321 - 322 (1995).
- [2] F. Gervais, in book "Handbook of Optical Constants of Solids II", ed. by E. D. Palik, pp. 761 - 775 (Academic Press, 1991).
- [3] S. K. Andersson and C. G. Ribbing, Physical Review B. vol. 49, no. 16, pp. 11336 - 11343 (1994).

# Infrared absorption measurements of titanium hydride films prepared by rf reactive sputtering

Setsuo NAKAO, Masato TAZAWA, Ping JIN, Tatsuya HIRAHARA and Kazuo SAITOH

National Industrial Research Institute of Nagoya,  
1-1 Hirate-cho, Kita-ku, Nagoya 462-8510, Japan

## Introduction

Titanium hydride (Ti:H) films have potential applications such as neutron mirror, hydrogen storage layer and standard for hydrogen quantitative analysis. In addition, it is interesting in optical properties of such hydride films. However, there are few reports on the formation [1] and optical characterization of Ti:H films.

In this study, Ti:H films were formed and their microstructures were examined. Titanium deuteride (Ti:D) films were also prepared to compare with the Ti:H films. Their optical properties were attempted to characterize by infrared absorption measurements.

## Experimental

Figure 1 shows the schematic diagram of the rf reactive sputtering apparatus for the sample preparation. Pure Ti metal was used as a target material. Si wafers were used as a substrate and they were attached to substrate holder cooled by water. After the chamber was pre-evacuated to less than  $10^{-4}$  Pa, Ar and  $H_2$  (or  $D_2$ ) gases were introduced. The flow rate of  $H_2$  (or  $D_2$ ) gas was changed from 1 to 5 ccm. The total gas pressure during deposition was about 2 Pa. Plasma was produced by rf power source at 13.56 MHz. The rf power was changed from 100 to 300 W. After the Ti target pre-sputtered for 30 min, a shutter was opened. The deposition time was changed from 1 to 180 min.

The surfaces of the films were observed by scanning electron microscopy (SEM). The composition of the films were analyzed by Rutherford backscattering spectrometry (RBS) measurement and elastic recoil detection analysis (ERDA) with a 1.7 MV tandem-type ion accelerator of NIRIN [2]. The crystal structure of the films was examined by x-ray diffraction (XRD) measurements. The transmittance spectra of the samples were also measured by FT-IR spectroscopy.

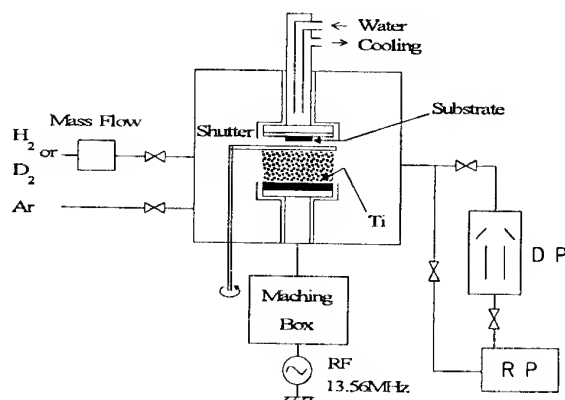


Fig.1. Schematic diagram of the rf reactive sputtering apparatus.

## Results and Discussion

Figure 2 shows typical XRD patterns of the samples deposited with Ar+ $D_2$  gas (a) and with Ar+ $H_2$  (b). Deposition time was 60 min for the samples (a) and (b). The sample (c) was deposited for 30 min without  $H_2$  (or  $D_2$ ) gas for comparison. For the sample (a) and (b), there are 3 peaks which are in agreement with the peaks of titanium deuteride (Ti:D) and hydride (Ti:H), i.e., the structure of the films is identified as the fcc  $CaF_2$  structure as expected from Joint Committee for Powder Diffraction Standard file (JCPDS No. 7-370 and No. 25-982). For sample (c), it is clearly different XRD patterns from samples (a) and (b) and the structure of the film is identified as the hcp Ti structure.

SEM observations showed that the films were composed of many grains and these grains developed in



crystal habit with deposition time, i.e., the surface roughness was increased with increasing the film thickness (deposition time). In the optical measurements, the thin films were employed to minimize the effects of surface roughness.

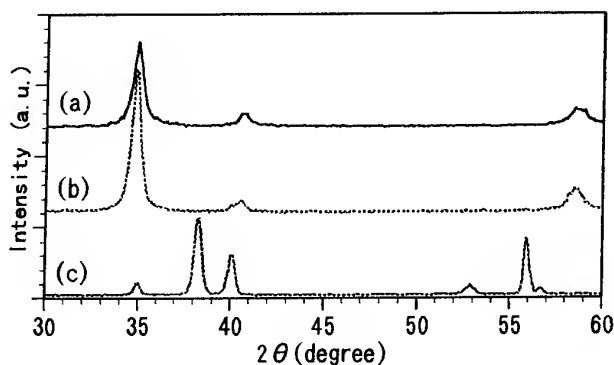


Fig. 2. XRD patterns of the samples deposited with Ar+D<sub>2</sub> (a) and with Ar+H<sub>2</sub> (b). The sample (c) was deposited with Ar for comparison.

Figure 3 shows the FT-IR transmittance of Si substrate (a) and Ti:D films deposited on Si substrates for 1 min (b) and 10 min (c). The thicknesses of the films were about 30 nm (b) and 190 nm (c) estimated from RBS measurements, respectively. For the films, (b) and (c), there is not an apparent spectral feature in the transmittance. However, the transmittance is decreased in the wide range as the thickness of the films is increased. These results suggest that the infrared absorption increased in the wide range with increasing the film thickness.

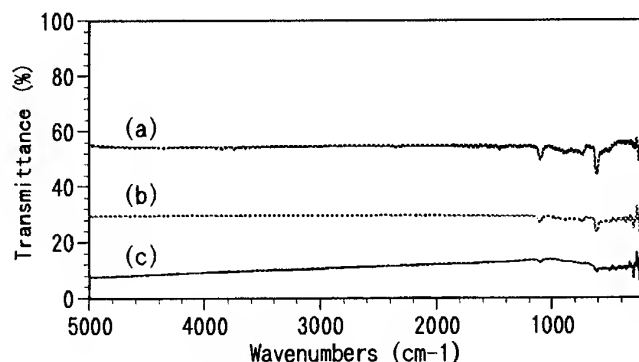


Fig. 3. FT-IR transmittance of Si (a) and Ti:D films deposited on Si for 1 min (b) and 10 min (c).

The results for RBS and ERDA measurements showed that the films included a large amount of O atoms and did not saturate with H or D atoms. Considering with the results of XRD measurements which only showed the Ti:H or Ti:D crystal structure as shown in Fig. 2, it might be said that the films included amorphous titanium oxide phase. The details of the microstructure are not known to date. Further study is underway.

#### Conclusion

Ti:H and Ti:D films were prepared by rf reactive sputtering and the optical properties in infrared region were examined. It was found that the films showed large infrared absorption in the wide range, although there was not a clear feature in the FT-IR transmittance.

#### References

- [1] H. Chatbi, M. Vergnat and G. Marchal, Appl. Phys. Lett. Vol.64, no.10, pp.1210-1211 (1994).
- [2] K. Saitoh, H. Niwa, M. Kobayakawa, S. Tanemura, M. Ikeyama, M. Takeda, H. Masuda, Y. Miyagawa, S. Nakamura, S. Miyagawa and K. Yasuda, Rep. Gov. Ind. Res., Nagoya, Vol. 9, no.6, pp.259-270 (1990).

## IDENTIFICACION OF OF A Ti – RELATED ABSORPTION BAND IN ZnSe

*Mireya Castillo*

*Universidad Nacional Experimental del Táchira*

*Apartado 436. San Cristóbal, Táchira.*

*VENEZUELA.*

Details of the spin properties and energy levels of substitutional titanium ions  $\text{Ti}^{+2} (d^2)$  on the zinc site in ZnSe have been studied by FT-IR in the range  $4000\text{-}400\text{ cm}^{-1}$ . Comparison with recently published theories in Ti based DMS shows excellent agreement.

## **Recent Developments on the High Power ECH Installation at the DIII-D Tokamak**

John Lohr, Dan Ponce, R.W. Callis, J.L. Doane,  
H. Ikezi, and C.P. Moeller,

*General Atomics  
San Diego, California, U.S.A.*

The 110 GHz gyrotron installation on the DIII-D tokamak has been incorporated into the experimental program as a research tool while in parallel being further characterized and upgraded. Two gyrotrons are in regular operation and a third is in testing. The first gyrotron is a Gycom "Centaur" model, which has reliably generated more than 800 kW for two second pulse lengths. The second gyrotron is a CPI VGT-8011A, which has regularly generated 750 kW at one second pulse length and has been tested at up to 1.09 MW for 600 ms pulse lengths.

These gyrotrons, operating both modulated and cw, have been used in power deposition profile measurements, transport studies, measurements of electron cyclotron current drive, heating, H-mode studies and magnetohydrodynamic mode stabilization. Using two different launchers, one injecting with a toroidal component and the other perpendicular to the magnetic field, comparisons between heating plus current drive and heating only were made to enhance the accuracy of the measurement of the electron cyclotron current drive. Changing the poloidal angle of the final launcher mirror permits the rf beam to be steered anywhere in the tokamak upper half plane and this feature, coupled with changes in the tokamak toroidal magnetic field, has been used in studies of off-axis electron cyclotron current drive, which is an essential element of advanced tokamak operation leading to reactor-relevant regimes of operation for modest sized tokamak devices.

Several experimental results have been obtained thus far. Injection of 1 MW of rf power into DIII-D yielded a DIII-D record electron temperature of 10 keV at low density. The direct measurement of transport coefficients in the electron channel using modulated rf gave a check on the internal self consistency of transport calculations based on equilibrium kinetic profiles. Another of the highest priority experiments has been the verification of theoretical calculations of electron cyclotron current drive efficiency. To date, analysis indicates that electron cyclotron wave driven currents greater than 100 kA at an efficiency of  $0.03 \times 10^{20}$  A/W-m<sup>2</sup> have been achieved. This is comparable to the fast wave current drive efficiency near the ion cyclotron resonance frequency. Engineering tests of the polarization and power deposition profiles showed that 100% X-mode could be generated for any plasma configuration, both for oblique and perpendicular injection and that the

power deposition was consistent with the spatial cross section of the beam for pure X-mode.

The high power, long pulse operation of the CPI gyrotron at DIII-D was at the same parameters that had been used during initial testing at CPI for shorter pulses [1], and, except for output window heating, there was no indication that longer pulses could not have been generated. The Gycom gyrotron has been extremely reliable for more than a year and can generate two second pulses whenever required without compromising the output power. The transmission lines for both tubes are evacuated windowless step-corrugated circular waveguides carrying the  $HE_{1,1}$  mode and launching a Gaussian beam into the DIII-D tokamak. About 75% of the rf power passing through the gyrotron windows for both systems is injected into DIII-D.

For studying the gyrotron performance, a rotating polarimeter was developed which is capable of performing direct beam polarization measurements in the evacuated waveguide for high power and long pulses. This instrument was also used to characterize the performance of remotely controllable vacuum compatible polarizing miter bends, which permit producing the proper ellipticity and tilt angle to generate the desired X-mode for any plasma configuration, resulting in optimization of the single pass absorption of the injected rf beam.

Measurements of the gyrotron current-voltage characteristics for the Gycom and CPI gyrotrons were made to understand cathode performance leading to an understanding of parasitic emission from the Gycom tube at 96 MHz.

A third gyrotron, also built by CPI, using a diamond disk output window and generating a Gaussian beam, has been installed at DIII-D and is being tested. At the time of this writing, this tube was generating 350 kW in a pulsed regime for mode mapping studies at the CPI facility. High power tests of the diamond window disk and thermal calculations indicate that this gyrotron should be capable of generating substantially longer pulses at one megawatt than have heretofore been achieved.

A description of the system will be presented and the results of the tokamak experiments to date will be summarized. Measurements and analysis of the gyrotron performance, including the beam polarization, and the first report of the operational experience with the diamond window gyrotron will be discussed. DIII-D has committed to a further upgrade of the electron cyclotron heating system as a part of the advanced tokamak research program and these plans will be presented.

This is a report of research sponsored by the U.S. Department of Energy under Contract No. DE-AC03-89ER51114.

[1] Kevin Felch *et al.*, IEEE Transactions on Plasma Science **24**, 558 (1996).

## STATUS OF THE 118 GHz - 0.5 MW - QUASI CW GYROTRON FOR TORE SUPRA AND TCV TOKAMAKS

C. TRAN, E. GIGUET, Ph. THOUVENIN

Thomson Tubes Electroniques - 2, rue Latécoère - 78141 Vélizy - France

P. GARIN, M. PAIN

Association Euratom - CEA - Département de Recherche sur la Fusion Contrôlée  
13108 Saint Paul Lez Durance - France

S. ALBERTI, M.Q. TRAN

Centre de Recherche en Physique des Plasmas - Association Euratom  
Ecole Polytechnique Fédérale de Lausanne - 21, av. des Bains - CH-1007 Lausanne - Switzerland

M. THUMM

Forschungszentrum Karlsruhe, Association Euratom - FZK  
Institut für Technische Physik - P.O. Box 3640 - D-76021 Karlsruhe - Germany

### Abstract

In the framework of a collaboration between CEA-Cadarache, CRPP-Lausanne, FZK-Karlsruhe and TTE Vélizy, a 0.5 MW-118 GHz-210 s gyrotron has been developed for experiments on Tore Supra and TCV tokamaks. The prototype has successfully performed its factory acceptance tests and is now under tests at CEA-Cadarache.

### Design and experimental set-up

A detailed description of the gyrotron design is presented in references [1] and [2]. The tube is composed of a triode type electron gun, an improved beam tunnel, a low-ohmic-losses cavity with an optimized non-linear output taper, a high efficient internal quasi-optical converter made of a rippled-wall launcher followed by three mirrors [3], a large collector making use of a beam sweeping coil, and a lateral output RF output through a liquid nitrogen edge-cooled single-disk sapphire window [4]. Four ion pumps located inside the tube and making use the remaining magnetic field generated by the superconducting magnet control the tube vacuum.

A matching optics unit (MOU) system is connected to the gyrotron window and consists in a vacuum vessel equipped with three moveable mirrors (two being corrugated) enabling the optimization of the RF beam matching to a 63.5 corrugated waveguide. The RF power is dissipated and measured in a metallic matched calorimeter. The schematic of the equipped gyrotron is shown on fig. 1.

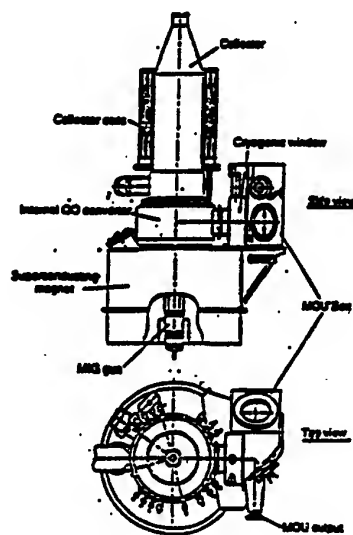


Fig. 1 : 118 GHz gyrotron and MOU schematic

### Long pulses experimental results at TTE Vélizy

The prototype was mounted on its test bench at Vélizy beginning of December 1997 and was conditioned up to 5 s - 0.5 MW by the end of January 98. The experiments consisted in short pulses mode purity measurements and MOU optimization by the mean of an infrared camera coupled with a phase reconstruction code,

parametric study in short pulses (see fig. 2 & 3), collector conditioning (see fig. 4) and beam spreading optimization, thermal characterization in long pulses and finally pulse enlargement up to 5 s - 0.5 MW within one day experiment and then 10 hours continuous tests at these nominal performances without any degasings exceeding  $20 \mu\text{A}$  (5 kV fed ion pumps) and with a success ratio of 97 % (on 190 pulses at a duty cycle of 2.8 %).

The operating parameters were the following : cathode voltage : 80.5 kV, anode voltage : 26.4 kV, beam current : 20.5 A. The performances reached were then : 0.5 MW, 30.3 % global efficiency (after the MOU and the 3 m-waveguide). The power extracted through the window can then be estimated : 0.54 MW and the power generated in the cavity : 0.6 MW, which leads to a an experimental interaction efficiency of 36.4 %.

The RF power measured in the load versus cathode voltage and anode voltage are presented on fig. 2 & 3.

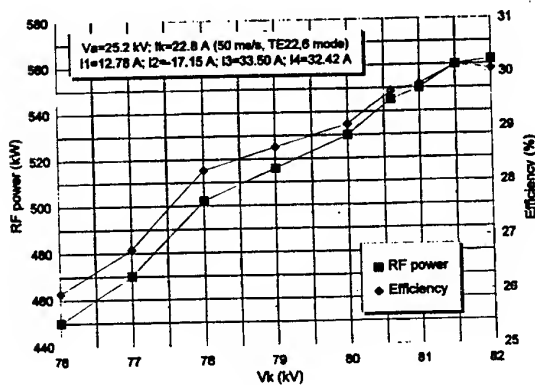


Fig. 2 : RF power and efficiency versus  $V_k$

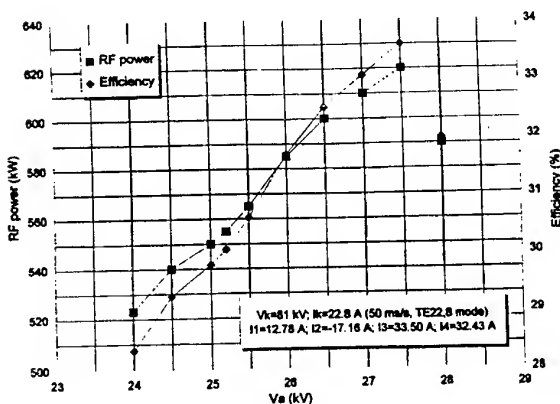


Fig. 3 : RF power and efficiency versus  $V_a$

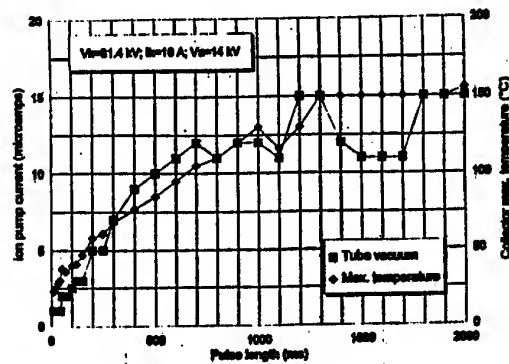


Fig. 4 : Collector outgasings and max. temperature in diode operation

All the temperatures are monitored by brazed thermocouples on the thermally most critical subassemblies of the gyrotron except for the window : beam tunnel, cavity, launcher, mirrors and collector and the measurements show that the equilibrium is reached after 4 s on those components (fig. 5 for example shows the frequency shift versus time due the cavity thermal expansion). The losses were also measured in the beam tunnel (3 kW) and in the cavity and launcher (50 kW). These results show that the gyrotron operates in very good conditions on its optimized operating point.

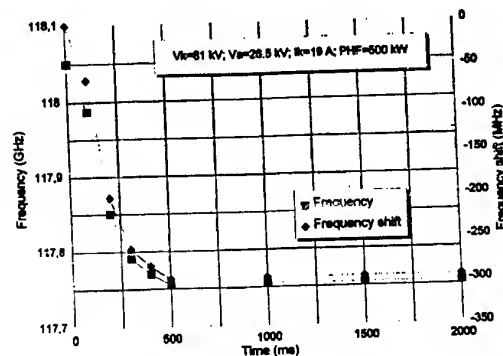


Fig. 5 : Frequency shift versus time

The constant low level outgasing of the tube recorded during the life test is shown on fig. 6 and the number of shots at pulses larger than 1 s is shown on fig.6, which corresponds approximately to the tube formation plus the acceptance tests procedure including the life test.

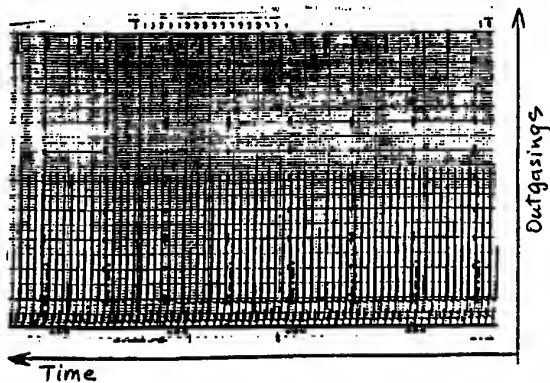


Fig. 6 : Gyrotron constant low level outgasings recorded during part of the life test

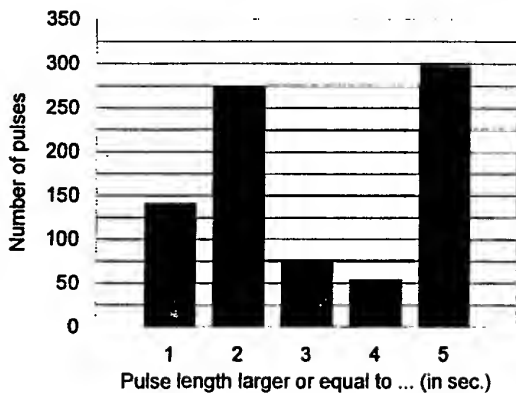


Fig. 7 : Number of pulses versus pulse length

#### Long pulses tests at CEA-Cadarache

After the life test, CEA and EPFL accepted the performances of the gyrotron which was housed and shipped to CEA-Cadarache for pulse enlargement up to 210 s.

The tube was installed at TORE SUPRA within 2 months, as planned. On fig. 7, one can see the superconducting magnet, the gyrotron with its collector coils, the MOU box and the corrugated waveguide connected to the MOU output guide.

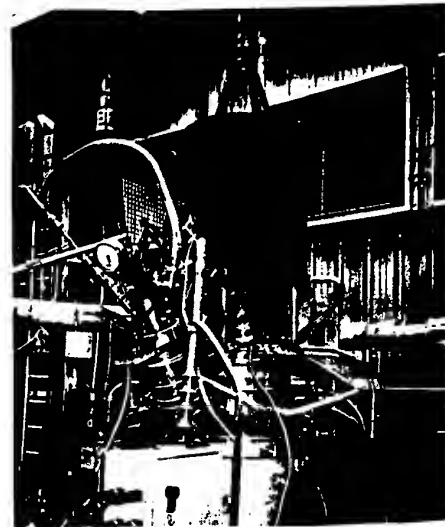


Fig. 8 : 118 GHz gyrotron installed at Cadarache

The high voltage has been applied on the gun, with cold filament without any problem. The tube filament is now to be heated.

#### Conclusion

The new 118 GHz gyrotron prototype has proven its capability to repetitively generate more than 0.5 MW at 5 s pulses at TTE factory site, within the specifications of CEA and EPFL.

It has been installed at CEA-Cadarache within the 2 months planned in the prototype time schedule.

The goal is now to re-obtain the same performances as those produced at Vélizy, in a very short time and then to enlarge the pulse length from 5 s to 210 s. This should be done by the end of September 1998.

#### References

- [1] E. Giguet et al. "Operation of a 118 GHz-0.5 MW gyrotron with cryogenic window : design and long pulse experiments", 20th Int. Conf. on IRMM Waves, Orlando, 1995
- [2] S. Alberti et al. "Long pulse operation of a 0.5 MW-118 GHz gyrotron with cryogenic window", 21st Int. Conf. on IRMM Waves, Berlin, 1996
- [3] O. Braz et al. "Cold tests and high power measurements on the advanced quasi-optical mode converter for a 118 GHz gyrotron", 20th Int. Conf. on IRMM Waves, Orlando, 1995
- [4] P. Garin et al. "Cryogenically cooled window : a new step to wards CW operation", 20th Int. Conf. on IRMM Waves, Orlando, 1995

## A DESIGN STUDY OF A 28GHz, 200kW GYROKLYSTRON AMPLIFIER

J. J. Choi, S. W. Bak, W. K. Han, D. M. Park, J. G. Yang\*, and S. M. Hwang\*

Kwangwoon University, Department of Radio Engineering

Seoul, Korea 139-701

\*Korea Basic Science Institute, Daejeon, Korea

### Abstract

A design study of a high efficiency/gain gyroklystron amplifier is currently underway to demonstrate amplified radiation power of 200kW operating at 28GHz. The key design features of the present gyroklystron amplifier include; (1) the amplifier is designed to be high gain so that a solid state input drive can saturate the gyroklystron, and (2) the amplifier is operated at a long pulse width of up to a 500msec pulse duration. Circuit analysis including efficiency optimization, amplifier stability, and thermal stress is in progress using numerical codes. Simulations show that stable amplifier radiation of 200kW is produced with a 54dB saturated gain from a five cavity configuration.

### Introduction

High power millimeter wave coherent radiation sources are needed for many applications such as ECR plasma heating, compact high gradient accelerator, high resolution radar, and fast material processing. Radiation generation by an amplifier configuration rather than an oscillator configuration is more attractive due to multi-purpose operation from low prf up to CW although scientific/engineering issues are more difficult to overcome in the amplifier scheme. Recently, stable gyroklystron amplifiers with peak radiation power of 200kW at 35GHz were successfully demonstrated at the US Naval Research Laboratory [1,2]. Hanbit plasma confinement device [3] (formerly known as TARA at MIT) which is now installed and operated at Korea Basic Science Institute (KBSI) needs a 500msec long single radiation pulse of 200kW for Hanbit plasma heating experiments. The present paper describes a design study of a high gain gyroklystron amplifier by the use of numerical simulation codes.

### Amplifier Design and Numerical Simulation

The amplifier is composed of a magnetron-injection-gun to produce a high power gyrating electron beam, beam-wave interaction cavities including a beam modulation cavity, bunching cavities, and a radiation extraction cavity, a CW comparable beam collector, and a 4" diameter vacuum window. An important scientific issue in the present amplifier design is that the amplifier should be operated with a long pulse duration of up to 500msec. A complete thermal analysis of rf ohmic loading in idler cavities, beam collector, and rf vacuum window is required by the use of ANSYS, HFSS, and EGUN codes. An high power electron beam of 70kV, 8.2A is produced by a double-anode magnetron-injection-gun and is compressed adiabatically through a magnetic compression powered by a DC-operated 10kG superconducting magnet. An input drive signal is coupled into the first cavity through a coaxial coupler [4]. The coaxial configuration is widely adopted in the TE<sub>0n</sub> type mode excitation in the cavity because of high mode purity and simple single port connection with an external drive source. The spent electron beam is decoupled from the amplified radiation and is collected on the water cooled copper collector which has a diameter of 4" to keep the beam power density on the collector surface below 500W/cm<sup>2</sup>. To minimize mode conversion and avoid undesired oscillations in the beam drift region right after the extraction cavity, an extensive theoretical examination should be taken. Electron trajectory studies by the use of EGUN code show that non-linear tapering of magnetic field on the beam collector region is



required to spread the electron beam over 10" long axial distance.

A key design feature of the present gyrokystron amplifier is to obtain high amplifier gain with a multi-cavity interaction circuit in order to avoid a bulky expensive input drive power system. Optimization of amplifier gain and efficiency is performed by iterative numerical simulations of a time-dependent slow time scale non-linear code [5]. It is previously shown [6] that the simulation code predicts essentially same results (within less than 5-10% difference) as other codes such as the Maryland gyrokystron code [7] known as MAGYKL and MAGIC code [8]. To saturate the amplifier with an input power than 1W (which can be delivered by a low-cost solid state power amplifier), three bunching cavities are needed to be inserted between the input drive cavity and the rf extraction output cavity. Cavity resonance frequency tuning is optimized to achieve maximum efficiency and gain rather than wide frequency bandwidth. Best design parameters are summarized in Table 1. As shown in Figure 1, the amplifier radiation power is linearly increasing with low input powers and is saturated at input power of 0.75W where output power is 200kW, electronic efficiency is 35%, and saturated gain is 54dB. Stability analysis shows that the output cavity becomes unstable at the beam current of 9A or more, indicating that the present gyrokystron amplifier operating at 8.2A is zero-drive stable.

#### Acknowledgment

This work is supported by Hanbit user development program managed by KBSI. The authors would like to acknowledge valuable discussion with Dr. A. K. Ganguly.

#### References

- [1] J. J. Choi, et. al., "Experimental Investigation of a High Power Two-cavity, 35GHz Gyrokystron Amplifier", to be published in IEEE Trans. Plasma Sciences, 1998.
- [2] J. Calame, et. al., to be published in Physics of Plasma, 1998.
- [3] S. M. Hwang, et. al., Proc. Open Magnetic System Plasma Confinement, Novosibirsk, Russia (1998).
- [4] A. H. McCurdy and J. J. Choi, "Design and Analysis of a Coaxial Coupler for a 35GHz Gyrokystron Amplifier," to be published in IEEE Trans MTT, 1998.
- [5] A. H. McCurdy, et. al., Phys. Rev. A 40(3), p.1402, 1989; private communication with A. K. Ganguly.
- [6] unpublished (work done by A. K. Ganguly, J. J. Choi, and M. Blank at NRL).
- [7] P. Latham, et. al, IEEE Trans. Plasma Sc. 22, p.804, 1994.
- [8] B. Goplan, et. al., MAGIC user's manual (MRC), Newington, VA, 1993.

Table 1. Design parameters of a five-cavity 28GHz gyrokystron amplifier

- beam voltage	70kV
- beam current	8.2A
- magnetic field	10kG
- beam alpha	1.4
- operating frequency	28GHz
- cavity mode	TE011
- saturated efficiency	35%
- saturated gain	54dB
- input power	0.75W
- maximum power	200kW
- number of cavity	5

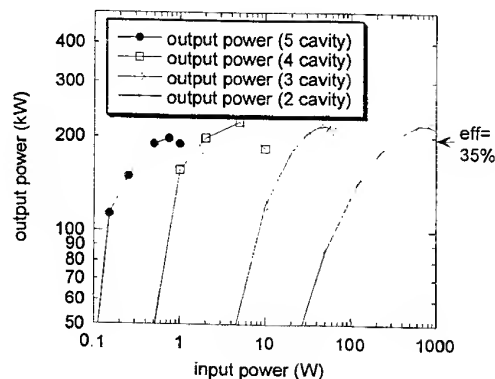


Figure 1. Simulated amplifier drive curves for 2, 3, 4, and 5 cavity configurations.

# 1 MW, 140 GHz Gyrotron with Brewster-Window

## Influence of Reflections

G.Dammertz, M. Kuntze, O. Braz<sup>1</sup>, K. Koppenburg<sup>1</sup>, B. Piosczyk, M. Thumm<sup>1</sup>

Forschungszentrum Karlsruhe, Association Euratom-FZK, ITP, P.O.Box 3640,  
D-76021 Karlsruhe, Germany

<sup>1</sup>also Universität Karlsruhe, Institut für Höchstfrequenztechnik und Elektronik, Kaiserstr. 12,  
D-76128 Karlsruhe, Germany

### Abstract

Even small reflections of the output power can have a big influence on the power generated inside a gyrotron cavity. The installation of a Brewster window without any reflections allows the investigation of this influence by externally adjustable reflections. The reflections are produced by external targets of different thicknesses or by a double disk window whose reflection coefficient can be changed continuously by changing the distance of the disks. A strong influence even for small reflections has been found if one operates the gyrotron at parameters with a narrow oscillation range. Thus, the effect of reflections seem to have to be considered especially at parameters generating high output power.

### Introduction

A TE<sub>22,6</sub> mode, 1MW, 140 GHz gyrotron has been used to investigate the behaviour of the oscillations with external reflections. The gyrotron was equipped with a single disk window of Si<sub>3</sub>N<sub>4</sub> ( $\epsilon_r=7.85$ ). The angle of the disk was chosen to be the Brewster angle ( $\alpha=70.36^\circ$ ) for this material. For this angle and for the proper linear polarisation the reflections turn out to vanish for a broad frequency range. This allows to produce and to change the reflections outside the gyrotron under well defined conditions.

The measurements showed a severe influence of the reflections on the output power.. For power reflections less than 5% a reduction of the generated power of more than a factor of 3 has been found. By tilting the calorimetric power measurement device, an increase in output power could be found by 20%, resulting in an output power of 1.6 MW and an efficiency of 36 % (efficiency with single stage depressed collector was 60%).

### Experimental set-up

The experimental set-up of the gyrotron has been described before [1]. The present new gyrotron, however, was equipped with a Brewster window of Si<sub>3</sub>N<sub>4</sub>. Just behind the window a thin target has been installed. From the gyrotron frequency, the dielectric constant and the thickness of the material the reflection coefficient can be calculated. Except from very few measurements thin disks of GFK-material (glass fibre strengthened material) with a dielectric constant  $\epsilon=4.7$  was used. The distance  $d$  from the window and the angle  $\alpha$  with respect to the window axes could be varied. By different thicknesses of this target the reflection coefficient has been changed. Behind the first target a second (fixed) target had been placed under an angle of about  $45^\circ$  in order to avoid the reflections going back to the gyrotron. These reflections were absorbed by special absorbing material. Using always the same second target the temperature increase of the material was measured and is a relative value of the power, as long as the distribution of the power does not change.

### Experimental results

The experiments were performed at the design values, this means at an accelerating voltage of 80 kV and a beam current of 40 A. Under these conditions the output power was calculated and measured with a calorimeter to be 1 MW.

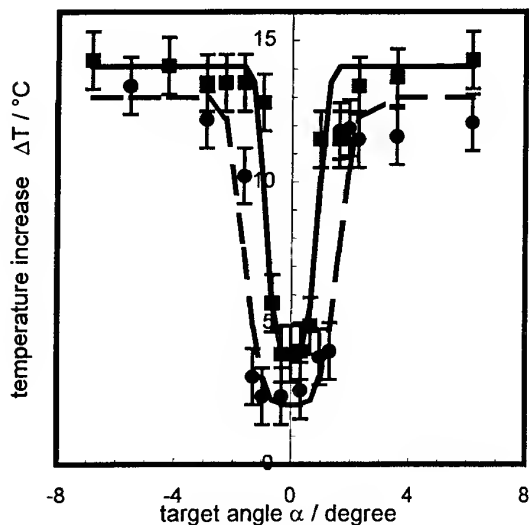
The measured temperature increase  $\Delta T_m$  of the second target does not yield the generated power. It has to be corrected due to the power reflection  $r^2$  of the first target. The generated power is proportional to the corrected temperature increase  $\Delta T = \Delta T_m / (1-r^2)$ .

a) Longitudinal position of the target

Inside the resonator the reflected wave adds with the original wave according to the phase and to the distance of the target. So one expects a sinusoidal dependence of the output power if one changes the distance between the first target and the window. This indeed was found though the effect was only measured at high reflection coefficients.

b) Different target angles

The angle between rf-beam axes and the first target has been changed. Only for very small angles ( $<2^\circ$ ) a strong degradation of the generated beam power has been found. The figure shows the result for the case that the electron beam is placed off axis with respect to the cavity by about 0.5 mm.



Generated power for different target angles  
squares and solid line:  $r^2 = 3,2 \%$   
circles and dashed line:  $r^2 = 13,6 \%$

For 25 % reflections the power had dropped by more than a factor of four. Placing the electron beam by about 0,3 mm off axis with respect to the resonator axis the allowed reflection coefficient is less than 2-3 %.

d) High power measurements

The experiments described so far were performed at the design values for an output power of 1 MW. At higher power the influence seems to be increased. Tilting the calorimeter ( the reflections were measured to be about 1% ) by about  $2^\circ$  lead to an increase in power by 20%. So at a beam current of 50 A an output power of 1.6 MW (efficiency: 36%) was measured compared to 1,35 MW without tilting.

## Conclusions

Up to now experiments only have been performed at a fixed accelerating voltage and a fixed beam current of 40 A. At these operating parameters the influence of small reflections is rather strong especially for not centred electron beams. For higher powers the oscillation range is reduced. The power measurements seems to indicate that under these conditions the influence of the reflections is even more increased. To prove this statement and to give a more accurate answer further measurements are necessary.

- [1] G. Dammertz, O. Braz, M. Kuntze, B. Piosczyk, M. Thumm  
3<sup>rd</sup> Int. Workshop on Strong Microwaves in Plasmas, Aug. 98, Nizhny Novgorod, 1997, vol.2, p. 660

The small angle for which one can observe the effect of power decrease seems to indicate, that a decrease of power only takes place if the launcher is hit directly by the reflected beam. For larger angles the power is still reflected to the mirror box, and after some further reflections inside the mirror box only part of it might go back to the resonator, but there does not seem to be a substantial influence of the output power on this stray radiation.

c) Double disk window.

To find the effect of power degradation as function of beam position more in detail, a double disk window was used as a first target. Unfortunately, the disks were matched to a frequency of 140 GHz, so the neighbouring  $TE_{23,6}$  mode ( $f=143.6$  GHz) was investigated. For this mode it turned out that with a centred electron beam strong degradation started at power reflections exceeding 17-18%.

## The design of the ECRH launcher in ITER

A.G.A. Verhoeven, O.G. Kruijt, P.R. Prins, F.J. van Amerongen, W.A. Bongers,  
L. de Jong, R. Kruisbergen, M.A. Makowski\*, E. Woldberg

FOM-Instituut voor Plasmafysica 'Rijnhuizen', Association EURATOM-FOM  
tel.: (31)30-6096999, fax: (31)30-6031204, e-mail: verhoeven@rijnh.nl  
P.O. Box 1207, 3430 BE Nieuwegein, the Netherlands

\*ITER JCT Garching, Germany

### Introduction

Electron cyclotron (EC) auxiliary power systems are very attractive for the future fusion research device ITER, the International Tokamak Experimental Reactor [1]. The coupling of EC waves to a plasma is rather simple, the delivered power density is very high and the absorption of the power in the plasma is for almost all conditions 100% in single pass. The ITER heating and current drive system is designed to deliver 50 MW of 170 GHz power, upgradeable to 100 MW. The major unresolved problem so far is a system to direct the individual mm-wave beams of 1 MW each to different positions in the ITER plasma. The system has to work in a very hostile environment, it is heated by plasma radiation, by neutrons and by losses of mm-wave power.

Therefore, a system was designed, under an ITER task, to direct 56 mm-wave beams to the plasma, more or less in the tokamaks equatorial plane. The principle of the steerable launcher is shown in figure 1. A waveguide transmits the power to a fixed mirror, after which a steerable mirror directs the beam to the plasma. Each steerable mirror rotates on its own support structure. The single launcher sets of one fixed and one steerable mirror each, are grouped to 7 horizontal rows of 8 launchers. All mirrors of one row are controlled by one push-pull rod. Each of the seven rows can be steered independently (figure 2).

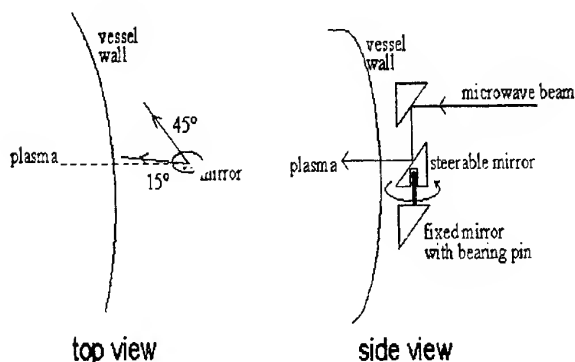


Figure 1. Principle of the construction and the range of the movement of the steerable mirror

The steerable mirrors can rotate around a vertical axis over an angle of at least 30°. The coolant supply channels of the rotatable mirrors consist of flexible couplings, which are positioned below each mirror, in or around the rotational axis, to minimize the mechanical load on the tube. The same construction is used at the push-pull rod bearings. Figure 2 gives an overview of the launching system.

### Heat load and cooling

The mirrors have to work in a hot environment and are heated by plasma radiation, by neutrons and by losses of microwavpower on the mirror surface. For the mirror surfaces the mm-wave losses are the dominant heating source [1]. Each construction part that cannot be cooled by heat conduction is cooled by a water channel. Each mirror has a layer of copper or glidcop for a high thermal conductivity and low mm-wave losses. Taken into account is a Beryllium coating, which will increase the mm-wave loss by about a factor of two.

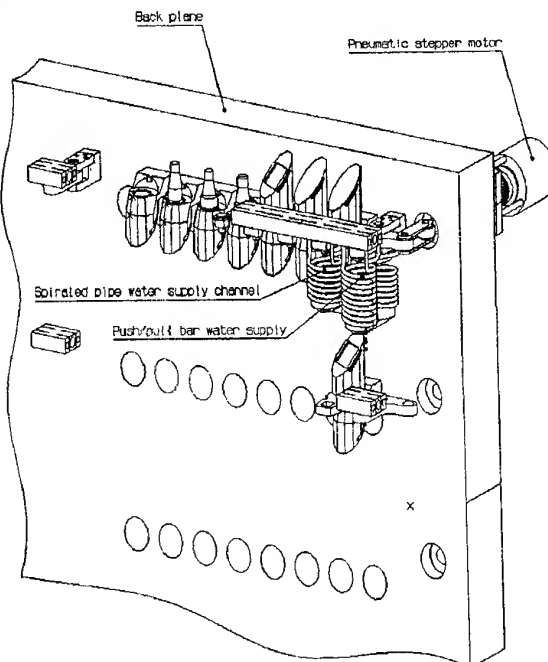


Figure 2. Overview of the launching system

Cooling water flows through channels in the copper layer. The distance between the cooling channels and the mirror surface should be small, for low heat resistance and low plasma-disruption forces. But as the copper layer is the barrier between good operation and failure-by-water-leakage, we consider 3 mm as a minimum distance between channels and vacuum. With channels in the stainless steel body the heat resistance would be too high.

The copper is intimately connected to the stainless steel mirror body by HIPping (Hot Isostatic Pressing). To maximize the heat transfer from copper to cooling water with a low flow rate, the cooling channels should be narrow. On the other hand there is a limitation, caused by the maximum pressure drop of 5 bar of the ITER water cooling circuit. Another limitation is the difficulty to drill narrow channels in copper. A diameter of 1.3 mm was found to be optimal.

#### Finite element calculations

The cooling channels are distributed in such a way that the temperature differences in the copper layer are more or less minimized. Finite element calculations were performed for the mirrors of figure 1. The calculations are done with a water flow of 3 liter per minute per mirror from the ITER cooling water plant, delivering 150 °C water at 40 bar. The outlet temperature is about 20 °C higher. In the simulations an average temperature of 160 °C is assumed. Figure 3 gives an impression of the temperature distribution in the surface area of the second mirror.

#### Prototype heat test

A mirror prototype for a check of the cooling capacity was made by brazing a copper layer on a stainless-steel body. The mirror was tested with a cooling water inlet temperature of 15 °C and an acetylene welding burner.

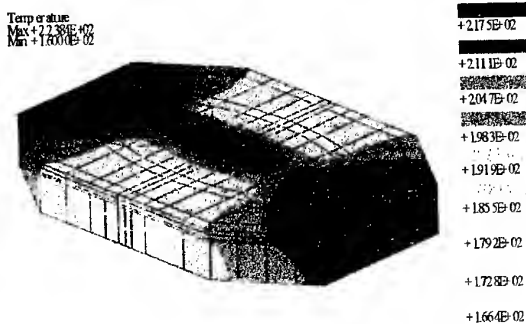


Figure 3: ITER mirror temperature distribution. Calculated with an average temperature of the water in the cooling channel of 160°C. The maximal temperature is 224°C, which is acceptable.

The flame was concentrated on the mirror center. With a cooling water flow of 3.2 litre per minute the concept proved its usability. The heat removal per channel was measured by thermocouples on the water in- and outlet. The flame entered 2 kW in the mirror surface. Figure 4 shows an infrared photograph of the mirror immediately after removing the flame.

The temperature in the center did not exceed about 40°C (compared with the 150°C cooling water in the final application, the cooling capacity of water with a temperature of 40°C is about a factor two worse).

#### Conclusions

The ITER launcher design was undertaken resulting in the proposal as described. First calculations indicate that the heat load can be handled. Initial experiments confirm the calculations. A lot more detailed design work and especially prototype testing have to be done.

#### Acknowledgements

This work was performed as part of the research programme of the association agreement of EURATOM and FOM with financial support from NWO and EURATOM.

#### References

1. M. Makowski, *et al.*, Proc. 10th Workshop on ECE and ECRH, EC10, Edited by A.J.H. Donne and A.G.A. Verhoeven (World Scientific, Singapore, 1998), pp. 549-559.
2. R. Prater, *et al.*, *ibid*, pp. 531-540.

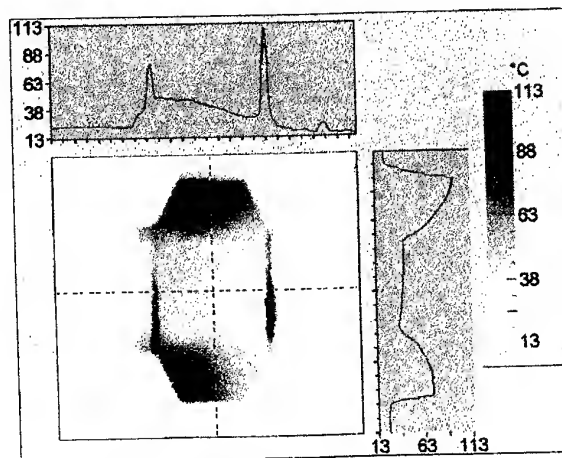


Figure 4: infra-red photograph with X/Y profile of the mirror immediately after removing the flame. The narrow hot zones left and right of the mirror are caused by heat absorption in the rubber seals of the test setup. The hot areas on top and bottom were caused by hot gas on places where in the case of heat load by a mm-wave beam, in the tail of the Gaussian profile, the heat production would be very low.

### Drift non-linearities in semiconductors giving rise to 1 THz radiation

R. Brazis<sup>1</sup>, R. Raguotis<sup>1</sup>, Ph. Moreau<sup>2</sup> and M. R. Siegrist<sup>2</sup>

<sup>1</sup>Semiconductor Physics Institute, A.Gostauto 11, 2600 Vilnius, Lithuania

<sup>2</sup>Centre de Recherche en Physique des Plasmas; Ecole Polytechnique Fédérale de Lausanne; PPB Ecublens, 1015 Lausanne; Switzerland

In a future test reactor plasma device like ITER it is essential to be able to diagnose the  $\alpha$ -particle temperature, motion and slow-down characteristics. This can be achieved by means of collective Thomson scattering using powerful radiation sources in the submillimetre wave region. At present no alternative diagnostic methods have been proposed, let alone tested, to obtain these characteristics. The exceedingly small cross-section of Thomson scattering requires a high power radiation source and a sensitive detection system and the fact that the information is contained in the spectrally-broadened shape of the scattered radiation imposes limits on the line width of the source. A source of this type does not currently exist. While free-electron lasers can supply the required power in the tens to hundreds of kW region and the pulse length of tens of milliseconds, they are bulky and expensive. Optically-pumped FIR lasers cannot be operated at pulse durations compatible with the integration time scales for heterodyne detection and gyrotrons do not currently operate at THz frequencies with sufficient power, although they would otherwise be ideal candidate sources. If the radiation of a gyrotron could be converted with reasonable efficiency ( $\sim 10\%$ ) to higher harmonics, the problem would be solved. Our current interest in the study of drift non-linearities in semiconductors giving rise to 1 THz radiation is stimulated by these diagnostic applications.

We determine the third harmonic generation efficiency in a semiconductor placed in an oscillating electric field using two Monte Carlo code modifications. The first one is designed for elemental crystals, and the second one has been developed for  $A^3B^5$  compound semiconductors.

The output of the code is the time dependence of the drift velocity of electrons. Making the Fourier transform of this velocity gives the spectrum of amplitudes and phases of the harmonic currents which are the sources of radiation emitted by the sample. Then, the third harmonic generation (THG) efficiency is defined by the square of the ratio of dividing the drift velocity amplitude to the pump wave field amplitude:

$$\eta_3 = K_0 \left( \frac{2}{1 + \sqrt{\epsilon_L}} \right)^2 \left| \frac{(enV_3)d}{E_1} \right|^2 \quad (1)$$

where  $K_0$  is the material-independent constant,  $\epsilon_L$  is the lattice dielectric constant,  $n$  is the electron density,  $d$  is the layer thickness and  $V_3$  is the 3<sup>rd</sup> harmonic drift velocity amplitude obtained from the Monte Carlo simulation.

Comparison with experimental results in n-type Si has allowed us to demonstrate the usefulness of this method in explaining the 3<sup>rd</sup> order nonlinearity in n-type Si for pumping intensities up to 2 MW/cm<sup>2</sup> at the fundamental frequency of 443 GHz. However, n-Si at room temperature is not the best possible choice with a power conversion efficiency not exceeding about 0.1% [1]. Cooling down the crystals to liquid nitrogen temperatures and using other materials like GaAs or InP seems to be much more promising.

For the electron motion in n-type Si six ellipsoidal X-valleys are considered, taking into account the nonparabolicity. One type of acoustic phonons in the equipartition and elastic approximation was used to model intravalley scattering, whereas intervalley scattering is accounted for by six types of large-momentum phonons. The phonon parameters of Brunetti et al. [2] have been used and direct comparison of simulation results with experimental data of the third harmonic generation at room temperature has been very successful [1].

The band structure of InP is similar to GaAs with 1.5 times higher separation between the  $\Gamma$  and X, and  $\Gamma$  and L valleys. The intervalley phonon energies and coupling constants are not much different from those in GaAs [3] but, the optical phonon energy in InP is 1.25 times higher than in GaAs. The difference between the optic and the static dielectric permeability determining the polar optic phonon scattering cross-section in InP is higher than in GaAs.

We have performed calculations for the three materials at lattice temperatures of 300 K and 80 K and compared them with the room temperature data of silicon where experimental results on the THG already exist [1]. The THG efficiency, which is proportional to the square of the 3<sup>rd</sup> harmonic drift velocity amplitude ratio to

the pumping wave field amplitude (Eq.1), can be improved by cooling the crystal down to liquid nitrogen temperatures (Fig.1).

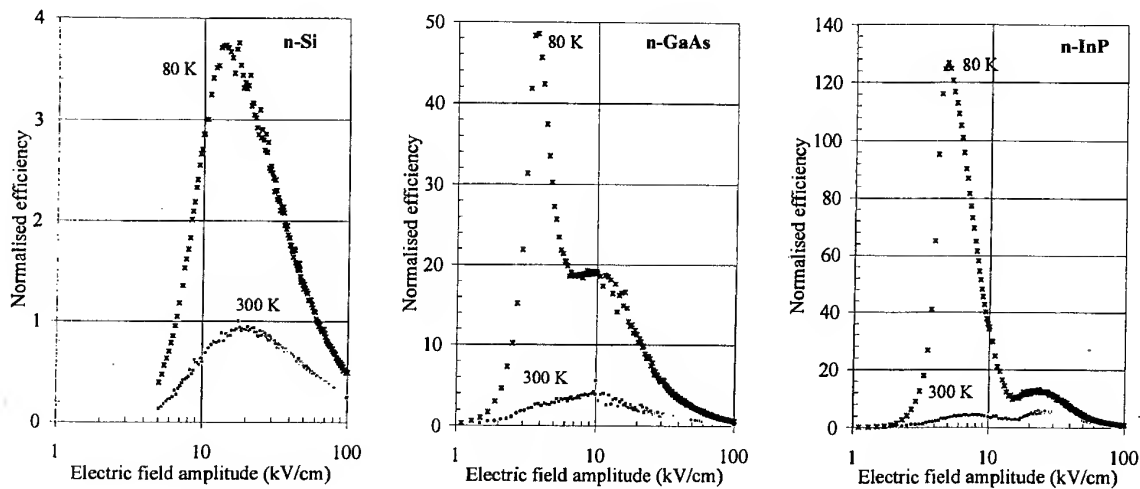


Fig.1. THG efficiency normalised to the maximum efficiency in n-type Si at  $T = 300$  K as a function of the pump field amplitude. The fundamental frequency is 333 GHz. Materials and temperatures are shown in the figure.

It is obvious that at very low field amplitudes the drift response is linear causing the THG efficiency to approach zero, whereas at high field amplitudes the heating of electrons randomizing their momentum should reduce the 3<sup>rd</sup> order nonlinear susceptibility again. Hence a maximum efficiency is expected in between which is indeed clearly observed (Fig.1, Si). The optimum conversion efficiency in n-type Si at the fundamental frequency of 333 GHz is around 20 kV/cm. Similar mechanisms of intervalley electron transfer in GaAs bring about a maximum efficiency around 10 kV/cm, whereas in InP it is at pumping field amplitudes slightly above 25 kV/cm [4]. What is striking, however, is the additional much more pronounced maximum which is observed in GaAs and InP at lower electric field amplitudes. It is seen from the comparison of data for GaAs and InP that the maximum position correlates with the optical phonon energy, and the maximum height correlates with the product of the optical phonon energy with the electron-polar-optic phonon scattering cross-section. Therefore we attribute the novel maximum of THG efficiency to the inelastic scattering of electrons on polar optic phonons. It does not take place in Si crystals which have no first order electric dipole related to optic phonon modes. When the lattice temperature is  $T = 300$  K then the effect of inelastic scattering of electrons by optic phonons is smeared out by randomising scatterings on other types of phonons. Nevertheless, the additional maximum of efficiency in InP is seen even at room temperatures. One can expect an even more pronounced effect in polar crystals with higher optic phonon energies or in p-type elemental semiconductors where the inelastic scattering on optic phonons is present owing to the deformation potential interaction.

In conclusion, we report here a novel effect of the maximum efficiency of the third harmonic generation which is more than two orders of magnitude higher than the THG efficiency experimentally observed up to now in n-Si. If one aims to optimise the output power and hence expands the pump beam in order to operate at the point of maximum efficiency, GaAs and InP seem to be superior, in particular at the temperature of liquid nitrogen. The low-temperature operation is favourable for the heat transfer from the non-linear sample subjected to the still quite powerful pump wave field.

This work was partially supported by the Swiss National Science Foundation.

#### References

1. M Urban, M R Siegrist, L Asadauskas, R Raguotis, and R Brazis, *Appl. Phys. Lett.*, **69**, 1776 (1996).
2. R Brunetti, C Jacoboni, T Nava, L Reggiani, G Bosman and R J J Zijlstra, *J. Appl. Phys.*, **52**, 6713 (1981).
3. K Brennan and K Hess, *Solid State Electronics*, **27**, 347 (1984).
4. R Brazis, R Raguotis and M R Siegrist, *J. Appl. Phys.* (1998), to be published.

## Beam-Shaping, Dual-Mirror Design using Measured Amplitude and Reconstructed Phase for the Input

B. M. Harper and R. J. Vernon

Department of Electrical and Computer Engineering  
University of Wisconsin, Madison, WI 53706

### Abstract

Beam shaping microwave reflector systems based on theoretical models of the output from Vlasov launchers have frequently not produced high-quality output beams. This paper discusses the design of such reflector systems using measured input amplitude patterns and phase distributions reconstructed from the amplitude data.

### Phase Reconstruction and Mirror Design

Internal beam-shaping reflectors are crucial for getting high powers out of some gyrotrons. Thermal limitations of the vacuum window as well as external injection of the microwave beam into a corrugated waveguide require very specific beam characteristics. Previous beam shaping reflectors have achieved satisfactory results but have shown room for improvement. One cause for error has been inaccuracy in the theoretical modeling of the input to the reflectors. Small inaccuracies in the amplitude and phase distribution of the theoretical patterns for the input beam can cause dramatic effects in the output beam's characteristics. It is possible to use measured data instead of theoretical data for the input to the mirror design. Measured amplitude data of the input to the two shaping reflectors has been available; however, both the amplitude and phase information of the beam are required for the design procedure. Since the amplitude and phase of a propagating beam are uniquely coupled, it is possible to obtain the phase information associated with a propagating beam from amplitude measurements over several cross-sections. An iterative, diffraction-based technique for obtaining the phase pattern associated with a propagating beam has been developed.

The reconstruction technique involves writing the measured amplitudes as currents and using numerical integration to "propagate" the beam from one plane to another. For a beam which is reasonably well behaved, the phase pattern can be obtained by using data from only two planes as long as there is a reasonable first estimate of the phase pattern at one of the planes. Using the amplitude data and a reasonable estimate for the phase pattern at one of the planes, the beam is propagated using numerical integration to the second plane. The phase distribution associated with the propagated beam is applied to the measured amplitude data at the second plane. These phase and amplitude patterns at the second plane are then back-propagated to the first plane. The back-propagated phase pattern at the first plane is applied to the measured amplitude data there. The process is then repeated until the solution converges, usually in only a few iterations. More planes can be added to this algorithm to improve the output. The amplitude and associated phase distribution are unique to the beam and only the "correct" applied phase will produce the proper amplitude distributions when propagated to the other planes. The phase and amplitude patterns now become the input for the reflector design.

The phase reconstruction technique was applied to a propagating beam at the input to the two shaping mirrors in the  $y=11$  cm,  $y=50$  cm, and  $y=122$  cm planes. Here the  $y$  direction is perpendicular to the axis of the gyrotron with  $y=0$  at the axis of the tube. The measured data at plane #1 with its reconstructed phase propagated to plane #3 and the measured data at plane #3 are shown in Fig. 1. The measured data at plane #3 with its reconstructed phase propagated back to plane #1 and the measured data at plane #1 are shown in Fig. 2.

The target output distribution depends on the size and type of vacuum window. The new diamond window can sustain very high peak power densities. With this new window, a new target power distribution was chosen, a fundamental Gaussian beam, the  $TEM_{00}$  mode, with a waist of  $0.58a$ . Here  $2a$  is the diameter of the window aperture which is 2.0". This allows 99.7% of the power in the beam to pass through the 2.0" aperture. The theoretical peaking factor of this beam is 5.94. The peaking factor (PF) is defined as the peak power density divided by the average power density over the aperture.

The dual-mirror design technique is similar to the phase reconstruction technique. The fields associated with a beam are propagated forward and backward using numerical integration. This design procedure requires precise amplitude and phase information at both the input and the output of the reflectors. The desired output beam is back-propagated to the surface of mirror #2 and then to mirror #1. The input is then propagated forward to the surface of mirror #1. The phase distributions of both the forward propagated and back-propagated beams are compared at the surface of mirror #1. The difference in the phases suggests a perturbed surface on mirror #1. The input beam is then propagated off of the perturbed surface to mirror #2. The phases of this forward propagated beam and the back-propagated output beam are compared at the surface of mirror #2. The difference in the phase distributions suggests a perturbation to the surface of mirror #2. The desired output beam is now back-propagated off of the perturbed surface



of mirror #2 to mirror #1. This procedure is repeated until the output beam couples sufficiently to the target output beam, usually in only 1 or 2 iterations.

### Experimental Results

Two shaping mirrors were designed using the iterative, dual-mirror, diffraction-based technique with the empirical input and new target output. Two iterations were used to obtain the surface perturbations. The theoretical design produced a peaking factor of 5.75, allowed 99.6 % of the power through the aperture, and had 99.9 % coupling to the  $TEM_{00}$  mode before masking of the unmanufacturable surfaces near the edges. After masking the theoretical design produced a PF of 5.74, allowed 99.5 % of the power through the aperture, and had 99.8 % coupling to the  $TEM_{00}$  mode.

Measured patterns agreed very well with the theory. The mirror system produced a PF of 5.94, allowed 98.9 % of the power through the aperture, and had 99.7 % coupling to the  $TEM_{00}$  mode (see Fig. 3). The beam propagated nearly along the y-axis, off by  $0.4^\circ$  in x and  $0.25^\circ$  in z.

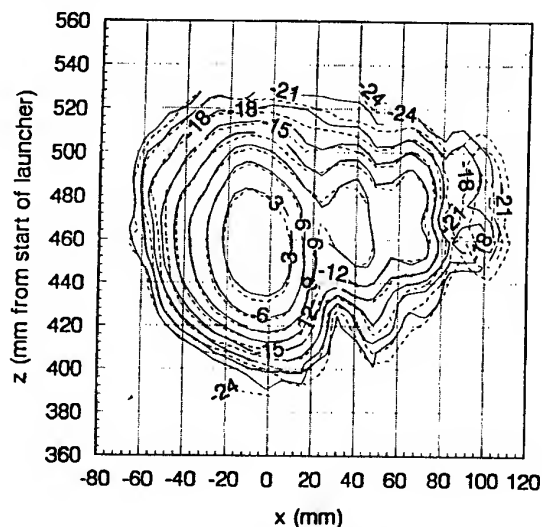


Fig. 1. Power density contours on the  $y = 50$  cm plane. Measured data at the  $y = 11$  cm plane with its reconstructed phase propagated to the  $y = 50$  cm plane are shown with measured data at the  $y = 50$  cm plane.

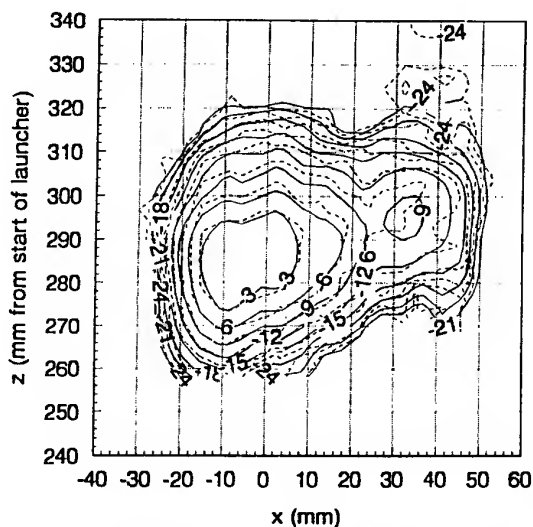


Fig. 2. Power density contours on the  $y = 11$  cm plane. Measured data at the  $y = 50$  cm plane with its reconstructed phase back-propagated to the  $y = 11$  cm plane are shown with measured data at the  $y = 11$  cm plane.

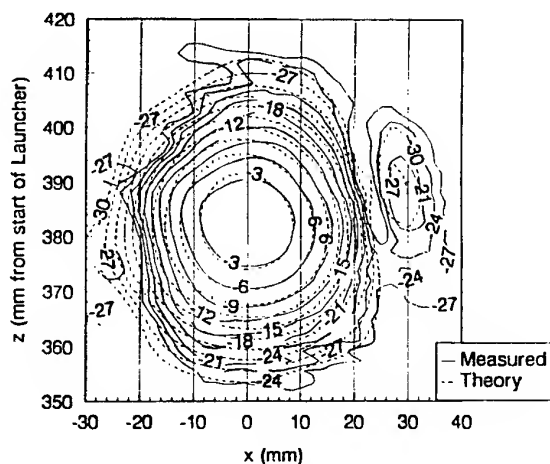


Fig. 3. Power density contours at the position of the vacuum window showing the reflector and theoretical outputs. The reflectors are in their nominal positions.

## Compact, Turn-key, Terahertz, Laser Systems for Fusion Plasma Diagnostics

W.A. Peebles<sup>#</sup>, David Brower, Yong Jiang, Lei Zeng, Patrick Pribyl<sup>#</sup>, Peter King<sup>\*</sup>

Electrical Engineering Department,  
University of California Los Angeles,  
Los Angeles, CA.90095, USA

<sup>#</sup>Also: *IR&T*, Innovative Research & Technology,  
326 25th St., Santa Monica, CA. 90402, USA

<sup>\*</sup> California Institute of Technology, Pasadena, California, USA

### Abstract

The terahertz spectral region is extremely useful for measurement of important fusion plasmas parameters, such as density profile, current profile and turbulence spectra. However, despite the obvious benefits this has not resulted in widespread application especially on smaller experiments. This is a direct result of the widespread belief that source technology in this spectral region is complicated and labor intensive. However, recent advances have resulted in turn-key, compact laser systems that have the potential for widespread application to fusion plasma diagnosis, as well as other application areas such as atmospheric physics, astrophysics, etc. This paper documents the contributions that terahertz technology has made to fusion plasma diagnosis as well as describing advances in optically pumped laser technology that will enable future widespread application.

### Introduction

Controlled thermonuclear fusion offers a future supply of safe, clean and virtually unlimited energy. Towards this end there is presently great worldwide interest in the detailed study of high temperature magnetic confinement fusion plasmas with a view to improving our understanding and advancing progress towards the above goal. Fusion science is almost unique in that it has always relied on and benefited from strong international collaboration. Presently, significant fusion efforts exist in the former Soviet Union, United Kingdom, France, Germany, Italy, Netherlands, Spain, USA, Japan, Korea, India, Australia etc.

Understanding high temperature fusion plasmas comes through detailed measurement and comparison with theoretical predictions. Much progress has been achieved in recent years and diagnostic instrumentation has played a critical role. In particular, the terahertz spectral region ( $0.3\text{THz} < f < 3\text{THz}$ ) has contributed to the operation, control and understanding of fusion plasmas. For example, interferometry has provided line integrated electron density information for control and profile determination as well as to study sawteeth and MHD instabilities. Polarimetry (Faraday rotation) has provided critical information on the evolution of the current profile in tokamaks and reversed field pinch plasmas. Finally, collective Thomson scattering has been employed to monitor the spectral properties of the background turbulence thought responsible for the anomalous transport of heat and particles. However, terahertz laser systems on fusion plasmas have typically been cumbersome, manpower intensive and expensive. This has resulted in their application being confined to larger laboratories where the resources exist to maintain routine operation. In order to motivate the need for increased access to terahertz systems the next section briefly presents some representative terahertz data from fusion plasmas.

### Fusion Plasma Data

Interferometers typically consist of optically pumped *twin frequency* FIR lasers separated in frequency by  $\sim 1\text{MHz}$  to provide a heterodyne capability. This ensures that there is minimal ambiguity over the temporal evolution of the plasma induced phase change. Figure 1a illustrates the evolution of phase (proportional to line integrated plasma density) for a multichannel (11 channels) interferometer system operating at 670 GHz on the MST reversed field pinch at the University of Wisconsin. Channels close to the center and edge plasma are illustrated. Initially there is a sharp rise and fall in plasma density followed by a slower rise accompanied by increasing density fluctuations associated with MHD. Injection via plasma guns cause a further increase in fluctuations. Reversed field pinch plasma have complicated and extensive MHD

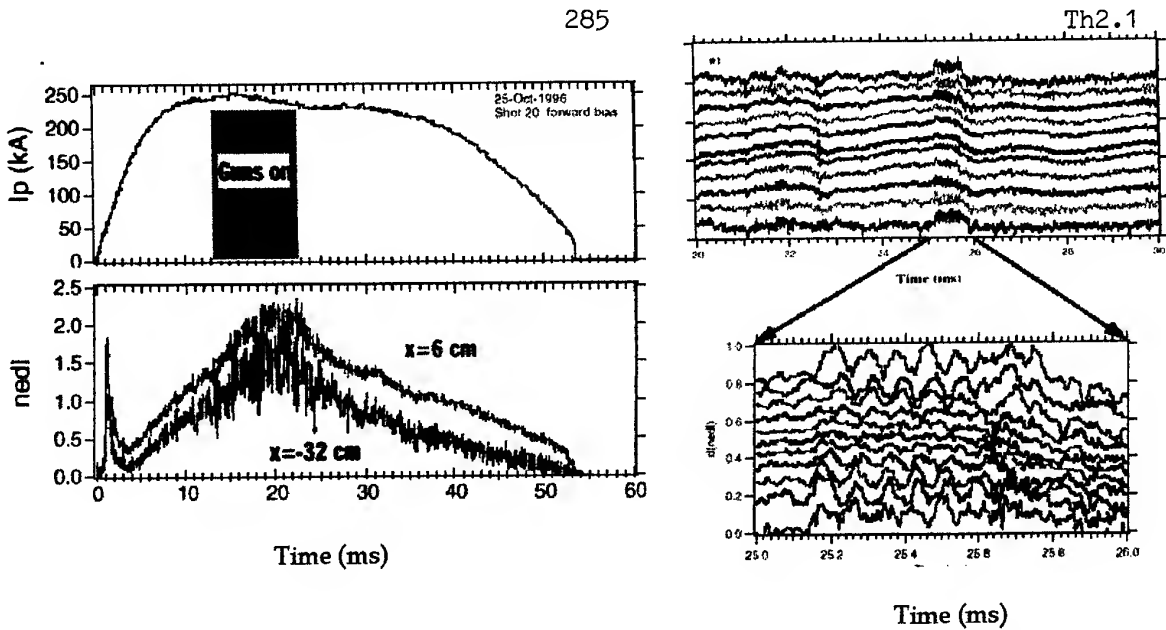


**Figure 1(a)** Evolution of plasma current and line integrated density. Note the increased density fluctuations (associated with MHD) especially during the injection via plasma guns. **(b)** Line integrated density data over a short time period during a quiescent phase. Note the clear indication of an  $m = 1$  MHD mode

structure as illustrated in Fig 1(b) where the line integrated density for all 11 channels is shown for a period of 10 and 1 ms respectively. As can be seen the mode structure can be identified as  $m = 1$  from the clear phase reversal across the plasma radius.

Adding a capability to measure the polarization properties of the emerging electromagnetic wave after passage through the plasma can significantly extend the usefulness of interferometers. Faraday rotation of the incident beam results in a polarization rotation proportional to the line integral of the product of density and magnetic field component along the propagation direction. Therefore simultaneous measurement of line integrated density and Faraday rotation allows data inversion to produce not only density but also, more importantly, current profile. For tokamak fusion plasmas the current profile is extremely important in that it determines the stability properties of the plasma. Data from the TEXT-U plasma at the University of Texas, Austin is illustrated in Fig 2.

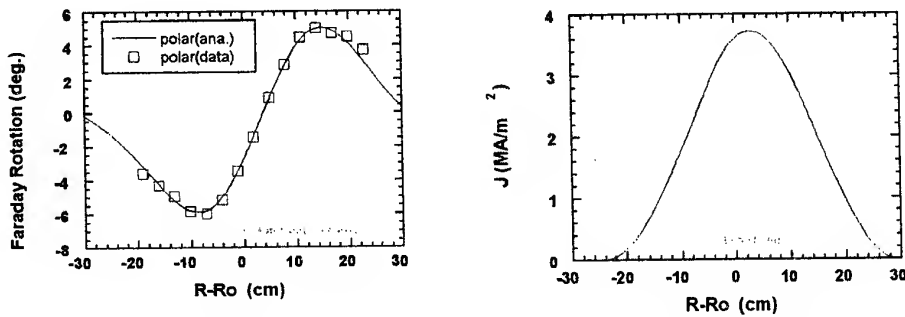


**Figure 2.** Faraday rotation data together with inverted current profile

Faraday rotation resulting from measurement in a poloidal plane is sensitive to the poloidal magnetic field resulting from the toroidal plasma current. Note that in Fig. 2 the sign of the rotation angle reverses around plasma center as to be expected. In fact the center of the current channel can be easily inferred from the zero crossing point of the Faraday rotation angle.

From the above data it is clear that terahertz laser systems can be utilized to provide information on the equilibrium profiles of both density and current as well as revealing important information on MHD and turbulence characteristics of the plasma. However, improvements in simplicity of operation, efficiency together with resultant lower costs would

increase application of such systems as well as improving routine measurement capability.

### Recent Improvements in Terahertz Laser Systems

As mentioned above, terahertz systems utilized for interferometry, polarimetry and collective scattering typically operate as twin frequency systems where two separate far-infrared (FIR) laser cavities are employed that operate at slightly ( $\sim 1$  MHz) different frequencies. One of the laser beams typically passes through the plasma and is then combined with a reference beam in a Schottky diode mixer. It should be noted that in the linear cavities employed feedback effects can lead to deleterious effects through frequency pulling. Existing systems typically employ complicated, cumbersome flowing gas, longitudinal high voltage DC discharge  $\text{CO}_2$  pump lasers. Recently, outside of the plasma community, compact, turnkey FIR lasers have emerged which offer significant promise for application to fusion plasma diagnosis. Compact, sealed-off, RF excited  $\text{CO}_2$  lasers have been utilized eliminating the need for gas flow and high voltage power supplies. Figure 3 illustrates one such system delivered to NASA by Innovative Research & Technology.

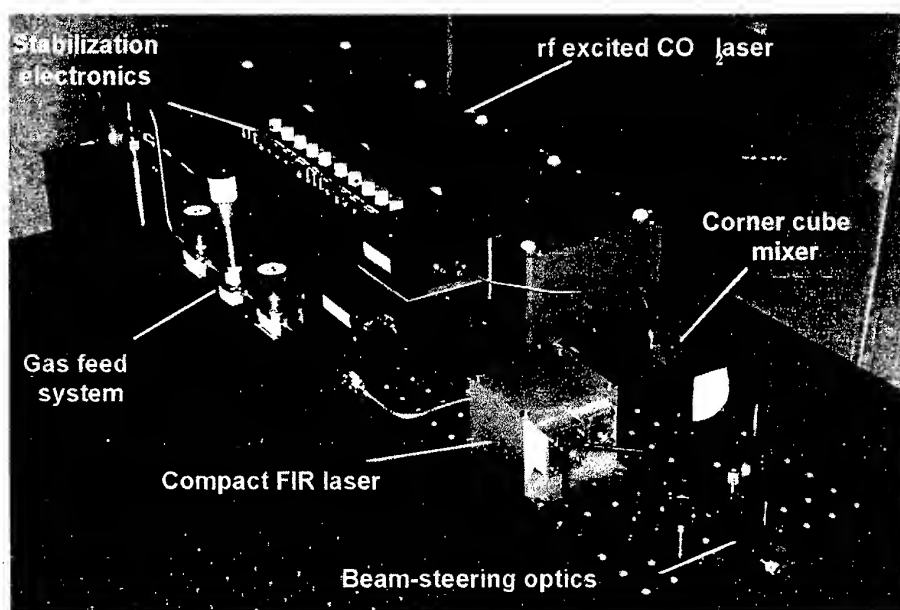


**Figure 3** Photograph illustrating turnkey compact 2.5 THz laser. The entire laser including gas feed, monitoring detector and feedback control electronics is mounted on a 1 ft. x 3.5-ft optical breadboard. A DEOS sealed-off, RF excited  $\text{CO}_2$  laser is employed to pump a folded FIR cavity. Distinct modulation frequencies are applied to the  $\text{CO}_2$  and FIR laser cavities for the purpose of feedback control. The analog electronics contains mixer bias, low noise amplifier plus feedback control for both the  $\text{CO}_2$  and FIR laser cavities. The next evolution will incorporate digital control and twin-frequency operation in a similar package size.

Another important development in recent years has been the utilization of far-infrared ring cavities. The ring cavity serves two purposes. First, it eliminates feedback of  $\text{CO}_2$  pump radiation from the FIR cavity and therefore simplifies stabilization. Second, it significantly mitigates the effect of far-infrared laser feedback to the FIR cavity. This occurs because the FIR ring laser operates *unidirectionally* and so radiation feedback is not resonant with the operating laser mode.

### Summary

Recent advances in FIR lasers have led to compact, lower cost, turnkey systems suitable for widespread application to fusion plasma diagnosis. Future beneficial developments would include increased efficiency, further reduction in size, commercial availability of three-frequency lasers, as well as lasers possessing a temporally rotating plane polarized output.

# The challenge of implementing THz plasma diagnostic systems on ITER

G. Vayakis for the ITER JCT and Home Teams

ITER JCT, San Diego JWS, 11025 N. Torrey Pines Road, La Jolla CA 92037, USA

## Introduction

Several diagnostic systems [1] planned for the International Thermonuclear Experimental Reactor (ITER) [2] work in the mm and sub-mm wave range (Table 1). These systems are all, in principle, "reactor friendly": They need comparatively small penetrations through the inner wall which faces the plasma (first wall) and neutron shield, and the signal can be routed in complex paths to minimise neutron streaming. In addition, the front end requires little or no maintenance, because it is resistant to damage from the plasma, even in disruptive events, and essentially immune to neutron irradiation effects [3]. Preliminary designs for all these systems have been evolved through an iterative process with most of the effort taking place in the ITER Home Teams [4].

Significant issues have been encountered in this design process: access to the plasma through the plasma facing components, access to the front end for installation and maintenance, calibration to provide immunity to machine movements during the long pulses planned, long transmission lines, relatively ambitious frequency ranges, and very high reliability requirements. Although it is fair to state there are examples of these problems being dealt with in the present generation of magnetic fusion devices, ITER presents an unusual challenge in that the problems occur simultaneously. The dominant design drivers are that the access to the plasma is restricted to an unusual degree, due to the stringent thermal and mechanical requirements on the first wall and neutron shield structures, and planned maintenance or calibration procedures that involve dedicated in-vessel access impose an unacceptable burden on machine availability. Two strategies have emerged, given the difficulties and costs associated with each transmission line, and the ambitious nature of the measurement targets: use of broad-band, oversize transmission lines, and waveguide sharing between measurements.

In this paper we discuss two designs, that of the Electron Cyclotron Emission (ECE) system, and that of the divertor reflectometer. Additional information on these and other systems can be found in the references cited within Table 1.

Table 1: List of mm and sub-mm wave systems proposed for ITER.

System	Location	Mode *	Frequency Range (GHz)	Transmission within cryostat	Measurement
ECE [5]	Main Horizontal Port	O	120 - 240 + 100 - 1000 (survey)	QO and oversize circular corrugated wg. (see text)	Electron temperature by the detection of cyclotron radiation, typically at the first two harmonics.
		X	240 - 360 + 100 - 1000 (survey)		
Reflectometer (Main Plasma) [6,7]		O	20 - 155	Oversize circular corrugated wg.	Electron density profile, employing radar-like techniques to measure the distance of layers of reflection (cutoff layers) in the plasma from the machine walls.
		X	84 - 220		
	In- vessel (high field side)	O	20 - 155	Oversize rectangular wg.	
		X	10 - 110 (2 bands)	Rectangular/ circular corrugated wgs.	
Reflectometer (Plasma Position) [8,7]	In vessel (on backplate)	O	15 - 60	Oversize rectangular wg.	
Reflectometer (Divertor) [9,7]	In divertor cassette (see fig. 2)	O	20 - 960 (3 bands)	Oversize rectangular and circular corrugated wg. (see text)	
		X	90 - 180		
ECA [10]		X	~ 300		
Interferometry [7]		O	300 - 960		
Collective Scattering (mm option) [11]	Main Horizontal Port	O	80 - 90	Circular corrugated wg. (Tx), QO (Rx)	Ion and $\alpha$ particle temperature by the frequency-broadened scattered spectrum of externally launched radiation.

\* O and X refer to the E-plane parallel and perpendicular to the magnetic field, respectively. The nominal magnetic field of ITER is 5.68 T at a major radius  $R = 8.14$  m.

### The ECE system

The design of the ITER ECE system, whose front end is shown in Figure 1, has been shaped by the following considerations:

(i) Selection of an adequate sightline distribution: Two sightlines were found adequate to cover the vertical range ( $\sim 0.8$  m) of typical ITER plasmas (including startup), without degrading the core resolution significantly. These, using polarisation splitters, can support the 4 planned instruments: Two (O & X mode) survey instruments (Michelson interferometers covering the range 0.1 - 1 THz) and two (O & X mode) heterodyne instruments for fast profile measurements.

(ii) Choice of an appropriate front end: In order to reach the spatial resolution limits imposed by the physics of the emission process, and thus achieve the target resolution in the core (0.1 m), well defined antenna patterns over a very broad band (100 GHz-1 THz) are a requirement (to avoid potential degradation of the resolution due to the antenna side lobes). The present design employs a Quasi-Optical (QO) Gaussian beam telescope arrangement, using off-axis ellipsoidal mirrors forming a dog-leg to decrease the neutron leak rate.

(iii) Optimisation of the front end to minimise the perturbation to the first wall and shield: The size for the first mirror has been iteratively decreased, subject to the core resolution requirement, with the focal length as a free parameter. It is found [5] that a mirror size of 200 mm gives acceptable performance for all frequencies above 100 GHz. Thus, good performance in X-mode is available down to 1/2 full field.

(iv) Calibration mechanism: to ensure the accuracy of the measurements, an end-to-end absolute spectral calibration mechanism has been incorporated in both sightlines. On ITER, and any reactor grade device, it will be difficult, and expensive in operation time, to introduce an in-vessel calibration source at frequent intervals as is current practice (e.g. on JET). At the same time, there is no other comprehensive way of checking the full system performance. This mechanism has two parts: a passively cooled metal mirror, rotated using a mechanism in the interspace vacuum, and a calibration source in vacuum, which will be the subject of future R&D. The key issue here is the stability of the source.

(v) Robustness and ease of maintenance: the first two mirrors are held in a rigid, pre aligned, assembly, with a single set of coolant connections to the shield block, which is a maintained a single component once irradiated. It is expected to survive the machine life ( $\sim 20$  yrs). The calibration source assembly, and the shutter/mirror are the only other components that require removal of the diagnostic block for replacement.

(vi) Vacuum boundaries. For the difficult to reach primary vacuum, a single quartz window qualified to 0.5 MPa, and inclined at  $15^\circ$  to reduce standing waves, is used for both polarisations. For the second barrier, following a deposited beam splitter, separate Brewster silicon nitride windows are used for each polarisation.

### The divertor reflectometer

Similar principles to those used in the ECE design drove the design of the divertor reflectometry (Figure 2), with some additional considerations, primarily the extreme scarcity of first wall space, and the need to share this space with the other mm-wave systems (Table 1). In the present, tentative, configuration, to cover the extreme frequency range (in O-mode), it is planned to use three sub-systems: A "low mm" (20-60 GHz) system and "high mm" (60 -  $\sim 300$  GHz) system for profiles, and a "comb" type transmission/reflection combined system in the sub-mm range, which in effect can also be used as an interferometer.

(i) Selection of an adequate sightline distribution: To meet the requirement of 0.1 m resolution along each divertor leg would require  $\sim 20$  sightlines for each type of measurement to be accommodated in the divertor (Table 1). Reflectometry alone needs 5 antennas / sightline to accommodate the 3 bands, resulting in 100 waveguides, clearly an impracticable number. The present design is a compromise based on a total maximum number of waveguides with priority given to the more "robust" measurements [7]. It turns out that it is possible to accommodate 5 sightlines on the outer leg, and 3 sightlines on the inner leg by making full use of two out of the 4 maintenance ports (20 waveguides per port).

(ii) Choice of an appropriate front end, and (iii) Optimisation of the front end to minimise the perturbation to the first wall and shield: These two issues are inextricably linked for the divertor. There are strong limits imposed by the cassette geometry, which cannot be altered without increasing the (already high) local heat loads near the cassette gaps. Thus the front ends for all systems consist of truncated rectangular waveguide, viewing the plasma through the cassette gaps. This will have as yet unquantified effects on the performance because of parasitic reflections. Several bends are necessary to bring the radiation out of the cassette, further degrading the performance.

(iv) Calibration mechanism: In order to calibrate the instrument to antenna distance, it is planned to employ one of the unavoidable parasitic leaks near the antenna front end as a reference point.

(v) Thermal loads on the front end components: These will be very high (up to 3 MW/m<sup>2</sup>) and require the use of refractory materials for the first few cm of waveguide. Small changes in antenna pattern during the pulse are unavoidable.

(vi) Robustness and ease of maintenance: All the waveguides for each of the two cassettes are incorporated into two replaceable assemblies, each with a single set of cooling connections. Since the ports used are also the divertor maintenance ports, a quick-release folding set of circular corrugated guides is used to connect the cassette waveguides with the permanent transmission line structures in the port. A special QO coupler is needed for each line to transform the radiation from the HE<sub>11</sub> mode in the corrugated guide to the TE<sub>10</sub> mode within the rectangular guide. Special baffles are necessary to ensure cross talk is minimised at the gaps that are necessary to allow for thermal distortions and other movements of the cassette, as well as mechanical tolerances.

(vii) Vacuum boundaries: Similarly to the ECE, the first boundary is likely to be a simple circular quartz window. For the second boundary, Brewster windows appropriate to the line polarisation may be used.

(viii) Location of the instrumentation: The distance to the diagnostic hall is prohibitively large ( $> 100$  m). Therefore it is planned that the electronics should reside in an underground area of infrequent access and difficult environment (radiation during maintenance operations, and stray fields during machine operation).

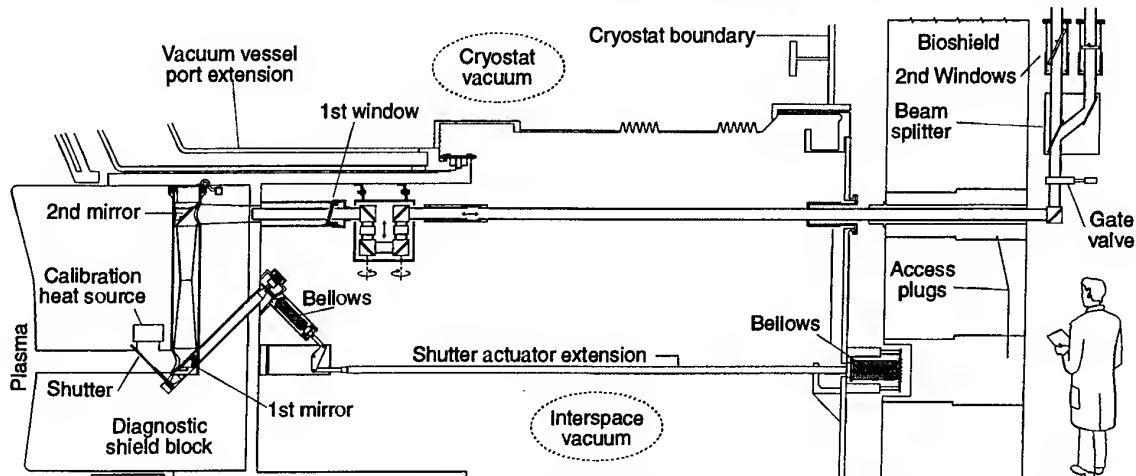


Figure 1: Drawing of the ECE system to the second vacuum boundary. The joint assembly compensating for machine movements, the first window assembly and shutter actuators can be replaced *in situ*.

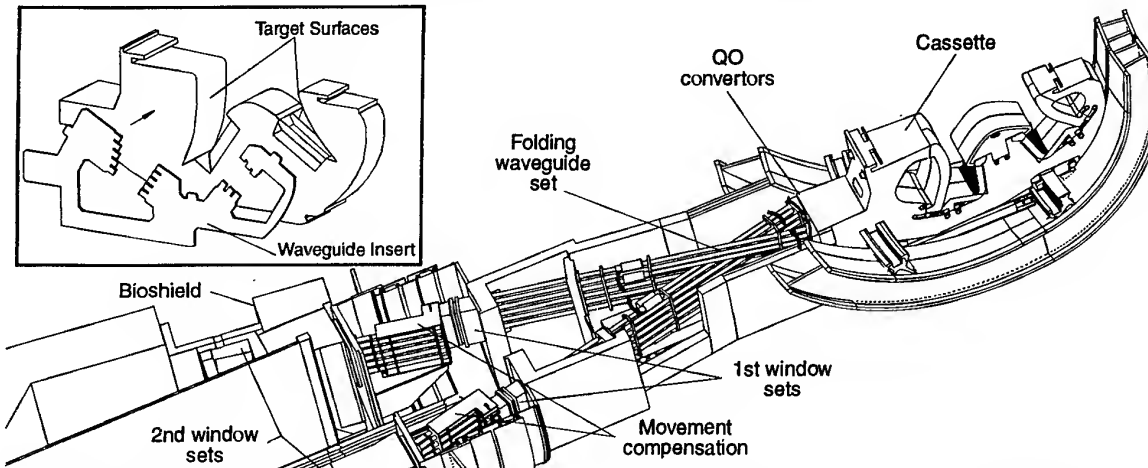


Figure 2: View of one of the divertor transmission systems to the second vacuum boundary, showing key sub-assemblies. Inset: the assembly of the waveguide insert into the divertor cassette.

This report is an account of work undertaken within the framework of the ITER EDA Agreement. The views and opinions expressed herein do not necessarily reflect those of the Parties to the ITER Agreement, the IAEA or any agency thereof. Dissemination of the information in this paper is governed by the applicable terms of the ITER EDA Agreement.

1. A E Costley et al, in *Diagnostics for Experimental Thermonuclear Fusion Reactors* (Plenum Press, New York, P. Stott et al, eds.) 41 (1998)
2. G Janeschitz et al, *ibid.* 1
3. V S Voitsenya et al, in *Diagnostics for Experimental Thermonuclear Fusion Reactors* (Plenum Press, New York, P. Stott et al, eds.) 61 (1996)
4. K. Young et al, *ibid.* 13
5. D V Bartlett and H Bindslev, in *Diagnostics for Experimental Thermonuclear Fusion Reactors* (Plenum Press, New York, P. Stott et al, eds.) 171 (1998)
6. V Vershkov et al, *ibid.* 107
7. G Vayakis et al, *ibid.* 97
8. N L Bretz et al, *ibid.* 129
9. M. Manso et al, *ibid.* 155
10. D V Bartlett et al, in *Diagnostics for Experimental Thermonuclear Fusion Reactors* (Plenum Press, New York, P. Stott et al, eds.) 183 (1996)
11. F Orsitto et al, in *Diagnostics for Experimental Thermonuclear Fusion Reactors* (Plenum Press, New York, P Stott et al, eds.) 255 (1998)

## Correlation Radiometry for Temperature Fluctuation Measurements in Fusion Plasmas

Hans J. Hartfuss

Max-Planck-Institut für Plasmaphysik, EURATOM-Ass., Boltzmannstr. 2, 85748 Garching, Germany

### Abstract

Radiometry of electron cyclotron emission can be used as an electron temperature fluctuation diagnostic if the conditions on temporal, radial and poloidal resolutions are fulfilled. The natural sensitivity limit set by inherent intensity fluctuations can be overcome by applying crosscorrelation radiometry. Three different methods are qualitatively described and briefly compared.

### Introduction

A significant amount of the anomalously high radial electron heat transport in fusion plasmas is assumed to be driven by fluctuations of density, electric field, temperature or magnetic field. Temperature fluctuations have been measured at the plasma edge with probes for many years. More recently methods for measurements in the inner confinement region have been developed based upon the correlation techniques described below. High sensitivity to small fluctuation amplitudes is required since relative amplitudes below 1% might significantly contribute to transport. None of the existing plasma core temperature diagnostics fulfill these requirements, therefore new approaches needed to be found. This paper describes the diagnostic problem and the various techniques applied to detect turbulent temperature fluctuations. Two methods, both based on correlation radiometry of electron cyclotron emission (ECE), have successfully been applied. The crossed sightline technique as developed at the W7-AS stellarator [1] and the correlation of ECE channels overlapping in real space but separated in frequency space as developed at the TEXT tokamak [2]. For a comparison of the methods the crossed sightline set-up at W7-AS has been supplemented in such a way that the application of the second method is simultaneously possible. The two methods agree within error bars [3]. By combining reflectometry and ECE radiometry in the same plasma volume, it could be shown that density and temperature fluctuations are in-phase correlated [4]. This result can be explained in the frame of a convective microturbulence model. Details of the temperature fluctuation behaviour are not the subject of this paper. They can be found in the literature [5,6,7].

### ECE radiometry as fluctuation diagnostic

Radiometry of ECE has established itself as an electron temperature diagnostic with good spatial and temporal resolution. Observation of the continuous cyclotron emission spectrum along a major radius from the low field side of toroidal fusion devices like tokamaks and stellarators allows for the accurate determination of the electron temperature by measuring the radiation temperature. Localized measurements are possible due to the local monotonously varying B-field, which directly determine the frequency of the emission. Referring to Fig. 1, the time resolution of a simplified radiometric system is determined by the post-detection bandwidth  $B_V$  and can be made easily as high as a few MHz. Concerning spatial resolution, radial and poloidal resolution must be distinguished.

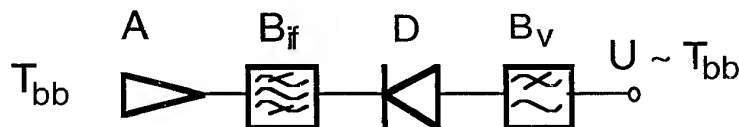


Fig. 1: Simplified radiometer: A = antenna, D = detector,  $B_{ff}$  and  $B_V$  = pre- and post-detection bandwidths. The output voltage is proportional to the radiation temperature  $T_{bb}$ .

The radial resolution is determined by the pre-detection bandwidth  $B_{ff}$  which in the established wideband multichannel heterodyne radiometer systems is defined by the width of the intermediate frequency bandfilter [9, and references therein]. A fundamental lower limit is set by the relativistic spectral broadening of the emission and the optical depth of the plasma which define a kind of natural linewidth of the cyclotron emission. This leads to a radial resolution of typically 0.5 - 1 cm for plasmas in the keV temperature range. The corresponding bandwidth is about  $B_{ff} = 400$  MHz. The spatial resolution in poloidal direction is diffraction limited and determined by the type of optical arrangement used. With antenna-lens or antenna-mirror combinations and Gaussian optics, 1-2 cm poloidal



resolution can be obtained. Good spatial resolution in fluctuation measurements is crucial. Finite sample volume effects do not only restrict the wave number range of the fluctuation diagnostic but lead to increased correlation lengths, reduced mean frequency and increased phase velocities derived. The temporal and spatial resolution of the order of 1 MHz and a few cm respectively, which is possible with standard ECE radiometers is sufficient for temperature fluctuation measurements. The main diagnostic problem is the high sensitivity required for small fluctuation amplitudes of the order of 0.1 %. The ratio of noise and signal,  $i(t) / I(t)$ , in radiometry at extremely high radiation temperatures is governed exclusively by inherent intensity fluctuations,  $i(t)$ , called wave noise or thermal noise superimposed to the mean intensity  $I(t)$  of the blackbody type emitter. It is determined by the radiometer's bandwidth ratio of post- and pre-detection bandwidths,

$$\frac{\sqrt{\langle i(t)^2 \rangle}}{\langle I(t) \rangle} = \sqrt{\frac{2B_v}{B_{if}}},$$

which is about 5 % for the typical ECE radiometer parameters as given previously. This phenomenon sets a severe limit to fluctuation measurements burying completely "true" temperature fluctuations if they occur at a relative level lower than about 5%. Noise from the radiometer itself is completely negligible under these conditions.

### Correlation radiometry

**Crossed sightline correlation.** The problems can be overcome by applying cross correlation techniques and making use of the coherence properties of thermal radiation. If the same plasma volume is observed with two independent radiometers along two different lines of sight, as given in Fig. 2, both radiometers show the same inherent noise level together with the small "true" temperature fluctuations of the viewed volume. However, if the angle between the two sightlines exceeds a minimum one, the two signals in the separated sightlines are not coherent and as a result the thermal or wave noise is not correlated while the intensity fluctuations due to true temperature fluctuation of the plasma are correlated. Cross correlation of the upper and the lower sightlines of Fig. 2 then suppresses the uncorrelated components and reveals the correlated ones. The amount of data determines the significance level finally reached. Stationary plasma conditions with at least 1 s duration are necessary for this kind of measurement to obtain a sensitivity level of 0.1%.



**Fig. 2:** Crossed sightline correlation radiometry. A common plasma volume is viewed along two different lines of sight. Temperature fluctuations in the plasma volume result in correlated intensity fluctuations while the inherent wave noise in the two sightlines is uncorrelated.

With this method temperature fluctuations have been measured for the first time in the W7-AS stellarator [1,8]. Fluctuation spectra and the radial dependences of the integrated fluctuation level have been investigated under various conditions of plasma heating, density and magnetic field. Both radiometers of the two sightlines are multichannel instruments measuring simultaneously at various discrete radial positions. This allows for the characterization of radial and poloidal correlation lengths of the temperature fluctuations by correlating neighbouring channels [5].

**Single sightline correlation.** The second method successfully applied has been developed at the TEXT tokamak [2,6]. It makes use of the fact that the ECE emission exhibits a kind of natural linewidth which means that the cyclotron emission from one radial position has a finite spectral width or equivalently that the emission at a single frequency consists of contributions from nearby radial locations. The measurement with two different radiometer frequency channels with the sum of the bandwidths not exceeding the natural linewidth of about 400 MHz then results in incoherent signals whose intensity fluctuations are uncorrelated. Again the true temperature fluctuations are correlated

because the two channels separated in frequency space overlap in real space as shown in Fig. 3. Typical filter bandwidth  $B_{if}$  is 100 MHz with about 200 MHz separation between the radiometer channels.

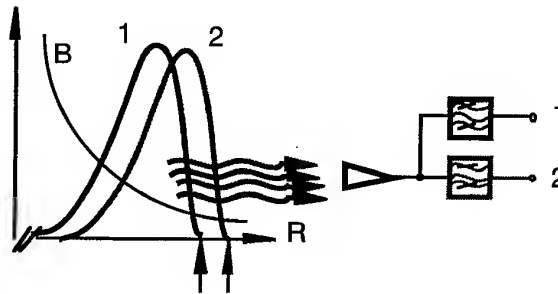


**Fig. 3:** The emission into two separated frequency intervals 1 and 2 originates from almost the same radial position. Crosscorrelation of the separated channels of a single sightline discriminates the uncorrelated wave noise against the correlated temperature fluctuations.  $B$  = B-field along the radial coordinate  $R$ .

**Autocorrelation.** A third method to decorrelate thermal noise is possible even with a single sightline and a single channel. Both the temperature fluctuation level and the spectrum can be evaluated from the autocorrelation function under certain assumptions. If the spectrum of the temperature fluctuations is limited and clearly differs in shape from the white spectrum of the thermal fluctuations they become separable in the autocorrelation function. To make this possible, the postdetection bandwidth which determines the spectral width of thermal fluctuations must be made much larger than the width of the fluctuation spectrum. Under these conditions the thermal noise generates a peaked autocorrelation function of width  $\sqrt{\ln 2/\pi}/B_V$  which can be separated from the broad autocorrelation function of the temperature fluctuations with some experience if the former is sufficiently narrow. This method demands therefore for high video bandwidth  $B_V$  which in turn increases the inherent noise.

### Summary and discussion

Single and crossed sightline correlation radiometry have successfully been applied to measure and characterize electron temperature fluctuations in the core of fusion plasmas. The most general method which needs no assumptions on the properties of the fluctuations is the crossed sightline method. It operates with the full bandwidth  $B_{if}$ , resulting in the lowest inherent fluctuation level possible. However, it demands two identical separated radiometers. In the single sightline approach  $B_{if}$  must be smaller by at least a factor of about 3, which increases the inherent noise. On the other hand it allows measurements with a single radiometer. For given access with finite aperture to the plasma vessel, the full aperture can be used for one radiometer, increasing the diffraction limited resolution in poloidal direction compared to the crossed sightline case where the full aperture must be shared by two viewing beams which necessarily results in poorer spatial resolution. The third method though in principle possible, has gained no practical significance.

### References

1. S Sattler, H J Hartfuss and W7-AS Team, Phys. Rev. Lett. 72, 653 (1994)
2. G Cima et al, Phys. Plasmas 2, 720 (1995)
3. C Watts et al, Comparison of Temperature Fluctuation Measurements using Different Techniques, Proc. of 10th Joint Workshop on ECE and ECRH, Ameland, The Netherlands, Singapore: World Scientific, p. 147
4. M Haese, H J Hartfuss, Rev. Sci. Instrum. accepted for publication (1998)
5. H J Hartfuss et al, Plasma Phys. Control. Fusion 38, A 227 (1996)
6. C Watts et al., Phys. Plasmas 3, 2013 (1996)
7. C L Rettig et al, Rev. Sci. Instrum. 68, 484 (1997)
8. S Sattler and H J Hartfuss, Plasma Phys. Control. Fusion 35, 1285 (1993)
9. H J Hartfuss et al, Plasma Phys. Control. Fusion 39, 1693 (1997)

## Passive Ranging by Measurement of Phasefront Curvature

Duncan A. Robertson & Jim C.G. Lesurf

Millimetre Wave and Terahertz Technology Group, School of Physics and Astronomy, North Haugh  
University of St. Andrews, St. Andrews, Fife KY16 9SS, SCOTLAND

### Abstract

We demonstrate passive ranging on a +10dBm 94GHz source by measuring the curvature of the arriving phasefront using a quasi-optical 3-port spatial interferometer with 0.5m port separation. Range to the source was measured to an accuracy of  $\pm 25$ m at 1km and the bearing accuracy of the instrument was  $\pm 0.1$  arcmin.

### Introduction

The principle of passive range and bearing measurements on coherent sources using quasi-optical spatial interferometers has been demonstrated before[1]. Three ports collect signal from a distant source and an interferometric receiver compares the phase offsets between them to establish the phasefront curvature from which the source bearing and range can be determined. However, the W-band system in [1] used Schottky detectors which limited range measurements to 65m and was slow to use as it employed moving mirror interferometers. In this work, we have built a fully symmetric quasi-optical receiver circuit, which has no moving parts and uses heterodyne radiometers, that can measure the range and bearing of a source in near real time, to ranges of the order of kilometres.

The technique offers the significant advantage over radar that it can be used to determine the range and bearing to an emitting source completely passively, and is hence covert. Furthermore, it allows the location of an emitter from a single observation point without the need for conventional triangulation techniques [2].

### System Design

The spatial interferometer was designed using Gaussian Beam Mode techniques and was built using standard half-cube components on a dowelled baseplate with a side extension to accommodate the required input port span and aperture size - Fig. 1. The outer ports form a two-port monopulse circuit but only the sum pattern is generated. The centre port signal is converted to circular polarisation by a reflection quarter wave plate (RQWP) and is combined with the sum pattern to form sum+centre and sum-centre signals which are then analysed and detected by four radiometers. Fig. 2 is a schematic illustration which indicates how the power falling on the four radiometers depends on the source bearing and range.

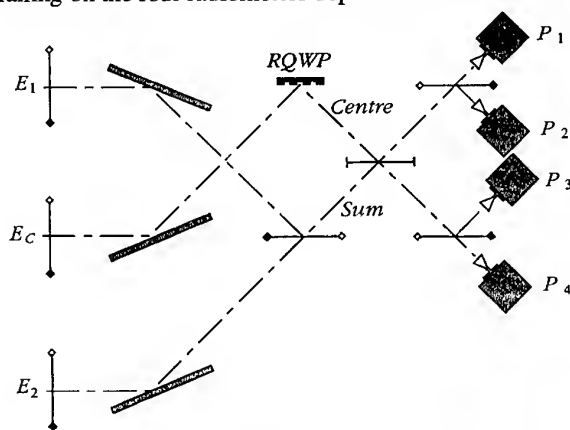


Fig 1 The Quasi Optical Receiver Circuit.

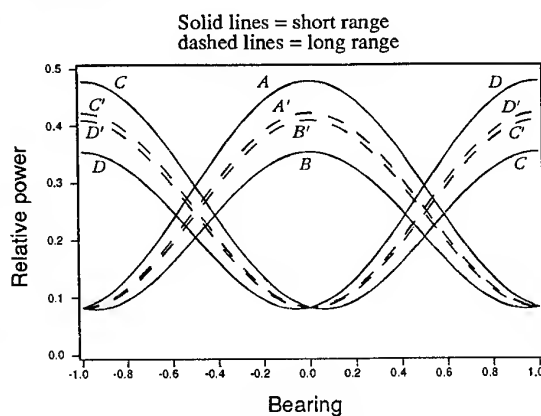


Fig 2 Detected power as a function of  $R$  and  $\phi$

Analysis of the system shows that provided the range  $Z \gg X^2/\lambda$ , where  $X$  is the port spacing and  $\lambda$  is the wavelength, the range  $Z$ , and bearing  $\phi$ , depend on the detected powers  $P_1$  to  $P_4$  approximately according to the expressions (where  $a$  is a scale factor and we ignore whole-cycle phase ambiguities):

$$Z = \frac{aX^2 [P_1 + P_2 + P_3 + P_4]^2}{\lambda [(P_1 - P_2)^2 + (P_3 - P_4)^2]} \quad \text{and} \quad \phi = \text{Arctan} \left\{ \frac{P_1 - P_2}{P_3 - P_4} \right\}$$

The source used in the experiments was a 10mW 94GHz Gunn oscillator which was 100% amplitude modulated with a PIN switch driven by an 8kHz square-wave. The source was located at ranges of 300m to 1000m in a nearby field. The real range was measured using a Leica laser rangefinder surveying instrument.

At the receiver, the detected waveforms were low-pass filtered to recover the 8kHz fundamental and then sampled by computer for 0.3s. The software performed a PSD measurement to accurately measure the amplitude of the sinewave in each channel, from which the range and bearing were calculated.

At each range, the transmitter power was adjusted to give a constant received power level to avoid detector nonlinearity problems and to prevent any possible false cueing of the results. Many data points were taken at each range on many different days to investigate the statistics of the results. The input ports had 2° 3dB beamwidths and were spaced 0.5m apart. The DSB radiometers had an IF bandwidth of 500MHz.

### Experimental Results

Gain fluctuations in the receiver channels were predicted to be significant in limiting the range accuracy. The channel-to-channel gain fluctuations were measured both in the lab and outside and found to be less than 0.005dB. This would give a predicted range accuracy of about  $\pm 5\text{m}$  at 1km range for our system.

Data collection runs varied from about 10mins to over an hour with a 2.5s intersample interval. The raw sampled voltages, computed detected powers, range and bearing were all saved for each measurement point. For three typical days, Fig. 3 shows the mean measured range against real range and Fig. 4 shows the RMS range error. The 24<sup>th</sup> and 25<sup>th</sup> were fine, clear, warm days whilst the 26<sup>th</sup> was a cold, damp, blustery day.

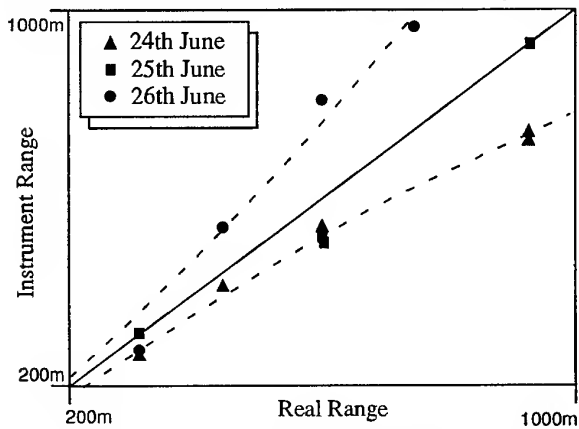


Figure 3 Instrument range for three different days.

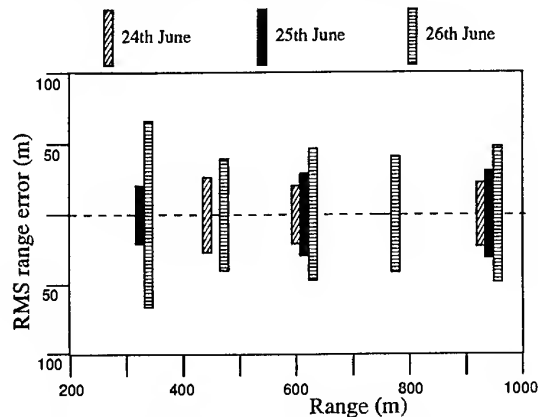


Figure 4 RMS fluctuations in observed range.

From Figs. 3 and 4 it is clear that the instrument performance varied from day to day and with the weather conditions. The dotted lines in Fig. 3 show theoretically how the measured range would alter if the polariser grid which overlays the centre with the sum of the sides moved by  $\pm 10\mu\text{m}$  from its nominal position. This could easily be caused by thermal expansion in the receiver hardware. The RMS range error in Fig. 4 is clearly better for the fine days (typically  $\pm 25$  to  $\pm 30\text{m}$  at 1km) than on the cold blustery day (nearer  $\pm 50\text{m}$  at 1km). The 300m range results were irregular since the beam passed close to a road and multipath from vehicles was evident.

Gain fluctuations cannot solely be responsible for the magnitude of the range error measured and atmospheric effects and mechanical vibrations were certainly significant. However, by injecting a known common-mode signal into the receiver, to calibrate out relative gain fluctuations between channels, the overall accuracy of the measurement could be improved.

### Discussion

We have demonstrated the ability to measure range and bearing to a source at 1km completely passively by measuring the phasefront curvature of the arriving signal. The results obtained with our spatial interferometer at 94GHz validate our theoretical predictions, and sources of experimental errors have been identified. Atmospheric fluctuations were apparent and will ultimately limit the performance of such a system.

### Acknowledgements

The authors would like to thank the Defence Evaluation and Research Agency, Malvern for sponsoring this work, the University's Mechanical and Electronic Workshops who built the receiver hardware, and Paul Cruickshank and Phillip Bentley who helped with the experiments.

### References

- [1] M.R. Robertson & J.C.G. Lesurf, *Int. J. I.R. & M.M. Waves*, **15** (11), 1841-50 (1994).
- [2] D.D. Vaccaro, *Electronic Warfare Receiving Systems*, Artech House, 1993.

## Compact video-rate passive millimetre-wave imager

S. Price, R.N. Anderton, J.R. Borrill, P.R. Coward, M.J. Roberts, N.A. Salmon, G.N. Sinclair, M.R.M. Wasley, K. St J. Murphy and R. Appleby

Defence Evaluation and Research Agency, St. Andrews Rd, Gt. Malvern, Worcs, WR14 3PS, UK

D. Dunn, P. Papakosta, I. Thomas and A.H. Lettington

JJ Thomson Physical Laboratory, University of Reading, Whiteknights, PO Box 220, Reading, RG6 6AF, UK

### 1. Introduction

Practical applications of passive millimetre-wave imaging are currently limited because existing systems cannot provide wide field-of-view images with video-rate frame update times. A fully staring passive millimetre-wave focal plane array could provide good performance, but would require thousands of receivers and would be prohibitively expensive. This paper describes a compact, mechanically scanned, passive millimetre-wave imager which produces wide field-of-view images ( $40^\circ \times 20^\circ$ ) of high quality with a 25Hz frame update rate. This mechanically scanned imager is relatively inexpensive because the scene is imaged using just a small number of high-performance 28-33GHz receivers.

### 2. Principle of operation

The imager consists of five key components: an offset rotating mirror which produces a conical scan pattern, a converging mirror and plane mirror made of polarising grids, a large-area, free-space, ferrite Faraday rotator which rotates the plane of polarisation of the beam non-reciprocally by  $45^\circ$  and a 32-channel receiver array. Polarisation-rotation techniques are used to fold the antenna optics which allows the imager to be compact. A ray trace of the antenna and scanner is shown in figure 1.

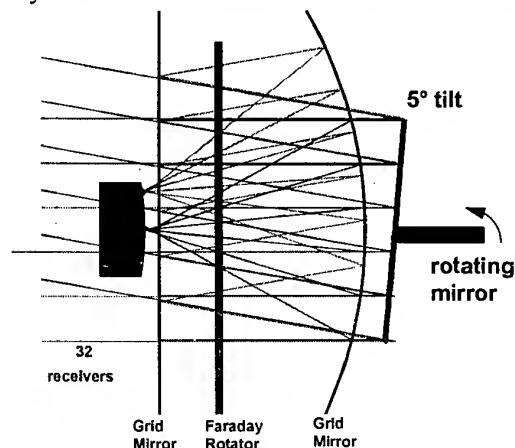


Figure 1: Ray trace of antenna and scanner

Plane polarised radiation from the scene is transmitted through the vertical polarising grids of the plane mirror, passes through the ferrite Faraday rotator where its plane of polarisation is rotated by  $45^\circ$  and is transmitted by the grid of the converging mirror (which is a sphere of radius 1500mm positioned with its grids at  $45^\circ$  to the vertical). The radiation reflects off the rotating mirror, passes back through the converging mirror and is rotated a further  $45^\circ$  in the ferrite Faraday rotator. The radiation is now reflected by the plane mirror (as it is orthogonal to its original state) and it acquires a further  $45^\circ$  rotation in the Faraday rotator before being reflected and focused by the converging mirror. Prior to reaching the receivers the radiation is rotated by another  $45^\circ$  in the Faraday rotator which enables it to pass through the plane mirror. The imager produces high quality images with a beamwidth of  $0.9^\circ$  and a temperature sensitivity of approximately 2K.

Each image covers an angular field-of-view of  $40^\circ \times 20^\circ$  and is updated at a frame rate of 25Hz.

### 3. System components

The scanning mechanism of the imager consists of a counter-balanced, aluminium disc of diameter 770mm which is tilted on its shaft by  $5^\circ$ . A 600W dc servo motor rotates the disc at any frequency up to a maximum of 1500rpm which gives an image frame rate of 25Hz. The rotating disc is the only moving component within the imager. The scanning mechanism produces a conical scan pattern with an angular deviation of  $20^\circ$ .

A free-space Faraday rotator of area  $1\text{m}^2$  has been constructed for DERA by St. Andrews University. It consists of a large panel of commercially available anisotropic barium hexaferrite-loaded rubber, which was magnetised

before being located between two matching layers made of ABS (polyacrylonitrile-butadiene-styrene). The Faraday rotator operates across the frequency band 28-33GHz, with an insertion loss of 0.63dB averaged over the panel and an isolation of 20dB over a 2GHz bandwidth (and at least 15dB over a 3.5GHz bandwidth). The dominant loss in the system optics is that due to the Faraday rotator.

The imager scans over a wide field-of-view with a large effective aperture (750mm) antenna whilst maintaining diffraction-limited performance over the entire field-of-view at frequencies in the 30GHz band. This includes the entire length of the receiver array, which covers the equivalent of 20° in object space. To achieve this performance the scanner has to be located in object space, that is, before the antenna focuses incoming radiation onto the receiver array feeds. Consequently, the scanner has to be at least as wide as the effective aperture of the antenna. The entrance pupil of the antenna is the rotating mirror, which is placed at what would be the centre of curvature of the converging mirror if the folding by the plane mirror were undone. The focal plane shares this centre of curvature and has half the radius of the converging mirror. The result is a system free of coma or astigmatism; analogous to a Schmidt camera without the corrector plate. This is important as these off-axis aberrations would be extremely severe, given both the large field-of-view of the imager and the compact fl optics. Distortion is corrected in the scan conversion and chromatic aberration does not occur with a reflecting system. Hence, the only aberration to be accommodated is spherical aberration. For the system described, at 30.5GHz, the spherical aberration introduces errors equivalent to less than an eighth of a wavelength path difference and so can be safely ignored.

The grids that make up both the plane and converging mirrors are linear polarisers consisting of parallel lines etched in copper metallisation on a 0.25mm PTFE/glass fibre substrate. The grid lines are 180µm wide and the gaps between them 300µm wide. This gives better than 95% transmission with the E-plane normal to the lines and better than 96% reflection with the E-plane parallel to the lines, at both the 30GHz band and 94GHz band. The grids are supported by expanded polystyrene shaped to the required profile of the mirror. The expanded polystyrene produces negligible loss or change of refractive index.

The measured insertion loss of the antenna over the 28GHz to 33GHz waveband is 5.5dB  $\pm$  0.5dB, compared with a predicted insertion loss of 4.5dB  $\pm$  1dB.

The feed-horn assembly of the imager consists of 32 smooth-walled, pyramidal feed-horns which are arranged in two horizontal arrays. The horns are positioned such that the beams diverge outwards on a radius of curvature of 750mm. The feed-horns are optimised to give a 10dB taper at the edge of the main aperture. This is the standard condition for maximum gain, which was measured to be 41.5dB  $\pm$  1dB. The imager has 32 direct detection RF receiving channels which operate over the bandwidth 28 to 33GHz. The feed-horn of each channel is connected via waveguide and a waveguide to K-connector transition to a first stage, GaAs FET amplifier. This amplifier has a bandwidth of 28 to 33GHz and amplification of approximately 33dB. A second amplifier has a bandwidth of 26 to 40GHz and supplies around 30dB of amplification. The output of the second amplifier passes through a bandpass filter before reaching a Schottky diode detector which produces a voltage proportional to the radiometric temperature of the scene. The noise temperature of each receiver channel is approximately 400K. The output signal from each detector is digitised by a 16 bit ADC and transferred to a data acquisition card in a PC. A scan conversion routine transforms the data which is collected in a conical scan pattern into a format that is displayed on a monitor in real time. A software program calibrates the image and optimises the image display parameters.

#### 4. Conclusions

A mechanically scanned, passive millimetre-wave imager has been designed and constructed which is both compact and affordable. The imager is capable of producing wide field-of-view images of high quality, at video rate, using a small array of 28-33GHz direct detection receivers.

The novel design of the antenna and scanner will allow future imagers to be more compact and lighter in weight. These imagers could operate at higher frequencies, with larger apertures and faster frame rates with little or no modification.

# Measurement of Bunch Shape of Electrons by Coherent Radiation

M. Ikezawa, Yu. Shibata and K. Ishi

Research Institute for Scientific Measurements, Tohoku University, Sendai, 980-8577, Japan

## Abstract

Coherent radiation is emitted from a bunch of accelerated electrons. By the Fourier analysis of its spectrum, we can determine the distribution of the electrons in the bunch. The principle of the method and measurements of bunch shapes of four linear accelerators are reviewed.

## 1. Introduction

In the millimetre and sub-millimetre wave region, coherent synchrotron radiation is emitted from a short bunch of electrons of the linear accelerator[1-5]. The spectral intensity  $P(\lambda)$  of the coherent radiation of the wave vector  $\mathbf{k}$  at the wavelength  $\lambda$  is related to the structure factor  $F(\lambda)$  of the bunch as

$$P(\lambda) = N^2 p(\lambda) |F(\lambda)|^2 \quad (1)$$

$$F(\lambda) = \int S(\mathbf{x}) e^{i\mathbf{k}\cdot\mathbf{x}} d\mathbf{x} \quad (2)$$

where  $N$  is the number of electrons in a bunch,  $p(\lambda)$  is the radiation intensity from an electron and the structure factor  $F(\lambda)$  is the Fourier transform of the electron distribution function,  $S(\mathbf{x})$ , at the position  $\mathbf{x}$  in the bunch.

The distribution function  $S(\mathbf{x})$  is expressed as the product of the distribution function  $h(z)$  along the direction of the trajectory of the electron and that perpendicular to it  $g(x, y)$ . The structure factor is written as

$$F(\lambda) = \int g(x, y) e^{i(k_x x + k_y y)} dx dy \int h(z) e^{ik_z z} dz \quad (3)$$

The first factor has a similar effect to the van Cittert-Zernike theorem for an extended light source. The second factor mainly determines the shape of the spectrum. We can determine the longitudinal distribution function  $h(z)$  from an observed spectrum  $P(\lambda)$ .

From the spectrum of coherent radiation, we obtain the modulus of the structure factor. To restore its phase, we employ the Kramers-Kronig relation. Then, the distribution function is obtained by the inverse transform of Eq.(3).

We have observed that five kinds of radiation are enhanced by the coherence effect in the long wavelength region[6-16]. Among them the coherent transition radiation[10,11] and, in particular,

the diffraction radiation[14] are suitable for the measurement of the bunch shape, because they are emitted from a straight trajectory with a small disturbance to the electron beam.

## 2. Linear Accelerator

Observations were done using linear accelerators (linac) at the Laboratory of Nuclear Science

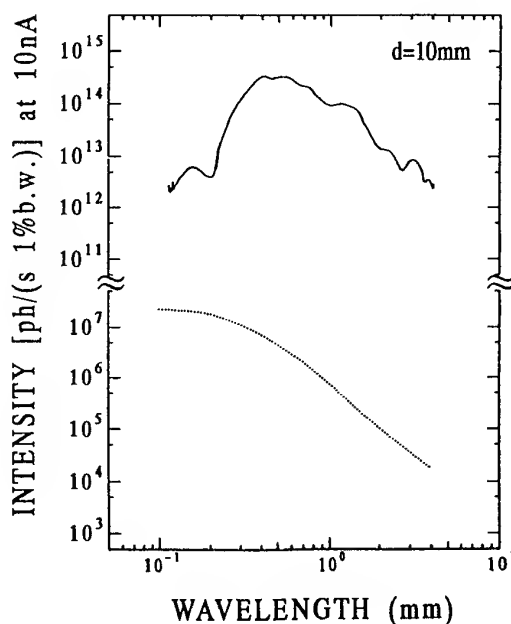


Fig.1. Spectra of superposed diffraction and transition radiation.

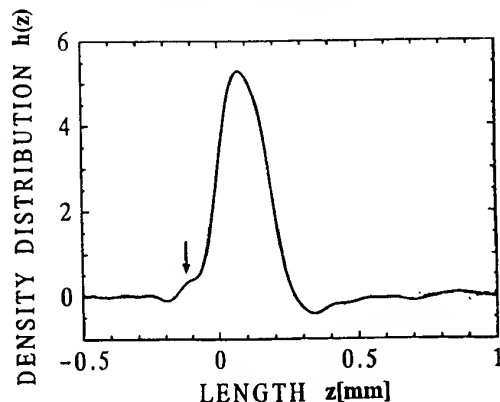


Fig.2. Bunch shape of LNS linac.

Table I. Linear accelerators				
Facility	RF-Band	Energy (MeV)	Beam Diameter (mm)	Bunch Length (mm)
LNS	S	150 ~ 180	~ 3	0.26 ~ 0.28
NERL	S	~ 35	~ 7	0.4 ~ 4 (variable)
RRI	L	~ 40	~ 10	~ 8
ISIR	L	~ 28	~ 18	~ 9

(LNS) of Tohoku University, the Nuclear Energy Research Laboratory (NERL) of The University of Tokyo, the Research Reactor Institute (RRI) of Kyoto University and Institute of Scientific and Industrial Research (ISIR) of Osaka University. In Table I the radio frequency (RF) of the accelerators, the energy of the electron and the diameter of the beam at the observation point are summarized.

### 3. Determination of Bunch Shape

Using the accelerator of LNS, we observed a superposition of diffraction radiation and transition radiation. The spectrum of coherent radiation is shown in Fig.1 by the solid curve, and the dashed one is calculated incoherent radiation. From these spectrum and the value of the number of electron

in the bunch,  $N = 1.8 \times 10^8$ , the amplitude of the bunch form factor and subsequently its phase were derived. The result of the longitudinal distribution function along the trajectory is shown in Fig.2. It has the half width of 0.26 mm and is close to a Gaussian curve.

The distribution of Fig.2 has a small structure shown by the arrow, which has been confirmed to be due to a small structure in the spectrum at the wavelength of 0.15 mm in Fig.1. This example and the method of the Fourier transform as well indicate that the resolution of the distribution function is determined roughly by the short-wavelength limit of the observation of the spectrum.

Examples of the distribution functions of electrons in the bunch of the linac of NERL[17] are shown in Fig.3. The bunch length of this linac is variable. The observed shape is asymmetric and the width changes from 0.4 (1.2 ps) to 4 mm (13 ps).

Results of the bunch lengths of L-band accelerators [12, 13] are given in the last column of Table I.

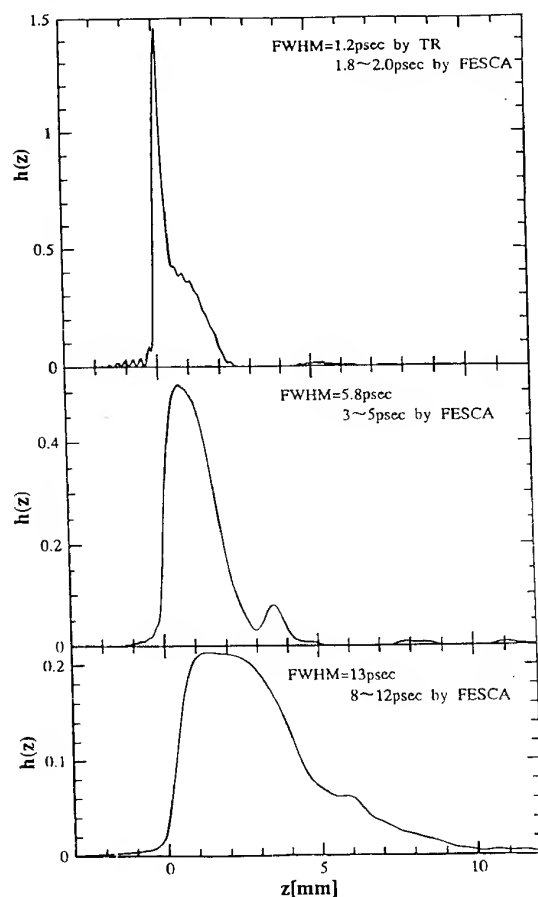


Fig.3. Bunch shape of NERL linac.

### References

- [1] J. Schwinger : Phys. Rev. 70(1946)798.
- [2] L. I. Schiff : Rev. Sci. Instrum. 17(1949)6.
- [3] J. S. Nodvick and D. S. Saxon : Phys. Rev. 96(1954)180.
- [4] L. A. Vardanyan et al. : AN Armenian SSR Fiz. 10(1975) 350.
- [5] D. J. Winham : Phys. Rev. D35(1993)4674.
- [6] T. Nakazato et al. : Phys. Rev. Lett. 63(1989) 1245.
- [7] Y. Shibata et al. : Nucl. Instrum. & Methods A301(1991)161.
- [8] K. Ishi et al. : Phys. Rev. A43(1991)5597.
- [9] Y. Shibata et al. : Phys. Rev. A45(1992)R8340.
- [10] T. Takahashi et al. : Phys. Rev. E48(1993) 4674.
- [11] Y. Shibata et al. : Phys. Rev. E49(1994)785.
- [12] Y. Shibata et al. : Phys. Rev. E50(1994)1479.
- [13] T. Takahashi et al. : Phys. Rev. E50(1994) 4041.
- [14] Y. Shibata et al. : Phys. Rev. E52(1995)6787.
- [15] K. Ishi et al. : Phys. Rev. E52(1995)R5212.
- [16] Y. Shibata et al. : Phys. Rev. E57(1998)1061.
- [17] M. Uesaka, T. Watanabe et al. : to be published.



## The quasi-optic diffraction tomography system for non-destructive evaluation

A. A. Vertiy <sup>(1),(2),(3)</sup>, S. P. Gavrilov <sup>(1),(2),(3)</sup>, I. V. Voinovskiy <sup>(3)</sup>, V. N. Stepanuyk <sup>(3)</sup>

1. TÜBITAK -M.R.C., Turkish- Ukrainian Joint Research Laboratory, P.K. 21, 41470,

Gebze- Kocaeli, Turkey, phone: 90(262)6412300, e-mail: alex@mam.gov.tr

2. IRE, National Academy of Science of Ukraine, 12 Acad. Proskura St., Kharkov, Ukraine.

3. Concern "Nauka", State Research Center "Fonon", 37 Pobedy Ave., 252056, Kiev, Ukraine.

### Abstract

Possibilities of the first-order diffraction tomography in the case of using of millimeter electromagnetic waves for object sounding (quasi-optical tomography) are studied.

Dielectric objects have been taken as objects under investigation. Experimental images obtained by using antennas of dielectric type and radiation frequency  $f \approx 135 \text{ GHz}$  are represented.

It is shown that in the frequency band under consideration, the images of investigated objects with characteristic dimension  $A \approx 7\lambda \div 12\lambda$  may be obtained by first-order diffraction tomography method (in Born, Rytov or high frequency approximation for the scattered electromagnetic field).

### 1. Introduction

Possibilities of the first-order diffraction tomography in the case of using of millimeter electromagnetic waves for object sounding (quasi-optical tomography) do not studied well. On the other hand, application of millimeter waves in diffractive tomography may sufficiently increase its possibilities. For example, increasing of sounding radiation frequency gives us possibility to get Fourier image of the object investigated at higher special frequencies. Wave fields in quasi-optical approach may be represented as narrow beams of plane waves weakly diverging when they propagate in medium. Apertures of a millimeter waves antennas forming such beams, have small sizes ( $A \approx 10\lambda$ ). For sounding volumetric objects, it is very suitable to use shaped quasi-optical beams.

### 2. Experimental set-up and reconstruction

Millimeter wave tomography set up allowing to measure phase and amplitude of  $U$  and  $U_I$  fields at straight line is shown in Fig. 1.

Signal from oscillator 1 with operating frequency in  $\Delta f \approx 135 \div 136.5 \text{ GHz}$  band is divided by directional branch into two signals. One of these signals is given to up-converter 2, and the other to down-converter 8. Signal from reference generator 10 with frequency  $f \approx 1 \text{ GHz}$  is also supplied to up-converter 2. As a result a signal radiated by antenna 3 which is represented by an end of a dielectric waveguide (electric vector  $\vec{E}$  of the wave is directed along straight line 6) is shifted up by frequency at  $1 \text{ GHz}$  relatively to operating frequency of oscillator 1. Sample 5 may be rotated round its axis and move along straight line 6 (step motors are used to move and rotate). The signal received by antenna 7 is given to down-converter 8.

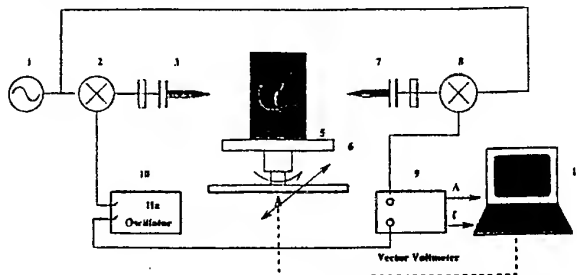


Fig.1. Scheme of tomograph with dielectric antennas which allows to measure phase and amplitude of total  $U$  and incident  $U_I$  fields.

The signal from the operating oscillator 1 is given to the same down-converter, with the result that signal at the output of device 8 is shifted "down" and its frequency  $\nu_{out} \approx 1 \text{ GHz}$ . This signal is fed then to vector

voltmeter 9. A signal from generator 10 of frequency  $\nu \cong 1$  GHz is supplied to the same voltmeter. Amplitude  $A$  and phase  $\Phi$  measured by vector voltmeter 9 are taken to be equal to amplitude and phase of the fields at straight line 6. Analogue signals corresponding to the measured amplitude and phase are given then to system 11 of processing and obtaining of image which also manages the stepping motors. The images of investigated objects with characteristic dimension  $A \approx 7\lambda \div 12\lambda$  are obtained by first-order diffraction tomography method (in Born, Rytov or high frequency approximation for the scattered electromagnetic field).

Fig.2 shown images of  $|Q(\vec{r})|$  cross sections of the objects under experimental investigations: 2 cylinders with approximately circle cross-section manufactured from paper and having the following dimensions: height  $h \cong 35\lambda$  ( $\lambda \cong 2$  mm), diameter  $D \cong 12\lambda$ . One of these samples have two chinks cut out along their axes with the widths of  $d_1 \cong 3.5\lambda$ ;  $d_2 \cong 6.5\lambda$ . The thickness of the wall  $t = 0.05\lambda$ .

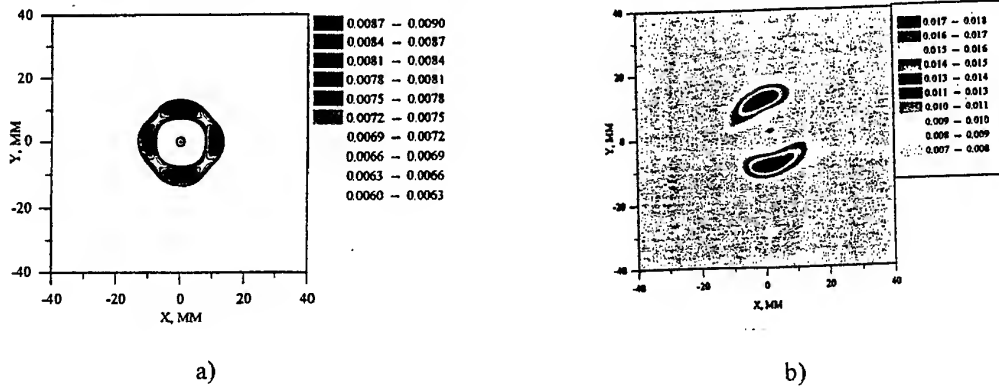


Fig.2. The Image of the paper cylinder without ( a) and with ( b) two chinks.

Schemes for obtaining tomographic images of objects using of the waveguide structures are shown in Fig.3, 4.

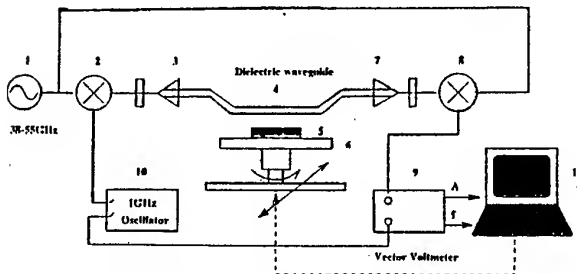


Fig.3. Tomograph block- diagram with guide structure in a form of dielectric waveguide.

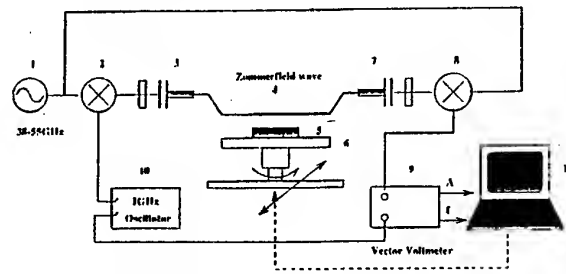


Fig.4. Tomograph block- diagram with guide in a form of wire.

These systems operate like tomograph shown in Fig.1. But instead of dielectric antennas 3 and 7, matching devices 3 and 7 in which ends of waveguide line 4 ( rectangular dielectric waveguide shown in Fig 3 or wire shown in Fig.4 are used ) are employed. The object is placed under dielectric waveguide, is shown.

In Fig.5a the experimentally obtained image of ferrite disks. The distance between the top surface of the disk and lower surface of the waveguide is  $t \cong 2$ mm. Fig. 5b illustrates image of the ferrite structure.

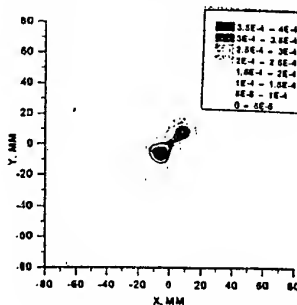


Fig.5a. Experimentally obtained image of the ferrites.

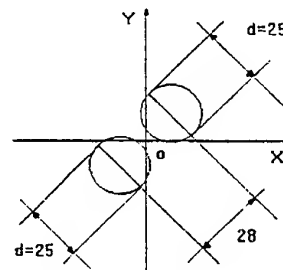


Fig5b. The image of the ferrite structure

## Concealed Weapons Detection Sensor and Signal Processing Demonstration

Al Pergande<sup>a</sup>, Dayton Eden<sup>b</sup>, Mike McKinley<sup>b</sup>, Surachai Sutha<sup>a</sup>, and Ed Weatherwax<sup>a</sup>

<sup>a</sup>Lockheed Martin Electronics & Missiles 5600 Sand Lake Road, Orlando, Fla 32819

<sup>b</sup>Intelligent Machine Technology Corp. 2200 Regency Dr., Irvine, Tx 75062

The combination of infrared (IR) and millimeter wave (MMW) passive imaging systems can provide detailed visual images of concealed weapons and other objects. While an infrared system can provide 'video quality' images, it can not detect objects through many common clothing items. Millimeter waves pass through most types of cloth, but provide a lower resolution image. The fusion of both imaging types can provide a viewer much better detection of concealed objects than either system alone.

### 1.0 Millimeter Wave Radiometer

The radiometer used in this test was built by Intelligent Machine Technology (IMT) of Irvine, TX. It combines a single RF receiver, a focusing system, and a motion control system. The testbed is designed to operate at W-band; nominally at 94 GHz with a 5 GHz bandwidth. The lens is a 30 cm refractive telecentric with a speed of  $f/1$ . It is fixed to the housing, and the receiver element moved mechanically to provide focus control and scanning. Its field of view (FOV) is approximately 24 degrees in azimuth and 18 degrees in elevation. The focal plane is presently scanned over an area 12.7 cm wide and 9.6 cm high. The RF detector has four gain stages with a minimum overall gain of 50 dB. The camera with the receiver has a noise-equivalent temperature contrast ( $\Delta T$ ) of 1.25K when operating in its fastest sampling mode of 2 msec per pixel, and an 80 msec sample time ( $\tau$ ) yields a  $\Delta T \sim 0.2K$ . Image collection time ranges from 3 minutes to 90 minutes.

Figures 1 and 2 are typical images collected with the radiometer, with dark warm and light cold. Figure 1 shows a seated man with a Beretta pistol in his coat pocket at a range of 15 feet. He is wearing a fairly thick Nylon and polyester filled windbreaker. The temperature sensitivity is 0.5 K, and the gun is essentially at body temperature. Figure 2 is a close up taken at a range of 4 feet, and at a slightly greater sensitivity (0.4K). Here, a plastic Glock pistol can be seen inside a sport coat pocket. Details of the coat, such as the lapels, are visible. Both images were taken indoors at an ambient temperature of 25 C. In general, weapons, metal and plastic objects are visible underneath most types of clothing. The physical temperature of the object has little to do with its detectability - reflectivity and absorption are much more important in MMW detection.

### 2.0 Infrared Quantum Well Camera.

The IR system used to detect concealed weapons was a staring focal plane array (FPA) using Quantum Well (QW) technology. The camera uses  $f/1.7$  diffraction limited reimager optics with a 10.4 degree horizontal by 10.2 degree vertical FOV for the 256 X 256, 50 micron pitch FPA. An afocal lens assembly mounted in front of the reimager reduces the FOV to approximately 2.2 degrees (horizontal and vertical). The closed cycle cooler-based camera has a minimum resolvable temperature (MRT) at the low spatial frequency targets of 0.007 Kelvin (7 millikelvin). Near the Nyquist frequency, the MRT was as low as 0.033 to 0.034 Kelvin (33 to 34 millikelvin). The QW IR camera provides a higher quality video image than the MMW sensor as expected. It is much more sensitive to the actual temperature of the detected object. A gun that is at body temperature is quite difficult to see, although if the observed subject has just entered a warm area from a cooler one, there can be a strong temperature difference due to the thermal lag of the weapon, which provides a clear image of the weapon.

### 3.0 IR-MMW Sensor Fusion

Having two sensors with differing capabilities and resolutions suggests the use of sensor fusion to improve weapon detection. Our preliminary work involved taking near simultaneous data with both systems described above, and then performing the fusion/detection work off line. Simultaneous images were taken from slightly differing view points, as the two sensors do not share a common aperture at this time. The concealed weapons detection (CWD) algorithm should first perform a quick evaluation of the scene to find Regions of interest (ROI) and then perform more extensive processing on the ROI for actual weapon detection.

The video imagery from the sensor is filtered to remove noise, and contrast enhanced for display. Image contrast enhancement is based on an intensity histogram equalization technique. Second, the filtered video imagery is analyzed to locate potential carriers of concealed weapons based on the carrier's motion. For stationary CWD sensors, the carrier's motion is detected using a relatively simple algorithm, such as change detection based on frame differencing. The figure 3 example of frame differencing shows a significantly higher density of dark pixels in a particular image region, corresponding to the subject motion.

A silhouette mask is generated to indicate a region of the image that corresponds to each carrier. Pixels in such a region are then analyzed in detail to detect concealed weapons. The ROI mask not only increases the efficiency of the algorithm by concentrating the processing resources on where concealed weapons are likely to be found, but also reduces the number of potential false alarms due to background objects.

Although the two sensors in the multisensor CWD demonstration system were roughly co-boresighted, there is a significant discrepancy between the pixel resolutions of the IR and MMW sensors. Therefore, it is not effective to fuse or combine data of the two sensors at the pixel level. A post detection fusion approach is selected for this study. Because the pixel resolution and the frame rate of the IR sensor are higher than those of the MMW sensor, it is more efficient to establish the ROI based on the IR imagery. In this scheme the IR sensor provides cueing of the common ROI for further processing. Candidate detection regions nominated by the two sensor paths are combined via an AND logic fusion scheme to suppress false alarms.

In the imagery used for the fusion experiments, the gun is merely suggested by the IR system, but the MMW system has no trouble detecting it, even though it has been in contact with the carrier for some time, and has equalized in temperature. Candidate regions are for both the IR and the MMW scene. Since the weapon may be either warmer or colder than the subject, both hot and cold areas are nominated. After the fusion only common regions nominated by both IR and MMW are retained as fused detections. Experimental results are summarized in the form of receiver operating characteristic curves shown in Figure 3. Comparison of the three curves clearly shows the benefits of sensor fusion in increasing probability of detection while lowering the number of false alarms.

#### 4.0 Conclusion

Multiple sensors provide a higher probability of detecting concealed weapons. A fast IR system can cue a slower, but more robust, MMW system improving overall system performance. Additional work is needed to produce a real time MMW sensor, and further validate the CWD concept and performance.

This work was sponsored by DARPA, under the guidance of Mr. Dave Ferris at USAF Rome Laboratory. We thank our sponsors and their technical representatives for their suggestions and advice in conducting this effort. We would also like to thank Jon Albritton for work on the QW camera, Jim Yonge for Sensor Fusion Data processing, and everyone who sat so patiently while the radiometer took their pictures.



Fig 1 Man with Beretta 15 feet.

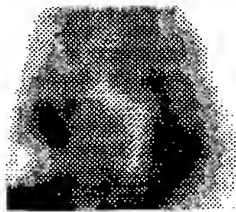


Fig 2 Glock Pistol at 4 feet.

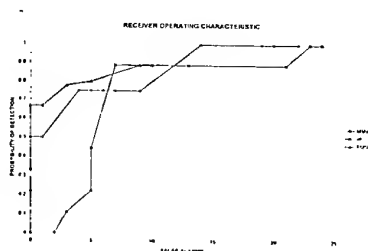


Fig 3. ROC improvement.

## Terahertz Spectroscopy of Biomolecules

A. G. Markelz\* and E. J. Heilweil

Physics Laboratory, B208/Bldg. 221, NIST, Gaithersburg, MD. 20899-0001 USA

### Abstract

Collective vibrational modes associated with the 3D tertiary structure of biomolecules were measured using pulsed terahertz spectroscopy. Clear reproducible absorptions are seen for solid samples of bovine serum albumin and calf thymus DNA in the frequency range of 0.06 THz to 2.0 THz under controlled humidity conditions.

### Introduction

There is an increasing interest in the low frequency collective vibrational modes occurring in proteins and oligonucleotides due to the possibility of using these absorption lines as a direct probe of the biomolecule's conformational state. Prohofsky and collaborators has predicted dominant DNA twisting and librational modes in the 0.6 – 3.0 THz range.[1-3] Similarly, protein collective vibrational modes have been calculated to lie in the far-infrared (FIR) for bovine pancreatic trypsin inhibitor (BPTI) and human lysozyme.[4,5] These modes are due to collective motion of the tertiary subunits beating against one another, or coherent movement of a portion of a subunit. With reported signal to noise ratios of 10,000:1, pulsed terahertz spectroscopy, (PTS), is a preferable method for low frequency mode assignment over standard FIR techniques[6], and using time resolved measurements using PTS may allow for the determination of the sequence of intermediate tertiary forms involved in a conformational state change. Towards this end we have performed measurements on biomolecular samples using PTS. These measurements demonstrate the existence of unique FIR absorptions for calf thymus DNA (CT-DNA) and bovine serum albumin (BSA). These absorptions increase with pathlength and are both hydration and conformation dependent. These results suggest that PTS is a viable technique for time resolved FIR measurements of protein folding.

### Experimental

We used a PTS system based on photoconductive switches embedded in Hertzian dipole antennas.[7] The generating antenna's fabrication, illumination and biasing conditions are discussed elsewhere.[8] The receiver antenna, fabricated on low temperature grown GaAs, was a 25 mm long stripline antenna with 10  $\mu$ m wide leads, 30  $\mu$ m apart. At the center of the strip line, 30  $\mu$ m wide tabs extend from the leads to produce a 5  $\mu$ m photoconductive gap. The receiver was optically gated with 1.2 nJ pulses of the NIR light focused to < 10  $\mu$ m spot. While signal can be achieved with 1/10<sup>th</sup> this gating energy, the output spectrum is more susceptible to antenna coupling effects. The current induced in the receiver antenna by the incident THz field was measured using lock-in detection as a function of delay time between generation and detection. Representative waveforms for transmission through a CT-DNA thin film are shown in Figure 1. The dynamic range of power spectrum determined by the Fourier transform of the measured waveforms was  $\geq 10^2$  for 0.06-2.0 THz. Data was taken with 0.015 THz resolution. Both antennas were mounted on high purity hyper-hemispherical silicon lenses to enhance optical coupling of the submillimeter light. The optical configuration for the THz output is shown in the inset of Figure 1. The THz spotsize at the sample focus, measured by scanning a metal aperture, was 4 mm FWHM of the field amplitude. The PTS system was enclosed in a dry nitrogen purged box to diminish FIR absorption due to ambient humidity.

The native BSA and native CT-DNA samples were formed by pressing 7 mm diameter pellets of the as sent lyophilized samples using a standard hand press. Denatured BSA samples were made by first dissolving the lyophilized powder into a phosphate buffer solution (pH=7.07). The solution was then heated to 90°C for 20 minutes. The resultant opaque gel was allowed to dry in a fume hood and then crushed to a powder and subsequently pressed into pellets for transmission measurements. A 76  $\mu$ m thick DNA thin film sample was prepared by dissolving the DNA in a buffer solution, then the resulting uniform gel was dried slowly in a fume hood.

For spectra taken with the samples directly exposed to the dry nitrogen atmosphere of the PTS system were mounted in 6 mm diameter metal apertures and the transmission was referenced to an empty aperture. For humidity dependence measurements, the samples were mounted in a controlled humidity cell 90 minutes prior to data taking. The transmissions were referenced to an empty cell with the same relative humidity (r.h.).

\* NIST/NRC postdoctoral associate. Work funded by NIST/ATP program.

## Results and Discussion

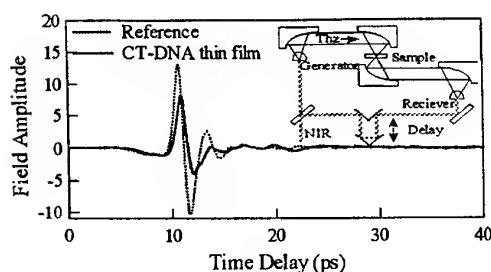


Figure 1. Waveforms for CT-DNA thin film THz transmission measurements at 77% r.h. Inset shows PTS optical setup.

In Figure 2 we show representative transmission spectra for BSA pellets as a function of humidity and conformation. The samples in the figure were all 20 mg pressed pellets. The noise level increased rapidly above 1.5 THz for the denatured BSA pellet runs and the data has been subsequently truncated. While the transmission at low frequencies rapidly rises below 0.50 THz for the native BSA at 77% r.h., there is a distinct absorption at 0.15 THz. The entire transmission spectrum appears to shift to higher frequencies for the native BSA with <10% r.h. and the low frequency absorption shifts to 0.31 THz. The denatured BSA with <10% r.h. has overall lower transmission at the lower frequencies.

From Figure 1 we determine a real index for CT-DNA of 1.9 directly from the phase delay of the waveform. This value is identical to the value determined by a single frequency microwave measurement of Wittlin et al.[9] The pathlength dependence and relative humidity dependence for CT-DNA pressed pellets are shown in Figure 3. The transmission is pathlength dependent and increasing humidity lowers the net transmission with a stronger effect at the lower frequencies. We do not observe spectral shifts as seen for the BSA samples as a function of r.h. Wittlin et al. derived low frequency extinction coefficients from an assumed 5 oscillator fit to their transmission data covering 0.06 THz – 17 THz, and the single frequency index measurement. In order to cover the low frequency range, the measurements in ref. 9 used both single frequency microwave and standard FTIR transmission measurements, and the two measurements did not agree in their overlapping frequency range. This discrepancy demonstrates how PTS has a distinct advantage over the methods used in ref. 9, in that by measuring multiple thickness samples we can directly measure the extinction coefficient over the entire range of 0.06 – 2.0 THz. While we are in agreement with Wittlin et al.'s observed trend of increasing low frequency absorption with increasing humidity, the spectral structure seen in Fig. 3 does not appear in their derived extinction coefficients. Further measurements are required to confirm these spectral features.

We have demonstrated the use of PTS for measuring low frequency absorptions of biomolecular samples. Future work will include measurements on controlled density thin film samples and application of this technique to probe THz absorption changes after photo-initiation of conformational change.

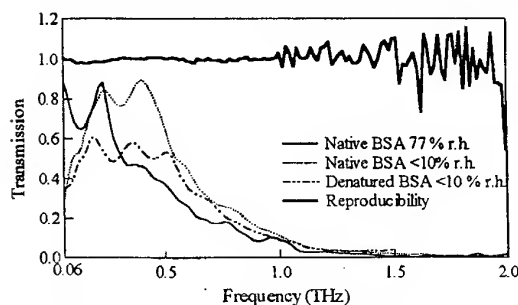


Figure 2. THz transmission of BSA pellets. Thick solid line shows spectral reproducibility defined by the ratio of two consecutive 100 scan averages.

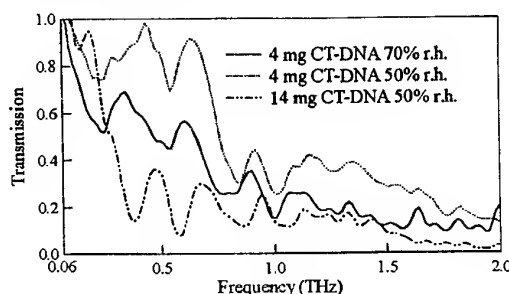


Figure 3. CT-DNA THz transmissions demonstrating dependence on path length and relative humidity.

## References

1. W. Zhuang, Y. Feng, and E. W. Prohofsky, *Phys. Rev. A* **41**, 7033 (1990).
2. L. Young, V. V. Prabhu, E. W. Prohofsky, and G. S. Edwards, *Phys. Rev. A* **41**, 7020 (1990).
3. Y. Feng, W. Zhuang, and E. W. Prohofsky, *Phys. Rev. A* **43**, 1049 (1991).
4. S. Hayward and N. Go, *Annu. Rev. Phys. Chem.* **46**, 223 (1995).
5. A. Roitberg, R. B. Gerber, R. Elber, and M. A. Ratner, *Science* **268**, 1319 (1995).
6. R. A. Chevillat and D. Grischowsky, *Opt. Lett.* **20**, 1646 (1995).
7. N. Katzenellenbogen and D. Grischowsky, in *Ultra-Wideband, Short-Pulse Electromagnetics*, edited by Betroni et al. (Plenum Press, New York, 1992).
8. A. G. Markelz and E. J. Heilweil, *Appl. Phys. Lett.* **72**, 2229 (1998).
9. A. Wittlin, L. Genzel, F. Kremer, S. Haseler, and A. Poglitsch, *Phys. Rev. A* **34**, 493 (1986).

## Far-infrared Spectra of Highly Viscous Liquids: Glycerol, Glycerol Triacetate, O-Terphenyl

T.S. Perova<sup>1</sup>, D.H. Christensen<sup>2</sup>, O. Faurskov Nielsen<sup>2</sup>, U. Rasmussen<sup>2</sup> and J.K. Vij<sup>3</sup>

<sup>1</sup>Vavilov State Optical Institute, St.-Petersburg, 199034, Russia

<sup>2</sup>Department of Chemistry, University of Copenhagen, 5-Universitetsparken, DK-2100, Copenhagen, Denmark

<sup>3</sup>Department of Electronic & Electrical Engineering, Trinity College, Dublin-2, Ireland

The understanding of dynamical processes in highly viscous liquids such as glycerol and o-terphenyl has attracted much attention for many decades. Despite the suggestion [1-3] that most of the dynamics in the disordered state can be understood in terms of vibrations no far-infrared spectra have been studied for these highly viscous liquids. Here we present far-infrared spectroscopic studies of three highly viscous liquids: glycerol, glycerol triacetate (triacetin) and o-terphenyl in the temperature range 256 - 353 K. Glycerol and triacetin are chosen for the reason that despite similarities in molecular structure only glycerol has a possibility of forming hydrogen bonds. Thus a comparison of the far-infrared spectra of these two liquids can be very useful for understanding the role of hydrogen bonding in low-frequency spectra. Another interesting peculiarity of these two highly viscous liquids is the inhomogeneity of their structures which can be reflected in unusual properties in FIR and low-frequency Raman spectra (see for example Ref. [4]).

Far-infrared spectra were obtained using a Bruker 120-HR FTIR spectrometer. The spectra were recorded in the region 25-500  $\text{cm}^{-1}$  using different beam splitters. Fig. 1 show the spectra of glycerol and triacetin in the region 50-500  $\text{cm}^{-1}$  at room temperature. The spectra of glycerol in this range show much broader bands than the spectra of triacetin. This probably reflects the presence of hydrogen-bonded molecules with a wide distribution of different H-bond stretching and bending vibrations, lattice translations and librations as shown from the normal mode analysis performed in Ref. [2] for crystalline glycerol.

We focus our attention to the low-frequency part of the far-infrared spectra, in particular, in the range 25-250  $\text{cm}^{-1}$ . Far-infrared spectra of all studied liquids in this range were obtained at temperatures from 256 K to 353 K. These experimental results are discussed by comparison with the low-frequency Raman data [1,3-6] and with the normal mode analysis performed in Refs.[2,7] for glycerol and in Ref. [8] for o-terphenyl.

Far-infrared spectra of glycerol and triacetin in the range 25-250  $\text{cm}^{-1}$  do not show many differences in the temperature range 256-328 K. This result is different from the behaviour of low-frequency Raman spectra of glycerol in the same temperature range [1,3,5]. In particular as was shown in Refs. [1,3,5], the Raman spectra of glycerol shows a noticeable peak at around  $\sim 33 \text{ cm}^{-1}$  developed at temperatures below  $\sim 270 \text{ K}$ . The peak gets even more pronounced at lower temperatures [1,3]. However, this change was mainly observed in the Raman intensities which included basically two main contributions: relaxational and vibrational processes. Thus, the fact that at temperatures close to  $T_c$  (which is 278 K for glycerol [9]) the low-frequency peculiarity getting much more pronounced in Raman spectra probably tell us only that the relaxational process decays faster (the Rayleigh line getting more narrow) than changes in the vibrational processes. In order to perform a more proper comparison of the results one should compare the reduced Raman spectra (so-called  $R(\nu)$  representation [10]) with the far-infrared spectra. After these corrections the low-frequency Raman spectra [4,5] compares favourably to the far-infrared spectra.

The band fitting performed for the far-infrared spectra shows that four bands with the frequency maxima:  $\sim 55$ ,  $\sim 95$ ,  $\sim 135$  and  $182 \text{ cm}^{-1}$  have contributed to the spectra of glycerol in the range 25-250  $\text{cm}^{-1}$ . These frequencies are in a good agreement with the calculated frequencies, obtained in Ref. [2] for crystalline glycerol and in Ref. [7] for glycerol in the liquid state.

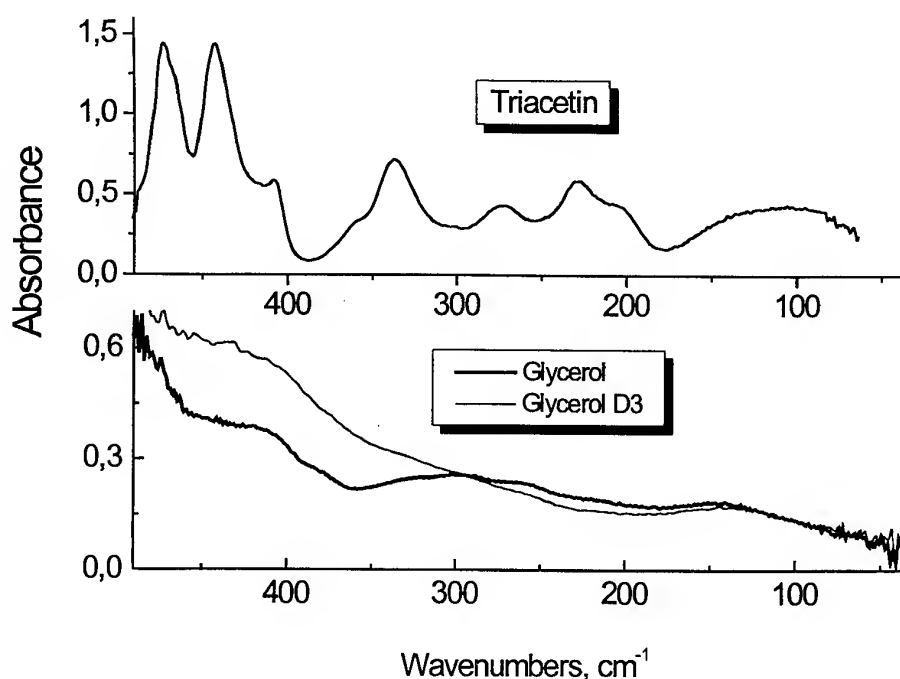


Fig. 1. Far-infrared spectra of glycerol, deuterated glycerol (glycerol D3) and glycerol triacetate (triacetin) at room temperature.

Far-infrared spectra of *o*-terphenyl in the temperature range 256-353 K shows large differences due to the phase transition from the crystalline to the liquid state at a temperature of 329 K. The experimentally observed frequency maxima are in a good agreement with the normal mode analysis performed in Ref. [8].

The authors thanks the European Commission for funding this work through the INTAS-96-1411 grant. DHC, OFN and UR thanks the Danish National Science Research Council and Chemistry Institute, University of Copenhagen for the financial support. JKV thanks Forbairt, Ireland for partial funding under its basic programme of research.

#### References:

1. C.H. Wang and R.B. Wright, *J. Chem.Phys.*, 55, 3300 (1971).
2. F.J. Bermejo, A. Criado, A. de Andress, E. Enciso and H. Schober, *Phys.Rev.B*, 53, 5259 (1996).
3. V.Z. Gochiyaev, V.K. Malinovsky, V.N. Novikov, and A.P. Sokolov, *Phil.Mag.B*, 63, 777 (1991).
4. T.S. Perova and J.K. Vij, *J.Molec.Liquids*, 69, 1 (1996).
5. S.A. Kirillov, T.M. Kolomiyets, O. F. Nielsen, D.H. Christensen, U. Rasmussen and T.S. Perova, *Proceed. of the 16th International Conference on Raman Spectroscopy*, 6-11 September, 1998, Cape Town, South Africa.
6. W. Steffen, B. Zimmer, A. Patkowski, G. Meier, E.W. Fisher, *J. Non-Cryst.Solids*, 171-174, 37 (1994).
7. T. Uchino and T. Yoko, *Science*, 273 480 (1996).
8. A. Criado, F.J. Bermejo, A. de Andres and J.L. Martinez, *Mol. Physics*, 82, 787 (1994).
9. C. Alba-Simionesco, V. Krakoviack, M. Krauzman, P. Migliardo and F. Romain, *J. Raman Spectr.*, 27 715 (1996).
10. O. Faurskov Nielsen, *Ann.Rep.Prog.Chem.Sec.C., Phys.Chem.*, 90,3 (1993); 93, 57 (1996).



# Rotational spectra of protonated rare gas ions observed with tunable far-infrared spectrometer

Fusakazu Matsushima, Hitoshi Odashima, and Kojiro Takagi

Department of Physics, Toyama University  
Gofuku 3190, Toyama 930, Japan

## Abstract

Pure rotational transitions of protonated rare gases, such as  $\text{HeH}^+$ ,  $\text{NeH}^+$ , and  $\text{KrH}^+$ , have been investigated in the 1 - 5 THz region with a high-precision far-infrared spectrometer using a tunable radiation source. Measured transition frequencies of these species including their isotopic species were analyzed to obtain Dunham coefficients  $Y_{kl}$  and isotopically independent parameters  $U_{kl}$  and  $\Delta_{kl}$ .

## Introduction

The protonated rare gas ions are the simplest polar molecule. Recently, all protonated rare gases have been studied in one or more of the millimeter, far-infrared and infrared regions. As for far-infrared region above 1 THz, rotational transitions of  $\text{ArH}^+$  [1] was observed in 1988 with a technique of high-precision spectroscopy using a tunable radiation source. The same type of tunable far-infrared spectrometers in NIST and Toyama University have been applied to observe other protonated rare gas ions such as  $\text{HeH}^+$  [2],  $\text{NeH}^+$  [3] and  $\text{KrH}^+$  [4,5].

First we studied rotational spectra of  $\text{HeH}^+$  and its isotopic species because  $\text{HeH}^+$  is the first protonated rare gas in the periodic table. The procedure of measurement and analysis of  $\text{HeH}^+$  was successfully applied to the studies of  $\text{NeH}^+$  and  $\text{KrH}^+$ . Study of  $\text{XeH}^+$  is also in progress.

Details of our spectrometer and examples mainly from  $\text{NeH}^+$  measurements are described here.

## Experimental

Our far-infrared spectrometer (Fig.1) [2,5] is based on a tunable far-infrared technique developed by Evenson [6]. Two  $\text{CO}_2$  laser radiations ( $\nu_I$  and  $\nu_{II}$ ) are mixed in a metal-insulator-metal (MIM) diode to generate far-infrared radiation of high spectral purity. Microwave radiation ( $\nu_{\text{MW}}$ ) tunable up to 18 GHz is added to generate tunable sidebands ( $\nu_{\text{FIR}}$ );

$$\nu_{\text{FIR}} = |\nu_I - \nu_{II}| \pm \nu_{\text{MW}} \quad (1)$$

With an appropriate choice of the pair of normal  $\text{CO}_2$  laser lines, tunable FIR radiation up to 5.7 THz is generated.

The sample cell is an ac discharge tube made of Pyrex glass with a length of 1.4 m and inner diameter of 16 mm and has polypropylene windows of 1mm thickness at each end. Discharge cell is cooled with liquid nitrogen. A sinusoidal wave voltage from a signal generator is amplified by an audio power amplifier and a step up transformer to make discharge.

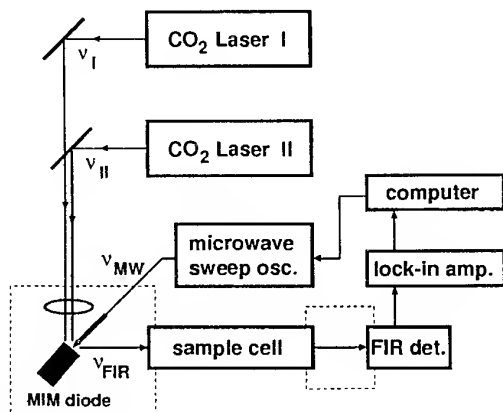


Fig. 1 Tunable far-infrared spectrometer.

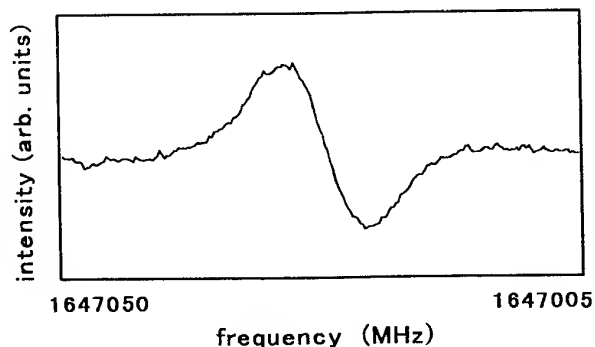


Fig. 2  $J=3 \leftarrow 2$  rotational line of  $^{20}\text{NeD}^+$

Table I. Observed rotational transitions. Figures denote J quantum number of  $J+1 \leftarrow J$  transition.

$\text{HeH}^+$		$\text{NeH}^+$		$\text{KrH}^+$	
$^4\text{HeH}^+$	0, 1	$^{20}\text{NeH}^+$	0 ~ 4	$^{82}\text{KrH}^+$	1 ~ 6
$^4\text{HeD}^+$	1 ~ 3	$^{20}\text{NeD}^+$	2 ~ 8	$^{82}\text{KrD}^+$	3 ~ 12
$^3\text{HeH}^+$	0, 1	$^{22}\text{NeH}^+$	1 ~ 3	$^{84}\text{KrD}^+$	1 ~ 13
$^3\text{HeD}^+$	1, 2	$^{22}\text{NeD}^+$	3 ~ 7	$^{86}\text{KrD}^+$	1 ~ 13

Optimum condition of ac discharge is different for each rare gas species. For  $\text{NeH}^+$  ion, the sinusoidal ac discharge had a frequency of 1.2 kHz, the peak to peak voltage of  $\sim 4.5$  kV, and the root mean square current density of  $\sim 180$  mA/cm<sup>2</sup>. The gas mixing ratio of Ne and H<sub>2</sub> (or D<sub>2</sub>) was typically 36:1 and the total pressure of the sample was  $\sim 56$  Pa. Though an oil-sealed rotary pump was enough to exhaust the sample gas, a mechanical booster pump was sometimes used to enhance some weak spectral lines. The far-infrared radiation after passing through the sample cell is detected by a silicon composite bolometer.

Two kinds of modulation technique were adopted. The velocity modulation technique [7] which is based on the Doppler shift of spectral lines of ions accelerated by the discharge field is effective for light ions such as  $\text{HeH}^+$  and  $\text{NeH}^+$ . The source modulation was used for  $\text{KrH}^+$  because velocity modulation is less effective for heavy ions.

### Results and discussions

The  $J=3 \leftarrow 2$  rotational line of  $^{20}\text{NeD}^+$  around 1.65 THz is shown in Fig.2 as a typical trace. Two CO<sub>2</sub> laser lines, 9 $\mu\text{m}$  P(30) and 10 $\mu\text{m}$  R(30) lines, were used to synthesize FIR radiation. Microwave frequency was scanned by 45 MHz to record the trace.

Rotational lines of protonated rare gas ions observed with our spectrometer are summarized in Table I. The accuracy of the frequency measurement was better than 0.3 MHz. In particular, the lowest  $J=1 \leftarrow 0$  transition of  $^4\text{HeH}^+$  observed at 2010.1839(2) GHz will be an important future probe for detecting this species in space.

Rotational constants of each species in Table I were obtained by using the formula for vibration-rotation term values of a  $^1\Sigma$  state given by

$$E_v(J) = T_v + B_v J(J+1) - D_v [J(J+1)]^2 + H_v [J(J+1)]^3 + L_v [J(J+1)]^4. \quad (2)$$

The vibration-rotation term values for each isotopic species are also calculated by using Dunham parameters  $Y_{kl}$ . These Dunham parameters are expressed using isotopically invariant parameters  $U_{kl}$  and  $\Delta_{kl}$ . For example, all the isotopic species of  $\text{NeH}^+$  can be calculated by using the formula

$$Y_{kl} = \mu_c^{-(k/2+1)} U_{kl} \left[ 1 + \frac{m_e \Delta_{kl}^{\text{Ne}}}{M_{\text{Ne}}} + \frac{m_e \Delta_{kl}^{\text{H}}}{M_{\text{H}}} \right] \quad (3)$$

where  $\mu_c$  denotes the reduced mass of the isotopic species. Observed rotational frequencies in Table I were analyzed together with microwave and infrared data [8-13] to determine the parameter sets for  $\text{NeH}^+$ ,  $\text{NeH}^+$  and  $\text{KrH}^+$ . Parameters  $\Delta_{02}^{\text{H}}$  of  $\text{HeH}^+$ ,  $\Delta_{02}^{\text{H}}$  and  $\Delta_{01}^{\text{Ne}}$  of  $\text{NeH}^+$ , and  $\Delta_{02}^{\text{H}}$  of  $\text{KrH}^+$  were determined for the first time. For all these protonated rare gas ions,  $\Delta$  parameters with  $k=0$ ,  $l=1,2$  were determined with unprecedented accuracy, and provide important information for breakdown of the Born-Oppenheimer approximation.

This research was supported by a Grant-in-Aid from the Ministry of Education, Science and Culture of Japan.

### References

- 1 J.M. Brown, D.A. Jennings, M. Vanek and K.M. Evenson, J. Mol. Spectrosc. **28**, 587 (1988).
- 2 F. Matsushima, T. Oka and K. Takagi, Phys. Rev. Lett. **78**, 1664 (1997).
- 3 F. Matsushima, Y. Ohtaki, O. Torige, and K. Takagi, J. Chem. Phys. *in press*.
- 4 H. Linnarts, L.R. Zink and K.M. Evenson, J. Mol. Spectrosc. **184**, 56 (1997).
- 5 H. Odashima, F. Matsushima, A. Kozato, S. Tsunekawa, K. Takagi, and H. Linnartz, J. Mol. Spectrosc., **189** *in press*.
- 6 K.M. Evenson, D.A. Jennings, and F.R. Petersen, Appl. Phys. Lett. **44**, 576 (1984).
- 7 C.S. Gudeman, M.H. Begemann, J. Pfaff, and R.J. Saykally, Phys. Rev. Lett. **50**, 727 (1983).
- 8 P. Bernath and T. Amano, Phys. Rev. Lett. **48**, 20 (1982).
- 9 M.W. Crofton, R.S. Altman, N-N. Haese and T. Oka, J. Chem. Phys. **91**, 5882 (1989).
- 10 M. Wong, P. Bernath and T. Amano, J. Chem. Phys., **77**, 693 (1982).
- 11 R.S. Ram, P.F. Bernath and J.W. Brault, J. Mol. Spectrosc., **113**, 451 (1985).
- 12 J.W.C. Johns, J. Mol. Spectrosc., **106**, 124 (1984).
- 13 H.E. Warner, W.T. Conner, and R.C. Woods, J. Chem. Phys., **81**, 5413 (1984).

## Far-infrared Spectra of Molecular Mixtures in the Liquid State: Comparison with the Low-frequency Raman Spectra

T.S. Perova<sup>1</sup>, D.H. Christensen<sup>2</sup>, O. Faurskov Nielsen<sup>2</sup>, U. Rasmussen<sup>2</sup>, P. Perov<sup>1</sup>  
and J.K. Vij<sup>3</sup>

<sup>1</sup>Vavilov State Optical Institute, St.-Petersburg, 199034, Russia

<sup>2</sup>Department of Chemistry, University of Copenhagen, 5-Universitetsparken, DK-2100, Copenhagen, Denmark

<sup>3</sup>Department of Electronic & Electrical Engineering, Trinity College, Dublin-2, Ireland

A significant problem in a comparison of the far-infrared (FIR) and low-frequency Raman (LFR) spectra is that the later technique is dominated by the broad, intense Rayleigh-line. These difficulties may be overcome by use of the so-called  $R(\nu)$  representation of the low-frequency Raman spectrum, because the Rayleigh-line is suppressed in this representation [1]. The  $R(\nu)$ -function can be directly compared to the absorption coefficient,  $\alpha(\nu)$ , found by far-infrared spectroscopy. The following correlation between the peak position of low-frequency vibrational spectra (far-infrared and low-frequency Raman) and the isothermal compressibility of liquids has been established [2]

$$\nu_{calc.} = \frac{1}{2\pi c} \sqrt{\frac{3}{\rho K_T r^2}} \quad (1)$$

Here  $\rho$  is the density,  $K_T$  is the isothermal compressibility,  $r$  is the intermolecular distance, which to a first approximation may be interpreted as the structural radius of the molecule.

In this paper the far-infrared and low-frequency Raman spectra of mixtures of different organic liquids at various compositions are presented. The correlation between the behaviour of frequency maximum of the low-frequency vibrational spectra (far-infrared and low-frequency Raman) and isothermal compressibility of mixtures was observed for many liquids. (see also Ref. [3]). Figs. 1 and 2 in particular show the results of such a comparison for the mixtures of water and glycerol. The far-infrared spectra for different water contents in glycerol is shown in Fig. 1. Fig. 2 shows the dependence of frequency maximum of the wide band observed by FIR and LFR techniques at around 135 - 200  $\text{cm}^{-1}$  on the concentration of water in water/glycerol mixture. The calculated frequencies using formula (1) are also shown in Fig. 2. For these calculations the isothermal compressibilities obtained in Ref. [4] for water/glycerol mixtures have been used. As one can see from Fig. 2 there is quite a good correlation in between the experimental and the calculated values.

However, a large discrepancy of the frequency maximum for these types of vibrational spectra have been found in some cases. In particular an acetone+chloroform mixture shows a different concentration behaviour of the frequency maximum for the far-infrared and low-frequency Raman spectra. The results can be explained by taking into account the different sensitivity of the aforementioned techniques to the complex formation [5]. It is well known that the chloroform is a standard proton donor whilst acetone is a strong proton acceptor. As was shown in [6] the molecular complexes involving chloroform have demonstrated a broad band in the far-infrared region with the frequency maximum at around 100  $\text{cm}^{-1}$ . This can influence the low-frequency vibrational spectra. As it follows from our study of acetone+chloroform mixtures, the far-infrared spectrum is much more sensitive to the molecular complex formation than low-frequency Raman spectrum. This insensitivity of the low-frequency Raman spectra with respect to intermolecular modes of complex consisting of rigid molecular subunits is in accordance with the isothermal compressibility behaviour found in [7].

The authors thanks the European Commission for funding this work through the INTAS-96-1411 grant. DHC, OFN and UR thanks the Danish National Science Research Council and Chemistry Institute, University of Copenhagen for the financial support. JKV thanks Forbairt, Ireland for partial funding under its basic programme of research.

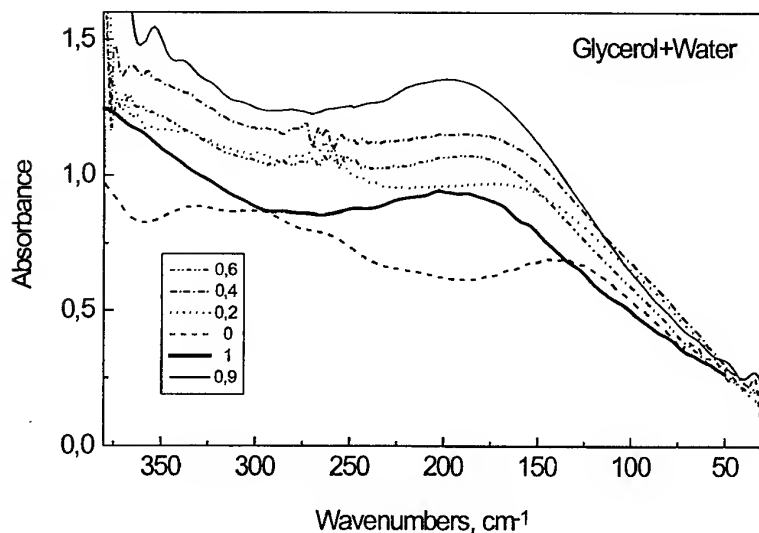


Fig. 1

FIR spectra of water/glycerol mixtures. Figures in box show the mole fraction of water in glycerol.

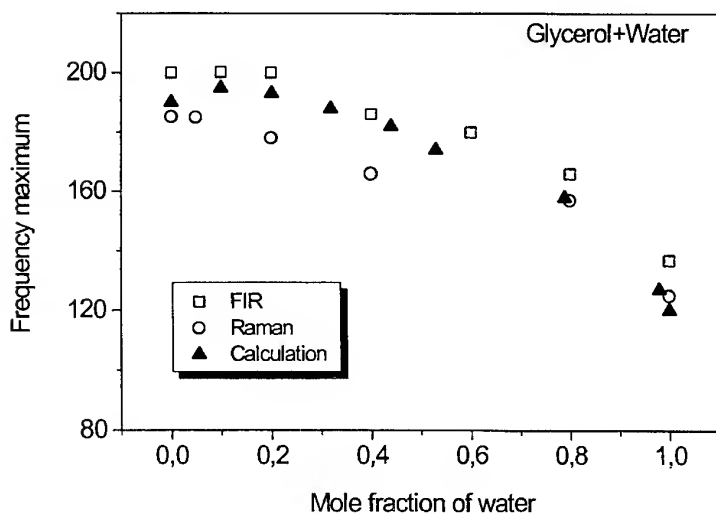


Fig. 2

The dependence of band maximum of far-infrared and Raman spectra on mole fraction of water in glycerol together with the calculated values using formula (1).

#### References:

1. O.Faurskov Nielsen, Annu.Rep.Prog.Chem.Sect.C, 90, 3 (1993); 93, 57 (1997).
2. V.S. Libov and T.S. Perova, Russ.J.Phys.Chem., 54, 549 (1980).
3. T.S. Perova, Adv.Chem.Phys., 87, 427 (1994).
4. W.M. Slie, A.R. Donfor, Jr., and T.A. Litovitz, J.Chem.Phys., 44, 3712 (1966).
5. E. Knozinger and O. Schrems, Vibrational Spectra and Structures, A series of Advances, vol. 16, Ed. by J.R. Durig, Elsevier, (Amsterdam - Oxford - New York - Tokyo), 1987.
6. A.V.Yarkov, M.A. Belkin and O.A. Raevsky, Spectrochim Acta, 47A, 5631 (1991).
7. N.Van Nhu, S.N.Bhat and F.Kohler, Ber.Bunsenges.Phys.Chem., 91, 525 (1987).

## Revisiting Water at Terahertz Frequencies

J R Birch and D H Martin

Dorking, Surrey, UK, and Brentwood, Essex, UK

Water is structurally an anomalous liquid (for example, the density maximum near 4°C). It is hugely important in natural processes. In particular, it is a major constituent of biological cells and there are indications that intracellular water undergoes structural modifications which play a crucial part in the cell cycle. This leads directly to a general question: can additives/solutes significantly modify the structure of water?

Water molecules are strongly dipolar and their motion in the liquid leads to spectra which show several dielectric relaxations and resonances. The form of the attenuation spectrum is likely to be a sensitive monitor of any modifications of structure induced by additives/solutes (or in other ways). With this in mind, we have revisited our earlier measurements of the terahertz spectra of water and of aqueous solutions and have found aspects of interest in this context. These are described in the paper. Terahertz measurements on a wider range of solutions and suspensions will be required to study this question further (and a purpose of this paper is to encourage spectroscopists in this direction).

## INFLUENCE OF THE MICROWAVE IRRADIATION ON THE INTERACTION OF THE WATER WITH THE NA-DNA IN THE FILMS.

T.V.Bolbuch<sup>1</sup>, G.M.Glibitskiy<sup>1</sup>, E.A.Andreev<sup>2</sup>, V.N.Kharkyanen<sup>2</sup>.

1- Institute of Radiophysics and Electronics, National Academy of Sciences of Ukraine, Kharkiv 310085, Ukraine;

2 - Institute of Physics, National Academy of Sciences of Ukraine, Kyiv 252028, Ukraine.

The application of the infra-red spectroscopy for investigation of the mechanism of the microwave irradiation (MI) influence on nucleic acids is the perspective method of explaining the nature of the conformation dynamics of the biopolymer. The data on the kinetics of the desorption of the water molecules from the surface of the film of the DNA was obtained at MI (frequency 41.0 GHz) of the Na-DNA in the damp films (96% relative humidity) with simultaneous writing down of infra-red spectrums on  $\nu = 3400 \text{ cm}^{-1}$  (it is the frequency of the valent oscillation of the similar sample without influence). Also the spectrum of Na-DNA film in the diapason of  $1600\text{-}1700 \text{ cm}^{-1}$  was studied and tendency to delay the destruction of the hydrated shell of the secondary structure was found in the hydration process.

The obtained results is the evidence of the MI influence on the dehydrating process of the Na-DNA molecules in the humidity films. It shows in the growth of structural stability of DNA hydrate encirclement. The purpose of investigation was the comparative analysis of dehydration kinetics of the Na-DNA in the damp films with and without MI with the help of the infra-red spectroscopy data.

The construction of the cuvette is shown in figure 1.

The Na-DNA film is located on the fluorite window. The cuvette allows to damp the film by placing the hermetical passage in the glass which is connected with metric trap to dry the films. The cuvette with the damped film of the Na-DNA is installed in the cuvette chamber of the infra-red spectrometer UR-20, where the waveguide section has been already mounted.

This section is connected to Г4-141 generator with the frequency 41.0 GHz. The radiating waveguide element is placed near the fluorite window, where the film of the Na-DNA is located (as it is shown in figure 2).

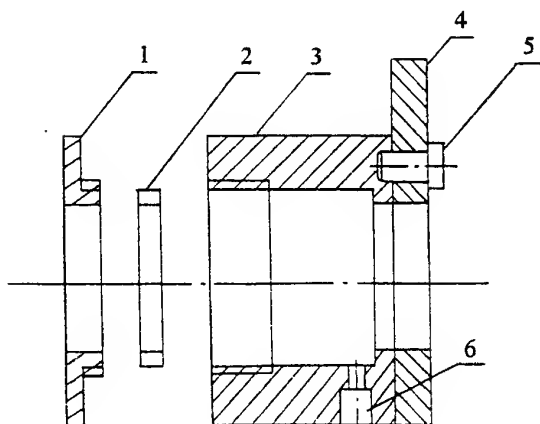


Figure 1. The construction of the cuvette. 1 - cover, 2 - insert, 3 - cuvette, 4 - holdfast, 5 - screw, 6 - glass.

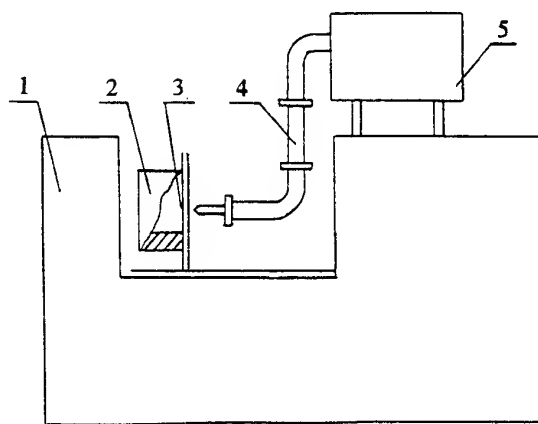


Figure 2. Outline of the experimental arrangement used for determining the optical density of infra-red spectra. 1 - spectrophotometer, 2 - cuvette, 3 - film of Na-DNA, 4 - waveguide, 5 - generator.

This design allows to radiate with microwaves the exposed object and to investigate the surface of this object by infra-red radiation simultaneously. The curve of the kinetics of the desorption of the water

from Na-DNA film which was determined at relative humidity of 96% in the beginning of the experiment is shown in the figure 3.

The optical density of absorption stripe at  $3400\text{ cm}^{-1}$  (frequency of valent oscillation of the OH - group) is placed along the axis of the ordinate, the time of the desorption  $T$  of the water molecules is placed along the axis of the absciss.

It is obviously shown on figure 3 that the desorption kinetics curve under the influence of radiation is located above the same kinetic curve when desorption of the similar sort takes place without an influence.

The dependence of the relative intensity  $R$  of the stripe absorption on time  $T$  is shown in figure 4.

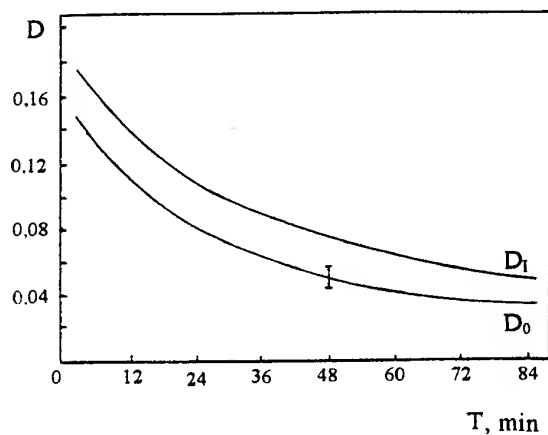


Figure 3. The dependence of infra-red optical density ( $\nu=3400\text{ cm}^{-1}$ ) on time:  $D_0$  - corresponds to Na-DNA films without MI,  $D_1$  - corresponds to Na-DNA films with MI.

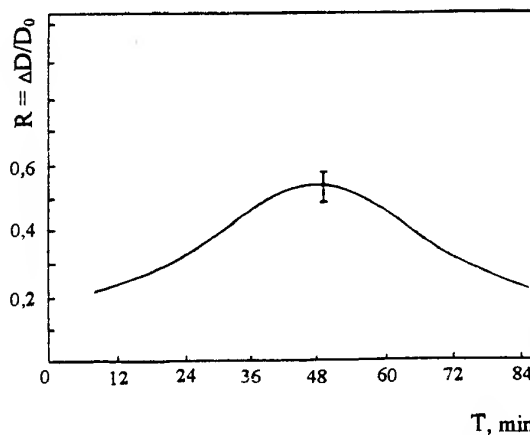


Figure 4. The dependence of the relative intensity ( $R_v$ ) of infra-red absorption on time.

The dependence has an unmonotonous character hence the more stable structure of the hydrated encirclement of Na-DNA exists at the MI. The size of the relative intensity with  $\nu=3400\text{ cm}^{-1}$  of Na-DNA film by desorption of the water has maximum at relative humidity in the interval of 5 - 8 water molecules on the nucleotide in which the regular ion-hydrated encirclement of the A - form of Na-DNA is formed.

Thus, the obtained results are the evidence of the MI influence on the dehydrate process of the Na-DNA molecules which shows itself in the rising of structural stability of hydrate surroundings.

## **Development of submillimeter wave gyrotrons (Gyrotron FU Series) as radiation sources**

**T.Idehara, I.Ogawa, S.Mitsudo and M.Pereyaslavets**

*Faculty of Engineering, Fukui University, Fukui 910-8507, Japan*

High frequency, medium power gyrotrons in Fukui University (Gyrotron FU series) have been developed as radiation sources which cover a wide range in millimeter to submillimeter wave region, and already applied to studies on high frequency ESR and submillimeter wave scattering of plasma. The main items which the series has achieved are summarized.

### **1. Introduction**

The development of gyrotrons are proceeding in two directions. One is the development of high power, millimeter wave gyrotrons as the power sources for an electron cyclotron heating of the plasma, an electron cyclotron current drive of tokamaks and for ceramic sintering. The other is the development of high frequency, medium power gyrotrons as millimeter to submillimeter wave sources for plasma scattering measurement, ESR experiment and so on.

Gyrotrons developed in Fukui University are ones of the latter, that is, high frequency, medium power gyrotrons covering a wide frequency range in millimeter to submillimeter wavelength region. ('Gyrotron FU series'). The series has achieved a frequency step tunability from 38 GHz to 889 GHz by many single mode operations at the fundamentals and the second and third harmonics of electron cyclotron frequency.[1]

The series has also achieved main items which are not only useful for extending their applications to wide fields but make significant operation mechanisms of gyrotron clear. These are summarized as follows, 1) Achievement of moderately high power in wide range of millimeter to submillimeter wave region. Achieved powers are several hundred watt to several kW at fundamental operations and several tens watt to several kW at the second harmonics, 2) Single mode operations at higher harmonics, which are important for high frequency operations of gyrotron under limited field intensity, 3) Studies on mode competition and mode cooperation. These give some insights for high efficient, single mode operations at the second harmonics, 4) Amplitude modulation due to the modulation of velocity distribution function of beam electron, 5) Frequency step-switching and frequency modulation due to the modulation of beam electron mass, 6) Completely cw operations for high stabilities of amplitude and frequency of the output, and 7) Operations in high purity modes due to installation of carefully designed cavity.



Gyrotron FU II, which is one of gyrotrons included in the series, has been used for submillimeter wave scattering measurement of CHS plasma in National Institute for Fusion Science, and Gyrotrons FU I and FU IVA for millimeter to submillimeter wave ESR experiment. In this paper, some of the items mentioned above are presented somewhat in detail.

## 2. Development of Gyrotron FU series

### 2.1 Present status of high frequency, harmonic gyrotrons in Fukui University

Gyrotron FU series is including 7 gyrotrons. Each gyrotron consists of a sealed-off gyrotron tube and a superconducting magnet except Gyrotron FU III, which has a demountable tube. Table 1 summarizes the present status of gyrotrons included in Gyrotron FU series.

Table 1 Present status of Gyrotron FU series

Gyrotron FU I	70-200 GHz	Radiation source for ESR experiment
Gyrotron FU E	90-300 GHz	Radiation source for ESR experiment
Gyrotron FU IA	38-215 GHz	Radiation source for plasma scattering measurement of WT-3 Studies on mode competition and mode cooperation
Gyrotron FU II	70-400 GHz	Radiation source for plasma scattering measurement of CHS
Gyrotron FU III	100-640 GHz	3rd harmonic operations in single modes, Amplitude modulation, Frequency step-switching
Gyrotron FU IV	160-850 GHz	Frequency modulation, cw operation for high stabilities of amplitude and frequency
Gyrotron FU IVA	160-889 GHz	Higher frequency operations by 3rd harmonics, High purity mode operation, Radiation source for ESR

The design was carried out by computer simulations. We are using narrow cavities to get a good mode separation and then to operate the gyrotron in many single modes at the fundamentals, second harmonics and even at the third harmonics. Such a situation is important for our high frequency, harmonic gyrotrons. For example, the diameter of the latest gyrotron, Gyrotron FU IVA, is only 3.0 mm. The design of this cavity was carried out precisely to minimize the mode conversion from the main cavity mode to its competing modes by D. Wagner from University of Stuttgart and M. Thumm from Forshungszentrum Karlsruhe. A schematical drawing of the gyrotron is shown in Fig. 1. It consists of a 17 T superconducting magnet and a sealed-off tube. A triode magnetron injection type gun operates in the magnetic field leaking from a superconducting magnet. The mirror ratio, that is the ratio of the main field intensity at the cavity region to the intensity at the cathode of electron gun, is about 45.

### 2.2 Frequency step tunability in millimeter to submillimeter wave region (38 GHz to 889 GHz)

Gyrotron FU series has achieved frequency step-tunabilities in the wide ranges by single mode operations at the fundamental and the second and third harmonics as shown in Table 1. The maximum frequency is 889 GHz which was achieved recently by the latest gyrotron, Gyrotron FU IVA. The corresponding wave length is 337  $\mu\text{m}$ . Fig. 1 summarizes all frequencies which Gyrotron FU series has achieved up to the present.

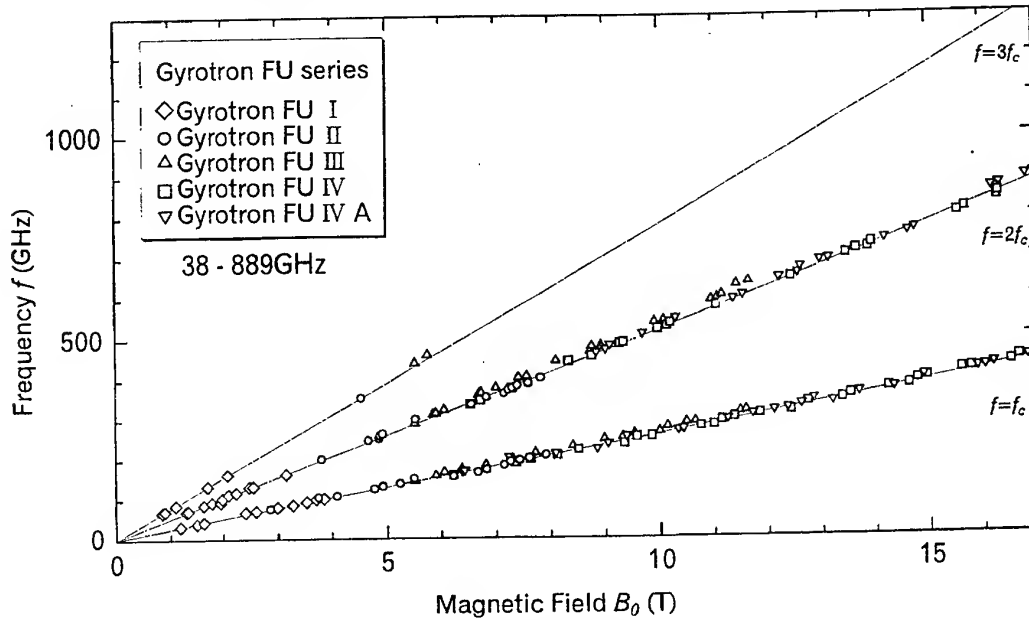


Fig. 1 All frequencies observed up to the present as functions of field intensity  $B_0$ .

### 3.3 Amplitude modulation, frequency step switching and frequency modulation

An amplitude modulation, frequency step-switching and frequency modulation of submillimeter wave gyrotrons are useful for their applications to wider fields as radiation sources. Gyrotron FU III has achieved amplitude modulation of its output. The 100 percent modulation of the output ( $\Delta P_{\text{out}}/P_{\text{out}}=1.0$ ) was attained, when the modulation of anode voltage  $\Delta V_a/V_a$  is only several percent ( $\Delta V_a/V_a \sim 0.076$ ). Frequency modulation was achieved by Gyrotron FU IV. Modulation of beam energy  $eV$  results in the modulation of cyclotron frequency  $f_c$ , which in turn modulates the output frequency  $f$ . The observed maximum modulation amplitude  $\Delta f$  is around 15 MHz and the observed modulation efficiency  $\Delta f/\Delta V$  is around 0.124 MHz/V. Frequency step switching was performed by switching cathode voltage and then switching operating cavity modes.

### References

- [1] T. Idehara, et al, Phys. Plasmas, 2, 3246 (1995).

## Wide-Band Frequency Tunable Single Mode Gyrotron

K. Yokoo, M. Iguchi, N. Sato, and J. Nishihara

Research Institute of Electrical Communication,  
Tohoku University

Katahira 2-1-1, Aoba-ku, Sendai 980-8577, Japan  
Tel. +81-22-217-5510, Fax. +81-22-217-5513

**Abstract** The paper describes a wide-band frequency tunable gyrotron operating at a single guided wave mode in a long resonator constructed from a standard X-band rectangular waveguide. Oscillation frequency covers a full range of the X-band and changes stepwise following the higher order of axial modes in the resonator.

### 1. Introduction

A wide-band frequency tunable and high power electromagnetic wave source is very important for many applications, such as spectroscopy for material science, plasma diagnostics, as well as electrical communication. Frequency step tunable high power gyrotrons have been demonstrated for wide bands in millimeter wave region, where the operation modes change at each frequency step of oscillations due to the change of resonant mode in the resonator [1], [2]. However, we can generate an electromagnetic wave over a wide frequency band at a same guided wave mode by selecting an axially higher order of mode in a long waveguide resonator.

The paper describes the experimental results of a wide-band step tunable gyrotron operating at the  $TE_{10}$  mode in a long waveguide resonator constructed from the X-band standard rectangular waveguide, and shows a very wide-band oscillation ranging from 8.5 to 12 GHz, as a first step of experimental studies.

### 2. Experiments of frequency tunable gyrotron

Fig. 1 shows a schematic construction of the concept for a wide-band frequency tunable gyrotron, where a center circled large orbit electron beam interacts with an electromagnetic wave of the  $TE_{10}$  guided wave mode in the X-band waveguide resonator. Fig. 2 shows oscillation frequencies and output powers of the backward wave gyrotron operating at the  $TE_{10}$  mode in the waveguide without resonator. The oscillation frequency covers a wide frequency band ranging from 8.5 to 12 GHz, as a function of magnetic flux density, though the highest oscillation frequency is limited by the applicable field of the magnet. However, the output powers were order of tenth watts due to the limited length of interaction zone and the beam current. In order to obtain a saturation power in the conventional backward wave interaction of gyrotron, an extremely long interaction zone is required at a low beam current. The problem will be overcome by using the interaction between the beam and the wave of axially higher order of modes in a long waveguide resonator instead of the backward wave interaction.

Fig. 3 shows oscillation frequencies and output powers of the  $TE_{10}$  gyrotron operating in a long waveguide resonator of nearly 2 m, which is formed from a X-band standard waveguide and a waveguide iris, as a function of magnetic flux density. The frequency range of oscillations is nearly same as that of the backward wave oscillation, as shown in Fig. 2. However, nearly tenth times of output powers are easily obtained, though the length of the resonator and the output coupling have not been precisely optimized for the beam current used in the experiments.

Fig. 4 shows an expanded view of the oscillation frequencies at the magnetic flux density around 0.38 T. The oscillations are step tunable at the same guided wave mode of the  $TE_{10}$  and the frequency steps are about 50 MHz following the separation of resonant frequencies between the axial modes in the resonator. These frequency steps are adjustable by adding some changeable reactance in the resonator. Fig. 5 shows the tuning characteristics

of the oscillation frequencies using an E-H tuner mounted in the long waveguide resonator, where the frequency steps are adjusted by the length of E-plane branch in the tuner.

### 3. Conclusion

The paper described a wide-band step tunable gyrotron operating at a single guided wave mode of the waveguide resonator and showed a very wide-band oscillation ranging from 8.5 to 12 GHz. In addition, the paper showed that the frequency steps were adjusted by applying a changeable reactance in the resonator.

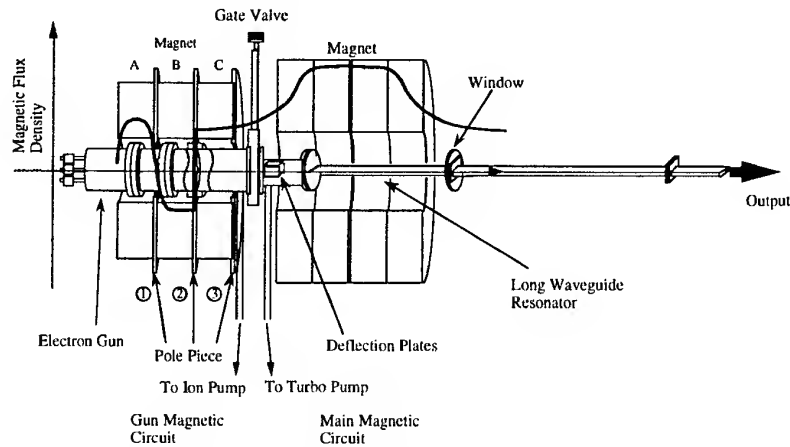


Fig. 1 : Schematic diagram of frequency tunable gyrotron

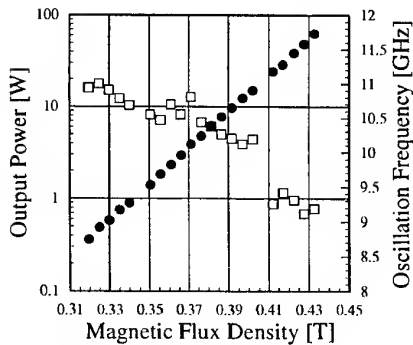


Fig. 2 : Oscillation characteristics of backward wave gyrotron

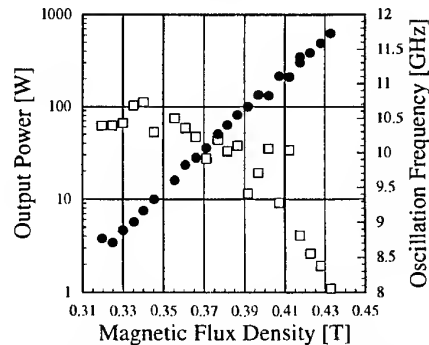


Fig. 3 : Oscillation characteristics of step tunable gyrotron in a long waveguide resonator

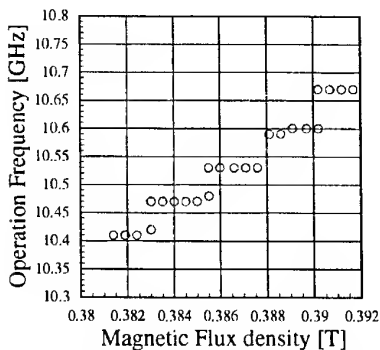


Fig. 4 : Step tunable oscillations in a long waveguide resonator

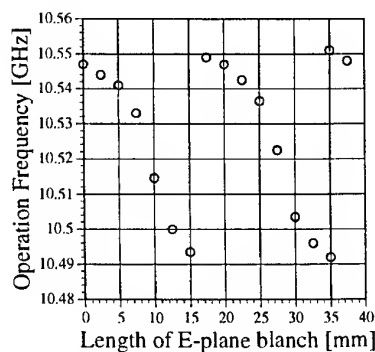


Fig. 5 : Tuning characteristics for frequency steps using an adjustable reactance

1. K.E. Kreischer, J.B. Schutkeker, B.G. danly, and R.J. Temkin, Int. J. Electronics, 57, 835-850 (1984)
2. O. Braz, M. Krtze, and M. Thumm, Conf. Digest of 22nd Int. Conf. on IR & MM Waves, 148-149 (1997)

## A CAVITY DESIGN FOR SECOND HARMONIC GYROTRON OPERATION

G.F. Brand

*School of Physics, University of Sydney NSW 2006, AUSTRALIA*

### Introduction

This paper describes a novel resonant cavity design that overcomes the problem that arises when attempting to operate gyrotrons at the second harmonic of the electron cyclotron frequency. The problem is competition from more easily excited low frequency fundamental modes. Usually, in any attempt to increase the high frequency power, the fundamental grows at the expense of the second harmonic[1,2].

We have shown that the principle of employing a blazed grating to separate second harmonic from fundamental works very well outside the gyrotron tube. In our earliest work[3] the grating was located at the far end of the oversized waveguide, in order to demonstrate that this was indeed an effective method of separating second harmonic from fundamental. It is clearly much more effective to perform the separation as soon as the radiation emerges from the output window of the gyrotron. This is done by mounting the grating at the position of the second reflector of the quasioptical antenna.[4] The performance of such an antenna is improved by using a parabolic blazed grating.[5]

However if the aim is to design a true submillimeter wavelength gyrotron, a better solution would be to inhibit the growth of any fundamental. The starting current for excitation of any mode depends among other things on the  $Q_{\text{diff}}$  of the gyrotron resonant cavity for that mode. If  $Q_{\text{diff}}$  is large, the mode is easier to excite, if it is small it is more difficult. The Sydney gyrotrons operate with beam currents between 20 and 50 mA and our resonant cavities have slight constrictions at their output ends to ensure that  $Q_{\text{diff}}$  is large.

In the proposed new cavity this separation is carried out internally. The new design incorporates a structure rather like a cylindrical blazed grating at the output end so  $Q_{\text{diff}}$  will be very high for second harmonic frequencies but low for the fundamental. The grating will reflect the second harmonic back into the cavity so it can build up while the fundamental will be unable to.

### Separation of fundamental and second harmonic with a blazed grating

The (Fraunhofer) diffraction pattern reflected from a blazed diffraction grating can be described as the product of a diffraction term and a finer interference term. We can separate out second harmonic radiation, wavelength  $\lambda_2$ , from fundamental, wavelength  $\lambda_1 = 2\lambda_2$  as follows.[3] First we ensure that as much second harmonic as possible lies in the direction of its principal diffraction maximum. This leads to a value for the period  $D$ ,

$$D = \frac{\lambda_2}{2\theta_b}, \quad (1)$$

where  $\theta_b$  is the blaze angle. For the second harmonic all the other interference maxima coincide with diffraction zeros. Furthermore, the fundamental interference maxima lie in quite different directions.

### Design of the new cavity

Now let us apply this relation to the design of a gyrotron resonant cavity. We will locate a cylindrical version of the blazed grating at the output end of the cavity as shown in Fig. 1.

Microwaves in a cylindrical waveguide can be treated approximately as plane waves traveling at an angle to the axis of the waveguide. The angle  $\alpha$  is given by

$$\sin \alpha = \frac{\kappa_c}{\kappa}, \quad (2)$$

where  $\kappa_c = \chi_{mn}/R_{wg}$  is the cutoff wavenumber of the  $TE_{mn}$  mode,  $\chi_{mn}$  is the Bessel zero,  $R_{wg}$  is the radius of the waveguide and  $\kappa = \omega/c$  is the free space wavenumber.

As an illustration, let us consider the resonant cavity shown in Fig. 1 whose cylindrical region has the same radius  $R$  of 3.0 mm and length  $L$  of 10.0 mm as the current GYROTRON V cavity and design around the  $TE_{091}$  mode with a frequency of 462.2 GHz (wavelength 0.65 mm), in the middle of the second harmonic range of our gyrotron.

Suppose, for example, the blaze angle  $\theta_b$  is  $20^\circ$ . The period  $D$ , from Eq. (1), will be 0.95 mm. Now let us require that this second harmonic beam be diffracted back into the cavity along the same path as the incident beam. That is,  $\phi' = -\phi$ . The angle  $\phi$  will then be, from the blazed grating equations,  $\phi = \theta_b = 20^\circ$  and  $\phi' = -20^\circ$ . With this value of  $\phi$ ,  $\alpha = 90^\circ - \phi = 70^\circ$  and by Eq. (2) the radius of the waveguide should be  $R_{wg} = 3.19$  mm.

Any fundamental mode would travel towards the output window at an angle of  $\phi' = 20^\circ$ .

It would appear at this point that the scheme is feasible; the second harmonic is trapped so its  $Q_{diff}$  is high and the fundamental escapes so its  $Q_{diff}$  is low. However we should carry out more detailed calculations.

### Scattering matrix calculations

We have used scattering matrices to calculate the resonant frequencies, diffraction  $Q$ s and the mode composition of the output. The same approach was used earlier to design a cavity with minimal mode conversion[6] at the output end.

The results of a calculation are given in Table 1 below. They confirm  $Q_{diff}$  is high for the second harmonic and low for any fundamental that may be excited at the same magnetic field.

This work has been supported by the Australia Research Council, the University of Sydney and the Science Foundation for Physics in the University of Sydney.

- 1 K.D. Hong, G.F. Brand and T. Idehara, J. Appl. Phys, 74, 5250 (1993).
- 2 G.F. Brand, T. Idehara, T. Tatsukawa and I. Ogawa, Int. J. Electronics, 72, 745 (1992).
- 3 K.D. Hong, G.F. Brand and T. Idehara, J. Appl. Phys, 74, 2197 (1993).
- 4 G.F. Brand and G.P. Timms, J. Electrical and Electronic Engineering, Australia, 15, 7 (March 1995).
- 5 G.P. Timms and G.F. Brand, Rev. Sci. Instr., 69, 2155 (1998).
- 6 G.F. Brand, Int. J. Infrared Millimeter Waves, 17, 711 (1996).

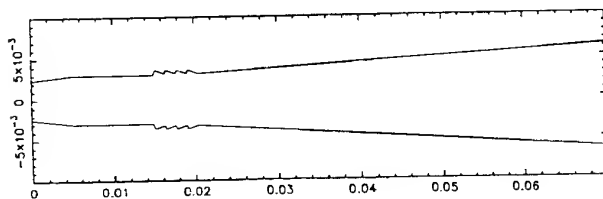


Fig. 1 Sketch of the new cavity. The electron gun lies to the left, the output window to the right. (dimensions are in mm)

Table 1. Calculated resonant frequencies and  $Q_{diff}$ s for one second harmonic and several fundamental resonances.

	mode	frequency (GHz)	$Q_{diff}$
second harmonic	$TE_{091}$	462.17	122 000
fundamental	$TE_{041}$	212.31	6 500
	$TE_{151}$	236.75	13 300
	$TE_{051}$	262.26	14 300

## Resonator with grating for a quasi-optical gyrotron operating at the third harmonic frequency of 260 GHz.

D. Guyomarc'h, J. P. Hogge, M. Siegrist.

Centre de Recherches en Physiques des Plasmas  
Association Euratom – Confédération Suisse  
Ecole Polytechnique Fédérale de Lausanne  
CH - 1015 Lausanne, Switzerland

Didier.Guyomarch@epfl.ch, Jean-Philippe.Hogge@epfl.ch, Mark.Siegrist@epfl.ch

A resonator incorporating a diffractive grating has been designed and cold-tested. It will be used as cavity of a quasi-optical gyrotron with fundamental frequency of 87 GHz in order to impose operation at the third harmonic.

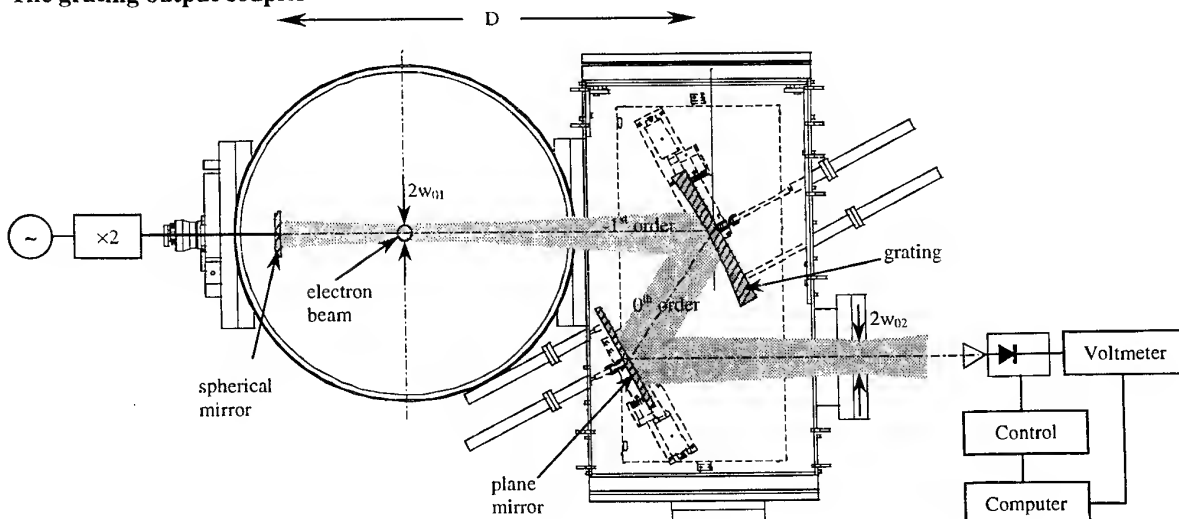
Collective Thomson scattering (CTS) is one method to get information on the ion velocity distribution in a tokamak plasma. The feasibility to measure the ion temperature has been demonstrated at CRPP [1]; however, other methods exist which are simpler and more accurate, so that it is unlikely that CTS will ever be used to routinely measure the temperature of the bulk ions. But there is renewed interest in CTS in connection with future reactor-type machines where  $\alpha$ -particle diagnostics are required for which no proven technique exists yet.

For CTS, a high power source with pulses of several milliseconds duration at a wavelength of a few hundred  $\mu\text{m}$  is required. Optically pumped far-infrared lasers, which have been used until now, cannot produce the required pulse length. Gyrotrons achieve the power and pulse duration required, but their frequency is too low. Currently, only the free electron laser could be considered as a radiation source. Unfortunately, it generates a wide mode spectrum and is a large and expensive piece of equipment.

Efficient frequency conversion of gyrotron radiation might be a solution. A two-step process would probably be required. A 110 GHz gyrotron could be operated at its third harmonic, followed by a passive solid state tripler, producing radiation at about 1 THz (300  $\mu\text{m}$  wavelength). High frequencies in gyrotrons are principally limited by the use of an high magnetic field ( $> 10$  tesla) required from superconducting (sc) coils. The use of the third harmonic emission allows existing gyrotron with a sc coil designed for fundamental radiation (4 tesla).

Passive frequency tripling with laser radiation in Si has been investigated at CRPP. At the maximum power of 2 MW (limited by surface breakdown effects) and 200 ns pulses, 2 kW of third harmonic radiation at 225  $\mu\text{m}$  was produced [2]. This is a conversion efficiency of 0.1 %, but the conversion efficiency scales with the power squared at least in the small signal regime. More efficient coupling schemes and materials are currently under investigation.

### The grating output coupler



Top-view of the cold test cavity arrangement experimented in the gyrotron configuration.

It has been shown [3], [4] that power can be efficiently coupled out of a Fabry-Pérot resonator in the millimeter wave range by replacing one of the mirrors of the cavity by a diffraction grating placed in the Littrow mount. If  $d$  is the groove spacing,  $\theta$  the angle of incidence,  $\lambda$  the wavelength and  $n$  the order of diffraction, the condition  $2d \sin \theta = n\lambda$  defines the Littrow mounting of the grating at the  $-n$  order. If additionally  $\lambda/d > 2/3$ , only the  $n = -1$  and  $n = 0$  diffracted waves can exist. The zeroth order (or specular reflection) provides the output power while the  $-1$  order provides the feedback in the resonator.

In a quasi-optical gyrotron cavity, a grating coupler offers several advantages : with respect to the resonator, 1) it acts as a semi-transparent spherical mirror required to produce a gaussian beam, 2) it can refocus the output beam in order to produce a flat phase front for the transmission through the output coupler window, and 3) it is frequency selective and hence able to suppress unwanted modes ; in particular, it prevents the growth of harmonics of lower order than the design value. Encouraging results have been obtained with a grating coupled resonator at the fundamental of 92 GHz [3], [4]. A new grating has now been designed for the same resonator geometry, optimized for the third harmonic.

Under the  $-1$  order Littrow mounting condition, the efficiency for the  $-1$  order depends only on the angle of incidence  $\theta$  and the groove depth  $h$  normalized to the period  $d$ . If we divide the groove period of a grating designed for the fundamental by 3, we obtain a grating in Littrow mount for  $-1$  order at a « tripling frequency » ; for a grating designed for the third harmonic under the  $-1$  order Littrow mounting, no feedback into the resonator will be provided for the fundamental.

Considering waves with any phase shapes incident on a grating, the Littrow condition is satisfied if the vertex of the grooves coincide with the intersection of the grating support and the wavefronts which are separated in phase by  $\pi/2$ . With an elliptical surface, the output beam can be focused to an optimum waist size for the coupling into an  $HE_{11}$  corrugated waveguide.

### Experimental set-up

For the QOG, we shall consider only sinusoidal grooves whose relatively smooth surface minimizes the risk of rf breakdown. For practical reasons, the TM polarization is preferred for the experiment because the  $-1$  order efficiency is relatively insensitive to the angle of incidence in the domain of interest. The cold test experimental set-up is shown on the figure. The RF source is a carcinotron ( $P_{RF} = 200$  mW,  $f_{RF} = 130$  GHz), followed by a frequency doubler. The resonator is composed of a spherical mirror and a diffraction grating placed in Littrow mount (both in copper OFHC). To couple the RF power into the cavity, a WR-03 rectangular waveguide through the center of the spherical mirror.

The angle of incidence  $\theta = 28^\circ$  on the grating and the normalized sinusoidal groove depth  $h/d = 0.31$  lead to an  $-1$  order efficiency for TM mode  $e_{-1TM} = 99\%$  which means that we extract only 1 % of the power in the cavity. The support of the grating is an ellipsoid of revolution with semi axes  $a = 1182$  mm and  $b = 960$  mm. With a waist  $w_{01} = 11$  mm, the spot size on the spherical mirror is 12 mm and on the grating is 22.6 mm. The output waist  $w_{02} = 16.7$  mm is at a distance of 500 mm from the grating.

The output pattern is recorded by a standard rectangular horn and a Schottky diode mounted on a computer-controlled XY table allowing scans over a  $10 \times 10$  cm<sup>2</sup> area.

### Conclusion

We have design a grating designed to operate in  $-1$  Littrow mount at the third harmonic of a QOG with fundamental frequency of 87 GHz. The cold test cavity has been characterized both at the fundamental and the third harmonic.

*We would like to acknowledge the assistance of Mr. A. Gorgerat and other mechanical engineers of the CRPP workshop for their contribution.*

*This work was partially supported by the Swiss National Science Foundation.*

- [1] R. Behn, D. Dicken, J. Hackmann, S. A. Salito, M. R. Siegrist, P. A. Krug, I. Kjelberg, B. Duval, B. Joye and A. Pochelon, Phys. Rev. Lett. **62** (24), 2833 (1989).
- [2] M. R. Siegrist, F. Keilmann, Ch. Nieswand, M. Urban, Infrared Phys. Technol. **36**, 407 (1995)
- [3] M. Q. Tran, H. Cao, J. Ph. Hogge, W. Kasperek, T. M. Tran and P. J. Paris, J. Appl. Phys. **73** (5), 2089 (1993).
- [4] J. P. Hogge, T. M. Tran, P. J. Paris, M. Q. Tran, Phys. Plasmas **3** (9), 3492 (1996).



## Continuously tunable 35-190 GHz powerful gyrotrons at GYCOM

E. V. Zasytkin, I. I. Antakov, I. G. Gachev, S. N. Vlasov and E. V. Sokolov

GYCOM Co. Ltd, 46 Uljanov Str. 603600 Nizhny Novgorod, Russia

To drive powerful broadband gyrokystrons, high-power millimeter-wave sources tunable in the frequency range of about 1% are required. Unfortunately, the electron frequency tuning band of a conventional high-Q cavity gyrotron coincides approximately with the unloaded cavity bandpass which does not exceed 0.1% usually (see, for example [1]). Therefore, at GYCOM a line of research related to the elaboration of mm-wave tunable gyrotrons was being developed simultaneously with the development of gyrokystrons. As a result, a series of 35-, 70- and 93- GHz powerful continuously tunable gyrotrons was designed, fabricated and tested at GYCOM last years.

To attain broadband tuning of the radiation frequency in gyrotron, the cavity eigen-frequency should be changed simultaneously with dc magnetic field changing. There are two possible ways of the cavity eigen-frequency variation: a) changing of the cavity length with help of a movable piston, b) changing the cavity transverse dimensions. In the first case, the frequency tuning band  $\Delta\omega/\omega$  is determined by [2]

$$\frac{\Delta\omega}{\omega} = \frac{q^2}{4} \left( \frac{\lambda}{L} \right)^2 \frac{\Delta L}{L}, \quad (1)$$

where  $q$  is the axial wavenumber of the operating mode,  $\lambda$  is the operating wavelength,  $L$  is the cavity length,  $\Delta L$  is the cavity length variation. As follows from (1), a significant tuning band may be obtained at the use of a short cavity only.

Two pulsed gyrotrons with a variable cavity length operating at 34- and 93 GHz in the  $TE_{011}$  cavity mode have been developed aiming mostly as gyrokystron drivers. In 34-GHz oscillator, the output power of 24 kW at the central frequency of 34.05 GHz has been produced with 20% efficiency at 2.7-A beam current and 45-kV beam voltage (Fig. 1). The following half-power oscillation frequencies were observed: above the central frequency - 34.45 GHz, below that - 33.96 GHz. Tube operated usually with a 100  $\mu$ s pulse duration and 15-Hz repetition frequency. Figs. 2 depicts the performance characteristics of a 93-GHz pulsed tunable gyrotron. As it follows from this figure, the output power of about 2 kW with 6% efficiency has been attained at 22-kV beam voltage and 1.1-A beam current. A half-power tuning band of 1.4% has been measured. The required dc magnetic field in the cavity (1.25 T for 34-GHz tube and 3.6 T for 93-GHz that) was provided by a superconducting coil cooled in a cryostat by liquid helium. The cryostat used in those experiments was very compact: its height was 85 cm, outer diameter was 38 cm, and its weight was about 80 kg.

A second approach has involved a study of a gyrotron with the cavity constituted by two mirrors separated by thin longitudinal slots. In that cavity, a non-symmetrical modes with fixed polarization and zeroth RF electric field at the slots are used as the operating those. The oscillation frequency is being tuned continuously due to the change of the distance between mirrors.

This principle of the operating frequency variation has been realized experimentally in a 70-GHz CW tuneable gyrotron developed for Thomson scattering plasma diagnostics and some spectroscopy applications. This tube has been designed to operate in the  $TE_{131}$  cavity mode. To prevent mirrors overheating, their output edges were attached to the cooled part of the tube and were immovable while the distance between their input edges (from the cathode side) was varied. It means that in this gyrotron design, parallel shifting of the mirrors has been changed by their rotation about an axis lying at the plane of the slots and passing through the point of the output edges attachment. At the assumption of small rotation, a frequency tuning band is given by [2]

$$\frac{\Delta\omega}{\omega} \approx 0.72 \left( \frac{\lambda}{L} \right)^2 \frac{l}{L}, \quad (2)$$

where  $l$  is the distance between the axis of rotation and middle of the cavity.

Fig. 3 shows the output power as a function of the operating frequency for the case when both cavity eigen-frequency and magnetic field were varied simultaneously. Maximum output power of 1.4 kW CW with 22% efficiency and 11% tuning band in the  $TE_{13}$  mode, and 0.9 kW CW with 14% efficiency and 7.4% tuning band in the  $TE_{42}$  mode have been demonstrated. A 17.5-kV, 0.36-A electron beam was used in this experiment.

Last year, a 190-GHz CW second-harmonic gyrotron with fixed cavity parameters was designed and tested at GYCOM. The required dc magnetic field strength in the cavity of 3.7 T was provided by the same cryomagnet used in 34- and 94-GHz experiments. The output power of 0.55 kW with a 6.2% efficiency has been observed at

the operating frequency of 191.5 GHz (Fig. 4). At the base of this tube, a 190-GHz tunable gyrotron is now being developed.

# REFERENCES

1. I. I. Antakov, E. V. Zasyplin, E. V. Sokolov, *Int. J. Infrared and MM Waves*, 14, No. 5, 1001 (1993)
2. I. I. Antakov *et al*, *Electronnaya Tekhnika, Ser. Elektronika SVCh*, 8, 20 (1975) (in Russian).

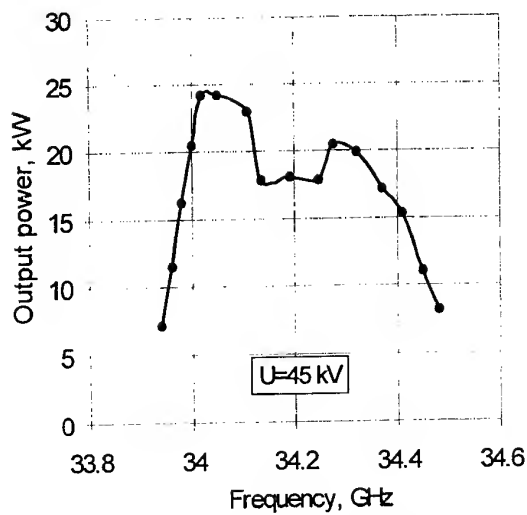


Fig. 1 Output power vs operating frequency for 34-GHz tunable pulsed gyrotron

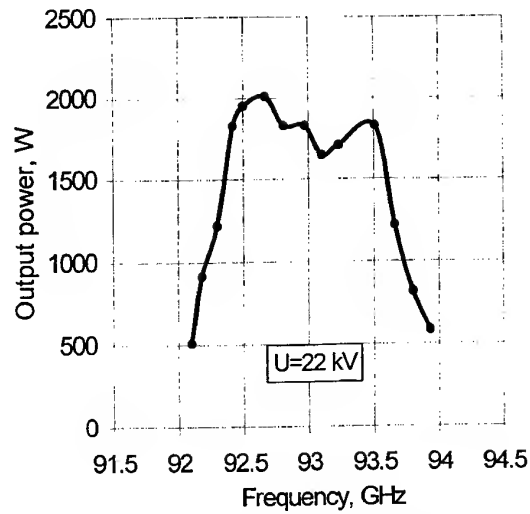


Fig. 2 Output power as a function of frequency for 93-GHz tunable pulsed gyrotron

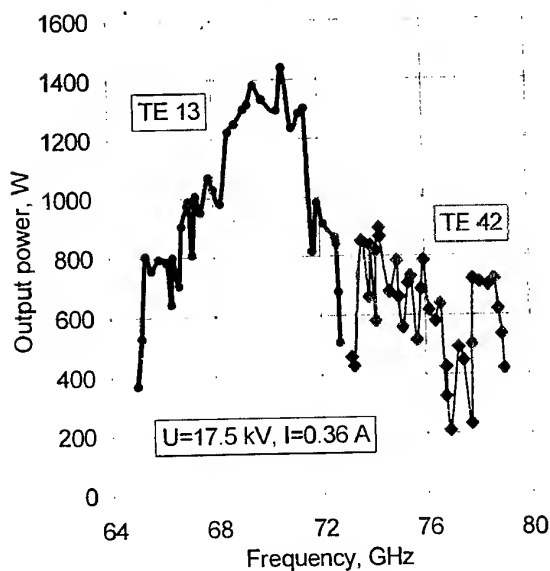


Fig. 3 Output power vs operating frequency for 70-GHz CW tunable gyrotron

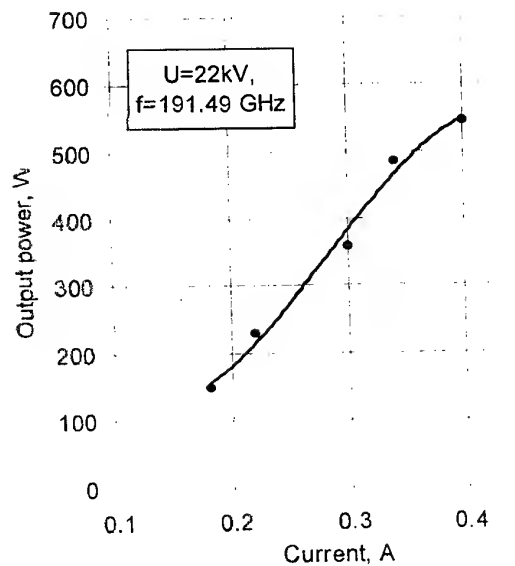


Fig. 4 Output power vs beam current for 190-GHz CW second harmonic gyrotron

## Gyrottron at the 5th Cyclotron Harmonic

V.L. Bratman, A.E. Fedotov, Yu.K. Kalynov, V.N. Manuilov,  
M.M. Ofitserov, S.V. Samsonov, and A.V. Saviolov

Institute of Applied Physics, Russian Academy of Sciences,  
Nizhny Novgorod, 603600, Russia

### Abstract

A Large Orbit Gyrottron with a 300 keV/30 A/20 ns electron beam provides radiation power of 100 kW at the 5th cyclotron harmonic (TE<sub>5,1</sub> operating mode, wavelength of 4 mm). Next experiment with an unique electron beam (250 keV/15 A/10  $\mu$ s, 0.6 mm in diameter) is in progress.

### Introduction

A high-harmonic gyrottron with a strong magnetic field is one of the simplest candidates for development of powerful sources in the whole submillimeter wavelength range [1,2]. Already at subrelativistic electron energies a second-harmonic gyrottron provides generation at wavelengths of about 0.35 mm [1]. According to simulations and modeling experiments the use of moderately relativistic electron energies of order of several hundred kilovolts allows an effective generation of higher cyclotron harmonics at the wavelengths down to 0.1 mm [2]. In the present paper, new results of modeling experiments in millimeter wavelength band with a short-pulse Large Orbit Gyrottron (LOG) at the 1st–5th cyclotron harmonics are reported. In addition, a theoretical analysis of mode interaction and results of tests for a new long-pulse electron optical system of a LOG are presented.

### Selective excitation of harmonics

Power of cyclotron radiation of an electron in a uniform magnetic field changes approximately as  $(\beta_{\perp})^{2s}$ , where  $\beta_{\perp}$  is the transverse electron velocity normalized to speed of light,  $s$  is the harmonic number. The same factor describes a coupling of an electron beam with a fixed waveguide mode for the stimulated radiation. Therefore, the increase in the transverse velocity up to relativistic value makes generation of higher harmonics significantly more effective. For a gyrottron with a traditional cavity in the form of a weakly non-uniform cylindrical waveguide, coupling with higher harmonics increases also due to enlargement of diffraction  $Q$  for shorter wavelengths. Correspondingly, for electron energies of order of several hundred kilovolts, starting currents for first harmonics are of the same order of magnitude. This is clearly not sufficient for excitation of higher harmonics because the spectrum of cavity modes is very dense for each harmonic. A significant mode selection is achieved, in particular, in a LOG, where electrons excite only corotating modes which azimuthal indices are equal to the resonant harmonic

number. Due to non-equidistant spectrum of the gyrottron modes, resonant values of magnetic field for different harmonics can be separated by the magnitude of order of the corresponding resonance lines. In this case, when the electron current slightly exceeds the starting value for a higher harmonic, numerical simulations based on a time-domain multi-mode code predict a single-mode regime of the operation (Fig. 1a).

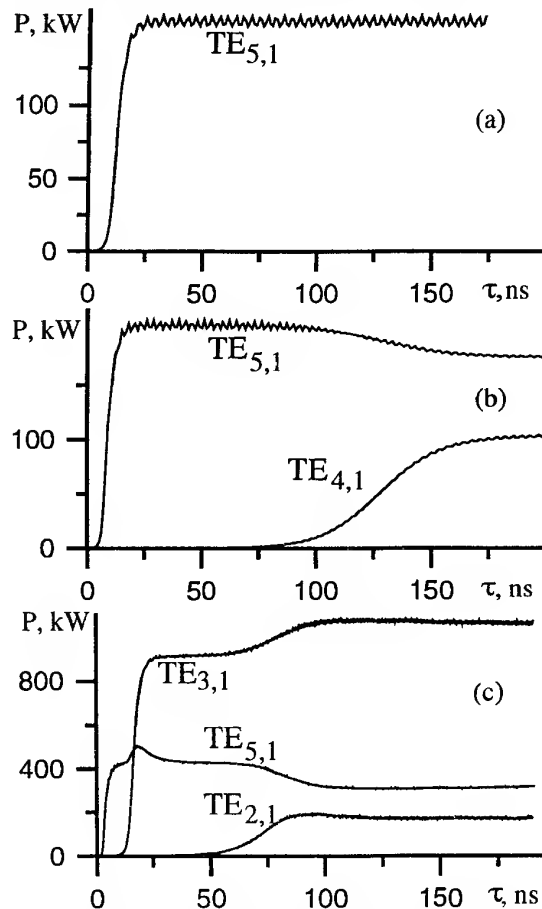


Fig.1. Simulations for 5th-harmonic-LOG at different excess over threshold,  $I/I_{st}$ : 3 (a), 5 (b) and 10 (c).

In the simulations, the TE<sub>5,1</sub> mode at the 5th cyclotron harmonic is assumed to be the operating one, and all other modes are considered as spurious. Thus, the magnetic field and the beam current are chosen so that the starting condition is fulfilled for the TE<sub>5,1</sub> mode only. Along with this mode, the most dangerous modes TE<sub>2,1</sub>, TE<sub>3,1</sub>, and TE<sub>4,1</sub> at the corresponding cyclotron harmonics,  $s = 2-4$ , are

taken into account. It is assumed also that the voltage, beam current and electron pitch-factor are constant. For a larger current, the single-frequency operation of the  $TE_{5,1}$  mode is unstable: after a comparatively long period, the neighboring  $TE_{4,1}$  mode is also excited (Fig.1b). Let us notice, that the starting condition for the  $TE_{4,1}$  mode is not satisfied in the absence of the operating mode, and its excitation is caused by the operating mode. The deceleration of particles in the field of the operating mode increases the electron cyclotron frequency, and particles become nearer to the resonance with the  $TE_{4,1}$  mode. With the further increase of the current, the output power of the parasitic mode increases at the expense of the operating mode, and the time of its excitation decreases. If the current is large enough, the parasitic mode can completely suppress the operating one. Beginning from some current, the excitation of other modes occurs. Fig.1c demonstrates the regime, where the 3rd harmonic suppresses the 4th one, whereas the power of the 2nd harmonic remains quite small. In this regime, the time of the 3rd harmonic excitation is comparable with that for the 5th harmonic.

### Experiment

The experimental study of LOG is carried out at the high-current direct-action electron accelerator "Sinus-6" with a field-emission injector. The accelerator provides electron energy of 300-700 keV, total current of 3-8 kA and pulse duration of 20 ns. The selection of the "most rectilinear" particles by a narrow anode outlet (Fig.2) is used. For the operating beam having passed through the outlet, the diameter is 1.5 mm, the current is 30 A at the electron energy 300 keV and the 10 ns flat-top of a voltage pulse. The initially rectilinear beam is pumped by the kicker in the form of a rectangular current frame sloping to the z-axis, producing practically homogeneous transverse magnetic field near the beam and, therefore, providing a weak sensitivity to spread in the particle position. Sensitivity to the velocity spread was reduced using a relatively short cavity, where electrons underwent only 3-5 gyro-rotations. After pumping in the kicker, electrons with the pitch factor  $g=1.3-1.5$  enter a gyrotron cavity (Fig.2). Three different cavities were tested in "hot" experiments: a "short" and a "long"

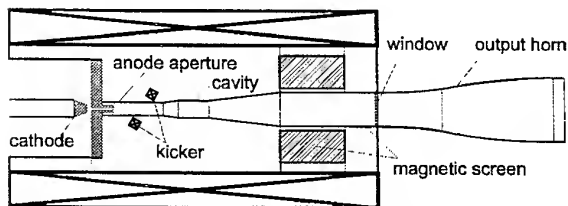


Fig.2. The schematic of LOG.

traditional cavities with the length of cylindrical part of 23 and 42 mm, as well as a cavity with a smooth matched output. The length of HF field in the last "matched" cavity coincided with the length for the "long" cavity, but its  $Q$  was twice lower. The

calculated excess of the operating current over threshold,  $I/I_{st}$ , was equal to 2, 10 and 20, respectively, for the pitch-factor of 1.5. In accordance with the multi-mode simulations (Fig.1), the most selective excitation of harmonics up to  $s=5$  was observed for the case of minimal excess over threshold, namely, in the "short" cavity. When decreasing the magnetic field from 1.2 T down to 0.8 T, we clearly observed successive excitation of the  $TE_{s,1}$  modes at the harmonics  $s=1-5$ , which was confirmed by measurements of the radiation frequency and mode pattern (Table 1). Approximately

Table 1

$s$	1	2	3	4	5
$\lambda$ , mm	13.9	8.4	6.1	4.8	4.0
$P$ , kW	1500	1500	600	200	120

the same power of 100 kW at the 5th harmonic was selectively observed in a LOG with the "matched" cavity. The radiation power at the 5th harmonic was twice lower and simultaneous powerful generation at lower harmonics was obtained in the "long" cavity.

The results obtained for the short-pulse LOGs are used for design and construction of a long-pulse LOG. A quasi-Pierce electron-optical system producing 250 keV/ 15 A/ 10  $\mu$ s high-quality electron beam gyrating around the axis in a magnetic field of 1.6 T with a pitch-factor 1.5 was tested experimentally. The formation of a very dense (5 kA/cm<sup>2</sup>) rectilinear beam was based on combination of non-adiabatic electrical and adiabatic magnetic compression with a cross-section ratio of 1000. This beam is now used for the realization of a LOG with designed power of 50-100 kW and wavelength of 2 mm at the 5th cyclotron harmonic. The developed concept allows elaboration of relatively compact powerful sources in millimeter/submillimeter wavelength band.

### Acknowledgments

This work was supported by the Russian Interdisciplinary Scientific and Technological Program "Physics of Microwaves" and the Russian Foundation for Basic Research, Grant No. 96-02-18971.

1. T. Idehara et al., Proc. of 22nd Int. Conf. on Infrared and Millimeter Waves, T1.5 (Wintergreen, Virginia, 1997).
2. V.L. Bratman et al., Proc. of 22nd Int. Conf. on Infrared and Millimeter Waves, M4.1 (Wintergreen, Virginia, 1997).

## A High-Power, Short Pulse Dielectric Cherenkov Maser Amplifier Operating in the Superradiant Regime

S. M. Wiggins, D. A. Jaroszynski, A. W. Cross, A. D. R. Phelps, K. Ronald, P. Aitken,  
B. W. J. McNeil and G. R. M. Robb

Department of Physics and Applied Physics,  
University of Strathclyde, Glasgow, G4 0NG, UK.

M. I. Yalandin, V. G. Shpak, S. A. Shunailov and M. R. Ulmaskulov

Institute of Electrophysics, Russian Academy of Science,  
620049, Ekaterinburg, Russia.

N. S. Ginzburg, N. Yu. Novozhilova, I. V. Zotova, A. S. Sergeev and N. Yu. Peskov

Institute of Applied Physics, Russian Academy of Science,  
603600, Nizhny Novgorod, Russia.

### Abstract

A high-power ( $\sim 2$  MW), short duration ( $\sim 1$  ns), Ka-band dielectric Cherenkov maser operating in the superradiant regime has been investigated. In this regime, slippage of the wave through the electron pulse is significant. A strong dependence of the microwave power on the risetime of the current pulse suggests that coherent spontaneous emission acts as the source in the superradiant pulse evolution.

### Introduction

The Cherenkov maser involves the coupling of a slow guided electromagnetic wave in a dielectric lined waveguide and the slow space-charge mode of a relativistic electron beam. The synchronism condition for excitation of the Cherenkov instability is  $\omega = k_z v_0 - \omega_p / \gamma_0$  where  $v_0$  is the electron axial velocity,  $\omega_p = (e^2 n / \gamma_0 m \epsilon_0)^{1/2}$  is the plasma frequency,  $n = I / e v_0 \sigma$  is the electron density,  $I$  is the beam current,  $\sigma$  is the beam cross-sectional area,  $\gamma_0 = (1 - \beta_0^2)^{-1/2}$  is the relativistic factor and  $\beta_0 = v_0 / c$ . In experiments described here, a single-pass Cherenkov amplifier amplifies an RF field due to its spontaneous radiation; both coherent and incoherent. The radiation spikes of interest arise from coherent spontaneous emission of electrons in the leading edge of the pulse. As the wave group velocity is less than the electron axial velocity, the spikes slip backwards into the electron pulse, enabling them to interact with 'fresh' electrons. In this superradiant regime the microwave power scales as the square of the number of emitters [1,2]. The first observation of Cherenkov superradiance was by Ginzburg *et al.* [3] using a similar accelerator to that used in the experiments reported here.

### Experimental Set-up

A RADAN 303 accelerator with a subnanosecond slicer has been used to inject typically 0.5 ns, 0.8-1.3 kA, 240 keV electron pulses [4]. These

electron pulses are generated from a magnetically insulated coaxial diode which utilises a cold explosive emission cathode. The fast rising electron beam current and accelerating voltage pulses are measured using a Faraday cage strip line current probe and an inline capacitive voltage probe respectively. Signals have been recorded using a 7 GHz Tektronix 7250 digitizing oscilloscope. The high current electron pulses are transported through a cylindrical stainless steel waveguide lined with a dielectric medium in a longitudinal guiding magnetic field of 5 T. The waveguide is of length 30 cm with an inner diameter of 9.8 mm. The dielectric medium is a maximum of 20 cm in length and consists of a quartz tube ( $\epsilon = 3.8$ ) with inner diameter 5.7 mm and outer diameter 8.0 mm. A Mylar film ( $\epsilon = 3.0$ ) of thickness 0.9 mm lines the outside of the quartz tube. The hollow electron beam diameter is 4.0 mm. The radiation has been measured using a hot-carrier germanium detector. A schematic of the experimental set-up is shown in figure 1.

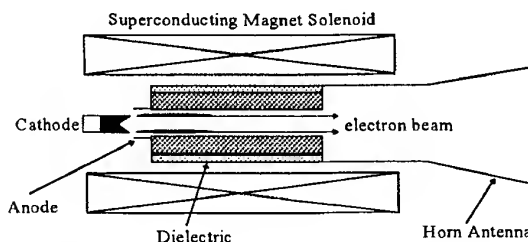


Figure 1 Schematic of experimental set-up

### Experimental Results

Total peak power for the 20 cm dielectric has been found to be 2.8 MW. The mode is a mixture of  $TM_{01}$  and  $HE_{11}$  at a frequency of  $\approx 30$  GHz. The output power depends very strongly on the temporal profile of the applied voltage pulse. Figure 2 shows the variation of the detected power with voltage pulse

risetime for a dielectric liner of length 20 cm. The RF signal decreases sharply as the risetime increases i.e. as the derivative of the profile decreases. This shows that the main source of the signal is coherent spontaneous emission of radiation by electrons in the leading edge of the current pulse.

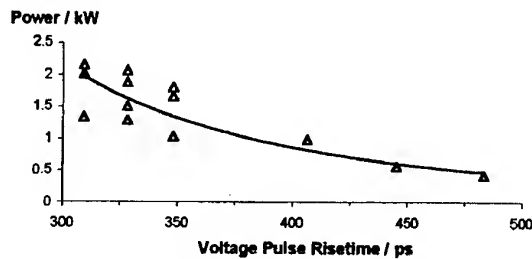


Figure 2 Power dependence on the voltage pulse risetime

To establish the dependence of the power on the charge in the current pulse, only shots with unchanged voltage pulse amplitude, width and risetime have been considered. This has been possible with simultaneous capture of the voltage and microwave pulses, as shown in figure 3. Saturation was observed for the 20 cm dielectric so a 16 cm dielectric has been used here. The microwave output consists of short duration (~100 ps) spikes that are not cleanly resolved by the detection system. They arise from sub-structure in the density and energy/phase distribution in the electron pulse.

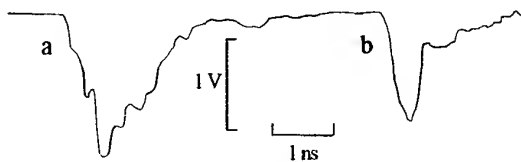


Figure 3 Typical (a) microwave pulse and (b) voltage pulse

The charge has been varied by adjusting the anode-cathode gap distance. This is accompanied by a change in the mean electron energy. For our geometry it ranges from 310 kV for a current of 1.3 kA to 380 kV for a current of 0.8 kA. The variation of the mean energy does not significantly change the interaction strength between electrons and electromagnetic wave because of both the wide bandwidth of the maser and the wavelength insensitive filling factor. Thus, in the measurement of peak power as a function of charge, the influence of energy can be neglected to first order. The power as a function of charge is presented in figure 4. As the electron pulse consists of electrons with a wide energy distribution, some of the lower energy electrons are not involved in the interaction. A lower estimate of the residual non-resonant charge has

been achieved by tuning the beam line out of synchronism by decreasing of the voltage pulse amplitude and width. This has been estimated as 81 units and is depicted in figure 4 by the arrow. Excluding this charge, the power scales as  $Q^{2.66}$ .

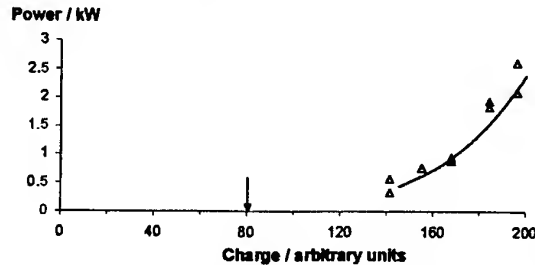


Figure 4 Power dependence on charge

It must be stressed that this is a lower estimate for the non-resonant charge and a higher value would lower the power scaling. This strong scaling of the power with charge demonstrates the superradiant nature of the interaction. The scaling of power with interaction length has been investigated for dielectrics from 9 cm to 16 cm in length. Figure 5 displays the exponential nature of the scaling of power with interaction length, an indication that the system is still evolving in the exponential regime [1]. By extrapolating to the beginning of the interaction region, an estimate of the start-up power is ~100 W.

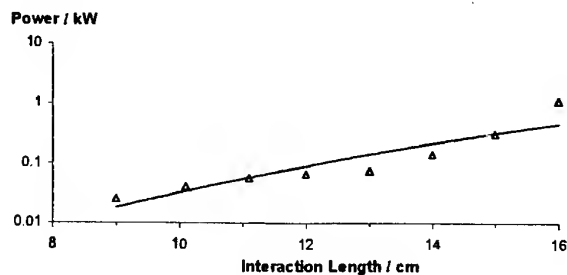


Figure 5 Power dependence on interaction length

#### Acknowledgments

This work has been supported by the United Kingdom DERA and EPSRC and by the Russian Fund for Fundamental Research, Grant No. 98-02-17308.

#### References

1. R Bonifacio, N Piovella and B W J McNeil Phys. Rev. A 44, R3441 (1991).
2. D A Jaroszynski *et al.* Phys. Rev. Lett. 78, 1699 (1997).
3. N S Ginzburg *et al.*, A D R Phelps *et al.* and V G Shpak *et al.* Nucl. Instrum. Methods Phys. Sect. A 393, 352 (1997).
4. V G Shpak *et al.* Proc. BEAMS '96 - 11<sup>th</sup> Int. Conference on High-Power Particle Beams, Prague, Czech Rep., 913 (1996).

## A NEW FAR-INFRARED (FIR) SOURCE

J.E. Walsh, J.C. Swartz, J.H. Brownell and M.F. Kimmitt

Department of Physics and Astronomy,  
Dartmouth College, Hanover, New Hampshire 03755-3528

A new source of coherent, tunable, FIR radiation has been developed [1]. The essential features of the device are the beam in a scanning electron microscope (SEM) and a diffraction grating mounted in the e-beam focal region. The beam moving over the grating induces a surface current which in turn is responsible for the emission. When the beam current density is low, the total power generated is the result of an incoherent sum of the radiation produced by each electron in the beam. In this limit, the emission is in effect a shot noise process. If, however, the beam current density is high, as it may be in the SEM, the distributed feedback from the grating is sufficient to cause beam bunching and growth of a coherent mode of radiation. The grating is functioning as an open surface resonator and in recognition of this role the device has been termed a grating coupled oscillator (GCO).

A schematic diagram of the SEM is shown in Fig. 1. The beam is produced on a tungsten hairpin cathode and focussed and positioned over the grating with the aid of the microscopes internal electron optical elements. Beam voltages vary over a range extending from 20-40 kV and total current levels up to approximately 1 mA can be extracted. Coherent radiation can be obtained with beam diameter as large as 35  $\mu\text{m}$  and in the present apparatus the lower limit to the beam diameter is about 20  $\mu\text{m}$ . The coherent oscillation "turns on" when the beam current density reaches a point where the beam plasma frequency times the duration of an electron transit over the grating exceeds about 0.75. A typical power versus beam current curve is shown in Fig. 2.

The wavelength,  $\lambda$ , is determined by the so called Smith-Purcell relation [2]:

$$\lambda = \frac{\ell}{|n|} \left( \frac{1}{\beta} - \cos \theta \right) \quad (1)$$

In Eq. 1,  $\ell$  represents the grating period,  $\beta$  the velocity of a beam electron relative to the speed of light,  $\theta$  is the angle of emission relative to the direction of the beam, and  $|n|$  is the order of diffraction. In the present device the emission is taken in the normal direction and diffraction orders up to  $|n| = 3$  have been used effectively. The choice of dominant order is controlled by the grating profile.

To date, radiation over a wavelength band extending from 250  $\mu\text{m}$  (1.2 THz) out to 1 mm (0.3 THz) has been obtained. Basic scaling relations developed to guide the design of the experiments indicate that coverage of the entire 10-1000  $\mu\text{m}$  band should be possible.

A summary of these considerations and a review of the progress with GCO experiments will be presented.

Support from ARO Contract DAAH04-95-1-0640, DoD/AF DURIP Contract F49620-97-1-0287, and Vermont Photonics, Inc., is gratefully acknowledged.

---

[1] J. Urata, M. Goldstein, M.F. Kimmitt, A. Naumov, C. Platt and J.E. Walsh, Phys. Rev. Lett. **80**, 516 (1998).

[2] S.J. Smith and E.M. Purcell, Phys. Rev. **92**, 1069 (1953).

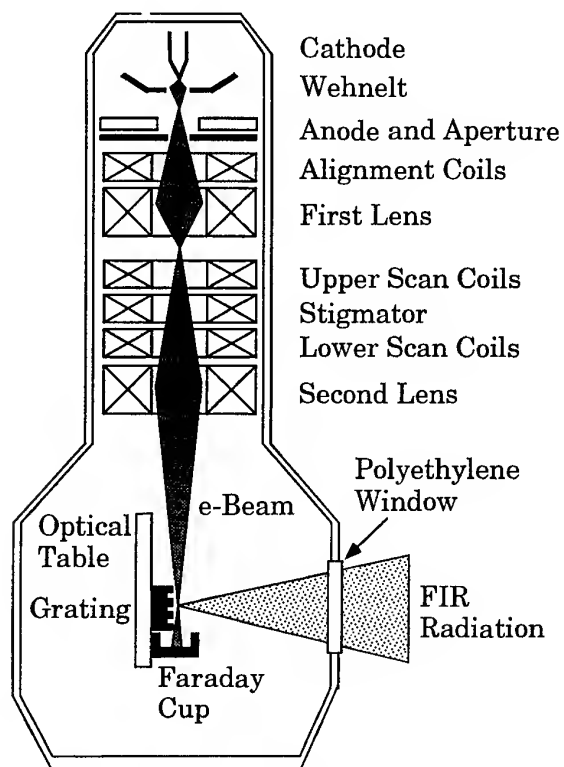


FIG. 1. Diagram of the SEM optical system.

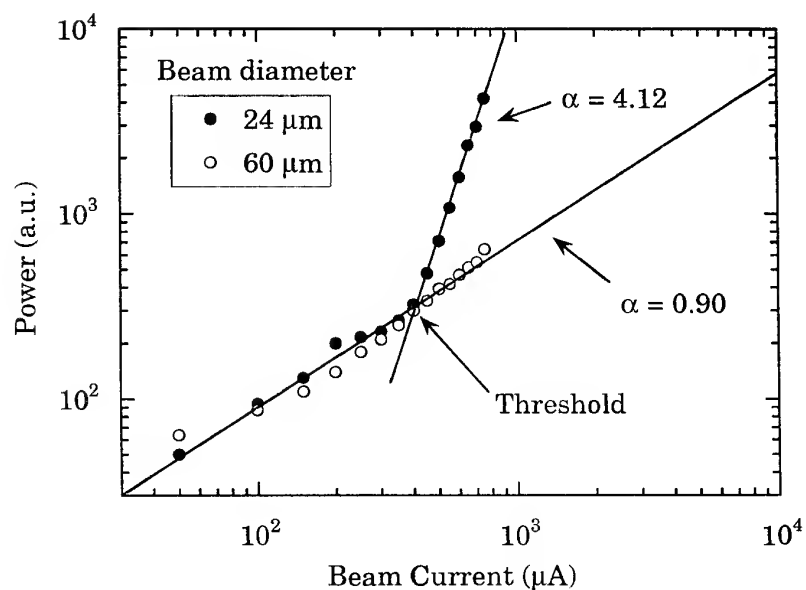


FIG. 2. GCO emission vs. electron beam current.



## A High Brightness Photoinjector for Free Electron Laser Applications

F.V. Hartemann\*, E.C. Landahl\*, N.C. Luhmann, Jr,

University of California, Davis  
Department of Applied Science  
P.O. Box 808, L-794  
Livermore, CA 94550

\*Also with the Institute for Laser Science and Applications at Lawrence Livermore National Laboratory

J.P. Heritage

University of California, Davis  
Department of Electrical and Computer Engineering  
Davis, CA 95616

G.P. Le Sage

Lawrence Livermore National Laboratory  
P.O. Box 808, L-280  
Livermore, CA 94550

C.H. Ho

Synchrotron Radiation Research Center  
No. 1 R&D Road VI, Hsinchu Science-Based Industrial Park  
Hsinchu 3007, Taiwan, Republic of China

### Introduction

Relativistic electron bunches properly phased within a few tens of femtoseconds can radiate coherently when passed through a short magnetic wiggler where the radiation wavelength is limited by the bunch length and the radiated power is determined by the peak current and number of the electron bunches. [1] A properly prebunched beam should result in high gain, permitting saturation using a short free electron laser (FEL) wiggler and producing a corresponding broadband pulse. [2] (Figure 1) In a waveguide, the FEL can be operated at grazing (where the axial bunch velocity matches the electromagnetic wave group velocity) so that the output pulse is extremely short and chirped over the full interaction bandwidth. A negative group velocity dispersion region can further compress the pulse to achieve high peak powers. [3] (Figure 2)

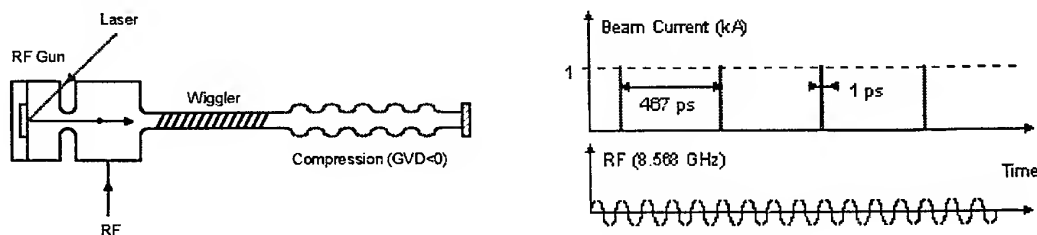


Figure 1. Basic concept of the photoinjector driven chirped pulse free electron laser.

The production of bursts of short, high peak current, relativistic electron bunches can be achieved using an rf photoinjector, where a 1.5 cell accelerating cavity has its cathode illuminated with a series of ultrashort UV laser pulses. The resulting photoelectrons have low energy spread and can be accelerated when the laser pulses arrive at the cathode properly timed with respect to the rf phase in the cavity. Optimization of parameters to produce 2.2 MW, 1.5 ps pulses of coherent synchrotron radiation with an instantaneous bandwidth of 125 to 225 GHz have resulted in the design and operation of an X-band photoinjector to be an FEL electron source. [4] Initial FEL experiments are expected to commence by Fall, with a long term aim of developing a facility providing output in the 100 mm to 3 mm region using a 11 period adjustable planar wiggler with a 3 cm period. At shorter wavelengths, power is expected to drop below 100 kW as the coherence condition is no longer maintained.

In addition to its use in a fast wave structure for generating coherent synchrotron radiation, the X-band photoinjector should produce a high quality electron beam which has a variety of other uses. Accelerator physics

should be possible on the X-band photoinjector not possible at other photoinjector frequencies, and the resulting dense beam (and its synchronization to an external laser) can be exploited to perform a number of laser-electron scattering experiments at relativistic energies and high laser intensities. These include studies of Kapitza-Dirac scattering [5] (electron diffraction off a standing laser wave), Pondermotive scattering (vacuum laser acceleration) [6], and nonlinear Compton scattering (development of a compact alternative to 3<sup>rd</sup> generation X-ray light sources) [7]. The X-band photoinjector is also ideally suited to perform as an injector for high gradient electron accelerators and other novel accelerator schemes such as laser plasma wakefield [8] and inverse free electron laser accelerators [9-10].

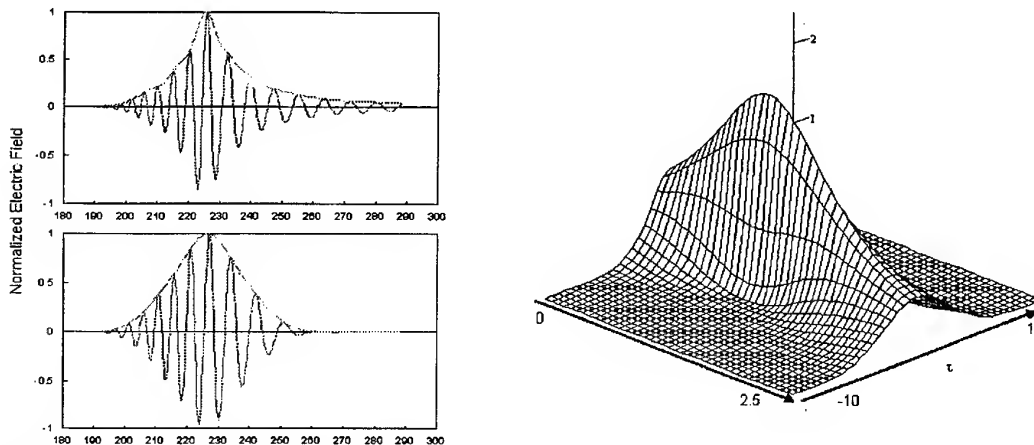


Figure 2. Left: Chirped pulse exiting the FEL plotted against normalized time  $\tau = \omega t$  according to simulation (top) and theory (bottom). Right: Compression of the FEL pulse in a negative GVD structure. Intensities are normalized to the fields at input and the distance is measured in units of the distance required to remove all chirp, which is set by the physical parameters of the GVD structure.

#### X-band Photoinjector Design and Photoelectron Production

The rf gun was designed using the LANL codes SUPERFISH and PARMELA and is based on a scaled and optimized version of a 1 1/2 cell S-band rf gun. Both a cold test gun and a high power gun have been fabricated and tested. The high accelerating gradients are provided by an X-band rf system consisting of a Traveling Wave Tube amplifier and a SLAC SL-3 8.424 GHz klystron which produces 11 MW, 2  $\mu$ s pulses which when delivered to the gun results in an average accelerating gradient of 150 MV/m. The fill time of the cavity is long enough for hundreds of electron bunches to be produced per rf pulse; these bursts could be repeated at up to 30 Hz with the implementation of a high repetition rate laser system.

The laser system is based on Chirped Pulse Amplification (CPA) and is designed to produce sub-picosecond, GW peak power pulses (center wavelength 800 nm) which can be converted with an efficiency > 1% into UV, at which point the photon energy is above the work function of copper. Production of 1 nC bunches of photoelectrons on a copper cathode in less than a picosecond at a repetition rate of 10 Hz should be possible with this design. High repetition rates can be achieved by sending a train of pulses into the CPA system. The resulting pulses will have a smaller energy than when singly amplified, but equivalently high photoelectron yields should still be possible with the use of a high quantum efficiency cathode such as Cs<sub>2</sub>Te instead of copper.

Emittance growth in the photoinjector is minimized using a solenoid bucking pair around the rf cavity. A Faraday cup was used to measure the first photoelectrons produced, which was accomplished using partial rf power and a commercial mode locked laser oscillator followed by our CPA system illuminating a copper cathode. [11] Following this initial demonstration, a laser upgrade is underway to improve the timing and amplitude stability of the amplified laser pulses and to implement a high repetition rate semiconductor laser oscillator. The semiconductor laser is designed to produce stable pulses at up to the fourth sub-harmonic of the rf (2.1 GHz) and can be driven using a field pickup inside the photoinjector cavity itself to insure timing synchronism. An electro-optic fiber switch is being evaluated for use as a pulse train modulator at the laser repetition rate.

### Cathode Illumination

The implementation of the above switch will allow for stable pulse trains to be generated by our amplifier system using a feedback loop. In addition, we will be able to program in a desired output pulse train envelope for cathode illumination. In this manner, the shot to shot charge of the photoinjector can be adjusted to explore and mitigate wakefields in the photoinjector itself and later optimize the multibunch FEL.

Optimal X-band photoinjector operation requires sub-picosecond pulses, which are coincidentally also ideal for exploring temporal shaping of laser pulses (accomplished using a phase and amplitude mask in the Fourier plane of the compression gratings). [12-13] To our knowledge, detailed studies of temporal pulse shaping has not been undertaken on photoinjectors. For example, by generating a flat-top (instead of gaussian) pulse in time a uniform electron density could be created at the cathode. In addition our broadband laser amplifier will be able to put varying pulse lengths onto the cathode while maintaining constant energy per pulse (down to 30 fs) and permit experimental exploration of the laser limits on electron bunch duration for X-band photoinjectors.

The importance of spatial shaping of the photocathode illumination laser has already been demonstrated and will be implemented on our system as well. An additional benefit of working at X-band is that the laser can be brought into the cavity at near normal incidence ( $3^\circ$ ). In existing S-band photoinjectors a separate port must be made in the photoinjector wall to accommodate the laser entrance. The short size of X-band cavities makes this normal incidence possible and means that a square profiled laser pulse is easier to achieve. (At oblique incidence angles a great deal of care must be taken to ensure that the short laser pulse illuminates a cathode area at the same time.) We expect that the ease of placing the illuminating laser on the cathode will allow us to explore more subtle variations in spatial profile. Along with new PARMELA simulations, this added laser control will greatly expand the parameter space available for photoinjector design.

### Acknowledgements

This work was supported in part by DoD/AFOSR (MURI) under F49620-95-1-0253, AFOSR (ATRI) under F30602-94-2-001, ARO under DAAH04-95-1-0336, and in part under the auspices of the U.S. Department of Energy by the Lawrence Livermore National Laboratory under contract No. W-7405-ENG-48 through the Institute for Laser Science and Applications.

### References

- [1] A. Gover, F.V. Hartemann, G.P. Le Sage, N.C. Luhmann, Jr., R.S. Zhang, and C. Pellegrini, "Time and Frequency Domain Analysis of Superradiant Coherent Synchrotron Radiation in a Waveguide Free Electron Laser," *Physical Review Letters* 72, 1192 (1994).
- [2] F.V. Hartemann, G. P. Le Sage, D. B. McDermott, and N.C. Luhmann, Jr., "Coherent Synchrotron Radiation in a Cylindrical Waveguide with a Helical Wiggler," *Phys. Plasmas* 1, 1306 (1994).
- [3] F.V. Hartemann, G.P. Le Sage, A. L. Troha, N.C. Luhmann, Jr., and S.N. Fochs, "Transform-limited Coherent Synchrotron Radiation Wavepackets in a Chirped Pulse Free Electron Laser," *Phys. Plasmas* 3, 2446 (1996).
- [4] G. P. Le Sage *et al.*, "Theory and Design of a Photoinjector-Driven Chirped Pulse Free-Electron Maser," *IEEE Trans. Plasma Sci.* 24, 781 (1996).
- [5] P.L. Kapitza and P. A. M. Dirac, "The Reflection of Electrons from Standing Light Waves," *Proc. Cambridge Philos. Soc.* 29, 297 (1933).
- [6] F. V. Hartemann *et al.*, "Nonlinear Pondermotive Scattering of Relativistic Electrons by an Intense Laser Field at Focus," *Phys. Rev. E* 51, 4833 (1995).
- [7] F. V. Hartemann and A.K. Kerman, "Classical Theory of Nonlinear Compton Scattering," *Physical Review Letters* 76, 642 (1996).
- [8] E. Esarey, P. Sprangle, J. Krall, and A. Ting, "Overview of Plasma-based Accelerator Concepts," *IEEE Trans. Plasma Sci.*, 24, 252 (1996).
- [9] E.D. Courant, C. Pellegrini, and W. Zakowicz, *Phys. Rev. A* 32, 2813 (1985).
- [10] F.V. Hartemann *et al.*, "Chirped Pulse Inverse Free Electron Laser Vacuum Accelerator," presented at the Eighth Advanced Accelerator Concepts Workshop (1998) and submitted to *Physical Review Letters*.
- [11] E.C. Landahl *et al.*, "Phase Noise Reduction and Photoelectron Acceleration in a High-Q RF Gun," *IEEE Trans. Plasma Sci.* 26, 814 (1998).
- [12] J.P. Heritage, A.M. Weiner, and R.N. Thurston, "Picosecond Pulse Shaping by Spectral Phase and Amplitude Manipulation," *Opt. Lett.* 10, 609 (1985).
- [13] A.M. Weiner, J.P. Heritage, and E.M. Kirschner, "High-resolution Femtosecond Pulse Shaping," *J. Opt. Soc. Am. B* 5, 1563 (1988).

## Coherent Smith-Purcell Radiation in the Millimeter Wave Region

Kimihiko Ishi, Yukio Shibata, Mikihiro Ikezawa, Toshiharu Takahashi,<sup>A</sup> Tomochika Matsuyama,<sup>A</sup> Katsuhei Kobayashi,<sup>A</sup> and Yoshiaki Fujita<sup>A</sup>

Research Institute for Scientific Measurements, Tohoku University, 2-1-1 Katahira, Sendai, 980-8577, Japan

<sup>A</sup>Research Reactor Institute, Kyoto University, Kumatori, 596-0821, Japan

### Abstract

Coherent Smith-Purcell radiation, generated by the passage of short-bunched electrons from a linear accelerator above a lamellar-type grating, has been observed in the millimeter wave region. The intensity of the radiation decreases with the increase of the beam height, or the distance of the beam from the grating. The radiation intensity varies sharply with the depth of the groove. The observed properties of radiation are discussed on the basis of a three dimensional theory of Smith-Purcell radiation.

### 1. Introduction

Since the discovery of Smith-Purcell radiation (SPR) [1], many researchers confirmed the dispersion relation of SPR [2],

$$n\lambda = g\left(\frac{1}{\beta} - \cos\theta\right), \quad (1)$$

where  $\lambda$  and  $n$  are the wavelength and the order of SPR, respectively,  $g$  is the grating period,  $\beta$  the ratio of the velocity of electrons to the light velocity in vacuum, and  $\theta$  the emission angle. Properties of SPR, however, have not been studied well by the experiment except for the dispersion relation. This is mainly due to the difficulty in controlling the electron beam with the precision of the wavelength of the radiation.

When we use a high-energy beam of electrons, the required precision in controlling the beam position is relaxed by the Lorentz factor,  $\gamma = (1 - \beta^2)^{-1/2}$ .

Using short-bunched beams of linear accelerators of 40 MeV ( $\gamma=78$ ) and of 150 MeV ( $\gamma=293$ ), we observed coherent SPR in the millimeter wave region [3]. Radiation from every electron in a bunch adds coherently in the spectral region where the wavelength is comparable to or longer than the longitudinal length of the bunch.

We examined the dependences of SPR on the beam height, and on the groove depth, by observing the SPR enhanced by the coherence effect in the millimeter wave region. We used lamellar-type gratings to generate SPR. The observed SPR

is compared with the three dimensional theory of SPR based on the modal expansion method [4].

### 2. Experiment

The experimental setup is schematically shown in Fig. 1. The short-bunch beam of electrons from the linear accelerator passed near a grating G made of aluminum to emit SPR.

The SPR was reflected by the plane mirror M1 to a grating-type far-infrared spectrometer which covered the wavelength region from 0.1 mm to 6 mm. The radiation was detected with a helium-cooled Si bolometer. The acceptance angle of the measuring system was  $33 \text{ mrad} \times 72 \text{ mrad}$ .

In the experiment we prepared lamellar-type gratings with 6mm period. At first, we observed the dispersion relation of SPR. Next we examined the dependences of SPR on the beamheight and on the groove depth. When we measured the dependence of SPR on the beam height, we moved the grating perpendicularly to the beam trajectory by a pulse motor. To observe the dependence on the groove depth, we prepared gratings whose groove depth was variable.

A short-bunch beam of electrons of 40 MeV was generated by an L-band liner accelerator of Kyoto University. The beam conditions were as follows: Duration of a burst of electrons was 33 ns and its repetition rate was 55 Hz. The average beam current was  $1.5 \mu\text{A}$ , and hence the number of electrons per bunch  $N_e$  was  $4 \times 10^9$ . The cross section of the beam was shaped by the aluminum collimator C in Fig. 1 which had an opening of  $10 \times 12 \text{ mm}^2$ .

### 3. Experimental results and discussion

#### 3.1. Dependence on beam height

The dependence of the intensity of SPR on the beam height  $h$  was measured at the wavelengths of 2.5 mm. The results are shown by open circles in Fig. 2. The intensity is plotted in logarithmic scale.

In Fig.2, the exponential dependence of the intensity on the beam height,  $\exp(-4\pi h/\beta\gamma\lambda)$ , which is widely accepted to explain the dependence, is shown by the dotted line. The observed intensities

decrease more rapidly than the line as the beam height increases.

Following the three dimensional theory of the SPR [4], the intensity of the SPR is written as,

$$\frac{dP}{d\lambda} = P_0 \int T(\theta, \phi) R(g, \theta, \phi) H(h, \theta, \phi) d\phi, \quad (2)$$

where  $P_0$  is a constant and the factor  $T$  is a function of the emission angle  $\theta$  and  $\phi$ , and the factor  $R$  is a complicated function, which depends on the cross section of the lamellar grating, and  $g$  is the grating constant. The dependence of SPR on the beam height  $h$  is included in the factor  $H(h, \theta, \phi)$  as,

$$H(h, \theta, \phi) = \exp\left(-\frac{4\pi h}{\beta\gamma\lambda} \sqrt{1+t^2}\right), \quad (3)$$

where  $t = \beta\gamma \sin\theta \sin\phi$ . The solid curve in Fig. 2 shows the theoretical dependence of Eq.(3) integrated over the acceptance angle of the optical system and the beam cross section. The solid curve agrees well with the experimental results.

### 3.2. Dependence on groove depth

We measured the dependence of the SPR intensity on the groove depth at the wavelength of 2.4 mm with the 6 mm period grating, and also the dependence at  $\lambda = 4.8$  mm with the 12 mm period grating. The results are shown by the filled circles for  $\lambda = 2.4$  mm and open circles for  $\lambda = 4.8$  mm in Fig. 3, where the abscissa is the groove depth normalized by the grating constant.

According to the theory, the two measurements should coincide. The observed dependences of filled and open circles in Fig. 3 are almost similar to each other. Both curves show structure of five minima in a range from 0.04 to 0.92 of  $d/g$ .

We have calculated the relative variation of the SPR intensity as a function of the groove depth, and the result is shown by the solid curve in the lower part of Fig. 3, which has structure similar to the experimental ones. The theory is qualitatively in agreement with the experiment.

### References

1. S.J.Smith and E.M.Purcell, Phys. Rev. 92, 1069 (1953).
2. B.M.Bolotovskii and G.V.Voskresenskii, Usp. Fiz. Nauk 94, 377 (1968) [Sov. Phys. Uspekhi 11, 143 (1968)].
3. K.Ishi, Y.Shibata, T.Takahashi, S.Hasebe, M.Ikezawa, K.Takami, T.Matsuyama, K.Kobayashi, and Y.Fujita, Phys. Rev. E51, R5212 (1995).
4. Y.Shibata, S.Hasebe, K.Ishi, S.Ono, M.Ikezawa, T.Nakazato, M.Oyamada, S.Urasawa, T.Takahashi, T.Matsuyama, K.Kobayashi, and Y.Fujita, Phys. Rev. E57, 1061 (1998).

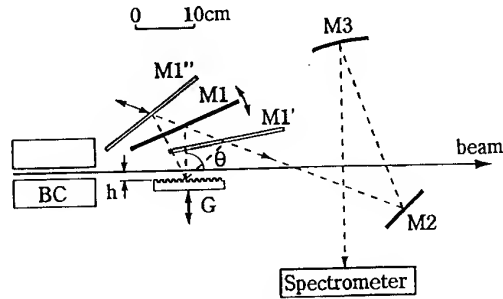


Fig. 1. Schematic diagram of experimental setup. G: Grating; M1, M2: plane mirrors; M3: collecting mirror;  $\theta$ : emission angle;  $h$ : beam height. The broken lines show the optical axes, and the mirror M1 is moved along positions M1' and M1''.

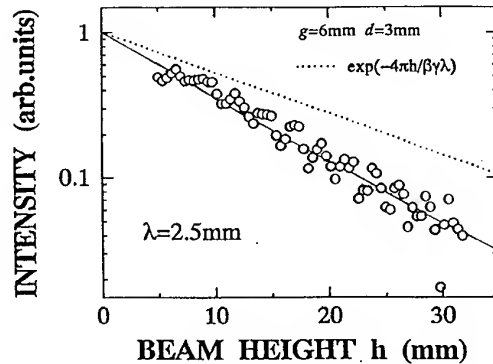


Fig. 2. Dependence of intensity on the beam height at  $\lambda = 2.5$  mm. The solid curve shows the calculated intensity based on the three dimensional theory and the dotted curve shows the exponential function of  $\exp(-4\pi h/\beta\gamma\lambda)$ .

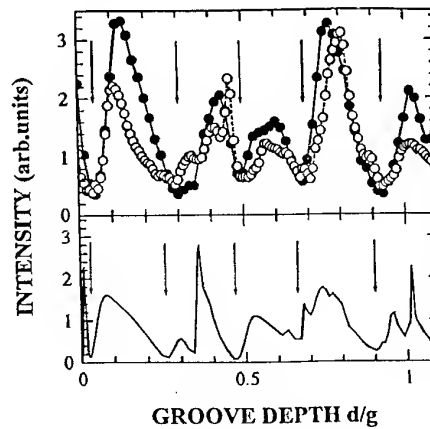


Fig. 3. Dependence of the SPR intensity on the groove depth; experiment (upper) and theory (lower). The filled circles show intensities observed with the 6 mm-period grating at  $\lambda = 2.4$  mm and the open circles those with 12 mm-period grating at  $\lambda = 4.8$  mm.

## Energy-Phase Correlation in a Bunched Electron Beam. A New Scheme for Free-Electron Generators of Radiation

A. Doria, G.P. Gallerano, E. Giovenale, S. Letardi, G. Messina, C. Ronsivalle

ENEA, Dipartimento Innovazione, Divisione Fisica Applicata  
Via E. Fermi 45, P.O. Box 65, 00044 Frascati (Rome) – ITALY

### Introduction

During the recent years a new concept arose, in the field of free-electron radiation sources for the generation of coherent radiation in the Millimetre (MM) and Sub-Millimetre (sub-MM) spectral range [1]. The basic idea is to exploit the repeatability of the electron bunches generated by a radio-frequency (RF) accelerator and the coherent nature of the electron distribution respect to the RF phase; this emission mechanism is called "Coherent Spontaneous Emission" (CSE). Within this frame many devices are now operating in the world [2]. A new scheme is now proposed that goes beyond the CSE by using the manipulation of the single electron bunch in the energy-phase space. In fact, when a certain correlation in energy and phase is reached, the CSE is enhanced because the phase emission of a single electron interferes constructively with that of the other electrons in the bunch.

### The Theory

The CSE occurs when an electron bunch has a length comparable with the period of the radiation that will be generated in the undulator. Under these conditions, in fact, all the electrons in the bunch have a similar phase and emit coherently, i.e. the emission is proportional to  $N^2$ , where  $N$  is the number of electrons in the single bunch ( $\sim 10^8$ ), while the incoherent emission is proportional to  $N$ . Moreover if the electron current is generated in a RF accelerator it carries the modulation of the RF itself and of all its harmonics with a relative amplitude dependent on the bunch shape [1]. These harmonic act as external driving forces. This means that when this current is propagated along the undulator it can generate only the harmonics of the RF that fall within the spontaneous emission curve allowed by the general device parameters (electron energy, undulator field, undulator parameter, etc.). The power emitted on the single harmonic  $l$  can be calculated from the time averaged flux of the Poynting vector as follows [1]:

$$P_{l,0,n} = \frac{\beta_{gl}}{2Z_0} |A_{l,0,n}|^2 \quad \text{where} \quad A_{l,0,n} = -\frac{Z_0}{\beta_{gl}} I_P \frac{C_l}{2} \frac{K}{\beta\gamma} F \frac{L}{\sqrt{ab}} \left[ \frac{\sin(\theta_l/2)}{\theta_l/2} \right] e^{i\theta_l/2} \quad (1)$$

and where  $\theta_l = \left( \frac{\omega_l}{c} \frac{1}{\beta_z} - k_{0,n} - k_u \right) L$  is the usual definition of the phase shift parameter describing the FEL

resonance condition in a waveguide [3],  $a$  and  $b$  are the waveguide transverse dimension,  $Z_0 = 377 \, \Omega$  is the free space impedance,  $I_P$  is the peak current in the bunch,  $\beta_{gl}$  is the normalized group velocity of the waveguide mode at the frequency  $\omega_l$  with wave vector  $k_{0,n}$ ,  $F$  is a form factor describing the overlapping between the e-beam transverse distribution and the waveguide mode, and  $C_l$  is the coefficient of the Fourier expansion of the

normalized bunch profile at the  $l$ -th harmonic as defined in [1]. The phase factor  $e^{i\theta_l/2}$  in (1) has the important physical meaning of showing that the external driving current and the radiated field are no longer in phase when the electron drift velocity does not match the resonance condition  $\theta_l = 0$ .

We can now treat the electron bunch as an ensemble of  $N_e$  particles distributed in the phase space  $(\Psi, \gamma)$ , each having energy  $\gamma_j$  and phase  $\Psi_j = \omega_{RF} t_j$ . The total radiated power can be calculated as follows [4]:

$$P_{l,0,n} = \frac{\beta_{gl}}{2Z_0} |A_{l,0,n}|^2 \quad \text{where} \quad A_{l,0,n} = -\frac{Z_0}{\beta_{gl}} \frac{q}{T_{RF}} \frac{KL}{\sqrt{ab}} F \sum_{j=1}^{N_e} \frac{1}{\beta_j \gamma_j} \frac{\sin(\theta_j/2)}{\theta_j/2} e^{i \left( \frac{\theta_j}{2} + l \Psi_j \right)} \quad (2)$$

From eq.2 it can be easily seen that the emitted power  $P_{l,0,n}$  can be maximised when the single electron contribution in the sum of the expansion coefficient  $A_{l,0,n}$  interferes constructively with the others. This happens when the phase term of each electron depends only on the harmonic number, i.e.  $\left( \frac{\theta_j}{2} + l \Psi_j \right) = \phi_l$ . This relation indicates an ideal correlation in the distribution of energy and phase in the phase space that can be easily

obtained [4] substituting the expressions of  $\theta$  and  $\psi$  and remembering that  $\psi = 0$  for  $\beta_z = \beta_{z0}$ . Finally the ideal phase matching curve is:

$$\psi = -\pi \frac{L}{cT_{RF}} \left( \frac{1}{\beta_z(\gamma)} - \frac{1}{\beta_{z0}} \right) \quad (3)$$

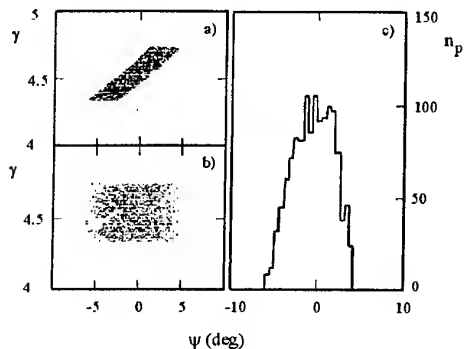


Fig. 1

gives a total output power one order of magnitude higher than for the uncorrelated case (see Fig. 2b), moreover the higher harmonics components are enhanced (see Fig. 2a) while in the uncorrelated case are depressed by the Fourier coefficients of the bunch shape (see Fig. 2b).

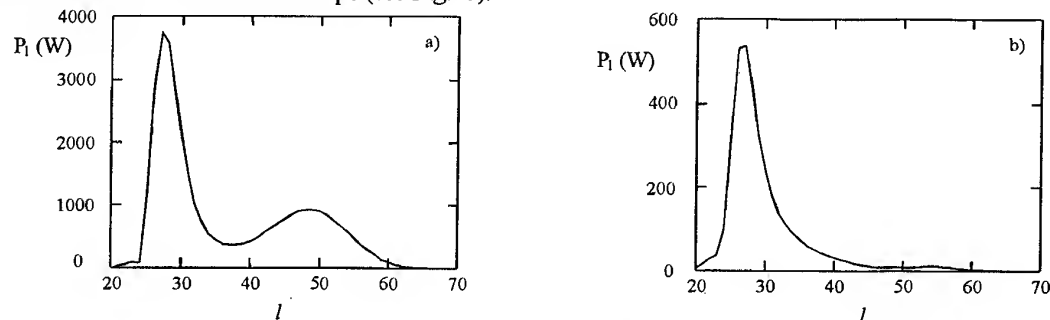


Fig. 2

To test the feasibility of this idea a device has been designed [4] with the PARMELA simulation code. A RF-Linac with 3+1/2 cavities has been considered as electron accelerator, then, after 5 cm of drift space, a Phase-Matching device (PMS) has been considered to rotate the electrons in the phase space (see Fig. 3b). In this way the electron distribution approaches the "ideal" one, while at the exit of the Linac (see Fig. 3a) it shows a minimum energy spread but no correlation in phase.

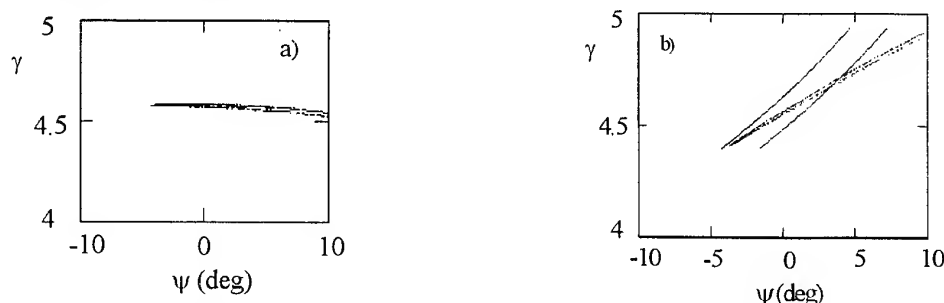


Fig. 3

The spectra obtained from the simulation confirm the theoretical model. An experiment based on these results is in preparation at the ENEA Frascati research centre.

#### References

1. A. Doria, R. Bartolini, J. Feinstein, G.P. Gallerano, R.H. Pantell, IEEE-JQE 29, 1428, (1993)
2. F. Ciocci, R. Bartolini, A. Doria, G.P. Gallerano, E. Giovenale, M.F. Kimmitt, Phys. Rev. Lett. 70, 928, (1993)
3. J.M. Ortega, R. Prazeres, F. Glotin, D.A. Jaroszynski, Phys. Rev. E 57, 1053, (1998).
4. A. Doria, G.P. Gallerano, A. Renieri, Opt. Commun. 80, 417, (1991)
5. A. Doria, G.P. Gallerano, E. Giovenale, S. Letardi, G. Messina, C. Ronsivalle, Phys. Rev. Lett. 80, 2841, (1998).

## A Smith-Purcell Experiment

G Doucas<sup>1</sup>, M F Kimmitt<sup>2</sup>, G Korschinek<sup>3</sup>, C Wallner<sup>3</sup> and J E Walsh<sup>4</sup>

1. Particle and Nuclear Physics Laboratory, University of Oxford,  
Oxford OX1 3RH, UK

2. Department of Physics, University of Essex, Colchester CO4 3SQ, UK

3. Fachbereich der Technischen Universität München, Garching, Germany

4. Department of Physics and Astronomy, Dartmouth College, Hanover,  
New Hampshire 03755-3528, U S A

### Abstract

An experiment to generate Smith-Purcell radiation in the far-infrared region using relativistic electrons is described. The electrons are produced by a pulsed, laser-driven electron gun positioned at the terminal of a Van de Graaff accelerator.

### Introduction

The interaction of an electron beam with a metallic grating surface produces an electromagnetic wave known as Smith-Purcell (S-P) radiation, named after the first observers of this phenomenon[1]. In a series of experiments over the past few years we have observed radiation over a wavelength range from more than 1mm down to less than 10 $\mu$ m using electron energies between 25keV and 50MeV [2][3][4][5]. Our initial objective in this research was to test the S-P dispersion relationship over a wide wavelength range. The spectrum of this radiation,  $\lambda_{SP}$ , is given by the equation

$$\lambda_{SP} = \lambda_G (1/\beta \cos\theta)$$

where  $\lambda_G$  is the grating period,  $\beta$  is the electron velocity in units of  $c$ , the velocity of light and  $\theta$  is the angle of emission relative to the electron beam direction. All of our results confirm this relationship.

The second objective was to measure the radiated power from S-P sources and to study its variation with angle [6]. We have recently developed a theory [7] describing the S-P effect in terms of the surface charges induced on the grating by the passing electrons and 'dragged' along by it. The source of the emitted radiation is the acceleration imposed on the moving charge by the grooves of the grating. The calculation leads to a formula describing the spectral distribution of emitted, incoherent power at a specific wavelength in terms of the beam and grating parameters. We have then compared this theory with our experimental results and found satisfactory agreement over the wavelength range 400-1500 $\mu$ m where we have made accurate power measurements [8].

The third and most important objective was to use our results in the design of a useful source for spectroscopic purposes. The S-P effect offers the attractive prospect of a compact and efficient method of generating tunable radiation, especially in the far infrared (FIR) where suitable sources are very sparse. Very recently we have taken the first step to achieving this goal with a CW source of FIR radiation [9]. This has been recognised as a major advance in FIR source development [10].

The present experiment, which is being carried out on a modified Van de Graaff accelerator at the Technical University in Munich, is designed to measure the radiated power of S-P radiation in the 30-120 $\mu$ m region and compares it with theory.

### Experimental Arrangement

One of our early experiments was based on a Van de Graaff accelerator at Oxford University [2]. This used a triode electron gun which was pulsed to give 6 $\mu$ s long pulses of electrons which were then accelerated to 3.6MeV. Beam currents reached a maximum of 200mA with current densities of 1.4Acm<sup>-2</sup>. S-P radiation was measured from 400-1500 $\mu$ m using an InSb electron bolometer as



the detector. The Munich experiment is planned to extend measurements to shorter wavelengths. The major difference from the Oxford experiment is the use of a photocathode. This is excited by quadrupling the photon energy of a 1064nm Nd:Yag laser from 1.16 to 4.65eV. Preliminary studies indicated that tantalum is a suitable material for the cathode and this is illuminated with the 266nm laser beam of 5.5mj energy and 20ns pulse duration. With a 3mm<sup>2</sup> spot size a maximum beam current of 500mA has been obtained without plasma production. It was expected that the photocathode would produce a significantly better emittance compared with Oxford and, with the higher current, a much improved current density. So far this has not been achieved, probably due to poor focusing of the electrons after acceleration to 2MeV by the Van de Graaff.

The important parameters of an electron beam for producing SP radiation are current density and small size. For incoherent output the power is proportional to the current interacting with the grating and the height of the electrons above the grating must be a small fraction of the emitted wavelength. We are at present modifying the focusing arrangements of the Munich experiment to achieve a smaller beam as so far only very modest power output has been obtained.

### Detection and Analysis

The InSb electron bolometer used at Oxford has a response time of ~500ns, much longer than the 20ns photoexcited electron beam in this experiment. Because of the hoped-for improved emittance and higher current density, the wavelength range chosen was 50-120 $\mu$ m, where Ge:Ga extrinsic photoconductors have fast response (20-30ns) and an excellent noise equivalent power of  $<10^{-11}$  WHz<sup>-1/2</sup>. Because the resistance of the detector used is ~15k ohm current amplifiers were designed to achieve the necessary bandwidth to display the short pulse.

Initial analysis of the output will be with a large, evacuable Czerny-Turner grating monochromator [11]. This is an f/3 instrument using 250mmx200mm gratings and has an excellent throughput. Assuming that good signal-to-noise is obtained, this will be replaced by a Martin-Puplett interferometer for a more detailed study of the output, with higher resolving power.

### Acknowledgements

Support for this research from the British Council is gratefully acknowledged. We are indebted to David Smith, of Oxford University, for the design and construction of suitable current amplifiers.

### References

- [1] S J Smith and E M Purcell Phys. Rev. **92**, 1069 (1953)
- [2] G Doucas, J H Mulvey, M Omori, J E Walsh and M F Kimmitt Phys. Rev. Lett. **69**, 1761 (1992)
- [3] K J Woods, J E Walsh, R E Stoner, H G Kirk and R C Femow Phys. Rev. Lett. **74**, 3808 (1995)
- [4] M Goldstein, J E Walsh, M F Kimmitt, J Urata and C L Platt Phys. Rev. Lett. **71**, 452 (1997)
- [5] J H Brownell, J E Walsh, H G Kirk, R C Femow and S H Robertson Nucl. Instr. and Meth. **A393**, 323 (1997)
- [6] G Doucas, J H Mulvey, M Omori, J E Walsh and M F Kimmitt Nucl. Instr. and Meth. **A331**, 609 (1993)
- [7] J H Brownell, J E Walsh and G Doucas Phys. Rev. E, **57**, 1075 (1998)
- [8] J H Brownell, G Doucas, M F Kimmitt, J H Mulvey, M Omori and J E Walsh J. Phys. D: Appl. Phys. **30**, 2478 (1997)
- [9] J Urata, M Goldstein, M F Kimmitt, A Naumov, C Platt and J E Walsh Phys. Rev. Lett. **80**, 516 (1998)
- [10] Richard Temkin Science **280**, 854 (1998)
- [11] G N Harding, M F Kimmitt, J H Ludlow, P Porteous, A C Prior and V Roberts Proc. Phys. Soc. **77**, 1069 (1961)

# Proposal of THz FEL using a Photomixing Field Emission Cathode

Kuniyoshi Yokoo

Reserch Institute of Electrical Communication, Tohoku University

Katahira 2-1-1, Aoba-ku, Sendai 980-8577, Japan

Phone: +81-22-217-5510, FAX: +81-22-217-5513

e-mail: yokoo@riec.tohoku.ac.jp

**Abstract** The paper proposes a frequency tunable, medium power, and compact electromagnetic wave source at frequencies in excess of terahertz using a photomixing of semiconductor field emitter array and discusses the radiation power and the efficiency of the source.

## 1. Introduction

The terahertz (THz) wave radiation from photoconductive antennas has been reported by photo-excitation of femtosecond laser pulses or two continuous and frequency-offset pump lasers [1][2]. In the former, a pulse current as narrow as sub-picosecond generated by the laser pulses flows through the antennas and radiates a very wide band electromagnetic wave ranging from millimeter to submillimeter waves, because the Fourier-transformed amplitude spectrum of the pulse currents covers these frequency ranges. On the other band, the latter generates a modulation current at the intermediate frequency of the pump lasers by photomixing of the frequency-offset pump lasers in the photoconductor. Then, these photo-excitation technique is expected to be a wide band frequency tunable and compact electromagnetic wave source at the THz wave for a spectroscopy of material science. However, the radiation power from the photoconductive antennas is the order of microwatt or less due to the limitation of applicable voltage on the photoconductors and the optical pump powers.

The paper proposes an application of the photomixing technique to a gated field emitter array (FEA) to generate modulation beams at frequencies in excess of terahertz. A semiconductor FEA produces excess emission current by photo-excitation due to generation of electron-hole pairs in the semiconductor emitter tips. A modulated emission at the intermediate frequency is produced in the FEA by the photomixing of frequency-offset pump lasers, as same as the photoconductors. These bunched electron beam generates easily a wide band and medium power electromagnetic wave over THz by an interaction between the beam and a wave in RF circuits, such as metal grating and dielectric loaded waveguide, and in some kind of radiative antennas. The medium power and wide band frequency tunable sources are very promising for many applications for molecular spectroscopy, terahertz radiometers and plasma diagnostics, as well as for future ultra high speed communication.

## 2. Terahertz Wave Radiation System using FEA

Figures 1 and 2 show conceptual configurations of wide-band THz wave sources based on photomixing technique of FEA. A modulation electron beam at the intermediate frequency of the pump lasers, such as single mode semiconductor lasers and Ti sapphire lasers, is generated by the photomixing in the semiconductor emitter tips and interacts with an electromagnetic wave in a radiative RF cuicuit and on the metal grating, as shown in Figs.1 and 2, respectively. In Fig.1, the electron transit time is adjusted to emphasize the radiation power at the specific frequency. On the other hand, there are two operation modes in the configuration shown in Fig.2. The beam interacts with the surface wave on the grating, so called a conventional backward wave interaction, and couples with the wave of the Fabry-perot mode, that is, the

stimulated Smith-Purcell radiation. The radiation frequency is widely tunable by changing the frequency of one of pump lasers and adjusting the beam velocity, as well as by changing the mirror spacing of the Fabry-Perot resonator in the Smith-Purcell radiation. In addition, the wave source is highly efficient, because the energy of spent electrons can be recovered by potential depletion on the collector.

### 3. Estimation of Radiation Power and Efficiency

The emission current of a photomixing field emission cathode is approximately given by

$$I = \frac{e\eta_{ex}P_0}{h\nu} \left[ 1 + \frac{2\sqrt{mP_1P_2}}{P_0} \frac{1}{\sqrt{1+\omega^2\tau^2}} \sin\omega t \right] \quad (1)$$

Where  $P_1$  and  $P_2$  are average powers of two pump lasers and  $P_0=P_1+P_2$  is the total incident power.  $\eta_{ex}$  is the extrinsic quantum efficiency determined by the intrinsic quantum efficiency and effective absorption coefficient for electron-hole pair generation in the emitter tips,  $h\nu$  and  $\omega$  are the average photon energy and the intermediate angular frequency of the pump lasers, respectively,  $m$  is the mixing efficiency, and  $\tau$  is the effective relaxation time relating to the conduction and the recombination of carriers.

The efficiency of electromagnetic wave radiation is given by the average and the modulation current and the beam and the RF voltages, as shown in Eq.(2).

$$\eta = \frac{I_1 V_1}{I_0 V_0} = \frac{2\sqrt{mP_1P_2}}{P_0} \frac{1}{\sqrt{1+\omega^2\tau^2}} \frac{V_1}{V_0} \quad (2)$$

Where  $V_0$  is the acceleration voltage of the beam and  $V_1$  is the effective RF voltage determined by the beam-wave coupling in an interaction circuit.

An ideal efficiency for  $\omega\tau \ll 1$  and  $P_1=P_2=P_0/2$  is approximated as  $\sqrt{m}V_1/V_0$ . The radiation power is approximately given by  $P_{out}=\eta I_0 V_0=6.25 \times 10^{-3} \eta_{ex} \sqrt{m} V_1$ , since the average emission current given by the first term in Eq.(1) is  $6.25 \times 10^{-3} \eta_{ex} [A]$  for the average optical pump power of 10mW and the beam voltage of 10kV. Then, the radiation power and the efficiency are about 20mW and 0.3%, respectively, for the values of  $\eta_{ex}=0.1$ ,  $m=0.1$  and  $V_1/V_0=10^{-2}$ , through the used values might be underestimated.

### 4. conclusion

The paper described the generation of modulation electron beams at frequencies in excess of THz using a photo-mixing semiconductor FEA. These bunched electron emission enable to generate a wide band and tenth mW order of output power of electromagnetic wave over THz with considerably high efficiency.

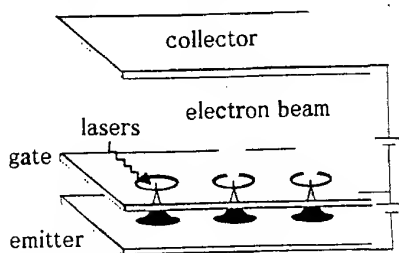


Fig.1. Conceptual view of THz wave source based on photomixing field emission and transit time interaction

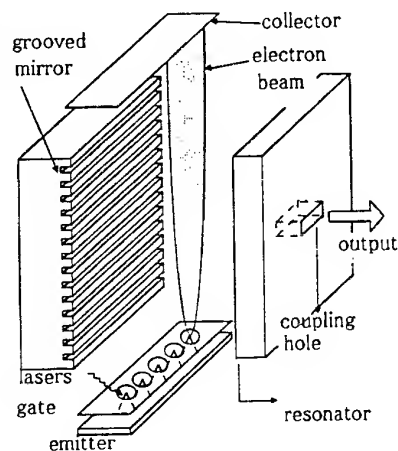


Fig.2. Schematic THz wave source based on travelling wave interaction of bunched beam by FEA.

- [1] M.Tani, S.matsuura, K.sakai, and S.Nakashima, Applied Optics 36, 7853 (1997)
- [2] E.R.brown, F.W.Smith, and K.A.McIntosh, J.apply.phys.73, 1480 (1993)

## Prebunched Free Electron Laser in the Millimeter Wave Region

Yukio Shibata, Satoshi Sasaki, Kimihiro Ishi, Syuiichi Ono, Yuta Inoue, Mikihiro Ikezawa, Toshiharu Takahashi,<sup>A</sup> Tomochika Matsuyama<sup>A</sup>, Katsuhei Kobayashi,<sup>A</sup> Yoshiaki Fujita,<sup>A</sup> and Evgueni Bessonov<sup>B</sup>

Research Institute for Scientific Measurements, Tohoku University, 2-1-1 Katahira, Sendai, 980-8577, Japan

<sup>A</sup>Research Reactor Institute, Kyoto University, Kumatori, 590-0494, Japan

<sup>B</sup>Lebedev Physical Institute, Russian Academy of Science, Leninsky pr.53, GSP V333, Moscow, 117924, Russia

### Abstract

Using a short-bunch beam of electrons from a linear accelerator, we have constructed a free electron laser (FEL) of a new type consisted of an open resonator and a bending magnet. The output of the FEL has a quasi-continuous spectrum composed of the higher harmonics of the RF of the accelerator.

### 1. Introduction

Coherent radiation such as coherent synchrotron radiation or coherent transition radiation is emitted from bunched electrons in the long wavelength region where the size of the bunch is near to or shorter than the wavelength [1-3]. By superposing the wavepackets of coherent synchrotron radiation on the subsequent electron bunches in a resonator, we have constructed a new type of FEL [4].

We observed the detuning curve, and the spectrum of the output of the resonator. We also examined the radiation field in the resonator. The output of the FEL had a broad-band spectrum in the millimeter wave region [4].

### 2. Experiment

A short-bunch beam of electrons of 35 MeV generated by an L-band linear accelerator (lineac) of Research Reactor Institute, Kyoto University, was guided to the resonator under magnetic field of 80 Gauss. The resonator is schematically shown in Fig.1, where the trajectory of the electron beam is shown by the solid curve. The bunches of electrons emit coherent synchrotron radiation in the millimeter wave region [1,2].

The wave packets of the coherent synchrotron radiation emitted from the bunches go back and forth in the resonator and are superposed on the subsequent bunches to stimulate emission from the bunches.

The resonator consisted of a plane mirror M1 of Al-foil and of a concave mirror M2 of fused quartz. The focal length and the aperture of M2 were 1200

mm and 130 mm in diameter. The mirror M2 had a window of 2 cm in diameter at its center. The output of the resonator was extracted through the window, and was guided to a grating-type far-infrared spectrometer. The radiation was detected with a He-cooled Si bolometer.

The RF of the lineac was 1300.8 MHz, and the energy  $E$  and its spread  $\Delta E/E$  were 35 MeV and 7 %. The width of the macro-pulse was 2  $\mu$ s in duration, and the pulse was repeated at 13 Hz. The beam current was 6  $\mu$ A in average and hence the number of electrons in a bunch was  $1.1 \times 10^9$ .

### 3. Results and Discussion

First we observed detuning curve or the variation of intensity with the cavity length at the wavelength  $\lambda$  of 2.3 mm. The results are shown by solid curve in Fig. 2. The observed curve had periodic structure whose period was  $\lambda/2$ . The structure was composed of main peak, secondary peak and a few sub-peaks. When the mirror M2 was tilted by 2 degrees to make the resonator ineffective, the output intensity decreases sharply. The result is shown by the dotted curve in Fig. 2.

The main peak was observed to be polarized in the orbital plane of the beam.

Next, fixing the cavity length at the maximum peak of the detuning curve, we observed the output spectrum. The result is shown by the solid curve in Fig. 3. The output was observed over a wide range in the millimeter wave region as a continuous spectrum: It is in fact composed of many lines of higher harmonics of RF of the accelerator.

The total output power was evaluated to be 52  $\mu$ W at the beam current of 6  $\mu$ A.

Finally, we observed the radiation field in the resonator, replacing the mirror M2 in Fig. 1 by the mirror which had a transparent slit of 4 mm width along the horizontal direction. The cavity length was fixed at the maximum peak of Fig. 2, and the radial distribution of the output intensity was observed through the slit by moving a small mirror behind the slit. The result is shown by the

solid curve in Fig. 4. The observed distribution of the intensity had a peak at the center of the mirror M2 and was nearly symmetric with respect to the mirror center.

The main peak was assigned to the  $TEM_{00}$  mode of the resonant cavity, because the synchrotron radiation should have the symmetry of this mode. The theoretical distribution of the  $TEM_{00}$  mode, shown by the dotted curve in Fig. 4, is in agreement with the observation.

The energy stored in the resonator is expressed as,

$$E(\omega) = \sum_{mode} |E_{mn}(\omega)|^2 g(\omega, Q, L) \left\{ \frac{\sin(N\omega T_b/2)}{\sin(\omega T_b/2)} \right\}^2,$$

$$g(\omega, Q, L) = \frac{1}{1 - 2R_{mn} \cos(\omega T + \phi_{mn}) + R_{mn}^2},$$

where  $E_{mn}$ ,  $\phi_{mn}$  are the radiation field and phase of the  $mn$ -mode, respectively,  $L$  is the cavity length,  $N$  is the number of bunches in the macropulse and  $T_b$  is the time interval between the successive bunches, and  $T = 2L/c$ . The loss of the resonator  $R_{mn}$  is related to the quality factor  $Q_{mn}$  as  $R_{mn} = \exp(-2\pi/Q_{mn})$ .

The equations show that the output of the resonator is composed of a subset of the higher harmonics of the RF of the accelerator and that the frequencies of the subset satisfy the resonance condition,

$$\omega T + \phi_{mn} = 2K\pi,$$

where  $K$  is integer. The phase factor  $\phi_{mn}$  is related to the band width of the spectrum of the output of the resonator. The theoretical value of  $\phi_{00}$  was 55 degree, and the calculated value of  $g(\omega, Q, L)$ , fitted to the observed intensity at  $\lambda = 2.3$  mm, is shown by the dotted curve in Fig. 3.

### References

1. T. Nakazato et al., Phys. Rev. Lett. **63**, 1245 (1989).
2. K. Ishi et al., Phys. Rev. **A43**, 5597 (1991).
3. Y. Shibata et al., Phys. Rev. **E49**, 785 (1994).
4. Y. Shibata et al., Phys. Rev. Lett. **78**, 2740 (1997).

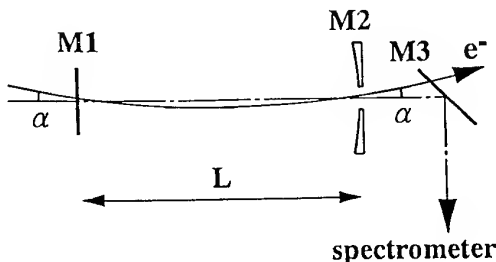


Fig. 1. Schematic layout of the resonator.

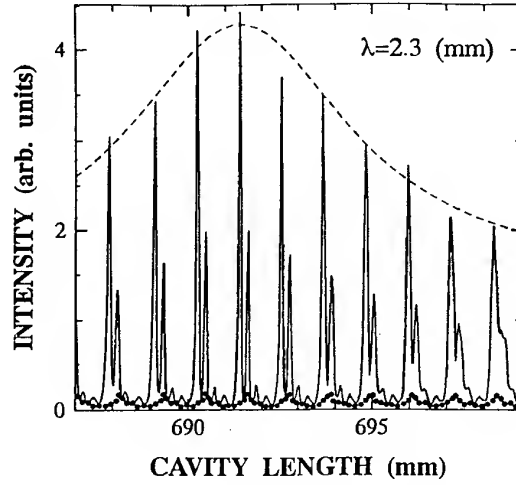


Fig. 2. Detuning curve of the intensity observed at  $\lambda = 2.3$  mm. The dashed curve is the calculated envelope of the peaks with  $Q=30$ .

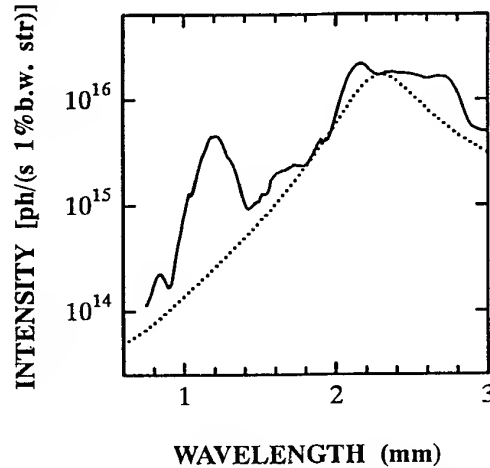


Fig. 3. Observed spectrum out of the resonator. The cavity length was fixed at the maximum peak in Fig. 2.

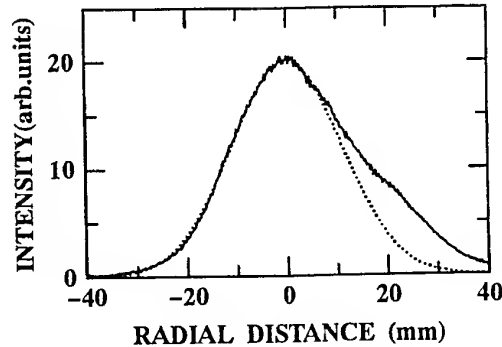


Fig. 4. Distribution of the intensity of the main peak along the radial distance of the resonator. The dotted curve is the theoretical distribution of the  $TEM_{00}$  mode.

# A Ka-band CHI-wiggler Free-Electron Maser: Experimental Results

J.M. Taccetti, R.H. Jackson, H.P. Freund, D.E. Pershing and V.L. Granatstein

Naval Research Laboratory  
Code 6840, Vacuum Electronics Branch  
Washington, DC 20375-5347, USA

## Abstract

Due to the nature of the Coaxial Hybrid Iron (CHI) wiggler, a resonance between the transverse wiggler and cyclotron motions of the beam exists which can enhance the free-electron maser (FEM) interaction. Amplification with a bandwidth on the order of a few percent was achieved. In spite of beam propagation problems, the gain was about 5 dB for operation below gyroresonance, and 7 dB above it.

## Introduction

The free-electron laser interaction provides the possibility for high-power, high-frequency radiation sources, although almost always coupled with the need for high-voltage operation. The CHI wiggler [2, 3] configuration overcomes this obstacle by allowing the use of short periods and gap spacings while maintaining excellent beam focusing properties and high magnetic fields. This reduces the overall system size while maintaining the ability to operate at high frequencies and power levels. The Ka-band FEM, with  $g/\lambda_w > 1$  ( $g$  is the coaxial gap width and  $\lambda_w$  the wiggler period), demonstrates the operation of this wiggler configuration and its potential for applications to higher-frequency devices.

## Experimental Setup

The FEM amplifier consists of three main sub-systems: the interaction area, the electron beam and the rf circuit. The interaction area is made up of a CHI wiggler with  $\lambda_w = 6.4$  mm, a  $60 \lambda_w$  uniform section and a coaxial gap width of  $1.09 \lambda_w$ . The electron beam is formed in a thermionic hollow-cathode diode, with design voltage and current of 100 kV and 10 A, respectively. The beam is collected immediately after traversing the wiggler. The rf is coupled in at a point between the gun and the wiggler, using a novel wideband TE<sub>01</sub> outer coaxial to TE<sub>01</sub> inner coaxial coupler. A similar design is used to monitor approximately 25 % of the power after the interaction, while the rest of the rf is dumped into a water load/calorimeter. The inner coaxial section of the wiggler is held concentrically (mounted horizontally) by three sets of three tungsten 'spokes' each.

Two DC breaks with accompanying current monitors were used to determine the fraction of the beam which makes it from the gun to the wiggler and from there to the collector. A misalignment in the magnetic axis of the electron gun and that of the interaction region is believed to be the cause of serious beam propagation problems experienced during the experiment. Only about 10 % of the beam making it to the wiggler reached the collector in a typical measurement. Rf amplification was nevertheless achieved.

The voltage pulse applied has a FWHM of 2.4  $\mu$ s. The 1  $\mu$ s input rf pulse was timed such that it coincided with the flatter section of the voltage pulse. Our setup allowed the detailed study of the dependence of the rf output pulse shape on the variations in the voltage pulse.

## Experimental Results

A transition (or gyroresonant) field  $B_T$  can be defined in terms of the original energy of the beam,  $\gamma$ , the axial velocity of the beam,  $\beta_z$ , and  $k_w = 2\pi/\lambda_w$ . This field,  $B_T = (mc^2/e)\gamma\beta_z k_w$ , is that for which the wiggler motion and the cyclotron motion of the beam are resonant. Operation below and above this value is termed Group I and Group II operation, respectively. The dependence of  $B_T$  on  $\beta_z$  demonstrates how its value is not constant but rather varies dynamically during the interaction.

Rf amplification of Group I orbits was achieved at  $0.76 B_T$ . The output rf pulse shape varied with voltage, as expected, but was not overly sensitive. Varying the input power from 0 to 1.2 kW resulted in a gain of approximately 4 dB for all these values. The beam voltage in this case was 113.1 kV, and the estimated  $\alpha = v_{\text{transverse}}/v_{\text{axial}}$  was 0.39. This value of  $\alpha$  was obtained by assuming a grazing intersection of the uncoupled TE<sub>01</sub> coaxial mode dispersion curve and the CHI beam line, a safe assumption due to the mode selectivity of the output rf monitor. This high  $\alpha$  indicates a large amount of axial energy of the

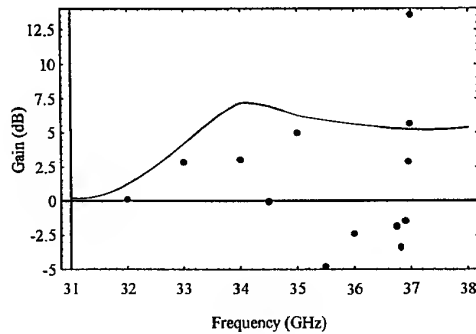


Figure 1: Gain as a function of drive frequency in Group I. Points are measured values, and the solid line is from CHIFEL simulations (details in text).

beam is being coupled to transverse motion before entering the wiggler. This is supported by comparison of measurements of gain as a function of frequency against a simulation (performed on CHIFEL [1]), as shown on Fig. 1, where the simulation is shown as a solid line. Both agree fairly well on the low frequency side. The high frequency discrepancy is believed to be due to reflections in the rf circuit caused by limitations of the output rf monitor. In the simulation, the maximum beam width was chosen such that all of the 2.1 A (as in the experiment) makes it through the interaction region. For interaction to occur in the simulation, the voltage had to be lowered to 102 kV, from the 116.3 kV used in the experiment, indicating again that a large fraction of the beam energy is turned into transverse motion prior to entering the wiggler.

Group II operation was also achieved at  $1.1 B_T$ . The output rf pulse was in this case much more sensitive to slight variations in voltage. This is due to the proximity to  $B_T$ , as a variation in axial velocity causes a variation in  $B_T$ , which in turn causes a quite drastic change in  $\alpha$ . The gain measured as a function of input power in this case was from 5 to 7 dB in the range from 0 to 1.2 kW input power. The bandwidth was about 5 % and centered about 35 GHz.

Regions of cyclotron oscillation were found and mapped out in Group I. No oscillations were found in Group II, although, as mentioned above, the output rf pulse was very sensitive to variations in beam voltage.

### Conclusion

Operation of the first FEM amplifier utilizing a CHI-wiggler configuration has been demonstrated, with a gap to wiggler period ratio in excess of one. The dependence of the output rf on the voltage has been studied on either sides of gyroresonance, approaching to within 10 % of it on the Group II side. It was found that operation is limited by cyclotron oscillations on Group I, and by high sensitivity to voltage on Group II. In conclusion, in spite of beam propagation problems, the CHI wiggler displays exceptional potential for higher frequency operation.

### Acknowledgement

This work was supported in part by the Office of Naval Research and the Naval Research Laboratory through a contract with the University of Maryland.

### References

- [1] H. Freund, R. Jackson, D. Pershing, and J. Taccetti. *Phys. Plasmas*, 1:1046, 1994.
- [2] R. H. Jackson, H. P. Freund, D. E. Pershing, and J. M. Taccetti. *Nucl. Instrum. Methods*, A341:454, 1994.
- [3] J. Taccetti, R. Jackson, H. Freund, D. Pershing, M. Blank, and V. Granatstein. *Nucl. Instrum. Methods*, A358:193, 1995.

## Detailed mm-waves measurements at the Dutch free-electron maser

W.A. Bongers, G.F.IJ. Kramer, J.A. Rietveld, A.G.A. Verhoeven, P. Manintveld, V.L. Bratman\*, M. Caplan\*\*, G.G. Denisov\*, C.A.J. van der Geer, A. Montvai, A.J. Poelman, J. Plomp, A.V. Savilov\*, P.H.M. Smeets, A.B. Sterk, W.H. Urbanus

FOM-Instituut voor Plasmafysica 'Rijnhuizen', Association EURATOM-FOM P.O. Box 1207, 3430 BE Nieuwegein, the Netherlands tel.: (31)30-6096999, fax: (31)30-6031204, e-mail: bongers@rijnh.nl  
\*IAP, Nizhny Novgorod, 603600 Russia, \*\*LLNL, Livermore, CA 94551, USA

### Abstract

The mm-wave output power of the Dutch free-electron maser, FEM, developed for applications on future fusion research devices such as ITER, has been analyzed. This paper gives an overview of the high-power measurements and the diagnostic set up used. This set up enables to measure energy, power and frequency-spectrum of the FEM mm-wave pulses as a function of time. Further, the spatial power distribution of the output beam was measured. To demonstrate the wide-band tuneability of the FEM, the cavities were remotely tuned at 200 and 167 GHz. First generation of mm-wave power was achieved in October 1997. Up to now the highest power measured is 730 kW at 206 GHz at a beam current of 7.2 A and a energy of 1.77 MeV.

### Introduction

In the first phase of the project, the so-called inverse set-up is used. The electron gun is mounted inside the high-voltage terminal within the pressure vessel. The undulator and wave-guide system are outside the vessel at ground potential for easy access and fine-tuning of the entire system [1]. In this set up the electron beam current is delivered from the capacitance of the high voltage terminal (1 nF); the accelerating voltage drops and the pulse length is limited to 10 - 20  $\mu$ s.

### mm-wave setup

The mm-wave cavity consists of a 15x20 mm<sup>2</sup> waveguide, which carries the HE<sub>11</sub> mode [2], inside the undulator and so-called stepped waveguides located upstream and downstream of the undulator, see fig. 1. In the stepped waveguides the mm-wave beam is split into two identical off-axis beams, as to separate the mm-wave beams from the electron beam. At the position of full separation mirrors are mounted to reflect the mm-wave beams back into the undulator. The upstream mirrors provide 100% reflection, while the downstream mirrors can be adjusted to tune the reflection coefficient. The two off-axis output beams from the splitter are bend by two pairs of 45° mitre bends into the combiner to merge into one output beam. This beam is directed by one waveguide mitre bend and a wide band confocal mirror set to the Brewster-angle window. A small part of the output power is fed to a mixer with a LO (Local Oscillator) to measure the frequency spectrum shifted to a 1-GHz IF band. A fast wide-band detector measures the power calibrated to the calorie meter, placed behind another wide band confocal mirror set. The absorption sheet has a calibrated dissipation of 42-48% in the frequency range of

160-220 GHz. The temperature profile is measured by a Thompson-cooled infrared camera and calculated to an absolute power profile by an iterative calorimetric model taking convection, radiation, conduction, pulse time and duty-cycle into account.

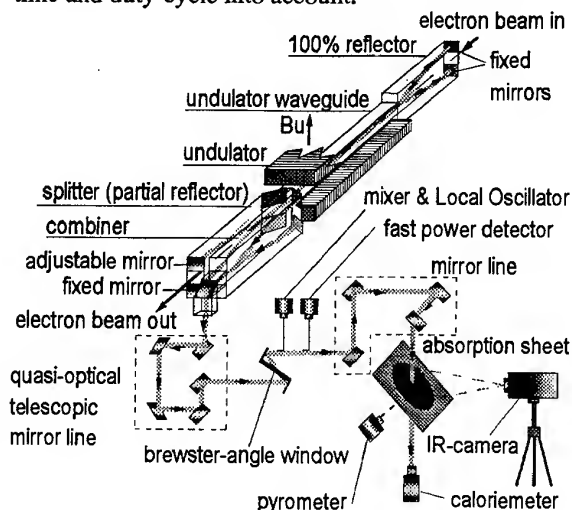


Fig. 1. The mm-wave system, showing the 100% reflector, the undulator, the splitter/combiner, the out-coupling waveguide and the confocal mirror system to the window. The high power measurement system is composed of a mixer and a local oscillator, a fast detector, and a confocal wide band mirror system focusing the beam to the calorie meter. For mm-wave beam pattern measurements, an absorption sheet, before the calorie meter, can be inserted and observed by an infrared camera and a pyrometer.

### High-power measurements

The fast detector trace and the FFT (Fast Fourier Transform) of the IF signal of the mixer are given in fig. 2, for the 200 and 167 GHz cavity settings. For these cases a smooth curve was measured, indicating single-frequency operation. This was confirmed by the FFT, which shows one frequency, and which follows the detector signal well in time, indicating that the frequencies of the main signals were measured. The spatial power distributions of the mm-wave beam are given in fig. 3. The Gauss-fits taken between the top of the signal and a level just above the noise level result in a Gaussian mode content of 99.83 % and 99.81 % for the 206 GHz and the 169 GHz signals, respectively. Note that the beam sizes are constant for the various frequencies, i.e. the confocal mirror systems have a large bandwidth.



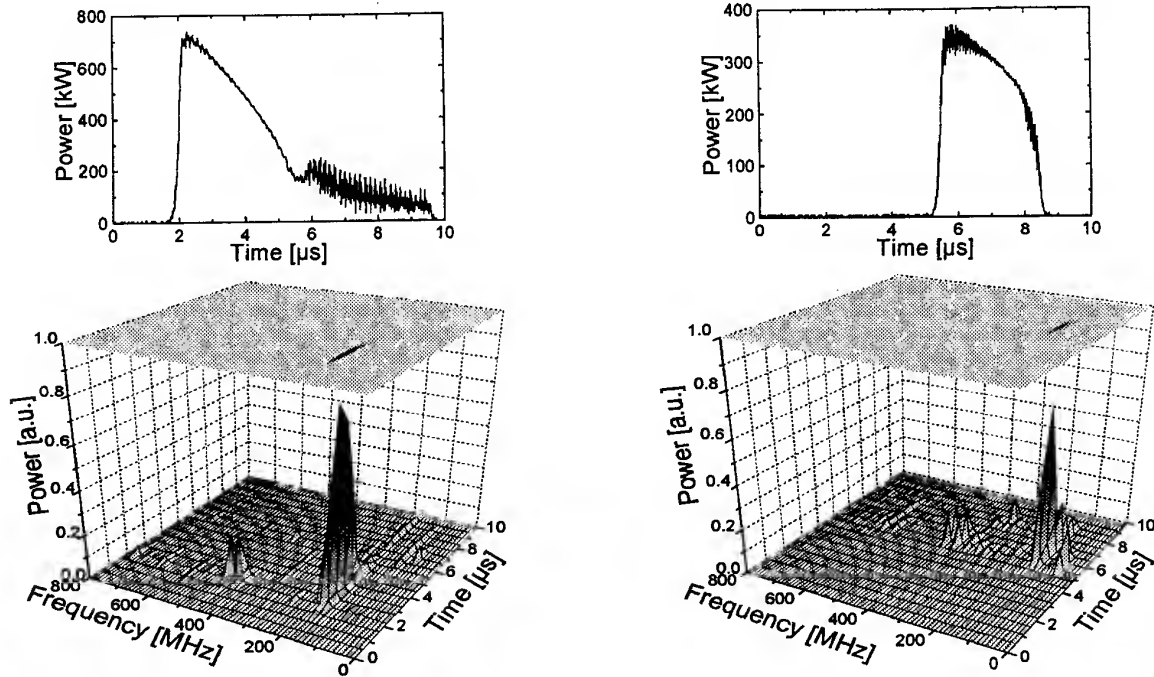


Fig. 2. Highest powers achieved: left, 730 kW at 200 GHz setting and, right, 350 kW at 167 GHz setting, measured by the fast detector. The lower figures show the FFT IF spectrums of the same shots around LO frequencies of 205.7 GHz and 169.5 GHz. The corresponding beam energies and currents are 1.77 MeV, 7.2 A and 1.61 MeV, 7.0 A respectively.

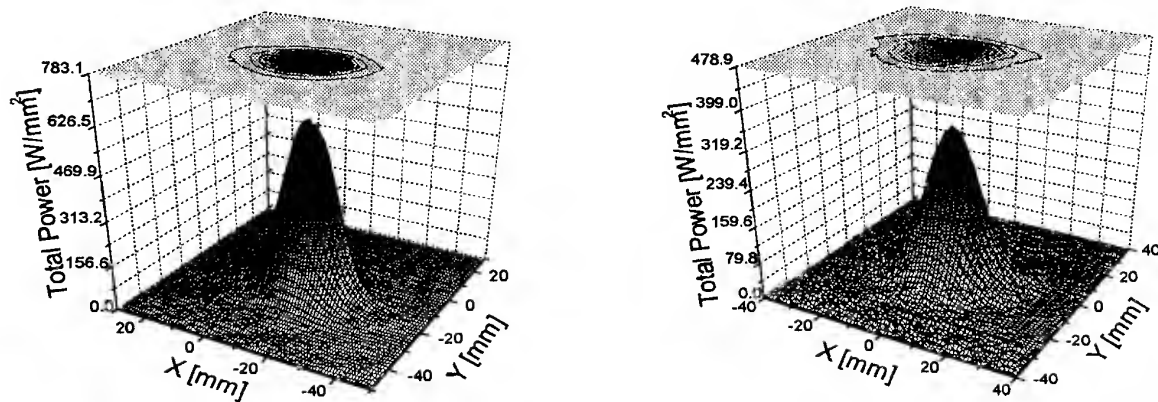


Fig. 3. Power profiles of the mm-wave beam at cavity settings of 200 GHz (left) and 167 GHz, measured with the IR-camera. The Gaussian-mode content is 99.83 % and 99.81 %, respectively.

### Conclusions

The FEM has been operated at two different frequency settings; FEM is tuneable over a wide band. The diagnostics system performs well. For various frequencies the power, spatial power distribution and frequency have been analysed as a function of time. The highest mm-wave power measured so far is 730 kW for an electron beam current of 7.2 A.

### Acknowledgements

This work was performed as part of the research program of the association agreement of EURATOM and FOM with financial support from NWO and EURATOM.

### References

1. W.A. Bongers, et al., in Proc. 10th Workshop on ECE and ECRH, EC10, Eds. A.J.H. Donne and A.G.A. Verhoeven, World Scientific, Singapore (1998) pp. 507-514.
2. G.G. Denisov, and M. Yu. Shmelyov, in Proc. 21st Intl. Conf. on IR and mm-Waves, Berlin, BF3, Eds. M. von Ortenberg and H.U. Müller, IR and mm-Waves, Vol. 1, (1996).
3. A.G.A. Verhoeven, et al., First generation of mm-waves in the Dutch Free-Electron Maser, this conference.

## Design, Performance and Applications of Compact Far-Infrared Laser Magnetic Resonance Spectrometers

H.-W. Hübers, H. P. Röser

German Aerospace Center (DLR)  
Institute of Space Sensor Technology  
Rudower Chaussee 5, 12489 Berlin, Germany  
heinz-wilhelm.huebers@dlr.de

### Introduction

Radicals, such as OH, NO and ClO, play a key role in many chemical reactions for example in the atmosphere of the earth or in combustion processes. Their high reactivity and short lifetimes make the analysis challenging. One of the most sensitive techniques is the laser magnetic resonance (LMR) spectroscopy [1]. Two different compact far-infrared (FIR) LMR spectrometers have been built at the DLR and will be described here.

### Design

Both LMR spectrometers are shown in fig. 1. In one spectrometer the Zeeman tuning of the energy levels is achieved by using a superconducting solenoid while in the other a pair of permanent magnets is used. The superconducting magnet is inside a LHe cryostat with a room temperature bore of 54 mm diameter. It can generate a maximum flux density of 3.5 T over a length of 120 mm with a homogeneity < 0.5%. In order to improve the homogeneity two correction coils can be used.

The permanent magnet system (for details see ref. 2) consists of two NdFeB magnets. The magnets are located on top of the pole pieces of an U-type iron yoke. The pole pieces are mounted on sliding tables. A fingerlike structure at the bottom of the iron yoke closes the magnetic field and allows to move the pole pieces against each other. With an electric motor the distance between the magnets can be changed from 80 mm to 25 mm corresponding to a flux density of 100 mT to 500 mT in the center between the magnets.

The laser system of both LMR spectrometers consists of an optically pumped FIR gas laser. The CO<sub>2</sub> laser delivers a maximum output power of 30 W and is tunable to about 80 different lines. The FIR laser has a confocal resonator of 1 m length. A polyethylene window separates the absorption cell from the part which contains the lasing medium. The absorption cell is a Duran™ tube while the lasing part is a 20 mm inner diameter copper tube. An intracavity iris diaphragm allows to suppress higher modes. A 45° mirror can be moved into the resonator in order to couple out a small fraction of the laser power. In both systems modulation coils are used to generate a small oscillating magnetic field. Its overlap with the homogeneous volume of the magnet and the laser mode defines the detection volume. A LHe cooled Ge:Ga photoconductor is used as a detector. The signal is amplified by a low noise amplifier and detected phase sensitively with reference to the oscillating magnetic field.

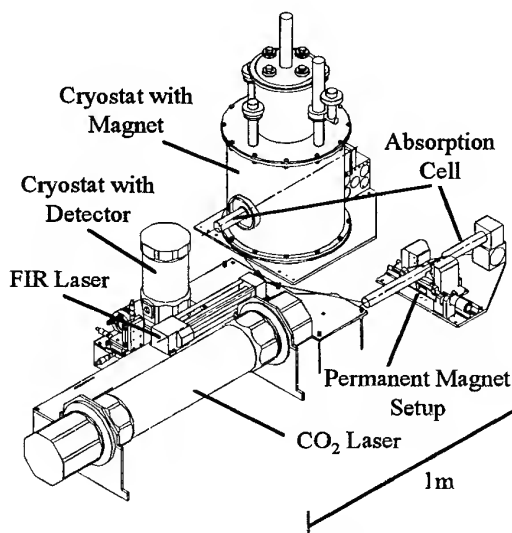


Fig. 1: The LMR spectrometers.

### Performance

Fig. 2 shows a spectrum of the OH radical measured with the LMR spectrometer with the superconducting magnet. It is the transition  ${}^2\Pi_{3/2}$ ,  $J=3/2$ ,  $m_J=-1/2$  ( $-$ )  $\rightarrow$   $J=5/2$ ,  $m_J=1/2$  ( $+$ ) at a flux density of 1.281 T. The OH was generated from H<sub>2</sub> and O<sub>2</sub> in a dc discharge in a sidearm of the absorption cell. The FIR laser was operated at 2522.8 GHz. (lasing medium CH<sub>3</sub>OH, CO<sub>2</sub> pump line 9P36). The first derivative of a Voigt profile was fitted to the spectrum. The difference between the measured and the fitted line profile is less than 1% of the peak-to-peak height (lower trace). The small deviation from the theoretical line shape is due to the inhomogeneity of the magnetic field. The proper setting of the magnetic field of the correction coils was critical to achieve this result. From a measurement of the line shape between 200 and 1300 Pa with He as the

broadening gas we determined the pressure broadening parameter. Our result of 0.0126(5) Pa/MHz is in good agreement with an earlier measurement performed with a tunable FIR spectrometer (0.0120(5) Pa/MHz [3]).

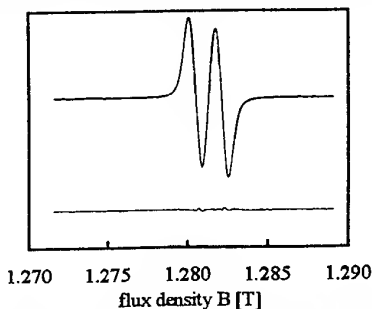


Fig. 2: Spectrum of OH (superconducting magnet LMR).

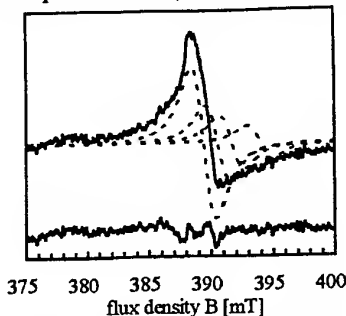


Fig. 3: Spectrum of O<sub>2</sub> (permanent magnet LMR).

In fig. 3 a spectrum of the O<sub>2</sub> rotational transition ( $N=13, J=14, m_J=-14 \rightarrow N=15, J=14, m_J=-14$ ) at 2.5 THz is shown. It was measured with the permanent magnet LMR spectrometer. The line shape is asymmetric due to the inhomogeneity of the magnetic field. The spectrum was fitted by taking into account the Voigt profile of the transition, the homogeneity of the magnetic field and the laser mode profile. The difference between measured and fitted line shape is about 10% of the peak-to-peak signal (lower trace). The dotted lines are the calculated contributions from different parts of the volume between the magnets to the total line shape. When the magnets are moved together these parts reach successively the flux density necessary for absorption. The signal-to-noise ratio is determined only by the innermost part of the volume between the magnets. This detection volume is about 0.1 cm<sup>3</sup> compared to about 10 cm<sup>3</sup> for the LMR spectrometer with the superconducting magnet. The smaller detection volume is the reason for the lower sensitivity of the permanent magnet system.

### Applications

Beside laboratory spectroscopy the LMR spectrometer with the superconducting magnet will be used for atmospheric research. Its sensitivity is sufficient for the in-situ detection of OH in the lower stratosphere and upper troposphere [4]. Fig. 4. shows the design of the airborne LMR spectrometer. A possible application in medicine and biology is indicated in fig. 5 which shows the O<sub>2</sub> concentration in expired human air. The LMR spectrometer with permanent magnets needs an improved sensitivity for applications. However, finite element simulations show [5] that the homogeneous volume between the permanent magnets can be increased with specially shaped pole pieces. A sensitivity comparable to the LMR with the superconducting magnet is possible. In addition, current developments of compact optically pumped FIR lasers for space borne applications [6] let it seem feasible to build a transportable, table top LMR spectrometer with permanent magnets.

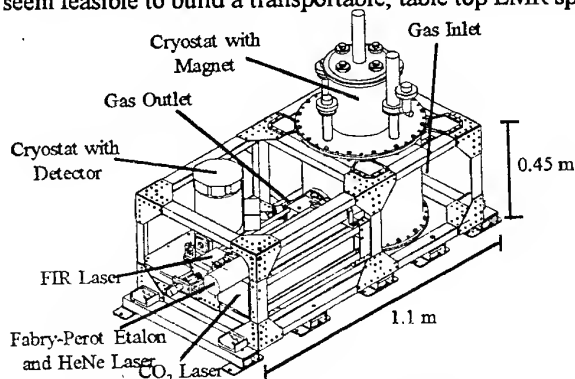


Fig. 4: Design of the airborne LMR spectrometer.

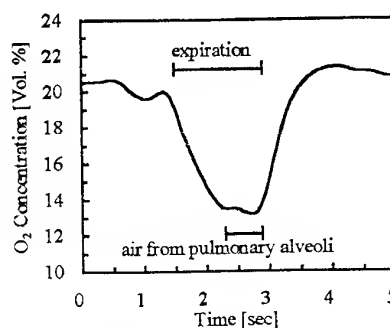


Fig. 5: Human expiration cycle measured with a LMR spectrometer.

### References

1. K. M. Evenson, R. J. Saykally, D. A. Jennings, R. F. Curl, J. M. Brown, *Chemical and Biochemical Applications of Lasers*, p. 95, edited by C. Bradley Moore (Academic, New York, 1980).
2. H.-W. Hübers, L. Töben, H. P. Röser, *Rev. Sci. Instrum.* **69**, 290 (1998).
3. K. Park, L. R. Zink, K. M. Evenson, K. V. Chance, I. G. Nolt, *J. Quant. Spectrosc. Radiat. Transfer* **55**, 285 (1996).
4. H.-W. Hübers, L. Töben, H. P. Röser, *Proc. of the 4th Europ. Symp. on Ozone Research*, Schliersee (1997).
5. H.-W. Hübers, unpublished results.
6. E. R. Muller, W. E. Robotham, R. P. Meisner, R. A. Hart, J. Kennedy, L. A. Newman, to appear in: *Proc. of the 9th Int. Symp. on Space THz Technology*, Pasadena (1998).

# DUAL-FREQUENCY VECTOR DETECTION IN THE 8-800 GHz INTERVAL. APPLICATION TO SPECTROSCOPY AT HIGH MAGNETIC FIELD.

**P. Goy, S. Caroopen**

*AB MILLIMETRE, 52 rue Lhomond 75005 Paris, France*  
tel: 01 47 07 71 00, fax: 01 47 07 70 71, E-mail: abmm001@ibm.net,

**M. Gross,**

*Laboratoire Kastler-Brossel, Département de physique de l'Ecole normale supérieure,*  
24 rue Lhomond, 75231 Paris cedex 05, France,

**K. Katsumata, H. Yamaguchi, M. Hagiwara, H. Yamazaki,**

*The Institute of Physical and Chemical Research (RIKEN), Wako, Saitama, 351-01, Japan,*  
tel: 81 48 462 1111, fax: 81 48 462 4649.

Since 1989, there is a millimeter-submillimeter vector analyzer (1) in which the microwave at  $F_{mm}$  is created by multiplication in a Schottky device powered by a source  $S_1$ , at the frequency  $F_1$ . One has:

$$F_{mm} = N \times F_1 \quad (1),$$

where the integer  $N$  is the harmonic order, and can take several values. For a reasonable efficiency,  $N$  is limited to about 10. With the 8-18 GHz sweeper contained in the analyzer, the frequency coverage is up to ca 180 GHz. With a Gunn oscillator in the 80-115 GHz range, the frequency coverage is up to ca 1000 GHz. Symetrically, the detection is operated in a Schottky harmonic mixer powered by a source  $S_2$  similar to  $S_1$ . The frequency  $F_2$  of  $S_2$  is maintained parallel to  $F_1$  by a PLL circuit (2), with a  $F_{s1}$  frequency reference from a first synthesizer:

$$F_2 - F_1 = F_{s1} \quad (2).$$

From the output of the harmonic mixer is extracted the detected signal, at the frequency  $F_{if}$ :

$$F_{if} = |F_{mm} - NF_2| = N \times F_{s1} \quad (3).$$

This signal is sent into the dual-channel, narrow-band, heterodyne vector receiver, working at the frequency  $F_r$ . The harmonic  $N$  will be selected if the 1st synthesizer is tuned to the following  $F_{s1}$  value (Eq.3):

$$F_{s1} = F_r/N \quad (4).$$

The non-linear Schottky devices can work at different  $N$  values at the same time, so that one observes a comb of harmonics (Eq.3) at the output of the harmonic mixer. In particular, a second microwave frequency  $F'_{mm}=N'F_1$  can also be detected, when selecting the harmonic  $N'$  at the harmonic mixer output, at  $F'_{if}$ :

$$F'_{if} = (N'/N) \times F_{if} \quad (5).$$

For receiving  $F'_{if}=N'F_{s1}=(N'/N)F_r$  on the 2nd channel of the receiver together with  $F_{if}=NF_{s1}=F_r$  on the 1st, the 2nd channel of the vector receiver must be off-tuned from its basic frequency  $F_r$  by a front-end heterodyne mixing with a second synthesizer tuned at  $F_{s2}$ , so that:

$$F_{s2} = |F'_{if} - F_{if}| = |N' - N| \times F_{s1} \quad (6).$$

The dual-frequency vector detection described above is of very great interest when performing mm-smm spectroscopy at high magnetic field. During a long- and time-consuming magnetic sweep, it is interesting to double the data points. Moreover, there is a drastic improvement on the reliability of obtained results, since fake signals appear correlated, in contrast with good signals (which are frequency dependent, in most cases). The experimental setups for spectroscopy with high magnetic fields cannot be small. The long source-to-detection distance entails parasitic drifts of the detected phase (Fig.1). However, the dual-frequency acquisition permits an extremely accurate compensation of these drifts, by ratioing the dual-frequency results obtained during the same sweep (Fig.2). Vector detection is especially powerful in resolving lineshape problems. In particular, the sense of rotation in the polar plane (Figs.3, 4) is an indication of the sign of the slope of the curve in the Frequency/Field diagram. A Lorentzian resonance appears as a circle in the polar plane, and split resonances appear as "potatoes" (Fig.4). Thanks to dual-frequency acquisition and vector Lorentzian fitting, split resonances are clearly resolved, despite splittings below the resonance widths (Figs.5-6).

## REFERENCES

- 1 - Shown in operation for the first time at Würzburg in October 1989, during the 14th Int. Conf. on IR & mm Waves, see also P.Goy, M.Gross, J.M.Raimond, 15th Int. Conf. on IR & mm Waves, Orlando FL, *SPIE 1514*, 172 (1990), R.E.Temkin, Ed., and 18th Int. Conf. on IR & mm Waves, Colchester, *SPIE 2104*, 487 (1993), J.R.Birch, T.J.Parker, Eds.
- 2 - P.Goy, M.Gross, Millimeter and/or submillimeter network vector analyzer, French Patent Sep 1st 1989, European Pat. EP 0 420 767 Apr 3rd 1991, US Pat. N° 5 119 035 Jun 2nd 1992.
- 3 - K.Katsumata, H.Yamaguchi, M.Hagiwara, H.Yamazaki, P. Goy, M.Gross, to be published.

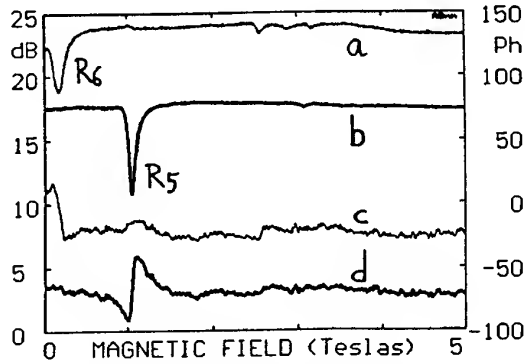


**Fig. 1.** Dual-frequency Fmm microwave transmission through a Fe12 sample at 5K. Experimental traces obtained in a single magnetic field  $B$  sweep: *a*, *b*, amplitudes (dB), *c*, *d*, phases (degrees) at 666 and 555 GHz, respectively. The strong resonances occur at  $R_6$ , close to  $B=0$ , and at  $R_5$ , close to  $B=1T$ , for 666 and 555 GHz, respectively.

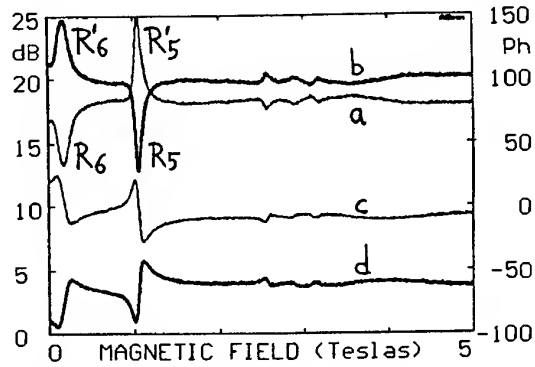


**Fig. 2.** The ratio of complex numbers gives their amplitudes ratio and their phases difference. When making the ratio of data shown in Fig. 1, the phase drifts are cancelled, as shown in *c* (which is  $c-d$  of Fig. 1) and *d* (which is  $d-c$  of Fig. 1). In the lines *a* (which is  $a/b$  of Fig. 1) and *b* (which is  $b/a$  of Fig. 1) expressed in dB, the peaks  $R_6$  and  $R_5$  are significant. The upwards peaks  $R_6'$  and  $R_5'$ , added by ratioing, are not.

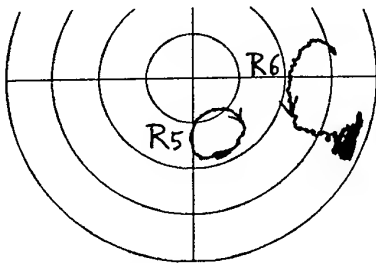


**Fig. 3.** Polar plots of Fig. 1. The clockwise resonance  $R_5$  at 555 GHz, left, belongs to a Fmm/ $B$  branch with a negative slope. The counterclockwise resonance  $R_6$  at 666 GHz, right, belongs to a Fmm/ $B$  branch with a positive slope.

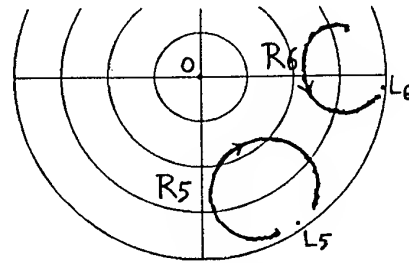


**Fig. 4.** Polar plots of the (double) resonances  $R_5$  and  $R_6$  of Fig. 2. The phase drifts elimination allowed by the dual-frequency acquisition permits to obtain pure "potato" lineshapes. The double Lorentzian fits are superimposed.  $OL_5$  and  $OL_6$  are the leak vectors associated with the double resonances  $R_5$  and  $R_6$ , respectively.

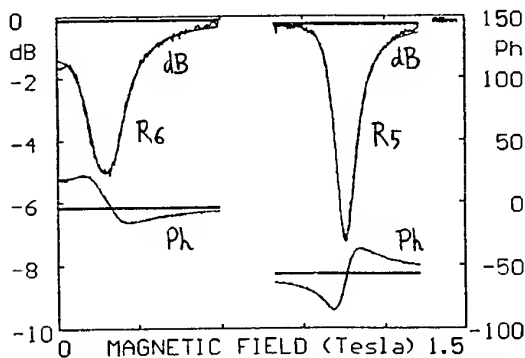


**Fig. 5.** Cartesian representation of Fig. 4, same as Fig. 2 in which only resonances  $R_6$  and  $R_5$  would be shown. The horizontal lines correspond to the leak vectors  $OL_6$  and  $OL_5$ . The fact that each of the resonances is actually a double resonance is not as clearly visible as in the polar plot of Fig. 4, where experimental traces cannot be fitted by simple circles.

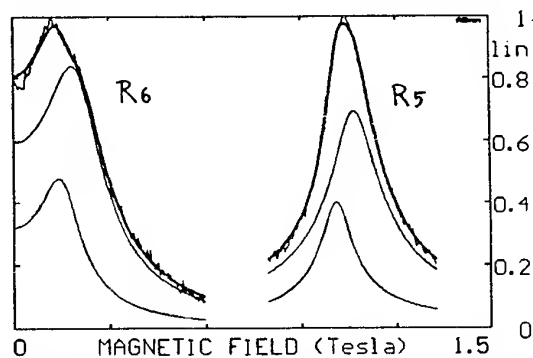


**Fig. 6.** Plots of the linear amplitudes calculated after removing the leak vectors  $OL_6$  and  $OL_5$  from the (double) resonances  $R_6$  and  $R_5$  of Fig. 5. Top: experimental traces and fits. Bottom: the two single Lorentzian components of each double resonance. Splittings smaller than the resonance widths could thus be shown.

A high resolution Fourier Transform spectrometer  
for the spectral region below  $60\text{ cm}^{-1}$

A Atkins, G Poulter and J R Birch\*

Graseby Specac Ltd, River House, 97 Cray Avenue,  
St Mary Cray, Orpington, Kent BR5 4HE

\*Also at JB Research, 9 Clifton Terrace, Cliftonville,  
Dorking, Surrey RH4 2JG, UK.

## ABSTRACT

A high resolution, Martin Puplett polarising interferometer has been constructed for both conventional and dispersive Fourier transform spectroscopy in the wavenumber region below  $60\text{ cm}^{-1}$ . The high wavenumber limit is imposed by the pure rotational spectrum of atmospheric water vapour, as the interferometer was designed to be operated in the open laboratory environment. The maximum optical path difference that can be achieved is 200 cm.

## INTRODUCTION

Quantitative studies of the near millimetre wavelength optical constants of reasonably transparent solids are required in an increasing number of areas of Terahertz Technology. These cover the design of Gaussian beam-based systems including radomes, covert surveillance, remote sensing of resources, anti-collision radars for cars, helicopters and aircraft, and the detection of hidden small arms as well as more conventional applications in physics, chemistry, astronomy and biology.

The present paper reports on the design of a high resolution Fourier transform spectrometer that can be used to give continuous cover over the wavenumber region from 1 to around  $60\text{ cm}^{-1}$ . Prior to this work, most broad band near millimetre Fourier transform measurements did not extend significantly below  $3\text{ cm}^{-1}$ .

## THE INTERFEROMETER

The interferometer was based on a polarising wire grid configuration using roof top reflectors to terminate each of the active arms of the interferometer. The moving mirror arm was mounted on a 1 metre linear slide driven by a stepping motor. Depending on the spectral region required, a liquid helium cooled indium antimonide hot electron bolometer or a DTGS pyroelectric detector, were used to detect the interferograms.

Large aperture polarising wire grids acting as beamdividers were used to put the interferometer into a Martin-Puplett configuration with polarisation modulation imposed by a rotating grid at the source, a standard water cooled 125 W mercury lamp.

The performance of the interferometer will be illustrated by the results of measurements on materials such as Macor, PEEK, silicon, beryllia, polyethylene and TPX.

## A FAST SWEEPABLE BROADBAND SYSTEM FOR DIELECTRIC MEASUREMENTS AT 90 – 100 GHz

R. Heidinger<sup>1)</sup>, R. Schwab<sup>1)</sup>, F. Königer<sup>2)</sup>,

<sup>1)</sup>Forschungszentrum Karlsruhe, Institut für Materialforschung I,  
Postfach 3640, D-76021 Karlsruhe, Germany

<sup>2)</sup>PROMETH GmbH, Alt Zeilsheim 21, D-65931 Frankfurt, Germany

### Abstract

For dielectric materials measurements in the frequency range between 90 GHz and 100 GHz, a fast and high accuracy system was realised. The resonator parameters of a ( quasi-)hemispherical Fabry-Perot mirror set-up can be analysed for a series of up to nine basic  $TEM_{00q}$  modes. Sources of errors by unequal distribution of losses in the mirror system were reduced by the coupling geometry and corrected for in the determination of dielectric loss measured in specimens with non-resonant specimen thickness.

### Introduction

Although it is well-known that the open resonator technique produces some of the lowest values of uncertainty for determining the dielectric properties, namely permittivity ( $\epsilon_r$ ), and dielectric loss tangent ( $\tan\delta$ ) of low loss dielectrics at mm-wavelengths, and offers the potential to determine anisotropies and inhomogeneities in the dielectric materials [ 1 ], it has not yet found a wide spread use in laboratories. Certainly, the need for highly stable frequency sources and mechanical resonator set-ups has created some kind of experimental conflict with the desired wide range tunability in order to inspect a larger series of  $TEM_{00q}$  resonances for improving the amount of information and of confidence. A frequent solution to the problem is either setting various resonator lengths for a given frequency and sweeping over the resonance in a very limited frequency span, or setting up a generator system which still covers a band wide enough to have access to different  $TEM_{00q}$  modes at a fixed resonator length. The latter method is more directly combined with automated resonator analysis which is indispensable for dense data sets, as in spatially and/or temperature dependent measurements. Contrasting to mainly purpose built wide band systems for frequencies above 50 GHz, Komiyama et al. [ 2 ] reported the use of a more standardly available configuration where a commercial synthesiser combined with frequency multiplier could be used to cover the entire W band. However, measurements were restricted then to single frequencies at which the specimen was at resonant thickness. This promising approach is taken up in the present paper which describes a similar configuration at 90 – 100 GHz and shows that by a special treatment of the scattering losses in the resonator,  $\tan\delta$  levels down to  $10^{-5}$  can be accurately determined for arbitrary specimen thickness.

### Characteristics of the experimental set-up

The frequency generation was realised by feeding an active frequency multiplier ( Millitech FEX-10-07041 ) by pulse modulated signals ( modulation frequency: 27.8 kHz ) from a sweepable synthesised source ( HP 83630A ) at 14.6 – 17 GHz. With an input power of +11 dBm, an overall output power of + 6 dBm was achieved between 88 – 100 GHz. Signals transmitted ( cf. Fig. 1 ) through a Fabry-Perot resonator in (quasi-) hemispherical geometry ( cf. Fig. 2 ) were analysed using a diode detector adapted to a scalar network analyser ( HP 8757 E ).

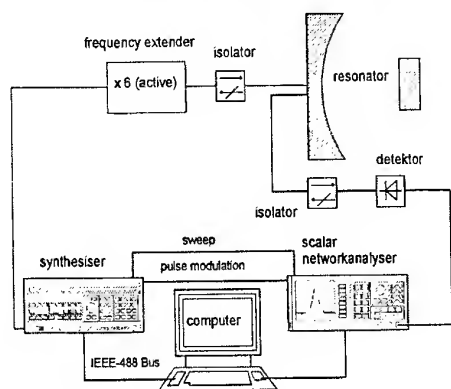


Fig.1 Block diagram of the mm-wave set-up

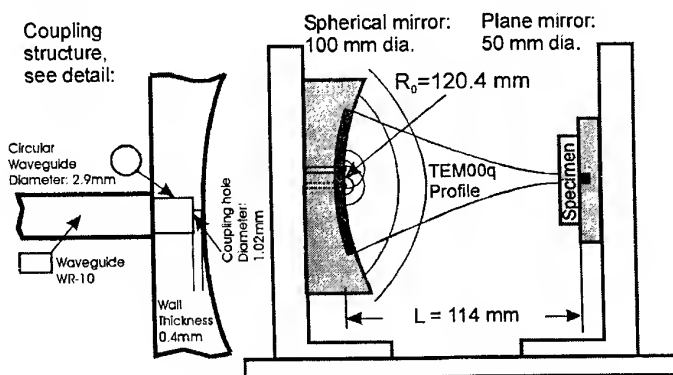


Fig.2 Geometrical data of the resonator set-up

The basic resonance parameters were analysed by fitting a Lorentzian line shape with the option for distortion by signal leakage [ 3 ]. The determined centre frequency and the quality factor for the empty resonator (  $Q_0, f_0$  ) and the filled resonator (  $Q_1, f_1$  ) can be used to calculate the dielectric parameters by standard formula ( cf. [ 2 ] ).

#### Evaluation of loss data for specimens with arbitrary thickness

For  $\tan\delta$ , the formulae are simplified using a filling and loading factor (  $F_F$  and  $F_L$  ):  $\tan\delta = F_F (Q_1^{-1} - (Q_0/F_L)^{-1})$ . Whereas these factors are easily given for specimens with resonant thickness, they become quite intricate at arbitrary specimen thickness. In addition, there is a non-standard formulation of the loading factor required if the losses are not equally distributed between the plane and the spherical mirror of the resonator system [ 3 ]:  $F_L^M = (2/(\Delta+1))((M\Delta+1)/(M+1)) F_L$ , where the  $\Delta$  parameters varies strongly with the permittivity and the thickness of the specimen [ 2 ]. The degree of the perturbation of the mirror system is quantified by the so-called M-factor [ 3 ], which relates the losses at the plane mirror to the losses at the spherical mirror. Finding that the major source of unequal losses arises from the scattering losses at the coupling holes introduced at the spherical mirror, special care was given to avoid any irregularity at their formation. This implied formation of holes by electro-erosion and careful tapering of its original wall thickness of 0.4 mm down to 0.2mm. By this way, M-factors of 0.65 were realised which come much closer to 1 than for the first resonator systems analysed this way [ 3 ]. Clearly this correction is most effective for very low loss specimens where  $Q_0$  is comparable to  $Q_1 / F_L^M$ . The importance of the factor correction is shown in Table 1 for data observed in single crystal Quartz ( extraordinary ray orientation ).

$f_0$ [GHz]	$Q_0$	$f_1$ [GHz]	$Q_1$	$Q_1/F_L$	$(\tan\delta)_{st}$ [ $10^{-5}$ ]	$\Delta$	M	$Q_1/F_L^M$	$(\tan\delta)_{cor}$ [ $10^{-5}$ ]
88.63	198812	98.21	75799	84160	0.8	4.45	0.624	98603	1.8
89.94	202858	90.38	91066	107734	1.3	3.12	0.637	121597	2.1
91.26	205794	91.61	123213	144887	1.4	1.96	0.645	155817	2.0
92.57	207936	92.89	154159	179286	1.5	1.35	0.648	185266	1.8
93.88	204417	94.19	169799	197072	1.7	1.08	0.623	198893	1.8
95.20	203794	95.50	172991	203780	1.9	1.00	0.613	203783	1.9
96.51	200919	96.82	160636	194905	2.3	1.06	0.593	196556	2.4
97.83	191294	98.12	143814	167250	1.7	1.32	0.543	174375	2.1
99.14	200537	99.40	124401	144446	1.4	1.88	0.578	157346	2.1

**Table 1:** The effect of the correction for non-equal distribution of resonator losses by substituting  $F_L$  by  $F_L^M$  shown in dielectric loss measurements on a s. c. Quartz specimen (extraordinary ray) of thickness 5.108 mm.

#### Dielectric measurements

The measurement set-up was used to investigate two of the major window materials for high power gyrotrons, which are Sapphire and CVD diamond. Details on the materials are given in Ref. 4 and 5. The anisotropy of Sapphire like single crystal Quartz causes a double data set: ordinary/extraordinary ray ( E-field perpendicular / parallel to optical axis ). The  $\tan\delta$  data at 90-100 GHz fall onto the interpolated frequency trend between 30-40 GHz and 144-146 GHz while the permittivity is identical for in the three cases: 9.4 / 11.6 for Sapphire and 5.67 for CVD diamond.

Material	Sapphire (ordinary ray)	Sapphire (extraordinary ray)	CVD-Diamond (‘FZK’ disc)	CVD-Diamond (‘Super-FZK’ disc)
30 – 40 GHz	$0.4 \times 10^{-4}$	$0.2 \times 10^{-4}$	$1.2 \times 10^{-3}$	$1.8 \times 10^{-5}$
90 – 100 GHz	$1.1 \times 10^{-4}$	$0.6 \times 10^{-4}$	$6.6 \times 10^{-4}$	$0.9 \times 10^{-5}$
144 – 146 GHz	$1.9 \times 10^{-4}$	$1.0 \times 10^{-4}$	$5.0 \times 10^{-4}$	$0.7 \times 10^{-5}$

**Table 2:** The dielectric loss data of gyrotron window materials measured over an extended frequency interval.

#### Literature

- [1] J.R. Birch, R.N. Clarke, The Radio and Electronic Engineer, 52 (11/12) (1982), pp. 565-584
- [2] B. Komiya, M. Kiyokawa, T. Matsui, IEEE Trans. on Microwave Theory and Techniques, 39(10) (1991), pp. 1792-96
- [3] R. Heidinger, G. Link, Digest 18<sup>th</sup> Int. Conf. IR & MM Waves, Colchester (UK), 1993, SPIE vol. 2104, pp. 64-65
- [4] R. Heidinger, J. Nucl. Mater., 212-215 (1994), pp. 1101-1106
- [5] R. Heidinger, R. Spörl, M. Thumm, R.S. Sussmann, J.R. Brandon, C.N. Dodge, Digest of this conference



# DIELECTRIC PROPERTIES OF MATERIALS UP TO MILLIMETER WAVELENGTHS USING WHISPERING GALLERY DIELECTRIC RESONATORS

G. Annino\*, M. Cassettari, I. Longo, M. Martinelli

*Istituto di Fisica Atomica e Molecolare, C.N.R., via del Giardino 7  
56127 Pisa, Italy*

*\* now with Scuola Normale Superiore and INFN, Piazza dei Cavalieri 7  
56126 Pisa, Italy*

In the open dielectric resonators the radiation is confined by internal reflection at the surfaces of the resonator. In particular in a planar cylindrical resonator working in the whispering gallery (WG) modes the electromagnetic field is confined by the total reflection mechanism near the boundary of dielectric volume, thus minimizing the radiation losses. The size of such resonators is then typically much greater than the wavelength of radiation and this allows a wide band resonance frequency range which spans from microwave to visible radiation [1-2].

The use of WG resonators is convenient in many research fields, such as high-field EPR spectroscopy, dielectrometry and in the built up of integrated components. A resonator with resonance frequency tunable in a continuous way in a definite frequency range is often required in these applications, especially when radiation sources with poor or no tunability are employed. In these cases it is necessary to change effectively and in a controlled way the frequency of resonance of the resonator, without a sensible degradation of its characteristics. This problem was experimentally solved [3] by axially moving a conducting disc parallel to a plane surface of the resonator.

Here are presented the results of an analytical non-perturbative calculation method describing the field distribution and resonance frequency  $\nu_0$  for all the possible distances  $z$  of the conducting disc from the resonator surface. The method is based on a set of approximate solutions derived from the normal modes of the cylindrical infinite waveguide. The resonance frequency and the distribution of the fields are obtained from the suitable boundary conditions [4,5]. Some results of these calculations are reported in Fig. 1 for WGE (quasi-TM) and WGH (quasi-TE) modes of a WG resonator made with polyethylene ( $\epsilon=2.13$ ) 0.8 mm thick and having 30 mm in diameter, in a frequency range near 250 GHz.

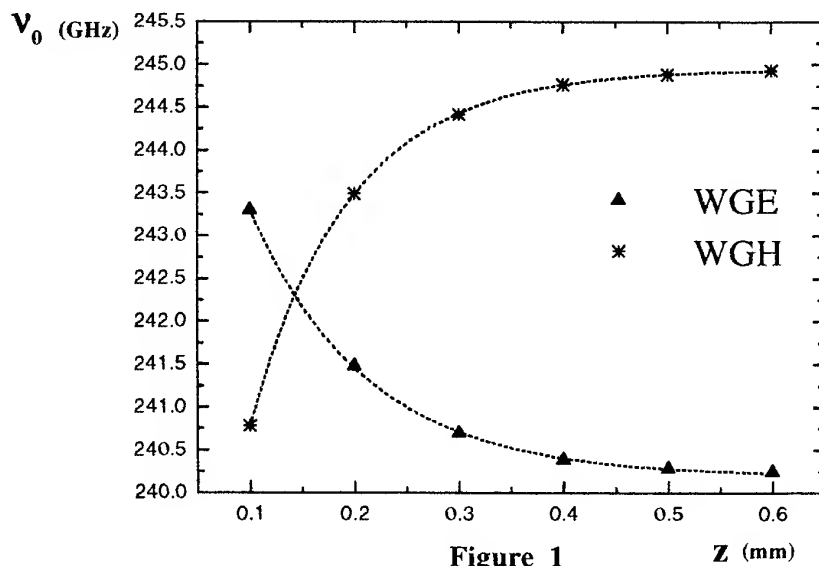


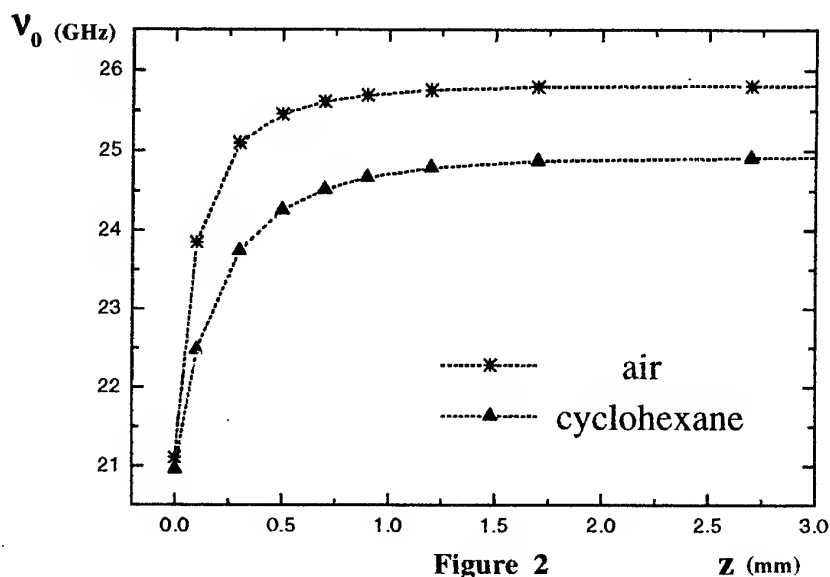
Figure 1

Z (mm)

The calculated values, which are well fitted by an exponential law (dashed curves), span some free spectral ranges of the resonator; the tuning method employed allows then an effective matching between the source and the resonator. The experimental analysis confirms these predictions, while the Q factor shows a weak dependence on the z value.

Using this calculation procedure and experimentally detecting the field distribution and the Q factor of the resonator it is possible to determine the complex dielectric constant of the material forming the resonator. Moreover, when the dielectric properties of the resonator are known, the dielectric constant of a fluid surrounding the resonator itself can be obtained by measuring the change of the properties of the resonator when it is plunged in the liquid. As an example, the Fig. 2 reports the calculated resonance frequencies of a WGH mode of an alumina WG resonator ( $\epsilon=9.6$ , diameter 80mm, thickness 2.6mm) plunged in air (stars) or in cyclohexane ( $\epsilon=2.01$ , triangles), tuned by a conducting disc at about 25 GHz.

It can be remarked that when a fixed frequency source is used, analogous information can be obtained measuring the shift of the tuning disc necessary to recover the resonance frequency when the resonator is plunged in the liquid.



#### REFERENCES

- [1] X. H. Jiao, P. Guillon, L.A. Bermudez, P. Auxemery, *IEEE Trans. On Micr. Theory and Techniques*, vol. 35, no. 12, 1169 (1987).
- [2] T. Bacr, *Optics Letters*, vol. 12, no. 6, 392 (1987).
- [3] D. Cros, "Les 'whispering gallery' modes des rsonateurs dielectriques: application aux oscillateurs et combineurs de puissance millimetriques", *These de Doctorat*, Université de Limoges (1990).
- [4] G. Annino, M. Cassettari, I. Longo, M. Martinelli, *IEEE Trans. On Micr. Theory and Techniques*, vol. 45, 2025 (1997).
- [5] G. Annino, M. Cassettari, I. Longo, M. Martinelli, *Chem. Phys. Lett.*, vol. 281, 306 (1997).

## The Use of a 250 GHz Gyrotron in a DNP/EPR Spectrometer

K.E. Kreisler, C. Farrar, R.G. Griffin, and R.J. Temkin

Plasma Science and Fusion Center / Francis Bitter Magnet Laboratory  
Massachusetts Institute of Technology  
Cambridge, MA 02139

### Abstract

A 100 watt, 250 GHz cw gyrotron is presently being constructed for use as a microwave source in EPR and NMR spectroscopic studies. This gyrotron will operate in the  $TE_{031}$  mode and will produce a Gaussian beam appropriate for transmission to the sample. The gyrotron will eventually be upgraded to generate second harmonic radiation at 500 GHz. The gyrotron will be used to study dynamic nuclear polarization, which can result in significant enhancement of the NMR signal.

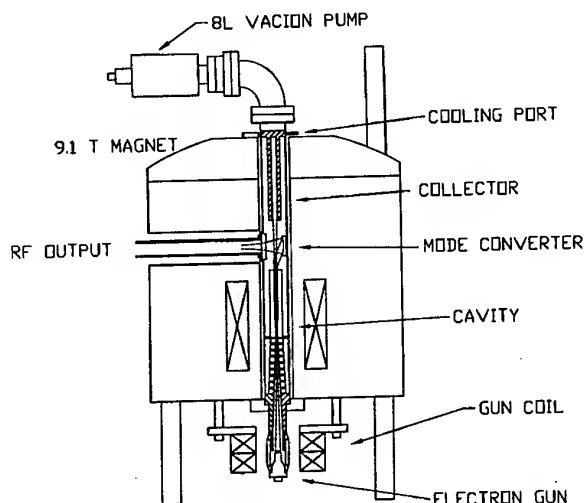
### 250/500 GHz Gyrotron

The main goal of this research program is to design and construct a gyrotron-based spectrometer suitable for dynamic nuclear polarization/nuclear magnetic resonance (DNP/NMR) and electron paramagnetic resonance (EPR) at 250 and 500 GHz. The motivation for this effort is the recent success at MIT with similar instrumentation at 140 GHz [1,2]. In those experiments, dramatic signal enhancements were observed in DNP/NMR studies, including enhancements of 50-200 in  $^{15}\text{N}$  MAS spectra of the protein T4 lysozyme. In addition, the resolution of EPR spectra due to g value dispersion was significantly increased. We anticipate similar improvements with the systems that are presently being built for our studies at higher frequencies.

The early months of this project were spent completing a detailed design of a fundamental free-running gyrotron oscillator operating at 250 GHz. Parameters for this device, which were optimized for 100 W of output power, are listed in Table I. A variety of constraints were considered in our study, including electron beam formation, rf interaction, and thermal heating of internal components. Of particular concern was the selection of a cavity design that would provide efficient operation and have manageable ohmic heating of the cavity walls. This required choosing the cavity mode and Q so that the rf field is large enough to extract the beam energy, and yet not so large that it overheats the walls and causes damage. We selected the  $TE_{031}$  mode as the operating mode of the gyrotron. Our studies indicated that this mode would provide the optimum coupling between the electron beam and rf field in the interaction cavity. This mode has also been extensively studied in other gyrotron experiments at MIT. Nonlinear simulations of the cavity were performed to confirm that high efficiency could be achieved. These codes indicated that about 150 watts of rf power would be generated by a 12 kV, 40 mA beam, and that about one-third of this power would be lost in the cavity walls due to ohmic heating. An overall efficiency of 21% is expected. The MIT gyrotron will be similar to a tube presently operating at Fukui University [3].

Once the gyrotron operating parameters were determined, a mechanical design was completed. Figure 1 shows the basic features of the gyrotron system. The tube will be operated in the vertical direction in order to simplify support and alignment. Unlike the 140 GHz NMR gyrotron, the tube was designed to be fully assembled outside the magnet. This will allow us to bake the tube to 250-300° C prior to operation, and should significantly improve reliability during cw operation. One major modification from the original proposal was the addition of a radial bore in the magnet to allow the transmission of the microwave power through a side vacuum window on the tube. As a result, the electron beam and microwave power can be separated just after the interaction in the gyrotron cavity. This reduces ohmic losses in the output waveguide, and simplifies the design of the beam collector. It also increases the vacuum pumping conductance to the cavity and electron gun, which will improve reliability during cw operation. A quasi-optical mode converter will be used to convert the  $TE_{031}$  cavity mode to a Gaussian beam. This converter will consist of a step-cut Vlasov converter, a focusing mirror, and a steering mirror. We anticipate a conversion efficiency of 85-90%. The rf beam will be about 1 cm in diameter.

The superconducting magnet, built by Cryomagnetics, Inc., has been successfully tested. The magnet has a 6.4 cm diameter warm bore and a simple NbTi coil to provide up to 9.4 T at the gyrotron cavity. Helium losses are



Mode	TE-031
Voltage (kV)	12
Current (mA)	40
Efficiency (%)	21
Magnetic field (T)	9.06
Velocity ratio	1.6
Diffraction Q	4950
Total Q	3400
Cavity radius (mm)	1.94
Cavity length (mm)	18
Cavity losses (W)	48
Cavity beam radius (mm)	1.02

Table I - Characteristics of the 250 GHz gyrotron

Figure 1 - Schematic of the 250 GHz gyrotron

below 25 mL/hr. The magnet is very compact, with a diameter of 61 cm. A simple diode-type gun will be constructed using a cathode assembly built by Semicon, Inc. The low operating voltage (10-20 kV) has greatly simplified the design, and eliminated the need for oil for cooling and high voltage insulation. The gun was also designed to allow quick replacement of the cathode. The gun simulation code EGUN has been used to verify that the beam perpendicular velocity spread will be less than 5%. Other auxiliary equipment includes a high-stability power supply for the electron gun that provides both high voltage and filament power, a 1 kW chiller that regulates the cooling water temperature for the cavity and collector to  $\pm 0.1^\circ \text{C}$ , and a room-temperature shim coil at the gun for optimizing the electron beam characteristics. The beam voltage and cavity temperature must be kept as steady as possible to achieve gyrotron frequency stability of 100 kHz or less.

### EPR Spectrometer

The implementation and characterization of DNP experiments requires a knowledge of the EPR spectrum and the relaxation rates of the paramagnetic centers used as the polarizing agents. A solid-state 250 GHz EPR spectrometer is presently being built by Millitech, Inc., and will be capable of both cw and pulsed experiments. The transmitter power will be provided by an 84 GHz injection locked oscillator tripled to 252 GHz. Approximately 2 mW of output power is expected. A PIN switch before the tripler will be used to provide pulses of 100 nsec or less. The receiver signal will be subharmonically mixed with a 124.8 GHz signal from another injection locked oscillator. The 2.4 GHz IF signal will then be sent to a quadrature detection system. The transmitter, receiver, and detection system will all be locked to a 100 MHz reference oscillator in order to maintain phase coherence. The EPR and NMR experiments will be conducted in a five-inch bore 8.8 T magnet being built by Magnex, Inc. This field corresponds to 375 MHz for  $^1\text{H}$  NMR, and 247 GHz for  $g=2$  electrons. The magnet will have both superconducting and room-temperature shim coils in order to achieve 0.1 ppm homogeneity at the center of the bore. A sweep coil will also be built into the magnet to allow the field to be varied from 8.2 to 9.4 T. This magnet will be delivered during the latter part of 1998.

This research is supported by the U.S. National Institutes of Health.

### References

- [1] G.J. Gerfen, L.R. Becerra, D.A. Hall, R.G. Griffin, R.J. Temkin, and D.J. Singel, *J. Chem. Phys.*, Vol. 102, 9494-9497 (1995).
- [2] D.A. Hall, D.C. Maus, G.J. Gerfen, S.J. Inati, L.R. Becerra, F.W. Dahlquist, and R.G. Griffin, *Science*, Vol. 276, 930-932 (1997).
- [3] T. Idehara, K. Yoshida, N. Nishida, I. Ogawa, M.L. Pereyaslavets, and T. Tatsukawa, *Int. J. Infrared and Millimeter Waves*, Vol. 19, 793-801 (1998).

Dielectric loss measurements with a confocal Fabry-Perot resonator

J. M. Dutta and C. R. Jones

Department of Physics

North Carolina Central University, Durham, NC 27707 USA

A measurement method which combines coherent optical resonance techniques with conventional microwave techniques, has been optimized to investigate the dielectric loss properties of materials under investigation for the gyrotron window applications. The theory of the method applied is reviewed and the results of some of the candidate materials are presented.

## The Precision of Quasi-optical Null-Balanced Bridge Techniques for Transmission Coefficient Measurements.

S. Hadjiloucas, J.W. Bowen and L.S. Karatzas

Department of Cybernetics, The University of Reading, P.O. Box 225, Whiteknights, Reading. RG6 6AY, U.K.

We present an analysis of the errors involved when performing transmission coefficient measurements after balancing at a null a quasi-optical transmissometer based on a Martin-Puplett Mach-Zehnder hybrid polarising interferometer configuration. Each element in the optical system shown in Figure 1 can be described by a Jones matrix which relates the polarisation state of the emergent beam to that of the incident beam. Under manual operation, the user iteratively balances the instrument to a null by successive movements of the roof-top reflector and the rotating grid. It can be shown that the power  $P$  at the detector is:

$$P = \left| \left( \frac{1 - \sin 2\theta}{4} \right) e^{-jkd} - \frac{T}{2} e^{-j\phi} \right|^2 P_0 \quad (1)$$

where  $P_0$  is the modulated source power output,  $\theta$  is the angle of the grid wires to the vertical,  $T$  is the sample transmittance ( $0 < T < 1$ ),  $k$  is the source wavenumber and  $kd$ , and  $\phi$  are the phase delays through the sample and reference arms of the interferometer respectively. It is found that a null at the detector is obtained when the phase difference between the two paths of the interferometer is zero so that  $T = (1 - \sin 2\theta)/2$ . The reference grid transmits all of the incident polarisation when  $\theta = -45^\circ$  and gives a null when  $\theta = -45^\circ + \gamma$  where  $\gamma$  is half the angle between the adjacent nulls. Thus we find that under balanced conditions  $T = \cos^2 \gamma$ . A plot of the power output at the detector as a function of  $\theta$  with amplitude transmission coefficient of a) 25%, b) 50% and c) 75% is shown in Figure 2. It can be observed that for very transmitting or very absorbing samples, the observed null angles become difficult to resolve. The relation between power output as a function of roof-top reflector distance and grid angle is shown in the contour plot in Figure 3, where each dark contour corresponds to the locus of a null-balance measurement. An error in  $\gamma$  can be directly linked to an error in the measured transmittance  $T$  using:

$$\sigma_T(T, SNR) = \left( \frac{\partial T}{\partial \gamma} \right) \sigma_{\gamma_{TOTAL}}(T, SNR), \text{ where: } \frac{\partial T}{\partial \gamma} = -2 \sin \sqrt{T} \cos^{-1} \sqrt{T} \quad (2)$$

The  $\sigma_{\gamma_{TOTAL}}(T, SNR)$  term is composed of the following two errors in determining the null position: a) the precision in determining the angle (quantisation error) of the rotating grid  $\sigma_{\gamma_Q}$  and b) the precision in determining the balanced position in  $\theta$  due to the noise equivalent power  $NEP$  of the detector (at a bandwidth  $B$  related to the time constant of the PSD used). In order to further incorporate the source output power in the analysis, the signal to noise ratio  $SNR$  at the detector given from  $SNR = P_0 / NEP \sqrt{B}$  may be used to calculate a  $\sigma_\gamma(T, SNR)$  error term. Since these errors are independent, their variances may be added separately and therefore:

$$\sigma_{\gamma_{TOTAL}}(T, SNR) = \sqrt{\sigma_{\gamma_Q}^2 + \sigma_\gamma^2(T, SNR)} \quad (3)$$

The error  $\sigma_\gamma(T, SNR)$  in the rotating grid angle due to the  $SNR$  when the instrument is assumed to be completely balanced in  $d$  can be calculated from (1) after setting  $kd = \phi$ ,  $P = NEP \sqrt{B}$  and

$$\theta = \theta_0 \pm \sigma_\gamma(T, SNR) \text{ or } P = \left[ \frac{1 - \sin(2\theta_0 \pm 2\sigma_\gamma(T, SNR))}{4} - \frac{T}{2} \right]^2 P_0. \text{ Since } \theta = -\frac{\pi}{4} + \cos^{-1} \sqrt{T} \text{ it follows that:}$$

$$\sigma_\gamma(T, SNR) = \left[ \mp \sin^{-1} \left[ 1 - \left( \pm 4 \sqrt{P_0^{-1} NEP \sqrt{B}} + 2T \right) \right] \mp \pi / 2 \pm 2 \cos^{-1}(\sqrt{T}) \right] / 2. \quad (4)$$

where the upper and lower signs are used for transmittances above and below 50% respectively. A plot of  $\sigma_{\gamma_{TOTAL}}(T, SNR)$  assuming a quantisation error of 0.017 rad with a source power  $P_0$  of 1 mW and a range of detector  $NEP$  values at a bandwidth of 1 Hz as a function of sample transmittance is shown in Figure 4. A Plot of (2) is shown in Figure 5. The theoretical limits to the measurable sample transmittance  $T_{lim}$ , beyond which the nulls become unresolvable, are calculated using (1) after setting  $kd = \phi$ ,  $\theta_{max} = 3\pi/4$  for  $T < 50\%$  and  $\theta_{max} = \pi/4$  for  $T > 50\%$ . It can be shown that  $T_{lim} = [1 - \sin(2\theta_{max})] / 2 \pm 2 \sqrt{P_0^{-1} NEP \sqrt{B}}$  (Figure 6). A similar analysis for the phase errors involved will be presented at the conference.

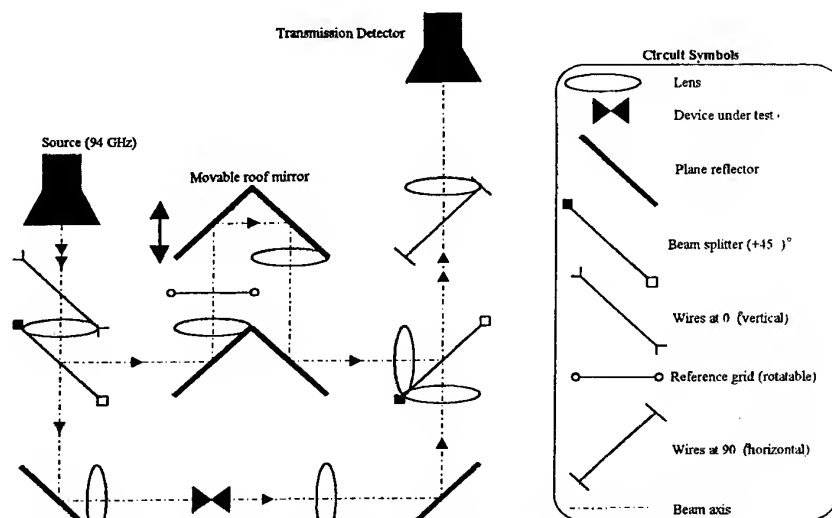


Figure 1. Null-balance transmissometer configuration

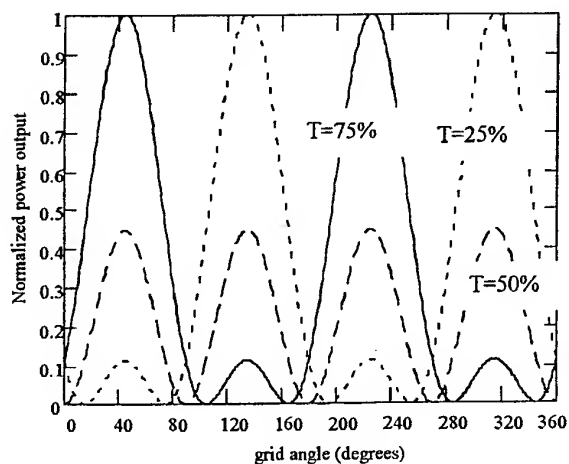
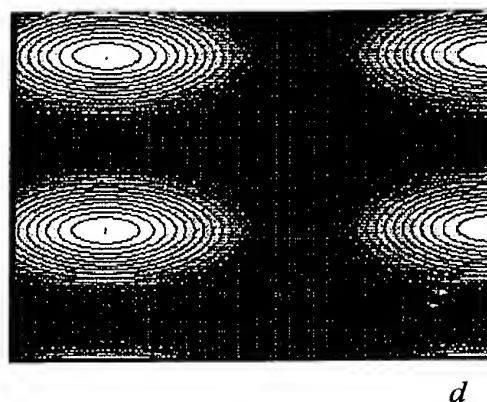
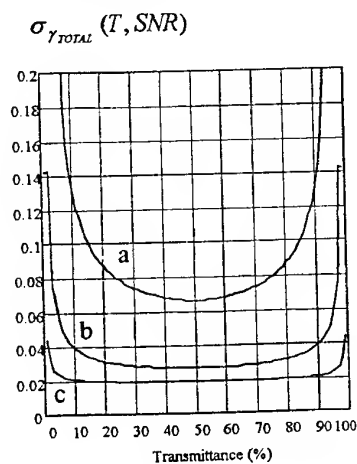
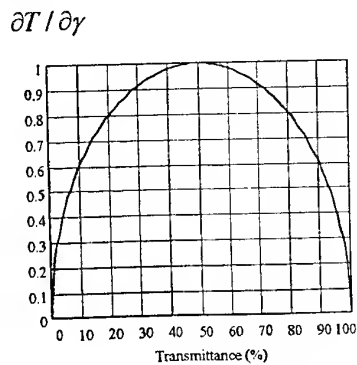
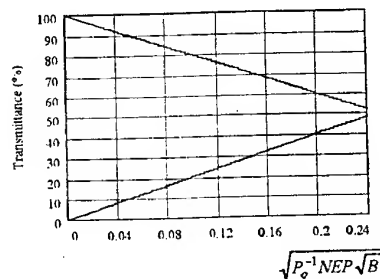
Figure 2. Normalised power output as a function of grid angle for different sample transmissions when the instrument is completely balanced in  $d$ .

Figure 3. Contour plot showing the relation between power output as a function of roof-top reflector distance and grid angle for a sample transmittance of 50%. Darkest sections correspond to a null.

Figure 4. A plot of  $\sigma_{\gamma TOTAL}$  for a)  $10^{-6}$  b)  $10^{-7}$  c)  $10^{-8}$   $\text{W Hz}^{-1/2}$ .Figure 5.  $\partial T / \partial \gamma$  as a function of sample transmittance  $T$ .Figure 6. Theoretical limits to the measurable sample transmittance  $T_{lim}$  as a function of SNR for a unit bandwidth

## Operation of a High Performance, Three Stage, Harmonic-Multiplying Inverted Gyrotron

H. Guo, J. Rodgers, V. L. Granatstein, G. Nusinovich, M. Walter, and J. Zhao  
Institute for Plasma Research, University of Maryland College Park, MD 20742-3511  
Fax: 301-405-9437, Tel: 301-405-5018

Several years ago, it was suggested that a new member be added to the family of high power, millimeter-wave gyro-amplifiers, namely the Phase-coherent, Harmonic-multiplying, Inverted Gyrotron (PHIGTRON). Experiments have now been carried out to evaluate its performance. The novel phigtron is a hybrid gyrotron which consists of a gyro-TWT as a prebunching input section operating at the fundamental cyclotron resonance and a two-cavity second harmonic gyroklystron as an output section. Phase locking, amplification and mode selection have been studied. Frequency doubling amplifier peak power of 320kW was achieved in the  $TE_{03}$  mode with a bandwidth about 0.6%, gain of 35dB and efficiency of 30% at frequencies about 33.4GHz. This measured performance considerably advances the state-of-the art for millimeter wave gyrotron amplifiers. The proof-of-principle phigtron experiments have established the following points: First, the weakly relativistic ( $V_b < 100$ KV) harmonic-multiplying scheme can be used for phase and frequency control with a compact driver, and highly efficient and stable harmonic operation. Second, the mode selective input coupler and interaction circuit are effective for suppressing spurious mode competition. Third, combined traveling-wave ballistic bunching is effective for high gain and broadband gyrotron operation. Fourth, the use of up-tapered magnetic field profile can effectively reduce the negative effect of beam velocity spread and voltage fluctuations on the efficiency and phase stability.

The phigtron has the potential of becoming a high average power, millimeter wave device with good efficiency, low noise, high gain, compact driver, and medium bandwidth for radar and other advanced applications.

The authors acknowledge helpful scientific discussions with B. Levush, K. R. Chu, B. Danly, T. M. Antonsen, Jr., and A. T. Lin. This work has been supported by the DoD MURI program under AFOSR grant F4962001528306.



## Development of High Power Gyrotron with Diamond Window

Keishi Sakamoto, Atsushi Kasugai, Masaki Tsuneoka, Koji Takahashi, Yukiharu Ikeda,  
Tsuyoshi Imai

RF Heating Lab., JAERI, Naka-machi, Ibaraki, 311-0193 Japan

Tsuyoshi Kariya, Yoshika Mitsunaka

Electron tube division, Toshiba Co., Otawara-shi, Tochigi, 324-8550 Japan

### Abstract

The diamond window was fabricated and installed on 170GHz gyrotron. In the pulse extension experiment, 520 kW / 6.2 sec, and 450 kW / 8 sec were attained. The total operation number of more than 1 sec was 1300 shots, and the total output energy was 1.8 GJ. No trouble was found both on the gyrotron and the diamond window. The temperature increase of the diamond disk stabilized after 5 sec with an edge cooling by water. It is concluded that the diamond window is useful and reliable, and gives a solution for the window problem on the gyrotron development.

### Introduction

On the development of high power, long pulse gyrotron, an output window has been supposed as the most serious and annoying problem. In the development in JAERI, the gyrotron performance was limited by the temperature increase of the window, where Sapphire or Silicon Nitride double disk windows were used [1]. Recently, however, the large sized synthetic diamond disk which has low  $\tan\delta$  and high thermal conductivity has been developed [2]. Using this diamond disk, the window assembly which has an edge cooling system by water was developed. The high power transmission test of this window assembly was carried out at 110 kW / 10 sec / 170 GHz, and the stable power transmission and the stabilization of the window temperature were confirmed [3]. This window assembly was installed on the 170 GHz gyrotron and the high power test was carried out.

### Diamond window gyrotron

A cross sectional view and a picture of the diamond window assembly are shown in Fig.1 and Fig.2, respectively. The diameter of the disk is 96 mm. The aperture of the window is 83 mm. The thickness of the disk is 2.23 mm, which corresponds to  $3\lambda_g$ . Here,  $\lambda_g$  is a wavelength in the diamond disk. Periphery of the disk, 2 mm, is cooled by water. The diamond disk was welded to the gyrotron output port. The baking of the gyrotron was performed for degassing at 450 deg.C in a large baking oven of Toshiba Co. The pressure in the baking oven is  $\sim 10^{-3}$  Pa. The baking was done for two days flat top ( which is shorter than standard gyrotrons because of re-baking ), and two days for heating up and four days for cooling down. The final vacuum pressure in the gyrotron was  $\sim 10^{-8}$  Pa. No vacuum leakage was found after the baking. In Fig.3, the picture of the diamond window gyrotron which is installed on the test stand is shown.

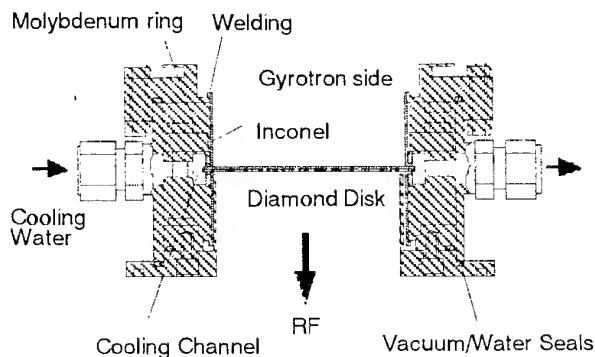


Fig.1: Cross sectional view of the diamond window assembly.

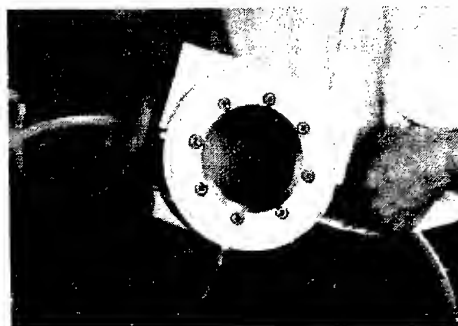


Fig.2: Picture of diamond window assembly.

### Experimental result and discussion

The gyrotron experiment was done on the JAERI gyrotron test stand. The corrugated waveguide of 88.9 mm in diameter was connected to gyrotron via mirror optics unit (MOU). The RF power is output from the window with a flat power profile and converted to  $HE_{11}$  profile using two phase correction mirrors in the MOU. The waveguide was tapered down from 88.9 mm to 31.75 mm, and terminated by a metal dummy load. The transmission line was evacuated to avoid the breakdown in the waveguide and dummy load. The window was cooled by water in which a corrosion inhibitor (c.c.15, Freeston Ltd.) was added to protect a brazing material between the diamond disk and the Inconel cylinder. The flow rate of the cooling water was 20 liters / min.

The pulse extension experiment was done at the output power  $P_{RF} \sim 520$  kW. Here, the beam voltage  $V_b = 84$  kV, beam current  $I_b = 31$  A, depressed collector voltage  $V_d = 32$  kV. The monitoring items are an outgassing in the gyrotron, window arcing, temperatures of the center and the edge of the diamond disk, cooling water temperature of the window, etc. The temperature of the window center was measured with a calibrated infrared camera whose detecting wavelength is 3-5.4  $\mu\text{m}$ . The other temperatures were obtained using thermocouples. In Fig.4, the time dependence of the temperature increase of the window is shown. Initial temperature of the cooling water was 283K. The closed circles are measured data and the dashed curve is a simulation result. Here,  $\tan\delta \sim 1.3 \times 10^{-4}$ , thermal conductivity of 1800 W/mK, and the transmission power of 520 kW, heat transfer coefficient of 1.2 W/cm<sup>2</sup>/K are assumed. The results show a good agreement. The maximum temperature increase was  $\sim 145$  deg.C, but almost stabilized after  $\sim 5$  sec. It is found that the diamond disk has a capability of at least by this temperature. The solid line in Fig.4 is a simulation result of the temperature increase when the Gaussian beam (1/e radius of 21mm) of 1 MW is transmitted through the window of  $\tan\delta \sim 2 \times 10^{-5}$ . This suggests a potential of the diamond window for multi-megawatt power transmission if the high quality diamond disk such as  $\tan\delta \sim 2 \times 10^{-5}$ , which is already developed, is used [3].

In the experiment, the pulse extension was tried up to 6.2 sec at  $P_{RF} = 520$  kW, and 8 sec at  $P_{RF} = 450$  kW. It should be noted these values were limited by the experimental time, not by the limit of the diamond window nor a gyrotron failure. Total number of the operation of greater than 1 sec was  $\sim 1300$ . Total output energy was  $\sim 1.8$  GJ. After the experiment, the surface of the diamond disk was inspected, but no damage and no trouble were found.

It is concluded that the synthetic diamond disk is useful and reliable for gyrotron output window. It should be pointed out that the diamond window has a potential for multi-megawatt and CW power transmission of millimeter wave when the disk of lower  $\tan\delta$  is used.

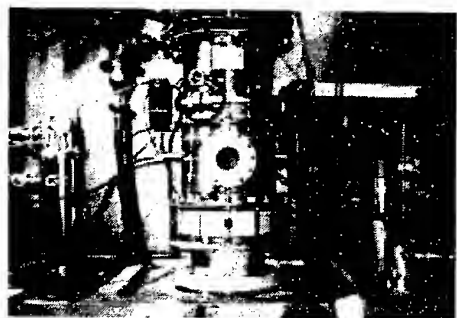


Fig.3: Picture of 170 GHz gyrotron with diamond window assembly installed on the test stand.

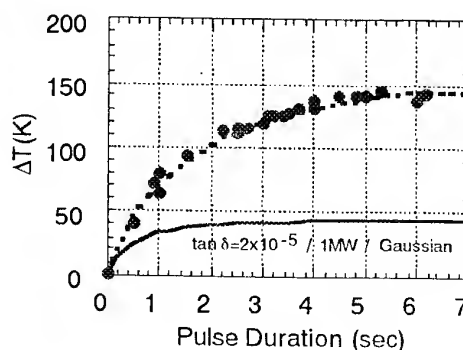


Fig.4: Time dependence of temperature increase of the diamond window  $\Delta T$ . Dashed line is simulation results at  $P_{RF} = 520$  kW,  $\tan\delta = 1.3 \times 10^{-4}$ , flat power profile.

### References

1. K. Sakamoto, A. Kasugai, M. Tsuneoka, et al., Int. J. Infrared and Millimeter Waves, **18**, 1637 (1997).
2. R. S. Sussmann, J. R. Brandou, G.A. Scarsbrook, et al., Diamond and Related Materials., **3**, 303(1994).
3. A. Kasugai, K. Sakamoto, K. Takahashi, et al., Rev. Sci. Inst., **69**, 2160 (1998).

## Experimental Results of Two High Powered Coaxial Gyroklystrons

M.Castle, W. Lawson, B.Hogan, J.Cheng, X. Xu, V.L. Granatstein, M.Reiser

Work supported by the U.S. Dept. of Energy  
Institute for Plasma Research  
University of Maryland  
College Park, MD 20742 USA

### Introduction

In linear accelerating structures in the near future, high power microwave amplifiers will propel the particles to energies that exceed 1 TeV. These amplifiers must be efficient and stable. Current linear colliders are powered by klystrons. Typical performance of a state of the art klystron is at SLAC where they have produced a PPM klystron that exceeds 50 MW power at 60% efficiency.[1] At University of Maryland, we have been exploring the merits of gyroklystrons as potential drivers for linear colliders. A series of experiments at the 30 MW level culminated 6 years ago with about 32 MW at 19.76 GHz.[2]

In the intervening time, our project has upgraded our test bed to accommodate a 100 MW power level. A new magnetron injection gun was designed and installed and our modulator was altered to produce a small orbit gyrating beam of up to 800 A at 500 kV. A coaxial design was undertaken to have the drift tube cut-off to the operating modes and to increase isolation. The microwave transport, which includes two nonlinear uptapers to guide the signal to the diagnostics were doubled in radius. A new output window, new beam dump and dumping magnet to channel the spent beam into the tube wall, and new input waveguide system all were constructed to accommodate higher power levels.

### Fundamental System

The fundamental system for the 100 MW gyroklystron operates at about 8.57 GHz in the TE<sub>01</sub> output mode. Two different tubes were tested. The first tube had two cavities, an input cavity for impressing an input signal on the beam and an output cavity to couple the beam power back into microwave energy. This tube was tested for only a short time due to output power levels far below what was expected. A maximum power of about 0.5 MW was achieved. The major limitation seemed to be poor coupling of beam power in the input cavity.

For the second tube, the input cavity design was redone. The Q of the input cavity was increased to 73 and a second window was placed along the input waveguide to minimize reflections. The symmetric injection setup, that is, input waveguide split and injected on either side of the input cavity, which had been employed in the previous tube for mode purity reasons was abandoned in favor of one port injection, which was seen to be better in the cold testing.

Other significant upgrades from the first tube to the second tube were made. A buncher cavity was added in the drift space between the input and output cavities to enhance the azimuthal bunching process begun in the input cavity and to increase the gain of the system.

The main microwave diagnostic used in our system is a anechoic chamber with a 10" diameter input from the system. An open piece of X-band waveguide that has been placed in a lossy dielectric mold to minimize reflections, serves as the chamber's antenna. It is on a motorized track and can be swept in one dimension for mode patterns for two components of the far field. A crystal detector is attached to this setup and by these methods we obtain the pulse shape, mode pattern, and first measurement of the power in the system. A directional coupler was constructed by the advent of the second tube to verify these preliminary results in two ways: a crystal detector placed on the coupled port for the coupler, and a water calorimeter load at the end of the transmitted port which gives an estimate of average power over a certain number of shots. The repetition rate of this tube was 0.5 Hz and the pulse length is about 1.2  $\mu$ s. The calibrated numbers for the anechoic chamber and the directional coupler were  $-30 \pm 0.5$  dB and  $-62.3 \pm 0.5$  dB, respectively.

The second tube's maximum output power was 75 MW at a nominal operating point of 469 kV and 506 A for an efficiency of almost 32% and a gain of 29.7 dB. This was validated from all three sources of power measurements. The optimized input frequency at the nominal point was 8.601 GHz, a detuning from the design by 33 MHz and the pulse length was 1.7 microseconds for FWHM. The magnetic field in the output cavity at the nominal operating point was 4.99 kG. To attempt to estimate realistic  $\alpha$ (perpendicular to parallel velocity ratio) and velocity spread parameters, from the nominal 1.5 and

6.4% respectively, the tube was resimulated at various lower alpha values and at the realistic nominal magnetic field values. An operating point that corresponded very closely to the data was found with an alpha of 1.01 and a spread of 4.4%. This lower alpha value can be seen as the limitation to output power in this tube.

The second tube was nevertheless a very stable tube. Broad areas of magnetic field and voltage and current were able to be swept without encountering instabilities. The main limitation to the experiment was a cut in the pulse that was encountered when the cathode magnetic field was turned below a nominal value, whereby alpha was raised. The pulse would rise to almost its maximum and then drop down for about 0.5 microseconds and then resume its seemingly natural "uncut" trace. A loop antenna was placed in the back of the gun structure to observe backstreaming instabilities in the system, yet no great instabilities were observed at this loop. This phenomenon was not fully understood.

#### **Second Harmonic System**

A second harmonic design has been developed at 17.14 GHz in the TE02 mode. As of this writing it was about to go on-line in the system. Changes to the fundamental include: different microwave transitions to minimize mode conversion, and three new cavities in the microwave circuit. All three cavities have been fully designed and cold tested. The input cavity Q was lowered to increase stability to spurious oscillatory modes, while the buncher and output cavities were made to operate at the second harmonic frequency in the TE02 mode. The output cavity was pre-detuned by 26 MHz to optimize efficiency in accordance with a time dependent simulation. The simulated efficiency at an alpha of 1.5, current of 720 A, and spread of 6.4% was 41%.

#### **Conclusion**

Significant efforts have been made to characterize the performance of two 100 MW coaxial gyrokystrons. The fundamental system was a success. It achieved a very respectable power level of 75 MW. It uncovered some performance issues we will attempt to address in various ways in the second harmonic system, such as limitations on the current, alpha, and frequency detuning.

1 SLAC Klystron development home page. <http://www.slac.stanford.edu/grp/kly/index.html>

2 H.W. Mathews et.al., "Experimental Studies of stability and amplification in a two cavity second harmonic gyrokystron", IEEE Trans. Plasma Sci. vol. 20, pp.205-215, 1992

# Status Report on a 110 GHz, 1 MW CW Gyrotron with a CVD Diamond Window

K. Felch<sup>+</sup>, P. Borchard<sup>+</sup>, S. Cauffman<sup>+</sup>, R.W. Callis<sup>%</sup>, P. Cahalan<sup>+</sup>, T.S. Chu<sup>+</sup>, D. Denison<sup>&</sup>,  
H. Jory<sup>+</sup>, M. Mizuhara<sup>+</sup>, D. Remsen<sup>%</sup>, G. Saraph<sup>+</sup> and R.J. Temkin<sup>&</sup>

<sup>+</sup>Communications and Power Industries, Palo Alto, CA, USA

<sup>%</sup>General Atomics, San Diego, CA, USA

<sup>&</sup>Plasma Science and Fusion Center, MIT, Cambridge, MA, USA

## Abstract

A 110 GHz, 1 MW gyrotron, which employs a CVD diamond output window, has been designed, constructed and is currently undergoing initial tests. The design and initial tests on the gyrotron are summarized.

## Introduction

The output window was the key factor that limited the achievable pulse duration in a previous 110 GHz, 1 MW gyrotron developed at CPI.[1] The earlier 110 GHz tube had utilized a double-disc, sapphire window that was face-cooled with a fluorocarbon coolant. According to thermomechanical analyses of this window, it is limited to 450 kW CW or 1 MW for 800 ms pulse duration. Temperature measurements on the window, taken during long-pulse tests on the tube, confirmed this analysis.[1] The tube was operated at power levels of 1.0 MW for 0.6 s and 0.53 kW for 2.0 s.[2] To address the window limitations, a single-disc, CVD (chemical-vapor-deposition) diamond window, that employs water cooling around the edge of the disc, was incorporated into a second 110 GHz, 1 MW gyrotron. Calculations predict that the CVD diamond window should be capable of full 1 MW CW operation. An added advantage of the CVD diamond window is that the output mode can be a fundamental Gaussian rather than the "flattened" Gaussian that was used on the earlier tube to maximize the power-handling capability of the window. This greatly simplifies the coupling of the output power to a low-loss transmission line outside the tube. Below we summarize the key elements of the tube design and discuss initial test results.

## Design Features

The design configuration for the 110 GHz, 1 MW gyrotron with a CVD diamond window is shown in Figure 1. The designs of the magnetron-injection gun, TE<sub>22,6</sub>-mode cavity and 61-cm diameter collector are similar to those of an earlier 110 GHz, 1 MW gyrotron.[1] The design of the internal converter is also similar to the earlier

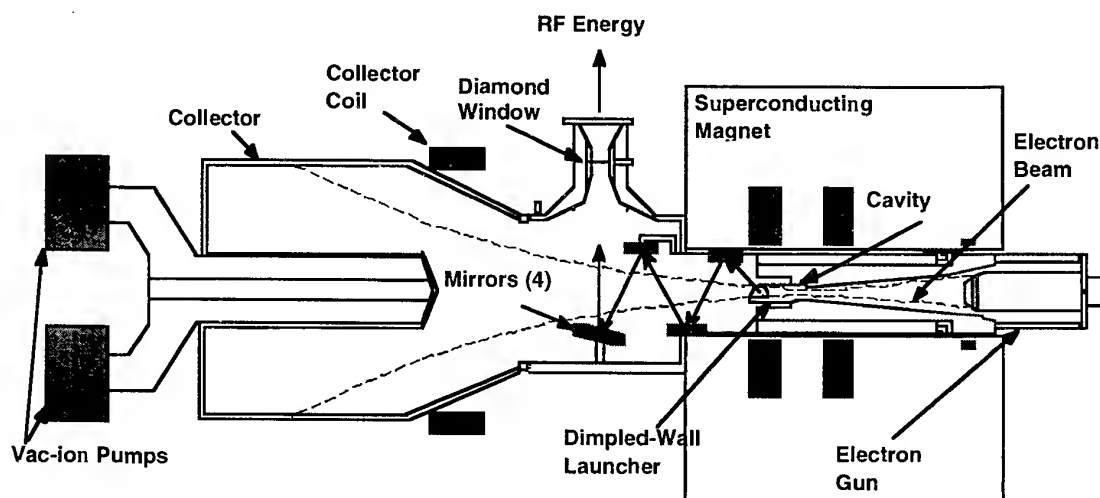
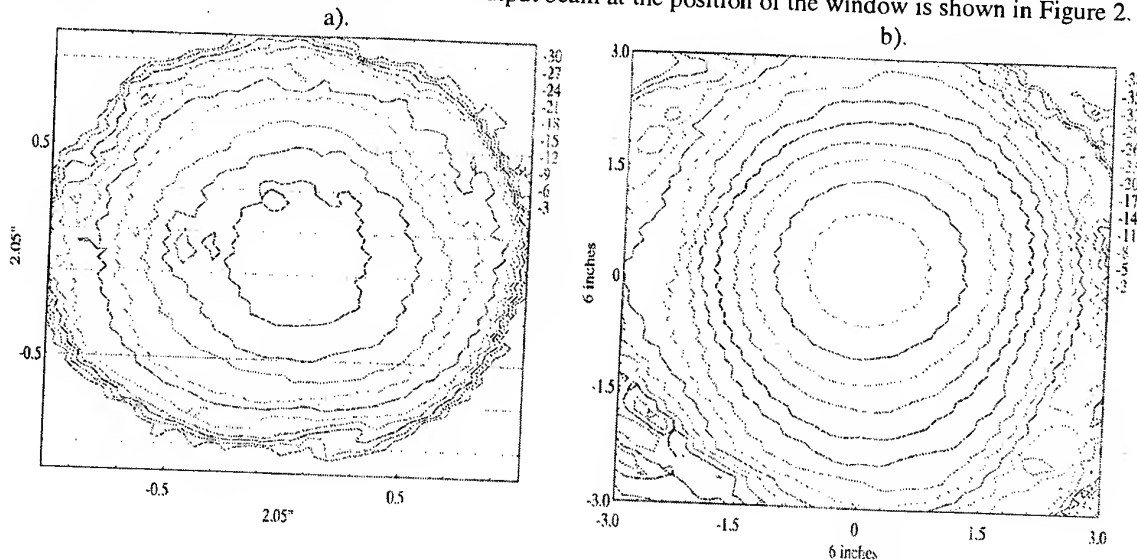


Figure 1. Schematic diagram of 110 GHz, 1 MW gyrotron with a CVD diamond window.

tube except that the design of the last two mirrors was carried out using phase reconstruction techniques based on measurements of the output radiation from the first two mirrors.[3] The resulting Gaussian mode has excellent Gaussian beam characteristics and is transmitted through the 5.08-cm-diameter window aperture with more than 98% efficiency. The measured profile of the output beam at the position of the window is shown in Figure 2.



**Figure 2. Cold-test mode patterns at a). window and b). 59 cm from output window. (Intensities shown are in dB relative to the peak.)**

The CVD diamond window has an overall diameter of 7.0 cm and is 0.117 cm thick. The window is edge-cooled by water. Measurements of the loss tangent for the CVD diamond disc were made at FZK at a frequency of 145 GHz. These measurements indicated that all regions of the window had a loss tangent of less than  $1.0 \times 10^{-4}$  and that much of the window had a loss tangent value of less than  $5.0 \times 10^{-5}$ . Assuming a loss tangent of  $1.0 \times 10^{-4}$  at a frequency of 110 GHz, thermal analyses predict a maximum temperature rise in the window of  $107^\circ\text{C}$ , for an incident power of 1 MW. The resulting maximum tensile stress, including atmospheric pressure, is 42 MPa, which is well below measured ultimate tensile stress values for CVD diamond.

### Initial Tests

Following the fabrication and processing of the tube, tests on the tube were begun. At this writing, the tube has been operated at power levels up to 750 kW during short-pulse (1 ms) operation and 600 kW for pulse durations of 400 ms. Mode patterns taken during the tests agree quite well with the cold tests shown in Figure 2. The goal of these tests is to achieve 1 MW power levels for 10-s pulses.

### Acknowledgments

This work was supported by the U.S. Department of Energy, Office of Fusion Energy, under Prime Contract DE-FC02-93ER54209, by subcontract through the Massachusetts Institute of Technology, Cambridge and under Prime Contract DE-AC03-89ER51114, by subcontract through General Atomics.

### References

1. K. Felch, et al., "Long-Pulse and CW Tests of a 110 GHz Gyrotron with an Internal, Quasi-Optical Converter," IEEE Trans. Plasma Sci., vol. 24, no. 3, pp. 558-569, June 1996.
2. H. Jory, et al., "Recent Activities with CPI Gyrotrons for ECRH," in Proc. Second Europhysics Topical Conference on Radio Frequency Heating and Current Drive of Fusion Devices, pp. 257-260, January 1998.
3. D. Denison, M. Shapiro, R. Temkin, "Internal Mode Converter Mirror Shaping from Measured Field Intensity," 1998 IEEE Int. Conf. Plasma Science, Conference Record, pg. 324, June 1998.

## Design Of A Multi-Megawatt 95 GHz Gyroklystron Experiment

W. Lawson and M. R. Arjona

Electrical Engineering Department and Institute for Plasma Research  
University of Maryland, College Park, MD 20742

### Abstract

In this paper we present the three cavity design of a 95 GHz gyrokystron. The 500 kV, 30-70 A beam is produced by a MIG with an average perpendicular-to-parallel velocity ratio of 1.5 and a parallel velocity spread below 5%. The microwave circuit has a first-harmonic  $TE_{011}$  input cavity which is driven at 47.5 GHz, and second-harmonic  $TE_{021}$  buncher and output cavities which are resonant at 95 GHz. A peak power of 7.56 MW is obtained with 51.6 dB gain and 33.6% efficiency. A complete description of the system is presented.

### Introduction

The range in frequencies near 95 GHz is currently of great interest for radar applications due to the low atmospheric absorption. Because of the dependence of breakdown on frequency, there is also interest to develop an amplifier for high energy RF acceleration of electrons in W-Band. The power tubes that are commercially available at these frequencies have maximum output powers of about 3 kW and research tubes have peak powers below 100 kW. At the University of Maryland, we have a program to develop high power gyrotron amplifiers for electron-positron collider applications. We have designed, constructed, and tested a variety of gyrokystron tubes, including a 2<sup>nd</sup> harmonic, two-cavity tube which produced peak powers above 30 MW at 19.7 GHz [1]. In this paper we scale this 19.7 GHz tube to 95 GHz. Details of the Magnetron Injection Gun (MIG) design are presented in the next section. The microwave circuit design is discussed in the section preceding the summary.

### Magnetron Injection Gun

The magnetron injection gun which generates our injected beam is shown in Fig. 1. The gun design is based on the gun for the 19.7 GHz tube. A scaling code was used to obtain the starting dimensions. After being scaled, the design was adjusted by changing the boundaries in both anodes and cathode until the required parameters were obtained with the minimum velocity spread. *Egun* was used to simulate the performance of the electron gun.

Our MIG is designed for minimum velocity spread at a current of 45 A. The parameters of the gun and the results of the simulation are summarized in Table I. The control anode voltage required to produce the proper velocity ratio is 65.1 kV and the magnetic compression is about 30. At 10 A/cm<sup>2</sup>, the cathode loading is a little high, but well within the state-of-the-art. The electric field is less than 100 kV/cm everywhere.

Because the cathode angle is low, the beam is non-laminar and the axial velocity spread varies significantly with beam current. As expected, the minimum velocity spread occurs at 45 A. The axial velocity spread remains below 10% for all currents between 30 A and 65 A. The required change in the control anode voltage to keep  $\alpha$  at 1.5 throughout this range in currents is  $\pm 3.5$  kV.

### Microwave Circuit

Our amplifier circuit is made of input, buncher, and output cavities that are connected by drift regions. The input cavity interacts at the first harmonic in the  $TE_{011}$  mode. Simulations showed that a buncher cavity was necessary in order to increase the power that can

Fig.1 The 500 kV, 45 A Electron Gun Simulation

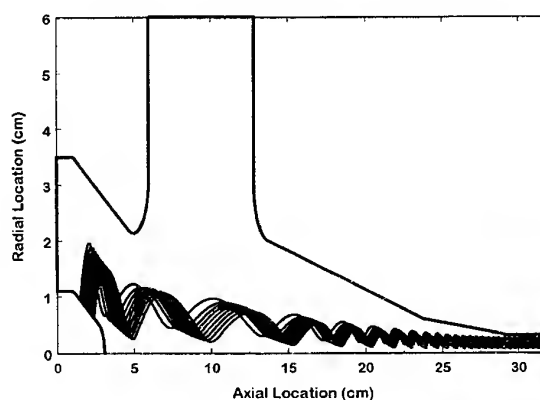


Table I: Electron gun specifications and simulated performance.

Emitter radius (cm)	0.78
Emitter width (cm)	0.958
Emitter angle (deg)	20
Cathode loading (A/cm <sup>2</sup> )	9.58
Cathode magnetic field (G)	900
Cathode-anode gap (cm)	2.262
Average velocity ratio	1.5
Axial velocity spread (%)	4.69
Average beam radius (cm)	0.163
Peak anode field (kV/cm)	81
Peak cathode field (kV/cm)	94
Space-charge current (A)	98

be extracted from the output cavity at the second harmonic (in the  $TE_{021}$  mode). A picture of the circuit design is shown in Fig. 2. The starting parameters for the circuit came from scaling the input and output cavities from the 19.7 GHz design and adding the buncher cavity. The buncher and output cavities have dolph-chebychev radial wall transitions. This proved in simulations to minimize mode conversion from the  $TE_{02}$  to the  $TE_{01}$  mode. The initial dimensions were adjusted to get the desired first (47.5 GHz) and second harmonic (95 GHz) frequencies. This is done using a simulation code called *Coax*. This code takes for input the cavity's dimensions and starting points for the frequency and quality factor (Q) search. It then iterates the frequency and Q until it finds a solution. The azimuthal mode is an input to the code, but a field plotting routine is required to verify that the mode found by *Coax* has the correct radial and axial mode numbers.

After the dimensions were modified to the correct values, two different codes were run to get the system efficiency. These codes are *Hpm\_gen* and *Gycoax*. Both codes are partially self-consistent, but they take very different approaches to solving the problem and serve as a check of the results. Furthermore, *Gycoax* has been compared extensively to experimental results for other gyroklystrons and has always given good agreement. The dimensions of the microwave circuit and the simulated results from *Hpm\_gen* are given in Table II. Note that the quality factors are at least an order of magnitude below the resistive Q of a copper cavity. That means that over 90% of the output power can be extracted from the system and that the buncher Q must be realized with additional loss (e.g. lossy ceramics [1]).

To assure stability another code was used: *Qpb*. This code gives the Q (for each cavity) below which the device will be stable as a function of magnetic field and beam power. The threshold Qs for the input, buncher, and output cavities are approximately 730, 1225, and 1730, respectively, indicating that the system will be stable.

In Fig. 3 we plot the relationship between efficiency and velocity spread as computed by both large-signal codes. Note that the agreement is quite good. Our MIG is predicted to produce a beam with 4.7% spread. We can see from the figure that the efficiency for an ideal beam (zero spread) is over 36%. Note that this our design's efficiency is less than 3% lower than that of the ideal beam and that the efficiency remains above 30% for velocity spreads up to about 6.5%.

### Summary

The three cavity gyroklystron presented in this paper is predicted to produce over 7 MW at 95 GHz – more than 2 orders of magnitude above the state-of-the-art for amplifiers. This high power is obtained from the interaction between a second harmonic output cavity and a 45A, 500kV beam which is produced by a double-anode MIG. According to simulations, the beam quality is sufficiently high to produce an interaction efficiency of 33.6% with a high gain (>50 dB). The tube is predicted to be zero-drive stable. In the future we hope to build and test this microwave system.

### REFERENCES

1. V. L. Granatstein and W. Lawson, "Gyro-Amplifiers as Candidate RF Drivers for TeV Linear Colliders" IEEE Trans. on Plasma Science, vol. 24, pp. 648-665 (1996).

Fig. 2 The 95 GHz Circuit Design

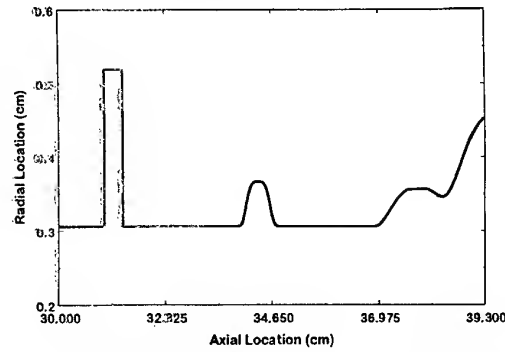


Fig. 3 Dependence of Efficiency on Velocity Spread

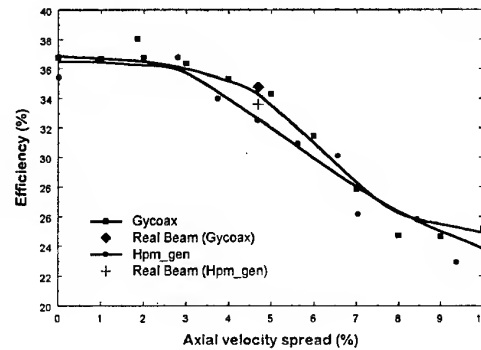


Table II: Microwave circuit parameters and simulated results.

Input Cavity	
Drive frequency (GHz)	47.5
Resistive quality factor (Q)	600
Radius (mm)	5.19
Length (mm)	4.00
Input drive power (W)	52
Buncher Cavity	
Maximum radius (mm)	3.663
Length (mm)	20.20
Required Q	1075
Output Cavity	
Main section radius (mm)	3.457
Overall length (mm)	23.70
Required Q	1345
Drift Regions	
Radius (cm)	0.306
Length I-B (cm)	2.50
Length B-O (cm)	2.09
Amplifier performance	
Power (MW)	7.56
Efficiency (%)	33.6
Gain (dB)	51.6



## Optimisation of the Electron Beam-Cavity System of 170 GHz Gyrotron for ITER .

V.E.Zapevalov, V.A.Flyagin, N.Kuftin, M.A.Moiseev, N.A.Zavolsky.

Institute of Applied Physics, Russian Academy of Sciences, GYCOM Ltd. (46 Ulyanov Street, 603600 Nizhny Novgorod, Russia),

### Abstract

The report presents improved method and results of numerical and experimental study of the possibility to optimise processes of mode interaction in the electron beam-cavity system for the 170 GHz/1 MW gyrotrons with different operating mode for ITER. Parameters are optimized to achieve maximum efficiency of the gyrotron with an acceptable Ohmic load on the cavity. The influence of unwanted mode conversion at the output of the resonator, mode competition, electron beam potential depression, ion compensation of the space charge and beam energy recovery is investigated.

### Introduction

Electron-cyclotron heating and current control in planned ITER plasma set-ups require gyrotrons with the level of CW power up to 1 MW and frequencies 170 GHz and efficiency not less than 50%. In the framework of the international ITER project, from the preliminary analyses possible operating modes have been chosen and the general design concept of the gyrotron has been developed [1]. The report presents improved method and results of numerical simulation and experimental study of the possibility to optimise processes of mode interaction in the electron beam-cavity system for the 170 GHz/1 MW gyrotrons with different operating mode for ITER including the possibility for energy recovery (CPD-regime [2-5]).

### Numerical simulation

Stable single-mode generation in an oversized cavity at sufficiently high efficiency  $\eta$  and the megawatt level of output power  $P$  becomes an extremely complicated problem as the operating frequency grows [1,4]. An essential circumstance here is, that this problem has to be solved within a number of limitations. The most difficult is the limitation on density of ohmic losses in cavity walls - energy removal is limited by possibilities of the cooling system, which are, as a rule, not higher than 2-3 kW/cm<sup>2</sup>. For spatially developed modes conventionally used in gyrotrons at the cavity with the Gaussian field structure one can find the following estimate for efficiency depending on parameters

$$\eta \approx \eta_{\max}^{3/4} \cdot \frac{(1 + g^2)^{1/4} \cdot v_s^{5/4} \cdot (\lambda^{5/2} P_{\text{ohm}})^{3/4}}{3 \cdot m^{1/4} \cdot U_0^{1/2} \cdot P^{1/2}} \quad (1)$$

(where  $\eta_{\max}$  is  $\eta$  at  $I_0 = I_{0,\text{opt}}$ ,  $\lambda$  is wavelength in millimeters,  $g$  - pitch factor,  $v_s$  is the root of equation  $J_m'(v_s) = 0$  corresponding to the considered mode TE<sub>m,p</sub> with azimuthal ( $m$ ) and radial ( $p$ ) indexes, and  $J_m'(v)$  is argument derivative of Bessel function  $J_m(v)$ ,  $P_{\text{ohm}}$  (kW/cm<sup>2</sup>) is specific power of Ohmic losses in a cavity). It was taking into account Distinction of values of real Ohmic Q-factor and ideal one by 1.5-2 times was accepted. Results of numerical simulation for the detailed model of gyrotrons are shown in the fig.1. Admissible values of  $m/p$  and  $R_0/R_r$  are limited by lower efficiency due to voltage depression and mode competition.

Effects of beam voltage depression and mode interaction as well as undesired mode conversion, methods of mode selection and energy recovery are investigated also. Fig. 2. shows the possibility of gyrotron efficiency improvements with single-stage depressed collector (CPD).

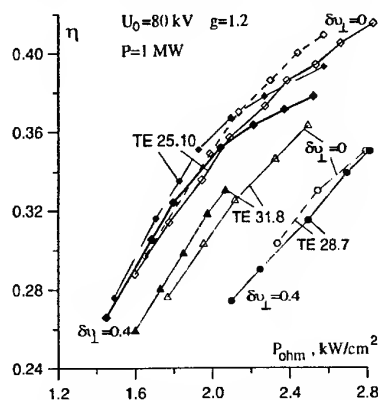


Fig. 1. Dependence of efficiency on specific power of Ohmic losses.

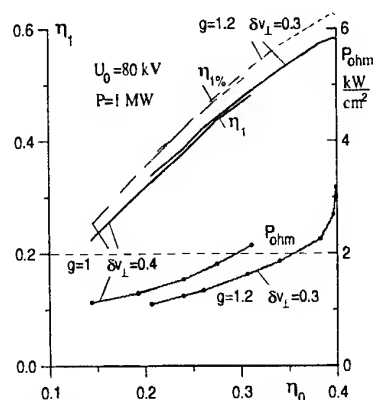


Fig. 2. Efficiency with CPD  $\eta_1$ ,  $\eta_{1\%}$  and  $P_{\text{ohm}}$  vs. cavity efficiency  $\eta_0$ .

### Experimental investigation of short pulse gyrotron

Finally basing on the analysis of technical limitations the  $TE_{28.7}$  and  $TE_{25.10}$  operating modes have been chosen for experimental tube which give us the possibility to check different scientific and technical solution. Magnetic system of the tube includes a main superconducting solenoid and a cathode coil for fine adjustment of electron beam parameters. All the gyrotrons uses the optimized magnetron injection guns, which forms a quasi-laminar helical beam [2]. The converter [1, 3] separates RF radiation from the worked-out electron beam, transforms a complicated cavity mode to an optimised wave beam and allows one to minimise harmful action of possible reflections of RF power back to the gyrotron.

Experimental investigation of short pulse prototype of the 170 GHz gyrotron were made on the automated set-up and dependencies of gyrotron parameters on the beam current, accelerating voltage and magnetic field is analyzed. Fig.3. shows output power and efficiency dependencies on the beam current for two cavity version of the  $TE_{25.10}$  gyrotron. The output power level 1 MW was achieved at the  $TE_{28.7}$  and  $TE_{25.10}$  operating modes in design regime with efficiency 32% and 34%, correspondingly. The maximum output power near 1.3 MW with efficiency 32% was achieved at the  $TE_{25.10}$  operating mode. Calculation and experimental data are in a good correlation.

The same  $TE_{25.10}$  gyrotron has been operated also with a single-stage depressed collector (CPD). Measurements of the RF-output power and efficiency in dependence on the retarding collector voltage were provided (fig.4). Output power of 1MW/0.1ms was obtained at the beam parameters of 80 kV/40 A. The improved efficiency with single-stage depressed collector was over 60%.

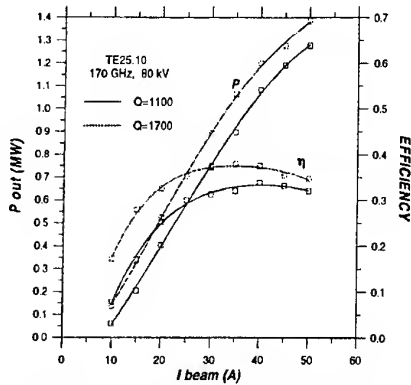


Fig.3 Output power and efficiency vs. beam current for the  $TE_{25.10}$  gyrotron

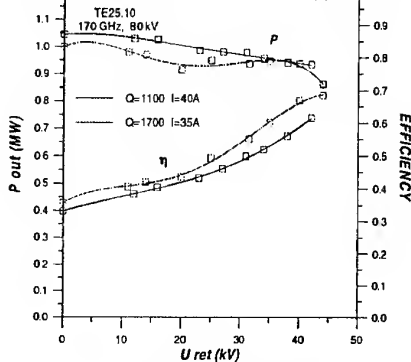


Fig.4. Output power and efficiency vs. retarding voltage.

### Conclusion

The possibility to make 170 GHz/1 MW gyrotron for ITER is proved by calculations and experiments. The data presented prove that in a gyrotron for ITER it is possible to obtain single-frequency generation at the operating mode with output power 1 MW and efficiency 33–36% at pitch factor  $g=1.2-1.4$ , velocity spread  $\delta v_{\perp}=0.4$  and specific power of Ohmic losses in the cavity wall less than  $2 \text{ kW/cm}^2$ . The use of a collector with single-stage recovery makes efficiency by 1.6 times higher, up to 55–65%. Calculation results and experimental data for the 170 GHz/1 MW gyrotron for ITER are in a good correlation.

### References

1. G.G.Denisov, V.A.Flyagin, V.E. Zapevalov Conf. Proc. 20 Int. Conf. on IR & MM waves. Orlando, USA.197 (1995)
2. K.Sakamoto, M.Tsuneoka, A.Kasugai et al., Phys. Rev. Letters, V.73, No.26, 3532-(1994).
3. V.L.Bratman, G.G.Denisov, A.V.Savilov. Int. J. of Infrared and MM Waves, V.16, No.3, 459.(1995).
4. A.L.Goldenberg, et al., Int. J. of Infrared and MM Waves, V.18, No.1, 43 (1997)
5. M.Yu.Glyavin, et al., Int. J. of Infrared and MM Waves, V.18, No.11, 2129 (1997).
6. A.N.Kuftin, et al. Int. J. Electronics, 72, 1145 (1992).
7. V.E.Zapevalov et al., Conf. Proc. 22 Int. Conf. on IR & MM waves. Wintergreen, USA., pp. 108 (1997)

## High Power Operation of an 8.6 GHz Coaxial Gyroklystron

W. Lawson, J. Cheng, B. Hogan, V. L. Granatstein, and X. Xu

Electrical Engineering Department and Institute for Plasma Research  
University of Maryland, College Park, MD 20742

### Abstract

We have conducted experiments on two X-Band coaxial gyrokystron tubes which were designed for collider applications. Calibrated measurements indicate that we have achieved a maximum peak power in excess of 75 MW at 8.6 GHz in a three-cavity first-harmonic tube with a gain near 30 dB and an efficiency near 32%. In this paper we detail the results of these experiments.

### Introduction

At the University of Maryland, we have been investigating the suitability of high power gyrokystrons as drivers for linear colliders for over a decade. [1] To this end, we have designed, constructed, and tested a number of gyrokystron tubes operating from X-Band to Ka-Band. With a 440 kV, 160-260 A beam, we were able to produce about 30 MW of peak power in 1  $\mu$ s pulses near 9.87 and 19.7 GHz with first- and second-harmonic gyrokystron tubes, respectively. The peak efficiencies were near 30% and the large-signal gains were 25-35 dB.

The focus in the past few years has been to upgrade the system to achieve peak powers near 100 MW. Our approach has been to increase beam current by enlarging the average beam radius. Subsequently, the tube cross-sectional dimensions are increased and an inner conductor is required to maintain cutoff to the operating mode in the drift regions. In this paper we discuss the experimental test facility, the computer simulations, and the experimental results from our first two X-Band tubes.

### Experimental Test Facility

The voltage pulse is generated with a modulator which is capable of producing 2  $\mu$ s flat-top pulses with voltages and currents up to 500 kV and 800 A, respectively. Our single-anode MIG is capable of producing a 500 kV, 720 A beam with an average orbital-to-axial velocity ratio of  $\alpha = 1.5$  and an axial velocity spread of  $\Delta v_z/v_z < 10\%$ . The beam parameters are given in Table I for the operating point where maximum amplification occurred. The voltage and current are measured quantities; all other values come from EGUN simulations and are based on the MIG geometry and the magnetic field profile. The axial fields at the centers of the three cavities are given in Table I.

The 3-cavity microwave circuit is shown in Fig. 1 and the key dimensions are given in Table I. The inner conductor is supported by two thin tungsten pins and forces the drift tubes to be cutoff to the  $TE_{01}$  mode at 8.6 GHz. Lossy ceramics are placed in the drift regions to suppress spurious modes. The rings on the inner conductor generally alternate between carbon-impregnated alumino-silicate (CIAS) and 80% BeO-20% SiC. Two layers of lossy ceramics are placed along the outer conductor in the drift regions. The 2-cavity circuit omits the buncher cavity and has a longer drift region.

The input cavity is defined by a decrease in the inner conductor radius. The cavity loss is roughly evenly divided between the coupling aperture and a CIAS ring on the inner conductor which is placed adjacent to the cavity. The power to the input cavity is supplied by a 150 kW coaxial magnetron. The buncher cavity has identical dimensions for the metal components. However, the Q is determined

Table I. The system parameters.

Beam parameters	
Beam Voltage (kV)	470
Beam Current (A)	505
Average Velocity Ratio	1.05
Axial velocity spread (%)	4.4
Magnetic field parameters	
Input cavity field (kG)	5.69
Buncher cavity field (kG)	5.38
Output cavity field (kG)	4.99
Input and buncher cavity parameters	
Inner radius (cm)	1.10
Outer radius (cm)	3.33
Length (cm)	2.29
Quality factor	$70 \pm 15$
Output cavity parameters	
Inner radius (cm)	1.01
Outer radius (cm)	3.59
Length (cm)	1.70
Quality factor	$135 \pm 10$
Drift tube parameters	
Inner radius (cm)	1.83
Outer radius (cm)	3.33
Length (between I-B) (cm)	5.18
Length (between B-O) (cm)	5.82
Amplifier Results	
Drive Frequency (GHz)	8.60
Output power (MW)	75
Pulse length ( $\mu$ s)	1.7
Gain (dB)	29.7
Efficiency (%)	31.5

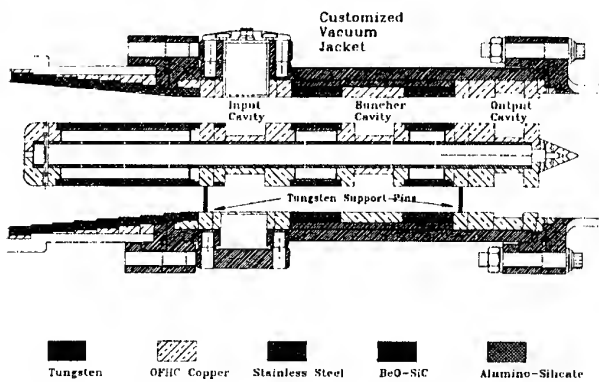


Figure 1. The three-cavity microwave circuit.

For the 6% spread predicted for a 500 A beam, the simulated interaction efficiency is about 40%. All microwave cavities are expected to be stable at the design operating point. The theoretical efficiency for the 2-cavity tube is slightly less, but the predicted gain is significantly lower. Consequently, the 2-cavity tube was gain-limited and produced less than 1 MW of output power.

The experimental results for the 3-cavity tube have been listed in Table I. The time dependence of the beam voltage, beam current, and the amplified signal are shown in Fig. 3. The peak values indicated in Table I represent the average value of the signal in the flat top region. The peak power is about 75 MW, which represents an efficiency of nearly 32%. The corresponding gain is almost 30 dB and the pulse width is 1.7  $\mu$ s (FWHM). Attempts to increase the peak power further by raising the beam's velocity ratio result in a sharp cut in the output signal near the maximum value which is usually indicative of an instability.

An EGUN simulation using the parameters of the operating point indicate that the beam's velocity ratio at the entrance to the circuit is near one. Simulations of the amplifier performance at the operating point are given by the dashed line in Fig. 2. The measured efficiency is given by the cross. Agreement is seen to be excellent.

### Summary

In summary, we have developed an X-band coaxial gyrokystron which has increased the state-of-the-art in peak power for gyrokystrons by nearly a factor of 3. In the near future we will test a 2<sup>nd</sup> harmonic tube, with the goal of obtaining about 100-150 MW of peak power at 17.136 GHz. We will investigate the limitations on velocity ratio in greater detail and attempt to increase the nominal velocity ratio to the original design value. This work was supported by the U. S. Department of Energy.

1. V. L. Granatstein and W. Lawson, *IEEE Trans. on Plasma Science*, vol. 24, p. 648 (1996).

entirely by CIAS ceramics. The output cavity is defined by radial changes on both walls and the lip radii are equal to the drift tube radii. The quality factor is dominated by the diffractive Q which is adjusted by changing the length of the coupling lip.

### Theoretical And Experimental Results

A large-signal code is used to design the circuit and magnetic field configuration and to estimate the performance of the tube at the actual operating point. A small-signal start-oscillation code is used to determine the stability properties of the cavities and set limits on the cavity quality factors. The solid line in Fig. 2 shows the expected performance of the 3-cavity tube as a function of velocity spread for  $\alpha=1.5$ .

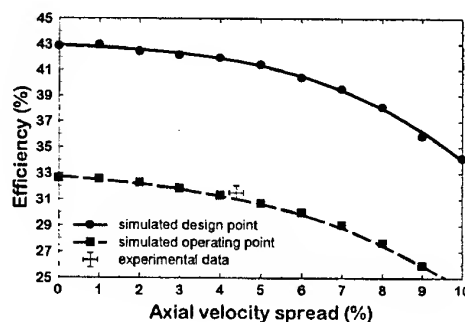


Figure 2. Efficiency versus velocity spread.

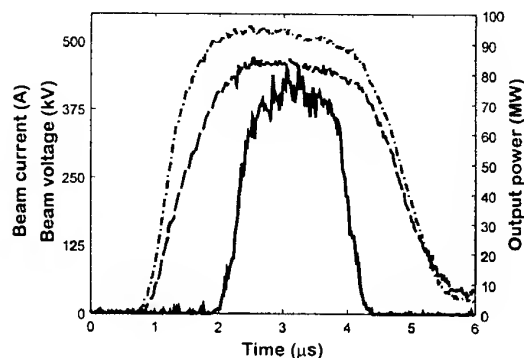


Figure 3. Time dependence of the output pulse.

## Development of 140 GHz/ 1MW gyrotron with a dual RF beam output

V.E. Myasnikov, M.V. Agapova, A.N. Kostyna, L.G. Popov,  
G.G. Denisov, A.A. Bogdashov, V.E. Zapevalov.

GYCOM Ltd., 46 Ulyanov St., Nizhny Novgorod, 603 600, Russia

### Abstract

A 140 GHz/1MW – gyrotron with a dual RF beam output has been developed. The first sample of this tube with two output windows based on BN disk has been tested. A maximal RF power of 840 kW with efficiency of 34% has been achieved.

For both wave beams their profiles measured at the window flange position were in good agreement with the simulations.

### Introduction

The development of a gyrotron with more than 10 s pulse duration (up to CW regime) and output power of 1 MW in the frequency range of 110 – 170 GHz does not seem to be unrealizable dream now.

The present status of 110 – 170 GHz long-pulse gyrotrons developed by GYCOM [1,2,3] is following:

- 110GHz gyrotron: 930 kW at pulse duration of 2.0 s and 330 kW at pulse duration of 10s;
- 140GHz gyrotron: 960 kW at pulse duration of 1.2 s and 140 kW at pulse duration of 9.3s;
- 170GHz gyrotron: 1000 kW at pulse duration of 1.0 s, 500 kW at pulse duration of 5.0 s and 270 kW at pulse duration of 10s;

There is a common set of problems, which one should solve while creating 1 MW power level gyrotron for longer pulse and especially for CW operation.

Solutions of this problems which has been found for gyrotrons mentioned above need additional verification at longer pulses.

The main limitation for pulse duration increasing more than 1÷2 s at 1 MW power level is the capacity of output window. Developing the gyrotron with a dual RF beam output we hoped to overcome this restriction. We expect that this will allow us to reach the following regimes in frequency range of 140 GHz :

- 1 MW/5-6 s and 0.5 MW/10s when BN single disk edge cooling window is used;
- 1 MW/(10 s - CW) when diamond window is used.

The 140 GHz gyrotron with a dual RF beam output has been manufactured and its initial test has been carried out. The picture of the gyrotron is shown in Fig.1.

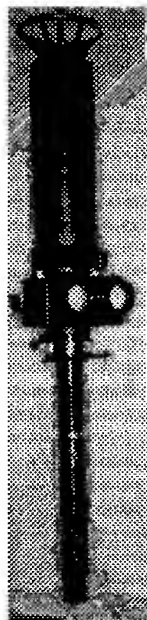


Fig.1. The gyrotron with a dual RF beam output.

### Design and configuration

As a basis for developing of this tube the design of TE<sub>22,6</sub>/0.5 MW/3 s gyrotron[1] was taken. To form two wave beams a new quasi-optical (QO) converter had to be created. It was

suggested that these beams should have the same power and polarization. Propagating both in the parallel direction these beams are more suitable for power transportation.

The new QO converter scheme is presented in Fig.2. The design of irradiator, barrel and parabolic mirrors was similar to the prototype. The corrugated mirror (2) installed after the turning mirror (1) is used for separating wave beam to two parts. The additional mirrors (3) are necessary to form two parallel rf-beam with equal polarization. The calculated diffraction losses are of 6÷7 %. The power distribution simulated for each window surface is shown in fig.3a.

The RF beams could be combined together outside the gyrotron by using diffraction mirror, if necessary. Inserting of additional water-cooled mirrors has caused modification of the gyrotron body assembly in its design and manufacturing.

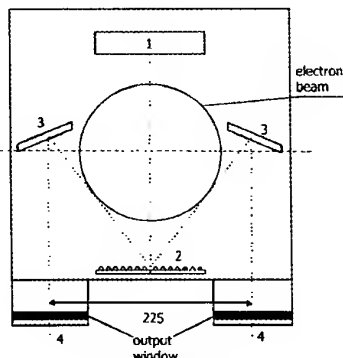


Fig.2. Scheme forming two equal parallel RF beam

### Experimental Results

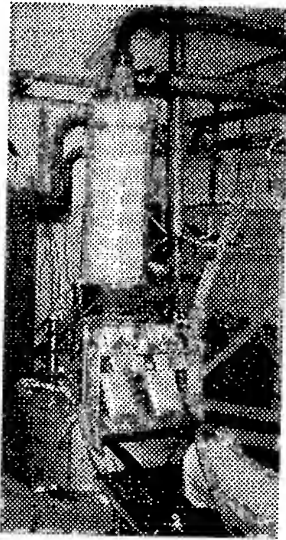


Fig. 4. The gyrotron with external mirrors.

The test has been carried out with new GYCOM cryomagnet with a bore diameter of 160 mm.

The picture of the gyrotron in cryomagnet is shown in Fig.4. The outside mirrors were installed to match gyrotron output radiation with the load.

The measurements have been performed with pulse duration up to 200 ms. The pulse length was limited by brick load design. The output power of 840 kW with efficiency of 34 % was obtained at beam current of 34.4 A and beam voltage of 72 kV. The frequency was measured to be of 140.25 GHz.

The measured RF power is plotted in Fig.5 depending on the beam voltage.

The RF power through both windows as measured with the experimental accuracy ( $\pm 5\%$ ) was found to be the same.

The power distributions at the output window flange positions were the same too. This fact is illustrated in Fig.3b by the burn pattern made on a thermosensitive paper.

The total power measured after external mirrors was 680 kW yielding transmission coefficient of 80 %. The real losses 20% were a bit higher than expected 12  $\div$  13 % including 6  $\div$  7 % of inside diffraction losses and 5 % reflection from BN disk at the start of the pulse.

The transmission coefficient should be increased by using larger dimension external mirrors with a surface specially profiled.

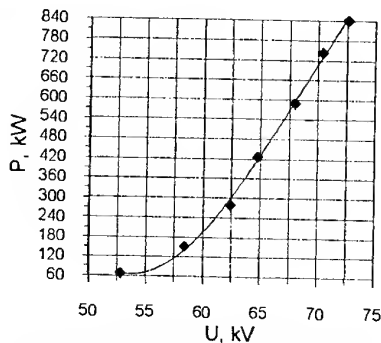
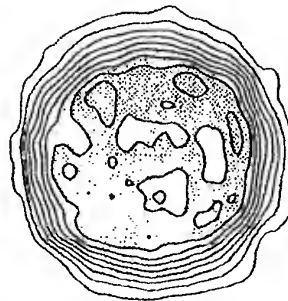
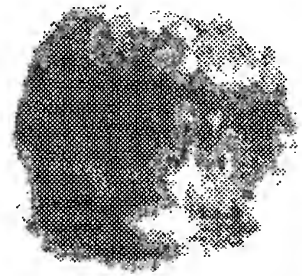


Fig.5. Measured output power versus beam voltage.



a



b

Fig.3. a- calculated power distribution at the window surface;  
b- measured power distribution at the window flange position.

### Conclusion

The initial tests on 140 GHz gyrotron with a dual RF beam output have validated a possibility to separate generated wave beam in to two beams with equal power, distribution and polarization. The stable gyrotron operation was observed up to beam current of 35 A. Not so high efficiency of 34 % is assumed to be connected with small deflections in magnetic field distribution of used cryomagnet compared to conventional one. Further tests will be aimed at enlarging the pulse length up to 10 s.

### References

- [1]. V.E. Myasnikov et al. "Megawatt power long-pulse 140 GHz gyrotron". 21<sup>st</sup> International Conference on Infrared and Millimeter Waves. July, 1996, Berlin.
- [2]. V.E. Myasnikov et al. "Long-pulse operation of 110-GHz 1-MW gyrotron". 22<sup>nd</sup> International Conference on Infrared and Millimeter Waves. July, 1997, Wintergreen.
- [3]. V.E. Myasnikov et al. "Long-pulse operation of 170GHz/ 1MW gyrotron for ITER". This digest.

## The Benefits of Millimeter Waves for Materials Processing

G. Link<sup>1</sup>, L. Feher<sup>1</sup>, S. Rhee<sup>1</sup>, M. Thumm<sup>1,2</sup>

Forschungszentrum Karlsruhe GmbH, <sup>1</sup>ITP, Postfach 3640, D-76021 Karlsruhe

<sup>2</sup>Universität Karlsruhe, IHE, Kaiserstr. 12, D-76128 Karlsruhe

### Introduction

The heating process is one of the most crucial steps in the processing of advanced ceramics. Due to the low penetration depth of the IR-radiation in a standard resistance heated furnace, temperature gradients are induced in the ceramic parts leading to thermal stresses, if not an optimized time-temperature program with small heating rates is applied. These problems can be solved by using microwave sintering techniques, because of a volumetric heating mechanism. Furthermore, the densification process of ceramic bodies seems to be enhanced by sintering in a microwave field, which has been demonstrated by several authors [1,2]. This means a possible reduction of the maximum sintering temperatures and dwelling times compared to the processing in a standard sintering furnace. Due to these effects microwave technology gives the unique possibility not only for a reduction of processing time and thus for energy consumption but offers also the chance to influence microstructure and physical properties of the ceramic materials.

### Gyrotron Installation

At the Forschungszentrum Karlsruhe, Germany, a compact gyrotron system has been established since 1994 in order to investigate technological applications in the field of high temperature materials processing. Beside the improvement of the system design, research activities are mainly engaged in studies on debinding and sintering of various types of advanced structural and functional ceramics. The compact prototype system includes a 30 GHz gyrotron which allows continuous wave operation at the second harmonic of the electron cyclotron frequency in the TE<sub>02</sub> cavity mode. The fully computer controlled millimeter wave (mm-wave) output power of up to 10 kW is coupled into an applicator of about 100 l volume via an advanced quasi-optical transmission line [3].

The use of mm-waves distinguishes from the widespread magnetron frequencies of 0.915 GHz and 2.45 GHz, respectively. First of all the heating is more efficient by a factor of 10 to 100 due to the fact that the absorbed power is proportional to the frequency and the dielectric loss, which is increasing with frequency for most advanced ceramics. The problem of hot spots inside the ceramic parts is less critical with short wavelengths since their distance is small enough to be leveled out by thermal conduction. Finally, a homogeneous field distribution inside an applicator and therefore an homogeneous heating is much easier to establish with shorter wavelengths provided that an optimized applicator geometry is used. For this purpose a Microwave Raytracing- (MiRa-) Code was developed [4]. It is a gridless analytical approach which allows the simulation of large and complex applicator geometries and design studies on small computers. Existing codes and techniques imply an enormous amount of memory allocation and cost intensive computation time. Calculations for the original applicator with cylindrical symmetry did not yield a homogeneous field distribution as assumed before due to focusing effects and caustics. In order to avoid such effects polygonal applicator designs were simulated with different numbers of polygonal edges. A hexagonal geometry with the beam launched inside hitting one edge first results in the most homogeneous field distribution [5].

### Results of Millimeter Wave Sintering Experiments

In order to reduce radiation losses from the sample surfaces leading to temperature gradients and therefore to mechanical stresses, the samples are placed in an optimized thermal isolation box. Such a box consists of ceramic fiber boards transparent to mm-waves and opaque to IR-radiation.

One of the most interesting class of functional ceramics are piezoceramics based on the system lead-zirconate-titanate (PZT). As lead oxide tends to evaporate during the sintering process, shortening of the processing time and a possible reduction of the sintering temperature will help to reduce this difficulty. This problem is the more severe the higher the surface to volume ratio of the samples is as present in the ultrasonic sensor elements shown in Figure 1. This PZT piezoarray consists of 75 x 75 columns with a single column cross-section of 100 x 100  $\mu\text{m}$  and 400  $\mu\text{m}$  height. First results revealed that using mm-waves the sintering temperature of the conventional process can be reduced from 1200 °C down to 1100 °C and the dwelling time from 60 min. down to 10 min. only.

Another interesting ceramic material for special applications such as denture are materials with compositions in the ternary system  $\text{TiO}_2\text{-ZrO}_2\text{-MgO}$ . The sintering kinetics of different types of these materials have been investigated in comparison with conventional sintering experiments. For different compositions conventionally high densities can only be achieved by sintering at temperatures as high as 1500 °C and sintering times as long as 24 hours. When using the mm-wave technique similar densities were reached at 1400 °C with a dwelling time of 20 min. only. But the most remarkable differences can be seen in the microstructure (c.f. Figure 2) and the mechanical properties. Whereas the conventionally sintered samples show very coarse grains and are extremely brittle the microwave treated samples are fine-grained and show acceptable mechanical properties with  $K_{IC}$ -values of about  $2\text{-}3 \text{ MPam}^{0.5}$  and HV5-values of about 800.

The development of new techniques for the production of nanocrystalline oxide ceramic powders with average grain sizes smaller than 50 nm provides the opportunity for the production of ceramic materials with novel mechanical properties, such as low temperature creep and plastic deformation at temperatures well below the melting point [6]. But such novel material properties can only be exploited if the problem of grain growth during the sintering process can be solved. With conventional sintering techniques it is practically impossible to avoid strong grain growth due to the need of long processing time. The application of high power mm-waves for sintering seems to be a promising technical approach to high-density nanocrystalline ceramics. Therefore sintering experiments with nanocrystalline  $\text{Al}_2\text{O}_3$ -,  $\text{TiO}_2$ - and  $\text{ZrO}_2$ -powders [7] with average particle sizes in the range of 25 to 40 nm have been performed. The weakly agglomerated powders were compacted with the pulsed magnetic compression technique [8] to green densities of up to 83 % TD and were mm-wave sintered afterwards. Densification to reasonable densities of about 94 % TD and average grain sizes of about 100 to 150 nm was demonstrated already at 950 °C for  $\text{TiO}_2$  and 1150 °C for the others. Hereby no holding time was applied.

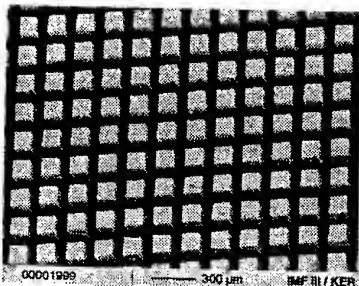


Fig. 1 PZT piezoarrays; mm-wave sintered (1100°C 10 min.).

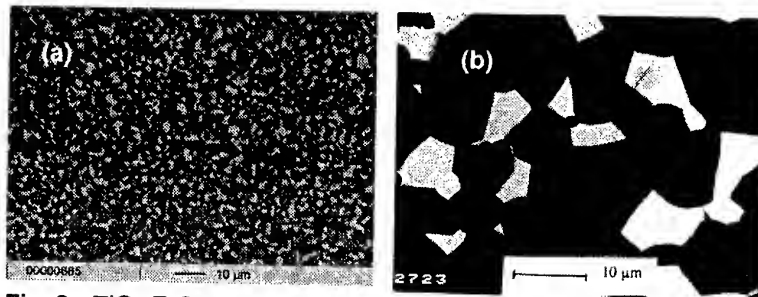


Fig. 2  $\text{TiO}_2\text{-ZrO}_2\text{-MgO}$  ceramic; (a) mm-wave sintered (1400 °C, 20 min.); (b) conventionally sintered (1500°C 24h).

### Summary and Conclusions

Sintering tests in a gyrotron installation at the Forschungszentrum Karlsruhe have been performed in order to study the densification behavior of several types of structural and functional ceramics under mm-wave radiation. For the investigated types of ceramics it was shown that mm-wave sintering is superior to conventional heat treatment. In order to reach the desired densities with the mm-wave technique the necessary processing times are markedly shorter and the sintering temperatures are lower. These changes of the sintering conditions, as could be shown with PZT piezoceramics,  $\text{TiO}_2\text{-ZrO}_2\text{-MgO}$ -ceramics and nanocrystalline oxide ceramics result in a finer grained microstructure, which can lead to improved mechanical properties.

### References

1. M.A. Janney, H.D. Kimrey, MRS Symp. Proc., **189**, 215-227 (1991).
2. G. Link, et al.; MRS Symp. Proc., **430**, 157 (1996)
3. A. Möbius, et al. 21th Int. Conf. on IR and mm-Waves, Berlin, paper AT11 (1996).
4. L. Feher, G. Link, M. Thumm; MRS Symp. Proc., **430**, 363 (1996).
5. L. Feher, G. Link, M. Thumm; Conf. Proc. of Microwave and High Frequency Heating, Fermo, Italy; ed. by A Breccia, R. De Leo, A.C. Metaxas; 442 (1997).
6. J. Karch, R. Birringer, H. Gleiter, Nature, **330**(10), 556 (1987).
7. I.V. Beketov et al., Conf. Proc. 4th Euro-Ceramics, Riccione; **1**, ed. by C. Galassi; 77 (1995).
8. V.V. Ivanov et al., Conf. Proc. 4th Euro-Ceramics, Riccione; **2**, ed. by C. Galassi; 169 (1995).



# OPEN RESONATOR SET-UP FOR SPATIALLY RESOLVED AND TEMPERATURE DEPENDENT MM-WAVE PROPERTY MEASUREMENTS

R. Schwab, R. Heidinger, R. Spörl

Forschungszentrum Karlsruhe, Institut für Materialforschung I,  
Postfach 3640, D-76021 Karlsruhe, Germany

## Abstract

The homogeneity of mm-wave properties in superconductors and low loss dielectrics is shown to be assessable using novel arrangements of Fabry-Perot resonators which allow remote control of the specimen position under a minimum mm-wave beam waist of the analysed mm-wave gaussian TEM<sub>00q</sub> modes. The special aspects of mapping the surface resistance are exemplified for a 3 inch YBCO wafer and of mapping the dielectric loss tangent for a 4 inch CVD diamond wafer. The extension of the experimental set-up is discussed for temperature variable measurements.

## Introduction

The characterisation of materials properties in the mm-wave range was in the past focused to provide data characterising a given material with a well-defined set of mm-wave properties, such as surface resistance  $R_s$  and penetration depth  $\lambda$  in (super-)conductors, and permittivity  $\epsilon_r$  and dielectric loss tangent  $\tan\delta$  in dielectrics. Variations of these properties within a specimen were considered as a special deficiency of the sample similar to geometrical imperfections (f.e. warped shape) [1]. Starting with superconductor applications, where potentially critical material processing became unavoidable, new concern was given to cope with inhomogeneities and even to quantify them. As the task of developing dielectrics for extreme mm-wave power loads, namely in gyrotron windows, put new emphasis on the control of materials processed by highly advanced technologies, such as Microwave Plasma Assisted Chemical Vapour Deposition (MPA-CVD), specially adapted measuring techniques became of special concern. Clearly, the good accessibility to the specimen position and the few restrictions to the specimen geometry made the open resonator technique one of the promising candidates to provide a spatially resolved data set ('mapping'). In this paper, the successful development of systems based on a (quasi-)hemispherical Fabry-Perot resonator is reported.

## Minimisation of the analysed specimen area

The open resonator technique allows to quantify the mm-wave properties of materials by analysing the centre frequency and quality factor of the resonator before and after introducing a specimen ( $f_0, Q_0$  and  $f_1, Q_1$  resp.). For the present installations which are operated around 145 GHz, the high frequency components and the signal processing to obtain the resonator parameters have been described in detail recently [2]. For inhomogeneous specimens, the parameters  $f_1$  and  $Q_1$  are given by a weighted average of the local mm-wave properties. In this context, only differences occurring over the area of (disc-shaped) flat specimens will be considered which is certainly valid for thin specimens. In thicker specimens, inhomogeneities along the disc axis may also be present which for the moment can only be demonstrated by reversing the specimen in the resonator set-up [3]. The primary task of scanning a given specimen was to install a highly mechanically stable resonator in a (quasi-)hemispherical geometry where the specimen is attached to a plane mirror which can be reproducibly moved perpendicular and along the resonator axis (cf. Fig. 1a,b)

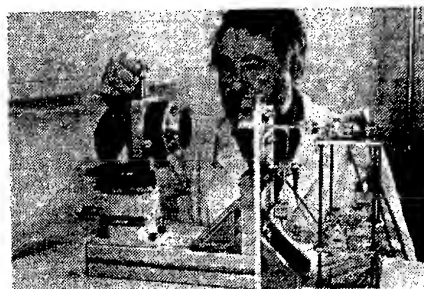
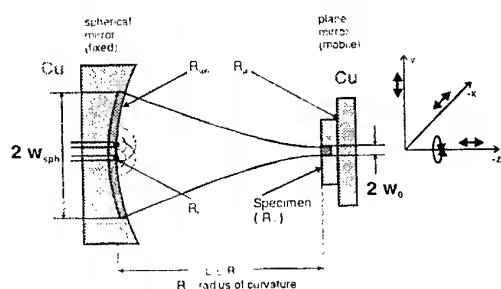


Fig.1 a) Schematic diagram of the resonator set-up, b) Manual version of scanning configuration

The effective area contributing to the material response is related to the beam waist of the analysed  $TEM_{00q}$  modes in the open resonator, more precisely to its value at the plane mirror,  $w_0$ . Its value tends to zero, as the mirror separation  $L$  approaches the radius of curvature of spherical mirror  $R_0$ . However, at the same time the beam waist at the spherical mirror grows and causes diffractive losses at the mirror edges and thus affects severely the quality factor of the resonator. Therefore an optimum mirror separation has to be found experimentally. For the given mirror geometries, the separation was set to  $L = 117.5$  mm ( cf. Fig.2 ), and the manually driven positioning elements were replaced by a rotary and a linear computer controlled drive. The limits of the contributing area were determined from line scans over a circular test mirror, made of two half circles from copper and brass. It was found at the border line that contributions from both materials appeared only within the double beam waist of about 7 mm, which sets the upper limit to the effective spot size (cf. Fig.3).

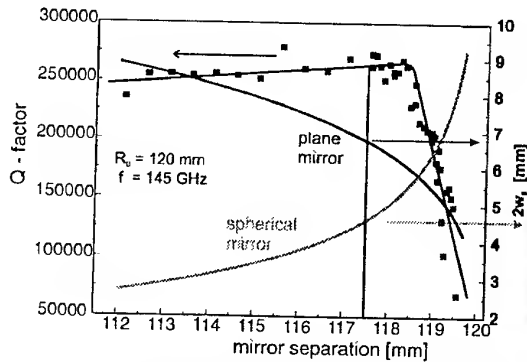


Fig. 2 The calculated beam width parameters and the measured Q-factors of the observed resonances as a function of the mirror separation  $L$

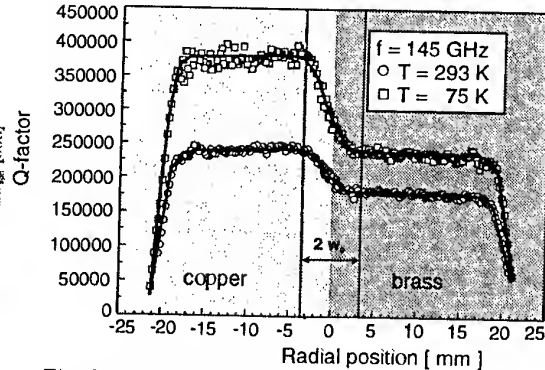


Fig. 3 Observed Q-factors for line scans over a mirror composed of two copper and brass half circles

### $R_s$ mapping at cryogenic temperatures

The surface resistance of conducting materials,  $R_s$ , can be determined from the effective total surface resistance of the resonator set-up,  $R_{eff}$ , where the plane mirror is superseded by the conductor. The value of  $R_{eff}$  is directly determined from the measured Q-factor via the geometry factor  $\Gamma$ :  $R_{eff} = \Gamma/Q$  with  $\Gamma = (1/4)\omega\mu_0 L$  for a hemispherical resonator geometry. The separation of  $R_{eff}$  into contributions from the specimen, the spherical mirror and the coupling holes ( cf. Fig. 1a ) can be managed by proper calibration measurements with well-defined conductor materials [ 4 ]. The quality of a resonator set-up is mainly given by a small and constant value of contribution of the coupling hole  $R_h$ . This value could be kept at  $R_h = 50 (\pm 5)$  m $\Omega$  for the present set-up. The error in  $R_h$  also sets the lower resolution level for  $R_s$ . Evidently, measurements for homogeneity analysis of superconducting films have to be performed at cryogenic temperatures. A gas flow cryostat system with two thermal screens was developed to house the Fabry-Perot resonator. Temperatures below 15 K can be reached at the specimen which was demonstrated by measuring the superconductive transition in a  $Nb_3Sn$  sample. For high  $T_c$  superconductors, measurements are most commonly performed at 77 K. For mapping, the positioning of the plane mirror must be set reproducibly under remote control even at the very low temperatures. This key problem was solved by a thermal decoupling of the positioning elements which are located in the vacuum vessel, but operate close to room temperature ( cf. Fig. 4a ). This 'CRYOSCAN' system ( cf. Fig. 4b ) has been used successfully for mapping YBCO wafers made by different film growing techniques for characteristic types of  $R_s$  inhomogeneities [ 5 ]. One example is given later together with the description of temperature dependent measurements (cf. Fig. 6 ).

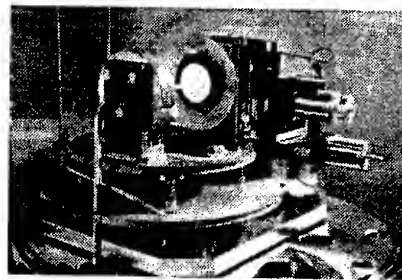
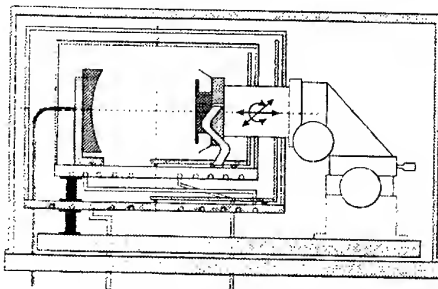


Fig. 4 a) Schematic diagram of the cryostat set-up, b) 'CRYOSCAN' system for  $R_s$  mapping

### Dielectric loss mapping at room temperature

Whereas for mm-wave properties in HSTL films, the exact values of the centre frequency is of minor importance ( as long as it is ensured that the resonator is operated at a mirror separation  $L$ , where  $Q$  is insensitive to limited variations in  $L$  and thus in  $f_0$  and in  $f_1$  ), these parameters can play an important role when investigating low loss dielectrics. As these materials are 'transparent' for mm-waves, they modify the effective resonator length by their permittivity  $\epsilon_r$  which is the basis for evaluating  $\epsilon_r$  from  $f_0$  and  $f_1$ . Even dielectric loss measurements are affected, as both the filling and the loading factor  $F_F$  and  $F_L$ , which determine the evaluation of  $\tan\delta$  by the formula [ 2 ]:

$$\tan\delta = F_F (Q_1^{-1} - (Q_0/F_L)^{-1}),$$

dependent strongly on number of half-wavelengths  $N_\lambda$  in the specimen, and thus on sample thickness and permittivity. As the behaviour of open resonators with extreme radial variations in effective length have not yet been systematically investigated, our mapping of dielectric properties has been limited to cases where only minor changes in centre frequencies occur. This implies a restriction to special geometrical conditions ( excellent mirror alignment and specimen preparation ) and to specimens which show only inhomogeneities in dielectric loss but not in permittivity. In this case, the factors  $F_F$  and  $F_L$  can be set constant, and  $\tan\delta$  can be calculated directly from the variation of  $Q_1$  during the scanning. A good case is given for CVD diamond wafers where  $\epsilon_r$  is constant even when  $\tan\delta$  changes by orders of magnitude [ 6 ]. The power of the technique is shown in Fig. 5, where an local absorptive area ( 'hot spot' ) was identified. The actual mapping system for  $\tan\delta$  is equipped for room temperature measurements with an enlarged plane mirror and position element that allow to scan over a radius of 75 mm, thus accommodating 6 inch wafers.

### System operation for temperature variable measurements

The temperature dependence of mm-wave properties can provide key data sets by which the interaction mechanisms are identified. Therefore the CRYOSCAN system was designed to perform also temperature variable measurements at selected, well defined positions to better approach the fundamental aspects of the material response. Similar to a previous system for integral cryogenic measurements [ 7 ], the cryostat was designed with enough thermal mass for free heating operation. The measurement procedure first identifies locations of special interest at 77 K, and then goes on with selected free heating runs after cooling below 15 K. As an example, three spots with different  $R_S$  values on an inhomogeneous YBCO wafer exhibit characteristic differences in the offset, slope and the critical temperature of the individual  $R_S$  curves ( cf. Fig 6a,b ). Scanning of CVD diamond bears only potential of characteristic differences for temperature curves far above room temperature [ 6 ], therefore it is foreseen to equip the present room temperature system with heating elements.

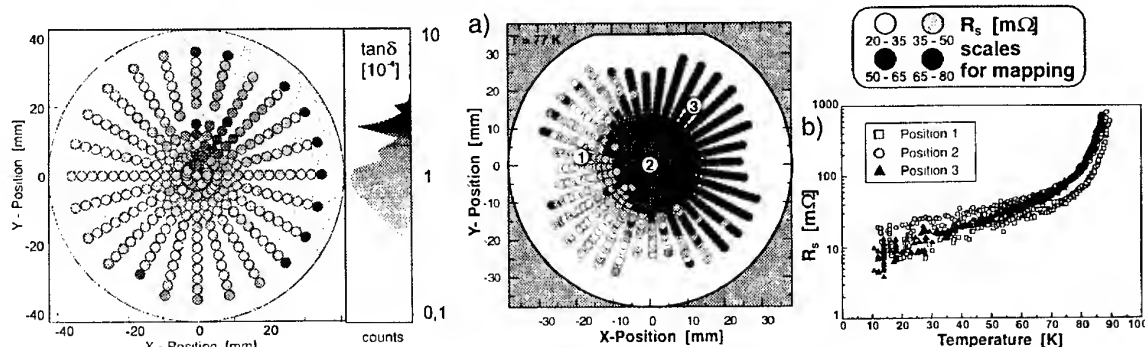


Fig.5 Dielectric loss mapping in a 4 inch CVD diamond wafer showing a local absorptive spot at 145 GHz

Fig. 6 a )  $R_S$  mapping in an inhomogeneous 3 " YBCO wafer  
b) Temperature dependent  $R_S$  curves for selected spots  
All measurements performed at 145 GHz.

### Literature

- [1] J.R. Birch, R.N. Clarke, The Radio and Electronic Engineer, 52 (11/12) (1982), pp. 565-584
- [2] R. Schwab, R. Spörl, J. Burbach, R. Heidinger, F. Königer, Proc. of ITG Conference on Displays and Vacuum Electronics, Garmisch-Partenkirchen (D), 1998, ITG Report No. 150, pp. 363-368
- [3] R. Heidinger, R. Schwab, R. Spörl, M. Thumm, Digest 22<sup>nd</sup> Int. Conf. IR & MM Waves, Wintergreen (USA), 1997, pp.142-143
- [4] R. Schwab, R. Heidinger, Digest 21<sup>st</sup> Int. Conf. IR & MM Waves, Berlin (D), 1996, ISBN 3-00-000800-4, Paper ATh7
- [5] R. Schwab, R. Heidinger, J. Geerk, F. Ratzel, M. Lorenz, Digest of this conference
- [6] R. Heidinger, R. Spörl, M. Thumm, R.S. Sussmann, J.R. Brandon, C.N. Dodge, Digest of this conference
- [7] R. Heidinger, G. Link, Digest 18<sup>th</sup> Int. Conf. IR & MM Waves, Colechester (UK), 1993, SPIE vol. 2104, pp. 64-65

## Visualization of Photo-Excited Free Carriers with a Scanning Near-Field Millimeter-Wave Microscope

Tatsuo Nozokido<sup>†</sup>, Hiroaki Minamide<sup>††</sup>, Jongsuck Bae<sup>††</sup>, Tetsu Fujii<sup>††</sup>, Masatoshi Ito<sup>††</sup>,  
and Koji Mizuno<sup>†,††</sup>

<sup>†</sup>Photodynamics Research Center, The Institute of Physical and Chemical Research (RIKEN)  
19-1399 Aza-Koeji, Nagamachi, Aoba-ku, Sendai 980-0868, Japan.  
e-mail: nozokido@postman.riken.go.jp.

<sup>††</sup>Research Institute of Electrical Communication, Tohoku University,  
2-1-1 Katahira, Aoba-Ku, Sendai 980-8577, Japan.

### Abstract

Scanning near-field microscopy in the millimeter-wave region can be used to map electronic transport properties of objects with the resolution of sub-wavelength. In this paper, visualization of photo-excited free carriers in a silicon substrate by scanning near-field millimeter-wave microscopy using a new type of probe is demonstrated.

### Introduction

We have demonstrated a novel type of scanning near-field millimeter-wave microscopy using a metal slit at the end of a rectangular metallic waveguide as a scanning probe and an image reconstruction algorithm based on computerized tomographic (CT) imaging [1,2]. This slit-type probe has several advantages over conventional point-type probes [3-5], such as high transmission efficiency, wide bandwidth, and its easiness of fabrication. The benefit of using millimeter-waves in scanning near-field microscopy lies in the promise of new types of material contrast. A good example is the mapping of electronic transport properties. We have applied our scanning near-field millimeter-wave microscope to visualize photo-excited free carriers in a silicon substrate.

### Photo-excited free carriers in silicon

The complex refractive index,  $n^* = n_r + jn_i$ , and bulk reflectance of intrinsic silicon at 60 GHz as a function of free carrier density can be calculated by applying Drude's theory [6]. The result is shown in Fig. 1. It's seen from the figure that the reflectance can be changed from 0.3 to 0.95 for a free carrier density variation of  $10^{18} / \text{cm}^3$ .

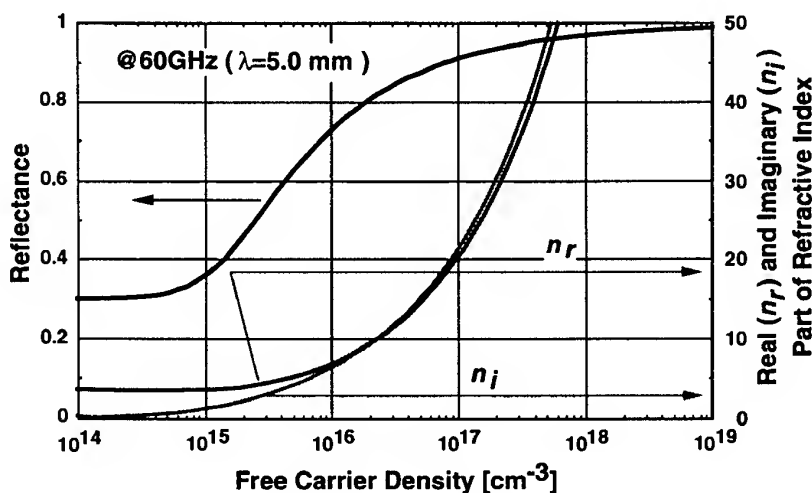


Fig. 1

Complex refractive index and bulk reflectance of intrinsic silicon at 60GHz as a function of free carrier density.

### Experimental Setup

Figure 2 is a schematic drawing of our experimental setup, and also shows the slit-type probe used in our experiments. A reduced-height waveguide forms the slit; the wide dimension of the slit and that of the waveguide are identical but the waveguide height is tapered down to  $80\mu\text{m}$  ( $\lambda/60$ ). The frequency used in our experiments was 60 GHz ( $\lambda=5\text{mm}$ ). The object was a  $2.2\text{mm} \times 2.2\text{mm} \times 20\mu\text{m}$  undoped (intrinsic) silicon substrate ( $\rho=15\text{ K}\Omega\cdot\text{cm}$ ), supported by a quartz plate. The 840nm near-infrared (NIR) radiation of a CW laser was incident on the object through the quartz plate and generated free carriers. The object was scanned linearly for different object-rotation angles,  $\theta$ . The  $S_{11}$  signals from the probe were obtained in reflection mode through a vector network analyzer (WILTRON 360B) and processed using an image reconstruction algorithm based on CT imaging [7].

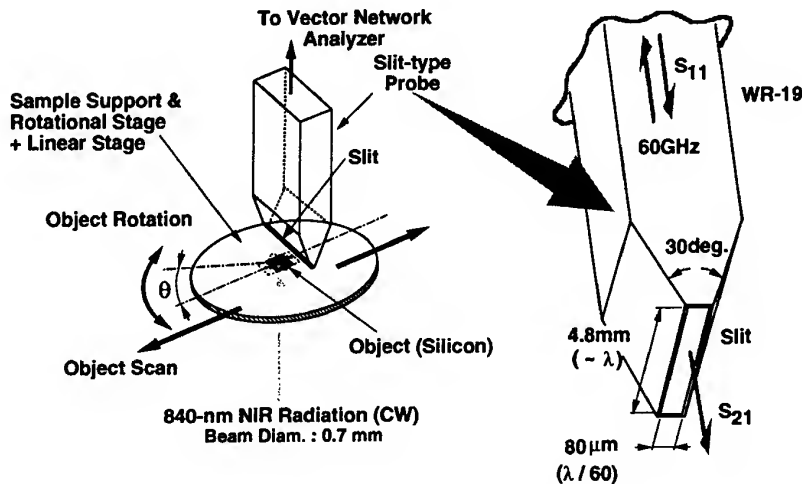


Fig.2

Experimental setup for scanning near-field millimeter-wave microscopy in reflection mode to visualize photo-excited free carriers.

### Experimental Results

Figure 3 shows the millimeter-wave images, which were obtained for the following conditions:

· CW NIR laser power absorbed by the silicon substrate	: 26.1mW
· Laser beam spot size on the Si substrate	: $0.7\text{mm}^{\phi}$ ( $\sim\lambda/7$ )
· Field of view	: $3350\mu\text{m}$
· Sampling interval for linear motion	: $40\mu\text{m}$
· Total sampling points for linear motion	: 121 pt.
· Sampling interval for rotational motion	: 1.5 deg.
· Total sampling points for rotational motion	: 121 pt.
· Probe-to-Object separation	: $25\mu\text{m}$
· Image resolution	: $\sim 200\mu\text{m}$ ( $\lambda/25$ ).

For an excitation power of 26.1mW, the density of free carriers generated is estimated to be as high as  $10^{18}/\text{cm}^3$ . Figure 3(a) and 3(b) are images with and without free carrier excitation, respectively. Figure 3(c) is the free carrier image which is derived by subtracting Fig. 3(b) from Fig. 3(a). The distribution of photo-excited free carriers could be clearly visualized. Figure 4 is the one-dimensional intensity variation along the line x-x in Fig. 3(c) for various photo-excitation intensity levels. The image intensity at the center of the laser beam spot is nearly proportional to the NIR power absorbed by the silicon substrate.

An "N" shaped distribution of free carriers was generated on the silicon substrate and imaged. In the experimental setup shown in Fig. 2, a 530nm CW laser was used as an excitation source and a shadow mask was inserted in the laser beam path in order to illuminate an "N" shaped region on the silicon substrate, with a line width of  $0.25\text{mm}$  ( $\lambda/20$ ). Figure 5 shows the results. Figure 5(a) and 5(b) are images with and without free carrier excitation, respectively. Figure 6(c) is the free carrier image.

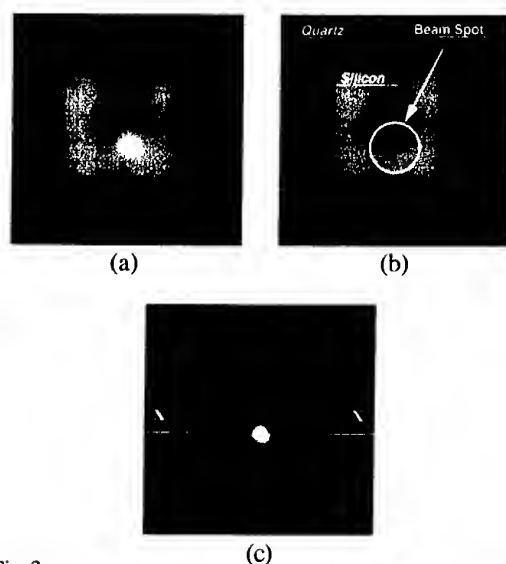


Fig.3

Intensity images of a high-resistivity silicon substrate: with free carrier excitation (a), without free carrier excitation (b), and free carrier image (c).

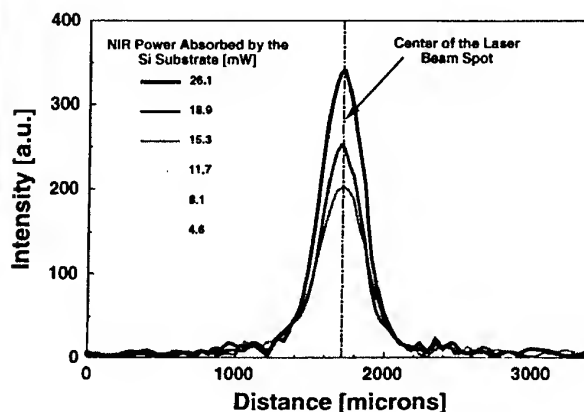


Fig.4

One-dimensional intensity variation along the line x-x in Fig.3(c) for various photo-excitation intensity levels.

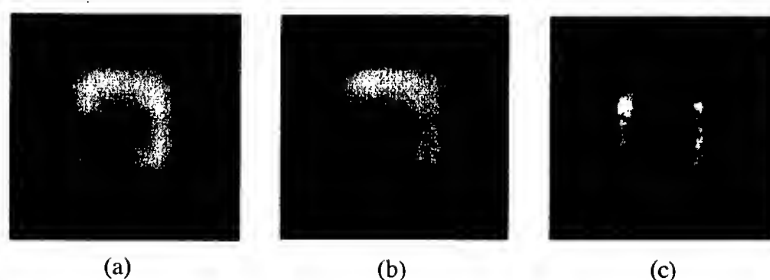


Fig.5

Intensity images of a high-resistivity silicon substrate: with free carrier excitation (a), without free carrier excitation (b), and free carrier image (c).

### Summary

Visualization of photo-excited free carriers has been successfully demonstrated with a scanning near-field millimeter-wave microscope using a slit-type probe. Although we have succeeded in visualizing free carriers only under steady-state conditions, by utilizing a high-speed millimeter-wave detection system it is possible to image transition phenomena of free carriers such as generation, extinction and transfer processes if they are cyclic. Scanning near-field microscopy in the millimeter-wave region, which can image free carrier distribution with resolution much smaller than the wavelengths used, is also applicable to map doping profiles of semiconductor substrates, and to map defect profiles in combination with photo excitation.

### References

- [1] T. Nozokido, J. Bae, T. Fujii, M. Itoh, and K. Mizuno: Conf. Dig. 22nd International Conference of Infrared and Millimeter Waves, 302 (1997).
- [2] J. Bae, T. Okamoto, T. Fujii, K. Mizuno, and T. Nozokido: Appl. Phys. Lett. **71**, 3581 (1997).
- [3] D. W. Pohl, W. Denk and M. Lanz, Appl. Phys. Lett. **44**, 651 (1984).
- [4] U. Dürig, D. W. Pohl and F. Rohner, J. Appl. Phys. **59**, 3318 (1986).
- [5] E. Betzig and J. K. Trautman, Science **257**, 189 (1992).
- [6] H. Alius and G. Dodel, Infrared phys. Technol. **35**, 73 (1994).
- [7] A. C. Kak and M. Slaney, in Principles of Computerized Tomographic Imaging, Chapter 3, IEEE Press, New York (1988).

## **Induced Anisotropy Studying by the Methods BWO-spectroscopy.**

**E. A. Vinogradov**

**General Physics Institute, Russian Academy of Sciences,  
Vavilov str 38, 117942, Moscow, Russia.  
fax: (095)135 84 45, e-mail: eavin@kapella.gpi.ru**

### **Abstract**

**It was developed and used different methods for studying induced (including by outer magnetic field) anisotropy magnetic fluid, thin films etc. Very high sensitivity was achieved on the base homodyne type BWO-spectrometer MASS-4 (8-0.2 mm. waverange).**

## T-Rays in the Near-Field

Klaas Wynne\*, Dino Jaroszynski

Dept. of Physics and Applied Physics, University of Strathclyde, 107 Rottenrow, Glasgow G4 0NG, UK  
E-mail: k.wynne@strath.ac.uk, dino@phys.strath.ac.uk, URL: <http://dutch.phys.strath.ac.uk/FRC/>

### INTRODUCTION

Several attempts have been made at using terahertz pulses (T-rays) for imaging[1] including T-ray tomography and real-time imaging.[2] In a typical T-ray imaging setup, the rays are focussed to a diffraction-limited spot, a sample is placed in the focus and scanned perpendicularly to the beam. However, since the peak wavelength of a typical terahertz pulse is about 1 mm, spatial resolution is limited in practice to a few millimeters. At visible wavelengths, the spatial resolution limit has been overcome by using near-field methods. A near-field method for improving the spatial resolution in T-ray imaging has been reported as well.[3] A metal aperture with a diameter of 140  $\mu\text{m}$  was placed in the focus of the T-ray beam and the sample was placed directly behind this aperture. Although this method works in principle, it can be seen that if one wants to achieve a resolution on the order of 1  $\mu\text{m}$  with 1 mm waves, this will lead to unacceptable loss of signal intensity. In this paper, we demonstrate a new method of achieving sub-wavelength spatial resolution in T-ray imaging. T-rays can be generated by the optical rectification of femtosecond laser pulses at optical wavelengths. Therefore, if the optical beam is focussed to its diffraction limit in the generation crystal, the T-rays will emerge in a beam, which in the near-field region may have a diameter of less than 1  $\mu\text{m}$ . If the sample is placed directly on the generation crystal, it can be imaged in the far-infrared with sub-wavelength resolution. This experimental setup was used to study the propagation of evanescent waves inside waveguides. It has been predicted[4] that waves can travel at superluminal velocities in such waveguides. Because our T-ray setup gives access to all the pertinent information of the pulse traveling through the waveguide, we have been able to analyze the propagation characteristics of these evanescent waves fully for the first time. It is found that although the phase velocity can tend to infinity or even become negative, the group velocity is at all times subluminal. However, absorptive pulse shaping in the waveguide can cause the peak of the pulse to travel superluminally. In the shortest waveguides, it is found that resonances occur even for the evanescent waves. This effect is most likely caused by surface plasmons traveling through the waveguide.

### IMAGING SETUP

In our experiment, the T-rays are generated through optical rectification of femtosecond pulses in ZnTe. The laser source is a Ti:sapphire oscillator and regenerative amplifier producing 150 fs pulses at 800 nm with a repetition rate of 250 kHz. About 280 mW is focussed onto a <110> cut ZnTe crystal with a thickness of 1 mm or 500  $\mu\text{m}$ , mounted on an x-y translation stage to allow lateral translation. The T-rays emitted by the ZnTe crystal are recollimated and focused with two  $f = 38.1$  mm off-axis parabolic mirrors. The second off-axis parabolic mirror has a hole to allow an 800 nm gating beam to be overlapped with the T-ray beam in another 500  $\mu\text{m}$  <110> cut ZnTe crystal. The gating beam has an average power of 8 mW, is temporally delayed by a fast-scanning optical delay line and focussed into the detection crystal. The delay dependent retardation of the probe beam is measured by sending it through a quarter-wave plate and a polarizer, and balanced detection by a pair of photodiodes. The T-rays generated and detected this way have about three cycles and a spectrum that extends from 5 to 100  $\text{cm}^{-1}$  as published previously.[5]

To obtain the highest spatial resolution one would like to focus the 800 nm T-ray generation beam to the smallest possible spot size. As ZnTe is used as the optical rectification crystal, the minimum spot size is 200  $\mu\text{m}$ , determined by two-photon absorption. When the ZnTe generation crystal is scanned several millimeters perpendicularly to the generation beam, little variation of the T-ray field-strength ( $\pm 4\%$ ) or transit-time ( $\pm 5$  fs) is observed. To determine the resolution of the imaging system, a knife-edge consisting of a piece of aluminum foil mounted directly onto the ZnTe generation crystal, was scanned through the beam. At each position, a time-scan over 20 ps was taken to determine the time-dependence of the THz pulse. These data are then Fourier transformed in order to plot the position and frequency dependent transmission. The transmission is determined as  $T = \tilde{E}(\omega, x) / \tilde{E}(\omega, 0)$  where  $\tilde{E}(\omega, 0)$  is the complex amplitude spectrum of the field at a position where the knife-edge does not absorb. The intensity FWHM of the T-ray beam varies from  $110 \pm 13 \mu\text{m}$  at 80  $\text{cm}^{-1}$  ( $\lambda = 125 \mu\text{m}$ ), to  $232 \pm 85 \mu\text{m}$  at 10  $\text{cm}^{-1}$  ( $\lambda = 1 \text{ mm}$ ). Thus, at the longer wavelengths, the spatial resolution is



more than 2.6 times higher than the diffraction limit of  $0.61 \lambda$ . Reflective optics suitable for T-rays, rarely have a numerical aperture larger than  $NA = 0.5$  and therefore the result should be compared to an expected free-space diffraction limited spot of  $0.61 \lambda / 0.5$ . Images were taken of thin metal wires and a young leaf from a Chinese elm bonsai (*Ulmus parvifolia* Jacq.), demonstrating that the method is suitable for practical high-resolution imaging.

Near-field imaging with T-rays had been demonstrated before[3] using a metal pinhole to enhance the spatial resolution. In the method described here similar spatial resolution is obtained ( $140 \mu\text{m}$  FWHM at  $30 \text{ cm}^{-1}$ ) but without any loss of T-ray intensity. The main source of noise in our experiment is a fluctuation in the center frequency of the Ti:sapphire oscillator spectrum and use of the amplifier was required to lift the terahertz signal above the noise floor. Hence, the resultant two-photon absorption in the ZnTe generation crystal prevented us from attaining an even higher spatial resolution at present. In principle, there is no reason why a resolution of about  $0.5 \mu\text{m}$  could not be obtained.

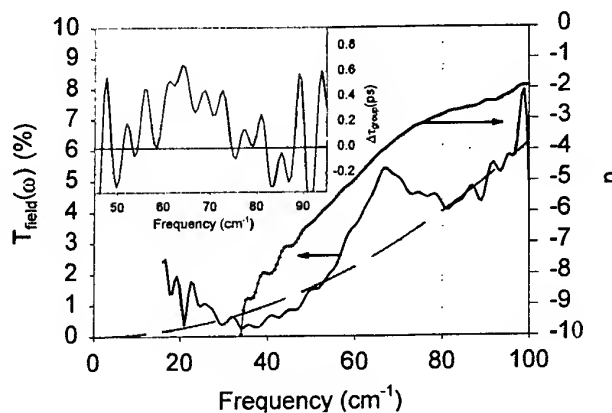


Figure 1. Transmission of evanescent waves through a  $50 \mu\text{m}$  diameter,  $40 \mu\text{m}$  length, nickel waveguide. Show is the electric field transmission and the effective refractive index. The dashed line is a fit to an  $\omega^{-2}$ -dependence and the inset shows the group delay relative to free-space.

#### PHOTON TUNNELING

To investigate the properties of evanescent waves inside waveguides, several metal cylindrical pinholes were used. First, the transmission through pinholes with a diameter of  $150$ ,  $200$  and  $400 \mu\text{m}$  and lengths ranging from  $40 \mu\text{m}$  to  $1 \text{ mm}$  was measured. The accumulated phase above the cutoff frequency of the  $\text{TE}_{11}$ -mode  $\omega_c = \{3.682 c\}/d$  is given by  $\phi = (\omega_c L/c) ((\omega/\omega_c)^2 - 1)^{1/2}$ , [6] where  $d$  is the diameter of the waveguide and  $L$  its length. In accordance with this theoretical prediction, it is found in the long waveguides that the phase velocity tends to infinity and the group velocity to zero, as the cutoff frequency is approached. Due to reshaping of the transmitted pulse close to cutoff, it is observed in the intermediate length waveguides that parts of the pulse travel faster than through an equivalent amount of free space. This is consistent with special relativity, as the group velocity derived from the data is always subluminal.

As the waveguides get shorter, it is observed that the cutoff becomes much smoother than predicted by theory. In addition, the theory predicts an effective refractive index at frequencies below cutoff that is identical zero. In stark contrast, in the experiments it is seen that the refractive at these frequencies becomes negative. For example, in the  $200 \mu\text{m}$  diameter,  $80 \mu\text{m}$  length waveguide the refractive index varies from  $1$  at high frequencies to  $-5$  at  $10 \text{ cm}^{-1}$ . In all cases, the phase velocity goes to infinity at the predicted waveguide cutoff frequency. In experiments in  $50$  (See Figure 1) and  $100 \mu\text{m}$  diameter waveguides, (nearly) all the transmitted light is in evanescent waves as the cutoff frequencies are at  $117$  and  $59 \text{ cm}^{-1}$  respectively. Transmission resonances are observed at  $65 \text{ cm}^{-1}$  in the  $50 \mu\text{m}$  pinhole and at  $80 \text{ cm}^{-1}$  in the  $100 \mu\text{m}$  pinhole. This is unexpected for the  $50 \mu\text{m}$  waveguide as the (exponentially decaying) evanescent waves should not give rise to any resonances. A possible explanation for both the smoothing of the cutoff and the resonances is that the femtosecond THz pulse excites surface plasmons that can travel through the waveguide as non-evanescent waves. The waveguide gives rise to a negative dielectric constant near cutoff, thereby creating the ideal conditions for coupling into and out of surface plasmons. This may open up the possibility of using these photon tunnel-barriers as efficient sensors that could be used in a quasi parallel fashion.

On of us (KW) would like to thank EPSRC for financial support.

#### REFERENCES

1. D.M. Mittleman, R.H. Jacobsen and M.C. Nuss, IEEE J. Selected Topics Quantum Electron. **2**, 679-692 (1996).
2. Q. Wu, T.D. Hewitt and X.-C. Zhang, Appl. Phys. Lett. **69**, 1026-1028 (1996).
3. S. Hunsche, M. Koch, I. Brener and M.C. Nuss. THz Imaging in the Near-Field. in CLEO/QELS'97 Technical Digest. 1997. Baltimore: OSA.
4. R.Y. Chiao and A.M. Steinberg, Prog. Opt. **37**, 345-405 (1997).
5. R. McElroy and K. Wynne, Phys. Rev. Lett. **79**, 3078-3081 (1997).
6. S.Y. Liao, Microwave Circuit Analysis and Amplifier Design (Prentice-Hall, Englewood Cliffs, 1987).

## MULTIMODE OPEN RESONATOR IN THE DEFECTOSCOPY OF THIN-FILMS.

V.Derkach, A.Pojedinchuk, A.Brovenko and A.Vertij

The Usikov' Institute for Radiophysics and Electronics of Academy of Sciences of Ukraine,  
12 Ac Proskura St., Kharkov, 310085, Ukraine  
Phone (0572) -44-85-94, Fax (0572) - 441-105

### Introduction

The methods of the resonant quasioptical interferometry based on the use of open resonators (OR) can be effectively used in the non-destructive testing of dielectric materials. The investigated object can be placed both inside the OR and outside it [1]. The high measurement accuracy is necessary for testing the dielectric parameters of thin films. In this case it is advisable to place the object inside the resonator.

In the present paper the mathematics of the resonator method of analysis and reconstruction of permittivity function  $\varepsilon = \varepsilon(r)$  of thin ( $h \ll \lambda$ ) dielectric samples is considered. The results of the model experiments in the two-millimeter range of electromagnetic waves are presented.

### Description of the method

The essence of the method consists in the use of the multimode millimeter-wave open resonator as the analyzer of the spectrum of spatial frequencies of the waves passing through the object. It is known that in an empty two-mirror resonator with square-law phase correction the axial-symmetric modes TEM<sub>lpq</sub> (l, p and q is the indexes of modes) are exited. These modes are gaussian wave beams [2]. In the infinite aperture mirror approximation they are described the Laguerre-Gaussian functions in a cylindrical coordinate system with sufficient accuracy. At a smooth change of frequency or distance between the reflectors at the certain geometrical parameters of the resonator, in the OR the set of modes TEM<sub>lpq</sub> with different indexes l,p,q and corresponding configurations of fields in cross section are exited. The modes with different indexes represent the elementary linearly independent fields.

In the case when a thin dielectric film with the permittivity  $\varepsilon = \varepsilon(r)$  is placed inside the resonator, its resonant properties change. The object presence changes only the mode resonant frequencies ( $w_{lpq}$ ) provided the absorption and dispersion losses in the object are not taken into account. Thus the frequency shift  $\Delta w_{lpq}$  depends on the mode configuration and function  $\varepsilon(r)$ . With the experimentally measured  $\Delta w_{lpq}$  and using well known expressions of Laguerre-Gaussian functions the function  $\varepsilon(r)$  is restored.

The action of the object on the OR properties, namely, on the resonant frequencies determined executed on the basis of the theory of small disturbance [3]. As the result we have the Fredholm-type integral equation of the first kind

$$\int_0^{\tau} K(p,s)Y(s)ds = g(p) \quad (1)$$

in the unknown function  $Y(s) \equiv \Delta\varepsilon(r) = \varepsilon(r) - 1$ . Here  $K(p,s)$  and  $g(p)$  are known, and  $K(p,s)$  is a real function, which is continuous in s and discrete in p. Besides  $y(s) \in L_2(0, \tau)$  and  $g(p) \in R^1$  ( $R^1$  is a real straight line with the metrics  $\rho(g_1, g_2) = |g_1 - g_2|$ ).

The reconstruction of the behavior of function  $\varepsilon = \varepsilon(r)$  implies the solution of equation (1). It is necessary to note that the function  $g(p)$  can be experimentally determined only at some of points  $p_i$  with limited accuracy. Therefore this integral equation represents a non-correct problem. The solution depends on the experimental data involving the measurement errors and the requirement of stability of the exact solution in relation to insignificant changes of the initial data is not carried out. Nevertheless, function  $y(s)$  can be determined by the method of regularization with some accuracy [4]. Then integral equations (1) are reduced to the integral equation of the second kind:

$$y_\alpha(t)\alpha + \int_0^\tau \left\{ \int_c^d \hat{K}(p,t) \hat{K}(p,x) dp \right\} y_\alpha(x) dx = \int_c^d \hat{K}(p,t) \hat{g}(p) dp \alpha \quad (2)$$

Here  $y'_\alpha(0) = y'_\alpha(\tau) = 0$ , and regularization parameter  $\alpha$  is defined by well-known method of generalized discrepancy [5]. The integral in (2) can be substituted by their discrete analogs obtained by the rectangle formula. And then we arrive at the system of linear algebraic equations of the form

$$(C\alpha + H)y_\alpha = z \quad (3)$$

Here  $C$  is a diagonal unit matrix and  $H$  is a positively definite matrix. This system is solved by the method of a square root.

#### Model experiments

Based on the obtained formulas the calculation algorithm for function  $\Delta\epsilon(r)$  was developed. Some model experiments in the two-millimeter wave range were carried out with the open resonator as a gauge. The OR with mirror curvature  $R_{1,2} = 30\lambda$ , aperture size  $2b = 30\lambda$ , intermirror space  $L \cong 24\lambda$  was taken to work at wavelength  $\lambda = 2,2\text{mm}$ . The Teflon film of  $h \cong 0,01\text{mm}$  was located at a maximum of the electrical component of an electromagnetic field of resonant mode. The frequency shifts of 10 axially symmetric modes with radial index  $p = 0 - 9$  were measured.

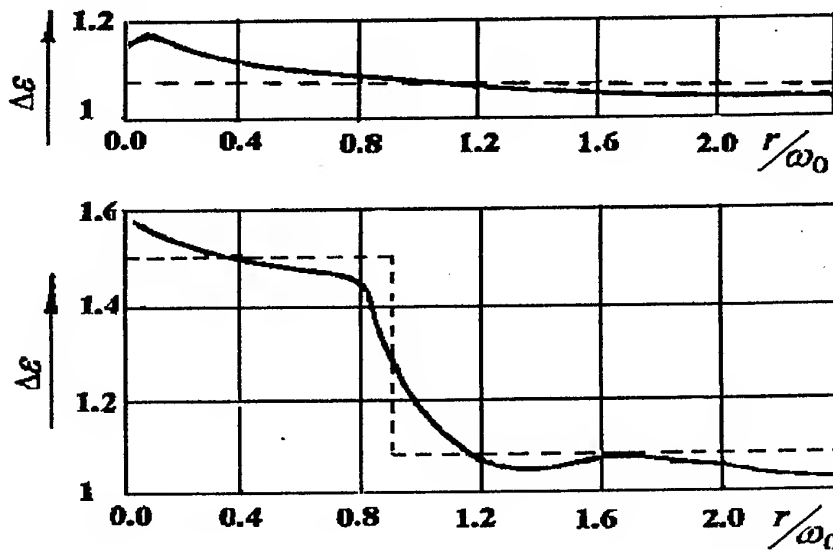


Fig.1

Fig. 1a shows  $\Delta\epsilon(r/w_0)$  for a homogeneous Teflon film with the uniform  $\epsilon(r)$  distribution. The solid curve is for the restored function  $\Delta\epsilon$ , the dotted curve shows the Teflon permittivity  $\Delta\epsilon = \epsilon_{\text{tef}} - 1$ . The curve for  $\Delta\epsilon(r/w_0)$  of an inhomogeneous Teflon film is in Fig 1b. The permittivity inhomogeneity Teflon film was modeled by varying the film thickness in the center of the film. The function restoration accuracy can be raised by increasing of the modes number..

1. A.A. Vertiy, I.V. Ivanchenko, V.N. Derkach, Proc. of Intern. Conf. San Diego. USA. 2250. 373 (1994).
2. H.Kogelnik Foreign electronics.. 3. 102. (1967)
3. V.V.Nikolsky Variational methods for internal tasks of electrodynamics. M.:Nauka, 460 (1967)
4. A.N.Tikhonov Methods for solution of incorrect problems M.:Nauka, 288 (1986)
5. A.F.Verlan, A.N.Sizikov Integrabel equations. Kiev., 554 (1986)
6. N.S.Bakhvalov Numerical methods. M, Nauka, 632 (1975)

## SURFACE IMPEDANCE MAPPING AT CRYOGENIC TEMPERATURES OF HTSC-WAFERS AT 145 GHZ

R. Schwab<sup>1)</sup>, R. Heidinger<sup>1)</sup>, J. Geerk<sup>2)</sup>, F. Ratzel<sup>2)</sup>, M. Lorenz<sup>3)</sup>, H. Hochmuth<sup>3)</sup>

<sup>1)</sup> Forschungszentrum Karlsruhe, Institut für Materialforschung I

P.O. Box 3640, D-76021 Karlsruhe, Germany

<sup>2)</sup> Forschungszentrum Karlsruhe, Institut für Nukleare Festkörperphysik

P.O. Box 3640, D-76021 Karlsruhe, Germany

<sup>3)</sup> Universität Leipzig, Fakultät für Physik und Geowissenschaften

Linnéstrasse 5, D-04103 Leipzig, Germany

### Abstract

Highly qualified YBCO - thin films provide superior surface resistances even at mm-wavelength. On the other hand, mm-wave measurements are a sensitive tool for homogeneity studies of large sized wafers. This approach is used to map advanced materials produced by magnetron sputtering and by pulsed laser deposition.

### Introduction

Passive high frequency components based on high- $T_c$ -superconductors (HTSC) have shown superior performance at minimal size and weight and they are being introduced into commercial applications in communication and satellite technology. The basic materials for these devices are HTSC-wafers composed of a few hundred nanometer thick HTSC-film epitaxially grown on a dielectric substrate. For a number of components double-sided large area wafers (typical 3 inch in diameter) are required which challenges design and operation of the deposition technologies. New aspects arise also for materials characterisation since the spatial homogeneity of the key materials parameters, which for the high frequency dissipation is the surface resistance  $R_s$ , become a critical concern. The use of the open resonator technique in the mm - wave range is one of the most promising candidates to cope with this problem and actually the CRYOSCAN system [1] has shown to provide quantitative mappings of  $R_s$ . In this paper systematic  $R_s$ -mappings for HTSC-wafers from two of the most promising deposition processes, i.e. sputtering and pulsed laser deposition, are discussed.

### Sample preparation and experimental details

The  $R_s$ -mappings were performed on double-sided YBCO-wafers where on a 3 inch r-plane oriented sapphire disc (thickness 430  $\mu\text{m}$ )  $\text{YBa}_2\text{Cu}_3\text{O}_{7-\delta}$  was grown epitaxially on both sides with the c-axis oriented perpendicular to the surface. To reduce the large lattice mismatch and to suppress the undesired interdiffusion of sapphire and YBCO, a buffer layer of  $\text{CeO}_2$  is deposited prior to the YBCO-film. Wafer 1 (400 nm YBCO) and Wafer 2 (500 nm YBCO) were produced by the inverted magnetron sputtering method [2], where the substrates were placed in a radiation heater and the deposition could be carried out simultaneously on both sides of the substrate. Wafer 3 and Wafer 4 (both 250 nm YBCO) were produced by the pulsed laser deposition method [3] which is a particularly simple and fast deposition process.

The investigated samples are selected from a series of wafers produced from each deposition method during the optimisation runs of the processes. The samples were fixed on the plane mirror of the focussed quasi hemispherical Fabry-Perot resonator and the complete mirror system is cooled down and stabilised at a temperature of 77 K using  $\text{LN}_2$  in the gasflow cryostat. With a radial and a rotational degree of freedom a specific position of the sample can be moved into the focussed beam of the open resonator set-up at 145 GHz (spot size < 7 mm). A complete surface mapping is achieved by radial linescans at specified angles. From the resonance parameter at each position the surface resistances are assessed.

### Discussion of the surface resistance mappings

The  $R_s$ -mapping as obtained for Wafer 1 is plotted in Fig. 1a in form of circles distinguished by different shades of grey. From this  $R_s$ -mapping specific loss patterns in the samples are seen. For a better survey about the actual values a bar graph showing the quantity of data points in a certain  $R_s$ -range is plotted in Fig. 1b. The mapping may essentially be divided in three regions, i.e. a light grey and a grey area with low or moderate  $R_s$  and a black area where the losses of this wafer are strongly degrading. Even points where  $R_s$  exceeds the upper measurement limit (1  $\Omega$ ) are found indicated by crossed white circles. The symmetry of this pattern is related to the movement of the wafer during the deposition process and the degraded part was caused by an object screening the deposition which now is removed. Also seen in Fig 1a is a band around the wafer edge, which is not accessible by the method for quantitative measurements because of diffraction losses at the edge. A substantially much more homogenous wafer is shown in Fig. 2a together with the corresponding bar graph in Fig 2b. The mottled map results mainly from measurement statistics but there may also be a contribution from randomly distributed minor imperfections. In Fig. 2c the second side of this wafer is presented with equivalent  $R_s$ -values. Showing

essentially the same homogeneity, in this side however two isolated points are found where strongly increased  $R_S$  in the centre and in the left could be localised.

The  $R_S$ -mappings of Wafer 3 and Wafer 4 (Fig. 3a,b) reveal a pattern of rotational symmetry where an extended central area with higher losses is surrounded by an area of lower losses. Although the geometrical pattern looks similar and reveals again the symmetry of wafer movement during deposition, the absolute values in both wafers are different (cf. Fig. 3c). Further Wafer 4 shows improved homogeneity which is reflected in the reduced data distribution.

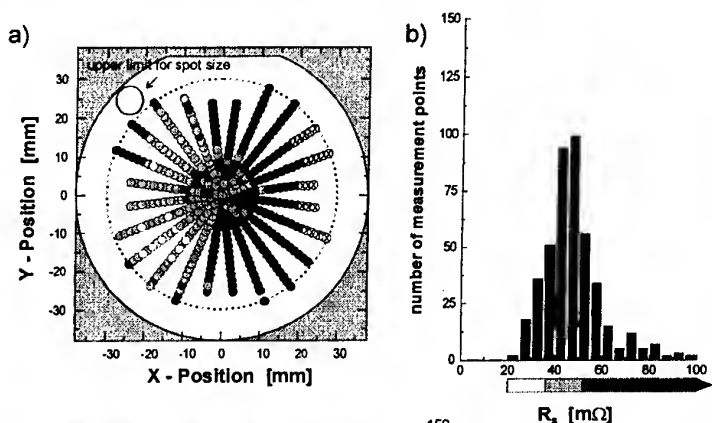


Fig 1:

- a)  $R_S$ -mapping of Wafer 1 at 77 K and 145 GHz  
b) Distribution of measured  $R_S$ -values

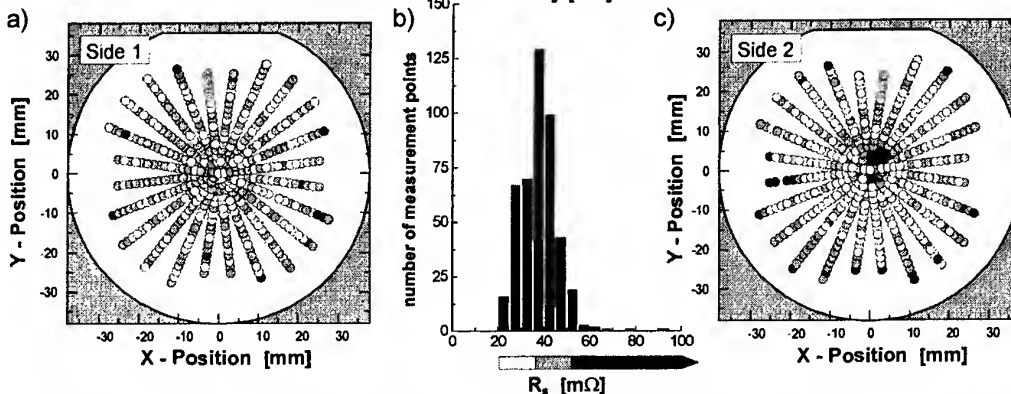


Fig. 2: a)  $R_S$ -mapping of Wafer 2: Side 1    b) Distribution of measured data for Wafer 2: Side 1    c)  $R_S$ -mapping of Wafer 2: Side 2

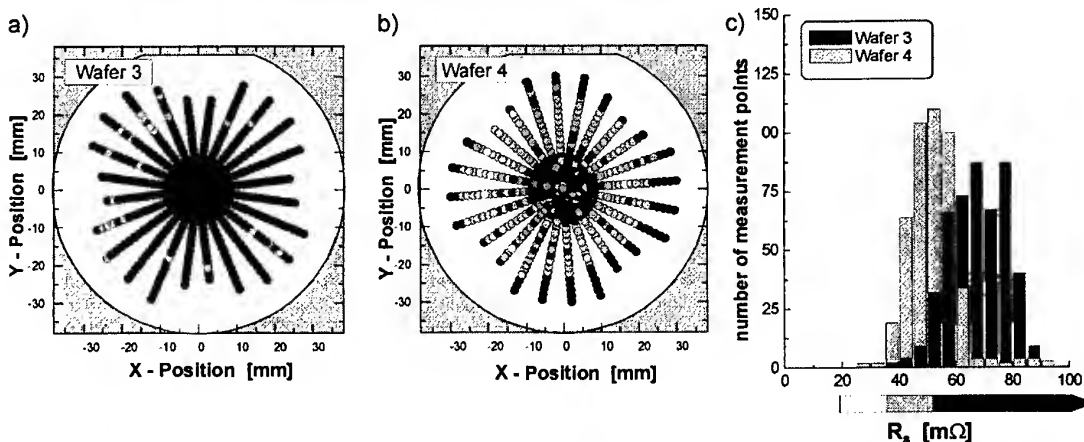


Fig. 3: a)  $R_S$ -mapping of Wafer 3    b)  $R_S$ -mapping of Wafer 4    c) Data distribution of both wafers

#### Literature

- [1] R. Schwab, R. Heidinger, R. Spörl, Digest of this conference
- [2] J. Geerk, G. Linker, O. Meyer, Mat. Sci. Rep. 4, 1989, 193
- [3] M. Lorenz, H. Hochmuth, D. Natusch, H. Börner, G. Lippold, K. Kreher, W. Schmitz, Appl. Phys. Lett. 68 (23), 1996

# ELECTROMAGNETIC SIMULATION OF A 32GHz, TE<sub>021</sub> GYROTRON

J. J. Barroso, K. G. Kostov\*, and R. A. Corrêa

National Institute for Space Research (INPE), PO. Box 515, 12227-970 São José dos Campos, SP, Brazil

\*on leave from Dept. of General Physics, Sofia University, 5 J. Bourchier Blvd, Sofia-1126, Bulgaria

## Abstract

A simulation study based on experimental parameters of a 32GHz gyrotron operating in the TE<sub>021</sub> mode is presented. Beam electrons with typical energy of 40 keV and transverse-to-axial velocity ratio ranging from 0.8 to 2.0 are injected into the cavity to drive electromagnetic oscillations from noise. Using an electromagnetic PIC code, a parameterization study is carried out to determine the dependence of output power upon pitch ratio and beam current.

## Introduction

Particle simulations can provide insights that complement and enlarge those gained by traditional approaches, thus adding feedback for improvement in theory. Gyrotron simulations using particles have begun since the 1980's, either making relativistic predictions of the saturated RF output characteristics of a gyrotron amplifier [1] or examining the scaling of the transient growth rate with the beam current [2]. Being fully nonlinear, simulation is then capable of handling growth in time and space from linear through large amplitudes. In the particle model, the motion of a large assembly of charge particles is followed in their self-consistent electric and magnetic fields. In this paper, we report on a simulation study of a high-power, pulsed gyrotron operating in the TE<sub>021</sub> mode at 32 GHz using a 2½ dimensional, fully relativistic electromagnetic particle code [3]. Beam equilibrium parameters are based on experimentally observed values [4], and in all the computer runs a monoenergetic annular electron beam with guiding centers located on the second radial maximum of the TE<sub>021</sub> mode is injected into the cavity to drive the electromagnetic oscillations from noises. Results of the simulation are detailed in the second Section and followed by discussion in the Conclusions.

## Results of the Simulation

Fig. 1 illustrates the elements of the particle modeling. Simulations are initiated by continuously injecting the beam

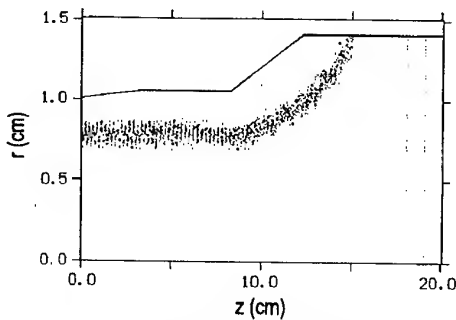


Fig. 1. Real-space (r-z) diagram of the simulated beam at t=48 ns

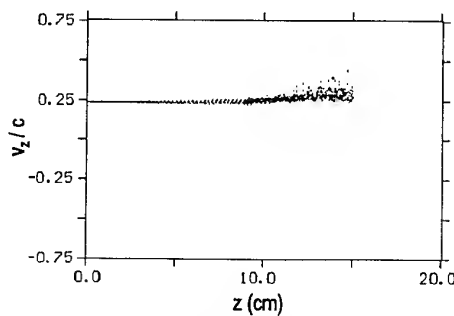


Fig. 2. Axial velocity vs. axial distance of the electron beam at t=48 ns

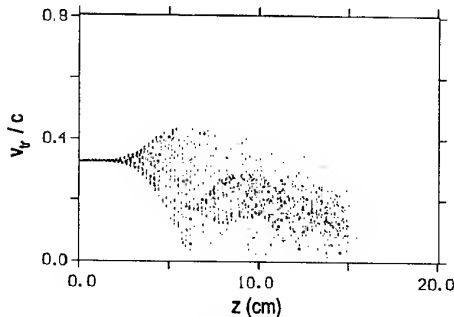


Fig. 3. Transverse velocity vs. axial distance of the beam at t=48 ns

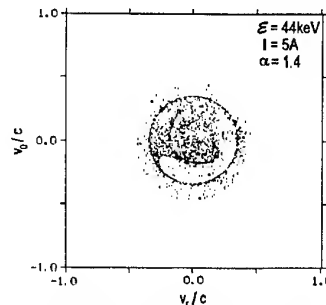


Fig. 4. Particle positions in the  $v_\theta - v_r$  parameter space

electrons with prescribed parameters into the cavity. The inlet is at the beginning of a downtapered section and an absorbing disk is placed in the output guide to absorb the outgoing travelling wave. The axial component of the applied guiding magnetic field is constant over the distance  $0 \leq z \leq 9.0$  cm and decreases linearly to reach a zero value at  $z = 17.5$  cm, so that the spent beam is dumped beyond the output taper, where the electrons are no longer in

resonance with the wave. We have used over ten thousand particles to simulate the beam and a mathematical spatial grid, having dimensions  $0.2\text{mm} \times 0.3\text{mm}$ , which is fine enough to resolve a Larmor radius in order to measure the charge density and then calculate the fields. At time  $t=48\text{ns}$  an injected 44-keV, 5-A beam with pitch ratio of 1.4 has clearly become modulated as shown in Fig. 1. The corresponding plots of the axial and transverse velocities vs. the axial distance are given in Fig. 2 and Fig. 3 at a time  $t=48\text{ns}$  when the RF fields have saturated into the simulation. The simulated self-consistent axial profile of the operating  $\text{TE}_{021}$  mode is shown in Fig. 5 for  $\Omega_B/\omega_c = 0.97$  where  $\Omega_B$  is the relativistic cyclotron frequency and  $\omega_c$  is the waveguide cutoff frequency. We can distinguish the quasi-stationary cavity field confined in the region  $0 \leq z \leq 9.0\text{cm}$  and a pure outgoing traveling wave that propagates to the right. This indicates the effectiveness of the conducting disk in absorbing all the output radiation, thus preventing the wave from reflecting back to the cavity.

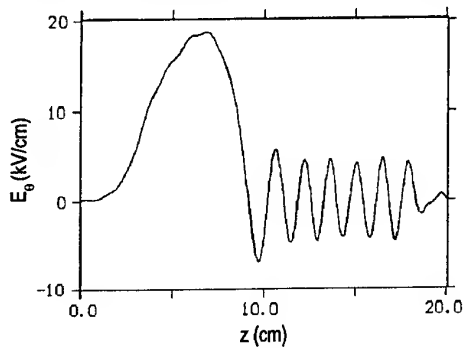


Fig. 5. Self-consistent electric field profile

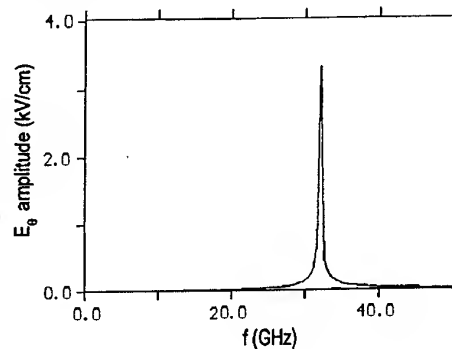


Fig. 6. Frequency spectrum at  $r=1\text{cm}; z=17\text{cm}$

The associated frequency spectrum of the electric field at  $r=1.0\text{cm}$ ,  $z=17.0\text{cm}$  is given in Fig. 6, which is characterized by a single-frequency component peaked at 32.03GHz, being slightly above the 31.90GHz cutoff frequency of the regular section of the waveguide cavity with radius 1.05cm. For a 44-keV, 5A beam with pitch ratio of 1.4, Fig. 7 shows the time history of the output power as determined by integration of the Poynting flux across the observation section at  $z=17.0\text{cm}$ . A parameterization of the gyrotron's settings were carried out to determine how sensitive the output power is to changes in pitch ratio and beam current.

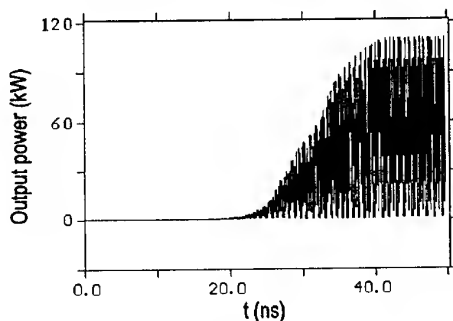


Fig. 7. Time history of the output power

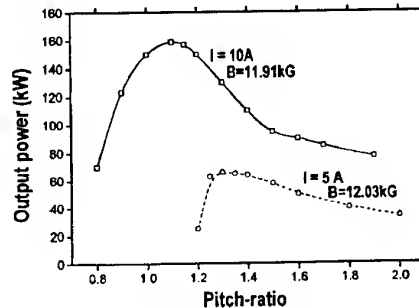


Fig. 8. Simulated pitch-ratio parameterization

The results of this study are presented in Fig. 8 which shows the output power as function of the pitch ratio with the beam current as a parameter. The output power was optimized with respect to the applied magnetic field, and we see that the maximum values of both output power and efficiency increase with beam current.

### Conclusions

The operation of 32GHz gyrotron was examined using an electromagnetic PIC code that provided a comprehensive picture of cyclotron resonance interaction of TE-mode cavity fields with a helical electron beam. Beam currents of 5 and 10A with pitch angle  $\alpha = v_{\perp}/v_{\parallel}$  varying from 0.8 to 2.0 have been considered. For each value of current, optimization of the conversion efficiency with respect to the external magnetic field has given 40% efficiency at  $\alpha=1.1$  and 10A, while for the low-current case the maximum efficiency has been 32% at  $\alpha=1.3$ .

### References

1. M. Caplan, A.T. Lin, and K.R. Chu, *Int. J. Electronics*, 53(6), 659 (1982).
2. A.T. Lin, Z.H. Yang, and K.R. Chu, *IEEE Trans. Microwave Theory Tech.*, 16(2), 129 (1988).
3. V.P. Tarakanov, "User's Manual for code KARAT", Berkeley Research Ass., Inc., Springfield, VA, USA, (1994).
4. J.J. Barroso, P.J. Castro, A.A. Pimenta, V.A. Spassov, R.A. Corrêa, T. Idehara, and I. Ogawa, *Int. J. Infrared Millimeter Waves*, 18(11), 2147 (1997).

## A 4.5 MW - Electron Gun for a Coaxial Cavity Gyrotron

B. Piosczyk

Forschungszentrum Karlsruhe, Association EURATOM-FZK, Postfach 3640, D-76021 Karlsruhe, Germany,  
e-mail: bernhard.piosczyk@itp.fzk.de

### Introduction

The mechanical complexity of a coaxial gyrotron is increased due to the existence of the coaxial insert. In order to investigate the related specific problems, in particular in view of cw operation and to demonstrate a technically feasible solution a new electron gun has been designed and is now under fabrication. Since the gun is foreseen to be used in an experimental set up [1] at FZK the design of the gun is adapted to the existing equipment, in particular to the superconducting (sc) magnet.

The electron gun has two electrodes (diode type). The arrangement of the electron emitter ring and the anode is similar to that of a conventional magnetron injection gun (MIG) for gyrotrons. Thus, the emission of the electrons is not, as in the presently used inverse magnetron injection gun (IMIG) directed towards the inner rod [2] but towards the anode. The suggested gun has the following important advantages over the IMIG gun geometry:

- reduced diameter of the gun at a given diameter of the emitter
- negligible influence of the inner rod on the beam properties
- possibility of independent polarization of the inner rod

The design has been performed in order to satisfy the requirements on the electron beam both for the  $TE_{28,16}$  mode at 140 GHz and the  $TE_{31,17}$  mode at 165 GHz. This can be fulfilled by an individual optimization of the anode shape for both cases with an unchanged surface contours of the cathode and the inner rod.

### Requirements on the electron beam and design of the gun

The required parameters are given in the first part of Table 1. The nominal operating voltage has been chosen to be 90 kV and 80 kV, respectively. The needed beam radius  $R_b$  in the cavity is different in both cases. Since the cathode radius stays unchanged a different magnetic compression has to be used. The design of the gun has been performed for a magnetic field distribution of an existing sc-magnet consisting of three independently adjustable solenoidal coils, a main coil and two gun coils.

Fig. 1 shows as an example the contours of the electrodes together with the trajectories and potential lines of the gun for the  $TE_{28,16}$  mode. The conditions are very similar for the  $TE_{31,17}$  mode. Therefore in the following only the case of the  $TE_{28,16}$  mode will be considered.  $\beta_{\perp}$  and  $\beta_{\parallel}$  are the normalized transverse and axial

**Tab. 1:** Nominal electron beam and gun parameters. Results of EPOSR and BFCRAY are in brackets.

operating mode		$TE_{28,16}$	$TE_{31,17}$
frequency :	$f / \text{GHz}$	140	165
beam current	$I_b / \text{A}$	50	50
cathode voltage	$U_c / \text{kV}$	90	80
beam radius at the cavity :	$R_b / \text{mm}$	10.0	9.41
magnetic compression	$b$	32.7	36.9
magnetic field in the cavity	$B_{\text{cav}} / \text{T}$	5.55	6.58
velocity ratio	$\alpha = \beta_{\perp} / \beta_{\parallel}$	1.53 [ 1.38 / 1.35 ]	1.45 [ 1.38 / 1.33 ]
velocity spread - rms value	$\delta\beta_{\perp, \text{rms}} / \%$	2.2 [ 0.7 / 2.0 ]	1.9 [ 2.0 / 1.6 ]

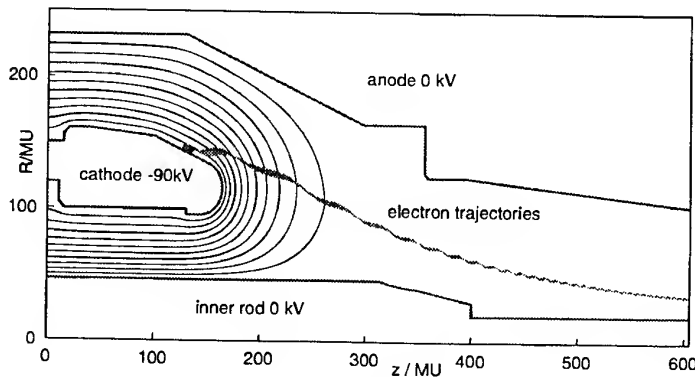


**Fig. 1:** Electron trajectories at nominal conditions. 1MU = 0.4 mm.



velocities. The average radius of the emitter is 57.2 mm, its tilt angle towards the axis is  $21.80^\circ$ . The coaxial insert is supported from the bottom of the gun. The insert consists of two parts, a rigid outer part which ranges up to the gun region and ends at  $z = 400$  MU (Fig. 1) and a radially adjustable inner part with a total length of about 120 cm ending approximately 30 cm above the cavity. The range of the radial adjusting is  $\Delta r = \pm 2$  mm with a reproducibility of  $\pm 0.1$  mm. The adjustment can be performed in the fully assembled tube. The insert has been designed to be sufficiently rigid to keep the amplitude of mechanical vibrations at acceptable values. The part inside and above the cavity is made of copper. The total amount of rf-power dissipated in the insert is about 1 kW at the design rf-output of 1.5 MW. To remove the heat losses water cooling is provided.

#### Beam and gun parameters under nominal operating conditions

The electron gun has been optimized using the EGUN-code. The trajectories have been calculated from the gun up to the resonator. The electron trajectories are of non-laminar type as shown in Fig. 1.

The nominal beam parameters are given in Tab. 1. The maximum electric field of 6.3 kV/mm is at the nose of the cathode. The electric field at the inner rod is only slightly lower. Compared to that the electric field at the anode is small. At the emitter surface the electric field is about 3.8 kV/mm at zero current and decreases to about 3.5 kV/mm at the nominal current of 50 A. The magnetic compression  $b = \{R_c/R_b\}^2$  is defined by the ratio of the radius  $R_c$  of the emitter and the beam radius  $R_b$ . For the nominal parameters the calculations have been verified with the trajectory codes EPOSR and BFCRAY\*. The calculated  $\alpha$ -value varies between 5 and 10% for the different codes. Fig. 2 gives the dependence of the transverse and axial velocity versus the starting position at the emitter surface also calculated with the three codes. The agreement of the different calculations is reasonable. In Fig. 3 the dependence of beam parameters on the beam current are given for the  $TE_{28,16}$ -mode. The  $\alpha$ -value decreases with current and the spread has a minimum around the design current of 50 A.

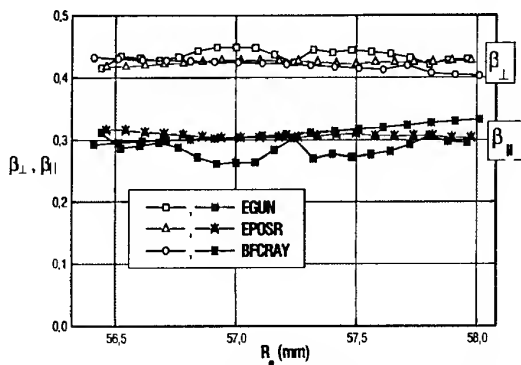


Fig. 2:  $\beta_{\perp}$  and  $\beta_{\parallel}$  versus the starting position at the emitter surface for the  $TE_{28,16}$ -mode parameters.

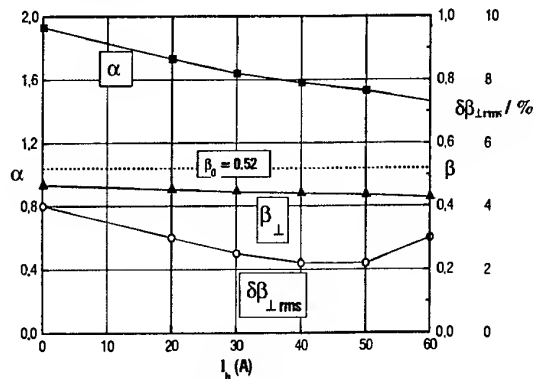


Fig. 3:  $\alpha$ ,  $\beta_{\perp}$  and  $\delta\beta_{\perp,rms}$  versus  $I_b$ .  $\beta_0$  corresponds to the electron energy  $eU_c = 90$  keV

#### Operation of the coaxial gyrotron with a polarized inner rod

In the suggested design the presence of the inner rod enables an operation of the gun with the inner rod polarized with respect to the anode. This allows a variation of the electron beam energy with nearly no influence on the transverse momentum  $p_{\perp} \sim \beta_{\perp}$  as has been confirmed in numerical calculations. The operation is similar to that of a three electrode gun (triode gun) where the voltage between the cathode and the modulation anode mainly determines  $\beta_{\perp}$  and the beam energy is given by the voltage between the cathode and the anode. Since according to experimental observations the current  $I_{rod}$  to the inner rod is small,  $I_{rod} < 0.001 \cdot I_b$ , the polarization of the rod can be done nearly powerless. Therefore, an operation with the polarized coaxial insert enhances the efficiency similar as use of a single stage depressed collector without the necessity of having an insulated collector. The polarization of the insert leads to a radial dependence of the potential inside the cavity. This results in an additional energy spread which has been estimated to be below 1% for relevant parameters. However, this has practically no influence on the gyrotron efficiency.

#### References

- [1] B. Piosczyk, et al.: 165 GHz,  $TE_{31,17}$ -coaxial cavity gyrotron with quasi-optical rf-output, this conference
- [2] V. Lygin, et al.: Inverse magnetron injection gun for a coaxial cavity 1.5 MW, 140 GHz gyrotron, Int.J.Electronics, 1995, vol.79,2 227-235

\* the calculations with EPOSR and BFCRAY have been performed by Dr. V. Manuilov, IAP Nizhny Novgorod and Dr. E. Borie, FZK Karlsruhe, respectively.

# Investigations of Beam Instabilities in the Compression Region of Gyrotrons Using Kinetic Theory and Particle-in-Cell Simulations

Stefan Illy, Edith Borie

Forschungszentrum Karlsruhe, Institut für Technische Physik, Association EURATOM-FZK  
Hermann-von-Helmholtz-Platz 1, D-76344 Eggenstein-Leopoldshafen, Germany

## Introduction

Beam instabilities that arise in the compression zone of a gyrotron oscillator can degrade the beam quality and hence adversely affect the operating characteristics of these devices. We investigated a class of space charge instabilities that are related to unstable Bernstein modes. These have been studied mainly because they can degrade the beam quality [1–3].

In order to investigate this class of instabilities further, a fully electromagnetic particle-in-cell (PIC) code has been developed to model an annular electron beam in the  $z$ - $r$  plane. The instabilities are also investigated using small signal analysis based on kinetic theory, similar to that of Chen et al. [1] and of Li and Antonsen [2]. Use of the code makes it possible to study effects that cannot be taken into account in the linear dispersion relation, such as the effect of static self-fields. The dependence of growth rate and frequency spectrum on beam parameters was calculated both with simulation and the analytic method and showed good agreement. A detailed analysis of the electromagnetic fields calculated in the simulation showed that the unstable waves are not, as frequently assumed in the past, purely electrostatic.

## Small signal analysis

The derivation of the dispersion relation from the Vlasov equation and Maxwell's equations is standard and can be found in many textbooks. The dielectric tensor  $\tilde{\epsilon}$  was rederived and agrees with the expressions given in [4]. For the investigation of space charge instabilities we assumed that  $E_y = 0$  (in cylinder coordinates, this corresponds to neglecting TE-modes) and that waves propagate in the  $x$ - $z$  plane. We obtain the following dispersion relation:

$$k_x^2 \epsilon_{xx} + k_x k_z (\epsilon_{xz} + \epsilon_{zx}) + k_z^2 \epsilon_{zz} - \frac{\omega^2}{c^2} (\epsilon_{xx} \epsilon_{zz} - \epsilon_{xz} \epsilon_{zx}) = 0. \quad (1)$$

If only electrostatic waves are considered, one can obtain a similar dispersion relation from Poisson's equation and charge conservation. In this case the last term of Eq. (1) is not present [1].

In Fig. 1 we present numerical solutions of (1) for different values of the propagation vector compo-

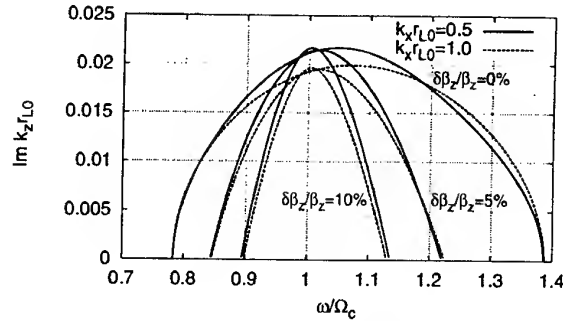


Figure 1:  $\text{Im } k_z$  vs.  $\omega$  for  $\beta_z = 0.279$ ,  $\beta_\perp = 0.418$ ,  $\omega_p/\Omega_c = 0.070$  ( $\omega_p$  is the plasma frequency and  $\Omega_c$  is the relativistic cyclotron frequency) and several values of the velocity spread  $\delta\beta_z$  and  $k_x$ .

nent  $k_x$  and the velocity spread  $\delta\beta_z$  (parameters in caption). The choice of the  $k_x$  values was influenced by the fact that there may be a standing wave in the electron beam restricting  $k_x$  to a typical range of  $0.5 \leq k_x r_L \leq 1.0$ . One observes a broad frequency band centered around  $\Omega_c$  where unstable wave propagation is permitted. The width of the frequency band decreases if  $\delta\beta_z$  is increased, but there is almost no influence on the maximum growth rate. A subsequent detailed analysis showed that the dependence of the growth rate  $\text{Im } k_z$  on beam parameters can be reduced to the expression  $\text{Im } k_z \propto \omega_p \beta_\perp \Omega_c$  for  $\omega = \Omega_c$ .

## PIC Simulations

Both the electromagnetic and the electrostatic dispersion relation give almost the same results (for the considered beam parameters). In addition, the analytic model uses several approximations that may not be valid in the case of a real gyrotron beam. The particle-in-cell simulation of the hollow electron beam should give further information about the properties of the instability and the validity of the analytic model.

The particle-in-cell code T2hPIC was especially developed for the purpose of investigating beam instabilities and is described in [5]. The simulation was performed for an electron beam in a cylindrical region with a constant magnetic field ( $B_{z,appl} = 1$  T), in order to have conditions as close as possible to those assumed in the analytical theory. The rectangular grid is sufficiently fine to re-

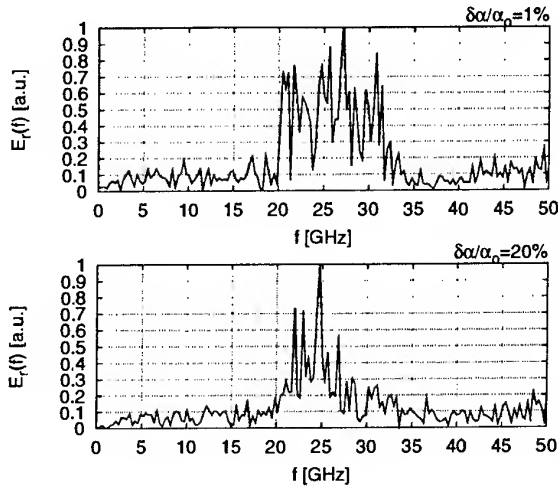


Figure 2: Frequency spectra of the time dependent contribution to  $E_r$  for different values of the velocity spread  $\delta\alpha$ .

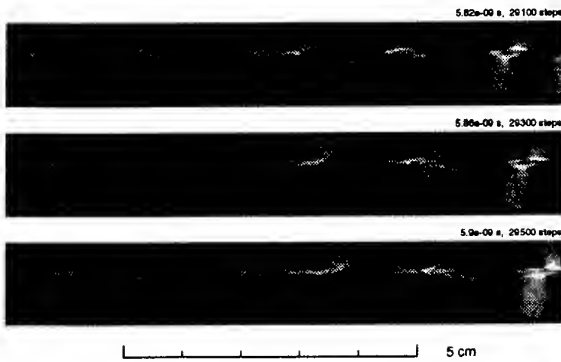


Figure 3: Contours of the time dependent contribution to  $E_r$  at time intervals of approximately a cyclotron period (200 time steps). Scaling:  $-10^5$  V/m (black) ...  $10^5$  V/m (white).

solve the instability and long enough to permit an instability to grow ( $L \approx 9.5$  cm). Except for the symmetry axis, the computational region was limited by open boundary conditions, in order to avoid accumulation of fluctuations in the electromagnetic fields that might mask the space charge instability. In the first simulation only the field components corresponding to a TM-wave were kept, a flat charge density profile was used and the static contribution to  $E_r$  was suppressed in order to be able to compare the results with those of the small signal theory better.

Fig. 3 shows simulation results for beam parameters  $U = 80$  kV,  $I_b = 100$  A and  $\alpha = 1.5$ . It is a series of contours of the time dependent contribution to  $E_r$ , at time intervals of approximately a cyclotron period. One observes that fairly strong fluctuations occur in the region occupied by the electron beam.  $k_z$  is not zero, as would be expected for ideal Bernstein waves. However,  $k_x \gg k_z$ . The amplitude of the fluctuations increases from left to right. Closer examination shows that the extrema

move slowly from left to right, with a drift velocity of about  $0.025c$ . This is a clear indication that the instability is convective.

In addition, we examined the frequency spectra of all three field components at the radial center of the beam at position  $z = 0.5L$ . The spectrum of  $E_r$  shows a broad peak around  $\Omega_c$  (Fig. 2), in good agreement with the results of the analytic model. The spectra show no structure at higher harmonics of  $\Omega_c$ . If the instability were associated with an electrostatic wave then the condition  $\mathbf{k} \times \mathbf{E} = 0$  would require that  $B_\phi = 0$ . The analysis of the magnitude and spectrum of  $B_\phi$  shows that this is not the case. This indicates the existence of electromagnetic contributions to the space charge instability. Giving velocity spread to the injected electrons results in a shrinking of the allowed frequency band, in agreement with the small signal analysis.

The averaged amplitude  $|E_r(z)|$  was fitted to the function  $f(z) = ae^{z/d_g}$  for  $0.4L < z < 0.9L$ . For  $U = 80$  kV,  $I_b = 100$  A,  $\alpha = 1.5$  we obtain the growth length  $d_g = (\text{Im } k_z)^{-1} = 4.1$  cm. The corresponding results from the small signal theory for  $\omega = \Omega_c$  are  $d_g = 4.2$  cm and  $d_g = 4.6$  cm for  $k_x r_L = 0.5$  and  $k_x r_L = 1.0$ , respectively. The results of the simulation are in very satisfactory agreement for other values of  $I_b$  and  $\alpha$ . The simulations were then repeated including more realistic assumptions. The results are summarized as follows:

- Using a more realistic (hat shaped) beam profile tends to decrease the growth of the instability ( $d_g = 5.6$  cm).
- Inclusion of the static self field  $E_{r,stat}$  did not show a clear tendency (here  $d_g = 4.9$  cm, but it increases for other beam parameters).
- A velocity spread of  $\delta\alpha/\alpha = 20\%$  given to the injected electrons results in an additional damping of the instability ( $d_g = 5.9$  cm).
- Inclusion of the TE-polarization results in a significant increase of  $d_g$  up to 8.1 cm.

In the future it will be interesting to consider the effect of a nonuniform magnetic field on the instability, and to try to understand why the inclusion of TE-polarization damps the instability.

## References

- [1] K. R. Chen and K. R. Chu: IEEE Trans. on Microwave Theory and Techniques, 34(1):72-79, 1986.
- [2] H. Li and T. M. Antonsen, Jr.: Physics of Plasmas, 1(3):714-729, 1994.
- [3] T. M. Tran *et al.*: Physics of Plasmas, 4(8):3043-3048, 1997.
- [4] G. Bekefi: *Radiation Processes in Plasmas*. John Wiley & Sons, New York, 1966.
- [5] S. Illy: Dissertation, Universität Karlsruhe und Forschungszentrum Karlsruhe (FZKA 6937), 1997.

## Development of a submillimeter wave gyrotron (Gyrotron FU V)

T.Idehara, I.Ogawa S.Mitsudo, M.L.Pereyaslavets, T.Tsuchida and M.Ui

*Faculty of Engineering, Fukui University  
3-9-1 Bunkyo, Fukui-shi 910-8507, Japan*

The latest gyrotron in the Gyrotron FU series in Fukui University, named Gyrotron FU V which consists of a helium-free 8T superconducting magnet and a demountable gyrotron tube, has been designed and constructed. Complete cw operation of the gyrotron will enable us to use it as a time-unlimited power source covering a wide range in the millimeter to submillimeter wave region.

### 1. Introduction

The Gyrotron FU series in Fukui University is being developed to provide high frequency sources for plasma diagnostics and far-infrared spectroscopy. The series has achieved the frequency step-tunability in wide range from 38 GHz to 889 GHz [1] and frequency and amplitude modulations. [2] Some gyrotrons in the series have applied to plasma scattering measurement [3] and ESR experiment [4] as submillimeter wave sources.

In almost all gyrotrons which have been developed up to the present, superconducting magnets are used. Therefore, operation duration of the gyrotron is limited by supplied liquid helium. To remove a complicated tasks to treat liquid helium, we have designed and constructed a new gyrotron, Gyrotron FU V, which consists of a helium-free, 8T superconducting magnet, subsidiary coils installed at a electron gun region and a demountable tube.

Operations of conventional gyrotrons are pulsed. However, medium power, submillimeter wave gyrotrons for infrared spectroscopy need to be operated in long pulses or completely cw. cw operation has been achieved with output powers of several tens of watts by a series of the high frequency gyrotrons at the University of Sydney [5], while a long pulse operation up to 600 msec with output powers of several hundreds of watts has been obtained by one of the submillimeter wave gyrotrons (Gyrotron FU II) at Fukui University. [3] cw operation has the other advantage that the frequency and amplitude of the output is more stable.[6]

Gyrotron FU V is designed for complete cw operation, which enables us to apply the gyrotron to wide fields as a time-unlimited, cw source covering a wide range in millimeter to submillimeter wave region. In this paper, the design and the construction of the gyrotron are presented.

### 2. Experimental apparatus and calculation results

Gyrotron FU V consists of a demountable gyrotron tube and magnet system as shown in Fig. 1. The helium-free superconducting magnet gives a main field in the cavity region whose intensity can be raised up to 8 T and three copper subsidiary field coils in the electron gun region. Both fields can be adjusted independently to control the electron beam trajectory. A constant current, high voltage power supply is used for gun cathode and a resistance divider connected across this supply is used for gun anode. The shape of the cavity installed in the gyrotron is a simple cylinder with a linear up-teper at its output end. In the present design,

mode conversions from the cavity mode to its competing modes are severe to obtain the pure mode output. In future, we are intending to install a precisely designed cavity for a high quality output mode.

For completely cw operation of gyrotron, water coolings of both the beam collector and the resonant cavity are important. The water flow rate is of the order of 2.5 l/min. Usually, we require that the water temperature at the outlet is never greater than 20 degrees above that at the inlet. As a consequence, the maximum input power to beam collector is 3.5 kW.

Starting currents of many cavity modes for fundamental and second harmonic operations are calculated and plotted in Fig.2 as functions of the main field intensity. Single mode operations of these modes at the second harmonics are useful for the applications to submillimeter wave spectroscopy. The experimental results will be presented in detail.

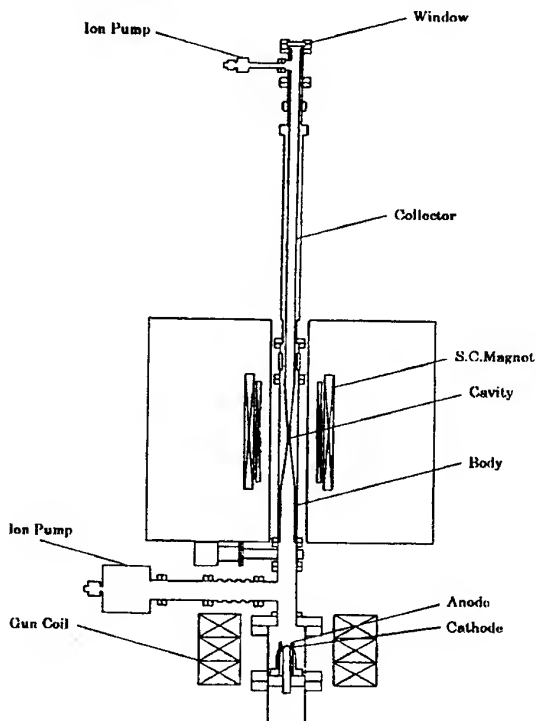


Fig. 1 Schematic drawing of Gyrotron FU V.

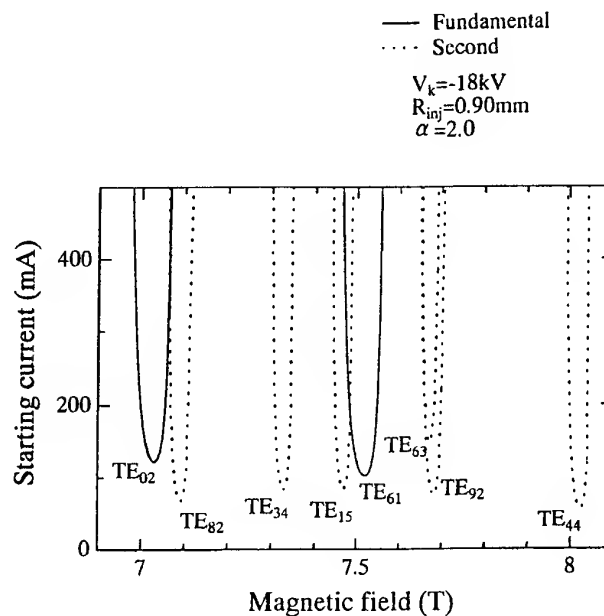


Fig.2 Calculated starting current of each cavity mode as a function of main field intensity

## References

- [1] T. Idehara, Y. Shimizu, K. Ichikawa, S. Makino, K. Shibutani, K. Kurahashi, T. Tatsukawa, I. Ogawa, Y. Okazaki and T. Okamoto, *Phys. Plasma* **2**, 3246 (1995).
- [2] T. Idehara, Y. Shimizu, S. Makino, K. Ichikawa, T. Tatsukawa, I. Ogawa and G.F. Brand, *Int. J. Infrared and Millimeter Waves* **18**, 391 (1987).
- [3] I. Ogawa, K. Yoshisue, H. Ibe, T. Idehara and K. Kawahata, *Rev. Sci. Instrum.* **65**, 1788 (1994).
- [4] T. Tatsukawa, T. Maeda, H. Sasai, T. Idehara, M. Mekata, T. Saito and T. Kanemaki, *Int. J. Infrared and Millimeter Waves* **16**, 293 (1995).
- [5] K.D. Hong, G.F. Brand and T. Idehara, *J. Appl. Phys.* **74**, 5250 (1993).
- [6] T. Idehara, K. Yoshida, N. Nishida, I. Ogawa and M.L. Pereyaslavets, *Int. J. Infrared and Millimeter Waves* **19**, no. 6 (to be published).

## High Power, Coherent InGaAs/InP Semiconductor, Laser Design Operating At 1.55

### Microns

Dr. A.R.Jha, Technical Director,  
Jha Technical Consulting Services,  
12354 Charlwood St, Cerritos, CA (USA)

### ABSTRACT

Diode-pumped solid state (DPSS) lasers employing diode arrays and optical crystals suffer from excessive weight, low conversion efficiency, and high fabrication cost. This paper reveals a unique design of coherent, high performance InGaAsP/InP strained-layer quantum-well (QW) semiconductor laser capable of delivering CW power output greater than 500 mw at 1.55 microns. It is important to mention that InGaAsP/InP strained-layer double-quantum-well (DQW) laser diodes are capable of yielding even higher optical power output with improved differential quantum efficiency (DQE) and with lower threshold current at 20 deg C. Compact packaging, minimum power consumption, eye-safe operation and minimum cost are the major benefits of this laser design.

### INTRODUCTION

InGaAsP/InP or InGaAs/InGaAsP semiconductor laser diodes with QW or DQW or MQW (multiple-quantum-well) heterostructures offer higher optical power levels with improved differential quantum and conversion efficiencies. Preliminary design analysis indicates that the InGaAsP/InP laser is capable of delivering even 1 watt of CW power at 1.55 microns. These semiconductor laser diodes are fabricated from epitaxial material layers grown on InP substrates with excellent lifetime characteristics. Inclusion of strained-layer InGaAs quantum-wells into an InGaAsP heterostructure allows this semiconductor laser diode to generate IR energy over 1.55 to 2.10 micron range without cryogenic cooling. As mentioned earlier, InGaAsP/InP laser diodes with InGaAs-DQW active layers can deliver optical power output of several hundred milliwatts per facet. Total differential quantum efficiency (TDQE) and optical power output as a function of cavity length and drive current can be computed at a given operating temperature.

Note the thickness of heavily strained InGaAs-QW active regions imbedded within the InGaAsP heterostructure determines the emission wavelength, whereas the mole fraction of indium and gallium in the  $\text{In}_{1-x}\text{Ga}_x\text{As}$ -quantum-well determines the internal transparent current density (ITCD). For a InGaAs-QW active region with In mole fraction of 0.75, the ITCD is about 56 A/sq.cm, which leads to total current density of 155 A/sq.cm for a DQW laser diode, assuming an injection efficiency of 72 %. For a cavity length of 2 mm, the threshold current density is about 300 A/sq.cm. at 25 deg., a value which compares well to InGaAsP/InP diode operating at 1.55 microns.

The InGaAsP/InP heterostructure diode employs the binary compound known as InP, which offers highest thermal conductivity and heat transfer efficiency. These parameters are considered most desirable for CW operations stated earlier the optical power and quantum efficiency are dependent on drive current, cavity length and diode temperature.

### DESIGN APPROACH FOR A SEMICONDUCTOR DIODE LASER

The critical elements required to test and evaluate the diode laser include a well-regulated power supply, water cooler with temperature control, optical cavity, and low-loss fiber optic cable. The InGaAsP/InP- QW laser diodes are arranged in parallel inside an optical cavity of appropriate length complete with collimating optics. The optical output is coupled to a low-loss single mode optical fiber. The power supply provides the drive current with precision control. The optical cavity and associated optics are cooled by water and its temperature is controlled to optimize the differential quantum efficiency and power output. The high power capability of this laser design has been demonstrated through computer modeling.

### **CONCLUSIONS**

Compact packaging, high differential quantum efficiency, low threshold current, non-cryogenic operation, high power CW capability, improved reliability and eye-safe operation are the major benefits of this laser. Potential applications include eye-safe surgical lasers, LIDARs, optical communication equipment, IR countermeasures systems and directed energy weapon systems.

### **ACKNOWLEDGEMENT**

The author wishes to thank Dr.S. Monen for computer analysis and comprehensive review of the paper.

## **A new boundary description in absorbing-boundary conditions for two dimension TLM models**

Chendong Zhu, Liquan He and Wei Hong

State Key Lab of Millimetre Waves, Southeast University, Nanjing, P R China 210096

In this paper, an algorithm is presented which uses a new boundary representation in an absorbing-boundary condition (ABC) based on the perfectly matched-layer (PML) approach for the 2D transmission-line matrix (TLM). In the conventional TLM method which was established by Johns[1], there is a halfway between two nodes. However, since fields are defined on the nodes and since the distance between the closest nodes and boundary is half of that of two nodes, the value at the boundary is not directly obtained from the TLM solution.

The paper uses a technique by which the boundary is placed across the nodes rather than halfway between them. Now the field value at the absorb boundary can be directly incorporated into the TLM model. Thus the flexibility and versatility of TLM simulations are increased. Such a TLM simulation can be easily combined with other methods such as FD-TD. In this paper, the return loss of a WR-28 rectangular waveguide is calculated, which is compared with the conventional method.

- [1] P.B.Johns and R.L.Beurle, "Numerical solution of 2-dimensional scattering problems using a transmission-line matrix," Proc.Inst. Elec.Eng., vol.118, no.9, pp.1203-1208,1971.



## POWER DIVIDERS IN MILLIMETER WAVES

Robson L.M. Lima and Humberto C.C. Fernandes

Department of Electrical Engineering - Technological Center  
Federal University of Rio Grande do Norte. P. O. Box 1583 - Tel/Fax: +55 84 2153731 / 32  
E-mail: humbeccf@ct.ufrn.br ; 59.072-970 - Natal/RN - Brazil

**Abstract:** The Transverse Transmission Line (TTL) Method in the Fourier transform domain is used to project and analyze unilateral power dividers with three-ports in millimeter wave by the first time. In addition, broadband power dividers have been analysed by using series connections of two fin lines, having essential applications to divide power and to work like an impedance transformer. Results of power at each output arm are obtained to different ratios of slot widths power dividers.

### 1. Introduction

This work presents an electromagnetic application to obtain the effective dielectric constant, the attenuation constant and the characteristic impedance of the arms of the power divide in millimeter wave frequencies, consisting of the unilateral fin lines with semiconductor substrate as shown in Fig. 1. The power in the output arms of this device to different ratios of slot widths utilizing the TTL [1] method, by first time, is also presented. In addition, broadband power dividers have been analysed by using series connections of two fin lines, having essential applications to divide power and to work like an impedance transformer [2]. Broadband power dividers having unequal power divisions can be designed by choosing different ratios of slot widths, corresponding to different line impedances.

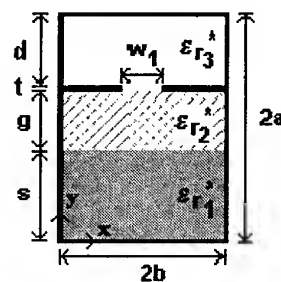


Fig. 1. Cross section of an arbitrary bilateral fin lines with semiconductor substrate.

The TTL method, the Maxwell's equations in Fourier transform domain, are used to obtain the electromagnetic fields in terms of the transversal electromagnetic fields.

By applying the boundary conditions to the tangential electric fields, the fields in all dielectric in all dielectric regions are determined as functions of the electric fields in the slots. Applying the boundary conditions to the magnetic fields at the interface, an inhomogeneous equations system is obtained, in which the current densities in the fins are related to the electric fields in the slots. Applying the boundary conditions to the magnetic fields at the interface, an inhomogeneous equations system is obtained, in which the current densities in the fins are related to the electric fields in the slots. By expanding these fields in terms of suitable basis functions and using the moment method and the Parseval's theorem, the current densities are eliminated, and an homogeneous equations system is obtained [3]. The LLUSSE.FOR and POWDIV.FOR computer programs, are developed in FORTRAN 77 language and the results obtained show rapid convergence and exactness.

### 2. Development

In the TTL method starting from the Maxwell's equations in Fourier transform domain, the tangential electromagnetic fields are obtained in terms of the transversal electromagnetic fields in the  $i$ -region of the structure [3].

$$\vec{E}_i = \vec{E}_{xi} + \vec{E}_{yi} + \vec{E}_{zi} \quad (1)$$

$$\vec{H}_i = \vec{H}_{xi} + \vec{H}_{yi} + \vec{H}_{zi} \quad (2)$$

Then are obtained the electromagnetic fields in the directions  $x$  and  $z$ , as function of the fields in the direction  $y$ .

By applying the boundary conditions to the tangential electric fields, the fields in all dielectric regions are determined as functions of the electric fields in the slots. An inhomogeneous equations system is obtained, by applying the boundary conditions to the magnetic fields at the dielectric interface, in which the current densities in the fins are related to the electric fields in the slots.

$$[Y] \cdot [\tilde{E}] = [\tilde{J}] \quad (3)$$

By expanding these fields in terms of suitable basis functions and using Galerkin's method and Parseval's theorem, it is possible to eliminate the current densities. Then an homogeneous equation system is obtained with two variables.

The characteristic equation for determining the complex propagation constant ( $\Gamma = \alpha + j\beta$ ), is obtained by setting the determinant of the system matrix equal to zero. The effective dielectric constant is determined by means of the relation  $\epsilon_{eff} = (\beta/k_0)^2$  [3].

The characteristic impedance is then determined

$$Z_c = \frac{V_x^2}{2P} \quad (4)$$

where the voltage in slot and the transmitted power are given by the expressions shown below:

$$V_x = \int_{-w/2}^{+w/2} \tilde{E}_{xt} dx \quad (5)$$

$$P = \frac{1}{8} \text{Re} \sum_{-\infty}^{+\infty} \left[ \int_0^{2a} (\tilde{E}_x \tilde{H}_y - \tilde{E}_y \tilde{H}_x) dy \right] \quad (6)$$

The powers in the output arms are obtained by analyzing series connections of two fin lines [2].

### 3. Results

Computer programs are developed in FORTRAN 77 language, and the results obtained for the effective dielectric constant and of the attenuation constant are presented as functions of the frequency, of the arbitrary dimension  $s$  (mm), and of the dimensions of the slots  $w_1$  and  $w_2$  (mm), in 3-D. The results were compared with references in 2-D, in which the substrate is a lossless material and for the symmetric not arbitrary structure [1], and the agreement was observed.

Results of the power at each output arm are obtained to different ratios of slot widths power dividers, in 2-D, also. It's important to note that such power dividers are reactive devices. For example, a 1:1 power divider that uses 300 Ohms input line and two 150 Ohms output lines is reported to a power division of  $3.4 \pm 0.2$  dB at each output arm over entire Ka band, for comparison with the literature [2].

### 4. Conclusions

In conclusions, results in 3-D were presented, and compared with references in 2-D, for an unilateral finline on semiconductor substrate, using the TTL method and applied to results of power dividers. These results increase the possibility of application in millimeter wave devices [4]-[5]. This work was supported by CNPq.

### References

1. H. C. C. Fernandes, E. A. M. Souza and I. S. Queiroz Jr, "High precision analysis of finlines on semiconductor substrate", International Journal of Infrared and Millimeter Waves, Vol. 16, N° 1, pp.185-200, Jan. (1995).
2. Bharathi Bhat, and Shibani K. Koul, "Analysis, design and applications of fin lines", Artech House, (1987).
3. H. C. C. Fernandes, "A Direct Method (TTL) Applied To General Planar Devices And Structures Of Millimeter Waves", Int. Conf. on Millimeter and Submillimeter Waves and Applications III, part of the SPIE'96, Denver-Colorado Conf. Proc. pp. 5-10, USA, Aug. (1996).
4. K. Ogusu, "Dielectric waveguide and power divide with metallic reflector", IEEE Trans. Microwave Theory and Techniques, vol. MTT-32, pp113-116, Jan. (1984).
5. L.C. Freitas Jr., H.C.C. Fernandes and S.A.P. Silva, "A Coupler with Losses in Millimeter Waves", 1997 SBMO/IEEE MTT-S International Microwave and Optoelectronics Conference, Natal, Brazil, pp. 59-64, Aug. (1997).

# A New Method of Circular Groove Guide Analysis

Hong-hui Yan, Guo-qin Huang, Hong-sheng Yang

Dept. of Electronic Engineering  
National Key Laboratory of Millimeter Waves  
Southeast University, Nanjing, 210096, P. R. China

**Abstract** — Using the Fourier transform and the mode matching technique, the circular groove guide is analyzed. While deriving a series of simultaneous equations basing on boundary conditions, we get the characteristic equation of this guide structure that is strict than those before.

## I. INTRODUCTION

Comparing with those traditional guides, the circular groove guide has many attractive advantages [1], such as large power capacity, low loss, large scale, wide bandwidth and so on. Although this guide structure has studied for long time, it is also necessary to derive the exact characteristic equation. In this paper, we distinguish the cross section in new way. Using the Fourier transform and the mode matching technique gets the characteristic equation [4]. The comparison with those characteristic equations in [1][2][3] is given in section III.

## II. ANALYSIS

The geometry of circular groove guide is shown as Fig. 1. The inner radius of region (I),(III) is  $a$ . And  $a \cos(\phi_0) = c$

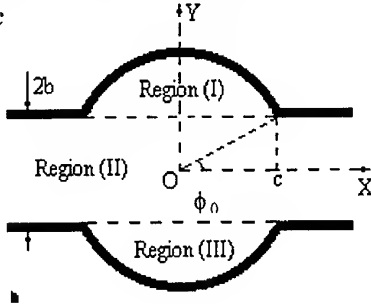


Fig.1 The geometry of circular groove guide  
The time factor and the z-direction propagating wavenumber are  $e^{j\omega t}$  and  $e^{-j\beta z}$ , respectively.

At first, we consider the TM mode case. In region (I), (II) and (III), the field can be expressed as:

$$E_z^I = \sum_{m=0}^{\infty} P_m \left[ -\frac{N_m(Ta)}{J_m(Ta)} J_m(Tr) + N_m(Tr) \right] \cdot \sin(m\phi + \varphi) \quad (1)$$

$$E_z^{II} = \frac{1}{2\pi} \int_{-\infty}^{\infty} (\tilde{E}_z^+ e^{jy\xi} + \tilde{E}_z^- e^{-jy\xi}) e^{-jx\zeta} d\zeta \quad (2)$$

$$E_z^{III} = \sum_{m=0}^{\infty} Q_m \left[ -\frac{N_m(Ta)}{J_m(Ta)} J_m(Tr) + N_m(Tr) \right] \cdot \sin(m\phi + \varphi) \quad (3)$$

$$T^2 + \beta^2 = K^2 = \zeta^2 + \xi^2 + \beta^2 \quad (4)$$

Where  $K$  is free space wavenumber,  $\zeta$  and  $\xi$  are wavenumbers of x direction and y direction in region (II) respectively.  $\varphi$  is the polarization direction.

At the boundary between region (I) and (II), we have

$$E_z^{II} = \begin{cases} E_z^I & |x| < c \\ 0 & |x| > c \end{cases} \quad (5)$$

Substitution of (1) and (2) into (5) yields

$$\begin{aligned} & \frac{1}{2\pi} \int_{-\infty}^{\infty} (\tilde{E}_z^+ e^{jy\xi} + \tilde{E}_z^- e^{-jy\xi}) e^{-jx\zeta} d\zeta \\ &= \begin{cases} \sum_{m=0}^{\infty} P_m \left[ -\frac{N_m(Ta)}{J_m(Ta)} J_m(Tr) + N_m(Tr) \right] \sin(m\phi + \varphi) & |x| < c \\ 0 & |x| > c \end{cases} \end{aligned}$$

Taking the Fourier transform of the above expression,

$$\begin{aligned} & \tilde{E}_z^+ e^{jy\xi} + \tilde{E}_z^- e^{-jy\xi} \\ &= \sum_{m=0}^{\infty} P_m \int_{-\phi_0}^{\phi_0} e^{jbc \tan(\phi) \zeta} \frac{-b}{\sin^2 \phi} \sin(m\phi + \varphi) \\ & \quad \cdot \left[ -\frac{N_m(Ta)}{J_m(Ta)} J_m\left(T \frac{b}{\sin \phi}\right) + N_m\left(T \frac{b}{\sin \phi}\right) \right] d\phi \\ &= \sum_{m=0}^{\infty} P_m F_m \quad (6) \end{aligned}$$

The condition  $H_x^{II} = H_x^I$  at the same boundary gives

$$\begin{aligned} & \frac{1}{2\pi} \int_{-\infty}^{\infty} (\tilde{E}_z^+ e^{jy\xi} - \tilde{E}_z^- e^{-jy\xi}) j\xi e^{-jbc \tan(\phi) \zeta} d\zeta \\ &= \sum_{m=0}^{\infty} P_m \left( \frac{\cos \phi \sin \phi}{b} \left[ -\frac{N_m(Ta)}{J_m(Ta)} J_m\left(T \frac{b}{\sin \phi}\right) + N_m\left(T \frac{b}{\sin \phi}\right) \right] \right. \\ & \quad \cdot \cos(m\phi + \varphi) \cdot m + \sin \phi \cdot \sin(m\phi + \varphi) \\ & \quad \cdot \left. \left[ -\frac{N_m(Ta)}{J_m(Ta)} J_m\left(T \frac{b}{\sin \phi}\right) \cdot T + N_m\left(T \frac{b}{\sin \phi}\right) \cdot T \right] \right) \end{aligned}$$

$$= \sum_{m=0}^{\infty} P_m G_m \quad (7)$$

In the same way, the expressions on the boundary between region (II) and (III) are derived:

$$\tilde{E}_z^+ e^{-jb\xi} + \tilde{E}_z^- e^{jb\xi} = \sum_{m=0}^{\infty} Q_m S_m \quad (8)$$

$$\begin{aligned} & \frac{1}{2\pi} \int_{-\infty}^{\infty} (\tilde{E}_z^+ e^{-jb\xi} - \tilde{E}_z^- e^{jb\xi}) j\xi e^{jbctg(\phi)\zeta} d\zeta \\ &= \sum_{m=0}^{\infty} Q_m H_m \end{aligned} \quad (9)$$

Where

$$S_m = \int_{\pi+\phi_0}^{\phi_0} e^{-jbctg(\phi)\zeta} \left[ -\frac{N_m(Ta)}{J_m(Ta)} J_m\left(T\frac{-b}{\sin\phi}\right) + N_m\left(T\frac{-b}{\sin\phi}\right) \right] \cdot \sin(m\phi + \varphi) \frac{b}{\sin^2\phi} d\phi \quad (10)$$

$$\begin{aligned} H_m &= \frac{\cos\phi \sin\phi}{-b} \left[ -\frac{N_m(Ta)}{J_m(Ta)} J_m\left(T\frac{-b}{\sin\phi}\right) + N_m\left(T\frac{-b}{\sin\phi}\right) \right] \\ &\cdot \cos(m\phi + \varphi) \cdot m + \sin\phi \cdot \sin(m\phi + \varphi) \\ &\cdot \left[ -\frac{N_m(Ta)}{J_m(Ta)} J_m\left(T\frac{-b}{\sin\phi}\right) \cdot T + N_m\left(T\frac{-b}{\sin\phi}\right) \cdot T \right] \end{aligned} \quad (11)$$

Eliminating  $\tilde{E}_z^+$  and  $\tilde{E}_z^-$  from (6), (7), (8) and (9), we get:

$$\begin{aligned} & \frac{1}{2\pi} \int_{-\infty}^{\infty} \xi (ctg(2b\xi) \sum_{m=0}^{\infty} P_m F_m - \frac{1}{\sin(2b\xi)} \sum_{m=0}^{\infty} Q_m S_m) e^{-jbctg(\phi)\zeta} d\zeta \\ &= \sum_{m=0}^{\infty} P_m G_m \end{aligned} \quad (12)$$

$$\begin{aligned} & \frac{1}{2\pi} \int_{-\infty}^{\infty} \xi \left( \frac{1}{\sin(2b\xi)} \sum_{m=0}^{\infty} P_m F_m - ctg(2b\xi) \sum_{m=0}^{\infty} Q_m S_m \right) e^{jbctg(\phi)\zeta} d\zeta \\ &= \sum_{m=0}^{\infty} Q_m H_m \end{aligned} \quad (13)$$

Multiplying (12) by  $G_n$  and integrating from  $(\pi - \phi_0)$  to  $\phi_0$ , multiplying (13) by  $H_n$  and integrating from  $(-\pi + \phi_0)$  to  $-\phi_0$ , respectively, we obtain:

$$\begin{pmatrix} A_{mn} - B_{mn} & D_{mn} \\ I_{mn} & -E_{mn} - L_{mn} \end{pmatrix} \begin{pmatrix} P_m \\ Q_m \end{pmatrix} = 0 \quad (14)$$

Where

$$A_{mn} = \int_{\pi-\phi_0}^{\phi_0} G_m \cdot G_n \cdot d\phi \quad (15)$$

$$\int_{\pi-\phi_0}^{\phi_0} \frac{1}{2\pi} \int_{-\infty}^{\infty} \xi ctg(2b\xi) F_m G_n e^{-jbctg(\phi)\zeta} d\zeta d\phi = B_{mn} \quad (16)$$

$$\int_{\pi-\phi_0}^{\phi_0} \frac{1}{2\pi} \int_{-\infty}^{\infty} \xi \frac{1}{\sin(2b\xi)} S_m G_n e^{-jbctg(\phi)\zeta} d\zeta d\phi = D_{mn} \quad (17)$$

$$E_{mn} = \int_{\pi+\phi_0}^{\phi_0} H_m \cdot H_n \cdot d\phi \quad (18)$$

$$\begin{aligned} & \int_{\pi+\phi_0}^{\phi_0} \frac{1}{2\pi} \int_{-\infty}^{\infty} \xi \frac{1}{\sin(2b\xi)} F_m H_n e^{jbctg(\phi)\zeta} d\zeta d\phi \\ &= I_{mn} \end{aligned} \quad (19)$$

$$\begin{aligned} & \int_{\pi+\phi_0}^{\phi_0} \frac{1}{2\pi} \int_{-\infty}^{\infty} \xi ctg(2b\xi) S_m H_n e^{jbctg(\phi)\zeta} d\zeta d\phi \\ &= L_{mn} \end{aligned} \quad (20)$$

The requirement that the determinant be zero gives:

$$\begin{vmatrix} A_{mn} - B_{mn} & D_{mn} \\ I_{mn} & -E_{mn} - L_{mn} \end{vmatrix} = 0 \quad (21)$$

The characteristic equation is obtained by substituting (15), (16), (17), (18), (19) and (20) into (21).

In the same way, we can obtain the characteristic equation of TE mode by assuming  $E_z = 0$  and  $H_z \neq 0$

### III. CONCLUSION

Basing on the Fourier transform and mode matching method, we derive the characteristic equation of circular groove guide. The proceeding is easy to understand and exact than before. For example, in paper [1], it assumes that  $c \approx a$  when deal with the boundary condition between region (A) and (B); in paper [2], it only deals with the dominant mode properties; in paper [3], it only considers the first-order field component expressions of TE and TM modes, so the characteristic equation is also approximate. However, in this paper, we did not make any assumptions and the characteristic equation is strict.

### IV. REFERENCES

- [1] H. S. Yang, J. L. Ma, and Z. Z. Lu, IEEE trans. on MTT vol.43, No.2, pp755-764, 1995
- [2] J. L. Ma, H. S. Yang, and Z. Z. Lu, Journal of Southeast University, vol.25, No.3, pp30-33, 1995
- [3] H. S. Yang, J. L. Ma, and Z. Z. Lu, 2<sup>nd</sup> international symposium on recent advances in microwave technology, pp.239-240, 1989
- [4] B. T. Lee, J. W. lee, H. J. Eom, and S. Y. Shin, IEEE trans. on MTT vol.43, No.9, pp2162-2165, 1995

## Calculation of Eigenmode Mixtures in Oversized Corrugated Rectangular Waveguides

D. Wagner,<sup>1</sup> M. Thumm,<sup>2</sup> W. Kasperek<sup>1</sup>

<sup>1</sup>Universität Stuttgart, Institut für Plasmaforschung, Pfaffenwaldring 31, D-70569 Stuttgart, Germany

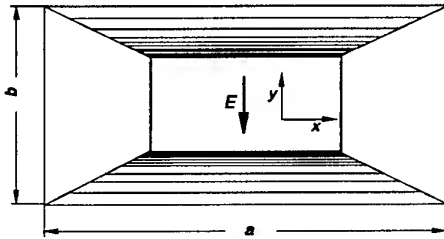
<sup>2</sup>Forschungszentrum Karlsruhe, Institut für Technische Physik and, Universität Karlsruhe, Institut für Höchstfrequenztechnik und Elektronik, P.O.Box 3640, D-76021 Karlsruhe, Germany

### 1. Introduction

Oversized circular corrugated waveguides propagating the hybrid  $HE_{11}$  mode are widely used for high power microwave transmission. In waveguides with rectangular cross section corrugated walls with a groove depth close to  $\lambda/4$  similarly lead to a drastic reduction of the ohmic losses due to the almost vanishing tangential magnetic fields at the waveguide walls. Radiated from the open-ended waveguide these hybrid eigenmodes exhibit desirable radiation characteristics such as low sidelobes and cross polarization. Compared to overmoded corrugated circular waveguides the rectangular cross section offers additionally useful optical effects which were explored most recently for high-power resonators [1] and waveguide antennas [2]. The eigenmodes of such waveguides were derived on the assumption of an anisotropic longitudinal wall impedance caused by the corrugations [3,4]. However this method has some limits since the exact geometry of the grooves cannot be taken into account. Hybrid  $HE_{mn}$  eigenmodes of the corrugated rectangular waveguide with both  $E_z$  and  $H_z$  components can be represented as a superposition of  $TE_{mn}$  and  $TM_{mn}$  eigenmodes of the smooth wall waveguide. Since any corrugation geometry can be modelled by steps in smooth wall waveguides (staircase representation) the scattering matrix formalism can be used in order to analyse such hybrid eigenmode mixtures.

### 2. Calculation Method

The waveguide geometry is shown in Fig.1, where the top and bottom walls are transversely corrugated and the sidewalls are smooth. Assuming a symmetric corrugation, an incident  $TE_{10}$  fundamental mode can only couple to pairs of  $TE_{1n}/TM_{1n}$  modes, where  $n$  is an odd number. Therefore only these modes have to be taken into account.



Each step in a waveguide can be represented by a scattering matrix taking into account all propagating and additional evanescent modes coupling to the incident mode [5]. The simplest rectangular corrugation profile can be divided into two waveguide steps. Cascading the scattering matrices of the two steps gives the overall scattering matrix of the groove ( $S_0$ ). In order to find the eigenmodes one has to solve the eigenvalue problem:

$$S_{012} \cdot A = \Lambda \cdot A \quad (1)$$

Fig.1 Corrugated rectangular waveguide

where  $A$  is the complex modal amplitude vector of the input wave,  $S_{012}$  is the forward overall transmission matrix and  $\Lambda$  is the eigenvalue. After solving the eigenvalue problem (1) the superposition of the modal fields of the  $TE_{1n}/TM_{1n}$  eigenmode mixture gives the field distribution of the hybrid  $HE_{1n}$  eigenmodes. The longitudinal wavenumber  $k_z$  and therefore the normalized eigenvalue  $n$ , corresponding to the second index of the hybrid mode  $HE_{1n}$ , can then be numerically deduced from the phase variation of the  $E_z$  and  $H_z$  components in longitudinal direction:

$$n = \sqrt{k_0^2 - k_z^2 - \left(\frac{\pi}{a}\right)^2} \cdot \frac{b}{\pi} \quad (2)$$

The losses per unit length are calculated by numerically integrating the tangential magnetic field over the waveguide walls:

$$P_L = \frac{R_s}{2p} \cdot \iint_{S_0} (|H_x|^2 + |H_y|^2 + |H_z|^2) \cdot ds \quad (3)$$

where  $R_s$  is the surface resistance of the waveguide wall,  $p$  is the corrugation period and  $S_0$  is the inner surface of one corrugation period.

### 3. Computational Results

For the calculations an oversized waveguide with  $a/b=2$  and  $k_0 \cdot b=42.7$  (where  $k_0=2\pi/\lambda$  is the vacuum wavenumber,  $a$  and  $b$  are the waveguide width and height respectively) has been chosen. The corrugation profile is rectangular with  $p=\lambda/3$  and  $w/p=2/3$ , where  $p$  is the corrugation period and  $w$  is the groove width. In Fig.2 the computed eigenmode mixture of the lowest order hybrid mode  $HE_{11}$  is plotted as a function of groove depth  $d$ . Fig.3 shows the field distribution of the  $HE_{11}$  mode for  $d=0.2\lambda$  which is the optimum depth for the corrugations chosen. The eigenvalues of several hybrid  $HE_{1n}$  modes as a function of the groove depth  $d$  are shown in Fig.4. The attenuation of the  $HE_{11}$  mode as a function of the groove depth  $d$  is plotted in Fig.5.

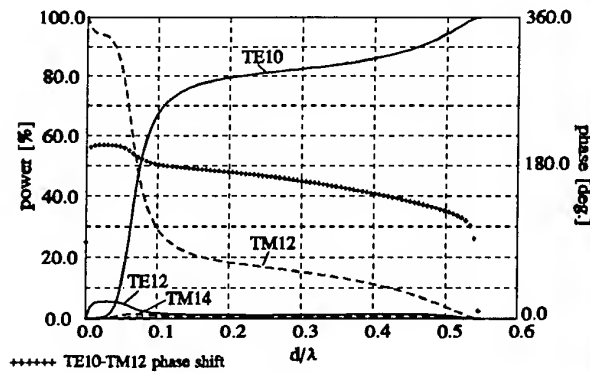


Fig.2 Calculated eigenmode mixture of the  $HE_{11}$  mode

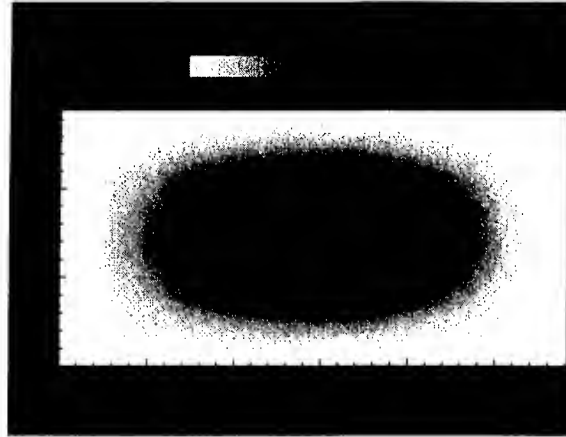


Fig.3 Calculated z-component of the Poynting vector of the  $HE_{11}$  mode over the waveguide cross section

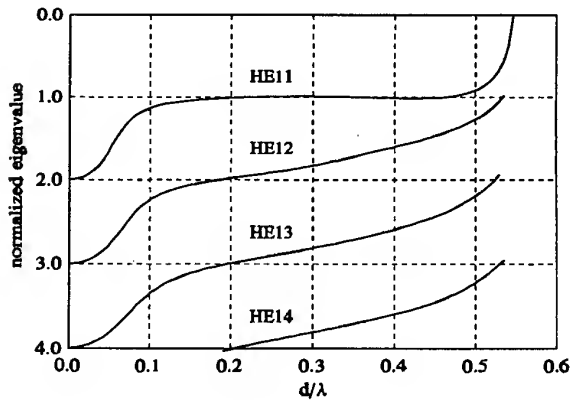


Fig.4 Calculated normalized eigenvalues of  $HE_{1n}$  modes

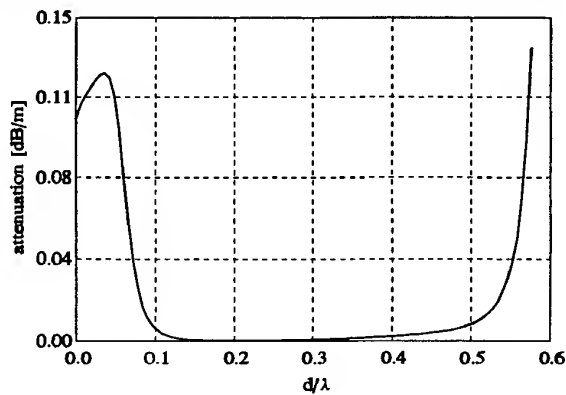


Fig.5 Calculated attenuation of the  $HE_{11}$  mode

### 4. Conclusions

$HE_{1n}$  eigenmodes of corrugated rectangular waveguides are described in terms of  $TE_{1n}/TM_{1n}$  modes using the scattering matrix formalism. By this method all geometrical parameters are taken into account. Therefore the results differ slightly from those obtained with the surface impedance model. The method holds also for higher order hybrid modes and corrugation geometries different from the ideal rectangular one (e.g. sinusoidal corrugations).

### 5. References

- [1] A.G.A.Verhoeven et al., Conf. Digest, 18th Int. Conf. on Infrared and Millimeter Waves, Colchester (UK), 1993, 19.
- [2] A.Chirkov et al., this conference.
- [3] P.J.B.Clarricoats, A.D.Oliver, Corrugated Horns for Microwave Antennas, London: Peter Peregrinus Ltd., 1984.
- [4] J.L.Doane, Int. J. of Infrared and Millimeter Waves, 8, 13-27, 1987
- [5] D.Wagner et al., Proc. EC-8, 8th Joint Workshop on ECE and ECRH, 1992, 575-581.

# A Small-sized Compound Antenna for the Auto-identification of Dual-Polarization Waves

Wu Qun

Dept. of Radio Engineering, Harbin Institute of Technology, PRC

Gun-Sik Park

Physics Education Department, Seoul National University, Korea

**Abstract** A novel antenna for dual-polarization reception based on individual operating principle of Cassegrain and parabolic antennas is investigated. By using front and back feed groups which are perpendicular to each other for the E-field polarization, and metallic gratings, which act as a polarization selector, simultaneous reception or transmission for two kinds of linearly-polarized waves which are mutually orthogonal has been realized. In this paper, experimental and measured results are given.

**Keywords:** dual-polarization; Cassegrain antenna; parabolic antenna; polarizer

**1. Introduction** For the applications of millimeter and microwave to radar for traffic control or target tracking, automatic identification for two kinds of linearly-polarized electromagnetic wave which are perpendicular to each other are needed during the signal reception or transmission simultaneously. To do so, traditionally, two sets of antennas either Cassegrain or parabolic reflector types are used so that different linear polarization can be separated. In some occasions, compact structure is seriously confined for system applications. In this paper, a newly-developed compact compound antenna system is presented. It consists of front feed, back feed, a paraboloidal reflector and a secondary reflector(hyperboloidal shaped polarizer).when the two groups of feeds are fixed in a form of perpendicular to their polarization vectors each other in a Cassegrain antenna system, and the polarizer is determined in term of required polarization selection.

**2. Design considerations** To realize required functions by using a sets of antenna system, basically, there are two considerations: one is system structure, as shown in Fig.1. Two feed clusters come face to face with each other in cross apertures. Front feed is located at the focus of main reflector .the another is polarizer, or metallic gratings form, as shown in Fig.2. The subreflector consists of a horizontal gratings which reflects an incident horizontally polarized wave from the back feed to the paraboloid, while the vertically polarized wave from front feed passes through the subreflector essentially unaffected. To ensure antenna system's performance, the gratings play an important role in the system. The outmost surface of the subreflector faced to the main reflector outlined a curve surface, which is approximately a perfect reflected hyperboloid to the wave from back feed. In addition, it needs to but only provide good isolation between two types of linear polarization waves, but also reduce diffraction effect as much as possible by optimum design of gratings sizes. We may consider this antenna system to be an integration of both Cassegrain and paraboloid antennas. Both two feed clusters are conducted to the back of the main reflector by waveguide feed for signal processing by using a hybrid connector(magic T). As shown in Fig.1, both of the feeds are E-plane sectoral horns. Since the front feed is horizontal polarized source, the main

reflector and front feed are composed of a paraboloid antenna because of being essentially invisible to perpendicular polarization. The gratings are designed based on parallel-plate polarizer theory[1][2][3]. For paraboloid antenna application in this system,  $F/D=0.4$  is selected. Analysis approaches of the Cassegrain and paraboloid reflector antenna theory are given by Ref.[4].

**3.Measured results** For paraboloid antenna channel, as a typical example, radiation pattern is shown in Fig.3. In Fig.3, the radiation pattern is drawn in terms of the relationship of normalized radiation intensity  $E/E_{\max}$  vs. degrees, which shows that the tendency is in good agreement with the design prediction even the introduction of a polarizer. A gain of 20 dB is obtained. The main lobe width is  $2\theta_{0.5} = 7.5 \pm 0.5^\circ$  and the sidelobe level is -16dB. For Cassegrain antennas channel, a gain of 22dB is obtained. The main lobe width is  $2\theta_{0.5} = 7.2 \pm 0.5^\circ$  and sidelobe level is -15dB. Measured result of polarization isolation of the gratings for two orthogonal linearly-polarized waves shows that can reach as high as 40dB and more.

**4. Conclusion** In our research, it has been well proved that this antenna can receive or transmit two linearly-polarized waves simultaneously for the orthogonal linear polarization. The validity and the applicability of the grating type for dual-polarization identification are examined. This combination of Cassegrain and paraboloid antennas provides a compact structure and realistic polarization-selection applications for the front end of radar or traffic control, satellite tracking, direction-finding system and other purposes in a system application at microwave or millimeter wave bands.

## References

- [1] Richard C.Johnson, Henry Jasik, Antenna Engineering Handbook, McGraw-Hill Book Company, 1993.
- [2] Zhang Deqi, Principle of Microwave Antennas. Beijing Institute of Technology Press, 1985.
- [3] Wang Huzhuang, Wu jian and Xie Yinfang, "Mono-aperture Compound Antenna Adapted for Object Surveying with Various Polarizations," Journal of Zhejiang University, vol. 27, no. 4, pp. 438-445, July. 1993.(in Chinese)
- [4] A.W.Love, Reflector Antennas, IEEE Press, 1978.

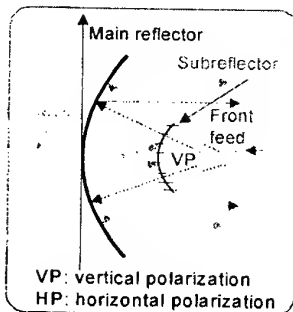


Fig.1. Illustration of the Antenna structure

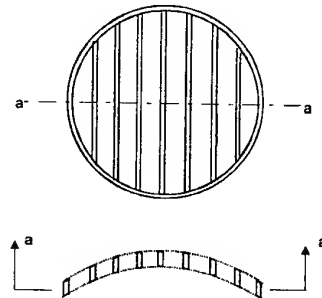


Fig.2. Schematic view of the subreflector

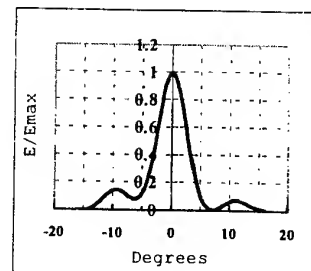


Fig.3. Radiation pattern of paraboloid antenna channel



# AN EDUCATIONAL PROGRAM FOR RESULTS IN 3D ON FINLINE COUPLER

Humberto César Chaves Fernandes, Luiz Carlos de Freitas Júnior  
and Sidney Alexandre Pinto Silva

Department of Electrical Engineering - Technological Center  
Federal University of Rio Grande do Norte - P.O Box 1583  
Tel/Fax: +55 84 2153731 , E-mail: humbecf@ct.ufrn.br  
59.072-970 - Natal - RN - Brazil

**Abstract:** Computer programs are developed in FORTRAN 77 and MATLAB for WINDOWS languages, given the results in 3-D of the dispersion and of the coupling, as functions of the frequency, conductivity and permittivity for the unilateral finline coupler asymmetric in E-plane, on semiconductor substrate. The characteristic impedance and complex propagation constant, for the odd and even-modes excitation are obtained by Transverse Transmission Line (TTL) method. These programs are easily used in graduate and undergraduate courses with good efficiency, and the results are very good.

## 1. INTRODUCTION AND DEVELOPMENT

In this work are used computer programs to obtain the main characteristics parameters of structures with the finline and was developed supported in the theory enveloped in designers these structures.

The structure is basically a slotline inserted in the E-plane of a rectangular waveguide, shown in Fig. 1. This report pertains to application of computer programs in design of directional coupler, most particularly the *Parallel-Coupled Fin-Line Coupler* shown in the Fig 2. This type of coupler offers forward wave coupling, i. e., if a signal is fed to port 1, port 3 is the coupled port and port 4 is the isolated port.

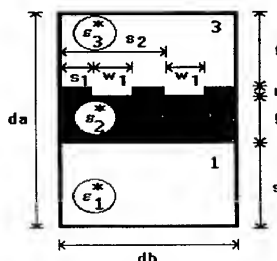


Fig. 1 - Cross section of arbitrary unilateral coupled slots.

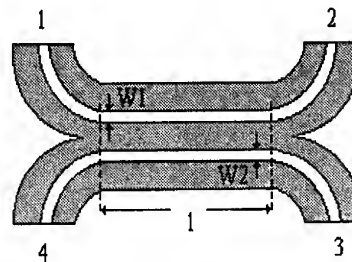


Fig. 2 - Top and internal view of the finline with unilateral fin-line coupler.

In the direct and concise TTL method, the Maxwell's equations in Fourier transform domain, are firstly used to obtain the electromagnetic fields in terms of the transversal electromagnetic fields [1]. By applying the boundary conditions, the fields in all dielectric regions are determined as functions of the electric fields in the slots.

An inhomogeneous equation system is obtained, in which the current densities in the fins are related to the electric fields in the slots. By expanding these fields in terms of suitable basis functions and using the moment method and the Parseval's theorem, the current densities are eliminated, and an homogeneous equation system is obtained with two variables.

The complex propagation constant is obtained by setting the determinant of the system matrix equal to zero. The effective dielectric constant is determined by means of the relation between the phase constant and the wave number of the free space.

## 2. THEORY

For the unilateral fin-line with two coupled slots in the Fig 1, when used to be a parallel coupled fin-line coupler, the results obtained for even and odd modes of the phase constant using this TTL method, are used to given the coupling length  $L$  [2], where a complete transfer of power from port 1 to port 3 is present:

$$L = \pi / (\beta_{\text{even}} - \beta_{\text{odd}}) \quad (1)$$

The amplitude of the coupling coefficient between ports 1 and 3 is:

$$|S_{13}| = \sin(\pi l / 2L) \quad (2)$$

where the length of the coupling region  $l$ , for any  $L$  can be calculated by using (2).

The expression for the coupling is defined as:

$$C_3 = 20 \cdot \log \left( \frac{1}{|S_{13}|} \right) \quad (3)$$

### 3. RESULTS

Computer programs were developed to given the numerical results of the planar structures analyzed.

In Fig. 3a, curves of the characteristic impedances of the unilateral finline are showed. The structure is a WR-28,  $d_a = 7.112$  mm and  $d_b = 3.556$  mm,  $g = 0.254$  mm,  $s = 3.302$  mm,  $x_1 = 0.789$  mm,  $x_2 = 2.567$  mm,  $w_1 = w_2 = 0.2$  mm. Was considered a dielectric substrate with relative permittivity  $\epsilon_{r2} = 2.22$  and values of  $\sigma_2$  between 0 S/m and 1 S/m. The range of frequency is 25 GHz until 40 GHz. Results of the coupling in the port 3 as functions of the frequency and  $L = 0.5$  mm are shown in Fig 3b.

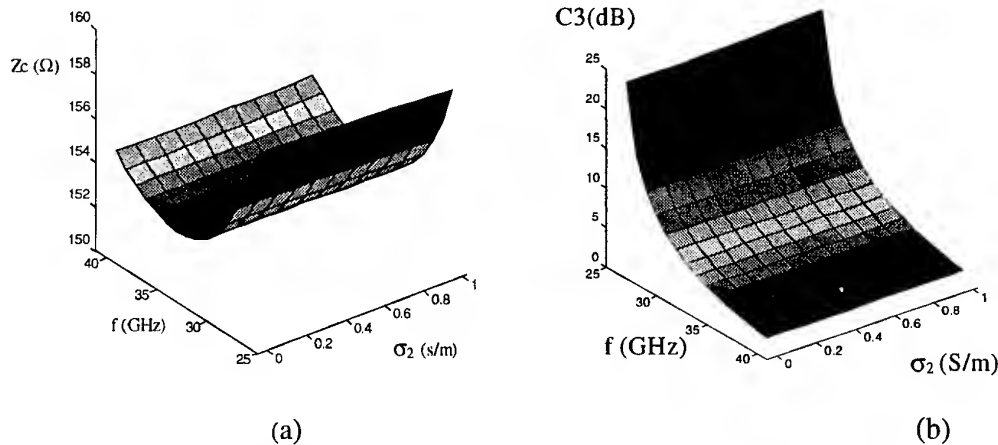


Fig. 3 - Characteristic impedance  $Z_{c1} = Z_{c2} = Z_c$  of the coupled unilateral finline for odd mode in (a) and coupling as functions of the frequency and conductivity in (b).

### 4. CONCLUSIONS

Computer programs, with good appeal, are developed for to be used in graduate and under graduate courses. The theory and numerical results were presented to the unilateral fin lines and coupler with semiconductor substrate. The full wave analysis of the Transverse Transmission Line method - TTL in the FTD was used in determination of the electric and magnetic fields in all dielectric regions. Good results were presented and compared with that of the literature [3]. This work was supported by CNPq and CAPES.

### REFERENCES

1. H. C. C. Fernandes, "Attenuation And Propagation In Various Fin-line Structures", International Journal of Infrared and Millimeter Waves, Vol. 17, N° 08, 12 pp., Aug. (1996).
2. B. Bhat, S. K. Koul, "Analysis, design and applications of fin lines", Artech House, Norwood, MA (1987).
3. D. Mirshekar-Syahkal and J. B. Davies, "An Accurate , Unified Solution to Various Fin Lines Structures of Phase Constant, Characteristic Impedance and Attenuation ", IEEE Trans. on MTT-30, pp. 1854-1861 , Nov. (1982).

## The high quality mirrors for microwave range.

Vladimir Parshin

Applied Physics Institute of RAS, 46 Ulyanov Street, Nizhny Novgorod, 603600, Russia.

Fax: 007 8312 362061; E-mail: parsh@appl.sci-nnov.ru

### Abstract

The results of reflection losses measurements from the mirrors coated by thin layer of - Ag, Cu, Au, and Al are presented.

At the frequency range 70 - 200 GHz the losses are only 15% - 20% higher than calculated ones coming from the DC conductivity.

### Introduction

The present work is the compound of the work on the installation creation for the measurement of extremely small absorption in dielectrics (like diamond [1]) at MM and SubMM ranges of wavelengths.

The key part of this installation is the high Q-factor Fabry-Perot resonator. The absorption sensitivity of installation directly depends on its quality. That's why the special attention was devoted to the resonator mirrors. Some of technologies for the production of mirrors were tested with the purpose of getting the mirror with the min. possible reflection losses (with the max. reflectivity). The most "reflective" metals such as Ag, Cu, Au and Al were tested. Certainly, the silver coating mirror was found to be the optimal one[2].

### Mirrors

The most reliable and at the same time comparatively not expensive way of production mirrors was the following one: The Silver layer with the thickness of  $\sim 0.0005$  mm was put on the spherical optically polished glass and brass mirrors (This thickness is approximately equal to the skin-layer at the lowest frequency of the range of measurements.) To prevent an oxidation of the Silver it was coated by Aluminium with the thickness  $\sim 10^{-5}$  mm. The coatings were produced during one pumping cycle by means of vacuum vaporisation in a special chamber evacuated down to the pressure  $\sim 10^{-7}$ .

On the open air the Aluminium film transforms into Aluminium Oxide ( $\text{Al}_2\text{O}_3$ ), which protects well the Silver coating against the oxidation. At the same time the film of  $\text{Al}_2\text{O}_3$  doesn't introduce the additional losses because of the negligible thickness (It was tested by special experiment).

The reflective coefficients of such coatings practically coincide both with glass and brass mirrors.

### Resonator

Parameters of resonator			
Frequency of measurement	GHz	78	195
Resonance curve width	kHz	133	348
Q-factor of resonator	$[10^3]$	586	560
Resonator length	mm	385	390
Mirror radius	mm	240.450	
Mirror diameter	mm	120	
Refraction losses		$<10^{-5}$	
Coupling film thickness	mm	0.012	0.012
Calculated coupling losses		$21 \cdot 10^{-5}$	$125 \cdot 10^{-5}$
Atmospheric absorption		$1 \cdot 10^{-5}$	$26 \cdot 10^{-5}$
Experimental reflection losses		$85 \cdot 10^{-5}$	$135 \cdot 10^{-5}$
Calculated reflection losses		$73 \cdot 10^{-5}$	$117 \cdot 10^{-5}$
Experimental reflection coefficient R		0.9991	0.9986

For the reflection losses measurements the installation [3] based on the Fabry-Perot resonator was used. The resonator is connected with the microwave generator and the measuring tract by means of teflon film which is situated in the centre of resonator at the  $45^\circ$  angle. For the coupling losses calculation we used the value of the teflon refractive index = 1.414 (the film thickness = 12 micron).

We used an open, non vacuumed resonator, so for calculation of the atmosphere absorption the model [4] was used.

Full set of resonator parameters for the two frequencies is presented on the table.

### Result

The frequency dependence of reflection losses is presented on the Figure together with the theoretical (-) dependence for "thick" silver layer. (For its calculation we used silver conductivity =  $5.71 \cdot 10^{17} \text{ sec}^{-1}$  at  $20^\circ \text{ C}$ ).

There are three series of measurements presented which were made at the essentially different conditions of atmosphere absorption: at the humidity of 6%, 15%, and 40% (the dependencies 1,2,3, respectively). However, the scattering of the results from series to series does not exceed the average error of measurement. This fact confirms the accuracy of measurements and calculations. Nevertheless, we see the shift of the measured results

in comparison with the calculated ones. This practically constant shift in a wide frequency range needs a special consideration. I can only say that it may be connected with some calculation errors.

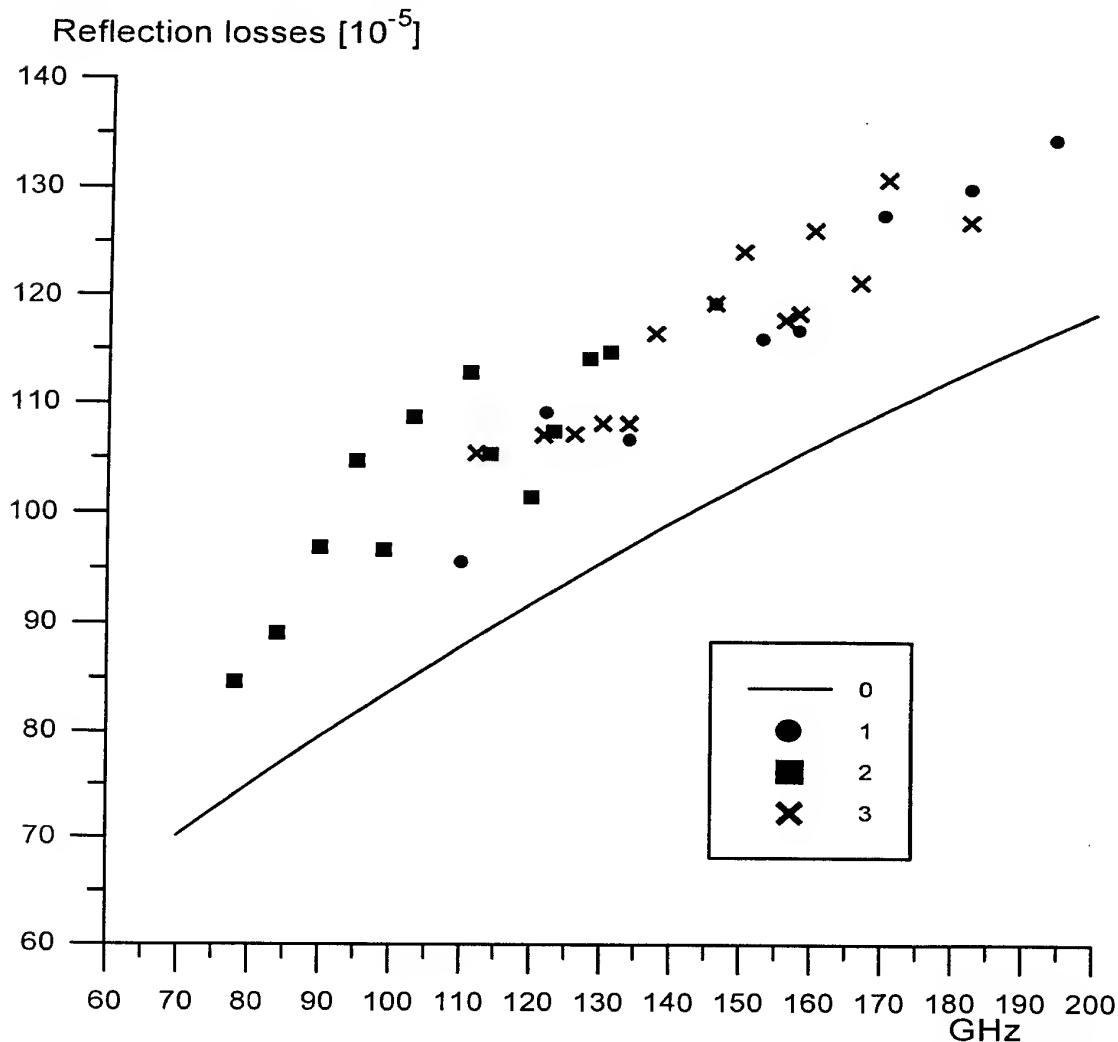


Figure. The measured reflection losses frequency dependencies for silver mirror are recalculated for 20°C and theoretical (0) curve.

### Conclusion

As a result of this work we got the mirrors with the reflection losses which are only 15% - 20% higher than the calculated ones coming from the DC conductivity. This result was obtained by using the most conductive metal (Ag), so I can say that we got the practical limit in reflectivity of the resonator mirrors at room temperatures.

The further progress in this field is possible with the cryogenically cooled mirrors or/and with the multilayer dielectric mirrors like those at an optical range. But all of these ways are rather expensive.

### Acknowledgement

Experiments described were supported partially by Russian State Program "Fundamental Physics of Microwaves".

The author expresses his deep gratitude to this source of support.

### References

1. V.V.Parshin, V.Ralchenko and V.Konov. Digest of this conference.
2. Yu.A.Dryagin, V.V.Parshin. Int. J. of IR & MM Waves. 1992, Vol. 13, N.7, pp.1023-1032.
3. A.F. Krupnov, V.V. Parshin at all. IEEE Trans. on MTT (Submitted No. M-5268)
4. Hans J.Liebe. Int. J. of IR & MM Waves. 1989, Vol. 10, N.2.

## COMPARATIVE ANALYSIS OF MM-WAVE VCO STRUCTURES

Eugene A. Machusky

Design Bureau "Storm"

National Technical University of Ukraine "Kyiv Polytechnical Institute",  
build-11, Politechnichna, 16, Kyiv, Ukraine, 252056  
tel/fax (044)-274-10-15, e-mail: pers@rtus.ntu-kpi.kiev.ua

At the present time there is no generalized analysis of different voltage controlled oscillators realizations. The task is complicated due to the very detailed equivalent circuits of such oscillators. At the same time some practical restrictions (especially large difference of real load and real active element resistance and large difference of active element impedance components) give the possibility of choosing optimal structure analytically.

The minimal set of voltage controlled oscillator (VCO) elements is an active diode, a varactor, a load, a matching inductance. The simplest representation of active diode is a serial connection of capacitance  $C_A$  and negative resistance  $R_A$ . Good quality varactor is simply capacitance  $C_V$ . Useful load is represented by resistance  $R_L$ . Matching inductance is  $L_M$ . The complete set of simplest VCO-structures is presented in Fig.1. Such realizations are possible in mm-wave band using discrete or monolithic technology.

Procedure of analysis is the following: establishing the balance equations  $R_Y = \Sigma R = 0$ ,  $X_Y = \Sigma X = 0$  and parameters  $V = X_V/X_A$  and  $Q_A = |X_A/R_A|$  on the central frequency  $\omega$  to estimate the varactor coupling factor  $p = (\delta X_V / \delta \omega) / (\delta X_Y / \delta \omega)$ , resistance transformation factor  $D = R_H / |R_A|$  and normalized matching inductance  $\bar{X}_L = |X_L|/|X_A|$ . The results are presented in Fig.1. Frequency tuning band is well estimated by  $\omega_{\max}/\omega_{\min} = (C_{V\max}/C_{V\min})^p$ .

Typically in mm-structures  $R_L \gg |R_A|$  therefore practically necessary condition is  $D \gg 1$ . From the view point of resistance matching the best structures are N 4, N5, N6, N7, because of  $Q_A \gg 1$ .

Structures N 1, N4, N6, N7 have better varactor coupling factor and corresponding frequency tuning band under condition  $V > 1$ , it means that average capacity of varactor must be less than capacity of active element at the central frequency. Opposite is true for structures N 2, N3, N5, N8.

Structures N1, N3, N8 give active resistance balance only if the load resistance is equal or less than negative active element resistance. This is unpracticed because real loads (transmitting lines, antennae) have wave resistance of tens - hundreds Ohm, but real active elements (IMPATT, TE-diodes) have few Ohm negative resistance especially at the maximum power point.

Structures N2, N6, N8 have very strong dependence of resistance transformation factor  $D$  on the varactor capacitance and corresponding  $V$  changing and the result is very large output power variation. Structure N4 has the same disadvantage with the low capacitance (or high  $V$ ) varactor. Variation of  $Q_A$  during the frequency tuning is less expressed because of little change of  $C_A$  and  $R_A$  that is the power variation in structures N5, N7 is small. Unpracticed structures N1, N3 and structure N8 (under  $V \gg 1$  condition) have no power variation.

At the millimeter wavelengths it is not simple to realize a very low meaning of matching inductance. Structures N1, N4, N6, N7 have more inductance and are preferable from this point of view.

Structure N5 has complicated practical realization because of necessity of close spacing of circuit elements and bias shunting by matching inductance without additional capacity element.

The best practical structure is N7: active element is shunt connected to the load line, varactor and active element are spaced by matching inductance.

Very close spacing of active element and varactor at millimeter wavelengths is often a difficult task. For reasonable matching the diode elements the spacing must be about half wavelengths at the central frequency. Such spacing leads to the crucial decreasing of varactor coupling factor to  $p = VQ_A/(VQ_A + \pi D)$ . Practical meanings of resistance transformation factors  $D$  are 20...100. Active element  $Q$  is 3...10. Typical  $V$  is 0.5...2.  $C_{V\max}/C_{V\min}$  is often about 3...10. Let us take  $Q_A = 5$ ,  $V = 1$ ;  $C_{V\max}/C_{V\min} = 5$ ,  $D = 50$ . Frequency tuning of lumped element structures does not exceed (with  $p = V/(2(V+1)) = 1/4$ );  $\omega_{\max}/\omega_{\min} = (C_{V\max}/C_{V\min})^p = 5^{1/4} \approx 1.5$ . Varactor coupling of half wavelength spaced structures is about  $VQ_A/(VQ_A + \pi D) \approx 1/32$  and corresponding frequency tuning is  $\omega_{\max}/\omega_{\min} = 5^{1/32} \approx 1.05$ .

Best realization examples in microstrip, fin-line, waveguide iris and quasi-optical techniques will be presented.

N 1		$p=0,5V/(V+1)$ $D=1$ $\bar{X}_L = V+1$	Poor resistance matching
N 2		$p=0,5/(V+1)$ $D=V^2$ $\bar{X}_L = V/(V+1)$	Large power variation, low inductance and poor resistance matching at reasonable varactor coupling
N 3		$p=0,5/(V+1)$ $D=1$ $\bar{X}_L = V/(V+1)$	Poor resistance matching and low inductance
N 4		$p=0,5V/(V+1)$ $D=Q_A^2(V+1)^2$ $\bar{X}_L = V+1$	Large power variation at reasonable varactor coupling
N 5		$p=0,5/(V+1)$ $D=Q_A^2$ $\bar{X}_L = V/(V+1)$	Complicated realization and low inductance
N 6		$p=0,5V/(V+1)$ $D=Q_A^2V^2$ $\bar{X}_L = V+1$	Large power variation
N 7		$p=0,5V/(V+1)$ $D=Q_A^2$ $\bar{X}_L = V+1$	Best practical structure
N 8		$p=0,5/(V+1)$ $D=V^2/(V+1)^2$ $\bar{X}_L = V/(V+1)$	Poor resistance matching, low inductance and large power variation

Fig. 1. Comparative structures parameters

## Modeling of microwave images of buried cylindrical objects

A. A. Vertiy <sup>(1),(2),(3)</sup>, S.P. Gavrilov <sup>(1),(2),(3)</sup>

1. TÜBITAK -M.R.C., Turkish- Ukrainian Joint Research Laboratory, P.K. 21, 41470, Gebze- Kocaeli, Turkey, phone: 90(262)6412300, e-mail: alex@mam.gov.tr
2. IRE, National Academy of Science of Ukraine, 12 Acad. Proskura St., Kharkov, Ukraine.
3. Concern "Nauka", State Research Center "Fonon", 37 Pobedy Ave., 252056, Kiev, Ukraine.

### Abstract

In this paper some results of electromagnetic simulation of microwave image of cylindrical dielectric objects embedded in lossy dielectric homogeneous half-space are given. For image reconstruction of objects, a plane wave spectrum of diffracted field is used.

A complex function of space coordinates representing the normalized polarization currents was reconstructed. A modulus of the complex function is the image of the object under investigation. The reconstruction algorithm is based on Fourier inverse formulas.

### 1. Introduction

This spectrum can be obtained from amplitude and phase measurements of back-scattered field in the case when the plane wave incidents on a lossy half-space containing the cylindrical object. We supposed that a part of the spectrum connected with plane inhomogeneous and surface ( lateral wave and evanescent wave ) waves propagating along a plane boundary of two dielectrics, may be measured by a diffraction grating placed closely to the boundary.

For direct problems the integral representation for diffracted fields was used. In the inverse a complex function of space coordinates representing the normalized polarization currents was reconstructed. A modulus of the complex function is the image of the object under investigation.

The reconstruction algorithm is based on Fourier inverse formulas [1]. Calculation was carried out in Born approximation for scattered field for electrodynamical parameters of mediums:  $\varepsilon_1(x, y) = 1.0$ ;  $\varepsilon_2(x, y) = 5.0$  and  $\varepsilon_3(x', y') = 4.0$ ;  $\mu_1 = \mu_2 = \mu_3 = 1.0$ ;  $\sigma_1 = \sigma_2 = \sigma_3 = 0$ , where  $\varepsilon, \mu$  are permittivity and magnetic permeability;  $\sigma$  is conductivity;  $x, y$  are coordinates; indexes 1; 2; 3 denote the number of medium: 1-for medium (air) with sources of the plane wave; 2-for medium containing the cylindrical object; 3-for the object, respectively. Within Born approximation, scattered field  $\psi(x', y') \equiv 0$  and expression for normalized polarization current  $K(x', y')$  reduces to

$$K(x', y') = \left[ \frac{k_3^2(x', y')}{k_2^2} - 1 \right] \quad (1)$$

with

$$k_j^2(x, y) = \omega^2 \varepsilon_j(x, y) \mu_0 + i \omega \mu_0 \sigma_j(x, y), j = 2, 3, \quad (2)$$

where  $\omega$  is frequency of electromagnetic fields;  $\varepsilon_j(x, y)$  is dielectric permittivity of the  $j$ -th medium;  $\sigma_j(x, y)$  is the conductivity of the  $j$ -th medium;  $\mu_0$  is the vacuum magnetic permeability, and does not depend on incident and diffracted fields. If the electrodynamical parameters of the object under investigation do not depend on coordinates  $x', y'$ , then according to expression (1) functions  $K(x', y')$  also does not depend on this coordinates.

Then the expression for Fourier-image of the scattered field  $\hat{\psi}(v, y_1)$  has the form [1] of

$$\hat{\psi}(v, y_1) = C(v, y_1) K \iint_S e^{-2i\pi(\alpha x' + \beta y')} dx' dy' \quad (3)$$

where  $K$  is value taking on a constant value in the region  $S$  according to (1), and which is equal to 0 out of the object region  $S$ ;  $\alpha = \alpha(v)$ ;  $\beta = \beta(v)$ . In the present paper the results are given to the region  $S$  of a rectangular form with borders along the  $X$  axis:  $x_1 = a$ ;  $x_2 = b$ ; ( $b > a$ ) and along the axis  $Y$ :  $y_1 = c$ ;  $y_2 = d$  ( $d > c$ ).

The object reconstruction is shown when the calculation of the diffracted field are performed at a fixed probing line  $y = y_1 = \text{const} < 0$  for incident plane wave with the frequency varying from  $\omega_i$  to  $\omega_f$  with a step of  $\Delta\omega \cong 0.125$  GHz. It was defined that the image of the reconstructed object may be obtained by using the evanescent spectrum only.

## 2. The object reconstruction

Fig.1 a), b) and c) show the reconstructed image of the rectangular cylinder with crosssection  $S = 0.11 \times 0.03 \text{ m}^2$  (rectangular contour) in the case when  $\varepsilon_1 = 1; \varepsilon_2 = 5; \varepsilon_3 = 4$  by using data collected at probing line  $y_1 = -0.035 \text{ m}$  in the frequency bands:  $\delta\omega_1 \cong 6.5 \div 4.5 \text{ GHz}$  (case a);  $\nu = -22 \div 22 \text{ m}^{-1}$ ,  $\delta\omega_2 \cong 12 \div 10 \text{ GHz}$  (case b);  $\nu = -33 \div 33 \text{ m}^{-1}$ ,  $\delta\omega_3 \cong 136.5 \div 134.5 \text{ GHz}$  (case c);  $\nu = -65 \div 65 \text{ m}^{-1}$ , where  $\nu$  is the space frequency of scattered field.

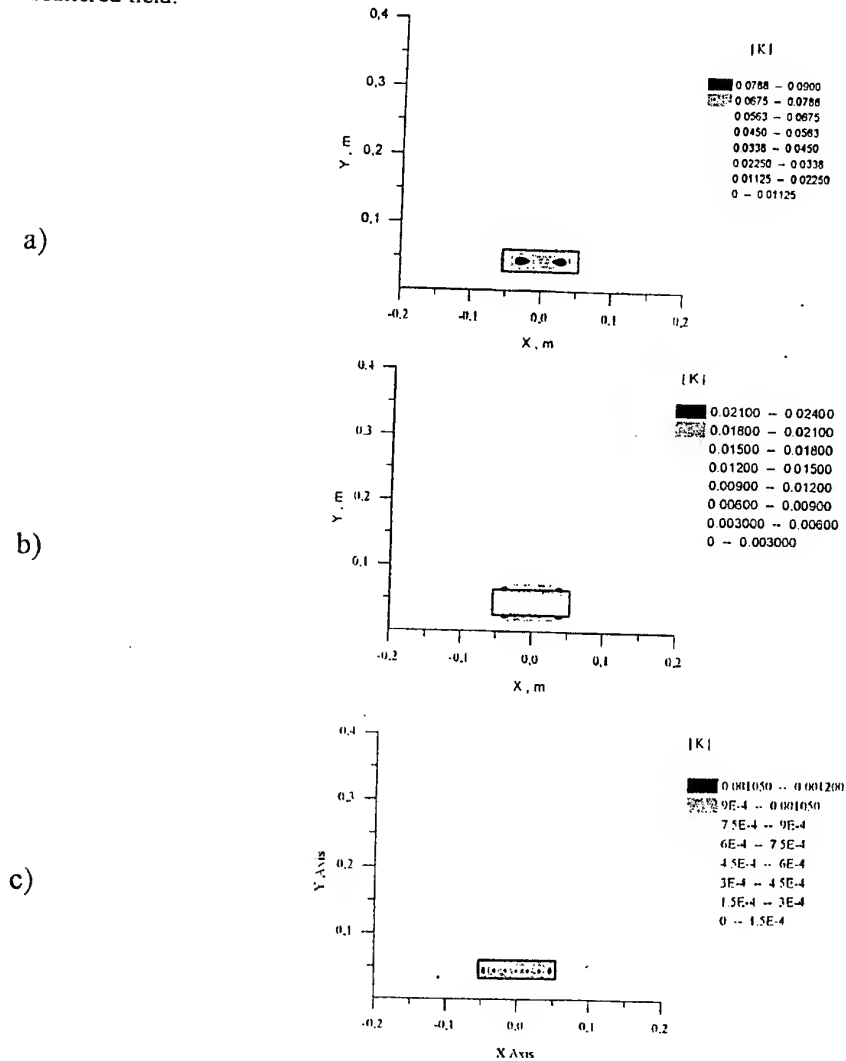


Fig. 1. Reconstructed images of the rectangular cylinder

## References

1. L. Chommeloux, Ch. Pichot, J.-Ch. Bolomey. Electromagnetic Modeling for Microwave Imaging of Cylindrical Buried Inhomogeneities.-IEEE Trans. Microwave Theory Tech., MTT-34,10, 1064-1075 (1986).



# DYNAMICS OF JOSEPHSON JUNCTION UNDER 'GREEN' NOISE

S. A. Guz, M. V. Sviridov

Department of Physics, Moscow Institute of Physics and Technology,  
Institutskiy per. 9, Dolgoprudny, Moscow region, 141700 Russia

The Fokker-Planck equation is mostly used to study thermal fluctuations in a Josephson junction [1]. However, this is impossible to apply when a power spectral density,  $S(\omega)$  of external stationary noise,  $N(t)$  fulfils condition  $S(0) = 0$ , and a diffusion coefficient  $D = 2\pi S(0)$  of this equation is equal to zero accordingly. Therefore, we use the Krylov-Bogoljubov averaging method to analyze the phase locking between the wave functions of Cooper pairs in the Josephson junction. Such a noise has been named "green" noise in [2]. The example of green noise has been presented in [3] where the Josephson junction has been considered as a microwave antenna of the black-body radiation passing through the lens. Then green noise can arise by reason of background illumination for example. In the high-frequency region  $\lambda \ll a$ , where  $\lambda$  is the wavelength of the radiation, the power spectrum of this noise is

$$S(\omega) \approx \eta^2 \left( \frac{2e}{\hbar} \right)^2 \frac{a^2}{l^2} \cdot \frac{1}{2\pi^4 c^2} \cdot \frac{\hbar \omega^3}{\exp(\hbar \omega / k_B T_b) - 1}, \quad (1)$$

where  $T_b$  is temperature of the background radiation,  $a$  is a radius of the lens,  $l$  is its focal length, being equal to a distance between the lens and the junction,  $\eta$  is the conversion factor of the radiation flow, passing through the Eyrie's disk  $\pi(\lambda l / 2a)^2$  in the focal plane of the lens, into the junction voltage. The value  $\eta$  can be estimated by the relation  $U = Ed$ , where  $U$  is a junction voltage,  $E$  is an electric field of radiation, and  $d$  is a typical size of input leads of the junction. Then we find  $\eta^2 \approx 2d^2 / \epsilon_0 c$ , where  $\epsilon_0$  is the vacuum dielectric constant. There is no effective penetration of the radiation the lens aperture if  $\lambda \gg a$ . Then the spectrum can be evaluated by the theory of the Rayleigh scattering:

$$S(\omega) \approx \frac{128\pi a^6 \omega^4 \eta^2}{9c^2 l^2} \cdot \frac{\hbar \omega}{\exp(\hbar \omega / k_B T_b) - 1}. \quad (2)$$

We use the equation of a resistively shunted Josephson junction model:

$$\mathcal{G} \frac{d^2 \varphi}{dt^2} + \frac{d\varphi}{dt} + \Omega_0 \sin \varphi = \Omega + N(t), \quad (3)$$

where  $\varphi$  is the phase difference between the wave functions of Cooper pairs,  $\mathcal{G} = RC$  is the relaxation time,  $R$  and  $C$  are the resistance and capacitance of the junction respectively,  $\Omega_0 = 2eI_0 R / \hbar$ ,  $I_0$  is the Josephson junction maximum (critical) current,  $\Omega = 2eIR / \hbar$ ,  $I = \text{const}$  is the direct current.

The averaging method requires that the evolution of the system under study include two different time scales. In our case the first scale is given by  $\Omega_0^{-1}$ . The order of magnitude of this value is  $10^{-12} \div 10^{-10}$  s, and it is farther considered as the "slow" time. The second "fast" time is given by the correlation time  $\tau_0$  of the noise  $\xi$  which is the solution of differential equation (3) at the linear case  $\Omega_0 = 0$  and  $\Omega = 0$  [2], i.e.  $\mathcal{G} d^2 \xi / dt^2 + d\xi / dt = N(t)$ . If the noise  $N$  has wide band enough, the time  $\tau_0$  has the same order with the relaxation time  $\mathcal{G}$  and may be less than  $10^{-13}$  s at the current technology. Therefore we suppose that a small parameter is  $\Omega_0 \tau_0 \ll 1$ . Then the well-known procedure of a two-time-scale averaging method [2] can be used. Using  $\tau_0$  as the time unit, we have  $\Omega_0 \ll 1$ , and write the solution of equation (3) by an asymptotic expansion:

$$\varphi(t) = \xi(t) + L\bar{x}(t, \Omega_0) + \Omega_0 Lu(t, \bar{x}) + O(\Omega_0^2), \quad (4)$$

where  $L = (\mathcal{G} d/dt + 1)^{-1}$  is the integral operator and  $x = L^{-1}(\varphi - \xi)$ .

In the first approximation of the averaging method we find

$$\mathcal{G} \frac{d^2}{dt^2} \langle \varphi \rangle + \frac{d}{dt} \langle \varphi \rangle + \Omega_n \sin(\langle \varphi \rangle) = \Omega. \quad (5)$$

This equation coincides with (1), except that the noise  $N = 0$  is absent and old constant  $\Omega_0$  is replaced by new

$$\Omega_n = \Omega_0 \langle \cos \xi \rangle = \text{const.} \quad (6)$$

This can be treated as the new critical current  $I_n = \hbar \Omega_n / 2eR$ . Now we have the stable solutions  $\langle \varphi \rangle = \text{const}$  of (5) at  $|I| \leq I_n$ . It means that the superconducting branch  $\langle V(I) \rangle = (\hbar/2e) \langle d\varphi/dt \rangle = 0$  of the current-voltage ( $I$ - $V$ ) characteristic exists at green noise within the region  $|I| \leq I_n$ .

The term  $v = \Omega_0 L u$  of (4) is satisfied the Langevin equation  $\mathcal{G} d^2 v / dt^2 + dv/dt = \Omega_0 f$ , where  $f = -\sin(L\bar{x} + \xi) + \langle \sin(L\bar{x} + \xi) \rangle$ . This follows from the second approximation of the averaging method. The random force  $f$  has the correlation time less than  $\tau_0$  and we obtain the diffusion law  $\langle v^2 \rangle = At$  for  $t \gg \tau_0$ . The diffusion coefficient is

$$A = \Omega_0^2 \int_{-\infty}^{+\infty} \langle f(t) f(t+\tau) \rangle d\tau. \quad (7)$$

The time  $\tau_d = A^{-1}$  determines the lifetime of the locking state of the Cooper pairs' wave functions.

Now we go back to the problem of the background illumination. This radiation and process  $\xi$  are Gaussian. Then we have from (6) that

$$I_n = I_0 \exp(-\Delta^2/2),$$

where  $\Delta^2 = \langle \xi^2 \rangle$  is the variance of the process  $\xi$ . It is expressed through its spectrum  $G(\omega)$  as

$$\Delta^2 = \int_{-\infty}^{+\infty} G(\omega) d\omega = \int_{-\infty}^{+\infty} \frac{S(\omega)}{\omega^2 (\mathcal{G}^2 \omega^2 + 1)} d\omega = \eta^2 \left( \frac{2e}{\hbar} \right)^2 \frac{a^2 \beta^2 \hbar}{2\pi^4 l^2 c^2 \mathcal{G}^2} \int_0^{+\infty} \frac{x dx}{(\beta^2 x^2 + 1)(\exp x - 1)}, \quad (8)$$

where  $\beta = k_B T_b \mathcal{G} / \hbar$ . The numerical integration of (8) for  $d = 0.001$  m,  $a = 0.01$  m,  $l = 0.05$  m, and  $T_b = 300$  K gives  $\Delta^2 \approx 0.4$ . This shows that the effective critical current  $I_n$  may possess value within the interval  $[0, I_0]$  versus specific situation.

Using the well-known properties of the Gaussian process, we can obtain from (7) that

$$A = \Omega_0^2 \exp\left\{-\Delta^2\right\} \int_{-\infty}^{+\infty} \sinh \rho(\tau) d\tau.$$

where zero current  $I = 0$  is taken for the sake of simplicity, and  $\rho(\tau) = \langle \xi(t) \xi(t+\tau) \rangle$ . If  $\Delta \ll 1$ , we can put  $\sinh \rho \approx \rho + \rho^3/6$  and obtain:

$$A \approx 2\pi \Omega_0^2 G(0) + \frac{\Omega_0^2}{6} \int_{-\infty}^{+\infty} \rho^3(\tau) d\tau. \quad (9)$$

We see from (2) and (8) that the asymptotic dependence of the spectral density  $G(\omega)$  on the frequency is  $G(\omega) \propto S(\omega)/\omega^2 \propto \omega^4$  at  $\lambda \gg a$ . Hence the first term in the right-hand side of (9) is equal to zero strictly and the diffusion coefficient has the order of magnitude  $A \sim \Omega_0^2 \Delta^6 \tau_0 = (2eI_0 R / \hbar)^2 \Delta^6 \tau_0$ . It may be very large value. Let us assume that we measure  $I_n$  to detect the intensity of green noise [3]. The phase-sensitive detector methods may give the accuracy less than 0.01 %. Since we can take  $\Delta = 0.01$  and obtain  $\Omega_0 \approx 3.2 \cdot 10^{10} \text{ s}^{-1}$  at  $I_0 = 10^{-4} \text{ A}$ ,  $R = 0.1 \text{ Ohm}$ ,  $\tau_0 \sim \mathcal{G} = 10^{-13} \text{ s}^{-1}$ . Then  $A \sim 10^2 \text{ s}^{-1}$  and the lifetime of the superconducting state is  $\tau_d = A^{-1} \sim 10^{-2} \text{ s}$ . It is the enormous time in contrast to the characteristic time  $\Omega_0^{-1} \sim 3 \cdot 10^{-11} \text{ s}$  of transient phenomenon in the Josephson junction. Accordingly, the  $I$ - $V$ -characteristic remains broken at the point  $I = I_n$  with very high the accuracy ( $\sim 10^{-7} \%$ ).

## References

1. V. Ambegaokar, B. I. Halperin, Phys. Rev. Lett., **22**, 1364 (1969).
2. S. A. Guz, M. V. Sviridov, Physics Letters A, **A 240**, 43 (1998).
3. M. V. Sviridov, A. R. Gabidullin, Appl. Phys. A, **A 57**, 539 (1993).

# A novel method for the exact calculation of Wannier-Stark localization in superlattices

Y. Ergun\*, R. Amca\*, I. Sokmen\*\*, H. Sari\*, S. Elagoz\*, N. Balkan\*\*\*

\* Cumhuriyet University, Physics Department, 58140, Sivas, Turkey

\*\* Dokuz Eylül University, Department of Physics, Izmir, Turkey

\*\*\* University of Essex, Department of Physics, Colchester, UK

## Abstract

We present a novel method for the exact calculation of the Wannier-Stark (WS) localization in a long periodic potential representing a 50Å/30Å, GaAs/Ga<sub>1-3</sub>Al<sub>x</sub>As superlattice with an Al concentration of x=30%. Electric field dependence of the electron wave function is shown to have unique localization dynamics. Our calculations predict a second order effect involving the change of the dipole field with increasing WS field. It is suggested that this change may give rise to parasitic effects in Bloch oscillations, and, therefore to noise in coherent terahertz emission.

## Introduction

Bloch oscillations have been investigated in semiconductor superlattices (SL) by using coherent optical excitations of Bloch wave-packets in the WS Regime. The displacement of the Bloch oscillating wave-packet with a high spatial resolution can be used to investigate the spatial amplitude of the oscillating wave packet as a function of time [1]. In the experiments the dipole field created by oscillating Bloch wave packets is determined by using the field shift of the WS ladder transitions as sensitive detector. Displacements are then derived directly from the shift without any adjustable parameters. The accuracy of the results is primarily determined by the sensitivity of the detector, i. e. the WS localization parameters. Current aims at calculating these parameters using a simple method.

## Results and discussions

When a uniform external electric field lifts the degeneracy in a superlattice, each quantum well in the periodic chain has its own eigen states and the wave functions become well localized [2-5]. If the energy difference of localized states between adjacent wells belonging to the same band index  $n$  is  $|eFL|$  or more, the derivative of the matrix element  $I$ , with respect to  $k$  vector must be zero [5]. The interband matrix element  $I$ , is given by;

$$I(n, k; n', k') = \int_0^{\Lambda} dx. e^{i(k'-k)x} \cdot u_{F,n,k}^* \cdot u_{F,n',k'}(x) \quad (1)$$

where  $n$  is the band index and  $F$  is the electric field and  $u$  is the periodic part of the field dependent Bloch function. We have reported elsewhere [6] a vanishing interband matrix element for a simple potential profile where a step-like increment in the potential simulates the effect of an external field along to growth direction of the SL. Here we apply the

same method to WS localization. Following Emin and Hart [5], we write the Hamiltonian as,  $H = \frac{p^2}{2m^*} + V_E(z) + V_S(z)$

here the first two terms represent the periodic part of the Hamiltonian and  $V_S(z)$  is the step-like potential. Schrodinger equation of the field dependent periodic structure in terms of the dimensionless reduced co ordinate  $\tilde{z} = z / \Lambda$  becomes:

$$\frac{\partial^2 \psi_{\tilde{F},n,k}(\tilde{z})}{\partial^2 \tilde{z}} - \left(\frac{\pi}{\tilde{F}}\right)^{2/3} \left[ \sum_{i=1}^{N-1} (\tilde{F}(\tilde{z}-i)S(\tilde{z}-i) + \tilde{V}_0 S(\tilde{z}-i-t_\Lambda))S(i+1-\tilde{z}) - \tilde{\epsilon}_{\tilde{F}}(n,k) \right] \psi_{\tilde{F},n,k}(\tilde{z}) = 0 \quad (2)$$

where,  $\tilde{F} = eF / E_0$  ( $E_0$  is the zero field ground state energy of the well with a normalized well width, 1.  $\tilde{\epsilon}_{\tilde{F}}(n,k)$

is the eigen energy in the  $n$ 'th band which has wave vector  $k$  in electric field  $F$ .  $\tilde{V}_0$  is the barrier height normalized with respect to  $E_0$  and  $\tilde{t}_\Lambda = t_\Lambda / \Lambda$  is the reduced well width. Wave function can therefore be represented by Airy functions both in the well and barrier regions, hence numerical calculations can be carried out. In the calculations we used a GaAs/GaAlAs superlattice comprising  $N=11$  wells and barriers with widths 50 Å and 30 Å respectively, and  $m_e^*$  is taken

as a variable. (For the results presented in this paper  $m_e^* = 0.45m_e$  corresponding to heavy hole effective mass). In figure 1 the first two subband wave functions are shown for an electric field  $F=1 \times 10^5$  V/cm. It is evident that the first subband wave function accumulates to the left hand side and the second subband wave function move to right hand-side of the quantum wells as expected. Eigenfunction of the total Hamiltonian must satisfy,

$$H\varphi_{\tilde{F}}^m(\tilde{z}) = \tilde{\epsilon}_m \varphi_{\tilde{F}}^m(\tilde{z}), \quad \varphi_{\tilde{F}}^m(\tilde{z}) = \sum_{n,k} A_m(n,k) \psi_{n,k,\tilde{F}}(\tilde{z}) \quad \text{where } \tilde{\epsilon}_m \text{ is the reduced eigen energy of the real system,}$$

and  $\varphi_{\tilde{F}}^m(\tilde{z})$  is the superposition of the electric field dependent Bloch functions belonging to the  $m$ 'th eigenvalue. One

possible treatment of the field dependent Bloch functions has been given by Emin and Hart [14] which involves the expansion of coefficients  $A_m(n,k)$ . An alternative and simpler approach would be the expansion in terms of field dependent Wannier functions for all the states. Because these are peaked functions they would be better suited to the solution of localization problems. Wannier function for the  $n$ 'th band and at a site  $p$  is expressed by field-dependent Bloch functions as

$$W_{\tilde{F}}^n(\tilde{z} - p) = N^{-1/2} \sum_k e^{-ikp} \psi_{n,k,\tilde{F}}(\tilde{z}) \quad (3)$$

The wave function of the total Hamiltonian can be written independent of  $k$  as,

$$\varphi_{\tilde{F}}^m(\tilde{z}) = \sum_{n',p'} c_{n',p'}^m W_{\tilde{F}}^{n'}(\tilde{z} - p'), \quad c_{n',p'}^m = N^{-1/2} \sum_{k'} A_m(n',k') e^{ik'p'} \quad (4)$$

If we apply the full Hamiltonian to eq.6, then multiply this by  $W_{\tilde{F}}^{n'*}(\tilde{z} - p)$  the integration over the full space gives the effective Schrodinger equation in Dirac representation. If we take the inter-matrix element from ref.[14] and carry out the appropriate intermediate calculations we can express the inter-band coupling of the field dependent Bloch function as:

$$i\tilde{F} \sum_{n',p',k'} C_{n',p'}^m e^{i(p-p')k'} \left( \frac{\partial}{\partial k'} I(n,k;n',k') \right) + i\tilde{F} \sum_{n',p',k'} C_{n',p'}^m e^{i(p-p')k'} \left( \frac{\partial}{\partial k'} I(n,k;n',k') \right)_{k=k'} + \tilde{F} \sum_{n',p',k'} C_{n',p'}^m p \delta_{pp'} \delta_{kk'}$$

This leads to the eigenvalue equation 
$$\sum_{p',n'} \left[ \frac{1}{N} \sum_k e^{ik(p-p')} \tilde{\epsilon}(n,k) \delta_{n,n'} - \epsilon'_m \delta_{p,p'} \delta_{n,n'} + \tilde{F} p \delta_{p,p'} \delta_{n,n'} \right] c_{n',p'}^m = 0 \quad (5)$$

It is obvious from eq. (5) that for a given site index  $p$  the energy of the localized state is equal to the sum of the field induced potential and the average subband energy:  $\tilde{\epsilon}_m = \tilde{\epsilon}(\tilde{F}, n) + \tilde{F}p$ . Therefore, the eigen values have the ladder structure as expected (WS Ladder). This is shown in Fig.2 where the energy splitting of both the first and second subband as a function of applied field is depicted. Fig. 3 shows the localized wave functions for the first subband at different electric field strengths. In order to eliminate the edge effects we only look at the first three wells on either side the sixth well which is marked as 0. It is worth pointing out the remarkable sensitivity of the localization characteristics on the applied field. For the centre well and the next well on the right-hand side, increasing the electric field results in an increase in the localization. The two adjacent wells on the left-hand side show a decrease in localization with field. In a terahertz emission experiments this behaviour would imply the growth of electric dipole field as observed. However, although it is a very small effect, the field dependence of the localization shows an opposite behaviour for the third well on the left and the second well on the right-hand side of the center well. Namely localization increases in the third left-hand side well and decreases in the second right hand side well. This small effect might give rise to parasitic effects and noise in experiments concerning field dependent oscillations and terahertz emission as often observed at elevated temperatures [7].

### Conclusion

A simple novel method for the exact numerical calculation of W.S. localization parameters are presented. Our results indicate a second order anomalous behaviour of the localization characteristics but in principle, give results similar to those by others, and predict the experimental results involving Bloch oscillations.

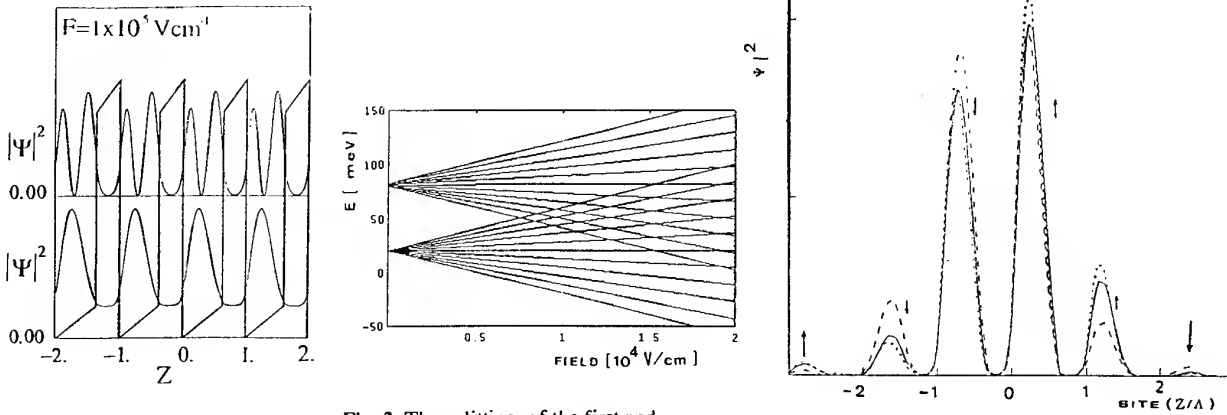


Fig. 2 The splitting of the first and the second subbands of the 11 superlattice

Fig. 1 Electron wave function for the first two subbands of the superlattice in a uniform electric field of  $F=100$  kV/cm

Fig.3 Localization characteristics of the six central wells of the superlattice. Long broken line:  $F=10$  kV/cm, Full line: 50 kV/cm, Short broken line : 100 kV/cm

### References

1. V. G. Lyssenko, M. Sudzius, G. Valussis, F. Loser, T. Hasche, K. Leo, M. M. Dignam, K. Kohler Proc. of Hot Carriers in Semiconductors -X Berlin (1997)
2. D. Emin, and C. F. Hart, Phys. Rev. B. 36 7353 (1978)
3. J. Leo, and A. MacKinnon, Phys. Rev. B. 43 5166 (1991)
4. L. Kleinman, Phys. Rev. B. 41 3857 (1990)
5. Emin, and C. F. Hart, Phys. Rev. B. 43 5169 (1991)
6. Sari, H. Metin, I. Sokmen, S. Elagoz, and Y. Ergun. Superlattices Microstruct., 17 (1995) 457.
7. P. Leisching, P. Haring Bolivar, R. Schwedler, K. Leo, H. Kurtz, K. Kohler and P. Ganser. Semicond. Science and Technol. 9, 419 (1994)

## Efficiency Enhancement in the Relativistic Microwave Oscillator

E. Odarenko, A. Shmat'ko

Dept. of Radiophysics, Kharkov State University  
Svobody Sq., 4, 310077, Kharkov, UKRAINE

### Abstract

The non-linear theory of the relativistic resonant O-type oscillator with dc nonuniform focusing magnetic field is considered. The theoretical analysis of the physical phenomena within the framework of the three-dimensional model is carried out. The effect of the relativistic mass-factor, beam current and focusing field displacement on the oscillator efficiency is investigated.

### Introduction

Resonant O-type oscillator with prolonged interaction (orotron, diffraction radiation generator, ledatron, laddatron etc.) which uses relativistic electron beam is analyzed. The charged particles velocity increase in the interaction space allows to enhance the output power and efficiency of the interaction between the rf field and electron beam. However the system being considered is the multiparametrical. Hence the search problem of the efficiency enhancement additional opportunities by means of the electron-beam system parameters change is actual. The application of the nonuniform focusing field in the non-relativistic devices allows to enhance the efficiency of the both starting and non-linear steady-state regimes. Therefore the study of the nonuniform focusing field application possibility in the relativistic devices is actual.

The solution of this problem can be separated on two stages:

- the investigation of the device with uniform focusing field (displacement may be varied);
- the investigation of the device with nonuniform focusing field (both displacement and space distribution may be varied).

In the present report some aspects of the relativistic oscillator investigation first stage are considered.

### Theoretical model

The electron devices multidimensional model must be used for more complete investigation of the physical processes. It is necessary for accounting of the different phenomena caused by transversal motion of electrons and rf field nonuniformity in the electrodynamic system. The relativistic electron beam passes near the slow-wave system surface (e.g. grating) through the high-quality resonator. The rf field structure is assumed to be fixed. Theoretical analysis is carried out on the base of the non-linear self-consistent equations set solution. This set consists of the motion and excitation equations.

Three-dimensional vector equation of the charged particle motion in the electromagnetic field can be specified as

$$\frac{d\vec{v}}{dt} = -\frac{|e|\hbar}{m_0\gamma} \left\{ \vec{E} + [\vec{v}\vec{B}] - \frac{\vec{v}}{c^2} (\vec{v}\vec{E}) \right\}; \quad (1)$$

where  $\vec{v}$  is the velocity vector of electron,  $t$  is the time,  $e$  and  $m_0$  - charge and rest mass of the electron,  $\gamma = (1 - v^2/c^2)^{-1/2}$  is the relativistic factor,  $\vec{E}$  and  $\vec{B}$  - electric and magnetic field vectors respectively,  $c$  is the light velocity.

The equation of the rf field excitation in the high quality electrodynamic system can be specified as

$$\frac{dF}{d\tau} - id_s F = \frac{G}{2\pi\Delta} \int_V \int_0^{2\pi} f(\xi) \Psi(Z) \left( 1 - i \frac{dZ}{d\xi} \right) \exp[i(\theta + \Phi b\xi + \varphi)] d\varphi dV. \quad (2)$$

Here  $F$  is the complex oscillations amplitude,  $\tau = \omega_s' t / 2Q$ ,  $\omega_s = \omega_s' - i\omega_s' / 2Q$  is the eigen frequency of the s-th resonator mode,  $d_s = 2Q(\omega - \omega_s) / \omega_s$ ,  $\omega$  is the oscillations frequency,  $Q$  is the

quality factor,  $G$  is the interaction efficiency parameter ( $G$  directly proportional to beam current),  $\xi$  and  $Z$  - longitudinal and transversal coordinates,  $f(\xi)$  and  $\Psi(Z)$  - longitudinal and transversal amplitude envelope functions,  $\Phi$  is the normalized interaction space length,  $b$  is the relative synchronism mismatch parameter,  $\varphi$  is the oscillations phase,  $V$  is the interaction space volume.

The numerical solution of the initial equations set is carried out for Gaussian form of the function  $f(\xi)$  (orotron-type devices).

### Discussion

Figure 1 shows the dependence of the maximum electron efficiency  $\eta$  over the oscillation zone on the parameter  $\gamma_0$  ( $\gamma_0 = \gamma|_{v=v_0}$ ,  $v_0$  is the initial electron velocity). The curve 1 is plotted for  $\omega_c/\omega=0.4$ , curve 2 -  $\omega_c/\omega=0.15$ . Here  $\omega_c$  is the cyclotron frequency. The focusing field displacement increase results in the efficiency enhancement but does not change the function  $\eta(\gamma_0)$  form. Results being obtained at  $\omega_c/\omega=0.4$  are similar to known from the one-dimensional theory of the relativistic devices. Thus longitudinal electron-wave interaction is the main energy exchange mechanism in this case.

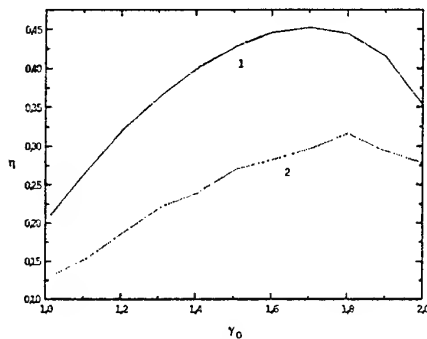


Fig.1.

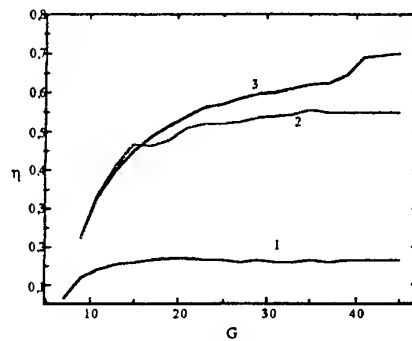


Fig.2.

Figure 2 shows the dependence  $\eta(G)$  for different values of the parameter  $\omega_c/\omega$  (curve 1 - 0.1, curve 2 - 0.2, curve 3 - 0.4). All curves are plotted at  $\gamma_0=1.6$ . The focusing field displacement increase results in efficiency enhancement in the whole range of the parameter  $G$  change. There is the settling of electrons onto the grating in the case  $\omega_c/\omega=0.1$ . The settling results in electron bunches density decrease and, in turn, in the decrease of the energy which electrons are giving to wave. Figure 3 shows the dependence of the rf current module on the longitudinal coordinate for two values of the magnetic field displacement (curve 1 -  $\omega_c/\omega=0.4$ , curve 2 - 0.1). The dashed curve shows the function  $f(\xi)$ . It is seen that the electron bunch forms nearer to interaction space middle in the case of stronger magnetic field. Therefore the efficiency enhances because the rf field amplitude is maximum at  $\xi=0.5$ .

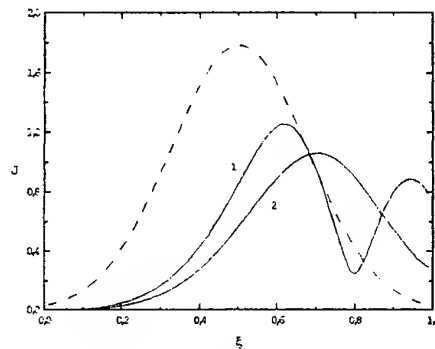


Fig.3.

### Conclusions

The efficiency of the relativistic resonant oscillator depends on the both focusing field displacement and beam current. The magnetic displacement increase results in the efficiency enhancement. The settling of the electrons onto the grating is the main cause of the efficiency reduction in the case of weak focusing field. The beam current increase results in efficiency enhancement for fairly strong magnetic field only.

## Double Resonance in Gyrodevices

G.S. Nusinovich and J. Zhao

Institute for Plasma Research  
University of Maryland  
College Park, MD 20742-3511 USA

In many gyrodevices (i.e., gyromonotrons, gyroklystrons) a beam of gyrating electrons excites standing waves in resonators. Such waves can be represented as a superposition of forward and backward waves that have opposite Doppler shifts of the operating frequency in the reference frame moving with electrons. Correspondingly, for certain axial wave numbers, both forward and backward waves can simultaneously be in cyclotron resonance with gyrating electrons at different cyclotron harmonics. The theory describing the interaction between electrons and the resonator field in the case of such a double resonance is developed. It is shown that this double resonance can be beneficial when the device operates at symmetric modes, while in the case of operation at nonsymmetric modes, it always lowers the efficiency. The latter effect is especially important when the electron velocity spread is large. (A full-length paper describing this study is published in *Phys. Rev. E*, July 1998.)

This work has been supported by the U.S. Department of Energy, Division of High Energy Physics.

## Experimental study of trapped electrons effect in helical electron beams of a millimeter wave range gyrotrons

A.N.Kuftin., V.E.Zapevalov

Institute of Applied Physics, Russian Academy of Sciences,  
46 Ulyanov Street, 603600 Nizhny Novgorod, Russia

### Abstract

The basic properties of helical electron beams formed in the magnetron -injection gun of powerful millimeter wave range gyrotrons are investigated experimentally at the presence of electrons, reflected by the magnetic mirror and locked in adiabatic trap and the excluding of a such electrons. Guns for 1 MW power level 83GHz, 110GHz, 140GHz and 170GHz gyrotrons, forming beams with the different topology are considered. The experimental results show that the trapped electrons significantly affect the beam parameters.

### Introduction

In the magnetron-injection gun (MIG) of the powerful gyrotrons, which form helical electron beams (HEB), a portion of electrons acquired in the gun the surplus oscillatory energy owing to the velocity spread, appears to be caught in the adiabatic trap. It was mentioned [1], that the trapped electrons are the main factor that lead to electron flow instability. The trapped electrons effect on the helical beam parameters for the case of stable beams was considered theoretically [2] and studied experimentally in centimeter wave range gyrotrons HEBs [3]. In [3] it was noted that the transition to more short-wave gyrotrons having a relatively small Langmuir radius and the trajectory step in the near-cathode region, should, facilitate the improvement of the HEBs quality. In this case attenuation of the trapped electrons phasing and, consequently, their influence on the velocity spread  $\delta v_{\perp}$  and relative oscillatory energy  $t_{\perp}$  are expected.

Parameters of HEBs can be different when the operating frequency changes and other conditions stay the same, due to variation of mirror ratio-  $\alpha$  ( $\alpha=B_0/B_c$ , where  $B_0$  and  $B_c$ - are magnetic fields in the operating space and at the cathode, respectively). According to the adiabatic theory this coefficient  $\alpha$  will be growing and average velocity falling in higher-frequency ranges at the same other conditions [1,4]. Below some results of the experiments, aimed at ascertaining the character of the trapped particles effect on the parameters of the millimeter wave range gyrotrons are given.

### Measurements and Experimental Results

The measurements were carried out by the modified method of the retarding field in the scale down regime [3] at the automated experimental set up [4]. Beams with trapped electrons - "resulting beam" (or 1D regime) are compared with beams, in which these electrons are intercepted by a special additional diaphragm - "primary beam" (or 2D regime). Scaled regimes are used, during which the magnetic field, voltage and current decrease in comparison with the operating values, according to the scaling relations which guarantee the invariability of the

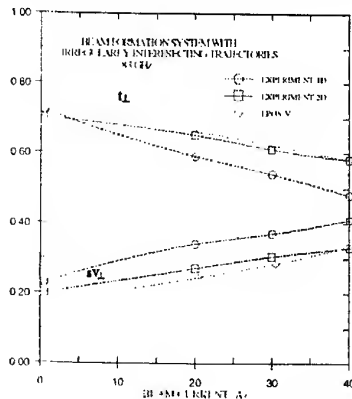


Fig.1.  $t_{\perp}$  and  $\delta v_{\perp}$  vs. beam current.

forms of trajectories. The relative velocity spread  $\delta v_{\perp}$ , relative oscillatory energy  $t_{\perp}$ , function of distribution electron on oscillatory velocities  $f(v_n)$  changing with the beam current grow are traced.

a) The measurements for 83 GHz gyrotron guns ( $\alpha=19$ ) [4] were carried out in a scale down regime described above. According to [4] HEB parameters depend significantly on HEB topology. Guns forming mixed (irregularly intersecting), regularly intersecting, boundary (between quasilaminar and regularly intersecting HEB) and quasilaminar HEB are considered. For example, in Fig. 1 the 1D and 2D -marked lines show the average relative oscillatory energy  $t_{\perp}$  and the oscillatory velocities spread  $\delta v_{\perp}$  in MIGs, as functions of the beam current in the 1D and 2D case. It is seen that the characteristics of the MIG become different but not in the great degree as [3], the velocity spread decreases and the oscillatory energy increases. For the 2D case, the changing of values  $\delta v_{\perp}$  and  $t_{\perp}$  satisfactorily agrees with the results of the trajectory analysis



performed without taking into account reflected electrons (see [4,6]).

b) MIG for 110 GHz gyrotron, ( $\alpha \approx 22.5$ ) forming boundary and quasilaminar HEB [6] were also investigated in 1D and 2D regimes. The attributes of the MIG primary beam acquire another form in 1D-regime compare with 2D case. It is seen that the dependence become a little bit different, the velocity spread decreases and the oscillatory energy increases. The changing of values  $\delta v_{\perp}$  and  $t_{\perp}$  satisfactorily agrees with the results of the trajectory analysis.

c) For 140 GHz gyrotron guns ( $\alpha \approx 28$ ) forming boundary and quasilaminar HEB [7], were also investigated in 1D and 2D regimes and dependencies of the average relative oscillatory energy  $t_{\perp}$  and the oscillatory velocities spread  $\delta v_{\perp}$  as functions of the beam current were received. The velocity spread dependence  $\delta v_{\perp}(I)$  of the MIG primary beam get another form for quasilaminar HEB, and practically the same for boundary one. It is seen that the oscillatory energy  $t_{\perp}(I)$  dependence have no changes for both HEB topology. Like the previous case, the change of values  $\delta v_{\perp}$  and  $t_{\perp}$  satisfactorily agrees with the results of the trajectory analysis. More detail information on electron beam property are included at the electron distribution function in the oscillatory velocities  $f(v_{\perp})$  [5]. Evolution of the  $f(v_{\perp})$  as the beam current grows has been traced. Fig.2. presents such  $f(v_{\perp})$  functions for the primary boundary beam and resulting one respectively with current 10, 30, and 50A. The

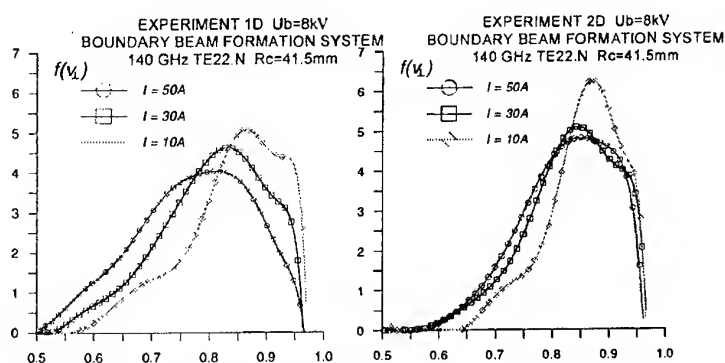


Fig.2. Electron distribution functions upon the oscillatory velocities.

distribution functions even for the relatively small beam current 10A have the Gaussian like shape in the 2D case only. When the beam current grows the  $f(v_{\perp})$  shape becomes more wide, especially for resulting beams. Even at the 50 A beam current the distribution functions have no tendency to get additional maximum.

Two version of the 170 GHz gyrotron guns forming boundary beams for the  $TE_{25,10}$  ( $\alpha \approx 31.5$ ) and  $TE_{28,7}$  ( $\alpha \approx 30$ ) operating modes [8] also are considered.

In all the investigated cases, the beam corresponds the operating current value does not lose its stability. We may state that, in spite of the considerable influence of the reflected electrons on the velocity distribution of helical beams, there is a mechanism of particle removal from the trap that does not disturb HEB stability.

### Conclusions

The results of experiment in the wide mirror ratio interval show essential influence trapped electrons on parameters of a millimeter wave range gyrotrons HEB. The interception of the reflected electrons decreases the velocity spread. The beam parameters with the excluded trapped electrons satisfactory agree with the calculated ones obtained from the trajectory analysis. Attenuation of the trapped influence on the velocity spread and  $t_{\perp}$  of millimeter wave range gyrotrons beam compare centimeter one are shown.

Acknowledgment: This research was supported in part by the Russian Foundation for Fundamental Researches (Grant 96-02-16217-A).

### References

1. Sh.E.Tsimring, Lectures on Microwave Electronics at the Third Winter Workshop -Seminar for Engineers. Book 4.,3, Saratov, Sar. State University, (1974).
2. V.E.Zapevalov, V.N.Manuilov, Sh.E.Tsimring Izvestiya VUZov, Radiofizika, 33, 1406(1990).
3. Sh.E.Tsimring, V.E.Zapevalov, Int. J. Electronics, 81, No2, 199(1996).
4. A.N.Kuftin et al, Int. J. Electronics, 72, 1145(1992).
5. V.K.Lygin. Int. J. Infrared and Millimeter Waves, 16, 363(1995).
6. Denisov G.G., Kuftin A.N., Maligin V.I. et al., Int. J. Electronics, 72(5-6), 1079(1992).
7. Mjasnikov et al., Conf. Proc. 21 Int. Conf. on IR & MM waves., Berlin, Germany, ATH1(1996)
8. V.E.Zapevalov et al., Conf. Proc. 22 Int. Conf. on IR & MM waves. Wintergreen, USA., 108 (1997)

## Non-stationary analysis of the helical electron beams with different topology

P.V.Krivosheev, V.K.Lygin and V.N.Manuilov

Institute of Applied Physics of Russian Academy of Sciences,  
46 Uljanov Street, 603600, Nizhny Novgorod, Russia

### Abstract

Numerical simulation results of the helical electron beams (HEBs) properties based on the PIC method and quasi-stationary electric field model are presented. The distribution of the space charge in HEBs is investigated. The velocity and energy distribution functions of electrons are presented. The process of the cathode bombardment by reflected electrons is studied.

### Introduction

During recent years in many countries the intense efforts to develop the high power CW and quasi-CW gyrotrons for nuclear fusion (ITER program) and technology applications have been undertaken. Formation of HEBs in gyrotrons is performed by magnetron-injection guns (MIGs). The essential difference of MIGs in comparison with many other electron-optic systems forming conventional laminar beams are following: small ratio of the beam thickness to the transverse dimensions of the electron-optic systems, essentially larger electrons trajectories (in the scale of trajectory step  $h$ ) and rather large oscillatory velocity spread  $\delta v_{\perp}$ . The latter factor decreases the gyrotron efficiency and causes the reflection of a part of electrons with the maximum oscillatory velocity from the magnetic mirror between the cathode and the working space. Reflected electrons may initiate the beam instability in some regimes [1].

The static model of the HEBs and corresponding codes [2-4] allow to predict the variation of the  $t_{\perp}$  value (the ratio of the beam oscillatory energy to the total one) as the beam current  $I$  grows with good enough accuracy. However the difference in calculated and measured values of  $\delta v_{\perp}$  in spite of the identical methods of the  $\delta v_{\perp}$  definition [4] remained still essential [5]. The main reason for this deviation is evidently the absence in the static numerical model of the electrons reflected from the magnetic mirror and then captured into the adiabatic trap between the cathode and the cavity. The first works dealing with the non-stationary processes in HEBs were [6,7]. Below the new results of the HEBs properties simulation as well as some methodical aspects of the used code based on the PIC method are described.

### Brief description of the numerical simulation method

The numerical simulation of the HEB formation processes was carried out within the quasi static assumption of the electric field. The self-consistent beam magnetic field was not taken into account. At each time step the electric field was found from the Poisson's equation solution with the space charge density  $\rho$  depending on the coordinates  $r, z$  and the current time  $t$ . To solve the Poisson's equation and find the electric field  $E$  the approach [2] based on the auxiliary charges method and introducing of three additional meshes – a potential mesh and two space charge meshes aimed to calculate the potentials produced by nearest and distant from the point of view charges separately was used. Electric field components then were calculated using potentials in 9 nodes nearest to the point of observation and the algorithm allowing to cut all blank nodes [2].

The numerical simulation was carried out with and without taking into account the initial velocity spread on the cathode. In the latter case the azimuthal velocity spread was considered only [1,4]. The above mentioned distribution was chosen such as to take into account both the influence of the emitter surface roughness and the thermal electron velocities on the velocity spread [4]. The function of the initial azimuthal velocity distribution  $f(v_{\phi 0})$  was chosen close to Gaussian function.

At the initial time moment  $t=0$  it was assumed that the electrode potentials jump from zero to the final values and at the same time the emission with constant current density begins. The trajectory calculation of each big particle is performed up to the moment when it leaves the calculation region through its right edge or intersects with the cathode surface (below the axial-symmetry geometry and quasi-critical regime of the gun were considered and so the radial drift is absent and the particle cannot reach the surface of any other electrode). The right edge of the calculation region was chosen on the right from the point of magnetic field maximum  $B_0$  on the distance approximately equal to the cavity diameter, where  $B_z$  decreases to  $B_z=0.95 B_0$ .

At each time moment  $t_i = i \cdot \Delta t$  ( $i=1, 2, \dots$ )  $N_z \cdot N_v$  particles start from the emitter ( $N_v$  – the number of the

velocity groups with different  $v_{\phi 0}$  and corresponding values of particle charge calculated according to the function of the initial velocity distribution  $dI/dv_{\phi 0}$  on the cathode,  $N_z$  – the number of elementary rings with surface  $S_k$ ). Then the particle trajectory integration with the time step  $dt$  is carried out. At the end of the integration interval  $\Delta t$  the coordinates, velocities and charges of all particles are remembered and then the new solution of the Poisson's equation is found. This cycle forms a time iteration. After that all described steps are repeated up to specified final time moment.

### The results of non-stationary analysis

The calculations were performed for MIGs in the regime close to critical that is typical of the HEBs formation systems of the centimeter wave length range. The diode type guns with accelerating potential  $U_0=60$  kV were considered. The emission current value  $I$  was chosen in such a manner as to provide the ratio  $t_j=I/I_L \approx 0.1-0.2$ . Here  $I_L$  – Langmuir current of the gun. The variation of the pith-factor value  $g_0$  (the ratio of the oscillatory velocity to the longitudinal drift one,  $t_j=g_0^2/(1+g_0^2)$ ) in "cold" system from  $g_0=1$  up to  $g_0=2.0$  was provided by changing the amplitude  $B_0$  of the magnetic field in the working region.

The calculations were performed for three values of  $g_0=1, 1.2$  and  $2.0$  for each gun. The dispersion of initial velocity distribution was chosen using the static code so that  $\delta v_{\perp} \approx 20\%$  for  $t_j=0$ . When  $g_0=1$  and  $1.2$  there are no reflected electrons and the beam parameters again are close to the calculated ones using the static model. However, in this case the tendency of increasing the relaxation time is observed in comparison with zero initial velocities model. The most interesting are the versions with  $g_0=2.0$ . In this case in time interval  $T_1$  a little bit less than  $T_{||}$  ( $T_{||}$  is the time of the particle motion from the cathode to the interaction region) the part of particles from the "head" of the beam with maximum oscillatory velocities reflects in the plane where  $B(z)/B_0 \approx 0.8$  from the magnetic mirror and then turns back to the cathode. Finally in time  $\sim 2.5 T_1$  the reflected electrons reach the cathode. From this moment the cathode bombardment by reflected electrons begins. On the average the zone of bombardment is to some extent shifted ( $\sim 0.2-0.3d$ ,  $d$  – the larmour diameter in the cathode region) to the left in comparison with emitter edges. The averaged energy  $W_c$  of electrons bombarding the cathode may exceed some kilovolts. For laminar flow the value of  $W_c$  is to some extent greater than for the regular intersecting flow. When reflected electrons reach the cathode region they cause the additional cathode electric field depression  $\Delta E$ . However, it is not exceed 50% of  $\Delta E$  caused by the initial beam. When the relaxation processes are finished the full space charge of locked into the adiabatic trap electrons for laminar flow is 2-3 times bigger than for regular intersecting one. The time of the relaxation proses  $Tr$  in any case exceeds  $10-15 T_{||}$ . The value of  $Tr$  is greater for laminar flow. The middle life-time of the electrons in the adiabatic trap is about  $3-5 T_{||}$ . The value of  $t_1$  becomes lower and  $\delta v_{\perp}$  – greater in comparison with the static model of the beam. The maximum deviation in  $\delta v_{\perp}$  is observed for the laminar flow and minimum – for boundary one. The stabilization of the beam potential depression  $\Delta U$  is observed for  $t > (5-6) T_{||}$ . At the same time after that the small oscillations of  $\Delta U$  is observed. The frequency spectra of oscilations is calculated.

### Acknowledgment

The described research was made possible in part by the Grant No. 96-02-16217-A from the Russian Foundation of Fundamental Reseaches.

### References

1. Sh.E. Tsimring, Izvestiya Vysshikh Uchebnykh Zavedenii, Radiofizika 15, 1247 (1972).
2. V.K. Lygin, V.N. Manuilov and Sh.E. Tsimring, Elektronnaya tekhnika, ser. I, Elektronika SVCH 7, 36 (1987).
3. V.N. Manuilov and Sh.E. Tsimring, Izvestiya Vysshikh Uchebnykh Zavedenii, Radiofizika 4, 491 (1981).
4. V.K. Lygin, Int. J. of IR and MM waves 16, 363 (1995).
5. A.N. Kuftin, V.K. Lygin, Sh.E. Tsimring, V.E. Zapevalov, Int. J. Electronics 72, 1145 (1992).
6. E. Borie, C. Cruber, T. Westermann, Int. J. Electronics 78, 789 (1995).
7. B.V. Rasky, Sh.E. Tsimring, IEEE Transactions on plasma science 24, 992 (1996).

## Theoretical Study of the Gyrotron Backward Wave Oscillator

S. H. Chen

National Center for High-Performance Computing

K. R. Chu

Department of Physics, National Tsing Hua University  
Hsinchu, Taiwan, ROC

Gyro-BWO has become a promising candidate of a tunable high-power radiation source for its broadband tunability achieved by varying the magnetic field or the beam voltage and its insensitivity to the beam quality and voltage fluctuation [1-3]. Injection-locking technique has also been employed on the gyro-BWO for the phase control and spectral purity [4].

In this talk, we report studies of the saturated behavior of the gyro-BWO with a particle tracing code which calculates the self-consistent field profile in a weakly non-uniform structure (Fig.1). Four issues have been examined and results are summarized below:

### 1. Mechanism for efficiency enhancement

Previous gyro-BWO experiment [2] attributed the unexpected high efficiency to the non-uniform magnetic field profile, which was verified in subsequent numerical modeling [5]. On the other hand, almost the same efficiency has been obtained in a later gyro-BWO experiment [4] employing a uniform magnetic field. Our numerical results indicate that wave reflection from the tapered output end can also result in significant (up to 80%) efficiency enhancement. The calculated efficiency is in good agreement with earlier experimental results [4].

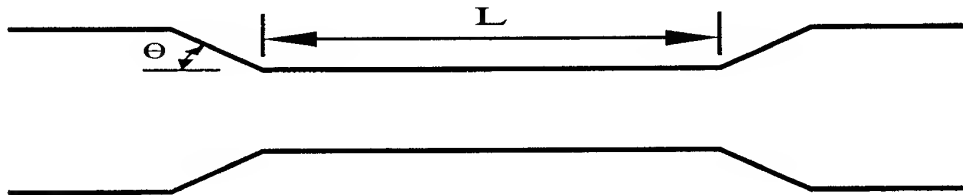


Fig. 1

### 2. Effects of the interaction length ( $L$ in Fig. 1) on mode density and efficiency

An important issue in the gyro-BWO research is the mode competition or transition that might occur during the magnetic field and voltage tuning. Mode competition or mode switching can limit the tuning bandwidth at higher beam current [4], discretize the tuning spectrum [6], or cause ripples in the continuous tuning spectrum [2]. We show that the density of modes in the frequency domain increases with the interaction length, which will in turn result in enhanced possibility of mode switching during magnetic-field and voltage tuning. The interaction efficiency ( $\eta$ ) as a function of the interaction length ( $L$ ) was also examined. Results indicate a rapid rise of  $\eta$  as  $L$  is increased from a couple up to a few free space wavelengths. However,  $\eta$  remains relatively constant with further increase in  $L$ . Physical reasons for this consistency will be discussed.

### 3. Magnetic field and voltage tuning characteristics

Stable voltage tuning bandwidth of 5% was observed at beam current  $I_b=3A$  in a previous experiment [4], but the tuning bandwidth dropped to less than 1% for  $I_b \sim 5A$ . The magnetic field tuning curve in the same experiment showed a rippled structure even at  $I_b=3A$ . The experiment of Ref. 4 employed a long interaction structure, hence the deterioration in tunability might be attributed to the high mode density. A new experiment with a much shorter interaction length has been designed to improve the tunability. Theory predicts a 3% voltage

tunability and 10% magnetic field tunability at  $I_b=5A$ .

#### 4. Phase control by injection locking

The numerical model applied in the study of free-running gyro-BWO's has been extended to handle the injection-locked gyro-BWO by proper modification of the boundary condition of the wave at the output end. The locking power as a function of the frequency and the phase relations between the output and injected waves have been calculated. The results are found to be in good agreement with Adler's theory. The numerical data will be further compared with the data of the newly designed gyro-BWO experiment.

1. J. M. Wachtel and E. J. Wachtel, Appl. Phys. Lett. 37, 1059(1980).
2. S. Y. Park, R. H. Kyser, C. M. Armstrong, R. K. Parker and V. L. Granatstein, IEEE Trans. Plasma Sci. 18, 321(1990).
3. T. A. Spencer, R. M. Gilgenbach and J. J. Choi, J. Appl. Phys 72, 1221(1992).
4. C. S. Kou, S. H. Chen, L. R. Barnett, H. Y. Chen and K. R. Chu, Phys. Rev. Lett. 70, 924(1993).
5. A. K. Ganguly and S. Ahn, Int. J. Electronics 67, 261(1989).
6. M. A. Basten, W. C. Guss, K. E. Kreischer, R. J. Temkin, and M. Caplan, Int. J. Infr. Millimeter Waves 16, 889(1995).

# THE DIFFRACTION RADIATION OSCILLATOR WITH THE WIDE-BAND ELECTRONIC FREQUENCY CHANGE

M.Demchenko, I.Ivanchenko, V.Korneynikov

Usikov Institute of Radiophysics & Electronics of the NAS of Ukraine  
12, Ac.Proskura St., 310085 Kharkov, Ukraine. Tel. (380572)448594,  
fax: (380572)441105, e-mail: buran@ire.kharkov.ua

## Introduction

Over the last 10 years the small-size oscillators of the high-coherent microwave electromagnetic radiation have been developed in the Institute of Radiophysics and Electronics of the NAS of Ukraine. These oscillators called the diffraction radiation oscillators (DRO) overlap the entire millimeter wavelength band. The DRO is the modification of the average middle power oscillator such as an orotron. A Smith-Purcell's effect is used in a DRO. This effect consists in producing electromagnetic radiation when the electron beam is moving near the periodical structure, particularly a reflected diffraction grating. In contrast to the orotron, the diffraction grating in the DRO covers partially one of the reflectors of quasi-optical open resonator (OR) as the positive back-coupling contour of an oscillator. It leads to the spectrum oscillations rarefaction, to a decrease in ohmic losses, to an increase of the load quality factor in the oscillation system. The DRO distinctive feature is the high-oscillation stability and high-radiation coherence. An electronic frequency change is about (20 - 40)MHz. However, the substantially larger electronic frequency change is sometimes required for practical uses, but the good spectral and power characteristics should remain unchanged. It was shown here that this problem can be resolved by selecting an oscillator electro-dynamical system.

## Research method and experimental results

The quasi-optical OR is used as the electro-dynamical system in the basic DRO. The OR of this kind is usually formed by the lower cylindrical reflector with the local diffraction grating (the width of the diffraction grating  $B \approx 2.4 \lambda$ ) and by the upper spherical reflector with the steepness radius of about  $R=110\text{mm}$ . The expansion of electronic frequency change band in these oscillators by decreasing the Q-factor in any way gives rise to the deterioration of the spectral and power radiation characteristics. To achieve the project aim we used the long-focus OR as the DRO electro-dynamical system. In the above OR the reflector aperture and the distance between them are compared to the working wavelength. The quasi-optical condition  $J^2/L\lambda \ll (L/J)^2$ , (where  $L$  is the reflectors separation,  $J$  is the reflector aperture radius) is violated for this OR geometry as well as for its

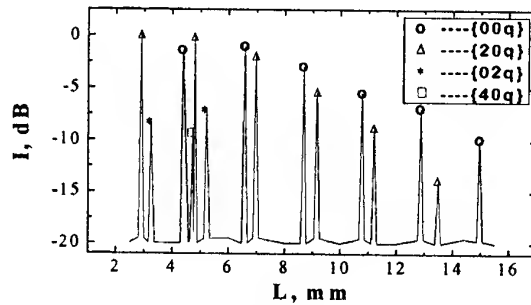


Fig.1. Spectrum and amplitude field distributions for a small-aperture sphere-cylindrical OR with the long-focus reflectors.

short-focus analogy just as the Fresnel numbers are of the same order as in the short-focus OR. The same situation is also observed in the long-focus OR for the small values  $L$ , but the spectrum density shows a significant increase and the selective OR properties tend to worsen. It is obvious that for the small  $L$  ( $L/R < 0.1$ ) a decrease of the reflector aperture is equivalent to some filtering action due to the increase in diffraction losses for the higher modes. It allows to retain the selective properties of the OR and to increase simultaneously the density of the electromagnetic field in the interaction space with an electron beam in contrast to the quasi-optical OR.

To define the DRO output characteristics it is necessary to know the field distribution near the diffraction grating along the interaction space. However, in this case the traditional methods for studying the resonance field space distribution are unacceptable. In this paper we developed the original method for the OR excitement where the Sommerfeld wave propagating along the metal string is used to excite the OR by means of an electrical dipole coupled with this transmission line. In Fig.1 the OR spectrum is shown for the following parameters:  $J=12\text{mm}$ , the dipole length  $l=0.3\lambda$ ,  $L/R=(0.03\lambda - 1.1\lambda)$ . The quality-factor of the excited modes is about  $(5 - 7) \cdot 10^2$ . One can see the fundamental mode presents here in contrast to the long-focus OR with the diffraction grating on the reflector surface.

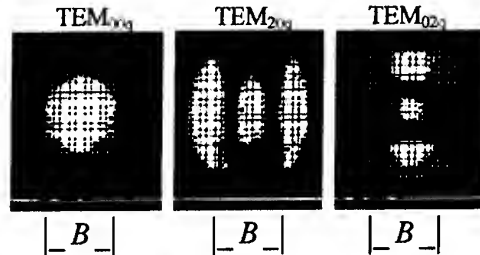


Fig.2. The amplitude field distributions of the lowest modes small-aperture OR.

Sommerfeld line together with the dipole is placed on the mechanical scanner, which makes it possible to meet the required conditions for investigating into both the spatial amplitude and phase field distributions within the OR. The study of the «cold» OR was carried out in the 4-mm wavelength band. The amplitude field distributions of the three lower modes are shown in Fig.2. The obtained field pictures suggest that the OR of this kind can be used as the positive back-coupling contour in the small-size DRO. As a result, a series of these devices was developed. The aperture radius of the OR reflector is about 10mm and the reflectors separation varies within the interval of the longitudinal index from  $q$  to  $3q$ .

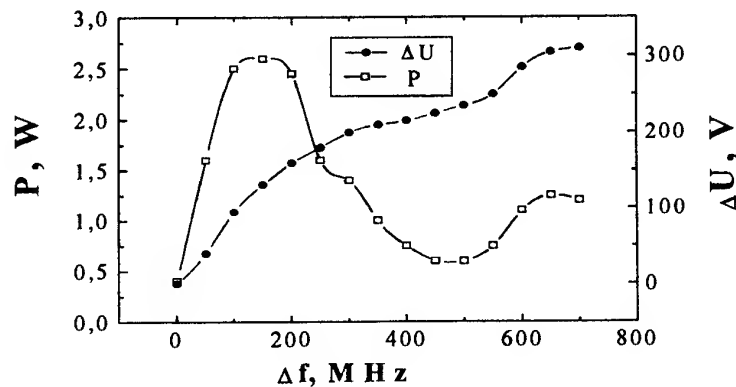


Fig.3. The electronic frequency change and the output power of the microwave oscillator.

The frequency band of the electromagnetic radiation is (66 - 73)GHz. The accelerating voltage varies from 2.6kV to 3.3kV. In Fig.3 the electronic frequency change and the DRO output power are shown for the working beam current  $I=90\text{mA}$ . One can see that the electromagnetic radiation frequency can be changed to 700MHz if the accelerating voltage is changed to 300V.

#### Conclusion

We used the small-aperture OR formed by the long-focus reflectors as the positive back-coupling contour in the new modification of the microwave DRO. The reflector aperture and their separation are compared to the working wavelength. The oscillators of this kind have an electronic frequency change which is 10 times as greater than the basic DRO and their output radiation power and spectrum quality are comparable. The steepness of the mechanical frequency change is  $\approx 3.7 \text{ GHz/mm}$  and of electronic frequency change is  $\approx 2 \text{ MHz/V}$ .

The practical application of the compact DRO with the small long-focus reflectors extend the functional capabilities of the microwave oscillators, and the new prospects are offered for the development of the multicascade systems of the microwave diffraction electronics.

## LOCAL "PHASE" INHOMOGENEITIES REVELATION IN OPTICAL OPAQUE DIELECTRIC

Igor Ivanchenko

Usikov Institute of Radiophysics & Electronics of the NAS of Ukraine  
12, Ac. Proskura St., 310085 Kharkov, Ukraine. Tel. (380572)448594,  
fax: (380572)441105, e-mail: buran@ire.kharkov.ua

### Introduction

One of the significant practical problems in modern defectoscopy is the discovery and identification of local inhomogeneities in the optical opaque solid state dielectrics. Among the numerous experimental methods the special importance is attached to the nondestructive control radio-wave methods. The receive-transmitting antennae of the various types are used in millimeter wavelength band for the dielectric material investigations. Under these conditions the standard methods allow to discover the foreign inclusions in an examined object at a resolving capacity determined by the well-known Rayleigh criterion. At the same time if the highest homogeneous and isotropic samples are required, it is necessary to combine simultaneously the high resolving capacity and sensitivity of experimental techniques for radiostructure analysis. This problem is very important when the local "phase" inhomogeneities and small anisotropy areas are required to discover within the material under investigation.

### Research methods and results

The experimental research was carried out in the 4-th - and 2-nd millimeter wavelength band both for the basic and cross polarization of the probing wave bunch. As the object under study was the dielectric matrix formed by the two homogeneous and isotropic textolite plates with dimensions of  $100 \times 120 \text{ mm}^2$  and thickness of 1.5mm each. The matrix was conditionally divided into the six cells with dimension of  $30 \times 30 \text{ mm}^2$ . The different local inhomogeneities were placed in each cell. These elements have imitated the possible foreign inclusions in the dielectric materials. In the complete form the being measured matrix was placed on the mobile frame of the complex [1]. The probing wave bunch with a diameter of  $D = 0.4 \lambda$  was formed with the aid of the special metal-dielectric antenna. The receiving and transmitting antennae were identical. Scanning of the dielectric matrix was performed with respect to the fixed antennae.

The "strong" inhomogeneities such as the cavities, metal and dielectric elements were recorder with confidence due to the intensity change of the probing wave. The exception was one of the cells where two  $15 \times 5 \text{ mm}^2$  teflon films with a thickness of  $20 \mu\text{m}$  were separated from each other at 2mm. Both the amplitude method and the phase one were insensitive to the inhomogeneity of this kind. It is known that the resonance methods make it possible to increase the sensitivity of the radio-wave method. The quasi-optical open resonators (OR) are effectively used in millimeter wavelength band. It allows to increase the phase sensitivity as

$$\frac{\Delta \varphi_s}{\Delta \varphi} = 1 + \frac{\lambda Q}{2\pi d}, \quad (1)$$

where  $Q$  is the quality factor,  $\lambda$  is the working wavelength,  $L$  is the situation between the OR reflectors. However, the use of the ordinary OR in this case will be limited by the resonance field cross-section size which is more than  $3 \lambda$  even in the gauss bunch throat. Therefore, the stronger focusing of the resonance field is required. The field of that kind can be formed in the short-focus OR.

The symmetric short-focus OR was used in the experiments. The resonator is formed by the spherical reflectors with a steepness radius of  $R = 3.6 \lambda$  and an aperture radius of  $J = 2.3 \lambda$  and it is incorporated in the two-channel interferometer scheme. In an optimized OR the field size on the matrix surface is  $W \approx \lambda$  at 72GHz when the basic mode is excited with  $Q = 2.3 \times 10^3$ .

In Fig.1 the obtained results are shown. As is seen, the amplitude measurement method does not permit to record the inhomogeneities within the matrix (see Fig.1a). If we use the phase measurement scheme, with the phase information being transferred from the EHF-band to the low frequency using the Doppler frequency shifter, then film radio-pictures have a fine resolution (see Fig.1,b). One can see that the film contours are washed away when the radius  $W$  of the probing resonance bunch is increased (see Fig.1,c) and when the value  $W \approx 2.5 \lambda$  (such as in the quasi-optical OR) the radio-pictures are transformed into a certain inhomogeneous formation (see Fig.1,d).



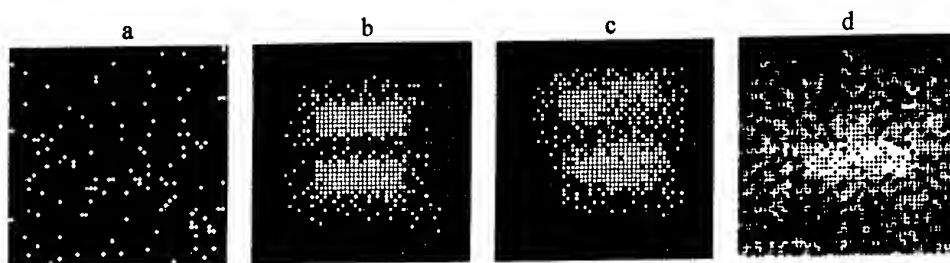


Fig.1. Amplitude (a) and phase (b,c,d) field pictures of the dielectric matrix within the "phase" inhomogeneities at 72GHz.

With the transition to the 3-d channel interferometer it is possible to obtain additional information about the local "phase" inhomogeneities with the small anisotropy  $\varepsilon$ , which can not be determined by the well-known Rayleigh criterion [3]. The oriented polyethylene film with a thickness of  $h=0.03\lambda$  was placed in one of the matrix cell. The coupling element in the receiving OR reflector was isotropic to the resonance field polarization. A measurement scheme was calibrated on the linear field polarization in the OR when the matrix was absent (see Fig.2,a). This linear polarization is retained when the resonance curve is being scanned and when the

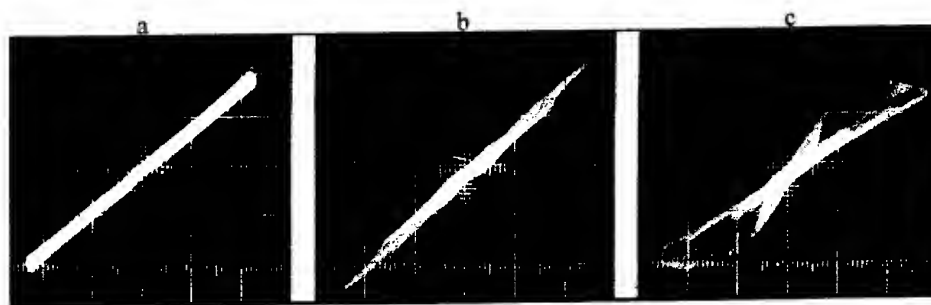


Fig.2. Polarization change during the transition of the resonance curve: a - the empty OR, b - isotropic sample within OR, c - anisotropic sample within OR.

homogeneous matrix part is in the OR (see Fig.2,b). If the film occurs in the field "spot", the picture is transformed and shows the double-ray refraction effect within the system (see Fig.2,c). The anisotropy is determined from the following expression:

$$\left| n_{\perp} - n_{\parallel} \right| = \frac{\Delta\varphi L}{h} \left( \frac{2\pi L}{\lambda} + Q \right)^{-1}, \quad (2)$$

where:  $n_{\perp}, n_{\parallel}$  are the diagonal elements of the permittivity tensor of the sample under investigation,  $\Delta\varphi=12^\circ$  is the phase shift between the orthogonal components of the vector  $\mathbf{E}$ . In our case the anisotropy is equal to  $1.08 \cdot 10^{-2}$  for the following OR parameters:  $Q=2.3 \cdot 10^3$ ,  $L=3.6\lambda$ .

#### References

1. A.A.Vertiy, I.Ya.Gudym, I.V.Ivanchenko, Yu.V.Karelin, N.A.Popenko, Instruments and Experimental Techniques. 38, No.3, 355 (1995).
2. R.J.Primich, R.A.Hayami, IEEE Trans. Microwave Theory and Techn. 12, No.1, 33 (1964).
3. M.Born, E.Wolf. Principles of Optics. - Pergamon Press, 1964.

# Off-Axis Expansion Solution of Laplace's Equation: Application to Accurate and Rapid Calculation of Coil Magnetic Fields

Robert H. Jackson

Vacuum Electronics, Code 6840  
Naval Research Laboratory  
4555 Overlook Avenue S.W.  
Washington, D.C. 20375-5347, USA

## Abstract

A flexible algorithm for calculation of general off-axis magnetic fields is presented. The technique employs a partial power series decomposition of Laplace's equation where the series coefficients are derivatives of the on-axis field. Analytic on-axis formulas are available for four *basic* coils: loop, annular disk, thin solenoid and full coil. High order analytic derivatives have been developed for each of these permitting highly accurate off-axis field calculations for a variety of magnetic systems. Comparisons of this formulation with simulation codes will be presented for coils and PPM stacks.

## Introduction

Knowledge of a Laplace solution on a subset of a region can be used to obtain the solution throughout the entire (source free) region. Starting with the equations for the fields, the technique proceeds in the following manner. (Also, see the derivations in [1-4].)

$$\nabla^2 \Phi(x) = 0 \quad (1)$$

$$\mathbf{F} = -\nabla \Phi(x) \quad (2)$$

Instead of representing  $\Phi$  in the usual complete power/Fourier series decomposition, it is decomposed as a partial power series with unspecified functional coefficients.

$$\Phi(x) = \sum_{n=0}^{\infty} A_n(x_1, x_2) x_3^n \quad (3)$$

The Laplacian is split into a "normal" component (e.g. in  $x$  or  $r$ ) in which the solution dependence is unknown and a "planar" component (e.g. in  $z$ ,  $x$ - $y$ ,  $r$ - $z$ ) in the coordinates containing the known solution.

$$\nabla^2 = \nabla_n^2 + \nabla_p^2 \quad (4)$$

Substitution of Eqs. (3) and (4) into Eq. (1) yields the following result.

$$\sum_{n=0}^{\infty} [A_n(x_1, x_2) \nabla_n^2 \{x_3^n\} + \nabla_p^2 \{A_n(x_1, x_2)\} x_3^n] = 0 \quad (5)$$

Performing the "normal" partials in the first term leads to a recursion relating  $A_{n+2}$  and the "planar" derivative of  $A_n$ . This recursion can be solved to give an explicit expression for  $A_n$  in terms of multiple applications of the planar Laplacian to either  $A_0$  or  $A_1$ . In cylindrical coordinates the directions are  $r$ -normal and  $z$ -planar. The coefficients resulting from application of Eq. (5) in cylindrical coordinates combined with Eqs. (3) and (2) produce the equations below for the axial and radial field components, where  $f_0$  is the on-axis field.

$$F_z(r, z) = \sum_{n=0}^{\infty} (-1)^n \frac{f_0^{(2n)}(z)}{2^{2n} (n!)^2} r^{2n} \quad (6)$$

$$F_r(r, z) = \sum_{n=0}^{\infty} (-1)^{n+1} \frac{f_0^{(2n+1)}(z)}{2^{2n+1} n! (n+1)!} r^{2n+1}$$

An expression for the vector potential is obtained through the usual flux-contour integral relationship.

$$A_\theta(r, z) = \sum_{n=0}^{\infty} (-1)^n \frac{f_0^{(2n)}(z)}{2^{2n+1} n! (n+1)!} r^{2n+1} \quad (7)$$

Implementation on early digital computers showed serious instabilities [3]. However, the results in [4] showed that this was caused by implementation issues and not by inherent problems with the technique.

## Cylindrically Symmetric Magnetic Coils

The basic cylindrical coils are shown schematically in Fig. [1]. The ideal current loop is the fundamental element. The other three coils can be built up from the loop by integration over the current distribution.

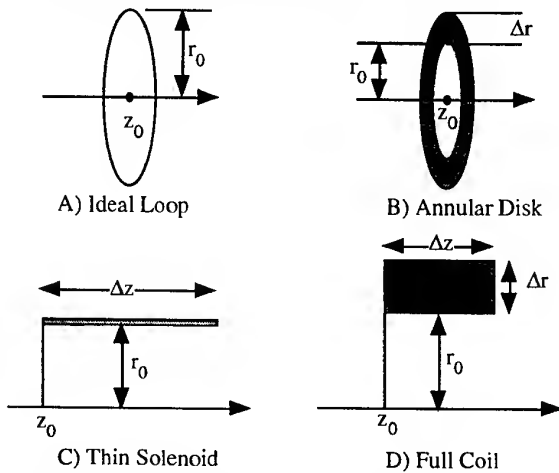


Figure 1. Schematic geometries for the four basic cylindrical coil types. Note that all of the on-axis field equations are referenced to the lower, left-hand corner source coordinates.

The on-axis field equations for the basic coils are:

1) Ideal Loop

$$B_z(0, z) = \left[ \frac{\mu_0 I}{2 r_0} \right] \frac{1}{(1 + x^2)^{3/2}}$$

2) Thin Solenoid

$$B_z(0, z) = \left[ \frac{\mu_0 J}{2} \right] \left[ \frac{x}{\sqrt{1 + x^2}} - \frac{(x - \eta)}{\sqrt{1 + (x - \eta)^2}} \right]$$

3) Annular Disk

$$B_z(0, z) = \left[ \frac{\mu_o J}{2} \right] \left[ \frac{1}{\sqrt{1+x^2}} - \frac{\rho}{\sqrt{\rho^2+x^2}} + \ln \left( \frac{\rho + \sqrt{\rho^2+x^2}}{1 + \sqrt{1+x^2}} \right) \right]$$

4) Full Coil

$$B_z(0, z) = \left[ \frac{\mu_o J r_0}{2} \right] \times \left[ x \ln \left( \frac{\rho + \sqrt{\rho^2+x^2}}{1 + \sqrt{1+x^2}} \right) - (x-\eta) \ln \left( \frac{\rho + \sqrt{\rho^2+(x-\eta)^2}}{1 + \sqrt{1+(x-\eta)^2}} \right) \right]$$

Where dimensions are normalized as shown below.

$$x = \frac{z-z_0}{r_0}, \quad \eta = \frac{\Delta z}{r_0}, \quad \rho = \frac{r_0 + \Delta r}{r_0}$$

Expansion solutions, Eqs. (6) and (7), require high order derivatives of the above on-axis formulas. This is accomplished by analytic differentiation of the normalized component [denoted by  $b(x)$ ] of each equation. For the loop, computing the first few derivatives by "hand" indicates that the  $n^{\text{th}}$  derivative of  $b(x)$  can be put into the general form [4]:

$$b^{(n)}(x) = \frac{P_n(x)}{\sqrt{1+x^2} (1+x^2)^{n+1}} \quad (8)$$

$$P_{n+1} = (1+x^2)P_n' - (2n+3)xP_n$$

Starting with the known on-axis equation,  $P_0 = 1$ , Eqs. (8) provide the means to generate derivatives of the loop equation to any desired order. (Note that the ' indicates differentiation with respect to the argument.) With some modifications, the same technique works for the annular disk on-axis equation. Rewrite the disk on-axis formula as:

$$B_z(0, z) = \left[ \frac{\mu_o J}{2} \right] (b(x) - b(\xi) - \ln(\rho)) \quad (9)$$

where  $\xi$  is related to  $x$  by

$$\xi = \frac{x}{\rho} = \frac{(z-z_0)}{\rho r_0} = \frac{(z-z_0)}{(r_0 + \Delta r)}$$

and where the normalized function  $b$  is given by

$$b(x) = \frac{1}{\sqrt{1+x^2}} - \ln(1 + \sqrt{1+x^2}) \quad (10)$$

Applying the loop technique to Eq. (10) results in:

$$b(x)^{(n)} = \frac{P_n(x)}{(\sqrt{x^2+1}+1)^n (x^2+1)^n} + \frac{Q_n(x)}{\sqrt{x^2+1} (\sqrt{x^2+1}+1)^n (x^2+1)^n} \quad (11)$$

As above,  $P_n$  and  $Q_n$  must satisfy recursion relations, which are shown below.

$$P_{n+1}(x) = (x^2+1)(P_n' + Q_n') - x(2nP_n + (3n+1)Q_n) \quad (12)$$

$$Q_{n+1}(x) = (x^2+1)((x^2+1)P_n' + Q_n') - x((3n(x^2+1)P_n + (2n+1)Q_n))$$

Using Eqs. (9), (11) and (12), it is possible to generate derivatives of the annular disk function to any desired order [4]. It appears that the derivatives for the solenoid and full coil remain to be computed.

However, it can be demonstrated [4] that the solenoid and full coil derivatives are closely related to the loop and disk derivatives respectively. The appropriate relations will simply be stated here.

Thin Solenoid:

$$b^{(n+1)}(x)|_{\text{solenoid}} = b^{(n)}(x)|_{\text{loop}} - b^{(n)}(x-\eta)|_{\text{loop}}$$

Full Coil:

$$b^{(n+1)}(x)|_{\text{coil}} = \left[ b^{(n)}(x)|_{\text{disk}} - b^{(n)}(\xi)|_{\text{disk}} \right] - \left[ b^{(n)}(x-\eta)|_{\text{disk}} - b^{(n)}(\xi - \frac{\eta}{\rho})|_{\text{disk}} \right]$$

We are now in possession of high order analytic derivatives of all four basic cylindrical coil types.

### Analytic and Numeric Comparisons

The figures below compare expansion solutions with full coil, Fig 2, and PPM stack, Fig. 3, simulations (only half of the simulation points are shown.)

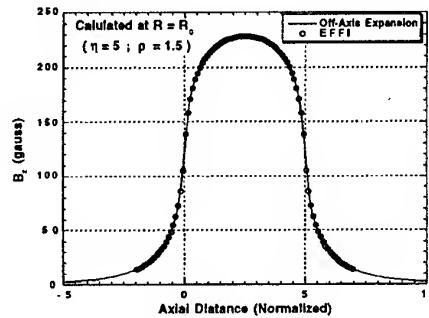


Figure 2. Coil comparison with the EFFI code.

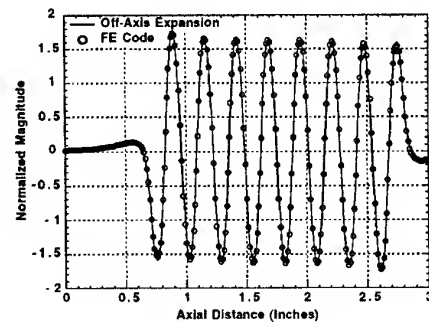


Figure 3. PPM comparison with an FE code,  $r/r_0 = 0.65$ .

### References

1. See Sections 13.2 and 14.2 in *Vacuum Tubes*, K. R. Spangenberg, McGraw-Hill (1948).
2. P. S. Farago, *Free-Electron Physics*, Penguin Books (1970).
3. J. R. Vaughan, IEEE Trans. Electron Devices, **ED-19**, 144-151 (1972).
4. R. H. Jackson, "Off-Axis Expansion Solution of Laplace's Equation: Application to Accurate and Rapid Calculation of Coil Magnetic Fields," submitted to IEEE Trans. Electron Devices.

# THE FEATURES OF THE SMOOTH ANODE MAGNETRON OPERATING IN A MODE CLOSE TO THE CRITICAL

O.P. Kulagin

Usikov Institute of radiophysics and electronics of National Academy of Sciences of Ukraine, 310085, Ukraine, Kharkov, Ac.Proscura St., 12,  
fax: 0572-441105, e-mail: eremka@ire.kharkov.ua.

## Abstract

The processes in the cylindrical magnetron with smoothbore anode, operating in a mode close to critical, have been considered. The investigation shows, that space charge in the system is the active nonlinear medium. The equations, describing the excitation of oscillations in this medium, have been derived. The autosoliton solution for the system is obtained. The results allow to take a new look into mechanism of generation of mm oscillations in the magnetron with surface wave.

## I. Introduction.

The conventional (classical) magnetrons generate with the operating magnetic field  $H > H_k$  (here  $H_k$  is the critical magnetic field). At the same time, oscillations of the cyclotron-frequency type are described. These oscillations take place in the magnetrons with smoothbore anode with  $H \sim H_k$ . It is noted in the literature that this type is of no practical interest [1,2,3].

On the other hand, over the last decades significant results were obtained on the millimeter wave generators - the surface wave magnetrons (SWM) which operate directly with  $H \sim H_k$  and with the very high experimentally confirmed values of efficiency [4]. Probably, in these devices some other mechanism of electron-wave interaction is realized, which differs from the traveling wave type oscillations in the conventional magnetrons. In order to understand this mechanism, it is seems necessary to analyze in more detail the processes in a smooth anode magnetron with  $H \sim H_k$ . Just this topic is the aim of the work.

## II. The equivalent distributed line.

The experiment conducted on the cylindrical magnetron with slots cutted in the cavity showed the following [5]: in the case, where the disturbing potential  $\Delta\varphi$  is applied to one of the anode segments, the difference in current between the segments may be approximate as (here  $S_1, S_2$  are the coefficients of approximation):

$$\Delta I = -S_1 \Delta\varphi + S_2 \Delta\varphi^3 \quad (1)$$

Thus, the space charge in a region between the cathode and anode is the active nonlinear medium. It is necessary to note that these results were obtained under the condition when the generation of usual magnetron oscillations of resonance type does not arise. Basically, this case is equivalent to the cylindrical magnetron with a smoothbore anode in which the space charge is exposed to some disturbance. Accordingly, in this case the magnetron may be presented by following equivalent distributed line (fig.1):

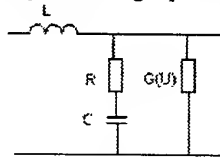


fig.1

where  $G(U)$  is the nonlinear conductivity of the medium between the anode and the virtual cathode of the magnetron,  $C$  - is the capacity of this medium,  $L$  - is the inductivity of the anode,  $R$  - are the high frequency losses (all above-mentioned values are related to the unit of length).

## III. Analysis of the theoretical model.

The system of equations describing propagation of the oscillations in the above-noted line, has the following form:

$$\frac{\partial U}{\partial x} + L \frac{\partial I}{\partial t} = 0; \quad \frac{\partial I}{\partial x} + \frac{\partial Q}{\partial t} + G(U)U = 0; \quad \frac{\partial U}{\partial t} = \frac{1}{C} \frac{\partial Q}{\partial t} + R \Delta x^2 \frac{\partial^2 Q}{\partial t^2}; \quad (2)$$

where  $x$  is the direction of the electron drift,  $\Delta x$  is the characteristic length of disturbance,  $Q$  is the charge, related to the unit of length,  $U$  is the potential of disturbance,  $I$  is the current of disturbance,  $G(U) = -g + g\gamma U^2$  (we designate  $\frac{S_1}{\Delta x} = g$ ;  $\frac{S_2}{\Delta x} = g\gamma$ ).

We will seek for the solution of the system in the form of the wave, for which the correlation is justified:

$$I \approx \sqrt{\frac{C}{L}} U ; \quad \frac{\partial}{\partial t} = -\frac{1}{\sqrt{LC}} \frac{\partial}{\partial x} \quad (3)$$

(we assume that nonlinearity caused by the conductivity  $G(U)$  is compensated by the dissipation processes) In the case, which is of some interest for us, the dissipation is completely compensated by the positive feedback. Proceeding from this, one can obtain the solution of the initial system of equations (2), having the form of the stationary solitary wave relating to the separatrix on a phase plane:

$$U = \mp \sqrt{\frac{1}{\gamma}} \operatorname{th} \left[ \sqrt{\frac{gL}{2RC}} \frac{1}{\Delta x} \left( x - V_0 t \mp \frac{\Delta x}{2} \right) \right] \quad (4)$$

The signs "-" and "+" in the obtained solution correspond to the front and back part of disturbance. The wave determined by (4) is the autosoliton - the disturbance auto-supported by the system positive feedback [6]. The autosoliton parameters are completely defined by the system parameters and are not dependent upon the character of some external disturbance. At first sight, (4) seems to be one of the particular solutions. However, the essential peculiarity of this solution is that different nonstationary disturbances in the analyzed system, as they are being evolved, are closely approximate to the autosoliton shape. The quantity of emerging autosolitons is determined from the condition of a complete compensation of losses by the feedback.

#### IV. Conclusion.

Are the obtained solutions of any practical interest? As we previously noted, there are some experimental data on the low efficiency of generation in the smoothbore anode magnetrons [3]. However, all these data were obtained when the conditions of the two-flow state of an electron cloud were realized in the magnetron. At the same time, in the SWM which also operate with  $H \sim H_k$ , but demonstrate a very high efficiency in the mm-wave band, the one-flow state occurs. This state is characterized by the relatively higher space charge density and by the negligible dispersion of electron velocity, which, to a large extent, is inherent to the two-flow state (the electron cloud is the current tube rotating around the cathode and the electron flow is approximate to the laminar type) [4,7]. It goes without saying that in this case a higher efficiency of the autosoliton regime is available.

The high efficiency of the SWM should be directly attributed to the fact that the nonlinear system constituted by the space charge and the anode resonator system, which are equally important to these millimeter wave generators, do not appear to be competing with each other during the oscillation generation process, but, on the contrary, successfully interact. So, one is led to the conclusion that the subsequent investigations in this field may be useful for improving the generation mechanisms for mm and sub-mm bands.

#### V. References.

1. V.N. Shevchik, G.N. Shvedov, A.V. Soboleva. The wave and oscillating phenomena in electron flows on the super high frequencies. Saratov: Published by Saratov university. 1962 - 335p.
2. W.H. Louisell. Coupled mode and parametric electronics. New York-London, Wiley, 1960 - 351p.
3. I.V. Lebedev. Technics and devices of super-high frequencies. v.II: The electron vacuum devices of super-high frequencies. Moscow: High school. 1972 - 376p.
4. A.Ya.Usikov, E.A.Kaner, I.D.Truten and others. Electronics and radiophysics of millimeter and submillimeter waves - Kiyev: Naukova dumka. 1986 - 368p.
5. G.Ya.Levin, A.Ya.Usikov., S.N.Terekhin, O.P.Kulagin. Solitons and autosolitons in magnetrons. //Preprint of IRE NAS of Ukraine, №94-1, Kharkov, 1994, 16p.
6. B. Kerner., V. Osipov. Autosolitons. - Moskow.: Nauka, 1991.- 200p.
7. G.Ya.Levin. The theory of the surface wave magnetron. // Preprint of IRE NAS of Ukraine, №240, Kharkov, 1984, 40p.

# MILLIMETER-WAVE COLD-CATHODE COAXIAL TWT

Victor D. Yermka, Maxim O. Khorunzhiy

The Usikov Institute of Radiophysics & Electronics of the National Academy  
of Sciences, 12, Acad. Proskura st., 310085, Kharkiv, Ukraine

Tel.: 38-0572-448-519. Fax: 38-0572-441-105.

E-mail: eremka@ire.kharkov.ua

## ABSTRACT

A description is given of the TWT design comprising a slow-wave structure (formed by spiraling round, coaxially arranged, slotted waveguides into a helix), a cold-cathode electron-optical system responsible for producing a tubular electron beam and a magnetic focusing system. Numerical simulation is employed to analyze the TWT power and frequency responses. It is suggested that a high-power source operating in the mm-wave range can be developed.

## 1. INTRODUCTION

The merits and limitations of the standard waveguide spiraled into a helix and utilized in the TWT as a SWS were first positively appraised by V. Valterson [1]. In the modified helical waveguide which was used as the SWS of the MW amplifier the circular slot for the tubular electron beam was provided in its wide wall [2,3].

## 2. DISCUSSION

The findings of an investigation into this SWS in the TWT suggest that an effective amplification can be achieved in a limited frequency range due to the backward wave excitation. The electron-backward wave interaction occurs with the TWT self-excitation and the deterioration of its amplifying properties. One of the major shortcomings of the SWS is the low coupling impedance. Therefore we had to make an extensive search for a suitable SWS circuit incorporating a spiraled waveguide built on a new concept [4]. We have utilized two round-shaped, slotted helical and coaxially arranged waveguides placed opposite each other, which served the purpose of the SWS of the mm-wave TWT. The frequency range at which the wave-guiding properties of such an electrodynamic system remain unchanged is on a par with that of the standard rectangular waveguide [4]. The input and output of the signal being amplified in the SWS of the experimental TWT breadboard are provided by the standard rectangular waveguide with transitions to a round-shaped waveguide. The amplifier signal input and output are matched to the load.

A study has been made into the forced oscillation in the two electromagnetic-field coupled slotted cylinders that were spiraled into a helix and coaxially arranged. The strongest coupling between the cylinders occurs with  $\delta \leq \lambda/4$  and is featured by a high Q-factor for one of the four split-type oscillations. Thus, with a specified Q-factor there is a possibility of selecting the optimal parameters of the TWT electrodynamic system. In this paper the results obtained from evaluating the SWS parameters for the experimental TWT specimen are given.

The cold electron emitters with a circular emitting surface which could be conceptually utilized to develop high-power mm-wave sources are currently being explored. In order to be able to produce the tubular electron beam in the laboratory breadboard model of the coaxial TWT the EOS having a matrix metal-point field emission cathode has been employed [5].

The computer simulation indicated that the limitation of the diode EOS comprising the matrix metal-point field emitter was the low focusing effectiveness ascribed to the significant transverse electron velocity components. The solid flare angle of electron microjets from the point tip surface of 1-2 steradians the trajectory slopes of the boundary beam electrons are equal to  $30^\circ - 45^\circ$  whereas the corresponding quantity of the transverse velocity  $v_\varphi$  becomes commensurate with the longitudinal component  $v_z$  of the electron motion velocity ( $\bar{v}_\varphi / \bar{v}_z \approx 0.5-1.0$ ). The above-cited magnitude of the velocity components ratio is more than 10 times less than that of the electron beams produced by the EOS with hot cathode. The effectiveness of the electron beam in the magnetic field can be evaluated from the magnitude relation of the root-mean square transverse  $\bar{v}_\varphi$  to the longitudinal  $\bar{v}_z$  velocity components  $\bar{v}_\varphi / \bar{v}_z$ . In the EOS with thermionic cathode the magnitude  $\bar{v}_\varphi / \bar{v}_z \leq 0.1$ , which provides for good quality focusing and the  $\approx 100\%$  passage of current. With an ideally focused electron beam (the parallel electron trajectories in an output anode plane)  $\bar{v}_\varphi / \bar{v}_z = 0$ . The

computer simulation of the EOS comprising the matrix metal-point field cathode and represented by the coaxial TWT with the selected electrode geometry and the magnitude of their voltages indicates that the transverse electron velocities in an output anode plane are equal to  $\bar{v}_\phi / \bar{v}_z < 0.1$  and, consequently, the electron beam is effectively focused by the MFS magnetic field which is used to focus the electron beam from the thermionic cathodes.

An additional advantage of the above-mentioned EOS is its high cost-effectiveness the sharp current-voltage curve, the possibility of providing a low-voltage current modulation for the 0control electrode and the first anode, an inertialess response of the current to the voltage variations, a high beam-current density ( $100 \text{ A/sm}^2$  and up).

In selecting the size of the interaction gap we proceed from the assumption that the electron transit angle in it is equal to  $2\beta \bar{v}_z < \pi/2$ . All the coils of the coaxial spiraled waveguides are expected to be identical and in the helical interaction gap  $2\vartheta$  the electrons meet the waves in one and the same phase. The relation for the electron transit angle  $\Theta$  between the gap of the two coils is given as

$$\Theta = 2\pi m, \quad (1)$$

where  $m$  is the number wavelengths being laid along the coil. Using (1) we find that the pitch  $L$  of the helical waveguides is determined from the relation

$$L/\lambda = m\sqrt{U_0}/505. \quad (2)$$

The 3-mm-wave TWT parameters were calculated by using the methods described in [5] for the width of the electron beam channel ( $\delta = 0.32 \text{ mm}$ ) with the channel occupations coefficient 0.6 and the electron beam current  $0.8 \text{ A}$ ,  $m=19$  for the average frequency of the amplification band being equal to 10%. The design value of the output signal average power was  $2 \text{ kW}$  at an operating voltage of  $10 \text{ kV}$ . The output signal corresponded to the  $20 \text{ dB}$  amplification. In the paper the electron efficiency value  $\eta_e$ , dissynchronism  $b$  and the length of the spiraled waveguides are graphically plotted against the Pierce parameter.

### 3. CONCLUSION

The first estimates that were made of the capabilities of the mm-wave TWT incorporating the mm-wave SWS formed by two cylindrical slotted helical and coaxial waveguides and of the EOS with a cold-field cathode testify to the fact that the development of high-power TWTs would offer great advantages.

### REFERENCES

1. B. Valtersson, Numero Special du Congres Tubes Hyperfrequences (Paris, France). 1956.
2. S. Ahn, A. Ganguly, IEEE Trans. on Electron Devices. Vol. ED-33, N9. -P.1348-1355(1986).
3. I. A. Man'kin, B. L. Usheronich, J. of Communications and technology & Electronics. V34, N11, -P.2366, (1989).
4. V. D. Yermka, Proc. SPIE. Vol. 1929. -P. 446-447.
5. USSR Pat. N1079096. Cl. H01J3/02 Electron gun/I. I. Golenitskiy, V. D. Yermka, R. I. Zacharova. et. al. (1983).

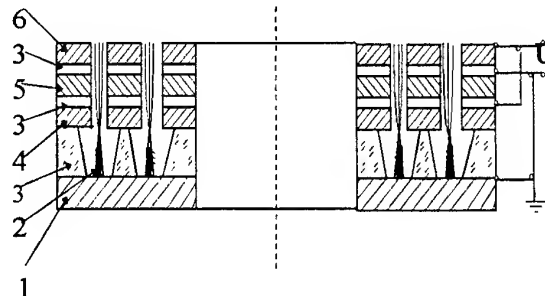


Fig. 1. Plot of electron gun.

1-substrate; 2-edge field emitter; 3-insulator; 4-first anode;  
5-focusing electrode; 6- second anode.

# THE MM-WAVE COLD CATHODE PENIOMAGNETRON

Victor D. Yermka

Usikov Institute of Radiophysics & Electronics of National Academy of Sciences of Ukraine,  
12, Acad. Proskura st., 310085, Kharkiv, Ukraine.  
Tel.: 38-0572-448-519. Fax: 38-0572-441-105.  
E-mail: yermka@ire.kharkov.ua

## ABSTRACT

The distinctive features of the peniotron device - a millimeter wave source with a peniotron mechanism of the electron-wave interaction on the high harmonics of the cyclotron frequency are considered. This device uses an adiabatic electronic-optical system (EOS) with a cold cathode. The EOS generates a large-orbit helical electron beam which releases the energy to the high frequency (HF) field in the space interaction of the source electrodynamic system (EDS). The EDS represents a coaxial cavity based on the round-shaped waveguide with an azimuthal periodic vane structure and slot-type resonators (magnetron waveguide). The scheme of the source makes it possible to operate in the modes of through gyroresonance or autoresonance. The first results of the investigation into the cold-cathode electron gun holds a greater promise for the devices based on such a system.

## 1. INTRODUCTION

The high performance of the peniotron mechanism of the electron-wave interaction of the high harmonics of the cyclotron frequency has been theoretically and experimentally demonstrated [ 1-3 ]. As part of an experiment the scheme of the highly efficient gyroresonance device has exhibited a good advantage offered by following three attributes:

- a) a magnetron waveguide with an axially directed rod (which provides the mode selection with a required azimuthal index);
- b) a peniotron interaction mechanism (which makes for the equality of all beam electrons);
- c) the mode of through gyroresonance (which helps achieve a high electronic efficiency). We have called this type of the device a «peniomagnetron» [ 2 ].

A possibility of developing the peniomagnetron with an EOS comprising a non-heated («cold») cathode is discussed below. This paper is the result of the conceptual evolution in [ 4 ].

## 2. ADIABATIC ELECTRON-OPTICAL SYSTEM

The power characteristics of the gyrodevices with a peniotron interaction mechanism, which operate on the high cyclotron frequency harmonics in oscillation and amplification modes, are largely dependent upon the EOS parameters that generate a thin-walled, tubular monohelical (rotating with a cyclotron frequency with respect to the system axis) electron beam (EB) with a high level (>70%) of rotational energy. The results of the studies on the EOS with a termionic cathode for peniotrons have been previously presented in [5].

The analytical relations given in [5] were the main criteria for selecting the parameters of a tree-electrode cold-cathode gun. These criteria were implemented by the computer simulation of the EOS and the magnetic focusing system (MFS) and by matching the gun with the magnetic field in the interaction space to reduce the radial EB pulsations. The construction of the gun (Fig.1) incorporates a cathode assembly with the ring-type emitting surface (RTES) 1, the focusing electrodes 2,3, the accelerating electrode 4, the matching electrode 5 and the anode 6. The matching electrode 5 ensures that the tubular EB is electrostatically focused to a certain degree and consistent with the magnetic field when there is a slight rise in the field (around 0.5 T/mm) in a transition region. The accelerating electrode 4 provides the prescribed magnitude of perveance. The focusing electrode 2 is combined with a field disc edge emitter (FDEE) made from refractory metal. The ring-type emitting surface is manufactured from the material having a high secondary electron emission factor  $\delta > 1$ . With a voltage pulse being fed across the electrodes 1 and 2 there occurred the pulse of the field emission current. The secondary electron emission process proceeded at the beginning of each anode voltage pulse with a duration of 0.5 to 3  $\mu$ s between the electrodes 1 and 4. The main current of the monohelical EB is set up by the secondary-emission electrons. A possibility of utilizing the chemically pure metals Pt, Mo, Ni, etc. as the materials for the ring-type emitting surface (RTES) has been examined. A comparison of the primary-emission electrons current to the FDEE and the secondary-electron emission current to the RTES indicates that their multiplication factor is on the order of  $10^3$ . To form the FDEE a technique for low-temperature metal evaporation has been employed [6]. A study on the FDEE made from Mo, Cr, W, Nb is currently being performed.



### 3. PENIOTRON INTERACTION MECHANISM IN STATIC CROSSED FIELD

The peniotron mechanism may probably occur in static electric and magnetic crossed fields [ 4 ]. Consider the electron-wave interaction in a coaxial waveguide with a longitudinal rib-type periodical structure in which the field of the electromagnetic wave, having azimuthal variations, is rotating counter clockwise (fig.2). The central coaxial is integrated with a secondary-emission cathode. The EOS forming the tubular EB is mounted at one end of the coaxial waveguide whereas the electron collector is placed at the other end. The central EOS pin has a galvanic connection with a secondary-emission cathode. The thin tubular EB formed by the EOS receives the cyclotron rotation by the static magnetic field reverse, placed at the input to the coaxial waveguide [ 4 ]. The EB also rotates counter clockwise under the action of the radial electric,  $E$ , and the axial magnetic,  $B$ , static fields. The particles outrun the wave for one period of its azimuthal variations for one revolution about the axis of the system. In this case the electric high frequency (HF) field is sensed by electrons as the complementary static electric field  $E$  of linear orientation.

This is a good indication that even in crossed fields the electron-wave and related peniotron interactions can be observed. A study into the possibility of integrating the positive features of magnetron - and peniotron-type interactions in the above-described device (peniotron) has been made. A large-orbit EB is injected into the peniomagnetron interaction space, and in this case the beam tube thickness is chosen as sufficient for its electrons to be involved in both of the parallel processes. A layer of electrons adjacent to the periodic structure provides an effective electron - wave interaction which is characteristic for the peniotron. In the region close to the system axis the drift of the electron-orbit driving centers is conducive to the electron bombardment of the secondary-emission cathode and the formation of the secondary-electron beam interacting with the HF-field in peniotron and magnetron modes. In this case by selecting the parameters of the electric and magnetic fields the secondary electrons can be phase-sorted in such a way as to get the latter involved in the effective energy exchange with the HF-field.

The design pulse of the devices output power is equal to 50 KW with an efficiency of 40% at a frequency of 100 GHz with a pulse operating voltage amplitude of 14 KV and a magnetic field strength of 0.36T on a 10-th cyclotron harmonic.

### 4. CONCLUSION

The combined peniotron and magnetron interaction mechanisms in a single system may appear beneficial in developing the efficient oscillators and amplifiers that are operated in short-wave bands.

### REFERENCES

1. Yermka V. D., Zhurakhovsky V. A., Shestopalov V.P., Journal of Communications Technology and Electronics, V.33, N9, 1900 (1989).
2. Yermka V.D., Zhurakhovskij V.A., Kovalenko A.M. ICMWFT'90. Sapl. Conf. Dig.-1990. Beijing, China. -P.52 (1990).
3. Ishihara T., Tadano H., Shimawaki H., e.a. IEEE Trans. on Electron Devices, V.43, N5, 827 (1996).
4. Yermka V.D., Zhurakhovskij V.A., Kulagin O.P. APMC'96, Conf. dig., New Delhi, India, P.282 (1996)
5. Yermka V.D., Golenitskiy I.I., Djubua B.Ch., e.a. ICMWFT'92. Sapl. Conf. Dig.-1992. Beijing, China. - P.351 (1992).
6. Dranova Zh., Yermka V.D., Mazilova T.I., Mikhailovskij I.M., Velikodnaya O.A. Conf.Dig. 9-th Int. Vacuum Microelectronics Conf. St.Petersburg.-P.169 (1996).

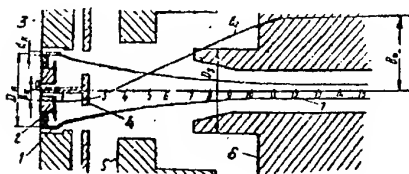


Fig.1

1-secondary-electron emission cathode; 2,3-focusing electrodes; 4-accelerating electrode; 5-matching electrode; 6-anode.

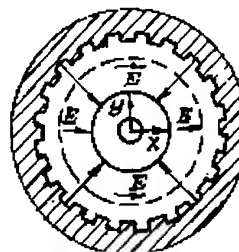


Fig.2.

Cross-section of the peniomagnetron interaction space

## Free Electron Maser Amplifier Experiments

C.G. Whyte, D.A. Jaroszynski, W. He, A.W. Cross, K. Ronald and A.D.R. Phelps

*Department of Physics and Applied Physics,  
University of Strathclyde,  
Glasgow, G4 0NG, Scotland.*

### Abstract

We present the initial experimental results from the Strathclyde Raman Free Electron Maser (FEM) amplifier experiment. The Free-electron Maser (FEM) has been designed to operate over a wide frequency range. Initial experiments will demonstrate high gain at 9.5GHz using a pulsed magnetron as the input source. Experiments are under way to demonstrate large bandwidth tunability using a broadband TWT.

### Introduction

FEM's with an axial guide magnetic field are one of the promising sources of powerful coherent radiation in the microwave, millimetre and sub-millimetre wavelength range. High efficiency (25%) operation of such devices was achieved by [1,2] in regimes with a reversed guide field when the cyclotron rotation of the beam electrons and their rotation imposed by the helical wiggler have opposite directions. Prior to reversed guide field operation it was observed that when these rotations were co-directed i.e. forward guide field regime, the efficiency was limited to ~12%. Theoretical interest [3] and evidence presented by [4,5] shows that for an FEM driven by an ideal (without any spread of parameters) electron beam of the same energy and operating transverse velocity the efficiency will be approximately the same in both guide field regimes. Recent simulations by [6] demonstrate a strong dependence of FEM efficiency on the spread of beam parameters and this dependence is different for different guide field configurations. It has been shown that for reversed guide field regimes (more general, for regimes far from the cyclotron resonance) the quality of the electron beam formed in the slowly up-tapered wiggler entrance is better than in regimes close to cyclotron resonance. As a result, FEMs operating in the reversed guide field regime are rather insensitivity to the initial spread of beam parameters. In contrast, the conventional guide field regime close to cyclotron resonance is more sensitive to beam quality and the presence of initial parasitic transverse velocity, present in all real electron beams, leads to a significant drop in efficiency.

### Method

A reverse guide field FEM amplifier operating in the Raman regime has been designed and constructed at Strathclyde. The FEM amplifier is designed for a near

grazing intersection of the beam line and waveguide mode to optimise the frequency range of operation as shown in figure 1.

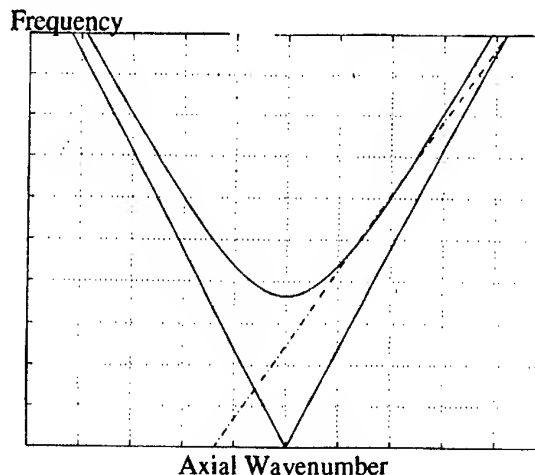


**Figure 1** Coupled dispersion diagram showing fundamental beam line with TE<sub>11</sub> cylindrical waveguide mode.

The maser may be tuned by either varying the beam voltage or by varying the undulator and guide magnetic field strengths. An undulator of more than 40 periods has been constructed to maximise gain. This will allow the investigation of the fundamental physical processes in the device in both the small signal and the saturated non-linear regimes when operating in the forward and reversed guide field regime.

The amplifier utilises DC solenoids to generate a maximum 0.3T guide field in the interaction region. DC field matching coils are used in the diode region, one of which has been clad in Maximag iron to maximise the on-axis field. The undulator consists of a bifilar helical coil of four 2mm diameter copper conductors wired with two pairs in parallel, each pair being connected in series to carry a maximum of 3kA per wire, or a total effective current of 12kA to give a maximum on axis field of 0.2T. The undulator magnetic field was tapered at the input by current return loops which have been used to reduce the effective current flowing in the undulator conductors stepwise over the first two periods. The undulator current is provided by an ignitron switched capacitor

bank charged to a maximum of 6kV, the discharge circuit is critically damped and produces a maximum peak current in excess of 7kA.

A quasi-resonant input coupler has been designed and cold tested in the laboratory and has a 2GHz bandwidth at 10GHz. In the final broadband device this input coupler design may be replaced by a quasi-optical design to achieve maximum bandwidth.

The high voltage power supply for the FEM consists of two four cable stacked Blumlein circuits which are charged positive and arranged to fire positive and negative to provide a maximum voltage of 300kV with a flat top pulse length of 100ns. The Blumlein cable pulser is switched using a field distortion triggered spark gap. The spark gap is triggered by a single 15ns trigger cable switched by a hollow anode thyatron. The cable is charged positive to 40% of the Blumlein charging voltage via a voltage divider on the main charging line. The thyatron is positioned at the charging end of the trigger cable, to produce a negative voltage pulse on the trigger electrode when the thyatron is fired. This has the additional benefit that any pulse appearing on the trigger electrode when the main spark gap fails will see the 50Ω cable in series with the thyatron and as a result the current loading on the thyatron will be reduced, moreover, as the thyatron has a hollow anode any reverse current demanded can be provided without damage to the switch. Due to the short (15ns) trigger pulse and the inherently low timing jitter (<5ns) of the thyatron, the timing jitter of the high voltage circuit of less than 20ns is more than adequate to ensure overlap of the 100ns high voltage pulse and the 1μs magnetron input power pulse.

A velvet cathode in a Pierce configuration gives a maximum beam current of 50A, representing 100% of the diode current. The electron gun diode has been modeled using a fully relativistic 2.5D code, including

space-charge effects, developed at Strathclyde. An example of these simulations is shown.

In the example no maximag cladding has been used on the diode coil and the on axis field at the cathode surface is therefore too low for optimal beam formation. However, the beam current for this example is still 53A.

As a velvet cathode electron gun is used in the experiments, the required vacuum is low and an O-ring sealed system pumped by a Diffstack can be used, the minimum base pressure in the system is approximately  $1 \times 10^{-7}$  mbarr.

The input power source was a 1μs pulse length, 25kW peak power magnetron operating at 9.5GHz. Future experiments will use a TWT to evaluate the broadband frequency performance of the system.

### Conclusion

Results will be shown for the Raman FEL amplifier performance. The measured small and large signal gain will be presented as well as cathode voltage, beam current, peak microwave output power, gain and efficiency.

### References

- [1] Kaminsky A.A., Kaminsky A.K., Rubin S.B. Particle Accelerators, 1990, vol.33, p.189.
- [2] Conde M.E., Bekefi G. Phys. Rev. Lett., 1991, vol.67 (22), p.3082.
- [3] Zhang SC and Elgin J., Phys Rev E, 1997, Vol 55, pp4684-4693.
- [4] Freund.H.P. & Antonsen.T.M. "Principles of free electron lasers" Second Edition 1996. ISBN 0 412 72540 1
- [5] Ginzburg N.S., Kaminsky A.K., Kaminsky A.A., Peskov N.Y., Sedykh S.N., Sergeev A.P., Sergeev A.S. International Workshop on High Power Microwave Generation and Pulse Shortening. Edinburgh, 10-12 June 1997.
- [6] N.Yu Peskov, N.S. Ginzburg, S.V. Samsonov, V.L. Bratman., Proc. of 19th Int. FEL Conf. Beijing, 1997.

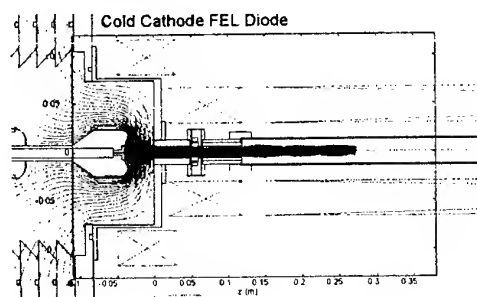


Figure 2 Schematic diagram of FEM electron optical system.

## Frequency-Broadband Gyrodevices Operating with Eigenwaves of Helically Rippled Waveguides

V.L.Bratman<sup>1)</sup>, A.W. Cross<sup>2)</sup>, G.G.Denisov<sup>1)</sup>, W. He<sup>2)</sup>, A.D.R.Phelps<sup>2)</sup>,  
K. Ronald<sup>2)</sup>, S.V.Samsonov<sup>1)</sup> and C.G. Whyte<sup>2)</sup>

<sup>1)</sup>Institute of Applied Physics, Russian Academy of Sciences  
46 Ulyanov St., Nizhny Novgorod, 603600, Russia

<sup>2)</sup>Department of Physics and Applied Physics, University of Strathclyde,  
Glasgow, G4 0NG, UK.

### Abstract

Helical corrugation of a circular waveguide coupling two partial rotating modes provides an unique dispersion for an eigenwave. This allows significant widening of the frequency bandwidth and increase in the efficiency for the gyro-TWT and gyro-BWO. The first experiments demonstrate high-efficiency operation.

### Introduction

The gyrotron traveling wave tube (gyro-TWT) and gyrotron backward wave oscillator (gyro-BWO) are known as wide-frequency-band varieties of gyrodevices. Due to the operation with electromagnetic waves having large group velocities, a gyro-TWT amplifier may have a wide instantaneous bandwidth while a gyro-BWO permits frequency tuning by varying the axial magnetic field or the electron beam voltage. For a microwave system in the form of a smooth cylindrical waveguide a large wave group velocity inevitably leads to a large axial wavenumber which makes these devices significantly more sensitive to particle velocity spread in comparison with a gyrotron. The most favorable wave dispersion for a gyro-TWT and gyro-BWO is that when the wave group velocity is sufficiently large and constant in the region of close-to-zero axial wavenumber. A similar dispersion can be realized in an oversized circular waveguide with a special helical corrugation of its inner surface [1].

### Helically rippled waveguides for gyro-TWT and gyro-BWO

The helical corrugation provides resonant coupling of two partial rotating waves of the smooth waveguide: a near-cutoff mode (A) with a small axial wavenumber and a traveling wave (B) with a large axial wavenumber (Fig.1). At properly chosen parameters of the corrugation, among eigenwaves  $W_{\pm}$  and  $W_1$  (Fig.1), which arise as a result of the coupling, the wave  $W_1$  has the desirable dispersion.

A theoretical analysis confirms attractive features provided by the use of the helical waveguides for gyro-TWTs and gyro-BWOs and demonstrates important advantages of the "helical" devices over the analogous "smooth" ones in sensitivity to electron

velocity spread, frequency bandwidth and stability to parasitic self-oscillations [2] (Fig.2). At present we are carrying out several experiments on helical gyro-TWT/BWOs with weakly (80 keV) and moderately (200 keV and 300-350 keV) relativistic electron beams. All the experiments have important common peculiarities.

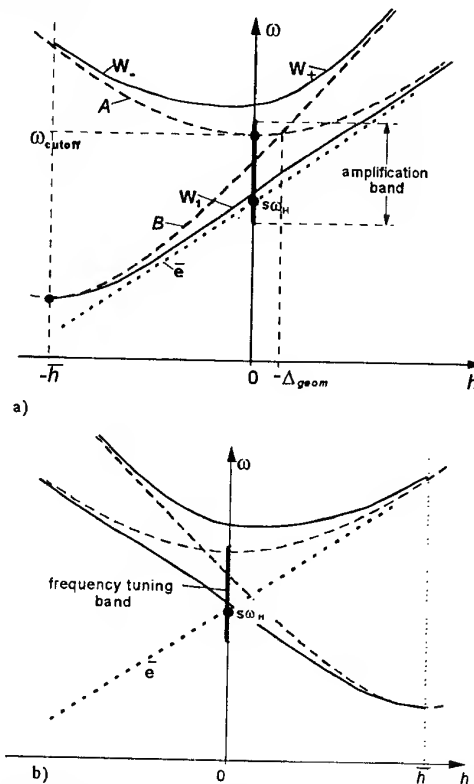


Fig.1. Wave dispersion diagram for a gyro-TWT (a) and a gyro-BWO (b) with helical waveguides.

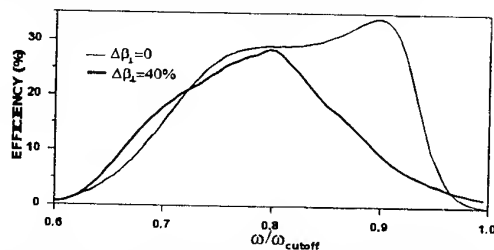


Fig.2. Simulated bandwidths for a 300 kV/80 A second harmonic helical gyro-TWT with various particle velocity spreads.

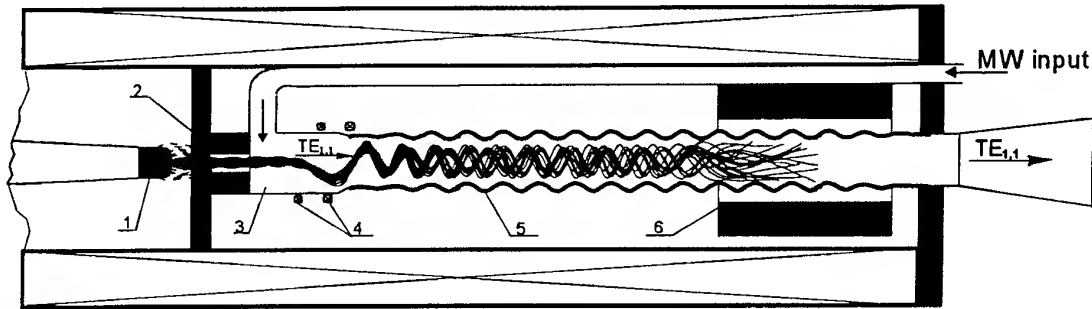


Fig.3. Schematic of a 300-kV second harmonic Ka-band helical gyro-TWT experiment: 1. Explosive-emission cathode. 2. Anode with a selecting aperture. 3. Wave launcher. 4. Kicker. 5. Helical waveguide. 6. Magnetic screen.

### Experiments

In order to significantly enhance the mode selection, a thin beam of electrons gyrating around the axis of the system is used. Such a beam can excite only co-rotating modes of a circular waveguide with the azimuthal index  $m$  equal to the cyclotron harmonic number  $s$ . In particular, we use the second-harmonic operation and the  $TE_{2,1}$  mode as a near-cutoff partial mode  $A$  which couples with the counter-rotating and forward/backward propagating  $TE_{1,1}$  mode (partial mode  $B$  in Fig.1) on the 3-fold helical corrugation. For frequencies below cutoff of the  $TE_{2,1}$  mode, the operating eigenwave  $W_1$  totally transforms at the end sections with a tapered amplitude of the corrugation into a  $TE_{1,1}$  mode of the smooth waveguide which simplifies input/output of RF power.

The first convincing results from the helical gyro-TWT were obtained in the X-band frequency range utilizing a 200 keV/ 25 A/ 100 ns electron beam (University of Strathclyde, Glasgow, UK). In the regime of single-frequency amplification, the gyro-TWT operating at the second cyclotron harmonic yielded the high output power of 1 MW, gain of 23 dB and efficiency of 20% [3].

A scheme for a Ka-band relativistic gyro-TWT/BWO experiment (IAP, Nizhny Novgorod, Russia) is shown in Fig.3. Using one helical waveguide we can switch between TWT and BWO modes of the operation by changing polarity of the axial magnetic field. First results for this configuration were obtained for the BWO mode when the wave launcher was closed by a cutoff insert reflecting the backward traveling wave to the output and allowing passage of the electron beam. A 350 keV/20 ns rectilinear electron beam was produced from a field-emission graphite cathode (Fig.3). The current of the beam passed through a selecting 1.5 mm-diameter anode aperture changed from 20 A to 50 A with variation of the axial magnetic field in the range 8-12 kG. A transverse velocity  $\beta_{\perp}=0.6$  was imparted to the electrons in a pulsed magnetic kicker. Because of the large change in the beam current an interaction length was optimized for

various magnetic fields (13 cm for 8-9.5 kG and 9 cm for 9.5-12 kG). The frequency was measured with a 1%-bandwidth filter.

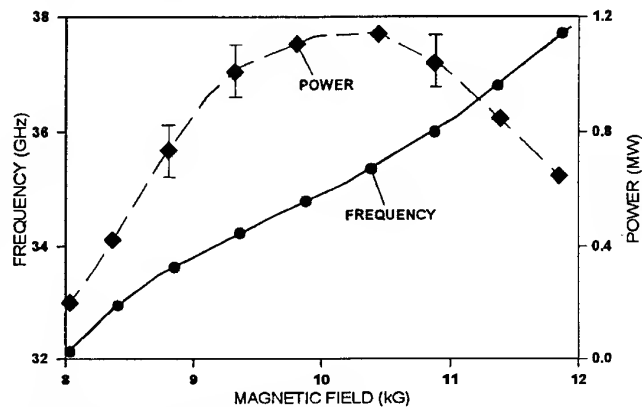


Fig.4. Results of an experiment on relativistic second harmonic helical gyro-BWO.

For the proper direction of the axial magnetic field the helical gyro-BWO oscillated at the second cyclotron harmonic with  $TE_{1,1}$  output mode. For a single-mode operation about 15% the magnetic tuning frequency range was measured (Fig.4). The measured maximum output power and efficiency amounted to 1.1 MW and 10%, respectively, which are close to the calculated values for a beam without velocity spread.

### References

1. G.G. Denisov, S.J. Cooke. New microwave system for gyro-TWT. The 21st Int. Conf. on IR and MM Waves. Berlin, 1996. Conf. Digest AT2.
2. G.G. Denisov, V.L. Bratman, A.D.R. Phelps, and S.V. Samsonov, Gyro-TWT with a helical operating waveguide: new possibilities to enhance efficiency and frequency bandwidth, IEEE Trans. on Plasma Sci., vol.26, (in press, being published June 1998).
3. V.L. Bratman, A.W. Cross, G.G. Denisov, W. He, A.D.R. Phelps, K. Ronald, S.V. Samsonov, C.G. Whyte, Experimental results from a helical waveguide gyro-TWT, (this Digest).

## Cold and Thermionic Cathode CARM Experiments

A.R. Young, W. He, K. Ronald, A.W. Cross, C.G. Whyte and A.D.R. Phelps

Department of Physics and Applied Physics,  
University of Strathclyde  
Glasgow, G4 0NG, Scotland, U.K.

### Introduction

Cyclotron Autoresonance Masers are effectively gyrotrons operating at a very high Doppler upshift so that the phase velocity of the interaction is close to the speed of light. This regime of operation offers certain advantages over the conventional gyrotron. The high Doppler upshift involved reduces the magnetic field requirement for any particular frequency and the phenomenon of autoresonance indicates the possibility for high efficiency as it reduces the problem of phase trapping. The dispersion relation of the beam is the same as that for a gyrotron, given by equation 1, which must be matched to a mode of a smooth cylindrical waveguide, given by equation 2.

$$\omega = s\omega_c + k_z v_z \quad [1]$$

$$\omega^2 = c^2(k_\perp^2 + k_z^2) \quad [2]$$

Where  $\omega$  is the angular frequency of the radiation,  $s$  is the harmonic number,  $\omega_c$  is the angular relativistic cyclotron frequency of the beam,  $k_z$  and  $k_\perp$  are the axial and transverse wavenumbers of the electromagnetic mode respectively and  $v_z$  and  $c$  are the axial velocity of the electron beam and the speed of light.

From equation 1 it is clear that for the regime of high Doppler upshifts as used for CARM experiments, spread in the parameter  $v_z$  will have a strong detrimental impact on the interaction, by comparison to the conventional gyrotron regimes where  $k_z \sim 0$ , yielding excellent tolerance to velocity spread. Nonetheless, the attractions of the CARM have encouraged researchers around the world, with many experiments being performed. Bratman et al (1995) [1] have demonstrated 26% efficiency at IAP Nizhny Novgorod, and Cooke et al (1996) [2] at the University of Strathclyde have demonstrated 2nd harmonic operation for the first time.

To realise the electron beam quality required for CARM operation, the practice of 'scraping' the electron beam has been applied in most experiments resulting in the real efficiency being somewhat less than the electronic efficiency. Recent cold cathode CARM experiments have been conducted where the entire electron beam formed in the accelerator was

used in the interaction. This was made possible by careful modelling of the electrode geometry using the 2.5D relativistic electron trajectory modelling software written at the University of Strathclyde. This cold cathode development was undertaken in preparation for thermionic cathode experiments using a similar accelerator geometry. Results of the 1st harmonic cold cathode experiments and the latest results from the thermionic cathode experiment will be reported.

### Experiments

The cold cathode experiments used a high current (~40A) high quality electron beam formed by space-charge-limited, explosive electron emission from a velvet cathode surface. Table 1 compares the parameters of the new 450kV diode with the 300kV one used previously in the 2nd harmonic CARM. As with all explosive cathode types, the duration of the beam is constrained by the expansion of the plasma formed at the cathode surface which changes both the impedance and geometry of the accelerator, and in these experiments the pulse duration was in the 100-200ns range. The cathode was driven by an 800kV, 15 stage Marx generator having an RC time of 3 $\mu$ s and a pulse terminating crowbar switch.

A 450kV electron beam was formed and passed through a 'kicker' magnet having the form of a single turn bifilar wiggler to produce a solid beam describing a spiral trajectory centred on the axis of the waveguide, as illustrated in figure 1. The electron beam pitch angle could be continuously tuned using the current flowing in the windings of the kicker magnet and this control was used to bring the electron beam into resonance with the  $TE_{1,1}$  mode of the waveguide at a frequency of 12.5GHz. The cavity was defined by a Bragg reflector at the output end of the waveguide which was designed and calibrated to provide selective feedback over the range of 12-15GHz.

The experiments used a rectifying crystal detector to measure the emitted microwave pulse shape and mode pattern. The mode pattern was consistent with the  $TE_{1,1}$  mode expected and the radiation frequency was confirmed using a cut-off filter.

Cathode	Original Pierce Cold	Modified Pierce Cold	Thermionic
Operating Voltage	300kV	450kV	500kV
Diode Current	60 A	40 A	30 A
Beam Current	60 A	40 A	30 A
Emission Current Density	44 $\rightarrow$ 82 A/cm <sup>2</sup>	23 $\rightarrow$ 30 A/cm <sup>2</sup>	2.3 $\rightarrow$ 2.7 A/cm <sup>2</sup>
Parallel Velocity / c	0.683 $\pm$ 0.026	0.8452 $\pm$ 0.0005	0.8618 $\pm$ 0.0003
Perpendicular Velocity / c	0.04 $\pm$ 0.02	0.039 $\pm$ 0.012	0.030 $\pm$ 0.009
Pulse Duration	100ns	100ns	>1 $\mu$ s

Table 1: Beam parameters for the three University of Strathclyde CARM diode configurations, 300kV cold cathode, 450kV cold cathode and 500kV thermionic

### Thermionic Cathode Progress

At this time, the thermionic cathode CARM experiment has been assembled (the cathode itself, built by EEV Ltd., is illustrated in figure 2) and has been vacuum tested. At the time of writing the cathode is being activated and will shortly be voltage conditioned. It is anticipated that the first results of operating this system will be presented at the conference. The parameters of the thermionic cathode based accelerator are also presented in table 1. It is anticipated that the improved reproducibility offered by the thermionic emission mechanism compared to the cold cathode explosive emission mechanism will help with the experiments investigating the nonlinear interaction mechanism itself.

### Acknowledgements

This research was sponsored by the EPSRC, EEV and the University of Strathclyde. D. Wilcox, I. Milsom and M. Carvey of EEV Ltd. and S.J. Cooke of Science Applications International Corporation are thanked for their ongoing advice and encouragement.

### References

1. Bratman V.L., Denisov G.G., Kolchugin B.D., Samsonov S.V. and Volkov A.B., Phys. Rev. Lett., **75**, 3102-3105, 1995
2. Cooke S.J., Cross A.W., He W. and Phelps A.D.R., Phys. Rev. Lett., **77**, 4836-4839, 1996

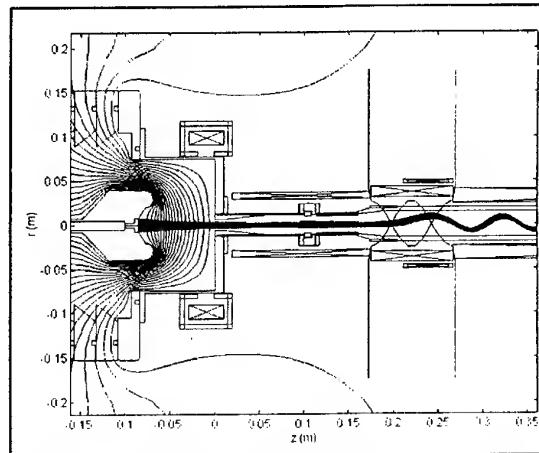


Figure 1: Modelled electron trajectories in the 450kV cold cathode diode showing the diode and magnet geometry

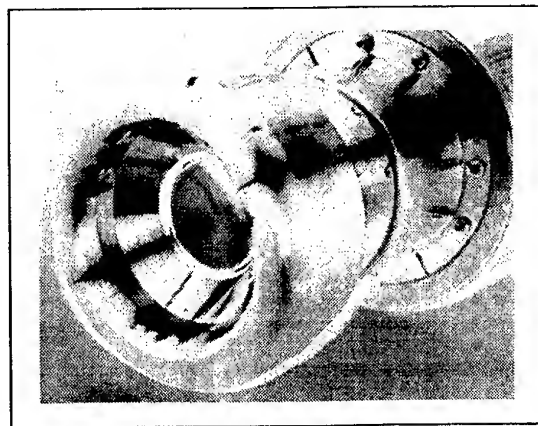


Figure 2: Photograph of the thermionic electron gun built by EEV and now installed at the University of Strathclyde

**Recent Developments of Scientific Instruments  
in the Millimeter Wave Division of ELVA-1 Ltd.**

D. Korneev

191025, Nevsky 74, 23H, St.Petersburg, Russia  
<http://www.nienschanz.ru/elva-1/>

A few instruments for scientific research like high temperature plasma diagnostics and EPR spectrometers are briefly described:

- \* 92-96 GHz Correlation Reflectometer for investigations of plasma turbulence.  
JET tokamak, UK
- \* 140 GHz Multichannel Interferometer for electron density measurements.  
TCABR tokamak, Brazil
- \* 130 GHz Multichannel Millimeter wave Scattering Diagnostics.  
H-1, Australian National University
- \* 90-140 GHz BWO Source for ECE Imaging Diagnostics.  
RTP tokamak, The Netherlands
- \* 95 GHz, 5 ns pulse EPR Spectrometer.  
Cornell University, USA

The main parameters of the instruments, and the principles of operation are presented, as well as technical approaches used in instrument design. New millimeter wave technologies which allow us to provide the specifications of the instruments are described.



**TEXTILE SEMICONDUCTORS - A NOVEL CLASS OF MM AND IR WAVE  
ABSORBING MATERIALS**

R. Brazis

Semiconductor Physics Institute, Gostauto 11, 2600 Vilnius, Lithuania  
e-mail: [brazis@uj.pfi.lt](mailto:brazis@uj.pfi.lt)

and

J.Koprowska

Textile Institute, Lodz, Poland

FIR and MM wave technology developments give rise to the necessity of suppressing a stray radiation which can affect detector systems or personnel. This work deals with a novel class of materials which are found to be non-reflecting and highly absorbing MM and IR waves. These are textile semiconductors obtained by chemical processing of polyacrylonitrile and other fibers. Experimental data on the material structure parameters and electromagnetic properties are to be presented.

## PUMPED PHONONS IN ATMOSPHERIC AEROSOLS.

Fröhlich illustrated the behaviour to be expected from isolated polar entities in biosystems when their phonon energy was increased above the value needed to maintain their Planckian equilibrium. In the contexts I shall discuss this will be called 'pumping'. Since phonons are bosons the relevant statistics are Bose-Einstein and Einstein Condensation comes to have something of the central role that the Exclusion Principle has for electrons. I describe Fröhlich's insights in this way to show that they are likely to be of much wider interest than they unquestionably have for atmospheric science.

Aerosols were a 'natural' in which to exploit pumped phonon phenomena and their contribution to understanding long standing problems in millimetre wave atmospheric behaviour has been recognised for perhaps ten years or so. What is however a recent development is to show that they become, when pumped, significant contributors to attenuation in the ten micron region despite their median radius being ten thousand times smaller than the wavelength. The atmosphere is naturally endowed with a splendid pumping source in the sun and this provides exciting new non linearities as well as exposing an array spectrum of the aerosols themselves. This can be used to measure their concentrations but also to dispose of, in a thoroughly satisfying way, so called 'continuum absorption' much used, and perhaps even loved, by those given to constructing models of atmospheric radiative transfer.

H.A.Gebbie,  
Dept. of Electronics, & Elec. Eng.  
Imperial College, London, SW7

## Problems in the relativistic theory of microwave plasma electronics

M V Kuzelev and A A Rukhadze

Moscow State University of Printing Art,  
ul. Pryanishnikova 2a, 127550 Moscow, Russia,

and

General Physics Institute, Russian Academy of Sciences,  
ul. Vavilova 38, 117942 Moscow, Russia.

A review of the theoretical studies on wide-band and high power microwave sources employing the stimulated Cherenkov radiation of REBs in a plasma waveguide is presented. The motivation for such studies lies in recent experiments on microwave plasma noise sources using intense REBs. Although only theoretical problems are discussed, all necessary estimates are obtained for actual General Physics Institute experiments. Comparison of theoretical and experimental results is given.

# Magnetic field dependence of THz radiation from InSb

Ping Gu, Masahiko Tani and Kiyomi Sakai

Kansai Advanced Research Center, CRL, Ministry of Posts and Telecommunications, Japan  
588-2 Iwaoka, Nishi-ku, Kobe 651-2401, Japan  
tel: +81-78-969-2198, fax: +81-78-969-2219, e-mail: guping@crl.go.jp

## Abstract

We report a strong magnetic field dependence of pulsed THz radiation from the (100) InSb surface irradiated with femtosecond laser pulses. The radiation power increased several times and the polarization also changed with the increase in the magnetic field. The mechanism of the magnetic field dependence of the THz radiation from semiconductor surfaces is discussed.

## 1. Introduction

Terahertz radiation from semiconductor surfaces can be strongly affected by a magnetic field. This was first reported by Zhang *et al.* [1] for (100) GaAs. Recently, THz radiation from InAs in strong magnetic fields was observed by Sarukura *et al.* [2]. The power was more than one orders of magnitude larger at the highest magnetic field (1.7 T) than that at zero magnetic field. However, there has been no clear experiment to identify the mechanism to increase the THz radiation power in the magnetic field. In this work we investigated the THz radiation from InSb surface in magnetic fields using a time-resolved detection system. InSb is expected to show a sensitive dependence of the THz emission on the magnetic field due to the extraordinary small effective electron mass and the very large electron mobility. It is suitable for the study of the influence of the magnetic field on the THz radiation from semiconductors. The time-domain waveforms of the horizontal and vertical radiation components were measured by changing the orientation of the photoconductive antenna detector. It was found that the total radiation power increased several times with the increase of the magnetic field from zero to 0.3 T. This indicates that the influence of the magnetic field on InSb is much stronger than on InAs or GaAs.

## 2. Experiment

The experimental setup for the detection of THz radiation from an InSb surface in a magnetic field (B) is shown in Fig. 1. The magnetic field (B) was applied in a direction parallel to the InSb sample surface as shown in Fig. 1. Thus, the orientation of the magnetic field is perpendicular to the surface electric field of the InSb sample. A mode-locked Ti:sapphire laser beam with 80 fs pulse width and 82 MHz repetition rate at 800 nm wavelength was split into two parts. The one part with an averaged power of 300 mW illuminated the InSb sample at an incident angle of 45° to generate THz radiation pulse.

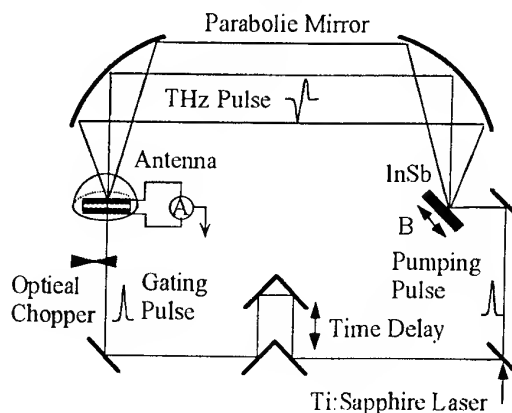


Fig.1. Experimental setup for the detection of THz radiation from a (100) InSb surface in a magnetic field.

The other part (7 mW) gated the photoconductive antenna detector. The THz radiation from the sample surface in the direction of the optical reflection was collected and focused on the detector with a pair of parabolic mirrors. The time-resolved waveforms of the radiation were obtained from the DC photocurrent in the antenna detector by varying the delay time between the pumping and gating pulses. The detector was a dipole antenna having a length of 30  $\mu\text{m}$  fabricated on low-temperature-grown GaAs. It was oriented either vertically or horizontally to detect vertical and horizontal components of THz radiation. The InSb sample was held at room temperature.

## 3. Results and Discussion

Figure 2 shows the temporal waveforms of the THz radiation for the horizontal (a) and vertical (b) polarization components from the InSb surface in the magnetic field. The amplitudes of the radiation are plotted in Fig. 3 against the magnetic field for the horizontal (●) and vertical (■) polarization components as well as the sum (▲) of the two components. The solid curves are fitting curves obtained by using the function

$$I(B) = a + bB^c \quad (1),$$

where  $a$  is the radiation amplitude at the magnetic field  $B = 0$ ,  $b$  and  $c$  are the constants expressing the magnetic field dependence of the radiation. In zero magnetic field, the radiation has a horizontal component only. The waveforms and amplitudes

remained almost the same at the magnetic field below 0.12 T for the horizontally polarized radiation. When the magnetic field was tuned above 0.12 T, the waveform became broad, and the radiation power increased with the magnetic field. However, when an external magnetic field as low as 0.05 T was applied to the sample, vertically polarized radiation was generated, and its radiation power depended quadratically on the external magnetic field. It is well known that the external magnetic field accelerates the moving carriers to the direction perpendicular to the magnetic field and also to the direction of the charge velocity due to the Lorentz force. This acceleration would change the direction of the moving carriers, and cause the carrier movement in vertical direction. This is the reason for the appearance of the vertical component in the external magnetic field. The acceleration of the moving

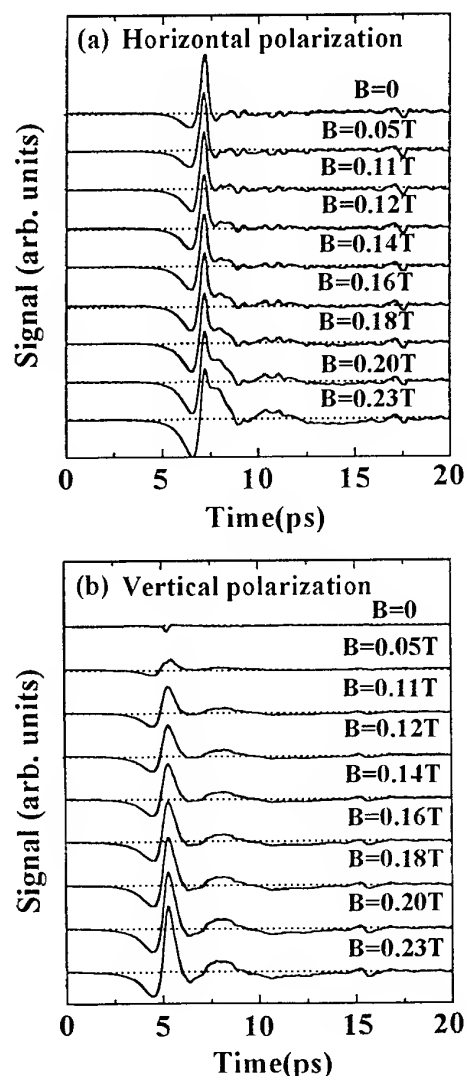


Fig. 2. The temporal waveforms of the horizontal (a) and vertical (b) components of the THz radiation from a InSb surface in an external magnetic field.

carriers given by an external magnetic field is inversely proportional to the carriers' effective mass ( $m_e^*$ ). The carriers' collision time ( $\tau = m_e^* \mu / e$ ) becomes longer with an increase in the carriers mobility. The electrons in InSb have a smaller effective mass and a higher mobility than those in InAs or GaAs. This means that the electrons in InSb are more easily modulated by an external magnetic field than in InAs or GaAs.

In magnetic field of  $B = 0.2$  T, the cyclotron frequency of the electrons in InSb is about 0.4 THz, and the electron collision time is 0.6 ps, which is almost the same as that of InAs. During this time, the electrons cannot move one circle (2.5 ps) at 0.2 T. This may not be enough to claim cyclotron radiation in the magnetic field as cause the change of the waveforms and the appearance of the slow radiation components as shown in Fig.2 (a) and (b). At a temperature below 77 K, the electron mobility in InSb increases by ten times compared to room temperature. This means that the electron collision time will increase by a factor of 10, and the electrons can move more than one circle before scattering. The measurement of the THz radiation from InSb in a high magnetic field (a few Tesla) and at low temperature ( $\sim 77$  K) will give more detailed information on the interaction of electrons and the magnetic field in InSb and the mechanism of the efficient THz radiation from semiconductors.

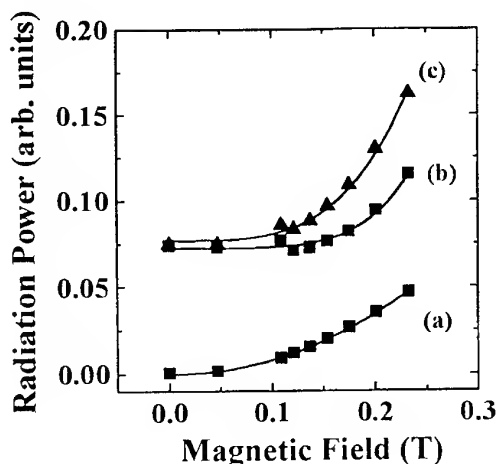


Fig. 3. Magnetic field dependence of the radiation amplitude for the horizontal (a) and vertical (b) components as well as the sum (c) of the two components.

## References

- [1] X.-C. Zhang et al., Appl. Phys. Lett. 62, 2003 (1993). X.-C. Zhang et al., Appl. Phys. Lett. 62, 2477 (1993).
- [2] N. Sarukura et al., CLEO'98, CTuB5.

## AUTHOR INDEX

<i>Author</i>	<i>Session</i>	<i>Page</i>	<i>Author</i>	<i>Session</i>	<i>Page</i>
Abe, H	Tu2.3	137	Blok, J H	M2.3	40
Abe, Y	W2.7	246	Boardman, A D	W3.6	262
Agapova, M V	M1.2	24	Bocquet, R	M6.6	110
	F1.8	375	Bogdashov, A A	F1.8	375
Aitken, P	M4.7	81	Bolbuch, T V	Th3.6	312
	Th4.7	327	Bongers, W A	M1.1	21
Alberti, S	Th1.2	271		Th1.5	278
Alikaev, V V	M1.2	24		Th5.9	346
Amca, R	P.16	421	Borchard, P	M1.6	32
Amerongen, F J van	Th1.5	278		F1.4	367
Anderton, R N	Th2.5	295	Borie, E	P.3	396
Andreev, E A	Th3.6	312	Borrill, J R	Th2.5	295
Annino, G	Th6.5	355	Botton, M	M4.5	77
Antakov, I I	Tu4.8	183	Bowen, J W	Tu5.3	189
	Th4.5	323		Th6.8	360
Antanavicius, R	Tu5.6	195	Bozzi, M	M2.6	46
Antonsen, T M	M4.5	77	Bozzi, R	Tu1.3	122
Antonsen Jr, T M	M1.6	32	Brand, G F	W2.5	242
Anuskevicius, R J	Tu5.6	195		W2.8	248
Appleby, R	Th2.5	295		Th4.3	319
Araujo, H	Tu6.1	203	Brandon, J R	W1.2	223
Arcioni, P	M2.6	46	Bratman, V L	M1.1	21
Arjona, M R	F1.5	369		Tu4.2	170
Arnold, A	Tu1.5	126		Th4.6	325
	Tu4.6	179		Th5.9	346
Aronzon, B	Tu6.2	206		P.29	446
Asadauskas, L	Tu6.2	206	Braz, O	Tu1.5	126
Atkins, A	Th6.3	352		Tu4.1	168
Avani, R N	Tu4.3	173		Tu4.6	179
Azarenkov, N A	W3.6	262		Th1.4	276
Bae, Jongsuck	M6.1	100	Brazis, R	Tu6.2	206
	F2.3	382		Th1.6	280
Bak, S W	Th1.3	274		P.32	451
Balkan, N	P.16	421	Brovenko, A	F2.6	388
Barker, R J	M4.2	71	Brower, D	Th2.1	284
Barnett, L R	M1.5	30	Brownell, J H	Th5.1	329
Barroso, J J	Tu4.5	177	Bruschi, A	Tu1.3	122
	P.1	392	Cahalan, P	F1.4	367
Baumgartner, M O	M6.5	108	Calame, J	M1.6	32
Belyantsev, A M	Tu2.4	139		M4.5	77
Benz, C	M2.1	34	Calame, J P	M1.4	28
Berceli, T	M4.6	79	Callis, R W	Th1.1	269
Bertolini, A	M6.4	106		F1.4	367
Bessonov, E	Th5.7	342	Caplan, M	M1.1	21
Bezant, C D	M3.3	58		Tu2.8	147
Birch, J R	Th3.5	311		Th5.9	346
	Th6.3	352	Carelli, G	M6.4	106
Blank, M	M1.3	26	Caroopen, S	Th6.2	350
	M1.6	32	Caryotakis, G	M4.3	74
	M4.5	77	Cassettari, M	Th6.5	355

## AUTHOR INDEX

<i>Author</i>	<i>Session</i>	<i>Page</i>	<i>Author</i>	<i>Session</i>	<i>Page</i>
Castillo, Mireya	W3.9	268	Davies, S R	Tu5.3	189
Castle, M	F1.3	365	Deksnys, A	M5.8	98
Cauffman, S	Tu1.2	119	Demchenko, M	P.22	432
	F1.4	367	Denison, D	F1.4	367
Chamberlain, J M	M3.3	58	Denison, D R	Tu1.2	119
	Tu5.2	186	Denisov, G G	M1.1	21
	Tu5.3	189		M1.2	24
Chang, T H	M1.5	30		Tu4.2	170
Chen, H Y	M1.5	30		W2.9	250
Chen, S H	M1.5	30		Th5.9	346
	P.21	430		F1.8	375
Cheng, J	F1.3	365		P.29	446
	F1.7	373	der Geer, C A J van	M1.1	21
Cheng, T S	M3.7	66		Th5.9	346
Chew, Khian-Hooi	W3.5	260	Derkach, V	F2.6	388
Chigryai, E E	W1.5	230	Diez, M C	M2.2	37
Chirkov, A	W2.9	250	Digby, J W	Tu5.2	186
Choi, J J	M1.4	28	Doane, J L	W1.1	220
	Th1.3	274		Th1.1	269
Christensen, D H	Th3.2	305	Dodge, C N	W1.2	223
	Th3.4	309	Doria, A	Th5.4	336
Chu, K R	M1.5	30	Dou, W B	Tu6.7	216
	P.21	430	Doucas, G	Th5.5	338
Chu, T S	M1.6	32	Dumelow, T	Tu3.5	159
	Tu1.2	119	Dutta, J M	Th6.7	359
	F1.4	367	Eden, D	Th2.8	301
Cirant, S	Tu1.3	122	Egorov, A	Tu2.2	135
Claassen, M	M2.7	48	Elagoz, S	P.16	421
Colgan, Ruth	Tu5.5	193	Empacher, L	W1.4	228
Collins, C E	Tu5.2	186	Ergun, Y	P.16	421
	Tu5.3	189	Erickson, N R	M5.2	86
Conciauro, G	M2.6	46	Evenson, K M	Tu2.7	145
Correa, R A	Tu4.5	177	Falcone, F	Tu5.7	197
	P.1	392	Farmer, K R	Tu5.4	191
Coward, P R	Th2.5	295	Farrar, C	Th6.6	357
Cronin, N J	Tu5.3	189	Feher, L	F2.1	377
Cross, A W	M4.7	81	Feiven, S A	Tu3.1	150
	Tu4.2	170	Felch, K	M1.6	32
	Th4.7	327		Tu1.2	119
	P.28	444		F1.4	367
	P.29	446	Fernandes, H C C	P.7	403
	P.30	448		P.11	411
Crowe, T W	M5.2	86	Fernandes, Humberto C C	Tu6.8	218
Dadoenkova, N N	Tu3.7	163	Filho, Geraldo F da Silveira	Tu6.8	218
Dammertz, G	Tu4.1	168	Fix, A Sh	M1.2	24
	Th1.4	276	Flyagin, V A	M1.2	24
Danly, B G	M1.3	26		F1.6	371
	M1.4	28	Foxon, C T	M3.7	66
	M1.6	32	Fredricksen, C J	M2.5	44
Darwish, A	M6.3	105	Freitas Jr, L C de	P.11	411

## AUTHOR INDEX

<i>Author</i>	<i>Session</i>	<i>Page</i>	<i>Author</i>	<i>Session</i>	<i>Page</i>
Freund, H P	Th5.8	344	Guz, S A	P.15	419
Freyer, J	M2.1	34	Ha, Hyun-Jun	Tu2.9	148
	M2.7	48	Hadjiloucas, S	Tu5.3	189
Fujii, T	F2.3	382		Th6.8	360
Fujii, Tetsu	M6.1	100	Hagiwara, M	Th6.2	350
Fujishima, H	M5.3	88	Han, W K	Th1.3	274
Fujita, Y	Th5.3	334	Hangyo, M	Tu2.1	132
	Th5.7	342	Hargreaves, T A	M1.6	32
Fujiwara, M	Tu6.4	210	Harper, B M	Th1.7	282
Fujiwara, Mikio	M2.4	42	Hartemann, F V	Th5.2	331
Fumeaux, C	M5.6	94	Hartfuss, Hans J	Th2.3	290
	Tu2.6	143	Hartnagel, H L	M2.6	46
Gachev, I G	Tu4.8	183		M5.1	83
	Th4.5	323		M5.4	90
Gallerano, G P	Th5.4	336	Hayakawa, A	Tu1.7	130
Gandini, F	Tu1.3	122	Hayashi, M	Tu3.4	157
Ganichev, S D	M3.5	62	He, Liquan	P.6	402
Gantenbein, G	Tu1.6	128	He, W	M4.7	81
	W1.4	228		Tu4.2	170
Garin, B M	W1.5	230		P.28	444
Garin, P	Th1.2	271		P.29	446
Garven, M	M1.4	28		P.30	448
Gaudreau, M	Tu4.4	175	Heidinger, R	W1.2	223
Gavrilov, S P	Th2.7	299		Th6.4	353
	P.14	417		F2.2	379
Gebbie, H A	P.33	452		F2.7	390
Geerk, J	F2.7	390	Heilweil, E J	Th3.1	303
Ghianni, F	M3.4	60	Helm, H	W2.6	244
	Tu6.3	208		W3.2	254
Giguët, E	Th1.2	271	Henini, M	M3.3	58
Ginzburg, N S	Th4.7	327	Heritage, J P	Th5.2	331
Giovenale, E	Th5.4	336	Herrmann, M	W2.3	238
Glibitskiy, G M	Th3.6	312	Herrmann, W H	M5.6	94
Gnedenkov, A Ph	M1.2	24		Tu2.6	143
Golubovic, D S	Tu2.5	141	Hesler, J L	M5.2	86
Gonzalo, R	Tu5.7	197	Hidehara, T	Th4.1	314
Good, G R	M1.6	32	Hirahara, T	W3.8	266
Goy, P	Th6.2	350	Hirano, A	W3.3	256
Granatstein, V	Tu4.4	175	Hirao, T	Tu6.4	210
Granatstein, V L	Th5.8	344	Hiromoto, N	Tu6.4	210
	F1.1	362	Hiromoto, Norihisa	M2.4	42
	F1.3	365	Ho, C H	Th5.2	331
	F1.7	373	Hochmuth, H	F2.7	390
Granucci, G	Tu1.3	122	Hofbeck, K	Tu2.2	135
Grenzer, J	Tu2.2	135	Hogan, B	F1.3	365
Griffin, R G	Th6.6	357		F1.7	373
Gross, M	Th6.2	350	Hogge, J P	Th4.4	321
Gu, Ping	P.35	454	Hollman, F	W1.4	228
Guo, H	F1.1	362	Hong, Wei	P.6	402
Guyomarc'h, D	Th4.4	321	Hosako, Iwao	M2.4	42



## AUTHOR INDEX

<i>Author</i>	<i>Session</i>	<i>Page</i>	<i>Author</i>	<i>Session</i>	<i>Page</i>
Hovenier, J N	M2.2	37	Kalynov, Yu K	Th4.6	325
	M2.3	40	Kanai, Y	Tu1.7	130
Huang, Guo-qin	P.8	405	Kanno, R	W3.3	256
Hubers, H W	M5.5	92	Karatzas, L S	Tu5.3	189
	Th6.1	348		Th6.8	360
Hung, C L	M1.5	30	Kasai, Y	M5.7	96
Hwang, S M	Th1.3	274	Kasperek, W	Tu1.6	128
Iatrou, C T	Tu4.1	168		W1.4	228
Idehara, T	P.4	398		W2.9	250
Iguchi, M	Th4.2	317		P.9	407
Ikeda, K Takahashi Y	F1.2	363	Kasugai, A	F1.2	363
Ikeuchi, Y	W3.3	256	Katsumata, K	Th6.2	350
Ikezawa, M	Th2.6	297	Kawashima, S	Tu1.7	130
	Th5.3	334	Keiding, S R	W3.2	254
Ikezi, H	W1.1	220	Ketterl, H	M3.5	62
	Th1.1	269	Kharyanen, V N	Th3.6	312
Illy, S	P.3	396	Khorunzhiy, M O	P.26	440
Ilyin, V I	M1.2	24	Kikuchi, H	Tu3.4	157
Imai, T	F1.2	363	Kimmitt, M F	Th5.1	329
Inoue, Y	Th5.7	342		Th5.5	338
Iola, N	M6.4	106	King, P	Th2.1	284
Irimajiri, Y	M5.7	96	Kiseliov, V K	Tu5.9	201
Ishe, K	Th2.6	297	Klaassen, T O	M2.2	37
Ishi, K	Th5.3	334		M2.3	40
	Th5.7	342		M3.4	60
Ishibashi, Y	W3.1	252		Tu6.3	208
Ito, M	F2.3	382	Kneubuhl, F K	M5.6	94
Ivanchenko, I	P.22	432		M6.5	108
	P.23	434		Tu2.6	143
Ivanov, D V P	Tu5.4	191	Kobayashi, H	W2.7	246
Ives, R L	Tu2.8	147	Kobayashi, K	Th5.3	334
	Tu4.4	175		Th5.7	342
	W1.3	226	Koniger, F	Th6.4	353
Jackson, R H	Th5.8	344	Konov, V	W1.6	232
	P.24	436	Konov, V I	W1.5	230
James, B G	M1.6	32	Kop'ev, P S	Tu2.2	135
Jaroszynski, D	F2.5	386	Kopnin, A N	W1.5	230
Jaroszynski, D A	Th4.7	327	Koppenburg, K	Tu1.4	124
	P.28	444		Th1.4	276
Jepsen, P Uhd	W2.6	244	Koprowska, J	P.32	451
Jha, A R	P.5	400	Komeev, D	P.31	450
Jiancong, Luo	M6.8	114	Komeynkov, V	P.22	432
Jiang, Yong	Th2.1	284	Korschinek, G	Th5.5	338
Jiayin, Qin	M6.8	114	Koschurinov, Yu	Tu2.2	135
Jin, P	W3.8	266	Kostov, K G	Tu4.5	177
Jones, C R	Th6.7	359		P.1	392
Jong, L de	Th1.5	278	Kostyna, A N	F1.8	375
Jory, H	M1.6	32	Kovalev, D Yu	Tu6.2	206
	F1.4	367	Kovsch, A	Tu2.2	135
Jung, Soon-Shin	Tu2.9	148	Kozyrev, A B	Tu2.4	139

## AUTHOR INDEX

<i>Author</i>	<i>Session</i>	<i>Page</i>	<i>Author</i>	<i>Session</i>	<i>Page</i>
Kramer, G F IJ	Th5.9	346	Lyubchanskii, M I	Tu3.7	163
Kreischer, K E	Tu4.3	173	Machusky, E A	M6.2	103
	Th6.6	357	Machusky, E A	P.13	415
Krivosheev, P V	P.20	428	Makowski, M	Pl.5	17
Kruijt, O G	Th1.5	278	Makowski, M A	Th1.5	278
Kruisbergen, R	Th1.5	278	Manabe, T	M5.7	96
Kubo, S	Tu1.7	130	Manintveld, P	M1.1	21
Kuftin, A N	M1.2	24		Th5.9	346
	Tu4.7	181	Mann, C M	M5.3	88
	P.19	426		Pl.4	13
Kuftin, N	F1.6	371	Mantovani, S	Tu1.3	122
Kulagin, O P	P.25	438	Manuilov, V N	Th4.6	325
Kunkel, H	Tu1.5	126		P.20	428
Kunkel, H R	Tu4.6	179	Marchetti, S	M6.4	106
Kuntze, M	Tu4.1	168	Margules, L	M6.6	110
	Th1.4	276	Markelz, A G	Th3.1	303
Kuzelev, M V	P.34	453	Martin, D H	Th3.5	311
Lalanne, P	Tu5.4	191	Martinelli, M	Th6.5	355
Landahl, E C	Th5.2	331	Martinez, B	Tu5.7	197
Langerak, C J	M3.3	58	Masuko, H	M5.7	96
Lanigan, William	Tu5.5	193	Matavulj, P S	Tu2.5	141
Laurinavicius, A	M5.8	98	Matsushima, F	Th3.3	307
Lawson, W	F1.3	365	Matsuyama, T	Th5.3	334
	F1.5	369		Th5.7	342
	F1.7	373	McKinley, M	Th2.8	301
Lawson, W G	M1.6	32	McNeil, B W J	M4.7	81
Lengfellner, H	Tu6.6	214		Th4.7	327
Leotin, J	Tu6.2	206	Mellera, V	Tu1.3	122
Lesurf, J C G	Th2.4	293	Meola, R	M2.7	48
Letardi, S	Th5.4	336	Messina, G	Th5.4	336
Levush, B	M1.3	26	Michel, G	Tu4.1	168
	M1.6	32		W2.2	236
	M4.5	77	Miles, R E	Tu5.2	186
Lim, Siew-Choo	Tu3.2	153		Tu5.3	189
	Tu3.6	161	Minamide, H	F2.3	382
Lima, R L M	P.7	403	MirJalili, G	M3.6	64
Lin, C I	M5.1	83		M3.7	66
	M5.4	90	Mitsudo, S	Th4.1	314
Link, G	F2.1	377		P.4	398
Lipphardt, B	Tu2.6	143	Mitsunaka, Y	F1.2	363
Lohr, J	Th1.1	269	Mizuhara, M	Tu4.4	175
Longo, I	Th6.5	355		W1.3	226
Lopetegi, T	Tu5.7	197		F1.4	367
Lorenz, M	F2.7	390	Mizuno, K	M5.3	88
Luhmann Jr, N C	M4.3	74		F2.3	382
	Th5.2	331		Pl.1	1
Lygin, V K	Tu4.7	181	Mizuno, Koji	M6.1	100
	Tu4.8	183	Mobius, A	Tu1.5	126
	P.20	428		Tu4.1	168
Lyubchanskii, I L	Tu3.7	163	Moeller, C	W1.1	220

## AUTHOR INDEX

<i>Author</i>	<i>Session</i>	<i>Page</i>	<i>Author</i>	<i>Session</i>	<i>Page</i>
Moeller, C P	Tu1.1	116	Ohgawara, T	Tu1.7	130
	Th1.1	269	Ohkuba, K	Tu1.7	130
Moeller, K D	Tu5.4	191	Ohkubo, Y	W2.7	246
Mogi, I	Tu3.4	157	Ohta, H	Tu3.3	155
Moiseev, M A	Tu4.8	183		Tu3.4	157
	F1.6	371		W3.3	256
Montvai, A	Th5.9	346	Okubo, S	Tu3.3	155
Moreau, Ph	Th1.6	280		Tu3.4	157
Moretti, A	M6.4	106		W3.3	256
Motokawa, M	Tu3.3	155	Ono, S	W3.3	256
	Tu3.4	157		Th5.7	342
Mottonen, V S	M5.4	90	Ortenberg, M von	M3.2	55
Muravjov, A V	M2.2	37	Osman, Junaidah	Tu3.2	153
	M2.3	40		Tu3.6	161
	M2.5	44		W3.1	252
Murphy, J Anthony	Tu5.5	193	Ostrikov, K N	W3.6	262
Murphy, K St J	Th2.5	295	Pain, M	Th1.2	271
Muzzini, V	Tu1.3	122	Parini, C G	W2.1	234
Myasnikov, V E	M1.2	24	Park, D M	Th1.3	274
Myasnoikov, V E	F1.8	375	Park, Gun-Sik	Tu2.9	148
Nagasawa, H	Tu3.4	157		P.10	409
Nakagawa, T	Tu6.4	210	Parker, T J	M3.6	64
Nakao, S	W3.8	266		M3.7	66
Nakashima, S	Tu2.3	137		Tu3.1	150
Nanba, T	W3.3	256		W3.4	258
Nardone, A	Tu1.3	122	Parkhomenko, M P	W1.5	230
Natarajan, V	W2.4	240	Parkurst, G M	Tu5.2	186
Neugebauer, F	M2.7	48	Parshin, V	W1.6	232
Nguyen, K	M1.6	32		P.12	413
	M4.5	77	Pavel'ev, D G	Tu2.2	135
Nguyen, K T	M1.4	28	Pavlov, S G	M2.2	37
Nielsen, O Fauriskov	Th3.2	305		M2.3	40
	Th3.4	309		M2.5	44
Nishihara, J	Th4.2	317	Peale, R E	M2.5	44
Noguchi, T	M5.7	96	Pedrozzi, M	Tu4.3	173
Nojiri, H	Tu3.3	155	Peebles, W A	Th2.1	284
	Tu3.4	157	Pendleton, R	W1.3	226
Novozhilova, N Yu	Th4.7	327	Perel, V I	M3.5	62
Nozokido, T	F2.3	382	Pereyaslavets, M	Th4.1	314
Nusinovich, G	F1.1	362		P.4	398
Nusinovich, G S	M4.1	70	Pergande, A	Th2.8	301
	M4.4	76	Perov, P	Th3.4	309
	P.18	425	Perova, T S	Th3.2	305
Obiya, Y	Tu1.7	130		Th3.4	309
Ochiai, S	M5.7	96	Perregrini, L	M2.6	46
Odarenko, E	P.17	423	Pershin, M A	M6.2	103
Odashima, H	Tu2.7	145	Pershing, D	M1.6	32
	Th3.3	307	Pershing, D E	Th5.8	344
Ogawa, I	Th4.1	314	Peskov, N Yu	Th4.7	327
	P.4	398	Petillo, J	M1.6	32

## AUTHOR INDEX

<i>Author</i>	<i>Session</i>	<i>Page</i>	<i>Author</i>	<i>Session</i>	<i>Page</i>
Phelps, A D R	M4.7	81	Robb, G R M	M4.7	81
	Tu4.2	170		Th4.7	327
	Th4.7	327	Roberts, M J	Th2.5	295
	P.28	444	Robertson, D A	Th2.4	293
	P.29	446	Rodgers, J	F1.1	362
	P.30	448	Rodriguez-Girones, M	M5.1	83
Pidgeon, C R	M3.1	52	Ronald, K	M4.7	81
Piironen, P V	M5.4	90		Tu4.2	170
Piosczyk, B	Tu1.4	124		Th4.7	327
	Tu4.1	168		P.28	444
	Th1.4	276		P.29	446
	P.2	394		P.30	448
Plaum, B	Tu1.6	128	Ronsivalle, C	Th5.4	336
Plomp, J	M1.1	21	Roser, H P	M5.5	92
	Th5.9	346		Th6.1	348
Poelman, A J	M1.1	21	Rothuizen, H	M5.6	94
	Th5.9	346		Tu2.6	143
Pojedinchuk, A	F2.6	388	Rukhadze, A A	P.34	453
Pollard, R D	Tu5.2	186	Rylkov, V	Tu6.2	206
	Tu5.3	189	Sage, G P Le	Th5.2	331
Ponce, D	Th1.1	269	Saito, F	Tu1.7	130
Popenko, N	Tu3.8	165	Saitoh, K	W3.8	266
Popov, L G	F1.8	375	Sakai, K	Tu2.1	132
Postnikova, A S	Tu4.7	181		Tu2.3	137
Poulter, G	Th6.3	352		W2.3	238
Poymanov, V D	Tu3.7	163		P.35	454
Prettl, W	M3.5	62	Sakamoto, K	F1.2	363
Pribyl, P	Th2.1	284	Salmon, N A	Th2.5	295
Price, S	Th2.5	295	Samsonov, S V	Tu4.2	170
Prins, P R	Th1.5	278		Th4.6	325
Puhlmann, N	M3.2	55		P.29	446
Qun, Wu	P.10	409	Saraph, G	F1.4	367
Radunovic, J B	Tu2.5	141	Sari, H	P.16	421
Raguotis, R	Th1.6	280	Sasaki, S	Tu1.7	130
Raisanen, A V	M5.4	90		Th5.7	342
Ralchenko, V	W1.6	232	Sato, N	Th4.2	317
Ralchenko, V G	W1.5	230	Savilov, A V	M1.1	21
Rasmussen, U	Th3.2	305	Savolov, A V	Th5.9	346
	Th3.4	309	Schall, M	W3.2	254
Ratzel, F	F2.7	390	Schikora, D	M3.2	55
Raum, M	M6.7	112	Schmat'ko, A	P.17	423
Rayner, M R	W2.1	234	Schomburg, E	Tu2.2	135
Reiser, M	F1.3	365	Schouten, R N	M2.3	40
Reiter, Gy	M4.6	79	Schumacher, R	Tu4.4	175
Remsen, D	F1.4	367		W1.3	226
Renk, K F	Tu2.2	135	Schunemann, K	M2.8	50
Repsas, K	M5.8	98	Schwab, R	Th6.4	353
Rhee, S	F2.1	377		F2.2	379
Rieckmann, C	W2.1	234		F2.7	390
Rietveld, J A	Th5.9	346	Sealy, P J	W2.4	240

## AUTHOR INDEX

<i>Author</i>	<i>Session</i>	<i>Page</i>	<i>Author</i>	<i>Session</i>	<i>Page</i>
Sergeev, A S	Th4.7	327	Sussmann, R S	W1.2	223
Seta, M	M5.7	96	Sutha, S	Th2.8	301
Shaaan, M	M2.6	46	Suzuki, T	M5.3	88
Shahabadi, M	M2.8	50	Sviridov, M V	P.15	419
Shapiro, M A	Tu1.2	119	Swartz, J C	Th5.1	329
Shastin, V N	M2.2	37	Taccetti, J M	Th5.8	344
	M2.3	40	Takagi, K	Th3.3	307
	M2.5	44	Takahashi, H	W2.3	238
Shayesteh, S Farjami	M3.6	64	Takahashi, M Ikezawa T	Th5.7	342
	M3.7	66	Takahashi, T	Th5.3	334
Shenggang, Liu	M4.2	71	Tan, X Q	Tu6.7	216
Shi, S C	M5.7	96	Tanaka, H	Tu3.3	155
Shibai, H	Tu6.4	210	Tanemura, S	W3.7	264
Shibata, Y	Th5.3	334	Tani, M	Tu2.1	132
	Th5.7	342		Tu2.3	137
Shibata, Yu	Th2.6	297		W2.3	238
Shpak, V G	Th4.7	327		P.35	454
Shunailov, S A	Th4.7	327	Tarkhanyan, Roland H	Tu3.9	167
Siegrist, M	Th4.4	321	Tazawa, M	W3.7	264
Siegrist, M R	Th1.6	280		W3.8	266
Silva, S A P	P.11	411	Temkin, R	Th6.6	357
Simon, A	M5.1	83	Temkin, R J	Tu1.2	119
	M5.4	90		Tu4.3	173
Simonetto, A	Tu1.3	122		F1.4	367
Sinclair, G N	Th2.5	295	Theiss, A J	M1.6	32
Singh, A	Tu4.4	175	Thompson, T	M6.3	105
Smeets, P H M	M1.1	21	Thouvenin, Ph	Th1.2	271
	Th5.9	346	Thumm, M	Tu1.4	124
Smith, Graham	Tu5.1	184		Tu1.5	126
Smith, S R P	Tu3.1	150		Tu1.6	128
	W3.4	258		Tu4.1	168
Sokmen, I	P.16	421		Tu4.6	179
Sokolov, E V	Tu4.8	183		W1.2	223
	Th4.5	323		W2.2	236
Song, L	M4.3	74		Th1.2	271
Sorolla, M	Tu5.7	197		Th1.4	276
Sozzi, C	Tu1.3	122		F2.1	377
Spinicchia, N	Tu1.3	122		P.9	407
Sporl, R	W1.2	223	Tilley, D R	Tu3.1	150
	F2.2	379		Tu3.2	153
Stamps, R L	W3.5	260		Tu3.6	161
Steenbrink, F W H J	Tu6.3	208		W3.1	252
Stepanuyk, V N	Th2.7	299		W3.5	260
Sterk, A B	Th5.9	346	Tonouchi, M T	Tu2.1	132
Sternberg, O	Tu5.4	191	Towlson, B M	Tu5.3	189
Stewart, K P	Tu5.4	191	Tran, C	Th1.2	271
Stolpe, I	M3.2	55	Tran, M Q	Th1.2	271
Strijbos, R C	M2.5	44	Tretyakov, M Yu	M6.6	110
Strumia, F	M6.4	106	Trimble, W	M2.5	44
Sun, Z L	Tu6.7	216	True, R B	M1.6	32

## AUTHOR INDEX

<i>Author</i>	<i>Session</i>	<i>Page</i>	<i>Author</i>	<i>Session</i>	<i>Page</i>
Tsuchida, T	P.4	398	Weinzierl, J	M2.6	46
Tsunekawa, S	M5.3	88	Weiss, C O	Tu2.6	143
Tsuneoka, M	F1.2	363	Wenckebach, W Th	M2.2	37
Tsuyoshi, T	F1.2	363		M2.3	40
Tupulov, A	Tu2.8	147		M3.4	60
Ui, M	P.4	398		Tu6.3	208
Umaskulov, M R	Th4.7	327	Whyte, C G	M4.7	81
Urbanus, W H	M1.1	21		Tu4.2	170
	Th5.9	346		P.28	444
Usachev, S V	M1.2	24		P.29	446
Ustinov, V	Tu2.2	135		P.30	448
Vaicikauskas, V	M3.8	68	Wiggins, S M	Th4.7	327
	Tu5.6	195	Williams, A	M6.3	105
Vaskevicius, R A	M5.8	98	Withers, S H	M2.5	44
Vayakis, G	Th2.2	287	Withington, Stafford	Tu5.5	193
Vengalis, B	M5.8	98	Woldberg, E	Th1.5	278
Verhoeven, A G A	M1.1	21	Wood, F	M1.4	28
	Th1.5	278	Wood, K	Tu6.1	203
	Th5.9	346	Wootton, S T G	Tu5.3	189
Vernon, R J	W2.4	240	Wylde, Richard	Tu5.1	184
	Th1.7	282	Wynne, K	F2.5	386
Vertij, A	F2.6	388		Pl.3	9
Vertiy, A A	Th2.7	299	Xizhang, Luo	M6.8	114
	P.14	417	Xu, X	F1.3	365
Veszely, Gy	M4.6	79		F1.7	373
Vij, J K	Th3.2	305	Yalandin, M I	Th4.7	327
	Th3.4	309	Yamada, T	Tu3.3	155
Vinogradov, E A	F2.4	385	Yamaguchi, H	Th6.2	350
Vlasov, S N	Th4.5	323	Yamamoto, K	Tu1.7	130
Vlieks, A	M4.3	74	Yamazaki, H	Th6.2	350
Voinovskiy, I V	Th2.7	299	Yan, Hong-hui	Tu5.8	199
von Ortenberg, M	Pl.2	5		P.8	405
Vorobjev, L E	M3.6	64	Yang, Hong-sheng	Tu5.8	199
Wagner, D	Tu1.6	128		P.8	405
	W2.9	250	Yang, J G	Th1.3	274
	P.9	407	Yang, T T	M1.5	30
Wakabayashi, K	Tu1.7	130	Yassievich, I N	M3.5	62
Walner, C	Th5.5	338	Yasui, T	M5.3	88
Walsh, J E	Th5.1	329	Yasuoka, Y	W2.7	246
	Th5.5	338	Yasuoka, Yoshizumi	Tu6.5	212
Walter, M	M4.1	70	Yeremka, V D	P.26	440
	F1.1	362		P.27	442
Wang, Jing-Ju	Tu3.6	161	Yin, H	M4.7	81
Wang, Xuan-Zhang	Tu3.6	161	Ymada, T	Tu3.4	157
Wang, Z G	Tu6.7	216	Yokoo, K	Th4.2	317
Wasley, M R M	Th2.5	295		Th5.6	340
Watanabe, K	Tu3.4	157	Young, A R	P.30	448
Watari, T	Tu1.7	130	Yu, M Y	W3.6	262
Weatherwax, E	Th2.8	301	Zahner, Th	Tu6.6	214
Webb, J F	W3.1	252	Zapevalov, V E	M1.2	24

## AUTHOR INDEX

<i>Author</i>	<i>Session</i>	<i>Page</i>
	Tu4.7	181
	F1.6	371
	P.19	426
Zasytkin, E V	Tu4.8	183
	Th4.5	323
Zavolsky, N A	F1.6	371
Zeng, Lei	Th2.1	284
Zepevalov, V E	F1.8	375
Zhang, J	M5.4	90
Zhao, J	M4.1	70
	M4.4	76
	F1.1	362
	P.18	425
Zhou, Xue-Fei	Tu3.6	161
Zhu, Chendong	P.6	402
Zhukov, A	Tu2.2	135
Ziemann, E	M3.5	62
Zink, L R	Tu2.7	145
Zolm, H	W1.4	228
Zotova, I V	Th4.7	327